frontiers | Research Topics

Novel biomarkers in tumor immunity and immunotherapy

Edited by
Takaji Matsutani, Esra Akbay and Eyad Elkord

Published in
Frontiers in Immunology
Frontiers in Oncology

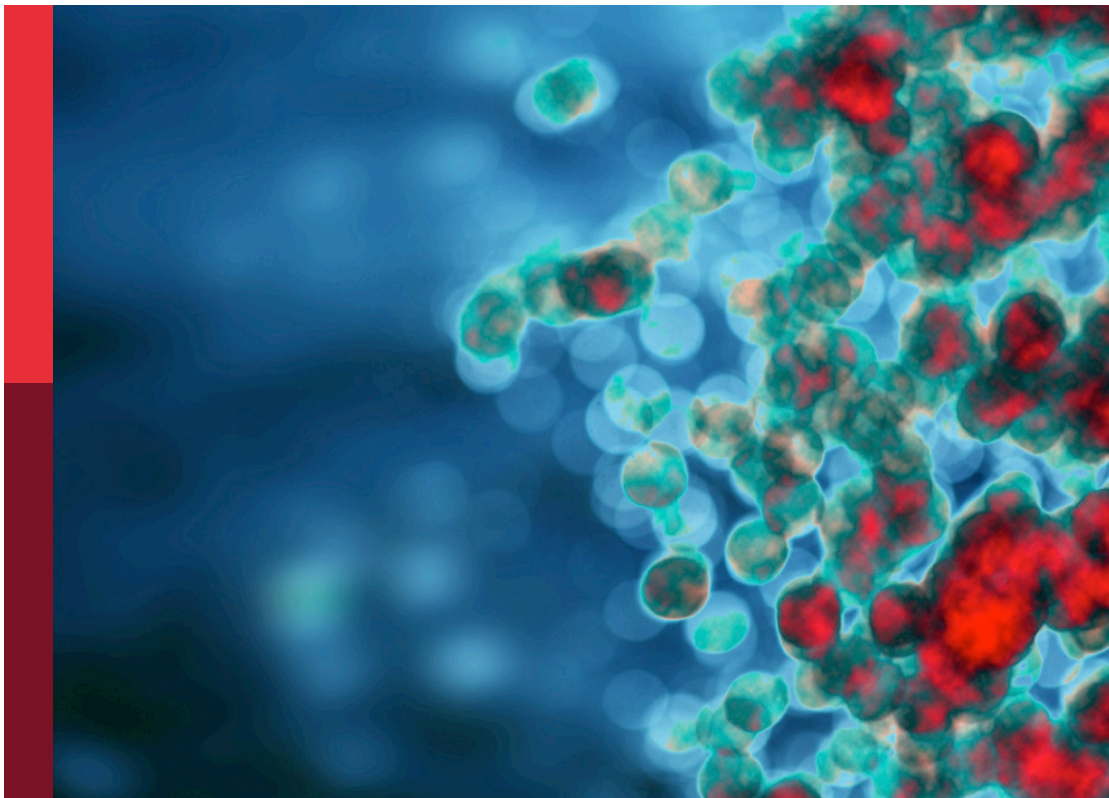

ISSN 1664-8714
ISBN 978-2-8325-4837-0
DOI 10.3389/978-2-8325-4837-0

About Frontiers

Frontiers is more than just an open access publisher of scholarly articles: it is a pioneering approach to the world of academia, radically improving the way scholarly research is managed. The grand vision of Frontiers is a world where all people have an equal opportunity to seek, share and generate knowledge. Frontiers provides immediate and permanent online open access to all its publications, but this alone is not enough to realize our grand goals.

Frontiers journal series

The Frontiers journal series is a multi-tier and interdisciplinary set of open-access, online journals, promising a paradigm shift from the current review, selection and dissemination processes in academic publishing. All Frontiers journals are driven by researchers for researchers; therefore, they constitute a service to the scholarly community. At the same time, the *Frontiers journal series* operates on a revolutionary invention, the tiered publishing system, initially addressing specific communities of scholars, and gradually climbing up to broader public understanding, thus serving the interests of the lay society, too.

Dedication to quality

Each Frontiers article is a landmark of the highest quality, thanks to genuinely collaborative interactions between authors and review editors, who include some of the world's best academicians. Research must be certified by peers before entering a stream of knowledge that may eventually reach the public - and shape society; therefore, Frontiers only applies the most rigorous and unbiased reviews. Frontiers revolutionizes research publishing by freely delivering the most outstanding research, evaluated with no bias from both the academic and social point of view. By applying the most advanced information technologies, Frontiers is catapulting scholarly publishing into a new generation.

What are Frontiers Research Topics?

Frontiers Research Topics are very popular trademarks of the *Frontiers journals series*: they are collections of at least ten articles, all centered on a particular subject. With their unique mix of varied contributions from Original Research to Review Articles, Frontiers Research Topics unify the most influential researchers, the latest key findings and historical advances in a hot research area.

Find out more on how to host your own Frontiers Research Topic or contribute to one as an author by contacting the Frontiers editorial office: frontiersin.org/about/contact

Novel biomarkers in tumor immunity and immunotherapy

This ebook is split into several files; this is part two of the ebook, please see the overview text of the Research Topic page to access the first part of the ebook.

Topic editors

Takaji Matsutani — Maruho, Japan

Esra Akbay — University of Texas Southwestern Medical Center, United States

Eyad Elkord — University of Salford, United Kingdom

Citation

Matsutani, T., Akbay, E., Elkord, E., eds. (2024). *Novel biomarkers in tumor immunity and immunotherapy*. Lausanne: Frontiers Media SA.

doi: 10.3389/978-2-8325-4837-0

Table of contents

frontiers | Frontiers in Immunology

TYPE Original Research
PUBLISHED 18 August 2023
DOI 10.3389/fimmu.2023.1207061

OPEN ACCESS

EDITED BY
Takaji Matsutani,
Repertoire Genesis, Inc., Japan

REVIEWED BY
Yinhao Chen,
Nantong University, China
Longchao Liu,
Chinese Academy of Sciences (CAS), China

*CORRESPONDENCE
Qingyi Zhu
zhuqy1971@126.com
Jian Yang
yangjian@njmu.edu.cn
Luming Sheng
shenluming2008@163.com

†These authors have contributed equally to this work

RECEIVED 17 April 2023
ACCEPTED 04 July 2023
PUBLISHED 18 August 2023

CITATION
Jiang S, Dong Y, Wang J, Zhang X, Liu W, Wei Y, Zhou H, Shen L, Yang J and Zhu Q (2023) Identification of immunogenic cell death-related signature on prognosis and immunotherapy in kidney renal clear cell carcinoma.
Front. Immunol. 14:1207061.
doi: 10.3389/fimmu.2023.1207061

Identification of immunogenic cell death-related signature on prognosis and immunotherapy in kidney renal clear cell carcinoma

Silin Jiang[1†], Yuxiang Dong[1†], Jun Wang[2†], Xi Zhang[3†], Wei Liu[1], Yong Wei[1], Hai Zhou[1], Luming Shen[1*], Jian Yang[1*] and Qingyi Zhu[1*]

[1]Department of Urology, The Second Affiliated Hospital of Nanjing Medical University, Nanjing, China, [2]Department of Urology, Nanjing University of Chinese Medicine, Nanjing, China, [3]The State Key Lab of Reproductive; Department of Urology, The First Affiliated Hospital of Nanjing Medical University, Nanjing, China

Background: Immunogenic cell death (ICD) is considered a particular cell death modality of regulated cell death (RCD) and plays a significant role in various cancers. The connection between kidney renal clear cell carcinoma (KIRC) and ICD remains to be thoroughly explored.

Methods: We conducted a variety of bioinformatics analyses using R software, including cluster analysis, prognostic analysis, enrichment analysis and immune infiltration analysis. In addition, we performed Quantitative Real-time PCR to evaluate RNA levels of specific ICD genes. The proliferation was measured through Cell Counting Kit-8 (CCK-8) assay and colony-formation assay in RCC cell lines.

Results: We determined two ICD subtypes through consensus clustering analysis. The two subtypes showed significantly different clinical outcomes, genomic alterations and tumor immune microenvironment. Moreover, we constructed the ICD prognostic signature based on TF, FOXP3, LY96, SLC7A11, HSP90AA1, UCN, IFNB1 and TLR3 and calculated the risk score for each patient. Kaplan-Meier survival analysis and ROC curve demonstrated that patients in the high-risk group had significantly poorer prognosis compared with the low-risk group. We then validated the signature through external cohort and further evaluated the relation between the signature and clinical features, tumor immune microenvironment and immunotherapy response. Given its critical role in ICD, we conducted further analysis on LY96. Our results indicated that downregulation of LY96 inhibited the proliferation ability of RCC cells.

Conclusions: Our research revealed the underlying function of ICD in KIRC and screened out a potential biomarker, which provided a novel insight into individualized immunotherapy in KIRC.

KEYWORDS

immunogenic cell death, kidney renal clear cell carcinoma, tumor immune microenvironment, prognostic signature, immunotherapy

Introduction

Renal cancer is one of the most common malignant tumors around the world (1). Renal cell carcinoma (RCC) accounts for 90% of renal cancer and kidney renal clear cell carcinoma (KIRC) accounts for the majority of RCC (2). Although surgical operation brings a good prognosis to early-stage KIRC patients (3), advanced and metastatic KIRC still have poor clinical prognosis and outcome due to their insensitivity to radiotherapy or chemotherapy regimens (4). With the improved awareness of the role of immunological factor in tumor progression and prognosis, immunotherapy, especially checkpoint inhibitors, has become an important approach for unresectable KIRC (5, 6).

Immunogenic cell death (ICD) is a particular cell death modality of regulated cell death (RCD) (7, 8). Previous researches have indicated that ICD can induce adaptive immune response against the antigens of dead or dying tumor cells through damage-associated molecular patterns (DAMPs), which include ATP release, calreticulin exposure, and HMGB1 (high mobility group box 1) secretion (9, 10). The pivotal factor of cancer immunotherapy is how to avoid the immune escape of cancer (11). Specific immunogenic chemotherapy induces ICD to transform immune cold tumors into hot ones and increase the sensitivity of tumor cells to checkpoint inhibitors in several tumor cell lines (12). However, evidence of the effectiveness of this procedure is still lacking, which prompts us to explore the possibility of using ICD in clinical application.

In this study, we categorized patients on the premise of their expression of ICD genes and evaluated the difference in prognosis and immunotherapy response. We further identified several ICD biomarkers and constructed a scoring signature in which risk score was prominently associated with clinical features and tumor progression. Eventually, we predicted several drugs with high sensitivity to high-risk patients. We furthermore speculated that LY96 may serve as a potential novel therapeutic target and we verified the findings by experiments. Our results provided new clues for the development of tumor immunotherapy for KIRC.

Materials and methods

Retrieval of ICD genes

We obtained 1,736 ICD-related genes using the keyword "immunogenic cell death" in the GeneCards database (https://www.genecards.org/). At the same time, we summarized 171 ICD-related genes from relevant literature (13, 14). Then, the intersection of two gene sets yielded 73 genes that were considered as ICD key genes and included in our research.

Acquisition and preprocessing of data

The TPM transcriptome data that involved 541 tumor samples and 72 normal samples and matched clinical data of KIRC were obtained from the TCGA database (https://portal.gdc.cancer.gov/). The E-MTAB-1980 dataset (https://www.ebi.ac.uk/arrayexpress/experiments/E-MTAB-1980/) was selected as external validation cohort, which comprised RNA sequencing data and clinical information of 101 KIRC samples. Samples without survival data were removed from the cohort.

Differentially expressed ICD genes and protein–protein interaction network

Differentially expressed ICD genes (DEIGs) were identified by the "limma" R package (15). The protein–protein interactions (PPIs) among DEIGs were constructed using the Search Tool for the Retrieval of Interacting Genes (STRING) database (https://string-db.org/). Cytoscape v3.9.1 was used to draw the network (16). MCODE was a plugin of Cytoscape, which we conducted to identify highly interconnected functional cluster.

Construction of ICD-related subtypes and functional enrichment analyses

The R package "ConsensusClusterPlus" was performed to identify ICD molecular subtypes. The maximum subtypes were set at nine and the maximum number of iterations was set to 1,000 to guarantee the reliability of statistical analysis. Samples were clustered into two subtypes according to the result. Differentially expressed genes (DEGs) between two ICD subtypes were identified with cutoffs of |log2 fold change (FC)| > 1 and false discovery rate (FDR)< 0.05 for functional enrichment analyses. Gene Ontology (GO) and Kyoto Encyclopedia of Genes and Genomes (KEGG) analyses were implemented to predict proper biological functions and pathways of DEGs between ICD subtypes through the "ClusterProfile" package. Gene set enrichment analysis (GSEA) was also performed to investigate proper mechanism of actions of DEGs *via* GSEA version 4.1.0 (http://software.broadinstitute.org/gsea/). KEGG, Hallmark, and Reactome gene sets were downloaded from the Molecular Signature Database (MSigDB, https://www.gsea-msigdb.org/gsea/downloads.jsp). The minimum gene set was set as 5 and the maximum gene was set as 5,000 based on the gene expression profile and phenotypic grouping. Each gene set was repeatedly permutated 1,000 times for each analysis. *p*-value< 0.05 was considered to be statistically significant.

Comparison of genomic alterations of different ICD subtypes

Somatic mutation data of KIRC patients were downloaded from the TCGA database in "maf" format. Waterfall plots were plotted by the "Maftools" R package to visualize and summarize gene mutation. We further downloaded the segmented copy number variation (SCNV) data of KIRC from the GDC portal using the "TCGAbiolinks" R package for somatic copy number analysis according to a previous study (17). The alteration of gene copy

number and GISTIC score for each sample were analyzed through GISTIC 2.0 software (https://cloud.genepattern.org/). We also calculated the burden of copy number loss or gain on the basis of total number of genes with copy number changes at focal and arm levels for further comparison between two ICD subtypes (18).

Tumor immune microenvironment of ICD subtypes

The ESTIMATE algorithm was conducted to evaluate the tumor immune microenvironment (TME) of KIRC patients (19). The ESTIMATE algorithm calculated the stromal and immune score to predict the infiltration of matrix and immune cells. The CIBERSORT algorithm was applied to convert the gene expression data into expression of 22 immune cell types (20). The immune cell type with low expression was removed. By analyzing the correlation and difference of immune cell types between two subtypes, we mapped the correlation heatmap and multiple-group barplot to visualize the results. Furthermore, we analyzed the difference of HLA and checkpoint genes expression between the two subtypes. The HLA and checkpoint genes were acquired from a previous study (21).

Construction and validation of ICD prognostic signature

Univariate Cox regression was performed to screen out prognosis-related ICD genes with the criteria $p< 0.05$ of training set. Dimension reduction was carried out through the supervised regression random forest algorithm of the "randomForestSRC" package (ntree = 1,000) (22). The top 10 significant genes were selected for further multivariate Cox regression. ICD risk score was calculated by the following formula:

$$\text{Risk score} = \sum_{i=1}^{N} \alpha_i x_i$$

N, α, and x represent the number of selected genes, coefficient, and expression value. Patients in the training and validation set were divided into two groups according to ICD risk score. Kaplan–Meier (KM) survival curve and ROC curve were used on both the training set and validation set to assess the reliability of the ICD Prognostic Signature. Area under the curve (AUC) was used to quantify the ROC curve. We then visualized the clinical features of two risk groups by a heatmap. Variation analyses of clinical factors between different risk groups and correlation analyses focused on ICD risk score and clinical factors were also conducted. Univariate and multivariate Cox regression analyses were used to figure out independent prognostic factors. A nomogram was plotted based on the R package "NomogramEX" (23) and proportional hazards assumption was examined. Calibration curves of 1, 3, and 5 years were plotted to assess the nomogram.

Immunotherapy response prediction

TIDE (Tumor Immune Dysfunction and Exclusion) was an algorithm that integrated the characteristics of T-cell dysfunction and T-cell exclusion to predict immunotherapy response in tumor patients. The TIDE webserver (http://tide.dfci.harvard.edu/) was used to analyze the normalized expression data, and assigned a TIDE score to each patient where >0 was determined as no responder and<0 was determined as responder. The Subclass Mapping (SubMap) method was also put into use to predict the response of different groups to anti-PD-1 and anti-CTLA4 immunotherapy. In this analysis, we compared the expression profile of the two ICD risk groups we defined with another published dataset containing 47 patients with melanoma that responded to immunotherapies (24).

Connectivity map analysis

The Cmap website (https://clue.io/) provides a connectivity map analysis to predict potential useful small molecular drugs using the 150 most significant up- and downregulated DEGs between two risk groups. All 300 DEGs included in our analysis were identified using the "limma" R package and showed a significant difference with the criterion of $p< 0.05$. The inclusion criterion for determining potential useful small molecular drugs was the absolute value of Cmap score greater than 90.

Cell culture and quantitative real-time PCR

Human RCC cell lines, including 786-O and 769-P, and the human renal tubular epithelial immortalized cell line HK-2 were obtained from the Cell Bank of the Chinese Academy of Sciences (Shanghai, China). 786-O and 769-P cells were cultured in Roswell Park Memorial Institute medium (RPMI-1640; Gibco) and HK-2 was cultured in DMEM/F-12 (Gibco). All these cells were maintained in medium supplemented with 10% fetal bovine serum (Gibco) and 1% penicillin/streptomycin (Thermo Fisher) at 37°C in a 5% humidified CO_2 atmosphere.

A total of nine paired fresh-frozen KIRC tissues and normal tissues were obtained from patients diagnosed with KIRC at The Second Affiliated Hospital of Nanjing Medical University.

The total RNAs were isolated from tissues or cells using Trizol reagent (Invitrogen Life Technologies) according to the manufacturer's instructions. The quantity and quality of the extracted total RNA were assessed by using a NanoDrop 2000c spectrophotometer (Thermo Scientific). The total RNA was reverse-transcribed using HiScript III All-in-one RT SuperMix Perfect for qPCR (Vazyme; R333). Quantitative real-time PCR (qRT-PCR) was performed with Taq Pro Universal SYBR qPCR Master Mix (Vazyme; Q712-02) using a CFX96 Touch Real-Time PCR Detection System (Bio-Rad). Beta-actin was used as an internal control, and the relative expression level for genes was calculated by the $2^{-\Delta\Delta Ct}$ method. The primers used for qRT-PCR are listed in Table S3.

Cell transfection

For transfection, cells were seeded in six-well plates and grown to 40%–60% confluence by the time of transfection. Small interfering RNA (siRNA) and its negative control reagents were purchased from GenePharma Company. siRNAs were transfected with Lipofectamine™ 3000 reagent (Invitrogen, USA) according to the manufacturer's instructions. Target sequences of the siRNAs are shown in Table S4.

Cell Counting Kit-8 assay

Cell proliferation was measured by using the Cell Counting Kit-8 (CCK-8) (Vazyme; A311-01) according to the manufacturer's instructions. Briefly, cells were seeded onto plastic 96-well plates at an initial density of 2×10^3 cells/well. Then, CCK8 solution was added to each well at the indicated times and incubated for an additional 2 h at 37°C. Thereafter, OD_{450} values were measured.

Colony formation assay

The clonogenic potential of transfected or infected cells was evaluated by plate colony formation assay. Cells were seeded onto plastic six-well plates at an initial density of 1×10^3 cells/well in appropriate growth media and incubated for 2 weeks. The cells were fixed with 4% paraformaldehyde, and stained with Crystal Violet Staining solution (Beyotime; C0121). The stained cell colonies were counted and analyzed.

Statistical analysis

Statistical analysis and figures were performed using R software v4.1.0 and GraphPad Prism 8 (San Diego, USA). Spearman analysis was performed to calculate correlation coefficients. Chi-square test was used for categorical data. The association between clinicopathologic data and expression profile was estimated by the Wilcoxon rank test and logistic regression. All results with p-value< 0.05 were considered statistically significant. The pheatmap and ggplot2 R packages were engaged for the mapping. KM survival and ROC curve based on survival and timeROC packages were performed to assess survival outcomes. Sangerbox (www.sangerbox.com) was used to improve the quality of figure. *, **, ***, and **** represent p< 0.05, p< 0.01, p< 0.001, and p< 0.0001, respectively.

Results

Identification of differentially expressed ICD genes and the protein–protein interaction network

From previous literatures and GeneCards database (25), 73 common genes were considered as ICD core gene (Table S1). Subsequently, the R package "limma" was applied to identify DEIGs (Figure 1A). A total of 61 DEIGs, namely, 52 upregulated and 9 downregulated genes, were screened out. A heatmap was used for visualization of the expression (Figure 1E). The PPI network of DEIGs was retrieved using the STRING database (Figure 1B) and visualized by the Cytoscape software (Figure 1C). Functional key subnetwork analysis was performed through the MCODE algorithm, consisting of the following modules: LY96, TLR4, IRF3, and RIPK1, which was considered as a significant module with a high MCODE score (Figure 1D).

Generation of two ICD subtypes through consensus clustering

To further reveal the relationship between expression of DEIGs and KIRC, we utilized the "ConsensusClusterPlus" R package to classify molecular subtype with KIRC patients according to the expression levels of DEIGs. Samples were clustered into two clusters after K-means clustering (Figures 2A, B). Then, KM survival analysis indicated that patients in the ICD-low subtype showed dismal prognosis compared with patients in the ICD-high subtype (Figure 2C). Furthermore, as displayed in Figure 2D, the genomic expression of ICD genes was compared in two clusters. Cluster C1 (n=383) was considered as ICD-high subtype for exhibiting a higher expression of ICD genes while cluster C2 (n = 145) was considered as ICD-low subtype. Differences of clinical features between the two distinct subtypes were also plotted for visualization in Figure 2D.

Functional enrichment analyses

In order to investigate the potential molecular mechanism and biological activity of ICD subtypes, subtype-related DEGs were figured out for functional enrichment analysis for GO and KEGG analysis. GO analysis demonstrated that DEGs were mainly involved in immune response, regulation of immune system process, defense response, and leukocyte activation (Figure 3A). KEGG analysis revealed that DEGs were mainly enriched in cancer-associated pathways, including the PI3K-Akt signaling pathway, EGFR tyrosine kinase inhibitor resistance, PD-L1 expression and the PD-1 checkpoint pathway in cancer, and the chemokine signaling pathway (Figure 3B), implying that immunogenic cell death acts as a crucial factor in the progression of RCC. Moreover, GSEA based on KEGG, Hallmark, and Reactome gene sets was used for further exploration. The results suggested that immunity and cancer-related pathways were highly concentrated in the ICD-high subtype, including the T- and B-cell receptor signaling pathway, the p53 signaling pathway, IL2-STAT5 signaling, and interleukin 1 and 17 signaling (Figures 3C–E).

Genomic alterations of different ICD subtypes

The somatic mutation landscape was also analyzed in two subtypes (Figures 4A, B). Although VHL, PBRM1, TTN, and SETD2 were the most frequent mutations, the relative frequency varied among different subtypes. We then analyzed the GISTIC scores and copy number gain/loss percentage in the ICD-high and -low group. The result revealed that the ICD-low subtype was more likely to have a higher GISTIC

10.3389/fimmu.2023.1207061

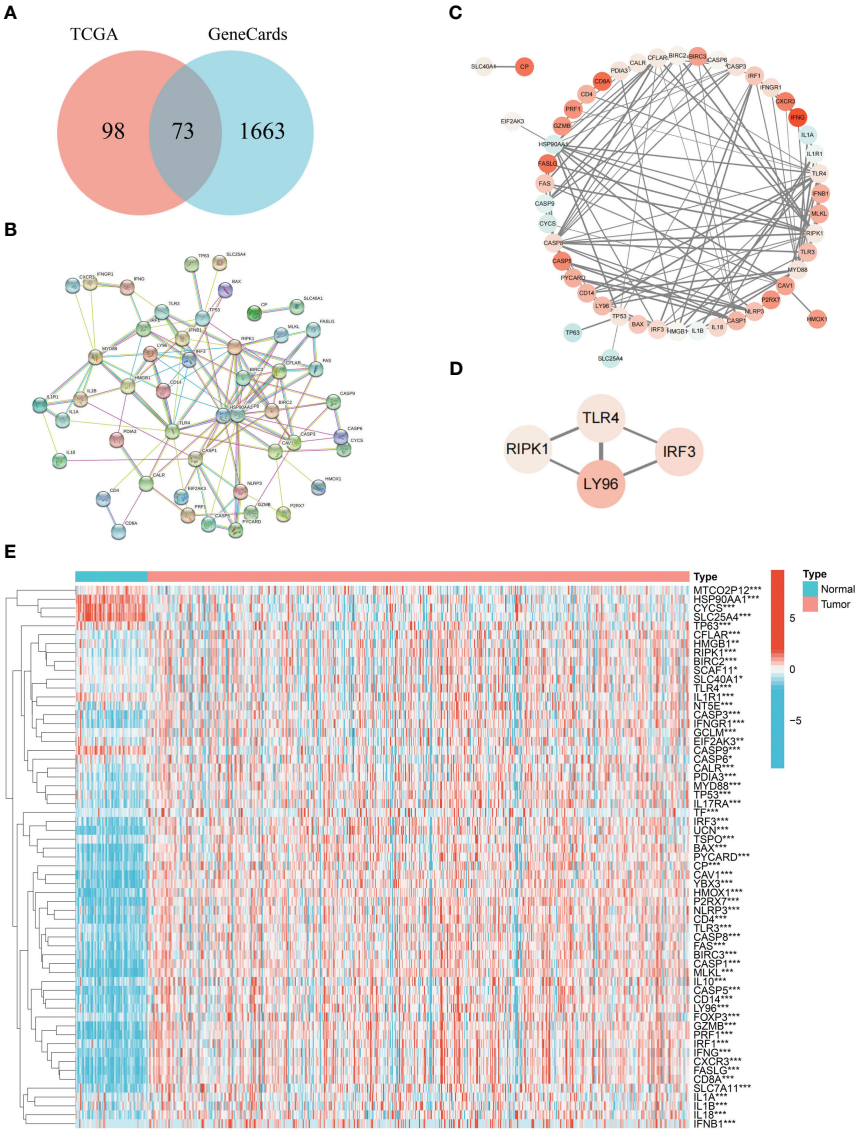

FIGURE 1
Acquisition of common ICD genes. **(A)** Venn diagram of the 73 common ICD genes. **(B)** Protein–protein interactions among the 73 common ICD genes. **(C)** Visualization of the PPI network conducted on Cytoscape. **(D)** Visualization of the functional subnet module. **(E)** Heatmap of differentially expressed ICD genes between normal and tumor samples in KIRC. * represents p< 0.05, ** represents p< 0.01, *** represents p< 0.001.

score (Figure 4C) and copy number gain/loss percentage (Figure 4D). The burden of copy number gain and loss in the ICD-high group was decreased compared with the ICD-low group at arm level while there was no remarkable difference at focal level (Figures 4E, F). It appeared that arm level copy number alterations mainly contributed to the difference in ICD expression level.

Assessment of tumor immune microenvironment and checkpoints in distinct subtypes

Accumulating evidence revealed that ICD had significant correlation with antitumor immunity. In our research, we analyzed the tumor immune microenvironment of two subtypes and discriminated immune-related characteristics between two subtypes. We first calculated the TME status using the ESTIMATE algorithm. As depicted in Figure 5A, the stromal score, immune score, and ESTIMATE score ($p< 0.05$) were significantly higher in the ICD-high subtype than those in the ICD-low subtype while tumor purity was the opposite.

Then, we calculated the fraction of 22 kinds of tumor-infiltrating immune cells (TIICs) through the CIBERSORT algorithm and removed the low-expression cell line. Grouping histogram showed the distribution of TIICs (Figure 5B). Macrophages and T cells accounted the most for the total. Pearson's correlation was performed to analyze TIIC correlation (Figure 5C). We next examined immune cell infiltration to assess differences in the immune context of the tumor immune microenvironment between two subtypes. The ICD-high subtype

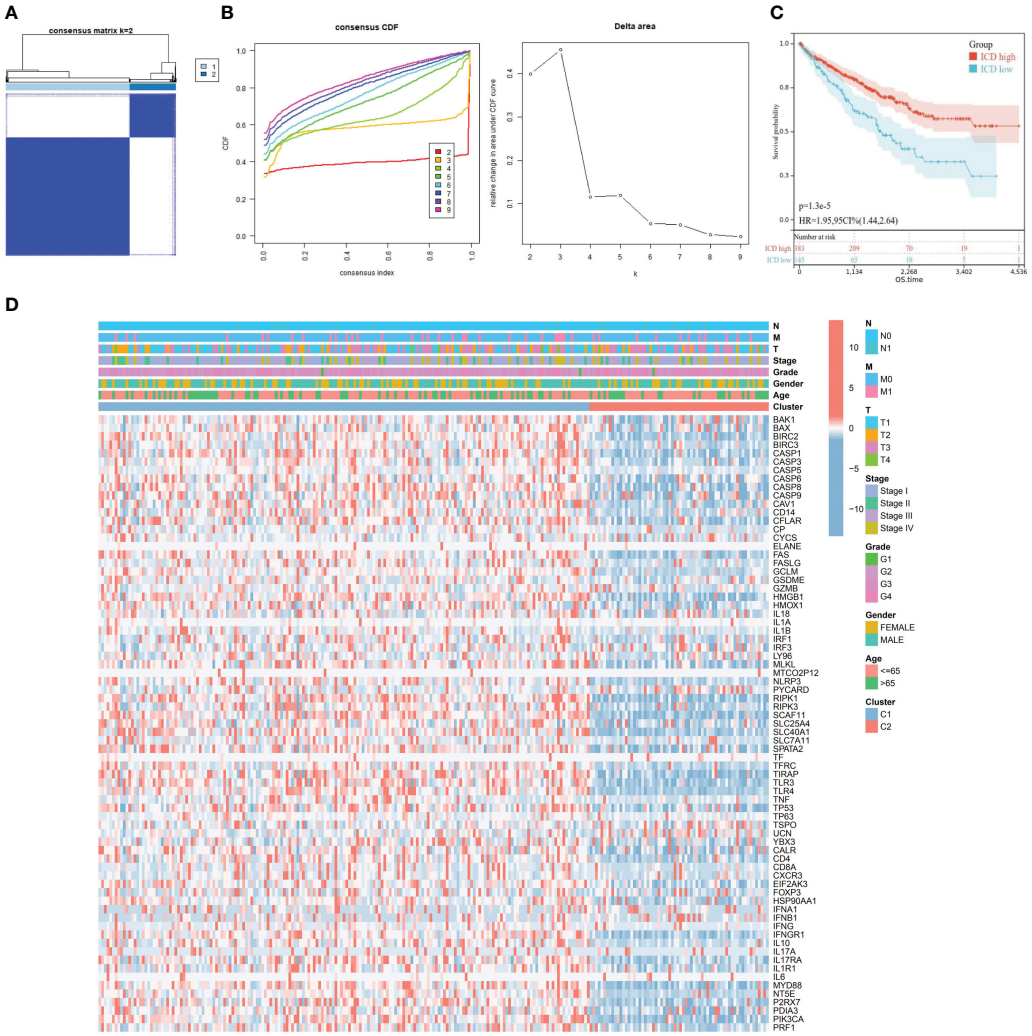

FIGURE 2
Construction of two ICD subtypes through consensus clustering. **(A)** Heatmap exhibits consensus clustering result for k = 2. **(B)** Consensus clustering cumulative distribution function (CDF) and delta area under the CDF curve for k = 2 to k = 9. **(C)** Kaplan–Meier curves of OS in ICD-high and ICD-low subtypes. **(D)** Heatmap of 73 ICD gene expression and clinical factors in different subtypes. Corresponding feature names are shown at the right of the heatmap.

showed high infiltration of CD8 T cells, activated CD4 memory T cells, follicular helper T cells, regulatory T cells (Tregs), and M0 macrophages, while the ICD-high subtype was characterized by high infiltration of resting CD memory T cells, monocytes, M1 and M2 macrophages, and resting dendritic cells (Figure 5D). Meanwhile, the expressions of HLA genes and immune checkpoint genes were different among the distinct subtypes. The result suggested that HLA genes (Figure 5E) and checkpoint genes (Figure 5F) were markedly higher in the ICD-high subtype.

Construction and validation of the ICD prognostic signature

For the purpose of predicting the prognosis accurately and credibly, we constructed an ICD prognostic signature based on supervised regression random forest algorithm. The top 10 significant genes—7 risk genes and 3 protect genes—were screened out (Figures 6A-C). KM analysis were carried out on the 1,023 combinations of the top 10 genes (Table S2). We selected the combination with the lowest p-value of KM analysis as ICD prognostic signature containing TF, FOXP3, LY96, SLC7A11, HSP90AA1, UCN, IFNB1, and TLR3. The ICD risk score was calculated as follows: ICD score = (0.10917254 * TF) + (0.16458303 * FOXP3) + (0.90393805 * LY96) + (0.50920311 * SLC7A11) + (−0.88020896 * HSP90AA1) + (0.99872821 * UCN) + (1.28833498 * IFNB1) + (−0.78540411 * TLR3). We allocated patients into high-risk and low-risk group according to their ICD risk score. KM survival analysis was performed to determine the overall survival (OS) time between different risk groups and ROC curve quantifying by AUC was utilized to examine prognosis on the training set (TCGA cohort) and validation set (E-MTAB-1980 cohort). According to our results, patients with low ICD risk score demonstrated a prominent survival benefit in both training set and validation set (Figures 6D, E). The AUC

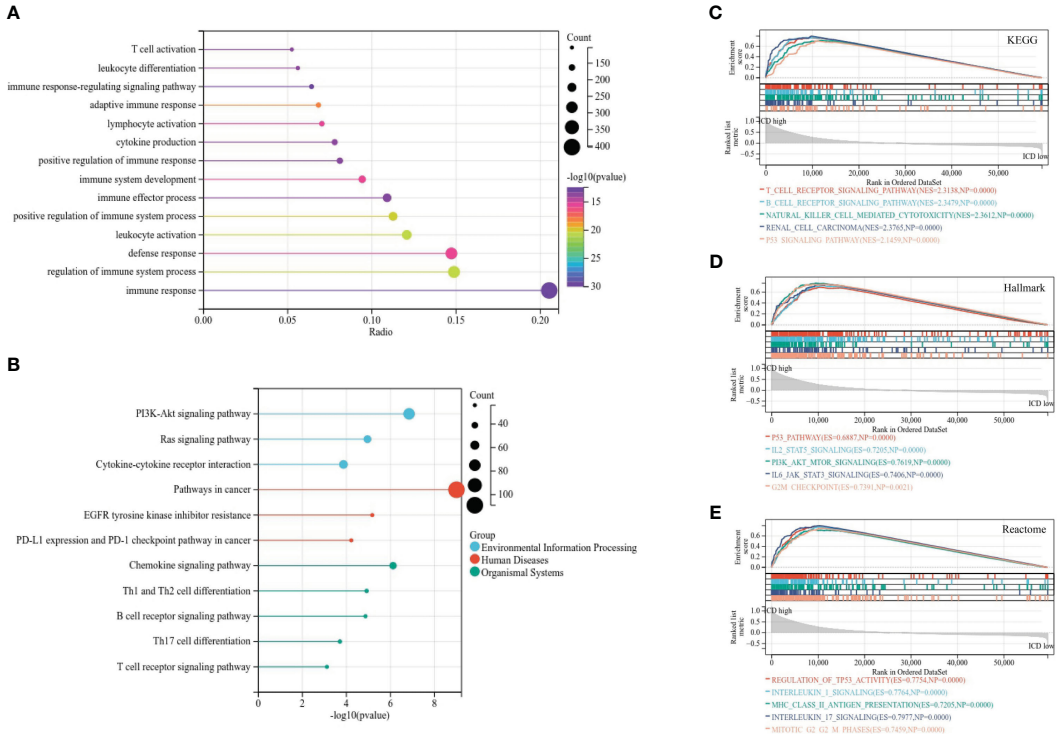

FIGURE 3
Functional enrichment analysis of differentially expressed genes in different subtypes. **(A, B)** Lollipop plot of GO **(A)** and KEGG **(B)** signaling pathway enrichment analysis. **(C–E)** GSEA analyses based on KEGG **(C)**, Hallmark **(D)**, and Reactome **(E)** gene sets.

curves showed that ICD risk score had an acceptable prognostic value for KIRC patients. The AUC values for predicting 1-, 3- and 5-year OS in the training set were 0.76, 0.72, and 0.76, respectively, and those in the validation set were 0.68, 0.71, and 0.72 (Figures 6G, H). Additionally, expressions of survival status and heatmap of each set were also presented (Figures 6F, I).

Clinical features of the prognostic ICD risk signature

After clinical information analysis, we first drew a heatmap to illustrate the difference between two risk groups (Figure 7A). Then, Chi-square test was performed to evaluate the clinical difference between two risk groups. Grade, stage, T staging, and M staging were considered to have a significant difference between the high- and low-risk group whereas age and gender had no difference (Figures 7B-G). Meanwhile, we further analyzed the correlation of ICD risk score and four diverse clinical parameters. The boxplots showed the substantially elevated ICD risk score in the higher grade, stage, T staging, and M staging according to the *p*-value of difference analysis between the groups (Figures 7H-K). Thus, it was surprising that the value of ICD risk score had the capability to assess tumor progression.

Establishment of nomogram to predict patient prognosis

We applied univariate and multivariate Cox regression analyses to explore independent prognostic factors. Clinicopathologic features including age, gender, grade, and stage with ICD risk score were displayed in the training set, which confirmed that ICD risk score was an independent prognostic factor of KIRC (univariate Cox: HR: 2.758, 95% CI: 2.231–3.404, *p*-value< 0.001; multivariate Cox: HR: 2.095, 95% CI: 1.671–2.827, *p*-value< 0.001, respectively) (Figures 8A, B). Owing to the high correlation between ICD risk score and prognosis, clinical parameters including age, N staging, and grade together with ICD risk score were incorporated to construct a nomogram. All features in the nomogram met the standard of *p*-value of proportional hazards assumption greater than 0.05. The nomogram was utilized to estimate 1-, 3-, and 5-year OS for KIRC patients (Figure 8C). As shown in Figures 8D–F, calibration curves of 1, 3, and 5 years were established to evaluate the performance of nomogram and presented great accuracy between actual observations and predicted values.

Relation between ICD signature and tumor immune microenvironment

Based on the findings above, we had confirmed the potential role of ICD in antitumor immune response. The relation between

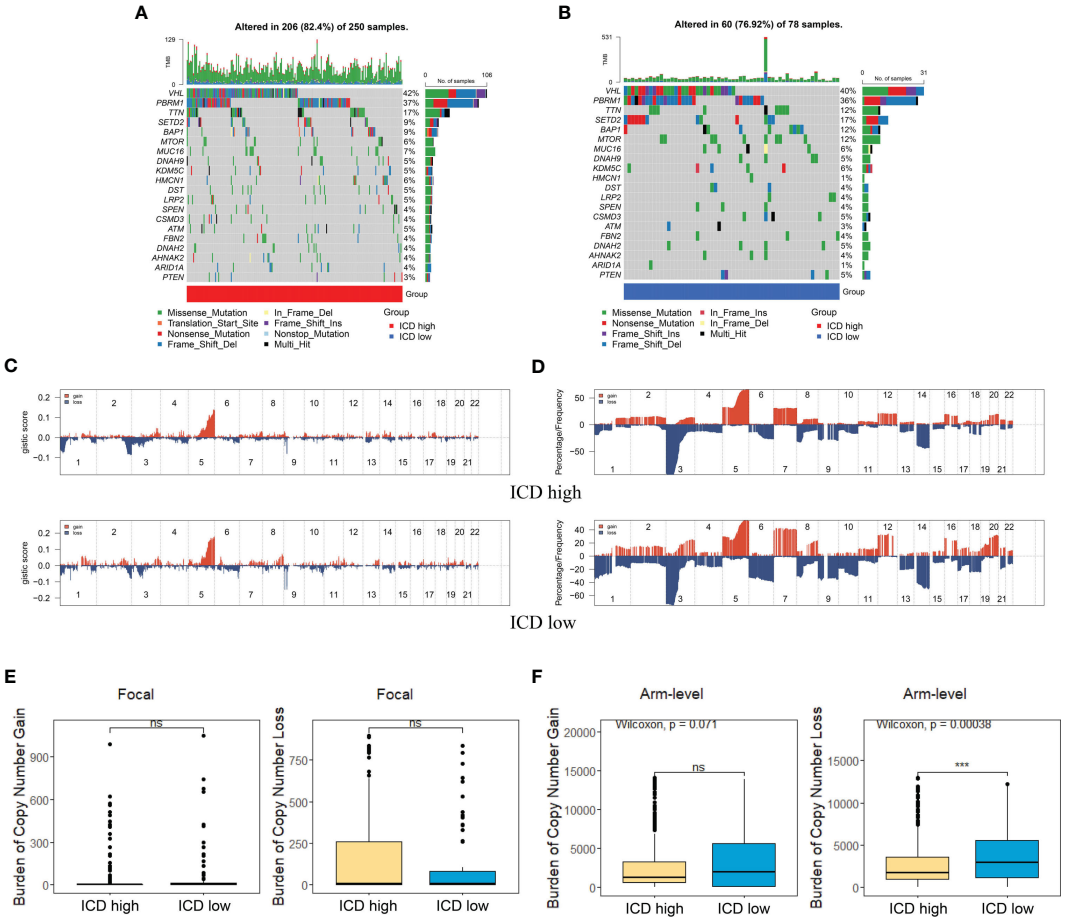

FIGURE 4
Comparison of genomic alternations between different subtypes. **(A, B)** Oncoprint display of the 10 most frequently mutated genes in the ICD-high subtype **(A)** and ICD-low subtype **(B)**. **(C, D)** Comparison of GISTIC score **(C)** and gain/loss percentage **(D)** of copy number profiles between different subtypes. **(E)** Focal level of CNV burden between two subtypes. **(F)** ICD-low subtype showed a higher arm level of CNV burden. *** represents p< 0.001.

ICD risk score and TIICs was scrutinized. The results demonstrated that patients with elevated ICD risk score exhibited a negative correlation with CD8 T cells, follicular helper T cells, activated NK cells, and a positive correlation with M0 macrophages (Figure 9A). The validation cohort showed the same tendency (Figure 9B).

To investigate the role of ICD risk score on response to immunotherapy, we used TIDE (http://tide.dfci.harvard.edu) analysis to quantify the rate of response to TIDE score for each patient. The results showed that the high-risk group had a higher percent of non-responder patients (Figure 9C). Notably, immunotherapy responder patients showed a lower ICD score compared with non-responder patients (p-value< 0.05) (Figure 9D). In addition to TIDE prediction, we also compared the expression profile of two risk groups with a published dataset containing 47 patients with melanoma that responded to immunotherapies. As for our result, the high-risk group was more conceivable to respond to anti-PD-1 therapy with the Bonferroni-corrected p-value of 0.011 (Figure 9E).

Prediction of small molecular drug

We employed the Connectivity Map (CMap) tool, which was widely used to discover potential small molecular drugs, with 150 up- and downregulated DEGs between two risk groups. We finally identified 12 candidate small molecular drugs with absolute CMap score > 90, namely, fostamatinib, YC-1, NM-PP1, torin-2, tipifarnib-P2, apigenin, SB-431542, cycloheximide, amonafide, linifanib, piperacillin, and ochratoxin-a (Table 1).

LY96 promotes the proliferation of KIRC *in vitro*

The eight ICD signature genes' expression was analyzed by qRT-PCR in nine pairs of KIRC and adjacent tissues (Figure S1). We measured the mRNA expression of LY96 in human renal cortex proximal convoluted tubular epithelial cell (HK-2) and two human

10.3389/fimmu.2023.1207061

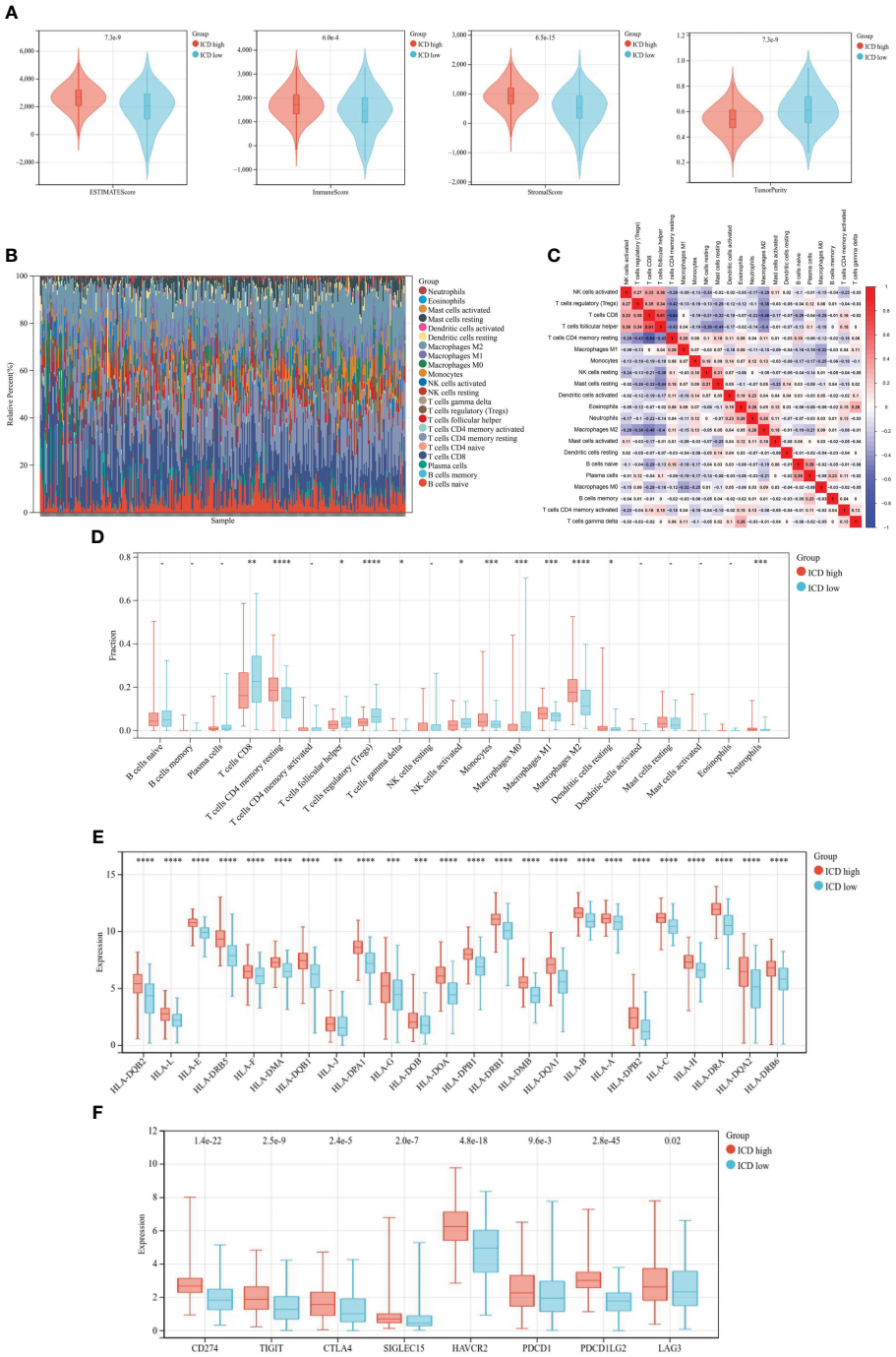

FIGURE 5
Immune landscape of different ICD subtypes. **(A)** Violin plots of ESTIMATE, immune, stromal scores, and tumor purity of ICD-high and -low subtypes. **(B)** Relative proportion of immune infiltration. **(C)** Correlation heatmap of 21 immune cells. **(D–F)** Box plots of differential expression of 21 immune cells **(D)**, HLA genes **(E)**, and immune checkpoints **(F)** between ICD-high and -low subtypes. *, **, ***, and **** represent $p< 0.05$, $p< 0.01$, $p< 0.001$, and $p< 0.0001$, respectively.

KIRC cell lines (786-0 and 769-P), and the highest expression was found in 786-O (Figure 10A). To evaluate the biological roles of LY96 in KIRC, small interfering RNA (siRNA) that specifically target LY96 was designed. According to the expression of LY96 in different cell lines, siRNA-LY96 was transfected into 786-O. The knockdown efficiency was confirmed by qRT-PCR analyses, which showed that more than 50% LY96 was knockdown. As shown in Figure 10B, the expression levels of LY96 were significantly decreased in siRNA-infected 786-O cells compared to negative control (NC) cells. CCK-8 and colony formation experiments demonstrated that downregulation of LY96 inhibited the proliferation ability of 786-O cells (Figures 10C, D).

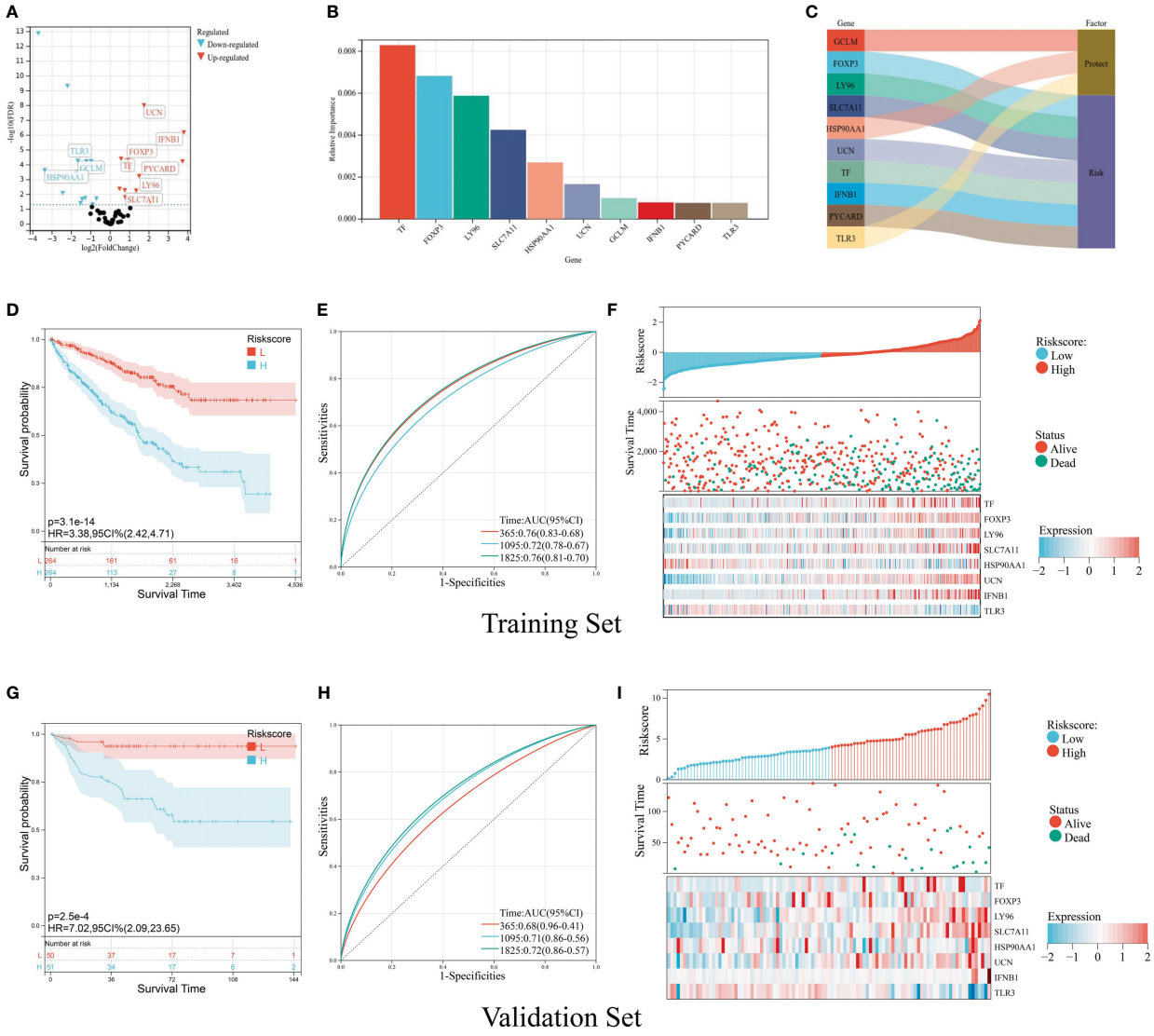

FIGURE 6
Construction and validation of the ICD prognostic signature. **(A)** Volcano plot of prognosis-related ICD genes preliminarily identified by univariate Cox analysis with the screening criteria $p < 0.05$. The red icons represent risk factors (HR > 1), and the blue icons represent protective factors (HR< 1). **(B)** The top 10 important ICD genes based on the relative importance calculated by random forest algorithm. **(C)** Sankey diagram demonstrated the prognosis effect of top 10 important ICD genes. **(D-F)** Kaplan–Meier curve of OS prognosis **(D)**, timeROC plot **(E)**, and risk plot including risk score distribution, survival status, and heatmap of eight signature genes **(F)** in the training set. **(G, I)** Kaplan–Meier curve of OS prognosis **(G)**, timeROC plot **(H)**, and risk plot including risk score distribution, survival status, and heatmap of eight signature genes **(I)** in the validation set.

Discussion

Cancer immunotherapy has made a revolution in cancer treatment through establishing a connection between the human immune system and cancer (26). Various types of immunotherapies, including cellular or antibody therapy (27), immune checkpoint therapy (28), CAR T-cell therapy (29), and cancer vaccination (30), have been applied to KIRC patients (31). ICD is a kind of RCD and considered sufficient to activate an adaptive immune response (32, 33). The mechanism of action encompasses the release of DAMPs, which can be recognized by innate pattern recognition receptors (PRRs) from dying tumor cells, which results in tumor-specific immune response (34). In addition, numerous drugs in other kinds of radiation therapy, chemotherapy, or immunotherapy have the potential to augment ICD (35). Overall, we believed that ICD therapy together with other therapies will be greatly beneficial for cancer treatment.

Our research identified 73 core ICD genes through searching previous studies and public databases. Consensus clustering analysis was applied to split patients into two subtypes based on ICD gene expression. Our research revealed that the ICD-low subtype tended to have a favorable clinical outcome. We then screened the DEGs between high and low subtypes of ICD and used them in biological function and pathway enrichment analyses. Based on the results of enrichment analysis, DEGs were mainly enriched in biological functions such as immune response, regulation of immune system process, defense response and leukocyte activation, and pathways associated with immunity and cancer-related signaling pathways, including the PI3K-Akt signaling pathway, P53 pathway, IL2-STAT5 signaling

FIGURE 7
Clinical relevance of the ICD prognostic signature. **(A)** Heatmap of clinical factors in different risk groups. **(B-G)** Clinical differences between high and low risk groups including age **(B)**, gender **(C)**, grade **(D)**, stage **(E)**, T staging **(F)**, and M staging **(G)**. **(H-K)** ICD score differences between groups of grade **(H)**, stage **(I)**, T staging **(J)**, and M staging **(K)**. *** represents p< 0.001.

pathway, PD-L1 expression and PD-1 checkpoint pathway in cancer, and B-cell receptor signaling pathway. STAT5 is regulated by the IL-2 family and significantly contributes to tumor cell survival and malignant progression of disease through influencing NK cell (36). P53 plays a key role in cancer-cell-autonomous functions. The loss of P53 can lead to the decrease of recruitment and activity of myeloid and T cells, and eventually result in immune evasion (37). Alissa Chackerian's team suggested that ICD can be induced by dinaciclib and enhance anti-PD1-mediated tumor suppression (38).

Furthermore, tumor immune infiltration landscape was calculated by the ESTIMATE and CIBERSORT algorithms. The score calculated by ESTIMATE for the two subtypes revealed that the ICD-high subtype was negatively correlated with tumor purity and positively correlated with immune, stromal, and estimate scores. Thus, HLA and checkpoint genes showed considerably high expression in the ICD-high subtype.

The ICD prognostic signature was built with TF, FOXP3, LY96, SLC7A11, HSP90AA1, UCN, IFNB1, and TLR3 to predict the prognosis by quantification metric. Patients in the high-risk group had significantly poorer prognosis compared with the low-risk group according to the KM survival analysis and ROC curve, and an external dataset was introduced for validation. We evaluated and found a significant correlation between risk score and clinical factors such as grade, stage, T staging, and M staging. Moreover,

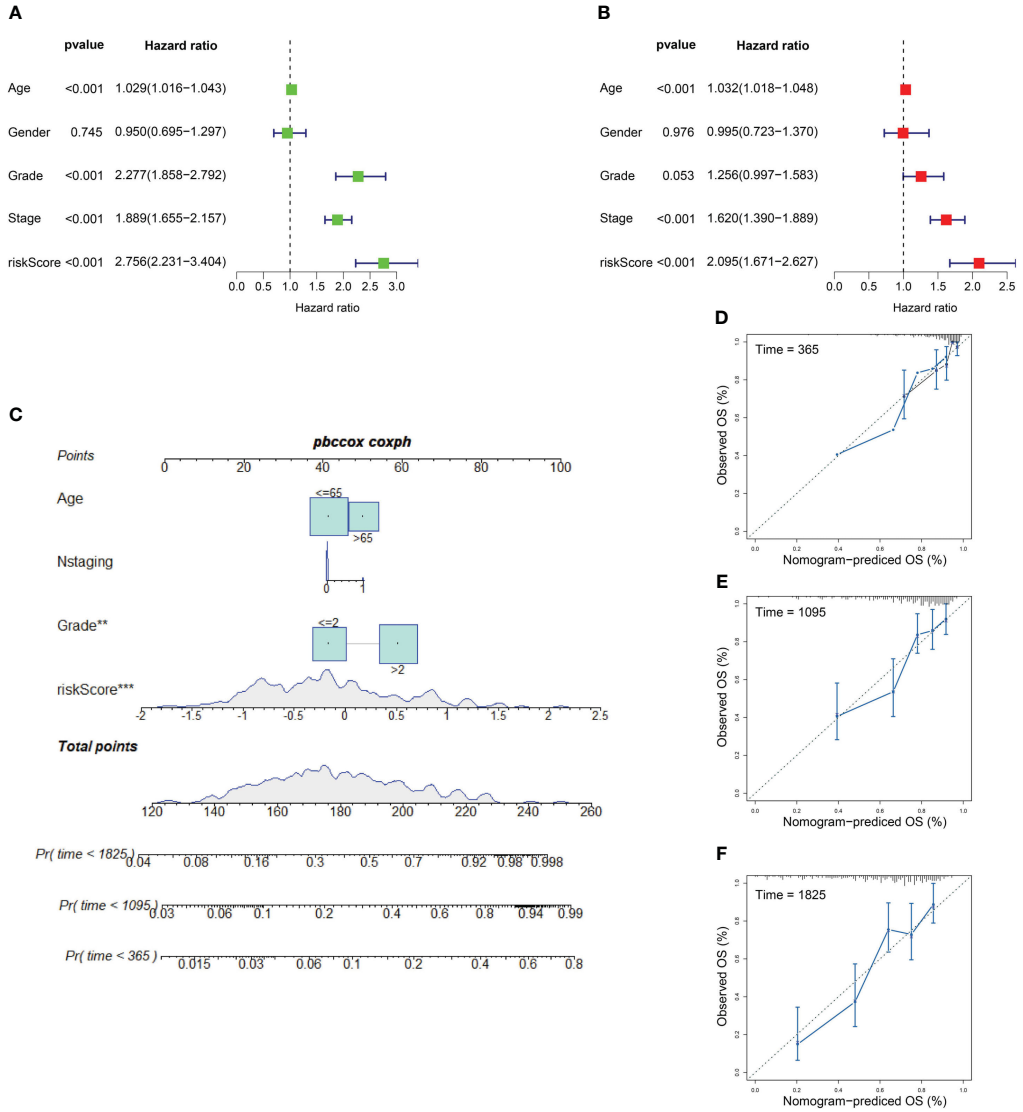

FIGURE 8
Independent prognostic factors and nomogram model. **(A, B)** Outcomes of univariate prognostic analysis **(A)** and multivariate prognostic analysis **(B)**. **(C)** Nomogram for evaluating the possibility of KIRC patients mortality at 1, 3, and 5 years. **(D–F)** Calibration for assessing the conformity between nomogram OS and observed OS at 1 year **(D)**, 3 years **(E)**, and 5 years **(F)**. ** represents p< 0.01, *** represents p< 0.001.

CD8 T cells, follicular helper T cells (Tfh), and activated NK cells showed a negative correlation with risk score whereas M0 macrophages showed a positive correlation. Tfh cells were accepted as a distinct lineage of helper CD4 T cells. Tfh is associated with the presence of tertiary lymphoid structures (TLS), which were commonly linked to better outcome (39, 40). It was reported by Timothy W. Hand and colleagues that Tfh cells promote the formation of TLS and drive antitumor immunity in colorectal cancer (41). In addition, Julie Niogret's team revealed that Tfh cells significantly contribute to CD8-dependent antitumor immunity and anti-PD-L1 efficacy (42). Our findings indicated that our signature was a good predictor of immunotherapy response rate. We then validated these results through TIDE analysis. A lower percentage of responders was observed in the high-risk group compared with the low-risk group. The result of submap analysis dramatically showed the better response of the high-risk group to anti-PD-1 therapy. Subsequently, we predicted the potential useful small molecular drugs through CMap analysis.

According to results of Cytoscape and supervised regression random forest algorithm, we determined LY96 (Lymphocyte antigen 96) as a hub gene to ICD in KIRC. LY96, also known as myeloid differentiation 2 (MD2), is a co-receptor to TLR4. LY96 is considered to play a key role in inflammation and immune-related diseases such as rheumatoid arthritis, Crohn's disease, and inflammatory diabetic cardiomyopathy (43–45). Several studies have shown that LY96 is correlated with tumorigenesis and progression (46). The interaction of LY96 and TLR4 promotes the release of pro-inflammatory cytokines and adhesive molecules, which accelerates colon cancer growth and lung metastasis (47). In gastric cancer, LY96 can activate

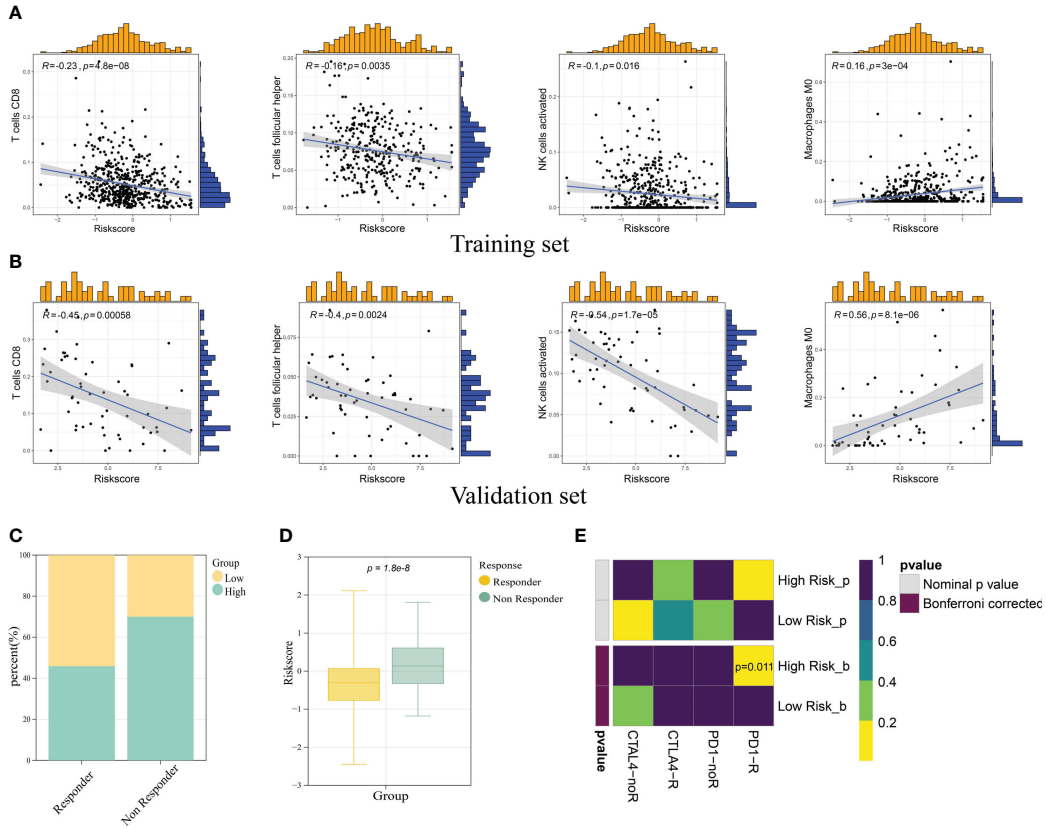

FIGURE 9
Correlation of ICD prognostic signature with immune cells and immunotherapy responses. Scatter plots revealed the correlation between risk score and infiltration of CD8 T cells, follicular helper T cells, activated NK cells, and M0 macrophages in the training set **(A)** and validation set **(B)**. **(C)** The immunotherapy responders had a higher percentage in the low risk group. **(D)** The immunotherapy responders had a lower risk score. **(E)** Submap analysis manifested the sensitivity of patients in different risk groups to PD1 and CTLA4 therapy.

TABLE 1 Candidate small molecular drugs analyzed by CMap tools.

Name	Score	MOA	Target
Fostamatinib	97.92	SYK inhibitor	SYK, FLT3, RET
YC-1	96.26	Guanylyl cyclase activator	HIF1A, GUCY1A2, GUCY1A3, GUCY1B3
NM-PP1	94.11	Mutant kinase inhibitor	CAMK2A, LCK, MAPK8, PRKACA, RIPK2, SRC
Torin-2	93.59	MTOR inhibitor	MTOR
Tipifarnib-P2	93.37	Farnesyltransferase inhibitor	FNTA, FNTB
Apigenin	90.81	Casein kinase inhibitor, cell proliferation inhibitor, cytochrome P450 inhibitor	AKR1B1, AR, CDK6, CFTR, CYP19A1, CYP1A2, CYP1B1, HSD17B1, MAOA, ODC1, XDH
SB-431542	90.08	TGF beta receptor inhibitor	TGFBR1, ACVR1C, ACVR1B
Cycloheximide	−93.2	Protein synthesis inhibitor	GSK3B, RPL3
Amonafide	−95.98	Topoisomerase inhibitor	TOP2A, TOP2B
Linifanib	−96.26	PDGFR receptor inhibitor, VEGFR inhibitor	CSF1R, KDR, PDGFRB, FLT1, FLT3, FLT4, CSF1, KIT, PDGFRA, RET, TEK
Piperacillin	−97.5	Bacterial cell wall synthesis inhibitor	none
Ochratoxin-a	−97.88	Phenylalanyl tRNA synthetase inhibitor	SLC22A6

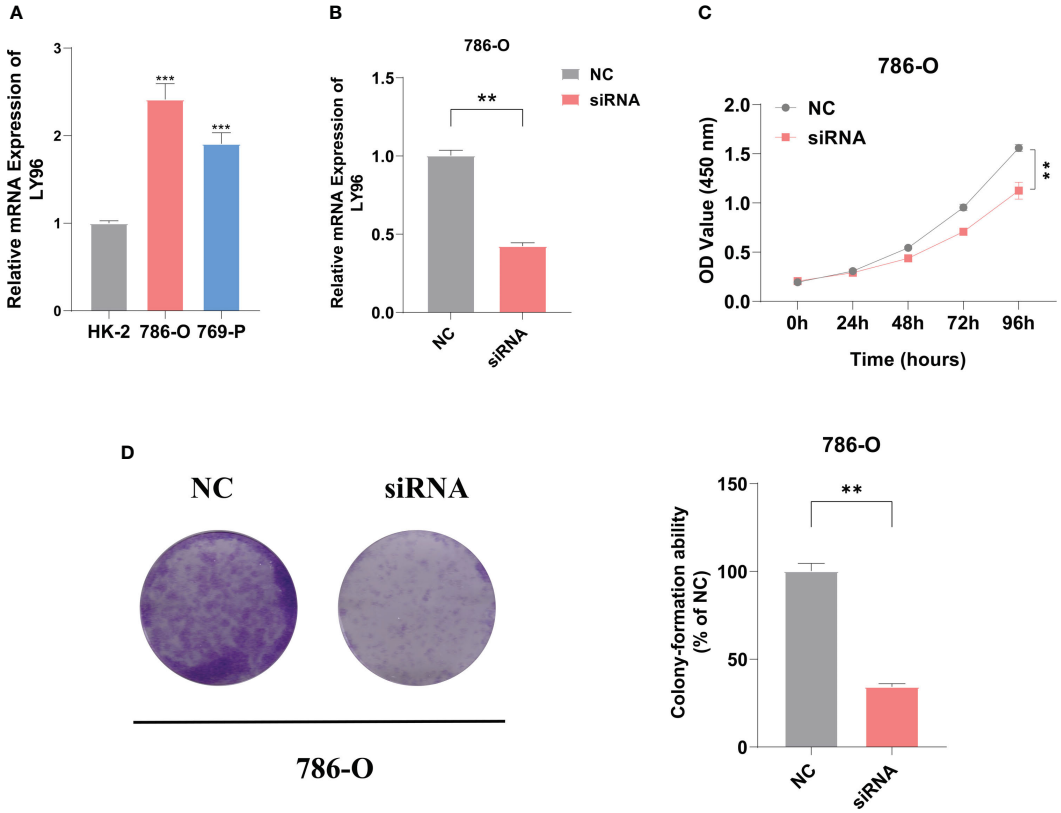

FIGURE 10
LY96 promotes the proliferation of ccRCC *in vitro*. **(A)** qRT-PCR verified the expression level of LY96 in RCC cell lines. **(B)** qRT-PCR analysis of LY96 mRNA in 786-O cells treated with negative control (NC) or LY96 siRNA. **(C)** CCK-8 was performed to determine the proliferation abilities of 786-O cells treated with negative control (NC) or LY96 siRNAs. **(D)** Colony formation was performed to determine the proliferation abilities of 786-O cells treated with negative control (NC) or LY96 siRNAs. ** represents p< 0.01, *** represents p< 0.001.

macrophage-mediated NF-κB and STAT3 pathways to promote tumor progression (48). The result of qRT-PCR validated the upregulated expression of LY96 in RCC cell lines and clinical samples. Additionally, CCK-8 and colony formation experiments demonstrated that downregulation of LY96 inhibited the proliferation ability of 786-O cells. We also validated the different expression of all signature genes in tissues.

In conclusion, our research evaluated the associations of prognosis, biological function and pathways, and immune infiltration landscape with ICD subtypes in KIRC. Furthermore, we constructed a prognosis-related ICD signature based on TF, FOXP3, LY96, SLC7A11, HSP90AA1, UCN, IFNB1, and TLR3. The signature was verified to have an independent prognostic value and provided an exact survival prediction. In addition, we determined LY96 as a potential biomarker. Based on previous studies, our research might provide a theoretical basis for the development of a novel immunotherapy for the treatment of KIRC. However, several limitations remain to be addressed in our study. The cohort in research mainly comprise Western samples, which may influence the usability of the findings to other populations. Further clinical trials were also required to verify our conclusion.

Data availability statement

The datasets presented in this study can be found in online repositories. The names of the repository/repositories and accession number(s) can be found in the article/Supplementary Material.

Ethics statement

The studies involving human participants were reviewed and approved by Department of Urology, The Second Affiliated Hospital of Nanjing Medical University, Nanjing. The patients/participants provided their written informed consent to participate in this study.

Author contributions

SJ: Data curation and Conceptualization. YD: Writing-Original manuscript. JW: Editing Methodology. XZ: Statistical analysis and R codes. WL, YW, HZ and LS: Writing-Review. JY: Validation and Software. QZ: Project administration. All authors contributed to the article and approved the submitted version.

Funding

This research was supported by the Medical Research Project of Jiangsu Commission of Health (No. ZD2021028 and No. Z2021074).

Conflict of interest

The authors declared that the research was conducted in the absence of any commercial or financial relationships that could be construed as a potential conflict of interest.

Publisher's note

Supplementary material

The Supplementary Material for this article can be found online at: https://www.frontiersin.org/articles/10.3389/fimmu.2023.1207061/full#supplementary-material

References

1. Guo F, Liu J, Han X, Zhang X, Lin T, Wang Y, et al. FBXO22 suppresses metastasis in human renal cell carcinoma *via* inhibiting MMP-9-mediated migration and invasion and VEGF-mediated angiogenesis. *Int J Biol Sci* (2019) 15:647–56. doi: 10.7150/ijbs.31293

2. Grimm MO, Leucht K, Foller S. Risk stratification and treatment algorithm of metastatic renal cell carcinoma. *J Clin Med* (2021) 10(22):5339. doi: 10.3390/jcm10225339

3. Qin S, Shi X, Wang C, Jin P, Ma F. Transcription Factor and miRNA Interplays Can Manifest the Survival of ccRCC Patients. *Cancers* (2019) 11(11):1668. doi: 10.3390/cancers11111668

4. Chen C, Yang RX, Zhang JX, Xu HG. Construction and validation of a prognostic model for kidney renal clear cell carcinoma based on podocyte-associated genes. *Cancer Med* (2022) 11:3549–62. doi: 10.1002/cam4.4733

5. Terranova-Barberio M, Pawlowska N, Dhawan M, Moasser M, Chien AJ, Melisko ME, et al. Exhausted T cell signature predicts immunotherapy response in ER-positive breast cancer. *Nat Commun* (2020) 11:3584. doi: 10.1038/s41467-020-17414-y

6. Liu W, Ren D, Xiong W, Jin X, Zhu L. A novel FBW7/NFAT1 axis regulates cancer immunity in sunitinib-resistant renal cancer by inducing PD-L1 expression. *J Exp Clin Cancer Res CR* (2022) 41:38. doi: 10.1186/s13046-022-02253-0

7. Huang Z, Wang Y, Yao D, Wu J, Hu Y, Yuan A. Nanoscale coordination polymers induce immunogenic cell death by amplifying radiation therapy mediated oxidative stress. *Nat Commun* (2021) 12:145. doi: 10.1038/s41467-020-20243-8

8. Li Z, Lai X, Fu S, Ren L, Cai H, Zhang H, et al. Immunogenic cell death activates the tumor immune microenvironment to boost the immunotherapy efficiency. *Advanced Sci (Weinheim Baden-Wurttemberg Germany)* (2022) 9:e2201734. doi: 10.1002/advs.202201734

9. Galluzzi L, Vitale I, Warren S, Adjemian S, Agostinis P, Martinez AB, et al. Consensus guidelines for the definition, detection and interpretation of immunogenic cell death. *J immunother Cancer* (2020) 8(1):e000337. doi: 10.1136/jitc-2019-000337corr1

10. Krysko DV, Garg AD, Kaczmarek A, Krysko O, Agostinis P, Vandenabeele P. Immunogenic cell death and DAMPs in cancer therapy. *Nat Rev Cancer* (2012) 12:860–75. doi: 10.1038/nrc3380

11. Ahtiainen M, Elomaa H, Väyrynen JP, Wirta EV, Kuopio T, Helminen O, et al. Immune contexture of MMR-proficient primary colorectal cancer and matched liver and lung metastases. *Cancers* (2021) 13(7):1530. doi: 10.3390/cancers13071530

12. Jia L, Pang M, Fan M, Tan X, Wang Y, Huang M, et al. A pH-responsive Pickering Nanoemulsion for specified spatial delivery of Immune Checkpoint Inhibitor and Chemotherapy agent to Tumors. *Theranostics* (2020) 10:9956–69. doi: 10.7150/thno.46089

13. Tang R, Xu J, Zhang B, Liu J, Liang C, Hua J, et al. Ferroptosis, necroptosis, and pyroptosis in anticancer immunity. *J Hematol Oncol* (2020) 13:110. doi: 10.1186/s13045-020-00946-7

14. Zhang Y, Chen Y. Stratification from heterogeneity of the cell-death signal enables prognosis prediction and immune microenvironment characterization in esophageal squamous cell carcinoma. *Front Cell Dev Biol* (2022) 10:855404. doi: 10.3389/fcell.2022.855404

15. Ritchie ME, Phipson B, Wu D, Hu Y, Law CW, Shi W, et al. limma powers differential expression analyses for RNA-sequencing and microarray studies. *Nucleic Acids Res* (2015) 43:e47. doi: 10.1093/nar/gkv007

16. Otasek D, Morris JH, Bouças J, Pico AR, Demchak B. Cytoscape Automation: empowering workflow-based network analysis. *Genome Biol* (2019) 20:185. doi: 10.1186/s13059-019-1758-4

17. Cancer Genome Atlas Research Network, Analysis Working Group: Asan University, BC Cancer Agency, Brigham, Women's Hospital, Broad Institute and Brown University, et al. Integrated genomic characterization of oesophageal carcinoma. *Nature* (2017) 541:169–75. doi: 10.1038/nature20805

18. Shen R, Li P, Li B, Zhang B, Feng L, Cheng S. Identification of distinct immune subtypes in colorectal cancer based on the stromal compartment. *Front Oncol* (2019) 9:1497. doi: 10.3389/fonc.2019.01497

19. Newman AM, Liu CL, Green MR, Gentles AJ, Feng W, Xu Y, et al. Robust enumeration of cell subsets from tissue expression profiles. *Nat Methods* (2015) 12:453–7. doi: 10.1038/nmeth.3337

20. Newman AM, Steen CB, Liu CL, Gentles AJ, Chaudhuri AA, Scherer F, et al. Determining cell type abundance and expression from bulk tissues with digital cytometry. *Nat Biotechnol* (2019) 37:773–82. doi: 10.1038/s41587-019-0114-2

21. Economopoulou P, Koutsodontis G, Strati A, Kirodimos E, Giotakis E, Maragoudakis P, et al. Surrogates of immunologic cell death (ICD) and chemoradiotherapy outcomes in head and neck squamous cell carcinoma (HNSCC). *Oral Oncol* (2019) 94:93–100. doi: 10.1016/j.oraloncology.2019.05.019

22. Yu X, Zeng Q. Random forest algorithm-based classification model of pesticide aquatic toxicity to fishes. *Aquat Toxicol (Amsterdam Netherlands)* (2022) 251:106265. doi: 10.1016/j.aquatox.2022.106265

23. Iasonos A, Schrag D, Raj GV, Panageas KS. How to build and interpret a nomogram for cancer prognosis. *J Clin Oncol* (2008) 26:1364–70. doi: 10.1200/JCO.2007.12.9791

24. Roh W, Chen PL, Reuben A, Spencer CN, Prieto PA, Miller JP, et al. Integrated molecular analysis of tumor biopsies on sequential CTLA-4 and PD-1 blockade reveals markers of response and resistance. *Sci Trans Med* (2017) 9(379):eaah3560. doi: 10.1126/scitranslmed.aah3560

25. Fishilevich S, Nudel R, Rappaport N, Hadar R, Plaschkes I, Iny Stein T, et al. GeneHancer: genome-wide integration of enhancers and target genes in GeneCards. *Database J Biol Database Curation* (2017) 2017:bax028. doi: 10.1093/database/bax028

26. Sun D, Wang J, Han Y, Dong X, Ge J, Zheng R, et al. TISCH: a comprehensive web resource enabling interactive single-cell transcriptome visualization of tumor microenvironment. *Nucleic Acids Res* (2021) 49:D1420–d1430. doi: 10.1093/nar/gkaa1020

27. Carter PJ, Rajpal A. Designing antibodies as therapeutics. *Cell* (2022) 185:2789–805. doi: 10.1016/j.cell.2022.05.029

28. Topalian SL, Taube JM, Anders RA, Pardoll DM. Mechanism-driven biomarkers to guide immune checkpoint blockade in cancer therapy. *Nat Rev Cancer* (2016) 16:275–87. doi: 10.1038/nrc.2016.36

29. Westin J, Sehn LH. CAR T cells as a second-line therapy for large B-cell lymphoma: a paradigm shift? *Blood* (2022) 139:2737–46. doi: 10.1182/blood.2022015789

30. Sellars MC, Wu CJ, Fritsch EF. Cancer vaccines: Building a bridge over troubled waters. *Cell* (2022) 185:2770–88. doi: 10.1016/j.cell.2022.06.035

31. Hsieh YC, Kirschner K, Copland M. Improving outcomes in chronic myeloid leukemia through harnessing the immunological landscape. *Leukemia* (2021) 35:1229–42. doi: 10.1038/s41375-021-01238-w

32. Sui M, Li Y, Wang H, Luo Y, Wan T, Wang X, et al. Two cases of intrahepatic cholangiocellular carcinoma with high insertion-deletion ratios that achieved a complete response following chemotherapy combined with PD-1 blockade. *J immunother Cancer* (2019) 7:125. doi: 10.1186/s40425-019-0596-y

33. Duan X, Chan C, Lin W. Nanoparticle-mediated immunogenic cell death enables and potentiates cancer immunotherapy. *Angewandte Chemie (International Ed English)* (2019) 58:670–80. doi: 10.1002/anie.201804882

34. Minnie SA, Hill GR. Immunotherapy of multiple myeloma. *J Clin Invest* (2020) 130:1565–75. doi: 10.1172/JCI129205

35. Rapoport BL, Anderson R. Realizing the clinical potential of immunogenic cell death in cancer chemotherapy and radiotherapy. *Int J Mol Sci* (2019) 20(4):959. doi: 10.3390/ijms20040959

36. Wiedemann GM, Grassmann S, Lau CM, Rapp M, Villarino AV, Friedrich C, et al. Divergent role for STAT5 in the adaptive responses of natural killer cells. *Cell Rep* (2020) 33:108498. doi: 10.1016/j.celrep.2020.108498

37. Li S, Gao J, Xu Q, Zhang X, Huang M, Dai X, et al. A signature-based classification of gastric cancer that stratifies tumor immunity and predicts responses to PD-1 inhibitors. *Front Immunol* (2021) 12:693314. doi: 10.3389/fimmu.2021.693314

38. Hossain DMS, Javaid S, Cai M, Zhang C, Sawant A, Hinton M, et al. Dinaciclib induces immunogenic cell death and enhances anti-PD1-mediated tumor suppression. *J Clin Invest* (2018) 128:644–54. doi: 10.1172/JCI94586

39. Rodriguez AB, Peske JD, Woods AN, Leick KM, Mauldin IS, Meneveau MO, et al. Immune mechanisms orchestrate tertiary lymphoid structures in tumors *via* cancer-associated fibroblasts. *Cell Rep* (2021) 36:109422. doi: 10.1016/j.celrep.2021.109422

40. Millar E, Browne L, Slapetova I, Shang F, Ren Y, Bradshaw R, et al. TILs immunophenotype in breast cancer predicts local failure and overall survival: analysis in a large radiotherapy trial with long-term follow-up. *Cancers* (2020) 12(9):2365. doi: 10.3390/cancers12092365

41. Overacre-Delgoffe AE, Bumgarner HJ, Cillo AR, Burr AHP, Tometich JT, Bhattacharjee A, et al. Microbiota-specific T follicular helper cells drive tertiary lymphoid structures and anti-tumor immunity against colorectal cancer. *Immunity* (2021) 54:2812–2824.e4. doi: 10.1016/j.immuni.2021.11.003

42. Niogret J, Berger H, Rebe C, Mary R, Ballot E, Truntzer C, et al. Follicular helper-T cells restore CD8(+)-dependent antitumor immunity and anti-PD-L1/PD-1 efficacy. *J immunother Cancer 9* (2021) 9(6):e002157. doi: 10.1136/jitc-2020-002157

43. Yang Y. Cancer immunotherapy: harnessing the immune system to battle cancer. *J Clin Invest* (2015) 125:3335–7. doi: 10.1172/JCI83871

44. Rychkov D, Neely J, Oskotsky T, Yu S, Perlmutter N, Nititham J, et al. Cross-tissue transcriptomic analysis leveraging machine learning approaches identifies new biomarkers for rheumatoid arthritis. *Front Immunol* (2021) 12:638066. doi: 10.3389/fimmu.2021.638066

45. Wang Y, Hwang J, Yadav D, Oda T, Lee PC, Jin JO. Inhibitory effect of porphyran on lipopolysaccharide-induced activation of human immune cells. *Carbohydr polymers* (2020) 232:115811. doi: 10.1016/j.carbpol.2019.115811

46. Nie K, Li J, Peng L, Zhang M, Huang W. Pan-cancer analysis of the characteristics of LY96 in prognosis and immunotherapy across human cancer. *Front Mol Biosci* (2022) 9:837393. doi: 10.3389/fmolb.2022.837393

47. Rajamanickam V, Yan T, Xu S, Hui J, Xu X, Ren L, et al. Selective targeting of the TLR4 co-receptor, MD2, prevents colon cancer growth and lung metastasis. *Int J Biol Sci* (2020) 16:1288–302. doi: 10.7150/ijbs.39098

48. Gradisar H, Keber MM, Pristovsek P, Jerala R. MD-2 as the target of curcumin in the inhibition of response to LPS. *J leukocyte Biol* (2007) 82:968–74. doi: 10.1189/jlb.1206727

frontiers | Frontiers in Immunology

TYPE Original Research
PUBLISHED 29 August 2023
DOI 10.3389/fimmu.2023.1206953

OPEN ACCESS

EDITED BY
Eyad Elkord,
University of Salford, United Kingdom

REVIEWED BY
Scott A. Read,
Western Sydney University, Australia
Ziyuan He,
Allen Institute for Immunology,
United States

*CORRESPONDENCE
Sven H. Loosen
sven.loosen@med.uni-duesseldorf.de
Tom Luedde
luedde@hhu.de

†These authors share last authorship

RECEIVED 16 April 2023
ACCEPTED 02 August 2023
PUBLISHED 29 August 2023

CITATION
Gorgulho J, Roderburg C, Beier F, Bokemeyer C, Brümmendorf TH, Luedde T and Loosen SH (2023) Peripheral blood CD3+HLADR+ cells and associated gut microbiome species predict response and overall survival to immune checkpoint blockade.
Front. Immunol. 14:1206953.
doi: 10.3389/fimmu.2023.1206953

Peripheral blood CD3+HLADR+ cells and associated gut microbiome species predict response and overall survival to immune checkpoint blockade

Joao Gorgulho[1,2], Christoph Roderburg[3,4], Fabian Beier[4,5], Carsten Bokemeyer[1], Tim H. Brümmendorf[4,5], Tom Luedde[3,4*†] and Sven H. Loosen[3,4*†]

[1]Department of Oncology, Hematology and Bone Marrow Transplantation with Section of Pneumology, University Medical Centre Hamburg-Eppendorf, Hamburg, Germany, [2]Mildred Scheel Cancer Career Center, University Cancer Center Hamburg, University Medical Center Hamburg-Eppendorf, Hamburg, Germany, [3]Department of Gastroenterology, Hepatology and Infectious Diseases, University Hospital Düsseldorf, Medical Faculty of Heinrich Heine University Düsseldorf, Düsseldorf, Germany, [4]Center for Integrated Oncology Aachen-Bonn-Cologne-Düsseldorf (CIOABCD), Aachen, Germany, [5]Department of Medicine IV, University Hospital Rheinisch Westfällisch Technische Hochschule (RWTH) Aachen, Aachen, Germany

Background: The search for biomarkers to identify ideal candidates for immune checkpoint inhibitor (ICI) therapy is fundamental. In this study, we analyze peripheral blood CD3+HLADR+ cells (activated T-cells) as a novel biomarker for ICI therapy and how its association to certain gut microbiome species can indicate individual treatment outcomes.

Methods: Flow cytometry analysis of peripheral mononuclear blood cells (PBMCs) was performed on n=70 patients undergoing ICI therapy for solid malignancies to quantify HLA-DR on circulating CD3+ cells. 16s-rRNA sequencing of stool samples was performed on n=37 patients to assess relative abundance of gut microbiota.

Results: Patients with a higher frequency of CD3+HLADR+ cells before treatment initiation showed a significantly reduced tumor response and overall survival (OS), a worst response and experienced less toxicities to ICI therapy. As such, patients with a frequency of CD3+HLADR+ cells above an ideal cut-off value of 18.55% had a median OS of only 132 days compared to 569 days for patients below. Patients with increasing CD3+HLADR+ cell counts during therapy had a significantly improved OS. An immune signature score comprising CD3+HLADR+ cells and the neutrophil-lymphocyte ratio (NLR) was highly significant for predicting OS before and during therapy. When allied to the relative abundance of microbiota from the Burkholderiales order and the species Bacteroides vulgatus, two immune-microbial scores revealed a promising predictive and prognostic power.

Conclusion: We identify the frequencies and dynamics of CD3+HLADR+ cells as an easily accessible prognostic marker to predict outcome to ICIs, and how these could be associated with immune modulating microbiome species. Two

unprecedented immune-microbial scores comprising CD3+HLADR+, NLR and relative abundance of gut bacteria from the Burkhorderiales order or Bacteroides vulgatus species could accurately predict OS to immune checkpoint blockade.

KEYWORDS

PD-1, HLA-DR, checkpoint inhibitors, microbiome, prognosis, biomarker

Introduction

Immune checkpoint inhibitors (ICI) contributed to a drastic change in the landscape of cancer therapy, giving hope to many advanced cancer patients, which are now able to achieve improved response and overall survival (1–3). Currently, more than 8 different such agents have been approved for a wide spectrum of cancer entities (4). Nonetheless, many patients only experience toxicities and/or fail to respond to ICI therapy. The question, which patients would mostly benefit from immune checkpoint blockade, remains yet unanswered, despite countless studies identifying different biomarker candidates. Among these are peripheral blood-based biomarkers such as specific lymphocyte subpopulations (5) and the neutrophil-to-lymphocyte ratio (NLR) (6), as well as the relative abundance of diverse taxa in the gut microbiome with a certain heterogeneity across cohorts (7).

The human leukocyte antigen-DR isotype (HLA-DR) is a major-histocompatibility complex class II (MHC-II) molecule present on the surface of antigen presenting cells (APCs), which together with a foreign peptide constitute a ligand for T-cells and engage T-cell response. It is known as an immune stimulation and late activation marker (8) for T-cells. CD3+HLADR+ cells are deemed as activated T lymphocytes, which are upregulated in autoimmune diseases (9) and HIV infection (10). In cancer patients they have had divergent results, with high CD3+HLADR+ levels being associated with shorter relapse-free survival in Hodgkin and non-Hodgkin lymphoma (11, 12), but with better response to neoadjuvant therapy in breast cancer (13). Studies assessing HLA-DR expression on lymphocytes as a potential biomarker for ICI therapy are scarce and focus mainly on single tumor entities (14).

The gut microbiome, which shows tremendous immune modulatory effects, mediated through different species (7), has recently emerged as another field of interest in terms of predicting response to immune checkpoint blockade. An active manipulation of the human microbiome through dietary interventions (15) or fecal microbiota transplantation (FMT) seems to increase efficacy to ICI therapy, and can even, in some cases, overcome a prior resistance to PD-1 and CTLA-4 antibodies (16). However, an association between activated T cells and specific microbiome species have, to our knowledge, not been studied. In the present analysis, we evaluate the prognostic role of CD3+HLADR+ cell frequencies and its dynamics during ICI therapy and analyze how they correlate with the relative abundance of microbiome species that could influence HLA-DR expression.

Abbreviations: (n)DC, (non-)Disease Control; APC, Antigen Presenting Cell; CPN, Cancer Patient Network; CR, Complete Remission; FMT, Fecal Microbiota Transplantation; HLA-DR, Human Leukocyte Antigen-DR Isotype; ICI, Immune Checkpoint Inhibitor; IL-12- Interleukin-12; IMS, Immune-Microbial Score; IRAE, Immune Related Adverse Event; MHC-II, Major Histocompatibility Complex II; NLR, Neutrophil to Lymphocyte Ratio; OS, Overall Survival; OUT, Operational Taxonomic Unit; PBMC, Peripheral Blood Mononuclear Cell; PD, Progressive Disease; PFS, Progression Free Survival; PR, Partial Remission; SD, Stable Disease; TMB, Tumor Mutational Burden; UICC, Union for International Cancer Control.

Patients and methods

Study population

70 patients with advanced stage solid neoplasia were prospectively recruited at the interdisciplinary cancer outpatient clinic at the University Hospital RWTH Aachen from August 2017 to September 2019 (see Table 1 for patient characteristics) before undergoing ICI therapy, as described before (17). The study was conducted in accordance with the ethical standards laid down in the 1964 Declaration of Helsinki and its later amendments and the protocol was approved by the ethics committee of the University Hospital RWTH Aachen, Germany (EK 206/09) with all patients delivering written informed consent.

Determination of response to ICI therapy

Patients were regularly consulted by a trained oncologist prior to each therapy cycle. Determination of response to ICI therapy was based on clinical and radiological evaluation by CT scan approximately every three months, evaluated by at least two independent experienced radiologists. Based on the assessment, patients were stratified into two groups: patients with a complete response (CR), partial response (PR) and stable disease (SD) were included in the “disease control” (DC) group, while the ones who exhibited progressive disease (PD) were enrolled in the “non-DC” group.

Assessment of peripheral PBMC subsets

One peripheral blood EDTA tube was drawn per patient (n=70) prior to ICI therapy initiation, at an early (after one to two cycles,

TABLE 1 Patient characteristics.

Parameter	Study cohort	Subgroup of patients for microbiome analysis
Cancer patients	n=70	n=37
Sex [%]:		
male-female	70.0 - 30.0	64.9 – 35.1
Age [years, median and range]	67.0 [38-87]	67.4 [38-87]
BMI [kg/m^2, median and range]	24.4 [15.9-42.3]	25.2 [15.9-40.0]
Tumor entity [%]		
NSCLC Melanoma Urogenital tract GIT Head and neck Other malignancies	34.2 20.0 12.9 14.3 10.0 8.6	29.7 29.7 13.5 10.8 5.4 10.8
Staging [%]		
UICC III UICC IV	10.0 90.0	13.5 86.5
ECOG PS [%]		
ECOG 0 ECOG 1 ECOG 2 ECOG 3	7.1 54.2 37.2 1.5	13.5 59.5 27.0 0.0
Therapeutic agent [%]		
Nivolumab monotherapy Pembrolizumab monotherapy Nivolumab/Ipilimumab Other (Avelumab, Durvalumab)	61.4 22.9 8.6 7.1	59.5 16.2 13.5 10.8
Smoker status [%]		
Never Yes, ex Yes, present Unknown	10.0 41.4 14.3 34.3	13.5 37.8 10.8 37.8
Prior therapy [%]		
Yes No	67.1 32.9	56.9 43.2
Side effects [%]		
Any CTC G3 or higher	38.6 7.1	45.9 10.8

BMI, body mass index; ECOG PS, "Eastern Cooperative Oncology Group" performance status, NSCLC, non-small cell lung cancer; GIT, gastrointestinal tract; CTC, common toxicity criteria.

n=51) and late time-point (after three to five cycles, n=47) during therapy. Freshly isolated cells were lysed using the Immunoprep Reagent System (Beckman Coulter) and staining was performed with two different flow cytometry panels. Panel 1 was stained with the antibody mix CD45-FITC/CD56-PE/CD19-ECD/CD3-PC5, to which the antibody CD-16 PE was added, and panel 2 was stained with the antibody mix CD45-FITC/CD4-PE/CD8-ECD/CD3-PC5, to which the antibody HLA-DR-PC7 was added (all antibodies from Beckman Coulter, Krefeld, Germany), according to manufacturer´s instructions. Flow-cytometry analysis was carried out and analyzed using NAVIOS cytometer and analysis software (Beckman Coulter). These analyses were performed within the clinical routine diagnostics of immune status by the hematological laboratory of the department of medicine IV of the University Medical Center Aachen, which includes standardized gating strategy to distinguish B cells (CD19+), NK cells (CD3-CD56+CD16+), and T cell subsets (CD3+CD4+, CD3+CD8+, CD3+CD56+CD16+, CD3+HLA-DR+) (Supplementary Figures 1A–D).

16s rRNA sequencing of stool samples and amplicon sequence analysis

Stool samples were obtained from n=37 patients before initiation of therapy and from n=15 patients after three to five cycles during therapy using a stool collection tube with 8ml DNA stabilization Buffer (Stratec Molecular GmbH, Berlin, Germany) and frozen aliquots were preserved at -80°C until further processing. Samples were sequenced at the ZIEL Institute for Food & Health Core Facility Mikrobiom/NGS (Freising, Germany) according to methods described before (18). Shortly, bead-beating and heat-treatment were used for cell lysis and gDNA columns (Macherey-Nagel, Düren, Germany) were employed to purify metagenomic DNA. The V3/V4 region of 16 S ribosomal RNA (rRNA) genes was amplified (25 cycles) from 24 ng DNA using primers 341F and 785R49. After purification using the AMPure XP system (Beckmann Coulter Biomedical GmbH), sequencing was carried out in paired-end mode (PE275) with pooled samples using a MiSeq system (Illumina, Inc., San Diego, California, USA) following the manufacturer's instructions and a final DNA concentration of 10 pM and 15% (v/v) PhiX standard library. The generated raw read files were pre-processed using the IMNGS platform (19), a pipeline based on the UPARSE approach (20) to build sample-specific sequence databases and OTU-based profiles. We then further analyzed generated data using the Rhea pipeline in R studio version 1.2.5, a set of R scripts for analysis of Operational Taxonomic Units (OTUs) (21). Only OTUs with a relative abundance > 0.5% total sequences in at least one sample were further analyzed. For precise identification of certain OTU sequences, the EzBioCloud database was used (22).

Statistical analysis

Shapiro-Wilk-Test was used to check for normal distribution of the data. By employing the Mann-Whitney-U-Test and Kruskal-Wallis-H-Tests, non-parametric data were compared. The median, quartiles and ranges of these data are displayed in box plot graphics. Kaplan-Meier curves aided in demonstrating the influence of a specific parameter on OS. The Log-rank test was used to evaluate statistical differences between subgroups. Repeated measures ANOVA was used for longitudinal analyses of CD3+HLADR+ frequencies at the three time-points (before ICI treatment, early and late time-point), reporting the main F-test. For calculation of the optimal cut-off of CD3+HLADR+ cell frequencies and counts, NLR and relative abundances of specific microbiome taxa to discriminate between short- and long-term survivors, the "Charité cut-off finder" was applied, which fits Cox proportional hazard models to the dichotomized survival status (deceased or alive) as well as the survival time (duration between first ICI administration and death/last follow-up) and defines the optimal cut-off as the value with the most significant split in log-rank test (23). In addition, uni- and multivariate Cox-regression was performed with parameters with a p-value of <0.100 in univariate testing being included into multivariate testing. The hazard ratio (HR) and the 95% confidence interval are displayed. Gut microbiome analysis was performed using the Rhea pipeline (21), mainly the normalization (to account for differences in sequence depth), beta- (computed based on generalized UniFrac distances) (24) and alpha-diversity (on the basis of species richness and Shannon effective diversity) (25), as well as taxonomic binning steps (using SILVA and RDP classifier) (26, 27). The Spearman correlation coefficient was used for correlation analyses between flow cytometry data and relative abundances of specific taxa in the gut microbiome. All statistical analyses were performed using SPSS 23 and 25 (SPSS, Chicago, IL, USA) and R studio version 1.2.5 (Posit PBC, Boston, MA, USA). A p-value of < 0.05 was considered statistically significant (* $p < 0.05$; ** $p < 0.01$; *** $p < 0.001$).

Results

Characteristics of the study population

70 patients with advanced solid malignancies receiving ICI therapy were included (detailed characteristics are shown in Table 1). The median age was 67.0 years (range 38 to 87 years).; 70.0% were males. The predominant cancer entity was NSCLC (34.2%), followed by malignant melanoma (20.0%), urogenital cancer (12.9%), GI-cancers (14.3%), head and neck tumors (10.0%) and others (8.6%). Only patients in UICC stadium III (10.0%) and IV (90.0%) were recruited. Immune related adverse effects (IRAE) of any grade were experienced by 38.6% of patients and 7.1% experienced IRAE graded ≥3. All patients were treated with immune checkpoint inhibitors only. Of all 70 patients, a subgroup of 37 and 16 patients were available for stool microbiome analyses at baseline and at 3 months after treatment initiation (see Table 1).

Baseline frequencies of peripheral blood CD3+HLA-DR+ cells significantly predict toxicity, response at 6 months and survival at 6 months after initiation of immune checkpoint blockade

First, we assessed differences between pretreatment CD3+HLADR+ cell frequency between ICI-responders (DC) and non-responders (non-DC) three and six months after therapy initiation. In this case, only a non-significant trend towards a higher CD3+HLADR+ cell frequency in non-responders compared to responders could be observed after 3 months, however a clear association between a better therapy response and lower pretherapeutic CD3+HLA-DR+ cell frequencies ($p_{3months}=0.051$, $p_{6months}=0.008$, Figures 1A, B) was observed. When looking at 3- and 6-months-survival, patients who were still alive six months after treatment initiation had a significantly lower initial CD3+HLA-DR+ cell frequency compared to non-survivors ($p=0.003$, $median_{survivor}=6.65\%$, $median_{deceased}=11.15\%$), while a similar trend towards lower CD3+HLADR+ cell frequency among patients who

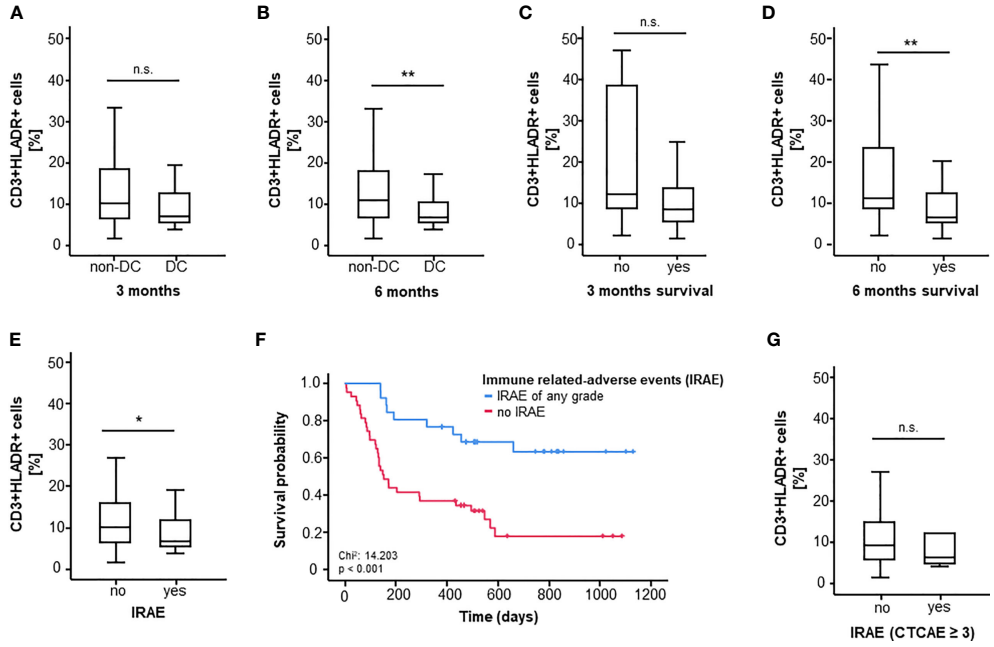

FIGURE 1
CD3+HLADR+ cell frequencies before ICI therapy significantly predict OS, response and toxicity. **(A, B)** High CD3+HLADR+ cell frequencies in the peripheral blood at baseline indicate a worse response to ICI therapy at 3 and 6 month ($p_{3months}$=0.051, $p_{6months}$=0.008). **(C, D)** High baseline CD3+HLADR+ cell frequencies indicate poor 3 and 6 months survival under immune checkpoint blockade ($p_{3months}$=0.067, $p_{6months}$=0.003). **(E)** Baseline CD3+HLADR+ cell frequencies are higher among patients who develop immune related adverse events (IRAE) under ICI therapy (p=0.043). **(F)** Overall survival is lower in patients who do not develop any grade of IRAE (median OS: 151 days vs. "not reached", p<0.001). **(G)** Baseline frequencies of CD3+HLADR+ cells do not differ between patients experiencing IRAE ≥ grade 3 and patients who do not (p=0.595). *: significant (p<0.05); **: highly significant (p<0.01); n.s.: not significant (p>0.05).

died within the first three months became apparent (p=0.067, Figure 1C, D).

In a further step, we looked at differences in CD3+HLADR+ cell frequencies with respect to treatment-related adverse events. Interestingly, patients not experiencing IRAE of any grade had significantly higher CD3+HLADR+ cell frequencies ($median_{yes}$=6.60% vs. $median_{no}$=10.00%, p=0.043, Figure 1E). Notably, in our cohort, patients who experienced IRAE of any type showed an improved overall survival (p<0.001, Figure 1F). However, the presence of HLA-DR expressing T cells before treatment failed to predict iRAE graded 3 or higher among all patients (p=0.595, Figure 1G).

Frequencies of peripheral blood CD3+HLADR+ cells are comparable across different clinical characteristics but associated with the ECOG performance status and can be influenced by the ICI regimen

For further characterization of the predictive role of CD3+HLADR+ values in ICI therapy, these were evaluated according to different clinical characteristics. Regarding tumor entity, sex, tumor stadium (UICC), smoking status and whether patients had previous lines of systemic therapy, no significant differences could be observed (Supplementary Figures 2A–E). Notably, there was a significantly higher peripheral blood CD3+HLADR+ frequency in patients with a higher ECOG performance status compared to patients with a lower ECOG performance status (p=0.026, Supplementary Figure 2F). Despite observing no significant difference between CD3+HLADR+ cell frequencies at baseline with respect to the administered ICI agent (Supplementary Figure 2G), HLADR+ cell frequencies were significantly higher at the early time-point in patients receiving a combined anti-PD-1/CTLA immune checkpoint blockade with Nivolumab and Ipilimumab (p=0.036, Supplementary Figure 2H).

Pretreatment circulating CD3+HLADR+ frequencies are an independent predictor of overall survival to ICI therapy

Based on the predictive power of activated T cells regarding 3- and 6-months-survival, we next took a deeper look at the prognostic role of these cells with respect to OS using Kaplan-Meier-curve estimates. In a first step, patients were split into two groups based on the median frequency of these cells. Interestingly, the median CD3+HLADR+ frequency (9.1%) at baseline significantly discriminated between short- and long-term survivors (p=0.035, Figure 2A). Since the median is likely not ideal to discriminate patients regarding OS, we then applied the Charité cut-off finder (further described in Patients and Methods) to establish a prognostically highly relevant cut-off value for CD3+HLADR+ cell frequencies (18.5%). Patients with a pretreatment CD3+HLADR cell frequency below this ideal cut-off survived

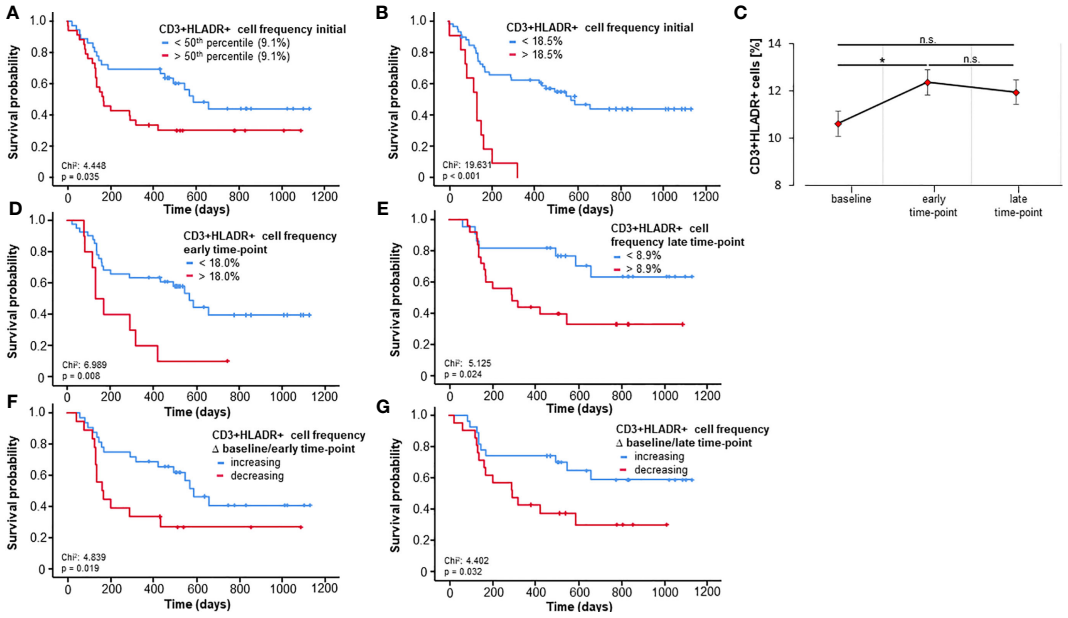

FIGURE 2
Baseline and longitudinal frequencies of circulating CD3+HLADR+ cells predict overall survival to immune checkpoint blockade. **(A)** Patients with baseline CD3+HLADR+ cell frequencies above the median (9.1%) have a significantly impaired overall survival (OS, p=0.035). **(B)** A baseline CD3+HLADR+ cell frequency above the ideal cut-off value (18.5%) indicate a significantly reduced median OS (132 vs. 569 days, p<0.001). **(C)** Frequencies of CD3+HLADR+ cells significantly increase from baseline to the early-time point (p=0.015) but remain unaltered thereafter (error bars indicate SEM). **(D, E)** Patients with CD3+HLADR+ cell frequencies above the ideal cut-off at the early and late time-point have a significantly impaired OS (p_{early}=0.008, p_{late}=0.024). **(F, G)** Increasing CD3+HLADR+ cell frequencies between baseline and the early or late time-point indicate a better outcome ($p_{baseline/early}$=0.019, $p_{baseline/late}$=0.032). *: significant (p<0.05); **: highly significant (p<0.01); n.s.: not significant (p>0.05).

significantly longer (median 569 days) than patients above this threshold (median 132 days, p<0.001, Figure 2B).

For further characterization of the role of CD3+HLADR+ cell frequencies as independent predictors of OS, we applied uni- and multivariate Cox-regression analyses. Univariate Cox-regression further sustained our hypothesis that the frequency of CD3+HLADR+ cells acts as a potent prognostic predictor in patients undergoing immune checkpoint blockade (HR: 1.068 [95%CI: 1.037 – 1.099], p<0.001, Table 2). Next, we included several prognostically relevant parameters such as CD3+CD8+ cell frequencies at baseline, ECOG PS, Hemoglobin, AST and ALT (p<0.110, Table 2) into multivariate Cox-regression analysis, which revealed peripheral blood CD3+HLADR+ cell frequencies as an independent predictor for OS in patients before commencement of ICI therapy (HR: 1.054 [95%CI: 1.007-1.103], p=0.024, Table 2).

Frequency of CD3+HLADR+ cells during ICI treatment can predict overall survival

Consequently, we evaluated the relevance of circulating activated T cells throughout therapy using two further time points beyond the baseline: an early time-point (after only one or two cycles of therapy, n=51) and a late time-point (after three to five cycles of therapy, n=47). First, we looked at how ICI could influence the abundance of these circulating cells during therapy. By employing repeated measures ANOVA analysis comprising the three time-points we could show that there was no significant effect across all time-points (F (1.35, 48.65) = 1.686, p=0.201, Figure 2C), however a significant difference could be demonstrated in the *post hoc* pairwise comparison using the Bonferroni correction between the baseline and the early-time point (p=0.015). As pretreatment frequencies of activated T cells were strong predictors of OS, we next hypothesized that longitudinal values could also be prognostically relevant and serve to monitor therapy during its course. As before, we calculated optimal cut-off frequencies of circulating CD3+HLADR+ cells at the early and late-time points (frequency of CD3+HLADR+$_{early}$: 18.0%, frequency of CD3+HLADR+$_{late}$: 8.9%). As hypothesized, patients with a frequency of activated T-cells above the ideal cut-off survived significantly shorter than patients with frequencies below (p_{early}=0.008, HR_{early}: 2.790 [95%CI: 1.261-6.177], p=0.011; p_{late}=0.024, HR_{late}: 2.714 [95%CI:1.104-6.667], p=0.030, Figures 2D, E). Next, we looked at how the ICI-induced dynamics of these frequencies (increasing/decreasing between baseline and early/late time-point) predicted OS. Notably, patients with increasing frequencies of CD3+HLADR+ cells between baseline and the early as well as late time points showed a significantly improved overall survival, with patients with increasing levels living a median of 587 days (Δ baseline/early time-point) and for Δbaseline/late time-point not reaching their median OS, while patients with decreasing frequencies of activated T cells had a median OS of only 162 and 292 days, respectively ($p_{early/baseline}$=0.019, $HR_{early/baseline}$: 2.338 [95%CI: 1.126-4.854], p=0.023, $p_{late/baseline}$=0.032, $HR_{late/baseline}$: 2.423 [95%CI: 1.052-5.576], p=0.018, Figures 2F, G).

TABLE 2 Uni- and multivariate Cox-regression analysis for the prediction of overall survival.

Parameter	univariate Cox-regression		multivariate Cox-regression	
	p-value	Hazard-Ratio (95% CI)	p-value	Hazard-Ratio (95% CI)
CD3+HLADR+ frequency	<0.001	1.068 (1.037-1.099)	0.024	1.054 (1.007-1.103)
CD3+CD8+ frequency	0.107	1.022 (0.995-1.050)	0.417	0.982 (0.940-1.026)
Age	0.679	1.006 (0.979-1.033)		
Sex	0.796	0.971 (0.474-1.773)		
UICC tumor stage	0.432	1.604 (0.494-5.213)		
ECOG PS	0.012	1.977 (1.164-3.356)	0.059	1.953 (0.976-3.907)
Leukocyte count	0.521	1.020 (0.961-1.082)		
Neutrophil count	0.440	1.000 (1.000-1.000)		
Lymphocyte count	0.275	1.000 (0.999-1.000)		
NLR	0.166	1.021 (0.992-1.051)		
Hemoglobin	0.001	0.865 (0.794-0.943)	0.087	0.915 (0.826-1.013)
Sodium	0.379	0.969 (0.903-1.040)		
Potassium	0.250	0.671 (0.341-1.323)		
ALT	0.005	1.012 (1.004-1.020)	0.147	1.014 (0.995-1.033)
AST	0.023	1.012 (1.002-1.022)	0.801	0.997 (0.977-1.018)
Bilirubin	0.022	1.069 (1.010-1.131)	0.232	1.050 (0.969-1.138)
Creatinine	0.788	0.948 (0.643-1.397)		
LDH	0.777	1.000 (0.998-1.002)		

UICC, Union for International Cancer Control; ECOG PS, Eastern Cooperative Oncology Group performance status; NLR, neutrophil to lymphocyte ratio; ALT, alanin aminotransferase; AST, aspartate aminotransferase; LDH, lactate dehydrogenase.

Frequency of CD3+HLADR+ cells predict toxicity, response and overall survival in patients undergoing monotherapy with a single ICI agent

Bearing in mind that, in our study, patients undergoing dual blockade contribute majorly to the significant increase in CD3+HLADR+ cell frequencies after the first cycle of therapy (Figure 2C, Supplementary Figure 2G–H), we have performed an analysis of response, OS and toxicity in patients undergoing ICI monotherapy (n=64) (Supplementary Table 2). As seen in the table, we could show that the role of CD3+HLADR+ cell frequencies in the peripheral blood towards predicting response ($p_{3months}$=0.089, $p_{6months}$=0.016), and toxicity (p=0.109) and OS remains (Ideal cut off: 18.5%, median OS 587 vs. 132 days, p<0.001, HR: 5.003 [95%CI: 2.308-10.845], p<0.001), even when regarding longitudinal values and their dynamics (p_{early}<0.001, HR_{early}: 4.508 [95%CI:1.860-10.925], p_{late}=0.031, HR_{late}: 2.640 [95%CI:1.056-6.603]; $p_{early/baseline}$=0.035, $HR_{early/baseline}$: 2.240 [95%CI: 1.038-4.830], p=0.040, $p_{late/baseline}$=0.038, $HR_{late/baseline}$: 2.410 [95%CI: 1.024-5.673], p=0.044), despite the exclusion of patients undergoing dual immune checkpoint blockade (n=6). The calculated ideal cut-offs using the Charité cut-off finder are the same for both patient populations (single agent vs. all). We then compared OS using Kaplan Meier estimates of monotherapy vs dual therapy patients, showing no significant differences (p=0.677).

An immune signature score comprising CD3+HLADR+ cell frequencies and the neutrophil-to-lymphocyte ratio is a highly significant OS predictor

The NLR, a well investigated biomarker for patients undergoing ICI (6), was validated in our cohort as a predictor of OS for all three time-points (baseline, early and late time-points), when using its respective ideal cut-off value ($NLR_{baseline}$:4.37, $p_{baseline}$<0.001; NLR_{early}:3.95, p_{early}=0.049; NLR_{late}:6.33, p_{late}=0.001; Figure 3A–C). Repeated measures ANOVA analysis demonstrated no significant change in NLR across all three time-points (F (2, 92) = 1.053, p=0.353, Figure 3D), Based on these results and the findings above related to CD3+HLADR+, we established an immune signature score combining CD3+HLADR+ and NLR and how it could predict OS. In this case, frequencies of CD3+HLADR+ and NLR above the ideal cut-off were seen as risk factors. Patients bearing e.g., two risk factors had a significantly shorter OS (median OS 132 days) compared to patients with no risk factors (median OS not reached) (p<0.001, HR: 12.454 [95%CI: 4.221-36.749], p<0.001,

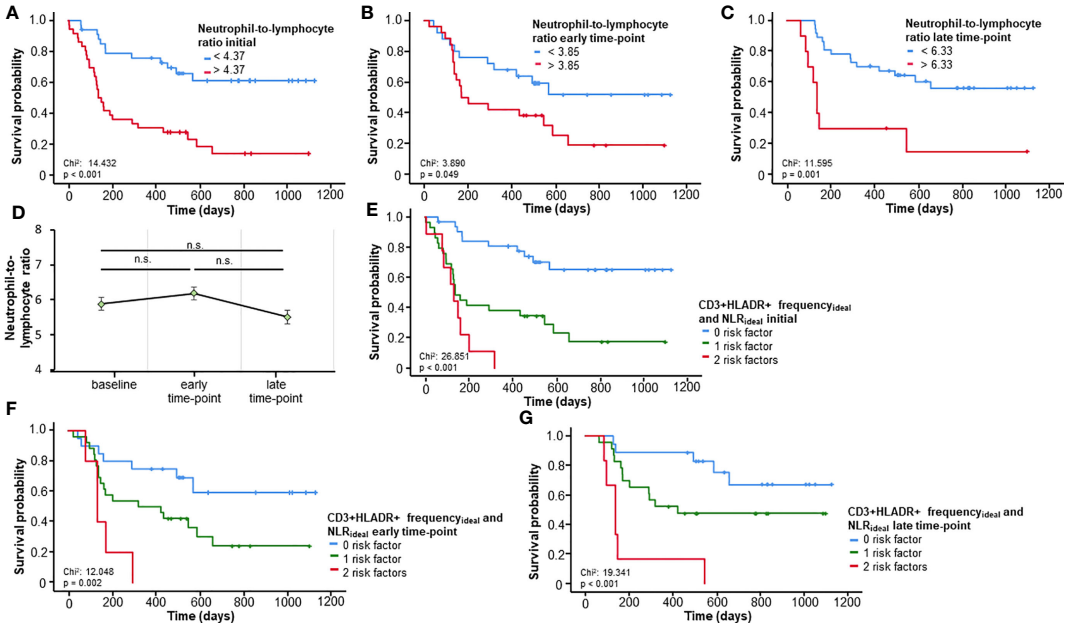

FIGURE 3
Prognostic relevance of the neutrophil-to-lymphocyte ratio (NLR) and a prognostic immune signature score including CD3+HLADR+ cell frequencies. **(A-C)** A NLR above the respective ideal cut-off value at baseline or the early/late time-point is associated with a significantly impaired overall survival (OS). **(D)** The NLR remains unaltered over time (error bars indicate SEM). **(E)** A novel immune signature score comprising baseline frequencies of CD3+HLADR+ cells and the NLR significantly predict OS. **(F, G)** The combined immune signature score shows a strong prognostic relevance for the early and late time-points. n.s.: not significant (p>0.05).

Figure 3E). This score could also significantly predict OS at the early and late-time points of therapy (p_{early}=0.002, HR_{early}: 2.000 [95%CI: 1.120-3.571], p_{early}=0.019; p_{late}<0.001, HR_{late}: 2.143 [95%CI: 1.157-3.970], p_{late}=0.015, Figures 3F, G).

Correlation between CD3+HLADR+ frequencies, T cell subsets and gut microbiome taxa

In a latter step, we took a glance at how the prognostically highly relevant CD3+HLADR+ cell frequencies correlated with other immune status parameters, clinical parameters and relative abundance of taxa from the gut microbiome measured by 16s rRNA sequencing. Figure 4 depicts an overview of gut microbiome analyzes, with patients showing no significant different beta-diversity related to time-point, response and survival at 6 months therapy (Figure 4A–C). Furthermore, relative abundances of specific taxa do not differ significantly between baseline and late-time point, despite interesting shifts in the proportions that some taxa represent within the gut microbiome. At the order level, the proportion of Bacteroidales decreased from 40% before therapy to about 25.5% at the late time point, while Clostridiales, which before therapy represented 52.1% of all orders, increased to 65.0% at the late time-point. At a family level, Lachnospiracae represented 38.9% before therapy, a proportion which decreased to 29.3% after treatment (Figure 4D–L).

Regarding the immune status, frequencies of CD3+HLADR+ cells significantly correlated with the frequency of CD3+CD8+ cells (p<0.001, r_s=0.521, Supplementary Figure 3A), and the frequency of CD3+CD4+ cells (p=0.002, r_s=-0.360, Supplementary Figure 3B). Concerning clinical parameters, CD3+HLADR+ cell frequencies correlated with the ECOG performance status (p=0.005, r_s=0.329, Supplementary Figure 3C). Finally, with regards to the measured microbiome taxa, the presence of activated T cells in the peripheral blood correlated with the relative abundance of the order Burkholderiales (p=0.006, r_s=-0.474, Supplementary Figure 3D). At a deeper taxa level inside this order, these frequencies showed further correlations to the family Sutterellaceae (p=0.001, r_s=-0.628, Supplementary Figure 3E) and within it the genus Sutterella (p=0.010, r_s=-0.474 Supplementary Figure 3F). Furthermore, a significant correlation could be established to the Genus Bacteroides (p=0.029, r_s=-0.365 Supplementary Figure 3G). More detailed values on these taxa are depicted in Supplementary Table 1.

Baseline CD3+CD8+ cell frequencies also play a role in toxicity, response and overall survival prediction to ICI therapy, yet inferior to CD3+HLA-DR+ cell frequency

Since CD3+HLA-DR+ cell frequencies positively correlate significantly with CD3+CD8+ cell frequencies in our cohort, while negatively correlating with CD3+CD4+ cell frequencies, we postulate that most of these CD3+HLA-DR+ cells are indeed CD3+CD8+HLA-DR+ cells. To further investigate this aspect, we looked at the role that baseline CD3+CD8+ cells play regarding response, toxicity and OS prediction for patients in our cohort

10.3389/fimmu.2023.1206953

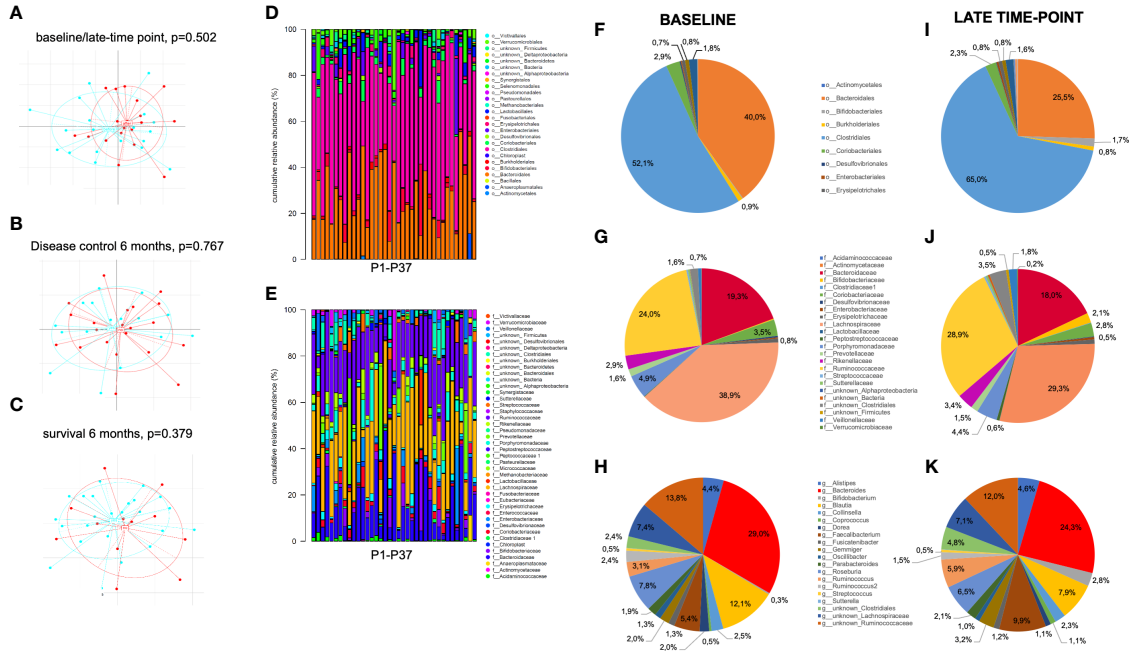

FIGURE 4
Overview of gut microbiota analyses in stool samples of patients before and after initiation of ICI treatment. **(A-C)** Beta-diversity across gut microbioma samples did not significantly differ between **(A)** pretherapeutic (blue) and late time-point (red), **(B)** responders (blue) vs. non-responders (red) and **(C)** patients who were still alive (blue) vs. deceased (red) at 6 months of ICI therapy. **(D, E)** Taxonomic binning at order **(D)** and family level **(E)** shows comparable relative abundance of different taxa across all 37 pretherapeutic samples. **(F-K)** Comparison of baseline to late time-point relative abundance of bacterial orders **(F, I)**, families **(G, J)** and the most frequent genus **(H, K)** show non-significant shifts of bacterial composition between both time points.

(Supplementary Table 3). CD3+CD8+ baseline cell frequencies seem to play a role in predicting disease control at 3 and 6 months (p=0.044 and p=0.026 respectively), toxicity of all grades (p=0.025), as is the case for CD3+HLA-DR+ cell frequencies. Also, by calculating an ideal cut-off for CD3+CD8+ cell frequency (23.65%) it is possible to discriminate between short- and long-term survivors, with patients with cell frequency values above 23.65% at baseline surviving a median of only 170 days compared to 658 days for patients below this value (HR: 2.323 [95%CI: 1.221-4.418], p=0.010). However, when using univariate Cox regression analysis, CD3+CD8+ cell frequencies at baseline do not pose as an independent predictor of overall survival, contrarily to CD3+HLA-DR+ cells (UVA: p=0.107). When adding CD3+CD8+ cells to the multivariate analysis, the independent prognostic power of CD3+HLA-DR+ cells is unaffected (HR: 1.054 [95%CI: 1.007-1.103], p=0.024, Table 2). Notably, despite the fact that the strong positive correlation between these two cell populations is not only present at baseline (p<0.001, rs=0.521) but also at early (p=0.004, rs=0.397) and late time-points (p=0.001, rs=0.484), contrarily to longitudinal values of CD3+HLA-DR+ and their dynamics that pose as predictors of overall survival through the course of therapy as shown above, longitudinal values of CD3+CD8+ and their dynamics don't show any type of predictive value, even when calculating an ideal-cut off (p_{early}=0.4, plate=0.056, p_{early}/baseline=0.319, p_{late}/baseline=0.995).

Relative abundance of specific gut microbiome taxa associated with CD3+HLADR+ cell frequencies can significantly predict overall survival

Here, we focused on four taxa that showed associations to the frequencies of CD3+HLADR+ cells: the Burkholderiales order, the Sutterellaceae family, Genus Sutterella and the Genus Bacteroides. Patients with a relative abundance of bacteria from the Burkholderiales order below the ideal cut-off of 0.422% lived significantly shorter (median OS 129 days) than patients with values above this cut-off (median OS not reached, p<0.001, HR: 6.219 [95%CI: 2.217-17.446], p=0.001, Figure 5A). Inside this order, a similar effect could be demonstrated for bacteria from the Sutterellaceae family related to an ideal cut-off of 0.405% (p=0.029, Supplementary Figure 4A) and within it the Genus Sutterella (Sutterella$_{ideal}$:0.254%, p=0.032, Supplementary Figure 4B) The Bacteroides genus failed to pose as a significant predictor of OS (p=0.064, Supplementary Figure 4C), but within it, we identified a prognostically significant OTU representing the species Bacteroides (B.) vulgatus (OTU3). Patients with a relative abundance of B. vulgatus above the ideal cut-off (7.146%) lived significantly longer (p=0.015, HR: 5.153 [95%CI: 1.186-22.397], p=0.029, Figure 5B) than patients below this value. When looking at these prognostically relevant taxa in a follow-up stool sample after

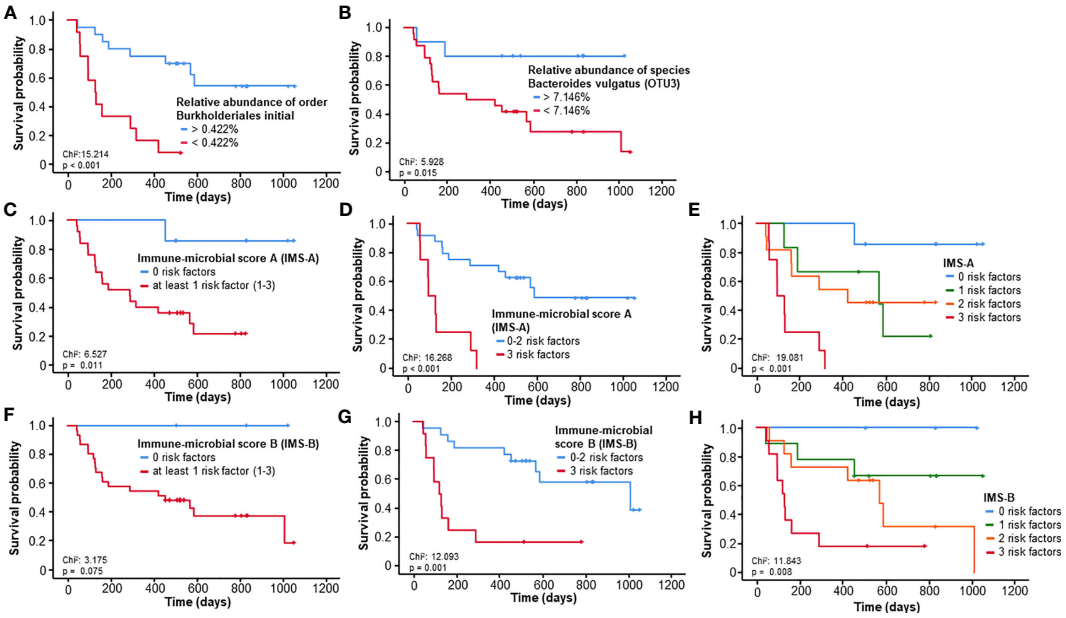

FIGURE 5
Prognostic relevance of specific gut microbiome taxa associated with CD3+HLADR+ cell frequencies. **(A, B)** A relative abundance of bacteria from the Burkholderiales order or Bacteroides vulgatus species below the ideal cut-off is associated with a significantly impaired outcome. **(C–E)** The immune-microbial score A (comprising ideal cut-offs of the NLR, the frequency of CD3+HLADR+ cells and the rel. abundance of the Burkholderiales order) is a strong predictor of survival in patients undergoing ICI therapy. **(F–H)** The immune-microbial score B (comprising ideal cut-offs of the NLR, the frequency of CD3+HLADR+ cells and the rel. abundance of Bacteroides vulgatus) is a strong predictor of survival in patients undergoing ICI therapy.

three to five cycles, these showed no prognostic relevance, possibly due to the low sample number (n=15). Nonetheless, patients with a relative abundance of B. vulgatus below the median (4.63%) at the late time-point showed a tendency towards better OS (p=0.092, Supplementary Figure 4D). In addition, also a tendency towards improved survival could be shown in patients with decreasing relative abundance of B. vulgatus between baseline and the late time-point (p=0.132, Supplementary Figure 4E).

A combined immune-microbial score including activated T cells, NLR and the relative abundance of Burkholderiales order or Bacteroides vulgatus species has an important prognostic role

We then proceeded to develop two immune-microbial scores (IMS), one at the order level, involving the ideal cut-offs of the relative abundance of Burkholderiales, the NLR and frequencies of CD3+HLADR+ cells, and one at species level, involving the relative abundance of B. vulgatus, NLR and CD3+HLADR+. Concerning the first score (IMS-A), patients with at least 1 risk factor already had a significantly impaired overall survival (p=0.011, HR: 8.914 [95%CI: 1.181-67.292], p=0.034, Figure 5C). An even more relevant discrimination could be achieved for patients with 3 risk factors vs patients with less (p<0.001, HR: 6.732 [95%CI: 2.352-19.272], p<0.001, Figure 5D). Figure 5E shows a depiction of all 4 groups and how each risk factor contributes to a further deterioration of OS (p=0.001, HR: 2.681 [95%CI: 1.513-4.750], p=0.001). For the second score (IMS-B), patients with at least 1 risk factor did not live significantly shorter (p=0.075, Figure 5F). However, a significant difference could be seen in patients with all 3 risk factors, which had an impaired median OS of 120 vs. 1009 days for less than 3 or no risk factors (p=0.001, HR: 4.853 [95%CI: 1.843-12.778], p=0.001, Figure 5G). Again, all 4 groups can be significantly distinguished from each other (p=0.008, HR: 2.625 [95% CI: 1.440-4.785], p=0.002, Figure 5H).

Discussion

To this day, extensive studies around possible biomarkers for ICI therapy have been performed, from invasive tissue-based approaches such as PD-L1 scoring and the study of the tumor microenvironment *via* profiling of co-inhibitory or co-stimulatory receptor expression *in situ* (28, 29), to minimally invasive ones studying different immunomodulators such as cytokines and cell frequencies such as the NLR in the peripheral blood (30), genetic profiles including tumor mutational burden (TMB) and microsatellite instability (MSI) (31) as well as a recently acknowledged key player in the immune system, the gut microbiome, whose manipulation through dietary interventions and FMT might impact response to ICIs (7, 16). So far, despite several candidates, only PD-L1 scoring and the TMB have found regular clinical use, still bearing some limitations (32).

In the present study, we show how easily measurable peripheral blood frequencies of CD3+HLADR+ (activated T) cells can serve as a notable predictor of response, outcome and possibly toxicity in patients undergoing immune checkpoint blockade in advanced solid malignancies. Furthermore, we show an unprecedented liaison between these cells and some microbial taxa residing in the gut of patients.

HLA-DR is an MHC-II class molecule expressed by APCs and is seen as a late activation marker for T cells, that is upregulated 48 hours after mitogen stimulation (8). Several studies have shown the role of high levels of HLA-DR+ T cells in HIV (33), autoimmune disease (34) and transplant rejection (35). In cancer, the presence of HLA-DR+ T cells in the peripheral blood has shown dichotomic results. Higher pretreatment frequencies of CD8+HLADR+ in breast cancer predicted better outcome to neoadjuvant chemotherapy (13). In squamous cell carcinoma of the lung and head and neck cancer, the same higher levels of circulating activated T lymphocytes predicted impaired overall survival (36, 37). In the ICI setting, little is known related to the biomarker role of peripheral CD3+HLADR+ cells, but Carlisle et al. report how an increase of a similar cell population after the first cycle of immunotherapy with ICI predicts better progress free-survival (PFS) and OS in RCC (14). In our cohort, we demonstrate how the peripheral blood CD3+HLADR+ frequencies can represent strong predictors of OS, with patients with higher pretreatment levels of this molecule having an impaired response and OS to ICI therapy. When frequencies of this cell population were above an ideal cut-off, patients were at a 4.5-times higher risk of impaired overall survival. We hypothesize that these high pretreatment levels support the model of a dysregulated immune system and within the CD3+HLADR+ population, some cells may have impaired antitumor immunity as suggested before (38, 39), which possibly cannot be reverted by immune checkpoint blockade. In addition, patients with a higher frequency of these activated T cells before therapy also have significantly less toxicity of any grade. Toxicity and response have been shown to go hand in hand in immune checkpoint blockade with patients with an immune system more prone to successful antitumoral directed activation by ICI demonstrating more side effects and an improved outcome (40), as is the case in our cohort. Further sustaining our thesis of dysregulated immune response and more erratic inflammation symbolized by higher pretreatment frequencies of activated T cells, ECOG status showed a strong correlation to pretreatment CD3+HLADR+ and a significant effect on OS. Not only pretreatment, but also sequentially assessed CD3+HLADR+ cell frequencies predict OS. Rather than the static CD3+HLADR+ frequencies, that can also likely depict activated T cells with impaired function unable to contribute to the antitumoral response, we also demonstrate how the dynamics of these cells, comparing early and late time-points to the baseline, can also significantly predict OS. Patients with increasing levels of CD3+HLADR+ levels as an immediate result of the first cycle(s) of immunotherapy, showing an ICI-mediated activation of T cells in the peripheral blood, which may consequently transit to the tumor microenvironment and contribute to enhanced antitumoral response, had a significantly prolonged OS, in line with prior findings (14). Interestingly, this effect was most pronounced in patients undergoing dual immune checkpoint blockade with nivolumab and ipilimumab. However, analyses excluding patients undergoing dual immune checkpoint blockade (n=6), using only patients under monotherapy (n=64), show an unaltered predictive and prognostic prediction power of CD3+HLA-DR+ cell frequencies at baseline and during ICI therapy. We also hypothesize that our CD3+HLADR+ cells are mostly CD8+ cells, since there is a significant positive correlation between both, while CD3+HLADR+ cells in our cohort negatively correlate with CD4+ cell frequencies. Our analysis concerning the predictive and prognostic prediction power of CD3+CD8+ cell frequencies shows a role for this cell population in the baseline, which cannot be verified with univariate analysis and when regarding longitudinal frequencies. Furthermore, the inclusion of this cell population in the multivariate analysis leaves the independent prognostic power of CD3+HLA-DR+ cell frequencies at baseline unaltered. Thus it is evident, that the prognostic relevance of CD3+HLA-DR+ is at least partly specific for this cell population and does not only reflect the CD8+ cell subset. Because of the complexity of the innumerous players within the immune system and the even broader individual cancer patient network (CPN), one single parameter is prone to high fluctuation between cohorts. To tackle this issue, we further analyzed a combined immune status score comprising frequencies of CD3+HLADR+ cells and a well-studied biomarker within the ICI framework, the NLR. The neutrophil to lymphocyte ratio has been shown to act as a potent prognostic predictor in ICI therapy in several cohorts, being a part of different immune signature scores shown before such as the Gustave Roussy score (41). Neutrophils have been described as facilitators of tumor growth and metastasis and stimulators of tumor angiogenesis (42). Our presented score can serve as an even better prognostic biomarker than the frequency of activated T cells by itself, with patients with values above the ideal cut-offs for both parameters before initiation of ICI treatment being at a 12.5-times higher risk of death than patients with values below the cut-offs for our cohort of patients. This immune status-based score can also serve as a biomarker to monitor therapy, also predicting OS of patients undergoing immune checkpoint blockade at an early and a late-time point during therapy.

Another important aspect of our study is the gut microbiome. We show how gut bacteria with significant correlations to the frequency of activated T cells in the peripheral blood belonging to the order Burkholderiales all the way to its genus Sutterella can successfully predict better OS in patients undergoing ICI therapy. Also, bacteria belonging to the species Bacteroides vulgatus were identified as a potential biomarker for outcome prediction in this setting, despite its genus Bacteroides only showing a trend towards better OS in patients with higher relative abundance of these bacteria. As already dissected by many reviews, the gut microbiome, despite its irrefutable role in immune modulation and its influence in cancer immunotherapy, is highly prone to fluctuation with many different studies reporting different prognostically relevant taxa, due to factors such as geography and different enterotypes, lifestyle and diet, different techniques to analyze samples and reference databases (43, 44). The relative abundance of the Burkholderiales order has been shown to impact relapse free survival (RFS) in lung tissue after resection of stage II cancer (45). In the gut, some genus inside this order have been shown in the past as successful predictors of OS, such as Burkhorderiales spp., whose supplementation lead to recovery of response to anti-CTLA4 treatment in melanoma mice by inducing interleukin 12 (IL-12)–dependent TH_1 immune responses (46), whilst results concerning another genus within this order,

Sutterella, are controversial, with one study showing how, contrarily to our findings, higher relative abundances could predict worsened OS in a NSCLC cohort undergoing ICI therapy (47), whilst favorable manipulation of the microbiome by Diosgenin therapy improved OS in patients with melanoma undergoing ICI therapy by increasing the relative abundance of the Sutterella genus (48). Little is known regarding the interaction of the Sutterella genus with the immune system, however it seems to exercise a mild pro-inflammatory activity, which we theorize could be beneficial towards immune system activation within ICI therapy, and its adhesion capacity to intestinal epithelial cells might suggest it has a immunomodulatory role (49). Some Bacteroides species play an anti-inflammatory role *via* recruitment of regulatory T-cells (Tregs), suppression of IL-17 and increase of anti-inflammatory IL-10 (50, 51). In addition, supplementation of Bacteroides spp. in melanoma mice lead to enhanced antitumoral effects and improved response to anti-CTLA-4 treatment (46). Here, we show how a higher relative abundance of the genus Bacteroides, which correlates negatively with CD3+HLADR+ cell frequencies, points non-significantly towards better OS and show how a certain species, Bacteroides vulgatus, can significantly predict OS. Interestingly, the negative correlation between Bacteroides in the gut and HLADR+ T cells in the peripheral blood can show how these possibly modulate T cell function by contributing to Treg recruitment and consequently to lesser activation of T cells. Since high levels of CD3+HLADR+ cells in a pretreatment setting seem to be unfavorable towards OS, it makes sense that high relative abundances of Bacteroides vulgatus, which can control the exaggerated presence of activated and somehow erratic T cells and the immune dysregulation some of them might represent, contribute to an improved OS in patients undergoing immune checkpoint blockade for advanced solid cancer, as shown before in a mouse model (52). Nevertheless, increasing CD3+HLADR+ cell frequencies after commencement of ICI therapy led to improved OS, since these most likely represent functional and active T cells that can combat the tumor effectively and are recruited to the TME as a result of checkpoint blockade. Simultaneously, a tendency towards better OS could be shown for patients with decreasing relative abundance of Bacteroides vulgatus after therapy initiation, most likely due to decreasing Treg recruitment, cells that result in impaired response to ICI therapy (53). In line with these findings, at a late time-point (after five cycles), a lower relative abundance of these bacteria also points towards improved outcomes. Finally, our immune-microbial scores (IMS-A and B), taking into account different factors of the complex interplay of the CPN such as CD3+HLADR+ frequencies, the NLR and microbial taxa (A: order Burkhorderiales, B: species Bacteroides vulgatus), serve as highly effective, unprecedented biomarkers in the prediction of outcome for patients with diverse advanced solid malignancies under different ICI agents.

In terms of limitations, the lack of other therapies besides ICI that our patient population is exposed to does not allow us to state whether CD3+HLADR+ cells and the presented microbial taxa as biomarkers are ICI specific or may also play a role in chemotherapy, radiotherapy or resection. In addition, the heterogeneity of our single-center patient cohort, where different cancer entities under different ICI agents are present, is one of our main limitations. Nonetheless, this same heterogeneity deems our patient population as a pan-cancer cohort, where the above depicted biomarkers show significance across a wide spectrum of malignancies and ICI drugs. Furthermore, the single-center design allows a more comprehensive and valid comparison of different demographic, clinical, radiological and laboratorial parameters across different time-points. Nevertheless, it should be noted that our analyses represent exploratory analyses only and the established cut-off values need external validation before an implementation into clinical routine could eventually be considered. Additionally, it is important to mention that since our flow cytometry data arise from a standardized and clinically established analysis by the laboratory of the hematological department of the University Medical Center Aachen, data are extracted from patient files, CD3+CD8+HLA-DR+ cell frequencies are beyond the scope of our manuscript, since their calculation does not belong to the accredited "immune status panel". Nonetheless, we strongly believe that using the implemented standardized workflow (including the clinically validated gating strategy) from this accredited institution for these patient samples has the invaluable benefit that the generation of these results is highly comparable and any potential individual experimental bias is greatly reduced. Finally, the divergent results concerning different taxa as predictors of OS to ICI across different studies show how the gut microbiome and the enterotype are highly dynamic parameters dependent on individual characteristics such as geography and ethnicity (54), an effect that should be further explored in a multi-center design using the same sampling strategy and 16s rRNA sequencing techniques.

In conclusion, despite its needed confirmation in a larger validation cohort, this study shows the potential role of CD3+HLADR+ cells as predictors of response and toxicity in patients undergoing immune checkpoint blockade and its role in the prediction of OS in these patients before and during therapy, an effect independent of tumor entity or ICI agent. Furthermore, not only its static values but also its dynamics during ICI therapy play a significant predictive role. To better depict the complex interplay between different host immune modulators within the cancer patient network and their interaction, we present unprecedented immune-microbial scores (IMS), which can accurately predict outcome of patients with advanced solid malignancies undergoing ICI therapy. Multicenter approaches, including different therapeutic modalities (e.g. mono vs. dual immune checkpoint blockade) and larger, independent cohorts should be performed to get a better insight on the precise role of CD3+HLADR+ cells and the combined parameters.

Data availability statement

The microbiome sequencing data presented in the study are deposited in the SRA repository, accession number is PRJNA1006689. Further raw data will be made available, upon reasonable request, and after confirming that data will be used within the scope of the originally provided informed consent.

Ethics statement

The studies involving humans were approved by the ethics committee of the University Hospital RWTH Aachen, Germany (EK 206/09). The studies were conducted in accordance with the local legislation and institutional requirements. The participants provided their written informed consent to participate in this study. Written informed consent was obtained from the individual(s) for the publication of any potentially identifiable images or data included in this article.

Author contributions

TL, SL, CR and JG designed the study. JG and SL recruited patients. JG and SL performed experiments. JG and SL performed statistical analysis and generated figures and tables. CB, CR, FB and TB provided intellectual input. JG, SL and TL drafted the manuscript. All authors contributed to the article and approved the submitted version.

Funding

Funding in the group of TL was provided by: The European Research Council (ERC) under the European Union's Horizon 2020 research and innovation programme (Grant agreement No. 771083); the Deutsche Forschungsgemeinschaft (DFG, German Research Foundation): 403224013, 279874820, 461704932, 440603844; and the Federal Ministry of Health (BMG): 2520DAT111 (DeepLiver). JG was supported by a short-term clinician scientist fellowship of the HATRICS[4] Mildred-Scheel Cancer Career Center Hamburg (MSNZ).

Conflict of interest

The authors declare that the research was conducted in the absence of any commercial or financial relationships that could be construed as a potential conflict of interest.

Publisher's note

Supplementary material

The Supplementary Material for this article can be found online at: https://www.frontiersin.org/articles/10.3389/fimmu.2023.1206953/full#supplementary-material

References

1. Li X, Hu W, Zheng X, Zhang C, Du P, Zheng Z, et al. Emerging immune checkpoints for cancer therapy. *Acta Oncol* (2015) 54(10):1706–13. doi: 10.3109/0284186X.2015.1071918

2. Brahmer J, Reckamp KL, Baas P, Crino L, Eberhardt WE, Poddubskaya E, et al. Nivolumab versus docetaxel in advanced squamous-cell non-small-cell lung cancer. *N Engl J Med* (2015) 373(2):123–35. doi: 10.1056/NEJMoa1504627

3. Robert C, Schachter J, Long GV, Arance A, Grob JJ, Mortier L, et al. Pembrolizumab versus ipilimumab in advanced melanoma. *N Engl J Med* (2015) 372(26):2521–32. doi: 10.1056/NEJMoa1503093

4. Vaddepally RK, Kharel P, Pandey R, Garje R, Chandra AB. Review of indications of FDA-approved immune checkpoint inhibitors per NCCN guidelines with the level of evidence. *Cancers (Basel)* (2020) 12(3):738. doi: 10.3390/cancers12030738

5. Peng L, Wang Y, Liu F, Qiu X, Zhang X, Fang C, et al. Peripheral blood markers predictive of outcome and immune-related adverse events in advanced non-small cell lung cancer treated with PD-1 inhibitors. *Cancer Immunol Immunother* (2020) 69(9):1813–1822. doi: 10.1007/s00262-020-02585-w

6. Sacdalan DB, Lucero JA, Sacdalan DL. Prognostic utility of baseline neutrophil-to-lymphocyte ratio in patients receiving immune checkpoint inhibitors: a review and meta-analysis. *Onco Targets Ther* (2018) 11:955–65. doi: 10.2147/OTT.S153290

7. Oh B, Boyle F, Pavlakis N, Clarke S, Eade T, Hruby G, et al. The gut microbiome and cancer immunotherapy: can we use the gut microbiome as a predictive biomarker for clinical response in cancer immunotherapy? *Cancers (Basel)* (2021) 13(19):4824. doi: 10.3390/cancers13194824

8. Reddy M, Eirikis E, Davis C, Davis HM, Prabhakar U. Comparative analysis of lymphocyte activation marker expression and cytokine secretion profile in stimulated human peripheral blood mononuclear cell cultures: an in vitro model to monitor cellular immune function. *J Immunol Methods* (2004) 293(1-2):127–42. doi: 10.1016/j.jim.2004.07.006

9. Crispin JC, Martinez A, Alcocer-Varela J. Quantification of regulatory T cells in patients with systemic lupus erythematosus. *J Autoimmun* (2003) 21(3):273–6. doi: 10.1016/S0896-8411(03)00121-5

10. Bogner JR, Matuschke A, Heinrich B, Schreiber MA, Nerl C, Goebel FD. Expansion of activated T lymphocytes (CD3 + HLA/DR +) detectable in early stages of HIV-1 infection. *Klin Wochenschr* (1990) 68(8):393–6. doi: 10.1007/BF01648577

11. Varoczy L, Gergely L, Miltenyi Z, Aleksza M, Illes A. Can CD3+/HLA-DR+ activated T cells predict the prognosis of non-Hodgkin's lymphoma patients? *Immunol Lett* (2005) 97(1):155–7. doi: 10.1016/j.imlet.2004.10.005

12. Cai F, Gao H, Yu Z, Zhu K, Gu W, Guo X, et al. High percentages of peripheral blood T-cell activation in childhood Hodgkin's lymphoma are associated with inferior outcome. *Front Med (Lausanne)* (2022) 9:955373. doi: 10.3389/fmed.2022.955373

13. Saraiva DP, Jacinto A, Borralho P, Braga S, Cabral MG. HLA-DR in cytotoxic T lymphocytes predicts breast cancer patients' Response to neoadjuvant chemotherapy. *Front Immunol* (2018) 9:2605. doi: 10.3389/fimmu.2018.02605

14. Carlisle JW, Jansen CS, Cardenas MA, Sobierajska E, Reyes AM, Greenwald R, et al. Clinical outcome following checkpoint therapy in renal cell carcinoma is associated with a burst of activated CD8 T cells in blood. *J Immunother Cancer* (2022) 10(7):e004803. doi: 10.1136/jitc-2022-004803.

15. Spencer CN, McQuade JL, Gopalakrishnan V, McCulloch JA, Vetizou M, Cogdill AP, et al. Dietary fiber and probiotics influence the gut microbiome and melanoma immunotherapy response. *Science* (2021) 374(6575):1632–40. doi: 10.1126/science.aaz7015

16. Fillon M. Fecal microbiota transplants may aid melanoma immunotherapy resistance. *CA Cancer J Clin* (2021) 71(4):285–6. doi: 10.3322/caac.21676

17. Gorgulho J, Roderburg C, Heymann F, Schulze-Hagen M, Beier F, Vucur M, et al. Serum levels of soluble B and T lymphocyte attenuator predict overall survival in patients undergoing immune checkpoint inhibitor therapy for solid Malignancies. *Int J Cancer* (2021) 149(5):1189–98. doi: 10.1002/ijc.33610

18. Lagkouvardos I, Klaring K, Heinzmann SS, Platz S, Scholz B, Engel KH, et al. Gut metabolites and bacterial community networks during a pilot intervention study with flaxseeds in healthy adult men. *Mol Nutr Food Res* (2015) 59(8):1614–28. doi: 10.1002/mnfr.201500125

19. Lagkouvardos I, Joseph D, Kapfhammer M, Giritli S, Horn M, Haller D, et al. IMNGS: A comprehensive open resource of processed 16S rRNA microbial profiles for ecology and diversity studies. *Sci Rep* (2016) 6:33721. doi: 10.1038/srep33721

20. Edgar RC. UPARSE: highly accurate OTU sequences from microbial amplicon reads. *Nat Methods* (2013) 10(10):996–8. doi: 10.1038/nmeth.2604

21. Lagkouvardos I, Fischer S, Kumar N, Clavel T. Rhea: a transparent and modular R pipeline for microbial profiling based on 16S rRNA gene amplicons. *PeerJ* (2017) 5: e2836. doi: 10.7717/peerj.2836

22. Yoon SH, Ha SM, Kwon S, Lim J, Kim Y, Seo H, et al. Introducing EzBioCloud: a taxonomically united database of 16S rRNA gene sequences and whole-genome assemblies. *Int J Syst Evol Microbiol* (2017) 67(5):1613–7. doi: 10.1099/ijsem.0.001755

23. Budczies J, Klauschen F, Sinn BV, Gyorffy B, Schmitt WD, Darb-Esfahani S, et al. Cutoff Finder: a comprehensive and straightforward Web application enabling rapid biomarker cutoff optimization. *PloS One* (2012) 7(12):e51862. doi: 10.1371/journal.pone.0051862

24. Chen J, Bittinger K, Charlson ES, Hoffmann C, Lewis J, Wu GD, et al. Associating microbiome composition with environmental covariates using generalized UniFrac distances. *Bioinformatics* (2012) 28(16):2106–13. doi: 10.1093/bioinformatics/bts342

25. Jost L. Partitioning diversity into independent alpha and beta components. *Ecology* (2007) 88(10):2427–39. doi: 10.1890/06-1736.1

26. Quast C, Pruesse E, Yilmaz P, Gerken J, Schweer T, Yarza P, et al. The SILVA ribosomal RNA gene database project: improved data processing and web-based tools. *Nucleic Acids Res* (2013) 41(Database issue):D590–6. doi: 10.1093/nar/gks1219

27. Lan Y, Wang Q, Cole JR, Rosen GL. Using the RDP classifier to predict taxonomic novelty and reduce the search space for finding novel organisms. *PloS One* (2012) 7(3):e32491. doi: 10.1371/journal.pone.0032491

28. Petitprez F, Meylan M, de Reynies A, Sautes-Fridman C, Fridman WH. The tumor microenvironment in the response to immune checkpoint blockade therapies. *Front Immunol* (2020) 11:784. doi: 10.3389/fimmu.2020.00784

29. Udall M, Rizzo M, Kenny J, Doherty J, Dahm S, Robbins P, et al. PD-L1 diagnostic tests: a systematic literature review of scoring algorithms and test-validation metrics. *Diagn Pathol* (2018) 13(1):12. doi: 10.1186/s13000-018-0689-9

30. Hernandez C, Arasanz H, Chocarro L, Bocanegra A, Zuazo M, Fernandez-Hinojal G, et al. Systemic blood immune cell populations as biomarkers for the outcome of immune checkpoint inhibitor therapies. *Int J Mol Sci* (2020) 21(7). doi: 10.3390/ijms21072411

31. Palmeri M, Mehnert J, Silk AW, Jabbour SK, Ganesan S, Popli P, et al. Real-world application of tumor mutational burden-high (TMB-high) and microsatellite instability (MSI) confirms their utility as immunotherapy biomarkers. *ESMO Open* (2022) 7(1):100336. doi: 10.1016/j.esmoop.2021.100336

32. Shum B, Larkin J, Turajlic S. Predictive biomarkers for response to immune checkpoint inhibition. *Semin Cancer Biol* (2022) 79:4–17. doi: 10.1016/j.semcancer.2021.03.036

33. Bentwich Z, Kalinkovich A, Weisman Z, Grossman Z. Immune activation in the context of HIV infection. *Clin Exp Immunol* (1998) 111(1):1–2. doi: 10.1046/j.1365-2249.1998.00483.x

34. Zhou H, Li B, Li J, Wu T, Jin X, Yuan R, et al. Dysregulated T cell activation and aberrant cytokine expression profile in systemic lupus erythematosus. *Mediators Inflamm 2019* (2019) p:8450947. doi: 10.1155/2019/8450947

35. Meloni F, Vitulo P, Bianco AM, Paschetto E, Morosini M, Cascina A, et al. Regulatory CD4+CD25+ T cells in the peripheral blood of lung transplant recipients: correlation with transplant outcome. *Transplantation* (2004) 77(5):762–6. doi: 10.1097/01.TP.0000116565.86752.6B

36. Nakamura H, Idiris A, Kato Y, Kato H. An increase in the percentage of HLA-DR-positive peripheral leukocytes predicts a poor prognosis in patients with squamous cell carcinoma of the lung. *Oncol Rep* (2004) 11(3):673–6. doi: 10.3892/or.11.3.673

37. Aarstad HJ, Heimdal JH, Klementsen B, Olofsson J, Ulvestad E. Presence of activated T lymphocytes in peripheral blood of head and neck squamous cell carcinoma patients predicts impaired prognosis. *Acta Otolaryngol* (2006) 126(12):1326–33. doi: 10.1080/00016480600702092

38. Vardhana S, Younes A. The immune microenvironment in Hodgkin lymphoma: T cells, B cells, and immune checkpoints. *Haematologica* (2016) 101(7):794–802. doi: 10.3324/haematol.2015.132761

39. Zajac AJ, Blattman JN, Murali-Krishna K, Sourdive DJ, Suresh M, Altman JD, et al. Viral immune evasion due to persistence of activated T cells without effector function. *J Exp Med* (1998) 188(12):2205–13. doi: 10.1084/jem.188.12.2205

40. Sung M, Zer A, Walia P, Khoja L, Maganti M, Labbe C, et al. Correlation of immune-related adverse events and response from immune checkpoint inhibitors in patients with advanced non-small cell lung cancer. *J Thorac Dis* (2020) 12(5):2706–12. doi: 10.21037/jtd.2020.04.30

41. Minami S, Ihara S, Ikuta S, Komuta K. Gustave roussy immune score and royal marsden hospital prognostic score are biomarkers of immune-checkpoint inhibitor for non-small cell lung cancer. *World J Oncol* (2019) 10(2):90–100. doi: 10.14740/wjon1193

42. Moses K, Brandau S. Human neutrophils: Their role in cancer and relation to myeloid-derived suppressor cells. *Semin Immunol* (2016) 28(2):187–96. doi: 10.1016/j.smim.2016.03.018

43. He Y, Wu W, Zheng HM, Li P, McDonald D, Sheng HF, et al. Regional variation limits applications of healthy gut microbiome reference ranges and disease models. *Nat Med* (2018) 24(10):1532–5. doi: 10.1038/s41591-018-0164-x

44. Gopalakrishnan V, Helmink BA, Spencer CN, Reuben A, Wargo JA. The influence of the gut microbiome on cancer, immunity, and cancer immunotherapy. *Cancer Cell* (2018) 33(4):570–80. doi: 10.1016/j.ccell.2018.03.015

45. Peters BA, Pass HI, Burk RD, Xue X, Goparaju C, Sollecito CC, et al. The lung microbiome, peripheral gene expression, and recurrence-free survival after resection of stage II non-small cell lung cancer. *Genome Med* (2022) 14(1):121. doi: 10.1186/s13073-022-01126-7

46. Vetizou M, Pitt JM, Daillere R, Lepage P, Waldschmitt N, Flament C, et al. Anticancer immunotherapy by CTLA-4 blockade relies on the gut microbiota. *Science* (2015) 350(6264):1079–84. doi: 10.1126/science.aad1329

47. Katayama Y, Yamada T, Shimamoto T, Iwasaku M, Kaneko Y, Uchino J, et al. The role of the gut microbiome on the efficacy of immune checkpoint inhibitors in Japanese responder patients with advanced non-small cell lung cancer. *Transl Lung Cancer Res* (2019) 8(6):847–53. doi: 10.21037/tlcr.2019.10.23

48. Dong M, Meng Z, Kuerban K, Qi F, Liu J, Wei Y, et al. Diosgenin promotes antitumor immunity and PD-1 antibody efficacy against melanoma by regulating intestinal microbiota. *Cell Death Dis* (2018) 9(10):1039. doi: 10.1038/s41419-018-1099-3

49. Hiippala K, Kainulainen V, Kalliomaki M, Arkkila P, Satokari R. Mucosal prevalence and interactions with the epithelium indicate commensalism of Sutterella spp. *Front Microbiol* (2016) 7:1706. doi: 10.3389/fmicb.2016.01706

50. Atarashi K, Tanoue T, Shima T, Imaoka A, Kuwahara T, Momose Y, et al. Induction of colonic regulatory T cells by indigenous Clostridium species. *Science* (2011) 331(6015):337–41. doi: 10.1126/science.1198469

51. Round JL, Mazmanian SK. Inducible Foxp3+ regulatory T-cell development by a commensal bacterium of the intestinal microbiota. *Proc Natl Acad Sci U.S.A.* (2010) 107 (27):12204–9. doi: 10.1073/pnas.0909122107

52. Huang J, Liu D, Wang Y, Liu L, Li J, Yuan J, et al. Ginseng polysaccharides alter the gut microbiota and kynurenine/tryptophan ratio, potentiating the antitumour effect of antiprogrammed cell death 1/programmed cell death ligand 1 (anti-PD-1/PD-L1) immunotherapy. *Gut* (2022) 71(4):734–45. doi: 10.1136/gutjnl-2020-321031

53. Saleh R, Elkord E. Treg-mediated acquired resistance to immune checkpoint inhibitors. *Cancer Lett* (2019) 457:168–79. doi: 10.1016/j.canlet.2019.05.003

54. Lee KA, Thomas AM, Bolte LA, Bjork JR, de Ruijter LK, Armanini F, et al. Cross-cohort gut microbiome associations with immune checkpoint inhibitor response in advanced melanoma. *Nat Med* (2022) 28(3):535–44. doi: 10.1038/s41591-022-01695-5

frontiers | Frontiers in Immunology

TYPE Original Research
PUBLISHED 18 September 2023
DOI 10.3389/fimmu.2023.1260492

OPEN ACCESS

EDITED BY
Esra Akbay,
University of Texas Southwestern Medical Center, United States

REVIEWED BY
Masaji Tani,
Shiga University of Medical Science, Japan
Shi-Ying Li,
Guangzhou Medical University, China

*CORRESPONDENCE
Satoshi Wada
st-wada@med.showa-u.ac.jp

RECEIVED 17 July 2023
ACCEPTED 04 September 2023
PUBLISHED 18 September 2023

CITATION
Ohkuma R, Miura S, Muto S, Toyomasu Y, Fujimoto Y, Ieguchi K, Onishi N, Shimizu T, Watanabe M, Takayanagi D, Goshima T, Horiike A, Hamada K, Ariizumi H, Shimokawa M, Hirasawa Y, Ishiguro T, Suzuki R, Iriguchi N, Tsurui T, Mura E, Takenoshita S, Numajiri K, Okabe N, Yoshimura K, Tsuji M, Kiuchi Y, Yajima T, Ishida H, Suzuki H, Yamochi T, Kobayashi S, Tsunoda T and Wada S (2023) Novel quantitative immunohistochemical analysis for evaluating PD-L1 expression with phosphor-integrated dots for predicting the efficacy of patients with cancer treated with immune checkpoint inhibitors. *Front. Immunol.* 14:1260492. doi: 10.3389/fimmu.2023.1260492

Novel quantitative immunohistochemical analysis for evaluating PD-L1 expression with phosphor-integrated dots for predicting the efficacy of patients with cancer treated with immune checkpoint inhibitors

Ryotaro Ohkuma[1,2], Sakiko Miura[3], Satoshi Muto[4], Yoshitaka Toyomasu[5], Yuki Fujimoto[1,2,6], Katsuaki Ieguchi[2,6], Nobuyuki Onishi[2,6], Takashi Shimizu[2,6], Makoto Watanabe[2,6,7,8], Daisuke Takayanagi[1,2,6], Tsubasa Goshima[1,2,6], Atsushi Horiike[1], Kazuyuki Hamada[4], Hirotsugu Ariizumi[1], Masahiro Shimokawa[1], Yuya Hirasawa[1], Tomoyuki Ishiguro[1], Risako Suzuki[1], Nana Iriguchi[1], Toshiaki Tsurui[1,7,8], Emiko Mura[1], Sachiko Takenoshita[6], Kazuki Numajiri[9], Naoyuki Okabe[4], Kiyoshi Yoshimura[1,6,10], Mayumi Tsuji[8], Yuji Kiuchi[7,8], Toshiki Yajima[11], Hideyuki Ishida[5], Hiroyuki Suzuki[4], Toshiko Yamochi[3], Shinichi Kobayashi[6], Takuya Tsunoda[1] and Satoshi Wada[1,2,6,7,8]*

[1]Division of Medical Oncology, Department of Medicine, School of Medicine, Showa University, Tokyo, Japan, [2]Department of Clinical Diagnostic Oncology, Clinical Research Institute for Clinical Pharmacology and Therapeutics, Showa University, Tokyo, Japan, [3]Department of Pathology, Showa University School of Medicine, Tokyo, Japan, [4]Department of Chest Surgery, School of Medicine, Fukushima Medical University, Fukushima, Japan, [5]Department of Digestive Tract and General Surgery, Saitama Medical Center, Saitama Medical University, Saitama, Japan, [6]Clinical Research Institute for Clinical Pharmacology and Therapeutics, Showa University, Tokyo, Japan, [7]Department of Pharmacology, School of Medicine, Showa University, Tokyo, Japan, [8]Pharmacological Research Center, Showa University, Tokyo, Japan, [9]Department of General Surgical Science, Graduate School of Medicine, Gunma University, Gunma, Japan, [10]Department of Clinical Immuno Oncology, Clinical Research Institute for Clinical Pharmacology and Therapeutics, Showa University, Tokyo, Japan, [11]Department of General Thoracic Surgery, Faculty of Medicine, Kagawa University, Kagawa, Japan

Introduction: Programmed cell death ligand 1 (PD-L1) expression in tumor tissues is measured as a predictor of the therapeutic efficacy of immune checkpoint inhibitors (ICIs) in many cancer types. PD-L1 expression is evaluated by immunohistochemical staining using 3,3´-diaminobenzidine (DAB) chronogenesis (IHC-DAB); however, quantitative and reproducibility issues remain. We focused on a highly sensitive quantitative immunohistochemical method using phosphor-integrated dots (PIDs), which are fluorescent nanoparticles, and evaluated PD-L1 expression between the PID method and conventional DAB method.

Methods: In total, 155 patients with metastatic or recurrent cancer treated with ICIs were enrolled from four university hospitals. Tumor tissue specimens collected before treatment were subjected to immunohistochemical staining with both the PID and conventional DAB methods to evaluate PD-L1 protein expression.

Results: PD-L1 expression assessed using the PID and DAB methods was positively correlated. We quantified PD-L1 expression using the PID method and calculated PD-L1 PID scores. The PID score was significantly higher in the responder group than in the non-responder group. Survival analysis demonstrated that PD-L1 expression evaluated using the IHC-DAB method was not associated with progression-free survival (PFS) or overall survival (OS). Yet, PFS and OS were strikingly prolonged in the high PD-L1 PID score group.

Conclusion: Quantification of PD-L1 expression as a PID score was more effective in predicting the treatment efficacy and prognosis of patients with cancer treated with ICIs. The quantitative evaluation of PD-L1 expression using the PID method is a novel strategy for protein detection. It is highly significant that the PID method was able to identify a group of patients with a favorable prognosis who could not be identified by the conventional DAB method.

KEYWORDS

phosphor-integrated dots, fluorescent nanoparticles, immunohistochemistry, imaging pathology, quantitative evaluation, PD-L1, immune-checkpoint inhibitors, biomarker

1 Introduction

Immune checkpoint inhibitors (ICIs) have been developed as antitumor agents with mechanisms completely different from those of conventional cytotoxic chemotherapies for patients with cancer. Immune checkpoint mechanisms were originally intended to regulate excessive autoimmune responses. However, in the cancer microenvironment, cancer cells use immune checkpoints to escape antitumor immune responses, involving pathways mediated by immune checkpoint molecules such as programmed death protein-1 (PD-1), cytotoxic T-lymphocyte-associated protein 4 (CTLA-4), and various other factors. PD-1 and its ligand programmed cell death ligand 1 (PD-L1) are fundamental factors in the immune checkpoints that interfere with immune escape (1). The clinical efficacy and safety profile of anti-PD-1 and anti-PD-L1 antibodies have been demonstrated in various cancer types (2). CTLA-4 negatively regulates immune function through its interaction with B7 (CD80/CD86) expressed on the surface of cancer cells, and its competitive action with CD28, which activates T cells (3, 4). Anti-CTLA-4 antibodies have shown efficacy in multiple types of cancers as monotherapy or in combination with other ICIs, especially the anti-PD-1 antibody. The therapeutic effects of ICIs have had a strong impact on cancer treatment, not only by improving response rates and prolonging progression-free survival (PFS) but also by providing a "long-tail effect," which is characterized by the long-term overall survival (OS) of patients with cancer. Thus, ICIs have become a significant breakthrough in cancer immunotherapy, showing remarkable efficacy against various cancer types by suppressing checkpoint-mediated immune escape (5). Table 1 summarizes the results of representative phase III pivotal studies that evaluated the efficacy of ICI treatment and served as the basis for approval (6–14). In contrast, many clinical trials have reported that ICIs are ineffective in all patients with cancer, especially ICI monotherapy, with an efficacy rate of only 10–30% (15). Therefore, further improvement in the efficacy of ICIs is necessary. The expression of PD-L1 molecules, high-frequency microsatellite instability, and tumor mutation burden have been identified as potential predictive biomarkers of the therapeutic response to ICIs; however, no definitive factors have been reported to correctly predict the treatment response to ICIs (16). Therefore, superior predictive biomarkers with high therapeutic efficacy and prognostic value are urgently needed.

To date, most studies on the biomarkers of ICI treatment have focused on the analysis of PD-L1 expression in tumor tissues using immunohistochemistry (IHC). PD-L1 expression in tumor tissue has been used as a biomarker in determining cancer treatment with ICIs (17), but is not used universally in many types of cancers. PD-L1 expression detected by IHC analysis has several limitations as a predictive biomarker. Although treatment responses to anti-PD-1 or anti-PD-L1 antibody therapies are associated with the expression of PD-L1 protein in tumor tissues, approximately 10–40% of PD-L1-negative patients also respond to anti-PD-1 or anti-PD-L1 therapies (18, 19). Conversely, we often encounter cases where

TABLE 1 Main results of the previous pivotal phase III trials of immune checkpoint inhibitors in advanced cancer.

		Trial	Phase	Follow-up duration	Cancer type	Regimen	Treatment line	PD-L1 expression	Median PFS, months (95% CI)	Median OS, months (95% CI)	Reference no.
Monotherapy	1	KEYNOTE-024	Phase III	5y	NSCLC	Pembrolizumab, 200 mg q3w	1st	TPS>50%	7.7 (6.1-10.2)	26.3 (18.3-40.4)	(6)
	2	CheckMate 057	Phase III	5y	Non-squamous NSCLC	Nivolumab, 3 mg/kg q2w	2nd, 3rd	All comers	2.5 (2.2-3.5)	11.1 (9.2-13.1)	(7)
	3	OAK	Phase III	–	NSCLC	Atezolizumab, 1200 mg q3w	2nd, 3rd	All comers	2.8 (2.6-3.0)	13.8 (11.8-15.7)	(8)
	4	ATTRACTION-2	Phase III	3y	Gastric cancer (adenocarcinoma)	Nivolumab, 3 mg/kg q2w	3rd~	All comers	1.6 (1.5-2.3)	5.3 (4.6-6.4)	(9)
	5	KEYNOTE-045	Phase III	2y	Urothelial cancer	Pembrolizumab, 200 mg q3w	2nd~	All comers	2.1 (1.9-2.1)	10.1 (8.0-12.3)	(10)
	6	CheckMate 141	Phase III	2y	Head and neck (Squamous carcinoma)	Nivolumab, 240 mg q2w	2nd~	All comers	2.1 (1.9-3.2)	7.7 (3.1-12.6)	(11)
	7	CheckMate 067	Phase III	6.5y	Malignant melanoma	Nivolumab, 3 mg/kg q2w	1st	All comers	6.9 (5.1-10.2)	36.9 (28.2-NR)	(12)
Combinationtherapy	8	CheckMate 067	Phase III	6.5y	Malignant melanoma	Nivolumab, 1mg/kg q3w + ipilimumab, 3mg/kg q3w	1st	All comers	11.5 (8.7-19.3)	72.1 (38.2-NR)	(12)
	9	KEYNOTE-189	Phase III	>2y	Non-squamous NSCLC	Pembrolizumab, 200 mg q3w + platinum doublet therapy, q3w	1st	All comers	9.0 (8.1-10.4)	22.0 (19.5-24.5)	(13)
	10	Impower 130	Phase III	–	Non-squamous NSCLC	Atezolizumab, 1200 mg q3w + CBDCA (q3w) + nab-PTX(q1w)	1st	All comers	7.0 (6.2-7.3)	18.6 (16.0-21.2)	(14)

NSCLC, non-small cell lung cancer; PD-L1, programmed cell death ligand 1; PFS, progression-free survival; OS, overall survival; TPS, Tumor Proportion Score; CI, confidence interval; no., number; q1w, once weekly; q2w, once every 2 weeks; q3w, every 3 weeks.

10.3389/fimmu.2023.1260492

PD-L1-positive patients do not respond to ICIs. This contradiction is considered to be caused by PD-L1 expression as determined by IHC and visual inspection by pathologists, which limits the objectivity of determining PD-L1 expression levels. In other words, the evaluation of PD-L1 expression performed by pathologists using IHC is limited because it does not provide a quantitative evaluation and lacks objectivity. Another limitation of the IHC method is that the immunohistochemical staining method of the PD-L1 molecule is based on the intensity of the color visualized by the chromogenic agent 3,3′-diaminobenzidine (DAB). In the conventional IHC method generally used in the clinical setting, tissue sections are incubated with primary antibodies and biotin-labeled secondary antibodies, followed by a reaction with streptavidin-labeled horseradish peroxidase (HRP) and a secondary antibody, and then with HRP and DAB chromogen. Therefore, in IHC-DAB, the staining intensity depends on the enzymatic activity of HRP and is greatly affected by the air temperature, reaction time, and HRP substrate concentration (20). Consequently, the quantitative sensitivity and dynamic range of conventional IHC methods using DAB for pathological diagnosis are poor.

As described above, the scoring method of the former IHC is dependent on the staining intensity, so it is not completely quantifiable. To overcome these limitations of IHC-DAB, we focused on the phosphor-integrated dot (PID) method using fluorescent nanoparticles, a novel protein quantification method developed by Konica Minolta, Inc. (Tokyo, Japan). Although existing IHC-DAB coloration systems have quantitative problems in low-expression groups, the PID system has a wide dynamic range, enabling the detection of both low- and high-expression groups (21). Fluorescent IHC can effectively improve the quantitative sensitivity of conventional IHC-DAB; however, tissue autofluorescence hinders sensitivity (22). To improve this fluorescent IHC autofluorescence deficiency, the PID method is further characterized by the 100-fold luminance of conventional fluorescent nanoparticles and high lightfastness, which is >10 times higher than those of existing fluorescent dyes (21). Given these characteristics, the system is expected to measure protein expression more quantitatively, including in a range undetectable by existing IHC. Compared to conventional IHC-DAB, the PID method provides more objective data on protein expression because it is possible to count the number of PID particles that bind in a one-to-one fashion with antibodies in each cell. Additionally, an image processing method was developed to calculate the PID particle counts for the acquired images. We compared the characteristics of the PID schemas with those of conventional IHC. We present a schema outlining the PID method (Figure 1A) and a table comparing the features of each method (Table 2). Recent studies have explored the application of fluorescent nanoparticles in quantitative diagnostics because of their high photostability and brightness; however, their clinical application has not yet been achieved. Although two previous studies evaluated PD-L1 expression using the PID method (23, 24), it is unclear whether it can be a predictive biomarker for the therapeutic efficacy of ICIs, such as anti-PD-1, anti-PD-L1, or anti-CTLA-4 antibodies.

Application of the PID method is expected to overcome the limitations of IHC-DAB in quantifying protein expression levels. Furthermore, PD-L1 expression, which is used as a companion diagnostic marker to determine indications for ICI treatment, is not a definitive biomarker. Thus, there is a need to identify superior biomarkers for predicting the efficacy of ICIs. In this study, we compared the correlation between conventional IHC-DAB and a novel PID method for detecting PD-L1 expression in patients with cancer treated with several ICIs. We analyzed whether the evaluation of PD-L1 protein expression using the PID method predicted the therapeutic efficacy of ICIs more reliably than the conventional DAB system.

2 Materials and methods

2.1 Ethics statement

The study was conducted in accordance with the guidelines of the Declaration of Helsinki and approved by the Ethics Committees of Showa University School of Medicine (approval number: 2772), Fukushima Medical University (approval number: 2019-262), Saitama Medical University (approval number: 2409), and Gunma University (approval number: HS2020-201). Informed consent was obtained from all patients involved in the study.

2.2 Patient selection

This study enrolled 155 patients with metastatic or recurrent cancer who were treated with ICIs. The patient cohort included patients with several types of cancer, including non-small cell lung carcinoma (NSCLC), gastric cancer, urothelial carcinoma, head and neck carcinoma, and malignant melanoma. This was a multicenter retrospective cohort study, and patients were diagnosed and treated at Showa University Hospital, Fukushima Medical University Hospital, Saitama Medical Center, and Gunma University Hospital from December 2015 to December 2022. All patients were treated with treatment regimens, including ICIs shown in Table 3, that were administered according to the clinical settings.

2.3 Assessment of the treatment response

Each patient's treatment response was evaluated using computed tomography scans as imaging assessments. The treatment efficacy was evaluated according to the Response Evaluation Criteria in Solid Tumors version 1.1 (25). Overall survival (OS) was defined as the date from the start of the first administration of treatment to the date of mortality due to any cause or the last follow-up. Progression-free survival (PFS) was

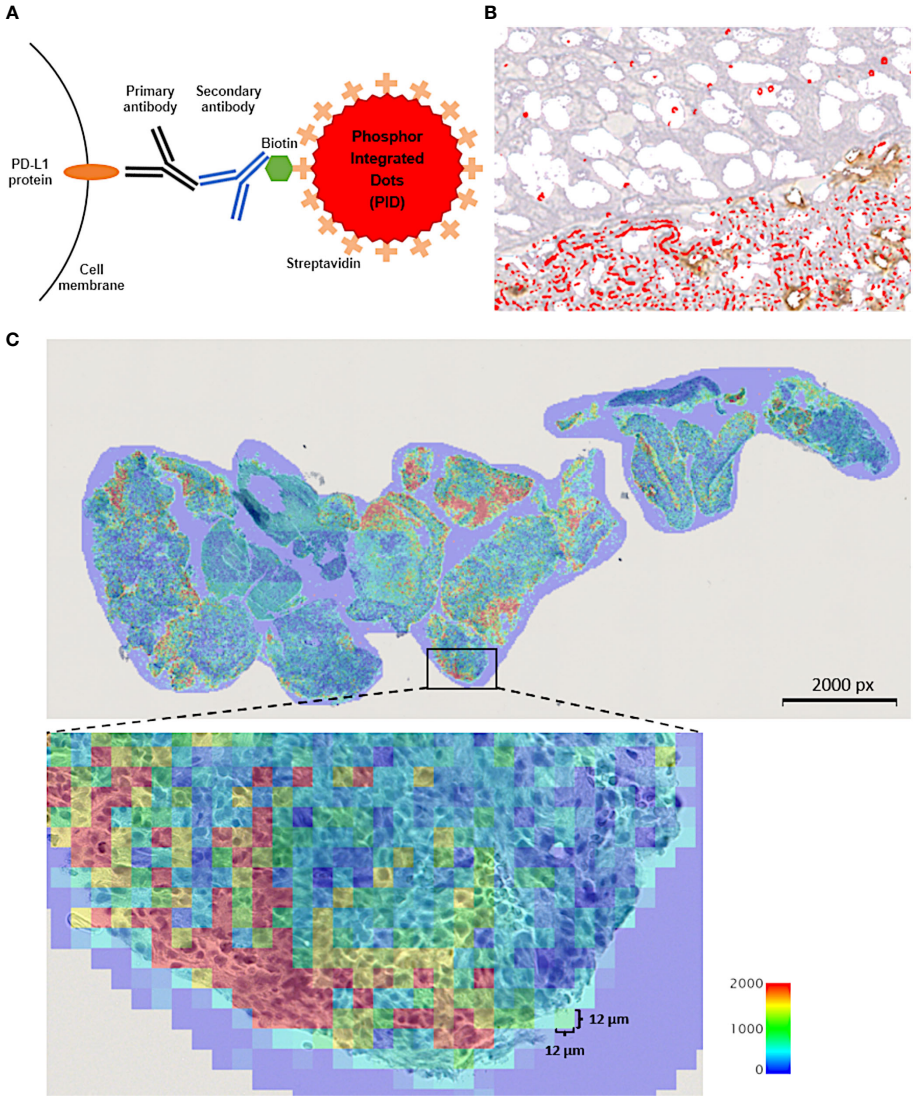

FIGURE 1
(A) Schematic explanation for the phosphor-integrated dot (PID) imaging of cancer tissues. The target protein, programmed cell death ligand 1 (PD-L1) molecules in this study, in tumor tissue were immunostained with monomeric and biotinylated monoclonal primary and monoclonal secondary antibodies. Then, the samples were stained with streptavidin-coated PID by biotin-streptavidin binding. **(B)** Immunohistochemistry of cancer tissue using PID staining. Red spots on the tumor cells indicate PID particles. **(C)** The number of PID particles were quantified in whole regions of tumor tissue specimen. The number of PD-L1-positive PID particles per 12 μm ×12 μm in the tumor cell nuclei were counted and shown as a heat map. The "PD-L1 PID score" for each case was calculated as the mean value of the number of PID particles per 12 μm × 12 μm area within each tissue specimen. px, pixel.

defined as the date from the start of treatment to the first documented progressive disease, mortality due to any cause, or the last follow-up, whichever occurred first. The cut-off date of follow-up was set as December 2022.

The "median PFS" or "median OS," based on the results obtained from the phase III pivotal clinical trials (Table 1), were used to uniformly evaluate the patient treatment efficacies of patient populations with different types of cancer. The patient population was divided into two groups (responder and non-responder) or three groups (long responder, responder, and non-responder), according to the treatment response prescribed above for each cancer type and treatment regimen. We then performed an analysis to compare PD-L1 expression evaluated by the PID method in each group.

2.4 Evaluation of PD-L1 expression using the IHC-DAB method

All tumor tissue specimens evaluated for PD-L1 expression were obtained before each patient received ICI treatment. The staining procedure for IHC using DAB and the evaluation method for PD-L1 expression were performed according to clinical routines, which have already been used for companion diagnosis when ICIs are administered to patients with cancer. We prepared formalin-fixed, paraffin-embedded tissue samples obtained by biopsy or resection. To evaluate their PD-L1 IHC assay, 155 slides were tested using Dako PD-L1 IHC 28-8 PharmDX kits (anti-PD-L1 28-8 rabbit monoclonal primary antibody; Dako,

TABLE 2 Methodology for quantifying protein expression.

Method	Advantage	Disadvantage
FACS	Suitable for measuring the total amount of protein present in the cell.	Not possible to evaluate both cell morphology and protein expression-dependent characteristics simultaneously.
IHC	Both cell morphology and protein expression-dependent characteristics can be evaluated simultaneously.	The intensity of DAB staining depends on the enzymatic activity of HRP and is greatly affected by reaction time, temperature, and HRP substrate concentration; thus, the quantitative sensitivity of IHC-DAB is low.
Fluorescent IHC	Effectively increases the quantitative sensitivity of conventional IHC.	Poor photostability and interference with tissue autofluorescence.
IHC with PIDs	High fluorescence intensity and high photostability. Newly developed image processing method enables calculation and quantification of the number of PID particles in the obtained images.	Requires specific equipment for PID analysis.

FACS, fluorescence-activated cell sorting; IHC, immunohistochemistry; PIDs, phosphor-integrated dots; DAB, 3,3′-diaminobenzidine; HRP, horseradish peroxidase.

TABLE 3 Clinicopathological characteristics of all patients.

Characteristic	
Age (y) (mean ± SD)	67.5 ± 9.4
Sex (n)	
Male	119
Female	36
Cancer type (n)	
Non-small cell lung carcinoma	109
Gastric cancer (adenocarcinoma)	28
Urothelial carcinoma	11
Head and neck cancer (squamous carcinoma)	4
Malignant melanoma	3
Site of pathological specimen (n)	
Primary tumor	129
Metastatic tumor	26
ICI Regimen (n)	
Nivolumab monotherapy	101
Pembrolizumab monotherapy	45
Pembrolizumab + platinum-based chemotherapy	4
Atezolizumab + platinum-based chemotherapy	3
Nivolumab + ipilimumab	1
Atezolizumab monotherapy	1
PD-L1 PID score (mean (min - max))	2043 (556-15757)
PD-L1 expression (IHC) (n)	
≥50%	27
1-49%	59
<1%	60
Not evaluable	9

SD, standard deviation; ICI, immune checkpoint inhibitor; PID, phosphor-integrated dots; IHC, immunohistochemistry.

Glostrup, Denmark) for nivolumab, PD-L1 IHC 22C3 PharmDX kits (anti-PD-L1 22C3 mouse monoclonal primary antibody; Agilent Technologies, Santa Clara, CA, USA) for pembrolizumab, and Ventana PD-L1 SP142 (anti-PD-L1 28-8 rabbit monoclonal primary antibody; Ventana, Antwerp, Belgium) for atezolizumab, according to the manufacturers' instructions. Two independent pathologists were experts in interpreting the clinical cut-off values of the assays used in this study and independently evaluated all 155 immunostained slides. IHC tests were scored by pathologists in accordance with a previous article (26). Missing or damaged tissue cores were excluded from the analysis, as was the case with <100 total tumor cells for scoring. The 28-8, 22C3 assays were used to evaluate PD-L1 expression in tumor cells, whereas the SP142 assay was used to assess PD-L1 expression in both tumor and immune cells (27). Two methods were used to evaluate PD-L1 expression. The Tumor Proportion Score was evaluated as the percentage of PD-L1-positive cells among the total tumor cells, and it is used as a companion diagnostic tool for lung cancer. The Combined Positive Score was evaluated as the ratio of the number of PD-L1-positive tumor cells plus tumor-infiltrating immune cells, e.g., lymphocytes and macrophages, to the total number of tumor cells, and it is used to evaluate PD-L1 expression in other types of cancer (26).

2.5 Evaluation of PD-L1 expression with the fluorescence properties of PIDs

We used the same tumor tissue specimens to evaluate PD-L1 expression as for the IHC-DAB method. Tissues collected before the patient received ICI treatment were used for analysis. The quantitative immunohistochemical detection of proteins using PID nanoparticles has been previously described (21). The pathological sections were incubated with a primary antibody against PD-L1 22C3 (Agilent Technologies, Santa Clara, CA, USA). The sections were incubated with the secondary antibody, which is Universal Secondary Antibody (Ventana, Antwerp, Belgium), for 30 minutes at 25°C. Envision Flex Target Retrieval Solution was activated at a low pH for 20 minutes at 95°C. The sections were then treated with PID-conjugated streptavidin (0.06 nM) for 2 hours at 25°C. The negative control was prepared using PID staining but without the primary antibody. Hematoxylin was

used for nuclear counterstaining. The sections were irradiated at 580 nm, and the fluorescence intensity was measured using a whole slide scanner (NanoZoomer S60; Hamamatsu Photonics K. K., Shizuoka, Japan) and a CMOS camera (ORCA-Flash version 4.0 LTPlus; Hamamatsu Photonics K. K., Shizuoka, Japan). Image capture, autofocusing, and shading correction were automated using the NDP.scan software (version 3.2.17, Hamamatsu Photonics K. K., Shizuoka, Japan) (Figure 1B). The number of PID particles was quantified using an automated exclusive QUIK software (version 1.0.1.0, Konica Minolta, Inc., Tokyo, Japan) in whole regions of the tumor tissue specimen. The input fluorescence images underwent high-pass filtering to eliminate background autofluorescence and noise. Subsequently, the positive bright spots resulting from the PIDs were accurately detected within fluorescence microscopy images. A previous article delved into examining the relationship between fluorescence intensity and particle count within a bright spot (21). Gonda et al. established a standard curve exhibiting a positive correlation between fluorescence signals and PID particle count. Employing this method, the fluorescence intensity of each positive bright spot analyzed in this study was translated into the corresponding PID particle count. The quantity of particles per 12 μm × 12 μm square area was visualized as a heat map. The "PD-L1 PID score" for each case was derived using the subsequent formula, computed as the mean value of the number of PID particles per 12 μm × 12 μm square area within each tissue specimen (Figure 1C). The unit of PID score is expressed as/144 μm^2.

$$PID\ score\ (/144\ \mu m^2) = \frac{Sum\ of\ number\ of\ PID\ particles\ in\ whole\ regions\ of\ the\ specimen}{Number\ of\ square\ areas\ of\ 12\ \mu m \times 12\ \mu m}$$

Therefore, the resulting fluorescent images were captured, processed, and homogenized using a computer image-processing method that quantified the number of PID nanoparticles.

2.6 Statistical analysis

Statistical tests were performed, and figures were created using GraphPad Prism 9.4.1 software (GraphPad Software Inc., San Diego, CA, USA). Student's t-test and Fisher's exact test were employed to compare the patient characteristics between the two groups. The Spearman correlation coefficient was used to analyze the associations between the variables. The comparison of PD-L1 expression values between the two groups was conducted using the Mann–Whitney U test. For multiple comparisons of PID scores between the three groups, statistical analyses were performed using one-way analysis of variance with the Dann–Bonferroni multiple comparison test. Statistical significance was defined at a p-value <0.05.

Regarding survival analyses, the survival durations (PFS and OS) of the patients were assessed using the Kaplan–Meier method and statistically analyzed using the log-rank tests. All tests were two-sided. When we compared between two groups using the log-rank tests, a p-value <0.05 was considered statistically significant. When performing comparisons among three groups with the Kaplan–Meier analysis, log-rank tests were performed for each of the triplicate pairs. P-values judged to be significantly different had to be adjusted and p-value <0.01667 (calculated 0.05 divided by 3) was determined to be statistically significant for comparison among three groups with Kaplan–Meier survival analysis.

3 Results

3.1 Clinicopathological characteristics

The clinicopathological characteristics of the patients are summarized in Table 3. Detailed patient information and data are presented in Supplementary Table S1. The median length of follow-up periods for all enrolled patients was 13.6 months (range, 0.5–69.1 months).

3.2 Correlation of PD-L1 expression between the IHC-DAB and PID methods

We investigated the correlation between PD-L1 expression measured by the IHC-DAB method and PD-L1 expression analyzed by the PID method using the Spearman correlation coefficient test. Nine patients were excluded from the IHC-DAB test because of low tumor cell counts (<100 total tumor cells); therefore, 146 patients were included in the analysis. A modest positive correlation was observed between PD-L1 expression measured using the IHC-DAB and PID methods (r=0.3272, p<0.0001; Figure 2). In contrast, there were some cases in which PD-L1 expression levels were not positively correlated between the

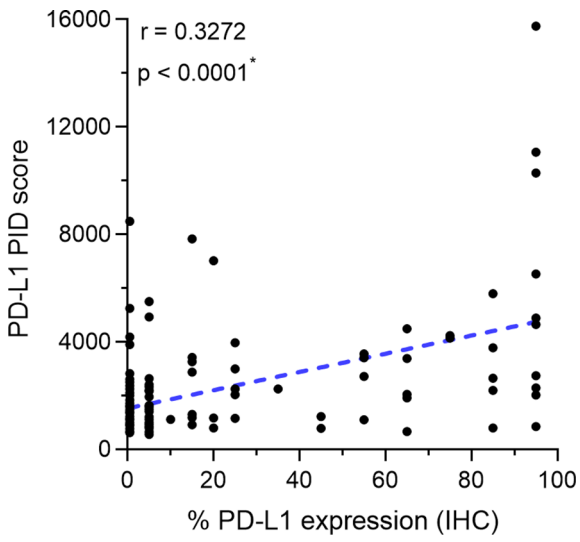

FIGURE 2
Correlation between programmed cell death ligand 1 (PD-L1) expression measured by immunohistochemical staining using 3,3′-diaminobenzidine chronogenesis (IHC-DAB) method and PD-L1 phosphor-integrated dot (PID) score. The Spearman correlation coefficient was used to analyze the correlation. A modest positive correlation is observed between PD-L1 expression measured by the IHC-DAB and PID methods (r=0.3272, p<0.0001). *Statistically significant: p<0.05.

two methods, such as a low PD-L1 PID score, despite the high PD-L1 expression measured using the IHC-DAB method. We show several images comparing PD-L1 expression between the IHC-DAB and PID methods in Figures 3A–D. Several patients exhibited a high PD-L1 PID score, irrespective of the low PD-L1 expression level assessed by IHC-DAB. We identified 7 patients with PD-L1 (IHC-DAB) levels below 20% yet possessing a high PD-L1 PID score (>4000). We conducted a comparative analysis between this patient subgroup and the remaining patients to assess background characteristics. The examination revealed no statistically significant differences in patient background characteristics between the two patient groups (Supplementary Table S2).

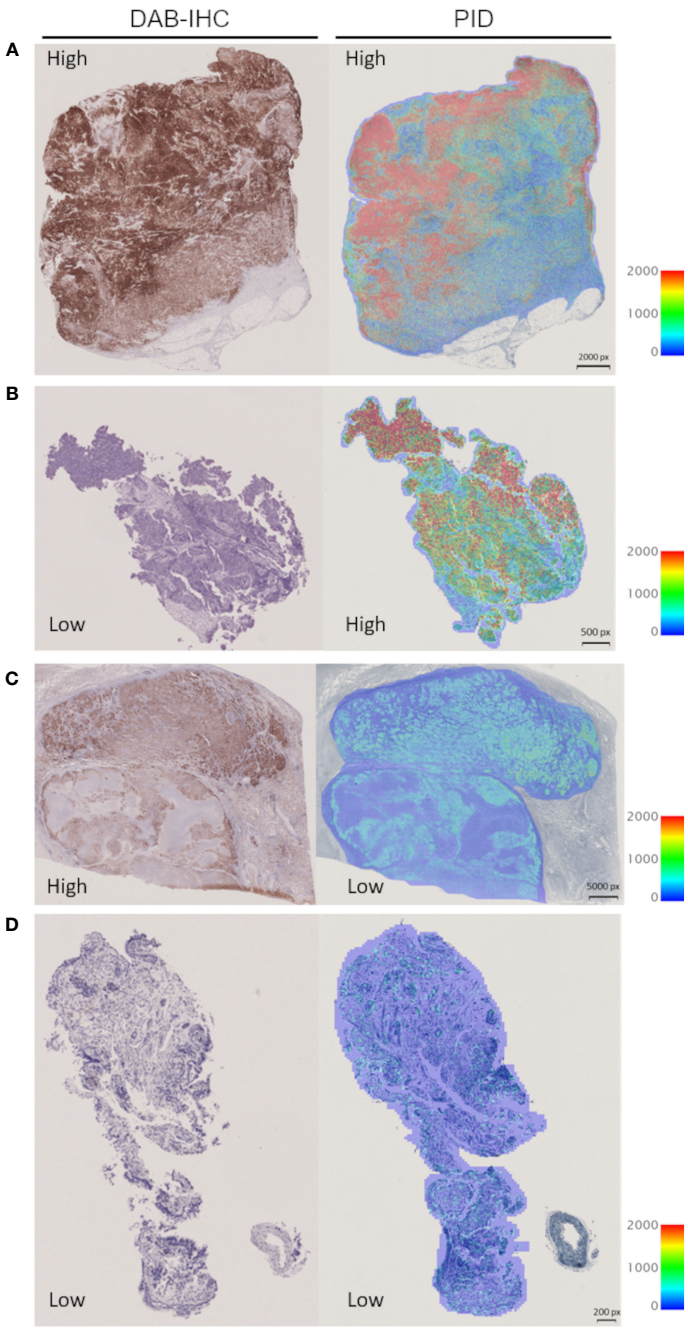

FIGURE 3
Representative images for visual comparison of programmed cell death ligand 1 (PD-L1) expression by the immunohistochemical staining using 3,3´-diaminobenzidine chronogenesis (IHC-DAB) and phosphor-integrated dot (PID) methods. **(A)** The case of high expression in IHC-DAB and high PID score: PD-L1 expression 90–100% (IHC-DAB), PD-L1 PID score 15757. **(B)** The case of low expression in IHC-DAB and high PID score: PD-L1 expression <1% (IHC-DAB), PD-L1 PID score 8487. **(C)** The case of high expression in IHC-DAB and low PID score: PD-L1 expression 90–100% (IHC-DAB), PD-L1 PID score 2024. **(D)** The case of low expression in IHC-DAB and low PID score: PD-L1 expression <1% (IHC-DAB), PD-L1 PID score 762. px, pixel.

3.3 Correlation between the PD-L1 PID score and patient survival

The correlation between the PD-L1 PID score and survival duration (PFS and OS) was analyzed using the Spearman correlation coefficient test (n=155). There were weak positive correlations between the PID score and PFS in the overall cohort of patients (r=0.2800, p<0.001, Figure 4A). Similar to PFS, a weak positive correlation with the PID score was observed for OS in the overall cohort (r=0.2712, p<0.001, Figure 4B). PD-L1 PID scores before ICI treatment, as determined by the PID method, correlated with prolonged PFS and OS in patients with cancer who received ICI treatment.

3.4 Comparison of PD-L1 PID scores by the treatment efficacy of patients

We verified whether PD-L1 expression levels obtained using the PID method before treatment initiation predicted the efficacy of ICI treatment in patients. The overall patient population was divided into two groups, responder and non-responder, based on their treatment response to ICIs, and PD-L1 PID scores were statistically compared between the two groups using Mann–Whitney U test (n=155). The duration of PFS for the responder group was defined by four criteria: PFS of each patient was 1) longer than "median PFS," 2) "median PFS"+3 months, 3) "median PFS"+6 months, 4) "median PFS"+12 months, based on "median PFS" data obtained from previous reported phase III pivotal trials evaluating ICI treatments (Table 1) (6–14). PD-L1 PID scores were not significantly different in the analysis that distinguished non-responders from responders according to the "median PFS" described above (p=0.5596, Figure 5A). However, PD-L1 PID scores were significantly higher in responders than in non-responders in this analysis for each patient's PFS: ≥"median PFS"+3 months, ≥"median PFS"+6 months, and ≥"median PFS"+12 months were defined as responders (p=0.0242, Figure 5B; p=0.0082, Figure 5C; and p=0.0323, Figure 5D, respectively). Regarding OS, the duration of OS for the responders was defined by the criteria in which each patient's OS was longer than the "median OS" reported in the previous pivotal trials (Table 1) (6–14). PD-L1 PID scores were significantly higher in responders than in non-responders according to prolonged OS (p=0.0136, Figure 5E).

Additionally, the patient population was divided into three groups: long responders, responders, and non-responders. PD-L1 expression as the PID score in each group was compared between the three groups with the "median PFS" reported from the pivotal trial as previously described (Table 1) (6–14). Multiple comparison test results were statistically analyzed using the Dann–Bonferroni multiple comparison test (n=155), and the PID scores were significantly higher in long responders than in responders (p=0.0498, Figure 6A; p=0.0190, Figure 6B), or non-responders (p=0.0179, Figure 6C; p=0.0363, Figure 6D). Based on these analyses of comparison between two and three groups, pre-ICI treatment PD-L1 expression measured as PID score by the PID method was associated with favorable PFS and OS in patients with cancer who received cancer immunotherapy with ICIs. The results regarding PFS suggest that PD-L1 PID scores might be predictive of better prognosis, as PID scores were higher in responders with longer PFS.

3.5 Kaplan–Meier survival analysis according to PD-L1 expression by the IHC-DAB method

Based on the cut-off values (50% and 1%) of PD-L1 expression by the IHC-DAB method, which is clinically applied (26), the patient cohort was divided into two groups, "high" and "low" according to PD-L1 expression levels by the conventional IHC-DAB method. Then, we compared both groups using Kaplan–Meier

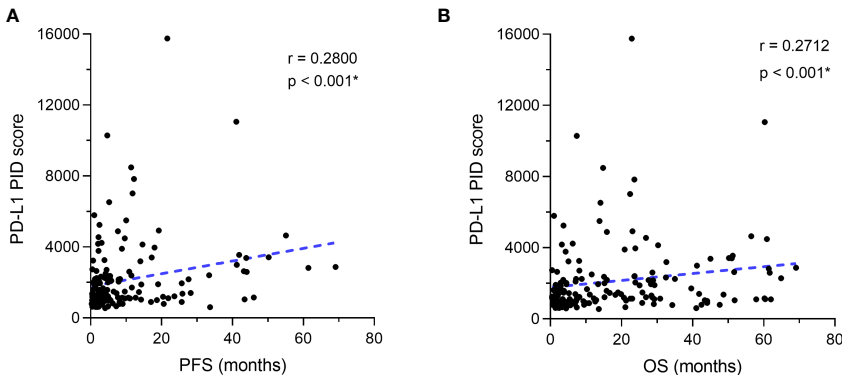

FIGURE 4
Correlation between programmed cell death ligand 1 (PD-L1) expression as the phosphor-integrated dot (PID) score and progression-free survival (PFS) and overall survival (OS). The Spearman correlation coefficient was used to analyze the correlation between the PD-L1 PID score and survival durations of **(A)** PFS and **(B)** OS. **(A)** There are weak positive correlations between the PID score and PFS in the overall cohort of patients. Similar to PFS, **(B)** a weak positive correlation with the PID score is observed for OS in the overall cohort. *Statistically significant: p<0.05.

10.3389/fimmu.2023.1260492

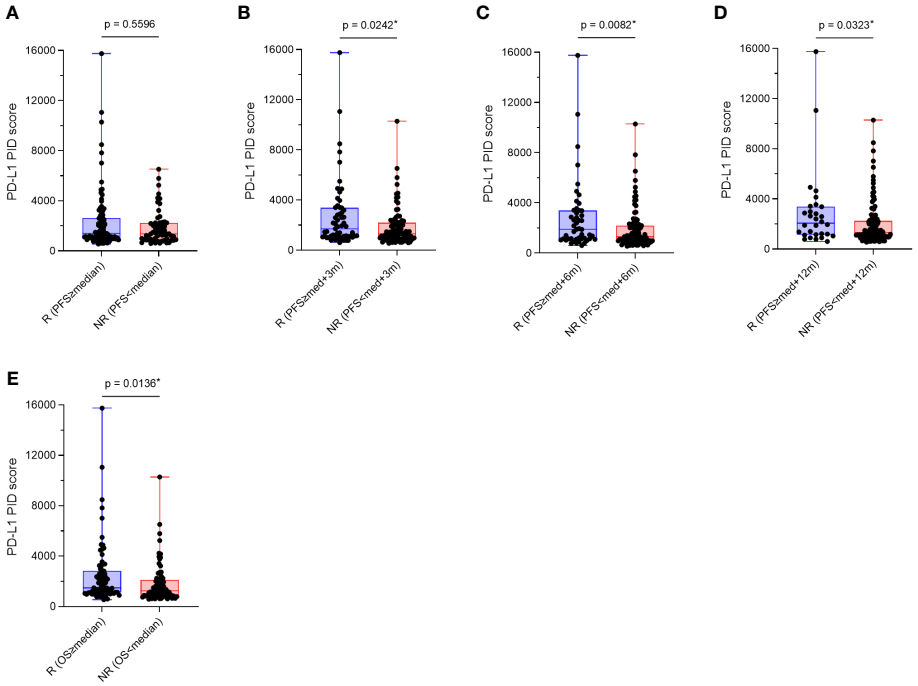

FIGURE 5
Comparison of programmed cell death ligand 1 (PD-L1) phosphor-integrated dot (PID) scores by treatment efficacy, responders and non-responders. Overall patient populations were divided into two groups, responders and non-responders, based on their treatment responses of immune checkpoint inhibitors, and PD-L1 PID scores were statistically compared between both groups. **(A)** PD-L1 PID scores are not significantly different in the analysis that distinguished non-responders from responders according to the "median PFS". **(B–D)** However, PD-L1 PID scores are significantly higher in responders than in non-responders in this analysis for each patient's PFS: **(B)** ≥"median PFS"+3 months, **(C)** ≥"median PFS"+6 months, and **(D)** ≥"median PFS"+12 months were defined as the responders. **(E)** Regarding OS, PD-L1 PID scores were significantly higher in R than in NR according to prolonged OS. R, responders; NR, non-responders; med, median. *Statistically significant: p<0.05.

survival analyses with the log-rank tests for PFS and OS. In the overall patient population (n=155), OS was significantly prolonged in the PD-L1 high (PD-L1(IHC) ≥50%) group (p=0.0347, Figure 7B), and a similar trend was observed with a cut-off value of 1%, which was not statistically significant (p=0.0697, Figure 7D). Regarding PFS, there were no significant differences between the high and low groups of PD-L1 expression by the IHC-DAB method with cut-off values of 50% (p=0.1607, Figure 7A) and 1% (p=0.1153, Figure 7C). We additionally performed sub-analyses for the NSCLC patient cohort because of the large number of patients (n=109), but the results were not statistically significant (Supplementary Figures 1A–D).

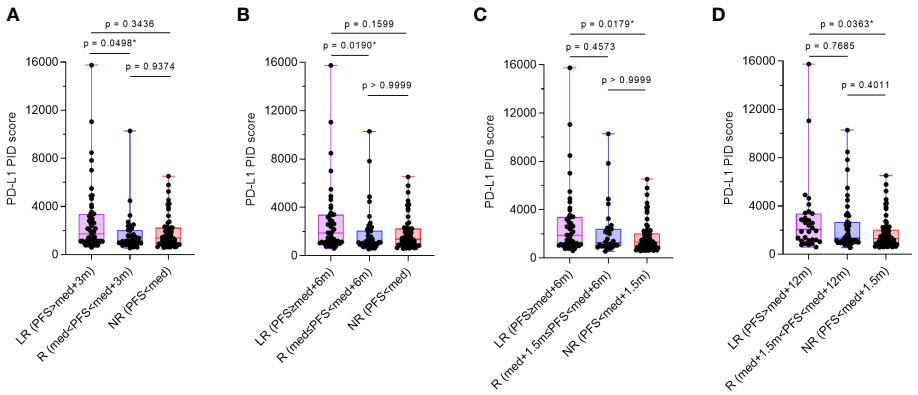

FIGURE 6
Comparison of programmed cell death ligand 1 (PD-L1) phosphor-integrated dot (PID) scores by treatment efficacy. The patient population was divided into three groups: long-responders, responders, and non-responders. One-way analysis of variance with the Dann–Bonferroni multiple comparison tests were performed to compare the three groups. **(A, B)** PID scores are significantly higher in long-responders than in responders (p=0.0292, **A**; p=0.0190, **B**) and **(C, D)** non-responders (p=0.0179, **C**; p=0.0363, **D**). LR, long-responders; R, responders; NR, non-responders; med, median. *Statistically significant: p<0.05.

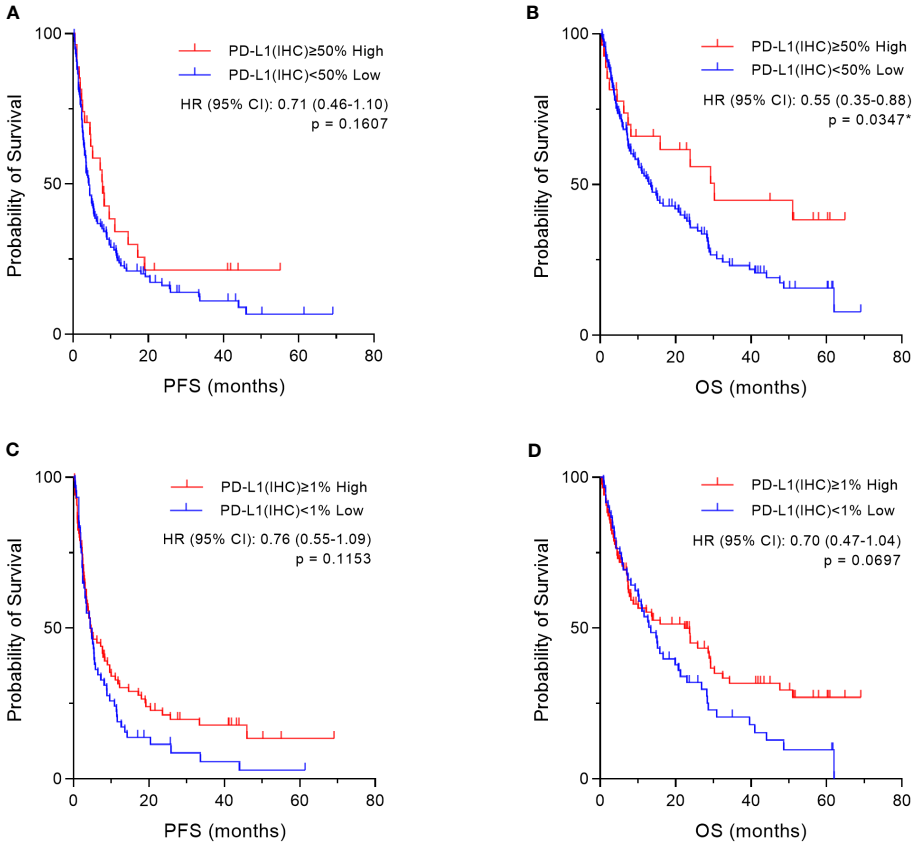

FIGURE 7
Kaplan–Meier survival analysis according to programmed cell death ligand 1 (PD-L1) expression by the immunohistochemical staining using 3,3´-diaminobenzidine chronogenesis (IHC-DAB) method in two groups. Based on the cut-off values (50% and 1%) of PD-L1 expression by the IHC-DAB method, the patient cohort was divided into two groups, "High" and "Low" according to PD-L1 expression levels by conventional IHC-DAB. In the overall patient population (n=155), we compared both groups using Kaplan–Meier survival analyses with log-rank tests for PFS and OS.
(A, C) Regarding PFS, there are also no significant differences between the "High" and "Low" groups of PD-L1 expression by the IHC-DAB method, which were defined by the cut-offs of **(A)** 50% and **(C)** 1%. **(B)** OS is significantly prolonged in the "High" (PD-L1(IHC) ≥50%) group, **(D)** and there is a similar trend with a cut-off value of 1%, which is not statistically significant. HR, hazard ratio; CI, confidence interval. *Statistically significant: p<0.05.

Furthermore, based on the PD-L1 cut-off values (50%, 1–49%, and 1%) evaluated by the IHC-DAB method, the patient population was divided into three groups according to PD-L1 expression levels, "High," "Medium," and "Low" groups, and then we compared the three groups using Kaplan–Meier survival analyses with the log-rank tests for PFS and OS. In the overall patient population (n=155), OS in the "High" (PD-L1(IHC) ≥50%) group was statistically prolonged compared to that of the "Low" (PD-L1 (IHC) <1%) group (p=0.0146, Figure 8B). However, no significant results were obtained for PFS (Figure 8A) when the three groups were categorized based on PD-L1 expression by the IHC-DAB method. Sub-analyses for the NSCLC patient cohort were also performed (n=109), and there were no statistically significant findings in the Kaplan–Meier survival analyses for both PFS (Supplementary Figure 2A) and OS (Supplementary Figure 2B). Therefore, these analyses indicated that the PD-L1 expression levels defined by the conventionally used IHC-DAB method with PD-L1 cut-off values were not associated with favorable PFS and OS, except for the "High" (PD-L1(IHC) ≥50%) group in OS.

3.6 Determining the cut-off value of the PD-L1 PID score

There are no criteria for defining high or low PD-L1 expression using the proportional integral derivative method. To determine an appropriate cut-off value for the PD-L1 PID score, we defined "high" and "low" PD-L1 expression by the IHC-DAB method as the outcomes and plotted receiver operating characteristic (ROC) curves regarding the PID scores. The PID score with the highest value, calculated by the formula [Sensitivity - (1 + Specificity)], was defined as the most appropriate cut-off value by the Youden index to distinguish between high and low PD-L1 expression groups (28). Appropriate ROC curves with statistical significance were obtained when PD-L1 IHC-DAB cut-off values of 50%, 20%, and 10% were applied, and the most appropriate cut-off value of the PD-L1 PID score was 1863 (Supplementary Figures 3A–H).

Moreover, we divided the PID scores into three groups for analysis, as was done for the IHC-DAB method. The cut-off values for dividing the patients into three groups were determined using

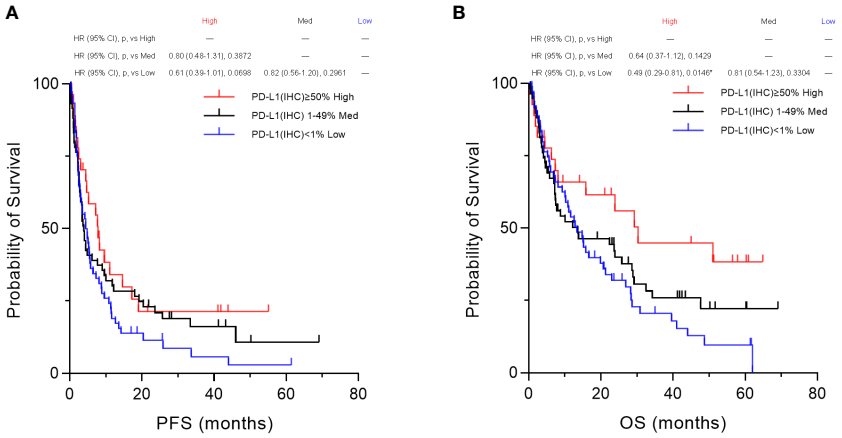

FIGURE 8
Kaplan–Meier survival analysis according to programmed cell death ligand 1 (PD-L1) expression by the immunohistochemical staining using 3,3´-diaminobenzidine chronogenesis (IHC-DAB) method between the three groups. Based on the PD-L1 cut-off values (50%, 1–49%, and 1%) evaluated by the IHC-DAB method, the patient population was divided into three groups of PD-L1 expression levels, "High," "Medium," and "Low" groups, and then we compared the three groups by performing Kaplan–Meier survival analyses with the log-rank tests for PFS and OS. **(A)** In the overall patient population (n=155), no significant results were obtained for PFS. **(B)** OS in the PD-L1 "High" (PD-L1(IHC) ≥50%) group was statistically prolonged compared to that of the PD-L1 "Low" (PD-L1(IHC) <1%) group (p=0.0146, **B**). HR, hazard ratio; CI, confidence interval; p, p-value; Med, medium. *Statistically significant: p<0.01667.

percentile values: 1) PID score ≥2359 (75th percentile) for the "High" group, 2) 948 (25th percentile)<PID score<2359 (75th percentile) for the "Medium" group, 3) PID score <948 (25th percentile) for the "Low" group (Supplementary Figure 4).

3.7 Kaplan–Meier survival analysis according to the PD-L1 PID score

Based on the cut-off value (1863) of the PD-L1 PID score that was obtained above, the patient cohort was divided into two groups, "High" and "Low" according to the PD-L1 expression levels by the PID method, and then we compared the two groups using Kaplan–Meier survival analyses with log-rank tests for PFS and OS. In the overall patient population (n=155), PFS and OS were significantly prolonged in the "High" PD-L1 PID score group (p=0.0005, Figure 9A and p=0.0011, Figure 9B, respectively). We further performed sub-analyses of the NSCLC patient cohort (n=109). PFS was significantly longer in the "High" PID score group than in the "Low" PID score group (p=0.0325, Supplementary Figure 5A), and a similar trend was observed for OS in the NSCLC patient cohort (p=0.0575, Supplementary Figure 5B).

Based on the percentile values, the PID scores were divided into three groups, "High," "Med," and "Low" groups, for survival analysis. Then, we compared the three groups using Kaplan–Meier survival analyses with the log-rank tests for PFS and OS.

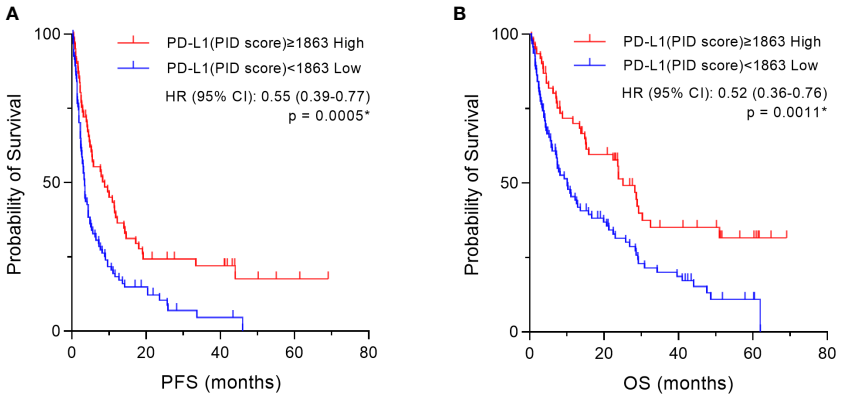

FIGURE 9
Kaplan–Meier survival analysis according to the programmed cell death ligand 1 (PD-L1) phosphor-integrated dot (PID) score in two groups. Based on the cut-off value (1863) of the PD-L1 PID score, the patient cohort was divided into two groups, "High" and "Low" according to PD-L1 expression levels by the PID method, and then we compared the two groups using Kaplan–Meier survival analyses with the log-rank tests for PFS and OS. In the overall patient population (n=155), both **(A)** PFS and **(B)** OS are prolonged in the "High" PD-L1 PID score group with high statistical significance. HR, hazard ratio; CI, confidence interval. *Statistically significant: p<0.05.

Only in these analyses of comparison among the three groups, a p-value <0.01667 was considered to be statistically significant. In the overall patient population (n=155), PFS was significantly prolonged in the "High" PD-L1 PID score group compared with the "Medium" (p=0.0011, Figure 10A) and "Low" PD-L1 PID score groups (p=0.0003, Figure 10A). Similar to PFS, the "High" PD-L1 PID score group had more favorable OS than the "Medium" (p=0.0012, Figure 10B) and "Low" PD-L1 PID score groups (p<0.0001, Figure 10B). In the NSCLC cohort (n=109), PFS and OS were longer in the "High" PD-L1 PID score group with strong statistical significance than in the "Medium" (p=0.0098, Supplementary Figure 6A; and p=0.0070, Supplementary Figure 6B, respectively) and "Low" PD-L1 PID score groups (p=0.0059, Supplementary Figure 6A; and p=0.0023, Supplementary Figure 6B, respectively). Therefore, the results demonstrated that when the PID score was used as the cut-off value for the PD-L1 expression level, the PID score more clearly predicted the treatment efficacy and prognosis of patients treated with ICIs.

4 Discussion

To evaluate whether quantitative detection of PD-L1 expression predicts the clinical outcomes of patients with cancer treated with ICIs, we demonstrated the expression of PD-L1 protein using two different immunohistochemical detection methods, the conventional IHC-DAB and PID system. From the results obtained herein, the quantitative evaluation of PD-L1 expression by the PID score appears to be more effective than the cut-off of PD-L1 expression by the IHC-DAB method in predicting the treatment efficacy and prognosis of patients with cancer treated with ICIs. PID scoring as a quantitative detection system is expected to resolve some limitations of the IHC-DAB method for quantifying protein expression levels.

Since the PID method was first reported in 2017 (21), researchers have focused on this technology and its practical applications. Gonda et al. published foundational articles on the PID system and established a novel method for quantitative protein evaluation by IHC using new fluorescent nanoparticles, called PIDs, with high sensitivity and a wide dynamic range (21). The PID method is strongly correlated with conventional human epidermal growth factor receptor 2 (HER2) testing methods using IHC-DAB (21, 29). In the present study, PD-L1 expression assessed using the conventional IHC-DAB method was positively correlated with that assessed using the PID method. Additionally, protein expression assessed by the PID method has been reported to have a positive linear correlation with that obtained by other methodologies such as fluorescence activated cell sorting analysis (21, 29) or enzyme-linked immunosorbent assay (ELISA) (24). Thus, the reproducibility of the PID method was confirmed by comparison with the other methods. It has also been verified whether protein expression evaluated using the PID method can be used as a biomarker for predicting treatment efficacy. The number of HER2-positive PID particles in breast cancer tissue analyzed from pretreatment biopsies have been shown to predict the therapeutic efficacy of the anti-HER2 antibody (trastuzumab) (21). Guo et al. showed that a high ratio of extranuclear-to-nuclear estrogen receptor alpha (ERα) in patients with hormone receptor-positive and HER2-negative breast cancer indicates a decreased likelihood of benefiting from hormone therapy (30). Similar to our study, the PID score for PD-L1 expression showed a higher prognostic value than protein detection using IHC-DAB (23). Quantitative

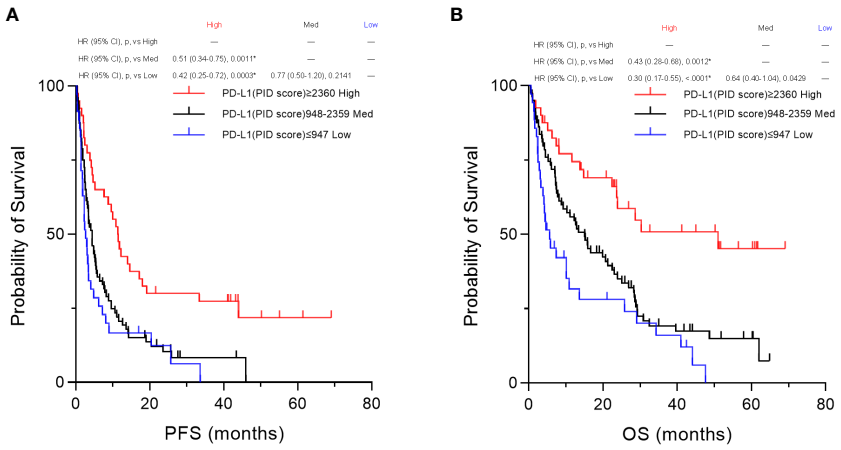

FIGURE 10
Kaplan–Meier survival analysis according to the programmed cell death ligand 1 (PD-L1) phosphor-integrated dot (PID) score between the three groups. Based on the 25th and 75th percentile values, PID scores were also divided into three groups for the survival analysis. We compared the three groups by performing Kaplan–Meier survival analyses with the log-rank tests for PFS and OS. In the overall patient population (n=155), both **(A)** PFS and **(B)** OS are significantly prolonged in the "High" PD-L1 PID score group compared with the "Medium" (PFS, p=0.0011, **A**; OS, p=0.0012, **B**) and "Low" PD-L1 PID score groups (PFS, p=0.0003, **A**; OS, p<0.0001, **B**). HR, hazard ratio; CI, confidence interval; p, p-value; Med, medium. *Statistically significant: p<0.01667.

evaluation of MYC protein expression using the PID method stratified OS in patients with diffuse large B-cell lymphoma more precisely than the conventional IHC-DAB method (31).

There have been limited studies on the quantitative evaluation of PD-L1 molecules using the PID method. In a previous study, PD-L1 expression in pancreatic ductal carcinoma was evaluated using IHC with PID, which could detect PD-L1 expression with higher sensitivity than conventional IHC-DAB. PD-L1 expression, evaluated using the PID method, predicts poor prognosis (23). Another study showed that digital immunostaining of PD-L1 expression was highly correlated with protein expression measured by other methods, such as ELISA and quantitative messenger RNA data generated by the nCounter system (24). Both studies are valuable in that they evaluated PD-L1 expression using the novel PID method, but they did not validate whether it predicts the efficacy of ICI treatment. In our study, we not only compared the PID method with the conventional IHC-DAB method in assessing PD-L1 expression but also analyzed the relationship between PD-L1 expression by IHC-DAB and treatment response to ICIs using pre-ICI treatment tissue specimens from 155 patients with cancer. When the patients were classified into responder and non-responder groups based on the duration of PFS and OS, the PD-L1 PID scores in the responder group were higher than those in the non-responders. As our data showed that PID scores tended to be higher in patients with a longer PFS, it is possible that PID scores were better at predicting long responders, which is a hallmark of ICI treatment. Furthermore, when we performed survival analysis by dividing patients into high and low PD-L1 PID score groups, PFS and OS were significantly prolonged in patients with high PID scores. However, when the PD-L1 expression level was evaluated using the conventional DAB method, neither PFS nor OS was significant and could not predict treatment response or prognosis. We found that the PD-L1 expression level evaluated using the PID method has the potential to be a better biomarker than the IHC-DAB method. There are several possible reasons why the two analysis methods gave different results. The main limitation of the IHC-DAB method is the dependence of the staining intensity on the enzymatic activity of HRP, which in turn is influenced by factors such as temperature, reaction time, and HRP substrate concentration. Furthermore, the efficacy of the IHC-DAB method is curtailed by the subjective selection of noteworthy fields of view by pathologists and their subsequent visual assessment of PD-L1 expression, which prevents quantitative evaluation and lacks objectivity. Conversely, the PID method features brightness levels 100 times greater than conventional fluorescent nanoparticles, along with 10 times greater lightfastness compared to existing fluorescent dyes (21). These distinctive attributes equip the PID method with the capacity to assess protein expression assessments in a more quantitative and accurate manner than the DAB method. Additionally, the capability of the PID method to comprehensively analyze entire regions of tumor tissue specimens permits the evaluation of PD-L1 expression in whole areas that conventional visual inspection by pathologists may not fully capture. These factors likely contribute to the disparities in results observed between the DAB and PID methods.

Furthermore, the PID method has been applied to research other than the search for predictive biomarkers of therapeutic efficacy. Guo et al. performed PID analysis using the nearest neighbor method, which takes advantage of the ability to analyze the location of detected proteins in cells and tissues. ERα expression in nuclear and extranuclear regions was detected and quantitatively analyzed, resulting in higher sensitivity and specificity than conventional IHC-DAB in patients with breast cancer (30). Suzuki et al. applied PID imaging to study antibody drugs to elucidate their mechanism of action. They evaluated the intratumor pharmacokinetics using PID imaging analysis, which can assess the distribution of proteins to tumor target sites at the microlevel, to analyze the intratumor distribution of a novel HER2-targeted antibody drug conjugate, trastuzumab deruxtecan (32). PID imaging analysis is expected to be used not only to detect biomarkers such as HER2 and PD-L1 expressed in tumor tissue but also as an ideal tool for elucidating the mechanism of action of antibody drugs in tumor tissue in the clinical setting. Moreover, as Inamura et al. analyzed the expression of colony stimulating factor-1 receptor-expressing tumor-associated macrophages in lung cancer tumor tissue (33), PID imaging technology will be increasingly applied to analyze the immune microenvironment in tumor tissue.

We found no significant difference in PID scores between responders and non-responders when using the "median PFS" reported in the pivotal trial as the cut-off, but significant results were obtained when patients were divided by "median PFS"+3 months, "median PFS"+6 months, and "median PFS"+12 months. In clinical trials of ICIs, PFS can be attributed to tumor shrinkage (pseudo-progression) following disease progression (PD) or to longer survival after PD, both of which suggest a delayed effect of ICIs. Previous studies have reported that excluding modified PFS, which excludes early PD events up to 3 months after randomization, is a more accurate surrogate endpoint for OS than actual PFS (34). Thus, considering the early PD of approximately 3 months, it is possible that a median PFS of 3 months or more would be reasonable to obtain significant results.

The present study has several limitations. It is a retrospective analysis, and there lies the aspect that it solely served as an exploratory investigation into the utility of PD-L1 expression through the PID method. In terms of the study design, the enrolled patients exhibited heterogeneity and encompassed various cancer types. The inclusion of diverse cancer types in this study gives rise to discrepancies in the approach to evaluating PD-L1 expression by the IHC-DAB method between NSCLC and other cancer types. Our assessment of PD-L1 expression by the IHC-DAB method aligns with the method employed in clinical practice. TPS serves as a companion diagnostic tool for lung

cancer, whereas CPS is utilized for assessing PD-L1 expression in other cancer types within clinical settings. Furthermore, the determination of the cut-off value of the PD-L1 PID score also remains a challenge. Currently, no recommended or established cut-off values exist for evaluating PD-L1 expression using the PID method. In this study, we established our own cut-off values utilizing ROC curves and percentile values. These cut-off values for PD-L1 PID scores may vary based on patient background, such as different cancer types. To resolve these issues and verify our results, conducting a prospective study with a homogenized patient population is imperative. We are in the process of planning a clinical trial to investigate PD-L1 expression through the PID method in the future.

5 Conclusions

We evaluated PD-L1 expression using highly sensitive quantitative immunohistochemistry with fluorescent nanoparticles (PIDs) in 155 patients with unresectable, recurrent, or metastatic cancer treated with ICIs, and compared it with that using the conventional IHC-DAB method. Evaluation of PD-L1 expression by the IHC-DAB and PID methods showed a positive correlation. The quantitative assessment of PD-L1 expression using the PID method predicted responders to ICI treatment. Furthermore, PFS and OS were significantly prolonged in the group with higher PD-L1 PID scores, suggesting that quantitative evaluation of PD-L1 expression by the PID method could be a biomarker for predicting treatment efficacy and patient prognosis of ICI treatment. It is significant that the PID method was able to identify the favorable prognosis group that could not be detected using conventional DAB staining. We propose prospective studies and further research on the quantitative evaluation of PD-L1 expression using the innovative PID method with the aim of adapting this methodology to clinical practice.

Data availability statement

The raw data supporting the conclusions of this article will be made available by the authors, without undue reservation.

Ethics statement

The studies involving humans were approved by the Ethics Committees of Showa University School of Medicine (approval number: 2772), Fukushima Medical University (approval number: 2019-262), Saitama Medical University (approval number: 2409), and Gunma University (approval number: HS2020-201). The studies were conducted in accordance with the local legislation and institutional requirements. The participants provided their written informed consent to participate in this study. Written informed consent was obtained from the individual(s) for the publication of any potentially identifiable images or data included in this article.

Author contributions

RO: Conceptualization, Data curation, Formal Analysis, Investigation, Methodology, Resources, Validation, Visualization, Writing – original draft, Software. SMi: Investigation, Methodology, Resources, Validation, Writing – review & editing. SMu: Investigation, Resources, Writing – review & editing. YT: Investigation, Resources, Writing – review & editing. YF: Methodology, Resources, Writing – review & editing. KI: Methodology, Resources, Writing – review & editing. NOn: Methodology, Resources, Writing – review & editing. TS: Methodology, Resources, Writing – review & editing. MW: Methodology, Resources, Writing – review & editing. DT: Methodology, Resources, Writing – review & editing. TG: Methodology, Resources, Writing – review & editing. AH: Investigation, Resources, Validation, Writing – review & editing. KH: Investigation, Resources, Validation, Writing – review & editing. HA: Investigation, Resources, Validation, Writing – review & editing. MS: Investigation, Resources, Validation, Writing – review & editing. YH: Investigation, Resources, Validation, Writing – review & editing. TI: Investigation, Resources, Validation, Writing – review & editing. RS: Investigation, Resources, Validation, Writing – review & editing. NI: Investigation, Resources, Validation, Writing – review & editing. TTsur: Validation, Writing – review & editing, Investigation, Resources. EM: Investigation, Resources, Writing – review & editing, Validation. ST: Writing – review & editing, Supervision, Validation. KN: Investigation, Resources, Writing – review & editing. NOk: Investigation, Resources, Writing – review & editing. KY: Supervision, Validation, Writing – review & editing, Investigation, Resources. MT: Supervision, Writing – review & editing, Validation. YK: Supervision, Writing – review & editing, Validation. TYaj: Investigation, Resources, Supervision, Writing – review & editing. HI: Supervision, Writing – review & editing, Investigation, Resources. HS: Supervision, Writing – review & editing, Investigation, Resources. TYam: Investigation, Resources, Validation, Writing – review & editing, Methodology. SK: Supervision, Validation, Writing – review & editing. TTsun: Conceptualization, Investigation, Project administration, Resources, Supervision, Validation, Writing – review & editing, Funding acquisition. SW: Conceptualization, Data curation, Investigation, Methodology, Project administration, Resources, Supervision, Validation, Writing – review & editing, Funding acquisition.

Funding

The authors declare that this study received funding from Konica Minolta, Inc. (Tokyo, Japan). The funder had the following involvement in the study: methodology and software.

Conflict of interest

The authors declare that the research was conducted in the absence of any commercial or financial relationships that could be construed as a potential conflict of interest.

The authors declare that this study received funding from Konica Minolta, Inc. (Tokyo, Japan). The funder had the following involvement in the study: methodology and software. The QUIK software used for data analysis in the present study was also supplied by this company.

Publisher's note

Supplementary material

The Supplementary Material for this article can be found online at: https://www.frontiersin.org/articles/10.3389/fimmu.2023.1260492/full#supplementary-material

References

1. Taube JM, Klein A, Brahmer JR, Xu H, Pan X, Kim JH, et al. Association of PD-1, PD-1 ligands, and other features of the tumor immune microenvironment with response to anti-PD-1 therapy. *Clin Cancer Res* (2014) 20:5064–74. doi: 10.1158/1078-0432.CCR-13-3271

2. Michot JM, Bigenwald C, Champiat S, Collins M, Carbonnel F, Postel-Vinay S, et al. Immune-related adverse events with immune checkpoint blockade: a comprehensive review. *Eur J Cancer* (2016) 54:139–48. doi: 10.1016/j.ejca.2015.11.016

3. Le Mercier I, Lines JL, Noelle RJ. Beyond CTLA-4 and PD-1, the generation Z of negative checkpoint regulators. *Front Immunol* (2015) 6:418. doi: 10.3389/fimmu.2015.00418

4. Chen L, Flies DB. Molecular mechanisms of T cell co-stimulation and co-inhibition. *Nat Rev Immunol* (2013) 13:227–42. doi: 10.1038/nri3405

5. Vaddepally RK, Kharel P, Pandey R, Garje R, Chandra AB. Review of indications of FDA-approved immune checkpoint inhibitors per NCCN guidelines with the level of evidence. *Cancers (Basel)* (2020) 12:738. doi: 10.3390/cancers12030738

6. Reck M, Rodríguez-Abreu D, Robinson AG, Hui R, Csőszi T, Fülöp A, et al. Five-year outcomes with pembrolizumab versus chemotherapy for metastatic non-small-cell lung cancer with PD-L1 tumor proportion score ≥ 50. *J Clin Oncol* (2021) 39:2339–49. doi: 10.1200/JCO.21.00174

7. Borghaei H, Gettinger S, Vokes EE, Chow LQM, Burgio MA, de Castro Carpeno J, et al. Five-year outcomes from the randomized, phase III trials checkMate 017 and 057: nivolumab versus docetaxel in previously treated non-small-cell lung cancer. *J Clin Oncol* (2021) 39:723–33. doi: 10.1200/JCO.20.01605

8. Rittmeyer A, Barlesi F, Waterkamp D, Park K, Ciardiello F, von Pawel J, et al. Atezolizumab versus docetaxel in patients with previously treated non-small-cell lung cancer (OAK): a phase 3, open-label, multicentre randomised controlled trial. *Lancet* (2017) 389:255–65. doi: 10.1016/S0140-6736(16)32517-X

9. Boku N, Satoh T, Ryu MH, Chao Y, Kato K, Chung HC, et al. Nivolumab in previously treated advanced gastric cancer (ATTRACTION-2): 3-year update and outcome of treatment beyond progression with nivolumab. *Gastric Cancer* (2021) 24:946–58. doi: 10.1007/s10120-021-01173-w

10. Fradet Y, Bellmunt J, Vaughn DJ, Lee JL, Fong L, Vogelzang NJ, et al. Randomized phase III KEYNOTE-045 trial of pembrolizumab versus paclitaxel, docetaxel, or vinflunine in recurrent advanced urothelial cancer: results of >2 years of follow-up. *Ann Oncol* (2019) 30:970–6. doi: 10.1093/annonc/mdz127

11. Gillison ML, Blumenschein G, Fayette J, Guigay J, Colevas AD, Licitra L, et al. Long-term outcomes with nivolumab as first-line treatment in recurrent or metastatic head and neck cancer: subgroup analysis of checkMate 141. *Oncologist* (2022) 27:e194–8. doi: 10.1093/oncolo/oyab036

12. Wolchok JD, Chiarion-Sileni V, Gonzalez R, Grob JJ, Rutkowski P, Lao CD, et al. Long-term outcomes with nivolumab plus ipilimumab or nivolumab alone versus ipilimumab in patients with advanced melanoma. *J Clin Oncol* (2022) 40:127–37. doi: 10.1200/JCO.21.02229

13. Rodríguez-Abreu D, Powell SF, Hochmair MJ, Gadgeel S, Esteban E, Felip E, et al. Pemetrexed plus platinum with or without pembrolizumab in patients with previously untreated metastatic nonsquamous NSCLC: protocol-specified final analysis from KEYNOTE-189. *Ann Oncol* (2021) 32:881–95. doi: 10.1016/j.annonc.2021.04.008

14. West H, McCleod M, Hussein M, Morabito A, Rittmeyer A, Conter HJ, et al. Atezolizumab in combination with carboplatin plus nab-paclitaxel chemotherapy compared with chemotherapy alone as first-line treatment for metastatic non-squamous non-small-cell lung cancer (IMpower130): a multicentre, randomised, open-label, phase 3 trial. *Lancet Oncol* (2019) 20:924–37. doi: 10.1016/S1470-2045(19)30167-6

15. Wada S, Kobayashi S, Tsunoda T. Future prospects for cancer immunotherapy - Strategies for ineffective cancers. *Hum Vaccin Immunother* (2022) 18:2031699. doi: 10.1080/21645515.2022.2031699

16. Hamada K, Tsunoda T, Yoshimura K. Emerging immune-monitoring system for immune checkpoint inhibitors. *Life (Basel)* (2022) 12:1229. doi: 10.3390/life12081229

17. Tsao MS, Kerr KM, Kockx M, Beasley MB, Borczuk AC, Botling J, et al. PD-L1 immunohistochemistry comparability study in real-life clinical samples: results of blueprint phase 2 project. *J Thorac Oncol* (2018) 13:1302–11. doi: 10.1016/j.jtho.2018.05.013

18. Borghaei H, Paz-Ares L, Horn L, Spigel DR, Steins M, Ready NE, et al. Nivolumab versus docetaxel in advanced nonsquamous non-small-cell lung cancer. *N Engl J Med* (2015) 373:1627–39. doi: 10.1056/NEJMoa1507643

19. Brahmer J, Reckamp KL, Baas P, Crinò L, Eberhardt WE, Poddubskaya E, et al. Nivolumab versus docetaxel in advanced squamous-cell non-small-cell lung cancer. *N Engl J Med* (2015) 373:123–35. doi: 10.1056/NEJMoa1504627

20. Thunnissen E, Allen TC, Adam J, Aisner DL, Beasley MB, Borczuk AC, et al. Immunohistochemistry of pulmonary biomarkers: A perspective from members of the pulmonary pathology society. *Arch Pathol Lab Med* (2018) 142:408–19. doi: 10.5858/arpa.2017-0106-SA

21. Gonda K, Watanabe M, Tada H, Miyashita M, Takahashi-Aoyama Y, Kamei T, et al. Quantitative diagnostic imaging of cancer tissues by using phosphor-integrated dots with ultra-high brightness. *Sci Rep* (2017) 7:7509. doi: 10.1038/s41598-017-06534-z

22. Stack EC, Wang C, Roman KA, Hoyt CC. Multiplexed immunohistochemistry, imaging, and quantitation: a review, with an assessment of Tyramide signal amplification, multispectral imaging and multiplex analysis. *Methods* (2014) 70:46–58. doi: 10.1016/j.ymeth.2014.08.016

23. Yamaki S, Yanagimoto H, Tsuta K, Ryota H, Kon M. PD-L1 expression in pancreatic ductal adenocarcinoma is a poor prognostic factor in patients with high CD8 + tumor-infiltrating lymphocytes: highly sensitive detection using phosphor-integrated dot staining. *Int J Clin Oncol* (2017) 22:726–33. doi: 10.1007/s10147-017-1112-3

24. Fujisawa T, Tsuta K, Yanagimoto H, Yagi M, Suzuki K, Nishikawa K, et al. Quantitative immunohistochemical assay with novel digital immunostaining for comparisons of PD-L1 antibodies. *Mol Clin Oncol* (2019) 10:391–6. doi: 10.3892/mco.2019.1801

25. Eisenhauer EA, Therasse P, Bogaerts J, Schwartz LH, Sargent D, Ford R, et al. New response evaluation criteria in solid tumours: revised RECIST guideline (version 1.1). *Eur J Cancer* (2009) 45:228–47. doi: 10.1016/j.ejca.2008.10.026

26. Paver EC, Cooper WA, Colebatch AJ, Ferguson PM, Hill SK, Lum T, et al. Programmed death ligand-1 (PD-L1) as a predictive marker for immunotherapy in solid tumours: a guide to immunohistochemistry implementation and interpretation. *Pathology* (2021) 53:141–56. doi: 10.1016/j.pathol.2020.10.007

27. Krigsfeld GS, Prince EA, Pratt J, Chizhevsky V, William Ragheb J, Novotny J, et al. Analysis of real-world PD-L1 IHC 28-8 and 22C3 pharmDx assay utilisation, turnaround times and analytical concordance across multiple tumour types. *J Clin Pathol* (2020) 73:656–64. doi: 10.1136/jclinpath-2020-206466

28. Bantis LE, Nakas CT, Reiser B. Construction of confidence regions in the ROC space after the estimation of the optimal Youden index-based cut-off point. *Biometrics* (2014) 70:212–23. doi: 10.1111/biom.12107

29. Hicks DG, Buscaglia B, Goda H, McMahon L, Natori T, Turner B, et al. A novel detection methodology for HER2 protein quantitation in formalin-fixed, paraffin embedded clinical samples using fluorescent nanoparticles: an analytical and clinical validation study. *BMC Cancer* (2018) 18:1266. doi: 10.1186/s12885-018-5172-1

30. Guo Z, Tada H, Kitamura N, Hamada Y, Miyashita M, Harada-Shoji N, et al. Automated quantification of extranuclear ERα using phosphor-integrated dots for predicting endocrine therapy resistance in HR+/HER2- breast cancer. *Cancers (Basel)* (2019) 11:526. doi: 10.3390/cancers11040526

31. Takayanagi N, Momose S, Kikuchi J, Tanaka Y, Anan T, Yamashita T, et al. Fluorescent nanoparticle-mediated semiquantitative MYC protein expression analysis in morphologically diffuse large B-cell lymphoma. *Pathol Int* (2021) 71:594–603. doi: 10.1111/pin.13131

32. Suzuki M, Yagishita S, Sugihara K, Ogitani Y, Nishikawa T, Ohuchi M, et al. Visualization of intratumor pharmacokinetics of [fam-] trastuzumab deruxtecan (DS-8201a) in HER2 heterogeneous model using phosphor-integrated dots imaging analysis. *Clin Cancer Res* (2021) 27:3970–9. doi: 10.1158/1078-0432.CCR-21-0397

33. Inamura K, Shigematsu Y, Ninomiya H, Nakashima Y, Kobayashi M, Saito H, et al. CSF1R-expressing tumor-associated macrophages, smoking and survival in lung adenocarcinoma: analyses using quantitative phosphor-integrated dot staining. *Cancers (Basel)* (2018) 10:252. doi: 10.3390/cancers10080252

34. Wang ZX, Wu HX, Xie L, Lin WH, Liang F, Li J, et al. Exploration of modified progression-free survival as a novel surrogate endpoint for overall survival in immuno-oncology trials. *J Immunother Cancer* (2021) 9:e002114. doi: 10.1136/jitc-2020-002114

frontiers | Frontiers in Immunology

TYPE Systematic Review
PUBLISHED 26 September 2023
DOI 10.3389/fimmu.2023.1265202

OPEN ACCESS

EDITED BY
Eyad Elkord,
University of Salford, United Kingdom

REVIEWED BY
Xin Yu,
Merck, United States
Bing Feng,
Pennington Biomedical Research Center, United States

*CORRESPONDENCE
Taotao Dong
dongtt82@163.com
Yawen Zheng
zhengyawen1993@gmail.com

RECEIVED 22 July 2023
ACCEPTED 08 September 2023
PUBLISHED 26 September 2023

CITATION
Shi H, Zhang W, Zhang L, Zheng Y and Dong T (2023) Comparison of different predictive biomarker testing assays for PD-1/PD-L1 checkpoint inhibitors response: a systematic review and network meta-analysis.
Front. Immunol. 14:1265202.
doi: 10.3389/fimmu.2023.1265202

Comparison of different predictive biomarker testing assays for PD-1/PD-L1 checkpoint inhibitors response: a systematic review and network meta-analysis

Haotong Shi[1], Wenxia Zhang[2], Lin Zhang[2], Yawen Zheng[2]* and Taotao Dong[2]*

[1]Cheeloo College of Medicine, Shandong University, Jinan, China, [2]Department of Obstetrics and Gynecology, Qilu Hospital of Shandong University, Jinan, China

Background: Accurate prediction of efficacy of programmed cell death 1 (PD-1)/programmed cell death ligand 1 (PD-L1) checkpoint inhibitors is of critical importance. To address this issue, a network meta-analysis (NMA) comparing existing common measurements for curative effect of PD-1/PD-L1 monotherapy was conducted.

Methods: We searched PubMed, Embase, the Cochrane Library database, and relevant clinical trials to find out studies published before Feb 22, 2023 that use PD-L1 immunohistochemistry (IHC), tumor mutational burden (TMB), gene expression profiling (GEP), microsatellite instability (MSI), multiplex IHC/immunofluorescence (mIHC/IF), other immunohistochemistry and hematoxylin-eosin staining (other IHC&HE) and combined assays to determine objective response rates to anti–PD-1/PD-L1 monotherapy. Study-level data were extracted from the published studies. The primary goal of this study was to evaluate the predictive efficacy and rank these assays mainly by NMA, and the second objective was to compare them in subgroup analyses. Heterogeneity, quality assessment, and result validation were also conducted by meta-analysis.

Findings: 144 diagnostic index tests in 49 studies covering 5322 patients were eligible for inclusion. mIHC/IF exhibited highest sensitivity (0.76, 95% CI: 0.57-0.89), the second diagnostic odds ratio (DOR) (5.09, 95% CI: 1.35-13.90), and the second superiority index (2.86). MSI had highest specificity (0.90, 95% CI: 0.85-0.94), and DOR (6.79, 95% CI: 3.48-11.91), especially in gastrointestinal tumors. Subgroup analyses by tumor types found that mIHC/IF, and other IHC&HE demonstrated high predictive efficacy for non-small cell lung cancer (NSCLC), while PD-L1 IHC and MSI were highly efficacious in predicting the effectiveness in gastrointestinal tumors. When PD-L1 IHC was combined with TMB, the sensitivity (0.89, 95% CI: 0.82-0.94) was noticeably improved revealed by meta-analysis in all studies.

Interpretation: Considering statistical results of NMA and clinical applicability, mIHC/IF appeared to have superior performance in predicting response to anti PD-1/PD-L1 therapy. Combined assays could further improve the predictive efficacy. Prospective clinical trials involving a wider range of tumor types are needed to establish a definitive gold standard in future.

KEYWORDS

anti-PD-1/PD-L1 inhibitors immunotherapy, biomarkers, predictive value of tests, solid tumor, meta-analysis

1 Introduction

Since the approval of anti-PD-1/PD-L1 inhibitors in the treatment of melanoma in 2014, the overall survival of patients has improved significantly. However, anti-PD-1/PD-L1 immunotherapy still has many shortcomings, such as PD-1/L1-induced immune-related adverse events (irAEs) and hyperprogression (1). It is important to predict patients' response to PD-1/PD-L1 immunotherapy based on the consideration of medical economics.

Various testing assays have been approved to predict the efficacy of anti-PD-1/PD-L1 immunotherapy response. Food and Drug Administration (FDA) has approved PD-1/PD-L1 IHC, TMB, proficient mismatch repair (pMMR) proteins, deficient mismatch repair (dMMR), and MSI-high (MSI-H) for specific tumor types and drugs as companion or complementary diagnostics (2). Similarly, European Communities (CE) and National Medical Products Administration (NMPA) have carried out their own standards on companion diagnostics and prediction assay applications.

PD-L1 IHC, the first approved companion diagnostic biomarker, aims to detect PD-1/PD-L1 expression on tumor cells or inflammatory cells. However, the efficacy of IHC may be influenced by the experience of pathologists, tumor types examined, and the used scoring methods. Researchers are now exploring the optimal detecting assay and scoring methods for specific tumors (3).

TMB has been found to increase neoantigens of major histocompatibility complexes (MHC) in various cancers, which leading to better immunotherapy response in patients. Increasing evidence indicates that different tumor types own various expression levels of TMB. TMB is usually assessed by next-generation sequencing (NGS) platforms, though standards of threshold and application methods need to be defined exactly to enhance accuracy across different tumor types. This would entail considerations such as genome coverage, workflow, and appropriate cutoff values (4). MSI and GEP display the difference in gene expression as well. MSI-H phenotype arises from numerous frameshift mutations due to deficits of the MMR system (5). Patients with MSI-H are more likely to suffer from various cancers, including colorectal cancer. MMR proteins, which could be detected by IHC, polymerase chain reaction (PCR), and gene sequencing, are now being used to identify MSI-H patients in various cancer types.

Detection and evaluation of tumor microenvironment (TME) have also been explored in recent years (6). For example, researchers have found that the epithelial-mesenchymal transition (EMT)- and stroma-related gene expression status is related to patients' tumorigenesis and drug resistance (7, 8). mIHC/IF and gene sequencing technique could offer more chances to verify (9). GEP could also allow the integrations of different gene signatures and training models to predict prognosis and drug response based on the results of DNA-microarray and RNA sequencing (RNA-Seq) (10–12). Some researchers have also explored the combined approaches, such as TMB+GEP or TMB+IHC, since such predictors could work through different mechanisms or may be positively correlated with each other. All biomarker assays mentioned above present novel opportunities to predict the response rate of PD-1/PD-L1 inhibitors.

Assessment and evaluation of diagnostic tests could also benefit from the increasing diagnostic test accuracy (DTA) studies and the continuous development of statistical methods. In the era of evidence-based medicine, meta-analysis plays an important role in integrating of different studies with pairs of intervention using various methodological methods. To enable the comparison of different assays with limited data and generate a whole scale ranking results, NMA turned out to be a better tool to indirectly compare and jointly analyze three or more DTA studies simultaneously.

In this study, we compared the diagnostic accuracy of seven biomarker testing assays, including PD-L1 IHC, TMB, GEP, MSI, mIHC/IF, other IHC&HE, as well as combined assays for predicting anti-PD-1/PD-L1 immunotherapeutic response. Diagnostic accuracy measures used in this study included sensitivity, specificity, relative sensitivity, relative specificity, PPV, NPV, relative predictive values, DOR, and superiority index (13). It is believed that the NMA performed here could provide stronger clinical evidence for current medical practice.

2 Methods

This NMA was performed according to the Preferred Reporting Items for Systematic Reviews and Meta-analyses (PRISMA) NMA checklist.

2.1 Eligibility criteria

The included research articles in this study were based on real-world data, and English translations were available. The studies were required to conduct PD-1/PD-L1 monotherapies and utilize at least two predictive biomarker testing assays on pre-treatment tissue samples. These assays could include PD-L1 IHC, TMB, GEP, MSI, mIHC/IF, HE for tumor-infiltrating lymphocytes (TIL), or other IHC methods. Each biomarker testing assay should provide sufficient information to determine the objective response rate (ORR) or non-progression rate (NPR) and allow for the calculation of sensitivity and specificity. If any testing assay had fewer than 15 tissue samples, it would not be considered. Hematologic cancers and flow cytometry studies on tumor lysates were excluded.

2.2 Search strategy and data collection

We systematically searched PubMed, Embase, and the Cochrane Library database for relevant studies and their errata (till February 2023). Additionally, we manually searched articles related to relevant clinical trials. For example, the search formula of Embase included: ("Immunohistochemistry " OR " Tumor mutational burden " OR " gene expression profiling " OR " multiplex immunofluorescence " OR " neoantigen load " OR " Immunofluorescence ")[Find articles with these terms] AND ("Pembrolizumab " OR " Nivolumab " OR " Durvalumab " OR " Toripalimab " OR " Camrelizumab " OR " Atezolizumab " OR " Avelumab " OR " Avelumab " OR " Budigalimab ")[Title, abstract or author-specified keywords] AND (Research articles)[Filter]. The intact search formula and results were in the Supplementary material.

Necessary information from eligible studies was extracted by three researchers independently and all inconsistencies were settled by discussion. The trial name, first author, year of publication, sample size, trial phase, tumor type, PD-1/PD-L1 antibody, and index test assay was recorded. To calculate sensitivity and specificity for each index test, we organized ORR-related information into a 2x2 table. We used Youden's index, which combines values for sensitivity and specificity to indicate test accuracy, to select the best-performing threshold among multiple thresholds. If a clinical trial has multiply publications, the one with most complete information was adopted.

2.3 Statistical analysis and quality assessment

The main outcomes were calculated by NMA. As for Bayesian NMA, the ANOVA model made it possible to use the original data and arm-based (AB) model (14). The latter shows superiority to contrast-based (CB) models by accommodating more complex variance-covariance structures. NMA was mainly performed with the R package "Rstan" (R version 4.2.2). In order to improve accuracy and compare diagnostic assays one by one, calculations were repeated 7 times (model_code = model, chains = 2, iterations = 10000, warmup = 5000, thin = 5), and then, we draw league tables for relative comparations. Given numerical variance, we chose the median of sensitivity, specificity, PPV, NPV, SROC, and superiority index.

The Midas module for DTA meta-analysis facilitated validation of results and assessment of heterogeneity by forest plot and I^2 analysis for every 7 biomarker modalities. Sensitivity, specificity, DOR, and summary receiver operating characteristic (SROC) curves and their associated area under the curve (AUC) were analyzed by Midas, which employs a bivariate mixed-effects logistic regression modeling framework and empirical Bayesian predictions. Publication bias of studies was also evaluated by Deeks' funnel plot asymmetry test ($p<0.05$ indicating significant asymmetry). The network graphs package on Stata were used to draw the network graphs. Meta-analysis and drawing figures were fulfilled in Stata (17.0 MP—Parallel Edition).

The QUADAS-C (Quality Assessment of Diagnostic Accuracy Study) tool was used to assess the risk of bias and applicability in each selected study. There were 4 sections for risk of bias: patient selection, index test, reference standard, and flow and timing; meanwhile, concerns regarding applicability were presented in 3 sections: patient selection, index test, and reference standard.

3 Results

3.1 Systematic review and characteristics of the included studies

3652 articles from databases and an additional 304 articles related to clinical trials were retrieved in total. After removing duplicates and glancing at the abstracts and titles, 294 articles were identified for full-text scrutiny. The literature search and study selection flow were recorded in Figure 1. Ultimately, a total of 49 studies involving 5322 patients were included in our analysis. 144 diagnostic index tests were extracted across all 49 studies, comprising PD-L1 IHC (n=46) (15–58), TMB (n=27) (15–33, 58–62), combined assays (n=22) (7, 16, 18, 20, 23, 31, 34–38, 61, 62), other IHC&HE (n=19) (7, 16–18, 21, 30, 33–35, 37–45), MSI (n=13) (21, 39, 46-53, 58, 61), GEP (n=13) (7, 16, 20, 23, 51, 53–56, 60, 62) and mIHC/IF (n=4)(36, 37, 43, 57). HE staining was used to score TIL. The situation where testing assays had been directly compared was represented by a network plot (Figure 2). 15 types of tumors accounted for the majority of the studies, while 7 studies (18, 20, 27, 31, 42, 60, 61) involved several solid tumors. 8 of 13 MSI tests (39, 46, 47, 50–53, 58) detected gastrointestinal cancer. The summary of included articles and details of studies can be found in Supplementary Tables 1, 2.

3.2 Sensitivity, specificity, PPV and NPV

The sensitivity and specificity of NMA were summarized in Table 1. Among the diagnostic index tests, mIHC/IF (0.76, 95% CI: 0.57-0.89) exhibited the highest sensitivity, whereas GEP (0.52, 95% CI: 0.42-0.63), multi-assay (0.46, 95% CI: 0.39-0.52) and MSI (0.42,

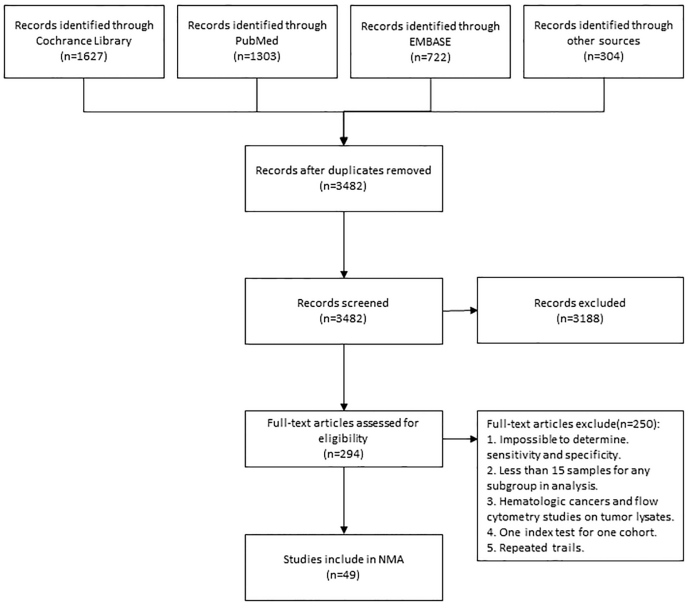

FIGURE 1
Flowchart Showing Literature Search and Study Selection. The study process followed the PRISMA guidelines. NMA, network meta-analysis.

95% CI: 0.30-0.53) have low efficacy. Other IHC&HE (0.66, 95% CI: 0.57-0.73), PD-L1 IHC (0.63, 95% CI: 0.59-0.67), and TMB (0.62, 95% CI: 0.56-0.68) presented similar sensitivities to rule out stable disease and progressive disease. As for specificity, MSI (0.90, 95% CI: 0.85-0.94) and combined assays (0.84, 95% CI: 0.79-0.87) performed better than the others. The specificities of the remaining testing assays were quite close, with TMB, other IHC&HE, PD-L1 IHC, GEP, and mIHC/IF having specificities of 0.65 (95% CI: 0.60-0.70), 0.63 (95% CI: 0.55-0.69), 0.61 (95% CI: 0.58-0.64), 0.61 (95% CI: 0.52-0.69) and 0.57 (95% CI: 0.39-0.73), respectively.

Table 1 also revealed that the PPV for each assay was below 0.60, indicating that positive results may not correctly predict the response to PD-1/PD-L1 checkpoint inhibitors. MSI (0.56, 95% CI: 0.45-0.67) had the highest PPV, while GEP (0.33, 95% CI: 0.28-0.38) was the lowest. However, all assays provided relatively good performance in NPV, with even the lowest being near 0.80 (GEP: 0.8, 95% CI: 0.77-0.83). This suggested that these assays were useful in providing evidence to refuse immunologic therapy due to the accuracy of figuring out non-responsive patients.

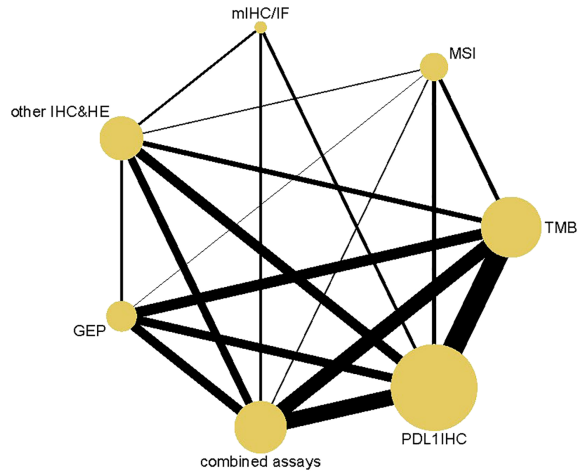

FIGURE 2
Network Plot. Both nodes and lines are weighted according to the number of studies involved in each treatment and direct comparison, respectively. PD-L1 IHC, Programmed cell death ligand 1 immunohistochemistry; TMB, Tumor mutational burden; GEP, Gene expression profiling; MSI, Microsatellite instability; mIHC/IF, Multiplex immunohistochemistry/immunofluorescence; other IHC&HE, Other Immunohistochemistry and hematoxylin-eosin staining.

3.3 Rankings, DOR and superiority index

Relative sensitivity, relative specificity, relative PPV, and relative NPV were shown in the league table (Table 2). From the league table for relative sensitivity (lower triangle of Table 2 (A), we can see that mIHC/IF, other IHC&HE, and PD-L1 IHC had similar efficacy and performed better than TMB, GEP, combined assays, and MSI according to the relative risk (RR) values. The upper triangle of Table 2(A) represented the relative specificity, MSI and multi-assay showed superiority to the other, meanwhile, the remaining tests exhibited comparable efficacy. Similarly, MSI and combined assays demonstrated higher relative PPVs among assays, as shown in the lower triangle of Table 2(B). There was no difference among relative NPVs (upper triangle of Table 2(B).

Table 1 presented the odds of responsive patients in test positives versus the odds of responsive patients in test negatives as measured by the DOR. MSI (6.79, 95% CI: 3.48-11.91) has the highest DOR as its high specificity, followed by mIHC/IF (4.44, 95% CI: 3.19-5.93), largely driven by its high sensitivity. In contrast, the DOR for gene expression profiling (GEP) was noticeably lower at

10.3389/fimmu.2023.1265202

TABLE 1 Sensitivity, specificity, PPV, NPV, and diagnostic odds ratio (DOR) and superiority index by network meta-analysis.

Test	Ranks	Sensitivity	Ranks	Specificity	Ranks	PPV	Ranks	NPV	Ranks	DOR	Ranks	Superiority Index
mIHC/IF	1	0.76 (0.57,0.89)	7	0.57 (0.39,0.73)	6	0.33 (0.28,0.38)	1	0.86 (0.79,0.91)	2	5.09 (1.35,13.90)	2	2.86 (0.14,9.00)
other IHC&HE	2	0.66 (0.57,0.73)	4	0.63 (0.55,0.69)	4	0.36 (0.31,0.41)	2	0.85 (0.82,0.88)	4	3.22 (1.97,5.05)	3	2.66 (0.20,7.00)
PD-L1 IHC	3	0.63 (0.59,0.67)	5	0.61 (0.58,0.64)	5	0.34 (0.32,0.37)	4	0.84 (0.82,0.85)	6	2.67 (2.17,3.25)	5	1.15 (0.14,5.00)
TMB	4	0.62 (0.56,0.68)	3	0.65 (0.60,0.70)	3	0.38 (0.34,0.42)	3	0.84 (0.82,0.86)	5	3.10 (2.21,4.25)	1	2.94 (0.20,7.00)
GEP	5	0.52 (0.43,0.63)	6	0.61 (0.52,0.69)	7	0.33 (0.28,0.38)	7	0.80 (0.77,0.84)	7	1.81 (1.31,2.40)	7	0.33 (0.14,1.00)
combined assays	6	0.46 (0.39,0.54)	2	0.84 (0.79,0.87)	2	0.48 (0.43,0.53)	6	0.82 (0.80,0.84)	3	4.44 (3.19,5.93)	6	1.14 (0.33,3.00)
MSI	7	0.42 (0.30,0.53)	1	0.90 (0.85,0.94)	1	0.56 (0.45,0.67)	5	0.83 (0.79,0.86)	1	6.79 (3.48,11.91)	4	1.65 (1.00,5.00)

PPV, Positive predictive value; NPV, Negative predictive value; PD-L1 IHC, Programmed cell death ligand 1 immunohistochemistry; TMB, Tumor mutational burden; GEP, Gene expression profiling; MSI, Microsatellite instability; mIHC/IF, Multiplex immunohistochemistry/immunofluorescence; other IHC&HE, Other Immunohistochemistry and hematoxylin-eosin staining.

1.81 (95% CI: 1.31-2.40). The high superiority index indicated biomarkers modality performs comparatively well in both sensitivity and specificity. In contrast, the low superiority index represents biomarkers that had a poor performance of at least one assessment measure. As Table 1 summarized, the ranks of superiority index from highest to lowest were TMB, mIHC/IF, other IHC&HE, MSI, PD-L1 IHC, combined assays, and GEP.

3.4 Heterogeneity and quality assessment

To further validate these present results, a meta-analysis was conducted and revealed the same ranks of sensitivity, specificity, and DOR as NMA (Table 3). The value of sensitivity and specificity were very similar, indicating reliable results from the ANOVA model used in the NMA. SROC generated through meta-analysis displayed the AUC for each biomarker testing assay. mIHC/IF had the largest AUC (0.80), while GEP exhibited the smallest (0.61) and AUC of all others were close to 0.70 (Figure 3). Ranking trends for AUC and DOR were similar, indicating the reliability of our ranking results for NMA.

However, the heterogeneity for each biomarker was high due to the absence of testing standards and various tumor types and thresholds. Although we chose the best performance threshold, I^2 was higher than 50% (Supplementary Figure 1). Nonetheless, publication bias wasn't obvious ($p>0.1$), according to Supplementary Figure 2. QUADAS-C tools allowed us to evaluate the quality (Supplementary Table 3).

3.5 Subgroup analysis

We conducted NMA for two subgroups of studies: 10 studies focused on non-small cell lung cancer (NSCLC) (7, 23, 32–34, 45, 54, 58) and 12 studies centered around gastrointestinal tumors (19, 33, 39, 46, 47, 50–53, 58, 59) as reported in Table 4 and Table 5. For NSCLC, mIHC/IF and multi-assay had high sensitivity (0.90, 95% CI: 0.44-1.00) and specificity (0.90, 95% CI: 0.84-0.95) separately. mIHC/IF, with only one study available, exhibited both high sensitivity and specificity (0.89, 95% CI: 0.69-0.98), suggesting its potential as a reliable biomarker modality. Further analysis based on the ranks of DOR and superiority index suggested mIHC/IF, multi-assay and other IHC&HE were better among the 6 testing assays investigated.

In the case of gastrointestinal cancers, MSI had high specificity (0.89, 95% CI: 0.82-0.92) and low sensitivity (0.40, 95% CI: 0.27-0.54). PD-L1 IHC along with other IHC&HE demonstrated relatively high DOR and superiority index, besides MSI.

Concerning that the majority of combined assays contained 3 models, namely, TMB+GEP (n=6) (16, 20, 23), TMB+PD-L1 IHC (n=6) (18, 20, 30), and PD-L1 IHC+other IHC&HE (n=5) (34–38). A meta-analysis was performed to explore sensitivity, specificity, DOR, and AUC (Supplementary Figure 3) in these models. TMB+PD-L1 IHC showed the best balance between sensitivity (0.89, 95% CI: 0.82-0.94) and specificity (0.68, 95% CI: 0.53-0.81) with high DOR (18, 95% CI: 9-37) and AUC (0.87, 95% CI: 0.84-

TABLE 2 Relative sensitivity, relative specificity, relative PPV, and relative NPV by network meta-analysis.

(A)						
mIHC/IF	0.92 (0.69,1.21)	0.96 (0.83,1.17)	0.85 (0.62,1.19)	0.87 (0.60,1.15)	**0.67 (0.46,0.90)**	**0.63 (0.43,0.83)**
RANK7	**GEP**	1.03 (0.99,1.11)	1.00 (0.83,1.17)	0.94 (0.79,1.08)	**0.73 (0.62,0.83)**	**0.68 (0.57,0.78)**
	RANK6	**PD-L1 IHC**	0.99 (0.88,1.12)	0.94 (0.86,1.04)	**0.73 (0.68,0.79)**	**0.68 (0.63,0.73)**
RANK1		**RANK5**	**other IHC&HE**	0.95 (0.82,1.10)	**0.74 (0.65,0.84)**	**0.69 (0.60,0.78)**
mIHC/IF	**RANK2**		**RANK4**	**TMB**	**0.78 (0.71,0.85)**	**0.72 (0.65,0.79)**
0.90 (0.70,1.21)	**other IHC&HE**	**RANK3**		**RANK3**	**combined assays**	**0.93 (0.87,0.99)**
0.86 (0.69,1.14)	1.00 (0.85,1.10)	**PD-L1 IHC**	**RANK4**		**RANK2**	**MSI**
0.85 (0.66,1.15)	0.96 (0.81,1.11)	1.01 (0.95,1.12)	**TMB**	**RANK5**		**RANK1**
0.72 (0.53,0.97)	**0.78 (0.64,0.99)**	**0.79 (0.69,0.91)**	0.85 (0.68,1.04)	**GEP**	**RANK6**	
0.63 (0.48,0.85)	**0.73 (0.58,0.84)**	**0.70 (0.65,0.83)**	**0.74 (0.61,0.90)**	0.80 (0.67,1.08)	**combined assays**	**RANK7**
0.57 (0.38,0.81)	**0.63 (0.46,0.82)**	**0.74 (0.68,0.81)**	**0.67 (0.48,0.88)**	0.78 (0.56,1.05)	0.89 (0.61,1.21)	**MSI**
(B)						
GEP	0.99 (0.94,1.03)	0.97 (0.91,1.04)	0.96 (0.92,1.00)	0.96 (0.91,1.00)	**0.94 (0.89,0.99)**	**0.94 (0.87,1.03)**
RANK7	**combined assays**	0.99 (0.93,1.05)	0.98 (0.94,1.01)	0.97 (0.94,1.00)	**0.96 (0.92,10.0)**	**0.96 (0.90,1.04)**
	RANK6	**MSI**	0.99 (0.93,1.04)	0.98 (0.93,1.03)	**0.97 (0.91,1.03)**	**0.97 (0.89,1.06)**
RANK1		**RANK5**	**PD-L1 IHC**	1.00 (0.97,1.03)	**0.98 (0.94,1.02)**	**0.98 (0.92,1.07)**
MSI	**RANK2**		**RANK4**	**TMB**	**0.99 (0.94,1.03)**	**0.99 (0.92,1.08)**
0.86 (0.70,1.09)	**combined assays**	**RANK3**		**RANK3**	**other IHC&HE**	**1.00 (0.93,1.09)**
0.68 (0.54,0.85)	**0.79 (0.68,0.90)**	**TMB**	**RANK4**		**RANK2**	**mIHC/IF**
0.64 (0.50,0.81)	**0.74 (0.62,0.88)**	0.95 (0.78,1.12)	**other IHC&HE**	**RANK5**		**RANK1**
0.61 (0.50,0.77)	**0.72 (0.62,0.81)**	**0.91 (0.81,1.03)**	0.97 (0.82,1.14)	**PD-L1 IHC**	**RANK6**	
0.60 (0.38,0.86)	**0.70 (0.46,0.96)**	**0.89 (0.59,1.22)**	**0.94 (0.64,1.31)**	0.97 (0.65,1.32)	**mIHC/IF**	**RANK7**
0.59 (0.46,0.76)	**0.69 (0.58,0.81)**	**0.88 (0.74,1.05)**	**0.94 (0.75,1.15)**	0.96 (0.80,1.13)	1.02 (0.69,1.50)	**GEP**

(A) Relative risk (RR) values and 95% CIs for sensitivity (lower triangle) and specificity (upper triangle) were in Table 2.
(B) Relative risk (RR) values and 95% CIs for PPV (lower triangle) and NPV (upper triangle) were in Table 2.
The values highlighted in bold indicated a significant difference between the two compared assays. Relative risk (RR) values <1.00 provided better predictive efficacy.
PD-L1 IHC, Programmed cell death ligand 1 immunohistochemistry; TMB, Tumor mutational burden; GEP, Gene expression profiling; MSI, Microsatellite instability; mIHC/IF, Multiplex immunohistochemistry/immunofluorescence; other IHC&HE, Other Immunohistochemistry and hematoxylin-eosin staining.

TABLE 3 Result validation by meta-analysis.

Ranks	Test	Sensitivity	Test	Specificity	Test	DOR
1	mIHC/IF	0.83 (0.14-0.99)	MSI	0.96 (0.88-0.99)	MSI	13 (6-9)
2	other IHC&HE	0.66 (0.55-0.75)	combined assays	0.85 (0.79-0.89)	mIHC/IF	12 (1-243)
3	PD-L1 IHC	0.63 (0.55,0.70)	TMB	0.68 (0.60-0.74)	multi-assay	5 (4-7)
4	TMB	0.63 (0.56-0.70)	other IHC&HE	0.63 (0.57-0.69)	other IHC&HE	3 (2-5)
5	GEP	0.58 (0.38-0.76)	PD-L1 IHC	0.63 (0.57.0.69)	TMB	4 (3,5)
6	combined assays	0.47 (0.39-0.55)	GEP	0.61 (0.51-0.69)	PD-L1 IHC	3 (2,4)
7	MSI	0.36 (0.23-0.52)	mIHC/IF	0.71 (0.45-0.88)	GEP	2 (1,4)

DOR, Diagnostic odds ratio; PD-L1 IHC, Programmed cell death ligand 1 immunohistochemistry; TMB, Tumor mutational burden; GEP, Gene expression profiling; MSI, Microsatellite instability; mIHC/IF, Multiplex immunohistochemistry/immunofluorescence; other IHC&HE, Other Immunohistochemistry and hematoxylin-eosin staining.

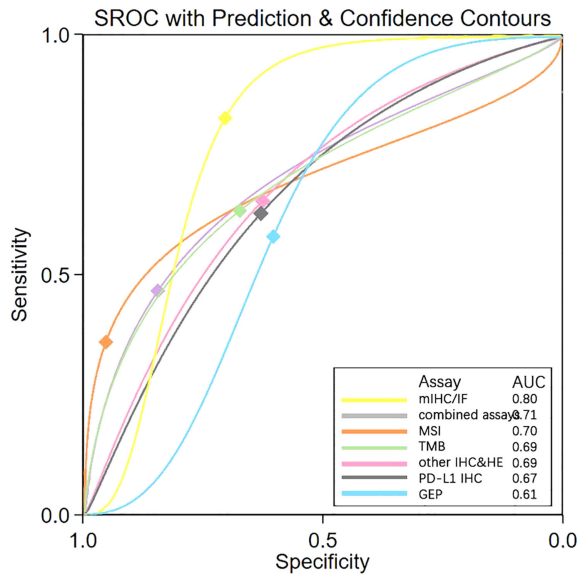

FIGURE 3
SROC Plot of "mIHC/IF" "combined assays" "MSI " "TMB" "other IHC&HE" "PDL1 IHC" and "GEP" by Meta-analysis. SROC, Summary receiver operating characteristic curves; AUC, Area under the curve; PD-L1 IHC, Programmed cell death ligand 1 immunohistochemistry; TMB, Tumor mutational burden; GEP, Gene expression profiling; MSI, Microsatellite instability; mIHC/IF, Multiplex immunohistochemistry/immunofluorescence; other IHC&HE, Other Immunohistochemistry and hematoxylin-eosin staining.

0.90). Conversely, the other models yielded higher sensitivity but lower specificity compared to a single assay in the meta-analysis (Supplementary Figure 3).

4 Discussion

In this article, we compared 7 common biomarker testing assays to assess their efficacy in predicting response to PD-1/PD-L1 checkpoint inhibitors. mIHC/IF had the highest sensitivity (0.76, 95% CI: 0.57-0.89) and AUC (0.80), the second highest DOR (5.09, 95% CI: 1.35-13.90) and superiority index (2.86), but relative lower specificity (0.57, 95% CI: 0.39-0.73). Although MSI exhibited the highest DOR (6.79, 95% CI: 3.48-11.91), its application is mainly limited to gastrointestinal tumors. Despite being the most commonly used method in clinical practice, PD-L1 IHC had not demonstrated obvious advantages in terms of sensitivity, specificity, DOR, as well as superiority index. Yet, when PD-L1 IHC is combined with TMB, a notable increase in sensitivity (0.89, 95% CI: 0.82-0.94) was observed.

Our conclusion is in alignment with those from a previous meta-analyses that had addressed similar topics (63, 64), which indicated that mIHC/IF was superior to PD-L1 IHC, TMB and GEP in predicting response to PD-1/PD-L1 checkpoint inhibitors and that combinatorial assays could improve predictive efficacy. Yet, to our best of knowledge, our study was the first to use NMA to demonstrate the objective benefits of mIHC/IF in predicting patients' response to PD-1/PD-L1 checkpoint inhibitors. Upon stratifying by tumor types, we also observed that mIHC/IF had both remarkable sensitivity and specificity in NSCLC. PD-L1, mIHC/IF and IHC also manifested relatively high DOR and superiority index in gastrointestinal cancers, which further substantiated the strengths of mIHC/IF.

To address the challenge of ranking multiple diagnostic tests simultaneously, statistical scientists have developed several new models based on the Bayesian setting for NMA of DTA studies (65), since traditional meta-analysis and NMA of intervention were not efficient enough to handle this issue. Multivariate extensions of meta-analysis models of DTA had been applied to NMA. In addition, the ANOVA model used in this NMA could facilitate ORR to be compared indirectly and rank testing assays directly (14). Researchers could also compare multiple thresholds per testing assay using certain models (66).

High sensitivity, DOR, and AUC of mIHC/IF collectively indicated its superiority in identification of potential patients who may benefit most from immunotherapy. mIHC/IF facilitates the acquisition of quantitative multiplexed data, which plays a pivotal role in deciphering the intricate relationship between tumor cells, their microenvironment, and antigen expressions at the single-cell level. This capability assumes paramount importance in understanding tumorigenesis, cancer progression, and immunotherapy responses. In all instances of mIHC/IF index testing, CD8 was included, and T cell antigen expression was examined. Various studies have established a link between T cells' cytotoxicity and pro-inflammatory activity with patients prognosis through its regulation of inherent immunological function by tumor antigens like CD8 or PD-1 (67–70), which further supports the potency of antigens on tumor-infiltrating lymphocytes (TILs). However, false negative results obtained from mIHC/IF screening may exclude some patients who may could benefit from immunotherapy, suggesting the need to explore additional proteins and combined assays to improve specificity. To enhance the precision in scoring staining, many researchers have incorporated artificial intelligence with mIHC/IF, rendering it a relatively convenient and cost-effective method when compared to combined assays (71). Thus, our study has concluded that mIHC/IF had the best performance and a broad range of applications.

PD-L1 IHC, the most widely used assay, exhibited suboptimal performance in sensitivity, specificity, and DOR. As previously mentioned, TME is excessively intricate and heterogeneous to be comprehensively elucidated by a singular mechanism. Furthermore, expressions of PD-1 and PD-L1 exhibit considerable interpatient variability. These two factors collectively contribute to the suboptimal performance of PD-L1 IHC as a predictive marker. The possible reasons for such unsatisfactory results varied, including the lack of experience for pathologists, sample type examined, and IHC assays used (72). A meta-analysis that scrutinized and compared different IHC assays using tumor proportion score (TPS) revealed that the sensitivity and specificity values were similar except SP142 with lower sensitivity (73). The quantification and assessment of PD-1 protein expression through

TABLE 4 Subgroup analysis of NSCLC by network meta-analysis.

Rank	Test	Sensitivity	Rank	Test	Relative Sensitivity	Rank	Test	DOR
1	mIHC/IF	0.90 (0.44,1.00)	**1**	mIHC/IF	1.42 (0.68,1.74)	**1**	mIHC/IF	1607584.12 (5.95,833493.27)
2	PD-L1 IHC	0.64 (0.56,0.72)	**2**	PD-L1 IHC	1.00 (1.00,1.00)	**2**	combined assays	6.55 (2.96,12.88)
3	TMB	0.59 (0.48,0.69)	**3**	TMB	0.92 (0.73,1.11)	**3**	other IHC&HE	6.20 (2.67,12.45)
4	other IHC&HE	0.55 (0.42,0.69)	**4**	other IHC&HE	0.87 (0.63,1.11)	**4**	PD-L1 IHC	3.30 (2.10,4.96)
5	GEP	0.44 (0.31,0.56)	**5**	GEP	0.68 (0.48,0.89)	**5**	TMB	2.88 (1.57,5.15)
6	combined assays	0.39 (0.27,0.50)	**6**	combined assays	0.61 (0.43,0.80)	**6**	GEP	1.68 (0.79,3.13)
Rank	**Test**	**Specificity**	**Rank**	**Test**	**Relative Specific-ity**	**Rank**	**Test**	**Superiority Index**
1	combined assays	0.90 (0.84,0.95)	**1**	combined assays	1.41 (1.25,1.59)	**1**	mIHC/IF	9.02 (1.00,11.00)
2	mIHC/IF	0.89 (0.69,0.98)	**2**	mIHC/IF	1.38 (1.06,1.61)	**2**	other IHC&HE	1.90 (0.33,7.00)
3	other IHC&HE	0.82 (0.71,0.89)	**3**	other IHC&HE	1.27 (1.08,1.47)	**3**	combined assays	1.07 (0.20,3.00)
4	GEP	0.67 (0.55,0.78)	**4**	GEP	1.04 (0.84,1.25)	**4**	PD-L1 IHC	0.83 (0.20,3.00)
5	TMB	0.66 (0.55,0.75)	**5**	TMB	1.02 (0.84,1.22)	**5**	TMB	0.65 (0.14,3.00)
6	PD-L1 IHC	0.64 (0.58,0.70)	**6**	PD-L1 IHC	1.00 (1.00,1.00)	**6**	GEP	0.18 (0.09,0.33)

DOR, Diagnostic odds ratio; PD-L1 IHC, Programmed cell death ligand 1 immunohistochemistry; TMB, Tumor mutational burden; GEP, Gene expression profiling; MSI, Microsatellite instability; mIHC/IF, Multiplex immunohistochemistry/immunofluorescence; other IHC&HE, Other Immunohistochemistry and hematoxylin-eosin staining.

TABLE 5 Subgroup analysis of gastrointestinal tumors by network meta-analysis.

Rank	Test	Sensitivity	Rank	Test	Relative Sensitivity	Rank	Test	DOR
1	other IHC&HE	0.72 (0.35,0.95)	**1**	other IHC&HE	1.00 (1.00,1.00)	**1**	other IHC&HE	7.24 (0.35,37.15)
2	PD-L1 IHC	0.56 (0.44,0.68)	**2**	PD-L1 IHC	0.84 (0.52,1.61)	**2**	MSI	5.73 (2.49,10.59)
3	TMB	0.55 (0.33,0.76)	**3**	TMB	0.82 (0.41,1.64)	**3**	PD-L1 IHC	2.73 (1.45,4.76)
4	MSI	0.40 (0.27,0.54)	**4**	MSI	0.60 (0.33,1.20)	**4**	mIHC/IF	1.92 (0.03,11.96)
5	mIHC/IF	0.37 (0.04,0.84)	**5**	mIHC/IF	0.55 (0.06,1.48)	**5**	TMB	1.62 (0.39,4.56)
6	GEP	0.06 (0.00,0.39)	**6**	GEP	0.10 (0.00,0.64)	**6**	GEP	0.45 (0,30,0.86)
Rank	**Test**	**Specificity**	**Rank**	**Test**	**Relative Sensitivity**	**Rank**	**Test**	**Superiority Index**
1	MSI	0.89 (0.82,0.92)	**1**	MSI	1.91 (1.09,4.19)	**1**	MSI	4.17 (1.00,7.00)
2	GEP	0.70 (0.28,0.96)	**2**	GEP	1.50 (0.49,3.52)	**2**	PD-L1 IHC	3.44 (0.33,7.00)
3	PD-L1 IHC	0.67 (0.60,0.73)	**3**	PD-L1 IHC	1.44 (0.81,3.14)	**3**	other IHC&HE	3.09 (0.14,9.00)
4	mIHC/IF	0.56 (0.17,0.91)	**4**	mIHC/IF	1.19 (0.32,2.88)	**4**	TMB	1.30 (0.14,7.00)
5	TMB	0.52 (0.32,0.71)	**5**	TMB	1.13 (0.50,2.65)	**5**	mIHC/IF	1.17 (0.11,7.00)
6	other IHC&HE	0.52 (0.21,0.82)	**6**	other IHC&HE	1.00 (1.00,1.00)	**6**	GEP	0.47 (0.09,3.00)

DOR, Diagnostic odds ratio; PD-L1 IHC, Programmed cell death ligand 1 immunohistochemistry; TMB, Tumor mutational burden; GEP, Gene expression profiling; MSI, Microsatellite instability; mIHC/IF, Multiplex immunohistochemistry/immunofluorescence; other IHC&HE, Other Immunohistochemistry and hematoxylin-eosin staining.

scoring methods varied among different assays, such as TPS, combined positivity score (CPS), and immune cell (IC) score (3). Gastrointestinal tumors were characterized by their most extensive proportions of MSI-H/dMMR, therefore, MSI status detection could be a reasonable approach to predict the response to immunotherapy. Subgroup analysis of gastrointestinal tumors indicated that MSI detection offered a valuable method for ruling out non-responsive patients due to its high specificity performance. MSI detection was also conducted in other solid tumors, including endometrial cancer, adrenocortical carcinomas, and multiple endocrine neoplasias (MENs). High specificity, DOR, and AUC of MSI suggested its potential applications in some other tumor types. Regrettably, generalization of MSI detections to a wider range of tumors may be prevented by the fact that most tumors in fact exhibit microsatellite stability (MSS) status.

Our efficacy rankings placed TMB and other IHC&HE in the middle, while GEP was ranked last, although they are closely related to crucial aspects of tumor immunology such as neoantigen, TME, and inflammatory gene signature. Nevertheless, it is important to note that the MSI status, TMB, and GEP serve as indicators of the gene phenotype, which is not directly associated with the primary mechanism of PD-1/PD-L1 immunotherapy compared to protein expression. The measurements obtained through MSI, TMB, and GEP reflect events upstream of gene expression, which may potentially diminish their predictive efficacy. Uncovering specific and precise gene pathways solely through these indicators can prove to be challenging. Whereas thresholds for TMB and GEP were mainly determined by proportions, other IHC&HE methods typically detected CD8 and TILs with different methods. This highlights the potential impossibility that some immature tests could have covered all types of tumors.

Combined assays provided more chances to improve the prediction accuracy in current challenging scenario. When TMB was combined with PD-L1 IHC, the performance of sensitivity was improved noticeably without sacrificing specificity. Ricciuti, B. et al. have explored the association of high TMB with other biomarkers and found that high TMB was related to higher proportions of tumor-infiltrating CD8+, PD1+ T cells, and high PD-L1 expression in cancer cells (74). Fumet, J.-D. et al. reported that tumors displaying high PD-L1/low CD8 TILs developed microenvironments conducive to tumor proliferation and exhibited poor outcomes (75). This may explain the enhanced efficacy of combined assays. Yet, the shortcomings of combined assays were high cost and technical complexity.

Despite nearly a decade of research on companion or complementary diagnostics for prediction purposes, the most effective indicators for PD-1/PD-L1 inhibitors have not yet been established for most tumors. While some testing assays such as mIHC/IF and combined tests hold potential values, there was still no perfect test with satisfactory sensitivity and specificity simultaneously in our analysis. Consequently, clinicians should exert appropriate caution when detecting predictive biomarkers and interpreting associated results. Additionally, it is believed that our NMA could provide supporting evidence to researchers and clinicians for amelioration of predictive tests in future.

5 Limitations

It is crucial to note that a high ORR doesn't necessarily translate into a high OS. It is essential to take care when interpreting results based on studies that relied solely on ORR which may not take into account of OS or progressive rate. To mitigate bias, it is worth noting that the threshold we chose with Youden's index may favor higher sensitivity and specificity. An article with two or more biomarker tests was selected, which may cause bias by giving up some robust data in each test. Moreover, there was a significant disparity between the number of studies conducted in PD-L1 IHC versus mIHC/IF. Last but not least, although our study mainly covered 15 types of tumors, the generalization of the conclusion still requires deliberation.

6 Conclusion

Various large prospective and retrospective studies have investigated biomarkers for the prediction of PD-1/PD-L1 checkpoint inhibitors response. According to our network meta-analysis, mIHC/IF had the best performance and a large range of applications. Given the diverse employment of mIHC/IF with different biomarkers across various studies, further investigations involving precise combinations are warranted to enhance prognostic prediction. When considering the selection of specific markers, it is crucial to take into account not only their efficiency and cost-effectiveness but also rely on substantiation from evidence derived from molecular mechanisms. Further exploration was required in combined assays of the high efficacy of TMB+PD-L1 IHC. Currently, there is a lack of studies or consensus regarding the workflow of companion or complementary diagnostics in this context. The existing approach is primarily based on clinicians' acknowledgment, and we anticipate that future research will provide more foundational evidence to support these practices. What' more, more evidence based medicine are needed to determine detailed testing modalities and thresholds for all types of tumors, e.g. advanced ovarian cancer. Clinicians should be cautious that the prognostic accuracy of each index test should be interpreted in a particular situation.

Data availability statement

The original contributions presented in the study are included in the article/Supplementary Material. Further inquiries can be directed to the corresponding author.

Author contributions

HS: Conceptualization, Data curation, Formal Analysis, Investigation, Writing – original draft. WZ: Investigation, Validation, Visualization, Writing – review & editing. LZ: Investigation, Validation, Visualization, Writing – review &

editing. YZ: Conceptualization, Data curation, Formal Analysis, Supervision, Writing – review & editing. TD: Conceptualization, Funding acquisition, Software, Supervision, Writing – review & editing.

Funding

The author(s) declare financial support was received for the research, authorship, and/or publication of this article. This work was supported by Innovation and Development Joint Funds of Natural Science Foundation of Shandong Province [ZR2021LZL009] and National Natural Science Foundation of China [82303956].

Acknowledgments

We acknowledge all the authors whose papers have been included in this network meta-analysis for their work, which made this analysis possible.

Conflict of interest

The authors declare that the research was conducted in the absence of any commercial or financial relationships that could be construed as a potential conflict of interest.

Publisher's note

Supplementary material

The Supplementary Material for this article can be found online at: https://www.frontiersin.org/articles/10.3389/fimmu.2023.1265202/full#supplementary-material

References

1. Makuku R, Khalili N, Razi S, Keshavarz-Fathi M, Rezaei N. Current and future perspectives of PD-1/PDL-1 blockade in cancer immunotherapy. *J Immunol Res* (2021) 2021:6661406. doi: 10.1155/2021/6661406

2. Health C for D and R. *List of cleared or approved companion diagnostic devices (In vitro and imaging tools)* . FDA. Available at: https://www.fda.gov/medical-devices/in-vitro-diagnostics/list-cleared-or-approved-companion-diagnostic-devices-in-vitro-and-imaging-tools (Accessed February 22, 2023).

3. Paver EC, Cooper WA, Colebatch AJ, Ferguson PM, Hill SK, Lum T, et al. Programmed death ligand-1 (PD-L1) as a predictive marker for immunotherapy in solid tumours: a guide to immunohistochemistry implementation and interpretation. *Pathology* (2021) 53(2):141–56. doi: 10.1016/j.pathol.2020.10.007

4. Sha D, Jin Z, Budzcies J, Kluck K, Stenzinger A, Sinicrope FA. Tumor mutational burden as a predictive biomarker in solid tumors. *Cancer Discovery* (2020) 10 (12):1808–25. doi: 10.1158/2159-8290.CD-20-0522

5. Baretti M, Le DT. DNA mismatch repair in cancer. *Pharmacol Ther* (2018) 189:45–62. doi: 10.1016/j.pharmthera.2018.04.004

6. Erin N, Grahovac J, Brozovic A, Efferth T. Tumor microenvironment and epithelial mesenchymal transition as targets to overcome tumor multidrug resistance. *Drug Resistance Updates* (2020) 53:100715. doi: 10.1016/j.drup.2020.100715

7. Wang L, Saci A, Szabo PM, Chasalow SD, Castillo-Martin M, Domingo-Domenech J, et al. EMT- and stroma-related gene expression and resistance to PD-1 blockade in urothelial cancer. *Nat Commun* (2018) 9(1):3503. doi: 10.1038/s41467-018-05992-x

8. Hugo W, Zaretsky JM, Sun L, Song C, Moreno BH, Hu-Lieskovan S, et al. Genomic and transcriptomic features of response to anti-PD-1 therapy in metastatic melanoma. *Cell* (2017) 168(3):542. doi: 10.1016/j.cell.2017.01.010

9. Gide TN, Quek C, Menzies AM, Tasker AT, Shang P, Holst J, et al. Distinct immune cell populations define response to anti-PD-1 monotherapy and anti-PD-1/Anti-CTLA-4 combined therapy. *Cancer Cell* (2019) 35(2):238–255.e6. doi: 10.1016/j.ccell.2019.01.003

10. Fan C, Oh DS, Wessels L, Weigelt B, Nuyten DSA, Nobel AB, et al. Concordance among Gene-Expression–based predictors for breast cancer. *New Engl J Med* (2006) 355:560–9.

11. Jamin SP, Hikmet F, Mathieu R, Jégou B, Lindskog C, Chalmel F, et al. Combined RNA/tissue profiling identifies novel cancer/testis genes. *Mol Oncol* (2021) 15(11):3003–23. doi: 10.1002/1878-0261.12900

12. Ayers M, Lunceford J, Nebozhyn M, Murphy E, Loboda A, Kaufman DR, et al. IFN-γ-related mRNA profile predicts clinical response to PD-1 blockade. *J Clin Invest* (2017) 127(8):2930–40. doi: 10.1172/JCI91190

13. Deutsch R, Mindt MR. Quantifying relative superiority among many binary-valued diagnostic tests in the presence of a gold standard. *J Data Science* (2021) 7:161–77. doi: 10.6339/JDS.2009.07(2).450

14. Nyaga VN, Aerts M, Arbyn M. ANOVA model for network meta-analysis of diagnostic test accuracy data. *Stat Methods Med Res* (2018) 27(6):1766–84. doi: 10.1177/0962280216669182

15. Hellmann MD, Callahan MK, Awad MM, Calvo E, Ascierto PA, Atmaca A, et al. Tumor mutational burden and efficacy of nivolumab monotherapy and in combination with ipilimumab in small-cell lung cancer. *Cancer Cell* (2018) 33(5):853–861.e4. doi: 10.1016/j.ccell.2018.04.001

16. Hodi FS, Wolchok JD, Schadendorf D, Larkin J, Long GV, Qian X, et al. TMB and inflammatory gene expression associated with clinical outcomes following immunotherapy in advanced melanoma. *Cancer Immunol Res* (2021) 9(10):1202–13. doi: 10.1158/2326-6066.CIR-20-0983

17. Hamid O, Molinero L, Bolen CR, Sosman JA, Muñoz-Couselo E, Kluger HM, et al. Safety, clinical activity, and biological correlates of response in patients with metastatic melanoma: Results from a phase i trial of atezolizumab. *Clin Cancer Res* (2019) 25(20):6061–72. doi: 10.1158/1078-0432.CCR-18-3488

18. Tang B, Yan X, Sheng X, Si L, Cui C, Kong Y, et al. Safety and clinical activity with an anti-PD-1 antibody JS001 in advanced melanoma or urologic cancer patients. *J Hematol Oncol* (2019) 12(1):7. doi: 10.1186/s13045-018-0693-2

19. Huang J, Mo H, Zhang W, Chen X, Qu D, Wang X, et al. Promising efficacy of SHR-1210, a novel anti-programmed cell death 1 antibody, in patients with advanced gastric and gastroesophageal junction cancer in china. *Cancer* (2019) 125(5):742–9. doi: 10.1002/cncr.31855

20. Cristescu R, Mogg R, Ayers M, Albright A, Murphy E, Yearley J, et al. Pan-tumor genomic biomarkers for PD-1 checkpoint blockade-based immunotherapy. *Science* (2018) 362(6411):eaar3593. doi: 10.1126/science.aar3593

21. Tanizaki J, Yonemori K, Akiyoshi K, Minami H, Ueda H, Takiguchi Y, et al. Open-label phase II study of the efficacy of nivolumab for cancer of unknown primary. *Ann Oncol* (2022) 33(2):216–26. doi: 10.1016/j.annonc.2021.11.009

22. Galsky MD, Saci A, Szabo PM, Azrilevich A, Horak C, Lambert A, et al. Impact of zumor mutation burden on nivolumab efficacy in second-line urothelial carcinoma patients: Exploratory analysis of the phase ii checkmate 275 study. *Ann Oncol* (2017) 28:v296–7. doi: 10.1093/annonc/mdx371.003

23. Shim JH, Kim HS, Cha H, Kim S, Kim TM, Anagnostou V, et al. HLA-corrected tumor mutation burden and homologous recombination deficiency for the prediction of response to PD-(L)1 blockade in advanced non-small-cell lung cancer patients. *Ann Oncol* (2020) 31(7):902–11. doi: 10.1016/j.annonc.2020.04.004

24. Hanna GJ, Lizotte P, Cavanaugh M, Kuo FC, Shivdasani P, Frieden A, et al. Frameshift events predict anti-PD-1/L1 response in head and neck cancer. *JCI Insight* (2018) 3(4):e98811. doi: 10.1172/jci.insight.98811

25. Carbone DP, Reck M, Paz-Ares L, Creelan B, Horn L, Steins M, et al. First-line nivolumab in stage IV or recurrent non-Small-Cell lung cancer. *N Engl J Med* (2017) 376(25):2415–26. doi: 10.1056/NEJMoa1613493

26. Lu M, Zhang P, Zhang Y, Li Z, Gong J, Li J, et al. Efficacy, safety, and biomarkers of toripalimab in patients with recurrent or metastatic neuroendocrine neoplasms: A multiple-center phase ib trial. *Clin Cancer Res* (2020) 26(10):2337–45. doi: 10.1158/1078-0432.CCR-19-4000

27. Liu D, Ma C, Lu P, Gong J, Ye D, Wang S, et al. Dose escalation and expansion (phase Ia/Ib) study of GLS-010, a recombinant fully human antiprogrammed death-1 monoclonal antibody for advanced solid tumors or lymphoma. *Eur J Cancer* (2021) 148:1–13. doi: 10.1016/j.ejca.2021.01.020

28. Gogas H, Dréno B, Larkin J, Demidov L, Stroyakovskiy D, Eroglu Z, et al. Cobimetinib plus atezolizumab in BRAFV600 wild-type melanoma: primary results from the randomized phase III IMspire170 study. *Ann Oncol* (2021) 32(3):384–94. doi: 10.1016/j.annonc.2020.12.004

29. Stratigos AJ, Sekulic A, Peris K, Bechter O, Prey S, Kaatz M, et al. Cemiplimab in locally advanced basal cell carcinoma after hedgehog inhibitor therapy: an open-label, multi-centre, single-arm, phase 2 trial. *Lancet Oncol* (2021) 22(6):848–57. doi: 10.1016/S1470-2045(21)00126-1

30. D'Angelo SP, Bhatia S, Brohl AS, Hamid O, Mehnert JM, Terheyden P, et al. Avelumab in patients with previously treated metastatic merkel cell carcinoma: long-term data and biomarker analyses from the single-arm phase 2 JAVELIN merkel 200 trial. *J Immunother Cancer* (2020) 8(1):e000674. doi: 10.1136/jitc-2020-000674

31. Marabelle A, Fakih M, Lopez J, Shah M, Shapira-Frommer R, Nakagawa K, et al. Association of tumour mutational burden with outcomes in patients with advanced solid tumours treated with pembrolizumab: prospective biomarker analysis of the multicohort, open-label, phase 2 KEYNOTE-158 study. *Lancet Oncol* (2020) 21 (10):1353–65. doi: 10.1016/S1470-2045(20)30445-9

32. Hayashi H, Sugawara S, Fukuda Y, Fujimoto D, Miura S, Ota K, et al. A randomized phase II study comparing nivolumab with carboplatin-pemetrexed for EGFR-mutated NSCLC with resistance to EGFR tyrosine kinase inhibitors (WJOG8515L). *Clin Cancer Res* (2022) 28(5):893–902. doi: 10.1158/1078-0432.CCR-21-3194

33. Rizvi NA, Hellmann MD, Snyder A, Kvistborg P, Makarov V, Havel JJ, et al. Cancer immunology. mutational landscape determines sensitivity to PD-1 blockade in non-small cell lung cancer. *Science* (2015) 348(6230):124–8. doi: 10.1126/science.aaa1348

34. Shimoda Y, Shibaki R, Yoshida T, Murakami S, Shirasawa M, Torasawa M, et al. Concurrent high PD-L1 expression and CD8+ immune cell infiltration predict PD-1 blockade efficacy in advanced EGFR-mutant NSCLC patients. *Clin Lung Cancer* (2022) 23(6):477–86. doi: 10.1016/j.cllc.2022.04.001

35. Raghav KP, Stephen B, Karp DD, Piha-Paul SA, Hong DS, Jain D, et al. Efficacy of pembrolizumab in patients with advanced cancer of unknown primary (CUP): a phase 2 non-randomized clinical trial. *J Immunother Cancer* (2022) 10(5):e004822. doi: 10.1136/jitc-2022-004822

36. Ficial M, Jegede OA, Sant'Angelo M, Hou Y, Flaifel A, Pignon JC, et al. Expression of t-cell exhaustion molecules and human endogenous retroviruses as predictive biomarkers for response to nivolumab in metastatic clear cell renal cell carcinoma. *Clin Cancer Res* (2021) 27:1371–80. doi: 10.1158/1078-0432.CCR-20-3084

37. Pignon JC, Jegede O, Shukla SA, Braun DA, Horak CE, Wind-Rotolo M, et al. irRECIST for the evaluation of candidate biomarkers of response to nivolumab in metastatic clear cell renal cell carcinoma: Analysis of a phase II prospective clinical trial. *Clin Cancer Res* (2019) 25(7):2174–84. doi: 10.1158/1078-0432.CCR-18-3206

38. Takada K, Takamori S, Yoneshima Y, Tanaka K, Okamoto I, Shimokawa M, et al. Serum markers associated with treatment response and survival in non-small cell lung cancer patients treated with anti-PD-1 therapy. *Lung Cancer* (2020) 145:18–26. doi: 10.1016/j.lungcan.2020.04.034

39. Pedersen KS, Foster NR, Overman MJ, Boland PM, Kim SS, Arrambide KA, et al. ZEBRA: A multicenter phase II study of pembrolizumab in patients with advanced small-bowel adenocarcinoma. *Clin Cancer Res* (2021) 27(13):3641–8. doi: 10.1158/1078-0432.CCR-21-0159

40. Miyama Y, Morikawa T, Miyakawa J, Koyama Y, Kawai T, Kume H, et al. Squamous differentiation is a potential biomarker predicting tumor progression in patients treated with pembrolizumab for urothelial carcinoma. *Pathol Res Pract* (2021) 219:153364. doi: 10.1016/j.prp.2021.153364

41. Ahmadzada T, Cooper WA, Holmes M, Mahar A, Westman H, Gill AJ, et al. Retrospective evaluation of the use of pembrolizumab in malignant mesothelioma in a real-world australian population. *JTO Clin Res Rep* (2020) 1(4):100075. doi: 10.1016/j.jtocrr.2020.100075

42. Naing A, Meric-Bernstam F, Stephen B, Karp DD, Hajjar J, Rodon Ahnert J, et al. Phase 2 study of pembrolizumab in patients with advanced rare cancers. *J Immunother Cancer* (2020) 8(1):e000347. doi: 10.1136/jitc-2019-000347

43. Kato K, Doki Y, Ura T, Hamamoto Y, Kojima T, Tsushima T, et al. Long-term efficacy and predictive correlates of response to nivolumab in japanese patients with esophageal cancer. *Cancer Sci* (2020) 111(5):1676–84. doi: 10.1111/cas.14380

44. Emens LA, Cruz C, Eder JP, Braiteh F, Chung C, Tolaney SM, et al. Long-term clinical outcomes and biomarker analyses of atezolizumab therapy for patients with metastatic triple-negative breast cancer: A phase 1 study. *JAMA Oncol* (2019) 5(1):74–82. doi: 10.1001/jamaoncol.2018.4224

45. Lambert SL, Zhang C, Guo C, Turan T, Masica DL, Englert S, et al. Association of baseline and pharmacodynamic biomarkers with outcomes in patients treated with the PD-1 inhibitor budigalimab. *J Immunother* (2022) 45(3):167–79. doi: 10.1097/CJI.0000000000000408

46. Kelly RJ, Lee J, Bang YJ, Almhanna K, Blum-Murphy M, Catenacci DVT, et al. Safety and efficacy of durvalumab and tremelimumab alone or in combination in patients with advanced gastric and gastroesophageal junction adenocarcinoma. *Clin Cancer Res* (2020) 26(4):846–54. doi: 10.1158/1078-0432.CCR-19-2443

47. Fuchs CS, Doi T, Jang RW, Muro K, Satoh T, Machado M, et al. Safety and efficacy of pembrolizumab monotherapy in patients with previously treated advanced gastric and gastroesophageal junction cancer: Phase 2 clinical KEYNOTE-059 trial. *JAMA Oncol* (2018) 4(5):e180013. doi: 10.1001/jamaoncol.2018.0013

48. Konstantinopoulos PA, Luo W, Liu JF, Gulhan DC, Krasner C, Ishizuka JJ, et al. Phase II study of avelumab in patients with mismatch repair deficient and mismatch repair proficient Recurrent/Persistent endometrial cancer. *J Clin Oncol* (2019) 37 (30):2786–94. doi: 10.1200/JCO.19.01021

49. Raj N, Zheng Y, Kelly V, Katz SS, Chou J, Do RKG, et al. PD-1 blockade in advanced adrenocortical carcinoma. *J Clin Oncol* (2020) 38(1):71–80. doi: 10.1200/JCO.19.01586

50. Overman MJ, McDermott R, Leach JL, Lonardi S, Lenz HJ, Morse MA, et al. Nivolumab in patients with metastatic DNA mismatch repair-deficient or microsatellite instability-high colorectal cancer (CheckMate 142): an open-label, multicentre, phase 2. *Lancet Oncol* (2017) 18(9):1182–91. doi: 10.1016/S1470-2045(17)30422-9

51. Kim ST, Cristescu R, Bass AJ, Kim KM, Odegaard JI, Kim K, et al. Comprehensive molecular characterization of clinical responses to PD-1 inhibition in metastatic gastric cancer. *Nat Med* (2018) 24(9):1449–58. doi: 10.1038/s41591-018-0101-z

52. Eng C, Kim TW, Bendell J, Argilés G, Tebbutt NC, Di Bartolomeo M, et al. Atezolizumab with or without cobimetinib versus regorafenib in previously treated metastatic colorectal cancer (IMblaze370): a multicentre, open-label, phase 3, randomised, controlled trial. *Lancet Oncol* (2019) 20(6):849–61. doi: 10.1016/S1470-2045(19)30027-0

53. Kwon M, Hong JY, Kim ST, Kim KM, Lee J. Association of serine/threonine kinase 11 mutations and response to programmed cell death 1 inhibitors in metastatic gastric cancer. *Pathol Res Pract* (2020) 216(6):152947. doi: 10.1016/j.prp.2020.152947

54. Higgs BW, Morehouse CA, Streicher K, Brohawn PZ, Pilataxi F, Gupta A, et al. Interferon gamma messenger RNA signature in tumor biopsies predicts outcomes in patients with non-small cell lung carcinoma or urothelial cancer treated with durvalumab. *Clin Cancer Res* (2018) 24(16):3857–66. doi: 10.1158/1078-0432.CCR-17-3451

55. McDermott DF, Huseni MA, Atkins MB, Motzer RJ, Rini BI, Escudier B, et al. Clinical activity and molecular correlates of response to atezolizumab alone or in combination with bevacizumab versus sunitinib in renal cell carcinoma. *Nat Med* (2018) 24(6):749–57. doi: 10.1038/s41591-018-0053-3

56. Sharma P, Retz M, Siefker-Radtke A, Baron A, Necchi A, Bedke J, et al. Nivolumab in metastatic urothelial carcinoma after platinum therapy (CheckMate 275): a multicentre, single-arm, phase 2 trial. *Lancet Oncol* (2017) 18(3):312–22. doi: 10.1016/S1470-2045(17)30065-7

57. Yeong J, Suteja L, Simoni Y, Lau KW, Tan AC, Li HH, et al. Intratumoral CD39 +CD8+ t cells predict response to programmed cell death protein-1 or programmed death ligand-1 blockade in patients with NSCLC. *J Thorac Oncol* (2021) 16(8):1349–58. doi: 10.1016/j.jtho.2021.04.016

58. Wang F, Wei XL, Wang FH, Xu N, Shen L, Dai GH, et al. Safety, efficacy and tumor mutational burden as a biomarker of overall survival benefit in chemo-refractory gastric cancer treated with toripalimab, a PD-1 antibody in phase Ib/II clinical trial NCT02915432. *Ann Oncol* (2019) 30(9):1479–86. doi: 10.1093/annonc/mdz197

59. Zeng D, Wu J, Luo H, Li Y, Xiao J, Peng J, et al. Tumor microenvironment evaluation promotes precise checkpoint immunotherapy of advanced gastric cancer. *J Immunother Cancer* (2021) 9(8):e002467. doi: 10.1136/jitc-2021-002467

60. Cindy Yang SY, Lien SC, Wang BX, Clouthier DL, Hanna Y, Cirlan I, et al. Pan-cancer analysis of longitudinal metastatic tumors reveals genomic alterations and immune landscape dynamics associated with pembrolizumab sensitivity. *Nat Commun* (2021) 12(1):5137. doi: 10.1038/s41467-021-25432-7

61. Friedman CF, Hainsworth JD, Kurzrock R, Spigel DR, Burris HA, Sweeney CJ, et al. Atezolizumab treatment of tumors with high tumor mutational burden from MyPathway, a multicenter, open-label, phase IIa multiple basket study. *Cancer Discovery* (2022) 12(3):654–69. doi: 10.1158/2159-8290.CD-21-0450

62. Cuppens K, Baas P, Geerdens E, Cruys B, Froyen G, Decoster L, et al. HLA-i diversity and tumor mutational burden by comprehensive next-generation sequencing as predictive biomarkers for the treatment of non-small cell lung cancer with PD-(L)1 inhibitors. *Lung Cancer* (2022) 170:1–10. doi: 10.1016/j.lungcan.2022.05.019

63. Lu S, Stein JE, Rimm DL, Wang DW, Bell JM, Johnson DB, et al. Comparison of biomarker modalities for predicting response to PD-1/PD-L1 checkpoint blockade: A systematic review and meta-analysis. *JAMA Oncol* (2019) 5(8):1195–204. doi: 10.1001/jamaoncol.2019.1549

64. Yarchoan M, Albacker LA, Hopkins AC, Montesion M, Murugesan K, Vithayathil TT, et al. PD-L1 expression and tumor mutational burden are independent biomarkers in most cancers. *JCI Insight* (2019) 4(6):e126908. doi: 10.1172/jci.insight.126908

65. Veroniki AA, Tsokani S, Rücker G, Mavridis D, Takwoingi Y. Challenges in comparative meta-analysis of the accuracy of multiple diagnostic tests. *Methods Mol Biol* (2022) 2345:299–316. doi: 10.1007/978-1-0716-1566-9_18

66. Owen RK, Cooper NJ, Quinn TJ, Lees R, Sutton AJ. Network meta-analysis of diagnostic test accuracy studies identifies and ranks the optimal diagnostic tests and thresholds for health care policy and decision-making. *J Clin Epidemiol* (2018) 99:64–74. doi: 10.1016/j.jclinepi.2018.03.005

67. Banchereau R, Chitre AS, Scherl A, Wu TD, Patil NS, de Almeida P, et al. Intratumoral CD103+ CD8+ t cells predict response to PD-L1 blockade. *J Immunother Cancer* (2021) 9(4):e002231. doi: 10.1136/jitc-2020-002231

68. Corgnac S, Malenica I, Mezquita L, Auclin E, Voilin E, Kacher J, et al. CD103 +CD8+ TRM cells accumulate in tumors of anti-PD-1-Responder lung cancer patients and are tumor-reactive lymphocytes enriched with Tc17. *Cell Rep Med* (2020) 1 (7):100127. doi: 10.1016/j.xcrm.2020.100127

69. Oja AE, Piet B, van der Zwan D, Blaauwgeers H, Mensink M, de Kivit S, et al. Functional heterogeneity of CD4+ tumor-infiltrating lymphocytes with a resident memory phenotype in NSCLC. *Front Immunol* (2018) 9:2654. doi: 10.3389/fimmu.2018.02654

70. Li Z, Zheng B, Qiu X, Wu R, Wu T, Yang S, et al. The identification and functional analysis of CD8+PD-1+CD161+ t cells in hepatocellular carcinoma. *NPJ Precis Oncol* (2020) 4:28–8. doi: 10.1038/s41698-020-00133-4

71. Berry S, Giraldo NA, Green BF, Cottrell TR, Stein JE, Engle EL, et al. Analysis of multispectral imaging with the AstroPath platform informs efficacy of PD-1 blockade. *Science* (2021) 372(6547):eaba2609. doi: 10.1126/science.aba2609

72. Doroshow DB, Bhalla S, Beasley MB, Sholl LM, Kerr KM, Gnjatic S, et al. PD-L1 as a biomarker of response to immune-checkpoint inhibitors. *Nat Rev Clin Oncol* (2021) 18(6):345–62. doi: 10.1038/s41571-021-00473-5

73. Torlakovic E, Lim HJ, Adam J, Barnes P, Bigras G, Chan AWH, et al. "Interchangeability" of PD-L1 immunohistochemistry assays: a meta-analysis of diagnostic accuracy. *Mod Pathol* (2020) 33(1):4–17. doi: 10.1038/s41379-019-0327-4

74. Ricciuti B, Wang X, Alessi JV, Rizvi H, Mahadevan NR, Li YY, et al. Association of high tumor mutation burden in non-small cell lung cancers with increased immune infiltration and improved clinical outcomes of PD-L1 blockade across PD-L1 expression. *JAMA Oncol* (2022) 8(8):1160–8. doi: 10.1001/jamaoncol.2022.1981

75. Fumet JD, Richard C, Ledys F, Klopfenstein Q, Joubert P, Routy B, et al. Prognostic and predictive role of CD8 and PD-L1 determination in lung tumor tissue of patients under anti-PD-1 therapy. *Br J Cancer* (2018) 119(8):950–60. doi: 10.1038/s41416-018-0220-9

frontiers | Frontiers in Immunology

TYPE Original Research
PUBLISHED 29 September 2023
DOI 10.3389/fimmu.2023.1236444

OPEN ACCESS

EDITED BY
Eyad Elkord,
University of Salford, United Kingdom

REVIEWED BY
Galal Metwally,
Zagazig University, Egypt
Minglei Zhuo,
Peking University, China

*CORRESPONDENCE
Pengxia Liu
liupengxia@imu.edu.cn
Changshan Wang
changshanwang@imu.edu.cn

†These authors have contributed equally to this work

RECEIVED 07 June 2023
ACCEPTED 12 September 2023
PUBLISHED 29 September 2023

CITATION
Wu R, Ma R, Duan X, Zhang J, Li K, Yu L, Zhang M, Liu P and Wang C (2023) Identification of specific prognostic markers for lung squamous cell carcinoma based on tumor progression, immune infiltration, and stem index. *Front. Immunol.* 14:1236444. doi: 10.3389/fimmu.2023.1236444

Identification of specific prognostic markers for lung squamous cell carcinoma based on tumor progression, immune infiltration, and stem index

Rihan Wu[1,2†], Ru Ma[1†], Xiaojun Duan[1,3†], Jiandong Zhang[1], Kexin Li[1], Lei Yu[1], Mingyang Zhang[1], Pengxia Liu[1*] and Changshan Wang[1*]

[1]School of Life Science, Inner Mongolia University, Hohhot, China, [2]The Department of Oncology, Affiliated Hospital of Inner Mongolia Medical University, Hohhot, China, [3]School of Basic Medicine, Inner Mongolia Medical University, Hohhot, China

Introduction: Lung squamous cell carcinoma (LUSC) is a unique subform of nonsmall cell lung cancer (NSCLC). The lack of specific driver genes as therapeutic targets leads to worse prognoses in patients with LUSC, even with chemotherapy, radiotherapy, or immune checkpoint inhibitors. Furthermore, research on the LUSC-specific prognosis genes is lacking. This study aimed to develop a comprehensive LUSC-specific differentially expressed genes (DEGs) signature for prognosis correlated with tumor progression, immune infiltration, and stem index.

Methods: RNA sequencing data for LUSC and lung adenocarcinoma (LUAD) were extracted from The Cancer Genome Atlas (TCGA) data portal, and DEGs analyses were conducted in TCGA-LUSC and TCGA-LUAD cohorts to identify specific DEGs associated with LUSC. Functional analysis and protein–protein interaction network were performed to annotate the roles of LUSC-specific DEGs and select the top 100 LUSC-specific DEGs. Univariate Cox regression and least absolute shrinkage and selection operator regression analyses were performed to select prognosis-related DEGs.

Results: Overall, 1,604 LUSC-specific DEGs were obtained, and a validated seven-gene signature was constructed comprising FGG, C3, FGA, JUN, CST3, CPSF4, and HIST1H2BH. FGG, C3, FGA, JUN, and CST3 were correlated with poor LUSC prognosis, whereas CPSF4 and HIST1H2BH were potential positive prognosis markers in patients with LUSC. Receiver operating characteristic analysis further confirmed that the genetic profile could accurately estimate the overall survival of LUSC patients. Analysis of immune infiltration demonstrated that the high risk (HR) LUSC patients exhibited accelerated tumor infiltration, relative to low risk (LR) LUSC patients. Molecular expressions of immune checkpoint genes differed significantly between the HR and LR cohorts. A ceRNA network containing 19 lncRNAs, 50 miRNAs, and 7 prognostic DEGs was constructed to demonstrate the prognostic value of novel biomarkers of LUSC-specific DEGs based on tumor progression, stemindex, and immune infiltration. In vitro experimental models confirmed

that LUSC-specific DEG FGG expression was significantly higher in tumor cells and correlated with immune tumor progression, immune infiltration, and stem index. *In vitro* experimental models confirmed that LUSC-specific DEG FGG expression was significantly higher in tumor cells and correlated with immune tumor progression, immune infiltration, and stem index.

Conclusion: Our study demonstrated the potential clinical implication of the 7-DEGs signature for prognosis prediction of LUSC patients based on tumor progression, immune infiltration, and stem index. And the FGG could be an independent prognostic biomarker of LUSC promoting cell proliferation, migration, invasion, THP-1 cell infiltration, and stem cell maintenance.

KEYWORDS

LUSC, prognosis, biomarker, tumor microenvironment, cancer stem cell

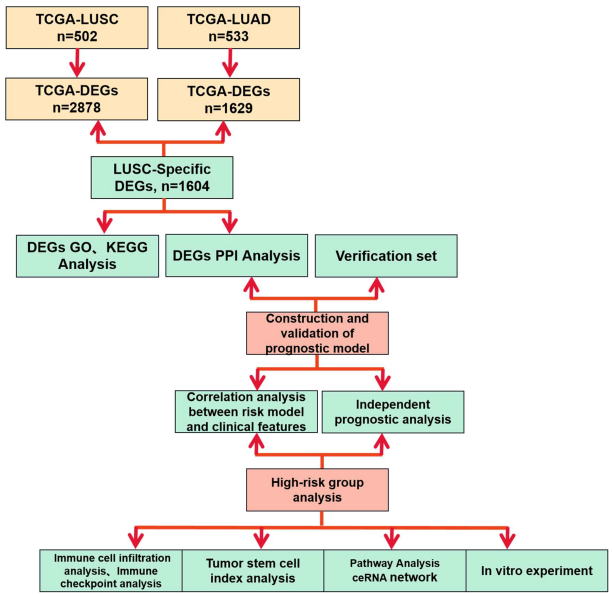

GRAPHICAL ABSTRACT

1 Introduction

Lung cancer is heterogeneous and fatal, with non-small cell lung cancer (NSCLC) as its main pathological subtype. Lung squamous cell carcinoma (LUSC) and lung adenocarcinoma (LUAD) are the primary subtypes of NSCLC (1); however, they differ in many aspects, including the origin of cells, genetic variation, epigenetics, and the outcome of antineoplaston drugs (2). Despite tremendous advances in diagnosis and treatment, including molecular targeted therapeutics and immunotherapy, the clinical outcomes of LUSC remain unsatisfactory (3). Patients with LUSC are often diagnosed in an advanced stage when existing therapy cannot be administered in a timely manner (4). LUSC patients are also not as sensitive as LUAD patients to chemotherapy, radiotherapy, and tumor immunotherapy. In addition, the prognosis of LUSC is poor, with an estimated 5-year survival rate of <15% (5). Therefore, distinguishing LUSC from LUAD is important to identify effective prognostic biomarkers.

Although studies based on the whole genome (6, 7), epigenetics (8), cancer stem cells (CSCs) (9, 10), and tumor microenvironment

Abbreviations: EMT, Epithelial-Mesenchymal Transition; NSCLC, Non-small cell carcinoma; LUAD, Lung adenocarcinoma; LUSC, Lung squamous cell carcinoma; mRNA, Message ribonucleic acid; FGG, Fibrinogen gamma; GO, Gene Ontology; KEGG, Kyoto Encyclopedia of Genes and Genomes; PPI, Protein-protein interaction; TCGA, The Cancer Genome Atlas; OS, Overall survival.

(TME) (11) have analyzed differentially expressed genes (DEGs) in LUSC and LUAD, research on the LUSC-specific prognosis genes is lacking. A previous study (4), involving 178 LUSC cases, conducted using the Cancer Genome Atlas (TCGA) Research Network reported complex genomic alterations in LUSC, including significant copy number alterations, which peaked for SOX2, PDGFRA/KIT, EGFR, FGFR1, CCND1, and CDKN2A. In LUSC, CDKN2A/RB1, NFE2L2/KEAP1, squamous differentiation genes, and PI3K/Akt were significantly altered. TP53 is the most commonly mutated gene with a mutation frequency of > 80% in LUSC. The overexpression and amplification of genes, SOX2 and TP63, are spectrum factors of LUSC (12). Despite progress in research on biomarkers for LUSC, oncology targets are rare. Recent studies on genetic biomarkers for LUSC have focused on a single gene based on the cognitions of CSCs and the TME in cancer progression, as well as drug resistance and response to immune checkpoint blockade. Traditional methods use differential expression detection to identify potential biomarkers but may miss out on useful genes. As the occurrence and development of malignant tumors is a long-term complex process involving genomic changes, the interaction between tumor cells and their immune microenvironment, and the participation of tumor stem cells, the behavior cognition of malignant tumors warrants extensive research.

Therefore, in this study, we aimed to compare DEGs of LUSC with LUAD using biological information analytical methods based on prognostic risk factors, including tumor invasion, metastasis, survival, immune infiltration, and tumor stem cell-related genes. DEGs in LUSC were employed to generate a risk model to evaluate the prognostic value of characteristic genes for possible prognostic indicators or therapeutic targets for LUSC. We further explored the associations between the specific prognostic markers FGG and tumor progression, immune invasion, and the tumor cell stem index to identify potential LUSC-specific survival prognostic biomarkers and therapeutic targets.

2 Methods

2.1 Data processing

We first retrieved LUSC (n=502) and LUAD (n=533) RNA sequencing datasets, and the clinical information of corresponding LUSC patients and 59 healthy volunteers from the TCGA database (https://portal.gdc.cancer.gov/).

2.2 Differentially expressed genes

The "limma" package was selected for DEGs analysis in TCGA-LUSC and TCGA-LUAD cohorts. For processing, a |log2 (fold change)| > 0.5 and adjusted P-value < 0.05 were considered the cut-off criteria for screening the DEGs between the tumor and normal samples. The "heatmap" package of the R program was used to generate a heatmap of the top 100 DEGs. Additionally, we employed a Venn diagram to indicate the specific DEGs in LUSC.

2.3 Functional enrichment analyses

The Gene Ontology (GO) and Kyoto Encyclopedia of Genes and Genomes (KEGG) pathway enrichment analyses of LUSC-specific DEGs were conducted with the "clusterProfiler" package of the R software; P < 0.05 was the statistical significance threshold. The bubble plot, circle graph, and heat map were plotted using R to visualize the top enrichment GO terms and KEGG networks. To explore the pathways and GO functions of unique differential genes in LUSC, the R "clusterProfiler" package was used for enrichment analysis based on KEGG and GO to search for common functions among DEGs, as well as related pathways of several genes. Statistical methods were used to calculate the cumulative hypergeometric distribution to analyze, within a group of genes, whether overpresentation occurs on a functional node, as follows:

$$P(X > q) = 1 - \sum_{x=1}^{q} \frac{\binom{n}{x}\binom{N-n}{M-x}}{\binom{N}{M}}$$

where 'N' is the total gene number within the annotation system, 'n' is the gene number annotated by the node or pathway itself to be examined, 'M' is the size of the DEGs set, and 'x' is the number of intersections between gene sets and nodes or pathways.

2.4 Protein–protein interaction axis for LUSC DEGs

The association between LUSC-specific DEGs was predicted using STRING (https://string-db.org). The PPI axis was visualized with the Cytoscape software at a confidence of 0.9. In the PPI network, the individual DEG's adjacent node numbers were computed, and the top 20 DEGs were displayed using a bar plot according to the number of adjacent nodes. Weighted gene co-expression network analysis (WGCNA) was conducted to screen out relevant modules and hub genes, which were used to develop the prognostic signature. TCGA and GTEx data based gene expression profiling interactive analysis (GEPIA) was used to predict gene interactive and customizable functions.

2.5 Construction and validation of a gene signature constructed from LUSC-specific DEGs

Based on the number of connections, the top 100 LUSC-specific DEGs were selected for subsequent analyses. We extracted the expression data of the 100 LUSC-specific genes from TCGA-LUSC patients and combined them with the clinical information of corresponding patients. The corresponding patients with TCGA-LUSC were randomly divided into a training cohort (TC, n = 336) and a validation cohort (VC, n = 145) in a 7:3 ratio. To identify

prognostic genes in LUSC, we conducted a univariate Cox regression analysis on 100 LUSC-specific DEGs. Those with a $P < 0.05$ were considered correlated with the LUSC prognosis. Subsequently, we used the least absolute shrinkage and selection operator (LASSO) and Cox regression analyses to obtain the genetic profile with the most significant prognosis from the LUSC-specific DEGs within the TCGA-LUSC patient population via the "glmnet" package in R. Individual patient risk score (RS) was computed based on the levels of the prognostic signature genes and the associated coefficients obtained from the LASSO-Cox regression model. LUSC patients were categorized into high risk (HR) and low risk (LR) cohorts based on the median RS. The overall survival (OS) of the different risk cohorts was analyzed using Kaplan–Meier analysis with the log-rank test using the "Kaplan–Meier survival" package in R. Moreover, the time dependent receiver operating characteristic (ROC) curve was generated via the "survival ROC" package in R to demonstrate the effectiveness of the genetic profile. To analyze the relationship between predictive and response variables, we employed the uni- and multivariate Cox regression analyses.

2.6 Single sample gene set enrichment analysis

The relative tumor infiltration levels of 29 immune-linked gene sets (16 immune cell types and 13 immune-linked pathways) between HR and LR groups were quantified by ssGSEA. The analysis was conducted using the "gsva" R package. Comparisons between the HR and LR cohorts were carried out via the Wilcoxon test.

2.7 Tumor stem cell index analysis

The mRNA expression based stemness index (mRNAsi) and epigenetically regulated mRNAsi (EREG-mRNAsi) in LUSC samples were computed using the OCLR algorithm for research on gastric cancer (13) and NSCLC (14). Subsequently, the differences in mRNAsi and EREG-mRNAsi between the HR and LR cohorts were compared using the Wilcoxon test. The two independent stemness indices range from 0 to 1, with a value closer to 1 suggesting stronger characteristics of CSCs.

2.8 Generation of the ceRNA axis

Differentially expressed lncRNAs (DE-lncRNAs) between tumor and healthy samples were recognized as follows: $|\log2 \text{ (fold change)}| > 1$ and P-value < 0.05. The target miRNAs of lncRNAs were estimated via the miRcode database (http://www.mircode.org/), and the target miRNAs of prognostic DEGs were estimated via the miRanda database (http://www.microrna.org/microrna/home.do). The common miRNAs predicted by the miRcode and miRanda databases, as well as the corresponding lncRNA and prognostic DEGs, were input into Cytoscape software to construct a ceRNA network.

2.9 Cell culture

LTEP-s, BEAS-2B, and NCI-H520 cells were purchased from the American Type Culture Collection (ATCC) and cultured in DMEM (HyClone, USA). NCI-H520 cells were cultured in RPMI-1640 medium (Biological Industries, USA). All cells were supplemented with 10% fetal bovine serum (FBS; Biological Industries, USA) and 1% penicillin/streptomycin (Sigma, USA) and cultured under standard culture conditions (37 °C, 5% CO_2) in culture medium recommended by the ATCC.

2.10 RNA extraction and real-time polymerase chain reaction assay

Total RNA was extracted using TRIzol Reagent (Invitrogen, Carlsbad, CA) according to the manufacturer's instructions. cDNA was synthesized using random primers and the PrimeScript RT Reagent Kit (Takara, China). Real-time polymerase chain reaction (qPCR) was performed using SYBR Premix Ex Tag (Takara, China). The PCR conditions were as follows: 95 °C for 15 s followed by 40 cycles of 95 °C for 5 s and 60 °C for 30 s. β-actin was used as the internal control. The primer sequences for real-time PCR are listed in Table 1.

2.11 Cell transfection

Small-interfering RNA (siRNA) oligonucleotides for FGG were designed and synthesized by Jima Bio (Suzhou, China). The primer sequences for the siRNAs are listed in Table 2. Transient transfection was performed using Lipofectamine 2000 Reagent (Invitrogen, USA) according to the manufacturer's instructions. After transfection for

TABLE 1 Primer sequences for real-time PCR used in the study.

Primer name	Primer sequences (5`–3`)	
FGG	Forward Primer	TTATTGTCCAACTACCTGTGGC
	Reverse Primer	GACTTCAAAGTAGCAGCGTCTAT
FGA	Forward Primer	AGACATCAATCTGCCTGCAAA
	Reverse Primer	AGTGGTCAACGAATGAGAATCC
JUN	Forward Primer	TCCAAGTGCCGAAAAAGGAAG
	Reverse Primer	CGAGTTCTGAGCTTTCAAGGT
CPSF4	Forward Primer	CATCGGGGTCATGCAGAGTC
	Reverse Primer	CTCGCCACACTTGTAACAGGT
HIST1H2BH-1F	Forward Primer	TCACCTCCAGGGAGATCCAG
	Reverse Primer	TTTGGGTTTGAACATGCGTCC
C3	Forward Primer	GGGGAGTCCCATGTACTCTATC
	Reverse Primer	GGAAGTCGTGGACAGTAACAG
CST3	Forward Primer	GTCGGCGAGTACAACAAAGC
	Reverse Primer	CACCCCAGCTACGATCTGC

TABLE 2 Primer sequences for siRNA used in the study.

Primer name	Primer sequences (5`–3`)	
FGG-homo-935	sense	CCUACUGGCACAACAGAAUTT
	antisense	AUUCUGUUGUGCCAGUAGGTT
FGG-homo-768	sense	GCGGGCUUUACUUUAUUAATT
	antisense	UUAAUAAAGUAAAGCCCGCTT
FGG-homo-1361	sense	GGUUAUGAUAAUGGCAUUATT
	antisense	UAAUGCCAUUAUCAUAACCTT

48 h, cells were used for functional assays, including migration, invasion, RNA extraction, and Western blotting.

2.12 Cell proliferation assay

Cells were seeded in 96-well plates at 1×10^3 cells per well and cultured in a final volume of 100 µL of culture medium supplemented with 10% FBS. The cell proliferation was determined using CCK-8. After incubation for 24, 48, 72, and 96 h, 20 uL of CCK-8 reagent was added for 3 h, and the absorption at a wavelength of 490 nm was determined.

2.13 Cell cycle assay

The cell suspension was diluted to 5×10^6 cells/mL, the supernatant was removed, and 70% 500 µL of cold ethanol was added and placed in a refrigerator at 4°C for 2 h. The cell pellet was mixed with 100 µL RNaseA (Solarbio, China) and placed in a 37°C water bath for 30 min; PI staining buffer was added in the dark for 30 min at 4°C. Red fluorescence at 488 nm was detected using flow cytometer.

2.14 Cell apoptosis assay

The cell culture medium was collected into a centrifuge tube. The cells were digested with Edta-free pancreatic enzymes and added into the cell culture medium, centrifuged, and precipitated. The cells were then re-suspended with 1 mL PBS precooled at 4 °C and the precipitated cells were centrifuged again. The cells were re-suspended with 1x binding buffer and the concentration was adjusted to 5×10^6/mL; 100 µL cell suspension was added to a 5 mL flow tube, mixed with 5 µL Annexin V/FITC (Solarbio, China), and incubated at room temperature for 5 min in the dark. A total of 5 µL propyl iodide solution (PI) and 400 µL PBS were added for immediate flow detection.

2.15 Wound healing assay

Cells were placed in 12-well plates. When cells grew to 90–95% confluence, cell monolayers were wounded by scratching with plastic micropipette tips and washed twice with PBS. The cells were rinsed with PBS and cultured in DMEM or RPMI 1640 supplemented with 1% FBS. Images of the different stages of wound healing were obtained via microscopy at 0, 24, and 48 h. Relative cell motility was quantified using Image-Pro Plus.

2.16 Transwell migration and invasion assay

Cell migration and invasion assays were performed in 24-well plates with 8-µm-pore size chamber inserts (Corning, USA). For the migration assays, 5×10^4 cells in 200 µL of serum-free culture medium were seeded into each well of the upper chamber with the noncoated membrane, and 800 µL of medium supplemented with 10% FBS was added to the lower chamber. For invasion assays, 1×10^5 cells in 200 µL of serum-free culture medium were seeded into each well of the upper chamber with the Matrigel-coated membrane, while 800 µL of medium supplemented with 10% FBS was added to the lower chamber. Cells that migrated through the membrane were fixed with 100% methanol, stained with 0.1% crystal violet for 30 min, imaged, and counted under a light microscope (Olympus, Japan).

2.17 Western blot assay

Cells grown in 6-well plates were lysed on ice using RIPA buffer. The lysis mixtures were centrifuged, and the supernatants were collected. Total protein was separated using SDS-polyacrylamide gel electrophoresis and transferred onto PVDF membranes (Millipore, USA). After blocking the membranes with non-fat milk, the membranes were incubated overnight with the following primary antibodies: anti-N-cadherin (1:1,000), anti-E-cadherin (1:1,000), anti-GAPDH (1:1,000) (Abcam, UK). The membranes were then incubated with horseradish peroxidase-conjugated secondary antibodies (1:2,000). The analysis was performed using an enhanced chemiluminescence system (Bio-Rad, USA). Binding was analyzed using Image J 6.0.

2.18 THP-1 cell infiltration

THP-1 cells were seeded at 1×10^6 per well in 6-well plates and treated with PMA (100 nmol; Sigma-Aldrich, USA) for 48 h. M1 macrophages were polarized by incubation with INF-γ (20 ng/mL; R&D System, USA) and LPS (100 ng/mL; Sigma, USA) for 48 h.

After transfection with si-NC or si-FGG in the absence or presence of coculture, a cell migration assay was conducted using 24-well Transwell plates (8.0 µm; Corning, NY, USA). The macrophages or cancer cells (5×10^4, LTEPs-si-NC, LTEPs-si-FGG) were planted into the upper chambers, while 600 µL RPMI 1640 containing 10% FBS were placed into the lower chambers. Thereafter, the Transwell plates were incubated at 37 °C, 5% CO_2 for 48 h, fixed in 4% formaldehyde for 30 min, and stained with 0.01% crystal violet. Non-migrating cells were carefully removed

with a cotton swab, while cells that migrated to the lower chambers were counted under a microscope.

2.19 Statistical analysis

All data analyses were conducted using the R language (version 3.5.1). The levels of immune checkpoint genes between the HR and LR cohorts were compared using the Wilcoxon test. Uni- and multivariate analyses were employed to screen for stand-alone prognostic markers for LUSC survival. $P < 0.05$ was set as the significance threshold.

3 Results

3.1 Identification of specific DEGs for LUSC

We analyzed DEGs between tumor and normal samples in TCGA-LUSC and TCGA-LUAD cohorts. Overall, 2,878 DEGs (1,466 upregulated and 1,412 downregulated) were identified in LUSC, relative to normal samples (Figure 1A). In addition, 1,629 DEGs were identified in LUAD, among which, 714 were highly expressed and 915 were scarcely expressed (Figure 1B). The top 100 DEGs in LUSC (Figure 1C) and LUAD (Figure 1D) are shown in the heat maps. We further applied an online Venn diagram to identify LUSC-specific DEGs (Figure 1E). Consequently, 1,604 specific DEGs for LUSC were obtained, as shown in a heat map (Figure 1F).

3.2 FEA and PPI analysis of the novel biomarkers in LUSC

To elucidate the physiological activities of these LUSC-specific DEGs, GO and KEGG enrichment analyses were carried out. GO terms revealed that these LUSC-specific DEGs were markedly enriched in immune-linked biological systems such as T cell-mediated immunity, immune response-related neutrophil activation, neutrophil degranulation, neutrophil-based immunity, and neutrophil activation (Figure 2A). KEGG analysis revealed that the LUSC-specific DEGs were associated with melanogenesis, small-cell lung cancer, the PI3K-Akt axis, viral myocarditis, human papillomavirus infection, ECM-receptor association, the Rap1 signaling pathway, Staphylococcus aureus infection, and glutathione metabolism (Figure 2B). PPI interaction networks containing 1,604 nodes and 14,209 edges further revealed the interactions between these LUSC-specific DEGs (Figure 2C). The top 20 DEGs are displayed in a bar plot based on the quantity of adjacent nodes (Figure 2D). The top 100 genes of connectedness were obtained using a collateral analysis. The genes with the top 100 connectedness were single factors. Then, Cox and LASSO regression analyses were employed for risk model construction. WGCNA was used to analyze the hub genes' biological behavior, and the correlation between alteration in hub gene expression and clinical characteristics was confirmed via external data from the GEPIA Database (http://gepia.cancer-pku.cn/). The results of WGCNA and GEPIA for hub genes suggested that all hub genes were significantly elevated in tumor tissues. Following the adjustment of confounding factors, we developed a prognostic profile using three genes with remarkable predictive ability.

3.3 Prognostic signature of LUSC-specific DEGs

Based on the counts of connections, the top 100 LUSC-specific DEGs in the PPI network were selected for further analysis. To identify the prognostic genes in LUSC, we further employed a univariate analysis of the 100 LUSC-specific DEGs. Eight were associated with the prognosis of patients with LUSC ($P < 0.05$); univariate Cox regression analysis results are shown in Supplementary Table 1. FGG, C3, FGA, ORM1, JUN, and CST3 served as risk hazards ($HR > 1$), whereas CPSF4 and HIST1H2BH served as a protective function ($HR < 1$) in LUSC (Figure 3A). LASSO analysis was employed to improve the robustness of the eight LUSC-specific DEGs. Eight genes carrying a P-value < 0.05 in the univariate Cox analysis were used to construct a LASSO regression. To reduce the feature dimension, we used the R software's "glmnet" package, set the parameter family as Cox, realized LASSO logistic regression, selected strong correlation features, and obtained the two graphs depicted in Figure 3; one is the graph of gene coefficient, and the other is the error graph of cross-validation. As shown in Figure 3B, the seven characteristic genes with a lambda.min of 0.0134 were FGG, C3, FGA, JUN, CST3, CPSF4, and HIST1H2BH. The seven genes and their corresponding coefficients were selected as the most prognostic gene signatures in LUSC. We further calculated the RS for individual patients with LUSC using the expression of the seven prognostic genes and associated coefficients retrieved from the LASSO-Cox analysis; LASSO analysis was then employed for characteristic genes and coefficients screening, as shown in Supplementary Table 2. Subsequently, the median of the RSs was utilized as a standard to separate the LUSC patients into HR and LR cohorts in both the TC and VC. The risk curve and distribution of OS status are shown in Figure 3C. Moreover, the expression patterns of the seven prognostic genes in the HR and LR cohorts verified the prognostic value of the seven markers. Figure 3C consists of three parts: upper (a), middle (b), and lower (b), all of which demonstrate that the HR cohort exhibited an elevated survival RS. Notably, the Kaplan–Meier analysis indicated that LR LUSC patients exhibited a markedly higher survival probability, compared to the HR cohort (Figure 3D; $P < 0.05$). The results of ROC analysis further tested the TC, which showed that this genetic profile could effectively estimate the OS of LUSC (Figure 3E).

The VC was also tested, and the risk curve and distribution of OS status are shown in Supplementary Figure 1. The survival and ROC curves of VC are shown in Figures 3F, G.

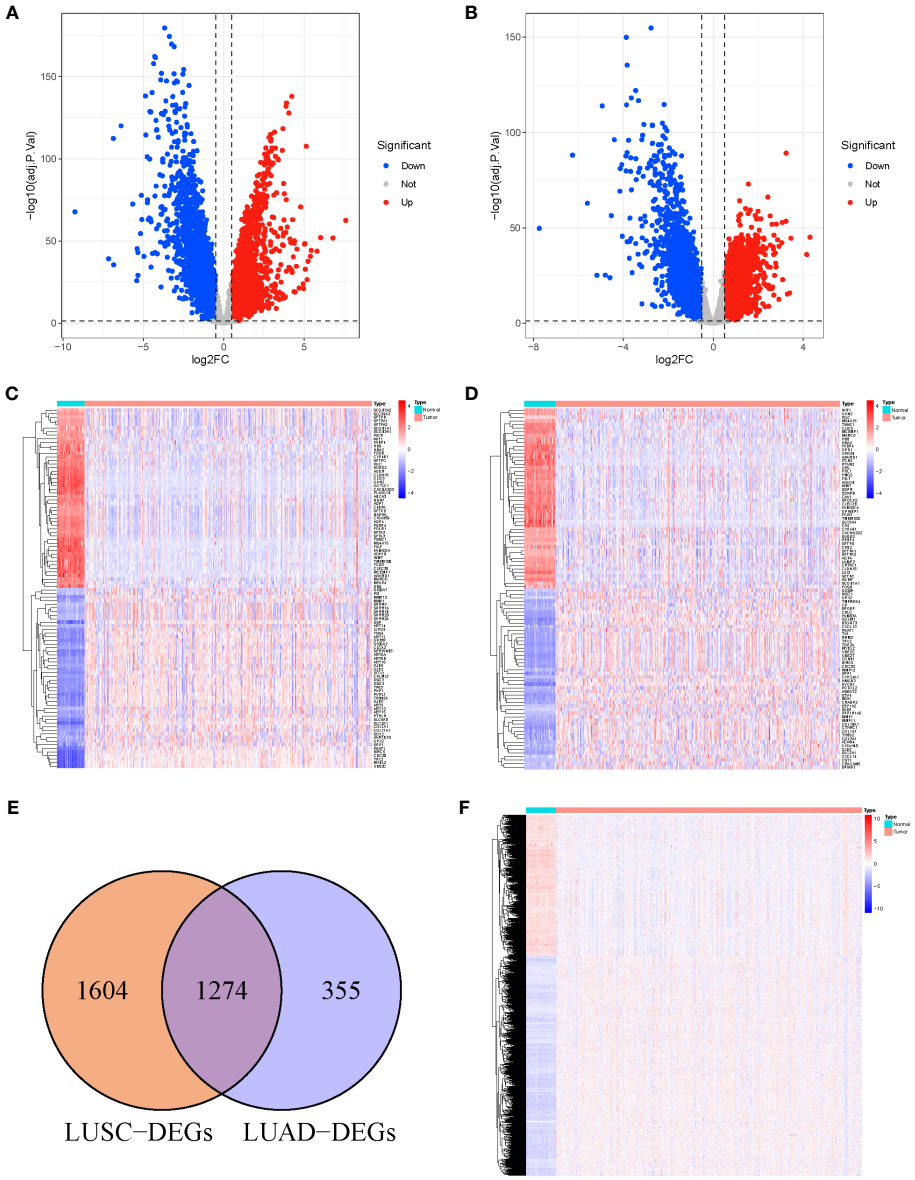

FIGURE 1
(A) Volcano Plots of 2,878 LUSC-DEGs. **(B)** Volcano Plots of 1,629 LUAD-DEGs. Multiples of the abscissa difference (Tumor/Normal) taken the logarithm of 2 and the ordinate representation of -$\log_{10}$(adj.P.Val). Each dot represents a gene. Red dots indicate gene upregulation (Tumor vs. Normal samples), blue dots indicate downregulation (Tumor vs. Normal samples), and gray dots indicate no significant differences in expression. **(C)** The heat map of the top 100 DEGs in LUSC. **(D)** The top 100 DEGs LUAD. The abscissa direction represents the DEGs, while the vertical direction represents the samples. Colors indicate normalized differential expression; high and low expressions are shown in red and blue, respectively. **(E)** The Venn diagram of 1,604 LUSC-specific DEGs calculated by subtraction of LUSC-DEGs and the cross-section of LUSC and LUAD DEGs. **(F)** The heat map of LUSC-specific DEGs. The abscissa direction indicates the DEGs, while the vertical direction indicates the samples. Colors indicate normalized differential expression; red represents elevated levels, and blue represents reduced levels.

3.4 The seven-gene signature of LUSC represents an independent stand-alone prognostic value

To elucidate whether the prognostic gene profile was independent of clinicopathological features such as age, pathological stage, and TNM stage, univariate and multivariate analyses were conducted. Univariate analysis revealed that age, as well as pathologic, pathologic T, and pathologic M stages, were strongly correlated with LUSC patients' OS (Figure 4A). Multivariate analysis based on the above clinicopathological characteristics further revealed that the RS was directly correlated with OS (Figure 4B; $P < 0.001$). The predictive efficiency of these clinicopathological characteristics was evaluated using ROC analysis, and the RS was employed as a predictor stand-alone indicator of LUSC outcome (Figure 4C). We observed marked differences between T1 and T2 of the T stage, and N0 and N1 of the N stage (Supplementary Figures 2, 3); however, there was no significant difference in other periods (Supplementary Figures 4–6). To explore the independent prognosis of risk models and

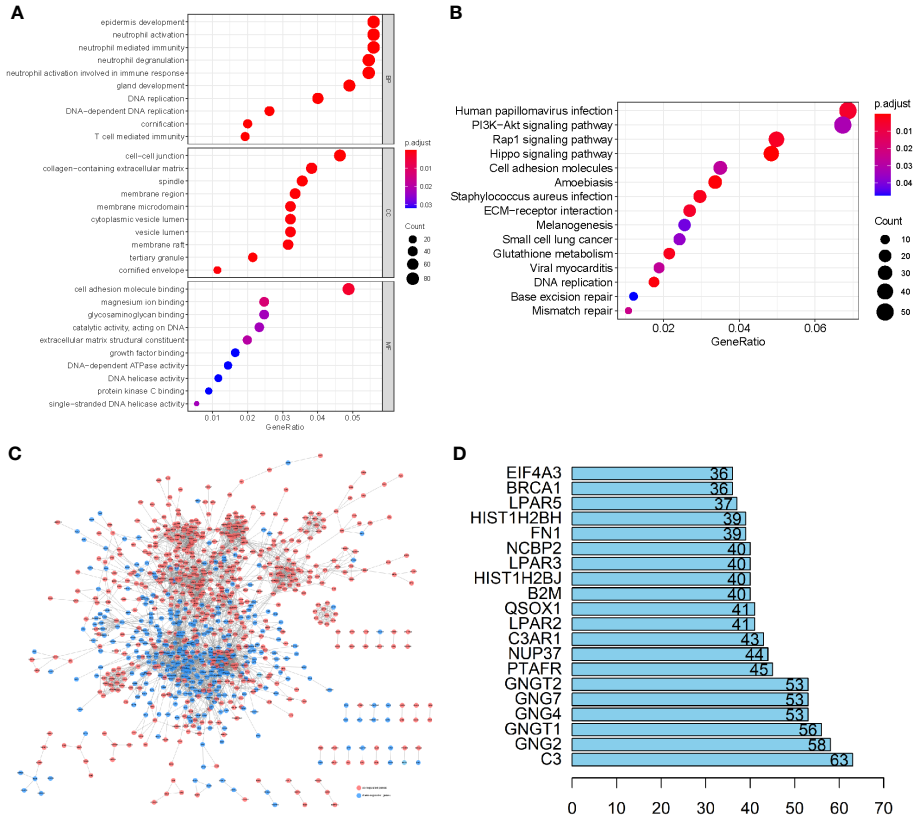

FIGURE 2
(A) GO enrichment analysis of the LUSC-specific DEGs. **(B)** The KEGG analysis of LUSC-specific DEGs. The ordinate and abscissa are the GO pathway sorted by the P-value and gene proportion. The shades of color denote the P-value, while the dot sizes represent the number of participating genes. **(C)** A PPI network containing 1,604 nodes and 14,209 edges further revealed the interactions of these LUSC-specific DEGs, where lines represent the interactions between them, red nodes refer to elevated gene expression, and blue nodes refer to diminished gene expression. **(D)** The bar plot of the top 20 DEGs in LUSC-specific DEGs.

clinicopathological factors, the Cox-independent prognostic analysis of age, the T, M, and N staging, and the RS showed that Pathologic_M and RiskScore were stand-alone prognostic indicators for LUAD ($P < 0.05$). We next analyzed RSs and various clinical features, including age, sex, tumor stage, T (size or extent of the tumor itself), M (distant metastasis), and N (tumor peripheral lymph node invasion and metastasis). A differential expression heat map of the genes was drawn (Figure 4D). Univariate and multivariate results were consistent, indicating that the conclusions were stable and easy to interpret.

3.5 Characteristics of immune infiltration in LUSC

Previous research has revealed a relationship between immune cell invasion and clinical prognosis in cancers, which may be utilized as drug targets to enhance the prognosis of patients (15, 16). Therefore, we quantified the tumor infiltration levels of 29 immune-related gene sets in the HR and LR cohorts. Immune checkpoint inhibitors were reported to be effective potent therapeutic methods against various cancers (17–19); hence, we assessed the levels of key immune checkpoint molecules in LUSC. The HR cohort was markedly correlated with elevated tumor infiltration levels in LUSC (Figures 5A, B; all P-values < 0.05); however, the tumor infiltration levels of NK cells showed no significant differences between the HR and LR cohorts. Importantly, the checkpoint scores between the HR and LR cohorts were significantly different. ssGSEA was performed on the samples from the HR and LR cohorts; we observed marked differences in the levels of certain immune cell infiltrates between the HR and LR cohorts. The infiltrating cells included aDCs, B cells, $CD8^+$ T cells, DCs, iDCs, macrophages, mast cells, neutrophils, pDCs, T helper cells, Tfh, Th1 cells, Th2 cells, TIL, and Tregs. There were also significant differences in the levels of some immune-linked pathways between the HR and LR cohorts, such as APC_co_inhibition, APC_co_stimulation, CCR, Check-point, Cytolytic_activity, HLA, Inflammation-promoting, MHC_class_I, Parainflammation, T_cell_co-inhibition, T_cell_co-stimulation, Type_I_IFN_Reponse, and Type_II_IFN_Reponse. Immune checkpoints refer to those that inhibit cytotoxic T lymphocyte activation, or cytotoxicity, as well as T lymphocyte (killer T cell) interaction. These findings suggest that the prognostic model is related to the function of antigen-presenting cells (APCs), cytotoxic T cells, immune checkpoints, and major histocompatibility complex (MHC). Thus, the risk model could also be an indicator of tumor immune response in LUSC.

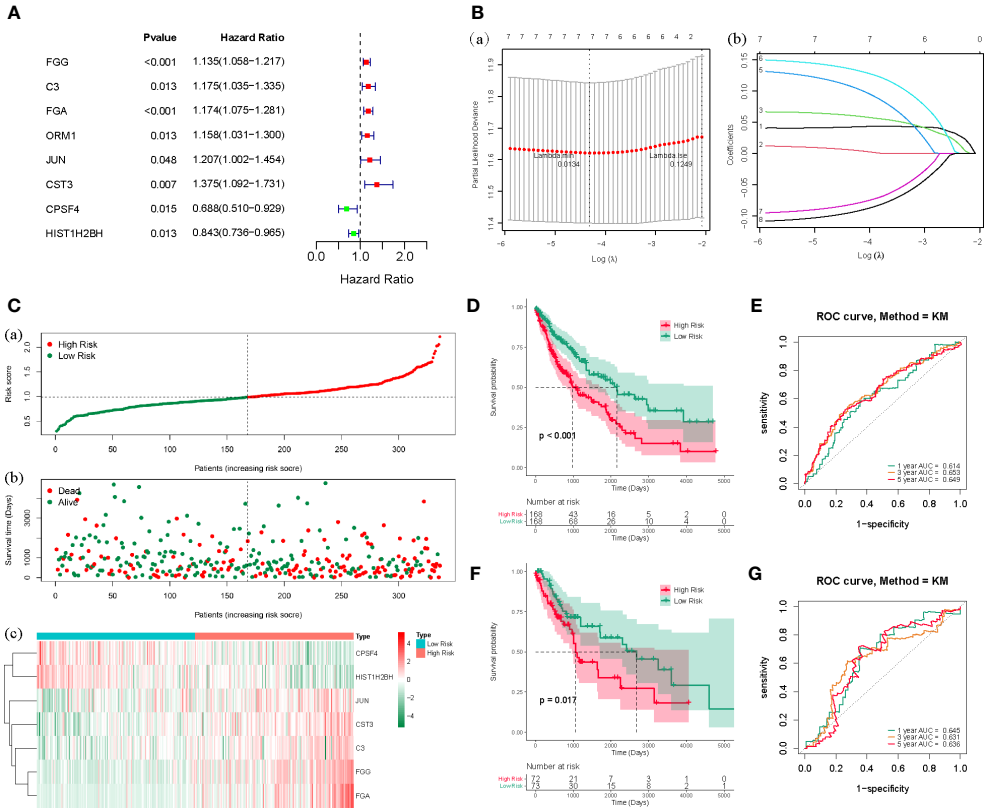

FIGURE 3
(A) The forest map of the eight risk genes (FGG, C3, FGA, CRM1, JUN, CST3, CPSF4, and HIST1H2BH) using univariate analysis. **(B)**, (a) LASSO analysis, where the screened characteristic gene ordinate is the gene coefficient; (b) the abscissa is the log(Lambda), and the ordinate denotes cross-validation error. In the analysis, we identified the position with the minimum error of cross-validation. In **(B)**, the dotted line on the left represents the position with the minimum error of cross-validation. Based on the position (lambda.min), we determined the associated horizontal coordinate log (Lambda) and the number of characteristic genes (shown above); we also found the optimal log(Lambda) value and the associated gene and its coefficient in the left figure **(A)**. **(C)** The risk curve and the distributions of OS status of the seven-gene TC ($P < 0.05$). The risk score (RS) of the TC in high- (HR) and low-risk (LR) cohorts (a), the OS status (b), and the heat map (c) are shown. The figure above (a) is consistent with the abscissa of the middle figure (b), indicating that RSs rose from left to right. The ordinate represents the RS and survival time, while the dotted line represents the median RS and the corresponding number of patients. Below (c) is the gene expression heat maps in the HR and LR cohorts. **(D)** The OS curve based on the HR and LR cohorts. **(E)** ROC curve of the seven-gene set in TCGA-LUSC training cohort (TC) 1-3-5-years OS. **(F)** TCGA-LUSC validation of survival curves for concentrated HR and LR cohorts. **(G)** ROC curves for 1-3-5-years OS in TCGA-LUSC validation cohort (VC).

Immune checkpoint molecules for immune function are crucial for TME and immunotherapy (20). To examine the potential association between molecular levels and immune checkpoints, we analyzed the expression of several key immune checkpoint sites, including TNFRSF18, TNFRSF14, CD160, CD48, CD244, TNFSF18, TNFSF4, CD28, ICOS, PD-1 (PDCD1), CD47, BTLA, TIGIT, CD80, CD86, TIM-3 (HAVCR2), PD-L1 (CD274), CD27, LAG3, CD276, LGALS9, CD226, CD70, TNFSF14, CEACAM1, PVR, and CD40. As shown in Figure 5C, apart from TNFSF18, TNFSF4, CD274, LAG3, and CD276, the levels of most immune checkpoint genes were markedly different between the HR and LR cohorts (Figure 5; all P-values < 0.05).

3.6 Cancer stem cell characteristics of the risk model

Cancer stem cells serve essential functions in tumor survival, metastasis, proliferation, and recurrence, owing to their self-renewal ability and production of heterogeneous tumor cells (21). MRNAsi reflects the gene expression characteristics of stem cells. We used mRNAsi as the stemness index to investigate the similarities between cancer and stem cells. The index ranged from 0 to 1; the value of mRNAsi close to 1 indicated enhanced stem cell features of the tumor cells. Thus, the mRNAsi and EREG-mRNAsi of LUSC samples were further computed using the OCLR algorithm and then compared between the HR and LR cohorts. Figures 6A, B) shows significant differences in the mRNAsi and EREG-mRNAsi between the two cohorts ($P < 0.05$).

3.7 Establishment of a ceRNA network for LUSC

LncRNAs and circRNAs are generally perceived as competing endogenous RNAs (ceRNAs) that bind to miRNAs. ceRNA analysis refers to the analysis of the entire ceRNA regulatory network; usually circRNA-miRNA-mRNA analysis or lncRNA-miRNA-

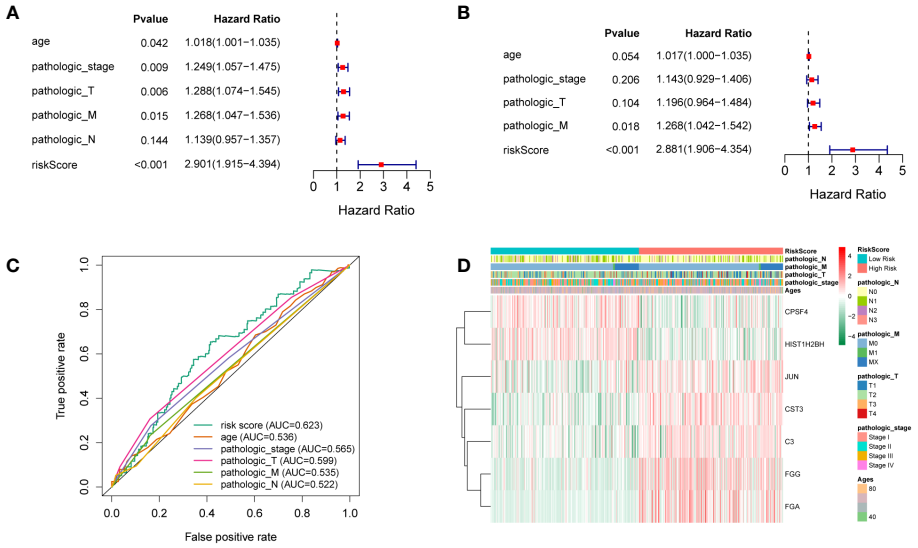

FIGURE 4
(A) Univariate analysis. **(B)** Multivariate analysis. **(C)** ROC curves of multiple indicators. **(D)** Heat maps of different clinicopathological features of TCGA-LUSC.

mRNA analysis is perceived as the core of the ceRNA regulatory network. With competitive binding of ceRNAs, such as lncRNA or circRNA with miRNA, the transcription level of the genes regulated by miRNAs will increase. To further elucidate the potential regulatory mechanism of these seven prognostic DEGs in LUSC prognosis, we generated a ceRNA network using the DE-lncRNAs and prognostic DEGs. The target miRNAs of DE-lncRNAs were predicted using the miRcode database, and the target miRNAs of prognostic DEGs were predicted using the miRanda database. A ceRNA network containing 19 lncRNAs, 50 miRNAs, and 7 prognostic DEGs demonstrated the molecular mechanism of LUSC-specific DEGs in LUSC prognosis (Figure 7).

3.8 FGG and Clinical Parameters in patients with LUSC

The prognostic values of FGG, C3, FGA, JUN, CST3, CPSF4, and HIST1H2BH7 genes in LUSC in the TCGA database suggest that they may play a role as key risk factors in tumors (Supplementary Figure 7). The expressions of seven prognostic genes in human LUSC cell lines NCI-H520 and LTEP-s were detected using q-PCR; FGG was significantly highly expressed in both LUSC cell lines (Supplementary Figure 8). We also examined the expression of FGG in surgically collected, paired, LUSC samples, and adjacent normal tissues from 6 patients. Remarkably, all LUSC specimens had markedly increased FGG protein levels compared with matched adjacent normal tissues (Figure 8). Our clinical observations reveal that FGG is significantly hyper-expressive in LUSC patient samples, further demonstrating the clinical value of FGG in LUSC.

3.9 FGG correlates with tumor progression, immune infiltration, and stem index in LUSC

Immunofluorescence showed that FGG was expressed in the nucleus of LUSC (Figures 9A, B). To demonstrate the biological function of FGG in LUSC cells, NCI-H520 (Figures 9C, E) and LTEP-s cell lines (Figures 9D, G) with FGG knockdown were successfully constructed.

Our results suggest that FGG can affect the tumor process of LUSC cells, as shown by the proliferation (Figures 9F, H), cloning (Figures 9I, J), invasion (Figures 9K, L), and migration (Figures 9M, N) of NCI-H520 and LTEP-s being significantly inhibited following FGG knockdown. In addition, the result of western blot showed that the expression of E-cadherin was increased while that of N-cadherin and VIMENTIN were decreased following FGG knockdown, which also corresponded to the inhibition of migration and invasion (Figures 9O, P). Subsequently, we evaluated the scores of 22 kinds of tumor immune cell infiltration in LUSC patients according to the expression of FGG and found that FGG was significantly correlated with 10 kinds of immune cell infiltration, including M1 macrophages (Figures 10A, B). *In vitro* Transwell experiments showed that the ability of NCI-H520 (Figure 10C) and LTEP-s cell lines (Figure 10D) with low FGG to recruit M1 mononuclear macrophages was significantly down-regulated. After FGG knockdown, KLF4, Nanog, CD44, and SOX2 in NCI-H520 cells were significantly decreased, while CD133 showed no significant changes (Figures 10E, F). After FGG knockdown, KLF4, Nanog, CD44, and SOX2 in NCI-H520 cells were significantly decreased, while CD133 showed no significant changes (Figure 10E). After FGG downregulation, the expressions of CD44 and CD133 in

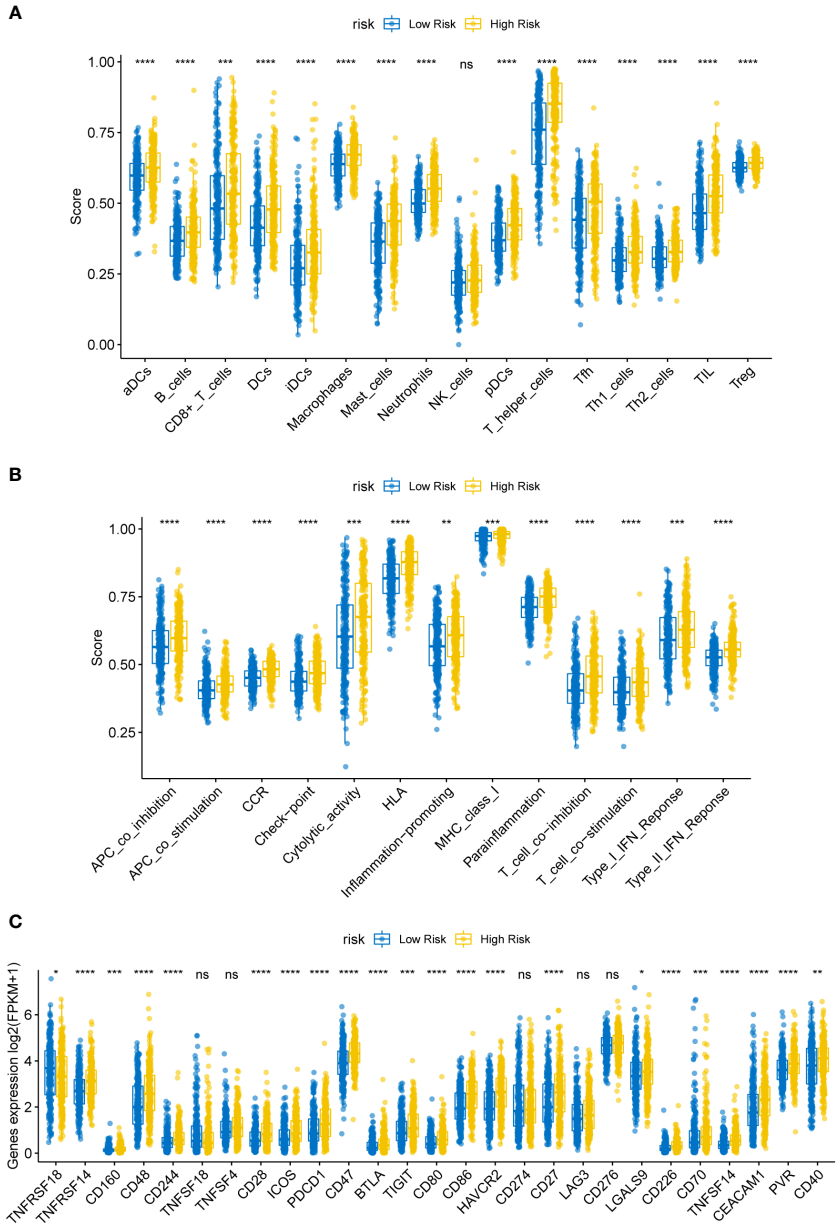

FIGURE 5
(A) Box plot of immune infiltrating cells in the high- (HR) and low-risk (LR) cohorts. The HR cohort was strongly associated with elevated tumor infiltration levels in LUSC (P < 0.05). **(B)** Box plot of tumor infiltrated pathway. **(C)** Box plot of immunoassay sites in the HR and LR cohorts. The levels of the remaining immune checkpoint genes were markedly different between the HR and LR cohorts (P-values < 0.05); ns, not significant. (*P<0.05, **P<0.01, ***P<0.001, ****P<0.0001).

LTEP-s cells were significantly decreased, while no significant changes in KLF4, Nanog, and SOX2 were observed (Figure 10F). These results indicate that FGG affected the tumor progression, immune infiltration, and stem index of LUSC cells.

4 Discussion

LUSC is a subtype of NSCLC and accounts for nearly 40% of all lung cancers. Early detection and the prognostic assessment of LUSC remain challenging, hence the poor 5-year survival rate of patients (22). Recent studies have improved the prognosis prediction for LUSC patients, focusing on biomarkers. For example, Shi et al. investigated DNA methylation profiling and proposed potential diagnostic biomarkers for LUSC (23). Chen et al. investigated the roles of IRGs in the deterioration of lung cancer and indicated the distinction between LUAD and LUSC from the perspective of the immune response (24). Liao et al. identified biomarkers with cancer stem cell characteristics in LUSC (14). To date, the prognostic gene signatures for prognostic prediction of LUSC are scarce and warrant further investigations. Several studies have proposed prognostic markers for survival prediction in patients with LUSC. Zhang et al. suggested that IRGPI could be used as a prognostic marker (25), while Li et al.

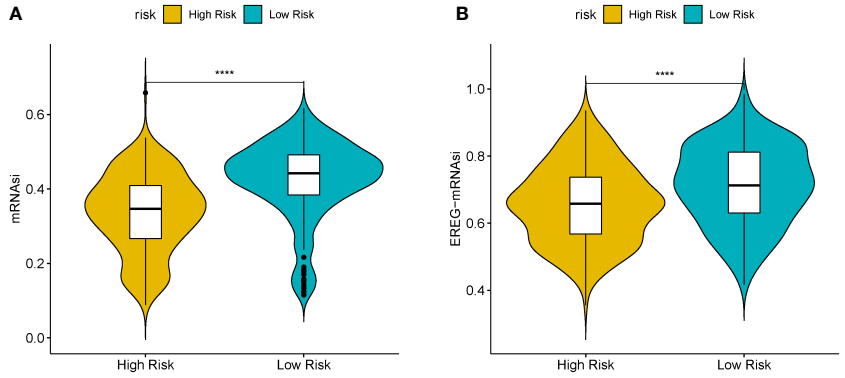

FIGURE 6
(A) Boxplots of mRNAsi in the high- (HR) and low-risk (LR) LUSC patients. **(B)** Boxplots of EREG-mRNAsi in the HR and LR LUSC patients. (*P<0.05, **P<0.01, ***P<0.001, ****P<0.0001).

constructed an mRNA signature to predict the outcomes of patients with LUSC (26). Liu et al. have identified an miRNA signature with potential clinical implications in the outcome prediction of LUSC (27). Indeed, several lncRNAs, such as VPS9D1-AS1 and MALAT-1, are correlated with the survival of LUSC patients (28, 29). Huang et al. reported a nine-long non-coding RNA signature for prognosis prediction of patients with LUSC (7). However, no prognostic indicators of LUSC have been established based on tumor progression, immune infiltration, and stem index analysis.

Recent studies have found that LUSC differs from LUAD in terms of genomic, epigenetic, CSC stemness, and TME characteristics. According to previous research, CSCs may lead to cancer recurrence and drug resistance (30, 31). The TME is a mutually adaptive environment in which tumor cells escape immunological surveillance. Tumor progression involves crosstalk between CSCs and the TME (32, 33), such as the induction of CSCs in EMT (34) and the interaction of angiogenesis and components of the TME (35). Herein, we adopted a comprehensive perspective of cancer biology based on tumor progression, TME, and CSC index for a better understanding of LUSC as an independent NSCLC from different dimensions. We recognized the importance of the particularly expressed genes in LUSC based on the TCGA database and DEGs in HR and LR cohorts; from this, we recognized the functions of independent genes as potential

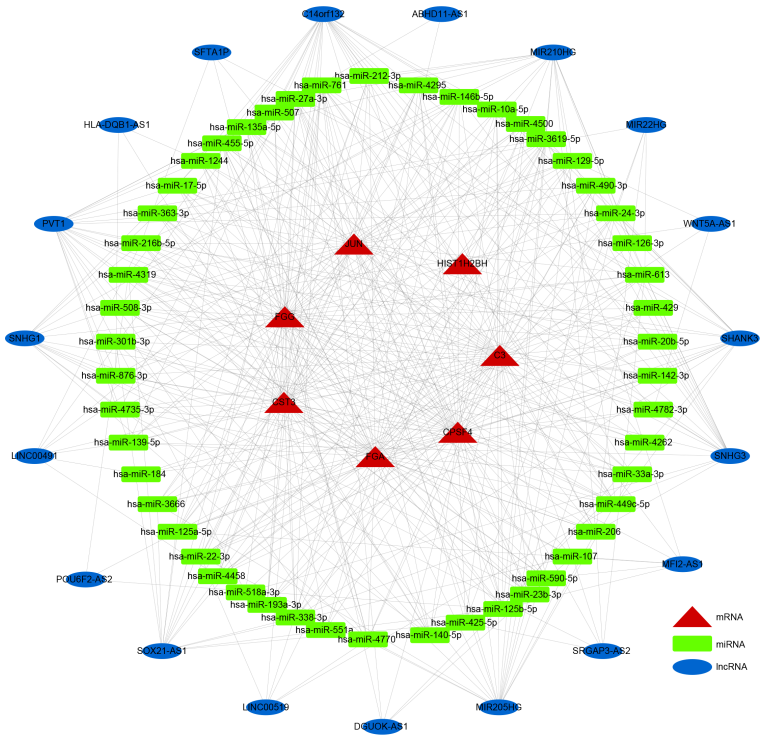

FIGURE 7
ceRNA network. Rectangles, ellipses, and triangles represent the miRNAs, lncRNAs, and mRNAs of the risk model genes, respectively.

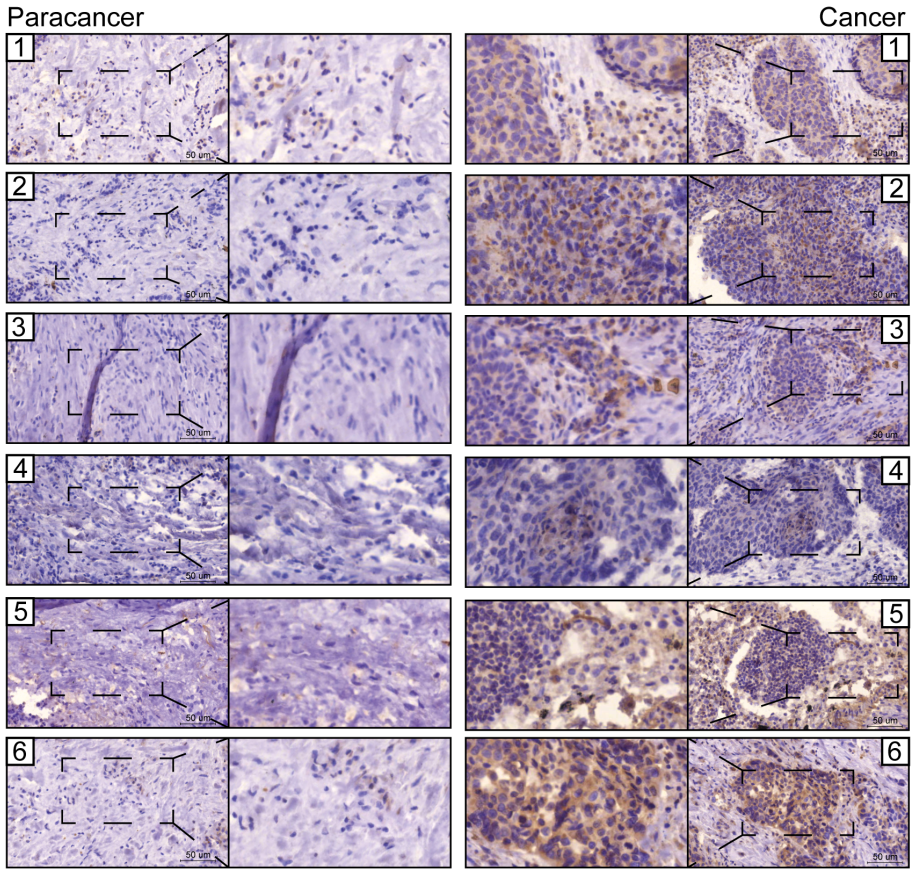

FIGURE 8
Representative images from immunohistochemical staining of FGG in lung cancers (n = 6) and normal tissues (n = 6). Scale bars: 100 μm and 50 μm.

predictors of tumor invasion, metastasis, tumor stem cell characteristics, and immune cell infiltration. Seven prognostic genes were varied in LUSC and were associated with the TNM stage and prognosis; these genes were FGG, C3, FGA, JUN, CST3, CPSF4, and HIST1H2BH. FGG, C3, FGA, JUN, and CST3 were associated with poor outcomes in LUSC patients, whereas CPSF4 and HIST1H2BH served as positive prognostic markers in LUSC patients.

In terms of clinicopathological features, the seven-gene biomarkers showed differences in tumor metastasis and invasion, and the significant differences between T1 and T2 of the T stage and N0 and N1 of the N stage suggested that the modification occurred during the early stage of tumor disease; however, the factors of dabbling were limited, such as the lack of the status of smoking status, driver factors, ORR of the various chemotherapy, and immune checkpoint blockade subgroups. Kaplan–Meier analysis showed that LUSC patients in the LR group exhibited significantly higher OS than those in the HR group, while ROC curve analysis results showed that this gene profile could effectively predict the OS of LUSC. Subsequently, our independent prognostic value analysis showed that protective genes were highly expressed in the low-risk group, while the risk genes were highly expressed in the high-risk group, indicating stable results. Moreover, the ROC curve showed that RS could be used as an independent prognostic factor effectively predicting LUSC outcomes. We also analyzed the relationships between HR and LR cohorts, immunoinfiltrating cells, and immune pathways, and showed that HR patients exhibited significantly elevated levels of tumor cell immune infiltration and that the molecular expression of immune checkpoint genes significantly differed between HR and LR patients.

Next, we analyzed the stem cell characteristics of the model and showed that mRNA was associated with prognosis and relevance; significant differences were noted in mRNAsi and EREG-mRNAsi between HR and LR patients, providing new insights into the clinical features, immune response, and TME of tumors based on the dry index. Finally, we constructed a ceRNA network containing 19 lncRNAs, 50 miRNAs, and 7 prognostic DEGs, demonstrating the prognostic value of novel biomarkers for Lusc-specific DEGs.

The prediction of the risk prognostic model constructed can potentially provide more reliable theoretical support for clinical application. However, bioinformatics is only a short practical perspective to this goal; therefore, we conducted specific molecular studies on prognostic genes. Based on the risk model constructed above, combined with RT-qPCR assay and survival analysis of the TCGA database, we screened LUSC-specific prognostic genes and found that FGG was closely correlated with LUSC results in univariate Cox analysis (P=0.000427708), and mRNA levels of FGG were stably expressed in NCI-H520 and

10.3389/fimmu.2023.1236444

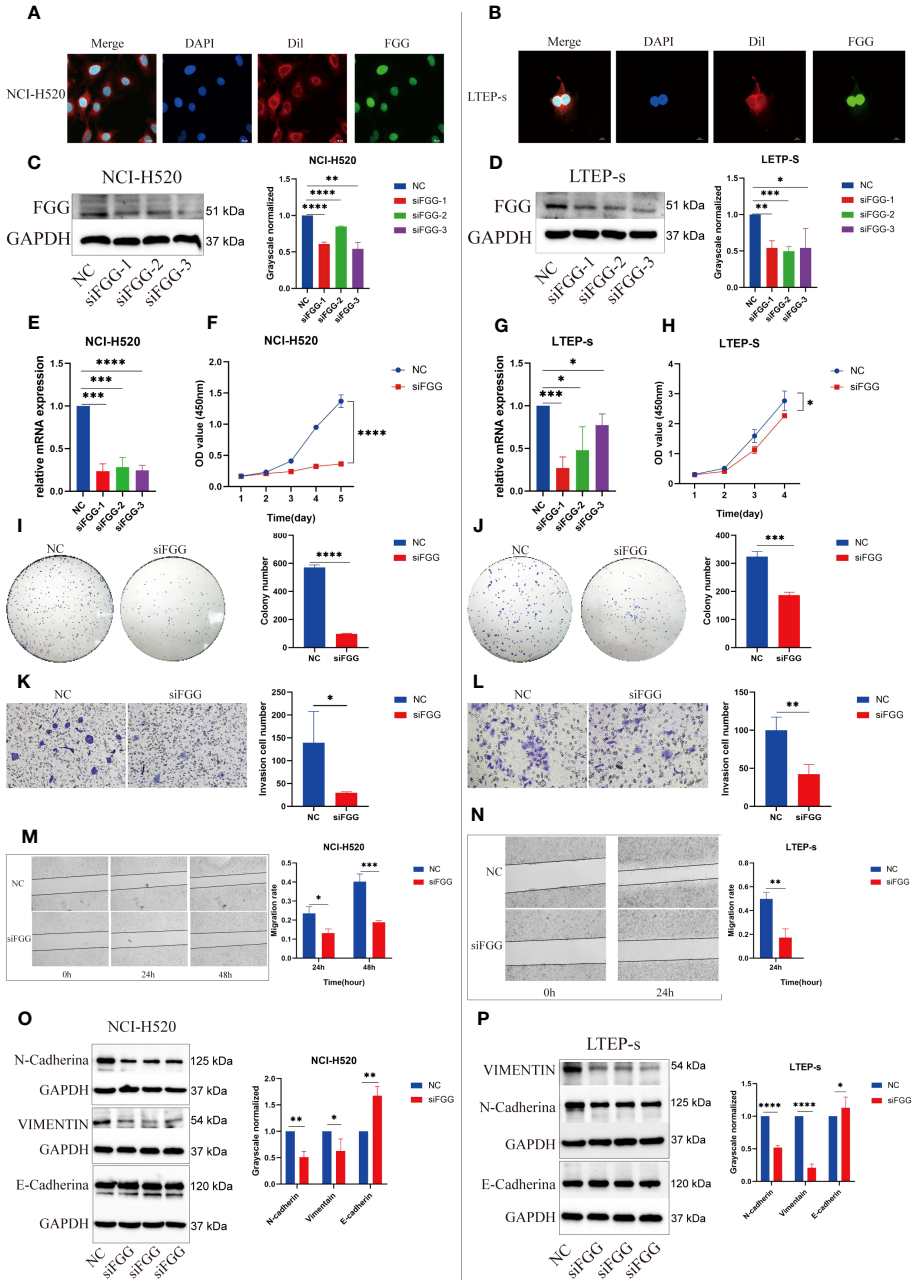

FIGURE 9
Expression locations of FGG detected using immunofluorescence in **(A)** NCI-H520 and **(B)** LTEP-s. FGG knockdown was determined using western blotting in **(C)** NCI-H520 and **(D)** LTEP-s cells. FGG knockdown was determined using Q-PCR in **(E)** NCI-H520 and **(G)** LTEP-s cells. CCK-8 assay was used to detect the proliferation of **(F)** NCI-H520 and **(H)** LTEP-s cells Viability line graph **(I)** NCI-H520 and **(J)** LTEP-s cell colony formation result. The result of the invasion of **(K)** NCI-H520 and **(L)** LTEP-s cells. The results of Wound Healing and migration of **(M)** NCI-H520 cells and **(N)** LTEP-s cells. Western blotting assay showing EMT markers N-cadherin, Vimentin, and E-cadherin expression following FGG knockdown in **(O)** NCI-H520 and **(P)** LTEP-s cells. The significant differences were analyzed using GraphPad Prism *t*-test, n=3 (*P<0.05, **P<0.01, ***P<0.001, ****P<0.0001).

LTEP-s cells and significantly up-regulated compared with normal airway epithelial cells. Therefore, their roles in tumor progression, immunoinfiltration, and dry characteristics were further analyzed.

FGG is the γ-chain of fibrinogen, a large, complex glycoprotein with a total molecular mass of approximately 340 kDa, comprising three pairs of polypeptide chains: Aα (encoded by the FGA gene), Bβ (FGB), and γ (36). FGG has a conserved globular domain, γC, at the COOH terminus, which is a major integrin binding site for fibrinogen. Yokoyama et al. found that the C-terminal region of FGG, as the primary integrin binding site of fibrinogen, participated in the process of thrombosis, angiogenesis, and inflammation (37, 38). Nobuaki Akakura et al. found that isolated γC and its mutant γC399tr induce endothelial cell apoptosis, and recombinant soluble γC399tr inhibited tumor growth, intratumoral vascular development, and metastasis *in vivo* (39). Previous studies have shown that fibrinogenemia, as a prognostic factor (40–42), is often

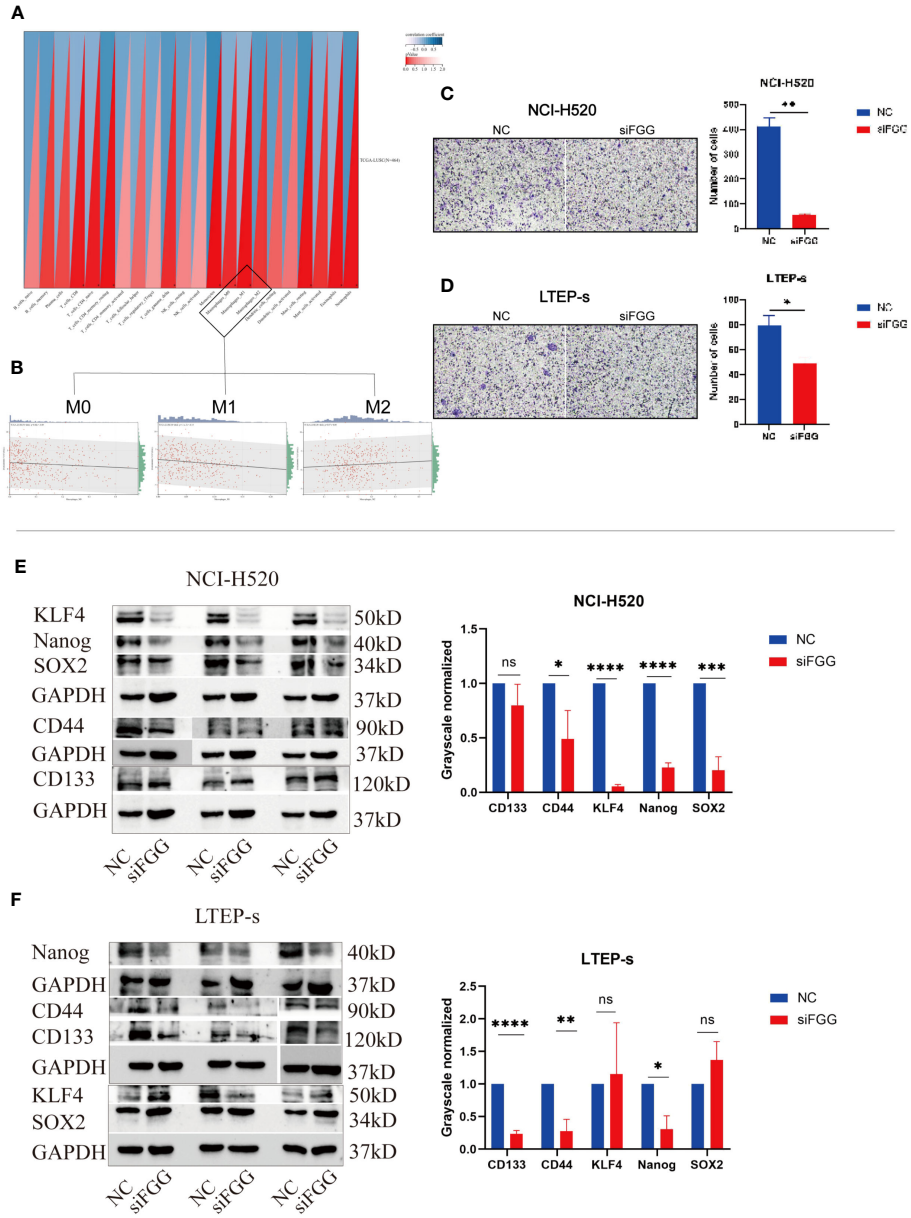

FIGURE 10
(A) Pearson's correlation coefficient of FGG with 22 immune cell infiltration scores in LUSC was calculated using the corr.test function of the R package psych (version 2.1.6), and 10 significantly correlated immune infiltration scores, including macrophages, were identified, **(B)** for further individual correlations plotted for FGG with M0, M1, and M2 macrophages, respectively (p=0.04, r=0.09, p=1.1e-03, r=0.15, p=0.07, r=0.09). Tranwell shows the infiltration of THP-1of **(C)** NCI-H520 cells and **(D)** LTEP-s cells. Western blotting assay showing the expression of stemness marker genes SOX2, Nanog, CD133, CD44, KLF4 following FGG knockdown in **(E)** NCI-H520 and **(F)** LTEP-s cells. "ns" No Significant.

observed in patients with malignant tumors and is closely related to tumor invasion, metastasis (43–45), angiogenesis (46), and tumor growth processes (47); further, its degradation products with carcinogenesis have been reported in tumors (41). However, Nagata et al. found that frameshift mutations in FGG led to hypofibrinemia, indicating that FGG was involved in the regulation of fibrinogen secretion (48). In addition, FGG inhibits platelet adhesion to fibrinogen by interacting with hepatitis B splicing protein (49). Dysregulation of FGG has also been reported in many malignant tumor types, such as liver cancer (50), stomach cancer (40), and prostate cancer (51), underscoring its potential relevance as a tumor marker. FGG is an important adverse prognostic factor for gastric cancer (35). Another study showed that serum FGG levels predicted the progression of prostate cancer (51). Additionally, FGG is thought to distinguish cancer from normal sera as a potential tumor marker in pancreatic cancer (52). Additional data show the possibility of urine FGG levels as a potential diagnostic marker for NSCLC (53). These findings suggest that FGG could hold diagnostic, prognostic, and therapeutic implications in cancer.

Our bioinformatics modeling demonstrated that FGG as a risk prognosticator is of significant research value in LUSC, and the

results of subsequent *in vitro* experiments are consistent with reports of abnormal expression of FGG mRNA in various cancers. Knockdown of FGG caused functional changes in LUSC tumor progression at the tumor cell level, significantly inhibited the proliferation and clonogenesis ability of NCI-H520 and LTEP-s cells, and blocked the cell cycle in the S phase (Supplementary Figure 9). It also inhibited the invasion and migration ability of tumor cells, by reducing the EMT process and promoting the early apoptosis of tumor cells. In terms of dry characteristics, FGG down-regulation decreased the expressions of KLF4, Nanog, CD44, and SOX2 in NCI-H520 cells, and the expressions of CD44, Nanog, and CD133 in LTEP-s cells. In terms of immune cell infiltration, the expression of FGG in LUSC tissues was significantly correlated with M0 and M1 type macrophages, while knockdown of FGG in LUSC cells significantly affected the degree of immune infiltration of M1 type macrophages (Supplementary Figure 10) formed by polarization of THP-1 cells, suggesting that FGG plays a specific role in the immune infiltration of LUSC.

In summary, our study successfully constructed a LUSC-specific DEGs based risk and prognosis model and verified the reliability of the risk model from the data model. According to the prognostic risk factors, including tumor invasion, metastasis, survival, immune infiltration, and tumor stem cell-related genes, DEGs in LUSC were used to determine associations between functional genes and tumor progression, immune invasion, and dry index. However, this prognostic model has some limitations, such as the relatively simple database and limited factors analyzed (such as lack of smoking status, drivers, ORRs of various chemotherapy treatments, and subsets of immune checkpoint blocking). Subsequently, *in vitro* studies of the LUSC-specific prognostic marker FGG will provide deeper insights into LUSC. As a risk factor in this prognostic model, FGG significantly inhibited the progression of LUSC tumor cells after knockdown and reduced the expression of dry marker genes and the infiltration level of M1 type macrophages, suggesting that FGG is a potential biomarker for independent poor prognosis of LUSC to identify LUSC patients with poor clinical outcomes and that it may play specific roles in dry maintenance and immune infiltration. However, the specific mechanism underlying the changes in tumor progression warrants further study.

5 Conclusion

This study established a seven-gene profile (FGG, C3, FGA, JUN, CST3, CPSF4, and HIST1H2BH) prognostic stratification system demonstrated in LUSC based on Tumor Progression, Immune Infiltration, and Stem Index. *In vitro* experiments confirmed that DEGs FGG could be independent prognostic biomarkers of LUSC promoting cell proliferation, migration, invasion, THP-1 cell infiltration, and stem cell maintenance.

Data availability statement

The original contributions presented in the study are included in the article/Supplementary Material. Further inquiries can be directed to the corresponding authors.

Ethics statement

The current study was approved by the institutional ethics review board of Affiliated Hospital of Inner Mongolia Medical University, Hohhot, Inner Mongolia Autonomous Region, China (NO.KY(2021021). The studies were conducted in accordance with the local legislation and institutional requirements. The participants provided their written informed consent to participate in this study.

Author contributions

RW contributed to the study's conception, design, and manuscript writing. RM conducted the *in vitro* experiment. XD performed the bioinformatics analysis. JZ and KL generated all the Figures and Tables. LY and MZ contributed to the manuscript editing. RW was responsible for funding acquisition. CW and PL reviewed and approved the manuscript. All authors contributed to the article and approved the submitted version.

Funding

This work was funded by the Youth Backbone Project of the Affiliated Hospital of Inner Mongolia Medical University (2022NYFYFG010).

Conflict of interest

The authors declare that the research was conducted in the absence of any commercial or financial relationships that could be construed as a potential conflict of interest.

Publisher's note

Supplementary material

The Supplementary Material for this article can be found online at: https://www.frontiersin.org/articles/10.3389/fimmu.2023.1236444/full#supplementary-material

References

1. Chen Z, Fillmore CM, Hammerman PS, Kim CF, Wong KK. Non-small-cell lung cancers: a heterogeneous set of diseases. *Nat Rev Cancer* (2014) 14(8):535–46. doi: 10.1038/nrc3775

2. Lu J, Wang W, Xu M, Li Y, Chen C, Wang X. A global view of regulatory networks in lung cancer: An approach to understand homogeneity and heterogeneity. *Semin Cancer Biol* (2017) 42:31–8. doi: 10.1016/j.semcancer.2016.11.004

3. Relli V, Trerotola M, Guerra E, Alberti S. Abandoning the notion of non-small cell lung cancer. *Trends Mol Med* (2019) 25(7):585–94. doi: 10.1016/j.molmed.2019.04.012

4. Ren S, Xiong X, You H, Shen J, Zhou P. The combination of immune checkpoint blockade and angiogenesis inhibitors in the treatment of advanced non-small cell lung cancer. *Front Immunol* (2021) 12:689132. doi: 10.3389/fimmu.2021.689132

5. Siegel RL, Miller KD, Jemal A. Cancer statistics, 2019. *CA: Cancer J Clin* (2019) 69 (1):7–34. doi: 10.3322/caac.21551

6. Cancer Genome Atlas Research Network. Comprehensive genomic characterization of squamous cell lung cancers. *Nature* (2012) 489(7417):519–25. doi: 10.1038/nature11404

7. Huang G, Huang Q, Xie Z, Zhou H, Cao J, Shi L, et al. A nine-long non-coding RNA signature for prognosis prediction of patients with lung squamous cell carcinoma. *Cancer Biomarkers section A Dis Markers* (2019) 26(3):239–47. doi: 10.3233/CBM-182275

8. Duruisseaux M, Esteller M. Lung cancer epigenetics: From knowledge to applications. *Semin Cancer Biol* (2018) 51:116–28. doi: 10.1016/j.semcancer.2017.09.005

9. Cao S, Wang Z, Gao X, He W, Cai Y, Chen H, et al. FOXC1 induces cancer stem cell-like properties through upregulation of beta-catenin in NSCLC. *J Exp Clin Cancer Res CR* (2018) 37(1):220. doi: 10.1186/s13046-018-0894-0

10. Deng K, Liu L, Tan X, Zhang Z, Li J, Ou Y, et al. WIP1 promotes cancer stem cell properties by inhibiting p38 MAPK in NSCLC. *Signal transduction targeted Ther* (2020) 5(1):36. doi: 10.1038/s41392-020-0126-x

11. Horvath L, Thienpont B, Zhao L, Wolf D, Pircher A. Overcoming immunotherapy resistance in non-small cell lung cancer (NSCLC) - novel approaches and future outlook. *Mol Cancer* (2020) 19(1):141. doi: 10.1186/s12943-020-01260-z

12. Bass AJ, Watanabe H, Mermel CH, Yu S, Perner S, Verhaak RG, et al. SOX2 is an amplified lineage-survival oncogene in lung and esophageal squamous cell carcinomas. *Nat Genet* (2009) 41(11):1238–42. doi: 10.1038/ng.465

13. Mao D, Zhou Z, Song S, Li D, He Y, Wei Z, et al. Identification of stemness characteristics associated with the immune microenvironment and prognosis in gastric cancer. *Front Oncol* (2021) 11:626961. doi: 10.3389/fonc.2021.626961

14. Liao Y, Xiao H, Cheng M, Fan X. Bioinformatics analysis reveals biomarkers with cancer stem cell characteristics in lung squamous cell carcinoma. *Front Genet* (2020) 11:427. doi: 10.3389/fgene.2020.00427

15. Tanaka A, Sakaguchi S. Regulatory T cells in cancer immunotherapy. *Cell Res* (2017) 27(1):109–18. doi: 10.1038/cr.2016.151

16. Cassetta L, Pollard JW. Targeting macrophages: therapeutic approaches in cancer. *Nat Rev Drug Discovery* (2018) 17(12):887–904. doi: 10.1038/nrd.2018.169

17. Wang Y, Zhang X, Yang L, Xue J, Hu G. Blockade of CCL2 enhances immunotherapeutic effect of anti-PD1 in lung cancer. *J Bone Oncol* (2018) 11:27–32. doi: 10.1016/j.jbo.2018.01.002

18. Ahern E, Cubitt A, Ballard E, Teng MWL, Dougall WC, Smyth MJ, et al. Pharmacodynamics of Pre-Operative PD1 checkpoint blockade and receptor activator of NFkB ligand (RANKL) inhibition in non-small cell lung cancer (NSCLC): study protocol for a multicentre, open-label, phase 1B/2, translational trial (POPCORN). *Trials* (2019) 20(1):753. doi: 10.1186/s13063-019-3951-x

19. Liu D, Schilling B, Liu D, Sucker A, Livingstone E, Jerby-Arnon L, et al. Integrative molecular and clinical modeling of clinical outcomes to PD1 blockade in patients with metastatic melanoma. *Nat Med* (2019) 25(12):1916–27. doi: 10.1038/s41591-019-0654-5

20. Li B, Chan HL, Chen P. Immune checkpoint inhibitors: basics and challenges. *Curr medicinal Chem* (2019) 26(17):3009–25. doi: 10.2174/0929867324666170804143706

21. Eun K, Ham SW, Kim H. Cancer stem cell heterogeneity: origin and new perspectives on CSC targeting. *BMB Rep* (2017) 50(3):117–25. doi: 10.5483/BMBRep.2017.50.3.222

22. Yang CY, Yang JC, Yang PC. Precision management of advanced non-small cell lung cancer. *Annu Rev Med* (2020) 71:117–36. doi: 10.1146/annurev-med-051718-013524

23. Shi YX, Wang Y, Li X, Zhang W, Zhou HH, Yin JY, et al. Genome-wide DNA methylation profiling reveals novel epigenetic signatures in squamous cell lung cancer. *BMC Genomics* (2017) 18(1):901. doi: 10.1186/s12864-017-4223-3

24. Chen M, Wang X, Wang W, Gui X, Li Z. Immune- and stemness-related genes revealed by comprehensive analysis and validation for cancer immunity and prognosis and its nomogram in lung adenocarcinoma. *Front Immunol* (2022) 13:829057. doi: 10.3389/fimmu.2022.829057

25. Zhang Z, Zhang S, Li X, Zhao Z, Chen C, Zhang J, et al. Reference genome and annotation updates lead to contradictory prognostic predictions in gene expression signatures: a case study of resected stage I lung adenocarcinoma. *Briefings Bioinf* (2021) 22(3):bbaa081. doi: 10.1093/bib/bbaa081

26. Li N, Li Y, Zheng P, Zhan X. Cancer stemness-based prognostic immune-related gene signatures in lung adenocarcinoma and lung squamous cell carcinoma. *Front Endocrinol* (2021) 12:755805. doi: 10.3389/fendo.2021.755805

27. Liu H, Li T, Dong C, Lyu J. Identification of miRNA signature for predicting the prognostic biomarker of squamous cell lung carcinoma. *PloS One* (2022) 17(3): e0264645. doi: 10.1371/journal.pone.0264645

28. Wang X, Su R, Guo Q, Liu J, Ruan B, Wang G. Competing endogenous RNA (ceRNA) hypothetic model based on comprehensive analysis of long non-coding RNA expression in lung adenocarcinoma. *PeerJ* (2019) 7:e8024. doi: 10.7717/peerj.8024

29. Ran R, Jin JW, Zhang WP. MALAT-1 expression correlates with prognosis in non-small-cell lung carcinoma: A systematic review and meta-analysis. *Dis Markers* (2021) 2021:5424623. doi: 10.1155/2021/5424623

30. Huang TH, Wu ATH, Cheng TS, Lin KT, Lai CJ, Hsieh HW, et al. In silico identification of thiostrepton as an inhibitor of cancer stem cell growth and an enhancer for chemotherapy in non-small-cell lung cancer. *J Cell Mol Med* (2019) 23 (12):8184–95. doi: 10.1111/jcmm.14689

31. Herreros-Pomares A, de-Maya-Girones JD, Calabuig-Fariñas S, Lucas R, Martínez A, Pardo-Sánchez JM, et al. Lung tumorspheres reveal cancer stem cell-like properties and a score with prognostic impact in resected non-small-cell lung cancer. *Cell Death Dis* (2019) 10(9):660. doi: 10.1038/s41419-019-1898-1

32. Malta TM, Sokolov A, Gentles AJ, Burzykowski T, Poisson L, Weinstein JN, et al. Machine learning identifies stemness features associated with oncogenic dedifferentiation. *Cell* (2018) 173(2):338–354.e315. doi: 10.1016/j.cell.2018.03.034

33. Tahmasebi S, Amiri M, Sonenberg N. Translational control in stem cells. *Front Genet* (2018) 9:709. doi: 10.3389/fgene.2018.00709

34. Shibue T, Weinberg RA. EMT, CSCs, and drug resistance: the mechanistic link and clinical implications. *Nat Rev Clin Oncol* (2017) 14(10):611–29. doi: 10.1038/nrclinonc.2017.44

35. Fukumura D, Kloepper J, Amoozgar Z, Duda DG, Jain RK. Enhancing cancer immunotherapy using antiangiogenics: opportunities and challenges. *Nat Rev Clin Oncol* (2018) 15(5):325–40. doi: 10.1038/nrclinonc.2018.29

36. Simurda T, Brunclikova M, Asselta R, Caccia S, Zolkova J, Kolkova Z, et al. Genetic variants in the FGB and FGG genes mapping in the beta and gamma nodules of the fibrinogen molecule in congenital quantitative fibrinogen disorders associated with a thrombotic phenotype. *Int J Mol Sci* (2020) 21(13):4616. doi: 10.3390/ijms21134616

37. Yokoyama K, Zhang XP, Medved L, Takada Y. Specific binding of integrin alpha v beta 3 to the fibrinogen gamma and alpha E chain C-terminal domains. *Biochemistry* (1999) 38(18):5872–7. doi: 10.1021/bi9827619

38. Yokoyama K, Erickson HP, Ikeda Y, Takada Y. Identification of amino acid sequences in fibrinogen gamma -chain and tenascin C C-terminal domains critical for binding to integrin alpha vbeta 3. *J Biol Chem* (2000) 275(22):16891–8. doi: 10.1074/jbc.M000610200

39. Akakura N, Hoogland C, Takada YK, Saegusa J, Ye X, Liu FT, et al. The COOH-terminal globular domain of fibrinogen gamma chain suppresses angiogenesis and tumor growth. *Cancer Res* (2006) 66(19):9691–7. doi: 10.1158/0008-5472.CAN-06-1686

40. Duan S, Gong B, Wang P, Huang H, Luo L, Liu F. Novel prognostic biomarkers of gastric cancer based on gene expression microarray: COL12A1, GSTA3, FGA and FGG. *Mol Med Rep* (2018) 18(4):3727–36. doi: 10.3892/mmr.2018.9368

41. Wang M, Zhang G, Zhang Y, Cui X, Wang S, Gao S, et al. Fibrinogen alpha chain knockout promotes tumor growth and metastasis through integrin-AKT signaling pathway in lung cancer. *Mol Cancer Res MCR* (2020) 18(7):943–54. doi: 10.1158/1541-7786.MCR-19-1033

42. Peng HH, Wang JN, Xiao LF, Yan M, Chen SP, Wang L, et al. Elevated serum FGG levels prognosticate and promote the disease progression in prostate cancer. *Front Genet* (2021) 12:651647. doi: 10.3389/fgene.2021.651647

43. Lyman GH, Khorana AA. Cancer, clots and consensus: new understanding of an old problem. *J Clin Oncol Off J Am Soc Clin Oncol* (2009) 27(29):4821–6. doi: 10.1200/JCO.2009.22.3032

44. Niu JY, Tian T, Zhu HY, Liang JH, Wu W, Cao L, et al. Hyperfibrinogenemia is a poor prognostic factor in diffuse large B cell lymphoma. *Ann Hematol* (2018) 97 (10):1841–9. doi: 10.1007/s00277-018-3382-x

45. Huang W, Wang S, Zhang H, Zhang B, Wang C. Prognostic significance of combined fibrinogen concentration and neutrophil-to-lymphocyte ratio in patients with resectable non-small cell lung cancer. *Cancer Biol Med* (2018) 15(1):88–96. doi: 10.20892/j.issn.2095-3941.2017.0124

46. Shiose S, Hata Y, Noda Y, Sassa Y, Takeda A, Yoshikawa H, et al. Fibrinogen stimulates *in vitro* angiogenesis by choroidal endothelial cells via autocrine VEGF. *Graefe's Arch Clin Exp Ophthalmol = Albrecht von Graefes Archiv fur klinische und experimentelle Ophthalmologie* (2004) 242(9):777–83. doi: 10.1007/s00417-004-0910-2

47. Adams GN, Rosenfeldt L, Frederick M, Miller W, Waltz D, Kombrinck K, et al. Colon cancer growth and dissemination relies upon thrombin, stromal PAR-1, and fibrinogen. *Cancer Res* (2015) 75(19):4235–43. doi: 10.1158/0008-5472.CAN-15-0964

48. Nagata K, Arai S, Taira C, Sugano M, Honda T, Okumura N. A novel frameshift mutation in the fibrinogen γC terminal region, FGG c.1169_1170 del AT, leading to

hypofibrinogenemia. *Thromb Res* (2017) 159:82–5. doi: 10.1016/j.thromres.2017.10.002

49. Chen JY, Chen WN, Liu LL, Lin WS, Jiao BY, Wu YL, et al. Hepatitis B spliced protein (HBSP) generated by a spliced hepatitis B virus RNA participates in abnormality of fibrin formation and functions by binding to fibrinogen γ chain. *J Med Virol* (2010) 82(12):2019–26. doi: 10.1002/jmv.21918

50. Gao HJ, Chen YJ, Zuo D, Xiao MM, Li Y, Guo H, et al. Quantitative proteomic analysis for high-throughput screening of differential glycoproteins in hepatocellular carcinoma serum. *Cancer Biol Med* (2015) 12(3):246–54. doi: 10.7497/j.issn.2095-3941.2015.0010.

51. Davalieva K, Kiprijanovska S, Maleva Kostovska I, Stavridis S, Stankov O, Komina S, et al. Comparative proteomics analysis of urine reveals down-regulation of acute phase response signaling and LXR/RXR activation pathways in prostate cancer. *Proteomes* (2017) 6(1):1. doi: 10.3390/proteomes6010001

52. Bloomston M, Zhou JX, Rosemurgy AS, Frankel W, Muro-Cacho CA, Yeatman TJ. Fibrinogen gamma overexpression in pancreatic cancer identified by large-scale proteomic analysis of serum samples. *Cancer Res* (2006) 66(5):2592–9. doi: 10.1158/0008-5472.CAN-05-3659

53. Zhang W, Gao Z, Zeng G, Xie H, Liu J, Liu N, et al. Clinical significance of urinary plasminogen and fibrinogen gamma chain as novel potential diagnostic markers for non-small-cell lung cancer. *Clinica chimica acta; Int J Clin Chem* (2020) 502:55–65. doi: 10.1016/j.cca.2019.11.022

frontiers | Frontiers in Immunology

TYPE Systematic Review
PUBLISHED 03 October 2023
DOI 10.3389/fimmu.2023.1270981

OPEN ACCESS

EDITED BY
Takaji Matsutani,
Repertoire Genesis, Inc., Japan

REVIEWED BY
Pengpeng Zhang,
Nanjing Medical University, China
Remya Raja,
Mayo Clinic Arizona, United States

*CORRESPONDENCE
Eva Andreuzzi
eva.andreuzzi@burlo.trieste.it

†These authors have contributed equally to this work and share first authorship

‡These authors share last authorship

RECEIVED 01 August 2023
ACCEPTED 18 September 2023
PUBLISHED 03 October 2023

CITATION
Fejza A, Carobolante G, Poletto E, Camicia L, Schinello G, Di Siena E, Ricci G, Mongiat M and Andreuzzi E (2023) The entanglement of extracellular matrix molecules and immune checkpoint inhibitors in cancer: a systematic review of the literature.
Front. Immunol. 14:1270981.
doi: 10.3389/fimmu.2023.1270981

The entanglement of extracellular matrix molecules and immune checkpoint inhibitors in cancer: a systematic review of the literature

Albina Fejza[1†], Greta Carobolante[2†], Evelina Poletto[2], Lucrezia Camicia[2], Giorgia Schinello[2], Emanuele Di Siena[2], Giuseppe Ricci[3,4], Maurizio Mongiat[2‡] and Eva Andreuzzi[3*‡]

[1]Department of Biochemistry, Faculty of Medical Sciences, UBT-Higher Education Institute, Prishtina, Kosovo, [2]Department of Research and Diagnosis, Division of Molecular Oncology, Centro di Riferimento Oncologico di Aviano (CRO) IRCCS, Aviano, Italy, [3]Obstetrics and Gynecology, Institute for Maternal and Child Health, IRCCS Burlo Garofolo, Trieste, Italy, [4]Department of Medicine, Surgery and Health Sciences, University of Trieste, Trieste, Italy

Introduction: Immune-checkpoint inhibitors (ICIs) have emerged as a core pillar of cancer therapy as single agents or in combination regimens both in adults and children. Unfortunately, ICIs provide a long-lasting therapeutic effect in only one third of the patients. Thus, the search for predictive biomarkers of responsiveness to ICIs remains an urgent clinical need. The efficacy of ICIs treatments is strongly affected not only by the specific characteristics of cancer cells and the levels of immune checkpoint ligands, but also by other components of the tumor microenvironment, among which the extracellular matrix (ECM) is emerging as key player. With the aim to comprehensively describe the relation between ECM and ICIs' efficacy in cancer patients, the present review systematically evaluated the current literature regarding ECM remodeling in association with immunotherapeutic approaches.

Methods: This review followed the Preferred Reporting Items for Systematic Reviews and Meta-analyses (PRISMA) guidelines and was registered at the International Prospective Register of Systematic Reviews (PROSPERO, CRD42022351180). PubMed, Web of Science, and Scopus databases were comprehensively searched from inception to January 2023. Titles, abstracts and full text screening was performed to exclude non eligible articles. The risk of bias was assessed using the QUADAS-2 tool.

Results: After employing relevant MeSH and key terms, we identified a total of 5070 studies. Among them, 2540 duplicates, 1521 reviews or commentaries were found and excluded. Following title and abstract screening, the full text was analyzed, and 47 studies meeting the eligibility criteria were retained. The studies included in this systematic review comprehensively recapitulate the latest observations associating changes of the ECM composition following remodeling with the traits of the tumor immune cell infiltration. The present study provides for the first time a broad view of the tight association between

ECM molecules and ICIs efficacy in different tumor types, highlighting the importance of ECM-derived proteolytic products as promising liquid biopsy-based biomarkers to predict the efficacy of ICIs.

Conclusion: ECM remodeling has an important impact on the immune traits of different tumor types. Increasing evidence pinpoint at ECM-derived molecules as putative biomarkers to identify the patients that would most likely benefit from ICIs treatments.

Systematic review registration: https://www.crd.york.ac.uk/prospero/display_record.php?ID=CRD42022351180, identifier CRD42022351180.

KEYWORDS

extracellular matrix, cancer, immune checkpoint inhibitors, pediatric cancer, gynecological cancer, gastrointestinal cancer, melanoma, breast cancer

1 Introduction

The development of immunotherapy represents a revolution in the treatment of cancer and the use of immune checkpoint inhibitors (ICIs) exerts a prominent anti-tumor activity in a broad range of tumor types. Nearly half of all patients with metastatic cancer are eligible to receive ICIs, with an increasing use of these agents seen in several (neo)adjuvant and maintenance settings (1–3). ICIs are often used in combination regimens, including those involving other classes of ICI, chemotherapy, anti-angiogenic and/or targeted therapies (4). Nonetheless, despite a portion of patients display remarkable and long-lasting disease regression in response to ICIs, two thirds of the patients do not benefit from these therapies (5). This is partially due to the occurrence of primary or acquired resistance, but also to the toxicity deriving from ICs blockade, that can be severe and even life-threatening. For these reasons, it is crucial to identify the patients that could benefit of ICIs and the search for predictive biomarkers of responsiveness to ICIs remains an active area of research and an urgent clinical need.

Immune checkpoint (IC) pathways are physiologic mechanisms aimed at attenuating T cell responses to prevent autoimmunity and maintain immune homeostasis. Tumors can viciously take advantage of the immune-inhibitory pathways to limit the extent of T cell activation and maintain immune tolerance. Indeed, ICs and their ligands are frequently upregulated in the tumor microenvironment (TME) of various cancer types, thus hindering the anti-tumor immune responses (1). Hence, with the aim to revitalize the anti-tumor immune response, ICIs have been developed as promising therapeutic agents. Most of the ICIs target the cytotoxic-T-lymphocyte-associated protein 4 (CTLA-4 or CD152), the programmed cell death 1 (PD-1 or CD279) or its ligand programmed cell death ligand 1 (PD-L1 or CD274 or B7 homolog 1) (1). Many drugs inhibiting these two checkpoint axes, i.e. ipilimumab for CTLA4, nivolumab and pembrolizumab for PD-1 and atezolizumab, avelumab, and durvalumab for PD-L1, have shown clinical activity and are currently used in the clinical practice (4). In the last few years, other checkpoint molecules have been identified and an increasing number of immunotherapies is under clinical development (e.g., blockade of LAG3, CD276, TIGIT and TIM3) (4, 6).

It is now well established that the efficacy of ICIs in cancer treatment is strongly affected not only by the specific characteristics of cancer cells and the expression levels of the immune checkpoint ligands, but also by other components of the TME. Indeed, the response to ICIs highly relies on the innate immune TME constituents, e.g. macrophages and natural killer cells (NK), on the tumor hypoxic levels, as well as on the efficiency of tumor-associated vasculature (7). A key cell type that strongly shapes the TME are cancer associate fibroblasts (CAFs), that represent the most abundant stromal cells within the tumor. CAFs exert multiple functions as modulating tumor angiogenesis and metabolism, secreting growth factors and immunomodulatory cytokines and driving the remodeling of the extracellular matrix (ECM). The tumor-associated ECM displays peculiar features, such as an altered composition and stiffness, and it has been shown to educate all the cells of the TME leading to the establishment of a pro-tumoral environment. Importantly, as detailed in the present systematic review, emerging evidence are pointing at the ECM as key constituent of the TME actively modulating the efficacy of ICIs.

The ECM is a complex network of molecules which, thanks to its mechanical as well as biochemical properties, strongly impacts on all the cellular TME components, thus affecting tissue homeostasis (8, 9). The ECM is composed of fibrillar proteins (such as collagens, laminins, fibronectin, elastin), proteoglycans and several glycoproteins. For their structural features, the ECM components can interact with a variety of proteins, receptors and soluble factors, influencing the behavior of tumor cells, as well as other tumor-associated cell types such as infiltrating immune cells, stromal cells, blood vascular and lymphatic endothelial cells and pericytes (10–15). As a consequence, the ECM profoundly influences important processes driving tumor growth and progression, such as epithelial-mesenchymal transition (EMT), immune response, angiogenesis and lymphangiogenesis (16–19).

Contrary to what previously thought, the ECM is not a mere static TME component, rather it undergoes continuous dynamic remodeling as well (20, 21). ECM remodeling is mainly due to three mechanisms: 1) altered expression of the components, as reported for collagens and Tenascin-C (22); 2) increased activity of lysis oxidase (LOX) enzymes, which leads to the formation of intermolecular cross-links between collagen I fibers themselves as well as with other molecules such as collagen III and IV and fibronectin (FN), thus resulting in increased tissue stiffness; 3) high protein degradation due to the activation of proteases, among which metalloproteases (MMPs) and ADAMs are the major players (23). These processes are exacerbated in the TME, leading to the formation of an abnormal ECM which utterly differs for composition and rigidity from the healthy tissues (8). Interestingly, a mounting amount of evidence indicate that the extent of ECM remodeling and its mechanical features strongly impact on the tumor immune response (24–26).

In the light of these findings, some ECM molecules, as well as fragments deriving from their proteolytic remodeling, are emerging as putative biomarkers to delineate the immune traits of the tumors, as well as the efficacy of immunotherapies. The aim of this systematic review is to identify and summarize all the published human research studies in this context. In particular, we aim to address the following questions: Can ECM remodeling regulate the tumor immune response? Is the ECM composition impacting on the efficacy of immune checkpoint inhibitors? Can ECM molecules/fragments represent a valuable biomarker to predict the outcome of cancer patients treated with immune checkpoint inhibitors?

2 Methods

2.1 Protocol and registration

The systematic review was designed based on the Preferred Reporting Ideas for Systematic Review and Meta-analyses [PRISMA (27)] systematic review checklist and was registered on PROSPERO, (ID: CRD42022351180, review protocol link: https://www.crd.york.ac.uk/PROSPERO/display_record.php?RecordID=351180).

2.2 Search strategy—eligibility criteria, information sources and search terms

Original research articles written in English and published before 20 January 2023 were eligible for inclusion. We included studies reporting any relation between ECM molecules and the immune traits of the tumors, as well as the response to immune checkpoint inhibition. We included studies regarding patients diagnosed with cancer, regardless of the cancer type, disease staging and PD-L1 expression status. Our inclusion criteria did not involve any age restrictions, since we wished to comprise both young and older patients. Articles not published in English, whose full text was not available, letters to the editor, case reports, and poster presentations were excluded.

To ensure a comprehensive retrieval of all the studies relative to ECM and ICIs efficacy, we chose to exploit three relevant and reliable databases: PubMed (MEDLINE), Scopus and Web of Science. The combination of mesh terms searched in the databases were "extracellular matrix molecules" or "extracellular matrix remodeling" and "immune checkpoint inhibitors" or "immunotherapy". Searches have also been performed using the names of the specific immune checkpoint inhibitors (Nivolumab, Pembrolizumab, Atezolizumab, Avelamab, Durvalumab, Ipilimumab, and Tremelimumab) and some specific ECM molecules (i.e. fibronectin, collagen, Emilin, tenascin-C, proteoglycans).

2.3 Study selection and data extraction

Duplicate articles were removed from the results of the literature search. Two independent authors screened the titles and abstracts of the remaining articles to ensure that the eligibility criteria were met. Any discrepancies between the authors were identified and discussed (with inputs from a third author if required). The remaining included articles assessed by full-text screening by two independent authors, using the same eligibility criteria.

2.4 Critical appraisal

Study quality and risk of bias were assessed by using the QUADAS-2 tool. The risk of bias in the studies was categorized based on the "yes" scores in the QUADAS-2 checklist. In particular, papers with all "yes" or maximum one "unclear or no" responses were classified as low risk. Instead, if two or more responses on the checklist were "unclear" or "no", papers were attributed as unclear or high risk, respectively. If two or more responses were "unclear" and at least one response as "no" the paper was attributed as high risk. Finally, we considered the last question of the QUADAS-2 checklist ("Were all patients included in the analysis?") as an important key factor for the evaluation of the study quality, therefore papers in which the response was "no" were classified as high risk papers.

3 Results

3.1 Literature selection

The systematic search identified a total of 5,070 articles: 1,501 articles were available in PubMed, 2,491 studies in Scopus, and 1,078 in Web of Science. Among those, 2540 were duplicates and 1521 articles were excluded since the publication type did not meet the eligibility criteria (reviews, non-English articles, editorials/commentaries, book chapters, conference abstracts). Two independent authors screened a total of 1,009 articles for their relevance in the topic by assessing the title, abstract or full-text. Among the 1,009 articles, 971 studies were excluded since unrelated to ECMs, relative to immunotherapy employed to treat other

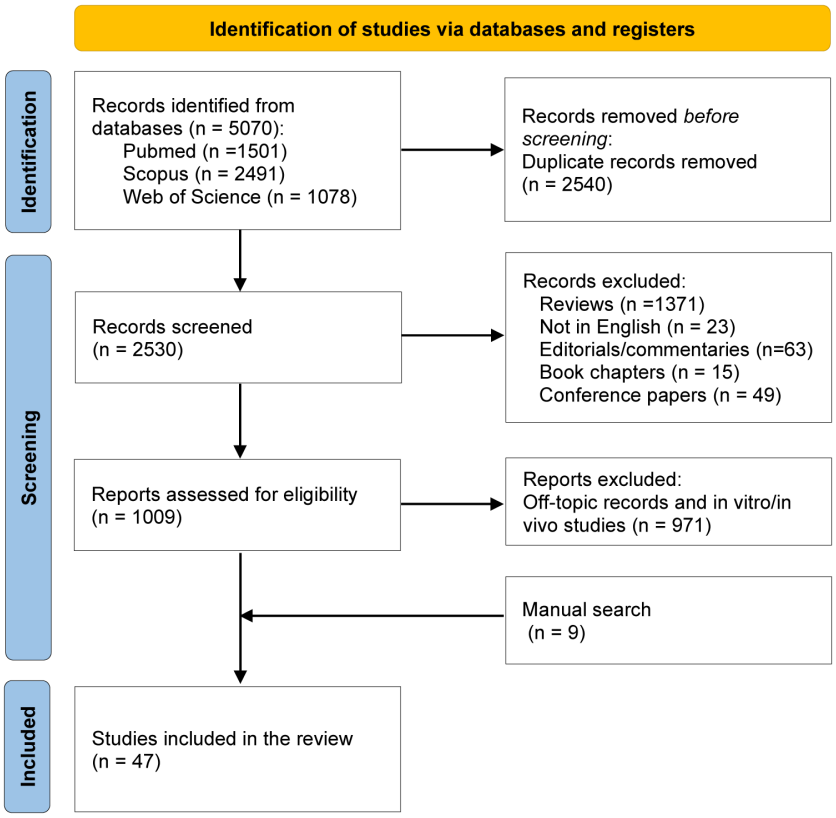

FIGURE 1
PRISMA flow diagram of the studies' screening and selection.

diseases, and *in vitro*/*in vivo* only studies. During the screening process, nine articles not identified by the database searches but relevant for the present review were added manually to the list. As a result, 47 articles were included and analyzed in this systematic review (Figure 1). These studies provide a clear overview of the importance of the tumor associated ECM in determining an immunosuppressive environment within the lesions. Moreover, they highlight the association between increased ECM stiffness and remodeling processes with the response to ICIs in different tumor types, further strengthening the value of ECM-derived molecules as predictive biomarkers. A summary of the main findings of each of the 47 retained studies is provided in the following sections and in Tables 1, 2.

The qualitative analysis of the selected papers indicated that three points were mainly exposed to considerable bias: the design of case-control studies, the definition of a threshold and the inclusion of all the patients in the analysis. Anyway, the overall risk of bias of the included studies assessed by QUADAS-2 was low for 62% of the papers, unclear for 23% and high for 17% (Figure 2).

The literature search spanned from inception to 2023, however most of the papers included in the present systematic review dated from the last five years. All tumor types in adult as well as in pediatric patients were included in the search, however none of these papers dealt with pediatric cancer. Among the tumor types, the majority of the papers were related to melanoma (7/47, 14.9%), breast cancer (BC) (6/47, 12.8%), colorectal cancer (CRC) (5/47, 10.6%) and hepatocellular carcinoma (HCC) (4/47, 8.5%). Half of the identified studies were carried out exploiting the patients' cohorts available to the research teams, whereas the other half was exclusively based on bioinformatic analyses.

3.2 ECM remodeling as a driver of the tumor immune environment

The ECM undergoes radical remodeling during tumor growth and progression, thereby replacing normal ECM with tumor-associated ECM (9, 75, 76). Several studies report a significant association between the altered ECM composition and the patient outcome in various cancer types, however the mechanisms underlying these changes remain elusive (10, 14, 23, 77–82). Most of these studies are focused on the effect of ECM alterations in modulating cancer cell behavior, whereas less attention has been given to their possible immunomodulatory roles. However, as described in the following paragraphs, the prominent role of some ECM components in affecting the immune cell infiltration and activity has been recently well documented.

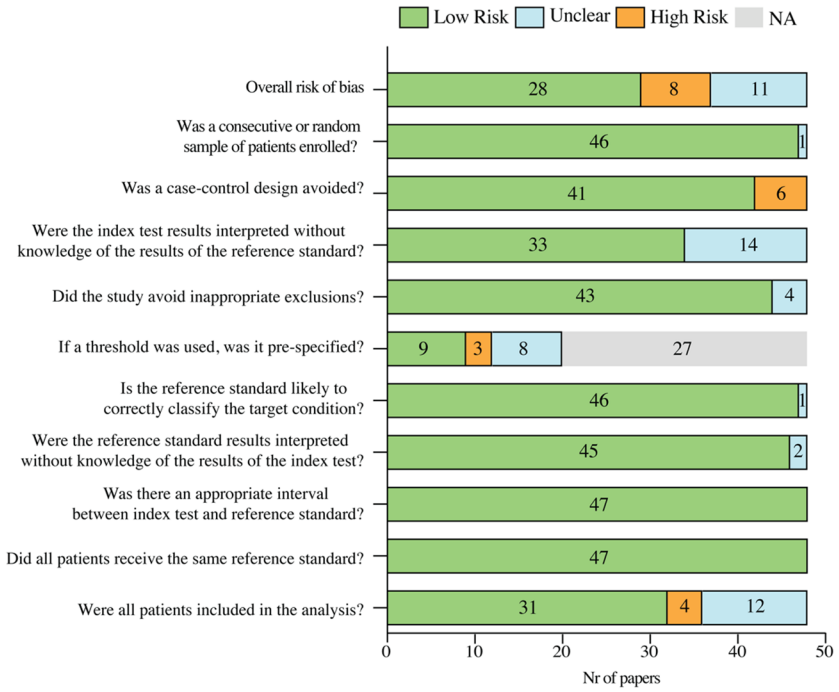

FIGURE 2
Risk of bias summary of the included papers, based on QUADAS-2 tool. NA, not applicable.

3.2.1 Altered expression of ECM components associating with the immune cell infiltration and IC expression

3.2.1.1 Collagens

Among the ECM components that have been associated with the traits of the tumor immune microenvironment, collagens are the most represented (Tables 1, 2).

The association between collagen deposition and the infiltration of immune cells has been well described in different cancer types. In triple negative breast cancer, high Th1 infiltration has been related to low collagen I content, whereas high Th2 and regulatory T cells (Treg) infiltration has been observed in collagen-rich lesions (38). Similar results were obtained by Yaegashi et al. in non-small cell lung carcinoma (NSCLC) (39). Yaegashi and colleagues identified three types of ECM barriers in NSCLC: the first represented by a low deposition of collagen V, the second showing an increase of collagen III and collagen I, and the third characterized by a high amount of collagen I fibers perpendicularly aligned to the tumor border. The diverse barriers were shown to be differentially permissive to immune cell infiltrates, with high density collagen V negatively correlating with NK infiltration and collagen I and III associating with decreased Treg infiltration (Yaegashi et al., 2021). A broad bioinformatic analysis showed that the collagen V gene (COL5A1) was overexpressed in a variety of tumor types including lung, breast, colorectal and gastric cancers, melanoma, liver hepatocellular carcinoma and prostate adenocarcinoma (34). The authors evidenced that COL5A1 expression increases during tumor progression, and it correlates with poor patient's outcome in some types of cancer. Importantly, COL5A1 levels significantly correlated with the presence of a plethora of different B and T cell subpopulations. Interestingly, heterogeneity was observed among the different cancer types, allowing to conclude that the effect of COL5A1 expression is strongly dependent on the specific TME.

In other studies, some interesting associations between ECM molecules and immune checkpoints molecules have been highlighted. This is the case for renal cell carcinoma, in which the presence of COL6A1 perfectly correlates with PD-1 staining (35). Comparable results have been obtained in PDAC, in which COL6A3, SPARC and fibrillin1 (FBN1) have been correlated not only with the presence of six different immune cell types ($CD4^+$ T cells, $CD8^+$ T cells, B cells, neutrophils, macrophages, and dendritic cells), but also with the expression level of the checkpoint molecules CTL4, PD-1, PD-L1 and PD-L2 (36). Similarly, in pancreatic adenocarcinoma (PAAD) the presence of $CD8^+$ T cells, M1 and M2 macrophages, Tregs and dendritic cells has been associated with COL10A1 expression, which seems to exert an immunosuppressive function within the TME (33). Indeed, COL10A1 also positively correlated with PD-L1 and CTLA-4, as well as with the newly identified immune checkpoints CD73 (83) and the human leukocyte antigen (HLA)-E (84). Possibly due to its involvement in the immune escape, COL10A1 associates with a poor PAAD patient prognosis (33).

Overall, this evidence has the potential to open the road towards the development of new predictive markers and novel strategies for targeted immunotherapy. In line with this hypothesis, the increased expression of COL1A2, together with other ECM-related molecules such as metalloprotease-2 (MMP2) and procollagen C-endopeptidase enhancer (PCOLCE), were shown to correlate with the survival of patients with advanced melanoma treated with neoadjuvant immunotherapy combining high-dose interferon α-

10.3389/fimmu.2023.1270981

TABLE 1 Characteristic and main findings of the included papers that show an association between ECM remodeling and tumor immune traits.

Ref	Molecule	Tumor type	Year	Enrolled Patient	Queried Databases	Association with immune traits
(28)	ABI3BP	LUAD	2023	/	TIMER, GEPIA, TCGA, HPA (n=504)	correlation with B and $CD4^+$ T memory cells, Tregs, B cells, T cells, $CD4^+$ T, DC activation, and Ecs
(29)	ADAM12	CRC	2021	/	Oncomine, UALCAN, TCGA, GEPIA, TIMER, TISIDB (n=86733)	correlation with $CD4^+$ T, B, $CD8^+$ T cells, neutrophils, macrophages, DC
(30)	ADAMs	PAAD	2020	/	TCGA (n=18313)	positive correlation with DC, B cells, neutrophils, $CD8^+$ T cells, macrophages
(31)	BGN	TNBC	2022	/	TCGA, GEO (n=116)	negative correlation with $CD8^+$ T cells
(32)		GC	2022	/	TCGA, GTEx (n=407)	positive correlation with NK cells and macrophages; negative correlation with Th17 cells
(33)	COL10A1	PAAD	2022	/	TCGA, GEO, GEPIA (n=182)	positive association with $CD8^+$ T cells, M1 and M2 Mac; positive correlation with PD-L1, CTLA-4, CD73, HLA-E
(34)	COL5A1	pan-cancer	2022	/	Oncomine, TCGA, CCLE, HPA, DNMIVD,cBioPortal	association with naive B cells, memory B cells, monocytes, macrophages, $CD8^+$ and $CD4^+$ T cells
(35)	COL6A1	RCC	2020	161	/	association with PD-L1 expression
(36)	COL6A3	PDAC	2020	/	TCGA, GEO (n=30)	association with $CD4^+$ and $CD8^+$ T, B cells, neutrophils, Mac and CD; association with CTLA-4, PD-1, PD-L1, PD-L2
(37)	Collagen alignment	BC	2021	/	TCGA, GEO	negative correlation with anti-tumor T cells
(38)	Collagen I	BC	2022	30	TCGA, GEO (n=1161)	positive association with Th1 and Tregs, negative association with Th1
(39)	Collagen I, III, V	NSCLC	2021	120	/	negative association of Coll I and III with Tregs and of Coll V with NK
(40)	Collagen, Elastin	BCC	2022	22	/	association with TILs counts
(41)	CTHRC1	CRC	2022	/	TCGA, GEO (n=242)	correlation with TAMs, M2 macrophages, Tregs, T cell exhaustion, and MDSCs
(42)		GC	2022	/	TCGA, GEO, GSA (n=375)	correlation with M2 Mac, NK cells, Th1 cells and DC
(43)	EMILIN2	CRC	2022	23	TCGA (n=844)	negative association with M2 Mac; positive association with M1 Mac
(44)		LLG	2021	97	CGGA, TCGA (n=1018)	positive correlation with B cells, $CD8^+$ T and $CD4^+$ T cells, DC, Mac and neutrophils
(45)		CCC	2022	/	TCGA, UCSC Xena (n=531)	positive correlation with CTLA-2, PD-1, LAG3, and TIGIT
(46)	LOXL3	HCC	2021	/	TCGA, TIMER, GTEx (n=52)	positive correlation with $CD4^+$ T and $CD8^+$ T cells, B cells, DC, neutrophils, Mac, B cells
(47)	LOXL4	HCC	2021	90	/	association with PD-L1 expression
(48)	MMP1	HCC	2022	/	TCGA, TIMER, GEO (n=11104)	association with activated DC, Mac, $CD4^+$ T cells and MDSC
(49)	MMP9	pan-cancer	2022	/	TCGA, GTEx (n=33)	positively correlates with T cells, macrophages, Th1 cells, and T cell exhaustion
(50)	PCOLCE	BC	2021	/	METABRIC (n=273)	association with PD-1/PD-L1 expression level
(51)		pan-cancer	2022	/	TCGA, CPTAC, GEO (n=33)	positive correlation with $CD4^+$ and $CD8^+$ memory cells, $CD4^+$ T, $CD8^+$ T, NK cells
(52)	PLOD2	pan-cancer	2022	/	GTEx, CCLE (n=21)	negative correlation with memory B cells, activated NK cells, $CD8^+$ T cells,Treg; positive correlation with Mac
(53)	SPP1	LUAD	2021	/	TCGA, CPTAC (n=551)	correlation with low $CD8^+$ Tcell infiltration and high M2-type macrophages
(54)	TNC	BC	2020	160	/	negative correlation with LC3B and $CD8^+$ T cells

(Continued)

TABLE 1 Continued

Ref	Molecule	Tumor type	Year	Enrolled Patient	Queried Databases	Association with immune traits
(55)		BC	2021	219	GEO	negative association with macrophages and $CD8^+$ T cells
(56)		OSCC	2020	68	GEO	positive correlation with $CD11^+$ cells and Tregs
(57)		LGG	2022	62	/	positive association with MDSC; negative association with effector T cells
(58)	Versican	NSCLC	2022	/	GEO	positive association with DC, negative correlation with $CD8^+$ T cells
(59)		MPM	2022	/	TGCA (n=12)	association with PD-1 overexpression and downregulation of CD127
(60)		CCa	2010	149	/	negative association with $CD8^+$ T cells
(61)		MM	2016	19	/	negative association with $CD8^+$ T cells
(62)		CRC	2017	122	/	negative association with $CD8^+$ T cells

BC, breast cancer; MM, myeloma; CCa, cervical cancer; MPM, pleural mesothelioma; CCC, clear cell carcinoma; CRC, colorectal cancer; NSCLC, non-small cell lung cancer; LGG, low grade glioma; OSCC, oral squamous cell carcinoma; LUAD, lung adenocarcinoma; HCC, hepatocellular carcinoma; PDAC, pancreatic ductal adenocarcinoma; PAAD, pancreatic adenocarcinoma.

TABLE 2 Characteristic and main findings of the included papers that show an association between ECM remodeling and ICIs efficacy.

Ref	Molecule	Tumor type	Year	Enrolled patients	Queried Databases	IC target	Sample type	Method	Main findings
(63)	BGN	CRC	2022	144	GEO, TCGA (N=435)	/	biopsy	RNA seq, IHC	positive association with M2 macrophages and Tregs; association with the prediction of the response to ICIs
(64)	COL6A1	BLCa	2023	58	TCGA (n=414)	PD-1	biopsy	RNA seq, IHC	predictive of poor response to anti-PD-1 treatment
(65)	Collagen fragments (C4G, PRO-C3)	CM	2020	54	/	CTLA-4	serum	ELISA	High C4G combined with low PRO-C3 predict improved OS
(66)	Collagen fragments (PRO-C3, C1M, C3M, C4M, VICM)	CM	2018	67	/	CTLA-4	serum	ELISA	High PRO-C3 and C4M independently predictive of worse OS ad PFS; high C3M/PRO-C3 and VICM independently associate with longer OS
(67)	Collagen fragments (PRO-C3, PC3X, C3M, C4M, VICM)	CM	2020	107	/	PD-1	serum	ELISA	High PRO-C3 and PC3X independently predictive of worse OS ad PFS; high C3M/PRO-C3 and VICM independently associate with improved OS
(68)	Collagen I, III	LUAD, LUSC	2020	451	TCGA (n=1580)	PD-1	biopsy	RNAseq, IHC	negative association with $CD8^+$ T cells; predictive of poor survival and response to anti-PD-1
(69)	CTHRC1	GBM, LGG	2021	/	CGGA, TCGA, GDC (n=1711)	PD-1	biopsy	RNA seq	predictive value for anti-PD-1 therapy efficacy
(70)	EMILIN2	CM	2021	/	TCGA (n=477)	PD-L1	biopsy	RNA seq	negative association with the response to anti PD-L1 therapy
(71)	HAPLN3	CM	2021	/	TCGA, GEO, dbGap (n=727)	CTLA-4	biopsy	RNA seq	part of TIR signature predictive of response to anti-CTLA-4 and patients' survival

(Continued)

TABLE 2 Continued

Ref	Molecule	Tumor type	Year	Enrolled patients	Queried Databases	IC target	Sample type	Method	Main findings
(72)	MMP12	HCC	2021	8	TCGA, GEO (n=467)	/	biopsy	RNA seq, WB, PCR	positive correlation with CTLA-4 and PD-L1; negative association with predicted ICIs efficacy
(73)	MMP2, COL1A2	CM	2021	30	/	CTLA-4	biopsy	transcriptomic Nanostring analysis	positive association with longer OS and RFS for patients treated with anti-CTLA-4
(74)	MMP9, LOX	GBM	2023	27	TCGA, CGGA, GEO (n=1876)	PD-1, PD-L1	biopsy	RNA seq, IHC, qPCR	part of a high risk signature correlated with poor prognosis and higher response to anti-PD1/L1 therapy

BC, breast cancer; CM, cutaneous melanoma; CCa, cervical cancer; BLCa, bladder cancer; GBM, glioblastoma; LGG, low-grade glioma; CRC, colorectal cancer; LUAD, lung adenocarcinoma; LUSC, lung squamous cell carcinoma; HCC, hepatocellular carcinoma; OS, overall survival; PFS, progression-free survival.

2b with the anti-CTLA-4 antibody ipilimumab (73). Similarly, COL6A1 expression has been indicated as a prognostic risk gene in bladder cancer, where high COL6A1 levels being predictive of a poor response to the PD-1 inhibitor tislelizumab (64).

An important association between collagen deposition and the efficacy of ICIs has been highlighted also in lung cancer. Taking advantage of a preclinical mouse model, Peng and colleagues (68) demonstrated that collagen induces $CD8^+$ T cell exhaustion through the binding with the leukocyte-associated immunoglobulin-like receptor 1 (LAIR1) acting as an immune checkpoint molecule (85). Notably, the inhibition of LOXL2 activity, which leads to the blockage of collagen deposition, sensitizes the lung tumors to anti-PD-L1 therapy. Consistently, in lung cancer patients, higher collagen I and III deposition associates with decreased $CD8^+$ T cells as well as increased levels of the exhaustion markers LAIR1 and TIM-3. Of note, collagen expression was shown to predict the response to anti-PD-1 therapy and the overall survival of these patients (68).

3.2.1.2 Versican

The ECM proteoglycan Versican (VCAN) exerts multiple functions by interacting with other ECM components and cell types impacting on tissue development, wound healing and cancer. Increased VCAN expression has been shown in solid tumors including ovarian, pancreatic, breast, lung, esophageal, bladder and colorectal cancer and to associate with patient's prognosis (86, 87). Many *in vitro* and *in vivo* studies have highlighted the role of VCAN in the modulation of inflammation. Moreover, some investigations have recently shown its association with the tumor immune environment in different cancer types (88). In 2022, Yang and colleagues reported that, in pleural mesothelioma, the expression of VCAN, in association with the other ECM molecules collagen I, fibulin and NG2, identifies patients characterized by immunosuppression and resistance to chemotherapy (59). In accordance with these evidences, the presence of VCAN and the rate of its proteolytic cleavage by the specific ADAMTS1 in lung cancer has been shown to play a pivotal role in dendritic cell activation (58). In detail, VCAN is located in the peritumoral stroma of NSCLC, where the VCAN-derived proteolytic fragment versikine induces dendritic cell (DC) accumulation and activation. This, in turn, allows the interaction of DC with transiting effector $CD8^+$ T cells, inducing their activation and infiltration within the tumor nest. Therefore, an active VCAN proteolysis and low total VCAN in the stroma associates with $CD8^+$ T cell infiltration in NSCLC (58), myeloma (MM) (61), CRC (62) and in cervical cancer (CCa) (60). These data suggest that VCAN remodeling may be exploited as a novel immune biomarker as well as a therapeutic target to promote antitumor $CD8^+$ T cell responses.

3.2.1.3 Tenascin-C

The third most represented molecule in the papers analyzed in this review is tenascin-C (TNC), a highly expressed glycoprotein in malignant solid tumors, including breast cancer and oral squamous cell carcinoma (OSCC) (9, 89, 90). The functions of TNC in modulating cancer cell migration, proliferation, invasion and angiogenesis have been extensively described (91–93), however only in recent years TNC has been associated with the immune response. Analyses of TNC deposition in breast cancer, low grade glioma (LGG) and OSCC indicated that a TNC-rich stroma associates with leukocyte infiltration in the tumor nest (55–57). Murdamoothoo and colleagues demonstrated that TNC can retain T cells within the stroma by inducing and directly binding CXCL2, an important T cell chemoattractant, thus preventing their infiltration and cytotoxic activity in the tumor nest (55). A similar function was observed in OSCC, in which, through the induction of CCL21, TNC has the capability to promote the retainment of $CD11c^+$ myeloid cells in the stroma leading to a more immune-suppressive environment within the tumor nest (56). In accordance with this evidence, Li and colleagues showed that, in triple-negative breast cancer (TNBC), TNC inversely correlates with $CD8^+$ T-cell tumor infiltration and positively correlates with poor patient prognosis (54). Furthermore, they assessed that the expression of TNC associates with the occurrence of autophagic defects in TNBC cells, defects known to counteract T cell-mediated tumor killing. The authors demonstrated that TNC blockage can sensitize TNBC cells to the cytotoxic effect of T lymphocytes, indicating that TNC may be explored as a new potential target for TNBC treatment (54).

3.2.1.4 Collagen triple helix repeat containing-1

Collagen triple helix repeat containing-1 (CTHRC1) is a secreted ECM protein transiently expressed during the repair process of injured arteries (94) and skin wound healing (95). In several solid tumors, CTHRC1 is upregulated and its expression has been associated with tumorigenesis and metastatic dissemination (96). In breast cancer, non-small cell lung cancer and oral cancer, CTHRC1 exerts a pro-tumorigenic effect by modulating the Wnt/β-catenin pathway (96). The association between CTHRC1 and the tumor immune environment has been described for the first time in a preclinical model of CRC, in which CTHRC1 was shown to promote liver metastasis by shaping the infiltrated macrophages towards a M2 phenotype through the direct interaction with the TGF-β receptors (97). This observation has been confirmed by Zhao et al., who evaluated CTHRC1 expression in gastric cancer (GC) through the integration of different datasets (42). Not only did the authors show that high CTHRC1 expression associates with worse patients' prognosis, but they also found that it correlates with the abundance of subtypes of immune infiltrating cells. In detail, elevated CTHRC1 expression was significantly correlated with the infiltration of M2 macrophages, as well as other innate immune cells, such as NK, Th1 and DC cells. Further analyses allowed to determine that CTHRC1 is highly expressed by cancer-associated fibroblasts (CAFs) and it is present in the vascular tissue surrounding the gastric lesions, where it may favor macrophage infiltration though the interaction with CAFs via the GRN/TNFRSF1A and AnxA1/FPR1 pathways (42). CAFs are likely the major source of CTHRC1 also in CRC, in which CTHRC1 expression is upregulated and it takes part in a gene-based signature with prognostic value (41). Indeed, the upregulation of CTHRC1, together with that of the Placental Derived Growth Factor C (PDGFC), PDZ and LIM Domain 3 (PDLIM3), Neurotrimin (NTM), and Solute Carrier Family 16 Member 3 (SLC16A3) genes, positively correlates with M2 macrophages, regulatory T cells (Tregs), and myeloid-derived suppressor cells (MDSCs) infiltration, as well as T cell exhaustion and associates with poor CRC patient survival (41). Taken together, these two papers confirm the immunosuppressive role of CTHRC1 in gastrointestinal cancers. However, the association between CAF-derived CTHRC1 and the tumor immune microenvironment characteristics do not seem to be tumor type-specific. Indeed, the expression of CTHRC1, together with ATP Binding Cassette Subfamily C Member 3 (ABCC3), macrophage scavenger receptor 1 (MSR1), PDZ and LIM domain protein 1 (PDLIM1), TNF Receptor Superfamily Member 12A (TNFRSF12A), and Chitinase-3-Like Protein 2 (CHI3L2), has been identified as a CAF-related gene signature with prognostic and predictive value for glioma patients treated with anti PD-1 therapy (69).

3.2.1.5 ABI family member 3 bind protein

ABI family member 3 binding protein (ABI3BP) is an ECM protein expressed in multiple organs, including the heart, kidney, lung, pancreas, and placenta, with low or variable expression in the spleen, liver, brain, bone, and skeletal muscle (98). ABI3BP expression has been associated with many physiological and pathological processes (99), and it is well known for its role in multiple cancer types, acting as a tumor suppressor by inhibiting cancer cell proliferation and migration and promoting cellular senescence (100–104). The role of ABI3BP in lung cancer has been investigated only recently and it has been indicated that this molecule is downregulated in the lesions compared to normal lung tissue and it gradually decreases as lung cancer progresses (28). Interestingly, in the same work, it has been demonstrated for the first time the association between ABI3BP expression and immune cell infiltration. Indeed, in lung cancer, ABI3BP expression positively correlates with B memory cells, $CD4^+$ T memory cell rest, Tregs, $CD8^+$ T cells, $CD4^+$ T cells, and CD activation. Even if the molecular mechanisms affecting the immune response are still unknown, these data suggest that increased ABI3BP expression may impact on tumor progression also by modulating the tumor immune microenvironment. In accordance with this hypothesis, the expression of ABI3BP in lung cancer correlates with patient's prognosis, with low expressing patients having a poorer outcome (28).

3.2.1.6 EMILIN-2

Elastin microfibril interfacer 2 (EMILIN-2) belongs to the EDEN protein family (105–107) and is often downregulated in epithelial tumors, in which it exerts a tumor suppressive function through multiple mechanisms (11, 77, 108, 109). EMILIN-2 directly acts on the survival and proliferation of cancer cells and, like other members of the EDEN family, such as Multimerin-2 (12, 13, 110–112), it also influences angiogenesis (109). Increasing evidence pinpoint this molecule as an important immunomodulator in the TME. Recently, EMILIN-2 has been shown to affect macrophage polarization through the engagement of TLR-4 (43). Indeed, in colorectal cancer low EMILIN-2 protein levels were shown to correlate with a low M1/M2 macrophage ratio and, consistently, with poor patient prognosis. A similar observation has been made in melanoma, in which the levels of EMILIN-2 are reduced compared to the healthy tissue, and patients displaying low EMILIN2 expression are characterized by poor overall survival (70). Importantly, in these patients EMILIN-2 has been shown to associate with the efficacy of PD-L1 blockage (70), suggesting that the evaluation of EMILIN2 in the tumor tissue may entail a possible predictive value.

Contrasting results have been found in other tumor types, as in low grade glioma (44) and clear cell renal cell carcinoma (ccRCC) (45), where the upregulation of EMILIN-2 associated with poor prognosis. This evidence was supported by the positive correlation of EMILIN-2 with macrophage subsets, T reg and T cell exhaustion, overall indicating an immunosuppressive effect of EMILIN-2 in these cancer types (44). In line with these findings, in ccRCC EMILIN-2 was shown to positively associate with the levels of several checkpoint molecules including CTLA-2, PD-1, LAG3, and TIGIT (45).

3.2.1.7 Biglycan

Biglycan (BGN) is an ECM proteoglycan with an essential role in mediating morphology, growth, differentiation and migration of epithelial cells and it is a well-known player in tumor development and progression (113–115). Several studies reported an up-regulation of BGN in a variety of solid tumors suggesting its potential diagnostic and prognostic value in ovarian, prostate,

head and neck, gastric and colorectal cancer (116–118). However, the function of BGN in tumor immunity has just recently been assessed. He and colleagues were the first to investigate the association between BGN and immune cell infiltration (63). These authors showed that, in CRC samples, elevated levels of BGN were correlated with immunosuppressive traits and an unfavorable patients' outcome. Indeed, BGN expression within CRC lesions positively corresponds to M2 macrophage and Treg infiltration. A bioinformatic model was applied to the same datasets indicating that CRC patients with high BGN expression levels were characterized by a higher expression of immune checkpoint molecules, as PD-L1, and were predicted to have a better response to ICIs. A similar immunosuppressive function of BGN has been found in GC (32) and in TNBC, in which high BGN levels have been negatively correlated with increased infiltration of $CD8^+$ T cells and associate with poor prognosis (31).

3.2.1.8 Osteopontin

Osteopontin (OPN), encoded by the SPP1 gene, is a non-collagenous bone matrix protein involved in the development of different organs (119). Many studies have assessed its role in the growth and metastatic dissemination of various solid tumors, such as breast and prostate cancer, squamous cell carcinoma, melanoma, osteosarcoma and glioblastoma, where OPN is often upregulated and correlates with a poor prognosis (120). *In vitro* and *in vivo* studies highlighted the role of OPN in determining the immune phenotype of the TME, since SPP1 expression directly correlated with $CD8^+$ T cell activation and M2 macrophage polarization (121–123). However, thus far the putative association of OPN with the immune traits of the TME in human tumors has been investigated only in lung cancer. SPP1 expression was demonstrated to be higher in lung adenocarcinoma (LUAD) compared with normal lung tissue, potentially impacting on the resistance to ICIs (53). The same study indicated that a high SPP1 expression associates with poor patient prognosis and, consistently with the *in vivo* observations, SPP1 expression correlates negatively with $CD8^+$ T cells and positively with M2 macrophage infiltration. Interestingly, the levels of SPP1 expression also positively correlated with the immune checkpoint CD276, particularly in patients displaying EGFR mutations (53).

3.2.1.9 Hyaluronan and proteoglycan link protein 3

Hyaluronan and proteoglycan link protein 3 (HAPLN3) is an ECM linker protein involved in the binding of proteoglycans to hyaluronic acid (124). HAPLN3 is expressed in most of the tissues and it is essential for generating hyaluronic acid-dependent ECM. Some studies have reported that HAPLN3 is overexpressed in breast cancer and in CRC and its high expression is linked to cancer occurrence and metastasis (125, 126). Interestingly, the analysis on circulating tumor DNA indicated that the methylation of HAPLN3 is significantly increased in metastatic prostate cancer and serves as a post-treatment risk predictor (127). Recently, HAPLN3 together with SEL1L Family Member 3 (SEL1L3), Bone Marrow Stromal Cell Antigen 2 (BST2), and Interferon Induced Transmembrane Protein 1 (IFITM1) have been included in a four-gene signature named TIR, which highly associates with the activation of $CD8^+$ T cells and immune cell infiltration in melanoma patients (71). When applied to a cohort of melanoma patients treated with the anti-CTLA-4 antibody ipilimumab, the TIR signature predicted the response to the therapy and the clinical outcome better than other known biomarkers as PD-L1 and IFN-γ, thus suggesting the potential use of the TIR signature as a predictive marker for those patients (71).

3.2.2 Tumor-associated ECM as a physical barrier for immune cell infiltration

The ECM properties, due to post-translational modifications such as the bio-physical structure and the stiffness, not only affects the recruitment/activation of immune, but also per se profoundly shape the tumor immune microenvironment (128). The major ECM components involved in these two properties are collagens. These molecules are synthesized as pro-procollagens and undergo several post-translational modifications that alter their traits (23). Modifications include glycosylation, pro-peptide alignment, disulphide bond formation and hydroxylation. Importantly, lysine hydroxylation of the pro-collagen chains by lysyl hydroxylases (PLODs) allows for spontaneous triple helix formation within the cell and secretion into the extracellular space. Once secreted, the pro-peptides on the C- and N-terminus are cleaved by proteases (such as the procollagen C-endopeptidase enhancer PCOLCE) leading to the formation of collagen fibrils. For further collagen fibers assembly, lysyl oxidases (LOX) catalyses the cross-linking of collagens as well as elastin, thus modulating the ECM stiffness. Finally, collagen fibers interact with integrins and other cell surface receptors (such as RHAMM and DDR1) that apply forces leading to the alignment of the fibers (23).

In cancer, the alteration of this complex and multistep process leads to abnormal mechanical and physical properties of the ECM. The higher stiffness and density of tumor-associated ECM constitute a mechanical barrier which protects the tumor from immune cell infiltration and immune-mediated destruction. Overall the TME is less permissive to leukocyte invasion, favoring the establishment of a more tolerant immune environment and also impairing the efficacy of ICIs (129).

This aspect is well represented in the study from Byers et al, in which the authors measured the stromal fibrillar morphology within the ECM in basal cell carcinomas (BCC) (40). The authors evaluated collagen, elastin, and reticulin and defined the presence of "gaps" between the fibers as lacunarity. A higher lacunarity represents a more permissive environment and directly correlates with the infiltration of tumor-associated T lymphocytes (TIL), as assessed in BCC.

In the same view, Xu et al. showed that PLOD2 (Procollagen-Lysine,2-Oxoglutarate 5-Dioxygenase 2), a member of PLOD family which mediates the formation of stabilized collagen cross-links generating a stiffer ECM, is overexpressed in a variety of tumors including gastric, bladder, lung, breast, and head and neck squamous cell cancer (52). Notably, in GC, PLOD2 expression was negatively correlated with the presence of memory B cells, activated NK cells, plasma cells, $CD8^+$ T cells, follicular helper T cells and Tregs; on the other hand, it was positively correlated with

macrophages, activated mast cells, resting NK cells, CD4 memory activated T cells and CD4 memory resting T cells. Overall, PLOD2 was shown to be significantly associated with the tumor immune infiltration and with a poor patients' outcome.

Another enzyme driving collagen rearrangements and recently associated with immune infiltrating cells is PCOLCE, which localizes in the TME of several cancer types. Bioinformatic analyses highlighted that PCOLCE is a prognostic predictor for PAAD, thymoma and CES (51). Even if the molecular mechanisms behind this observation are still unknown, PCOLCE expression correlates with the extent of $CD4^+$ T, $CD8^+$ T, NK cell infiltration. As well, Lecchi et al. developed a gene expression signature to identify high-grade breast cancer patients with poor prognosis (50). PCOLCE is one of the genes taking part in the $ECM3^+/IFN^-$ signature, together with other ECM genes such as Secreted Protein Acidic And Cysteine Rich (SPARC), Biglycan, EGF Containing Fibulin Extracellular Matrix Protein 2 (EFEMP2) and the basal membrane component Nidogen 2 (NID2). In breast cancer, the $ECM3^+/IFN^-$ signature was associated with low tumor-infiltrating lymphocytes, high levels of $CD33^+$ cells, absence of PD-1 expression or low expression of PD-L1.

As mentioned before, ECM stiffness and structural organization are strongly regulated by the activity of LOX enzyme family, which includes LOX and LOX-like (LOXL) 1-4 (23). Due to their involvement in different processes, as linking bi-directionally the ECM and acting directly on the activation of signaling pathways regulating cancer cell survival, proliferation and differentiation, LOXs have been identified as pivotal factors in the formation and progression of different tumor types as glioma, gastric and endometrial carcinoma (130–133). Among the LOX family of enzymes, LOXL3 has also been shown to play immunomodulatory functions in the TME. A detailed bioinformatic analysis highlighted that LOXL3 is upregulated in HCC compared with normal tissues and correlates with poor prognosis (46). In the same study, for the first time LOXL3 expression has been positively correlated with the infiltration extent of multiple immune cells, among which $CD8^+$ and $CD4^+$ T cells and macrophages, as well as with the expression of immune checkpoint molecules such as PD-L1 and CTLA-4. A functional enrichment analysis demonstrated that this effect was mainly based on ECM organization and regulation of cell–cell adhesion (46). However, in some cases, the immunomodulatory effect of the collagen modifying enzymes is not only related to ECM remodeling but also to different mechanisms that act in a synergic fashion. As an example, the lysyl oxidase 4 (LOXL4), whose upregulation induces higher ECM stiffness, during hepatocarcinogenesis was shown to be overexpressed by macrophages and to induce an autocrine expression of PD-L1, thus contributing to maintain T-cell exhaustion and supporting tumor progression (47). In accordance with this dual role of LOXL4 in HCC, a high expression of LOXL4 by macrophages and a low expression of the $CD8^+$ T cell marker CD8A can cooperatively predict poor survival of cancer patients.

Importantly, not only the density and stiffness of the collagen matrix, but also the fiber alignment represents a barrier for immune cell infiltration. This aspect has been described in breast cancer by Sun et al. Their study reported for the first time the implication of discoidin domain receptor 1 (DDR1), a tyrosine kinase collagen receptor, in shaping the immune infiltrate of breast cancer (37). DDR1 induces immune cell exclusion through its extracellular domain by promoting the alignment of collagen fibers. In agreement with this hypothesis, in TNBC, the expression of DDR1 negatively correlates with the intratumoral abundance of anti-tumor T cells (37).

3.2.3 ECM fragments as a reservoir of novel biomarkers for ICIs efficacy

ECM remodeling occurs on one side through the altered expression of the molecules, on the other side through their degradation mediated by the activation of target-specific proteases such as MMPs, disintegrins and ADAMs (23). Cancer cells and tumor associated cells express higher levels of proteases which contribute to the establishment of a pro-tumorigenic environment by multiple mechanisms (9, 23, 134). The proteolytic degradation of the ECM components allows the replacement of the normal ECM with tumor-derived ECM. This process favors the migration of cancer cells through the interstitial matrix by unlocking migratory tracks. Simultaneously, the enzymatic activity of MMPs and ADAMs induces the release of ECM-bond growth factors and proteolytic fragments, some of which exert a new biological activity respect to the molecule of origin. Some of these fragments are released in the blood stream and may be exploited to develop a liquid biopsy-based biomarkers. The association of proteolytic enzymes and ECM-derived fragments with the immune TME are described in the following paragraphs.

3.2.3.1 Proteolytic enzymes

MMP-9, together with MMP-2, are the most common progression markers correlated to cancer invasion and metastasis and, recently, MMP-9 levels have been associated with the presence of immune cell infiltration, particularly with M1 and M2 macrophages, in 33 tumor types (49). In accordance, Yu and colleagues included MMP-9, together with LOX and TIMP1 in a gene-based signature, which significantly correlates with the response to anti-PD1 and anti-PD-L1 immunotherapy and overall survival of glioma patients (74). Despite contradictory results that needed further analysis, the cancer immunomodulatory function of other MMPs has also been investigated. Such is the case for MMP-1, which is known to have a role in cancer invasion and epithelial-mesenchymal transition in HCC and other tumor types (135). MMP-1 expression has been associated with the presence of anti-tumor immune cells, such as activated DC, macrophages, T helper cells and $CD4^+$ T cells, as well as with the presence of MDSC cells, which, on the contrary, suppress the immune response (48). This suggests that MMP-1 functions and regulations in the TME are extremely complex and involve a number of yet elusive mechanisms. Always in the context of HCC, also MMP12 was found to be significantly increased and to associate with the CTLA-4 expression levels and with a poor ICI efficacy (72).

Like MMPs, ADAMs are often upregulated in tumors and high levels associate with a worse prognosis for the patients (136–141). Only recently, ADAMs have been linked to the immune cell infiltration and immune checkpoint molecule expression. In

detail, in HCC, the expression of nine components of the ADAMs family (ADAM8,9,10,12,19,28,TS2,TS12) was shown to increase along with tumor progression and to correlate with the presence of dendritic cells, B cells, neutrophils, $CD8^+$ T cells, and macrophages (30). Importantly, the same study showed that ADAM12, 19, TS2 and TS12 were positively correlated with the expression of the immune checkpoint molecules PD-1, PD-L1, PD-L2 and CTLA-4. In line with this evidence, in colorectal adenocarcinoma (COAD), one of the CRC subtypes, high ADAM12 expression associated with an altered immune cell infiltration and with a poor patients' outcome (29). In particular, ADAM12 expression positively correlated with the presence of $CD8^+$ T cells, $CD4^+$ T cells, macrophages, neutrophils, and DC; on the contrary, the correlation between ADAM12 expression and presence of B cells was not significant.

3.2.3.2 ECM-derived liquid biopsy biomarkers

The ECM remodeling by post-transcriptional modification enzymes and proteases generates fragments and peptides that can be detected in the peripheral blood and could be used as serological markers directly reflecting the disease and cancer progression (23, 142–144). The possibility to detect these fragments in the circulation represents an advantage compared to the analysis of tumor biopsies, considering the easy access through poorly invasive procedures, thus allowing to monitor the disease progression over time.

During collagen fibrillogenesis, the N-terminal propeptide of immature collagen is cleaved by specific proteases leading to the incorporation of the mature molecule in the ECM. The cleavage of the N-terminal region of pro-collagen III generates a fragment, named PRO-C3, which is released in the blood circulation and reflects the extent of collagen deposition, with high levels indicating an excessive collagen deposition (145). In accordance with this observation, and with the fact that collagen deposition is upregulated in immune-excluded tumors (23, 40, 129), high serum levels of PRO-C3 have been associated with poor outcome in CRC and metastatic breast cancer patients (146, 147). In melanoma, a high PRO-C3 levels correlated with low efficacy of the anti-PD-1 antibodies pembrolizumab or nivolumab (67).

The proteolytic cleavage of collagens produces the fragments C1M (collagen I), C3M (collagen III) and C4M (collagen IV) which were shown to be increased in cancer patients compared to healthy individuals (147, 148), and to associate with a poor response to anti-CTLA-4 blockage in melanoma patients (66). The same trend has been observed for PRO-C3, that together with C4M also correlated with shorter overall survival (66). In retrospective analyses, Jensen and colleagues calculated the C3M/PRO-C3 ratio as a parameter to evaluate the balance between collagen degradation and deposition, finding that a high C3M/PRO-C3 ratio was predictive of a better response to ipilimumab (66). The same observation has been observed in a prospective cohort of melanoma patients subjected to anti-PD-1 treatment, further strengthening the notion that a higher collagen degradation versus deposition favors a better outcome and response to ICIs (67).

The degradation of collagen IV by granzyme B generates a fragment distinct from C4M named C4G (149). In metastatic melanoma patients, high C4G levels at baseline corresponded to a good clinical response to anti-CTLA-4 therapy, in terms of both objective response rate and overall survival (65). Interestingly, and in line with the studies from Jensen (66) and Hurkmans (67), patients characterized by a combination of high C4G (indicating basal membrane degradation) and low PRO-C3 (suggestive of low collagen deposition) were characterized by a better chance to respond to ipilimumab compared to the patients displaying only high C4G levels (65).

Circulating fragments are generated not only by the degradation of collagen but also other ECM molecules. For example, extracellular vimentin is citrullinated and cleaved by MMPs giving rise to a fragment known as VICM (citrullinated and MMP-degraded vimentin) (150). VICM is released by tumor associated macrophages and has been detected in the serum of lung cancer patients (151, 152). In melanoma patients treated with ICIs, such as ipilimumab, nivolumab and prembolizumab, high levels of VICM before immunotherapy were linked to a survival benefit (66, 67). This finding fits well with the higher frequency of macrophages infiltrating the tumors of patients responding to ipilimumab compared with the non-responders (153).

Taken together, these studies highlight a prominent role of the ECM in affecting the immune response. From the evaluation of the 47 papers taken into account, we can infer that collagens are the most studied ECM components in this context, impacting on the infiltration and activation of immune cells by constituting a physical barrier to effector cells' infiltration and by influencing immune cells phenotype. Moreover, collagen remodeling represents a crossing-edge process among different tumor types and provides promising valuable biomarkers for ICIs efficacy. Nonetheless, from this study we can also conclude that other ECM components as glycoproteins and proteoglycans exert a prominent role in shaping the tumor immune response despite their effect is tumor-type specific.

4 Discussion

As a key component of the TME, the ECM is becoming a crucial source of novel diagnostic and prognostic biomarkers (75). Due to its intrinsic complexity and multimodular structure of its components, and thanks to the integration of inside-in and inside-out signals, the ECM takes part in a plethora of different processes within the tumor, being involved in a dynamic reciprocity with cancer cells, as well as tumor-associated cell types. The matrix signals affect gene expression programs shaping the phenotype of cancer cells, which in turn tightly control the ECM composition and its mechano-tensile properties. The changes in ECM composition, due to the altered expression of its components and to their overt post-transcriptional modifications, lead to the replacement of the normal ECM with a tumor-educated ECM, which supports tumor growth and progression. Only recently the abnormal ECM has also been

shown to impact on the susceptibility of tumor cells to immune cell-mediated killing (154). Indeed, increasing evidence suggest that the tumor-associated ECM as well as the ECM remodeling enzymes play a vital role in the modulation of the immune response, thus impacting not only on cancer progression but also on the susceptibility to ICIs therapy. Due to the extremely complex nature of the ECM, the literature regarding this topic is intricate, spanning several matrix molecules and processes, and covering a number of different tumor types. With the aim to comprehensively describe the relation between ECM and the efficacy of ICIs in cancer patients, the present review systematically evaluated the current literature regarding this topic, highlighting the value of ECM and ECM-derived molecules as predictive biomarkers for ICIs therapy efficacy (Figure 3).

The literature search strategy was intended to retrieve studies dealing with both adult and pediatric patients. However, none of the papers were related to pediatric cancers, likely because, in terms of absolute numbers, pediatric cancers are relatively rare and the use of ICIs is still under evaluation for these patients (155). Also, the TME of solid pediatric tumors has not been well investigated yet, despite it is known to be characterized by low mutational burdens and by a small number of TILs compared to adult malignancies (156). In accordance with these observations, the efficacy of checkpoint inhibition is poorer compared to that observed in the adults. Unlike pediatric patients, adult patients have been treated with immunotherapy for more than a decade, with the first ICI (anti-CTLA-4) being approved for the treatment of advanced-stage melanoma in 2011. Since then, the use of ICIs as single agents or in combinatorial approaches has greatly improved tumor regression rates and long-term cancer control for melanoma patients (157). More recently, the use of ICIs in breast and colorectal cancer has been explored, however promising results have been observed only in restricted subgroups of patients (158, 159). The use of ICIs to treat these three cancer types offered the possibility to analyze numerous patients' cohorts and to deeply investigate the characteristic of the ECM in relation to the therapy efficacy, as suggested by the fact that most of the papers included in the present systematic review regard melanoma, breast cancer and colorectal cancer.

Overall, the main processes and changes driving ECM remodeling in cancer have been well documented. However, it has become clear that each cancer type displays an unique ensemble of ECM molecules, ECM-remodeling enzymes and ECM-associated growth factors, collectively referred to as matrisome (160). This was confirmed also by the papers included in this study, with some mechanisms being strongly associated with a specific tumor type. The main ECM feature common to different tumor types is ECM stiffness, which highly impacts on immune cell infiltration representing a structural and physical barrier to the recruitment of effector T cells. An extreme matrix density and rigidity is also known to associate with impaired drug delivery to the tumors, thus pinpointing ECM stiffness as a double-edge sword deeply impaction on the efficacy of ICI (25).

On the other side, the activity of some ECM components is strongly tumor-type dependent. This can be at least partially explained by the fact that ECM molecules display multimodular

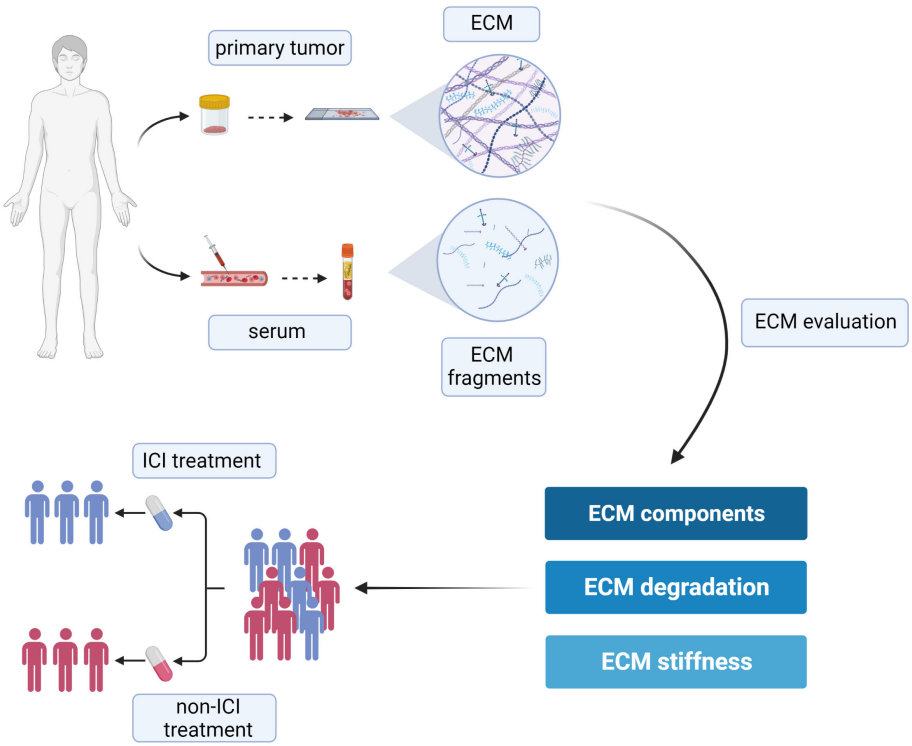

FIGURE 3
Schematic representation of the suitable approaches aimed at evaluating ECM remodeling as a tool to predict the efficacy of ICIs and to help the clinical decision-making process. Created with BioRender.com.

structures able to simultaneously modulate various biological functions and cell types, such as CAFS, immune cells and vascular cells. Thus, the overall association between the abundance of specific ECM proteins and the tumor immune traits are the result of a tight and complex molecular crosstalk between these cell types, through mechanisms that in part still remain elusive and need further investigation. In recent years, the crosstalk between immune and endothelial cells has been investigated to assess the impact of tumor associated vascularization on ICIs efficacy. These studies highlighted the synergic beneficial effect due to the simultaneous blockage of IC and the normalization of the vascular bed, leading to the design of novel therapeutic approaches based on the combination of ICIs and angiogenic drugs. On these grounds, it would be interesting to evaluate if the levels of ECM molecules exerting a role in both immunomodulation and angiogenesis may function as valuable biomarkers to stratify and identify the patients who benefit from the combination of anti-angiogenic therapy and ICIs.

The identification of tumor-specific matrisomes suggests that tumor ECM might not only represent a valuable reservoir of predictive biomarkers but also a new therapeutic target to improve ICIs treatments. The ECM components, indeed, may be exploited as new druggable targets to act on the bio-physical properties of the matrix and, in turn to synergize with ICIs therapy. The tumor-associated ECM may be therapeutically modulated in several ways, including the targeting of single ECM molecules or ECM-remodeling enzymes. For example, the administration of recombinant hyaluronidase to reduce hyaluronan accumulation has been used in phase I and II clinical trials in combination with pembrolizumab and atezolizumab for the treatment of stomach, lung and pancreatic cancer (161, 162). These trials will open the road for the clinical evaluation of other ECM/ICIs-based combinatorial therapy, as suggested by the promising data regarding the targeting of TNC and versican, which improved T cell mediated cancer cell killing in preclinical models (54). In addition, the ECM is under evaluation as a putative mean to improve drug delivery to the tumors. The use of tumor ECM-specific antibodies fused with cytokines (i.e. IL-2 and IL-12) or compounds (i.e. sunitinib) have in fact been shown to lead to increased concentrations of the drugs within the tumors, reduced severity of the side effects, and enhanced therapy efficacy (163–167). In the future, it is conceivable that similar approaches may be exploited also for the delivery of ICIs.

The potential weakness of the present systematic review resided in the fact that many of the studies are based on bioinformatic analyses. This represents a major limit since the altered mRNA levels not always coincide with the same alterations in the protein content. And this is particularly true when dealing with ECM molecules, which are extensively regulated not only at the transcriptional, but also post-translational level and undergo continuous remodeling. Nonetheless, we chose to comprise these studies since they were based on solid and strong results and provided deeper insights in the association between ECM and immune response, building the grounds for the development of new putative markers. Studies base on proteomic databases would certainly serve better this purpose, however these databases are limited compared to the RNAseq-based datasets. On these bases, we consider that more efforts should be put to attain a comprehensive proteomic profiling of the TME.

The use of ICIs represents an important therapeutic option for cancer treatment, with subgroups of patients gaining major and long-term benefits. Nonetheless, a large number of patients showing scarce response to ICIs and some experiencing unwanted side effects. For these reasons, the identification of the patients that would better benefit from immunotherapies is key to avoid over-treatments and unnecessary side effects. In addition, this approach would allow the National Health Systems to optimize more efficiently the resources. Indeed, many investigations aimed at identifying reliable predictive biomarkers for ICIs efficacy are ongoing (168). These approaches span from the analysis of cancer cell intrinsic features, such as the presence of specific gene mutations and their metabolic status, to the characterization of tumor associated stroma cells (169–172). Indeed, CAFs represent not only a promising prognostic biomarker (173, 174), but may also grant the possibility to predict ICIs efficacy, as highlighted in the present work. In this scenario, the ECM and its remodeling are entangled with the CAFs function and represent a passepartout to unravel the traits of the tumor immune environment. Indeed, the present systematic review indicates that ECM remodeling and ECM-derived fragments can represent a widow's cruse for the development of valuable biomarkers to predict the clinical outcome and to help identifying the patients that will better benefit from ICIs therapies. Importantly, the identification of circulating ECM fragments with predictive value would provide a fast and easily accessible liquid-biopsy based test to help clinicians to determine the most appropriate therapy for each patient. Nonetheless, further validations are needed, and it will be crucial to identify a threshold to successfully apply patient-tailored therapies. Given the complex network of ECM molecules, most of which have still not been evaluated in this context, we envision that the ECM will be extensively exploited for the development of new biomarkers to predict immunotherapy efficacy.

Data availability statement

The datasets presented in this study can be found in online repositories. The names of the repository/repositories and accession number(s) can be found below: https://doi.org/10.5281/zenodo.8348665.

Author contributions

AF: Data curation, Writing – original draft, Formal Analysis, Investigation, Methodology. GC: Data curation, Formal Analysis, Investigation, Writing – original draft. EP: Formal Analysis, Writing – review & editing. LC: Formal Analysis, Writing – review & editing. GS: Formal Analysis, Writing – review &

editing. ED: Formal Analysis, Writing – review & editing. GR: Writing – review & editing, Funding acquisition, Project administration. MM: Funding acquisition, Supervision, Writing – original draft. EA: Conceptualization, Data curation, Writing – original draft.

Funding

The authors declare financial support was received for the research, authorship, and/or publication of this article. This work was supported by the Italian Ministry of Health, through the contribution given to the Institute for Maternal and Child Health IRCCS Burlo Garofolo- Trieste, Italy, the Italian Association of Cancer Research (AIRC) (grant# IG-23643 to MM) and the Italian Ministry of Health (grant# RF-2018-12365425) to MM.

Conflict of interest

The authors declare that the research was conducted in the absence of any commercial or financial relationships that could be construed as a potential conflict of interest.

The author(s) declared that they were an editorial board member of Frontiers, at the time of submission. This had no impact on the peer review process and the final decision.

Publisher's note

References

1. Wei SC, Duffy CR, Allison JP. Fundamental mechanisms of immune checkpoint blockade therapy. *Cancer Discovery* (2018) 8(9):1069–86. doi: 10.1158/2159-8290.CD-18-0367

2. Johnson DB, Nebhan CA, Moslehi JJ, Balko JM. Immune-checkpoint inhibitors: long-term implications of toxicity. *Nat Rev Clin Oncol* (2022) 19(4):254–67. doi: 10.1038/s41571-022-00600-w

3. Lu Y, Wang W, Wang F. Clinical benefits of PD-1 inhibitors in specific subgroups of patients with advanced esophageal squamous cell carcinoma: a systematic review and meta-analysis of phase 3 randomized clinical trials. *Front Immunol* (2023) 14:14. doi: 10.3389/fimmu.2023.1171671

4. Iranzo P, Callejo A, Assaf JD, Molina G, Lopez DE, Garcia-Illescas D, et al. Overview of checkpoint inhibitors mechanism of action: role of immune-related adverse events and their treatment on progression of underlying cancer. *Front Med* (2022) 9:875974. doi: 10.3389/fmed.2022.875974

5. Wang J, Yang T, Xu J. Therapeutic development of immune checkpoint inhibitors. *Adv Exp Med Biol* (2020) 1248:619–49. doi: 10.1007/978-981-15-3266-5_23

6. Picarda E, Ohaegbulam KC, Zang X. Molecular pathways: targeting B7-H3 (CD276) for human cancer immunotherapy. *Clin Cancer Res* (2016) 22(14):3425–31. doi: 10.1158/1078-0432.CCR-15-2428

7. Petitprez F, Meylan M, de Reyniès A, Sautès-Fridman C, Fridman WH. The tumor microenvironment in the response to immune checkpoint blockade therapies. *Front Immunol* (2020) 11:784. doi: 10.3389/fimmu.2020.00784

8. Deng B, Zhao Z, Kong W, Han C, Shen X, Zhou C. Biological role of matrix stiffness in tumor growth and treatment. *J Transl Med* (2022) 20(1):540. doi: 10.1186/s12967-022-03768-y

9. Fejza A, Camicia L, Poletto E, Carobolante G, Mongiat M, Andreuzzi E. ECM remodeling in squamous cell carcinoma of the aerodigestive tract: pathways for cancer dissemination and emerging biomarkers. *Cancers (Basel)* (2021) 13(11):2759. doi: 10.3390/cancers13112759

10. Chen CG, Iozzo RV. Extracellular matrix guidance of autophagy: a mechanism regulating cancer growth. *Open Biol* (2022) 12(1):210304. doi: 10.1098/rsob.210304

11. Andreuzzi E, Fejza A, Capuano A, Poletto E, Pivetta E, Doliana R, et al. Deregulated expression of Elastin Microfibril Interfacer 2 (EMILIN2) in gastric cancer affects tumor growth and angiogenesis. *Matrix BiolPlus* (2020) 7(2590-0285 (2590-0285 (Linking):100029. doi: 10.1016/j.mbplus.2020.100029

12. Andreuzzi E, Colladel R, Pellicani R, Tarticchio G, Cannizzaro R, Spessotto P, et al. The angiostatic molecule Multimerin 2 is processed by MMP-9 to allow sprouting angiogenesis. *Matrix Biol* (2017) 1569-1802(Electronic):40–53. doi: 10.1016/j.matbio.2017.04.002

13. Colladel R, Pellicani R, Andreuzzi E, Paulitti A, Tarticchio G, Todaro F, et al. MULTIMERIN2 binds VEGF-A primarily via the carbohydrate chains exerting an angiostatic function and impairing tumor growth. *Oncotarget* (2015) 7(2):2022–37. doi: 10.18632/oncotarget.6515

14. Neill T, Xie C, Iozzo RV. Decorin evokes reversible mitochondrial depolarization in carcinoma and vascular endothelial cells. *Am J Physiol-Cell Physiol* (2022) 323(5): C1355–73. doi: 10.1152/ajpcell.00325.2022

15. Faisal SM, Comba A, Varela ML, Argento AE, Brumley E, Abel C, et al. The complex interactions between the cellular and non-cellular components of the brain tumor microenvironmental landscape and their therapeutic implications. *Front Oncol* (2022) 12:1005069. doi: 10.3389/fonc.2022.1005069

16. Danussi C, Spessotto P, Petrucco A, Wassermann B, Sabatelli P, Montesi M, et al. Emilin1 deficiency causes structural and functional defects of lymphatic vasculature. *Mol Cell Biol* (2008) 28(0270-7306(0270-7306 (Linking):4026–39. doi: 10.1128/MCB.02062-07

17. Mongiat M, Buraschi S, Andreuzzi E, Neill T, Iozzo RV. Extracellular matrix: the gatekeeper of tumor angiogenesis. *Biochem Soc Trans* (2019) 47(5):1543–55. doi: 10.1042/BST20190653

18. Spada S, Tocci A, Di Modugno F, Nisticò P. Fibronectin as a multiregulatory molecule crucial in tumor matrisome: from structural and functional features to clinical practice in oncology. *J Exp Clin Cancer Res* (2021) 40(1):102. doi: 10.1186/s13046-021-01908-8

19. van Tienderen GS, Rosmark O, Lieshout R, Willemse J, de Weijer F, Elowsson Rendin L, et al. Extracellular matrix drives tumor organoids toward desmoplastic matrix deposition and mesenchymal transition. *Acta Biomater* (2023) 158:115–31. doi: 10.1016/j.actbio.2022.11.038

20. Karamanos NK, Theocharis AD, Neill T, Iozzo RV. Matrix modeling and remodeling: A biological interplay regulating tissue homeostasis and diseases. *Matrix Biol* (2019) 75–76:1–11. doi: 10.1016/j.matbio.2018.08.007

21. He Z, Xin Z, Yang Q, Wang C, Li M, Rao W, et al. Mapping the single-cell landscape of acral melanoma and analysis of the molecular regulatory network of the tumor microenvironments. *Elife* (2022) 11. doi: 10.7554/eLife.78616.sa2

22. Virtuoso A, De Luca C, Cirillo G, Riva M, Romano G, Bentivegna A, et al. Tumor microenvironment and immune escape in the time course of glioblastoma. *Mol Neurobiol* (2022) 59(11):6857–73. doi: 10.1007/s12035-022-02996-z

23. Winkler J, Abisoye-Ogunniyan A, Metcalf KJ, Werb Z. Concepts of extracellular matrix remodelling in tumour progression and metastasis. *Nat Commun* (2020) 11 (1):5120. doi: 10.1038/s41467-020-18794-x

24. Hongu T, Pein M, Insua-Rodríguez J, Gutjahr E, Mattavelli G, Meier J, et al. Perivascular tenascin C triggers sequential activation of macrophages and endothelial cells to generate a pro-metastatic vascular niche in the lungs. *Nat Cancer* (2022) 3 (4):486–504. doi: 10.1038/s43018-022-00353-6

25. Zhu P, Lu H, Wang M, Chen K, Chen Z, Yang L. Targeted mechanical forces enhance the effects of tumor immunotherapy by regulating immune cells in the tumor microenvironment. *Cancer Biol Med* (2023) 20(1):44–55. doi: 10.20892/j.issn.2095-3941.2022.0491

26. Larsen AMH, Kuczek DE, Kalvisa A, Siersbæk MS, Thorseth ML, Johansen AZ, et al. Collagen density modulates the immunosuppressive functions of macrophages. *J Immunol* (2020) 205(5):1461–72. doi: 10.4049/jimmunol.1900789

27. Page MJ, McKenzie JE, Bossuyt PM, Boutron I, Hoffmann TC, Mulrow CD, et al. The PRISMA 2020 statement: an updated guideline for reporting systematic reviews. *BMJ* (2021) 372:n71. doi: 10.1136/bmj.n71

28. Feng Y, Han X, Zhang Z, Qiao H, Tang H. ABI3BP is a prognosis biomarker related with clinicopathological features and immunity infiltration of lung tumor. *Front Genet* (2022) 13:1085785. doi: 10.3389/fgene.2022.1085785

29. Huang Z, Lai H, Liao J, Cai J, Li B, Meng L, et al. Upregulation of ADAM12 is associated with a poor survival and immune cell infiltration in colon adenocarcinoma. *Front Oncol* (2021) 16(11):729230. doi: 10.3389/fonc.2021.729230

30. Qi B, Liu H, Dong Y, Shi X, Zhou Q, Zeng F, et al. The nine ADAMs family members serve as potential biomarkers for immune infiltration in pancreatic adenocarcinoma. *PeerJ* (2020) 8:e9736. doi: 10.7717/peerj.9736

31. Zheng S, Zou Y, Tang Y, Yang A, Liang JY, Wu L, et al. Landscape of cancer-associated fibroblasts identifies the secreted biglycan as a protumor and immunosuppressive factor in triple-negative breast cancer. *Oncoimmunology* (2022) 11(1):2020984. doi: 10.1080/2162402X.2021.2020984

32. Zhang S, Yang H, Xiang X, Liu L, Huang H, Tang G. BGN may be a potential prognostic biomarker and associated with immune cell enrichment of gastric cancer. *Front Genet* (2022) 13:765569. doi: 10.3389/fgene.2022.765569

33. Liu Q, Zhao H, Guo Y, Zhang K, Shang F, Liu T. Bioinformatics-based analysis: noncoding RNA-mediated COL10A1 is associated with poor prognosis and immune cell infiltration in pancreatic cancer. *J Healthc Eng* (2022) ;2022:7904982. doi: 10.1155/2022/7904982

34. Zhu H, Hu X, Feng S, Jian Z, Xu X, Gu L, et al. The hypoxia-related gene COL5A1 is a prognostic and immunological biomarker for multiple human tumors. *Oxid Med Cell Longev* (2022) 2022:6419695. doi: 10.1155/2022/6419695

35. Karabulut YY, Köse EÇ, Bozlu M, Tuncel F, Yüksek GE, Etit D, et al. The role of COL6A1and PD-1 expressions in renal cell carcinoma. *Turk J Urol* (2020) 46(4):282–7. doi: 10.5152/tud.2020.20062

36. Luan H, Zhang C, Zhang T, He Y, Su Y, Zhou L. Identification of key prognostic biomarker and its correlation with immune infiltrates in pancreatic ductal adenocarcinoma. *Dis Markers* (2020) 2020:8825997. doi: 10.1155/2020/8825997

37. Sun X, Wu B, Chiang HC, Deng H, Zhang X, Xiong W, et al. Tumour DDR1 promotes collagen fibre alignment to instigate immune exclusion. *Nature* (2021) 599 (7886):673–8. doi: 10.1038/s41586-021-04057-2

38. Zhou Y, Tian Q, Gao H, Zhu L, Zhang Y, Zhang C, et al. Immunity and extracellular matrix characteristics of breast cancer subtypes based on identification by T helper cells profiling. *Front Immunol* (2022) 13:859581. doi: 10.3389/fimmu.2022.859581

39. Yaegashi LB, Baldavira CM, Prieto TG, MaChado-Rugolo J, Velosa APP, da Silveira LKR, et al. *In situ* overexpression of matricellular mechanical proteins demands functional immune signature and mitigates non-small cell lung cancer progression. *Front Immunol* (2021) 12:714230. doi: 10.3389/fimmu.2021.714230

40. Byers C, Gill M, Kurtansky NR, Alessi-Fox C, Harman M, Cordova M, et al. Tertiary lymphoid structures accompanied by fibrillary matrix morphology impact anti-tumor immunity in basal cell carcinomas. *Front Med (Lausanne)* (2022) 9:981074. doi: 10.3389/fmed.2022.981074

41. Wang J, Akter R, Shahriar MF, Uddin MN. Cancer-associated stromal fibroblast-derived transcriptomes predict poor clinical outcomes and immunosuppression in colon cancer. *Pathol Oncol Res* (2022) 28:1610350. doi: 10.3389/pore.2022.1610350

42. Zhao L, Wang W, Niu P, Luan X, Zhao D, Chen Y. The molecular mechanisms of CTHRC1 in gastric cancer by integrating TCGA, GEO and GSA datasets. *Front Genet* (2022) 13:900124. doi: 10.3389/fgene.2022.900124

43. Andreuzzi E, Fejza A, Polano M, Poletto E, Camicia L, Carobolante G, et al. Colorectal cancer development is affected by the ECM molecule EMILIN-2 hinging on macrophage polarization *via* the TLR-4/MyD88 pathway. *J Exp Clin Cancer Res* (2022) 41(1):60. doi: 10.1186/s13046-022-02271-y

44. Wang Lc, Cui WI, Zhang Z, Tan Zl, Lv Q, Chen SH, et al. Expression, methylation and prognostic feature of EMILIN2 in Low-Grade-Glioma. *Brain Res Bulletin* (2021) 175:26–36. Cui W yao. doi: 10.1016/j.brainresbull.2021.07.013

45. Zhao G, Zheng J, Tang K, Chen Q. EMILIN2 is associated with prognosis and immunotherapy in clear cell renal cell carcinoma. *Front Genet* (2022) 13:1058207. doi: 10.3389/fgene.2022.1058207

46. Wang N, Zhou X, Tang F, Wang X, Zhu X. Identification of LOXL3-associating immune infiltration landscape and prognostic value in hepatocellular carcinoma. *Virchows Arch* (2021) 479(6):1153–65. doi: 10.1007/s00428-021-03193-4

47. Tan HY, Wang N, Zhang C, Chan YT, Yuen MF, Feng Y. Lysyl oxidase-like 4 fosters an immunosuppressive microenvironment during hepatocarcinogenesis. *Hepatology* (2021) 73(6):2326–41. doi: 10.1002/hep.31600

48. Dai L, Mugaanyi J, Cai X, Dong M, Lu C, Lu C. Comprehensive bioinformatic analysis of MMP1 in hepatocellular carcinoma and establishment of relevant prognostic model. *Sci Rep* (2022) 12:13639. doi: 10.1038/s41598-022-17954-x

49. Zeng Y, Gao M, Lin D, Du G, Cai Y. Prognostic and immunological roles of MMP-9 in pan-cancer. *BioMed Res Int* (2022) 2022:2592962. doi: 10.1155/2022/2592962

50. Lecchi M, Verderio P, Cappelletti V, De Santis F, Paolini B, Monica M, et al. A combination of extracellular matrix- and interferon-associated signatures identifies high-grade breast cancers with poor prognosis. *Mol Oncol* (2021) 15(5):1345–57. doi: 10.1002/1878-0261.12912

51. Gao H, Li Q. A pan-cancer analysis of the oncogenic role of procollagen C-endopeptidase enhancer (PCOLCE) in human. *Med (Baltimore)* (2022) 101(52): e32444. doi: 10.1097/MD.0000000000032444

52. Xu Q, Kong N, Zhao Y, Wu Q, Wang X, Xun X, et al. Pan-cancer analyses reveal oncogenic and immunological role of PLOD2. *Front Genet* (2022) 13:864655. doi: 10.3389/fgene.2022.864655

53. Zheng Y, Hao S, Xiang C, Han Y, Shang Y, Zhen Q, et al. The correlation between SPP1 and immune escape of EGFR mutant lung adenocarcinoma was explored by bioinformatics analysis. *Front Oncol* (2021) 11:592854. doi: 10.3389/fonc.2021.592854

54. Li ZL, Zhang HL, Huang Y, Huang JH, Sun P, Zhou NN, et al. Autophagy deficiency promotes triple-negative breast cancer resistance to T cell-mediated cytotoxicity by blocking tenascin-C degradation. *Nat Commun* (2020) 11(1):3806. doi: 10.1038/s41467-020-17395-y

55. Murdamoothoo D, Sun Z, Yilmaz A, Riegel G, Abou-Faycal C, Deligne C, et al. Tenascin-C immobilizes infiltrating T lymphocytes through CXCL12 promoting breast cancer progression. *EMBO Mol Med* (2021) 13(6):e13270. doi: 10.15252/emmm.202013270

56. Spenlé C, Loustau T, Murdamoothoo D, Erne W, Beghelli-de la Forest Divonne S, Veber R, et al. Tenascin-C orchestrates an immune-suppressive tumor microenvironment in oral squamous cell carcinoma. *Cancer Immunol Res* (2020) 8 (9):1122–38. doi: 10.1158/2326-6066.CIR-20-0074

57. Zhang P, Liu G, Hu J, Chen S, Wang B, Peng P, et al. Tenascin-C can serve as an indicator for the immunosuppressive microenvironment of diffuse low-grade gliomas. *Front Immunol* (2022) 13:824586. doi: 10.3389/fimmu.2022.824586

58. Papadas A, Deb G, Cicala A, Officer A, Hope C, Pagenkopf A, et al. Stromal remodeling regulates dendritic cell abundance and activity in the tumor microenvironment. *Cell Rep* (2022) 40(7):111201. doi: 10.1016/j.celrep.2022.111201

59. Yang H, Berezowska S, Dorn P, Zens P, Chen P, Peng RW, et al. Tumor-infiltrating lymphocytes are functionally inactivated by CD90+ stromal cells and reactivated by combined Ibrutinib and Rapamycin in human pleural mesothelioma. *Theranostics* (2022) 12(1):167–85. doi: 10.7150/thno.61209

60. Gorter A, Zijlmans HJ, van Gent H, Trimbos JB, Fleuren GJ, Jordanova ES. Versican expression is associated with tumor-infiltrating CD8-positive T cells and infiltration depth in cervical cancer. *Mod Pathol* (2010) 23(12):1605–15. doi: 10.1038/modpathol.2010.154

61. Hope C, Foulcer S, Jagodinsky J, Chen SX, Jensen JL, Patel S, et al. Immunoregulatory roles of versican proteolysis in the myeloma microenvironment. *Blood* (2016) 128(5):680–5. doi: 10.1182/blood-2016-03-705780

62. Hope C, Emmerich PB, Papadas A, Pagenkopf A, Matkowskyj KA, Van De Hey DR, et al. Versican-derived matrikines regulate Batf3-dendritic cell differentiation and promote T-cell infiltration in colorectal cancer. *J Immunol* (2017) 199(5):1933–41. doi: 10.4049/jimmunol.1700529

63. He ZX, Zhao SB, Fang X, JF E, Fu HY, Song YH, et al. Prognostic and predictive value of BGN in colon cancer outcomes and response to immunotherapy. *Front Oncol* (2021) 11:761030. doi: 10.3389/fonc.2021.761030

64. Zhang X, Liu J, Yang X, Jiao W, Shen C, Zhao X, et al. High expression of COL6A1 predicts poor prognosis and response to immunotherapy in bladder cancer. *Cell Cycle* (2023) 22(5):610–8. doi: 10.1080/15384101.2022.2154551

65. Jensen C, Sinkeviciute D, Madsen DH, Önnerfjord P, Hansen M, Schmidt H, et al. Granzyme B degraded type IV collagen products in serum identify melanoma patients responding to immune checkpoint blockade. *Cancers (Basel)* (2020) 12 (10):2786. doi: 10.3390/cancers12102786

66. Jensen C, Madsen DH, Hansen M, Schmidt H, Svane IM, Karsdal MA, et al. Non-invasive biomarkers derived from the extracellular matrix associate with response to immune checkpoint blockade (anti-CTLA-4) in metastatic melanoma patients. *J Immunother Cancer* (2018) 6(1):152. doi: 10.1186/s40425-018-0474-z

67. Hurkmans DP, Jensen C, Koolen SLW, Aerts J, Karsdal MA, Mathijssen RHJ, et al. Blood-based extracellular matrix biomarkers are correlated with clinical outcome after PD-1 inhibition in patients with metastatic melanoma. *J Immunother Cancer* (2020) 8(2):e001193. doi: 10.1136/jitc-2020-001193

68. Peng DH, Rodriguez BL, Diao L, Chen L, Wang J, Byers LA, et al. Collagen promotes anti-PD-1/PD-L1 resistance in cancer through LAIR1-dependent CD8+ T cell exhaustion. *Nat Commun* (2020) 11:4520. doi: 10.1038/s41467-020-18298-8

69. Chen Z, Zhuo S, He G, Tang J, Hao W, Gao WQ, et al. Prognosis and immunotherapy significances of a cancer-associated fibroblasts-related gene signature in gliomas. *Front Cell Dev Biol* (2021) 9:721897. doi: 10.3389/fcell.2021.721897

70. Fejza A, Polano M, Camicia L, Poletto E, Carobolante G, Toffoli G, et al. The efficacy of anti-PD-L1 treatment in melanoma is associated with the expression of the ECM molecule EMILIN2. *Int J Mol Sci* (2021) 22(14):7511. doi: 10.3390/ijms22147511

71. Mei Y, Chen MJM, Liang H, Ma L. A four-gene signature predicts survival and anti-CTLA4 immunotherapeutic responses based on immune classification of melanoma. *Commun Biol* (2021) 4:383. doi: 10.1038/s42003-021-01911-x

72. Huang H, Hu Y, Guo L, Wen Z. Integrated bioinformatics analyses of key genes involved in hepatocellular carcinoma immunosuppression. *Oncol Lett* (2021) 22 (6):830. doi: 10.3892/ol.2021.13091

73. Khunger A, Piazza E, Warren S, Smith TH, Ren X, White A, et al. CTLA-4 blockade and interferon-α induce proinflammatory transcriptional changes in the tumor immune landscape that correlate with pathologic response in melanoma. *PloS One* (2021) 16(1):e0245287. doi: 10.1371/journal.pone.0245287

74. Yu H, Wang M, Wang X, Jiang X. Immune-related matrisomes are potential biomarkers to predict the prognosis and immune microenvironment of glioma patients. *FEBS Open Bio* (2023) 13(2):307–22. doi: 10.1002/2211-5463.13541

75. Iozzo RV, Theocharis AD, Neill T, Karamanos NK. Complexity of matrix phenotypes. *Matrix Biol Plus* (2020) 6–7:100038. doi: 10.1016/j.mbplus.2020.100038

76. Girigoswami K, Saini D, Girigoswami A. Extracellular matrix remodeling and development of cancer. *Stem Cell Rev Rep* (2021) 17(3):739–47. doi: 10.1007/s12015-020-10070-1

77. Mongiat M, Ligresti G, Marastoni S, Lorenzon E, Doliana R, Colombatti A. Regulation of the extrinsic apoptotic pathway by the extracellular matrix glycoprotein EMILIN2. *Mol Cell Biol* (2007) 27(0270-7306(0270-7306 (Linking):7176–87. doi: 10.1128/MCB.00696-07

78. Mongiat M, Marastoni S, Ligresti G, Lorenzon E, Schiappacassi M, Perris R, et al. The extracellular matrix glycoprotein elastin microfibril interface located protein 2: a dual role in the tumor microenvironment. *Neoplasia* (2010) 12(4):294–304. doi: 10.1593/neo.91930

79. Chakravarthy A, Khan L, Bensler NP, Bose P, De Carvalho DD. TGF-β-associated extracellular matrix genes link cancer-associated fibroblasts to immune evasion and immunotherapy failure. *Nat Commun* (2018) 9(1):4692. doi: 10.1038/s41467-018-06654-8

80. Ahluwalia P, Ahluwalia M, Mondal AK, Sahajpal N, Kota V, Rojiani MV, et al. Prognostic and therapeutic implications of extracellular matrix associated gene signature in renal clear cell carcinoma. *Sci Rep* (2021) 11(1):7561. doi: 10.1038/s41598-021-86888-7

81. Fromme JE, Zigrino P. The role of extracellular matrix remodeling in skin tumor progression and therapeutic resistance. *Front Mol Biosci* (2022) 9:864302. doi: 10.3389/fmolb.2022.864302

82. Evers M, Schreder M, Stühmer T, Jundt F, Ebert R, Hartmann TN, et al. Prognostic value of extracellular matrix gene mutations and expression in multiple myeloma. *Blood Cancer J* (2023) 13(1):43. doi: 10.1038/s41408-023-00817-7

83. Chen S, Wainwright DA, Wu JD, Wan Y, Matei DE, Zhang Y, et al. CD73: an emerging checkpoint for cancer immunotherapy. *Immunotherapy* (2019) 11(11):983–97. doi: 10.2217/imt-2018-0200

84. Liu X, Song J, Zhang H, Liu X, Zuo F, Zhao Y, et al. Immune checkpoint HLA-E: CD94-NKG2A mediates evasion of circulating tumor cells from NK cell surveillance. *Cancer Cell* (2023) 41(2):272–87. doi: 10.1016/j.ccell.2023.01.001

85. Xie J, Gui X, Deng M, Chen H, Chen Y, Liu X, et al. Blocking LAIR1 signaling in immune cells inhibits tumor development. *Front Immunol* (2022) 13:996026. doi: 10.3389/fimmu.2022.996026

86. Wight TN, Kang I, Evanko SP, Harten IA, Chang MY, Pearce OMT, et al. Versican-A critical extracellular matrix regulator of immunity and inflammation. *Front Immunol* (2020) 11:512. doi: 10.3389/fimmu.2020.00512

87. Zhang Q, Wu J, Chen X, Zhao M, Zhang D, Gao F. Upregulation of versican associated with tumor progression, metastasis, and poor prognosis in bladder carcinoma. *BioMed Res Int* (2021) 2021:6949864. doi: 10.1155/2021/6949864

88. Hirani P, Gauthier V, Allen CE, Wight TN, Pearce OMT. Targeting versican as a potential immunotherapeutic strategy in the treatment of cancer. *Front Oncol* (2021) 11:712807. doi: 10.3389/fonc.2021.712807

89. Andreuzzi E, Capuano A, Poletto E, Pivetta E, Fejza A, Favero A, et al. Role of extracellular matrix in gastrointestinal cancer-associated angiogenesis. *IJMS* (2020) 21 (10):3686. doi: 10.3390/ijms21103686

90. Lepucki A, Orlińska K, Mielczarek-Palacz A, Kabut J, Olczyk P, Komosińska-Vassev K. The role of extracellular matrix proteins in breast cancer. *J Clin Med* (2022) 11(5):1250. doi: 10.3390/jcm11051250

91. Liot S, Balas J, Aubert A, Prigent L, Mercier-Gouy P, Verrier B, et al. Stroma involvement in pancreatic ductal adenocarcinoma: an overview focusing on extracellular matrix proteins. *Front Immunol* (2021) 12:612271. doi: 10.3389/fimmu.2021.612271

92. Tucker RP, Degen M. Revisiting the tenascins: exploitable as cancer targets? *Front Oncol* (2022) 12:908247. doi: 10.3389/fonc.2022.908247

93. Yoshida KI, Midwood KS, Orend G. Editorial: tenascins – key players in tissue homeostasis and defense. *Front Immunol* (2022) 12:834353. doi: 10.3389/fimmu.2021.834353

94. Pyagay P, Heroult M, Wang Q, Lehnert W, Belden J, Liaw L, et al. Collagen triple helix repeat containing 1, a novel secreted protein in injured and diseased arteries, inhibits collagen expression and promotes cell migration. *Circ Res* (2005) 96(2):261–8. doi: 10.1161/01.RES.0000154262.07264.12

95. Duan X, Yuan X, Yao B, Song W, Li Z, Enhejirigala, et al. The role of CTHRC1 in promotion of cutaneous wound healing. *Signal Transduction Targeted Ther* (2022) 7 (1):183. doi: 10.1038/s41392-022-01008-9

96. Mei D, Zhu Y, Zhang L, Wei W. The role of CTHRC1 in regulation of multiple signaling and tumor progression and metastasis. *Mediators Inflamm* (2020) 2020:9578701. doi: 10.1155/2020/9578701

97. Zhang XL, Hu LP, Yang Q, Qin WT, Wang X, Xu CJ, et al. CTHRC1 promotes liver metastasis by reshaping infiltrated macrophages through physical interactions with TGF-β receptors in colorectal cancer. *Oncogene* (2021) 40(23):3959–73. doi: 10.1038/s41388-021-01827-0

98. Matsuda S, Iriyama C, Yokozaki S, Ichigotani Y, Shirafuji N, Yamaki K, et al. Cloning and sequencing of a novel human gene that encodes a putative target protein of Nesh-SH3. *J Hum Genet* (2001) 46(8):483–6. doi: 10.1007/s100380170049

99. Delfín DA, DeAguero JL, McKown EN. The extracellular matrix protein ABI3BP in cardiovascular health and disease. *Front Cardiovasc Med* (2019) 6:23. doi: 10.3389/fcvm.2019.00023

100. Latini FRM, Hemerly JP, Freitas BCG, Oler G, Riggins GJ, Cerutti JM. ABI3 ectopic expression reduces in *vitro* and in *vivo* cell growth properties while inducing senescence. *BMC Cancer* (2011) 11:11. doi: 10.1186/1471-2407-11-11

101. Lin N, Yao Z, Xu M, Chen J, Lu Y, Yuan L, et al. Long noncoding RNA MALAT1 potentiates growth and inhibits senescence by antagonizing ABI3BP in gallbladder cancer cells. *J Exp Clin Cancer Res* (2019) 38(1):244. doi: 10.1186/s13046-019-1237-5

102. Cai H, Li Y, Qin D, Wang R, Tang Z, Lu T, et al. The depletion of ABI3BP by microRNA-183 promotes the development of esophageal carcinoma. *Mediators Inflamm* (2020) 2020:3420946. doi: 10.1155/2020/3420946

103. Nong B, Guo M, Wang W, Songyang Z, Xiong Y. Comprehensive analysis of large-scale transcriptomes from multiple cancer types. *Genes (Basel)* (2021) 12 (12):1865. doi: 10.3390/genes12121865

104. Ding Y, Li P, Wang W, Liu F. A potential four-gene signature and nomogram for predicting the overall survival of papillary thyroid cancer. *Dis Markers* (2022) 2022:8735551. doi: 10.1155/2022/8735551

105. Bot S, Andreuzzi E, Capuano A, Schiavinato A, Colombatti A, Doliana R. Multiple-interactions among EMILIN1 and EMILIN2 N- and C-terminal domains. *Matrix Biol* (2015) 41:44–55. doi: 10.1016/j.matbio.2014.10.001

106. Capuano A, Pivetta E, Sartori G, Bosisio G, Favero A, Cover E, et al. Abrogation of EMILIN1-β1 integrin interaction promotes experimental colitis and colon carcinogenesis. *Matrix Biol* (2019) 83:97–115. doi: 10.1016/j.matbio.2019.08.006

107. Pivetta E, Capuano A, Vescovo M, Scanziani E, Cappelleri A, Rampioni Vinciguerra GL, et al. EMILIN-1 deficiency promotes chronic inflammatory disease through TGFβ signaling alteration and impairment of the gC1q/α4β1 integrin interaction. *Matrix Biol* (2022) 111:133–52. doi: 10.1016/j.matbio.2022.06.005

108. Marastoni S, Andreuzzi E, Paulitti A, Colladel R, Pellicani R, Todaro F, et al. EMILIN2 down-modulates the Wnt signalling pathway and suppresses breast cancer cell growth and migration. *JPathol* (2014) 232(0022-3417(0022-3417 (Linking):391–404. doi: 10.1002/path.4316

109. Paulitti A, Andreuzzi E, Bizzotto D, Pellicani R, Tarticchio G, Marastoni S, et al. The ablation of the matricellular protein EMILIN2 causes defective vascularization due to impaired EGFR-dependent IL-8 production affecting tumor growth. *Oncogene* (2018) 37(25):3399–414. doi: 10.1038/s41388-017-0107-x

110. Lorenzon E, Colladel R, Andreuzzi E, Marastoni S, Todaro F, Schiappacassi M, et al. MULTIMERIN2 impairs tumor angiogenesis and growth by interfering with VEGF-A/VEGFR2 pathway. *Oncogene* (2012) 31(26):3136–47. doi: 10.1038/onc.2011.487

111. Andreuzzi E, Capuano A, Pellicani R, Poletto E, Doliana R, Maiero S, et al. Loss of multimerin-2 and EMILIN-2 expression in gastric cancer associate with altered angiogenesis. *Int J Mol Sci* (2018) 19(12):3983. doi: 10.3390/ijms19123983

112. Pellicani R, Poletto E, Andreuzzi E, Paulitti A, Doliana R, Bizzotto D, et al. Multimerin-2 maintains vascular stability and permeability. *Matrix Biol* (2020) 87:11–25. doi: 10.1016/j.matbio.2019.08.002

113. Diehl V, Huber LS, Trebicka J, Wygrecka M, Iozzo RV, Schaefer L. The role of decorin and biglycan signaling in tumorigenesis. *Front Oncol* (2021) 11:801801. doi: 10.3389/fonc.2021.801801

114. Sethi MK, Downs M, Shao C, Hackett WE, Phillips JJ, Zaia J. In-depth matrisome and glycoproteomic analysis of human brain glioblastoma versus control tissue. *Mol Cell Proteomics* (2022) 21(4):100216. doi: 10.1016/j.mcpro.2022.100216

115. Liu M, Wang W, Piao S, Shen Y, Li Z, Ding W, et al. Relationship of biglycan and decorin expression with clinicopathological features and prognosis in patients with oral squamous cell carcinoma. *J Oral Pathol Med* (2023) 52(1):20–8. doi: 10.1111/jop.13381

116. Zhao SF, Yin XJ, Zhao WJ, Liu LC, Wang ZP. Biglycan as a potential diagnostic and prognostic biomarker in multiple human cancers. *Oncol Lett* (2020) 19(3):1673–82. doi: 10.3892/ol.2020.11266

117. Hu S, Li P, Wang C, Liu X. Expression and the prognostic value of biglycan in gastric cancer. *Comput Math Methods Med* (2022) 2022:2656480. doi: 10.1155/2022/2656480

118. Zhao L, Liang J, Zhong W, Han C, Liu D, Chen X. Expression and prognostic analysis of BGN in head and neck squamous cell carcinoma. *Gene* (2022) 827:146461. doi: 10.1016/j.gene.2022.146461

119. Bastos ACS da F, Gomes AVP, Silva GR, Emerenciano M, Ferreira LB, Gimba ERP. The intracellular and secreted sides of osteopontin and their putative physiopathological roles. *Int J Mol Sci* (2023) 24(3):2942. doi: 10.3390/ijms24032942

120. Zhao H, Chen Q, Alam A, Cui J, Suen KC, Soo AP, et al. The role of osteopontin in the progression of solid organ tumour. *Cell Death Dis* (2018) 9(3):1–15. doi: 10.1038/s41419-018-0391-6

121. Zhang Y, Du W, Chen Z, Xiang C. Upregulation of PD-L1 by SPP1 mediates macrophage polarization and facilitates immune escape in lung adenocarcinoma. *Exp Cell Res* (2017) 359(2):449–57. doi: 10.1016/j.yexcr.2017.08.028

122. Klement JD, Paschall AV, Redd PS, Ibrahim ML, Lu C, Yang D, et al. An osteopontin/CD44 immune checkpoint controls CD8+ T cell activation and tumor immune evasion. *J Clin Invest* (2018) 128(12):5549–60. doi: 10.1172/JCI123360

123. Wei J, Marisetty A, Schrand B, Gabrusiewicz K, Hashimoto Y, Ott M, et al. Osteopontin mediates glioblastoma-associated macrophage infiltration and is a potential therapeutic target. *J Clin Invest* (2019) 129(1):137–49. doi: 10.1172/JCI121266

124. Spicer AP, Joo A, Bowling RA. A hyaluronan binding link protein gene family whose members are physically linked adjacent to chrondroitin sulfate proteoglycan core protein genes: THE MISSING LINKS *. *J Biol Chem* (2003) 278(23):21083–91. doi: 10.1074/jbc.M213100200

125. Kuo SJ, Chien SY, Lin C, Chan SE, Tsai HT, Chen DR. Significant elevation of CLDN16 and HAPLN3 gene expression in human breast cancer. *Oncol Rep* (2010) 24 (3):759–66. doi: 10.3892/or_00000918

126. Ding Y, Xiong S, Chen X, Pan Q, Fan J, Guo J. HAPLN3 inhibits apoptosis and promotes EMT of clear cell renal cell carcinoma *via* ERK and Bcl-2 signal pathways. *J Cancer Res Clin Oncol* (2023) 149(1):79–90. doi: 10.1007/s00432-022-04421-3

127. Bjerre MT, Nørgaard M, Larsen OH, Jensen SØ, Strand SH, Østergren P, et al. Epigenetic analysis of circulating tumor DNA in localized and metastatic prostate cancer: evaluation of clinical biomarker potential. *Cells* (2020) 9(6):1362. doi: 10.3390/cells9061362

128. He Y, Liu T, Dai S, Xu Z, Wang L, Luo F. Tumor-associated extracellular matrix: how to be a potential aide to anti-tumor immunotherapy? *Front Cell Dev Biol* (2021) 9:739161. doi: 10.3389/fcell.2021.739161

129. Nicolas-Boluda A, Vaquero J, Vimeux L, Guilbert T, Barrin S, Kantari-Mimoun C, et al. Tumor stiffening reversion through collagen crosslinking inhibition improves T cell migration and anti-PD-1 treatment. *Elife* (2021) 10. doi: 10.7554/eLife.58688.sa2

130. Kasashima H, Yashiro M, Okuno T, Miki Y, Kitayama K, Masuda G, et al. Significance of the lysyl oxidase members lysyl oxidase like 1, 3, and 4 in gastric cancer. *Gastroenterologia* (2018) 98(4):238–48. doi: 10.1159/000489558

131. Tenti P, Vannucci L. Lysyl oxidases: linking structures and immunity in the tumor microenvironment. *Cancer Immunol Immunother* (2020) 69(2):223–35. doi: 10.1007/s00262-019-02404-x

132. Lu X, Xin DE, Du JK, Zou QC, Wu Q, Zhang YS, et al. Loss of LOXL2 promotes uterine hypertrophy and tumor progression by enhancing H3K36ac-dependent gene expression. *Cancer Res* (2022) 82(23):4400–13. doi: 10.1158/0008-5472.CAN-22-0848

133. Xia QX, Yu J, Wang ZJ, Guan QW, Mao XY. Identification and validation of roles of lysyl oxidases in the predictions of prognosis, chemotherapy and immunotherapy in glioma. *Front Pharmacol* (2022) 13:990461. doi: 10.3389/fphar.2022.990461

134. Park KC, Dharmasivam M, Richardson DR. The role of extracellular proteases in tumor progression and the development of innovative metal ion chelators that inhibit their activity. *Int J Mol Sci* (2020) 21(18):6805. doi: 10.3390/ijms21186805

135. Lai YL, Gong CL, Fu CK, Yueh TC, Tsai CW, Chang WS, et al. The contribution of matrix metalloproteinase-1 genotypes to hepatocellular carcinoma susceptibility in Taiwan. *Cancer Genomics Proteomics* (2017) 14(2):119–25. doi: 10.21873/cgp.20024

136. Ueno M, Shiomi T, Mochizuki S, Chijiiwa M, Shimoda M, Kanai Y, et al. ADAM9 is over-expressed in human ovarian clear cell carcinomas and suppresses cisplatin-induced cell death. *Cancer Sci* (2018) 109(2):471–82. doi: 10.1111/cas.13469

137. Hubeau C, Rocks N, Cataldo D. ADAM28: Another ambivalent protease in cancer. *Cancer Lett* (2020) 494:18–26. doi: 10.1016/j.canlet.2020.08.031

138. Ao T, Mochizuki S, Kajiwara Y, Yonemura K, Shiraishi T, Nagata K, et al. Cancer-associated fibroblasts at the unfavorable desmoplastic stroma promote colorectal cancer aggressiveness: Potential role of ADAM9. *Int J Cancer* (2022) 150 (10):1706–21. doi: 10.1002/ijc.33947

139. Jain R, Gosavi S, Sethia D, Trimuke A, Salunke M. Evaluation of expression of ADAM 10 as a predictor of lymph node metastasis in oral squamous cell carcinoma-an immunohistochemical study. *Head Neck Pathol* (2022) 16(4):1055–62. doi: 10.1007/s12105-022-01466-1

140. Kalita A, Sikora-Skrabaka M, Nowakowska-Zajdel E. Role of some microRNA/ADAM proteins axes in gastrointestinal cancers as a novel biomarkers and potential therapeutic targets-A review. *Curr Issues Mol Biol* (2023) 45(4):2917–36. doi: 10.3390/cimb45040191

141. Sharma D, Singh NK. The biochemistry and physiology of A disintegrin and metalloproteinases (ADAMs and ADAM-TSs) in human pathologies. *Rev Physiol Biochem Pharmacol* (2023) 184:69–120. doi: 10.1007/112_2021_67

142. Willumsen N, Bager CL, Leeming DJ, Smith V, Karsdal MA, Dornan D, et al. Extracellular matrix specific protein fingerprints measured in serum can separate pancreatic cancer patients from healthy controls. *BMC Cancer* (2013) 13:554. doi: 10.1186/1471-2407-13-554

143. Willumsen N, Ali SM, Leitzel K, Drabick JJ, Yee N, Polimera HV, et al. Collagen fragments quantified in serum as measures of desmoplasia associate with survival outcome in patients with advanced pancreatic cancer. *Sci Rep* (2019) 9(1):19761. doi: 10.1038/s41598-019-56268-3

144. Karsdal MA, Nielsen SH, Leeming DJ, Langholm LL, Nielsen MJ, Manon-Jensen T, et al. The good and the bad collagens of fibrosis - Their role in signaling and organ function. *Adv Drug Delivery Rev* (2017) 121:43–56. doi: 10.1016/j.addr.2017.07.014

145. Nielsen MJ, Nedergaard AF, Sun S, Veidal SS, Larsen L, Zheng Q, et al. The neo-epitope specific PRO-C3 ELISA measures true formation of type III collagen associated with liver and muscle parameters. *Am J Transl Res* (2013) 5(3):303–15.

146. Kehlet SN, Sanz-Pamplona R, Brix S, Leeming DJ, Karsdal MA, Moreno V. Excessive collagen turnover products are released during colorectal cancer progression and elevated in serum from metastatic colorectal cancer patients. *Sci Rep* (2016) 6:30599. doi: 10.1038/srep30599

147. Lipton A, Leitzel K, Ali SM, Polimera HV, Nagabhairu V, Marks E, et al. High turnover of extracellular matrix reflected by specific protein fragments measured in serum is associated with poor outcomes in two metastatic breast cancer cohorts. *Int J Cancer* (2018) 143(11):3027–34. doi: 10.1002/ijc.31627

148. Bager CL, Willumsen N, Leeming DJ, Smith V, Karsdal MA, Dornan D, et al. Collagen degradation products measured in serum can separate ovarian and breast cancer patients from healthy controls: A preliminary study. *Cancer biomark* (2015) 15 (6):783–8. doi: 10.3233/CBM-150520

149. Hiebert PR, Wu D, Granville DJ. Granzyme B degrades extracellular matrix and contributes to delayed wound closure in apolipoprotein E knockout mice. *Cell Death Differ* (2013) 20(10):1404–14. doi: 10.1038/cdd.2013.96

150. Vassiliadis E, Oliveira CP, Alvares-da-Silva MR, Zhang C, Carrilho FJ, Stefano JT, et al. Circulating levels of citrullinated and MMP-degraded vimentin (VICM) in liver fibrosis related pathology. *Am J Transl Res* (2012) 4(4):403–14.

151. Willumsen N, Bager CL, Leeming DJ, Smith V, Christiansen C, Karsdal MA, et al. Serum biomarkers reflecting specific tumor tissue remodeling processes are valuable diagnostic tools for lung cancer. *Cancer Med* (2014) 3(5):1136–45. doi: 10.1002/cam4.303

152. Mortensen JH, Guo X, De Los Reyes M, Dziegiel MH, Karsdal MA, Bay-Jensen AC, et al. The VICM biomarker is released from activated macrophages and inhibited by anti-GM-CSFRα-mAb treatment in rheumatoid arthritis patients. *Clin Exp Rheumatol* (2019) 37(1):73–80.

153. Romano E, Kusio-Kobialka M, Foukas PG, Baumgaertner P, Meyer C, Ballabeni P, et al. Ipilimumab-dependent cell-mediated cytotoxicity of regulatory T cells ex vivo by nonclassical monocytes in melanoma patients. *Proc Natl Acad Sci U S A* (2015) 112 (19):6140–5. doi: 10.1073/pnas.1417320112

154. Kim SE, Yun S, Doh J. Effects of extracellular adhesion molecules on immune cell mediated solid tumor cell killing. *Front Immunol* (2022) 13:1004171. doi: 10.3389/fimmu.2022.1004171

155. Kattner P, Strobel H, Khoshnevis N, Grunert M, Bartholomae S, Pruss M, et al. Compare and contrast: pediatric cancer versus adult Malignancies. *Cancer Metastasis Rev* (2019) 38(4):673–82. doi: 10.1007/s10555-019-09836-y

156. Gupta A, Cripe TP. Immunotherapies for pediatric solid tumors: A targeted update. *Pediatr Drugs* (2022) 24(1):1–12. doi: 10.1007/s40272-021-00482-y

157. Carlino MS, Larkin J, Long GV. Immune checkpoint inhibitors in melanoma. *Lancet* (2021) 398(10304):1002–14. doi: 10.1016/S0140-6736(21)01206-X

158. Huyghe N, Baldin P, Van den Eynde M. Immunotherapy with immune checkpoint inhibitors in colorectal cancer: what is the future beyond deficient mismatch-repair tumours? *Gastroenterol Rep (Oxf)* (2020) 8(1):11–24. doi: 10.1093/gastro/goz061

159. Farshbafnadi M, Pastaki Khoshbin A, Rezaei N. Immune checkpoint inhibitors for triple-negative breast cancer: From immunological mechanisms to clinical evidence. *Int Immunopharmacol* (2021) 98:107876. doi: 10.1016/j.intimp.2021.107876

160. Izzi V, Lakkala J, Devarajan R, Kääriäinen A, Koivunen J, Heljasvaara R, et al. Pan-Cancer analysis of the expression and regulation of matrisome genes across 32 tumor types. *Matrix Biol Plus* (2019) 1:100004. doi: 10.1016/j.mbplus.2019.04.001

161. Edwards P, Kang BW, Chau I. Targeting the stroma in the management of pancreatic cancer. *Front Oncol* (2021) 11:691185. doi: 10.3389/fonc.2021.691185

162. Gordon-Weeks A, Yuzhalin AE. Cancer extracellular matrix proteins regulate tumour immunity. *Cancers (Basel)* (2020) 12(11):3331. doi: 10.3390/cancers12113331

163. Rybchenko VS, Aliev TK, Panina AA, Kirpichnikov MP, Dolgikh DA. Targeted cytokine delivery for cancer treatment: engineering and biological effects. *Pharmaceutics* (2023) 15(2):336. doi: 10.3390/pharmaceutics15020336

164. Momin N, Mehta NK, Bennett NR, Ma L, Palmeri JR, Chinn MM, et al. Anchoring of intratumorally administered cytokines to collagen safely potentiates systemic cancer immunotherapy. *Sci Transl Med* (2019) 11(498). doi: 10.1126/scitranslmed.aaw2614

165. Lutz EA, Jailkhani N, Momin N, Huang Y, Sheen A, Kang BH, et al. Intratumoral nanobody–IL-2 fusions that bind the tumor extracellular matrix suppress solid tumor growth in mice. *PNAS Nexus* (2022) 1(5):pgac244. doi: 10.1093/pnasnexus/pgac244

166. Frey K, Schliemann C, Schwager K, Giavazzi R, Manfred J, Neri D. The immunocytokine F8-IL2 improves the therapeutic performance of sunitinib in a mouse model of renal cell carcinoma. *J Urol* (2010) 184(6):2540–8. doi: 10.1016/j.juro.2010.07.030

167. Lo KM, Lan Y, Lauder S, Zhang J, Brunkhorst B, Qin G, et al. huBC1-IL12, an immunocytokine which targets EDB-containing oncofetal fibronectin in tumors and tumor vasculature, shows potent anti-tumor activity in human tumor models. *Cancer Immunol Immunother* (2007) 56(4):447–57. doi: 10.1007/s00262-006-0203-1

168. Lei Y, Li X, Huang Q, Zheng X, Liu M. Progress and challenges of predictive biomarkers for immune checkpoint blockade. *Front Oncol* (2021) 11:617335. doi: 10.3389/fonc.2021.617335

169. Cui Y, Zhang P, Liang X, Xu J, Liu X, Wu Y, et al. Association of KDR mutation with better clinical outcomes in pan-cancer for immune checkpoint inhibitors. *Am J Cancer Res* (2022) 12(4):1766–83.

170. Zhang P, Pei S, Liu J, Zhang X, Feng Y, Gong Z, et al. Cuproptosis-related lncRNA signatures: Predicting prognosis and evaluating the tumor immune microenvironment in lung adenocarcinoma. *Front Oncol* (2023) 12:1088931. doi: 10.3389/fonc.2022.1088931

171. Zhang P, Pei S, Gong Z, Ren Q, Xie J, Liu H, et al. The integrated single-cell analysis developed a lactate metabolism-driven signature to improve outcomes and immunotherapy in lung adenocarcinoma. *Front Endocrinol (Lausanne)* (2023) 14:1154410. doi: 10.3389/fendo.2023.1154410

172. Kovács SA, Fekete JT, Győrffy B. Predictive biomarkers of immunotherapy response with pharmacological applications in solid tumors. *Acta Pharmacol Sin* (2023) 44(9):1879–89. doi: 10.1038/s41401-023-01079-6

173. Ren Q, Zhang P, Zhang X, Feng Y, Li L, Lin H, et al. A fibroblast-associated signature predicts prognosis and immunotherapy in esophageal squamous cell cancer. *Front Immunol* (2023) 14:1199040. doi: 10.3389/fimmu.2023.1199040

174. Pei L, Liu Y, Liu L, Gao S, Gao X, Feng Y, et al. Roles of cancer-associated fibroblasts (CAFs) in anti- PD-1/PD-L1 immunotherapy for solid cancers. *Mol Cancer* (2023) 22(1):29. doi: 10.1186/s12943-023-01731-z

frontiers | Frontiers in Oncology

TYPE Original Research
PUBLISHED 04 October 2023
DOI 10.3389/fonc.2023.1209707

OPEN ACCESS

EDITED BY
Takaji Matsutani,
Repertoire Genesis, Inc., Japan

REVIEWED BY
Xianwen Wang,
Anhui Medical University, China
Bernett Lee,
Singapore Immunology Network (A*STAR), Singapore

*CORRESPONDENCE
Jia Wang
wangjia77@hotmail.com
Dianlong Zhang
zdldoctor@163.com

†These authors have contributed equally to this work and share first authorship

RECEIVED 21 April 2023
ACCEPTED 18 September 2023
PUBLISHED 04 October 2023

CITATION
Chen H, Wang S, Zhang Y, Gao X, Guan Y, Wu N, Wang X, Zhou T, Zhang Y, Cui D, Wang M, Zhang D and Wang J (2023) A prognostic mathematical model based on tumor microenvironment-related genes expression for breast cancer patients. *Front. Oncol.* 13:1209707. doi: 10.3389/fonc.2023.1209707

A prognostic mathematical model based on tumor microenvironment-related genes expression for breast cancer patients

Hong Chen[1†], Shan Wang[1†], Yuting Zhang[1†], Xue Gao[2], Yufu Guan[3], Nan Wu[1], Xinyi Wang[1], Tianyang Zhou[1], Ying Zhang[1], Di Cui[4], Mijia Wang[1], Dianlong Zhang[3*] and Jia Wang[1*]

[1]Department of Breast Surgery, Second Affiliated Hospital of Dalian Medical University, Dalian, China, [2]Department of Pathology, The First Affiliated Hospital of Dalian Medical University, Dalian, China, [3]Department of Breast and Thyroid Surgery, Affiliated Zhongshan Hospital of Dalian University, Dalian, China, [4]Information Center, Second Affiliated Hospital of Dalian Medical University, Dalian, China

Background: Tumor microenvironment (TME) status is closely related to breast cancer (BC) prognosis and systemic therapeutic effects. However, to date studies have not considered the interactions of immune and stromal cells at the gene expression level in BC as a whole. Herein, we constructed a predictive model, for adjuvant decision-making, by mining TME molecular expression information related to BC patient prognosis and drug treatment sensitivity.

Methods: Clinical information and gene expression profiles were extracted from The Cancer Genome Atlas (TCGA), with patients divided into high- and low-score groups according to immune/stromal scores. TME-related prognostic genes were identified using Kaplan-Meier analysis, functional enrichment analysis, and protein-protein interaction (PPI) networks, and validated in the Gene Expression Omnibus (GEO) database. Least absolute shrinkage and selection operator (LASSO) Cox regression analysis was used to construct and verify a prognostic model based on TME-related genes. In addition, the patients' response to chemotherapy and immunotherapy was assessed by survival outcome and immunohistochemistry (IPS). Immunohistochemistry (IHC) staining laid a solid foundation for exploring the value of novel therapeutic target genes.

Results: By dividing patients into low- and high-risk groups, a significant distinction in overall survival was found ($p < 0.05$). The risk model was independent of multiple clinicopathological parameters and accurately predicted prognosis in BC patients ($p < 0.05$). The nomogram-integrated risk score had high prediction accuracy and applicability, when compared with simple clinicopathological features. As predicted by the risk model, regardless of the chemotherapy regimen, the survival advantage of the low-risk group was evident in those patients receiving chemotherapy ($p < 0.05$). However, in patients

receiving anthracycline (A) therapy, outcomes were not significantly different when compared with those receiving no-A therapy ($p = 0.24$), suggesting these patients may omit from A-containing adjuvant chemotherapy. Our risk model also effectively predicted tumor mutation burden (TMB) and immunotherapy efficacy in BC patients ($p < 0.05$).

Conclusion: The prognostic score model based on TME-related genes effectively predicted prognosis and chemotherapy effects in BC patients. The model provides a theoretical basis for novel driver-gene discover in BC and guides the decision-making for the adjuvant treatment of early breast cancer (eBC).

KEYWORDS

breast cancer, tumor microenvironment, prognostic, resistance, therapeutic sensitivity

1 Introduction

Breast cancer (BC) is the most common malignancy in women. According to cancer burden data from the International Agency for Research on Cancer (World Health Organization, 2020), up to 2.26 million new BC cases were recorded globally, and together with lung and colorectal cancer, accounts for more than half of new female cancers (1). Long-term survival in BC patients varies with the stage status at the time of initial diagnosis. The overall 5-year BC survival rate is 98% for stage I, 92% for stage II, 75% for stage III, and a sudden drop to 27% for stage IV (2). Currently, the main BC treatments include surgery, radiotherapy, and systemic therapy (chemotherapy, endocrine therapy, and targeted medication) (3–6). However, 40% of BC patients are resistant to current available chemotherapy or targeted therapies (7). With the high heterogeneity of BC, the traditional immunohistochemical staining quadruple type is no longer able to provide more accurate personalized treatment for early BC (eBC) patients, especially considering the impact of new targets and targeted drugs. Multigene panels, such as PAM50 intrinsic BC subtypes, 21 Gene Recurrence Score and 70-gene Prognostic Signature have quietly stepped on to the historical stage, were incorporated into the TNM staging system by the American Joint Committee on Cancer (8^{th} edition) (8). Unequivocally, for prognosis predictions, multivariable indicators are more accurate and objective when compared with single biomarkers (9). Hence, to identify more biomarkers and guide precise personalized eBC treatment, more risk models based on gene expression profiles, are required.

Tumor progression is a complex process with interactions occurring among tumor cells, the tumor microenvironment (TME), and the immune system (10–12). The TME reflects the cellular environment of the tumor (13, 14), including cell components other than tumor cells, e.g., immune and stromal cells, extracellular matrix molecules, and cytokines (15, 16). Previous studies indicated that stromal cells have important roles in tumor growth, disease development (17, 18), and drug resistance (19). Immune cells exert regulatory and destructive effects toward tumor cells and may have dual promotional and antagonistic functions (20–22). Through crosstalk, they participate in tumor processes and development, are involved in mechanisms underpinning the TME, and contribute to tumor diagnostic and prognostic evaluation (23–26). Increasingly, the TME is considered a therapy target (27, 28); the prediction and prognostic value of tumor-infiltrating lymphocytes (TILs) in BC is gradually being recognized (29, 30). For example, ECOG2197 and ECOG1199 clinical studies identified an approximate 15% reduction in relapse and mortality rates for every 10% increase in TIL levels (30). The KEYNOTE-086 study indicated that higher TIL levels were associated with significant improvements in objective response rates for pembrolizumab (31). However, few studies have reported on how the TME may be used as a prognostic and predictive biomarker in assessing tumor immunity and treatment efficiency in BC patients. In our study, we show that TME may be used to accurately predict the prognosis in BC patients, independent of multiple clinicopathological factors, and predict the efficacy of chemotherapy and immunotherapy in these patients. Critically, low-risk patients in our prediction model may be exempted from the A-adjuvant chemotherapy regimens, thus providing guidance for patients with de-escalated individual treatment.

Yoshihara et al. developed the ESTIMATE algorithm where gene expression profiles were used to predict infiltrating stromal and immune cell levels in the TME (23). Previous studies reported the algorithm was effective in predicting TME status, with immune and stromal scores predicting tumor-associated normal cells penetration. However, studies focused exclusively on immune cells (32, 33) rather than stromal cells, and largely ignored their role in tumorigenesis and development. Secondly, due to complex reticular regulatory mechanisms in the TME, a single pathway or single cell subpopulation cannot fully identify mechanisms between the TME and tumors (34). Therefore, a comprehensive understanding of tumor-associated normal cells in tumor tissues may provide important insights into BC biology. In our study, we comprehensively evaluated molecular expression networks in stromal and immune cells to (1) understand the significance of TME-related genes and (2) provide a more accurate and comprehensive assessment of the TME during BC development and treatment.

We used several bioinformatics approaches to explore the TME during BC occurrence and progression. Based on TME-related genes expression, we constructed a new prognostic risk model to evaluate the prognostic value of the TME. Differences between the immune microenvironment in BC patients were comprehensively analyzed. Additionally, underlying signal pathways were preliminarily elucidated. This work provides new insights into the molecular mechanisms underpinning BC tumor occurrence and development, and may help predict prognosis in BC patients and assess therapeutic efficacy.

2 Methods

2.1 Clinical specimens

Two BC tissue specimens were obtained from patients at the Second Hospital of Dalian Medical University. Invasive breast cancer was pathologically confirmed in all patients not on chemotherapy or radiotherapy before tissue collection. Written informed consent was obtained from patients, and the study was approved by the Ethics and Human Subject Committee of the Second Hospital of Dalian Medical University (NO.2023191). Procedures were performed according to hospital guidelines and regulations.

2.2 Data sources

Gene expression matrices of enrolled patients were obtained from The Cancer Genome Atlas (TCGA) and the Gene Expression Omnibus (GEO) databases. We included 1,069 BC samples from TCGA as the training cohort. The gene-expression profiles of TCGA-BRCA in the Fragments Per Kilobase per Million (FPKM) format were obtained from the TCGA portal (http://cancergenome.nih.gov), and then the ID conversion was carried out through the operation of ENSG ID to GeneSymbol, and finally the data standardization was carried out, and the standardization method is log2 (X+1). In addition, the BC patients' clinical data (gender, age, histological type, and survival) were downloaded from TCGA. After searching the datasets with more than 150 human breast cancer samples with complete expression profile data, we selected the GSE42568, GSE88770, GSE48390, and GSE162228 dataset from the GEO as the validation cohort. These datasets were verified using the GPL570 platform. To ensure the scientificity and accuracy of the research, we successfully removed batch effect with COMBAT when combining GEO multi-data sets (Supplementary Figure S1). Additionally, clinical survival and outcome data of BC patients were also downloaded from this database.

2.3 Identifying differentially expressed genes (DEGs)

Data analysis was performed using the "limma" R package. Fold change > 1.5, $p < 0.05$, and false discovery rate (FDR) < 0.05 were set as the cutoffs to screen for DEGs.

2.4 DEG enrichment analysis

Gene ontology (GO) and Kyoto Encyclopedia of Genes and Genomes (KEGG) analyses were performed to enrich the DEGs into associated pathways using the "clusterProfiler" R package (version 3.14.3). $p < 0.05$ and FDR < 0.05 were considered significant.

2.5 Constructing and validating a risk model based on TME-related genes

Least absolute shrinkage and selection operator (LASSO) Cox regression analysis identified genes most correlated with OS, and 10-round cross-validation was performed to prevent overfitting. The risk score for each patient was then calculated based on the expression levels of genes. Risk score: -0.0419970982477039 * NPY1R - 0.162055812415471 * CELSR2 - 0.043004672153174 * STC2 - 0.0716026845406244 * SCUBE2 + 0.2810654696502 * GIMAP2 + 0.0773881988402307 * HLA-DPB1 - 0.0232515777318596 * CXCL14 - 0.721867840891611 * KLRB1 - 0.253187064109637 * BIRC3 - 0.0587584464454724 * IL18 - 0.242105852075788 * PSMB8 + 0.198881881356143 * CD1C + 0.0814403392760682 * TNFAIP8 + 0.076656198308623 * IRF1. According to the median risk score, BC patients were divided into high- and low-risk groups. Kaplan–Meier analysis was employed to estimate the difference in OS between the categorized patients via the R package "survival." The prognostic capability of the risk model was validated using time-dependent receiver operating characteristic (ROC) analysis with the R package "pROC".

2.6 Evaluation of risk model independence

Univariate and multivariable Cox regression analyses were performed to estimate whether the risk score was an independent predictor of BC prognosis. A subgroup analysis was conducted to confirm the independence of the risk model. The patients with BC in the training cohort were regrouped into new subgroups based on different clinical characteristics, and the patients in each subgroup were stratified into high- and low-risk groups, based on the median risk score.

2.7 Immunohistochemistry (IHC)

Patient tissue specimens were fixed in 10% neutral formalin, embedded in paraffin, and sectioned into 4 μm sections before staining. Sections were deparaffinized, rehydrated, and blocked for endogenous peroxidase activity. Next, antigen retrieval was performed in citrate buffer (pH 6.0) and sections autoclaved for 90 s at 121°C. After washing in phosphate buffered saline (3 min × 3), sections were blocked in goat serum at room temperature for 30 min and incubated with primary antibodies (PSMB8, (1:200), Proteintech Group, IL, USA; cIAP2, (1:200), Proteintech Group, IL, USA) overnight at 4° C. The next day, sections were incubated

with secondary antibodies (Maxin Biotechnologies, China) and treated with diaminobenzidine hydrochloride to visualize immunoreactivity. The immunohistochemical scoring was performed independently by two experienced pathologists, who had no knowledge of the clinicopathological information.

2.8 Nomogram construction

Nomograms are user-friendly clinical tools used to predict disease prognosis. The risk score and clinical parameters were subjected to univariate Cox regression analysis, and features with P values < 0.05 were subjected to multivariable COX regression analysis. Features with p values < 0.05 after multivariate analysis were incorporated into nomograms that were constructed to predict the 3- and 5-year OS rates. The nomogram was based on three independent prognostic factors: age, tumor stage, and the risk score. Factors corresponded to a specific point by drawing a line straight up to the point axis. The sum of the three factor points indicated the total points. By drawing a perpendicular line from the total point axis to the two-outcome axes, estimated 3- and 5-year OS probabilities were obtained. Observed 3- and 5-year OS rates were compared with predicted rates to further verify predictive performance. We assessed nomogram goodness-of-fit using calibration plots.

2.9 Immune analysis

The estimation of stromal and immune cells in malignant tumor tissues using expression data (ESTIMATE) method was applied to calculate the immune score, stromal score, and ESTIMATE score of the patients, via the R package "estimate". Tumor immune estimation resource (TIMER) analysis was conducted to evaluate the abundance of six types of immune cells (neutrophils, CD4 T cells, macrophages, CD8 T cells, dendritic cells (DCs), and B cells). The MCPcounter (microenvironment cell populations-counter) algorithm was also used to assess T cell, CD8 T cell, cytotoxic lymphocyte, B cell lineage, natural killer (NK) cell, monocytic cell lineage, myeloid DC, neutrophil, endothelial cell, and fibroblast abundance.

2.10 Immune infiltration analysis of hub genes

TIMER was used to analyze correlations between hub gene expression and the degree of lymphocyte infiltration. TISIDB was also used to analyze correlations between hub gene expression and immune molecule expression in BC. We used the GSCA Lite (A Web Server for Gene Set Cancer Analysis: http://bioinfo.life.hust.edu.cn/web/GSCALite) online tool to analyze the correlation between hub genes expression and sensitivity to current chemotherapeutic or targeted drugs for BC.

2.11 Statistical analysis

Statistical analyses were completed using R (version 3.6.3). Discontinuous data were presented as number (percentage), and continuous data were displayed as mean± standard deviation. The Wilcoxon rank sum test was utilized to compare two groups and the Kruskal-Wallis test to compare multiple groups. In addition, the survfit function of "survival" package in R was used to analyze the prognostic differences between the two groups, and the log-rank test was used to further evaluate the significance of prognostic differences between the two groups. Statistical significance was defined as $p < 0.05$.

3 Results

3.1 Immune scores and stromal scores are significantly associated with BC subtypes, hormone receptor status, and overall survival (OS)

We downloaded the gene expression profiles and clinical information of 1,069 BC patients from The Cancer Genome Atlas (TCGA). Based on gene expression, BC can be mainly classified into Luminal A, Luminal B, HER2-enriched, Basal-like, and Normal-like (35, 36). The ESTIMATE algorithm showed that the highest mean immune score of Normal-like subtype was highest among all five subtypes, followed by Basal-like subtype, HER2-enriched subtype, and Luminal A subtype. The Luminal B subtype cases had the lowest immune scores (Supplementary Figure S2A, $p < 0.0001$). However, stromal scores, from high to low, were Normal-like, Luminal A, HER2-enriched, Luminal B, and Basal-like (Supplementary Figure S2B, $p < 0.0001$). The mammary gland is a hormone-responsive organ- the endocrine system is closely related to its development and disease occurrence, therefore we performed correlation analyses between immune and stromal scores and hormone receptor status. As shown in Supplementary Figure S2C, patients with progesterone receptor positive (PR+) had lower immune scores when compared with progesterone receptor negative (PR-) patients ($p < 0.01$), while estrogen receptor positive (ER+) patients had lower scores when compared with estrogen receptor negative (ER-) patients ($p < 0.0001$). In contrast, PR+/ER+ patients had higher scores when compared with PR-/ER- patients, and ER+ patients had higher when compared with ER- patients in the stromal scores (Supplementary Figure S2D, $p < 0.0001$). Thus, stromal and immune scores were significantly associated with BC subtypes and hormone receptor status.

To identify potential OS correlations with immune scores and/or stromal scores, we divided our cohort into top and bottom halves (high vs. low score groups) based on their scores. Kaplan-Meier survival curves showed that median OS in the low score group was longer when compared with the high score group when based on immune scores (Supplementary Figure S2E, $p = 0.01$). Consistently, patients with lower stromal scores had longer median OS when

compared with patients with higher stromal scores (Supplementary Figure S2F, p = 0.85), although statistical significance was not observed.

3.2 Differentially expressed genes (DEGs) in BC and correlations with OS

To determine global gene expression profile correlations with immune scores and/or stromal scores, we compared Affymetrix microarray data in 1,069 BC patients. Heatmaps in Figure 1 showed distinct gene expression profiles of cases belong to immune scores/stromal scores groups. Based on immune scores, 943 genes were upregulated, and 71 genes downregulated in the high score group than the low score group (Figure 1A, fold change > 1.5, $p < 0.05$). Similarly, 1,011 genes were upregulated, and 50 genes were downregulated in the high score group (Figure 1B, fold change > 1.5, $p < 0.05$). Moreover, Venn diagrams (Figures 1C, D) showed that 498 genes were upregulated in the high-score group, while two genes were downregulated. We performed subsequent analyses by focusing on all DEGs obtained based on comparisons of immune and stromal scores. To determine potential DEGs functions, we performed functional enrichment analysis on 1,574 DEGs. Top Gene Ontology (GO) terms included immune system process, immune response, extracellular matrix, signalling receptor binding, and integrin binding (Figures 1E–G).

To explore individual DEG correlations with OS, we performed Kaplan-Meier survival curve analysis. In total, 421 DEGs out of 1,574 significantly predicted OS in the log-rank test ($p < 0.05$, selected genes are shown in Supplementary Figure S3).

3.3 Protein-protein interaction (PPI) of genes of prognostic value

To better understand interactions between prognostic value DEGs, we examined protein-protein interaction (PPI) networks in STRING. The network consisted of eight modules, which included 218 nodes and 704 edges. We selected the top three important modules for further analysis (Supplementary Figure S4). For descriptive convenience, we termed these modules MCODE1, MCODE2, and MCODE3 modules, respectively. In MCODE1 (Supplementary Figure S4A), ACKR3, CXCR3, and CCR5 had higher degree values. In MCODE2 (Supplementary Figure S4B), several immune response key genes occupied the module center and included HLA-DRB5, HLA-DRB1, CD247, and LCK. In MCODE3 (Supplementary Figure S4C), IL2RG, CD8B, and CD8A were significant nodes, as they had the most connections with other module members.

3.4 Functional enrichment analysis of genes of prognostic value

Consistent with PPI network analysis, functional enrichment analysis of these genes also identified strong associations with immune responses. Top GO terms included extracellular region and extracellular space (Supplementary Figure S5A), immune response (Supplementary Figure S5B), and antigen binding and signalling receptor binding (Supplementary Figure S5C). Additionally, all pathways from Kyoto Encyclopedia of Genes and Genomes (KEGG) analysis (Supplementary Figure S5D) were associated with immune responses.

3.5 Gene Expression Omnibus (GEO) database validation

To determine if genes identified by TCGA had prognostic significance in other BC patients, we downloaded and analyzed gene expression data from 435 BC patients (GSE42568, GSE88770, GSE48390, and GSE162228) from the GEO database. Interestingly, 15 genes were significantly and prognostically related to the validation set (Supplementary Figure S6, $p < 0.05$); NPY1R, CELSR2, STC2, SCUBE2, GIMAP2, HLA-DPB1, TFF1, CXCL14, KLRB1, BIRC3, IL18, PSMB8, CD1C, TNFAIP8, and IRF1.

3.6 Constructing a prognostic risk model based on TME-related genes

Subsequently, we performed least absolute shrinkage and selection operator (LASSO) Cox regression analysis to select highly relevant genes from these 15 genes. Finally, 14 were identified as related to the TME in BC, and optimal values of the penalty parameter were determined by 10-fold cross-validation (Figures 2A, B). We then constructed a prognostic model based on these genes, with the risk score of each sample from the training cohort calculated according to this model. Based on median risk score, BC samples from the training cohort were divided into high- and low-risk groups. To assess the OS in these groups, Kaplan-Meier curves were generated and showed that OS in the high-risk group was worse than that in the low-risk group, indicating the validity of the risk score prediction (Figure 2C, $p < 0.0001$). Additionally, the expression of the TME-related genes, survival status, and survival time distribution for patients according to risk scores are shown in Figure 2D. In terms of model diagnosis, the AUC of the time-dependent receiver operating characteristic (ROC) curves were 0.69 for 1-year survival, 0.74 for 3-year survival, and 0.74 for 5-year survival, respectively, suggesting acceptable stability of the risk model (Figure 2E). In addition, to explore if BC subtypes affect survival, we grouped patients according to subtypes and subsequently performed survival analyses. Clearly, no differences in survival due to subtypes were observed, suggesting that the BC subtype did not affect survival (Supplementary Figure S7, p = 0.26). Together, our risk model, constructed from TME-related genes, appeared to accurately predict prognosis in BC patients.

Next, to identify hub genes, we identified interactions between genes in the TME model by constructing a PPI network in STRING.

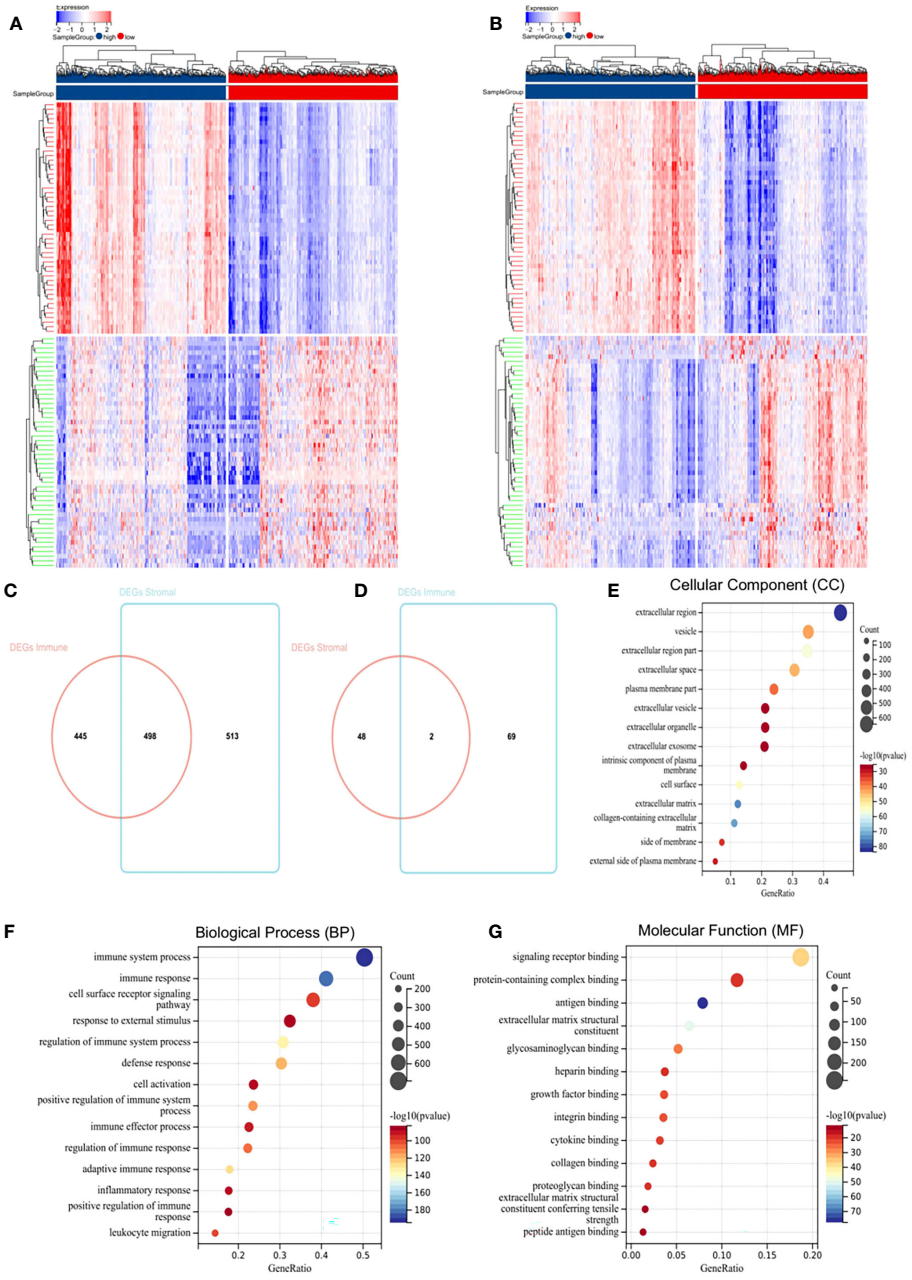

FIGURE 1
Differentially expressed genes (DEGs) in BC and their correlations with overall survival (OS). **(A)** Heatmap of the DEGs of immune scores. **(B)** Heatmap of the DEGs of stromal scores. **(C, D)** Venn diagrams showing the number of commonly upregulated **(C)** or downregulated **(D)** DEGs in stromal and immune score groups. **(E–G)** Gene Ontology analysis (GO) analysis.

The network included 13 nodes and six edges. PSMB8 and BIRC3 had the maximum neighboring genes and were identified as hub genes. The Kaplan-Meier analysis showed both were the prognostic indicators, and its high expression favored the prognosis (Supplementary Figure S2, $p < 0.05$). To verify this phenomenon still exists in the human body, we used immunohistochemistry to compare hub protein expression and identified high PSMB8 and BIRC3 expression trends in BC epithelial cells when compared with paracancerous cells (Figure 3).

3.7 The risk model is an independent BC prognosis indicator

Univariate Cox regression analysis showed that risk score could predict the prognosis of BC patients (Figure 4A, $p < 0.0001$). In the multivariable Cox regression analysis, risk score remained statistically significant (Figure 4B, $p < 0.0001$), indicating our risk model was an independent prognostic factor for BC. Additionally, BC patients in the training cohort were

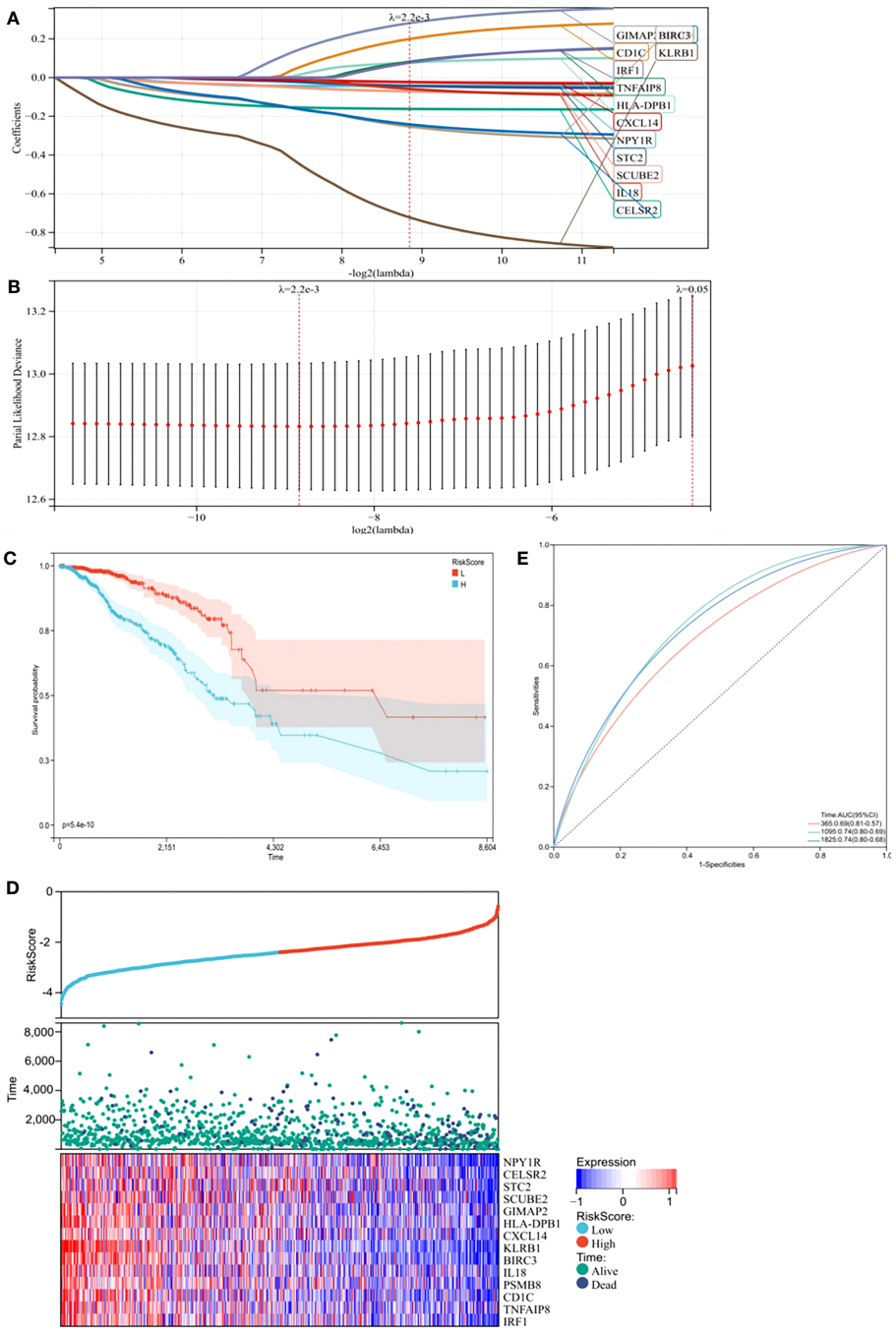

FIGURE 2
Construction of a prognostic model in the training cohort. **(A)** The Least absolute shrinkage and selection operator (LASSO) Cox regression analysis identified 14 genes most correlated with prognostics. **(B)** The optimal values of the penalty parameter were determined by 10-round cross-validation. **(C)** Patients in the high-risk group (blue) exhibited worse overall survival (OS) than those in the low-risk group (red). **(D)** Distribution of risk scores, survival profiles, and heat maps showing characteristic expressions of the low and high risky groups. **(E)** Time-dependent receiver-operating characteristic (ROC) curve.

regrouped into subgroups based on age (< 50 and ≥ 50 years old), and TNM stage (stage I, stage II, stage III, and stage IV). Regardless of subgroups, low-risk group patients still showed significantly longer survival (Figures 4C, D, $p < 0.05$), which indicated excellent risk model independence.

3.8 Establishing a nomogram

To create a quantitative method to predict OS, we integrated the risk score and independent clinicopathological prognostic factors, including age and TNM stage, to construct a nomogram (Figure 5A).

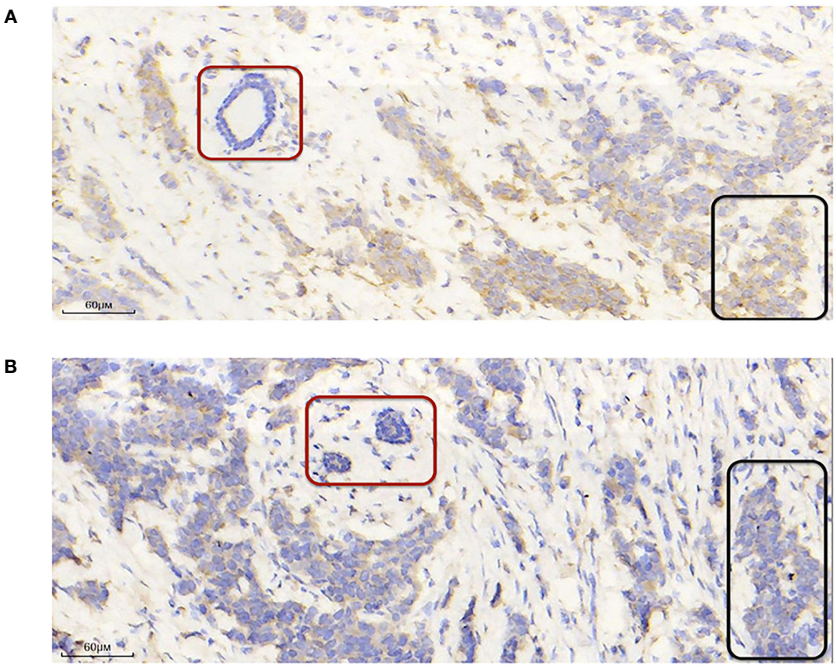

FIGURE 3
PSMB8 and BIRC3 expression. **(A)** Representative immunohistochemical image showing high and low PSMB8 expression. **(B)** Representative immunohistochemical image showing high and low BIRC3 expression. The red area indicates paracarcinoma epithelial cells and the black area indicates breast cancer epithelial cells.

To evaluate its prognostic value, we compared the concordance index (C-index) of the nomogram with TNM stage, and as shown in Table 1, the nomogram improved the prediction accuracy for BC. We compared predicted 3- and 5-year survival probabilities with actual probabilities and observed the calibration curve showed good concordance between these probabilities, thereby reflecting high nomogram accuracy and dependability (Figure 5B). Taken together, the nomogram, which integrated risk score, showed good performance and applicability, and has potential as a clinical tool to predict prognosis in BC patients.

3.9 Correlations between the risk model and clinicopathological features

Relationships between prognostic risk score and clinical characteristics were further investigated in the training cohort. Age, T category, M category and TNM stage were significantly related to risk score, whereas gender and N category were not (Figure 6A, $p < 0.05$). As observed Figure 6B, patients with HER2-enriched had the highest risk score, followed by Basal-like, Luminal B, and Luminal A subtypes, while Normal-like patients had the lowest scores ($p < 0.0001$). Association analysis with hormone receptor status showed that patients with PR+/ER+ had lower risk score when compared with PR-/ER- patients, and ER+ patients had lower risk score when compared with ER- patients (Figure 6C, $p < 0.0001$).

To better visualize the clinicopathological features in individual patients and assess correlations with survival, we used an alluvial diagram which showed that risk categories in the prediction model accurately predicted patient survival (Figure 6D).

3.10 Correlation between the risk model and immune infiltration

Association between the risk model and immune cell infiltration was assessed using several immune infiltration approaches. ESTIMATE algorithm data showed that immune, stromal, and ESTIMATE scores in the high-risk BC patient group were lower when compared with BC patients in the low-risk group (Figure 7A, $p < 0.0001$). The TIMER algorithm showed that B cell, neutrophil, CD4 T cell, dendritic cell (DC), and CD8 T cell abundance, but not macrophage, was statistically higher in the low-risk group when compared with the high-risk group (Figure 7B, $p < 0.0001$). Moreover, MCPcounter algorithm results showed that T cells, CD8 T cells, cytotoxic lymphocytes, B lineage cells, natural killer (NK) cells, monocytic lineage cells, myeloid DCs, neutrophils, endothelial cells, and fibroblasts were highly infiltrated in the low-risk group (Figure 7C, $p < 0.01$). Thus, our risk model correlated well with different immune microenvironment components.

Given the significant correlation of our risk model with the BC immune microenvironment, we next examined relationships between the risk model and immune cell subtype infiltration using Pearson's algorithm. As shown in Figure 7D, correlation values for B cells, CD4 T cells, CD8 T cells, DCs, and neutrophils with risk scores were −0.35, −0.48, −0.49, −0.43, and −0.39, respectively. As expected, immune cell infiltration levels were

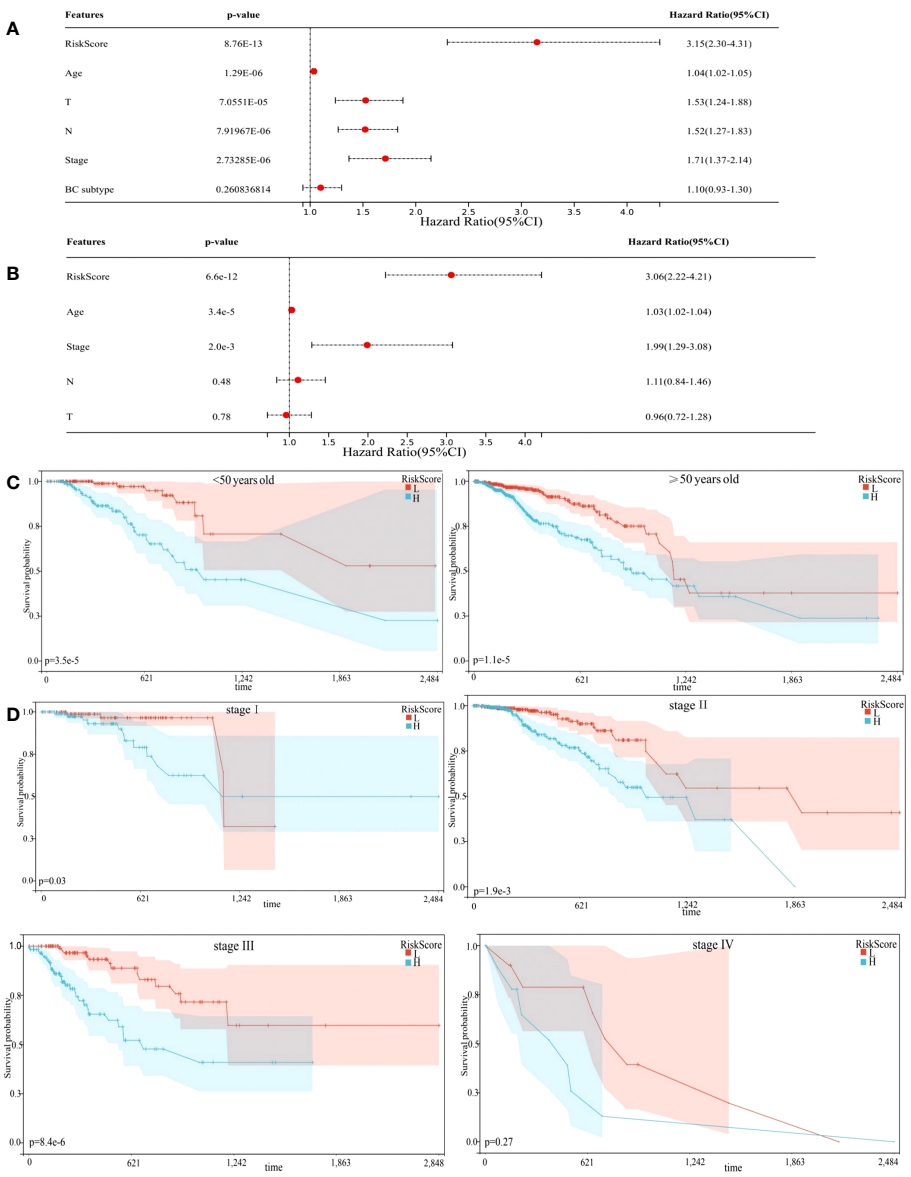

FIGURE 4
Prognostic model independence. **(A)** Results of Univariate Cox regression analysis. **(B)** Results of multivariable Cox regression analysis. **(C, D)** Subgroup analyses suggesting the independence of the prognostic model regarding age, and TNM stage.

significantly and positively correlated with prognosis (Figure 7D, $p < 0.0001$).

3.11 Practical analysis of the risk model

To further confirm model practicability and reliability, it was verified using a validation cohort. Risk scores, survival status, and gene expression are shown in Figure 8A. As expected, significant differences in OS were identified between groups, with longer OS in the low-risk group (Figure 8B, $p < 0.0001$). Furthermore, relationships between risk score and the BC immune microenvironment were confirmed in the validation cohort. From ESTIMATE, TIMER, and MCPcounter analysis, the low-risk group was significantly associated with high immune cell infiltration levels From ESTIMATE analysis, the low-risk group was significantly associated with high stromal, immune, and ESTIMATE scores (Figure 8C, $p < 0.0001$). In TIMER analysis, the abundance of the five aforementioned immune cell types, except macrophages, was statistically different between groups (Figure 8D, $p < 0.0001$), and immune cell abundance (all types) was significantly higher in the low-risk group than the high-risk group. The MCPcounter algorithm showed that T cells, cytotoxic lymphocytes, B lineage, monocytic lineage cells, myeloid DCs, endothelial cells, neutrophils, and fibroblasts were in a high infiltration state in the low-risk group (Figure 8E, $p < 0.05$). Therefore, our TME-related gene risk model was associated with BC prognosis and the immune microenvironment.

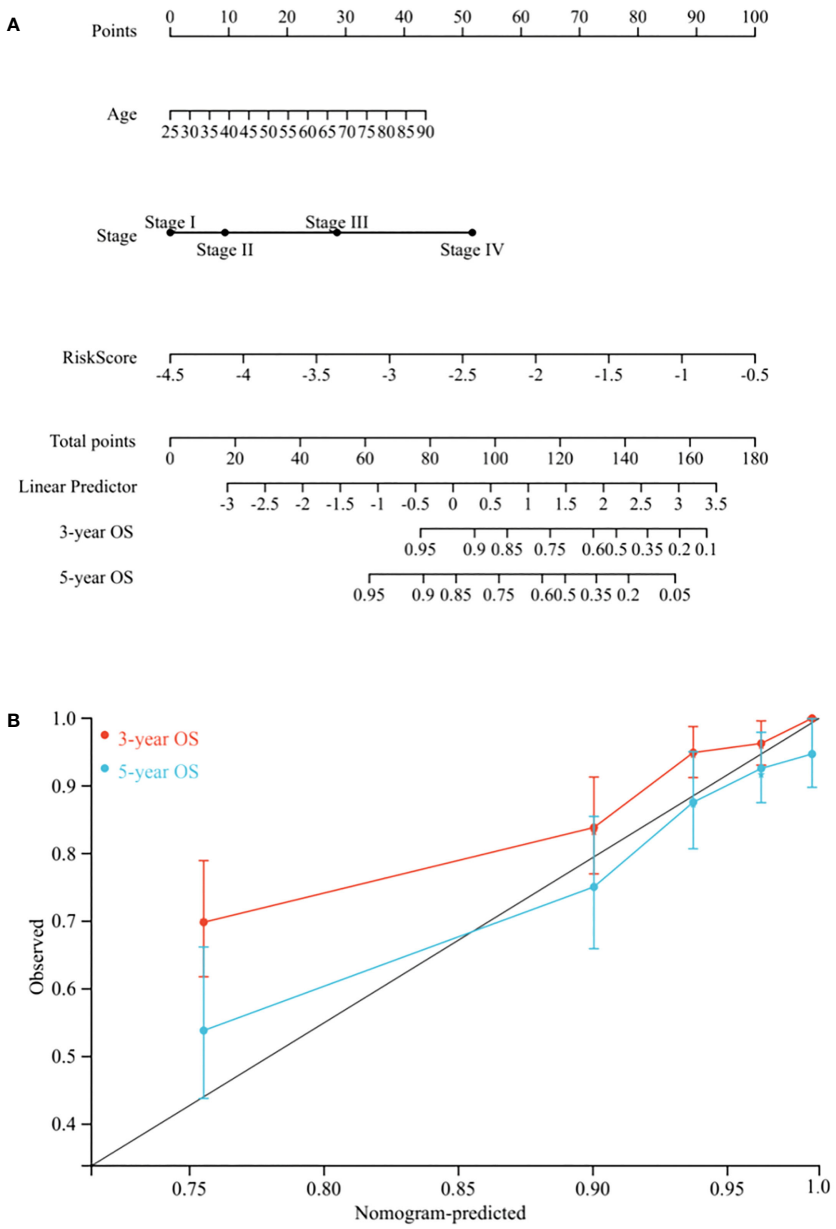

FIGURE 5
Nomogram construction. **(A)** Nomogram predicting 3-, and 5-year OS for BC patients in the training cohort based on risk score and other clinicopathological parameters (age and TNM stage). **(B)** The calibration curves of nomograms between predicted and observed 3- and 5-year OS in the training cohort. The gray line of 45° represents the perfect prediction of the nomogram.

3.12 The risk model predicts chemotherapy efficacy

As neoadjuvant and adjuvant chemotherapies are reportedly related to immune infiltration (37), we evaluated if chemotherapy influenced BC prognosis. According to the NCCN Guidelines in Oncology, anthracycline + cyclophosphamide (AC), AC followed by taxane (AC-T), and taxane + cyclophosphamide (TC) are major chemotherapy regimens. The OS advantage was observed in the low-risk group, regardless of whether they received chemotherapy or not. And whether in high-risk group or low-risk group, patients who received chemotherapy had a better prognosis (Figure 9A, $p < 0.0001$). In the low-risk group, the OS advantage was evident in patients who received TC and AC-T chemotherapy regimens when compared with those who received no chemotherapy (Figure 9B, $p < 0.05$). In contrast, the chemotherapy benefits in the high-risk group were observed for AC, TC, and AC-T chemotherapy

TABLE 1 The concordance indexes of tumor-node-metastasis (TNM) stage and nomogram system.

	C-index	95% Confidence Interval
Nomogram	0.800	0.76-0.84
TNM stage	0.763	0.72-0.81

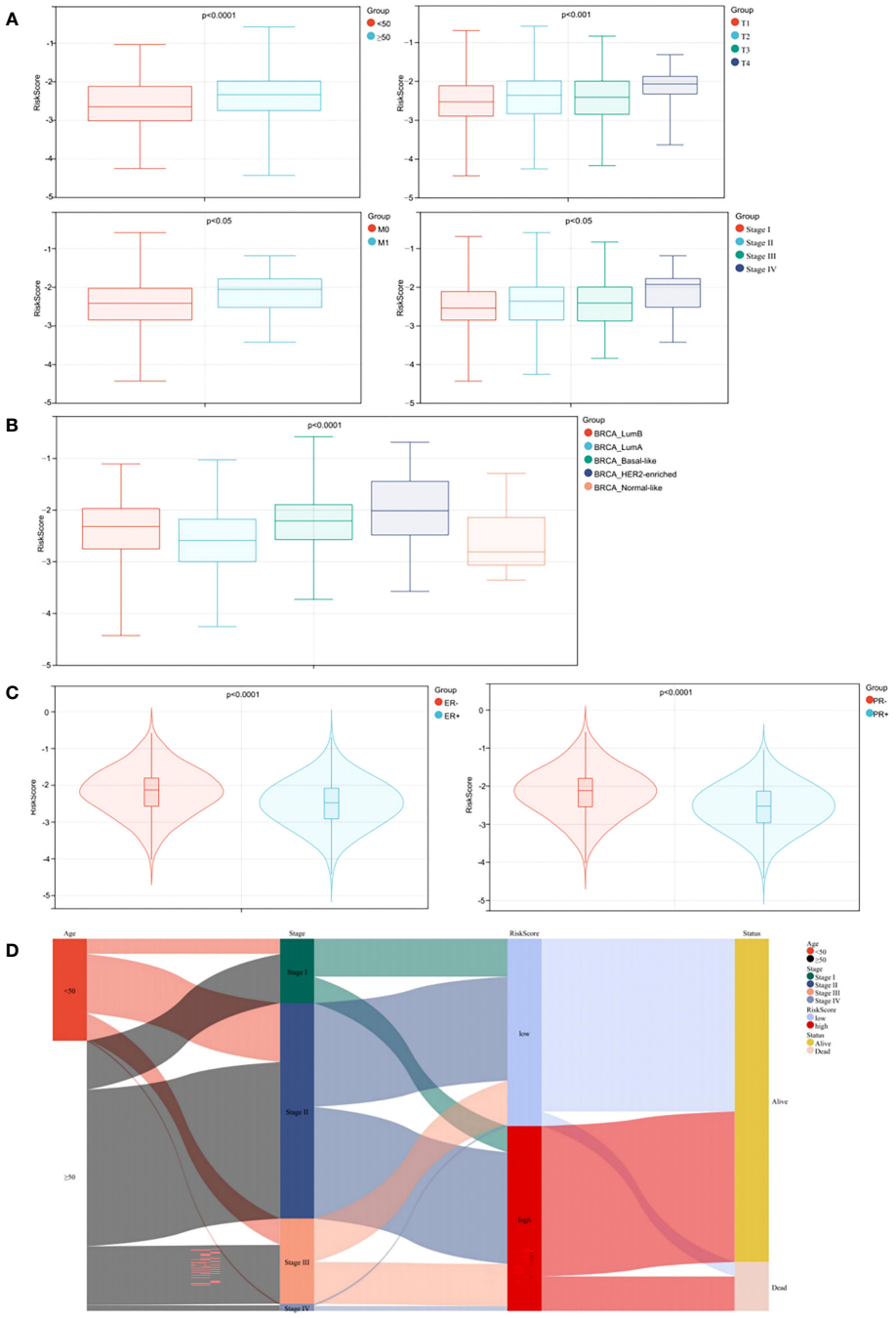

FIGURE 6
Stratified analysis of clinical characteristics for risk score in the prognostic model. **(A)** Correlation analysis of the risk score and the clinical characteristics. **(B)** Correlation analysis of the risk score and the BC subtypes. **(C)** Correlation analyses of the risk score and the status of PR/ER. **(D)** Alluvial diagram.

regimens (Figure 9C, $p < 0.05$). More importantly, subgroup interaction evaluations suggested that better chemotherapy outcomes were achieved in low-risk patients regardless of the chemotherapy regimen (Figure 9D, $p < 0.05$).

We also explored if the A-regimen was an indispensable chemotherapy agent in the low-risk group. As shown in Figure 9E, no significant differences in prognosis outcomes for patients treated with the A-regimen were identified, regardless of low- or high-risk ($p > 0.05$). Further subgroup analysis showed no significant differences in prognosis outcomes in low-risk patients who received the A-regimen when compared with those who did not (Figure 9F, $p > 0.05$). These observations suggested that the low-risk group selected by this prediction model has the opportunity to exempt the A-containing adjuvant chemotherapy regimen.

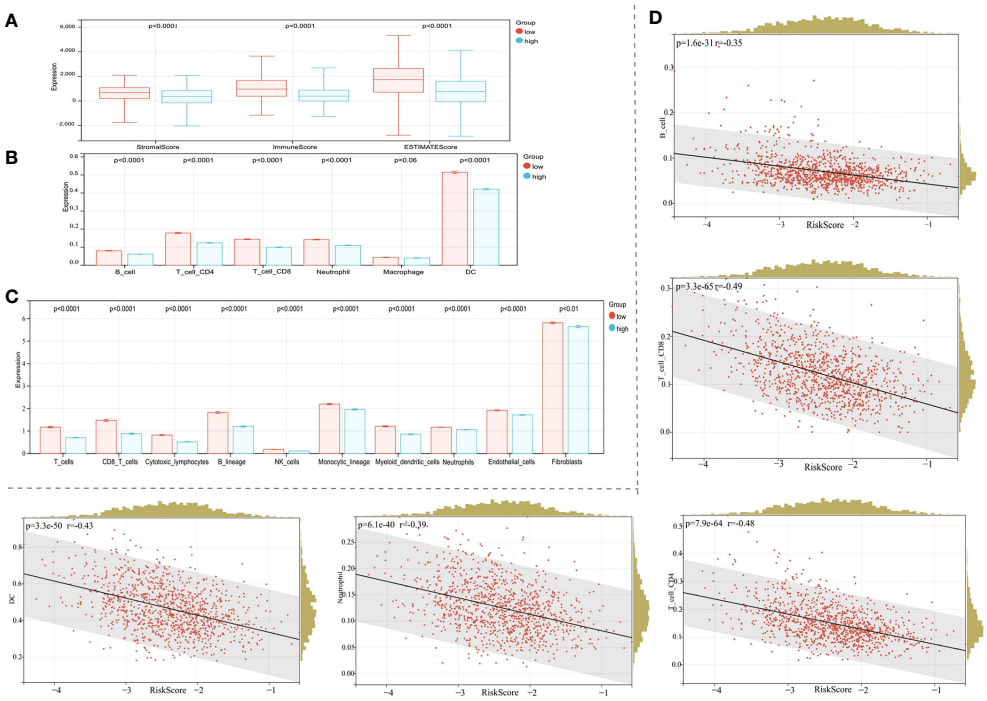

FIGURE 7
Correlation between the risk model and the immune microenvironment. **(A)** The ESTIMATE algorithm. **(B)** The TIMER algorithm. **(C)** The MCPcounter algorithm. **(D)** Correlations between the risk score and the infiltration of immune cell subtypes.

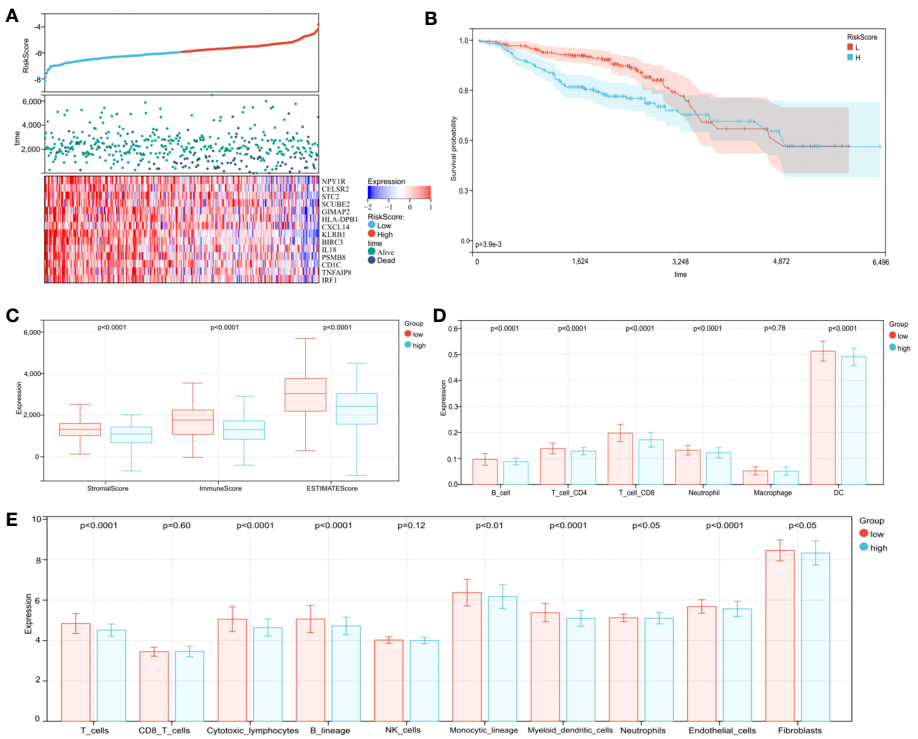

FIGURE 8
Validation of the prognostic risk model in the validation cohort. **(A)** Distribution of risk scores, survival profiles, and heat maps showing characteristic expressions of the low- and high-risk groups. **(B)** Patients in the high-risk group (blue) exhibited worse overall survival (OS) than those in the low-risk group (red). **(C)** The ESTIMATE algorithm. **(D)** The TIMER algorithm. **(E)** The MCPcounter algorithm.

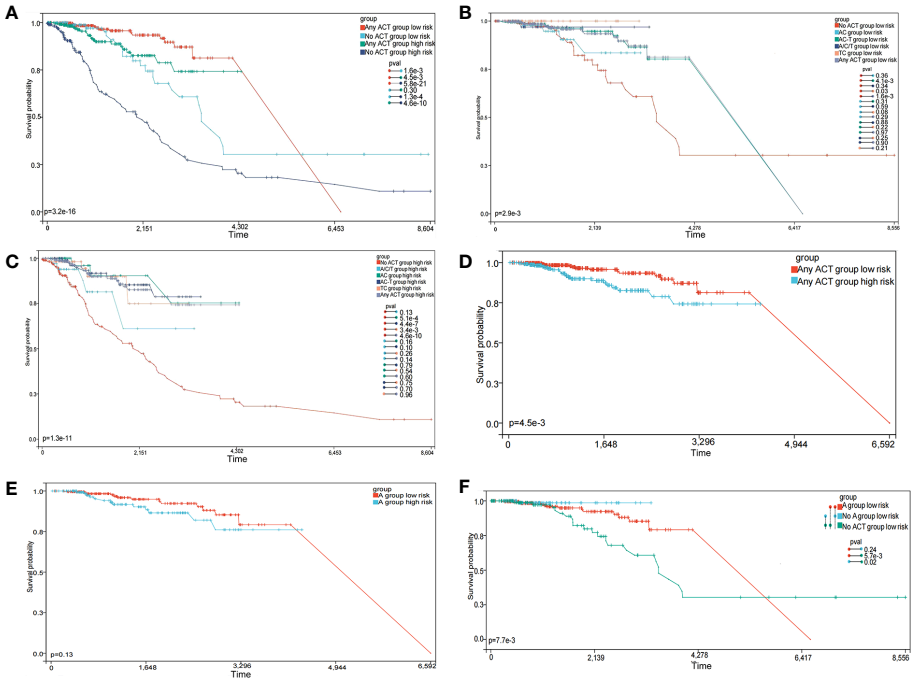

FIGURE 9
The prognostic model predicts chemotherapy efficacy. **(A)** Subgroup analysis of adjuvant chemotherapy (ACT) benefit for overall survival (OS) of low-and high-risk patients in the TCGA database. **(B)** OS analysis in patients with different chemotherapy regimens in the low-risk group. **(C)** OS analysis in patients with different chemotherapy regimens in the high-risk group. **(D)** OS analysis of treated patients in high- and low-risk groups. **(E)** OS analysis of patients receiving the anthracycline **(A)** regimens in high- and low-risk groups. **(F)** OS analysis of patients receiving A, no-A, and no treatment in the low-risk group.

3.13 The risk model predicts gene expression in immune responses, immune checkpoints, inflammation, and epithelial-mesenchymal transition

Immune checkpoint blockade with immunotherapies, including CTLA-4, CD28, and CD274 are promising treatment approaches for several malignancies (38). However, the bottleneck problem of immune checkpoint inhibitors (ICI) in the treatment of eBC is the lack of precise biomarkers identifying populations who may benefit from these therapeutics. In our study, we determined the expression levels of several key immune checkpoint regulators and inflammatory mediators to provide reference biomarker candidates for precision immunotherapy in early drug-resistant patients. As presented in Figure 10A, CD274, CD28, and CTLA-4 expression levels were significantly higher in the low-risk group ($p < 0.0001$). The Pearson algorithm was used to analyze correlations between immune checkpoints and our risk model. Correlation values of CTLA-4, CD28, CD274 and risk score were -0.37, -0.43 and -0.33, respectively (Figure 10B, $p < 0.0001$). Additionally, other immunomodulators or inflammatory mediators were increased in the low-risk group (Figure 10C, $p < 0.0001$). A previous study reported that HLA affected ICI efficacy (39), therefore we analyzed correlations between HLA family expression and our model, and showed this expression was significantly higher in the low-risk group when compared with the high-risk group (Figure 10D, $p < 0.0001$). We next explored ICI therapy responses, represented by the CTLA-4/PD1 inhibitors, by using the immunophenotype score (IPS), and showed that the IPS was slightly higher than that of the low-risk group in the patients treated with CTLA-4 and PD1 inhibitors (Figure 10E, $p < 0.05$). Overall, these results suggested that our model predicted the immunotherapy benefits for patients and may be a more effective biomarker to predict the efficacy of immunotherapy.

We further analyzed DEGs between low- and high-risk groups in TCGA. In total, 396 DEGs (7 upregulated and 389 downregulated genes, FDR p-value < 0.05) were identified in the high-risk group when compared with the low-risk group. Of these, SLC7A5, PRAME, CRABP1, CBX2, CA9, CALML5, and CD24 were significantly overexpressed in the high-risk group (Supplementary Figures S8A, B, FDR p-value < 0.05, fold change > 1.5). Furthermore, KEGG analysis showed that genes in the high-risk group were mainly involved in environmental information processing, human diseases, and organismal systems (Supplementary Figure S8C). From GO enrichment analysis, these genes in the high-risk group were mainly involved in extracellular matrix, vesicle, immune response, and antigen binding (Supplementary Figures S8D–F).

3.14 Risk model correlation with tumor mutation burden (TMB)

As shown in Figure 11A, BC patients in the high-risk group had a higher TMB than those in the low-risk group ($p < 0.05$). As suggested from previous studies, a high TMB leads to a poor prognosis in many

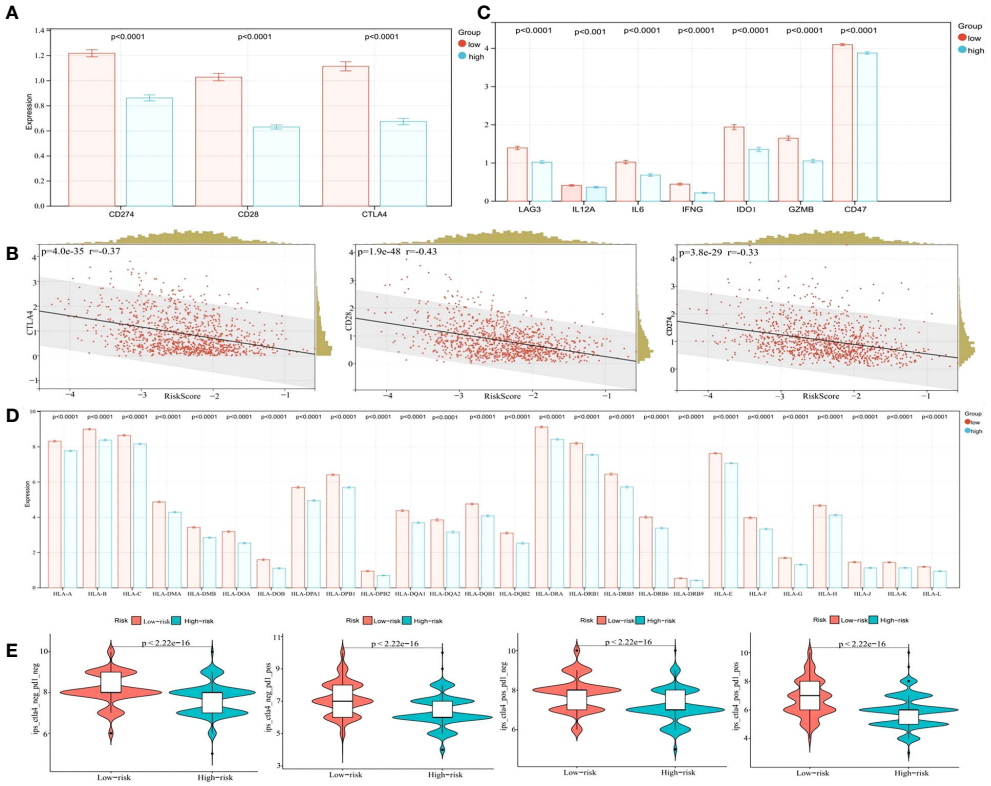

FIGURE 10
Bioinformatics analysis of the characteristics and signaling pathways among patients in different risk groups. **(A)** CD274, CD28, and CTLA4 mRNA expression between the low- and high-risk groups in the cohort from TCGA. **(B)** Correlation between the risk score and CD274, CD28, and CTLA4 mRNA expression. **(C)** LAG3, IL12A, IL12B, IL6, IFNG, IDO1, GZMB, and CD47 mRNA expression between the low- and high-risk groups in the cohort from TCGA. **(D)** The HLA family mRNA expression between the low- and high-risk groups in the cohort from TCGA. **(E)** Correlation of the risk score and the IPS.

cancers (40), consistent with our data. In correlation analysis between risk score and TMB, we identified a significant positive correlation (Figure 11B, $p < 0.05$). Further survival analysis indicated that the low-TMB group showed a significant survival benefit (Figure 11C, $p < 0.05$). Given the synergistic effect of TMB and the risk score, their effect on prognostic stratification was evaluated. As indicated from the results, TMB status did not interference the predictive ability of the risk score. Survival difference of the risk score subtypes was significant in both high- and low-TMB groups, and the subgroup with low risk-score and low TMB showed a better survival benefit, while the high-risk score and high TMB subgroup had a lower survival probability (Figure 11D, $p < 0.001$). Combined, risk score may act as a prognostic BC indicator, which is independent of TMB and can effectively predict TMB and treatment sensitivity.

3.15 Relationships among hub genes expression levels, tumor-infiltrating immune cells, immune molecules, and sensitivity to BC-targeting and chemotherapeutic drugs

We used the TIMER database to explore the relationships between hub genes expression (PSMB8 and BIRC3) and the level of infiltrating lymphocytes. Upregulated PSMB8/BIRC3 expression was associated with increased B cell, CD8+ T cell, macrophage, neutrophil, DC, and other infiltrating lymphocyte infiltration (Figures 12A, B, $p < 0.05$). Next, using the TISIDB database, we found that upregulated PSMB8/BIRC3 (Figures 12C, D) expression was associated with increased expression of immunostimulatory molecules, immunosuppressive molecules, MHC molecules, chemokines, and chemokine receptors, which provides important information for predicting potential therapeutic targets. Finally, we used GSCA Lite online tool to analyze the relationship between the expression of the hub genes and sensitivity to current immune or targeted therapies for BC (Figure 12E). PSMB8 expression levels were negatively correlated with sensitivity to many BC-targeting or chemotherapeutic drugs, including clofarabine and gemcitabine, and were positively correlated with abiraterone. BIRC3 expression levels were positively correlated with axitinib sensitivity and negatively correlated with dasatinib sensitivity. Thus, hub genes could function as new targets for predicting drug sensitivity and developing multi-targeted combined therapy for BC.

4 Discussion

We developed a 14-TME-related gene prognostic model based on statistical associations between eBC prognosis and drug

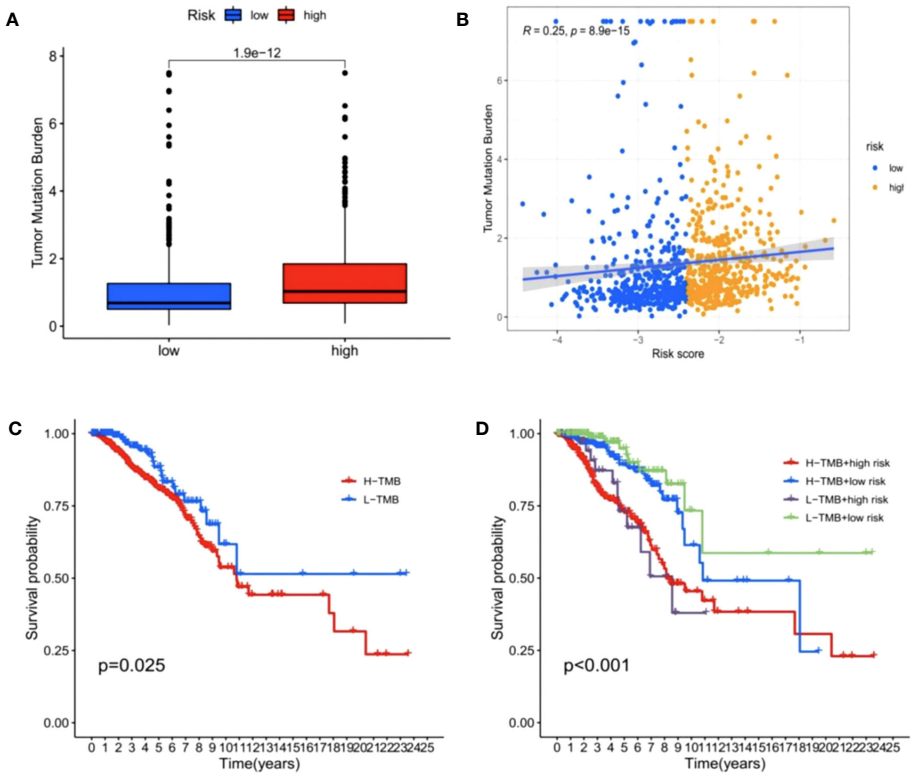

FIGURE 11
Correlations between risk score and tumor mutation burden (TMB). **(A)** The TMB was higher in the high-risk group than in the low-risk group. **(B)** The scatterplots depicted the positive correlation between the risk score and TMB. **(C)** Kaplan–Meier curves of overall survival (OS) in different TMB subgroups. **(D)** Kaplan–Meier curves of overall survival (OS) stratified by both TMB and the risk score.

resistance. (1) Our model exhibited strong predictive prognosis power in BC patients; (2) Enrichment analyses showed that immune-related pathways mediated the role of TME-related genes in BC; (3) we constructed a nomogram system, which was shown when compared with simple clinicopathological features, nomogram-integrated risk score had high prediction accuracy and applicability; (4) Our model provided predictive power for eBC patients to select the best treatments possible and avoid unnecessary chemotherapy agents; and (5) We found 2 novel therapeutic target genes, which provides a new direction for the development of BC precision medicine.

With the wide application of high-throughput technology and the continuous maturity of data sharing mechanism, unprecedented large-scale multi-omics cancer data have been accumulated in the international public databases, and cancer research has entered the era of “big data”. The focus of precision genomic medicine is to identify accurate specific survival prognostic factors from large medical datasets with clinical outcomes (41). Therefore, in recent years, some studies have aimed to explore microenvironment-related prognostic factors using bioinformatics analysis. However, the use of genomics, transcriptomic, and proteomic analysis of clinical tumor tissue is affected by the proportion of tumor cells present, and the method of evaluating the nontumor part of tumor samples (ESTIMATE) can provide an important context for genomic data analysis, a huge improvement in other capacity-limited methods (42). Additionally, many studies have not comprehensively explored the role of the genes related to stromal cells and immune cells in the BC TME and focused only on immune cell-related genes. In this study, we investigated infiltrating immune and stromal cell levels in tumor tissue in the ESTIMATE algorithm, and provided new perspectives for the comprehensive understanding on tumor-related normal cells in tumor tissue.

In our study, we used the ESTIMATE algorithm to assess the levels of infiltrating immune and stromal cell levels in tumor tissues. And we showed that the Basal-like subtype had a high immune score, consistent with previous findings showing that high levels of TILs were common in both the Basal-like type and the HER2-enriched types (43). The effect of tumor-infiltrating immune cells on the biological and clinical course of BC is well established in previous research (44). In accordance with the previous studies, we observed that BC patients with higher immune scores had the better prognosis, while no significant association of stromal scores with prognosis was observed. For another, LASSO regression was applied to construct risk models for 14 key TME prognostic genes, as used in previous studies (45, 46). The prognostic value of our risk model was also confirmed in the training and validation sets. The OS curves of the high-risk scoring group and low-risk scoring group were obviously separated, and patients with low-risk scores comprised a clear survival advantage, which vindicated our study design. The fly in the ointment was that we observed similar survival rates with the high- and low-risk groups in the validation set at late time points. Studies have shown that the survival curves

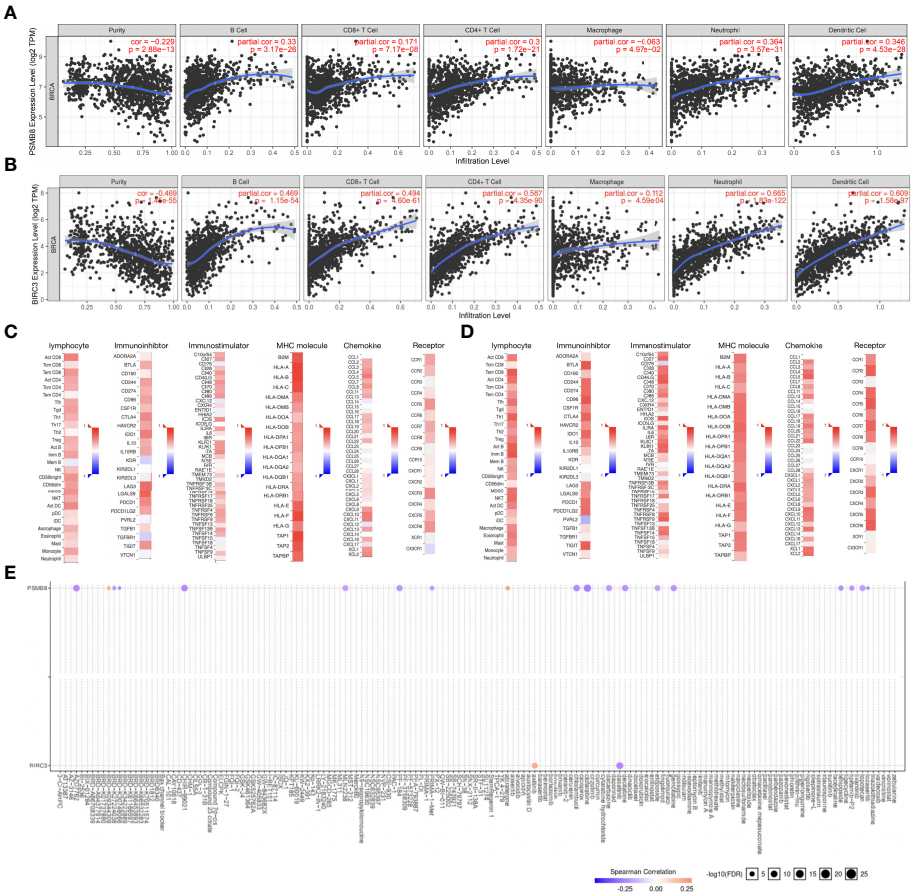

FIGURE 12
Relationships between hub gene expression and tumor-infiltrating immune cells, immune molecules, and sensitivity to BC-targeting and chemotherapeutic drugs. **(A)** Upregulation of PSMB8 expression is associated with increased infiltration of B cells, CD8+ T cells, macrophages, neutrophils, dendritic cells (DCs), and other infiltrating lymphocytes. **(B)** Upregulation of BIRC3 expression is associated with increased infiltration of B cells, CD8+ T cells, macrophages, neutrophils, dendritic cells (DCs), and other infiltrating lymphocytes. **(C)** The correlation between PSMB8 expression and lymphocytes, immunostimulatory molecules, immunosuppressive molecules, MHC molecule, chemokines, and chemokine receptors in BC. **(D)** The correlation between BIRC3 expression and lymphocytes, immunostimulatory molecules, immunosuppressive molecules, MHC molecule, chemokines, and chemokine receptors in BC. **(E)** The expression levels of PSMB8and BIRC3 are correlated with sensitivity to many BC-targeting and chemotherapeutic drugs.

crossing happens, when a relative few subject still being followed at late time points. When the sample reduce, there will also be a lot of uncertainty in the true position of the survival curves (47). Consistent with this, our data and results shown that the samples in the later stage of this survival curve have been reduced a lot compared to those at the start (Supplementary Figure S9). In addition, insufficient samples, differences in patient treatment regimens, and age deviation may also contribute to this phenomenon. Furthermore, model diagnosis using ROC analysis indicated that our risk model was a reliable indicator for predicting prognosis. Subgroup analysis further showed that risk score remained independent prognostic factor even when patients were regrouped based on clinical parameters. Finally, a nomogram, which may be used in clinical practice, was constructed and a calibration curve used to explore the predictive efficacy of our model for survival. Overall, our risk model of TME-related genes may be a mature reference for predicting prognosis in patients with BC that is feasible in clinical practice.

In this study, we selected 14 TME-related genes, including BIRC3, CELSR2, CXCL14, IL18, KLRB1, NPY1R, PSMB8, SCUBE2, STC2, CD1C, HLA-DPB1, GIMAP2, IRF1 and TNFAIP8, all of which were implicated in tumor progression and prognosis outcomes. BIRC3 is a member of the apoptosis inhibitor (IAP) family, with pro-survival and antiapoptotic effects in cancer cells (48). BIRC3 is associated with treatment resistance in BC; IL-1 upregulates BIRC3 and generates doxorubicin resistance in BC cells (49), thus BIRC3 appears to have important roles in the TME. PSMB8 is the catalytic subunit of the immunoproteasome and is implicated in glioblastoma, mucinous ovarian cancer, cutaneous squamous cell carcinoma, papillary thyroid carcinoma, and prostate cancer development and progression (50–52), consistent with our findings showing that PSMB8 was associated with high immune

infiltration and was a predictive protective gene. CELSR2 is part of the cadherin superfamily and was associated with poor prognosis (53). However, we confirmed CELSR2 was a protective gene and involved in changing the TME. These contradictory results highlight the need for more experimental studies on CELSR2. Furthermore, we found the first prognostic value of CD1C and GIMAP2 genes, which may provide new directions for further BC research.

In recent years, tumor immunity has attracted considerable research interest, while prognostic features related to the TME have great applications in identifying novel biomarkers. As described, BC growth and invasiveness are influenced by different cells in the TME. Many studies have reported that the degree of immune infiltration in the TME correlates with BC prognosis (30, 54). GO and KEGG analysis indicated that the DEGs between the high-risk and low-risk groups were mainly enriched in immune-related pathways. Specifically, ESTIMATE, TIMER and MCPCounter analysis showed that patients in the low-risk group had a relatively high immune infiltration status. When combined with the patient survival results, we showed that a good prognosis is associated with a high immune infiltration status, consistent with previous studies (30, 54). In the TME, tumor cells interact with different immune cell types by activating the immune checkpoint pathway (55, 56). We identified several immune checkpoint genes (e.g., CTLA-4, PDL1, LAG3, and CD28) which were highly expressed in the low-risk group, suggesting these patients may benefit from immunotherapy. The genomic instability may produce an immune response phenotype that affects the immune response and immunotherapy (57). We comprehensively analyzed correlation between the TMB and risk score and identified significant positive associations. Furthermore, the stratified prognostic analysis showed that the prognostic value of the risk score in the BC was independent of the TMB. Taken together, our results provide potential therapeutic targets and provide novel clinical applications for immunotherapies.

Chemotherapy is an important adjuvant treatment for eBC but has long been regarded as an immunosuppressive treatment modality. However, recent studies reported that chemotherapy has immune modulation effects (58, 59). The induced stress and apoptosis generated by chemotherapy produces new tumor immune antigens on cell surfaces and in the TME, which stimulate antitumor immune responses (60). Our results suggested that receiving chemotherapy was better than not receiving it, regardless of the immune microenvironment in low- or high-risk groups. A-based chemotherapeutic agents are represented by topoisomerase 2 inhibitors and have pivotal roles in eBC chemotherapy. However, it also exerts dose-dependent toxic side effects such as myelosuppression, cardiotoxicity, and gastrointestinal responses (61). Based on a pooled analysis of PlanB and SUCCESS C randomized clinical trials, six TC cycles provided similar efficacy to the A-regimen in most patients with HER2-eBC, and a significantly lower incidence of overall grade 3/4 toxicity was observed (62). The randomized neoadjuvant multicenter phase II trial, WGS-ADAPT-TN, found that additional A-containing chemotherapy was not associated with a significant invasive disease-free survival advantage in pathological complete response patients (63). Therefore, A-regimen removal is the trend, but how to accurately screen the population of chemotherapy is not unclear. We observed that A-use in the high-risk group may potentially promote immune cell infiltration and enhance antitumor immune responses. Interestingly, no prognosis differences were identified between A-use in low- and high-risk groups, and even an absence of A-regimen in the low-risk group did not affect long-term survival. This suggested that the no-A chemotherapy regimen seems feasible in low-risk patients despite chemotherapy benefit. Thus, we provide clinicians with an accurate tool that provides an opportunity for patients to choose the best treatment and avoid unnecessary chemotherapy.

Our study had some limitations. Firstly, our conclusions were based on open datasets and not sequencing data. Despite this weakness, the concordance between our TME-related gene risk model and survival in TCGA and GEO cohorts identified prognostic signatures in BC, but which still need to be further validated with sufficient sample data. Secondly, our data, which originated from databases, lacked experimental validation. In future studies, we will focus on these novel molecules using *in vitro* and *in vivo* analyses.

5 Conclusions

We comprehensively explored the role of the TME in BC patients using statistical analyses of public database data. First, the risk model we constructed based on TME-associated genes and successfully predicted the OS in BC patients. In addition, our model was inversely associated with BC immune cell infiltration and may be used as an independent prognostic marker to predict the efficacy of immunotherapy in BC patients. Importantly, we showed that outcomes in patients receiving the A-regimen in the low-risk group were not significantly different to those receiving the no-A regimen, suggesting this patient cohort may be exempted from A-containing adjuvant chemotherapy. The hub genes (BIRC3 and PSMB8) can be used as effective biomarkers to predict BC prognosis and used as novel targets to predict drug sensitivity.

Our work provides innovative perspectives for future BC research and the development of targeted therapeutic strategies for BC patients. Further studies are required to validate the clinical prognostic value of our risk model and explore underlying mechanisms associated with eBC.

Data availability statement

The original contributions presented in the study are included in the article/Supplementary Material, further inquiries can be directed to the corresponding author/s.

Ethics statement

The studies involving humans were approved by the Ethics and Human Subject Committee of the Second Hospital of Dalian

Medical University. The studies were conducted in accordance with the local legislation and institutional requirements. The participants provided their written informed consent to participate in this study.

Author contributions

HC conceived this study and wrote the manuscript. HC, SW and YuZ executed the data collection and data analysis. YuZ and XG performed immunohistochemistry analysis. YG, NW, XW, TZ, YiZ, DC, MW, and DZ assisted revising the manuscript. JW designed the study and was the director for the fund. All authors contributed to the article and approved the submitted version.

Funding

This study was supported by the "1+X" program cross-disciplinary innovation project (2022JCXKYB07), Wu Jieping Medical Foundation (320.6750.2022-19-81), and the Natural Science Foundation of Liaoning Province (2020-MS-266).

Conflict of interest

The authors declare that the research was conducted in the absence of any commercial or financial relationships that could be construed as a potential conflict of interest.

Publisher's note

Supplementary material

The Supplementary Material for this article can be found online at: https://www.frontiersin.org/articles/10.3389/fonc.2023.1209707/full#supplementary-material

References

1. Sung H, Ferlay J, Siegel RL, Laversanne M, Soerjomataram I, Jemal A, et al. Global cancer statistics 2020: GLOBOCAN estimates of incidence and mortality worldwide for 36 cancers in 185 countries. *CA Cancer J Clin* (2021) 71(3):209–49. doi: 10.3322/caac.21660

2. DeSantis CE, Ma J, Gaudet MM, Newman LA, Miller KD, Goding Sauer A, et al. Breast cancer statistics, 2019. *CA Cancer J Clin* (2019) 69(6):438–51. doi: 10.3322/caac.21583

3. Early Breast Cancer Trialists' Collaborative G, Davies C, Godwin J, Gray R, Clarke M, Cutter D, et al. Relevance of breast cancer hormone receptors and other factors to the efficacy of adjuvant tamoxifen: patient-level meta-analysis of randomised trials. *Lancet* (2011) 378(9793):771–84. doi: 10.1016/S0140-6736(11)60993-8

4. Bradley JA, Mendenhall NP. Novel radiotherapy techniques for breast cancer. *Annu Rev Med* (2018) 69:277–88. doi: 10.1146/annurev-med-042716-103422

5. Chargari C, Deutsch E, Blanchard P, Gouy S, Martelli H, Guerin F, et al. Brachytherapy: An overview for clinicians. *CA Cancer J Clin* (2019) 69(5):386–401. doi: 10.3322/caac.21578

6. Oikonomou EK, Kokkinidis DG, Kampaktsis PN, Amir EA, Marwick TH, Gupta D, et al. Assessment of prognostic value of left ventricular global longitudinal strain for early prediction of chemotherapy-induced cardiotoxicity: A systematic review and meta-analysis. *JAMA Cardiol* (2019) 4(10):1007–18. doi: 10.1001/jamacardio.2019.2952

7. Olver IN. New initiatives in the treatment of breast cancer. *Med J Aust* (2016) 205 (10):449–50. doi: 10.5694/mja16.01055

8. Giuliano AE, Connolly JL, Edge SB, Mittendorf EA, Rugo HS, Solin LJ, et al. Breast Cancer-Major changes in the American Joint Committee on Cancer eighth edition cancer staging manual. *CA Cancer J Clin* (2017) 67(4):290–303. doi: 10.3322/caac.21393

9. Zhang Y, Zhang Z. The history and advances in cancer immunotherapy: understanding the characteristics of tumor-infiltrating immune cells and their therapeutic implications. *Cell Mol Immunol* (2020) 17(8):807–21. doi: 10.1038/s41423-020-0488-6

10. Chen DS, Mellman I. Elements of cancer immunity and the cancer-immune set point. *Nature* (2017) 541(7637):321–30. doi: 10.1038/nature21349

11. Liu D, Dai X, Zhang W, Zhu X, Zha Z, Qian H, et al. Liquid exfoliation of ultrasmall zirconium carbide nanodots as a noninflammatory photothermal agent in the treatment of glioma. *Biomaterials* (2023) 292:121917. doi: 10.1016/j.biomaterials.2022.121917

12. Guo Q, Yin M, Fan J, Yang Y, Liu T, Qian H, et al. Peroxidase-mimicking TA-VOx nanobranches for enhanced photothermal/chemodynamic therapy of glioma by inhibiting the expression of HSP60. *Materials Design* (2022) 224. doi: 10.1016/j.matdes.2022.111366

13. Wu P, Gao W, Su M, Nice EC, Zhang W, Lin J, et al. Adaptive mechanisms of tumor therapy resistance driven by tumor microenvironment. *Front Cell Dev Biol* (2021) 9:641469. doi: 10.3389/fcell.2021.641469

14. Wang X, Wang X, Yue Q, Xu H, Zhong X, Sun L, et al. Liquid exfoliation of TiN nanodots as novel sonosensitizers for photothermal-enhanced sonodynamic therapy against cancer. *Nano Today* (2021) 39. doi: 10.1016/j.nantod.2021.101170

15. Hanahan D, Weinberg RA. The hallmarks of cancer. *Cell* (2000) 100(1):57–70. doi: 10.1016/S0092-8674(00)81683-9

16. Hanahan D, Coussens LM. Accessories to the crime: functions of cells recruited to the tumor microenvironment. *Cancer Cell* (2012) 21(3):309–22. doi: 10.1016/j.ccr.2012.02.022

17. Hanahan D, Weinberg RA. Hallmarks of cancer: the next generation. *Cell* (2011) 144(5):646–74. doi: 10.1016/j.cell.2011.02.013

18. Kalluri R, Zeisberg M. Fibroblasts in cancer. *Nat Rev Cancer* (2006) 6(5):392–401. doi: 10.1038/nrc1877

19. Straussman R, Morikawa T, Shee K, Barzily-Rokni M, Qian ZR, Du J, et al. Tumour micro-environment elicits innate resistance to RAF inhibitors through HGF secretion. *Nature* (2012) 487(7408):500–4. doi: 10.1038/nature11183

20. Chen D, Zhang X, Li Z, Zhu B. Metabolic regulatory crosstalk between tumor microenvironment and tumor-associated macrophages. *Theranostics* (2021) 11 (3):1016–30. doi: 10.7150/thno.51777

21. Khalaf K, Hana D, Chou JT, Singh C, Mackiewicz A, Kaczmarek M. Aspects of the tumor microenvironment involved in immune resistance and drug resistance. *Front Immunol* (2021) 12:656364. doi: 10.3389/fimmu.2021.656364

22. Zhu D, Ling R, Chen H, Lyu M, Qian H, Wu K, et al. Biomimetic copper single-atom nanozyme system for self-enhanced nanocatalytic tumor therapy. *Nano Res* (2022) 15(8):7320–8. doi: 10.1007/s12274-022-4359-6

23. Yoshihara K, Shahmoradgoli M, Martinez E, Vegesna R, Kim H, Torres-Garcia W, et al. Inferring tumour purity and stromal and immune cell admixture from expression data. *Nat Commun* (2013) 4:2612. doi: 10.1038/ncomms3612

24. Winslow S, Lindquist KE, Edsjö A, Larsson C. The expression pattern of matrix-producing tumor stroma is of prognostic importance in breast cancer. *BMC Cancer* (2016) 16(1):1–13. doi: 10.1186/s12885-016-2864-2

25. Wang J, Ikeda R, Che XF, Ooyama A, Yamamoto M, Furukawa T, et al. VEGF expression is augmented by hypoxiainduced PGIS in human fibroblasts. *Int J Oncol* (2013) 43(3):746–54. doi: 10.3892/ijo.2013.1994

26. Ren J, Ding L, Zhang D, Shi G, Xu Q, Shen S, et al. Carcinoma-associated fibroblasts promote the stemness and chemoresistance of colorectal cancer by transferring exosomal lncRNA H19. *Theranostics* (2018) 8(14):3932–48. doi: 10.7150/thno.25541

27. Genova C, Dellepiane C, Carrega P, Sommariva S, Ferlazzo G, Pronzato P, et al. Therapeutic implications of tumor microenvironment in lung cancer: focus on immune checkpoint blockade. *Front Immunol* (2021) 12:799455. doi: 10.3389/fimmu.2021.799455

28. Guo W, Wang T, Huang C, Ning S, Guo Q, Zhang W, et al. Platelet membrane-coated C-TiO2 hollow nanospheres for combined sonodynamic and alkyl-radical cancer therapy. *Nano Res* (2022) 16(1):782–91. doi: 10.1007/s12274-022-4646-2

29. Denkert C, von Minckwitz G, Darb-Esfahani S, Lederer B, Heppner BI, Weber KE, et al. Tumour-infiltrating lymphocytes and prognosis in different subtypes of breast cancer: a pooled analysis of 3771 patients treated with neoadjuvant therapy. *Lancet Oncol* (2018) 19(1):40–50. doi: 10.1016/S1470-2045(17)30904-X

30. Adams S, Gray RJ, Demaria S, Goldstein L, Perez EA, Shulman LN, et al. Prognostic value of tumor-infiltrating lymphocytes in triple-negative breast cancers from two phase III randomized adjuvant breast cancer trials: ECOG 2197 and ECOG 1199. *J Clin Oncol* (2014) 32(27):2959–66. doi: 10.1200/JCO.2013.55.0491

31. Adams S, Schmid P, Rugo HS, Winer EP, Loirat D, Awada A, et al. Pembrolizumab monotherapy for previously treated metastatic triple-negative breast cancer: cohort A of the phase II KEYNOTE-086 study. *Ann Oncol* (2019) 30(3):397–404. doi: 10.1093/annonc/mdy517

32. Qin Y, Deng J, Zhang L, Yuan J, Yang H, Li Q. Tumor microenvironment characterization in triple-negative breast cancer identifies prognostic gene signature. *Aging (Albany NY)* (2021) 13(4):5485–505. doi: 10.18632/aging.202478

33. Shen Y, Peng X, Shen C. Identification and validation of immune-related lncRNA prognostic signature for breast cancer. *Genomics* (2020) 112(3):2640–6. doi: 10.1016/j.ygeno.2020.02.015

34. Ning S, Dai X, Tang W, Guo Q, Lyu M, Zhu D, et al. Cancer cell membrane-coated C-TiO(2) hollow nanoshells for combined sonodynamic and hypoxia-activated chemotherapy. *Acta Biomater* (2022) 152:562–74. doi: 10.1016/j.actbio.2022.08.067

35. Sorlie T, Perou CM, Tibshirani R, Aas T, Geisler S, Johnsen H, et al. Gene expression patterns of breast carcinomas distinguish tumor subclasses with clinical implications. *Proc Natl Acad Sci USA* (2001) 98(19):10869–74. doi: 10.1073/pnas.191367098

36. Dai X, Li T, Bai Z, Yang Y, Liu X, Zhan J, et al. Breast cancer intrinsic subtype classification, clinical use and future trends. *Am J Cancer Res* (2015) 5(10):2929–43.

37. Mesnage SJL, Auguste A, Genestie C, Dunant A, Pain E, Drusch F, et al. Neoadjuvant chemotherapy (NACT) increases immune infiltration and programmed death-ligand 1 (PD-L1) expression in epithelial ovarian cancer (EOC). *Ann Oncol* (2017) 28(3):651–7. doi: 10.1093/annonc/mdw625

38. Denduluri N, Somerfield MR, Chavez-MacGregor M, Comander AH, Dayao Z, Eisen A, et al. Selection of optimal adjuvant chemotherapy and targeted therapy for early breast cancer: ASCO guideline update. *J Clin Oncol* (2021) 39(6):685–93. doi: 10.1200/JCO.20.02510

39. Chowell D, Morris LGT, Grigg CM, Weber JK, Samstein RM, Makarov V, et al. Patient HLA class I genotype influences cancer response to checkpoint blockade immunotherapy. *Science* (2018) 359(6375):582–7. doi: 10.1126/science.aao4572

40. Andor N, Maley CC, Ji HP. Genomic instability in cancer: teetering on the limit of tolerance. *Cancer Res* (2017) 77(9):2179–85. doi: 10.1158/0008-5472.CAN-16-1553

41. Kourou K, Exarchos TP, Exarchos KP, Karamouzis MV, Fotiadis DI. Machine learning applications in cancer prognosis and prediction. *Comput Struct Biotechnol J* (2015) 13:8–17. doi: 10.1016/j.csbj.2014.11.005

42. Carter SL, Cibulskis K, Helman E, McKenna A, Shen H, Zack T, et al. Absolute quantification of somatic DNA alterations in human cancer. *Nat Biotechnol* (2012) 30(5):413–21. doi: 10.1038/nbt.2203

43. Stanton SE, Disis ML. Clinical significance of tumor-infiltrating lymphocytes in breast cancer. *J Immunother Cancer* (2016) 4:59. doi: 10.1186/s40425-016-0165-6

44. Karn T, Pusztai L, Rody A, Holtrich U, Becker S. The influence of host factors on the prognosis of breast cancer: stroma and immune cell components as cancer biomarkers. *Curr Cancer Drug Targets* (2015) 15(8):652–64. doi: 10.2174/1568009615081510011012O9

45. Dai W, Feng Y, Mo S, Xiang W, Li Q, Wang R, et al. Transcriptome profiling reveals an integrated mRNA-lncRNA signature with predictive value of early relapse in colon cancer. *Carcinogenesis* (2018) 39(10):1235–44. doi: 10.1093/carcin/bgy087

46. Qu L, Wang ZL, Chen Q, Li YM, He HW, Hsieh JJ, et al. Prognostic value of a long non-coding RNA signature in localized clear cell renal cell carcinoma. *Eur Urol* (2018) 74(6):756–63. doi: 10.1016/j.eururo.2018.07.032

47. Pocock SJ, Clayton TC, Altman DG. Survival plots of time-to-event outcomes in clinical trials: good practice and pitfalls. *Lancet* (2002) 359(9318):1686–9. doi: 10.1016/S0140-6736(02)08594-X

48. Zhu H, Zheng C, Liu H, Kong F, Kong S, Chen F, et al. Significance of macrophage infiltration in the prognosis of lung adenocarcinoma patients evaluated by scRNA and bulkRNA analysis. *Front Immunol* (2022) 13:1028440. doi: 10.3389/fimmu.2022.1028440

49. Mendoza-Rodriguez M, Arevalo Romero H, Fuentes-Panana EM, Ayala-Sumuano JT, Meza I. IL-1beta induces up-regulation of BIRC3, a gene involved in chemoresistance to doxorubicin in breast cancer cells. *Cancer Lett* (2017) 390:39–44. doi: 10.1016/j.canlet.2017.01.005

50. Fan X, Zhao Y. miR-451a inhibits cancer growth, epithelial-mesenchymal transition and induces apoptosis in papillary thyroid cancer by targeting PSMB8. *J Cell Mol Med* (2019) 23(12):8067–75. doi: 10.1111/jcmm.14673

51. Liu Y, Yang HZ, Jiang YJ, Xu LQ. miR-451a is downregulated and targets PSMB8 in prostate cancer. *Kaohsiung J Med Sci* (2020) 36(7):494–500. doi: 10.1002/kjm2.12196

52. Miyamoto T, Honda Y, Izawa K, Kanazawa N, Kadowaki S, Ohnishi H, et al. Assessment of type I interferon signatures in undifferentiated inflammatory diseases: A Japanese multicenter experience. *Front Immunol* (2022) 13:905960. doi: 10.3389/fimmu.2022.905960

53. Xu M, Zhu S, Xu R, Lin N. Identification of CELSR2 as a novel prognostic biomarker for hepatocellular carcinoma. *BMC Cancer* (2020) 20(1):313. doi: 10.1186/s12885-020-06813-5

54. Papatestas AE, Lesnick GJ, Genkins G, Aufses AH Jr. The prognostic significance of peripheral lymphocyte counts in patients with breast carcinoma. *Cancer* (1976) 37(1):164–8. doi: 10.1002/1097-0142(197601)37:1<164::AID-CNCR2820370123>3.0.CO;2-H

55. Tan S, Xia L, Yi P, Han Y, Tang L, Pan Q, et al. Exosomal miRNAs in tumor microenvironment. *J Exp Clin Cancer Res* (2020) 39(1):67. doi: 10.1186/s13046-020-01570-6

56. Solinas C, Gombos A, Latifyan S, Piccart-Gebhart M, Kok M, Buisseret L. Targeting immune checkpoints in breast cancer: an update of early results. *ESMO Open* (2017) 2(5):e000255. doi: 10.1136/esmoopen-2017-000255

57. Mardis ER. Neoantigens and genome instability: impact on immunogenomic phenotypes and immunotherapy response. *Genome Med* (2019) 11(1):71. doi: 10.1186/s13073-019-0684-0

58. Zhang L, Zhou C, Zhang S, Chen X, Liu J, Xu F, et al. Chemotherapy reinforces anti-tumor immune response and enhances clinical efficacy of immune checkpoint inhibitors. *Front Oncol* (2022) 12:939249. doi: 10.3389/fonc.2022.939249

59. Demaria S, Volm MD, Shapiro RL, Yee HT, Oratz R, Formenti SC, et al. Development of tumor-infiltrating lymphocytes in breast cancer after neoadjuvant paclitaxel chemotherapy. *Clin Cancer Res* (2001) 7(10):3025–30.

60. Casares N, Pequignot MO, Tesniere A, Ghiringhelli F, Roux S, Chaput N, et al. Caspase-dependent immunogenicity of doxorubicin-induced tumor cell death. *J Exp Med* (2005) 202(12):1691–701. doi: 10.1084/jem.20050915

61. Armenian SH, Lacchetti C, Barac A, Carver J, Constine LS, Denduluri N, et al. Prevention and monitoring of cardiac dysfunction in survivors of adult cancers: American society of clinical oncology clinical practice guideline. *J Clin Oncol* (2017) 35(8):893–911. doi: 10.1200/JCO.2016.70.5400

62. de Gregorio A, Janni W, Friedl TWP, Nitz U, Rack B, Schneeweiss A, et al. The impact of anthracyclines in intermediate and high-risk HER2-negative early breast cancer-a pooled analysis of the randomised clinical trials PlanB and SUCCESS C. *Br J Cancer* (2022) 126(12):1715–24. doi: 10.1038/s41416-021-01690-6

63. Gluz O, Nitz U, Kolberg-Liedtke C, Prat A, Christgen M, Kuemmel S, et al. De-escalated neoadjuvant chemotherapy in early triple-negative breast cancer (TNBC): impact of molecular markers and final survival analysis of the WSG-ADAPT-TN trial. *Clin Cancer Res* (2022) 28(22):4995–5003. doi: 10.1158/1078-0432.CCR-22-0482

frontiers | Frontiers in Oncology

TYPE Original Research
PUBLISHED 04 October 2023
DOI 10.3389/fonc.2023.1134063

OPEN ACCESS

EDITED BY
Takaji Matsutani,
Repertoire Genesis, Inc., Japan

REVIEWED BY
Vivek Peche,
Washington University in St. Louis, United States
Firas Hamdan,
University of Helsinki, Finland

*CORRESPONDENCE
Zhengxin Wang
wangzhengxin@huashan.org.cn

RECEIVED 29 December 2022
ACCEPTED 22 August 2023
PUBLISHED 04 October 2023

CITATION
Sun C, Zhu G, Shen C, Huang S, Li R, Li J, Ma Z and Wang Z (2023) Identification and validation of PCSK9 as a prognostic and immune-related influencing factor in tumorigenesis: a pan-cancer analysis. *Front. Oncol.* 13:1134063. doi: 10.3389/fonc.2023.1134063

Identification and validation of PCSK9 as a prognostic and immune-related influencing factor in tumorigenesis: a pan-cancer analysis

Chao Sun[1], Guoji Zhu[2], Conghuan Shen[1], Shungen Huang[3], Ruidong Li[1], Jianhua Li[1], Zhenyu Ma[1] and Zhengxin Wang[1]*

[1]Department of General Surgery, Huashan Hospital, Fudan University, Shanghai, China, [2]Surgery Intensive Care Unit, Children's Hospital of Suzhou University, Suzhou, China, [3]Department of General Surgery, Children's Hospital of Suzhou University, Suzhou, China

Introduction: Proprotein convertase subtilisin/kexin-9 (PCSK9) has been primarily studied in the cardiovascular field however, its role in cancer pathophysiology remains incompletely defined. Recently, a pivotal role for PCSK9 in cancer immunotherapy was proposed based on the finding that PCSK9 inhibition was associated with enhancing the antigen presentation efficacy of target programmed cell death-1 (PD-1). Herein, we provide results of a comprehensive pan-cancer analysis of PCSK9 that assessed its prognostic and immunological functions in cancer.

Methods: Using a variety of available online cancer-related databases including TIMER, cBioPortal, and GEPIA, we identified the abnormal expression of *PCSK9* and its potential clinical associations in diverse cancer types including liver, brain and lung. We also validated its role in progression-free survival (PFS) and immune infiltration in neuroblastoma.

Results: Overall, the pan-cancer survival analysis revealed an association between dysregulated PCSK9 and poor clinical outcomes in various cancer types. Specifically, PCSK9 was extensively genetically altered across most cancer types and was consistently found in different tumor types and substages when compared with adjacent normal tissues. Thus, aberrant DNA methylation may be responsible for PCSK9 expression in many cancer types. Focusing on liver hepatocellular carcinoma (LIHC), we found that PCSK9 expression correlated with clinicopathological characteristics following stratified prognostic analyses. PCSK9 expression was significantly associated with immune infiltrate since specific markers of CD8+ T cells, macrophage polarization, and exhausted T cells exhibited different PCSK9-related immune infiltration patterns in LIHC and lung squamous cell carcinoma. In addition, PCSK9 was connected with resistance of drugs such as erlotinib and docetaxel. Finally, we validated PCSK9 expression in clinical neuroblastoma samples and

concluded that PCSK9 appeared to correlate with a poor PFS and natural killer cell infiltration in neuroblastoma patients.

Conclusion: *PCSK9* could serve as a robust prognostic pan-cancer biomarker given its correlation with immune infiltrates in different cancer types, thus potentially highlighting a new direction for targeted clinical therapy of cancers.

KEYWORDS

pcsk9, tumorigenesis, prognosis, immune infiltrate, pan-cancer

1 Introduction

The complex process of tumorigenesis involves interactions between the immune system and tumor. Currently, targeting cytotoxic T lymphocyte-associated protein 4 (CTLA-4) and PD-1 has provided superior anticancer effects in colorectal and lung cancer compared to conventional chemotherapy (1). However, most cancer patients continue to suffer poor outcomes from immunotherapies with observed overall objective response rates approximately 15–25% in various cancer types (2). Recently, the 3rd generation immune checkpoint blockades have received widespread attention, because of their combined immunotherapy strategies in the anti-tumor microenvironment (TME) (3, 4). In order to maximize the synergistic benefits in strengthening the immune response, it is vital to verify and highlight novel immune-related therapeutic targets in malignancies (5). Performing a pan-cancer investigation of putative genes could help determine its involvement in clinical prognosis and immunological functions due to the intricate relationship between carcinogenesis and TME.

In 2003, human *PCSK9* gene mutation was identified as the third genetic cause of autosomal dominant familial hypercholesterolemia for the first time (6). Low-density lipoprotein cholesterol (LDL-C) levels were shown to increase in response to PCSK9-mediated degradation of low-density lipoprotein cholesterol receptors (LDLR) (7, 8). Clinical research has finally confirmed the key role for PCSK9 in cholesterol metabolism, because the inhibition of LDL-C mediated by PCSK9 has expanded the therapeutic tools that can be used to treat individuals with residual LDL-C related cardiovascular risk (9). In addition to regulating cholesterol metabolism, *in vitro* and *in vivo* studies have also found that PCSK9 is involved in various other physiological processes (10). For example, inhibition of PCSK9 was demonstrated to reduced myocardial ischemia-/reperfusion injury via BNIP-3 mediated autophagic pathway and improved myocardial infarct size and subsequent cardiac function. By investigating the functional role of PCSK9 inhibitions in the metabolic targets, it could potentially lead to better understanding of the pathogenesis of myocardial infarction and ischemic stroke, as well as provide a potential therapeutic target for its management (11). Additionally, the knowledge gained from exploring the role of PCSK9 in cell proliferation and apoptosis could help to elucidate the potential involvement of this protein in cancer risk, providing insight into potential preventive strategies (12). A recent study showed that inhibiting PCSK9 enhanced the antigen presentation efficacy of PD-1 and influenced the tumor response to immune checkpoint treatment, although through a mechanism unrelated to its role in controlling cholesterol (13, 14). This novel finding highlighted that PCSK9 inhibition was a potential strategy for improving immune checkpoint treatment for cancer. Given its likely engagement with PD-1 in tumor immunotherapy, PCSK9 might provide useful insight into tumor development and immune treatment response. Therefore, it is vital to comprehensively assess PCSK9 clinical prognostic association with tumors.

In the current study, we thoroughly examined the relationships among *PCSK9* expression, methylation, mutation, and patient prognosis in 33 different cancer types. In order to further examine aberrant patterns and the possible clinical importance of PCSK9 across various cancer types, a survival association study was carried out. We also investigated the relationship between *PCSK9* expression and immunological checkpoints and six tumor-infiltrating immune cells in 33 TME. *PCSK9* expression changes in neuroblastoma was not verified in the databases used in this study. Therefore, we further verified the expression changes of *PCSK9* in neuroblastoma clinical samples as a supplemental study. Our results emphasize the potential relevance of PCSK9 across malignancies and indicated that it may be a predictive biomarker associated with immune infiltration in various tumors.

2 Materials and methods

2.1 Gene expression analysis

2.1.1 Tumor immune estimation resource database

In this study, *PCSK9* mRNA expression levels in different tumor disease tissues and normal tissues were retrieved from the TIMER database (15). Thirty-three cancer types were included: adrenocortical carcinoma (ACC), bladder urothelial carcinoma (BLCA), breast invasive carcinoma (BRCA), colon adenocarcinoma (COAD), lymphoid neoplasm diffuse large B-cell lymphoma (DLBC), esophageal carcinoma (ESCA), glioblastoma multiforme (GBM), head and neck squamous cell carcinoma (HNSC), kidney chromophobe (KICH), kidney renal clear carcinoma (KIRC),

kidney renal papillary cell carcinoma (KIRP), acute myeloid leukemia (LAML), brain lower grade glioma (LGG), liver hepatocellular carcinoma (LIHC), lung adenocarcinoma (LUAD), lung squamous cell carcinoma (LUSC), ovarian serous cystadenocarcinoma (OV), pancreatic adenocarcinoma (PAAD), prostate adenocarcinoma (PRAD), rectum adenocarcinoma (READ), skin cutaneous melanoma (SKCM), stomach adenocarcinoma (STAD), testicular germ cell tumors (TGCT), thyroid carcinoma (THCA), thymoma (THYM), uterine corpus endometrial carcinoma (UCEC), cervical squamous cell carcinoma (CESC), cholangiocarcinoma (CHOL), mesothelioma (MESO), pheochromocytoma and paraganglioma (PCPG), sarcoma (SARC), uveal melanoma (UVM), and uterine carcinosarcoma (UCS).

2.1.2 Gene expression profiling interactive analysis 2 database

The GEPIA2 database (http://gepia2.cancer-pku.cn/) was used to analyze *PCSK9* expression profiles between disease tumors and normal tissues (16). We also explored the distribution of *PCSK9* in specific tumor stages and drew a violin diagram of tumor stages. The distribution of *PCSK9* in different cancers and the clinical stage of the tumors were initially explored, and a violin map of the tumor stage was drawn.

2.1.3 TISIDB portal

TISIDB is a website for gene- and tumor-immune interaction (http://cis.hku.hk/TISIDB/index.php/) (17). It was used to analyze *PCSK9* gene expression in different immune subtypes, including C1 (wound healing), C2 (IFN-γ dominant), C3 (inflammatory), C4 (lymphocyte depleted), C5 (immunologically quiet), and C6 (TGF-β dominant) subtypes. *PCSK9* gene expression was also analyzed in different molecular subtypes of tumor samples from The Cancer Genome Atlas (TCGA).

2.2 Genetic alteration analysis

2.2.1 cBioPortal database

The mutation levels of the *PCSK9* gene were obtained from the online cBioPortal database (https://www.cbioportal.org/). We searched in the "mutation" module of the website to obtain the specific mutation site information on the *PCSK9* functional and structural domain map (18, 19).

2.2.2 UALCAN network

DNA methyltransferase alteration plays a vital role in chromatin structure and gene expression levels. The UALCAN network (http://ualcan.path.uab.edu) was used to analyze differential DNA methylation of *PCSK9* between tumor and normal tissues (20).

2.2.3 GSCALite platform

The GSCALite platform (http://bioinfo.life.hust.edu.cn/web/GSCALite/) was selected to obtain the copy number variations (CNV) of *PCSK9* between cancer tissues and adjacent tissues in 33 types of cancers in the TCGA (21).

2.3 Gene set enrichment analysis of PCSK9

Here, ssGSEA is used to calculate the enrichment score of each sample and obtain the correlation between *PCSK9* expression and pathway score. R software GSVA package was used to analyze, choosing parameter as method = 'ssgsea'. The correlation between genes and pathway scores was analyzed by Spearman correlation. ClusterProfiler package (version: 3.18.0) in R software was employed to analyze the Gene Ontology (GO) function of potential targets and enrich the Kyoto Encyclopedia of Genes and Genomes (KEGG) pathway, $p < 0.05$ or FDR <0.05 is considered to be a meaningful pathway (enrichment score with −log10 (P) of more than 1.3).

2.4 Stemness analysis of PCSK9

To analyze the stemness features, we performed the spearman correlation between mRNAsi of various tumors and *PCSK9* expression. This method refers to the OCLR algorithm constructed by Malta, which contains 11774 different gene profiles (22).

2.5 Survival prognosis analysis

2.5.1 PrognoScan database

The correlation of *PCSK9* expression with pan-cancer survival was analyzed using PrognoScan (23). Specifically, *PCSK9* expression levels were searched in all available microarray datasets in PrognoScan to determine its association with prognosis, including overall survival (OS) and disease-free survival (DFS). The threshold was set at a Cox p value < 0.05. We explored the impact of *PCSK9* expression on OS and DFS in each cancer type.

2.5.2 Kaplan-Meier Plotter database

Kaplan-Meier Plotter (https://kmplot.com/analysis/) is an online database containing gene expression and clinical information for 54,000 samples on 21 cancer types (24). To assess the clinical prognostic value of specific genes, patient samples were divided into two groups according to median gene expression (high vs. low expression). Kaplan-Meier survival curves were used to analyze pan-cancer OS rates. The association between *PCSK9* expression and OS in different tumor tissues was analyzed, and the 95% confidence interval (95% CI) and the hazard ratio (HR) of the log-rank p values were calculated. Furthermore, we analyzed the relationship between *PCSK9* expression in LIHC and OS and recurrence-free survival (RFS) and calculated log-rank p values and 95% confidence intervals (CIs) for risk ratios (HRs). The impact of various risk factors on tumor prognosis was also analyzed to explore the impact of different clinical characteristics on tumor prognosis.

2.5.3 GEPIA database

The survival analysis module in the GEPIA database was used to obtain the OS and DFS data of patients with different *PCSK9* expression across TCGA and Genotype-Tissue Expression Project (GTEx). The survival module was also used to explore the expression patterns between *PCSK9* and survival factors in tumor patients (16).

2.6 Immune correlation analysis

2.6.1 TIMER database

2.6.1.1 Immune infiltrating cells

To focus on the role of immune cells in the TME, the expression profile data of tumor samples in TCGA were analyzed using the "immune gene" module of the TIMER 2.0 database. The xCell algorithms were used to explore the potential relationship between the level of cancer-related immune cell infiltration and *PCSK9* gene expression in different cancer types found in TCGA. The tumor-infiltrating immune cells were correlated with gene expression to assess the level of immune cell infiltration in the TME.

2.6.1.2 Immune checkpoint

Over 40 common immune checkpoint genes were identified, and the correlation between *PCSK9* and the immune checkpoint genes was analyzed using the R software package in the SangerBox database (http://www.sangerbox.com/) and presented in a heat map.

2.6.2.3 Immune infiltration

TIMER is an ideal database for systematically analyzing immune infiltration in multiple cancer types. We analyzed the relationship between *PCSK9* expression and immune infiltrating cells, including B cells, CD4+ T cells, CD8+ T cells, neutrophils, macrophages, and dendritic cells. ESTIMATE is a tool for predicting tumor purity and stromal and immune cell infiltration into tumor tissue using gene expression data. The ESTIMATE algorithm was used to infer the immune score of each sample (25).

2.6.2.4 Copy number alterations and immune infiltration

The correlation between different somatic copy number alterations (SCNAs) and immune cell infiltration affecting *PCSK9* expression was also explored by using TIMER. Four types of alterations (arm-level deletion, diploid/ordinary, arm-level gain, high amplification) were analyzed and compared in the SCNAs. The infiltration level of each SCNA category was compared with that of normal tissue using a two-sided Wilcoxon rank-sum test.

2.7 Drug sensitivity analysis

The Drug Sensitivity Genomics Project (GDSC) and The Cancer Therapeutics Response Portal (CTRP)are two databases, which combine drug sensitivity and genome data sets to promote the new therapeutic biomarkers for cancer therapy. Through these two databases, we investigated the role of *PCSK9* expression in cancer therapeutic response. Pearson correlation analysis was performed to obtain the correlation between *PCSK9* mRNA expression and drug IC50. P-value was adjusted by FDR.

2.8 Neuroblastoma specimen collection

A total of 25 neuroblastoma (NB) patients from Children's Hospital of Soochow University (Suzhou, China) were consecutively enrolled in a study between January 2016 and December 2019 and followed up until December 2021. NB specimens and adjacent normal tissues were collected at the time, frozen in liquid nitrogen, and stored at −80°C until use. No patients received chemotherapy or radiotherapy or any treatment for the tumor before surgery or tissue biopsy. The sample collection and related experiments met the ethical requirements of the Children's Hospital of Suzhou University, Suzhou, China. The Clinical Research Ethics Committee approved this study at the Children's Hospital of Suzhou University, Suzhou, China, and all patients or their parents signed informed consent forms.

2.9 Western blot assay and quantitative real-time PCR

Proteins were isolated from tissues using RIPA lysis buffer (Biotime, Shanghai, China), separated using SDS-PAGE, and transferred onto a nitrocellulose membrane (Bio-Rad Laboratories, CA, USA). Then, we blocked proteins with 5% skim milk for 30 min and incubated the membranes with diluted primary antibodies. Primary antibodies for GAPDH (ab8245, 1:10000 dilution; Abam, Cambridge, UK), PCSK9 (ab181142, 1:1000 dilution; Abam, Cambridge, UK), CD11b (ab133357, 1:1000 dilution; Abam, Cambridge, UK), CD45 (ab40763, 1:5000 dilution; Abam, Cambridge, UK), CD68 (ab213363, 1:1000 dilution; Abam, Cambridge, UK), and BSA-1 (ab219724, Abam, Cambridge, UK) were purchased from Abcam (Cambridge, UK). After incubating with horseradish peroxidase-conjugated secondary antibodies, the immune complexes were detected with an ECL detection kit (Millipore, Billerica, MA, USA) and quantified using a Gel-Pro Analyzer (Media Cybernetics Corporation, USA). Total RNA was isolated from patients with NB by using Trizol and then converted into cDNA by reverse transcription (GoScriptTM Reverse Transcription system, USA). RT-qPCR was used to assay the mRNA expression of *PCSK9*, immune-related genes, and pathway-related genes. *PCSK9* primers were purchased from Sino Biological Inc. The primers used for qRT-PCR were as follows: *PCSK9*, 5′-GCT GAGCTGCTCCAGTTTCT-3′ (forward) and 5′-AAT GGCGTAGACACCCTCAC-3′ (reverse); and *GAPDH*, 5′-AAGGTGAAGGTCGGAGTCAAC-3′ (forward) and 5′-GGGG TCATTGATGGCAACAATA-3′ (reverse).

2.10 Statistical analysis

Gene expression data from the TCGA and GTEx databases were analyzed by using t-tests. The Kruskal-Wallis test was used to evaluate the difference among various tissues, and the Wilcoxon test was used to determine the gene expression differences between normal and tumor tissues. In PrognoScan, univariate Cox regression analysis was used to analyze the survival time of patients with the HR and *p* value. In GEPIA and Kaplan-Meier Plotter, log rank test was used to compare survival rate of patients stratified according to the different expression levels of *PCSK9*. Other online analysis websites of GEPIA2, cBioportal and GSCALite were also used. Spearman correlation analysis was calculated between the expression of *PCSK9* and the level of infiltrating immune cells, the level of immunosuppressant or immunostimulant factors and infiltration scores of six immune infiltrations. Correlations were considered statistically significant when $p < 0.05$ for all statistical analyses. The experimental data were analyzed using SAS 9.3 statistical software. Statistical analysis was performed using the *t* test. Differences were considered statistically significant at $p < 0.05$. OS was defined as the time interval between the date of surgery and the date of progression or death. Survival analyses were conducted by Kaplan–Meier curves (*p* values from log-rank test) by R version 3.5.3 and the survival package. HRs were calculated using the R package.

3 Results

3.1 mRNA expression level of *PCSK9* in human cancer

Abnormal *PCSK9* expression has been reported in various cancer types. Previous studies on *PCSK9* expression in cancer used several research methods, such as DNA microarrays, but were limited to relatively small sample sizes and limited numbers of cancer types. This study has provided a more comprehensive analysis of *PCSK9* expression in cancer. Since *PCSK9* has a potential role as an important new target for cancer diagnosis and prognosis, we analyzed the *PCSK9* mRNA levels across different cancers from TIMER, GEPIA, and UALCAN databases. Data from these databases indicated that *PCSK9* mRNA expression had inter-tumor heterogeneity, with some tumors having very high levels of *PCSK9* (BRCA, CESC, CHOL, COAD, ESCA, HNSC, LIHC, READ, SKCM, STAD, THCA, and UCEC). In contrast, others were characterized by low levels of *PCSK9* expression (LUAD, PRAD, KIRP, KIRC, PCPG, LUSC, and GBM) (Figure 1A). Different stages and subtypes of a tumor may exhibit differential expression of *PCSK9*. Thus, we further assessed *PCSK9* expression in different clinical stages and subtypes from GEPIA and UALCAN. Briefly, differential expression of *PCSK9* was obtained from GEPIA to correlate with clinical subtypes of tumors, including BRCA, COAD, ESCA, HNSC, STAD, LUSC, OV, and UCEC (Figure 1B). As shown in Figure 1C, *PCSK9* expression was elevated in some tumors, including BLCA, BRCA, CESC, HNSC, READ, STAD, THCA, COAD, ESCA, UCEC, and LIHC. Whereas lower *PCSK9* expression in later stages was observed only in KIRC, KIRP, and LUAD.

3.2 *PCSK9* genetic alterations (mutations and DNA methylation) in various cancers

It has been widely acknowledged that genomic mutations are closely associated with tumorigenesis. To determine the genomic mutations of *PCSK9* in tumors, we reviewed the genetic alterations of the *PCSK9* gene in cancer patients using the cBioPortal database. Notably, patients with ovarian epithelial tumors had the highest frequency of *PCSK9* genetic alterations (5%), including amplification of copy numbers and deep deletions (Figure 2A). In addition, several cancer types (e.g., non-small cell lung cancer, cervical squamous cell carcinoma, ESCA, LIHC, SARC, BLCA, and BRCA) had *PCSK9* mutations (amplifications or deep deletions). Tumors with dominant *PCSK9* mutations included cervical adenocarcinoma, esophageal squamous cell carcinoma, esophagogastric adenocarcinoma, renal non-clear cell carcinoma, COAD, HNSC, KIRC, PAAD. Deep deletions were more common in various neuroepithelial tumors, PCPG, LGG, and GBM. These results revealed the highly heterogeneous inheritance and expression changes of PCSK9 in different types of cancer.

We next differentiated the distribution of mutations and collected the types, sites, and case number of genetic alterations of *PCSK*. As shown in Figures 2B, C, there were 93 missense and 6 truncation mutations in *PCSK9*. The site S91T/E92Afs*78/S91L, in the inhibitor_I9 domain, was confirmed to have the highest abundance of mutations. We future searched the cBioPortal website for PCSK9-related tumor gene mutations and identified six types of tumors with a total of eleven protein changes: Melanoma (D321N, E84K, G176E, E405K, S249G), Uterine Endometrioid Carcinoma (V79M), Colorectal Adenocarcinoma (R272L), Diffuse Large B-Cell Lymphoma (Q454H), Serous Ovarian Cancer (R93H, S5G), and Esophageal Adenocarcinoma (C526F). Subsequently, we conducted a search on the PolyPhen-2 website (http://genetics.bwh.harvard.edu/pph2/) and found that in five tumor types (Melanoma, Uterine Endometrioid Carcinoma, Diffuse Large B-Cell Lymphoma, Serous Ovarian Cancer, and Esophageal Adenocarcinoma), the protein changes were predicted to be either "probably damaging" or "possibly damaging." However, the mutation in Colorectal Adenocarcinoma exhibited benign characteristics. Moreover, when we further correlated the prognosis of these six tumor types, we observed that three of them (Melanoma, Serous Ovarian Cancer, and Uterine Endometrioid Carcinoma) displayed worse prognoses, suggesting a potential association with inherent mutations (Supplementary Table 1).

DNA methylation is an epigenetic modification that can alter gene expression. The alteration of DNA methylation may be an essential factor in tumorigenesis. Through the UALCAN database, we explored *PCSK9* methylation between tumors and normal tissues. The results showed that the methylation of *PCSK9* was upregulated in various tumors, including BRCA, CHOL, HNSC, KIRC, KIRP, LGG, LUAD, LUSC, PRAD, SARC, and THCA (Figure 2D). Accordingly, these results indicated that *PCSK9* may mediate tumorigenesis by regulating DNA damage or methylation

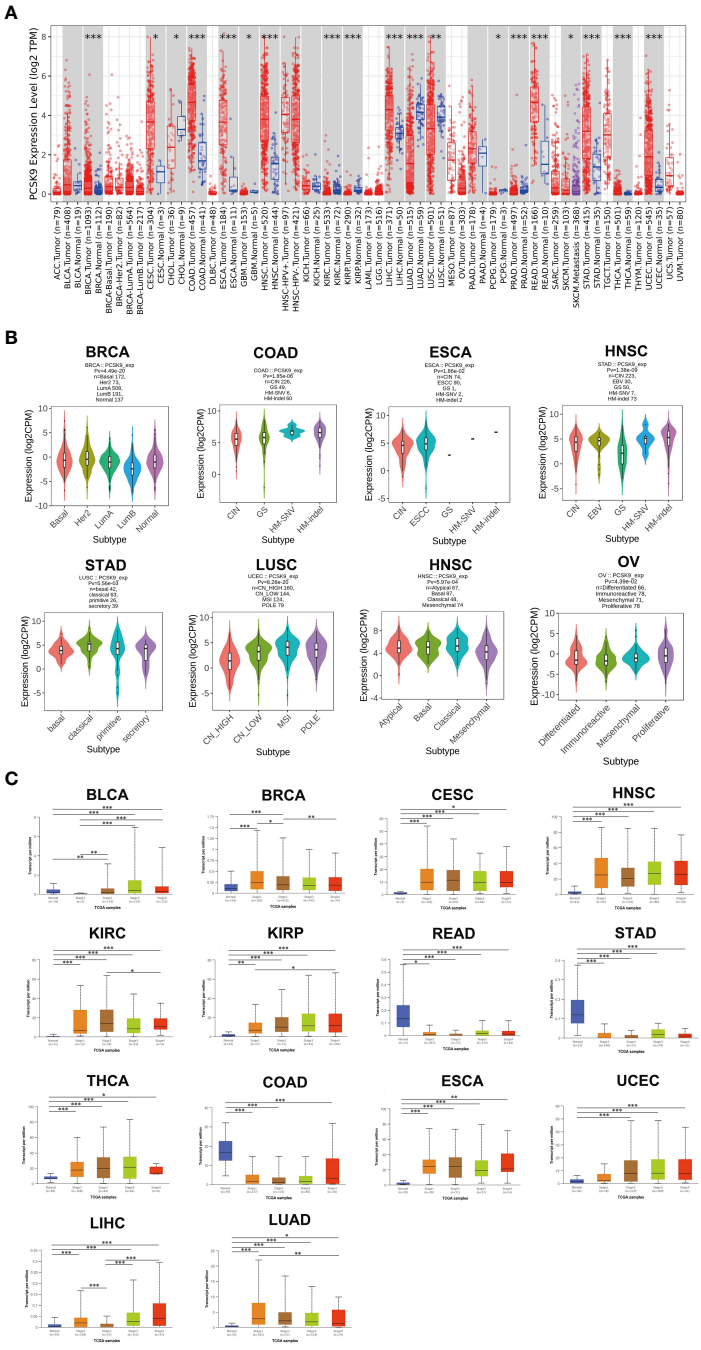

FIGURE 1
(A) PCSK9 expression levels in different cancer types. Increased or decreased expression of *PCSK9* compared with normal tissues across different cancer types from the TCGA database in TIMER (*p < 0.05, **p < 0.01, ***p < 0.001). **(B)** Pan-cancer *PCSK9* expression in different subtypes. (A–H), Pan-cancer differential expression of *PCSK9* in different cancer subtypes in the indicated tumor types from GEPIA. **(C)** Correlation between *PCSK9* expression and the main pathological WHO stages for BLCA, BRCA, CESC, HNSC, KIRC, KIRP, READ, STAD, THCA, COAD, ESCA, UCEC, LIHC, and LIHC (A–N) from the UALCAN database (*p < 0.05, **p < 0.01, ***p < 0.001).

status in human cancers. Furthermore, similar results were concluded from GSCALite data, which revealed a relatively high mutation frequency in diverse types of cancer. We also investigated the frequency of CNV changes of *PCSK9*. The results showed that tumors, including TGCT, BRCA, COAD, SKCM, PCPG, PRAD, LIHC, BLCA and KIRC, were significantly correlated with the CNV changes (Figure 2E).

3.3 Multifaceted prognostic value of *PCSK9* across cancers

The PrognoScan database was used to explore the relationship between *PCSK9* expression and prognosis in each cancer, results are summarized in Figure 3. Notably, *PCSK9* expression was significantly associated with five cancer types: brain, colorectal,

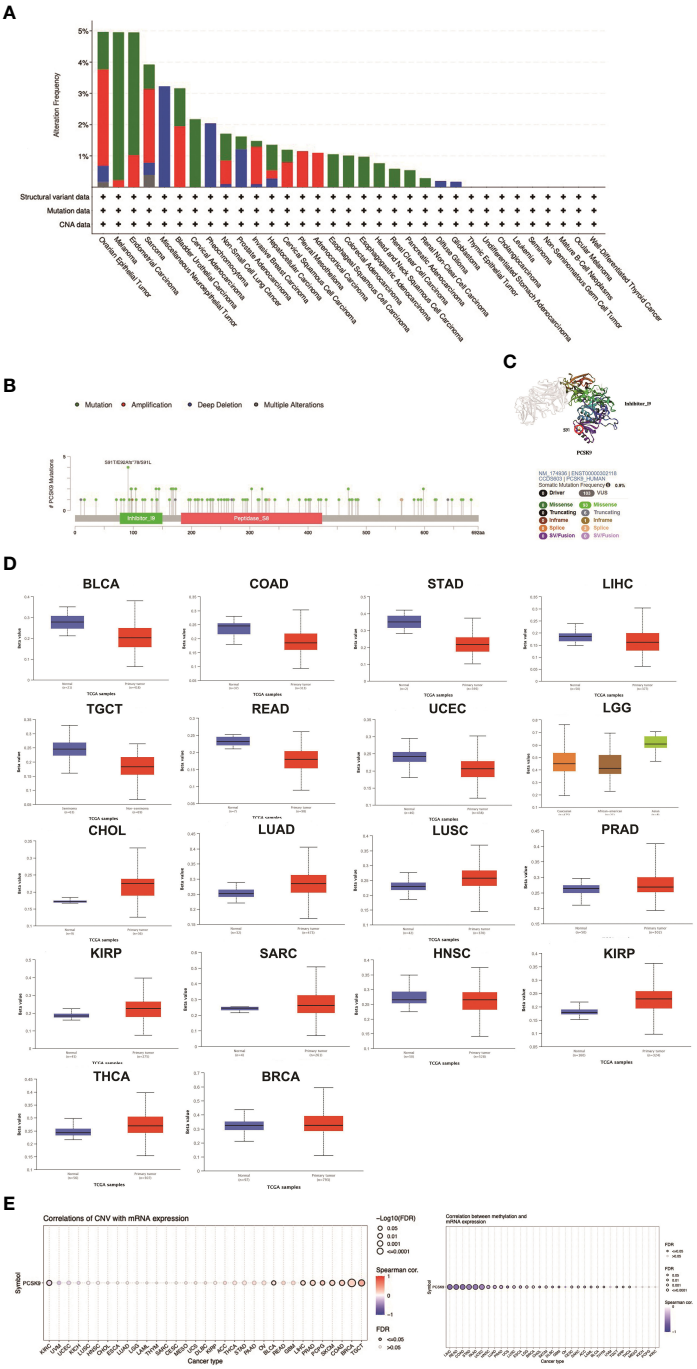

FIGURE 2
DNA methylation and mutation features of PCSK9 across cancer types. **(A)** The alteration frequency with different types of mutations was examined using the cBioPortal database. **(B, C)** The mutation site with the highest alteration frequency (E92Afs*78) in the 3D structure of PCSK9. **(D)** Promoter methylation level of PCSK9 across cancers. The results were obtained from the UALCAN database and GSCA database. **(E)** The correlation between PCSK9 expression and copy number variations (CNV) are shown from the GSCA database.

lung, head and neck, and ovarian cancer (Figure 3A). Among them, *PCSK9* showed a detrimental relationship in three cancer types, including colorectal cancer [OS: total = 177, HR = 1.46, Cox p = 0.048], lung cancer [OS: total = 56, HR = 1.43 Cox p = 0.028], lung cancer [RFS: total = 56, HR = 1.30, Cox p = 0.011] and head and neck cancer [RFS: total = 28, HR = 3.26, Cox p = 0.048]. However, *PCSK9* exhibited a protective effect in two other cancer types, brain cancer [OS: total = 67, HR = 0.01, Cox p = 0.030] and ovarian cancer [PFS (progression free survival): total = 110, HR = 0.89, Cox p = 0.044] (Figure 3A).

To evaluate the relationship between PCSK9 protein expression levels and the prognosis of tumor patients, the Kaplan-Meier Plotter database was used to study the PCSK9 protein expression level in 21 cancer tissues (Figure 3B). In some cancer tissues, such as BLCA

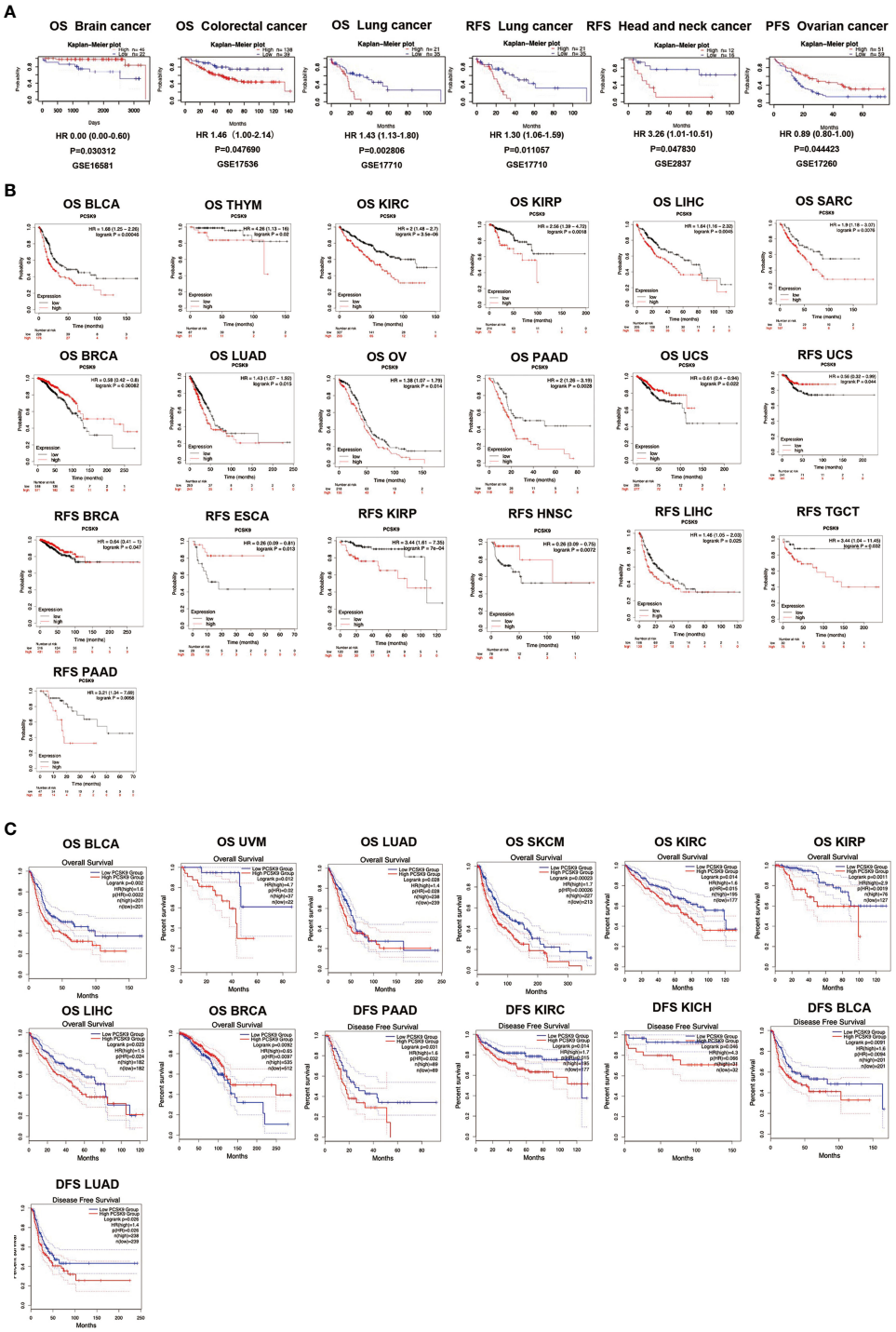

FIGURE 3
(A) Survival analyses of *PCSK9* expression across cancers (based on PrognoScan). OS (n = 67) in brain cancer cohort GSE16581. OS (n = 177) in colorectal cancer cohort GSE17536. OS (n = 56) in lung cancer cohort GSE17710. RFS (n = 56) in lung cancer cohort GSE17710. RFS (n = 28) in head and neck cancer cohort GSE2837. PFS (n = 110) in ovarian cancer cohort GSE17260. OS, overall survival; RFS, relapse free survival; PFS, progression free survival. **(B)** Kaplan-Meier survival curves of survival comparing high and low expression of *PCSK9* in the Kaplan-Meier Plotter database. Overall survival differences between groups in BLCA, THYM, KIRC, KIRP, LIHC, SARC, BRCA, LUAD, OV, PAAD, PCPG, and UCS. (M–T) Relapse-free interval difference between groups in UCS, BRCA, ESCA, KIRP, HNSC, LIHC, TGCT, and PAAD. **(C)** Kaplan-Meier survival curves of survival comparing high and low expression of *PCSK9* in the GEPIA database. (A–H) Overall survival differences between groups in BLCA, UVM, LUAD, SKCM, KIRC, KIRP, LIHC, and BRCA. (I–M) Disease-free interval difference between groups in PAAD, KIRC, KICH, BLCA, and LUAD.

(OS, HR = 1.68, p = 0.0005), THYM (OS, HR = 4.26, p = 0.02), KIRC (OS, HR = 2.56, p = 0.002), LIHC (OS, HR = 1.64, p = 0.005), SARC (OS, HR = 1.9, p = 0.008), LUAD (OS, HR = 1.43, p = 0.015), OV (OS, HR = 1.38, p = 0.014), PAAD (OS, HR = 2.00, p = 0.003), KIRP (RFS, HR = 3.44, p = 0.001), LIHC (RFS, HR = 1.46, p = 0.025), TGCT (RFS, HR = 3.44, p = 0.032), and PAAD (RFS, HR = 3.21, p = 0.006), high expression of PCSK9 correlated with poor OS and RFS. Other cancers exhibited a protective role for PCSK9 with low expression, such as BRCA (OS, HR = 0.58, p = 0.001; RFS, HR = 0.64, p = 0.047), UCS (OS, HR = 0.61, p = 0.022; RFS, HR = 0.56, p = 0.044), ESCA (RFS, HR = 0.26, p = 0.013), and HNSC (RFS, HR = 0.26, p = 0.007).

Similar work was also performed using the GEPIA database. High expression of PCSK9 was associated with a poor OS prognosis in BLCA (p = 0.002), UVM (p = 0.012), LUAD (p = 0.028), SKCM (p = 0.0002), KIRC (p = 0.014), KIRP (p = 0.001), LIHC (p = 0.023), and BRCA (p = 0.009) (Figure 3C). The data showed that high expression of PCSK9 was associated with an adverse DFS prognosis in PAAD (p = 0.031), KIRC (p = 0.014), KICH (p = 0.046), BLCA (p = 0.009), and LUAD (p = 0.026) (Figure 3C).

To verify the correlation between PCSK9 expression and multiple clinicopathological characteristics, we used LIHC as an example. The results indicated that PCSK9 was associated with a detrimental prognosis with five patient or tumor characteristics: female (OS: p = 0.01; PFS: p = 0.02), Asian race [OS: p = 0.01; PFS: p = 0.01], no hepatitis virus infection [OS: p = 0.03; PFS: p = 0.02], pathology stage 2 [OS: p = 0.01] and stage 3 [OS: p = 0.04], grade 2 [OS: p = 0.01], and AJCC stage 2 (OS: p = 0.01) and stage 3 (PFS: p = 0.03) (Figure 4A). A nomogram prediction model was generated by integrating the above clinicopathological parameters and *PCSK9* expression levels. The calibration curve is further evaluated to show that the predictions made by nomogram is in considerable agreement with the actual survival (Figures 4B–D).

3.4 Correlation of PCSK9 expression and stemness

Cancer progression involves the gradual loss of differentiated phenotypes and stemness features. Our correlation analysis revealed that the expression of *PCSK9* was positively correlated with the mRNAsi in COAD, LUAD and LIHC. As for tumors such as SKCM, BLCA and LGG, there is no correlation between the characteristics of stemness and the expression of *PCSK9* (Figures 5A, B).

3.5 KEGG, GO, and GVSA analysis of PCSK9

Taking BLCA as an example, we found that abnormal expression of *PCSK9* was associated with tumor invasion characteristics, cell hypoxia manifestations, and EMT-related markers (Figure 6A). In BRCA, *PCSK9* expression was involved in tumor inflammation signature, reactive oxygen species and transforming growth factor beta (TGF-β) (Figure 6B). The KEGG pathway analysis and GO enrichment analysis were performed to demonstrate the primary biological pathways and potential targets of major potential *PCSK9* mRNA. The results showed that PCSK9 positively regulated cellular adhesion, cholesterol and fatty acid metabolism, PI3K-Akt signaling pathway and immune-related functions in BRCA, LIHC and LUAD (Figures 7A–C).

3.6 Correlation of PCSK9 expression with immune infiltration and various subsets of immune cells

Tumor-infiltrating lymphocytes are independent predictors of sentinel node status and cancer prognosis. The correlation between the expression levels of PCSK9 protein and immune cells in pan-cancer tissues were analyzed using the TIMER database. PCSK9 expression levels significantly correlated with immune cells (CD8+ T cells in 14 types of cancer, dendritic cells (DCs) in 11 types of cancer, and macrophages in 13 types of cancer). We further studied whether PCSK9 expression correlated with the infiltration of different immune cell subtypes using the xCell online tool. The results showed that PCSK9 expression was significantly correlated with subtypes of infiltrating immune cells in various tumors, including HNSC, TGCT, ESCA, COAD, STAD, LUSC, and LIHC (Figure 8A). CD8+ T cells, DCs, and M2 macrophages were the immune cell subtypes most positively associated with PCSK9 expression in these different cancers.

Immune checkpoint inhibitors (ICIs) are novel tumor immunotherapy agents that play an essential role in tumor immunotherapy. Subsequently, we analyzed the correlation between PCSK9 expression and immune checkpoint gene expression levels using the R software package in the SangerBox database. The correlations between 46 immune checkpoint genes and PCSK9 protein expression levels were calculated, and a significant relationship was found in many cancer types with many of the 46 genes, such as THCA (40 of 46), BRCA (37 of 46), LUAD (37 of 46), BLCA (35 of 46), and TGCT (33 of 46) (Figure 8B). Furthermore, the results showed that the expression of PCSK9 in BRCA, BLCA, PRAD, THCA, LIHC, PCPG, and UVM was negatively correlated with immune checkpoint genes. Furthermore, a positive correlation was found in CESC, CHOL, LUAD, STAD, and TGCT. Notably, these immune checkpoint genes contained a broad spectrum of immune regulators, including signaling chemokines, immune stimulators, immune inhibitors, and major histocompatibility complex molecules, such as those related to regulatory T (Treg) cells (chemokine receptor 8, *CCR8*; forkhead box protein p3, *FOXP3*; signal transducer and activator of transcription 5B, *STAT5B*), B cells (*CD19*), macrophages (*CD68*), interleukin-10 (*IL10*), Th17 (signal transducer and activator of transcription 3 (*STAT3*), neutrophils (integrin subunit alpha m, *ITGAM*), natural killer (NK) cells killer cell immunoglobulin-like receptor 2DL (*KIR2DL*), DCs (major histocompatibility complex class II DR beta 1 (*HLA-DPB1*); histocompatibility complex class II DR alpha (*-DRA*; integrin subunit alpha X(*ITGAX*), Th1 cells (interferon gamma (*IFNy)*; tumor necrosis factor (*TNF*), Th2 cells (signal transducer and activator of transcription 6 (*STAT6*; signal transducer and

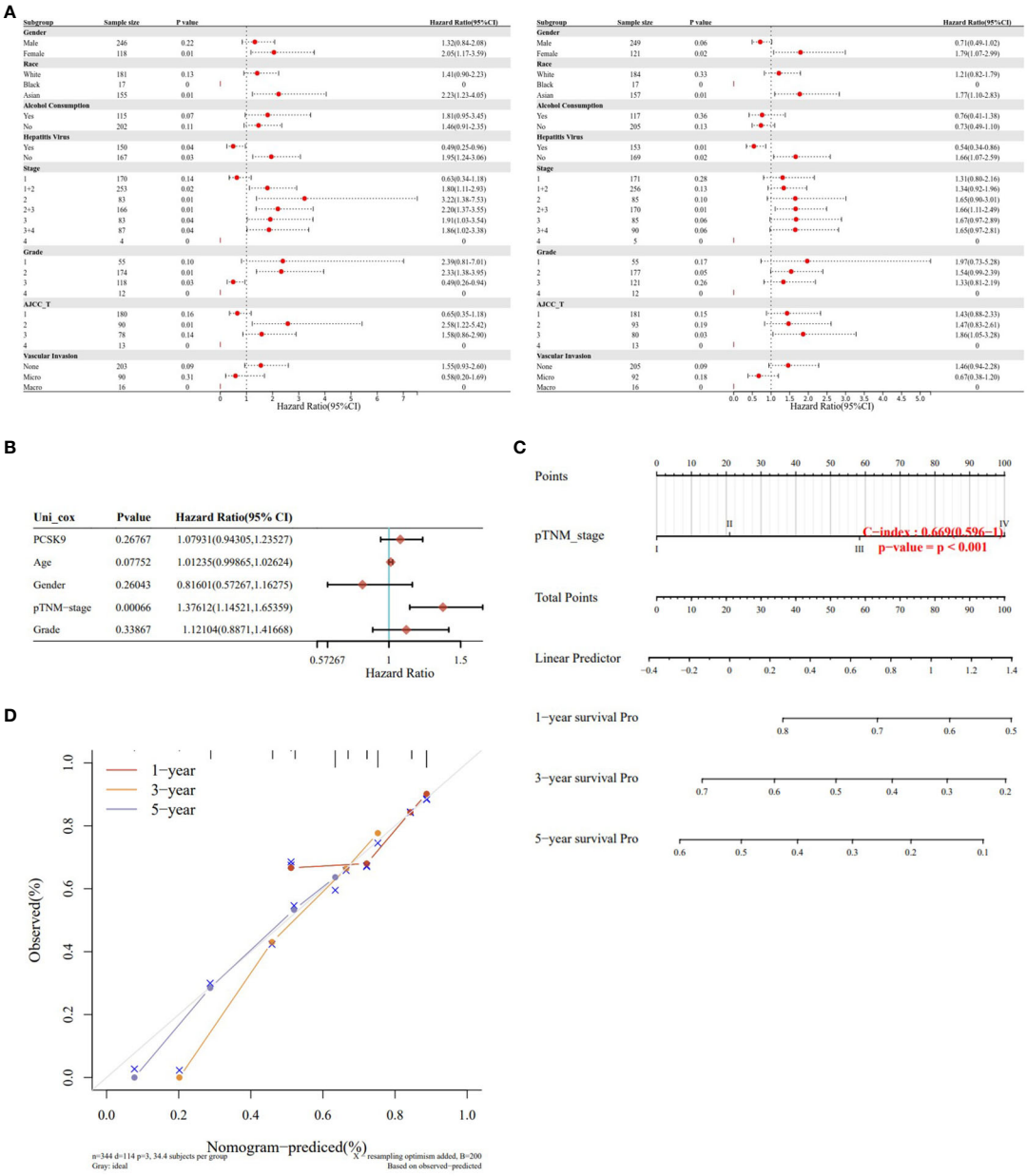

FIGURE 4
Survival analysis of PCSK9 expression in different clinicopathologic features in hepatocellular carcinoma. **(A)** Correlation of PCSK9 mRNA expression with OS in LIHC. **(B)** Correlation of PCSK9 mRNA expression with PFS in LIHC. OS, overall survival; PFS, progression free survival. **(C, D)** Development of a nomogram prediction model using PCSK9 expression levels and clinicopathological parameters for survival prediction.

activator of transcription 5A (*STAT5A*), and exhausted T cells (programmed cell death protein 1 (*PDCD1*); *CTAL4*; hepatitis A virus cellular receptor 2 (*HAVCR2*). Additionally, our results showed a significant correlation between PCSK9 expression with *PDCD1* and *CTLA4*, which referred to T cell exhaustion and led to the loss of T cell function in patients with common chronic infections and cancer.

Immune infiltration plays a vital role in the TME. To evaluate the association between PCSK9 expression and immune infiltration, we further investigated the relationships between the PCSK9 expression and immune cells in three different cancers (BLCA, BRCA, and LIHC) from the TIMMER database (Figure 8C). The immune cells included B cells, CD8+ T cells, CD4+ T cells, macrophages, neutrophils, and DCs. In BLCA, the expression level of PCSK9 significant and positively correlated with CD4+ T cells (R = 0.126, p = 8.55E−05), CD8+ T cells (R = 0.11, p = 6.00E−04), macrophages (R = 0.09, p = 4.88E−03), neutrophils (R = 0.158, p = 1.01E−06), and DCs (R = 0.162, p = 5.23E−07). In BLCA, the correlation between the expression level of PCSK9 with immune cells was significant, including CD8+ T cells (R = 0.246, p = 1.82E−06), CD4+ T cells (R = 0.086, p = 9.93E−02), macrophages (R = 0.167, p = 1.35E−03), neutrophils (R = 0.231, p = 8.38E−06), and DCs (R = 0.356, p = 2.50E−12). In LIHC, we also found a significant correlation of PCSK9 with B cells (R = 0.136, p = 1.17E−02), CD4+

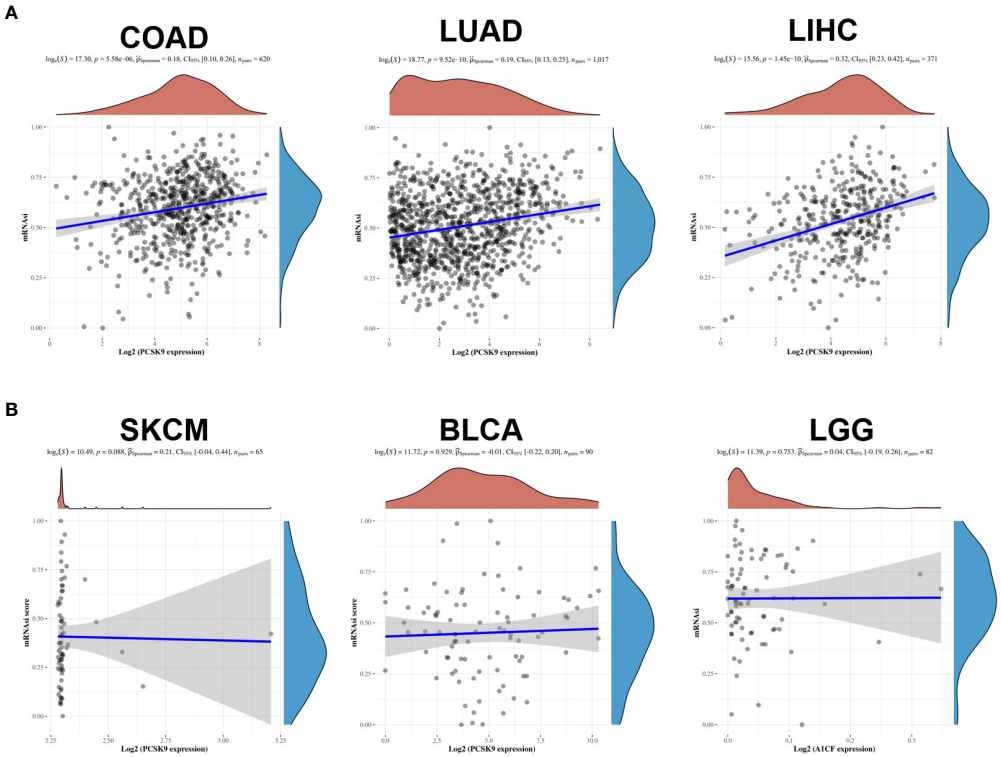

FIGURE 5
Associations of stemness indices with the PCSK9 expression in various cancers. **(A)** Positive correlations between mRNAsi and PCSK9 in COAD, LUAD and LIHC ($p < 0.05$). **(B)** No correlation between mRNAsi and PCSK9 expression in SKCM, BLCA and LGG ($p > 0.05$).

T cells (R = 0.132, p = 1.40E−02), macrophages (R = 0.143, p = 7.98E−03), neutrophils (R = 0.098, p = 7.03E−02), and DCs (R = 0.131, p = 1.60E−02). There was no correlation between PCSK9 and B cells in BRCA or BLCA ($p > 0.05$), or LIHC with CD8+ T cell ($p > 0.05$). In addition, PCSK9 expression strongly correlated with tumor-associated macrophages and DCs in these three cancers. These findings strongly suggested that PCSK9 affected the immune microenvironment by interacting with immune cell infiltration in various cancers.

Considering the heightened sensitivity of gamma delta T cells, particularly gamma 9 delta 2 T cells, towards alterations in the cholesterol pathway, it would be significant to include these cells as a specific control in the immune infiltration analysis. Thus, we further evaluated the immune cell infiltration scores associated with tumor samples obtained from the TCGA database. By utilizing the "corr.test" function in R software, we ultimately identified a significant correlation between PCSK9 expression and gamma delta T cell immune infiltration scores. Specifically, we observed a significant association between PCSK9 expression and gamma delta T cell infiltration in five types of tumors (TGCT, COAD, PRAD, LUSC and LIHC). These results indicated incorporating gamma delta T cells into the analysis would provide additional insights into the potential impact of PCSK9 and its role in modulating immune responses within the tumor microenvironment (Supplementary Figure 1).

To further unravel the potential predictive value of *PCSK9* gene alterations for ICI treatment, we then investigated the relationship between *PCSK9* alterations and six common immune infiltrates (B cells, CD4+ T cells, CD8+ T cells, macrophages, neutrophils, and DCs) across multiple cancer types. We demonstrated that *PCSK9* is frequently altered across different cancer types. Furthermore, we investigated the relationship between the *PCSK9* CNV and immune infiltration in various cancers (Figure 8D i–v). For six types of immune cells, we verified a correlation of the *PCSK9* CNV with immune infiltration. CD8+ and CD4+ T cells were associated with *PCSK9* deletions in LIHC, BLCA, BRCA, and THCA. Deletion of *PCSK9* was significantly related to infiltration of CD4+ T cells (p = 0.001), neutrophils (p = 0.001), and DCs (p = 0.05) in BRCA. These results suggested a possible mechanism by which immune cells may be affected by PCSK9 in the TME, which may help direct future immunotherapy treatments.

3.7 Correlation of PCSK9 expression and clinical chemotherapies

GDSC showed that high expression of *PCSK9* could make cancer more sensitive to IPA-3 (target PAK1), (5Z)-7-Oxozeaenol (target TAK1), Nutlin-3a (target MDM2), Navitoclax (target BCL2) and resistant to Docetaxel (target microtubule stabilizer), Epothilone B (target microtubule stabilizer), OSU-03012 (target PDK1) (Figure 9A). While in CTRP database, IC50 of QW-BI-011, CCT036477, CIL70, PRIMA-1, PRIMA-1-Met, teniposide, ML210, BRD-K92856060, BRD-K26531177 and avrainvillamide showed top 10 significant positive correlations with the expression level of

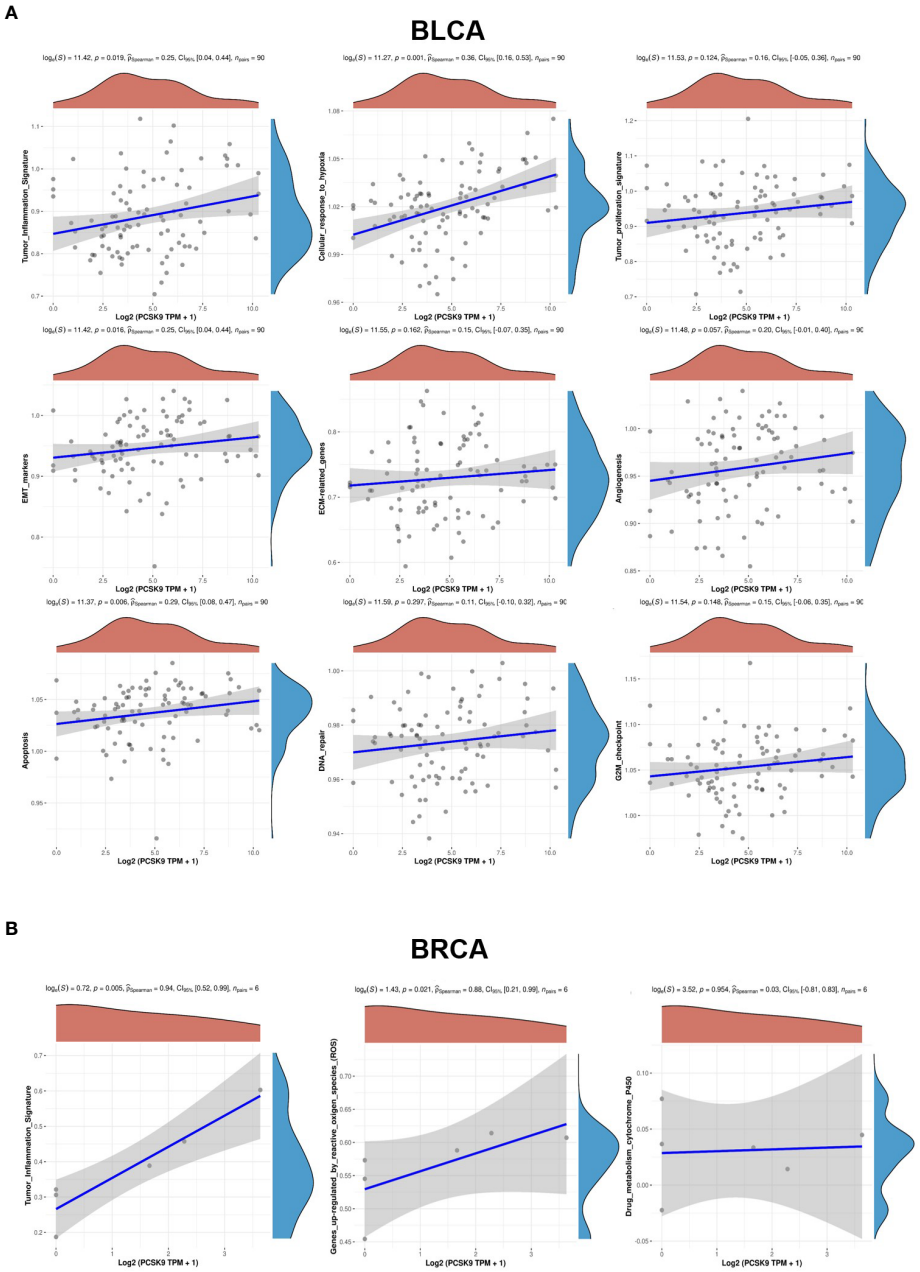

FIGURE 6
GVSA analysis of PCSK9 in various tumors. **(A)** BLCA, **(B)** BRCA.

PCSK9 (Figure 9B). Collectively, these results may provide new ideas for developing potential drugs relating to the expression of *PCSK9* for treating cancers.

3.8 Experimental verification of PCSK9 in neuroblastoma

To confirm PCSK9 expression in NB, we measured mRNA and protein levels of PCSK9 in paired NB and adjacent non-tumor tissues using qRT-PCR (n = 18; Figure 10A) and western blotting (n = 18; Figure 10A). Our findings revealed that PCSK9 expression in tumor tissues was significantly higher at both the transcriptional and protein levels than in adjacent normal tissues ($p < 0.001$).

Immune cells play an essential role in tumor immune tolerance. Immunotherapy (such as disialoganglioside GD2) has been incorporated into first-line treatment regimens of relapsed NB to significantly improve patient outcomes. Remarkably, immune cells, such as NK cells and macrophages, are thought to be the main effectors of anti-GD2 antibody potency in NB tumors. Thus, to investigate the role of immune cells in the NB TME, we used western blotting to measure the levels of CD11b, CD45, and CD68 expression in NB tissues (Figure 10B). The results showed that CD11b (PDC#2, PDC#4, and PDC#5) was positive for immune

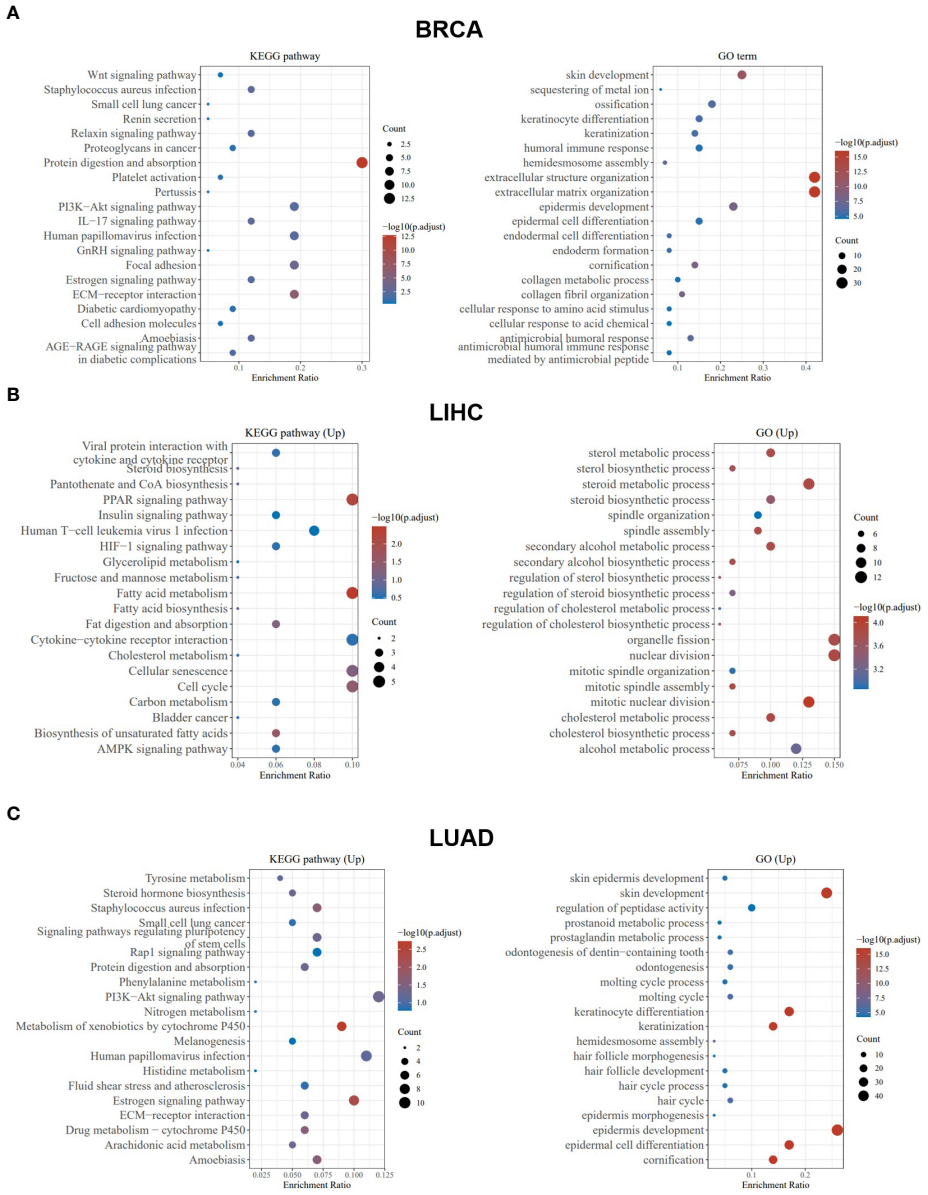

FIGURE 7
PCSK9-related KEGG pathway analysis and GO enrichment analysis. **(A–C)** KEGG pathway analysis and GO enrichment analysis of biological processes based on the PCSK9-interacted and PCSK9-correlated genes in BRCA, LIHC and LUAD.

infiltration of NB, which represented the potential involvement of NK cells in immune infiltration (Figure 10B).

Furthermore, we investigated the PCSK9 prognostic value in NB patients. Upregulated PCSK9 was associated with a lower PFS in the NB cohort, which was consistent with our database survival analysis (HR = 1.51, Figure 10C). Our findings showed that PCSK9 was negatively associated with NK cell infiltration in NB, implying a potential role of PCSK9 modulation in the NB microenvironment.

4 Discussion

Pan-cancer evaluations are increasingly being used to uncover functional genes, particularly those with immunological roles in oncology. To better understand the commonalities and heterogeneities during the fundamental biological processes of distinct malignancies, pan-cancer approaches have been employed. The data from such studies is beneficial for developing novel strategies of cancer prevention and treatment targets (26).

Reports of PCSK9 involvement in the management of dysregulated cholesterol levels and atherosclerotic cardiovascular diseases are well established. For example, PCSK9 inhibition during coronary artery disease is recognized as an effective therapeutic strategy. Additionally, several studies on cholesterol regulation in tumor sites have been proposed to be due to the corresponding association between PCSK9 and oncogenesis (27, 28). Therefore, PCSK9 regulation in physiological processes such as cancer cell death and cell proliferation is in addition to its role in cholesterol

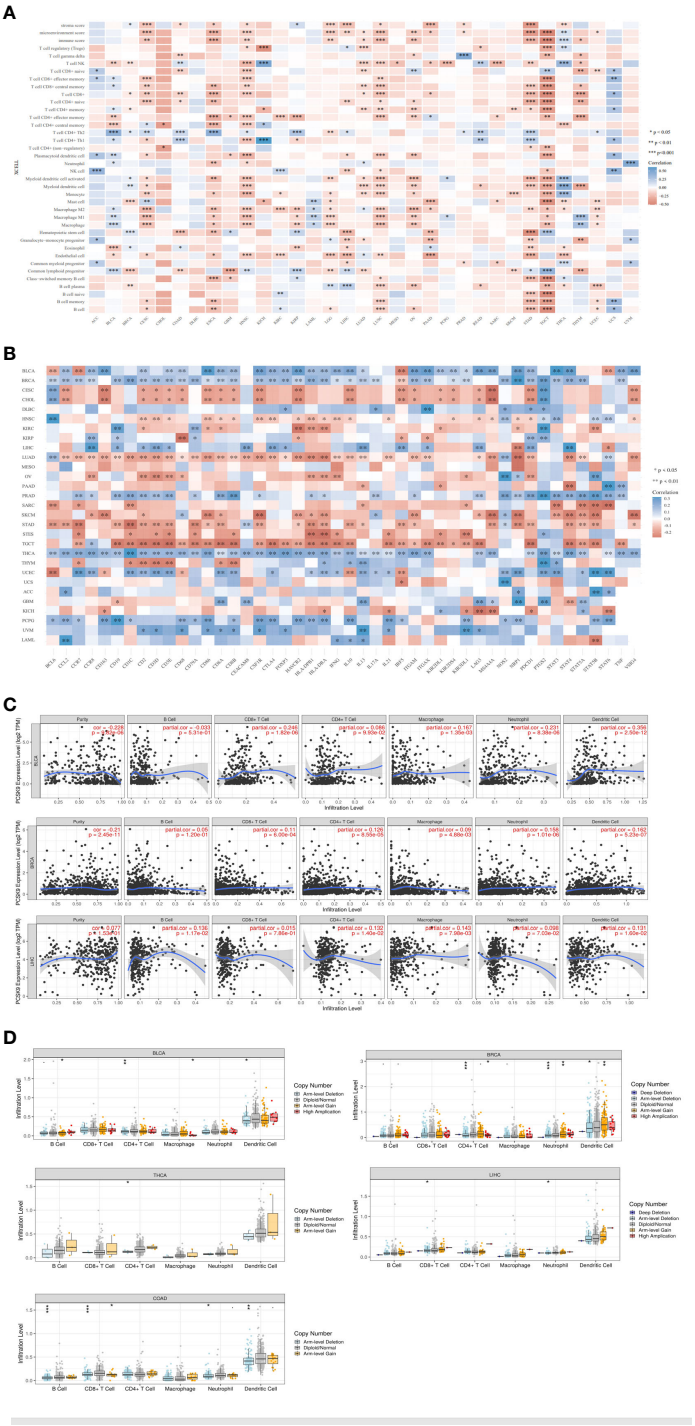

FIGURE 8
Correlation of *PCSK9* expression with immune infiltration and various subsets of immune cells. **(A)** Correlation of *PCSK9* expression with the levels of infiltrating immune cells based on xCell (*$p < 0.05$, **$p < 0.01$). **(B)** Correlation between *PCSK9* expression and immunosuppressive factors or immune stimulatory factors (*$p < 0.05$, **$p < 0.01$). **(C)** Correlation between *PCSK9* expression and infiltration scores of six immune infiltrates, including B cells, $CD4^+$ T cells, $CD8^+$ T cells, dendritic cells, macrophages, and neutrophils, in BRCA, BLCA, and LIHC. **(D)** The association between *PCSK9* copy number variations and immune infiltrates in LIHC, BLCA, BRCA, COAD, and THCA (i–v, *$p < 0.05$, **$p < 0.01$, ***$p < 0.001$).

homeostasis (10). The finding that PCSK9 and PD-1 might collaborate to enhance T cell immunological tolerance suggests a potential role in the immunotherapy of tumors. However, the function of PCSK9 in human cancers has not been determined, and it is not yet known if PCSK9 could have a significant impact on the immunological crosstalk associated with cancer and, in turn, affect the prognosis of different cancer types. Our novel findings are discussed below.

First, we conducted extensive data searches from TIMER to investigate the levels of *PCSK9* expression in diverse tumor types.

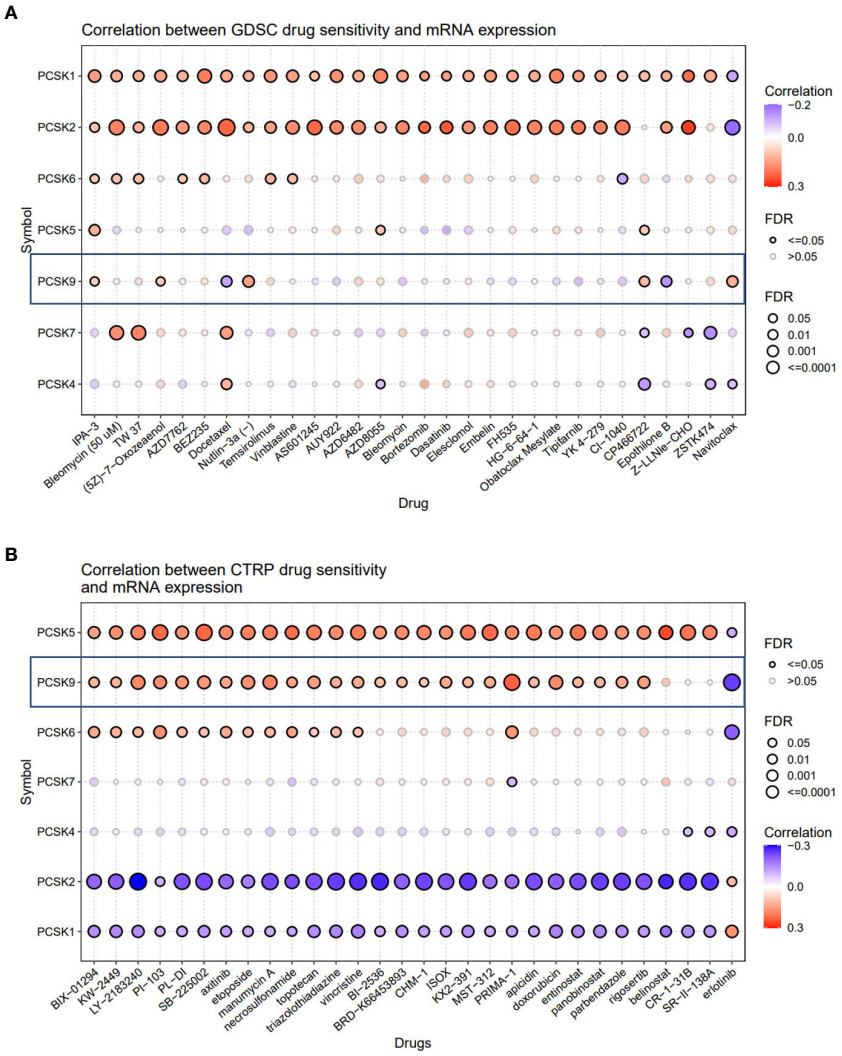

FIGURE 9
Correlation analysis between PCSK9 expression and drug sensitivity. **(A)** Correlation between PCSK9 and sensitivity of the top 10 anticancer drugs in GDSC database. **(B)** Difference of drug sensitivity between PCSK9-related expression groups in CTRP database.

The results revealed dysregulated *PCSK9* expression in different cancers. *PCSK9* expression was shown to be considerably higher in the following tissues: BRCA, CESC, CHOL, COAD, ESCA, HNSC, LIHC, READ, SKCM, STAD, THCA, and ECEC. Low levels of *PCSK9* were expressed in malignancies of the brain, kidney, lung, and prostate. Our results further detailed that tumor with substantial *PCSK9* expression may express different levels at various stages and subtypes, based on the GEPIA and UALCAN databases. DNA methylation has recently been demonstrated to serve significant regulatory functions in cancer development. In support of the positive relationship between DNA methylation and PCSK9 dysregulation, our study discovered that melanoma, non-small cell lung cancer, cervical squamous cell carcinoma, ESCA, LIHC, SARC, BLCA, and BRCA all had greater levels of *PCSK9* methylation. Taken together, aberrantly expressed *PCSK9* was related to cancer progression and cancer prognosis through modulation of *PCSK9* DNA methylation, an epigenetic hallmark of cancer.

Next, we visualized the prognostic landscape in human cancers using independent datasets from TCGA data in GEPIA and Kaplan-Meier Plotter. Our study indicated that *PCSK9* was a significant prognostic factor in various cancer types. However, an apparent heterogeneity was observed in different tumors regarding prognosis with some cancers exhibiting protective effects whilst others showed a pathogenic or an insignificant link. Concerning the heterogeneity, we further explored the correlation between *PCSK9* expression and several clinicopathological characteristics in different stages and grades of LIHC. The results showed that different factors could to some extent explain the heterogeneity of cancers that may have led to a protective or detrimental *PCSK9* prognostic relationship. These findings suggested that *PCSK9* may be a tumor molecular marker according to different forms of initiation and progression of LIHC.

Another significant discovery was the correlation between *PCSK9* expression and various infiltrating types of immune cells in the majority of cancer types. These cells, including Treg cells,

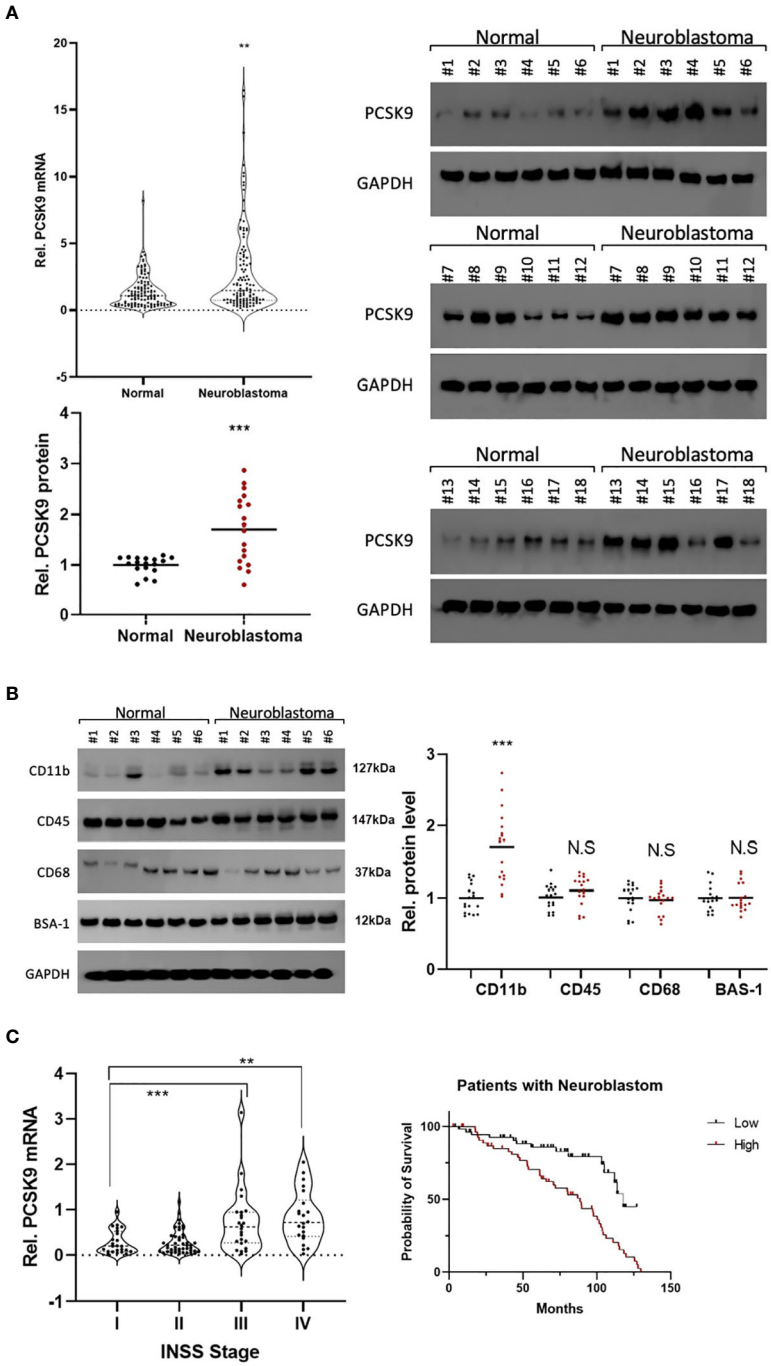

FIGURE 10
(A) Preliminary experimental verification of PCSK9 expression in neuroblastoma (NB). The mRNA and protein expression levels of PCSK9 in paired NB and adjacent non-tumor tissues by qRT-PCR (n=18; Figure 1A) and western blotting (n=18; Figures 1B, C) **p < 0.01, ***p < 0.001; **(B)** The association between NK cell-relevant immune checkpoints (CD11b, CD45, CD68) and PCSK9 expression in NB was detected by western blot in 18 NB tissue samples (***p < 0.001). **(C)** The association between PCSK9 expression in different clinical stages and survival analysis of patients. WHO stage III and IV showed highly expressed PCSK9 that correlated with poor progression-free survival (PFS, HR=1.51, 95% CI 1.25–1.71, p < 0.05).

DCs, macrophages, neutrophils, and tumor-infiltrating lymphocytes (B cells and T cells), are crucial for the development and spread of tumors (29, 30). For instance, Treg cells are thought to be suppressors of overactive immunological responses by producing CTLA4, IL-10, and TGF, which may allow tumor cells to evade the immune system (31, 32). Treg cells may also affect the proportion of CD4+ and CD8+ T cells and T cell differentiation (33). However, under the influence of the TME, Treg cells are immature and have a poor immune regulatory capacity, which could result in tumor immune escape. Studies have demonstrated the complex regulatory network of Treg cells in the TME, which makes Treg regulation in immunotherapy more challenging (34). Our research found a link between aberrant *PCSK9* expression and the presence of Tregs in a variety of malignancies (Figure 10A),

which may help to explain the synergistic effects of PCSK9 and PD-1 in immunotherapy.

The degree of CD8+ T cell infiltration into a tumor is yet another process that has been correlated with improved prognosis (35, 36). CD8+ T cells serve crucial functions in the immune system of the tumor, not only by attracting other immune cells and increasing the immunological response, but also by increasing the effectiveness of cancer immunotherapy, and ultimately improving the prognosis of patients (37). Furthermore, our examination of the pan-cancer population highlighted a correlation between PCSK9 expression and CD8+ T cell subpopulations in LIHC and LUAD. These findings suggested that PCSK9 might be involved in a significant and essential role in the immune infiltration.

Immune checkpoints that are abnormally expressed in the immune cell membrane or that act through receptors on cell membranes have the potential to be modulated by an oncogene (38). In this study, we gathered expression information on over 40 common immune checkpoint genes and investigated the connection between PCSK9 and these immune checkpoint genes. Using LIHC as an example, upregulated PCSK9 expression was positively linked with immunosuppressive checkpoint genes such as *PDCD1* (encoding PD-1), *CTLA4*, and *LAG3*, which are primarily expressed in exhausted T cells and consequently influence the prognosis of LIHC (39). A correlation of co-inhibition of *PCSK9* and *PDCD1* or *CTLA4* immune checkpoints could explain the enhanced effect of combining two or more ICIs in the 2nd generation immune therapy strategy (37). *FOXP3* and *CCR8* strongly correspond with *PCSK9* expression in LIHC, indicating that they may be involved in adaptive immune responses such as Treg cell-mediated immune response control (40). Next, we chose LUAD as another example, as we previously revealed that *PCSK9* was downregulated in LUAD patients, and associated with a poorer prognosis. In the immune checkpoint examination, a significant negative correlation existed between *PCSK9* and *CD163*, V-set and Ig domain-containing 4 (*VSIG4*), and membrane spanning 4-domains A4A (*MS4A4A*), which encode proteins exhibited on the surface of M2 macrophages, indicating the relationship with M2 macrophage polarization in the tumor microenvironment (41, 42). Furthermore, we also found a significant negative relationship between *PCSK9* overexpression and *NOS2*, which encodes a protein found on the surface of M1 macrophages. Collectively, these findings elucidated a possible stimulus function of M2 polarization and inflammation when considered jointly. Above all, these findings strongly suggest that *PCSK9* could be a future cancer immunotherapy target based on the interaction of immune cells in multiple cancer types.

The function of PCSK9 was not only to regulate cholesterol and prevent cardiovascular diseases, but also to potentiate the application of PCSK9 inhibitors in ischemia-reperfusion injury and enhance the synergistic anticancer effect of PD-1. All these highlighted the potential application prospect of PCSK9 inhibitors in clinic. Furthermore, recent research has unveiled an additional role of PCSK9 in the degradation of major histocompatibility complex I (MHC-I) receptors, exerting effects on the immune system and various physiological functions. This significant finding suggests a potential strategy of inhibiting PCSK9 to potentially augment T cell infiltration within tumors and enhance the response to immune checkpoint therapy. Overall, the discovery of PCSK9's regulation of MHC I levels on cell surfaces represents a crucial breakthrough, providing valuable insights into immune infiltration within tumor microenvironments. Our study further analyzed the signal pathways that may performed in the tumorigenesis and revealed the sensitivity of PCSK9 correlated with anti-tumor drugs in tumor treatment and their corresponding targets, such as PAK1, BCL2 and MDM2. These results indicated the potential role of PCSK9 in chemosensitivity or resistance in different cancers. However, our study's use of numerous datasets was not without its limitations. For example, past laboratory findings could not support a logical interpretation of the link between *PCSK9* expression and methyltransferase gene expression. Whilst useful conclusions could be drawn from our data based on numerous pan-cancer patient datasets, proof of concept clinical trials are needed to validate them. Specifically, the execution of functional tests and mechanistic investigations in *in vivo* and *in vitro* research, as well as clinical trials, are therefore needed for further analysis. Finally, even though we were able to show that *PCSK9* expression was associated with tumor immune cell infiltration and patient survival, we were not certain that *PCSK9* affected clinical survival through the immunological system; this requires further clinical trial verification.

Recently, the association between *PCSK9* and extracellular vesicle-derived miRNA has been studied in the context of cardiovascular disease (43). Studies have found that extracellular vesicles (EVs) can be induced by *PCSK9* and hence transport miRNAs to target cells, where the miRNAs can further modulate the expression of target genes, including LDLR and TLR4 (44). The interaction between *PCSK9* and EVs in tumorigenesis was interesting, but due to limited research, our pan-cancer analysis cannot reveal this point. Further study is of great significance to fully understand the specific mechanisms of the interaction between EVs and miRNAs to regulate the expression of *PCSK9* and its influence on tumor mechanisms. Interestingly, emerging data show that the circulating concentration of *PCSK9* in women is higher than that in men, which indicates that the potential roles of *PCSK9* may be different according to gender (45, 46). However, these researches of sex-related *PCSK9* mainly focused on cardiovascular diseases. As we mentioned that some studies have found that higher levels of *PCSK9* are associated with increased risk of colorectal cancer and liver cancer in both men and women. And some breast cancer patients showed that women with higher levels of *PCSK9* had a higher risk of developing metastatic disease. Hence, about the relationship between sex-related *PCSK9* and tumor, it needs to be further explained. Since the expression of *PCSK9* is sex-related, research is needed to explore if there are differences in the association of *PCSK9* and cancer risk between men and women. Although our pan-cancer analysis did not include related gender factors, the relationship between the abnormal expression of *PCSK9* related to gender and the prognosis, immune infiltration and treatment of tumor deserves further consideration. Since the current *PCSK9* inhibitors have been used in clinic, and the incidence of subsequent related tumors in these patients can be compared in a prospective study to help prove the potential of *PCSK9* in tumor immunotherapy.

To the best of our knowledge, this is the first report based on data mining and in-depth bioinformation analysis on the comprehensive

molecular characteristics of *PCSK9* across diverse cancer types. Furthermore, we found a strong correlation between *PCSK9* expression and an immune checkpoint marker and immune cell infiltration levels. Finally, our observation that aberrant PCSK9 expression was associated with a poorer prognosis and immunity in neuroblastoma is consistent with previous pan-cancer findings. Further investigations and clinical trials are warranted to validate the utility of PCSK9 as a reliable biomarker and explore its potential role in guiding immunotherapeutic interventions for cancer treatment.

Data availability statement

The data used to support the findings of this study can be available in the article. All the raw data of this study can be directed to the corresponding author upon request.

Ethics statement

The studies involving humans were reviewed and approved by the Ethics Committee of the Children's Hospital of Suzhou University (No. 20170606013). The studies were conducted in accordance with the local legislation and institutional requirements. Written informed consent for participation in this study was provided by the participants or the participants' legal guardians/next of kin.

Author contributions

Conception and design were performed by ZW. There was no administrative support. Study materials or patients were provided by SH. Data was collected and assembled by CS and GZ. Data analysis and interpretation were carried out by CHS, JL, ZM, and RL. The manuscript was written by all authors. The final version of the manuscript was approved by all authors.

Funding

This work was supported by the National Natural Science Foundation of China (Nos. 81873874 and 82071797) and Clinical Research Plan of SHDC (No. SHDC2020CR2021B).

Conflict of interest

The authors declare that the research was conducted in the absence of any commercial or financial relationships that could be construed as a potential conflict of interest

Publisher's note

Supplementary material

The Supplementary Material for this article can be found online at: https://www.frontiersin.org/articles/10.3389/fonc.2023.1134063/full#supplementary-material

SUPPLEMENTARY TABLE 1
PolyPhen-2 predicts the impact of mutations of PCSK9 on protein function.

SUPPLEMENTARY FIGURE 1
The correlation between PCSK9 expression and gamma delta T cell immune infiltration scores.

References

1. Han Y, Liu D, Li L. PD-1/PD-L1 pathway: current researches in cancer. *Am J Cancer Res* (2020) 10(3):727–42.

2. Bellmunt J, de Wit R, Vaughn DJ, Fradet Y, Lee JL, Fong L, et al. Pembrolizumab as second-line therapy for advanced Urothelial carcinoma. *N Engl J Med* (2017) 376 (11):1015–26. doi: 10.1056/NEJMoa1613683

3. Tang T, Huang X, Zhang G, Hong Z, Bai X, Liang T. Advantages of targeting the tumor immune microenvironment over blocking immune checkpoint in cancer immunotherapy. *Signal Transduct Target Ther* (2021) 6(1):72. doi: 10.1038/s41392-020-00449-4

4. Wu T, Dai Y. Tumor microenvironment and therapeutic response. *Cancer Lett* (2017) 387:61–8. doi: 10.1016/j.canlet.2016.01.043

5. Darvin P, Toor SM, Sasidharan Nair V, Elkord E. Immune checkpoint inhibitors: recent progress and potential biomarkers. *Exp Mol Med* (2018) 50(12):1–11. doi: 10.1038/s12276-018-0191-1

6. Abifadel M, Varret M, Rabès JP, Allard D, Ouguerram K, Devillers M, et al. Mutations in PCSK9 cause autosomal dominant hypercholesterolemia. *Nat Genet* (2003) 34(2):154–6. doi: 10.1038/ng1161

7. Romagnuolo R, Scipione CA, Boffa MB, Marcovina SM, Seidah NG, Koschinsky ML. Lipoprotein(a) catabolism is regulated by proprotein convertase subtilisin/kexin type 9 through the low density lipoprotein receptor. *J Biol Chem* (2015) 290(18):11649–62. doi: 10.1074/jbc.M114.611988

8. Raal FJ, Giugliano RP, Sabatine MS, Koren MJ, Blom D, Seidah NG, et al. PCSK9 inhibition-mediated reduction in Lp(a) with evolocumab: an analysis of 10 clinical trials and the LDL receptor's role. *J Lipid Res* (2016) 57(6):1086–96. doi: 10.1194/jlr.P065334

9. Fitzgerald K, White S, Borodovsky A, Bettencourt BR, Strahs A, Clausen V, et al. A highly durable RNAi therapeutic inhibitor of PCSK9. *N Engl J Med* (2017) 376(1):41–51. doi: 10.1056/NEJMoa1609243

10. Stoekenbroek RM, Lambert G, Cariou B, Hovingh GK. Inhibiting PCSK9 - biology beyond LDL control. *Nat Rev Endocrinol* (2018) 15(1):52–62. doi: 10.1038/s41574-018-0110-5

11. Ortona S, Barisione C, Ferrari PF, Palombo D, Pratesi G. PCSK9 and other metabolic targets to counteract ischemia/reperfusion injury in acute myocardial infarction and visceral vascular surgery. *J Clin Med* (2022) 11(13):3638–58. doi: 10.3390/jcm11133638

12. Macchi C, Ferri N, Sirtori CR, Corsini A, Banach M, Ruscica M. Proprotein convertase subtilisin/kexin type 9: A view beyond the canonical cholesterol-lowering impact. *Am J Pathol* (2021) 191(8):1385–97. doi: 10.1016/j.ajpath.2021.04.016

13. Liu X, Bao X, Hu M, Chang H, Jiao M, Cheng J, et al. Inhibition of PCSK9 potentiates immune checkpoint therapy for cancer. *Nature* (2020) 588(7839):693–8. doi: 10.1038/s41586-020-2911-7

14. Yuan J, Cai T, Zheng X, Ren Y, Qi J, Lu X, et al. Potentiating CD8(+) T cell antitumor activity by inhibiting PCSK9 to promote LDLR-mediated TCR recycling and signaling. *Protein Cell* (2021) 12(4):240–60. doi: 10.1007/s13238-021-00821-2

15. Pan JH, Zhou H, Cooper L, Huang JL, Zhu SB, Zhao XX, et al. LAYN is a prognostic biomarker and correlated with immune infiltrates in gastric and colon cancers. *Front Immunol* (2019) 10:6. doi: 10.3389/fimmu.2019.00006

16. Tang Z, Kang B, Li C, Chen T, Zhang Z. GEPIA2: an enhanced web server for large-scale expression profiling and interactive analysis. *Nucleic Acids Res* (2019) 47 (W1):W556–w560. doi: 10.1093/nar/gkz430

17. Ru B, Wong CN, Tong Y, Zhong JY, Zhong SSW, Wu WC, et al. TISIDB: an integrated repository portal for tumor-immune system interactions. *Bioinformatics* (2019) 35(20):4200–2. doi: 10.1093/bioinformatics/btz210

18. Gao J, Aksoy BA, Dogrusoz U, Dresdner G, Gross B, Sumer SO, et al. Integrative analysis of complex cancer genomics and clinical profiles using the cBioPortal. *Sci Signal* (2013) 6(269):pl1. doi: 10.1126/scisignal.2004088

19. Tomczak K, Czerwińska P, Wiznerowicz M. The Cancer Genome Atlas (TCGA): an immeasurable source of knowledge. *Contemp Oncol (Pozn)* (2015) 19(1a):A68–77. doi: 10.5114/wo.2014.47136

20. Chandrashekar DS, Bashel B, Balasubramanya SAH, Creighton CJ, Ponce-Rodriguez I, Chakravarthi B, et al. UALCAN: A portal for facilitating tumor subgroup gene expression and survival analyses. *Neoplasia* (2017) 19(8):649–58. doi: 10.1016/j.neo.2017.05.002

21. Liu CJ, Hu FF, Xia MX, Han L, Zhang Q, Guo AY. GSCALite: a web server for gene set cancer analysis. *Bioinformatics* (2018) 34(21):3771–2. doi: 10.1093/bioinformatics/bty411

22. Malta TM, Sokolov A, Gentles AJ, Burzykowski T, Poisson L, Weinstein JN, et al. Machine learning identifies stemness features associated with oncogenic dedifferentiation. *Cell* (2018) 173(2):338–54.e315. doi: 10.1016/j.cell.2018.03.034

23. Mizuno H, Kitada K, Nakai K, Sarai A. PrognoScan: a new database for meta-analysis of the prognostic value of genes. *BMC Med Genomics* (2009) 2:18. doi: 10.1186/1755-8794-2-18

24. Nagy Á, Lánczky A, Menyhárt O, Győrffy B. Validation of miRNA prognostic power in hepatocellular carcinoma using expression data of independent datasets. *Sci Rep* (2018) 8(1):9227. doi: 10.1038/s41598-018-27521-y

25. Yoshihara K, Shahmoradgoli M, Martínez E, Vegesna R, Kim H, Torres-Garcia W, et al. Inferring tumour purity and stromal and immune cell admixture from expression data. *Nat Commun* (2013) 4:2612. doi: 10.1038/ncomms3612

26. Kaubryte J, Lai AG. Pan-cancer prognostic genetic mutations and clinicopathological factors associated with survival outcomes: a systematic review. *NPJ Precis Oncol* (2022) 6(1):27. doi: 10.1038/s41698-022-00269-5

27. Lee S, Zhang C, Liu Z, Klevstig M, Mukhopadhyay B, Bergentall M, et al. Network analyses identify liver-specific targets for treating liver diseases. *Mol Syst Biol* (2017) 13(8):938. doi: 10.15252/msb.20177703

28. Marimuthu A, Subbannayya Y, Sahasrabuddhe NA, Balakrishnan L, Syed N, Sekhar NR, et al. SILAC-based quantitative proteomic analysis of gastric cancer secretome. *Proteomics Clin Appl* (2013) 7(5-6):355–66. doi: 10.1002/prca.201200069

29. Salgado R, Denkert C, Demaria S, Sirtaine N, Klauschen F, Pruneri G, et al. The evaluation of tumor-infiltrating lymphocytes (TILs) in breast cancer: recommendations by an International TILs Working Group 2014. *Ann Oncol* (2015) 26(2):259–71. doi: 10.1093/annonc/mdu450

30. Hwang WT, Adams SF, Tahirovic E, Hagemann IS, Coukos G. Prognostic significance of tumor-infiltrating T cells in ovarian cancer: a meta-analysis. *Gynecol Oncol* (2012) 124(2):192–8. doi: 10.1016/j.ygyno.2011.09.039

31. Whiteside TL. FOXP3+ Treg as a therapeutic target for promoting anti-tumor immunity. *Expert Opin Ther Targets* (2018) 22(4):353–63. doi: 10.1080/14728222.2018.1451514

32. Barbi J, Pardoll D, Pan F. Treg functional stability and its responsiveness to the microenvironment. *Immunol Rev* (2014) 259(1):115–39. doi: 10.1111/imr.12172

33. Whiteside TL. Human regulatory T cells (Treg) and their response to cancer. *Expert Rev Precis Med Drug Dev* (2019) 4(4):215–28. doi: 10.1080/23808993.2019.1634471

34. Tanaka A, Sakaguchi S. Regulatory T cells in cancer immunotherapy. *Cell Res* (2017) 27(1):109–18. doi: 10.1038/cr.2016.151

35. Ohtani H. Focus on TILs: prognostic significance of tumor infiltrating lymphocytes in human colorectal cancer. *Cancer Immun* (2007) 7:4.

36. Azimi F, Scolyer RA, Rumcheva P, Moncrieff M, Murali R, McCarthy SW, et al. Tumor-infiltrating lymphocyte grade is an independent predictor of sentinel lymph node status and survival in patients with cutaneous melanoma. *J Clin Oncol* (2012) 30 (21):2678–83. doi: 10.1200/JCO.2011.37.8539

37. Topalian SL, Drake CG, Pardoll DM. Immune checkpoint blockade: a common denominator approach to cancer therapy. *Cancer Cell* (2015) 27(4):450–61. doi: 10.1016/j.ccell.2015.03.001

38. Ito S, Horikawa S, Suzuki T, Kawauchi H, Tanaka Y, Suzuki T, et al. Human NAT10 is an ATP-dependent RNA acetyltransferase responsible for N4-acetylcytidine formation in 18 S ribosomal RNA (rRNA). *J Biol Chem* (2014) 289(52):35724–30. doi: 10.1074/jbc.C114.602698

39. Sun Y, Xue J. Expression profile and biological role of immune checkpoints in disease progression of HIV/SIV infection. *Viruses* (2022) 14(3):581–609. doi: 10.3390/v14030581

40. Shang B, Liu Y, Jiang SJ, Liu Y. Prognostic value of tumor-infiltrating FoxP3+ regulatory T cells in cancers: a systematic review and meta-analysis. *Sci Rep* (2015) 5:15179. doi: 10.1038/srep15179

41. Yang Z, Zhang M, Peng R, Liu J, Wang F, Li Y, et al. The prognostic and clinicopathological value of tumor-associated macrophages in patients with colorectal cancer: a systematic review and meta-analysis. *Int J Colorectal Dis* (2020) 35(9):1651–61. doi: 10.1007/s00384-020-03686-9

42. Troiano G, Caponio VCA, Adipietro I, Tepedino M, Santoro R, Laino L, et al. Prognostic significance of CD68(+) and CD163(+) tumor associated macrophages in head and neck squamous cell carcinoma: A systematic review and meta-analysis. *Oral Oncol* (2019) 93:66–75. doi: 10.1016/j.oraloncology.2019.04.019

43. Greco MF, Rizzuto AS, Zarà M, Cafora M, Favero C, Solazzo G, et al. PCSK9 confers inflammatory properties to extracellular vesicles released by vascular smooth muscle cells. *Int J Mol Sci* (2022) 23(21):13065–91. doi: 10.3390/ijms232113065

44. Macchi C, Greco MF, Favero C, Dioni L, Cantone L, Hoxha M, et al. Associations among PCSK9 levels, atherosclerosis-derived extracellular vesicles, and their miRNA content in adults with obesity. *Front Cardiovasc Med* (2021) 8:785250. doi: 10.3389/fcvm.2021.785250

45. Kajingulu FM, Lepira FB, Nkodila AN, Makulo JR, Mokoli VM, Ekulu PM, et al. Circulating Proprotein Convertase Subtilisin/Kexin type 9 level independently predicts incident cardiovascular events and all-cause mortality in hemodialysis black Africans patients. *BMC Nephrol* (2022) 23(1):123. doi: 10.1186/s12882-022-02748-0

46. Peng J, Liu MM, Jin JL, Cao YX, Guo YL, Wu NQ, et al. Association of circulating PCSK9 concentration with cardiovascular metabolic markers and outcomes in stable coronary artery disease patients with or without diabetes: a prospective, observational cohort study. *Cardiovasc Diabetol* (2020) 19(1):167. doi: 10.1186/s12933-020-01142-0

frontiers | Frontiers in Immunology

TYPE Original Research
PUBLISHED 12 October 2023
DOI 10.3389/fimmu.2023.1236806

OPEN ACCESS

EDITED BY
Takaji Matsutani,
Repertoire Genesis, Inc., Japan

REVIEWED BY
Shanqiang Qu,
Southern Medical University, China
Han Nie,
Nagasaki University, Japan

*CORRESPONDENCE
Wenjun Yi
yiwenjun@csu.edu.cn

RECEIVED 08 June 2023
ACCEPTED 29 September 2023
PUBLISHED 12 October 2023

CITATION
Zhu J, Chen Q, Zeng L, Gao H, Wu T, He Y, Xu J, Pang J, Peng J, Deng Y, Han Y and Yi W (2023) Multi-omics analysis reveals the involvement of origin recognition complex subunit 6 in tumor immune regulation and malignant progression. *Front. Immunol.* 14:1236806. doi: 10.3389/fimmu.2023.1236806

Multi-omics analysis reveals the involvement of origin recognition complex subunit 6 in tumor immune regulation and malignant progression

Jinfeng Zhu[1,2], Qitong Chen[1,2], Liyun Zeng[1,2], Hongyu Gao[1,2], Tong Wu[1,2], Yeqing He[1,2], Jiachi Xu[1,2], Jian Pang[1,2], Jing Peng[1,2], Yueqiong Deng[1,2], Yi Han[1,2] and Wenjun Yi[1,2]*

[1]Department of General Surgery, The Second Xiangya Hospital, Central South University, Changsha, Hunan, China, [2]Clinical Research Center For Breast Disease In Hunan Province, Changsha, Hunan, China

Background: Origin recognition complex 6 (*ORC6*) is one of the six highly conserved subunit proteins required for DNA replication and is essential for maintaining genome stability during cell division. Recent research shows that *ORC6* regulates the advancement of multiple cancers; however, it remains unclear what regulatory impact it has on the tumor immune microenvironment.

Methods: Unpaired Wilcoxon rank sum and signed rank tests were used to analyze the differences in the expression of *ORC6* in normal tissues and corresponding tumor tissues. Multiple online databases have evaluated the genetic alterations, protein expression and localization, and clinical relevance of *ORC6*. To evaluate the potential prognostic impact and diagnostic significance of *ORC6* expression, we carried out log-rank, univariate Cox regression, and receiver operating characteristic curve analysis. The ICGC-LIRI-JP cohort, CGGA-301 cohort, CGGA-325 cohort, CGGA-693 cohort, and GSE13041 cohort were used for external validation of the study findings. The associations between *ORC6* expression and immune cell infiltration, immune checkpoint expression, and immunotherapy cohorts was further analyzed. To explore the functional and signaling pathways related to *ORC6* expression, gene set enrichment analysis was performed. To clarify the expression and function of *ORC6* in hepatocellular carcinoma (LIHC) and glioma, we conducted *in vitro* experiments.

Results: Expression of *ORC6* is upregulated in the majority of cancer types and is associated with poor patient prognosis, notably in cases of LIHC and gliomas. In addition, *ORC6* may be involved in multiple signaling pathways related to cancer progression and immune regulation. High expression of *ORC6* correlates with an immunosuppressive state in the tumor microenvironment. The results of further immunotherapy cohort analysis suggested that patients in the *ORC6* high-

expression group benefited from immunotherapy. Inhibiting *ORC6* expression suppressed the proliferative and migratory abilities of LIHC and glioma cells.

Conclusion: High expression of *ORC6* may be used as a biomarker to predict the poor prognosis of most tumor patients. The high expression of *ORC6* may be involved in the regulation of the tumor immunosuppressive environment, and it is expected to become a molecular target for inhibiting tumor progression.

KEYWORDS

Orc6, pan-cancer, prognosis, immunotherapy, tumor microenvironment

1 Introduction

Worldwide, cancer presents a life-threatening situation and is one of the most economically burdensome diseases (1). Currently, no treatment for cancer is absolutely effective. As research advances, scientists are increasingly concentrating on the shared characteristics of different malignant tumors to uncover their underlying causes and create targeted inhibitors for cancer therapy (2). For instance, PD-L1 levels are often increased in different cancer types, and recent studies indicate that many oncogenic signaling pathways lead to this overexpression. Antagonistic antibodies against the inhibitory immune checkpoint receptor *PD-1* or its ligand *PD-L1* have shown promise in the treatment of various cancers, leading to significant improvement in patient survival rates (3). Protein tyrosine kinases from the human epidermal growth factor receptor family, such as *EGFR* and *HER2*, are important therapeutic targets for many malignancies, including non-small cell lung cancer, breast cancer, and gastroesophageal cancer, particularly colorectal cancer (4). Aldehyde dehydrogenase (ALDH) serves as a cancer stem cell biomarker across various cancers. Clinically, ALDHs are also regarded as indicators of poor prognosis in solid cancers. Targeting ALDHs may impede cancer stem cells in solid tumors, thereby achieving therapeutic effects (5). Therefore, analyzing the differential expression of genes across cancers, screening valuable genes, and exploring their correlation with clinical prognosis and the tumor immune microenvironment will promote the further development of tumor-targeted therapy and immunotherapy.

The origin recognition complex (ORC) is a vital six-subunit protein that is highly conserved across species and plays a crucial role in DNA replication. It is essential for maintaining genome stability during cell division (6). *ORC6*, the smallest subunit of human ORC, is primarily involved in chromosome segregation, DNA replication, and cell division. It localizes to replication forks to carry out these functions (7). *ORC6* is a cofactor in the mismatch repair (MMR) complex that promotes efficient mismatch repair (8). In recent years, research has identified a correlation between elevated *ORC6* expression and adverse prognostic outcomes in patients with colorectal cancer (9), renal clear cell carcinoma (10), gastric adenocarcinoma (11), and breast cancer (12). Current research on *ORC6* in tumors is restricted to specific types of human cancers. There has been no systematic multi-omics analysis across different types of cancer, notably in liver hepatocellular carcinoma (LIHC) and glioma (GBMLGG).

The research found that *ORC6* was frequently overexpressed in various cancer types and was associated with adverse survival outcomes. Additionally, the biological function of *ORC6* may be linked to RNA modifications, DNA methylation, and the tumor immune microenvironment. By examining *ORC6* across cancers, we observed that it significantly contributes to the development of LIHC and GBMLGG. Our study reveals that *ORC6* acts as an independent risk factor for the overall prognosis of LIHC and GBMLGG. Subsequently, we conducted *in vitro* experiments to elucidate whether *ORC6* promotes the progression of LIHC and GBMLGG. Together, our investigation provides a comprehensive understanding of the tumorigenic role of *ORC6* in different cancers and indicates that *ORC6* could be a dependable biomarker for predicting the clinical prognoses and immune landscapes in patients with LIHC and GBMLGG.

2 Materials and methods

2.1 Data preprocessing and differential expression analysis

We obtained a unified and standardized pan-cancer dataset (TCGA TARGET GTEx, https://xenabrowser.net/) from the UCSC database. Furthermore, we extracted the *ORC6* gene values from each sample and applied $\log_2$ (x+1) transformation for each value. The Sangerbox (13) online tool was used for visualization. In addition, we acquired validation cohorts from external sources, including the International Cancer Genome Consortium (ICGC), Chinese Glioma Genome Atlas Project (CGGA), and Gene Expression Omnibus (GEO) databases. These cohorts included the ICGC-LIRI-JP cohort, CGGA-301 cohort, CGGA-325 cohort, CGGA-693 cohort, and GSE13041 cohort. Cancer-type abbreviations are listed in Table 1.

2.2 Genetic alterations, localization, and interaction network of *ORC6*

The gene mutation type and frequency of *ORC6* in the TCGA pan-cancer dataset were explored by accessing cBioPortal (https://

10.3389/fimmu.2023.1236806

TABLE 1 Tumor types and abbreviations.

Abbreviation	Full name
ACC	Adrenocortical carcinoma
ALL	Acute Lymphoblastic Leukemia
AML	Acute myeloid leukemia
AST	Astrocytoma
BLCA	Bladder Urothelial Carcinoma
BRCA	Breast invasive carcinoma
CESC	Cervical squamous cell carcinoma and endocervical adenocarcinoma
CHOL	Cholangiocarcinoma
CML	Chronic myelogenous leukemia
COAD	Colon adenocarcinoma
COADREAD	Colon adenocarcinoma/Rectum adenocarcinoma
DLBC	Lymphoid Neoplasm Diffuse Large B-cell Lymphoma
ESCA	Esophageal carcinoma
GBM	Glioblastoma multiforme
GBMLGG	Glioma
HGG	High-grade glioma
HNSC	Head and Neck squamous cell carcinoma
KICH	Kidney Chromophobe
KIPAN	Pan-kidney cohort (KICH+KIRC+KIRP)
KIRC	Kidney renal clear cell carcinoma
KIRP	Kidney renal papillary cell carcinoma
LAML	Acute Myeloid Leukemia
LGG	Brain Lower Grade Glioma
LIHC	Liver hepatocellular carcinoma
LSCC	Lung squamous cell cancer
LUAD	Lung adenocarcinoma
LUSC	Lung squamous cell carcinoma
MEL	Melanoma
MESO	Mesothelioma
NSCLC	Non-small cell lung cancer
ODG	Oligodendroglioma
OV	Ovarian serous cystadenocarcinoma
PAAD	Pancreatic adenocarcinoma
PCPG	Pheochromocytoma and Paraganglioma
PRAD	Prostate adenocarcinoma
RB	Retinoblastoma
RCC	Renal cell carcinoma
READ	Rectum adenocarcinoma
SARC	Sarcoma
SKCM	Skin Cutaneous Melanoma
STAD	Stomach adenocarcinoma
STES	Stomach and Esophageal carcinoma
TGCT	Testicular Germ Cell Tumors
THCA	Thyroid carcinoma
THYM	Thymoma
UCEC	Uterine Corpus Endometrial Carcinoma
UCS	Uterine Carcinosarcoma
UM	Uveal Melanoma
UVM	Uveal Melanoma
WT	High-Risk Wilms Tumo

(Continued)

www.cbioportal.org/). We obtained the copy number variation (CNV) dataset at gene level 4 from all TCGA samples processed by GISTIC software (14) through GDC (https://portal.gdc.cancer.gov/). We used the unpaired Wilcoxon rank sum test or the Wilcoxon signed rank test to compare the values between the two groups and the Kruskal–Wallis test for differences among multiple groups.

The Human Protein Atlas (HPA, https://www.proteinatlas.org/) was utilized to obtain images of the subcellular localization of *ORC6* protein in cancer cells (HEK293 and PC-3) by immunofluorescence staining of cells. Furthermore, the subcellular localization of the *ORC6* gene was obtained through the Genecards database.

The comPPI website (http://comppi.linkgroup.hu/) was utilized to analyze the protein-protein interaction network of *ORC6*. The minimum interaction score was 1, and the edge width was scaled based on the interaction score.

2.3 The relationship among *ORC6* expression levels, clinical characteristics, and prognosis

The correlation of *ORC6* expression with clinical features was assessed by Spearman correlation analysis. We performed univariate Cox regression analysis to investigate the prognostic significance of *ORC6* expression in predicting the disease-free interval (DFI), progression-free interval (PFI), overall survival (OS), and disease-specific survival (DSS) in pan-cancer cohorts. We then utilized forest plots for a graphical representation of these results.

TCGA data were curated to extract *ORC6* expression levels in transcripts per million (TPM) format, followed by data normalization using log2(TPM+1). Survival data of matched samples were integrated and subsequently subjected to optimal grouping truncation using the 'surv_cutpoint' function from the 'survminer' package. The aim was to distinguish between the high and low *ORC6* expression groups. Prognostic differences between

the high- and low-expression groups were evaluated using the log-rank test. RNA-seq data in TPM format from TCGA and GTEx were uniformly processed through the Toil pipeline, as sourced from UCSC XENA (https://xenabrowser.net/datapages/). *ORC6* expression levels corresponding to TCGA cancer samples and GTEx normal tissue samples for each cancer type were extracted. The data were normalized using Log2(TPM+1). To assess the diagnostic accuracy for tumor detection, we employed the 'pROC' package to calculate sensitivity and specificity. Diagnostic value was quantified by the area under the curve (AUC), with a value of 1.0 indicating perfect diagnostics and 0.5 representing no diagnostic value. An AUC greater than 0.85 was considered to possess a high diagnostic value.

2.4 Correlation of *ORC6* expression with DNA methylation and RNA modification genes

The correlation of *ORC6* expression with DNA promoter methylation levels in cancer was explored by UALCAN(https://ualcan.path.uab.edu/) (15). The correlation of *ORC6* expression with marker gene expression associated with three classes of RNA modifications (N1-methyladenosine (m1A), 5-methylcytosine (m5C) and N6-methyladenosine (m6A)) (16) across cancers was assessed using Spearman correlation analysis.

2.5 Identification of corresponding characteristics of *ORC6*

To clarify the expression of *ORC6* and immune-related characteristics, we employed Spearman correlation analysis to calculate the correlation between *ORC6* and 5 types of immune-related genes (chemokines, chemokine receptors, immunosimulators, immunoinhibitors, and MHC). TISIDB (http://cis.hku.hk/TISIDB/) (17) to assess the immune cell infiltration status of *ORC6*.

To assess the impact of immunotherapy on ORC6 expression, we analyzed the immunotherapy advanced urothelial carcinoma cohort (IMvigor210 cohort) (18). The R package 'limma' was utilized for differential expression analysis of the target gene in the different groups. Additionally, we accessed the CAMOIP database (https://www.camoip.net/) (19) to obtain the prognostic information of the Auslander-Melanoma (20) immunotherapy cohort and assessed the effect of *ORC6* expression on the survival time of patients after immunotherapy.

The possibility of *ORC6* expression as a predictive marker for immunotherapy response was analyzed using the TISMO (http://tismo.cistrome.org/) (21) and TIDE (http://tide.dfci.harvard.edu/) (22) databases. To examine the correlation between *ORC6* expression and the half-inhibitory concentration (IC50) of the drug, we employed the R package 'pRRophetic' (23) for the analysis.

2.6 Single-cell and bulk transcriptome sequencing analysis

Tumor Immune Single-cell Hub (TISCH, http://tisch.comp-genomics.org/) is a scRNA-seq database that has been specifically developed to investigate the single-cell landscape of the tumor microenvironment (TME) (24). We screened single-cell datasets, including ALL_GSE132509, BRCA_GSE161529, CESC_GSE168652, CHOL_GSE138709, CRC_GSE166555, ESCA_GSE160269, HNSC_GSE103322, LIHC_GSE166635, LSCC_GSE150321, OV_GSE154600, PAAD_ CRA001160, PRAD_GSE141445, STAD_GSE134520, THCA_GSE148673 and UVM_GSE139829. UMAP plots were used for the visualization of cell types and *ORC6* expression levels.

2.7 Functional enrichment analysis

We utilized single-cell sequence data obtained from CancerSEA (http://biocc.hrbmu.edu.cn/CancerSEA/) (25) to examine the relationship between *ORC6* and 14 distinct cancer functional states.

To investigate the mechanisms underlying the impact of *ORC6* expression on the prognosis of tumor patients, we performed gene set enrichment analysis (GSEA) to explore the *ORC6*-related signaling pathways, as previously described in the literature (26, 27). We performed differentially expressed gene (DEG) analysis on the *ORC6*-low and *ORC6*-high subgroups of each cancer using the "limma" R package. The threshold was set at 30%, and genes with adjusted P values <0.05 were considered DEGs. We selected the h.all.v7.2.symbols.gmt gene set as our reference and employed it to determine the normalized enrichment score (NES) and false discovery rate (FDR). By examining the correlation between the *ORC6* gene expression matrix and the known functional genome, we evaluated the impact of coordinated changes in genes within the genome on phenotypic alterations. The presented findings were visualized as bubble plots with the aid of the R package "ggplot2". The CAMOIP (19) network server was employed to perform Kyoto Encyclopedia of Genes and Genomes (KEGG) and Gene Ontology (GO) analyses based on *ORC6* expression in TCGA-LIHC transcriptome data using the R package "clusterProfiler".

2.8 Cell lines and *ORC6* expression detection

The LIHC cell lines HCCLM3 and MHCC97-H and the hepatic epithelial cell line THLE-2 were acquired from BeNa Culture Collection. The HepG2, U-251 MG, and LN229 cell lines were obtained from Procell and cultured according to the manufacturer's instructions. Transfection was carried out in 6-well plates (NEST Biotechnology) using Lipofectamine 2000 (Invitrogen) according to the manufacturer's protocol in HepG2, HCCLM3, U-251 MG, and LN229 cells. The siRNA used in this study was synthesized by

GenePharma. Supplementary Table S1 lists the sequences of the siRNAs used in this study. The Western blot experimental steps were described in a previous study (28). The antibodies used in this study were anti-*ORC6* (Proteintech, 17784-1-AP, 1:1000) and anti-alpha tubulin (Proteintech, 11224-1-AP, 1:5000).

2.9 Cell viability and proliferation assays

Control and experimental cells were placed in 96-well plates at cell densities of 5,000 (HepG2 and HCCLM3) or 3,000 (U251 MG and LN229) cells per well, respectively. After incubation for 0, 24, 48, and 78 hours, cell viability was assessed by using the CCK-8 assay (GlpBio), and the optical density (OD) was measured at 450 nm with a microplate reader.

Cell proliferation was assessed using EdU (5-ethynyl-2'-deoxyuridine) staining. Briefly, control and experimental cells were seeded in 96-well plates and incubated overnight. After incubation with 10 μM EdU (RiboBio) for 2 hours, cells were fixed with 4% paraformaldehyde for 20 minutes, permeabilized with 0.5% Triton X-100 for 15 minutes, incubated with EdU reaction solution for 30 minutes, and finally incubated with Hoechst 33342 for 10 minutes. Images were taken using an inverted fluorescence microscope (Olympus).

2.10 Cell migration assays

Control and experimental cells were seeded onto a 6-well plate and cultured until reaching a confluence of 70% before undergoing transfection and continuing to be cultured normally. Scratch assays were performed when cell confluence reached approximately 90%, with images taken at 0 and 36 hours thereafter. For Transwell migration assays, 50,000 (HepG2 and HCCLM3) or 15,000 (U251 MG and LN229) cells were seeded into the chamber and cultured with serum-free medium within the insert and with 10% complete medium outside of the insert. After 24 hours, cells were fixed and stained, and then the cells within the insert were removed by gently swabbing with a cotton tip before imaging.

2.11 Statistical analysis

We used Student's t-test to determine the statistical significance of differences between the two groups. Paired t-tests were conducted to compare the expression levels of *ORC6* in tumor tissues with those in their paired normal tissues. We evaluated the prognostic significance of *ORC6* by conducting log-rank and univariate Cox regression analyses. Spearman correlation analysis was employed to assess the correlations between *ORC6* and its corresponding features. A p value < 0.05 was considered to indicate statistical significance.

3 Results

3.1 Expression landscape of *ORC6*

We conducted a comparative analysis of *ORC6* expression in tumor vs. normal tissues by merging the TCGA and GTEx databases. *ORC6* was found to be significantly upregulated in 33 tumors (all $p<0.05$), as illustrated in Figure 1A. However, no significant changes were observed in TCGT. Then, our analysis of tumor and matched normal tissue samples from the TCGA database revealed that *ORC6* expression was significantly elevated in tumor samples from BLCA, BRCA, CHOL, COAD, ESCA, HNSC, KICH, KIRC, KIRP, LIHC, LUSC, LUAD, PRAD, READ, STAD, THCA, and UCEC (Figure 1B, all $p<0.05$). Further protein score hints were provided by the HPA online database. *ORC6* showed high protein scores in the stomach, duodenum, colon, pancreas, lymph nodes, testis, and bone marrow but low protein scores in the liver (Figure 1C). Regarding its protein expression in tumors, we observed that *ORC6* was moderately/highly expressed in 100% of head and neck cancer (3/3) and testicular cancer (11/11) tissues and was moderately/highly expressed in 54.5% (6/11) of liver cancer tissues (Figure 1D). To clarify the localization of *ORC6* protein expression, we obtained immunofluorescence staining images of *ORC6* protein expression in HEK 293 and PC-3 cells through the HPA database (Supplementary Figure S1A). Further access to the Genecards database was performed for validation (Supplementary Figure S1B). We found that *ORC6* was mainly concentrated in the nucleus and cytoplasm. Finally, we constructed a PPI network using interaction data sourced from the ComPPI website. The results of our analysis showed that proteins found to be in close interaction with *ORC6* were primarily localized within the nucleus, as depicted in Supplementary Figure S1C. In summary, we identified that *ORC6* was generally highly expressed in tumors.

3.2 *ORC6* genetic alterations and epigenetic modifications

The frequency and type of *ORC6* gene genetic alterations across cancers were analyzed by the cBioPortal platform. As illustrated in Supplementary Figure S1D, the most frequent type of genetic alteration in *ORC6* was "amplification", followed by "deep deletion", "mutation" and "structural variation". SARC exhibited the greatest frequency of *ORC6* genetic mutations. These alterations included "deep deletions" in 2.35% of genes and "structural variants" in 0.39% of genes. In PRAD, the gene alteration frequency of *ORC6* was 2.63%, of which the frequency of "amplification" reached 2.43%. In both DLBC and UCS, *ORC6* genetic alterations were "deeply deleted". In UCEC and SKCM, the frequency of *ORC6* gene "mutation" reached 1.13%. In five different cancer types (ACC, ESCA, LIHC, KIRP, and PAAD), the *ORC6* gene only exhibited "amplified" genetic variants. The mutation frequency of the *ORC6* gene is generally low, at less than 3%. This could be due to the high conservation of genes within the ORC family (29). Subsequently, to explore the relationship between *ORC6* expression and genomic variations across different cancer types, we employed either the Wilcoxon rank-sum test or the Kruskal–Wallis rank-sum test. We observed differential expression of *ORC6* across three distinct variant groups (gain-variant, loss-variant, and no-variant) in 14 different cancers: BLCA, BRCA, CESC, COAD, HNSC, KIPAN, LIHC, LUAD, LUSC, OV, PRAD, STAD, STES, and UCS (Supplementary

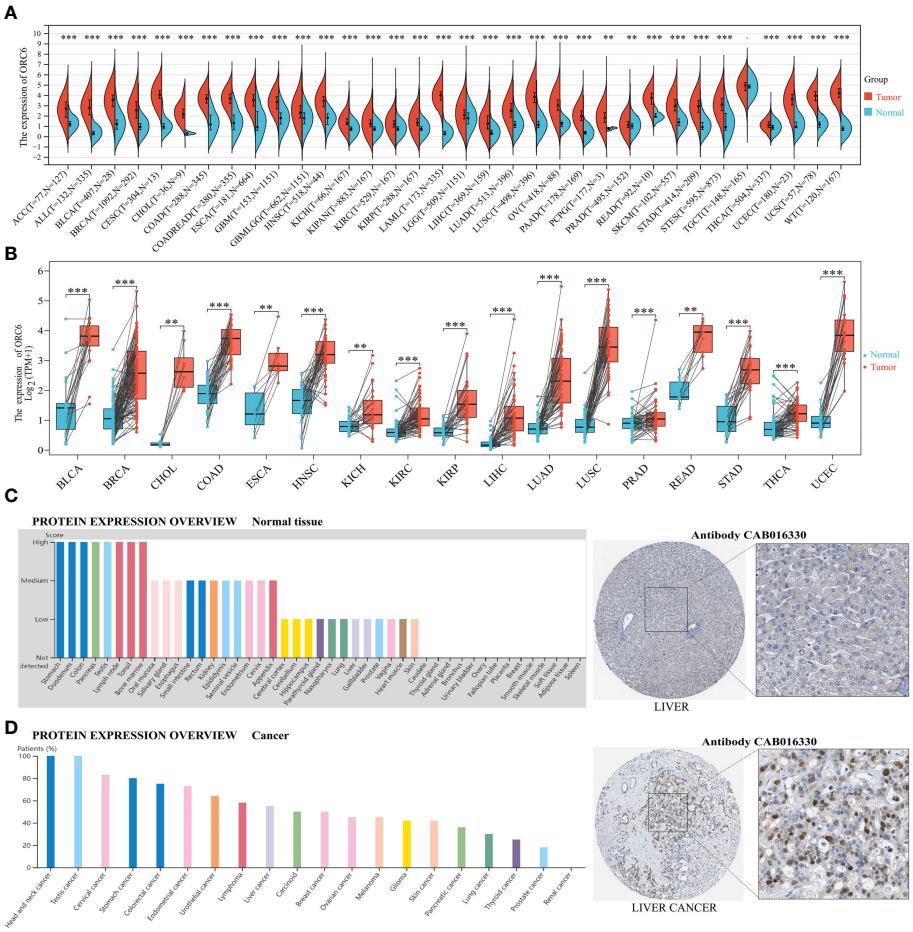

FIGURE 1
ORC6 expression profiles. **(A)** *ORC6* mRNA expression levels in pan-cancer tissues and corresponding normal tissues derived from TCGA and GTEx databases. **(B)** Differential expression of *ORC6* in tumor and paired adjacent tissues. **(C, D)** Protein expression analysis of *ORC6* in normal tissues and cancer tissues using the Human Protein Atlas database. The left panel shows the expression scores or positive percentages in each tissue, while representative immunohistochemistry images of normal liver tissue and liver cancer tissue are shown in the right panel. (**p < 0.01, ***p < 0.001).

Figure S1E, all p<0.05). Specifically, *ORC6* expression was generally higher in the gain-variant group than in the loss/neutral-variant group.

Numerous reports suggest that abnormal DNA methylation in the promoter region of genes can induce changes in chromatin structure and DNA stability, ultimately leading to the dysregulation of gene expression within the body (30). Therefore, we analyzed differences in the DNA promoter methylation levels of *ORC6* between tumor and normal tissues using UALCAN. As depicted in Supplementary Figure S2A, methylation levels were lower in BLCA, BRCA, HNSC, THYM, UCEC, and PRAD than in normal tissues (all p<0.05). In contrast, methylation levels were higher in PAAD, KIRC, LUSC, and SARC than in normal tissues (Supplementary Figure S2A, all p<0.05). Moreover, RNA modifications are critical in selectively regulating the expression of genes (31). Our analysis, as illustrated in Supplementary Figure S2B, reveals a strong positive correlation between *ORC6* expression and m1A-, m5C-, and m6A-related genes across almost all tumor types. These findings suggest that the ubiquitous overexpression of *ORC6* in tumors may be closely associated with its epigenetic modifications and genetic variations. This correlation further supports the potential of *ORC6* as a cancer regulatory factor and provides valuable clues for further exploring its role in cancer.

3.3 Correlation of *ORC6* expression with clinicopathological features

We also investigated the correlations between *ORC6* expression and various clinicopathological features. According to the results presented in Figure 2A, there was a positive correlation between *ORC6* expression and lymph node metastasis in several tumor types, and the correlations in HNSC (p=2.2e-4), KIPAN (p=6.8e-8), KIRC (p=5.6e-3), PRAD (p=4.0e-8), THCA (p=0.02) and other tumor types were the most robust. Figure 2B shows that the increase in *ORC6* expression was positively correlated with tumor metastasis in ACC (p=8.2e-3), KIPAN (p=1.9e-3), KIRC (p=4.3e-4), LUAD (p=9.5e-3), PRAD (p=0.01), and SKCM (p=0.03). Furthermore, increased *ORC6* expression was positively correlated with the T stage of ACC (p=4.8e-8), KIPAN (p=1.1e-9), KIRC (p=1.4e-5),

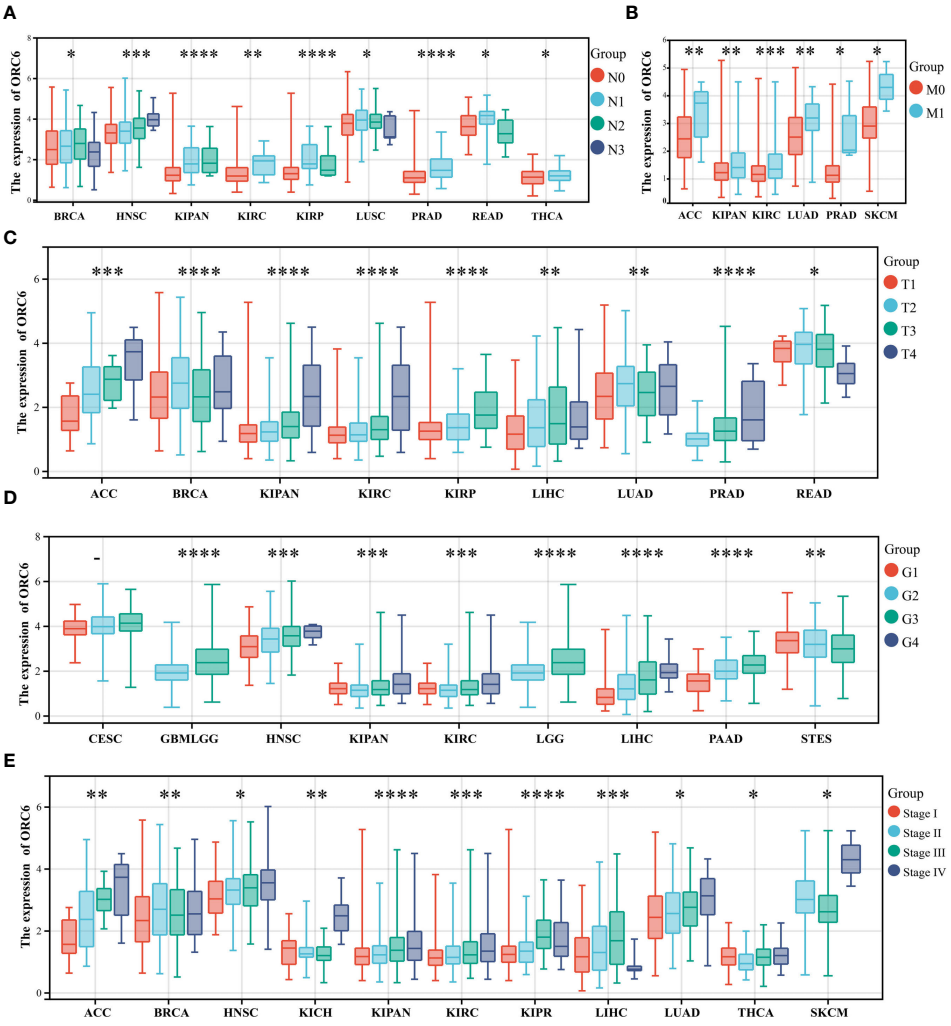

FIGURE 2
Correlations between clinical features and *ORC6*. **(A–E)** Correlation of *ORC6* expression with pan-cancer clinical N stage **(A)**, M stage **(B)**, T stage **(C)**, histological grade **(D)**, and clinical stage **(E)**. (*p<0.05, **p<0.01, ***p<0.001, ****p<0.0001).

KIRP (p=2.4e-8) and PRAD (p =7.0e-12) (Figure 2C). Figure 2D shows that the increased expression of *ORC6* was positively correlated with the histological grade of GBMLGG (p=9.2e-25), HNSC (p=5.6e-9), LGG (p=9.2e-25), LIHC (p=3.0e-15) and PAAD (p=2.9e-9) but negatively correlated with the histological grade of STES (p=6.3e-5). Similarly, increased *ORC6* expression was positively correlated with clinical staging (Figure 2E), and typical tumor types were ACC (p=6.3e-5), HNSC (p=1.5e-3), KIPAN (p=3.3e-9), KIRC (p=2.4e-4), and LUAD (p=0.01). From the above findings, it can be inferred that *ORC6* might play a role in tumor progression and metastasis.

3.4 Prognostic and diagnostic value of *ORC6*

To investigate the effect of *ORC6* on tumor prognosis, we plotted survival curves and assessed OS using the Kaplan–Meier method. As shown in Figure 3, in ACC, BRCA, GBMLGG, HNSC, KICH, KIRC, KIRP, LGG, LIHC, LUAD, LUADLUSC, MESO, OSCC, PAAD, PCPG, SARC and UCEC patients, high *ORC6* levels were highly correlated with poorer OS (Figure 3A; all p<0.05). Moreover, it is worth noting that high *ORC6* expression was exclusively correlated with improved OS in OV (Figure 3B; p<0.05).

Following this, we conducted Cox regression analysis to assess the correlation between *ORC6* expression and several survival outcomes, including OS, DSS, DFI, and PFI, for each tumor type. The results were then presented in the form of a forest plot. As shown in Figure 4A, our findings indicate that high *ORC6* expression was significantly associated with shorter OS in GBMLGG, KIPAN, KIRP, LGG, ACC, KIRC, MESO, LIHC, PCPG, PRAD, PAAD, KICH, LUAD, UVM, BRCA and HNSC patients (all p<0.05). High *ORC6* expression in GBMLGG, KIPAN, KIRP, KIRC, ACC, LGG, MESO, LIHC, PRAD, KICH, PCPG, BRCA, PAAD, UVM, and LUAD patients was associated with

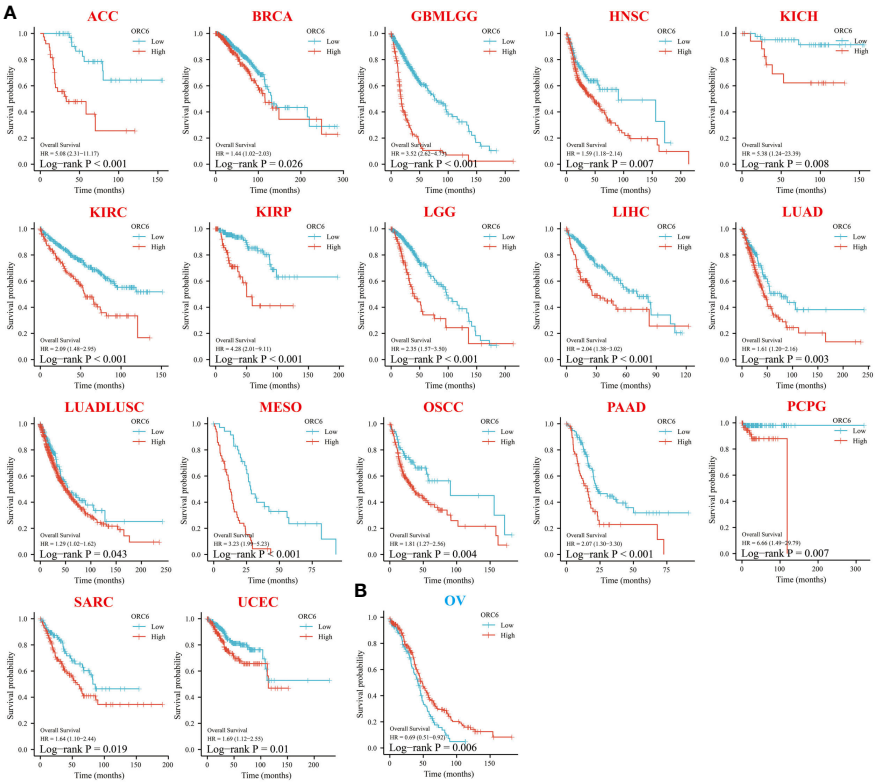

FIGURE 3
Relationship between *ORC6* expression and overall survival (OS) of patients. **(A, B)** Relationship between *ORC6* expression levels and prognosis in the indicated tumor types. In the abbreviation of tumor type, red represents poor prognosis, and blue represents good prognosis. The results are grouped by the best cutoff value, and the log-rank method was used for survival difference analysis.

poorer DSS (Figure 4B, all p<0.05). Regarding DFI, there was a significant association between high *ORC6* expression and lower DFI in KIRP, KIPAN, LIHC, BRCA, PRAD, PAAD, SARC, THCA, MESO, and LUAD patients, whereas high *ORC6* expression in OV patients was associated with improved prognosis for DFI (Figure 4C, all p<0.05). Furthermore, as illustrated in Figure 4D, high *ORC6* levels were strongly correlated with poorer PFI in GBMLGG, KIPAN, PRAD, KIRP, ACC, LIHC, LGG, UVM, KIRC, KICH, PAAD, BRCA, MESO, BLCA and HNSC (all p<0.05).

Moreover, we assessed the diagnostic accuracy of *ORC6* in different types of cancer using ROC curves. As shown in Figure 5, in ACC, BLCA, BRCA, CESC, CHOL, COAD, COADREAD, ESAD, ESCA, GBM, HNSC, LAML, LIHC, LUAD, LUADLUSC, LUSC, OSCC, OV, PAAD, READ, STAD, UCEC and UCS, *ORC6* could be used as a highly accurate diagnostic marker (Figures 5A–W, all AUC>0.85). In DLBC, GBMLGG, KICH, KIRC, KIRP, SKCM, and THYM, *ORC6* had moderate diagnostic performance (Supplementary Figures S3A–E, H, K; all AUC=0.7~0.85). In LGG, PRAD, TGCT, and THCA, *ORC6* had poor diagnostic values (Supplementary Figures S3F, G, I, J; all AUC=0.5~0.7). In conclusion, our study revealed that high expression of *ORC6* is generally linked to unfavorable prognosis in the majority of cancer types, and it has good diagnostic value.

3.5 Pathways and functions associated with *ORC6* expression

To explore the possible biological pathways influenced by *ORC6* that may contribute to tumorigenesis and progression, we conducted GSEA on data obtained from 33 tumors from TCGA. As illustrated in Figure 6A, we observed that immune-related pathways, including TNFα signaling via NFκB, IFN-α response, IFN-γ response, inflammatory response, IL-6/JAK/STAT3, IL-2/STAT5, complement and coagulation cascades, and allograft rejection pathways, were significantly enriched across a diverse range of tumors. Moreover, we observed a positive correlation between *ORC6* expression and MYC target V2, MYC target V1, MTORC1, mitotic spindle, G2 checkpoint, E2F target, DNA repair, and other pathways across cancers. Furthermore, KEGG analysis revealed that *ORC6* was mainly involved in the synthesis and degradation of various substances, drug metabolism, the cell cycle, ferroptosis, and neuroactive ligand-receptor interactions in LIHC (Figure 6B). GO analysis, including the BP, CC, and MF categories, indicated that *ORC6* was mainly related to immune response regulation and biological enzyme activity in LIHC (Figures 6C–E).

To explore *ORC6* expression in diverse TMEs, including ALL, BRCA, CESC, CHOL, CRC, ESCA, HNSC, LIHC, LSCC, OV,

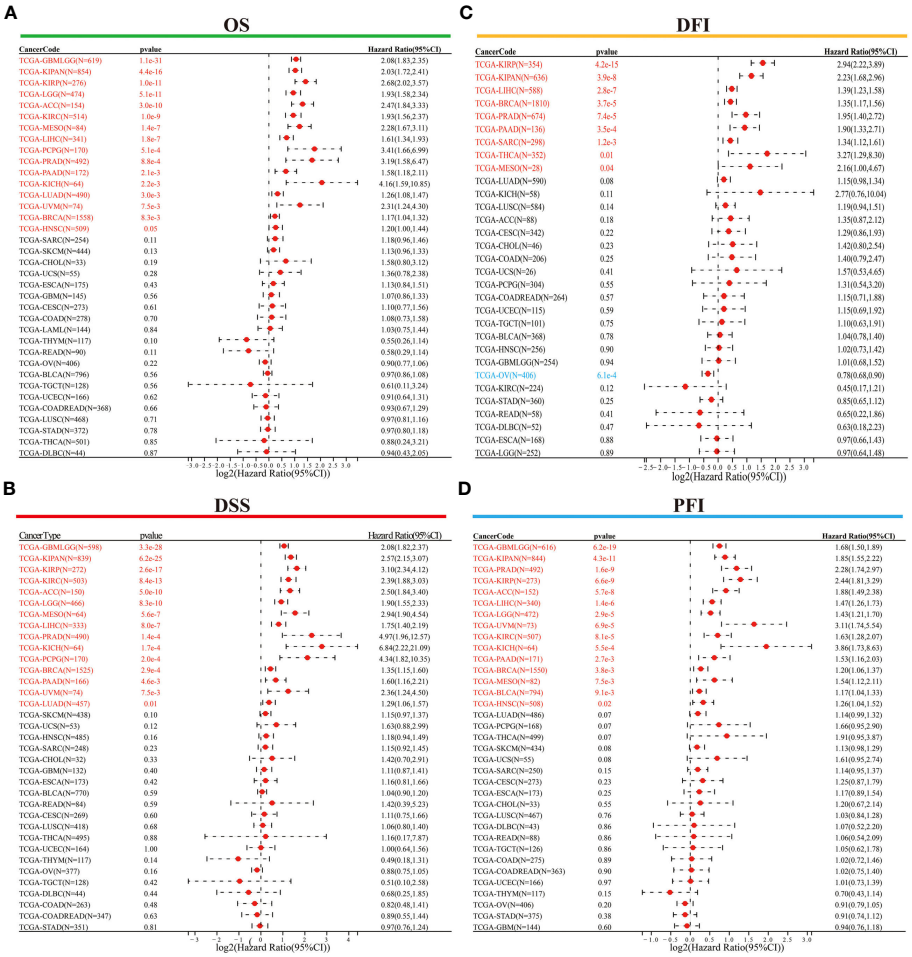

FIGURE 4
Univariate Cox regression analysis was performed to determine the prognostic role of *ORC6*. **(A–D)** Correlation of *ORC6* expression with OS **(A)**, DSS **(B)**, DFI **(C)**, and PFI **(D)**. (OS, overall survival; DSS, disease-specific survival; DFI, disease-free interval; PFI, progression-free interval).

PAAD, PRAD, STAD, THCA, and UVM, we investigated their expression distribution (Figures 7A–O). The results were interesting, as they showed that *ORC6* was primarily expressed at high levels in the malignant cells of these cancers. In STAD, it was predominantly expressed in pit mucus cells (Figure 7M). It is worth noting that in LIHC, *ORC6* was also found to be expressed in T-cell proliferation, which demonstrates its potential role in this immune response (Figures 7H, P). To further investigate the relationship between *ORC6* and the functional status of different cancers, we analyzed single-cell sequencing data obtained from CancerSEA for 14 types of cancer. In most tumors, *ORC6* showed a positive correlation with the cell cycle, proliferation, DNA damage, and DNA repair (Supplementary Figure S4). In contrast, *ORC6* was negatively associated with apoptosis, hypoxia, metastasis, and quiescence in most tumors (Supplementary Figure S4). These findings suggest a correlation between abnormal expression of *ORC6* and the advancement of cancer as well as the immune response of cancer.

3.6 Correlation between *ORC6* expression and the tumor immune landscape

Investigating the possible gene expression within tumors and its connection to immune cells can greatly aid in predicting the clinical outcome for patients with tumors and selecting appropriate diagnostic targets and intervention strategies (32). To gain further insights into the correlation between *ORC6* and immune cells in the TME, we used the TISIDB tool for analysis. The pan-cancer analysis indicated that the expression level of *ORC6* displayed an inverse correlation with the infiltration abundance of various immune cells, including Tem CD8 cells, Th1 cells, NK cells, pDCs, iDCs, eosinophils, monocytes, and neutrophils, while showing a positive correlation with the infiltration abundance of Act CD8 cells and Th2 cells (Figure 8A). This phenomenon was especially evident in LIHC (Figures 8B–K). Furthermore, in gliomas, which include GBM and LGG, *ORC6* expression was negatively correlated with the abundance of infiltrating immune cells, including Tem CD8,

10.3389/fimmu.2023.1236806

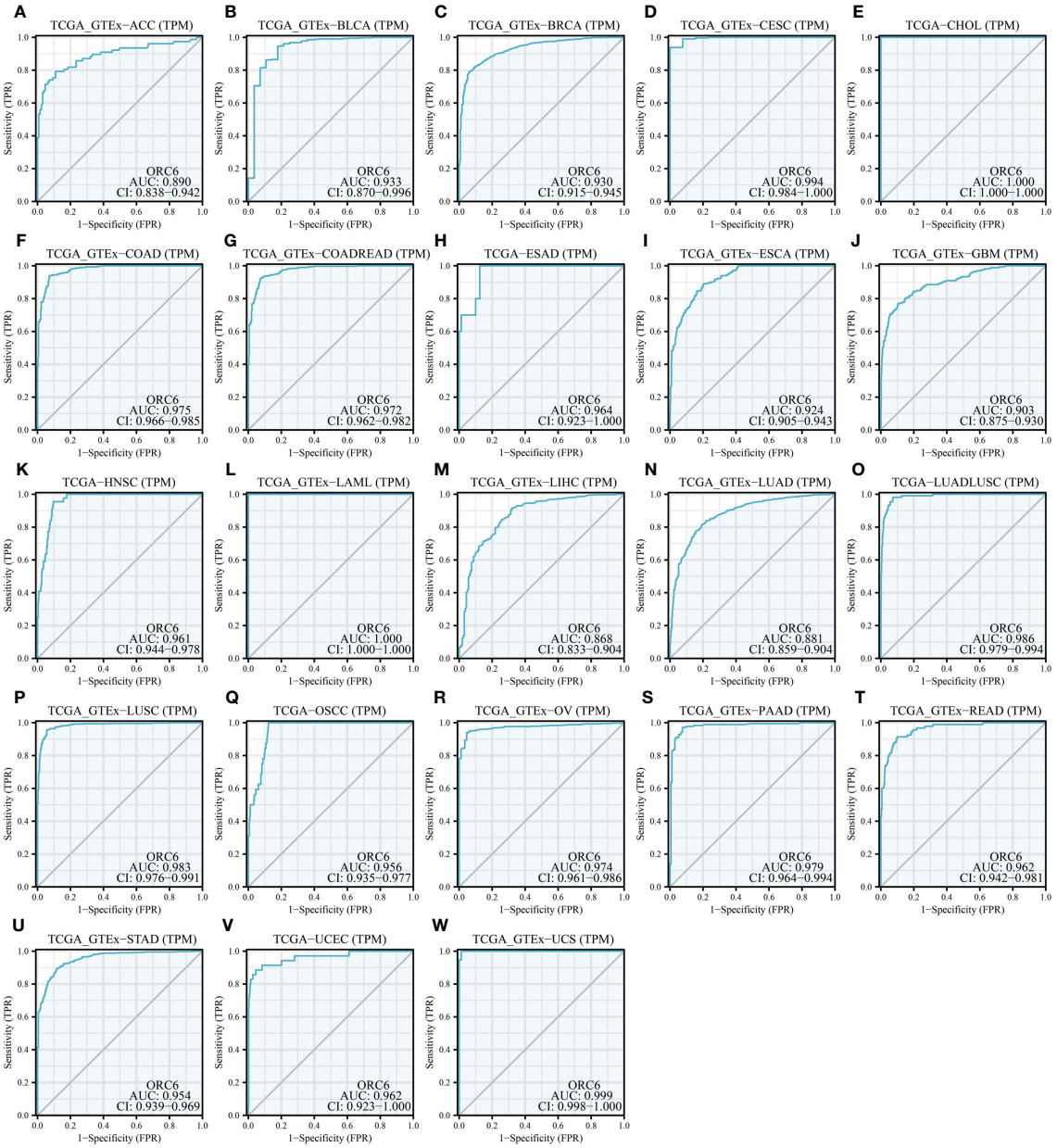

FIGURE 5
Diagnostic value of *ORC6*. **(A–W)** ROC curve of *ORC6* in ACC, BLCA, BRCA, CESC, CHOL, COAD, COADREAD, ESAD, ESCA, GBM, HNSC, LAML, LIHC, LUAD, LUADLUSC, LUSC, OSCC, OV, PAAD, READ, STAD, UCEC and UCS.

Tcm CD4, Tfh, Th1, Th17, Act B, lmm B, NK, MDSC, NKT, Act DC, pDC, iDC, macrophage, eosinophil, mast, monocyte, and neutrophil cells. In contrast, *ORC6* expression levels in THCA and KIRC were positively correlated with the majority of immune cell infiltration (Figure 8A).

Furthermore, we examined the association between *ORC6* expression and the expression of genes related to immune regulation (Figures 9A–E). The heatmap indicated that *ORC6* was coexpressed with most immune-related genes across cancers. Especially in DLBC, UVM, LIHC, KIRC, and THCA, *ORC6* was roughly positively correlated with 5 immune-related genes. In TGCT, GBM, and LUSC, *ORC6* was roughly negatively correlated with immune-related genes. Furthermore, the chemokine CCL14 was negatively correlated with *ORC6* expression across cancers (Figure 9A). Among the immune activation-related genes, MICB, PVR, ULBP1, CD276, and TNFRSF25 were positively correlated with *ORC6* expression in most tumors (Figure 9C). There was a positive correlation between the expression of *ORC6* and genes related to immunosuppression in several cancer types, such as DLBC, UVM, LIHC, KIRC, THCA, GBMLGG, LGG, and PRAD, as indicated in Figure 9D. Notably, in the advanced urothelial carcinoma cohort with immunotherapy, the response group had significantly higher *ORC6* expression (Figure 9F, p=0.00099). Furthermore, we observed that in the melanoma immunotherapy cohort, the high *ORC6* expression group had prolonged survival after immunotherapy (Figure 9G, p=0.027). Taken together, these results suggest that *ORC6* may be involved in

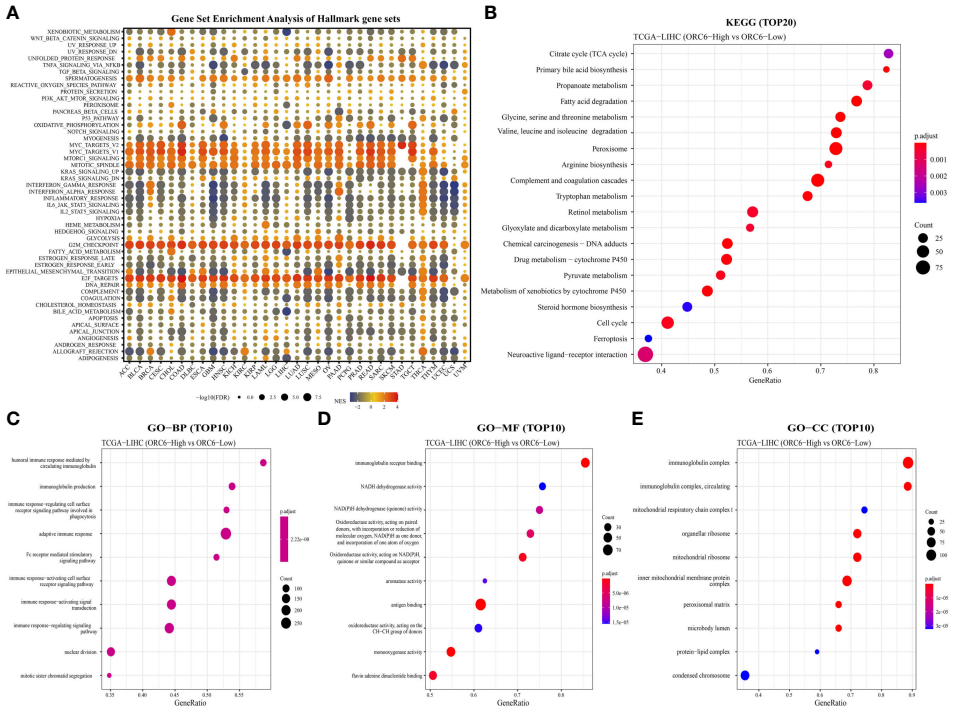

FIGURE 6
Gene set differential enrichment analysis of *ORC6* across cancers and in liver cancer. **(A)** This graph visualizes the potential signaling pathways that are associated with *ORC6* expression in different tumor types. The circles depict cancer enrichment projects. Their sizes vary based on their false discovery rate (FDR), while the colors represent the corresponding normalized enrichment score (NES) for each enrichment item. **(B)** The top 20 enriched KEGG results in HCC are shown. **(C–E)** The top 10 enriched gene ontology biological processes (BPs) **(C)**, molecular functions (MFs) **(D)**, and cellular components (CCs) **(E)** are also displayed.

immune cell infiltration and the expression of immunomodulatory genes and that high *ORC6* expression may indicate a better response to immunotherapy.

3.7 *ORC6* predicts immunotherapy response and chemotherapy efficacy

To elucidate the predictive function of *ORC6* expression in immunotherapy response, we evaluated it using the TISMO database. As depicted in Figure 10A, *ORC6* expression was markedly different in 5 subjects before and after ICB treatment and between responder and nonresponder cohorts. Moreover, *ORC6* expression was significantly different in the six cell lines before and after cytokine treatment (Figure 10B). Furthermore, we performed a biomarker assessment of *ORC6* by TIDE. The findings indicated that *ORC6* had a better predictive effect in 7 immunotherapy cohorts (Figure 10C). In addition, we performed a sensitivity analysis of chemotherapy drugs commonly used to treat LIHC. As shown in Figure 10D, the *ORC6* high-expression group was closely correlated with the reduction of IC50 of 5-fluorouracil, doxorubicin, gemcitabine, and imatinib (all $p<0.001$).

3.8 External cohort and *in vitro* experiments clarify the promotional effect of *ORC6* on LIHC and GBMLGG

After collating and analyzing the pan-cancer data mentioned above, it was observed that the elevated expression of *ORC6* was significantly associated with the unfavorable prognosis and malignancy of LIHC and GBMLGG patients (Figures 1–4). Consequently, our study will concentrate on LIHC and GBMLGG.

We collected clinical information and *ORC6* expression profiles of patients belonging to the TCGA-LIHC cohort. After performing a chi-square test analysis, we discovered a significant correlation between *ORC6* expression and tumor histological grade, alpha-fetoprotein (AFP) content, and vascular invasion in LIHC (Supplementary Table S2). Furthermore, via univariate and multivariate Cox regression analysis, we identified *ORC6* and pathological stage as independent prognostic risk factors for LIHC (Supplementary Table S3). Subsequently, a nomogram was developed to estimate the survival likelihood of patients at intervals of 1, 3, and 5 years, and its prediction efficiency was confirmed by the calibration curve, as illustrated in Figures 11A, B. This indicates that the model had a high accuracy in its predictive ability. Given that our analysis of *ORC6* was solely based on the TCGA database, we conducted external verification by collating clinical information and *ORC6* expression profiles of patients belonging to the ICGC-LIRI-JP cohort. The results showed that *ORC6* expression in LIHC was significantly higher than that in normal tissues (Figure 11C). It was positively correlated with the clinical stage and associated with poor overall survival (Figures 11D, E). Furthermore, univariate and multivariate Cox regression analyses revealed *ORC6*, sex, and clinical stage as independent risk factors for poor prognosis in LIHC (Figures 11F, G). To investigate the function of *ORC6* in LIHC cells, we carried out *in vitro* experiments. Initially, we

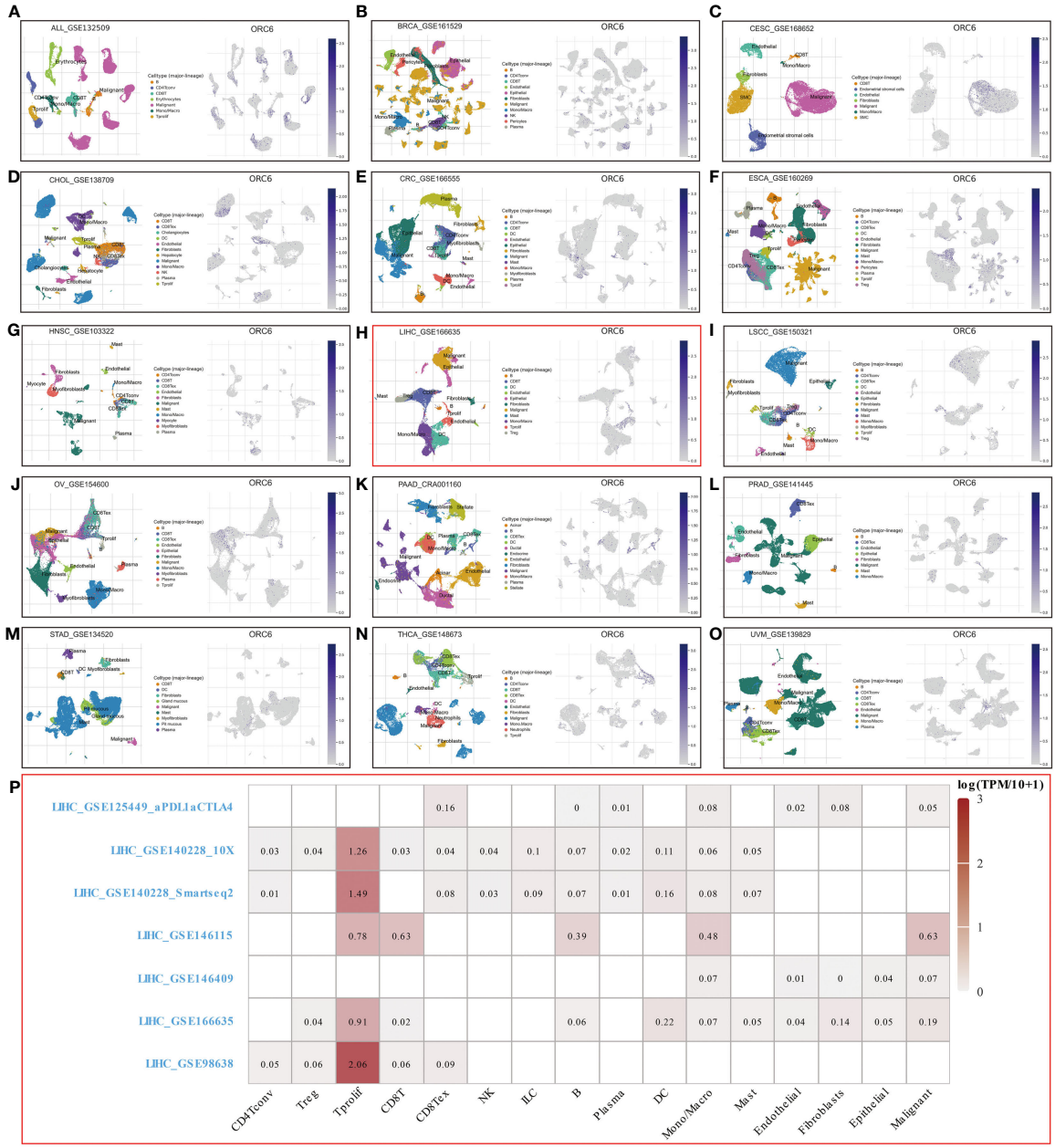

FIGURE 7
Single-cell sequencing analysis of *ORC6* expression in malignant cells. **(A–O)** *ORC6* in ALL **(A)**, BRCA **(B)**, CESC **(C)**, CHOL **(D)**, CRC **(E)**, ESCA **(F)**, HNSC **(G)**, LIHC **(H)**, LSCC **(I)**, OV **(J)**, PAAD **(K)**, PRAD **(L)**, THCA **(N)** and UVM **(O)** were mainly expressed in malignant cells; *ORC6* was mainly expressed in pit mucous in STAD **(M)**. **(P)** Expression distribution of *ORC6* in several LIHCs.

assessed the basal expression of *ORC6* in LIHC cell lines and normal hepatocytes. Our findings indicate that LIHC cell lines have noticeably increased *ORC6* expression compared to normal hepatocytes, as illustrated in Figure 12A. To assess the impact of *ORC6* downregulation in LIHC cells, we chose two LIHC cell lines with high expression (HepG2 and HCCLM3) and conducted an *ORC6* knockout assay (Figures 12B, C). Using the EdU cell proliferation test, a significant decrease in the proliferation of LIHC cells was observed after the knockout of *ORC6* expression (Figure 12D). In addition, similar results were obtained through CCK-8 analysis (Figures 12E, F). Subsequently, we conducted wound healing and Transwell tests to examine the impact of *ORC6* downregulation on the migratory capacity of LIHC cells. The results indicate that compared to the control cells, the downregulation of *ORC6* significantly inhibited the migration ability of LIHC cells (Figures 12G–L).

Subsequently, we compiled the *ORC6* expression and clinical information of patients in the TCGA-GBMLGG cohort. The chi-square test revealed a significant association between *ORC6* expression and age, histological type, WHO grade, IDH status, and 1p/19q codeletion in GBMLGG patients (Supplementary Table S4). Furthermore, our investigation revealed that *ORC6*, age, WHO

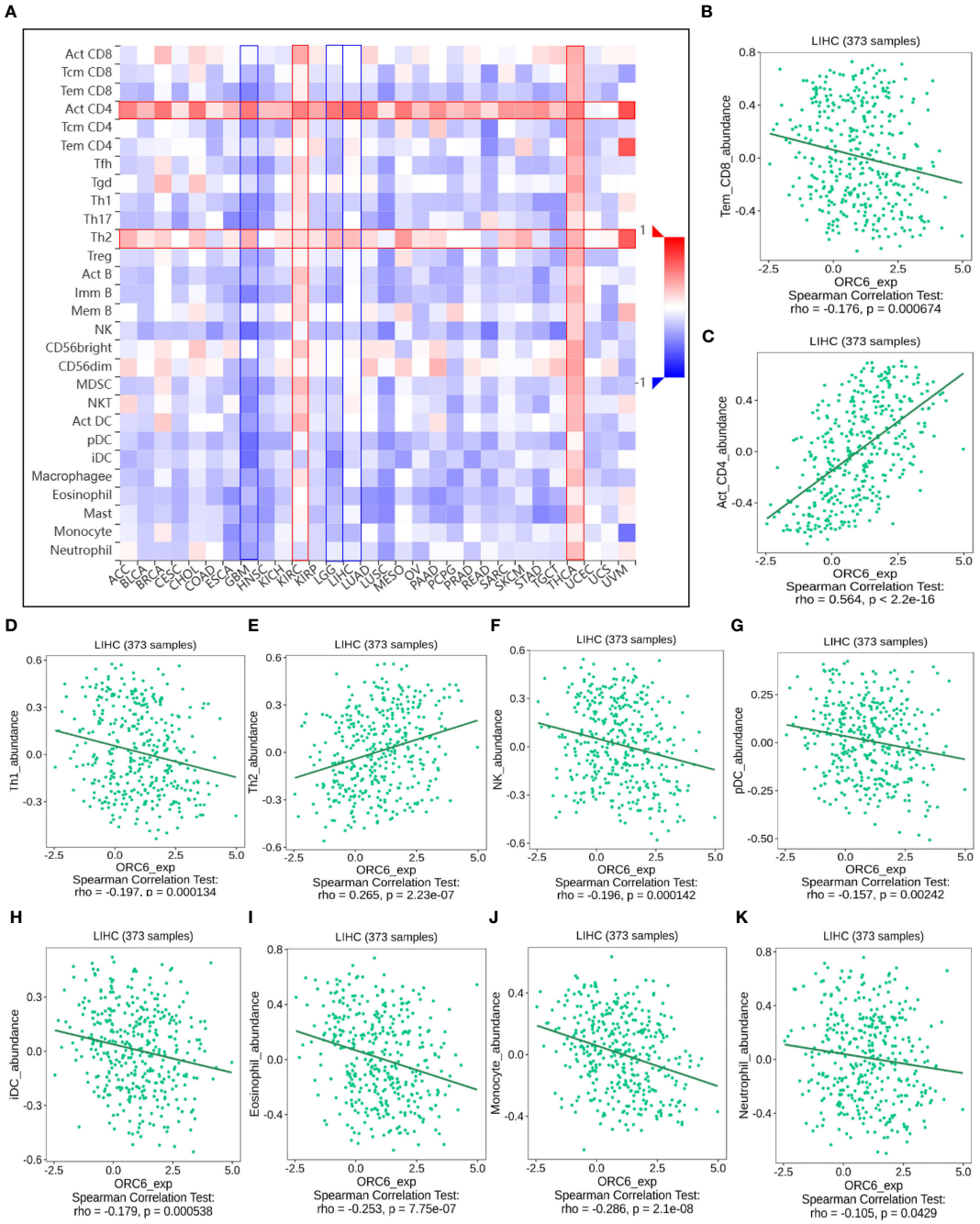

FIGURE 8
The relationship between *ORC6* levels and immune infiltration was analyzed by Timer 2.0. **(A)** *ORC6* expression correlates with immune cell infiltration across cancers. **(B–K)** Correlation of *ORC6* expression with the abundance of Tem CD8, Act CD4, Th1, Th2, NK, pDC, iDC, eosinophil, monocyte and neutrophil cell infiltration in LIHC.

grade, and 1p/19q codeletion were independent prognostic risk factors for GBMLGG patients, as confirmed by univariate and multivariate Cox regression analyses (Supplementary Table S5). Time-dependent ROC curve analysis further identified age, WHO grade, and *ORC6* as the top three effective predictors for 1-, 3-, and 5-year patient survival (Figure 13A, all AUC>0.7). Our results were validated in an external cohort. As demonstrated in Figures 13B–D, *ORC6* expression increased concomitantly with WHO grade in the CGGA-301, CGGA-325, and CGGA-693 cohorts. Moreover, high levels of *ORC6* expression were significantly associated with an unfavorable prognosis among GBMLGG patients in the CGGA-301, CGGA-325, CGGA-693, and GSE13041 cohorts (Figures 13E–H, all $p < 0.05$). In addition, the expression profile of *ORC6* in the GBMLGG cell line was analyzed using the CCLE database (Figure 13I). Further, the expression of *ORC6* protein was effectively inhibited in U251 MG and LN229 cells (Figures 14A, B). Consistent with findings in LIHC, the inhibition of *ORC6* expression led to decreased proliferation and migration of U251

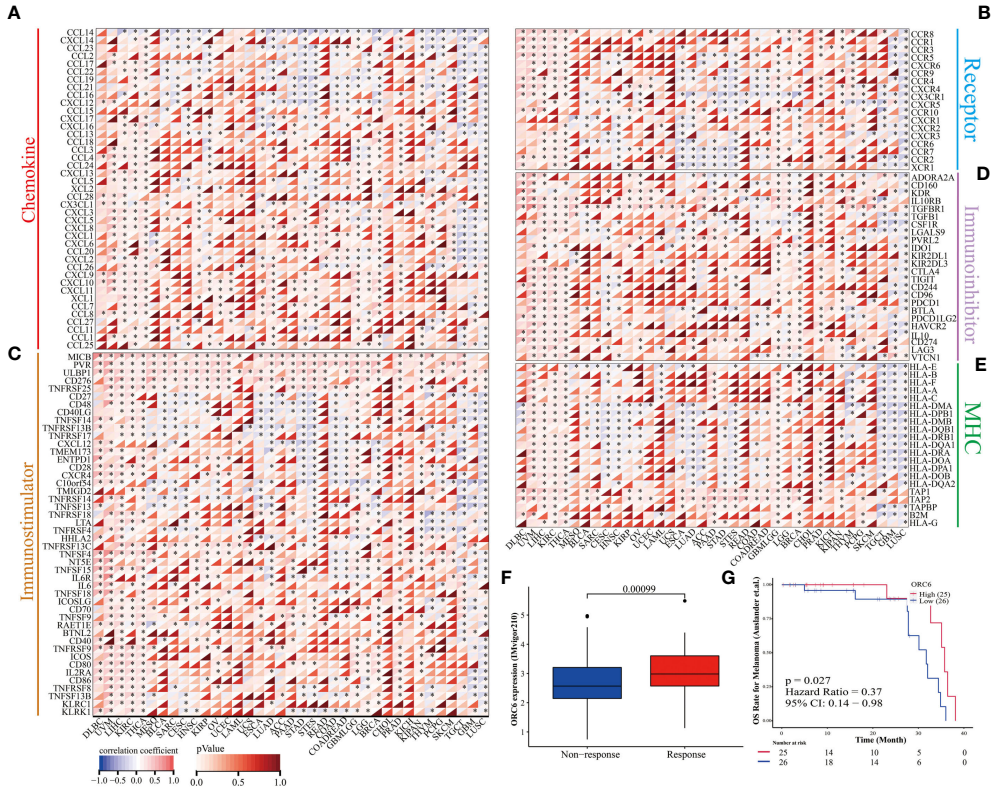

FIGURE 9
ORC6 expression and immunotherapy response. **(A–E)** Correlation analysis of *ORC6* expression with five types of immune regulation-related genes, including chemokine **(A)**, chemokine receptor **(B)**, immune stimulator **(C)**, immune inhibitors **(D)**, and MHC **(E)**. **(F)** Association of *ORC6* expression with immunotherapy response in the IMvigor210 cohort. **(G)** In the melanoma immunotherapy cohort, the log-rank method was used to analyze the difference in survival after immunotherapy between the high- and low-expression groups of *ORC6*. *p<0.05.

MG and LN229 cells (Figures 14C–J). In conclusion, our *in vitro* results strengthen the evidence supporting the carcinogenic effects of *ORC6* in LIHC and GBMLGG.

4 Discussion

Multi-omics data mining analysis is crucial for exploring tumor heterogeneity and complexity and identifying prognostic biomarkers. Prior studies have linked high *ORC6* expression to poor tumor prognosis, progression, and drug resistance in some cancers (33, 34), but its prognostic and biological significance in most cancer types remains unclear. We performed a comprehensive pan-cancer study of *ORC6* and revealed its important role in LIHC and GBMLGG. In addition, we verified that *ORC6* was highly expressed in LIHC and GBMLGG and could serve as an independent marker of poor prognosis. Further external cohort analysis and *in vitro* experiments supported our findings.

In this study, we observed that the expression of *ORC6* was higher in most tumors than in normal tissues, as well as in paired cancer and paracancerous tissues. Next, we analyzed the correlations between *ORC6* expression and clinicopathological features and discovered that *ORC6* expression was positively correlated with tumor size, metastasis, histological grade, lymph node metastasis, and clinical analysis, which further implied that *ORC6* expression was associated with tumor progression and metastasis. By utilizing log-rank and Cox regression analysis, it was determined that increased expression of *ORC6* was significantly linked to unfavorable prognosis in various types of tumors, in concurrence with previous research (10, 34, 35). Through ROC curves, we also found that *ORC6* was a highly accurate diagnostic marker for most tumor types. Single-cell functional analysis also indicated that *ORC6* expression was positively correlated with the cell cycle and proliferation of tumor cells. We found that *ORC6* and pathologic stage were independent prognostic risk factors for patients with LIHC. *ORC6*, age, WHO grade, and 1p/19q codeletion are independent risk factors for poor prognosis of GBMLGG, and this result is consistent with previous studies (36). Furthermore, the time-dependent ROC curves showed that *ORC6* was more accurate than sex, histological type, IDH, and 1p/19q colocation in predicting the 1-, 3-, and 5-year survival of GBMLGG patients. After silencing *ORC6* expression, we found that the proliferation and migration abilities of LIHC and GBMLGG cells were attenuated. The results of this study suggest that elevated *ORC6* levels may serve as a valuable prognostic marker for adverse outcomes in most tumor types. However, the validation of this study was limited to *in vitro* experiments, and further *in vivo* studies are needed to fully explore this possibility.

Genetic alterations and altered epigenetic regulation are considered major factors in cancer development and progression

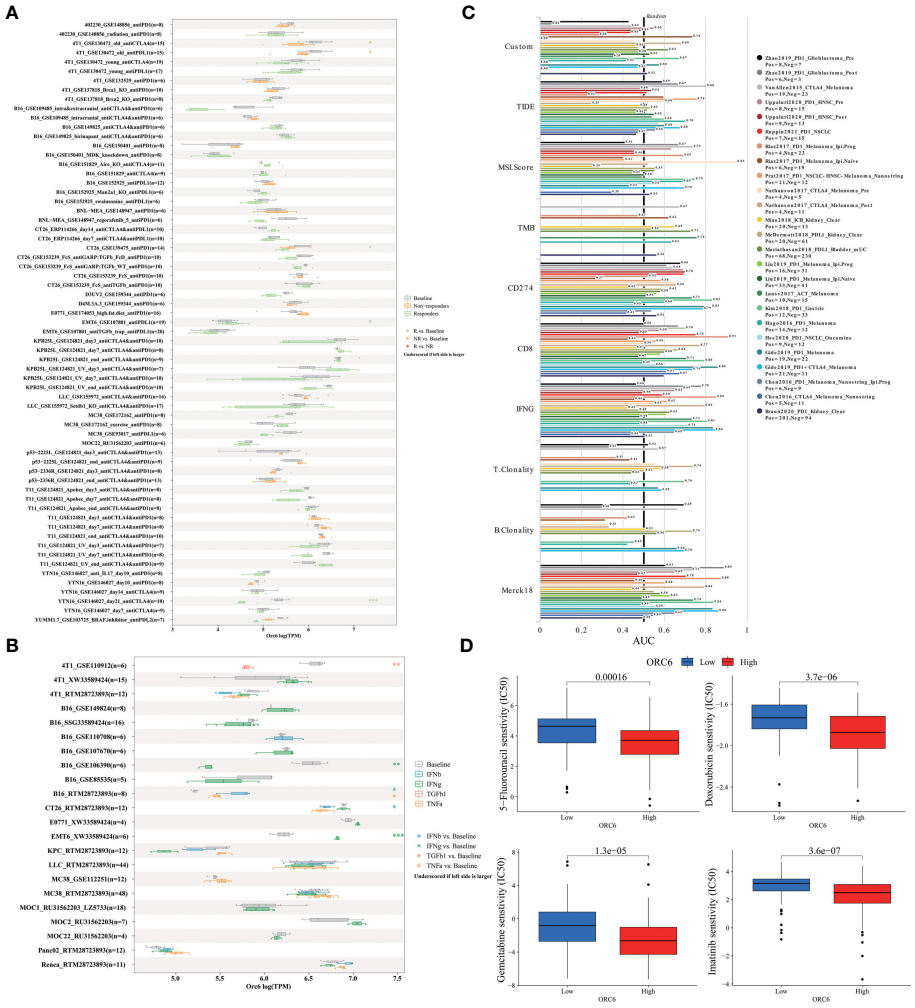

FIGURE 10
Correlation of *ORC6* expression with immunotherapy response, biomarkers, and drug sensitivity. **(A)** Differences in *ORC6* expression between the immunosuppressive treatment group and the control group. **(B)** Differences in *ORC6* expression between cytokine-treated and control groups. **(C)** The predictive role of *ORC6* as a biomarker versus other markers in different immunotherapy cohorts. **(D)** Relationship between *ORC6* expression and half-inhibitory concentration (IC50) of 5-fluorouracil, doxorubicin, gemcitabine and imatinib. *p < 0.05, **p < 0.01, ***p < 0.001.

(37, 38). In recent years, there has been growing recognition that RNA not only serves as an intermediary or effector molecule in protein synthesis but also plays a crucial and direct functional role in regulating gene expression. Consequently, the significance of RNA modifications has gained increasing prominence in scientific research and healthcare settings. Extensive evidence has suggested that the perturbation of RNA epigenetic pathways is associated with the development and progression of various human diseases, including cancer (39). In our study, we found that genetic alterations, DNA promoter methylation, and RNA modifications of *ORC6* have important effects on its expression. The main mutation forms of *ORC6* in tumors were "amplification" and "deep deletion", and the amplification was mainly concentrated in PAAD, BRCA, OV, BLCA, ACC, ESCA, LIHC, LUAD, etc. We also noticed that *ORC6* expression was markedly linked to CNV, mainly in BRCA, CESC, HNSC, LUAD, LUSC, OV, and STES. In BLCA, BRCA, HNSC, THYM, UCEC, and PRAD, as the levels of *ORC6* promoter methylation were reduced compared to those in normal tissues. However, in PAAD, KIRC, LUSC, and SARC, there was a significant increase in *ORC6* promoter methylation levels. Furthermore, we identified a positive correlation between *ORC6* expression and m1A-, m5C-, and m6A-related genes in almost all of the analyzed tumor types. Our single-cell functional analysis also indicated a close association between *ORC6* expression and DNA damage and repair mechanisms, which highlights the underlying mechanisms of aberrant *ORC6* expression in cancer from both genetic alteration and epigenetic modification perspectives.

Cancer progression, metastasis, invasion, and resistance to therapy are modulated by bidirectional interactions between cancer cells and the TME (40). Characteristics of TME include hypoxia, immunosuppression, chronic inflammation, acidosis, high interstitial fluid pressure, increased ECM stiffness, and depletion of essential nutrients. Immunotherapy mainly targets hypoxia and immunosuppression, which are presently active research topics (41). Precision medicine aims to develop targeted and immunotherapies to enhance the survival rate. Cancer

10.3389/fimmu.2023.1236806

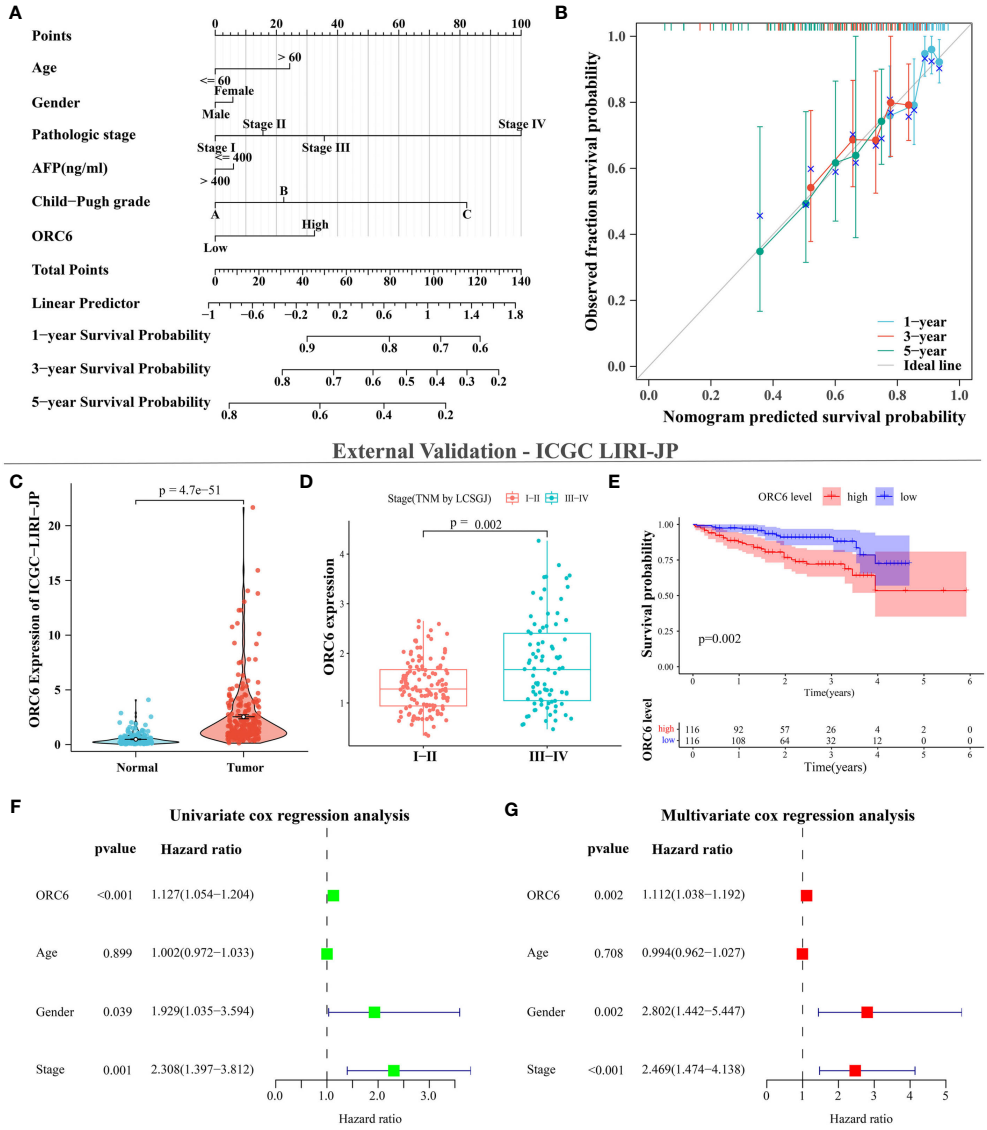

FIGURE 11
ORC6 is an independent risk factor for poor prognosis in LIHC. **(A)** Construction of line charts for 1-, 3-, and 5-year time points. **(B)** Calibration curves for 1-, 3-, and 5-year timepoints. **(C–G)** External data validation using the ICGC LIRI-JP cohort. **(C)** Differential expression analysis of *ORC6* between tumor and normal tissues. **(D)** Differential expression analysis of *ORC6* across different clinical stages. **(E)** Survival analysis of the high and low *ORC6* expression groups, with both univariate **(F)** and multivariate **(G)** Cox regression analyses used to establish the role of *ORC6* in LIHC.

immunotherapy presents an effective and groundbreaking method to fight cancer by manipulating or modulating the immune system to elicit a robust response against tumors (42). Successful cancer immunotherapy depends on overcoming the immunosuppressive environment in the TME of cancer patients (43). Increasing evidence suggests that immune dysregulation plays a critical role in allowing tumors to evade the host immune system (44), involving both innate and adaptive immunity. Research has revealed that tumor-infiltrating lymphocytes tend to exhibit dysfunctional behavior and may remain in a quiescent state near cancerous cells. Despite this, a few patients' T cells have been found to preserve their ability to proliferate and persist, leading to the complete eradication of sizable tumor deposits (45). This finding is consistent with our finding in single-cell sequencing that *ORC6* is predominantly expressed on Tprolif and malignant cells. Therefore, targeting ORC6 could potentially offer a precise method for identifying Tprolif and malignant cells, leading to novel avenues for tumor immunotherapy (46). Here, we found an inverse correlation between the expression level of *ORC6* and the abundance of immune cells widely believed to contribute to the suppression of tumor infiltration, including Tem CD8 cells, Th1 cells, NK cells, pDCs, iDCs, eosinophils, and monocytes (47–52). Interestingly, we noticed that *ORC6* expression levels were positively correlated with the abundance of Act CD4 and Th2 cells in the TME. Act CD4 refers to activated

10.3389/fimmu.2023.1236806

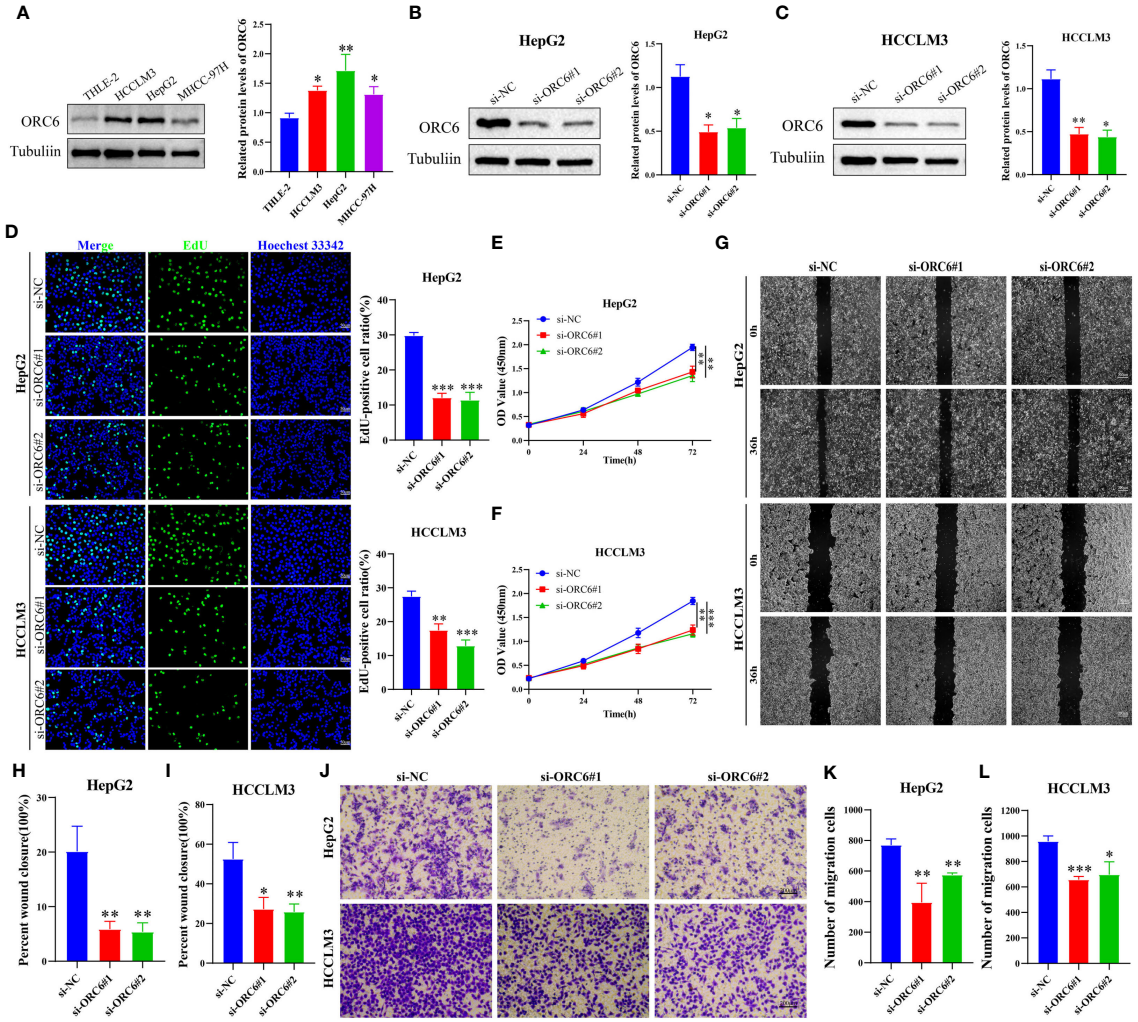

FIGURE 12
Silencing *ORC6* expression suppresses the proliferation and migration of LIHC cells. **(A)** Western blot analysis and quantitative measurements of *ORC6* protein levels in liver cells (THLE-2) and LIHC cells (HCCLM3, HepG2, and MHCC-97H). Western blot analysis and quantitative measurements of *ORC6* knockdown efficiency in HepG2 **(B)** and HCCLM3 **(C)** cells. **(D)** EdU staining and quantitative analysis were performed to evaluate changes in cell proliferation following *ORC6* knockdown. A CCK-8 assay was utilized to evaluate the effect of *ORC6* knockdown on cell viability in HepG2 **(E)** and HCCLM3 **(F)** cells. **(G–I)** A wound-healing assay was used to evaluate the changes in the cell migration rate among the si-NC, si-*ORC6*#1, and si-*ORC6*#2 groups of HepG2 and HCCLM3 cells. **(J–L)** Transwell assays were utilized to evaluate the changes in cell migration ability among the si-NC, si-*ORC6*#1, and si-*ORC6*#2 groups in HepG2 and HCCLM3 cells. *p < 0.05, **p < 0.01, ***p < 0.001.

CD4 T cells, a key component of the adaptive immune system. Recent studies have found that CD4+ T-cell infiltration defines an immune escape environment and predicts poor patient outcomes (53). Th2 refers to helper T-cell type 2, which is a specific type of T-cell in the immune system. Th2 cells play a critical role in the adaptive immune response by supporting B-cell function. Interestingly, the accumulation of Th2 cells within tumors, in addition to Hodgkin's lymphoma, has been associated with a poor prognosis in several types of cancers (54). At present, researchers are exploring ways to regulate Th2 cells to improve the effect of tumor treatment. Regulatory T cells (Tregs) are a subset of T cells crucial for maintaining immune homeostasis and tolerance. Research suggests that several subtypes of Tregs, including TNFR2+, LAG3+, TIM3+, and CTLA-4+ Tregs, demonstrate potent anticancer capabilities. However, in recent years, researchers have also discovered links between particular highly infiltrated Treg subtypes within tumors and favorable patient outcomes, such as CD30+OX40+ and BLIMP-1+FOXP3+ Tregs (55). This might elucidate the favorable correlation between *ORC6* and Treg infiltration abundance in BRCA, KIRC, MESO, and THCA, whereas an inverse correlation exists in the majority of other tumor types.

Cancer cells can secrete important cytokines and chemokines for the TME during growth and progression (56), these cytokines and chemokines can in turn regulate the TME and cell signaling pathways to affect cancer progression (57, 58). Our study revealed a positive correlation between *ORC6* expression and cytokines as well

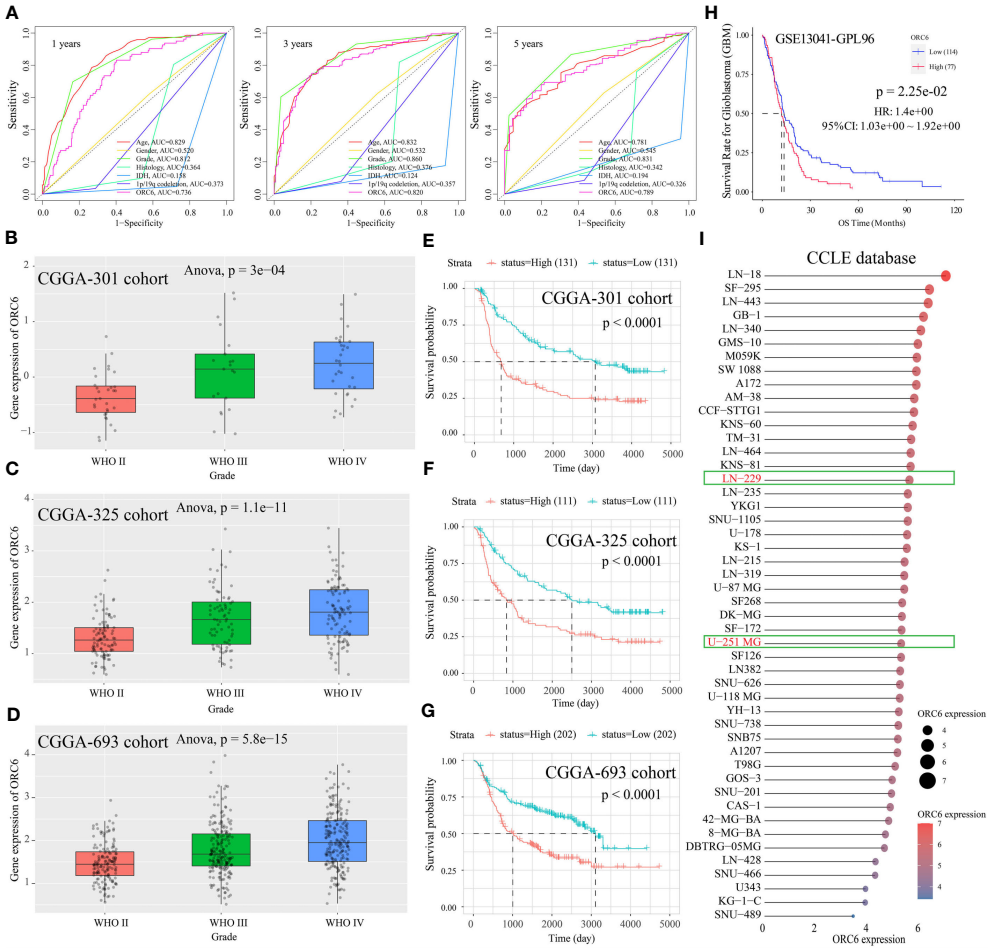

FIGURE 13
ORC6 effectively predicts the prognosis of the patients with GBMLGG. **(A)** Receiver operating characteristic (ROC) curves for predicting 1-, 3-, and 5-year overall survival (OS) of patients with GBMLGG. **(B–D)** Analysis of differential expression of *ORC6* in different WHO grades explored in the CGGA-301, CGGA-325, and CGGA-693 cohorts, respectively. **(E–H)** Survival differences between high and low *ORC6* expression groups were examined in the CGGA-301, CGGA-325, CGGA-693 and GSE13041 cohorts. **(I)** The Cancer Cell Line Encyclopedia (CCLE) database was used to analyze the expression of *ORC6* in GBMLGG cell lines.

as receptors in different types of tumors. Notably, GSEA revealed a strong association between *ORC6* expression and the cytokine-cytokine receptor interaction pathway, and our GSEA further highlights the close association between *ORC6* and immune-related pathways in multiple tumor types. Moreover, we discovered a positive association between *ORC6* expression and well-known targets for classical immune suppression and activation, such as PVR, MICB, ULBP1, CD276, CTLA4, TNFRSF25, PD-1 (PDCD1), TIGIT, PD-L2 (PDCD1LG2), HAVCR2, PD-L1 (CD274), and LAG3. Strikingly, our findings reveal that *ORC6* expression has a certain predictive effect on immunotherapy, cytokine therapy, and chemotherapy response. The current use of multifunctional carriers to deliver therapeutic drugs to lesion sites helps to significantly improve the effect of noninvasive treatment. Multifunctional carriers allow for multiple treatment options, including photodynamic therapy, photothermal therapy, chemotherapy, immunotherapy, or their synergistic treatments (59). Therefore, molecular probes targeting *ORC6* combined with multifunctional carriers are promising cancer treatment strategies (60). Collectively, these observations provide new insights into the complex regulation of immune cell-mediated tumor suppression and suggest that *ORC6* may serve as a promising predictive marker of immunotherapy efficacy in cancer treatment. Nevertheless, the mechanisms by which *ORC6* regulates the tumor immune microenvironment and tumor progression need to be further elucidated in the future.

5 Conclusion

ORC6 emerges as a promising prognostic biomarker across various cancer types, particularly in LIHC and GBMLGG. This study underscores the correlation between high *ORC6* expression

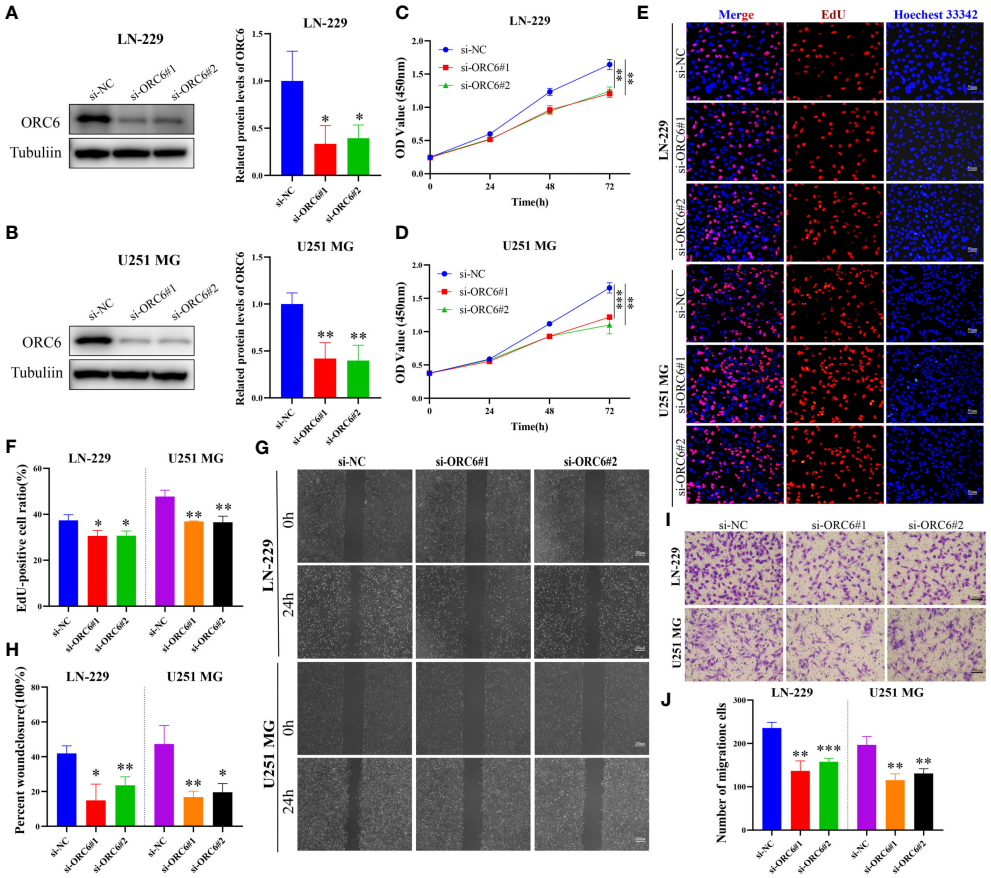

FIGURE 14
Knockdown of *ORC6* expression suppresses proliferation and migration of GBMLGG cells. **(A, B)** Western blot analysis and quantitative measurements of *ORC6* knockdown efficiency in LN-229 and U251 MG cells. **(C, D)** CCK-8 assay was used to evaluate the effect of *ORC6* knockdown on cell viability in LN-229 and U251 MG cells. **(E, F)** EdU staining and quantitative analysis were performed to evaluate the changes in cell proliferation after *ORC6* knockdown. **(G, H)** A wound healing assay was used to evaluate the changes in cell migration rate among the si-NC, si-*ORC6*#1, and si-*ORC6*#2 groups of LN-229 and U251 MG cells. **(I, J)** Transwell assays were used to evaluate the changes in cell migration ability among the si-NC, si-*ORC6*#1, and si-*ORC6*#2 groups in LN-229 and U251 MG cells. *p < 0.05, **p < 0.01, ***p < 0.001.

and the tumor immunosuppressive environment. These findings suggest a potential role for *ORC6* in tumor immune regulation, thereby offering further support for advancing the development of cancer immunotherapies.

Data availability statement

The datasets presented in this study can be found in online repositories. The names of the repository/repositories and accession number(s) can be found in the article/Supplementary Material.

Ethics statement

Ethical approval was not required for the study involving humans in accordance with the local legislation and institutional requirements. Written informed consent to participate in this study was not required from the participants or the participants' legal guardians/next of kin in accordance with the national legislation and the institutional requirements.

Author contributions

JZ conducted the formal analysis and wrote the original draft. WY performed the project administration. QC, LZ, HG, TW, YHe, and YD conducted the experiments. JX, JPang, JPeng, HG, TW, and YHan participated in software analysis. JZ, QC, LZ, and JPeng conducted data curation. JZ and WY contributed to writing, reviewing, and editing the article. WY provided funding acquisition. All authors read and approved the final submitted manuscript.

Funding

This study was funded by the Science and Technology Innovation Program of Hunan Province (Grant No.2021SK2026),

the Clinical Medical Boot Technology Innovation Project of Hunan Province (Grant No. 2021SK53504), the Health and Family Planning Commission of Hunan Province (Grant No. . 2022JJ70143), the Clinical Research Special Fund of Wu Jieping Medical Foundation (Grant No. 320.6750.2022-19-29), the Tumor Clinical Research of Public Welfare of Xiaoxiang the Clinical Research (Grant No. HTSF202207275503), the Innovation Platform and Talent Plan of Hunan Province (2023SK4019) and the National Natural Science Foundation of China (Grant No. 82270834, 82000756).

Conflict of interest

The authors declare that the research was conducted in the absence of any commercial or financial relationships that could be construed as a potential conflict of interest.

Publisher's note

Supplementary material

The Supplementary Material for this article can be found online at: https://www.frontiersin.org/articles/10.3389/fimmu.2023.1236806/full#supplementary-material

SUPPLEMENTARY FIGURE S1
ORC6 genetic alterations, localization, and interactions. **(A)** Immunofluorescence images and merged images of ORC6 protein, nucleus, endoplasmic reticulum (ER), and microtubules in HEK 293 and PC-3 cell lines. **(B)** ORC6 expression mapping was obtained through the Genecard website. **(C)** Protein-protein interaction (PPI) network presenting proteins that interact with ORC6. **(D)** Mutation types and frequencies of ORC6 in pan-cancer were obtained from the cBioPortal website. **(E)** The expression levels of ORC6 in various CNV status in pan-cancer. *p < 0.05, **p < 0.01, ***p < 0.001.

SUPPLEMENTARY FIGURE S2
ORC6 DNA methylation levels and the relationship between *ORC6* and RNA-modifying gene expression. **(A, B)** Promoter methylation levels of *ORC6* in different cancer types compared to normal adjacent tissues. Beta values represent DNA methylation levels ranging from 0 (unmethylated) to 1 (fully methylated). **(C)** The relationship between *ORC6* expression and gene expression related to three types of RNA modifications was analyzed by Spearman correlation. *p<0.05.

SUPPLEMENTARY FIGURE S3
Diagnostic value of *ORC6* across cancers. **(A-W)** ROC curve of *ORC6* in DLBC, GBMLGG, KICH, KIRC, KIRP, LGG, PRAD, SKCM, TGCT, THCA, and THYM.

SUPPLEMENTARY FIGURE S4
Correlation between *ORC6* expression and the functional status of 14 cancers. **(A)** The correlation between *ORC6* expression and the functional status of 14 cancers was analyzed using single-cell sequence data from the CancerSEA database.

References

1. Sung H, Ferlay J, Siegel RL, Laversanne M, Soerjomataram I, Jemal A, et al. Global cancer statistics 2020: globocan estimates of incidence and mortality worldwide for 36 cancers in 185 countries. *CA Cancer J Clin* (2021) 71(3):209–49. doi: 10.3322/caac.21660

2. Chen F, Zhang Y, Gibbons DL, Deneen B, Kwiatkowski DJ, Ittmann M, et al. Pan-Cancer Molecular Classes Transcending Tumor Lineage across 32 Cancer Types, Multiple Data Platforms, and over 10,000 Cases. *Clin Cancer Res* (2018) 24(9):2182–93. doi: 10.1158/1078-0432.CCR-17-3378

3. Yamaguchi H, Hsu JM, Yang WH, Hung MC. Mechanisms regulating pd-L1 expression in cancers and associated opportunities for novel small-molecule therapeutics. *Nat Rev Clin Oncol* (2022) 19(5):287–305. doi: 10.1038/s41571-022-00601-9

4. Friedlaender A, Subbiah V, Russo A, Banna GL, Malapelle U, Rolfo C, et al. Egfr and her2 exon 20 insertions in solid tumours: from biology to treatment. *Nat Rev Clin Oncol* (2022) 19(1):51–69. doi: 10.1038/s41571-021-00558-1

5. Xia J, Li S, Liu S, Zhang L. Aldehyde dehydrogenase in solid tumors and other diseases: potential biomarkers and therapeutic targets. *MedComm* (2023) 4(1):e195. doi: 10.1002/mco2.195

6. Liu S, Balasov M, Wang H, Wu L, Chesnokov IN, Liu Y. Structural analysis of human orc6 protein reveals a homology with transcription factor tfiib. *Proc Natl Acad Sci USA* (2011) 108(18):7373–8. doi: 10.1073/pnas.1013676108

7. Prasanth SG, Prasanth KV, Stillman B. Orc6 involved in DNA replication, chromosome segregation, and cytokinesis. *Science* (2002) 297(5583):1026–31. doi: 10.1126/science.1072802

8. Lin YC, Liu D, Chakraborty A, Kadyrova LY, Song YJ, Hao Q, et al. Orc6 is a component of the replication fork and enables efficient mismatch repair. *Proc Natl Acad Sci USA* (2022) 119(22):e2121406119. doi: 10.1073/pnas.2121406119

9. Hu Y, Wang L, Li Z, Wan Z, Shao M, Wu S, et al. Potential prognostic and diagnostic values of cdc6, cdc45, orc6 and snhg7 in colorectal cancer. *Onco Targets Ther* (2019) 12:11609–21. doi: 10.2147/OTT.S231941

10. Pan Q, Li F, Ding Y, Huang H, Guo J. Orc6 acts as a biomarker and reflects poor outcome in clear cell renal cell carcinoma. *J Cancer* (2022) 13(8):2504–14. doi: 10.7150/jca.71313

11. Mao R, Wang Z, Zhang Y, Chen Y, Liu Q, Zhang T, et al. Development and validation of a novel prognostic signature in gastric adenocarcinoma. *Aging (Albany NY)* (2020) 12(21):22233–52. doi: 10.18632/aging.104161

12. Chen S, Jin Z, Xin L, Lv L, Zhang X, Gong Y, et al. Expression and clinical significance of origin recognition complex subunit 6 in breast cancer - a comprehensive bioinformatics analysis. *Int J Gen Med* (2021) 14:9733–45. doi: 10.2147/IJGM.S342597

13. Shen W, Song Z, Zhong X, Huang M, Shen D, Gao P, et al. Sangerbox: A comprehensive, interaction-friendly clinical bioinformatics analysis platform. *iMeta* (2022) 1(3):e36. doi: 10.1002/imt2.36

14. Mermel CH, Schumacher SE, Hill B, Meyerson ML, Beroukhim R, Getz G. Gistic2.0 facilitates sensitive and confident localization of the targets of focal somatic copy-number alteration in human cancers. *Genome Biol* (2011) 12(4):R41. doi: 10.1186/gb-2011-12-4-r41

15. Chandrashekar DS, Karthikeyan SK, Korla PK, Patel H, Shovon AR, Athar M, et al. Ualcan: an update to the integrated cancer data analysis platform. *Neoplasia* (2022) 25:18–27. doi: 10.1016/j.neo.2022.01.001

16. Huang S, Sun L, Hou P, Liu K, Wu J. A comprehensively prognostic and immunological analysis of actin-related protein 2/3 complex subunit 5 in pan-cancer and identification in hepatocellular carcinoma. *Front Immunol* (2022) 13:944898. doi: 10.3389/fimmu.2022.944898

17. Ru B, Wong CN, Tong Y, Zhong JY, Zhong SSW, Wu WC, et al. Tisidb: an integrated repository portal for tumor-immune system interactions. *Bioinformatics* (2019) 35(20):4200–2. doi: 10.1093/bioinformatics/btz210

18. Balar AV, Galsky MD, Rosenberg JE, Powles T, Petrylak DP, Bellmunt J, et al. Atezolizumab as first-line treatment in cisplatin-ineligible patients with locally advanced and metastatic urothelial carcinoma: A single-arm, multicentre, phase 2 trial. *Lancet* (2017) 389(10064):67–76. doi: 10.1016/S0140-6736(16)32455-2

19. Lin A, Qi C, Wei T, Li M, Cheng Q, Liu Z, et al. Camoip: A web server for comprehensive analysis on multi-omics of immunotherapy in pan-cancer. *Brief Bioinform* (2022) 23(3):bbac129. doi: 10.1093/bib/bbac129

20. Auslander N, Zhang G, Lee JS, Frederick DT, Miao B, Moll T, et al. Robust prediction of response to immune checkpoint blockade therapy in metastatic melanoma. *Nat Med* (2018) 24(10):1545–9. doi: 10.1038/s41591-018-0157-9

21. Zeng Z, Wong CJ, Yang L, Ouardaoui N, Li D, Zhang W, et al. Tismo: syngeneic mouse tumor database to model tumor immunity and immunotherapy response. *Nucleic Acids Res* (2022) 50(D1):D1391–D7. doi: 10.1093/nar/gkab804

22. Fu J, Li K, Zhang W, Wan C, Zhang J, Jiang P, et al. Large-scale public data reuse to model immunotherapy response and resistance. *Genome Med* (2020) 12(1):21. doi: 10.1186/s13073-020-0721-z

23. Geeleher P, Cox N, Huang RS. Prrophetic: an R package for prediction of clinical chemotherapeutic response from tumor gene expression levels. *PloS One* (2014) 9(9): e107468. doi: 10.1371/journal.pone.0107468

24. Sun D, Wang J, Han Y, Dong X, Ge J, Zheng R, et al. Tisch: A comprehensive web resource enabling interactive single-cell transcriptome visualization of tumor microenvironment. *Nucleic Acids Res* (2021) 49(D1):D1420–D30. doi: 10.1093/nar/gkaa1020

25. Yuan H, Yan M, Zhang G, Liu W, Deng C, Liao G, et al. Cancersea: A cancer single-cell state atlas. *Nucleic Acids Res* (2019) 47(D1):D900–D8. doi: 10.1093/nar/gky939

26. Zhu J, Luo C, Zhao J, Zhu X, Lin K, Bu F, et al. Expression of lox suggests poor prognosis in gastric cancer. *Front Med (Lausanne)* (2021) 8:718986. doi: 10.3389/fmed.2021.718986

27. Tu Z, Peng J, Long X, Li J, Wu L, Huang K, et al. Sperm autoantigenic protein 17 predicts the prognosis and the immunotherapy response of cancers: A pan-cancer analysis. *Front Immunol* (2022) 13:844736. doi: 10.3389/fimmu.2022.844736

28. Zhu J, Huang Q, Liu S, Peng X, Xue J, Feng T, et al. Construction of a novel lncrna signature related to genomic instability to predict the prognosis and immune activity of patients with hepatocellular carcinoma. *Front Immunol* (2022) 13:856186. doi: 10.3389/fimmu.2022.856186

29. Chen Z, Speck C, Wendel P, Tang C, Stillman B, Li H. The architecture of the DNA replication origin recognition complex in saccharomyces cerevisiae. *Proc Natl Acad Sci USA* (2008) 105(30):10326–31. doi: 10.1073/pnas.0803829105

30. Saghafinia S, Mina M, Riggi N, Hanahan D, Ciriello G. Pan-cancer landscape of aberrant DNA methylation across human tumors. *Cell Rep* (2018) 25(4):1066–80 e8. doi: 10.1016/j.celrep.2018.09.082

31. Helm M, Motorin Y. Detecting rna modifications in the epitranscriptome: predict and validate. *Nat Rev Genet* (2017) 18(5):275–91. doi: 10.1038/nrg.2016.169

32. Zhang R, Guo Y, Liu Z, Kong L, Li C, He L, et al. Identification of irf8 as an immune infiltration-related biomarker in hepatocellular carcinoma by bioinformatics analysis. *MedComm (2020)* (2022) 3(3):e149. doi: 10.1002/mco2.149

33. Gavin EJ, Song B, Wang Y, Xi Y, Ju J. Reduction of orc6 expression sensitizes human colon cancer cells to 5-fluorouracil and cisplatin. *PloS One* (2008) 3(12):e4054. doi: 10.1371/journal.pone.0004054

34. Chen H, Bao L, Hu J, Wu D, Tong X. Orc6, negatively regulated by mir-1-3p, promotes proliferation, migration, and invasion of hepatocellular carcinoma cells. *Front Cell Dev Biol* (2021) 9:652292. doi: 10.3389/fcell.2021.652292

35. Wang XK, Wang QQ, Huang JL, Zhang LB, Zhou X, Liu JQ, et al. Novel candidate biomarkers of origin recognition complex 1, 5 and 6 for survival surveillance in patients with hepatocellular carcinoma. *J Cancer* (2020) 11(7):1869–82. doi: 10.7150/jca.39163

36. Qu S, Qiu O, Hu Z. The prognostic factors and nomogram for patients with high-grade gliomas. *Fundam Res* (2021) 1(6):824–8. doi: 10.1016/j.fmre.2021.07.005

37. Esteller M. Cancer epigenomics: DNA methylomes and histone-modification maps. *Nat Rev Genet* (2007) 8(4):286–98. doi: 10.1038/nrg2005

38. Lahtz C, Pfeifer GP. Epigenetic changes of DNA repair genes in cancer. *J Mol Cell Biol* (2011) 3(1):51–8. doi: 10.1093/jmcb/mjq053

39. Barbieri I, Kouzarides T. Role of rna modifications in cancer. *Nat Rev Cancer* (2020) 20(6):303–22. doi: 10.1038/s41568-020-0253-2

40. Hanahan D, Coussens LM. Accessories to the crime: functions of cells recruited to the tumor microenvironment. *Cancer Cell* (2012) 21(3):309–22. doi: 10.1016/j.ccr.2012.02.022

41. Zhang S-W, Wang H, Ding X-H, Xiao Y-L, Shao Z-M, You C, et al. Bidirectional crosstalk between therapeutic cancer vaccines and the tumor microenvironment: beyond tumor antigens. *Fundam Res* (2022). doi: 10.1016/j.fmre.2022.03.009

42. Gao Y, Shen M, Shi X. Interaction of dendrimers with the immune system: an insight into cancer nanotheranostics. *View* (2021) 2(3):20200120. doi: 10.1002/VIW.20200120

43. Flavell RA, Sanjabi S, Wrzesinski SH, Licona-Limon P. The polarization of immune cells in the tumour environment by tgfbeta. *Nat Rev Immunol* (2010) 10 (8):554–67. doi: 10.1038/nri2808

44. Lario S, Ramirez-Lazaro MJ, Sanjuan-Herraez D, Brunet-Vega A, Pericay C, Gombau L, et al. Plasma sample based analysis of gastric cancer progression using targeted metabolomics. *Sci Rep* (2017) 7(1):17774. doi: 10.1038/s41598-017-17921-x

45. Rosenberg SA, Restifo NP. Adoptive cell transfer as personalized immunotherapy for human cancer. *Science* (2015) 348(6230):62–8. doi: 10.1126/science.aaa4967

46. Zhang X, Liu X, Guo Y, Wu FG. Strategies for visualizing inflammation. *View* (2021) 2(1):20200025. doi: 10.1002/VIW.20200025

47. Lv B, Wang Y, Ma D, Cheng W, Liu J, Yong T, et al. Immunotherapy: reshape the tumor immune microenvironment. *Front Immunol* (2022) 13:844142. doi: 10.3389/fimmu.2022.844142

48. van der Leun AM, Thommen DS, Schumacher TN. Cd8(+) T cell states in human cancer: insights from single-cell analysis. *Nat Rev Cancer* (2020) 20(4):218–32. doi: 10.1038/s41568-019-0235-4

49. Vinay DS, Ryan EP, Pawelec G, Talib WH, Stagg J, Elkord E, et al. Immune evasion in cancer: mechanistic basis and therapeutic strategies. *Semin Cancer Biol* (2015) 35 Suppl:S185–S98. doi: 10.1016/j.semcancer.2015.03.004

50. Verneau J, Sautes-Fridman C, Sun CM. Dendritic cells in the tumor microenvironment: prognostic and theranostic impact. *Semin Immunol* (2020) 48:101410. doi: 10.1016/j.smim.2020.101410

51. Chusid MJ. Eosinophils: friends or foes? *J Allergy Clin Immunol Pract* (2018) 6 (5):1439–44. doi: 10.1016/j.jaip.2018.04.031

52. Ugel S, Cane S, De Sanctis F, Bronte V. Monocytes in the tumor microenvironment. *Annu Rev Pathol* (2021) 16:93–122. doi: 10.1146/annurev-pathmechdis-012418-013058

53. Gu Y, Chen Y, Jin K, Cao Y, Liu X, Lv K, et al. Intratumoral cd103(+)Cd4(+) T cell infiltration defines immunoevasive contexture and poor clinical outcomes in gastric cancer patients. *Oncoimmunology* (2020) 9(1):1844402. doi: 10.1080/2162402X.2020.1844402

54. Fridman WH, Pages F, Sautes-Fridman C, Galon J. The immune contexture in human tumours: impact on clinical outcome. *Nat Rev Cancer* (2012) 12(4):298–306. doi: 10.1038/nrc3245

55. Jiang Z, Zhu H, Wang P, Que W, Zhong L, Li XK, et al. Different subpopulations of regulatory T cells in human autoimmune disease, transplantation, and tumor immunity. *MedComm (2020)* (2022) 3(2):e137. doi: 10.1002/mco2.137

56. Hinshaw DC, Shevde LA. The tumor microenvironment innately modulates cancer progression. *Cancer Res* (2019) 79(18):4557–66. doi: 10.1158/0008-5472.CAN-18-3962

57. Mantovani A, Allavena P, Sica A, Balkwill F. Cancer-related inflammation. *Nature* (2008) 454(7203):436–44. doi: 10.1038/nature07205

58. Liotta LA, Kohn EC. The microenvironment of the tumour-host interface. *Nature* (2001) 411(6835):375–9. doi: 10.1038/35077241

59. Bian Y, Wang Y, Chen X, Zhang Y, Xiong S, Su D. Image-guided diagnosis and treatment of glioblastoma. *View* (2023) 4(3):20220069. doi: 10.1002/VIW.20220069

60. Zhu H, Yang C, Yan A, Qiang W, Ruan R, Ma K, et al. Tumor-targeted nano-adjuvants to synergize photomediated immunotherapy enhanced antitumor immunity. *View* (2023) 4(3):20220067. doi: 10.1002/VIW.20220067

frontiers | Frontiers in Oncology

TYPE Systematic Review
PUBLISHED 26 October 2023
DOI 10.3389/fonc.2023.1181248

OPEN ACCESS

EDITED BY
Takaji Matsutani,
Repertoire Genesis, Inc., Japan

REVIEWED BY
Xiaobin Shang,
Tianjin Medical University Cancer Institute and Hospital, China
Lei Yang,
Harbin Medical University, China
Hashem Obaid Alsaab,
Taif University, Saudi Arabia

*CORRESPONDENCE
Wei Qiu
15973881888@163.com

RECEIVED 07 March 2023
ACCEPTED 26 September 2023
PUBLISHED 26 October 2023

CITATION
Rugambwa TK, Abdihamid O, Zhang X, Peng Y, Cai C, Shen H, Zeng S and Qiu W (2023) Neutrophil–lymphocyte ratio and platelet–lymphocyte ratio as potential predictive markers of treatment response in cancer patients treated with immune checkpoint inhibitors: a systematic review and meta-analysis.
Front. Oncol. 13:1181248.
doi: 10.3389/fonc.2023.1181248

Neutrophil–lymphocyte ratio and platelet–lymphocyte ratio as potential predictive markers of treatment response in cancer patients treated with immune checkpoint inhibitors: a systematic review and meta-analysis

Tibera K. Rugambwa[1,2], Omar Abdihamid[3], Xiangyang Zhang[1], Yinghui Peng[1], Changjing Cai[1], Hong Shen[1], Shan Zeng[1] and Wei Qiu[4]*

[1]Department of Oncology, Xiangya Hospital, Central South University, Changsha, Hunan, China, [2]Department of Internal Medicine, Mbeya Zonal Referral Hospital and Mbeya College of Health and Allied Sciences, University of Dar-es-salaam, Mbeya, Tanzania, [3]Garissa Cancer Center, Garissa County Referral Hospital, Garissa, Kenya, [4]Department of Oncology, The First People's Hospital of Loudi, Loudi, Hunan, China

Background: The role of platelet–lymphocyte ratio (PLR) and neutrophil–lymphocyte ratio (NLR) as independent prognostic markers in different tumors is well established. However, there is a limited review of the potential of NLR and PLR as predictors of treatment outcomes from immune checkpoint inhibitors (ICIs).

Objective: To establish a correlation between NLR and PLR and the potential of clinical benefit from ICIs.

Methods: The literature search was performed for studies that reported the association between NLR, PLR, and treatment outcomes among cancer patients treated with ICIs. The outcomes of interest were objective response rate (ORR), disease control rate (DCR), and progressive disease (PD). ORR was the summation of patients who achieved complete response and partial response. DCR included patients who achieved stable disease. PD was the proportion of patients who progressed, relapsed, or discontinued the treatment. Statistical analysis was performed using the STATA 12.0 package. Heterogeneity was determined by the I^2 value. Quality assessment was performed using the Newcastle–Ottawa Scale. Egger's test was used to establish publication bias and sensitivity analysis.

Results: A total of 40 papers that met the inclusion criteria were included in the systematic review. However, only 17 studies were used in the meta-analysis to determine the correlation between NLR, PLR, and treatment response. We found

that treatment with ICIs and monitoring of outcomes and adverse events using PLR and NLR parameters have been studied in different tumors. Our analysis showed that low NLR correlated with higher ORR (OR = 0.62 (95% CI 0.47–0.81, p = 0.001) and higher DCR (OR = 0.23, 95% CI 0.14–0.36, p < 0.001). Higher NLR predicted a higher probability of PD (OR = 3.12, 95% CI 1.44, 6.77, p = 0.004). Similarly, low PLR correlated with higher ORR (OR = 0.69, 95% CI 0.5, 0.95, p = 0.025). Generally, patients with low NLR and PLR were more likely to achieve clinical benefit and better response (p-value < 0.001). Meanwhile, patients with high ratios were more likely to progress (p-value < 0.005), although there was significant heterogeneity among studies. There was no significant publication bias observed.

Conclusion: The study showed that high NLR and PLR either at baseline or during treatment is associated with poorer treatment outcome. Therefore, these ratios can be utilized in clinical practice with other markers to determine treatment efficacy from immunotherapy.

KEYWORDS

neutrophil-lymphocyte ratio, platelet-lymphocyte ratio, immune checkpoint inhibitors, predictive, biomarkers, response

1 Introduction

Chronic inflammation is one of the enabling characteristics in the acquisition of hallmarks of cancer, together with genomic instability (1). The inflammatory process is driven by key inflammatory cells, namely, lymphocytes, neutrophils, monocytes, and platelets (2). Interaction of these cells in the tumor microenvironment (TME) and the peripheral circulation not only facilitates the propagation and survival of cancer cells but also provides them with the ability to evade the immune system, induce angiogenesis, and metastasize to other sites (2).

Immunotherapy is one of the pillars of cancer treatment in combination with surgery, chemotherapy, radiotherapy, and the expanding targeted therapy. These drugs function by blocking immune checkpoints, which are programmed death-1 (PD-1) and its ligand (PDL-1), cytotoxic T-lymphocyte antigen 4 (CTLA-4), and lymphocyte-activation gene 3 (LAG-3), resulting in upregulation of T-cell activation, preventing tumor evasion and increasing CD8 T-cell response toward cancer cells (3).

Indication of immune checkpoint inhibitors (ICIs) is expanding rapidly from advanced disease settings to neo-adjuvant and adjuvant use in early disease (4–6) with the potential of complete treatment response and durable disease control in some patients (3). Currently, ICIs are indicated for multiple cancers with non-small cell lung cancer (NSCLC) and melanoma deriving the greatest benefit to gastrointestinal, genitourinary, and breast cancers and lymphomas just to mention a few (3).

The mechanism of action of immunotherapy depends on the inflammatory cells and tumor immunogenicity (3). Hence, in a state of lymphopenia (7), thrombocytosis (8, 9), and neutrophilia (10) either at baseline or during the course of treatment as is the case in most patients with advanced disease and poor performance status, it is less likely to achieve durable clinical response. In addition, tumors that can generate significant immune responses like melanoma and squamous cell carcinomas show dramatic responses in comparison to cold tumors like gliomas and pancreatic cancer (3).

The currently approved biomarkers to predict response to immunotherapy are PDL-1 levels, microsatellite instability status (MSI), and tumor mutation burden (TMB). However, these have been shown to be applicable in a small proportion of patients (2, 11). Although they have revolutionized the use of ICIs in cancer treatment, the fact that they are tissue-based makes them susceptible to tumor heterogeneity (12). In addition, they cannot distinguish between patients who will respond to therapy against those who will not (12).

Interaction between neutrophils, platelets, and lymphocytes reflects the balance between protumoral inflammation and anti-tumor activity (3). In some studies, the neutrophil–lymphocyte ratio (NLR) and platelet–lymphocyte ratio (PLR) was associated with a better response than PDL-1 levels (11, 13). Therefore, there is a need to develop a prognostic and predictive model that incorporates other potential biomarkers to be able to determine those who are more likely to benefit from treatment (14, 15).

A recent meta-analysis looked at the association of dynamic changes in NLR with survival outcomes and treatment response (16). The study concluded that lower baseline NLR and a downward trend of NLR during and post-treatment with immunotherapy were associated with longer survival and better tumor response (16). However, very few studies that were included reported on treatment response and disease control. Another meta-analysis on renal cell carcinoma (RCC) also showed high NLR correlated with worse survival outcomes (17).

Notably, a significant number of studies have focused on the role of NLR and PLR as prognostic factors, but very few have focused on treatment response with immunotherapy (18–21). Therefore, this study will focus on the role of NLR and PLR as predictive markers of response to immunotherapy.

2 Methods

2.1 Search strategy

The systematic review and meta-analysis were conducted in accordance with Preferred Reporting Items for Systematic Reviews and Meta-analyses (PRISMA) guidelines. A comprehensive literature search was conducted from PubMed, Embase, Web of Science, and Cochrane Library from 2015 to 2022. The search terms employed were "neutrophil-to-lymphocyte ratio" AND "immune checkpoint inhibitors" and "platelet-to-lymphocyte ratio" AND "immune checkpoint inhibitors" (Table S1).

The outcomes of interest were objective response rate (ORR), disease control rate (DCR), and progressive disease (PD) as defined by Response Evaluation Criteria in Solid Tumors (RECIST) 1.1. ORR was the summation of patients who achieved complete response and partial response. DCR included patients who achieved stable disease. PD was the proportion of patients who progressed, relapsed, or discontinued the treatment. The correlation was made according to cutoff values of NLR and PLR established at baseline and during the course of treatment as determined by the authors.

2.2 Inclusion and exclusion criteria

Studies that met the following criteria were included in the study:

- ☐ studies published from 2015 to 2022;
- ☐ studies that enrolled patients with solid tumors who received any of the ICIs;
- ☐ studies reporting clinical response (ORR, DCR, and PD) and prognostic value of inflammatory markers and ICIs; and
- ☐ prospective studies, retrospective studies, exploratory studies, and randomized controlled trials (RCTs).

2.2.1 Exclusion criteria

- ☐ Studies that did not document or analyze the association or prognostic value of inflammatory markers and ICIs;
- ☐ non-English studies;
- ☐ abstracts, reviews, meta-analyses, case reports, editorials, letters to the editor, and commentaries; and
- ☐ animal studies.

2.3 Data extraction

The following information was extracted:

- ☐ name of the first author,
- ☐ year of publication,
- ☐ type of cancer,
- ☐ number of patients,
- ☐ type of study design,
- ☐ inflammatory markers investigated, and
- ☐ numerical data for NLR, PLR, ORR, DCR, and PD from frequency tables.

2.4 Quality assessment

The Newcastle–Ottawa Scale (NOS) was used to assess the quality of included studies. Any study with a minimum of two stars was considered suitable to be included in the review and meta-analysis. However, the most important criterion was the availability of quality extractable data from an individual study (Table S2).

2.5 Statistical analysis

Authoritative statistical software (Stata 12.0: StataCorporation) was used to perform the meta-analysis. The OR and 95% CI values were applied to estimate the prognostic value of NLR and PLR for patients treated with ICIs. Individual OR and 95% CI values were combined to an overall OR and 95% CI. An OR < 1 indicated a better treatment outcome. The Higgins I^2 statistic was applied to detect the heterogeneity between studies; $p \leq 0.1$ and $I^2 > 50\%$ indicated a substantial heterogeneity between studies, and random-effects models were adopted. Egger's test and visual inspection of a funnel plot were carried out to evaluate the possibility of publication bias. Egger's test result was the primary indicator, and a symmetry funnel plot with a p-value ≥0.05 was considered an insignificant publication bias.

3 Results

3.1 Literature screening results

The literature search identified 1,062 studies from the database and registers. Out of those, 711 were removed as duplicates, 158 records were removed because they were not eligible, 80 reports could not be retrieved, and 73 reports either had missing information or were not related to the study. The final review and meta-analysis included 40 studies and 17 studies, respectively (Figure 1). The characteristics of studies, data extracted, and patient characteristics involved in the studies are represented in

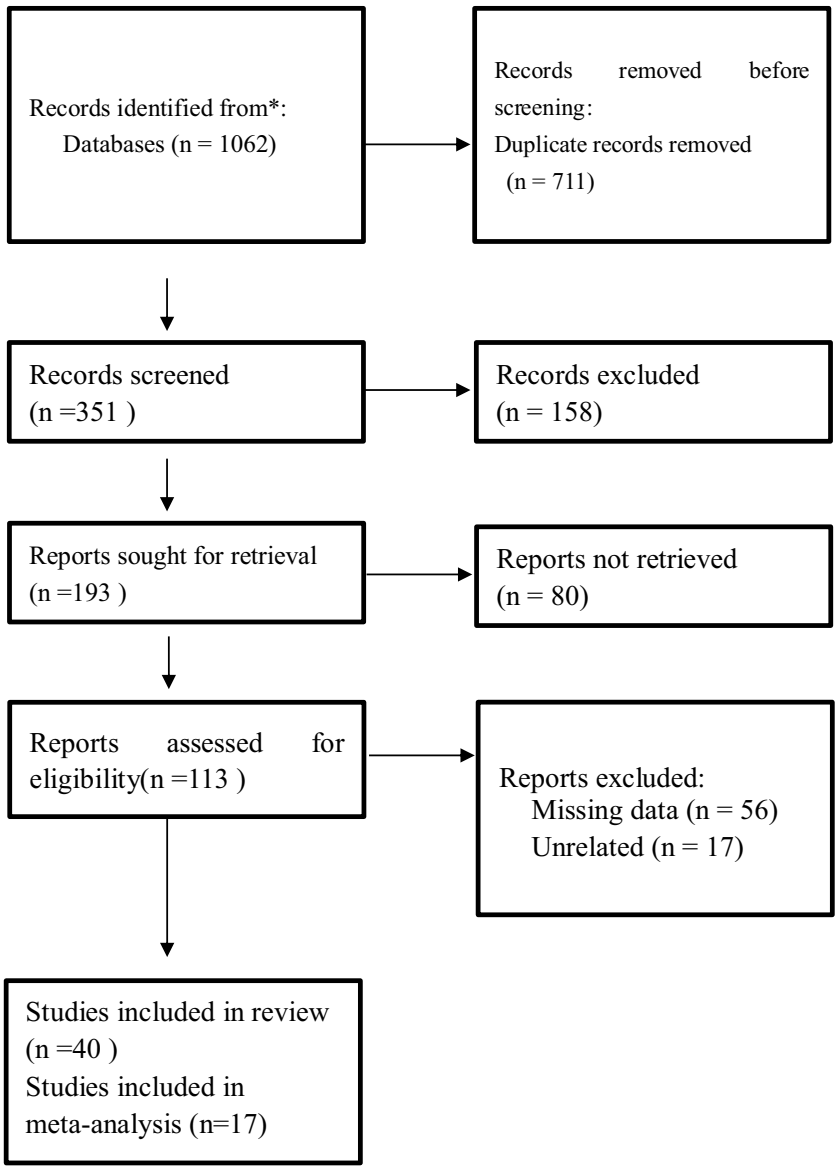

FIGURE 1
PRISMA flow diagram of study selection for inclusion in the systematic review and meta-analysis. PRISMA, Preferred Reporting Items for Systematic Reviews and Meta-analyses.

Tables 1 and 2. Important findings from the studies are summarized in Supplementary Table 3.

3.2 Research characteristics

A total of 40 studies were included in this systematic review, but only 17 studies (13, 22–37) qualified for meta-analysis. Regionwise, almost half of the included studies came from Asian countries (Japan, China, and Korea). The sample size in the included 40 studies ranged from 16 patients to 672 patients. Almost all studies were retrospective in nature except for one study that used a prospective study design (23) and received moderately high scores in the Newcastle–Ottawa Scale quality assessment. A total of 36 studies looked at distinct cancer types, and three studies looked at two or more types of tumors. Out of the 36 studies that looked at specific cancer types, NSCLC was the most frequently studied tumor. Fifteen studies focused only on ICI as a single agent, while the remaining studies included patients who received immunotherapy in combination with other cancer treatment modalities. Apart from reporting NLR and PLR, other blood cell counts included derived neutrophil–lymphocyte ratio (dNLR), absolute lymphocyte count (ALC), absolute neutrophil count (ANC), absolute platelet count (APC), absolute eosinophil count (AEC), and leukocyte count and its differentials. Receiver operating characteristic (ROC) curves were used in nine studies (25, 33, 36, 38–43) to determine the optimal cutoff value for NLR and PLR.

10.3389/fonc.2023.1181248

TABLE 1 Study Characteristics.

Author	Year	Design	Cancer	Patients	Marker	Outcome	NOS	Ref.no
Benzekry	2021	RC	NSCLC	298	NLR, PLR	DCR	6	20
Booka	2022	RC	GI	61	NLR, PLR	DCR,PD	8	35
Chen	2021	RC	NSCLC	151	NLR	ORR, DCR	6	15
Cheng	2022	RC	CERVICAL	70	NLR	ORR	8	54
Criscitiello	2020	RC	PAN CANCER	153	NLR, PLR	ORR, DCR	6	52
Dusselier	2019	RC	NSCLC	59	NLR, PLR	DCR-long responders PD-Early progressors	8	22
Eso	2021	RC	HCC	40	NLR	ORR, DCR, PD	8	44
Faccinetti	2018	PC	NSCLC	54	NLR	DCR, PD	6	23
Fan	2021	RC	GI	111	NLR, PLR	ORR, DCR, PD	8	36
Guida	2021	RC	MELANOMA	331	NLR	DCR	6	42
Guida	2022	RC	MELANOMA	272	NLR	DCR	6	43
Guven	2022	RC	PAN CANCER	231	NLR	ORR	8	53
Huang	2020	RC	NSCLC	61	NLR	DCR, PD	8	24
Hung	2021	RC	HCC	45	NLR, PLR	DCR, PD	8	45
Jiang	2020	RC	NSCLC	76	PLR	DCR, PD	8	11
Jung	2017	RC	MELANOMA	104	NLR	DCR, PD	8	75
Kim	2022	RC	GASTRIC	45	NLR	ORR, DCR	9	37
Lee	2021	RC	HNSCC	45	NLR	ORR, DCR	6	50
Moller	2021	RC	NSCLC	90	NLR	DCR, PD	7	26
Mountzios	2021	RC	NSCLC	672	NLR	ORR, DCR	7	27
Musaelyan	2022	RC	NSCLC	45	NLR, PLR	DCR-Responders PD-Non-responders	7	10
			MELANOMA	29				
Nakazawa	2022	RC	GASTRIC	58	NLR	DCR, PD	7	38
Namikawa	2020	RC	GASTRIC	29	NLR	DCR	7	39
Nenclares	2021	PC	HNSCC	100	NLR	DCR-Responders PD-Non-responders	6	51
Newman	2020	RC	NSCLC	137	NLR	DCR, PD	8	28
Ohashi	2020	RC	MELANOMA	16	NLR	ORR, PD	6	41
Ohba	2019	RC	NSCLC	32	NLR	ORR, DCR	8	29
Petrova	2020	RC	NSCLC	119	NLR, PLR	DCR, PD	9	31
Pu	2021	RC	NSCLC	184	NLR, PLR	ORR, DCR	8	32
Quaquarini	2022	RC	NSCLC	166	NLR	DCR, PD	9	33
Rebuzzi	2022	RC	RCC	422	NLR, PLR	ORR, DCR, PD	7	47
Russo	2018	RC	NSCLC	62	PLR	ORR	6	9
Simonaggio	2020	RC	RCC	86	NLR	DCR, PD	7	48
Spassova	2022	RC	MERKEL	114	NLR	DCR, PD	7	55
Tanaka	2022	RC	HCC	28	NLR	ORR-Responders PD-Non-responders	6	46
Wang	2022	RC	ESCC	69	NLR	ORR, DCR	8	40

(Continued)

TABLE 1 Continued

Author	Year	Design	Cancer	Patients	Marker	Outcome	NOS	Ref.no
Wu	2021	RC	NSCLC	136	NLR, PLR	ORR, PD	6	34
Yamamoto	2020	RC	UC	121	NLR, PLR	ORR	6	49
Yuequan	2021	RC	NSCLC	103	NLR, PLR	PR vs PD SD vs PD	8	76

RC, Retrospective cohort; PC, Prospective cohort; GI, Gastroinstestinal cancer; HCC, Hepatocellular carcinoma; HNSCC, Head and neck squamous cell carcinoma; RCC, Renal cell carcinoma; UC, Urothelial carcinoma; NLR, Neutrophil-to-lymphocyte ratio; NSCLC, Non-small cell lung cancer; CRC, Colorectal cancer; ESCC, Esophageal squamous cell carcinoma; PAN CANCER, Multiple cancers; PLR, Platelet-to-lymphocyte ratio; NOS, Newcastle Ottawa scale.

TABLE 2 Characteristics of patients involved in the studies that related NLR, PLR and treatment response.

Author, Country	Tumor type	Gender (M/F)	Age	ECOG PS High 0-1 Low >1	NLR values	PLR values	Treatment
Booka, Japan	Upper GI	49/12	<65-11 >65-50	PS<1-49 PS>2-12	3.9(0.9-31.7)	118(31-860)	Nivolumab Pembrolizumab
Benzekry, France	NSCLC	199/99	Median 62 (55,69)	Low-26 High-265	Mean-5.66 Median-3.85	Mean-273 Median-214	ICI-295 Comb-3
Chen, China	NSCLC	115/36	<63-70 >63-81	High-147 Low-4	>2.96=75 <2.96=76 (median)	>159=75 <159=76 (median)	ICI+Chemo=105 ICI+Angio=18 Both=28
Cheng, China	CERVIX	F=70	Median 51(29-77)	N/R	5.17(3.19-9.16)	270.5(174.19-363.49)	PD1+chemo=21 PDI+CHEMO+Angio=49
Christiello, Italy	-GI -Breast -Gynacologic -HNSCC -NSCLC -Melanoma& other skin cancers -MesothelICIma -NET -GUT	62/91	Median 58(31-80) >65=46 <65=107	Low=71 High=82	6	300	ICI=59 ICI+ICI=84 ICI+TARGET=10
Dusselier, France	NSCLC	44/15	Median 59.5(30.3-87.3)	Low=6 High=53	<5=21 >5=37	<160=19 169-262=31 >2=8	Nivolumab
Eso, Japan	HCC	35/5	Median 70.5(53-82)	N/R	2.56(0.39-14.0)	125(27.1-351)	Atezo/Bev
Facchinetti, Italy	NSCLC	45/9	Median 69(43-85)	LOW-15 High=39	To be retrieved	To be retrieved	Nivolumab
Fan, China	GI	56/55	>65=23 <65=88	N/R	>5=17 <5=94	<135=55 >135=56	ICI+Chemo=74 ICI+Target=44 ICI+RT=7
Guida, Italy	Melanoma	204/127	Median 63.4(53.3-73.8)	Low=78 High=252	NR	NR	Anti-PD1=246 Ipilimumab=80 Anti-PD1+Ipi=5
Guida, Italy	Melanoma (BRAF wt)	172/100	Median 63.2(52.0,73.0	Low=2 High=270	ΔNLR=0.86	ΔPLR=22.85	PD-1=209 CTLA4=57 PD-1+CTLA4=6
Guven, Turkey	Melanoma RCC NSCLC Others	155/76	Median 61(51-67)	Low=30 High=201	<5,<10% increase=76 >5, >10% increase=155		Niv=169 Atezo=28 Pembro=20 Ipi=13 Ave=1

(Continued)

TABLE 2 Continued

Author, Country	Tumor type	Gender (M/F)	Age	ECOG PS High 0-1 Low >1	NLR values	PLR values	Treatment
Huang, China	NSCLC	38/23	>.65=11 <65=50	High=60 Low=1	MEDIAN C1-2.72 C2=2.93 C3=2.56 C4=2.69		Niv=24 Pembro=6 Atezo=27 Niv/ipi=4 ICI+Chemo=5
Hung, China	HCC	41/4	61.8+/-9.6	Low=1 High=44	Serum NLR 4.0+/-2.2		Nivolumab
Jiang, China	NSCLC	66/10	61(35-74) median	Low=7 High=69		>168.13=27 <168.13=41	Niv=59 Durvalumab=17
Jung, Korea	Melanoma	51/53	58(50-66) median	Low=12 High=92	<5=84 >5=20		Ipilimumab
Kim, Korea	GC	34/11	Median 60(23-76)	NR	<2.9=23		Nivolumab
Lee, Korea	HNSCC	103/22	Median Median 57(33-87)	Low=19 High=106	>4=49 <4=76		PD-1=73 PD-L1=24 PD1/PDL1+CTLA4=28
Moller, Germany	NSCLC	60/30	Median 65(31-87)	High=90 Low=0	<6.1=61 >6.1=29		pembrolizumab
MountzICIs, Greece Germany	NSCLC	463/209	65 (median)	High=584 Low=88	Median 4.8(8.1)		ICI=460 ICI+Chemo=212
Musaelyan, Russia	NSCLC Melanoma	46/28	Median 62(59-69) 57(53-62)	N/R	N/R		Niv=41 Pembro=30 Atezo=3
Nakazawa, Japan	GC	45/13	Median=66	0=8 >1=50	**Baseline** DC 3.18+/-0.65 PD 4.85+/-0.49 After C2 DC 2.97+/-0.8 PD 5.43+/-0.7		Nivolumab
Namikawa, Japan	GC	19/10	Median 71(49-86)	High=28 Low=1	Baseline 1.8(0.5-9.4) Week 8 2.5(0.9-13.2)		nivolumab
Nenclares, UK	HNSCC	80/20	Median 62(31-85)	N/R	Baseline- responders (mean) 6.4+/-6.5 Non- responders 9.1+/-10.22)		ICI not specified
Newman, USA	NSCLC	80/57	Median 68.4(28-92)	N/R	Baseline <5=90 >5=47		1st line ICI=25 >2nd line=112 ICI+Chemo=8
Ohashi, Japan	Melanoma	8/8	Median 74.6(51-88)	High=15 Low=1	Baseline NLR Responders- 2.7(1.6-3.7) Non- responders-2.3 (1.4-3.3)		Nivolumab pembrolizumab

(Continued)

TABLE 2 Continued

Author, Country	Tumor type	Gender (M/F)	Age	ECOG PS High 0-1 Low >1	NLR values	PLR values	Treatment
Ohba, Japan	NSCLC	29/3	<70=26 >70=6	High=30 Low=2	Median 4.16(0.98-109.15) <4.11=19 >4.11=13		pembrolizumab
Park, Korea	NSCLC	62/21	65(42-82)	N/R	Cut-off value baseline 4.0	Cut off value baseline= 210	pembro=18 atezo=65
Petrova, Bulgaria	NSCLC	74/45	62.3+/-7.9	High=119 Low=0	Median NLR <5=57 >5=62	MEDIAN PLR <200=60 >200=59	Pembro
Pu China	NSCLC	134/50	Median 58(33-87) <70=153 >70=31	High=174 Low=10	NLR<5=115 >5=69	<200=99 >200=85	Pembro=98 Niv=86
Quaquarini, Italy	NSCLC	129/37	<65=54 >65=54	High=147 Low=19	<5=81 >5=85		Niv=84 Pembro=56 Atezo=26
Rebuzzi, Italy	RCC	305/117	Median 63.4(18-85) <70=314 >70=108	KPS>80% =367 KPS<80% =55	Mean=4.12	Mean=237	nivolumab
Russo, Italy	NSCLC	24/4	69(47-78)			PLR>160=2 PLR<160=12	nivolumab
Simonaggio, France	MRCC	67/19	Median 67(21.6-82)	High=73 Low=12	Median(95% CI) 3.26(1-37)		Nivolumab
	MNSCLC	47/28	65(31.2-86.7)	High=51 Low=24	Median 3.4(1.4-13)		Nivolumab
Spassova, Germany	MERKEL CELL CARCINOMA (MCC)	82/32	<70=40 >70=74	PS-0=64 PS>1=49 Not available=1	<4=54 >35=35 Not available=25		Avelumab=57 Niv=13 Pembro=44
Tanaka, Japan	HCC	22/6	73.5(56,89)	High=27 Low=1	3.13(1.19-23.7)		Atezo/Bev
Wang, China	ESCC	64/5	61(38-75)	PS-0=47 PS-1=22	NLR<4=36 NLR>4=33		Camrelizumab
Wu, China	NSCLC	101/35	<60=75 >60=61	HIGH PS<1=124 LOW PS>2=12	REPORTED IN TERMS OF DELTA (pre,medICI, post)		ICI-not specified Absolute values not provided
Yamamoto, Japan	UC	87/34	74(50-86)	Not provided	NLR cut off=3	PLR cut off=154	Pembro
Yuequan, China	NSCLC	68/35	Median 66(61,71)	High=97 Low=6	<5=69 >5=34		ICI=32 ICI+Chemo=71

Ave, Avelumab; Atezo, Atezolizumab; Bev, Bevacizumab; Chemo, chemotherapy; Comb, combination; ECOG-PS, Eastern Cooperative Oncology Group; GC, Gastric cancer; GI, Gastroinstestinal, GUT, Genitourinary tract; HCC, Hepatocellular carcinoma; HNSCC, Head and neck squamous cell carcinoma; ICI, Immune checkpoint inhibitor; Ipi, Ipilimumab; KS, Karnofsky status; M/F, Male/female; NET, Neuroendocrine tumor; NLR, Neutrophil-lymphocyte ratio; Niv, nivolumab; NSCLC, non-small cell lung cancer; N/R, not recorded; PD-1, Programmed death-1; PD-L1, Programmed death ligand 1; PLR, Platelet-lymphocyte ratio; Pembro, pembrolizumab; RCC, renal cell carcinoma; WT, wild type.

3.2.1 Non-small cell lung cancer

Up to 50% (18 studies) of the included studies (10, 11, 13, 22–28, 38, 39, 44–49) reported the association of NLR and PLR in non-small cell lung cancer patients treated with ICIs. The sample size ranged from 45 to 672 patients. The average number of patients was 142 patients. In total, there were 2,563 patients. One study only reported the ORR, five studies reported on DCR, four studies reported on ORR and DCR, and seven studies reported DCR and PD. None of the included studies had all the three components. Two studies compared numerical percentages between patients who responded to treatment (DCR) and those who progressed (PD). One study reported the correlation of ratios with overall short-term efficacy.

The studies were further divided on the basis of the presence or absence of a significant relationship between the ratios and end points. The subdivision produced a total of 51 reports. Out of those, five reports were on ORR, 27 reports were on DCR, and 19 reports were on PD.

3.2.1.1 Objective response rate

Three out of five reports showed a statistically significant relationship between the ratios and ORR. In one of the studies, ORR was higher in PLR-low patients compared to PLR-high patients (46.15% *vs.* 8.3%, $p < 0.0004$). In another study, those who had a decrease in NLR 12 weeks post-treatment were more likely to derive clinical benefit than those with increasing NLR (OR = 3.304, 95% CI 1.560–7.001, $p = 0.002$).

3.2.1.2 Disease control rate

Out of 29 reports, 16 reports showed a significant correlation between NLR, PLR, and DCR, while nine studies reported a lack of relationship. Most of the reports with significant association also noted a higher DCR among patients with low ratios either at baseline or after a few cycles of treatment.

3.2.1.3 Progressive disease

Ten reports showed a statistically significant correlation between the ratios and PD. Generally, patients with higher NLR and PLR tend to progress earlier and have a higher rate of PD as compared to those with low ratios.

3.2.2 Gastrointestinal cancer

Six studies (29–32, 50, 51) (17 reports) reported the correlation between ratios and study end points. Out of five reports for ORR, only one study showed a significant relationship with NLR at baseline compared with other times (NLR L *vs.* H Baseline 36.1% *vs.* 9.1%, $p = 0.018$; at V1 34.4% *vs.* 15.6%, $p = 0.083$; variation (baseline-V1) < 20% *vs.* >20%; 31.6% *vs.* 22.2%, $p = 0.430$).

Among nine reports that looked at DCR, five of them showed a positive correlation, while four reports lacked a statistically significant relationship. Those with low PLR and NLR had higher DCR than those with high ratios (PLR L *vs.* H) = 36.7% *vs.* 9.7%, $p = 0.012$; NLR (L *vs.* H) = 33.3% *vs.* 12.9%, $p = 0.058$).

Likewise, patients with higher ratios had higher rates of progressive disease than those with low ratios. In a retrospective study of 58 patients (50), mean NLR was significantly higher in the PD group at both baseline and post-treatment (Pre-rx, 318 *vs.* 4.85, $p = 0.045$; Post-rx, 2.97 *vs.* 5.43, $p = 0.025$). In another study (51), NLR showed a statistically significant relationship at week 4 post-treatment compared to other times ($p = 0.044$).

3.2.3 Melanoma

A study by Ohashi et al. with a small sample size of 16 patients reported no significant relation between NLR and ORR (52).

Another retrospective study (53) that looked at DCR reported a significant correlation between NLR and DCR despite the NRAS mutation status (OR = 0.88, 95% CI 0.77–1.00, $p = 0.005$). Also, a change in NLR and PLR correlated with lower response (ΔNLR with OR = 2.779, $p < 0.001$, ΔPLR OR = 2.022, $p < 0.009$) (40).

3.2.4 Hepatocellular carcinoma

Out of the three studies (33, 41, 54) (10 reports), three reports on DCR and three reports on PD showed a significant relationship. Only one study reported a lack of correlation between the ratios and ORR.

3.2.5 Urothelial carcinoma (renal [RCC] and bladder [UC])

Rebuzzi et al. (34) reported mean values of NLR and PLR among patients who achieved clinical response and those with progressive disease at baseline and after four doses of treatment (longitudinal variation). The mean value of NLR and PLR at baseline and after four doses of treatment was lower as compared with the group with progressive disease (NLR, 3.18 *vs.* 4.12, $p = 0.012$; PLR, 184 *vs.* 237, $p = 0.003$).

In the study by Simonaggio et al. (55), the NLR-low group had greater DCR in any NLR decrease at week 6 as compared to the NLR-high group (81% *vs.* 40%, $p = 0.0007$).

Likewise, in the study by Yamamoto et al. (42), NLR had a statistically significant association with ORR ($p = 0.016$), while PLR had a marginal significance ($p = 0.0536$).

3.2.6 Head and neck cancers

A study by Lee et al. (56) showed that those patients with high NLR were associated with poor response (OR = 0.3, 95% CI 0.11–0.84, $p = 0.022$). Similar findings were reported by Nenclares et al. (43) where NLR was significantly lower in responders (DCR) compared to non-responders ($p < 0.001$).

3.2.7 Across solid tumors

In both pan-solid cancer retrospective studies (35, 57), those with low ratios had a greater response rate as compared to those with high ratios. In a study by Guven et al., those patients with high NLR and greater than 10% NLR increase had the lowest ORR.

3.2.8 Other tumors

One study on cervical cancer (36) reported a significant relationship between NLR and ORR [NLR (L *vs.* H) 78.26% *vs.* 53.19%, OR = 0.316, 95% CI 0.1–0.991, $p = 0.048$], while there was no relationship with PLR [PLR (L *vs.* H) 70% *vs.* 58%, OR = 0.592,

95% CI 0.195–1.794, p = 0.354]. However, despite the lack of significance, ORR was higher in patients with low ratios than those with high ratios.

A study on advanced Merkel cell carcinoma by Spassova et al. (37) noted that the NLR-low group had more patients with disease control (ORR) than the NLR-high group (49% *vs.* 37%), while there was no difference in the group with disease progression.

3.3 Meta-analysis

As described in the Methods, a meta-analysis was conducted under two subgroups NLR and PLR for the treatment efficacy endpoint ORR, DCR, and PD. Each study that focused on these inflammatory markers was assessed independently. Forest plots were used to represent the pooled results (Figures 2A–F).

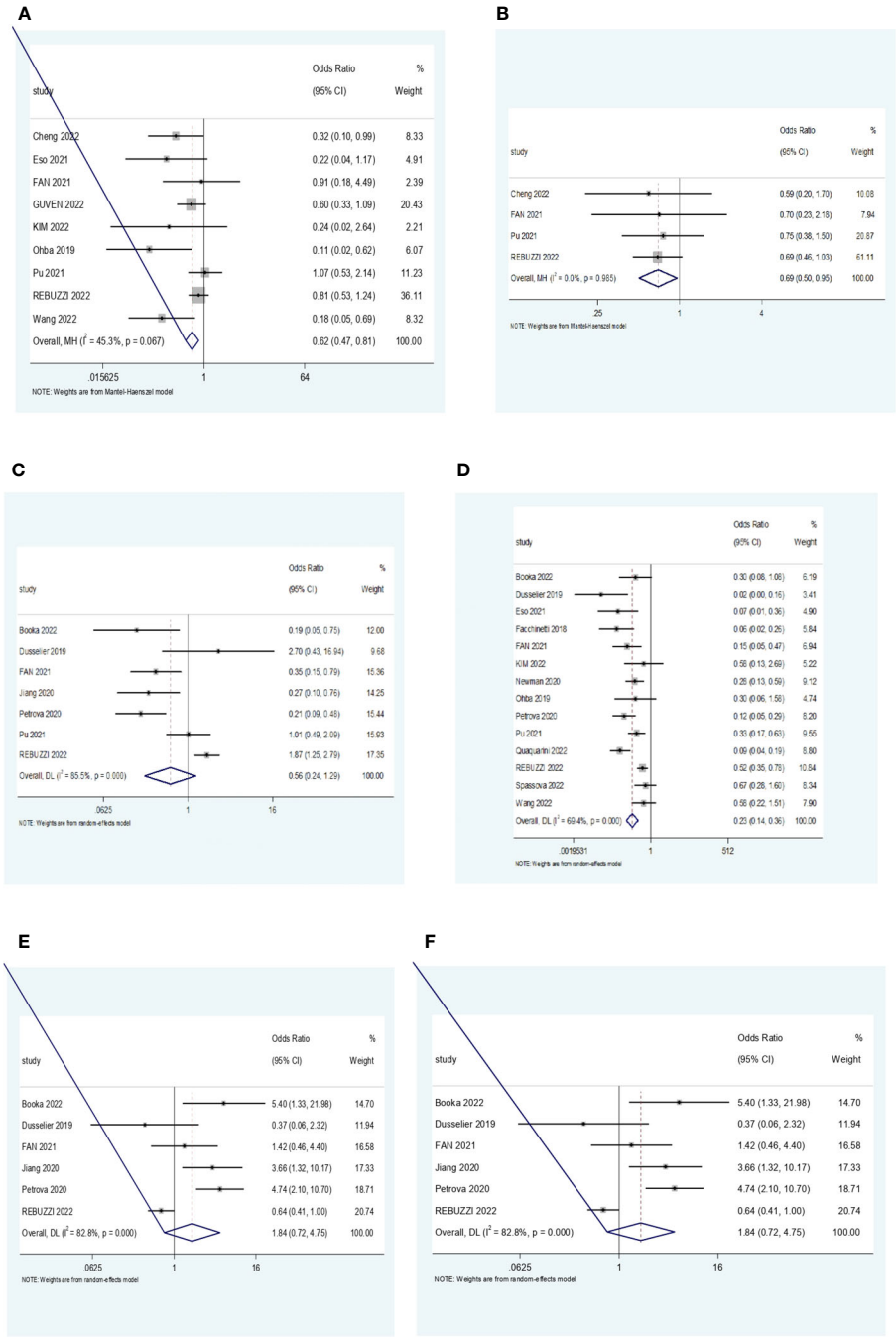

FIGURE 2
(A) Forest plot for the association NLR and ORR. **(B)** Forest plot for the association between PLR and ORR. **(C)** Forest plot for the association between NLR and DCR. **(D)** Forest plot for the association between PLR and DCR. **(E)** Forest plot for the association between NLR and PD. **(F)** Forest plot for the association between PLR and PD. NLR, neutrophil–lymphocyte ratio; ORR, objective response rate; PLR, platelet–lymphocyte ratio; DCR, disease control rate; PD, progressive disease.

3.3.1 Meta-analysis for ORR, DCR, and PD in NLR subgroup

A total of nine studies looked at the impact of NLR on ORR. All studies showed a positive correlation between a low NLR and a higher ORR. Out of the nine studies, five of them showed statistical significance ($p < 0.05$). The pooled effect estimate (OR) was found to be statistically significant at a value of 0.62 (95% CI 0.47–0.81, $p = 0.001$). Assessment of heterogeneity suggests that there is low heterogeneity between the studies included in the subgroup meta-analysis ($I^2 = 45.3\%$, $p = 0.067$).

Analysis of DCR included 14 studies, whereby 10 of them showed a statistically significant correlation in favor of low NLR, suggesting that patients with low ratios were more likely to have a better treatment response. The pooled effect estimate (OR) was found to be statistically significant at a value of 0.23 (95% CI 0.14–0.36, $p < 0.001$). Assessment of heterogeneity suggests that there is high heterogeneity between the studies included in the subgroup meta-analysis ($I^2 = 69.4\%$, $p = 0.000$).

Ten studies reported the correlation of NLR with progressive disease. Eight studies demonstrated that higher NLR was associated with a higher probability of disease progression. One study had contrasting results whereby low NLR was associated with PD. The overall estimate was statistically significant at a value of 3.12 (95% CI 1.44, 6.77, $p = 0.004$). Assessment of heterogeneity showed substantial heterogeneity among the included studies ($I^2 = 84.8\%$, $p = 0.000$).

3.3.2 Meta-analysis of ORR, DCR, and PD in PLR subgroup

Four studies were pooled to determine the impact of PLR levels on the ORR. All four studies showed a positive correlation between low PLR levels and ORR, but only one study was statistically significant. The pooled effect (OR) was found to be statistically significant at a value of 0.69 (95% CI 0.5, 0.95, $p = 0.025$). There was no heterogeneity among the studies ($I^2 = 0.0\%$, $p = 0.985$).

In the analysis of DCR, four studies showed a statistically significant positive correlation between low PLR and DCR, suggesting a better treatment response in PLR-low patients. Three studies favored high PLR, but only one of them was statistically significant. The overall estimate (OR) was 0.56 (95% CI 0.24, 1.29, $p = 0.172$), although it was not statistically significant. Assessment of heterogeneity showed high heterogeneity between the included studies ($I^2 = 85.5\%$, $p = 0.000$).

Six studies were analyzed for the relationship between PLR levels and PD. Four studies reported a positive correlation between high PLR and a higher probability of progressive disease. Meanwhile, two studies were contradicting, suggesting that low PLR levels were associated with the likelihood of disease progression. Out of the six studies, only two studies did not show a statistically significant correlation. The overall estimate was not statistically significant at a value of 1.84 (95% CI 0.72, 4.75, $p = 0.205$). There was substantial heterogeneity among the studies ($I^2 = 82.8\%$, $p = 0.000$).

3.3.3 Publication bias

Egger's test and funnel plots were used to assess publication bias (Figures 3A–F). All funnel plots had a symmetrical distribution of studies. However the findings from Egger's test showed that there was publication bias for studies that reported the association between ORR, DCR and NLR. After performing the trim and fill method, there was no significant change in the results.

4 Discussion

Our review and meta-analysis looked at the correlation between NLR and PLR and treatment response in patients treated with ICIs across different tumors. Generally, patients who had low ratios at baseline or decreasing trend during the course of treatment according to cutoff values pre-determined by authors based on previous studies or derived from the area under the curve (AUC) had a better treatment outcome and were more likely to obtain clinical benefit than those with higher values. Also, they had a lower rate of disease progression compared to the high-ratio group.

The findings of this study correspond with previous studies that looked at the correlation between inflammatory markers and treatment efficacy. A meta-analysis by Guo et al. studying the dynamics of NLR during ICI treatment also showed that patients with a significant upward trend of NLR did not respond to immunotherapy, while those with a downward trend were associated with better clinical and treatment outcomes (16). Similarly, Zhang et al. observed a significant correlation between NLR and ORR ($p = 0.003$) and a lack of significance between NLR and DCR ($p = 0.111$) in a meta-analysis involving patients with gastric cancer treated with immunotherapy (58).

There are limited studies on the effect of PLR and response to immunotherapy compared to NLR. Most of the literature focuses on PLR as a prognostic indicator (33, 34, 40, 41, 52–54). One of the studies included in this meta-analysis investigated blood markers before treatment that could be used as predictors of best clinical response (13). With the use of chi-square analysis, the PLR-H (<168.13) group had an inferior stable disease/partial response (SD/PR) rate than the PLR-L (<168.13). However, there were no significant differences in the best clinical response between PD-L1-positive and PD-L1-negative patients. Therefore, the study concluded that PLR could be a better predictive marker to differentiate the best response of ICIs than PD-L1 expression. Likewise in the study by Spassova et al. (37) and Musaelyan et al. (11), there was a lack of a statistically significant relationship between PDL-1 levels and clinical response. A study by Diem et al. also showed that elevated pre-treatment NLR and PLR were independently associated with poorer survival and lower response rates in lung cancer patients treated with nivolumab.

It is well-established that NLR is an independent prognostic factor in different cancers (59). The mechanism behind this observation is that some cancers express chemokines that drive the proliferation of tumor cells. Also, these chemokines drive the influx of myeloid-derived suppressor cells (MDSCs). Examples of those chemokines include CXCL5 and CXCL8, which interact with

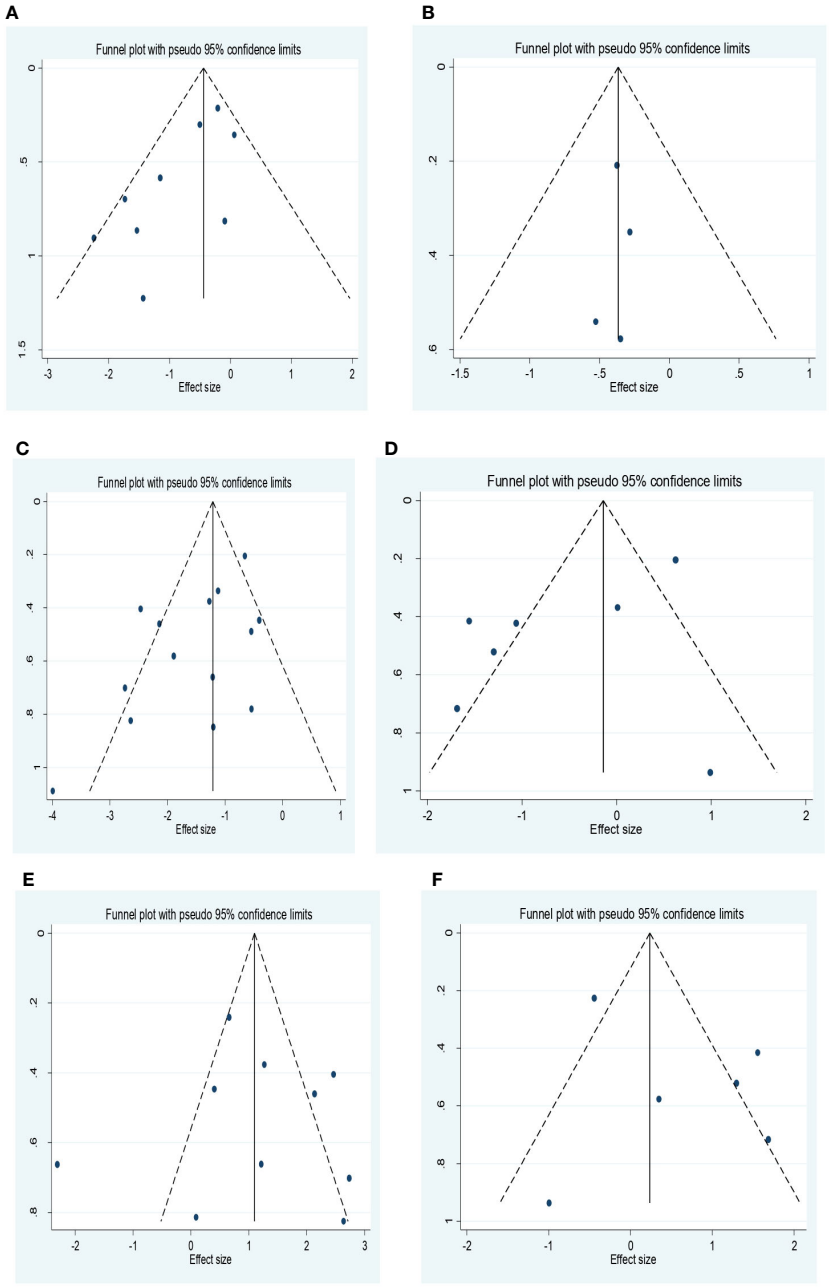

FIGURE 3
(A) Funnel plot for the association between NLR and ORR. **(B)** Funnel plot for the association between PLR and ORR. **(C)** Funnel plot for the association between NLR and DCR. **(D)** Funnel plot for the association between PLR and DCR. **(E)** Funnel plot for the association between NLR and PD. **(F)** Forest plot for the association between PLR and PD. NLR, neutrophil–lymphocyte ratio; ORR, objective response rate; PLR, platelet–lymphocyte ratio; DCR, disease control rate; PD, progressive disease.

receptor CXCR2 and CXCR1 expressed on neutrophils. This influx inhibits the tumor-suppressor activity of tumor-infiltrating lymphocytes (TILs) and cytotoxic CD8+ T cells. Additionally, they promote angiogenesis and metastatic potential of cancer cells (59). A study by Kargl et al. in NSCLC patients treated with immunotherapy demonstrated that cells of myeloid origin contributed to treatment failure (60).

Tumor-associated neutrophils (TANs) present in the TME, and neutrophils present in the blood or the bone marrow are linked with resistance to immunotherapy through adaptive immune cell polarization and suppression, tumor neoangiogenesis, immune evasion and exclusion, and tumor intrinsic characteristics. TAN-rich tumors display lower macrophage and TIL infiltration, making them resistant to ICIs. In gastric cancer patients, a sub-population of neutrophils was identified in the peripheral circulation that suppresses CD8+ cell activity. Arginase-1 (ARG1)-expressing human granulocytic cells downregulate T-cell proliferation and cytokine secretion. ARG1+ neutrophils increase with tumor stage in treatment-naive patients and negatively correlate with the number of CD8+ cytotoxic T-cell lymphocytes (61).

Platelet activation is stimulated by pro-inflammatory cytokines and participates in the recruitment of neutrophils (62). They play a fundamental role in systemic and local responses against cancer. They sequester tumor molecules, including RNA and protein transcripts, altering their RNA profiles. After their interaction with the TME, they are called tumor-educated platelets. They transport material from the TME to sites closer to the tumor, creating a favorable environment for the development of metastases. They contain a rich repertoire of RNA varieties, providing biomolecules for diagnosis and prognostic, predictive, or follow-up biomarkers (62).

The prognostic and predictive roles of NLR and PLR cut across most cancer types and in all forms of cancer treatment, not only in immunotherapy. However, the lack of standard cutoff values makes them difficult to apply in clinical practice. Also, baseline values are affected by underlying pre-clinical state, co-morbid systemic conditions, and other confounders.

The findings of this study have shown how heterogeneous the utilization of NLR and PLR as prognostic and predictive factors is. The study has shown that these ratios are predictive but not in all cancers. For example, the study by Wu et al. reported a lack of correlation between inflammatory markers and immune response (63). Moreover, in the same cancer type, one factor could be predictive while the other is not, which indicates that these markers cannot be used as a single entity; rather, they are more functional when combined with other markers in a predictive or prognostic model (64).

Examples of existing models and indexes that are multivariable include neutrophil–platelet score (NPS) (65), which is a systemic inflammation score based on the number of neutrophils and platelets. When tested in NSCLC patients, NPS predicted OS and DCR in pre-treated advanced NSCLC patients who received treatment with nivolumab or pembrolizumab (65). A study by Zhao et al. showed three models, namely, lung immune prognostic index (LIPI) based on pre-treatment blood levels of derived-NLR and lactate dehydrogenase (LDH), EPSILoN (ECOG-PS, smoking, liver metastases, LDH, and NLR), and modified LIPI were predictive and prognostic in immunotherapy (64).

Another study in melanoma patients built a multivariable predictive model for response and survival. A combination of performance status, number of liver and lung metastatic sites, serum LDH, blood NLR, type of treatment (monotherapy *vs.* combination), and line of treatment was predictive of ORR (14). Another is the Gustave Roussy Immune Score (GRIm-S), which is a composite of neutrophil–lymphocyte ratio (>6 = 1), albumin (<35 = 1), and LDH (>ULN = 1) established as a prognostic score and may aid in the selection of patients for phase 1 trials of immune checkpoint inhibitors (66). Additionally, the Pan-immune inflammation value (PIV), also called the aggregate index of systemic inflammation (AISI), which combines neutrophils, monocytes, platelets, and lymphocytes, is another useful prognostic index (67, 68).

Other prognostic models and indexes utilized in overall cancer treatment include systemic immune-inflammatory index (SII), which combines platelets and NLR (20); advanced lung cancer inflammatory index (ALI), which combines body mass index and the ratio of albumin to NLR (22, 69); and the immune metabolic prognostic index, which is an association of NLR, dNLR, lymphocyte–monocyte ratio (LMR), PLR, and SII (70, 71). In genitourinary tumors, there is a FAN score in urothelial carcinoma that relates to Fibrosis-4-index, albumin–bilirubin ratio, and NLR (72). The International Metastatic RCC Database Consortium (IMDC) predictive score combines hemoglobin levels, serum calcium levels, Karnofsky performance status, time to treatment, and number of platelets and neutrophils (73). The risk blood biomarker (RBB) accounts for the total leukocyte count and ratio of neutrophils, monocytes, and lymphocytes (74). More so, the Glasgow prognostic score (GPS-m) relates to C-reactive protein (CRP), albumin, and NLR (42, 75).

Prospective studies on inflammatory cells that constitute the TME and affect treatment response continue to report other cellular markers apart from neutrophils and platelets. One study reports that more infiltration of cytotoxic CD8+ TCLs present in the intratumoral area was associated with better disease control (37). The study by Musaelyan et al. suggested that other markers of T-cell activation like IL-18 and β2-microglobulin could be used to evaluate and monitor treatment response (11). Another study used artificial intelligence-powered analysis of TILs to generate immunophenotypes, which was shown to correlate with treatment response (76). A combined model of FOXP3+ TCLs and other clinical covariates including NLR was a better predictor of response to immunotherapy in urothelial carcinoma patients (77).

Apart from inflammatory cells, the use of gene expression like circulating tumor DNA (ctDNA) kinetics (78), single-nucleotide variants (SNVs) of PD-1 and PDL-1 (79), gene expression signatures (80), and tumor burden determined from FDG-PET derived metabolic tumor volume (MTV) (81) provide additional biomarkers that predict benefit from ICIs. Pioneer trial (NCT 03493581), which is a comprehensive biomarker analysis for treatment efficacy of ICI with chemotherapy in NSCLC patients, has identified up to 15 biomarker signatures associated with efficacy and progression-free survival (PFS) (82).

This study aimed to highlight the association between inflammatory markers NLR and PLR with disease control, objective response, and disease progression for patients treated with immunotherapy. The study has highlighted that at any point in time before, during, or after treatment, both low and high ratios of NLR and PLR correlate with treatment outcomes regardless of cutoff points, something that was not reported in previous meta-analyses.

Despite the highlighted correlation, the findings are limited by the fact that almost all the included studies were retrospective in nature with a risk of information bias and publication bias. The grouping of patients according to treatment response was not homogeneous. Some studies in the systematic review were not included in the meta-analysis due to the heterogeneous nature of reported data, particularly patients with SD and those with PD. Patients with stable disease were counted with those who progressed as non-responders, while in other studies, they were counted as part of disease control. Also, there was variation in reporting of the ratios, as some studies reported the means and medians, while others just the numerical data or percentages.

Our study was heavily skewed toward NSCLC and melanoma patients, which is attributed to the fact that these were the first tumor sites to obtain Food and Drug Administration (FDA) approval to use

ICIs in comparison to other sites. In addition, most patients involved in the studies were treated with pembrolizumab (anti-PD1), nivolumab (anti-PD1) and ipilimumab (anti-CTLA4), and atezolizumab (anti-PDL-1) with limited studies in other agents, hence making it challenging to generalize our findings.

In addition, most of the included studies did not report on the association between NLR and PLR and treatment response in patients treated with immunotherapy according to racial background. Therefore, determining the correlation according to racial background was not possible.

There is a paucity of literature that reported the association of NLR, PLR, and racial background in cancer patients treated with immune checkpoint inhibitors, while some studies that performed sub-group analysis according to country of origin reported contradicting results (58, 83, 84). However, sub-group analysis was not performed in this particular systematic review.

Despite the contradiction, it is evident that with effective treatment, a drop in NLR and PLR correlates with better treatment outcomes and improved survival.

5 Conclusion and recommendations

It is clear that the state of inflammation plays a significant role in treatment response to cancer treatment overall. Inflammatory cells serve as adjunct markers to the FDA-approved biomarkers. The fact that in some studies there was a lack of correlation between PDL-1 levels and treatment response calls for additional markers to augment the predictive and prognostic roles of PDL-1 levels, MSI status, and TMB.

These markers tend to be affected by other underlying co-morbid conditions and the overall state of the body, which compromises their prognostic and predictive functions. Therefore, there is a need to develop a comprehensive clinical model that is reflective of real-world settings and the models to be tested in clinical trials for validation before being incorporated into clinical practice.

Data availability statement

The original contributions presented in the study are included in the article/Supplementary Material. Further inquiries can be directed to the corresponding author.

Author contributions

(I) Conception and design: TR, HS, SZ, and WQ. (II) Collection and assembly of data: XZ, YP, and CC. (III) Data analysis and interpretation: OA and CC. (IV) Manuscript writing: all authors. (V) Final approval of manuscript: all authors.

Funding

This study was supported by grants from the National Natural Science Foundation of China (Nos. 82173342, 81874073, and 81974384), Reform and Development Fund for Colleges and Universities of Hunan Province (No. 2050205), and Nature Science Foundation of Hunan Province (Nos. 2021JJ31092 and 2021JJ31048).

Acknowledgments

The authors wish to acknowledge Fan Jing Li for his assistance in data analysis and Alphonce Nyalali for proofreading the manuscript.

Conflict of interest

The authors declare that the research was conducted in the absence of any commercial or financial relationships that could be construed as a potential conflict of interest.

Publisher's note

Supplementary material

The Supplementary Material for this article can be found online at: https://www.frontiersin.org/articles/10.3389/fonc.2023.1181248/full#supplementary-material

References

1. Pecorino L. *Molecular biology of cancer : mechanisms, targets, and therapeutics*. Oxford [u.a.]: Oxford Univ. Press (2016).

2. Ravindranathan D, Master VA, Bilen MA. Inflammatory markers in cancer immunotherapy. *Biology* (2021) 10(4):325. doi: 10.3390/biology10040325

3. Tan S, Day D, Nicholls SJ, Segelov E. Immune checkpoint inhibitor therapy in oncology: current uses and future directions: JACC: cardioOncology state-of-the-art review. *JACC Cardio Oncol* (2022) 4(5):579–97. doi: 10.1016/j.jaccao.2022.09.004

4. Schmid P, Rugo HS, Adams S, Schneeweiss A, Barrios CH, Iwata H, et al. Atezolizumab plus nab-paclitaxel as first-line treatment for unresectable, locally advanced or metastatic triple-negative breast cancer (IMpassion130): updated efficacy results from a randomised, double-blind, placebo-controlled, phase 3 trial. *Lancet Oncol* (2020) 21(1):44–59. doi: 10.1016/S1470-2045(19)30689-8

5. Chan JJ, Tan TJY, Dent RA. Integrating immunotherapy in the (neo)adjuvant setting of early breast cancer. *Curr Opin Oncol* (2020) 32(6):575–84. doi: 10.1097/CCO.0000000000000675

6. Fasano M, Corte CMD, Liello RD, Viscardi G, Sparano F, Iacovino ML, et al. Immunotherapy for head and neck cancer: Present and future. *Crit Rev Oncol/Hematol* (2022) 174:103679. doi: 10.1016/j.critrevonc.2022.103679

7. Ménétrier-Caux C, Ray-Coquard I, Blay JY, Caux C. Lymphopenia in Cancer Patients and its Effects on Response to Immunotherapy: an opportunity for combination with Cytokines? *J Immunother Cancer* (2019) 7(1):85. doi: 10.1186/s40425-019-0549-5

8. Hinterleitner C, Strähle J, Malenke E, Hinterleitner M, Henning M, Seehawer M, et al. Platelet PD-L1 reflects collective intratumoral PD-L1 expression and predicts immunotherapy response in non-small cell lung cancer. *Nat Commun* (2021) 12 (1):7005. doi: 10.1038/s41467-021-27303-7

9. Riesenberg BP, Li M, Spakowicz D, Hoyd R, Beane J, Yang Y, et al. Platelets impact the responsiveness of immune checkpoint blockade therapy in solid tumors. *J Clin Oncol* (2020) 38(15_suppl):e15023. doi: 10.1200/JCO.2020.38.15_suppl.e15023

10. Russo A, FranChina T, Ricciardi GRR, Battaglia A, Scimone A, Berenato R, et al. Baseline neutrophilia, derived neutrophil-to-lymphocyte ratio (dNLR), platelet-to-lymphocyte ratio (PLR), and outcome in non small cell lung cancer (NSCLC) treated with Nivolumab or Docetaxel. *J Cell Physiol* (2018) 233(10):6337–43. doi: 10.1002/jcp.26609

11. Musaelyan AA, Lapin SV, Urtenova MA, Odintsova SV, Chistyakov IV, Ulitin AM, et al. Inflammatory and autoimmune predictive markers of response to anti-PD-1/PD-L1 therapy in NSCLC and melanoma. *Exp Ther Med* (2022) 24(3):557. doi: 10.3892/etm.2022.11495

12. Wang Y, Tong Z, Zhang W, Zhang W, Buzdin A, Mu X, et al. FDA-approved and emerging next generation predictive biomarkers for immune checkpoint inhibitors in cancer patients. *Front Oncol* (2021) 11:683419. doi: 10.3389/fonc.2021.683419

13. Jiang M, Peng W, Pu X, Chen B, Li J, Xu F, et al. Peripheral blood biomarkers associated with outcome in non-small cell lung cancer patients treated with nivolumab and durvalumab monotherapy. *Front Oncol* (2020) 10:913. doi: 10.3389/fonc.2020.00913

14. Silva I, Ahmed T, McQuade JL, Nebhan CA, Park JJ, Versluis JM, et al. Clinical models to define response and survival with anti–PD-1 antibodies alone or combined with ipilimumab in metastatic melanoma. *J Clin Oncol* (2022) 40(10):1068–80. doi: 10.1200/JCO.21.01701

15. Li Y, Pan Y, Lin X, Hou J, Hu Z, Xu L, et al. Development and validation of a prognostic score for hepatocellular carcinoma patients in immune checkpoint inhibitors therapies: the hepatocellular carcinoma modified gustave roussy immune score. *Front Pharmacol* (2021) 12:819985. doi: 10.3389/fphar.2021.819985

16. Guo Y, Xiang D, Wan J, Yang L, Zheng C. Focus on the dynamics of neutrophil-to-lymphocyte ratio in cancer patients treated with immune checkpoint inhibitors: A meta-analysis and systematic review. *Cancers* (2022) 14(21):5297. doi: 10.3390/cancers14215297

17. Chen X, Meng F, Jiang R. Neutrophil-to-lymphocyte ratio as a prognostic biomarker for patients with metastatic renal cell carcinoma treated with immune checkpoint inhibitors: A systematic review and meta-analysis. *Front Oncol.* (2021) 11:746976. doi: 10.3389/fonc.2021.746976

18. Ksienski D, Wai ES, Alex D, Croteau NS, Freeman AT, Chan A, et al. Prognostic significance of the neutrophil-to-lymphocyte ratio and platelet-to-lymphocyte ratio for advanced non-small cell lung cancer patients with high PD-L1 tumor expression receiving pembrolizumab. *Trans Lung Cancer Res* (2021) 10(1):355–67. doi: 10.21037/tlcr-20-541

19. Liu D, Czigany Z, Heij LR, Bouwense SAW, van Dam R, Lang SA, et al. The value of platelet-to-lymphocyte ratio as a prognostic marker in cholangiocarcinoma: A systematic review and meta-analysis. *Cancers* (2022) 14(2):438. doi: 10.3390/cancers14020438

20. Liu J, Li S, Zhang S, Liu Y, Ma L, Zhu J, et al. Systemic immune-inflammation index, neutrophil-to-lymphocyte ratio, platelet-to-lymphocyte ratio can predict clinical outcomes in patients with metastatic non-small-cell lung cancer treated with nivolumab. *J Clin Lab Analysis* (2019) 33(8):e22964. doi: 10.1002/jcla.22964

21. Sun W, Zhang L, Luo M, Hu G, Mei Q, Liu D, et al. Pretreatment hematologic markers as prognostic factors in patients with nasopharyngeal carcinoma: Neutrophil-lymphocyte ratio and platelet-lymphocyte ratio. *Head Neck* (2016) 38 Suppl 1:E1332–40. doi: 10.1002/hed.24224

22. Dusselier M, Deluche E, Delacourt N, Ballouhey J, Egenod T, Melloni B, et al. Neutrophil-to-lymphocyte ratio evolution is an independent predictor of early progression of second-line nivolumab-treated patients with advanced non-small-cell lung cancers. *PloS One* (2019) 14(7):e0219060. doi: 10.1371/journal.pone.0219060

23. Facchinetti F, Veneziani M, Buti S, Gelsomino F, Squadrilli A, Bordi P, et al. Clinical and hematologic parameters address the outcomes of non-small-cell lung cancer patients treated with nivolumab. *Immunotherapy* (2018) 10(8):681–94. doi: 10.2217/imt-2017-0175

24. Newman J, Preeshagul I, Kohn N, Devoe C, Seetharamu N. Simple parameters to solve a complex issue: Predicting response to checkpoint inhibitor therapy in lung cancer. *Lung Cancer Manage* (2021) 10(2). doi: 10.2217/lmt-2020-0024

25. Ohba T, Takamori S, Toyozawa R, Nosaki K, Umeyama Y, Haratake N, et al. Prognostic impact of the Controlling Nutritional Status score in patients with non-small cell lung cancer treated with pembrolizumab. *J Thorac Dis* (2019) 11(9):3757–68. doi: 10.21037/jtd.2019.09.29

26. Petrova MP, Eneva MI, Arabadjiev JI, Conev NV, Dimitrova EG, Koynov KD, et al. Neutrophil to lymphocyte ratio as a potential predictive marker for treatment with pembrolizumab as a second line treatment in patients with non-small cell lung cancer. *Biosci Trends* (2020) 14(1):48–55. doi: 10.5582/bst.2019.01279

27. Pu D, Xu Q, Zhou LY, Zhou YW, Liu JY, Ma XL. Inflammation-nutritional markers of peripheral blood could predict survival in advanced non-small-cell lung cancer patients treated with PD-1 inhibitors. *Thorac Cancer* (2021) 12(21):2914–23. doi: 10.1111/1759-7714.14152

28. Quaquarini E, Sottotetti F, Agustoni F, Pozzi E, Malovini A, Teragni CM, et al. Clinical and biological variables influencing outcome in patients with advanced non-small cell lung cancer (NSCLC) treated with anti-PD-1/PD-L1 antibodies: A prospective multicentre study. *J Pers Med* (2022) 12(5):679. doi: 10.3390/jpm12050679

29. Booka E, Kikuchi H, Haneda R, Soneda W, Kawata S, Murakami T, et al. Neutrophil-to-lymphocyte ratio to predict the efficacy of immune checkpoint inhibitor in upper gastrointestinal cancer. *Anticancer Res* (2022) 42(6):2977–87. doi: 10.21873/anticanres.15781

30. Fan X, Wang D, Zhang W, Liu J, Liu C, Li Q, et al. Inflammatory markers predict survival in patients with advanced gastric and colorectal cancers receiving anti–PD-1 therapy. *Front Cell Dev Biol.* (2021) 9:638312. doi: 10.3389/fcell.2021.638312

31. Kim JH, Ryu MH, Park YS, Ma J, Lee SY, Kim D, et al. Predictive biomarkers for the efficacy of nivolumab as ≥ 3(rd)-line therapy in patients with advanced gastric cancer: a subset analysis of ATTRACTION-2 phase III trial. *BMC Cancer* (2022) 22 (1):378. doi: 10.1186/s12885-022-09488-2

32. Wang L, Zhu Y, Zhang B, Wang X, Mo H, Jiao Y, et al. Prognostic and predictive impact of neutrophil-to-lymphocyte ratio and HLA-I genotyping in advanced esophageal squamous cell carcinoma patients receiving immune checkpoint inhibitor monotherapy. *Thorac Cancer* (2022) 13(11):1631–41. doi: 10.1111/1759-7714.14431

33. Eso Y, Takeda H, Taura K, Takai A, Takahashi K, Seno H. Pretreatment neutrophil-to-lymphocyte ratio as a predictive marker of response to atezolizumab plus bevacizumab for hepatocellular carcinoma. *Curr Oncol* (2021) 28(5):4157–66. doi: 10.3390/curroncol28050352

34. Rebuzzi SE, Signori A, Stellato M, Santini D, Maruzzo M, De Giorgi U, et al. The prognostic value of baseline and early variations of peripheral blood inflammatory ratios and their cellular components in patients with metastatic renal cell carcinoma treated with nivolumab: The Δ-Meet-URO analysis. *Front Oncol.* (2022) 12:955501. doi: 10.3389/fonc.2022.955501

35. Guven DC, Sahin TK, Erul E, Cakir IY, Ucgul E, Yildirim HC, et al. The association between early changes in neutrophil-lymphocyte ratio and survival in patients treated with immunotherapy. *J Clin Med* (2022) 11(15):4523. doi: 10.3390/jcm11154523

36. Cheng M, Li G, Liu Z, Yang Q, Jiang Y. Pretreatment neutrophil-to-lymphocyte ratio and lactate dehydrogenase predict the prognosis of metastatic cervical cancer treated with combination immunotherapy. *J Oncol* (2022) 2022:1828473. doi: 10.1155/2022/1828473

37. Spassova I, Ugurel S, Kubat L, Zimmer L, Terheyden P, Mohr A, et al. Clinical and molecular characteristics associated with response to therapeutic PD-1/PD-L1 inhibition in advanced Merkel cell carcinoma. *J Immunother Cancer* (2022) 10(1): e003198. doi: 10.1136/jitc-2021-003198

38. Möller M, Turzer S, Ganchev G, Wienke A, Schütte W, Seliger B, et al. Blood immune cell biomarkers in lung cancer patients undergoing treatment with a combination of chemotherapy and immune checkpoint blockade. *Cancers (Basel)* (2022) 14(15):3690. doi: 10.3390/cancers14153690

39. Park CK, Oh HJ, Kim MS, Koh BG, Cho HJ, Kim YC, et al. Comprehensive analysis of blood-based biomarkers for predicting immunotherapy benefits in patients with advanced non-small cell lung cancer. *Trans Lung Cancer Res* (2021) 10(5):2103–17. doi: 10.21037/tlcr-21-100

40. Guida M, Bartolomeo N, Quaresmini D, Quaglino P, Madonna G. Basal and one-month differed neutrophil, lymphocyte and platelet values and their ratios strongly predict the efficacy of checkpoint inhibitors immunotherapy in patients with advanced BRAF wild-type melanoma. *J Transl Med* (2022) 20(1):159. doi: 10.1186/s12967-022-03359-x

41. Hung HC, Lee JC, Wang YC, Cheng CH, Wu TH, Lee CF, et al. Response prediction in immune checkpoint inhibitor immunotherapy for advanced hepatocellular carcinoma. *Cancers* (2021) 13(7). doi: 10.3390/cancers13071607

42. Yamamoto Y, Yatsuda J, Shimokawa M, Fuji N, Aoki A, Sakano S, et al. Prognostic value of pre-treatment risk stratification and post-treatment neutrophil/lymphocyte ratio change for pembrolizumab in patients with advanced urothelial carcinoma. *Int J Clin Oncol* (2021) 26(1):169–77. doi: 10.1007/s10147-020-01784-w

43. Nenclares P, Gunn L, Soliman H, Bover M, Trinh A, Leslie I, et al. On-treatment immune prognostic score for patients with relapsed and/or metastatic head and neck squamous cell carcinoma treated with immunotherapy. *J ImmunoTher Cancer* (2021) 9 (6). doi: 10.1136/jitc-2021-002718

44. Benzekry S, Grangeon M, Karlsen M, Alexa M, Bicalho-Frazeto I, Chaleat S, et al. Machine learning for prediction of immunotherapy efficacy in non-small cell lung cancer from simple clinical and biological data. *Cancers* (2021) 13(24). doi: 10.3390/cancers13246210

45. Liu X, Shi Y, Zhang D, Zhou Q, Liu J, Chen M, et al. Risk factors for immune-related adverse events: what have we learned and what lies ahead? *biomark Res* (2021) 9 (1):79. doi: 10.1186/s40364-021-00314-8

46. Huang L, Li L, Zhou Y, Yang Z, Wang M, Gao Y, et al. Clinical characteristics correlate with outcomes of immunotherapy in advanced non-small cell lung cancer. *J Cancer* (2020) 11(24):7137–45. doi: 10.7150/jca.49213

47. Khunger M, Patil PD, Khunger A, Li M, Hu B, Rakshit S, et al. Post-treatment changes in hematological parameters predict response to nivolumab monotherapy in non-small cell lung cancer patients. *PloS One* (2018) 13(10):e0197743. doi: 10.1371/journal.pone.0197743

48. Mountzios G, Samantas E, Senghas K, Zervas E, Krisam J, Samitas K, et al. Association of the advanced lung cancer inflammation index (ALI) with immune checkpoint inhibitor efficacy in patients with advanced non-small-cell lung cancer. *ESMO Open* (2021) 6(5). doi: 10.1016/j.esmoop.2021.100254

49. Wu M, Liu J, Wu S, Liu J, Wu H, Yu J, et al. Systemic immune activation and responses of irradiation to different metastatic sites combined with immunotherapy in advanced non-small cell lung cancer. *Front Immunol* (2021) 12. doi: 10.3389/fimmu.2021.803247

50. Nakazawa N, Sohda M, Ubukata Y, Kuriyama K, Kimura A, Kogure N, et al. Changes in the gustave roussy immune score as a powerful prognostic marker of the therapeutic sensitivity of nivolumab in advanced gastric cancer: A multicenter, retrospective study. *Ann Surg Oncol* (2022) 29(12):7400–6. doi: 10.1245/s10434-022-12226-4

51. Namikawa T, Yokota K, Tanioka N, Fukudome I, Iwabu J, Munekage M, et al. Systemic inflammatory response and nutritional biomarkers as predictors of nivolumab efficacy for gastric cancer. *Surg Today* (2020) 50(11):1486–95. doi: 10.1007/s00595-020-02048-w

52. Ohashi H, Takeuchi S, Miyagaki T, Kadono T. Increase of lymphocytes and eosinophils, and decrease of neutrophils at an early stage of anti-PD-1 antibody treatment is a favorable sign for advanced Malignant melanoma. *Drug Discoveries Ther* (2020) 14(3):117–21. doi: 10.5582/ddt.2020.03043

53. Guida M, Bartolomeo N, Quaglino P, Madonna G, Pigozzo J, Di Giacomo AM, et al. No impact of NRAS mutation on features of primary and metastatic melanoma or on outcomes of checkpoint inhibitor immunotherapy: An italian melanoma intergroup (IMI) study. *Cancers* (2021) 13(3):1–15. doi: 10.3390/cancers13030475

54. Tanaka T, Takata K, Yokoyama K, Fukuda H, Yamauchi R, Fukunaga A, et al. Pretreatment modified albumin–bilirubin grade is an important predictive factor associated with the therapeutic response and the continuation of atezolizumab plus bevacizumab combination therapy for patients with unresectable hepatocellular carcinoma. *Curr Oncol* (2022) 29(7):4799–810. doi: 10.3390/curroncol29070381

55. Simonaggio A, Elaidi R, Fournier L, Fabre E, Ferrari V, Borchiellini D, et al. Variation in neutrophil to lymphocyte ratio (NLR) as predictor of outcomes in metastatic renal cell carcinoma (mRCC) and non-small cell lung cancer (mNSCLC) patients treated with nivolumab. *Cancer Immunol Immunother CII* (2020) 69(12):2513–22. doi: 10.1007/s00262-020-02637-1

56. Lee YG, Chang H, Keam B, Chun SH, Park J, Park KU, et al. Outcomes and biomarkers of immune checkpoint inhibitor therapy in patients with refractory head and neck squamous cell carcinoma: Kcsg hn18-12. *Cancer Res Treat* (2021) 53(3):671–7. doi: 10.4143/CRT.2020.824

57. Criscitiello C, Marra A, Morganti S, Zagami P, Viale G, Esposito A, et al. Pretreatment blood parameters predict efficacy from immunotherapy agents in early phase clinical trials. *Oncol* (2020) 25(11):e1732–e42. doi: 10.1634/theoncologist.2020-0518

58. Zhang S, Qiu C, Yu H, Xu Y, Xu X. Prognostic value of neutrophil to lymphocyte ratio in gastric cancer patients receiving immune checkpoint inhibitors: a systematic review and meta-analysis. *Front Oncol* (2023) 13:1070019. doi: 10.3389/fonc.2023.1070019

59. Rapoport BL, Steel HC, Theron AJ, Smit T, Anderson R. Role of the neutrophil in the pathogenesis of advanced cancer and impaired responsiveness to therapy. *Mol (Basel Switzerland)* (2020) 25(7). doi: 10.3390/molecules25071618

60. Kargl J, Zhu X, Zhang H, Yang GHY, Friesen TJ, Shipley M, et al. Neutrophil content predicts lymphocyte depletion and anti-PD1 treatment failure in NSCLC. *JCI Insight* (2019) 4(24). doi: 10.1172/jci.insight.130850

61. Faget J, Peters S, Quantin X, Meylan E, Bonnefoy N. Neutrophils in the era of immune checkpoint blockade. *J Immunother Cancer* (2021) 9(7). doi: 10.1136/jitc-2020-002242

62. Honrubia-Peris B, Garde-Noguera J, García-Sánchez J, Piera-Molons N, Llombart-Cussac A, Fernández-Murga ML. Soluble biomarkers with prognostic and predictive value in advanced non-small cell lung cancer treated with immunotherapy. *Cancers* (2021) 13(17). doi: 10.3390/cancers13174280

63. Wu M, Liu J, Wu S, Liu J, Wu H, Yu J, et al. Systemic immune activation and responses of irradiation to different metastatic sites combined with immunotherapy in advanced non-small cell lung cancer. *Front Immunol* (2021) 12:803247. doi: 10.3389/fimmu.2021.803247

64. Zhao Q, Li B, Xu Y, Wang S, Zou B, Yu J, et al. Three models that predict the efficacy of immunotherapy in Chinese patients with advanced non-small cell lung cancer. *Cancer Med* (2021) 10(18):6291–303. doi: 10.1002/cam4.4171

65. Mielgo Rubio X, Sereno Moyano M, Chara LE, López-Castro R, Rubio-Martínez J, Velastegui A, et al. Neutrophil-platelet score (NPS), a predictive systemic inflammation score for PD-1 immune checkpoint inhibitors (ICI) in pretreated advanced non-small cell lung cancer (NSCLC) patients. *Ann Oncol* (2018) 29:viii510. doi: 10.1093/annonc/mdy292.035

66. Ma LX, Wang Y, Espin-Garcia O, Allen MJ, Jang GH, Zhang A, et al. Systemic inflammatory prognostic scores in advanced pancreatic adenocarcinoma. *Br J Cancer* (2023) 128(10):1916-21. doi: 10.1038/s41416-023-02214-0

67. Ginesu GC, Paliogiannis P, Feo CF, Cossu ML, Scanu AM, Fancellu A, et al. Inflammatory indexes as predictive biomarkers of postoperative complications in oncological thoracic surgery. *Curr Oncol (Toronto Ont)* (2022) 29(5):3425–32. doi: 10.3390/curroncol29050276

68. Şahin AB, Cubukcu E, Ocak B, Deligonul A, Oyucu Orhan S, Tolunay S, et al. Low pan-immune-inflammation-value predicts better chemotherapy response and survival in breast cancer patients treated with neoadjuvant chemotherapy. *Sci Rep* (2021) 11(1):14662. doi: 10.1038/s41598-021-94184-7

69. Shiroyama T, Suzuki H, Tamiya M, Tamiya A, Tanaka A, Okamoto N, et al. Pretreatment advanced lung cancer inflammation index (ALI) for predicting early progression in nivolumab-treated patients with advanced non-small cell lung cancer. *Cancer Med* (2018) 7(1):13–20. doi: 10.1002/cam4.1234

70. Bauckneht M, Genova C, Rossi G, Rijavec E, Dal Bello MG, Ferrarazzo G, et al. The role of the immune metabolic prognostic index in patients with non-small cell lung cancer (NSCLC) in radiological progression during treatment with nivolumab. *Cancers* (2021) 13(13). doi: 10.3390/cancers13133117

71. Castello A, Toschi L, Rossi S, Mazziotti E, Lopci E. The immune-metabolic-prognostic index and clinical outcomes in patients with non-small cell lung carcinoma under checkpoint inhibitors. *J Cancer Res Clin Oncol* (2020) 146(5):1235–43. doi: 10.1007/s00432-020-03150-9

72. Kawashima A, Yamamoto Y, Sato M, Nakata W, Kakuta Y, Ishizuya Y, et al. FAN score comprising fibrosis-4 index, albumin–bilirubin score and neutrophil–lymphocyte ratio is a prognostic marker of urothelial carcinoma patients treated with pembrolizumab. *Sci Rep* (2021) 11(1):21199. doi: 10.1038/s41598-021-00509-x

73. Zheng W, Zhu W, Yu S, Li K, Ding Y, Wu Q, et al. Development and validation of a nomogram to predict overall survival for patients with metastatic renal cell carcinoma. *BMC Cancer* (2020) 20(1):1066. doi: 10.1186/s12885-020-07586-7

74. Sánchez-Gastaldo A, Muñoz-Fuentes MA, Molina-Pinelo S, Alonso-García M, Boyero L, Bernabé-Caro R. Correlation of peripheral blood biomarkers with clinical outcomes in NSCLC patients with high PD-L1 expression treated with pembrolizumab. *Trans Lung Cancer Res* (2021) 10(6):2509–22. doi: 10.21037/tlcr-21-156

75. Namikawa K, Takahashi A, Mori T, Tsutsumida A, Suzuki S, Motoi N, et al. Nivolumab for patients with metastatic uveal melanoma previously untreated with ipilimumab: a single-institution retrospective study. *Melanoma Res* (2020) 30(1):76–84. doi: 10.1097/cmr.0000000000000617

76. Park S, Ock C-Y, Kim H, Pereira S, Park S, Ma M, et al. Artificial intelligence–powered spatial analysis of tumor-infiltrating lymphocytes as complementary biomarker for immune checkpoint inhibition in non–small-cell lung cancer. *J Clin Oncol* (2022) 40(17):1916–28. doi: 10.1200/JCO.21.02010

77. Adib E, Zarif TE, Freeman D, Labban M, Curran C, Sharma B, et al. FOXP3+ T-cell infiltration is associated with improved outcomes in metastatic urothelial carcinoma (mUC) treated with immune-checkpoint inhibitors (ICI). *J Clin Oncol* (2022) 40(6_suppl):549–. doi: 10.1200/JCO.2022.40.6_suppl.549

78. Sanz Garcia E, Laliotis G, Avery L, Spreafico A, Hansen AR, Eng L, et al. 9P Early circulating tumor DNA (ctDNA) kinetics and gene expression analysis to predict treatment outcomes with anti-PD-1 therapy. *Immuno-Oncol Technol* (2022) 16:100114. doi: 10.1016/j.iotech.2022.100114

79. Boutros A, Carosio R, Campanella D, Spagnolo F, Banelli B, Morabito A, et al. 24P The predictive and prognostic role of single nucleotide gene variants in PD-1 and PD-L1 in patients with advanced melanoma treated with PD-1 inhibitors. *Immuno-Oncol Technol* (2022) 16:100129. doi: 10.1016/j.iotech.2022.100129

80. Tarhini AA, Coleman SS, El Naqa I, Sukrithan V, Aakrosh R, McCarter M, et al. 18P Systematic evaluation of published predictive gene expression signatures in pan-cancer patient cohorts treated with immune checkpoint inhibitors in a real-world setting. *Immuno-Oncol Technol* (2022) 16:100123. doi: 10.1016/j.iotech.2022.100123

81. Dall'Olio FG, Garcia CA, Zrafi WS, Fortunati E, Bettayeb A, Zalcman G, et al. 4P FDG PET derived metabolic tumor volume (MTV) and its transcriptomic correlates as biomarker to predict efficacy of immune checkpoint inhibitors (ICB) alone or in combination with chemotherapy in advanced NSCLC: A multicentric study. *Immuno-Oncol Technol* (2022) 16:100109. doi: 10.1016/j.iotech.2022.100109

82. Barlesi F, Greillier L, Monville F, Audigier Valette C, Martinez S, Cloarec N, et al. 3MO Comprehensive biomarkers (BMS) analysis to predict efficacy of PD1/L1 immune checkpoint inhibitors (ICIs) in combination with chemotherapy: A subgroup analysis of the precision immuno-oncology for advanced non-small cell lung cancer (pioneer) trial. *Immuno-Oncol Technol* (2022) 16:100108. doi: 10.1016/j.iotech.2022.100108

83. Li Y, Zhang Z, Hu Y, Yan X, Song Q, Wang G, et al. Pretreatment neutrophil-to-lymphocyte ratio (NLR) may predict the outcomes of advanced non-small-cell lung cancer (NSCLC) patients treated with immune checkpoint inhibitors (ICIs). *Front Oncol* (2020) 10:654. doi: 10.3389/fonc.2020.00654

84. Shao Y, Wu B, Jia W, Zhang Z, Chen Q, Wang D. Prognostic value of pretreatment neutrophil-to-lymphocyte ratio in renal cell carcinoma: a systematic review and meta-analysis. *BMC Urol* (2020) 20(1):90. doi: 10.1186/s12894-020-00665-8

frontiers | Frontiers in Immunology

TYPE Original Research
PUBLISHED 31 October 2023
DOI 10.3389/fimmu.2023.1274431

OPEN ACCESS

EDITED BY
Takaji Matsutani,
Maruho, Japan

REVIEWED BY
Xiaoran Li,
University of Texas MD Anderson Cancer Center, United States
Yongbin Chen,
Chinese Academy of Sciences (CAS), China

*CORRESPONDENCE
Ming Gao
gaohaoming033@163.com

†These authors have contributed equally to this work and share first authorship

RECEIVED 08 August 2023
ACCEPTED 18 October 2023
PUBLISHED 31 October 2023

CITATION
Hou Y, Li X, Yang Y, Shi H, Wang S and Gao M (2023) Serum cytokines and neutrophil-to-lymphocyte ratio as predictive biomarkers of benefit from PD-1 inhibitors in gastric cancer. *Front. Immunol.* 14:1274431. doi: 10.3389/fimmu.2023.1274431

Serum cytokines and neutrophil-to-lymphocyte ratio as predictive biomarkers of benefit from PD-1 inhibitors in gastric cancer

Yidan Hou†, Xiaoli Li†, Yudan Yang, Hao Shi, Shaofang Wang and Ming Gao*

Department of Oncology, The First Affiliated Hospital of Zhengzhou University, Zhengzhou, Henan, China

Background: Immunotherapy is significantly revolutionizing cancer treatment and demonstrating promising efficacy in gastric cancer (GC) patients. However, only a subset of patients could derive benefits from targeted monoclonal antibody therapy against programmed death receptor 1 (PD-1). This study aims to identify suitable serum cytokines and blood cell ratios as predictive biomarkers to aid in the selection of GC patients likely to benefit from PD-1 inhibitors.

Materials and methods: This retrospective study included 41 GC patients who received PD-1 inhibitors combined with chemotherapy, 36 GC patients treated solely with chemotherapy, and 33 healthy controls. The study assessed the levels of seven cytokines: interleukin-2 (IL-2), IL-4, IL-6, IL-10, IL-17A, tumor necrosis factor-alpha (TNF-α), interferon-gamma (IFN-γ), and various inflammatory markers, including the neutrophil-to-lymphocyte ratio (NLR), total lymphocyte count (TLC), platelet-to-lymphocyte ratio (PLR), and lymphocyte-to-monocyte ratio (LMR). Measurements were obtained using the inpatient system. Univariate and multivariate Cox regression analyses were performed to evaluate the predictive significance of these hematologic parameters for clinical outcomes.

Results: Levels of IL-6, IL-10, TNF-α, NLR, and PLR were significantly elevated in GC patients compared to healthy controls, while TLC and LMR were higher in the control group. Among the 41 patients receiving PD-1 inhibitors and chemotherapy, baseline IL-2 was associated with OS and PFS. Additionally, IL-6 and IL-17A correlated with OS, while NLR was linked to PFS (all $P<0.05$). These factors were identified as independent prognostic indicators in both univariate and multivariate analyses. Furthermore, almost all cytokine levels increased following the initiation of PD-1 inhibitor treatment.

Conclusions: The introduction of PD-1 inhibitors alongside chemotherapy in GC impacts serum cytokine levels. IL-2, IL-6, IL-17A, and NLR exhibit potential as reliable circulating predictive biomarkers for identifying patients who may benefit from PD-1 inhibitors combined with chemotherapy.

KEYWORDS

gastric cancer, immune-checkpoint inhibitors, cytokines, predictive biomarker, blood cell ratio, overall survival, progression-free survival

Introduction

Gastric cancer is a significant global health concern, ranking fifth in terms of incidence and fourth in mortality worldwide (1). Certain regions, such as Eastern Asia, Eastern Europe, and South America, have particularly high rates of gastric cancer cases. In mainland China, a considerable number of patients are diagnosed at an advanced stage due to low screening rates and subtle clinical symptoms, resulting in missed opportunities for surgery and poorer prognoses (2). Fortunately, the development of immunotherapy for gastric cancer has shown promising results, changing traditional treatment approaches.

The immune checkpoint is a vital element of the immune system, consisting of receptors found on the surface of immune cells that can either positively or negatively regulate immune responses. For example, PD-1, located on the surface of T cells, functions as a natural brake to control the excessive activity of cytotoxic T effector cells when it binds to its ligand PD-L1. PD-L1 is commonly found in both normal tissues and tumor cells, and their interactions help limit immune-mediated tissue damage and support tumor cells in evading the immune system (3). Immunotherapy using Immune Checkpoint Inhibitors (ICIs) has emerged as a promising approach in the treatment of various cancers. ICIs target the PD-1/PD-L1 pathway to boost the reactivity of anti-tumor T cells. Notably, several PD-1 inhibitors (Nivolumab, Pembrolizumab, Sintilimab, Camrelizumab, Tislelizumab) and PD-L1 inhibitors (Atezolizumab, Avelumab, Durvalumab) have received approval for cancer therapy and have demonstrated effectiveness in an expanding range of malignancies, including gastroesophageal, melanoma, and lung cancers (4). However, despite these significant advancements, a considerable proportion of gastric cancer patients receiving ICIs do not derive therapeutic benefits (5). Numerous clinical studies have been conducted to identify biomarkers that can predict which gastric cancer patients are likely to respond well to ICIs therapy. Some potential biomarkers include PD-L1 expression, tumor mutational burden (TMB), microsatellite instability/mismatch repair (MSI/MMR) status, Epstein-Barr virus (EBV) infection, circulating tumor DNA (ctDNA), and gut microbiota. However, their practical application in day-to-day clinical practice still requires further confirmation (6).

Recent research has been rapidly uncovering the mechanisms linking infection, innate immunity, inflammation, and cancer (7). Cytokines, produced by activated immune cells, play a crucial role in this linkage. Pro-inflammatory cytokines such as IL-1β, IL-8, IL-12, TNF-α, IFN-γ, and anti-inflammatory cytokines like IL-4 and IL-10 have dual functions, activating anti-tumorigenic actions of T cells while also participating in tumor malignant transformation, growth, invasion, and metastasis (8). Cytokines can activate anti-tumorigenic actions of T cells and also contribute to tumor growth, invasion, and metastasis (9). Moreover, systemic inflammatory response (SIR) indicators, such as NLR, PLR, LMR, and TLC, have been reported to be associated with the prognosis of certain cancers (10). Changes in cytokine expression levels and cell composition in the tumor microenvironment (TME) can potentially influence the efficacy of ICIs in various malignancies (11). Therefore, multiplex cytokine and blood cell analysis could yield valuable prognostic assessments in patients.

This study aims to examine the association between baseline and post-treatment peripheral cytokines and blood cells in GC patients who received PD-1 inhibitors combined with chemotherapy. The goal is to identify clinically significant predictive factors for the efficacy of immunotherapy in patients with gastric cancer.

Abbreviations: PD-1, programmed death-1; GC, gastric cancer; IL-2, interleukin-2; TNF-α, tumor necrosis factor-alpha; IFN-γ, interferon-gamma; NLR, neutrophil-to-lymphocyte ratio; TLC, total lymphocyte count; PLR, platelet-to-lymphocyte ratio; LMR, lymphocyte-to-monocyte ratio; OS, overall survival; PFS, progression-free survival; PD-L1, programmed cell death-ligand 1; ICIs, immune checkpoint inhibitors; TMB, tumor mutational burden; MSI/MMR, microsatellite instability/mismatch repair; EBV, Epstein Barr virus; ctDNA, circulating tumor DNA; SIR, systemic inflammatory response; TME, tumor microenvironment; HR, hazard ratios; CI, confidence intervals; CR, complete response; PR, partial response; CAFs, cancer-associated fibroblasts; DCs, dendritic cells; TIL, tumor-infiltrating lymphocytes.

Materials and methods

Patient characteristics

December 2022. Among them, 41 GC patients received PD-1 inhibitors in combination with chemotherapy (Cohort 1), while 36 GC patients underwent chemotherapy alone (Cohort 2). The 33 healthy controls exhibited good health without any indications of tumors, viral infections, diabetes, connective tissue diseases, or liver/kidney impairments. Inclusion criteria for the 77 patients included: 1) histopathological confirmation of gastric cancer at stage II-IV according to the American Joint Committee on Cancer (AJCC); 2) receiving PD-1 inhibitors combined with chemotherapy (Cohort 1) or chemotherapy alone (Cohort 2) for a minimum of 3 cycles; 3) regular tumor assessments every 2 treatment courses using imaging evaluations, with Overall Survival (OS) and Progression-Free Survival (PFS) times recorded based on imaging results and follow-up phone calls; 4) blood samples collected for cytokine and blood cell analysis when tumor progression or response was observed; 5) physical condition scored according to the Eastern Cooperative Oncology Group guidelines (ECOG) ranging from 0 to 3 (12), and no dysfunction in vital organs detected. This study adhered to the principles outlined in the World Medical Association's Declaration of Helsinki and received approval from the Medical Ethical Committee of our hospital. Since only anonymous data were used for this retrospective study, the ethics committee waived the requirement for informed consent.

Treatment

In Cohort 2, 36 GC patients were treated: 19 received first-line Sox (Oxaliplatin, Teggio) chemotherapy, 15 received first-line Sox combined with albumin-bound paclitaxel, and 2 received first-line Xelox (oxaliplatin and capecitabine). The median number of cycles

for the first-line chemotherapy was 5, with a range from 3 to 10, and no subsequent PD-1 inhibitor treatment was administered. In Cohort 1, 41 patients were included: 14 received PD-1 inhibitors as part of the first-line therapy, while 27 received PD-1 inhibitors during subsequent-line therapy. The PD-1 inhibitors used were Sintilimab, Camrelizumab, and Tislelizumab, combined with chemotherapy over a 21-day cycle. The chemotherapy regimen was consistent with the description above. The median number of chemoimmunotherapy cycles was 5, with a range from 3 to 14.

Analysis of survival

Tumor assessments were performed after every two treatment courses using various imaging techniques such as CT, ultrasound, MRI, or PET-CT. The evaluation was conducted following the Response Evaluation Criteria of Solid Tumors 1.1 (RECIST1.1) criteria (13). PFS was calculated from the initiation of anti-tumor therapy to the date of disease progression. On the other hand, OS was measured from the date of the first treatment dose until death from any cause.

Blood sample collection and measurements

Plasma samples were collected from the patients before the first treatment and at the time of disease remission or progression. These samples were then centrifuged at 1000 g for 10 min at 4°C. After centrifugation, the supernatant (serum) was immediately extracted and analyzed on the spot or divided into aliquots and stored frozen at −80° C. Cytokine levels were assessed using the Human Cytokine 12 Plex Kit (Beijing ACRO Biosystems, catalog number: CRS- A002/A017/B001/B003/B005/B008) at the clinical laboratory department of our hospital. The panel of measured cytokines included IL-2, IL-4, IL-6, IL-10, IFN-γ, TNF-α, and IL-17A. Beyond that, blood routine examination was achieved by flow cytometry, NLR, PLR, and LMR were then calculated as the total neutrophil counts divided by the lymphocyte counts, platelet counts divided by the TLCs, and the TLCs divided by the total monocyte counts, respectively.

Cytokine cut-off value calculation

To assess the correlation between baseline blood parameters and survival, we categorized the baseline blood parameters into high-level and low-level groups. This categorization was based on either the median value or the optimal cut-off value (Tables S1-2). To ascertain the most suitable cut-off value for the studied indicators, we employed the web-based software X-tile (Table S3-4).

Statistical analyses

Patient characteristics underwent analysis using descriptive statistical methods. Continuous variables were summarized using medians and quartiles, and comparisons were conducted using the Mann-Whitney U test and the Kruskal-Wallis test. Categorical variables were presented as numbers (%) and analyzed using the chi-squared test and Fisher's exact test. For the evaluation of independent prognostic factors, both univariate and multivariate analyses were performed. Hazard ratios (HRs) and 95% confidence intervals (CIs) were reported. In the multivariable model, only elements with a p-value of <0.1 from the univariate analysis were incorporated. The significance threshold for multivariate analyses was set at $P < 0.05$. OS and PFS were illustrated using the Kaplan-Meier method, and the log-rank test was employed to compare the survival curves. All statistical analyses were executed using SPSS version 26.0 software, and the figures were generated using GraphPad Prism version 8.0.

Results

Patients' characteristics and survival outcomes

Table 1 presents the clinical characteristics and pre-treatment blood parameters of the 77 patients diagnosed with GC. Cohort 1 consisted of a higher percentage of patients in stages III-IV of the TNM classification (82.93% vs. 58.33%) and more patients who had not undergone gastric surgery (56.10% vs. 22.22%) compared to Cohort 2. The level of IL-6 was found to be higher in Cohort 1 than in Cohort 2 (12.06 vs. 4.85). Patients in Cohort 1, who received chemoimmunotherapy, experienced a significantly better PFS of 10.67 months compared to 8.1 months in Cohort 2 ($p = 0.003$). Additionally, Cohort 1 also showed an improved OS of 15.7 months compared to 10.83 months in Cohort 2 ($p = 0.021$). No statistically significant differences were observed between Cohort 1 and Cohort 2 regarding age, sex, ECOG score, presence of other chronic diseases (diabetes, hypertension, cardiopathy), history of smoking, and family history of cancer ($p > 0.05$).

Comparison of baseline blood parameters between GC patients and healthy individuals

To clarify the significance of cytokines in GC diagnosis, we included 33 healthy participants. As displayed in Table S5, there was no marked difference in age and gender distribution between the healthy controls and GC patients ($p > 0.05$), making subsequent results comparable. Figure 1 reveals that, aside from IL-2 and IL-4, levels of all other cytokines were elevated in GC patients compared to healthy individuals. Specifically, the differences in IL-6, IL-10, and TNF-αwere statistically significant ($p<0.0001$, $p<0.0001$, $p = 0.021$, respectively). It is worth highlighting that every blood cell component ratio studied exhibited statistical differences between the two cohorts. In healthy individuals, both TLC and LMR were higher ($p<0.0001$, $p<0.0001$), while GC patients had elevated NLR and PLR ($p = 0.0085$, $p = 0.0034$) (Table S6).

10.3389/fimmu.2023.1274431

TABLE 1 Characteristics of patients at baseline.

Clinical characteristics		GC patients (n=77) n (%)	Cohort 1 (n=41) n (%)	Cohort 2 (n=36) n (%)	P
Gender	male	53 (68.831%)	26 (63.415%)	27 (75.000%)	0.273
	female	24 (31.169%)	15 (36.585%)	9 (25.000%)	
Age	<60	41 (53.247%)	24 (58.537%)	17 (47.222%)	0.321
	≥60	36 (46.753%)	17 (41.463%)	19 (52.778%)	
ECOG score	≤2	63 (81.818%)	34 (82.927%)	29 (80.556%)	0.788
	>2	14 (18.182%)	7 (17.073%)	7 (19.444%)	
TNM stage	II	22 (28.571%)	7 (17.073%)	15 (41.667%)	**0.017**
	III-IV	55 (71.429%)	34 (82.927%)	21 (58.333%)	
Surgery history	Yes	46 (59.740%)	18 (43.902%)	28 (77.778%)	**0.002**
	No	31 (40.260%)	23 (56.098%)	8 (22.222%)	
Smoked	Yes	27 (35.065%)	15 (36.585%)	12 (33.333%)	0.765
	No	50 (64.935%)	26 (63.415%)	24 (66.667%)	
family cancer history	Yes	14 (18.182%)	6 (14.634%)	8 (22.222%)	0.389
	No	63 (81.818%)	35 (85.366%)	28 (77.778%)	
other chronic disease	Yes	20 (25.974%)	10 (24.390%)	10 (27.778%)	0.735
	No	57 (74.026%)	31 (75.610%)	26 (72.222%)	
mPFS (month)	median	8.87	10.67	8.1	**0.003**
mOS (month)	median	14.83	15.7	10.83	**0.021**
IL-2	median[Q1, Q3]	1.740[1.210,2.590]	1.960[1.420,2.600]	1.490[1.110,2.260]	0.213
IL-4	median[Q1, Q3]	1.990[0.910,3.310]	2.370[1.020,3.310]	1.930[0.800,3.080]	0.444
IL-6	median[Q1, Q3]	6.100[3.970,14.190]	12.060[5.020,18.060]	4.850[2.980,8.280]	**<0.001**
IL-10	median[Q1, Q3]	2.690[1.870,3.790]	2.860[1.870,3.840]	2.650[1.890,3.650]	0.748
TNF-α	median[Q1, Q3]	1.940[1.300,2.700]	1.870[1.470,2.550]	2.230[1.230,2.910]	0.537
IFN-γ	median[Q1, Q3]	2.060[1.460,2.590]	2.110[1.500,2.560]	1.940[1.460,2.620]	0.736
IL-17A	median[Q1, Q3]	5.680[2.900,9.260]	5.680[2.340,9.890]	5.720[3.190,8.910]	0.779
TLC	median[Q1, Q3]	1.320[1.040,1.700]	1.310[1.000,1.790]	1.370[1.200,1.690]	0.721
NLR	median[Q1, Q3]	2.338[1.571,3.444]	2.600[1.692,4.500]	2.338[1.571,2.628]	0.234
PLR	median[Q1, Q3]	149.231[109.924,209.375]	149.231[109.924,205.833]	149.693[114.557,223.171]	0.732
LMR	median[Q1, Q3]	3.478[2.370,4.238]	3.462[2.167,4.238]	3.714[2.726,3.953]	0.713

Eastern Cooperative Oncology Group Performance Status (ECOG PS). P < 0.05 was considered statistically significant and shown in bold type.

Correlation between blood indexes and clinical features in GC patients

As illustrated in Table S7, females exhibited notably higher baseline levels of IL-6 and PLR, while their NLR was significantly lower (p = 0.032, p = 0.046, p = 0.003, respectively). Elevated IL-6 levels were also observed in patients without a family history of cancer (p = 0.012) and in those aged above 60 years (p = 0.048). Patients who underwent gastric surgery had significantly increased levels of IFN-γ and NLR (p = 0.009, p = 0.017). Patients with an ECOG score of ≤2 had a notably raised TLC (p = 0.048). Conversely, LMR was distinctly lower in patients diagnosed with primary diseases such as hypertension, diabetes, and stroke (p = 0.028). There were no statistically significant differences in cytokine levels based on clinical stages or smoking histories (p > 0.05).

Associations between blood indexes and survival outcomes

Initially, we categorized baseline blood parameters into a high-level group and a low-level group based on the median value. As

10.3389/fimmu.2023.1274431

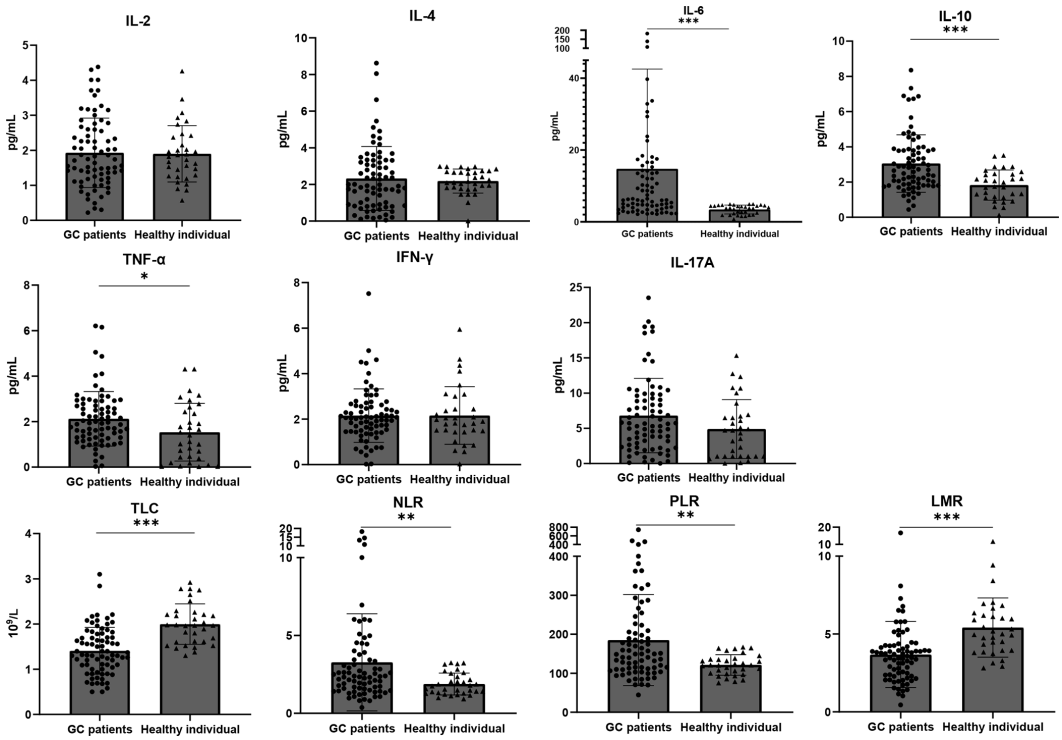

FIGURE 1
Baseline IL-6, IL-10, TNF-α, NLR and PLR are higher, TLC and LMR are lower in GC patients than in healthy individuals. Dot plots show the difference of baseline blood parameters between healthy volunteers (n = 33) and GC patients (n = 77). The top of the grey box shows the median value. All cytokines except for IL-2 and IL-4 were higher in GC patients, but only in the case of IL-6 ($p<0.0001$), IL-10 ($p<0.0001$) and TNFα ($p = 0.021$) these differences were statistically significant. TLC ($p<0.0001$) and LMR ($p<0.0001$) were higher in healthy individuals while NLR($p=0.0085$)and PLR ($p=0.0034$)were higher in GC patients. Error bars show the interquartile range. *$p < 0.05$, **$p < 0.01$, and ***$p < 0.001$.

outlined in Table 2, univariate analysis revealed a significant association between OS and several factors, including IL-2, IL-6, IFN-γ, IL-17A, NLR, and ECOG (all $p < 0.05$). To account for other potential influences on survival outcomes, a multivariable Cox regression analysis was conducted. It confirmed that the IL-2-high group had an improved OS, whereas the IL-6-high and IL-17A-high groups exhibited reduced OS (all $p < 0.05$) (Figures 2A–C). Regarding PFS, the univariate analysis indicated significant associations with IL-2, IL-4, IL-6, IL-10, IFN-γ, and NLR (all $p < 0.1$). Subsequent multivariate analysis confirmed that the NLR-high group had a reduced PFS ($p <0.01$) (Figure 2D**).** In a similar manner, we conducted an analysis of the prognostic impact of blood parameters (categorized by the median) after the initial 2 treatment cycles. The multivariable regression analysis revealed that the IL-6-low group exhibited an enhanced OS and PFS, whereas the IL-2-high groups showed increased OS. Conversely, the IL-17A-high group demonstrated a diminished PFS (all with $p < 0.05$) (Table S8).

As detailed in Table 3, the blood parameters of Cohort 1 were divided into high-level and low-level groups based on a cut-off value. Univariate analysis identified significant links between OS and parameters such as IL-2, IL-6, TNF-α, IFN-γ, IL-17A, NLR, and ECOG (all $p <0.05$). Further multivariate analysis verified that the IL-6-high and IL-17A-high groups had diminished OS (all $p < 0.05$) (Figures 3A, B). Similarly, univariate analysis revealed a significant relationship between PFS and variables like IL-2, IL-4, IL-6, IL-10, TNF-α, IFN-γ, NLR, and LMR (all $p < 0.1$). Upon multivariate assessment, the IL-2-high group was found to have a superior PFS (all $p < 0.05$) (Figure 3C). In a parallel manner, the Cox regression analysis of blood parameters (categorized by cut-off value) after the initial 2 treatment cycles indicated that the IL-2-high and IL-6-low groups experienced enhanced overall survival (OS) and progression-free survival (PFS), while the IL-17A-high groups displayed decreased PFS (all $p < 0.01$) (Table S9).

Interestingly, these relationships between blood parameters and clinical outcomes were exclusive to Cohort 1. When focusing on Cohort 2, where patients underwent only chemotherapy, these associations were not evident (Tables S10-11). This implies that baseline serum IL-2, IL-6, IL-17A, and NLR can independently forecast the efficacy of PD-1 inhibitors in GC patients.

Dynamic changes of cytokines once treatment was initiated in each cohort

As depicted in Figure 4, there was a general elevation from baseline to the moment the tumor exhibited its first complete response (CR) or partial response (PR) in all cytokines, with the exceptions being IL-6 and IL-17A in Cohort 1. Notably, the levels of IL-2, IL-4, IL-10, and IFN-γ were statistically significantly increases

10.3389/fimmu.2023.1274431

TABLE 2 Univariate and Multivariate analysis for PFS and OS of Cohort 1 baseline blood parameters grouped by median.

Characteristics	OS				PFS			
	univariate analysis		multivariate analysis		univariate analysis		multivariate analysis	
	HR (95% CI)	P	HR (95% CI)	P	HR (95% CI)	P	HR (95% CI)	P
IL-2	**0.217 (0.098-0.478)**	**0.000**	**0.382 (0.165-0.888)**	**0.025**	**0.432 (0.223-0.838)**	**0.013**	0.702 (0.294-1.674)	0.425
IL-4	0.745 (0.396-1.401)	0.361	-	-	**0.547 (0.287-1.041)**	**0.066**	0.73 (0.333-1.599)	0.431
IL-6	**2.944 (1.453-5.965)**	**0.003**	**3.018 (1.367-6.666)**	**0.006**	**2.212 (1.145-4.273)**	**0.018**	1.882 (0.866-4.089)	0.110
IL-10	0.74 (0.393-1.396)	0.353	-	-	**0.516 (0.265-1.002)**	**0.051**	0.668 (0.311-1.437)	0.302
TNF-α	0.88 (0.46-1.683)	0.699	-	-	0.919 (0.49-1.722)	0.791	-	-
IFN-γ	**0.355 (0.174-0.725)**	**0.004**	0.553 (0.251-1.218)	0.142	**0.567 (0.296-1.084)**	**0.086**	0.79 (0.372-1.677)	0.540
IL-17A	**1.978 (1.049-3.729)**	**0.035**	**2.143 (1.077-4.265)**	**0.030**	1.382 (0.739-2.587)	0.311	-	-
TLC	0.956 (0.501-1.824)	0.891	-	-	1.454 (0.727-2.908)	0.289	-	-
NLR	**2.162 (1.137-4.111)**	**0.019**	2.022 (0.981-4.166)	0.056	**2.38 (1.241-4.563)**	**0.009**	**2.886 (1.418-5.876)**	**0.003**
PLR	1.052 (0.559-1.981)	0.876	-	-	0.946 (0.508-1.763)	0.862	-	-
LMR	1.156 (0.607-2.203)	0.660	-	-	0.874 (0.467-1.635)	0.673	-	-
gender	0.921 (0.479-1.768)	0.804	-	-	0.875 (0.459-1.667)	0.685	-	-
age	0.74 (0.39-1.403)	0.357	-	-	0.968 (0.504-1.86)	0.922	-	-
ECOG (>2)	**10.172 (3.453-29.966)**	**0.000**	**7.481 (2.19-25.548)**	**0.001**	1.659 (0.723-3.81)	0.233	-	-
TNM stage (III-IV)	1.267 (0.526-3.055)	0.598	-	-	0.953 (0.391-2.322)	0.915	-	-
surgery history	1.33 (0.699-2.529)	0.385	-	-	0.957 (0.512-1.79)	0.891	-	-
other chronic basic diseases	1.001 (0.484-2.069)	0.999	-	-	1.072 (0.521-2.208)	0.850	-	-
smoked	0.903 (0.47-1.734)	0.758	-	-	0.97 (0.508-1.852)	0.927	-	-
family cancer history	1.373 (0.563-3.349)	0.486	-	-	0.765 (0.319-1.833)	0.548	-	-

Baseline blood parameters were grouped by the median. HR, hazard ratios; CI, confidence interval. basic disease (diabetes, hypertension, cardiopathy). Elements with a p-value of <0.1 in the univariate analysis and with a p-value of <0.05 in the multivariate analysis were in bold type.

(p = 0.044, p = 0.025, p = 0.034, p = 0.007, respectively). In contrast, Cohort 2 displayed a decline in IL-2, TNF-α, IFN-γ, and IL-17A from baseline to response. While IL-4, IL-6, and IL-10 demonstrated a rise from baseline to tumor response, none of these changes reached statistical significance. We calculated the percentage variations in cytokine levels from baseline to response to determine if these quantitative shifts during treatment correlated with survival outcomes. As illustrated in Figure 5, individuals in Cohort 1, where IL-2 levels increased by over 20% from baseline to response, showed a considerably improved OS (16.32 m vs. 13.03 m; p = 0.0154). This trend in IL-2 variation was also observed in Cohort 2 patients, but it did not maintain statistical significance (13.58 m vs. 12.49 m, p = 0.6537). We additionally computed the percentage variations in cytokine levels from baseline to the timepoint following 2 treatment cycles, but we did not observe any consistent trend.

Discussion

The detection of cytokines and blood cell parameters is preferable to other biomarkers due to their widespread use and minimally invasive sampling technique. In this study, we had access to two groups of patients treated either with immunochemotherapy or solely with chemotherapy. This allowed us to assess the biological impacts of incorporating Immune ICIs. Only associations that were notably significant in Cohort 1, distinct from those observed in Cohort 2 (chemotherapy-only group), were considered indicative of the effects related to ICIs. We employed statistical analysis to determine whether baseline levels and variations in cytokines and blood cell parameters could predict the efficacy of immunotherapy across different treatment outcomes. Initially, we compared baseline cytokine levels of GC patients against those found in healthy subjects. One significant observation was the universally elevated cytokine levels in GC patients, with the exceptions being IL-2 and IL-4. Notably, levels of IL-6, IL-10, and TNF-α were markedly increased in the GC patient group. As depicted in Figure 1, there were no significant differences in the levels of IL-2, IL-4, INF-γ, and IL-17A between GC patients and healthy controls. IL-2 is primarily secreted by T cells (14), and our study observed a decrease in the total lymphocyte count among gastric cancer patients. Consistent with our findings, Mohammad et al. (15), reported no significant differences in IL-2 levels between gastric cancer patients and healthy controls. Furthermore, another study noted that patients with

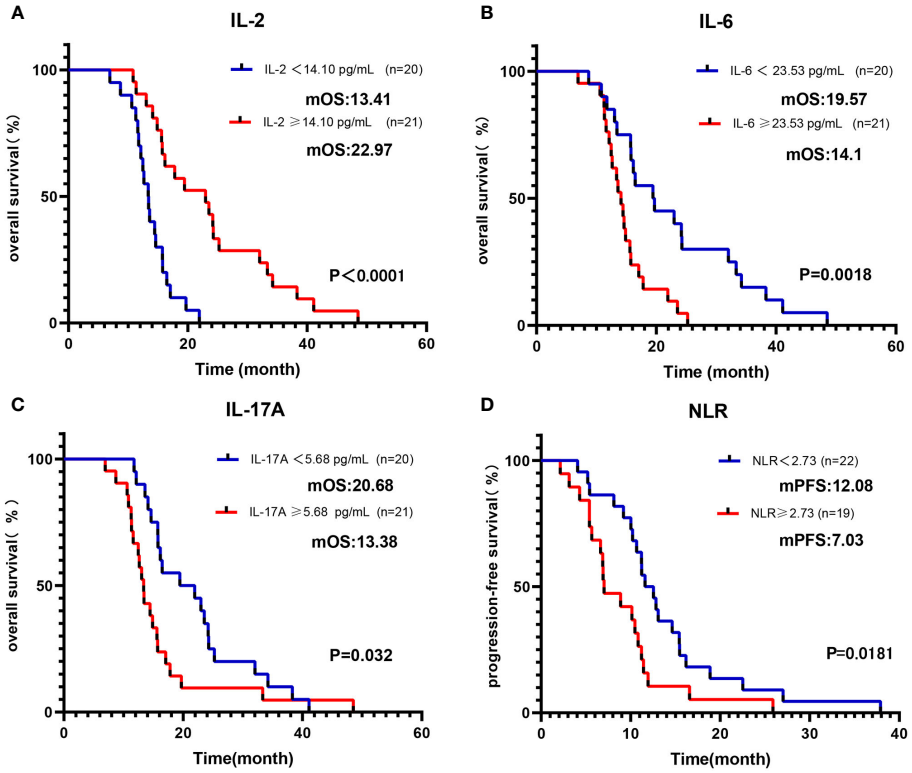

FIGURE 2
Kaplan-Meier curve of OS/PFS of Cohort 1 patients, grouped by median of baseline blood parameters. Kaplan-Meier OS curves according to baseline median of **(A)** IL-2; **(B)** IL-6; **(C)** IL-17A. Kaplan-Meier PFS curves according to baseline median of **(D)** NLR.

gastric cancer stage III or IV exhibited elevated levels of IL-2, while there was no distinction in the serum levels of IL-2 between patients with gastric cancer stage I or II and healthy controls (16), which aligns with our findings in Table S7. Increased IL-4 levels have been frequently observed in various types of cancers. However, the evidence regarding the pro- or antitumoral role of IL-4 is conflicting, and this function is closely linked to IL-4 levels and its interaction with other immunological modulators (17). IFN-γ, produced by numerous immune cell subsets (including T cells, natural killer cells, B cells, and others), possesses both pro-tumor and anti-tumor activities (18). Nitu et al. reported that no significant differences existed in the concentration of IFN-γ between patients and healthy controls (19), which is consistent with our findings. Norma et al. also identified that circulating levels of IL-6 and IL-10 were discernibly higher in GC patients compared to a healthy control group (20), aligning with our results. Numerous studies indicate the pivotal role of IL-6 in a variety of malignancies (21–23). Elevated serum IL-6 concentrations have been documented in several solid tumors, including those of the lung, breast, pancreas, and stomach (24). The STAT3 pathway, when activated by IL-6, up-regulates the expression of cyclins and down-regulates the expression of the cyclin-dependent kinase (Cdk) inhibitor p21. This mechanism consequently promotes tumor cell cycle progression, leading to metastasis and tumor cell proliferation (25). Additionally, IL-6 has been reported to prevent cellular senescence by increasing telomerase activity, thereby promoting tumor growth (26). Studies indicate that IL-10 primarily inhibits the differentiation and antigen-presenting properties of DCs (dendritic cells) during the early stages of immune response (27). As a result, IL-10 significantly suppresses the production of IL-2 from antigen-presenting cells. In the absence of Th1-associated cytokines (like IL-2), the T-cell-mediated response is inevitable (28). While TNF-α, a pro-inflammatory cytokine, has been linked to promoting tumor metastasis and correlated with advanced cancer stages (29–31), its presence in cancers has also been associated with immune suppression. Animal model research further supports TNF-α's role in promoting tumor growth and malignancy (32–35). Conversely, there are reports suggesting the benefits of the potent pro-inflammatory cytokine (TNF-α) in cancer treatments, especially given its recognition as a major factor in the anti-tumor activities of Coley's toxins (36). In this study, both NLR and PLR were statistically elevated in GC patients compared to healthy controls. The neutrophil-to-lymphocyte ratio in peripheral blood reflects the balance between systemic inflammation and immunity. Consistent with our results, Mishra et al. discovered that the NLR is higher in cancer patients and its elevated level is linked to a worse.

In SIR studies, elevated NLR levels after ICI treatment have been linked to reduced survival rates in advanced esophagus cancer and lung cancer (10, 37). Consistent with these findings, our patients with a pre-treatment NLR above the median demonstrated a notably worse PFS. This negative correlation may be indicative of the interplay between intense inflammation and compromised immune function (38). While some studies suggest that a higher PLR corresponds to a worse prognosis in lung cancer

10.3389/fimmu.2023.1274431

TABLE 3 Univariate and Multivariate analysis for PFS and OS of Cohort 1 baseline blood parameters grouped by cut-off value.

Characteristics	OS				PFS			
	univariate analysis		multivariate analysis		univariate analysis		multivariate analysis	
	HR (95% CI)	P	HR (95% CI)	P	HR (95% CI)	P	HR (95% CI)	P
IL-2	**0.215 (0.097-0.474)**	**0.000**	0.735 (0.267-2.026)	0.552	**0.195 (0.083-0.456)**	**0.000**	**0.354 (0.127-0.983)**	**0.046**
IL-4	0.713 (0.378-1.346)	0.297	–	–	**0.47 (0.243-0.909)**	**0.025**	0.62 (0.287-1.34)	0.224
IL-6	**2.969 (1.489-5.92)**	**0.002**	**3.092 (1.204-7.943)**	**0.019**	**1.815 (0.923-3.569)**	**0.084**	2.114 (0.935-4.78)	0.072
IL-10	0.65 (0.337-1.254)	0.199	–	–	**0.423 (0.209-0.859)**	**0.017**	0.511 (0.226-1.156)	0.107
TNF-α	**0.278 (0.111-0.701)**	**0.007**	0.697 (0.189-2.573)	0.588	**0.45 (0.183-1.107)**	**0.082**	1.828 (0.53-6.301)	0.339
IFN-γ	**0.355 (0.174-0.725)**	**0.004**	0.475 (0.179-1.262)	0.135	**0.45 (0.213-0.949)**	**0.036**	0.414 (0.17-1.006)	0.051
IL-17A	**2.704 (1.378-5.306)**	**0.004**	**2.715 (1.156-6.375)**	**0.022**	1.382 (0.739-2.587)	0.311	–	–
TLC	0.703 (0.332-1.491)	0.359	–	–	1.218 (0.63-2.354)	0.558	–	–
NLR	**2.967 (1.301-6.766)**	**0.010**	2.036 (0.758-5.463)	0.158	**2.22 (1.149-4.29)**	**0.018**	1.645 (0.653-4.141)	0.291
PLR	0.775 (0.374-1.606)	0.493	–	–	0.716 (0.352-1.46)	0.359	–	–
LMR	0.508 (0.213-1.211)	0.127	–	–	**0.54 (0.274-1.065)**	**0.075**	0.575 (0.207-1.594)	0.287
gender	0.921 (0.479-1.768)	0.804	–	–	0.875 (0.459-1.667)	0.685	–	–
age	0.74 (0.39-1.403)	0.357	–	–	0.968 (0.504-1.86)	0.922	–	–
ECOG (>2)	**10.172 (3.453-29.966)**	**0.000**	**7.546 (2.281-24.966)**	**0.001**	1.659 (0.723-3.81)	0.233	–	–
TNM stage (III-IV)	1.267 (0.526-3.055)	0.598	–	–	0.953 (0.391-2.322)	0.915	–	–
surgery history	1.33 (0.699-2.529)	0.385	–	–	0.957 (0.512-1.79)	0.891	–	–
other chronic basic disease	1.001 (0.484-2.069)	0.999	–	–	1.072 (0.521-2.208)	0.850	–	–
smoked	0.903 (0.47-1.734)	0.758	–	–	0.97 (0.508-1.852)	0.927	–	–
family cancer history	1.373 (0.563-3.349)	0.486	–	–	0.765 (0.319-1.833)	0.548	–	–

Baseline blood parameters were grouped by cut-off value. Elements with a p-value of <0.1 in the univariate analysis and with a p-value of <0.05 in the multivariate analysis were in bold type.

patients (38), there is a dearth of research examining whether PLR, TLC, and LMR values differ between cancer patients and healthy individuals.

Cytokines represent a broad category of intercellular signaling proteins that play a pivotal role in almost every aspect of human immunology. However, the interaction of cytokine signaling activities is highly complex due to the redundancy and pleiotropy exhibited by cytokines. Moreover, there exists an intricate network of "cytokine cascades," wherein the expression of a specific cytokine gene is invariably influenced by other cytokines (39). Cytokines are subject to regulation through various mechanisms. For instance, the anti-inflammatory cytokine IL-10 can suppress the expression of

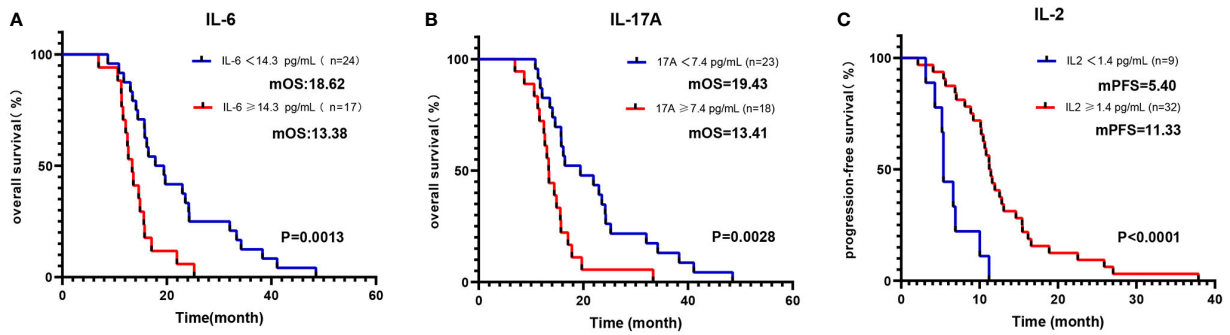

FIGURE 3
Kaplan-Meier curve of OS/PFS of Cohort 1 patients, grouped by cut-off values of baseline blood parameters. Kaplan-Meier OS curves according to baseline cut-off values of **(A)** IL-6; **(B)** IL-17A. Kaplan-Meier PFS curves according to baseline cut-off values of **(C)** IL-2.

10.3389/fimmu.2023.1274431

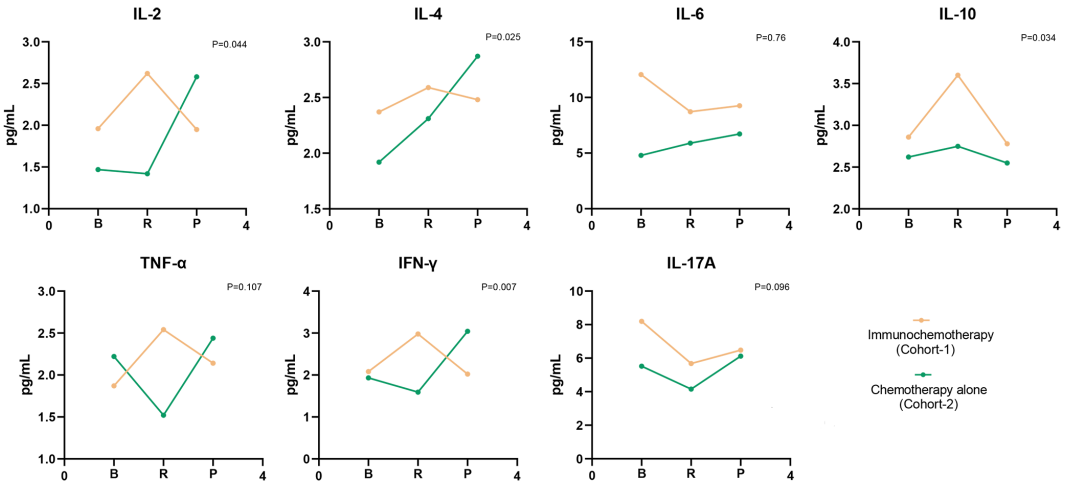

FIGURE 4
Evolution of cytokine levels in patients of two Cohorts. Values corresponded to the median of cytokine titers, and p values were obtained taking into account the difference of cytokine levels in the baseline and response period. B, baseline; R, response, include first complete response (CR) and partial response (PR); P, progression.

TNF-α and IFN-γ, a process referred to as feedback inhibition (40). IL-4, on the other hand, can suppress the production of IFN-γ by T cells, a phenomenon known as antagonism (41), IL-2, conversely, can enhance the production of IFN-γ (42), and IL-17A can synergistically stimulate TNF-α-induced IL-8 production (43).

To explore the prognostic and predictive role of cytokines, we examined the baseline and variations in cytokine levels and assessed their influence on patient outcomes across both cohorts. Cohort 2 had a higher number of patients in the early stages, and more had undergone radical surgery, which is traditionally considered a positive indicator for survival. However, the better OS in Cohort 1 implies that immunotherapy plays a more pivotal role in enhancing survival. A comparative analysis of the two cohorts allowed us to discern the specific effects associated with ICIs.

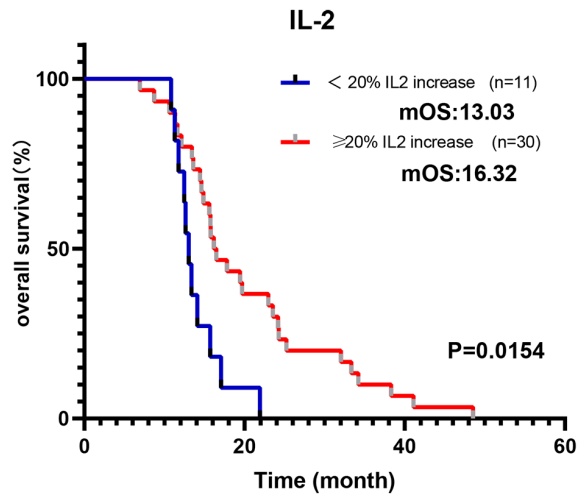

FIGURE 5
Modulation of IL-2 during immunochemotherapy treatment predicts a better prognosis. Cohort 1 patients whose IL-2 increased more than 20% from baseline to response indicate a longer OS.

Based on our findings, IL-2 can be perceived as a predictor of favorable response to ICIs. Higher baseline levels of IL-2 correlated with a significantly extended PFS and OS in Cohort 1, a distinction not observed in Cohort 2. IL-2 is a cytokine important in T-cell proliferation and promoting immune responses, as well as in increasing the activity of natural killer cells (44). Garrelds et al. identified that mice deficient in IL-2 are more prone to gastrointestinal inflammation, resembling human ulcerative colitis (45). Ren et al. documented that combining IL-2 with anti-PD-1 helps overcome tumor resistance to ICIs in mice by reactivating intratumoral CD8+ T cells rather than CD4+ Treg cells (46). Similarly, Ewan A et al. reported a two-year remission resulting from combined anti-PD-1 and intralesional IL-2 therapy in two patients with locoregional metastatic melanoma. This impressive response was partly due to an altered tumor microenvironment, including increased PD-L1 expression and CD8 T cell infiltration (47). Moreover, as shown in Figure 5, patients of Cohort-1 whose IL-2 increased more than 20% from baseline as a response, had a longer OS, which conforms to our preceding view.

IL-6 seems to be a predictor of resistance to ICIs, as patients with higher levels of this factor were found to have significantly worse OS. These observations perfectly agree with the study by Yu et al., who reported that increased circulating levels of IL-6 are associated with poor outcomes in liver cancer patients who received therapy with PD-1 inhibitors (48). IL-6 is a pro-inflammatory cytokine that may contribute to tumor progression by stimulating angiogenesis, invasion, and metastasis (8, 49). In some studies, increased IL-6 serum levels were reported to be associated with metastasis and poor prognosis in prostate, ovarian, and gastrointestinal cancers (21, 50, 51). Tsukamoto et al. indicated that increased IL-6 levels could indicate decreased efficacy of PD-1 blockade in patients with melanoma, and IL-6 blockade augments PD-L1 expression on tumor cells (52). Consistently, a study using IL-6-deficient mice bearing a murine colon cancer cell line found that the lack of IL-6 enhances the induction of effector T cells and

inhibits tumorigenesis. Additionally, PD-L1 expression levels on tumor cells were significantly increased in the IL-6-deficient mice compared with wild-type mice (53). These findings strongly indicate the negative immune role of IL-6, especially in patients receiving ICIs.

IL-17A is a prominent member of the IL-17 family of pro-inflammatory cytokines. Prior research has reported its upregulation in the serum and tumors of GC patients. Kang et al. suggested that IL-17A promotes gastric carcinogenesis by regulating the IL-17RC/NF-κB/NOX1 pathway (54). However, it is worth noting that Karl et al. (55) found decreased IL-17A levels in esophageal adenocarcinoma patients when compared to healthy controls. In our study, we observed a less pronounced elevation of IL-17A in GC patients in comparison to healthy controls (as shown in Figure 1). Furthermore, our study revealed that GC patients with lower levels of IL-17A experienced improved OS, as demonstrated in Figures 2C, 3B. Interestingly, IL-17A exhibited a noticeable decline from baseline to the point of maximum tumor remission. Accumulating evidence indicates that IL-17A activity may contribute to resistance to anti-tumor immunity and play a role in therapeutic failure. It is reported that the IL-17A signaling pathway can enhance the immunosuppressive activity of regulatory T cells (Tregs), leading to tumor growth and development (56). Liu et al. revealed that IL-17A increases PD-L1 expression through the p65/NRF1/miR-15b-5p axis, thereby promoting resistance to anti-PD-1 therapy. Blocking IL-17A improved the efficacy of anti-PD-1 treatment in murine models of MSS CRC (57). Another clinical analysis suggested that the activation of IL-17A signaling is associated with the failure of anti-PD-1 therapy in patients with colorectal cancer (58).

Prior research has shown that tumor cells release cytokines, vascular endothelial growth factors, and chemokines, which attract neutrophils into tumors. These neutrophils facilitate vascular invasion and contribute to the metastatic potential of tumor cells (59). Neutrophils also participate in creating an immunosuppressive microenvironment by releasing myeloperoxidase and arginase-1, and upregulating PD-L1. This, in turn, reduces the number of tumor-infiltrating lymphocytes (TIL) and leads to decreased effectiveness of immunotherapy (60). The correlation between peripheral blood NLR and clinical outcomes may be explained by the association between tumor-infiltrating lymphocytes and neutrophils, which results in reduced anti-tumor T-cell responses (61, 62).

As depicted in Figure 4, we observed changes in cytokine levels after treatment in both Cohorts. Cancer cells are the primary sources of cytokines, so successful treatment can lead to reductions in specific cytokines, as observed for IL-2, TNF-α, IFN-γ, and IL-17A in Cohort 2. However, patients treated with chemotherapy alone exhibited stabilization or an increase in levels of IL-4, IL-6, and IL-10 cytokines, which may suggest that the crucial cell compartments contributing to the presence of these cytokines might not be affected by chemotherapy, such as M2 macrophages in the tumor microenvironment (63, 64). Furthermore, the addition of ICIs increased concentrations of cytokines after treatment globally and appeared to counteract the effect of chemotherapy, which typically decreases cytokine levels. It is believed that cytokine levels reflect the immunosuppressive state to some extent, where a high level of cytokines indicates that the body is more sensitive to PD-1 antibodies (65). This finding is consistent with our observation that GC patients in Cohort 1 with more than 20% variation in IL-2 from baseline to the point of maximum remission had better OS.

Conclusion

In conclusion, ongoing studies are actively investigating the predictive role of peripheral blood indicators in the effectiveness and prognosis of immunotherapy. However, comprehensive data on the use of Immune Checkpoint Inhibitors (ICIs) in advanced gastric cancer patients, both domestically and internationally, are still limited. Therefore, further prospective validation is required. To sum up, serum cytokines have varying significance in assessing the response of gastric cancer (GC) patients to anti-PD-1 therapy. Baseline levels of IL-2, IL-6, IL-17A, and Neutrophil-to-Lymphocyte Ratio (NLR), as well as changes in IL-2 levels over time, may serve as convenient predictive biomarkers for identifying GC patients who are likely to benefit from the addition of anti-PD-1 monoclonal antibodies to chemotherapy.

Data availability statement

The raw data supporting the conclusions of this article will be made available by the authors, without undue reservation.

Ethics statement

The studies involving humans were approved by Research and Clinical Trial Ethics Committee of the First Affiliated Hospital of Zhengzhou University. The studies were conducted in accordance with the local legislation and institutional requirements. The ethics committee/institutional review board waived the requirement of written informed consent for participation from the participants or the participants' legal guardians/next of kin because The study was retrospective, with anonymous patient information obtained through the hospital record system, and all patients were deceased.

Author contributions

YH: Data curation, Formal Analysis, Writing – original draft. XL: Validation, Visualization, Writing – original draft. YY: Investigation, Software, Writing – review & editing. HS: Conceptualization, Writing – review & editing. SW: Investigation, Writing – review & editing. MG: Funding acquisition, Methodology, Writing – review & editing.

Funding

The author(s) declare financial support was received for the research, authorship, and/or publication of this article. This study was supported by Henan Province young and middle-aged health science and technology innovation leading talent training program (grant no. YXKC2022011); Beijing Science and Technology Innovation Medical Development Foundation (grant no. KC2021-JX-0186-48); Beijing Xisike Clinical Oncology Research Foundation (grant no. Y-HR2019-0303).

Conflict of interest

The authors declare that the research was conducted in the absence of any commercial or financial relationships that could be construed as a potential conflict of interest.

Publisher's note

Supplementary material

The Supplementary Material for this article can be found online at: https://www.frontiersin.org/articles/10.3389/fimmu.2023.1274431/full#supplementary-material

References

1. Sung H, Ferlay J, Siegel RL, Laversanne M, Soerjomataram I, Jemal A, et al. Global cancer statistics 2020: globocan estimates of incidence and mortality worldwide for 36 cancers in 185 countries. *CA Cancer J Clin* (2021) 71(3):209–49. doi: 10.3322/caac.21660

2. Zaanan A, Bouché O, Benhaim L, Buecher B, Chapelle N, Dubreuil O, et al. Gastric cancer: french intergroup clinical practice guidelines for diagnosis, treatments and follow-up (Snfge, ffcd, gercor, unicancer, sfcd, sfed, sfro). *Dig Liver Dis* (2018) 50 (8):768–79. doi: 10.1016/j.dld.2018.04.025

3. Vaddepally RK, Kharel P, Pandey R, Garje R, Chandra AB. Review of indications of fda-approved immune checkpoint inhibitors per nccn guidelines with the level of evidence. *Cancers (Basel)* (2020) 12(3):738. doi: 10.3390/cancers12030738

4. Havel JJ, Chowell D, Chan TA. The evolving landscape of biomarkers for checkpoint inhibitor immunotherapy. *Nat Rev Cancer* (2019) 19(3):133–50. doi: 10.1038/s41568-019-0116-x

5. Li K, Zhang A, Li X, Zhang H, Zhao L. Advances in clinical immunotherapy for gastric cancer. *Biochim Biophys Acta Rev Cancer* (2021) 1876(2):188615. doi: 10.1016/j.bbcan.2021.188615

6. Sundar R, Smyth EC, Peng S, Yeong JPS, Tan P. Predictive biomarkers of immune checkpoint inhibition in gastroesophageal cancers. *Front Oncol* (2020) 10:763. doi: 10.3389/fonc.2020.00763

7. Lin W-W, Karin M. A cytokine-mediated link between innate immunity, inflammation, and cancer. *J Clin Invest* (2007) 117(5):1175–83. doi: 10.1172/jci31537

8. Dranoff G. Cytokines in cancer pathogenesis and cancer therapy. *Nat Rev Cancer* (2004) 4(1):11–22. doi: 10.1038/nrc1252

9. Melero I, Normanno N. Harmful cytokines in cancer immunology and immunotherapy: biomarkers and targets? *Ann Oncol* (2021) 32(11):1311–3. doi: 10.1016/j.annonc.2021.09.010

10. Booka E, Kikuchi H, Haneda R, Soneda W, Kawata S, Murakami T, et al. Neutrophil-to-lymphocyte ratio to predict the efficacy of immune checkpoint inhibitor in upper gastrointestinal cancer. *Anticancer Res* (2022) 42(6):2977–87. doi: 10.21873/anticanres.15781

11. Ozawa Y, Amano Y, Kanata K, Hasegwa H, Matsui T, Kakutani T, et al. Impact of early inflammatory cytokine elevation after commencement of pd-1 inhibitors to predict efficacy in patients with non-small cell lung cancer. *Med Oncol* (2019) 36(4):6. doi: 10.1007/s12032-019-1255-3

12. Oken MM, Creech RH, Tormey DC, Horton J, Davis TE, McFadden ET, et al. Toxicity and response criteria of the eastern cooperative oncology group. *Am J Clin Oncol* (1982) 5(6):649–55. doi: 10.1097/00000421-198212000-00014

13. Eisenhauer EA, Therasse P, Bogaerts J, Schwartz LH, Sargent D, Ford R, et al. New response evaluation criteria in solid tumours: revised recist guideline (Version 1.1). *Eur J Cancer* (2009) 45(2):228–47. doi: 10.1016/j.ejca.2008.10.026

14. Rosenberg SA. Il-2: the first effective immunotherapy for human cancer. *J Immunol* (2014) 192(12):5451–8. doi: 10.4049/jimmunol.1490019

15. Shokrzadeh M, Mohammadpour A, Hoseini V, Abediankenari S, Ghassemi-Barghi N, Tabari YS. Serum cytokine of il-2, il-10 and il-12 levels in patients with stomach adenocarcinoma. *Arquivos gastroenterologia* (2018) 55(4):385–9. doi: 10.1590/s0004-2803.201800000-83

16. Forones NM, Mandowsky SV, Lourenco LG. Serum levels of interleukin-2 and tumor necrosis factor-alpha correlate to tumor progression in gastric cancer. *Hepato-Gastroenterology* (2001) 48(40):1199–201.

17. Li Z, Chen L, Qin Z. Paradoxical roles of il-4 in tumor immunity. *Cell Mol Immunol* (2009) 6(6):415–22. doi: 10.1038/cmi.2009.53

18. Gocher AM, Workman CJ, Vignali DAA. Interferon-gamma: teammate or opponent in the tumour microenvironment? *Nat Rev Immunol* (2022) 22(3):158–72. doi: 10.1038/s41577-021-00566-3

19. Kumari N, Agrawal U, Mishra AK, Kumar A, Vasudeva P, Mohanty NK, et al. Predictive role of serum and urinary cytokines in invasion and recurrence of bladder cancer. *Tumor Biol* (2017) 39(4):14. doi: 10.1177/1010428317697552

20. Sánchez-Zauco N, Torres J, Gómez A, Camorlinga-Ponce M, Muñoz-Pérez L, Herrera-Goepfert R, et al. Circulating blood levels of il-6, ifn-Γ, and il-10 as potential diagnostic biomarkers in gastric cancer: A controlled study. *BMC Cancer* (2017) 17 (1):384. doi: 10.1186/s12885-017-3310-9

21. Oka M, Yamamoto K, Takahashi M, Hakozaki M, Abe T, Iizuka N, et al. Relationship between serum levels of interleukin 6, various disease parameters and malnutrition in patients with esophageal squamous cell carcinoma. *Cancer Res* (1996) 56(12):2776–80.

22. Kim DK, Oh SY, Kwon HC, Lee S, Kwon KA, Kim BG, et al. Clinical significances of preoperative serum interleukin-6 and C-reactive protein level in operable gastric cancer. *BMC Cancer* (2009) 9:155. doi: 10.1186/1471-2407-9-155

23. Łukaszewicz-Zając M, Mroczko B, Kozłowski M, Nikliński J, Laudański J, Szmitkowski M. Higher importance of interleukin 6 than classic tumor markers (Carcinoembryonic antigen and squamous cell cancer antigen) in the diagnosis of esophageal cancer patients. *Dis Esophagus* (2012) 25(3):242–9. doi: 10.1111/j.1442-2050.2011.01242.x

24. Lippitz BE. Cytokine patterns in patients with cancer: A systematic review. *Lancet Oncol* (2013) 14(6):E218–E28. doi: 10.1016/s1470-2045(12)70582-x

25. Taniguchi K, Karin M. Il-6 and related cytokines as the critical lynchpins between inflammation and cancer. *Semin Immunol* (2014) 26(1):54–74. doi: 10.1016/j.smim.2014.01.001

26. Yamagiwa Y, Meng F, Patel T. Interleukin-6 decreases senescence and increases telomerase activity in Malignant human cholangiocytes. *Life Sci* (2006) 78(21):2494–502. doi: 10.1016/j.lfs.2005.10.015

27. Mocellin S, Marincola FM, Young HA. Interleukin-10 and the immune response against cancer: A counterpoint. *J Leukocyte Biol* (2005) 78(5):1043–51. doi: 10.1189/jlb.0705358

28. O'Garra A, Murphy KM. From il-10 to il-12: how pathogens and their products stimulate apcs to induce T(H)1 development. *Nat Immunol* (2009) 10(9):929–32. doi: 10.1038/ni0909-929

29. Gong K, Guo G, Beckley N, Zhang Y, Yang X, Sharma M, et al. Tumor necrosis factor in lung cancer: complex roles in biology and resistance to treatment. *Neoplasia* (2021) 23(2):189–96. doi: 10.1016/j.neo.2020.12.006

30. Cruceriu D, Baldasici O, Balacescu O, Berindan-Neagoe I. The dual role of tumor necrosis factor-alpha (Tnf-A) in breast cancer: molecular insights and therapeutic approaches. *Cell Oncol (Dordr)* (2020) 43(1):1–18. doi: 10.1007/s13402-019-00489-1

31. Mercogliano MF, Bruni S, Elizalde PV, Schillaci R. Tumor necrosis factor A Blockade: an opportunity to tackle breast cancer. *Front Oncol* (2020) 10:584. doi: 10.3389/fonc.2020.00584

32. Jiang M, Liu J, Yang D, Tross D, Li P, Chen F, et al. A tnfr2 antibody by countering immunosuppression cooperates with hmgn1 and R848 immune stimulants to inhibit murine colon cancer. *Int Immunopharmacol* (2021) 101(Pt A):108345. doi: 10.1016/j.intimp.2021.108345

33. Montfort A, Colacios C, Levade T, Andrieu-Abadie N, Meyer N, Ségui B. The tnf paradox in cancer progression and immunotherapy. *Front Immunol* (2019) 10:1818. doi: 10.3389/fimmu.2019.01818

34. Ji X, Peng Z, Li X, Yan Z, Yang Y, Qiao Z, et al. Neutralization of tnfα in tumor with a novel nanobody potentiates paclitaxel-therapy and inhibits metastasis in breast cancer. *Cancer Lett* (2017) 386:24–34. doi: 10.1016/j.canlet.2016.10.031

35. Yu M, Zhou X, Niu L, Lin G, Huang J, Zhou W, et al. Targeting transmembrane tnf-A Suppresses breast cancer growth. *Cancer Res* (2013) 73(13):4061–74. doi: 10.1158/0008-5472.Can-12-3946

36. Coley WB. The treatment of inoperable sarcoma by bacterial toxins (the mixed toxins of the streptococcus erysipelas and the bacillus prodigiosus). *Proc R Soc Med* (1910) 3(Surg Sect):1–48. doi: 10.1177/003591571000301601

37. Xiong Q, Huang Z, Xin L, Qin B, Zhao X, Zhang J, et al. Post-treatment neutrophil-to-lymphocyte ratio (Nlr) predicts response to anti-pd-1/pd-L1 antibody in sclc patients at early phase. *Cancer Immunol Immunother* (2021) 70(3):713–20. doi: 10.1007/s00262-020-02706-5

38. Chen T, Song C, Liang G, Xu X, Wang C, Zhang Z, et al. Neutrophil-to-lymphocyte ratio, platelet-to-lymphocyte ratio, and their variations as a basis for a prediction model in advanced nsclc patients receiving anlotinib. *Dis Markers* (2022) 2022:5879137. doi: 10.1155/2022/5879137

39. Jiang P, Zhang Y, Ru B, Yang Y, Trang V, Paul R, et al. Systematic investigation of cytokine signaling activity at the tissue and single-cell levels. *Nat Methods* (2021) 18 (10):1181. doi: 10.1038/s41592-021-01274-5

40. D'Andrea A, Aste-Amezaga M, Valiante NM, Ma X, Kubin M, Trinchieri G. Interleukin 10 (Il-10) inhibits human lymphocyte interferon gamma-production by suppressing natural killer cell stimulatory factor/il-12 synthesis in accessory cells. *J Exp Med* (1993) 178(3):1041–8. doi: 10.1084/jem.178.3.1041

41. Wurtz O, Bajenoff M, Guerder S. Il-4-mediated inhibition of ifn-gamma production by cd4(+) T cells proceeds by several developmentally regulated mechanisms. *Int Immunol* (2004) 16(3):501–8. doi: 10.1093/intimm/dxh050

42. Kasahara T, Hooks JJ, Dougherty SF, Oppenheim JJ. Interleukin 2-mediated immune interferon (Ifn-gamma) production by human T cells and T cell subsets. *J Immunol (Baltimore Md 1950)* (1983) 130(4):1784–9. doi: 10.4049/jimmunol.130.4.1784

43. Honda K, Wada H, Nakamura M, Nakamoto K, Inui T, Sada M, et al. Il-17a synergistically stimulates tnf-alpha-induced il-8 production in human airway epithelial cells: A potential role in amplifying airway inflammation. *Exp Lung Res* (2016) 42 (4):205–16. doi: 10.1080/01902148.2016.1190796

44. Pol JG, Caudana P, Paillet J, Piaggio E, Kroemer G. Effects of interleukin-2 in immunostimulation and immunosuppression. *J Exp Med* (2020) 217(1):e20191247. doi: 10.1084/jem.20191247

45. Garrelds IM, van Meeteren ME, Meijssen MA, Zijlstra FJ. Interleukin-2-deficient mice: effect on cytokines and inflammatory cells in chronic colonic disease. *Dig Dis Sci* (2002) 47(3):503–10. doi: 10.1023/a:1017995414697

46. Holcomb EA, Zou W. A forced marriage of il-2 and pd-1 antibody nurtures tumor-infiltrating T cells. *J Clin Invest* (2022) 132(3):e156628. doi: 10.1172/jci156628

47. Langan EA, Kümpers C, Graetz V, Perner S, Zillikens D, Terheyden P. Intralesional interleukin-2: A novel option to maximize response to systemic immune checkpoint therapy in loco-regional metastatic melanoma. *Dermatol Ther* (2019) 32(3):e12901. doi: 10.1111/dth.12901

48. Yu Y, Wang S, Su N, Pan S, Tu B, Zhao J, et al. Increased circulating levels of crp and il-6 and decreased frequencies of T and B lymphocyte subsets are associated with immune-related adverse events during combination therapy with pd-1 inhibitors for liver cancer. *Front Oncol* (2022) 12:906824. doi: 10.3389/fonc.2022.906824

49. Coussens LM, Werb Z. Inflammation and cancer. *Nature* (2002) 420(6917):860–7. doi: 10.1038/nature01322

50. George DJ, Halabi S, Shepard TF, Sanford B, Vogelzang NJ, Small EJ, et al. The prognostic significance of plasma interleukin-6 levels in patients with metastatic hormone-refractory prostate cancer: results from cancer and leukemia group B 9480. *Clin Cancer Res* (2005) 11(5):1815–20. doi: 10.1158/1078-0432.Ccr-04-1560

51. Scambia G, Testa U, Benedetti Panici P, Foti E, Martucci R, Gadducci A, et al. Prognostic significance of interleukin 6 serum levels in patients with ovarian cancer. *Br J Cancer* (1995) 71(2):354–6. doi: 10.1038/bjc.1995.71

52. Tsukamoto H, Fujieda K, Miyashita A, Fukushima S, Ikeda T, Kubo Y, et al. Combined blockade of il6 and pd-1/pd-L1 signaling abrogates mutual regulation of their immunosuppressive effects in the tumor microenvironment. *Cancer Res* (2018) 78 (17):5011–22. doi: 10.1158/0008-5472.Can-18-0118

53. Ohno Y, Toyoshima Y, Yurino H, Monma N, Xiang H, Sumida K, et al. Lack of interleukin-6 in the tumor microenvironment augments type-1 immunity and increases the efficacy of cancer immunotherapy. *Cancer Sci* (2017) 108(10):1959–66. doi: 10.1111/cas.13330

54. Kang JH, Park S, Rho J, Hong EJ, Cho YE, Won YS, et al. Il-17a promotes helicobacter pylori-induced gastric carcinogenesis *via* interactions with il-17rc. *Gastric Cancer* (2023) 26(1):82–94. doi: 10.1007/s10120-022-01342-5

55. Karstens KF, Kempski J, Giannou AD, Freiwald E, Reeh M, Tachezy M, et al. Systemic interleukin 10 levels indicate advanced stages while interleukin 17a levels correlate with reduced survival in esophageal adenocarcinomas. *PloS One* (2020) 15(4): e0231833. doi: 10.1371/journal.pone.0231833

56. Chen J, Ye X, Pitmon E, Lu M, Wan J, Jellison ER, et al. Il-17 inhibits cxcl9/10-mediated recruitment of cd8(+) cytotoxic T cells and regulatory T cells to colorectal tumors. *J Immunother Cancer* (2019) 7(1):324. doi: 10.1186/s40425-019-0757-z

57. Liu C, Liu R, Wang B, Lian J, Yao Y, Sun H, et al. Blocking il-17a enhances tumor response to anti-pd-1 immunotherapy in microsatellite stable colorectal cancer. *J Immunother Cancer* (2021) 9(1):e001895. doi: 10.1136/jitc-2020-001895

58. Llosa NJ, Luber B, Tam AJ, Smith KN, Siegel N, Awan AH, et al. Intratumoral adaptive immunosuppression and type 17 immunity in mismatch repair proficient colorectal tumors. *Clin Cancer Res* (2019) 25(17):5250–9. doi: 10.1158/1078-0432.Ccr-19-0114

59. Guo Y, Xiang D, Wan J, Yang L, Zheng C. Focus on the dynamics of neutrophil-to-lymphocyte ratio in cancer patients treated with immune checkpoint inhibitors: A meta-analysis and systematic review. *Cancers (Basel)* (2022) 14(21):5297. doi: 10.3390/cancers14215297

60. Oberg HH, Wesch D, Kalyan S, Kabelitz D. Regulatory interactions between neutrophils, tumor cells and T cells. *Front Immunol* (2019) 10:1690. doi: 10.3389/fimmu.2019.01690

61. Takakura K, Ito Z, Suka M, Kanai T, Matsumoto Y, Odahara S, et al. Comprehensive assessment of the prognosis of pancreatic cancer: peripheral blood neutrophil-lymphocyte ratio and immunohistochemical analyses of the tumour site. *Scand J Gastroenterol* (2016) 51(5):610–7. doi: 10.3109/00365521.2015.1121515

62. Ohki S, Shibata M, Gonda K, Machida T, Shimura T, Nakamura I, et al. Circulating myeloid-derived suppressor cells are increased and correlate to immune suppression, inflammation and hypoproteinemia in patients with cancer. *Oncol Rep* (2012) 28(2):453–8. doi: 10.3892/or.2012.1812

63. Kitajima M, Ziegler SF. Cutting edge: identification of the thymic stromal lymphopoietin-responsive dendritic cell subset critical for initiation of type 2 contact hypersensitivity. *J Immunol* (2013) 191(10):4903–7. doi: 10.4049/jimmunol.1302175

64. Dijkgraaf EM, Heusinkveld M, Tummers B, Vogelpoel LT, Goedemans R, Jha V, et al. Chemotherapy alters monocyte differentiation to favor generation of cancer-supporting M2 macrophages in the tumor microenvironment. *Cancer Res* (2013) 73 (8):2480–92. doi: 10.1158/0008-5472.Can-12-3542

65. Rahimi Kalateh Shah Mohammad G, Ghahremanloo A, Soltani A, Fathi E, Hashemy SI. Cytokines as potential combination agents with pd-1/pd-L1 blockade for cancer treatment. *J Cell Physiol* (2020) 235(7-8):5449–60. doi: 10.1002/jcp.29491

frontiers | Frontiers in Immunology

TYPE Original Research
PUBLISHED 31 October 2023
DOI 10.3389/fimmu.2023.1273422

OPEN ACCESS

EDITED BY
Takaji Matsutani,
Maruho, Japan

REVIEWED BY
Xuan Wu,
Zhengzhou University, China
Jin Zhang,
University of Mississippi Medical Center, United States

*CORRESPONDENCE
Yuan Tian
tytytianyuan@aliyun.com

†These authors have contributed equally to this work

RECEIVED 06 August 2023
ACCEPTED 16 October 2023
PUBLISHED 31 October 2023

CITATION
Li Z, Yin Z, Luan Z, Zhang C, Wang Y, Zhang K, Chen F, Yang Z and Tian Y (2023) Comprehensive analyses for the coagulation and macrophage-related genes to reveal their joint roles in the prognosis and immunotherapy of lung adenocarcinoma patients.
Front. Immunol. 14:1273422.
doi: 10.3389/fimmu.2023.1273422

Comprehensive analyses for the coagulation and macrophage-related genes to reveal their joint roles in the prognosis and immunotherapy of lung adenocarcinoma patients

Zhuoqi Li[1,2†], Zongxiu Yin[3†], Zupeng Luan[4†], Chi Zhang[5†], Yuanyuan Wang[6], Kai Zhang[7], Feng Chen[8], Zhensong Yang[9] and Yuan Tian[1,2*]

[1]Department of Otolaryngology-Head and Neck Surgery, Shandong Provincial ENT Hospital, Shandong University, Jinan, China, [2]Radiotherapy Department, Shandong Second Provincial General Hospital, Shandong University, Jinan, China, [3]Department of Pulmonary and Critical Care Medicine, Jinan Central Hospital Affiliated to Shandong First Medical University, Jinan, China, [4]Department of Radiation Oncology, Jinan Third People's Hospital, Jinan, China, [5]Department of Cardiology, The Second Hospital, Cheeloo College of Medicine, Shandong University, Jinan, China, [6]Department of Oncology, The Second Affiliated Hospital of Shandong University of Traditional Chinese Medicine, Jinan, China, [7]Generalsurgery Department, Wen-shang County People's Hospital, Wenshang, China, [8]Department of Thoracic Surgery, Shandong Cancer Hospital and Institute, Shandong First Medical University and Shandong Academy of Medical Sciences, Jinan, China, [9]Department of Gastrointestinal Surgery, Yantai Yuhuangding Hospital, Qingdao University, Yantai, China

Purpose: This study aims to explore novel biomarkers related to the coagulation process and tumor-associated macrophage (TAM) infiltration in lung adenocarcinoma (LUAD).

Methods: The macrophage M2-related genes were obtained by Weighted Gene Co-expression Network Analysis (WGCNA) in bulk RNA-seq data, while the TAM marker genes were identified by analyzing the scRNA-seq data, and the coagulation-associated genes were obtained from MSigDB and KEGG databases. Survival analysis was performed for the intersectional genes. A risk score model was subsequently constructed based on the survival-related genes for prognosis prediction and validated in external datasets.

Results: In total, 33 coagulation and macrophage-related (COMAR) genes were obtained, 19 of which were selected for the risk score model construction. Finally, 10 survival-associated genes (APOE, ARRB2, C1QB, F13A1, FCGR2A, FYN, ITGB2, MMP9, OLR1, and VSIG4) were involved in the COMAR risk score model. According to the risk score, patients were equally divided into low- and high-risk groups, and the prognosis of patients in the high-risk group was significantly worse than that in the low-risk group. The ROC curve indicated that the risk score model had high sensitivity and specificity, which was validated in multiple external datasets. Moreover, the model also had high efficacy in predicting the clinical outcomes of LUAD patients who received anti-PD-1/PD-L1 immunotherapy.

Conclusion: The COMAR risk score model constructed in this study has excellent predictive value for the prognosis and immunotherapeutic clinical outcomes of patients with LUAD, which provides potential biomarkers for the treatment and prognostic prediction.

KEYWORDS

lung adenocarcinoma, coagulation, tumor-associated macrophage, risk score model, prognosis, immunotherapy

1 Introduction

Although the screening and treatment of lung cancer have witnessed greater improvement in the past few years, there are still ongoing challenges in improving the clinical outcomes of patients (1, 2). Lung adenocarcinoma (LUAD), a kind of non-small cell lung cancer (NSCLC), was the most common lung malignancy with genetic and morphologic diversity, and the pathogenesis and treatment of LUAD still need further exploration (3, 4). The tumor microenvironment (TME) plays a critical role in tumor progression and treatment (5, 6). Tumor-associated macrophage (TAM) was an essential component of the tumor microenvironment, and it contributed to tumor growth, metastasis, and immunosuppression, as well as tumor resistance to chemotherapy and checkpoint blockade immunotherapy (7, 8).

There were also a number of studies about the roles of TAMs in NSCLC or LUAD. TAMs in the TME usually originated from two main sources: one was the bone marrow (BM)-derived monocytic precursors; another was the tissue-resident macrophages (TRMs) originated from embryonic precursors (8). After egress from the BM, monocytes (or M-MDSCs) were recruited to the TME via chemokines of the CC and CXC families, such as CCL2, CCL5, and CXCL12, that were produced by cancer cells early during tumorigenesis (9). Subsequently, the myeloid cells recruited to tumors would convert to TAMs under the activation of integrin (9). CCR2 and CX3CR1 were the receptors of the chemokines CCL2 and CX3CL1, respectively, and they were proven to play significant roles in macrophage migrating to lung cancer and M2 polarization (10).

TAMs shaped the TME of NSCLC. They accumulated close to tumor cells in the early stage of tumor formation to promote epithelial–mesenchymal transition and invasiveness of tumor cells, and they also caused a potent regulatory T-cell response that suppressed the adaptive immunity of tumor cells (11). TAMs can promote LUAD growth or metastasis by secreting some factors that can be adopted by the tumor cells in the TME, such as miR-942 (12), LINC00273 (13), and HB-EGF (14), as well as by upregulating CRYAB expression in tumor cells (15). The M2 subtype of TAM enhances the expression of VEGF-A and VEGF-C, which is significantly associated with angiogenesis and lymphangiogenesis, contributing to the progression of NSCLC (16). TAMs also have a great impact on the chemotherapy and anti-PD1/PD-L1 immunotherapy for LUAD (17, 18). Recent studies found that TAMs had a close relationship with coagulation. On the one hand, TAM was an important contributor to the coagulation in tumors by producing factor X (FX) and leading to cell-autonomous FXa-PAR2 signaling in these cells within the TME (19, 20). On the other hand, some coagulation-related factors can regulate the functions of TAMs, consequently influencing the progression of tumors. For example, thrombin and plasminogen activator inhibitor-1 (PAI-1) can facilitate the M2 polarization of TAMs in ovarian and breast cancer, respectively (21, 22). Tissue factor (TF) expression by tumor cells can recruit TAMs to the lung, supporting the formation of the premetastatic niche (23). The lung plays an important role in blood coagulation, and there was evidence that the lung is a primary site of terminal platelet production (24). Lung cancer is a non-negligible cause of the disturbance of blood coagulation, which can lead to venous thromboembolism, the second leading cause of death in cancer patients (5, 25). NSCLC has a relatively high risk of venous thromboembolism among lung cancer types, and LUAD is especially an independent risk factor for it (26, 27). The pathophysiology of this phenomenon was complex and not entirely understood, and several related risk factors were involved (25).

The study was designed to further explore the significance of coagulation and TAM infiltration in shaping the TME of LUAD and predicting the prognosis and immunotherapeutic clinical outcomes of LUAD patients.

2 Materials and methods

2.1 Data collection and preprocessing

The gene expression profiles of The Cancer Genome Atlas (TCGA)-LUAD cohort (converted to log2(FPKM+1)) were downloaded using the R package "TCGAbiolinks". The officially corrected survival information (overall survival (OS)) and clinical information (including age, stage, gender, grade, etc.) of LUAD patients in TCGA were downloaded from the cBioPortal database.

The gene expression profiles and clinical information of the GSE30219, GSE37745, GSE41271, GSE42127, GSE50081, GSE68465, and GSE72094 datasets were downloaded from the GEO database. In these datasets, the primary tumors were

collected by surgical resection from lung adenocarcinoma patients. The patients in these cohorts have been collected with high-quality gene expression data and complete clinical and follow-up information. None of the patients received preoperative chemotherapy or radiotherapy. The probes in the GEO datasets corresponding to more than one gene would be removed. When multiple probes corresponded to the same symbol, the average value would be taken.

We filtered out the samples with incomplete survival information in TCGA and the GEO datasets. The GSE68465 dataset was used as the training cohort, while the other datasets were taken as the validation cohorts. The GSE131907 dataset, containing single-cell transcriptome data from 15 lung adenocarcinoma patients, was also downloaded from the GEO database. The cellular annotation results, reported by Kim, were used for the subsequent analyses (28). A total of 535 coagulation-related genes were obtained from the coagulation-related pathways in the MSigDB and Kyoto Encyclopedia of Genes and Genomes (KEGG)databases. The detailed pathways and the numbers of the corresponding genes were listed in (Table 1), and the names of those 535 genes are listed in Supplementary Table S1.

2.2 The construction of the gene co-expression network by WGCNA analysis

Weighted Gene Co-expression Network Analysis (WGCNA) aimed to identify co-expressed gene modules, explore the relationships between the gene co-expression networks and the phenotypes of interest, and study the core genes in the network. WGCNA analysis was performed using the genes with the top 75% highest variation coefficient in the expression profile of the GSE68465 dataset. First, the correlation coefficient between every two genes was calculated, and the connections between genes in the network were made to obey a scale-free network using the weighted values of the correlation coefficients. Subsequently, a hierarchical clustering tree was constructed based on the correlation coefficients among these genes. Different branches of the clustering tree represented different gene modules, and different colors represented different modules. Next, the significance of the modules was calculated and used to calculate the correlation between the macrophage M2 infiltration scores and different modules, and the genes in each module, considered signature genes of the modules, were recorded.

TABLE 1 The coagulation-related pathways and the number of genes involved in each pathway.

Pathways	Count
GOBP_BLOOD_COAGULATION_INTRINSIC_PATHWAY	18
GOBP_COAGULATION	347
GOBP_NEGATIVE_REGULATION_OF_COAGULATION	52
GOBP_POSITIVE_REGULATION_OF_COAGULATION	24
GOBP_REGULATION_OF_COAGULATION	71
HALLMARK_COAGULATION	138
KEGG_COMPLEMENT_AND_COAGULATION_CASCADES	69
KEGG_PLATELET_ACTIVATION	124
KEGG_COMPLEMENT_AND_COAGULATION_CASCADES	86

2.3 Processing the single-cell RNA-seq data

The R package "Seurat" was used to preprocess the scRNA-seq data. First, we set the following thresholds in which the cells can be included in the study: (1) cells with more than 200 and less than 10,000 genes; (2) cells with less than 20% mitochondrial gene expression; and (3) cells with more than 100 and less than 150,000 UMIs. The "NormalizeData" function was used to normalize the scRNA-seq dataset, and 3,000 highly variable genes were identified using the "mvp" method of the "FindVariableFeatures" function. Subsequently, we made scale transformed for the data and performed principal component analysis (PCA) for dimensionality reduction. We eventually selected the top 20 principal components for the downstream analyses. Since the data were obtained from different samples, batch correction was performed using the R package "Harmony" to avoid the interference of the batch effect on the subsequent analyses. We used the UMAP algorithm to mine and visualize the data. Finally, we annotated the cell populations based on the signatures provided by the study of Kim et al. (28).

We identified differentially expressed genes (DEGs) between each cell type by using the "FindAllMarkers" function in the R package "Seurat", where min.pct = 0.1, logfc. threshold = 0.25, and only.pos = FALSE were set, while only genes with p-values of< 0.05 would be retained. We used the R package "scRNAtoolVis" to plot the volcano chart for the DEGs between different cell types.

2.4 Mutation and CNV analyses

R package "maftools" was employed to plot the waterfall maps of the mutation landscape of the 33 coagulation and macrophage-related (COMAR) genes in the TCGA-LUAD cohort. The CNV data of TCGA-LUAD was downloaded from the "UCSC Xena" website, and then the CNV frequency was presented in a plot finished by R software.

2.5 Construction of the COMAR prognostic model

The COMAR prognostic model was constructed based on 33 coagulation and macrophage-related genes. First, Kaplan-Meier survival analysis was performed to divide the patients into high and low-expression groups with the best cut-off value for each gene, and 19 genes that had significant differences in survival status between the two groups were identified. Next, multivariate Cox regression analysis for the 19 genes was used to construct the 10-gene prognostic model. In the COMAR prognostic model, patients'

risk scores were calculated based on the expression levels of each prognosis-related gene and their corresponding regression coefficients:

$$\text{Risk score} = \sum_{i=1}^{n} \text{expi} * \beta i$$

In the above formula, "*n*" represents the number of genes; "expi" represents the expression level of gene "i"; and "βi" represents the coefficient of gene "i". Patients were divided into high- and low-risk groups according to the median risk score, and survival analysis was performed using the R package "survminer" to analyze OS in the high- and low-risk groups. The "survminer" and "timeROC" packages were used to perform time-dependent ROC curve analysis to check the predictive efficacy of the prognostic models. Finally, risk scores would be calculated in the validation cohorts using the same formula.

2.6 Biological functional annotation

The GO_BP and GO_MF enrichment analyses were performed using the Gene Set Variation Analysis (GSVA) algorithm to calculate the score for each pathway in each sample. The differentially activated pathways in the high- and low-risk score groups were identified using the "limma" package, with the differential threshold set at FDR< 0.05. Differentially activated KEGG pathways between the high- and low-risk score groups were analyzed using Gene Set Enrichment Analysis (GSEA).

2.7 The estimation of immune cell infiltration in the TME

The CIBERSORT algorithm in the R package "IOBR" was applied to evaluate the immune cell abundance in the samples of the GSE68465 dataset. Specifically, the CIBERSORT algorithm was used to calculate the infiltration fractions of the 22 types of immune cells. CIBERSORT was considered superior to previous methods of deconvolution when analyzing unknown mixture content and noise. This algorithm could be used to statistically estimate the relative proportions of cell subgroups in complex tissues according to gene expression profiles, making it a useful tool for estimating the abundance of specific cell types in mixed tissues.

2.8 Collecting the immunotherapeutic cohorts

The GSE126044 dataset, containing seven LUAD patients who received anti-PD-1 immunotherapy, was downloaded from the GEO database. The GSE135222 dataset containing 27 NSCLC patients with anti-PD1/PD-L1 immunotherapy was also downloaded from the GEO database. We calculated the risk scores for each sample in these datasets using the same algorithm as the previous model and made a survival analysis. We also compared the difference in risk score between the patients with cancer progression and those with no progression after receiving immunotherapy.

2.9 Statistical analysis

All the analyses were performed in R software (version 4.1.2). For significance analysis between various values (such as expression levels, infiltration ratio, and various eigenvalues, etc.), the Wilcoxon rank-sum test was applied to compare the differences between two groups of samples, while the Kruskal–Wallis test was used to compare the differences between multiple groups of samples. For plot presentation, the "ns" represents $p > 0.05$; "*" represents $p< 0.05$; "**" represents $p< 0.01$; "***" represents $p< 0.001$; and "****" represents $p< 0.0001$. Survival curves in the prognostic analysis were generated by the Kaplan–Meier method, and the significance of the differences was determined by the log-rank test.

3 Results

3.1 Screening the macrophage-related genes through WGCNA

The flow chart of this study is shown in Figure 1. The CIBERSORT algorithm was used to calculate the content of macrophages M1 and M2 in the samples of the GSE68465 cohort. Next, the LUAD patients were divided into groups with high and low macrophages M1 and M2. Kaplan–Meier analysis indicated that there was no significant difference in the survival of LUAD patients between the high and low macrophage M1 groups (Supplementary Figure S1A), but patients in the low macrophage M2 group had a longer overall survival (Supplementary Figure S1B). This suggested that macrophage M2 played an important role in LUAD. Based on this result, WGCNA was used to identify macrophage M2-related genes in LUAD. First, the result of sample clustering showed no outliers in these LUAD samples (Supplementary Figure S1C). When the power value was 7, the degree of independence was > 0.85 for the first time, so 7 was selected as the optimal soft threshold power (Supplementary Figures S1D, S2E). There were nine gene modules identified in the WGCNA (Supplementary Figures S1F, S2G). The correlation analysis indicated that genes in the brown module (cor = 0.33, $p = 0.0001$) and blue module (cor = −0.41, $p = 0.0000$) were most significantly correlated with macrophages M2. Therefore, 408 genes in the brown module and 430 genes in the blue module (Supplementary Table S2) were selected for the subsequent analyses.

3.2 Acquiring the TAM marker genes using scRNA-seq data

After quality control for the scRNA-seq dataset GSE131907, 25,011 genes were detected in 50,515 cells. The violin plots showed the number of genes detected in each cell (nFeature), the total number of counts in each cell (nCount), and the percentage of mitochondrial genes in each cell (percent.mt) (Supplementary Figures S2A–C).

10.3389/fimmu.2023.1273422

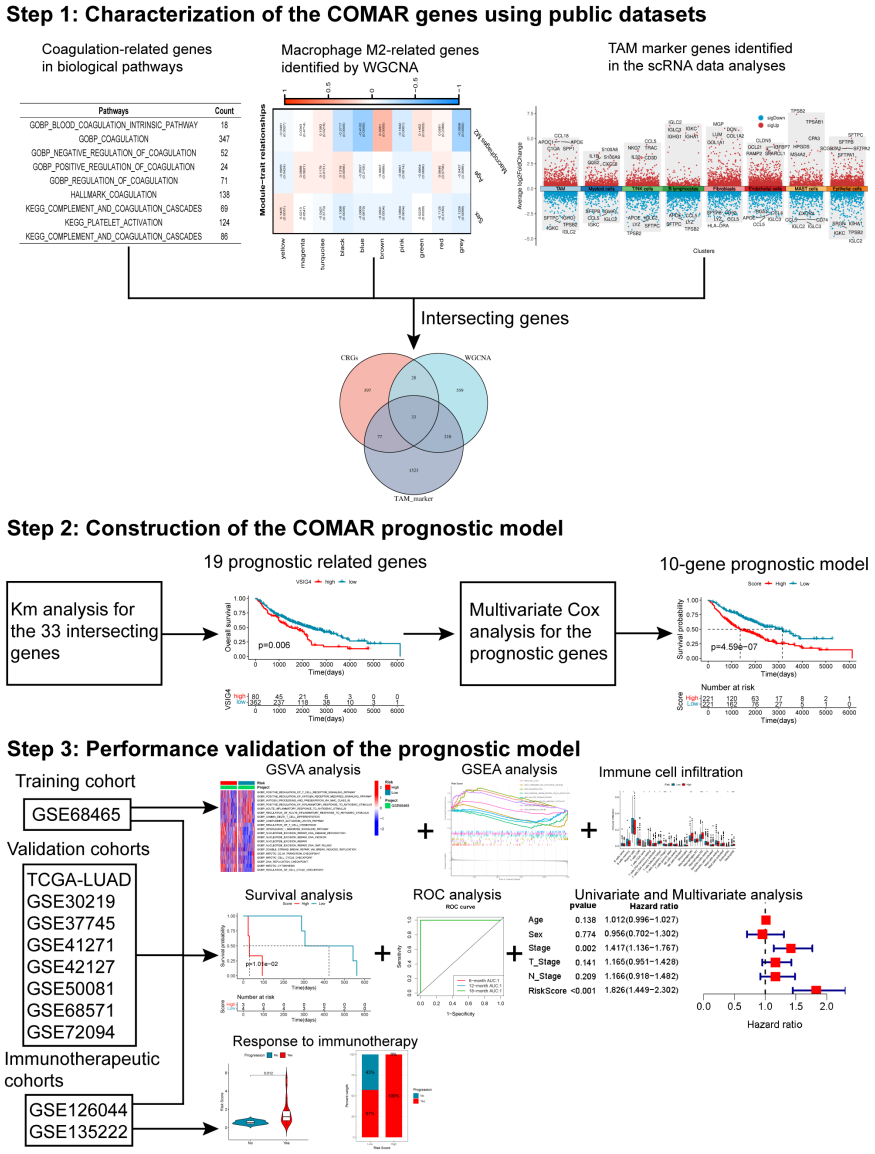

FIGURE 1
The flow chart of this study.

The correlation analysis indicated that nCount was significantly positively correlated with nFeature (Supplementary Figure S2D). Next, the 3,000 highly variable genes were plotted in the scatter plot (Supplementary Figure S2E). In total, 20 PCs were identified by PCA (Supplementary Figure S2F), which were selected for "harmony" analysis. According to the TSNE and cell type annotation, all cells were divided into two groups (34,279 immune cells and 16,236 nonimmune cells). The immune cell group consisted of B lymphocytes, mast cells, myeloid cells, T/NK cells, and TAM, while the nonimmune cell group included endothelial cells, epithelial cells, and fibroblasts (Supplementary Figures S3A, S4B). Differentially expressed genes for each cell type were analyzed and displayed in the volcano plot (Supplementary Figure S3C). The 1,815 differentially expressed genes in TAM were considered the TAM-associated genes (Supplementary Table S3).

3.3 Characterization of the COMAR genes and the landscape of their genetic and transcriptional alterations

The intersection of the 535 coagulation-associated genes, 838 macrophage M2-related genes, and 1,815 TAM-associated genes contained 33 genes, and these genes were selected for the subsequent analyses (Figure 2A; Supplementary Table S4). We first summarized the incidence of copy number variations and somatic mutations of the 33 COMAR genes in LUAD. Among 561 samples, 183 experienced mutations of coagulation-related genes, with a frequency of 32.62%. It was found that the TLR4 exhibited the highest mutation frequency, followed by ITGAX, while 11 genes did not show any mutations in LUAD samples (Figure 2C). The investigation of CNV alteration frequency indicated a prevalent

10.3389/fimmu.2023.1273422

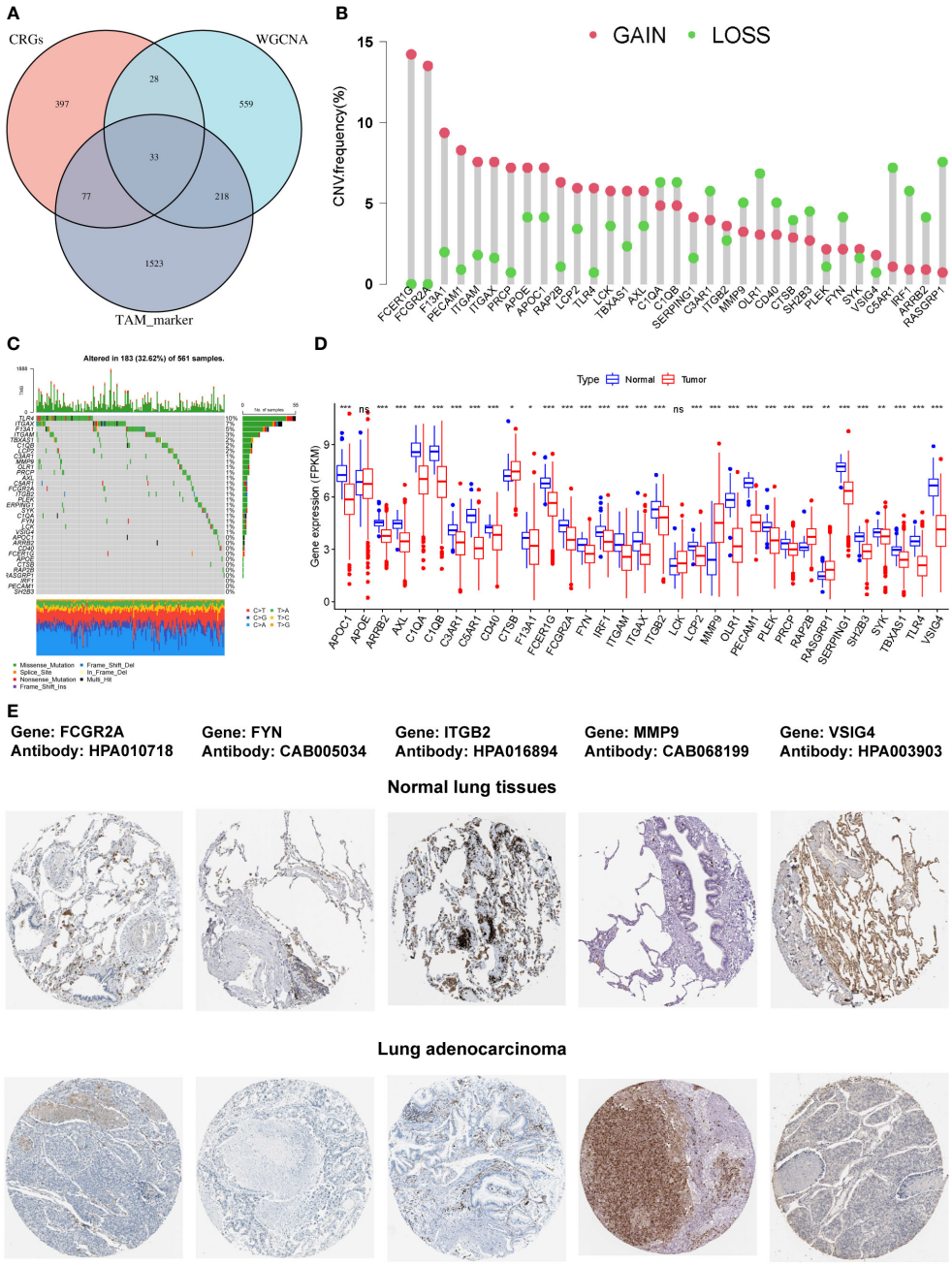

FIGURE 2
The characterization of the 33 COMAR genes and the landscape of their genetic and transcriptional alterations. **(A)** The determination of the 33 COMAR genes from the cross-talk of the coagulation-related genes, the macrophage M2-related genes identified by WGCNA, and the TAM markers. **(B)** The mutational frequency of the 33 coagulation-associated genes in 561 LUAD patients from the TCGA-LUAD cohort. Each column represents individual patients. Upper bar plots show TMB, and the numbers on the right indicate the mutational frequency of each gene. Right-bar plots show the proportion of each variant type. Stacked bar plots below show the fraction of conversions in each sample. **(C)** The CNV variation frequency of the 33 coagulation-related genes in the TCGA-LUAD cohort. The height of the column represents the alteration frequency. Red dots represent deletion frequency; blue dots represent amplification frequency. **(D)** The expression levels of the 33 genes between normal and LUAD cancer tissues in the TCGA-LUAD cohort. In the box plot, blue represents normal tissues, and red represents cancer tissue. The upper and lower ends of the boxes represent the interquartile ranges of values. Lines in the boxes represent median values. Blue or red dots show outliers. Asterisks above the boxes represent the *p*-value (*$p< 0.05$; **$p< 0.01$; ***$p< 0.001$; ns, $p> 0.05$). **(E)** The immunohistochemical staining images of FCGR2A, FYN, ITGB2, MMP9, and VSIG4 genes in normal lung tissues and LUAD tumor tissues. The names of genes and antibodies are listed at the top of the figure. The upper five images are the staining in the corresponding normal tissues, and the lower five images are the staining in the tumor tissues.

CNV alteration in these coagulation-related genes, with copy number amplification being much more significant than copy number deletion. Genes like FCER1G and FCGR2A were found with pretty prominent copy number amplification, while RASGRP1 and C5AR1 were found with obvious copy number deletion (Figure 2B). We also compared the relative RNA expression levels between LUAD and paired normal tissues and found that most of the genes were downregulated in LUAD compared with paired normal tissues (Figure 2D). Thus, there may be some other factors that may influence the expression of these genes, except for CNV. The Human Protein Atlas (HPA) database was applied to validate the protein expression of the COMAR genes, and the IHC staining images of FCGR2A, FYN, ITGB2, MMP9, and VSIG4 were obtained (Figure 2E). Each gene was stained using the same antibody in the normal lung tissue and LUAD cancer tissue. Among these genes, FCGR2A, FYN, ITGB2, and VSIG4 protein levels were increased in tumor tissues, while MMP9 protein level was decreased, which was consistent with their mRNA expression levels (Figures 2D, E).

3.4 Construction and validation of the prognostic model based on the COMAR genes

To investigate the clinical value of the 33 COMAR genes, we divided the patients in the training cohort GSE68465 into high- and low-expression groups for each gene with the best cut-off value and performed survival analysis. Results indicated that 19 genes were prognostic-related genes (Supplementary Figure S4). We then conducted a multivariate Cox regression analysis based on the 19 genes. Finally, 10 of the 19 genes were found in the prognostic model we constructed (Figures 3A–J). The specific calculation formula for the risk score model was listed as follows:

Risk score = (−0.26708659 * APOE expression level) + (−0.282614466 * ARRB2 expression level) + (0.410059345 * C1QB expression level) + (0.178659465 * F13A1 expression level) + (−0.303985307 * FCGR2A expression level) + (−0.271534215 * FYN expression level) + (−0.610784492 * ITGB2 expression level) + (0.15191577 * MMP9 expression level) + (0.120339218 * OLR1 expression level) + (0.446920184 * VSIG4 expression level).

The training LUAD patients were ranked by the risk score and divided into low-risk (n = 221) and high-risk (n = 221) groups (Figure 3M; Supplementary Table S5), and the patient's survival time became shorter with the risk score increasing generally (Figure 3N). The Kaplan–Meier curve showed a significantly poorer prognosis in the high-risk group than in the low-risk group (log-rank test, p = 4.59e–07) (Figure 3K). The ROC curve showed the AUCs of the patients at 1, 3, and 5 years were 0.693, 0.696, and 0.672, respectively (Figure 3L). The AUCs in the prediction of short-term prognosis were higher, and they were 0.745, 0.740, and 0.718 at 4-, 6-, and 9-month follow-up, respectively (Supplementary Figure S5A). Thus, the prognostic model might have stronger predictive efficacy for shorter-term prognosis. Moreover, this prognostic model had significantly superior predictive efficacy compared with other clinical factors such as age, sex, tumor stage, and differentiation status at 1-, 3-, and 5-year follow-ups (Supplementary Figures S5B–D).

To evaluate the robustness and generalizability of the 10-gene COMAR prognostic model, several external independent datasets, including GSE30219, GSE37745, GSE41271, GSE42127, GSE50081, GSE72094, and TCGA-LUAD, were used as the validation cohort for this model. In both validation cohorts, the patients in the low- and high-risk groups had significantly different prognoses, and the ROC curves all indicated high sensitivity and specificity (Figures 4A–G). Furthermore, univariate and multivariate Cox regression analyses were applied to evaluate whether the risk score model could act as an independent prognostic factor for LUAD. In both training and validation cohorts, the risk score was considered to be an independent prognostic factor among other clinical features such as age, sex, and tumor stage (Figures 5A–P). These results all indicated that the 10-gene coagulation-related risk score model had a better prognostic efficacy with high robustness and generalizability.

3.5 Relationship between the COMAR risk score and the tumor microenvironment

Different activations of hallmarks, GO_BPs, and GO_MFs in the GSE68465 dataset were investigated using the GSVA algorithm. Results indicated that some cancer hallmarks were much more enriched in the high-risk score group, such as MYC and MTOR-related pathways (Figure 6A; Supplementary Table S6). The high-risk score group had stronger molecular functions on DNA replication and transcription (such as DNA replication origin binding, helicase activity, and transcription initiation factor activity), while the low-risk score group exhibited greater molecular functions on immune activities (such as type I interferon receptor binding and T-cell receptor binding) (Figure 6B; Supplementary Table S6). Consistently, the immune biological pathways were mostly activated in the low-risk score group (such as positive regulation of T-cell receptor signaling pathway, positive regulation of antigen receptor-mediated signaling pathway, and positive regulation of inflammatory response to antigen stimulus), while pathways about DNA replication were activated in the high-risk group (such as DNA replication checkpoint and mitotic cell cycle checkpoint) (Figure 6C; Supplementary Table S6).

Similar to the results in the GO analyses, the KEGG GSEA indicated the high-risk score group was mostly enriched in the following pathways (DNA replication, cell cycle, and P53 signaling), while the low-risk score group was mostly enriched in the immune-related pathways (natural killer cell-mediated cytotoxicity, complement and coagulation cascades, and intestinal immune network for IgA production) (Figure 6D; Supplementary Table S6). To further explore the correlation between the risk score and tumor immune characteristics, the immune cell infiltration in these samples was investigated using the CIBERSORT algorithm. It was found that immune cell infiltration was overall higher in the low-risk score group than in the high-risk score group (such as naïve B cells, resting dendritic cells, naive CD4 T cells, resting memory CD4 T cells, and T follicular helper cells) (Figure 6E; Supplementary Table S7). However,

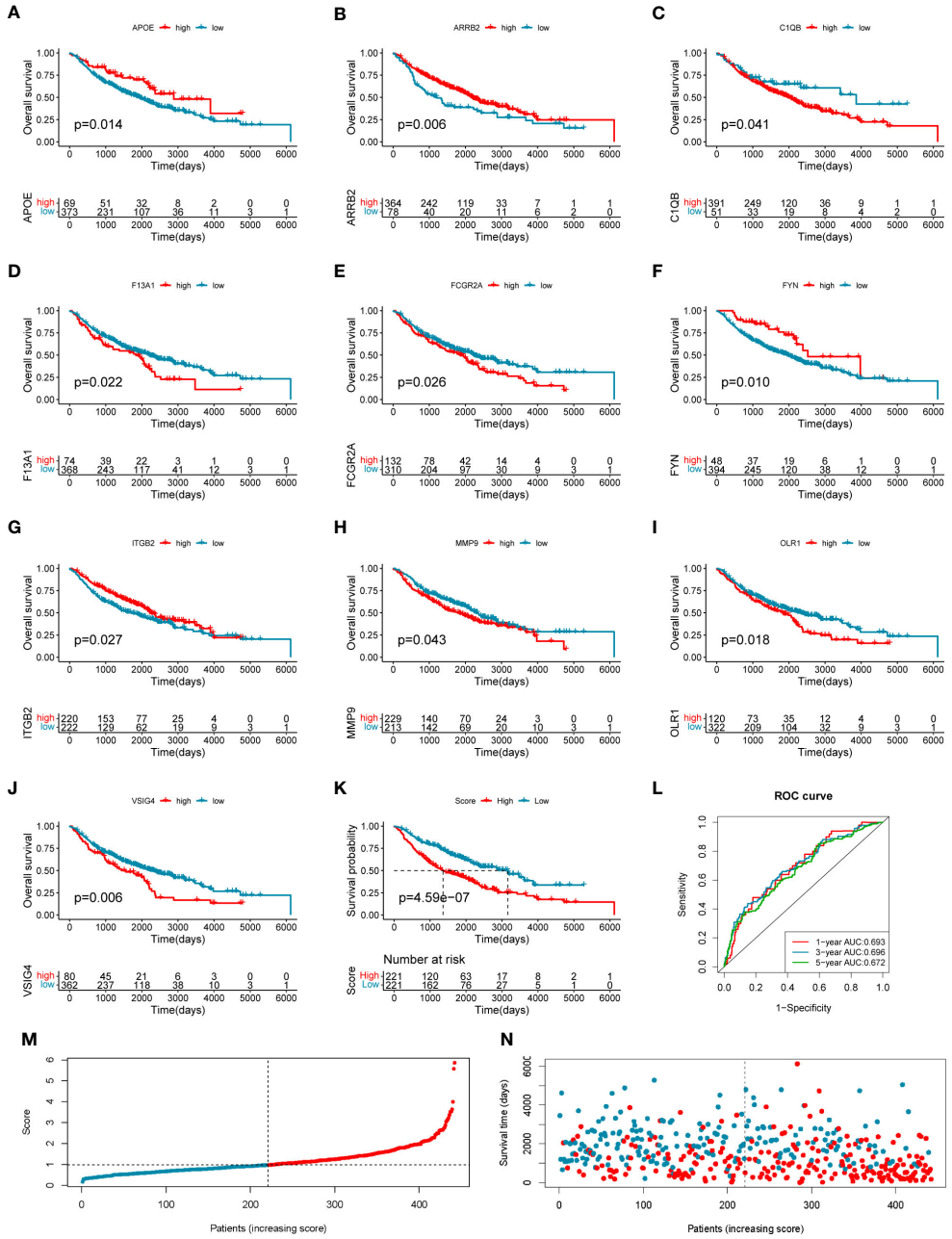

FIGURE 3
Construction of the 10-gene prognostic model in the training cohort. **(A–J)** The overall survival curves of the 10 genes involved in the prognostic model: **(A)** APOE, **(B)** ARRB2, **(C)** C1QB, **(D)** F13A1, **(E)** FCGR2A, **(F)** FYN, **(G)** ITGB2, **(H)** MMP9, **(I)** OLR1, and **(J)** VSIG4. The abscissa axis shows survival time, while the ordinate axis shows survival probability. Blue represents low expression, while red represents high expression. The grouping status of the patients is indicated at the bottom of the chart. $p< 0.05$ in the Log-rank test was considered statistically significant. **(K)** The overall survival curve of patients in high- and low-risk score groups in the training cohort. The abscissa axis shows survival time, while the ordinate axis shows survival probability. Blue represents patients with low-risk scores, while red represents patients with high-risk scores. The grouping status of the patients is indicated at the bottom of the chart. P< 0.05 in the Log-rank test was considered statistically significant. **(L)** The ROC curve for predicting the 1-, 3-, and 5-year survival of LUAD patients according to the risk score. The abscissa axis represents specificity and the vertical axis represents sensitivity. Different colors represent different predictive times. **(M)** The risk score distributions of the patients. **(N)** The survival status of the patients.

the infiltration of macrophage M0 and M2 was significantly higher in the high-risk score group (Figure 6E; Supplementary Table S7). Moreover, some immune-related functions were much more activated in the low-risk score group, including HLA, T-cell co-stimulation, and type II IFN response (Figure 6F).

3.6 Predictive efficacy of the 10-gene COMAR model in immunotherapy

The risk scores of LUAD patients treated with anti-PD1/PD-L1 blockade in the GSE126044 and GSE135222 datasets were

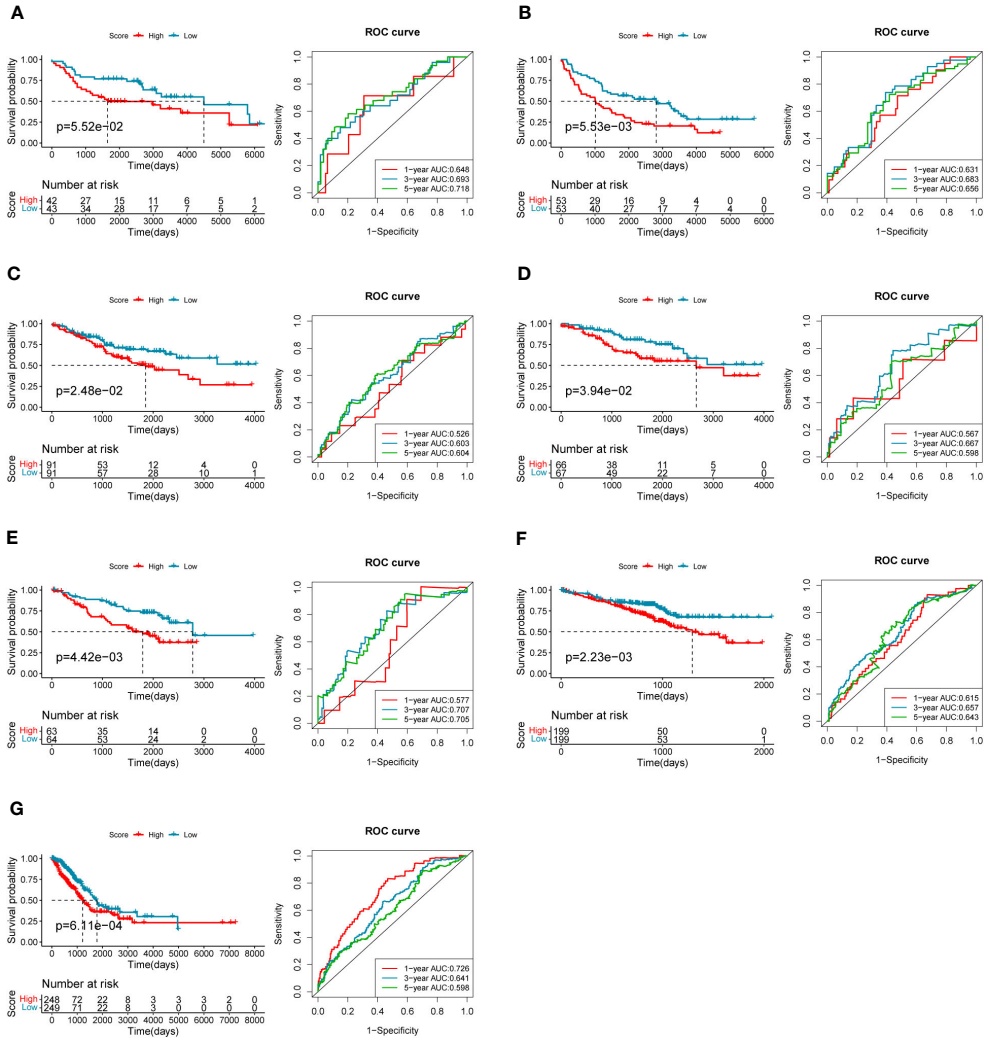

FIGURE 4
The predictive efficacy of the prognostic model in the external validation cohorts: **(A)** GSE30219 dataset, **(B)** GSE37745 dataset, **(C)** GSE41271 dataset, **(D)** GSE42127 dataset, **(E)** GSE50081 dataset, **(F)** GSE72094 dataset, **(G)** TCGA-LUAD dataset. On the left of each panel is the overall survival curve of patients in high and low-risk score groups. The abscissa axis shows survival time while the ordinate axis shows survival probability. Blue represents patients with low-risk scores while red represents patients with high-risk scores. The grouping status of the patients is indicated at the bottom of the chart. On the right of each panel is the ROC curve for predicting the 1-, 3-, and 5-year survival of LUAD patients according to the risk score. The abscissa axis represents specificity and the vertical axis represents sensitivity. Different colors represent different predictive times.

calculated using the risk score model. In the GSE126044 cohort, it was found that patients in the low-risk score group had significantly better progression-free survival (PFS) and overall survival (OS) versus high-risk score group (Figures 7A, C). Surprisingly, the corresponding ROC curves indicated that the AUCs at 6 months, 12 months, and 18 months were all 1 (Figures 7B, D). Similar results could also be found in the GSE135222 cohort. Patients in the low-risk score group had a remarkable advantage in prognosis (Figure 7E), and the AUCs of patients at 4 months, 8 months, and 12 months were 0.846, 0.8, and 0.854, respectively (Figure 7F). The risk score distributions and the survival status of the patients in the GSE135222 cohort are provided in Figures 7G, H. Moreover, patients who experienced progression of LUAD after anti-PD1/PD-L1 immunotherapy were found to have a higher risk score (Figure 7I), and they were all in the low-risk score group (Figure 7J). These results indicated that the 10-gene coagulation and macrophage-related model had a strong predictive efficacy for patients' prognosis with anti-PD1/PD-L1 immunotherapy.

3.7 Validation of the bioinformatic analytical results through the patient specimens and cancer cell lines

To further investigate the functions of the genes in the COMAR model in immunotherapy, first we made a correlation analysis in the TCGA-LUAD dataset and found the expression levels of all the genes in the COMAR model were positively correlated with PD-L1 expression level and the immunophenoscore (IPS) with anti-PD1 +CTLA4 or anti-PD1 along immunotherapy (Figure 8A). Next, we analyzed the protein expression levels of the COMAR genes and PD-L1 in the HPA database, and the immunochemical images of

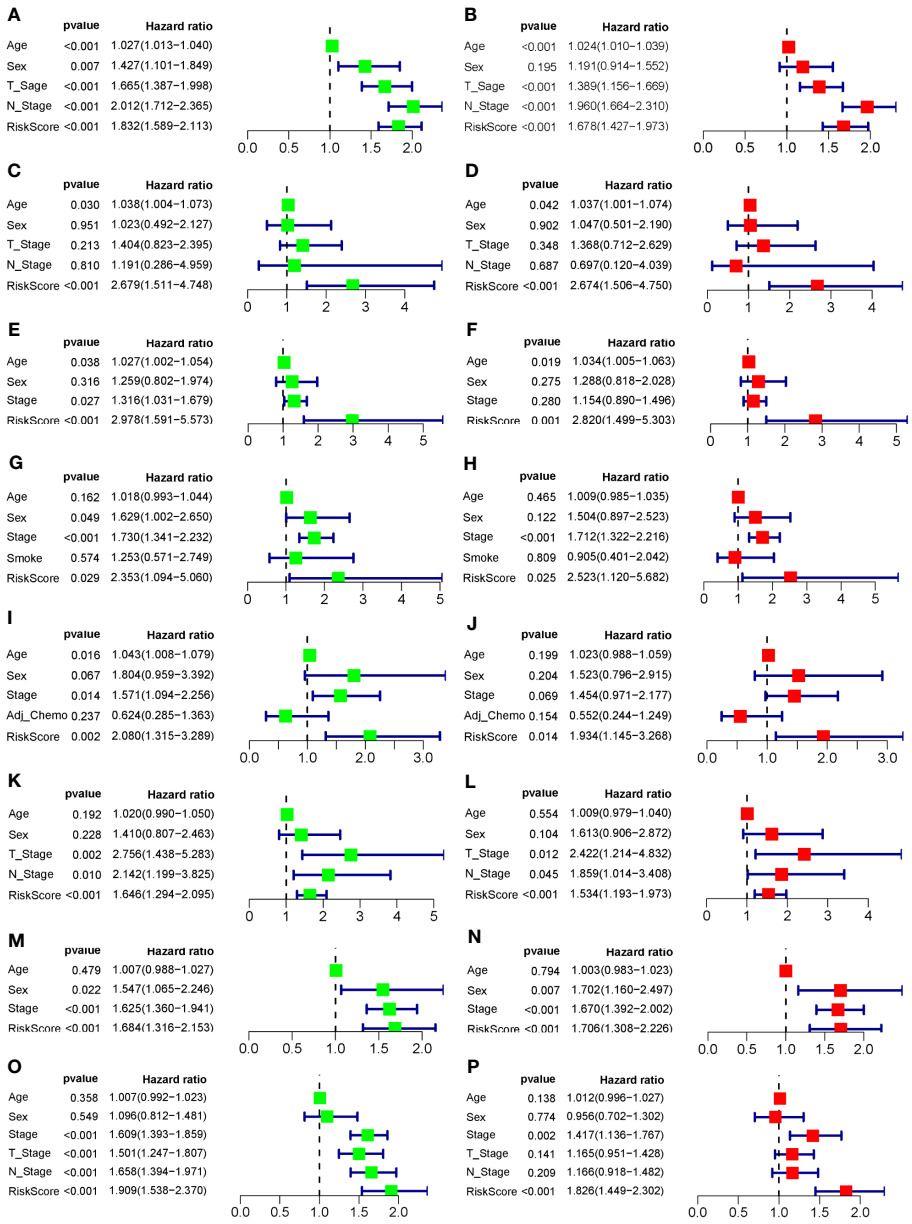

FIGURE 5
Forest plots of the univariate and multivariate Cox regression analyses for the prognostic model in the training and validation cohorts. **(A)** Univariate Cox regression analysis for the training cohort GSE68465. **(B)** Multivariate Cox regression analysis for the training cohort GSE68465. **(C)** Univariate Cox regression analysis for the validation cohort GSE30219. **(D)** Multivariate Cox regression analysis for the validation cohort GSE30219. **(E)** Univariate Cox regression analysis for the validation cohort GSE37745. **(F)** Multivariate Cox regression analysis for the validation cohort GSE37745. **(G)** Univariate Cox regression analysis for the validation cohort GSE41271. **(H)** Multivariate Cox regression analysis for the validation cohort GSE41271. **(I)** Univariate Cox regression analysis for the validation cohort GSE42127. **(J)** Multivariate Cox regression analysis for the validation cohort GSE42127. **(K)** Univariate Cox regression analysis for the validation cohort GSE50081. **(L)** Multivariate Cox regression analysis for the validation cohort GSE50081. **(M)** Univariate Cox regression analysis for the validation cohort GSE72094. **(N)** Multivariate Cox regression analysis for the validation cohort GSE72094. **(O)** Univariate Cox regression analysis for the validation cohort TCGA-LUAD. **(P)** Multivariate Cox regression analysis for the validation cohort TCGA-LUAD. The left column of each panel shows the *p*-value and hazard ratio of the factors, including risk score, and the right column shows the corresponding forest plot.

VSIG4 and PD-L1 of six patients stained using the same antibody for each gene were obtained.

It was found that patient 2003 with the strong staining intensity of PD-L1 could also be found with the strong staining intensity of VSIG4 in the specimens. Furthermore, the specimens of the other five patients with negative staining of PD-L1 were consistent with the negative VSIG4 staining results (Figures 8B–G). This indicated that the COMAR genes were positively correlated with PD-L1 expression at the proteinic level. We also explored the correlation between the 10 COMAR genes and immune checkpoint genes in LUAD cell lines using the data from the Cancer Cell Line Encyclopedia (CCLE) database (29). The results indicated that the expression levels of some COMAR genes, like ITGB2, were positively correlated with multiple immune checkpoints

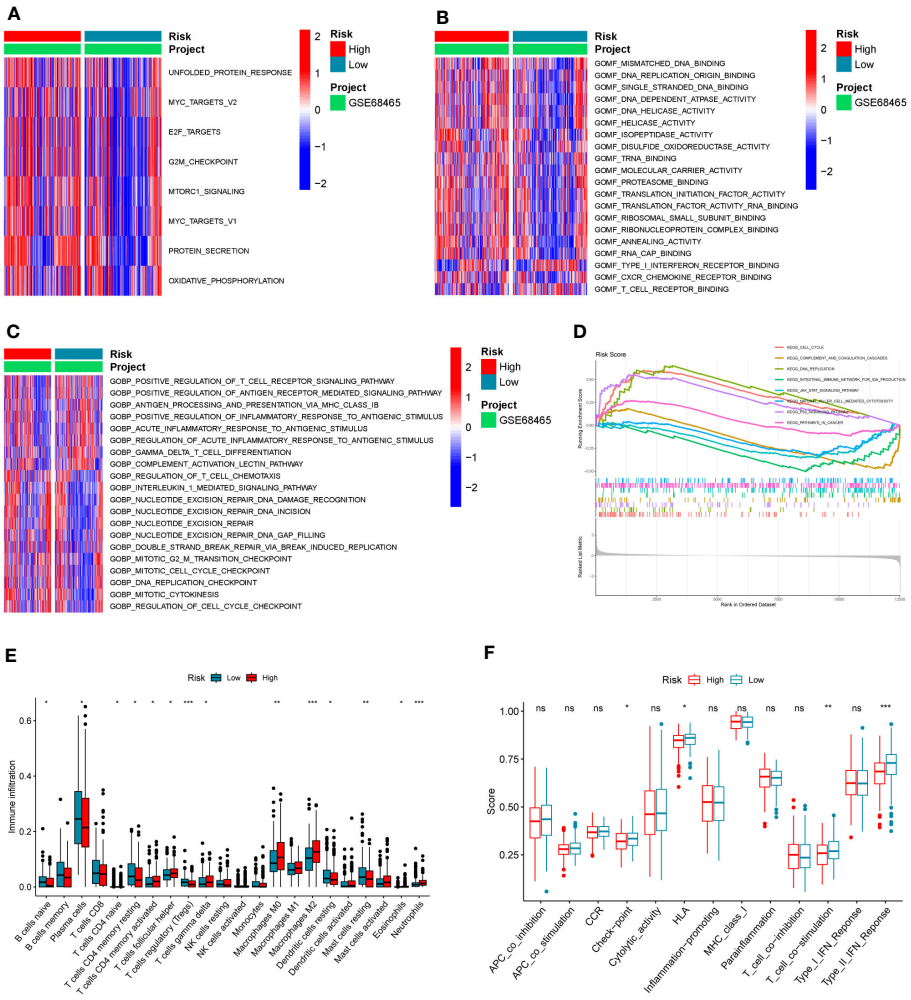

FIGURE 6
The association between the COMAR risk score and the TME characteristics. **(A–C)** GSVA enrichment analysis shows the differentially activated hallmarks **(A)**, GO_MFs **(B)**, and GO_BPs **(C)** between risk score low and high groups. The items of hallmarks, molecular functions, and biological processes are listed on the right. Red represents activation, while blue represents inhibition. **(D)** GSEA enrichment analysis shows the activated pathways in risk score high and low groups. The abscissa axis represents the ranked gene list according to their expression levels in two groups. The vertical axis represents the running enrichment score. Curves of different colors represent different pathways. The curves that have a high peak on the left side represent pathways that are enriched in the high-risk score group, while the curves that have a low peak on the right side represent pathways that are enriched in the low-risk score group. **(E)** Relative abundance of the 22 types of immune cells in risk score low and high groups. The abscissa axis represents the names of immune cells. The abscissa axis shows the immune cell types, and the vertical axis represents the infiltration fraction of each immune cell. **(F)** Score of functions in immune regulation in risk score low and high groups. The abscissa axis shows the items of immune functions, and the vertical axis shows the activation score of each immune function. "*p< 0.05; **p< 0.01; ***p< 0.001; ns, p> 0.05.

(Supplementary Figure S6A), which was consistent with the results in the patient specimens. Moreover, we obtained the immunofluorescent staining image of the VSIG4 gene in LUAD cell line A-549 from the HPA database and found that VSIG4 is mainly located in the plasma membrane and cytosol of cancer cell line A-549 (Supplementary Figure S6B).

4 Discussion

It had been extensively reported that lung cancer, especially for LUAD, could frequently cause coagulation aberration and even venous thromboembolism, which was a major cause of cancer-related deaths (25–27, 30–32). It has been proved that the TME plays a significant role in tumor progression and therapy. As an essential component of the TME, TAMs have been the focus of several studies. TAMs could facilitate the progression of most types of cancer, including LUAD, through promoting angiogenesis, suppression of specific immunity, and cancer growth and metastasis (7, 8, 11–16). TAMs could also be applied as the therapeutic target for cancers, and the ways include depleting them, reverting TAM polarization, checkpoint blockade, strategies to reshape and activate TAMs, metabolic approaches, and macrophage cell therapies (7, 8). TAMs played an important role in coagulation, which was closely related to cancer development. For example, TAMs could produce factor X (FX) and activate the cell-autonomous FXa-PAR2 signaling in the TME, which led to tumor immune evasion and a poor prognosis (19, 20). Some other

10.3389/fimmu.2023.1273422

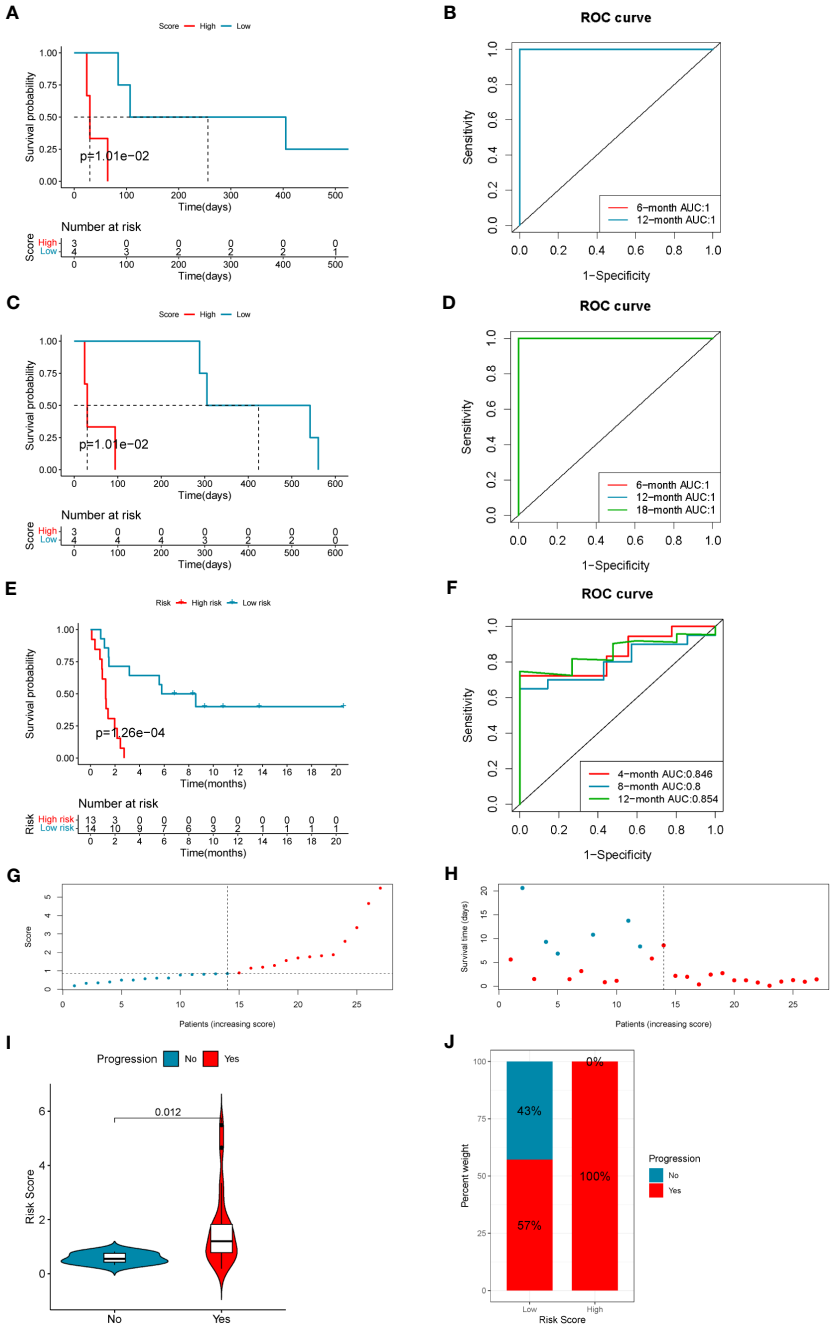

FIGURE 7
The 10-gene COMAR model predicts the immunotherapeutic outcomes of patients with LUAD. **(A)** The progression-free survival curve of patients with high and low-risk scores in the anti-PD-1 cohort GSE126044. **(B)** The ROC curve for predicting the 6- and 12-month progression-free survival of patients in the GSE126044 cohort. **(C)** The overall survival curve of patients with high and low-risk scores in the GSE126044 cohort. **(D)** The ROC curve for predicting the 6- and 12-month overall survival of patients in the GSE126044 cohort. **(E)** The progression-free survival curve of patients with high- and low-risk scores in the anti-PD-1/PD-L1 cohort GSE135222. **(F)** The ROC curve for predicting the 4-, 8-, and 12-month progression-free survival of patients in the GSE135222 cohort. For the survival charts, the abscissa axis shows survival time, while the ordinate axis shows survival probability. Blue represents patients with low-risk scores, while red represents high-risk scores. The grouping status of the patients is indicated at the bottom of the chart. For the ROC curves, the abscissa axis represents specificity, and the vertical axis represents sensitivity. Different colors represent different predictive times. **(G)** The risk score distributions of the patients in the GSE135222 cohort. **(H)** The survival status of the patients in the GSE135222 cohort. **(I)** Violin plot showing the risk score of patients with progression or no progression after anti-PD-1/PD-L1 blockade immunotherapy in the GSE135222 cohort. **(J)** The proportion of patients with progression or no progression after immunotherapy in low- and high-risk score groups in the GSE135222 cohort.

10.3389/fimmu.2023.1273422

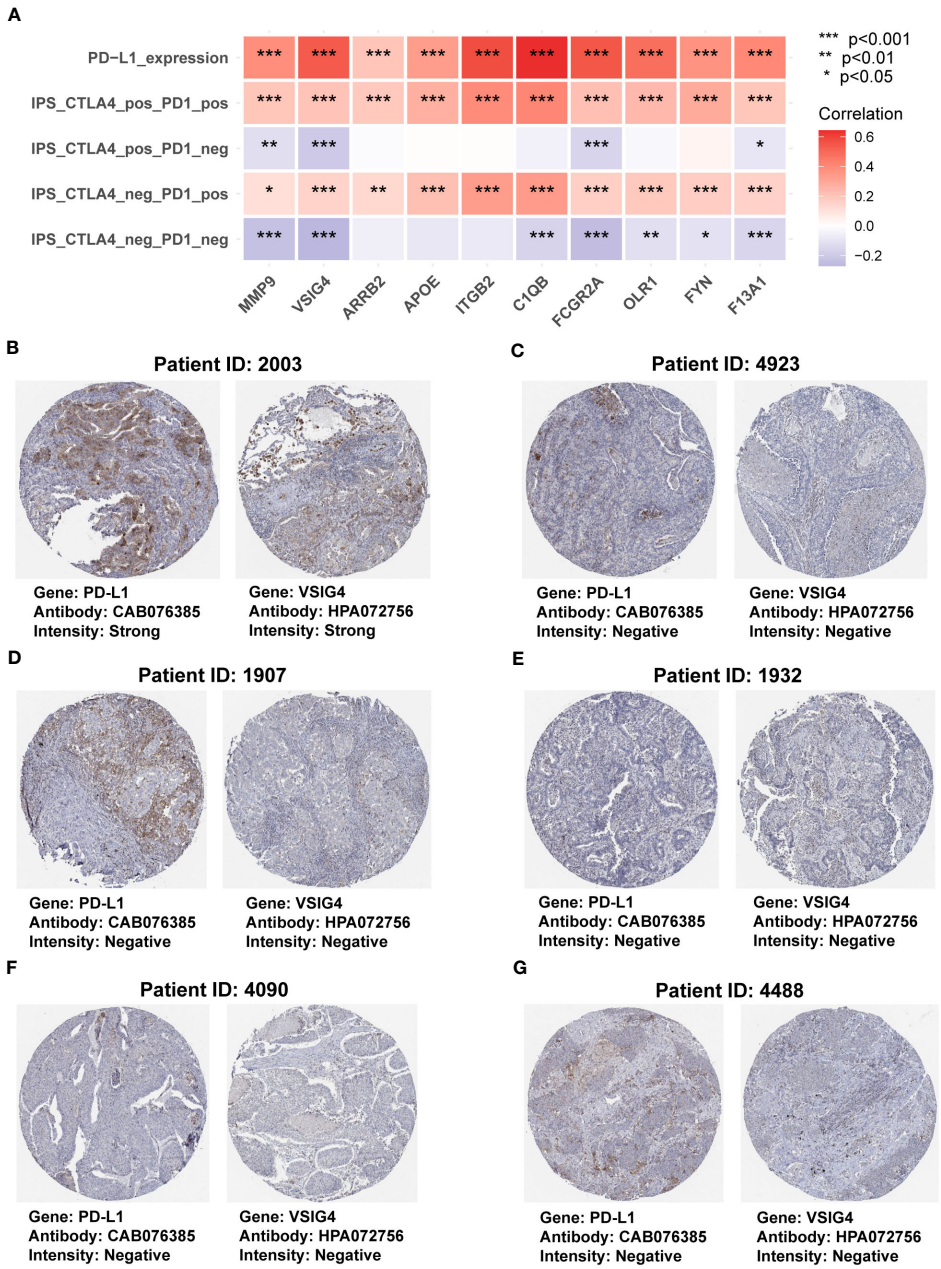

FIGURE 8
The correlation between genes in the COMAR model and anti-PD-1/PD-L1 immunotherapy. **(A)** Correlation analysis between the 10 genes involved in the COMAR model, PD-L1 expression, and IPS in immunotherapy. **(B–G)** Immunohistochemical staining images of the specimens of patient ID 2003 **(B)**, 4923 **(C)**, 1907 **(D)**, 1932 **(E)**, 4090 **(F)**, and 4488 **(G)**. Images were downloaded from the Human Protein Atlas (HPA) database. Gene names, antibodies, and staining intensity are listed at the bottom of each image. IPS, immunophenoscore. *p< 0.05; **p< 0.01; ***p< 0.001.

coagulation-associated factors could also strengthen the tumor-promoting effects of TAMs (21–23). Therefore, targeting the coagulation-related factors might effectively dampen the tumor-promoting functions of TAMs and boost the efficacy of cancer therapy. There have been some studies showing that targeting coagulation signaling could inhibit or reprogram TAMs and improve immunotherapy (19, 20). However, the regulatory mechanisms between coagulation and TAMs in tumor development still need to be further studied, and more biomarkers related to the coagulation process and TAM functions that could be used for cancer therapeutic targets and prognostic prediction should be explored.

In this study, we acquired the coagulation-related genes from the coagulation pathways provided by MSigDB and KEGG databases (Table 1; Supplementary Table S1). Then, we found high macrophage M2 content in the tumor was associated with a worse prognosis in LUAD patients while macrophage M1 was not (Supplementary Figures S2A, B), so the macrophage M2-related genes were identified using the WGCNA method in the bulk RNA-seq data (Supplementary Figures S2C–G; Supplementary Table S2).

Single-cell sequencing is an advanced technology that gives us an unprecedented opportunity to dissect cellular heterogeneity in various biological contexts by analyzing transcriptomic profiles of thousands to millions of cells simultaneously (33–36). Through analyzing the scRNA-seq data, we annotated all the cell types and characterized the TAM marker genes in the LUAD scRNA-seq data (Supplementary Figure S3C; Supplementary Table S3) (28). Finally, we adopted the intersectional genes of the three groups of genes and obtained 33 genes that are closely related to the coagulation process and TAM infiltration for further analyses (Figure 2A; Supplementary Table S4). Those genes were named COMAR genes.

Subsequently, we performed K-M survival analysis for those 33 COMAR genes and found that 19 genes were associated with the prognosis (Supplementary Figure S6). Based on the 19 genes, we constructed a prognostic model including 10 genes, which was effective and proved robust in predicting patients' prognosis (Figures 3–5). Among the 10 genes, ARRB2 was reported to be a tumor suppressor and could inhibit the progression of various kinds of cancer, including lung cancer (37–41). In our study, ARRB2 was found to be a protective factor for prognosis, which was consistent with the previous studies (Figure 3B). Moreover, it was found that ARRB2 was significantly downregulated in tumor versus normal tissues and presented with a higher frequency of CNV deletion (Figures 2B, D). Thus, we speculated that the expression of ARRB2 might be regulated by CNV in LUAD.

F13A1 was an important coagulation-related gene encoding factor XIII subunit A (FXIII-A), which was a transglutaminase involved in hemostasis, wound healing, tumor growth, and apoptosis (42). It was reported that F13A1 was a risky factor for the prognosis of patients with several types of cancer (43–45), which was consistent with our study (Figure 3D). Though F13A1 had a high frequency of CNV amplification (Figure 2B), it was downregulated in LUAD tumor tissues (Figure 2D). Considering its high mutation rate (Figure 2C), we speculated that mutational inactivation might be the reason for the low expression of F13A1.

C1QB was a risky factor for patients with some cancers, including NSCLC, according to previous studies (46–48), which was also consistent with our analyses (Figure 2C). CIQB might affect prognosis by regulating the TME because a study found that intrahepatic cholangiocarcinoma (ICC) with $APOE^{+}C1QB^{+}$ subtype of macrophage infiltration was associated with the chronic inflammation subtype of ICC and poor prognosis (46).

The FCGR2A gene encodes a member of the immunoglobulin Fc receptor gene family (49). Previous studies mainly focused on the polymorphisms of this gene that could influence the clinical outcomes of monoclonal antibody treatment in cancers like breast cancer (50), colorectal cancer (51, 52), and neuroblastoma (53). Only limited reports pointed out that high expression of FCGR2A was associated with a poor prognosis for cancer patients (49, 54). In our study, we also found that high expression of FCGR2A was associated with shorter survival in LUAD (Figure 3E). Moreover, FCGR2A, presented with a higher rate of CNV amplification, was downregulated in LUAD tumor tissues (Figures 2B, D), which was rarely reported. Thus, it needed to be further explored, and the regulatory mechanisms of its expression that were not consistent with CNV amplification also needed to be figured out.

FYN was a nonreceptor tyrosine kinase (RTK) member of the Src family kinase (SFK) (55). It was reported that FYN promoted tumor progression in glioma (56), melanoma (57), colon cancer (58), gastric cancer (59), and pancreatic cancer through various mechanisms (60). Furthermore, FYN was found to suppress LUAD by downregulating PI3K/AKT and inhibiting the epithelial-to-mesenchymal transition (61). This might partially account for the result of our study that FYN was a protective factor for the prognosis (Figure 3F).

ITGB2 participated in the YAP-induced cancer cell invasion by activating leukocyte-specific integrin β2 expression (62) and the myxofibrosarcoma aggressiveness conferred by SKP2 amplification (63). High expression in cancer-associated fibroblast (CAF) could promote oral squamous cell carcinoma proliferation by regulating PI3K/AKT/mTOR pathways to enhance glycolysis activity in CAFs (64). Moreover, high expression of ITGB2 was also reported to be correlated with poor prognosis in some cancers (65, 66). However, ITGB2 presented with opposite functions in NSCLC. It inhibited the proliferation and metastasis of NSCLC cells through suppressing EMT. Furthermore, low expression of it was associated with inferior prognosis in NSCLC (67), which was validated in an independent dataset, GSE68465 (Figure 3G).

MMP9 can degrade various components of the extracellular matrix to promote cancer cell invasion and liberate ligands for growth factor receptors from the extracellular matrix. It has been reported to play an important role in tumor-induced VEGF-dependent angiogenesis and prepping organs for the formation of distant metastases depending upon VEGFR-1 (68). Furthermore, it not only induced metastasis to the lung but was also involved in lung cancer invasion through multiple mechanisms (69). Consistent with previous reports, we found that MMP9 was also a risky factor for the prognosis of LUAD (Figure 3H).

The OLR1 gene encodes the LOX-1 receptor protein, which could facilitate the progression and metastasis of several cancers (70). OLR1 could also promote lung metastases of osteosarcomas through regulating the EMT (71). Similar to the above, OLR1 was also an unfavorable risky factor for the prognosis (Figure 3I). Its high frequency of CNV deletion might be the reason for its low expression in LUAD (Figures 2B, D).

VSIG4 was a multifunctional cell surface protein and presented as an immune checkpoint regulator, which suppressed T lymphocyte function and promoted cancer development and progression (72). In NSCLC tissues, VSIG4 could only be found expressed in macrophages, and the $VSIG4^{+}$ macrophages infiltrating the tumor tissues could facilitate tumor growth by inhibiting T-cell proliferation and cytokine production (73). This might mechanically explain why the high expression of VSIG4 was related to the poor prognosis of LUAD (Figure 3J).

Different from previous reports, APOE was found to be a protective factor for the prognosis of LUAD (Figure 3A), while it was reported to promote cancer proliferation and migration and contribute to an aggressive clinical course in patients with LUAD (74). When APOE was knocked out, lung tumor development and metastasis were suppressed via increasing TREM-1-dependent antitumor activity of NK cells (75). In general, most of the genes involved in the COMAR prognostic signature were limitedly

researched for their roles in LUAD. The regulatory mechanisms of coagulation aberrancy and TAM functions and the cross-talk relationships between them still need to be further studied.

For the correlation analysis between the COMAR risk score and the TME, patients in the low-risk score group were found to participate in much more activated immune-related biological pathways versus patients in the high-risk score group. These immune-related biological pathways might suppress tumor progression and contribute to a better prognosis for the low-risk group. In the GO_MF analysis, we found that the molecular functions of T-cell receptor (TCR) and type I interferon (IFN) receptor binding were enhanced in the low-risk score group (Figure 6B). For T cells, antitumor reactivity was defined by their unique TCRs (76), and high TCR abundance was associated with a better prognosis (77). Type I IFNs play a major role in the natural and therapy-induced immunological control of many malignancies, including lung cancer (78). The GO_BP analysis also indicated that positive regulation of the TCR pathway was activated in the low-risk score group. In addition, the gamma-delta T-cell differentiation was also found to be activated in the low-risk score group (Figure 6C). Gamma-delta T cells had antitumor functions in the TME and a high content of Vδ1 T cells; Vδ1 T cells were reported to be a subtype of gamma-delta T cells and were associated with superior prognosis and response to anti-PD-1 immunotherapy (79).

The GSEA of the KEGG pathway also indicated that several immune-associated pathways were enriched in the low-risk score group, including natural killer cell-mediated cytotoxicity (Figure 6D). Natural killer (NK) cells were cytotoxic lymphocytes of the innate immune system that were capable of killing viral infected and/or cancerous cells (80); when NK cells were commonly reduced in human tumors, immune surveillance escape would happen (81). The CIBERSORT analysis indicated that samples in the low-risk score group were infiltrated with a higher fraction of B cells, plasma cells, and CD4 cells, but less macrophage M2 (Figure 6E). B cells, plasma cells, and CD4 cells had been proven to play significant roles in promoting antitumor immunity and better clinical outcomes in the ICB immunotherapy (82–84), while macrophage M2 was associated with NSCLC progression, antitumoral immunosuppression, and resistance to anti-PD-1 immunotherapy (12, 15, 85, 86).

The results of the subsequent analyses in the LUAD immunotherapeutic cohorts corresponded to those of the TME analyses. Patients in the low-risk score group had significantly longer survival times and lower progression rates after accepting anti-PD-1 immunotherapy (Figure 7). The AUC values were pretty high, especially in the GSE126044 cohort (the AUC value = 1), which indicated the high sensitivity and specificity of this prognostic model (Figures 7B, D, F). Immune surveillance escape occurred by hijacking the corresponding inhibitory pathways via overexpressed checkpoint genes such as PD-L1 and CD47; thus, phagocytosis checkpoints have emerged as essential checkpoints for cancer immunotherapy (87). In the correlation analysis, we found that the 10 COMAR genes were positively correlated with immune checkpoint expression, such as PD-L1 and the IPS with anti-PD1 plus anti-CTLA4 or anti-PD1 along immunotherapy in both patient specimens and LUAD cell lines (Figure 8; Supplementary Figure S6A). Most of the genes in the COMAR model have also been reported to be positively correlated with PD-L1 expression and respond to ICB immunotherapy in multiple cancers (47, 88–93), which was consistent with the results of our study. These suggested that the 10 COMAR genes might serve as potential targets for ICB immunotherapy.

Certainly, there were also some limitations in our study. First, our study was mainly based on bioinformatic analyses of public datasets. Biological and molecular experiments *in vitro* and/or *in vivo* were needed to further explore the relevant mechanisms of the key COMAR genes. Second, due to our retrospective study, bias might be inevitable, and prospective experiments were needed for further validation. These limitations were also the focus of our future research. Our research had significant potential for future clinical guidance. First, the expression levels of key COMAR genes in LUAD could be examined before ICB immunotherapy and then applied for screening of immunotherapy patients. Second, researchers could explore the therapeutic target potential of these genes, which could be adopted for the development of targeted drugs.

In brief, the coagulation process and macrophage infiltration are two important factors that are usually aberrant in LUAD. They have cross-talk impacts on each other mutually and contribute to the concerto in regulating LUAD development. Based on the coagulation-related genes and the M2-TAM marker genes, a scoring model containing 10 prognostic genes (APOE, ARRB2, C1QB, F13A1, FCGR2A, FYN, ITGB2, MMP9, OLR1, and VSIG4) was constructed. This prognostic signature is super efficacious in predicting the prognosis and ICB immunotherapeutic outcomes of patients with LUAD, which provides potential biomarkers for LUAD treatment and prognostic prediction.

Data availability statement

The original contributions presented in the study are included in the article/Supplementary Material. Further inquiries can be directed to the corresponding author.

Ethics statement

Ethical approval was not required for the study involving humans in accordance with the local legislation and institutional requirements. Written informed consent to participate in this study was not required from the participants or the participants' legal guardians/next of kin in accordance with the national legislation and the institutional requirements.

Author contributions

ZLi: Data curation, Formal analysis, Investigation, Methodology, Writing – original draft. ZYi: Formal analysis, Data curation, Writing – original draft. ZLu: Data curation, Formal analysis, Writing – original draft. CZ: Data curation, Formal analysis, Writing – original draft. YW: Data curation, Formal analysis, Writing – review & editing. KZ: Data curation, Formal analysis, Writing – review & editing. FC: Data curation, Formal analysis, Writing – review &

editing. ZYa: Data curation, Formal analysis, Writing – review & editing. YT: Conceptualization, Funding acquisition, Investigation, Methodology, Project administration, Supervision, Validation, Writing – review & editing.

Funding

The author(s) declare financial support was received for the research, authorship, and/or publication of this article. The study was funded by the Clinical Research Fund of Shandong Medical Association Qilu Special Project (YXH2022ZX02016; YT), the Research Fund of Shandong Second Provincial General Hospital (2023MS01; YT), and the Clinical Research Special Support Fund of Wu Jieping Medical Foundation (320.6750.2023-16-12; YT).

Acknowledgments

We are very grateful to the Gene-Expression Omnibus (GEO) and The Cancer Genome Atlas (TCGA) databases for providing the transcriptome and clinical information.

Conflict of interest

The authors declare that the research was conducted in the absence of any commercial or financial relationships that could be construed as a potential conflict of interest.

Publisher's note

Supplementary material

The Supplementary Material for this article can be found online at: https://www.frontiersin.org/articles/10.3389/fimmu.2023.1273422/full#supplementary-material

References

1. Siegel RL, Miller KD, Wagle NS, Jemal A. Cancer statistics, 2023. *CA Cancer J Clin* (2023) 73(1):17–48. doi: 10.3322/caac.21763

2. Thai AA, Solomon BJ, Sequist LV, Gainor JF, Heist RS. Lung cancer. *Lancet* (2021) 398(10299):535–54. doi: 10.1016/s0140-6736(21)00312-3

3. Karasaki T, Moore DA, Veeriah S, Naceur-Lombardelli C, Toncheva A, Magno N, et al. Evolutionary characterization of lung adenocarcinoma morphology in Tracerx. *Nat Med* (2023) 29(4):833–45. doi: 10.1038/s41591-023-02230-w

4. Gillette MA, Satpathy S, Cao S, Dhanasekaran SM, Vasaikar SV, Krug K, et al. Proteogenomic characterization reveals therapeutic vulnerabilities in lung adenocarcinoma. *Cell* (2020) 182(1):200–25 e35. doi: 10.1016/j.cell.2020.06.013

5. Pitt JM, Marabelle A, Eggermont A, Soria J-C, Kroemer G, Zitvogel L. Targeting the tumor microenvironment: removing obstruction to anticancer immune responses and immunotherapy. *Ann Oncol* (2016) 27(8):11. doi: 10.1093/annonc/mdw168

6. Bejarano L, Jordao MJC, Joyce JA. Therapeutic targeting of the tumor microenvironment. *Cancer Discovery* (2021) 11(4):933–59. doi: 10.1158/2159-8290.CD-20-1808

7. Mantovani A, Marchesi F, Malesci A, Laghi L, Allavena P. Tumour-associated macrophages as treatment targets in oncology. *Nat Rev Clin Oncol* (2017) 14(7):399–416. doi: 10.1038/nrclinonc.2016.217

8. Mantovani A, Allavena P, Marchesi F, Garlanda C. Macrophages as tools and targets in cancer therapy. *Nat Rev Drug Discovery* (2022) 21(11):799–820. doi: 10.1038/s41573-022-00520-5

9. Christofides A, Strauss L, Yeo A, Cao C, Charest A, Boussiotis VA. The complex role of tumor-infiltrating macrophages. *Nat Immunol* (2022) 23(8):1148–56. doi: 10.1038/s41590-022-01267-2

10. Schmall A, Al-tamari HM, Herold S, Kampschulte M, Weigert A, Wietelmann A, et al. Macrophage and cancer cell cross-talk via Ccr2 and Cx3cr1 is a fundamental mechanism driving lung cancer. *Am J Respir Crit Care Med* (2015) 191(4):437–47. doi: 10.1164/rccm.201406-1137OC

11. Casanova-Acebes M, Dalla E, Leader AM, LeBerichel J, Nikolic J, Morales BM, et al. Tissue-resident macrophages provide a pro-tumorigenic niche to early Nsclc cells. *Nature* (2021) 595(7868):578–84. doi: 10.1038/s41586-021-03651-8

12. Wei K, Ma Z, Yang F, Zhao X, Jiang W, Pan C, et al. M2 macrophage-derived exosomes promote lung adenocarcinoma progression by delivering Mir-942. *Cancer Lett* (2022) 526:205–16. doi: 10.1016/j.canlet.2021.10.045

13. Chen J, Zhang K, Zhi Y, Wu Y, Chen B, Bai J, et al. Tumor-derived exosomal Mir-19b-3p facilitates M2 macrophage polarization and exosomal Linc00273 secretion to promote lung adenocarcinoma metastasis via hippo pathway. *Clin Transl Med* (2021) 11(9):e478. doi: 10.1002/ctm2.478

14. Zhang J, Li H, Wu Q, Chen Y, Deng Y, Yang Z, et al. Tumoral Nox4 recruits M2 tumor-associated macrophages via Ros/Pi3k signaling-dependent various cytokine production to promote Nsclc growth. *Redox Biol* (2019) 22:101116. doi: 10.1016/j.redox.2019.101116

15. Guo Z, Song J, Hao J, Zhao H, Du X, Li E, et al. M2 macrophages promote Nsclc metastasis by upregulating cryab. *Cell Death Dis* (2019) 10(6):377. doi: 10.1038/s41419-019-1618-x

16. Hwang I, Kim JW, Ylaya K, Chung EJ, Kitano H, Perry C, et al. Tumor-associated macrophage, angiogenesis and lymphangiogenesis markers predict prognosis of non-small cell lung cancer patients. *J Trans Med* (2020) 18(1):443–57. doi: 10.1186/s12967-020-02618-z

17. Gross DJ, Chintala NK, Vaghjiani RG, Grosser R, Tan KS, Li X, et al. Tumor and tumor-associated macrophage programmed death-ligand 1 expression is associated with adjuvant chemotherapy benefit in lung adenocarcinoma. *J Thorac Oncol* (2022) 17(1):89–102. doi: 10.1016/j.jtho.2021.09.009

18. Larroquette M, Guegan JP, Besse B, Cousin S, Brunet M, Le Moulec S, et al. Spatial transcriptomics of macrophage infiltration in non-small cell lung cancer reveals determinants of sensitivity and resistance to anti-Pd1/Pd-L1 antibodies. *J Immunother Cancer* (2022) 10(5):e003890. doi: 10.1136/jitc-2021-003890

19. Ruf W, Graf C. Coagulation signaling and cancer immunotherapy. *Thromb Res* (2020) 191(Suppl 1):S106–S11. doi: 10.1016/S0049-3848(20)30406-0

20. Kitano M, Macher-Göppinger S, Weiler H, Ruf W. Myeloid cell–synthesized coagulation factor X dampens antitumor immunity. *Sci Immunol* (2019) 4(39):eaaw8405. doi: 10.1126/sciimmunol.aaw8405

21. Zhang T, Ma Z, Wang R, Wang Y, Wang S, Cheng Z, et al. Thrombin facilitates invasion of ovarian cancer along peritoneum by inducing monocyte differentiation toward tumor-associated macrophage-like cells. *Cancer Immunol Immunother* (2010) 59(7):1097–108. doi: 10.1007/s00262-010-0836-y

22. Kubala MH, Punj V, Placencio-Hickok VR, Fang H, Fernandez GE, Sposto R, et al. Plasminogen activator inhibitor-1 promotes the recruitment and polarization of macrophages in cancer. *Cell Rep* (2018) 25(8):2177–91.e7. doi: 10.1016/j.celrep.2018.10.082

23. Gil-Bernabe AM, Ferjancic S, Tlalka M, Zhao L, Allen PD, Im JH, et al. Recruitment of monocytes/macrophages by tissue factor-mediated coagulation is essential for metastatic cell survival and premetastatic niche establishment in mice. *Blood* (2012) 119(13):3164–75. doi: 10.1182/blood-2011-08-376426

24. Lefrancais E, Ortiz-Munoz G, Caudrillier A, Mallavia B, Liu F, Sayah DM, et al. The lung is a site of platelet biogenesis and a reservoir for haematopoietic progenitors. *Nature* (2017) 544(7648):105–9. doi: 10.1038/nature21706

25. Khalil J, Bensaid B, Elkacemi H, Afif M, Bensaid Y, Kebdani T, et al. Venous thromboembolism in cancer patients: an underestimated major health problem. *World J Surg Oncol* (2015) 13:204. doi: 10.1186/s12957-015-0592-8

26. Zhang Y, Yang Y, Chen W, Guo L, Liang L, Zhai Z, et al. Prevalence and associations of Vte in patients with newly diagnosed lung cancer. *Chest* (2014) 146 (3):650–8. doi: 10.1378/chest.13-2379

27. Lee JW, Cha SI, Jung CY, Choi WI, Jeon KN, Yoo SS, et al. Clinical course of pulmonary embolism in lung cancer patients. *Respiration* (2009) 78(1):42–8. doi: 10.1159/000176208

28. Kim N, Kim HK, Lee K, Hong Y, Cho JH, Choi JW, et al. Single-cell Rna sequencing demonstrates the molecular and cellular reprogramming of metastatic lung adenocarcinoma. *Nat Commun* (2020) 11(1):2285. doi: 10.1038/s41467-020-16164-1

29. Ghandi M, Huang FW, Jané-Valbuena J, Kryukov GV, Lo CC, McDonald ER, et al. Next-generation characterization of the cancer cell line encyclopedia. *Nature* (2019) 569(7757):503–8. doi: 10.1038/s41586-019-1186-3

30. Galmiche A, Rak J, Roumenina LT, Saidak Z. Coagulome and the tumor microenvironment: an actionable interplay. *Trends Cancer* (2022) 8(5):369–83. doi: 10.1016/j.trecan.2021.12.008

31. Ben S, Huang X, Shi Y, Xu Z, Xiao H. Change in cytokine profiles released by mast cells mediated by lung cancer-derived exosome activation may contribute to cancer-associated coagulation disorders. *Cell Commun Signal* (2023) 21(1):97. doi: 10.1186/s12964-023-01110-7

32. Dou F, Li H, Zhu M, Liang L, Zhang Y, Yi J, et al. Association between oncogenic status and risk of venous thromboembolism in patients with non-small cell lung cancer. *Respir Res* (2018) 19(1):88. doi: 10.1186/s12931-018-0791-2

33. Levitin HM, Yuan J, Sims PA. Single-cell transcriptomic analysis of tumor heterogeneity. *Trends Cancer* (2018) 4(4):264–8. doi: 10.1016/j.trecan.2018.02.003

34. Kinker GS, Greenwald AC, Tal R, Orlova Z, Cuoco MS, McFarland JM, et al. Pan-cancer single-cell rna-seq identifies recurring programs of cellular heterogeneity. *Nat Genet* (2020) 52(11):1208–18. doi: 10.1038/s41588-020-00726-6

35. Potter SS. Single-cell Rna sequencing for the study of development, physiology and disease. *Nat Rev Nephrol* (2018) 14(8):479–92. doi: 10.1038/s41581-018-0021-7

36. Papalexi E, Satija R. Single-cell Rna sequencing to explore immune cell heterogeneity. *Nat Rev Immunol* (2018) 18(1):35–45. doi: 10.1038/nri.2017.76

37. Song Q, Ji Q, Li Q. The role and mechanism of B–Arrestins in cancer invasion and metastasis (Review). *Int J Mol Med* (2017) 41(2):631–9. doi: 10.3892/ijmm.2017.3288

38. Bostanabad SY, Noyan S, Dedeoglu BG, Gurdal H. Overexpression of beta-arrestins inhibits proliferation and motility in triple negative breast cancer cells. *Sci Rep* (2021) 11(1):1539. doi: 10.1038/s41598-021-80974-6

39. Sun WY, Hu SS, Wu JJ, Huang Q, Ma Y, Wang QT, et al. Down-regulation of beta-arrestin2 promotes tumour invasion and indicates poor prognosis of hepatocellular carcinoma. *Sci Rep* (2016) 6:35609. doi: 10.1038/srep35609

40. Raghuwanshi SK, Nasser MW, Chen X, Strieter RM, Richardson RM. Depletion of beta-arrestin-2 promotes tumor growth and angiogenesis in a murine model of lung cancer. *J Immunol* (2008) 180(8):5699–706. doi: 10.4049/jimmunol.180.8.5699

41. Kim JY, Shin JH, Kim MJ, Kang Y, Lee JS, Son J, et al. Beta-arrestin 2 negatively regulates lung cancer progression by inhibiting the Traf6 signaling axis for Nf-Kappab activation and autophagy induced by Tlr3 and Tlr4. *Cell Death Dis* (2023) 14(7):422. doi: 10.1038/s41419-023-05945-3

42. Supsrisunjai C, Hsu CK, Michael M, Duval C, Lee JYW, Yang HS, et al. Coagulation factor xiii-a subunit missense mutation in the pathobiology of autosomal dominant multiple dermatofibromas. *J Invest Dermatol* (2020) 140 (3):624–35 e7. doi: 10.1016/j.jid.2019.08.441

43. Fan T, Lu Z, Liu Y, Wang L, Tian H, Zheng Y, et al. A novel immune-related seventeen-gene signature for predicting early stage lung squamous cell carcinoma prognosis. *Front Immunol* (2021) 12:665407. doi: 10.3389/fimmu.2021.665407

44. Wang Y, Yan K, Lin J, Li J, Bi J. Macrophage M2 co-expression factors correlate with the immune microenvironment and predict outcome of renal clear cell carcinoma. *Front Genet* (2021) 12:615655. doi: 10.3389/fgene.2021.615655

45. Lehrer S, Dembitzer FR, Rheinstein PH, Rosenzweig KE. In primary glioblastoma fewer tumor copy number segments of the F13a1 gene are associated with poorer survival. *Thromb Res* (2018) 167:12–4. doi: 10.1016/j.thromres.2018.05.001

46. Bao X, Li Q, Chen J, Chen D, Ye C, Dai X, et al. Molecular subgroups of intrahepatic cholangiocarcinoma discovered by single-cell Rna sequencing-assisted multiomics analysis. *Cancer Immunol Res* (2022) 10(7):811–28. doi: 10.1158/2326-6066.CIR-21-1101

47. Jiang J, Ding Y, Wu M, Lyu X, Wang H, Chen Y, et al. Identification of Tyrobp and C1qb as two novel key genes with prognostic value in gastric cancer by network analysis. *Front Oncol* (2020) 10:1765. doi: 10.3389/fonc.2020.01765

48. Li Z, Zhou B, Zhu X, Yang F, Jin K, Dai J, et al. Differentiation-related genes in tumor-associated macrophages as potential prognostic biomarkers in non-small cell lung cancer. *Front Immunol* (2023) 14:1123840. doi: 10.3389/fimmu.2023.1123840

49. Fu T, Zhang L, Zuo M, Li F, Shi C, Chen H. Fcgr2a as one novel potential target for poor survival prognosis of clear cell renal cell carcinoma. *Med (Baltimore)* (2023) 102(11):e33324. doi: 10.1097/MD.0000000000033324

50. Gavin PG, Song N, Kim SR, Lipchik C, Johnson NL, Bandos H, et al. Association of polymorphisms in Fcgr2a and Fcgr3a with degree of trastuzumab benefit in the adjuvant treatment of Erbb2/Her2-positive breast cancer: analysis of the Nsabp B-31 trial. *JAMA Oncol* (2017) 3(3):335–41. doi: 10.1001/jamaoncol.2016.4884

51. Liu G, Tu D, Lewis M, Cheng D, Sullivan LA, Chen Z, et al. Fc-Gamma receptor polymorphisms, cetuximab therapy, and survival in the ncic Ctg Co.17 trial of colorectal cancer. *Clin Cancer Res* (2016) 22(10):2435–44. doi: 10.1158/1078-0432.CCR-15-0414

52. Zhang W, Gordon M, Schultheis AM, Yang DY, Nagashima F, Azuma M, et al. Fcgr2a and Fcgr3a polymorphisms associated with clinical outcome of epidermal growth factor receptor expressing metastatic colorectal cancer patients treated with single-agent cetuximab. *J Clin Oncol* (2007) 25(24):3712–8. doi: 10.1200/JCO.2006.08.8021

53. Cheung NK, Sowers R, Vickers AJ, Cheung IY, Kushner BH, Gorlick R. Fcgr2a polymorphism is correlated with clinical outcome after immunotherapy of neuroblastoma with anti-Gd2 antibody and granulocyte macrophage colony-stimulating factor. *J Clin Oncol* (2006) 24(18):2885–90. doi: 10.1200/JCO.2005.04.6011

54. Nie W, Yao Y, Luo B, Zhu J, Li S, Yang X, et al. Systematic analysis of the expression and prognosis of fcgamma receptors in clear cell renal cell carcinoma. *Front Oncol* (2022) 12:755936. doi: 10.3389/fonc.2022.755936

55. Sun S, Liu Y, Zhou M, Wen J, Xue L, Han S, et al. Pa2g4 promotes the metastasis of hepatocellular carcinoma by stabilizing Fyn Mrna in a Ythdf2-dependent manner. *Cell Biosci* (2022) 12(1):55. doi: 10.1186/s13578-022-00788-5

56. Comba A, Dunn PJ, Argento AE, Kadiyala P, Ventosa M, Patel P, et al. Fyn tyrosine kinase, a downstream target of receptor tyrosine kinases, modulates antiglioma immune responses. *Neuro Oncol* (2020) 22(6):806–18. doi: 10.1093/neuonc/noaa006

57. Zhang X, Huang Z, Guo Y, Xiao T, Tang L, Zhao S, et al. The phosphorylation of Cd147 by Fyn plays a critical role for melanoma cells growth and metastasis. *Oncogene* (2020) 39(21):4183–97. doi: 10.1038/s41388-020-1287-3

58. Yu B, Xu L, Chen L, Wang Y, Jiang H, Wang Y, et al. Fyn is required for Arhgef16 to promote proliferation and migration in colon cancer cells. *Cell Death Dis* (2020) 11(8):652. doi: 10.1038/s41419-020-02830-1

59. Yu J, Zhou Z, Wei Z, Wu J, OuYang J, Huang W, et al. Fyn promotes gastric cancer metastasis by activating Stat3-mediated epithelial-mesenchymal transition. *Transl Oncol* (2020) 13(11):100841. doi: 10.1016/j.tranon.2020.100841

60. Dong S-JS W, Qin J-J, Liu G-M. Fyn stimulates the progression of pancreatic cancer via Fyn-Glun2b-Akt axis. *Eur Rev Med Pharmacol Sci* (2020) 24(1):109–21. doi: 10.26355/eurrev_202001_19900

61. Xue F, Jia Y, Zhao J. Overexpression of fyn suppresses the epithelial-to-mesenchymal transition through down-regulating Pi3k/Akt pathway in lung adenocarcinoma. *Surg Oncol* (2020) 33:108–17. doi: 10.1016/j.suronc.2020.02.002

62. Liu H, Dai X, Cao X, Yan H, Ji X, Zhang H, et al. Prdm4 mediates Yap-induced cell invasion by activating leukocyte-specific integrin Beta2 expression. *EMBO Rep* (2018) 19(6):e45180. doi: 10.15252/embr.201745180

63. Li CF, Wang JM, Kang HY, Huang CK, Wang JW, Fang FM, et al. Characterization of gene amplification-driven Skp2 overexpression in myxofibrosarcoma: potential implications in tumor progression and therapeutics. *Clin Cancer Res* (2012) 18(6):1598–610. doi: 10.1158/1078-0432.CCR-11-3077

64. Zhang X, Dong Y, Zhao M, Ding L, Yang X, Jing Y, et al. Itgb2-mediated metabolic switch in Cafs promotes Oscc proliferation by oxidation of Nadh in mitochondrial oxidative phosphorylation system. *Theranostics* (2020) 10(26):12044–59. doi: 10.7150/thno.47901

65. Li C, Deng T, Cao J, Zhou Y, Luo X, Feng Y, et al. Identifying Itgb2 as a potential prognostic biomarker in ovarian cancer. *Diagnost (Basel)* (2023) 13(6):1169–82. doi: 10.3390/diagnostics13061169

66. Liu H, Wang J, Luo T, Zhen Z, Liu L, Zheng Y, et al. Correlation between Itgb2 expression and clinical characterization of glioma and the prognostic significance of its methylation in low-grade glioma(Lgg). *Front Endocrinol (Lausanne)* (2022) 13:1106120. doi: 10.3389/fendo.2022.1106120

67. Zu L, He J, Zhou N, Zeng J, Zhu Y, Tang Q, et al. The profile and clinical significance of Itgb2 expression in non-small-cell lung cancer. *J Clin Med* (2022) 11 (21):6421–33. doi: 10.3390/jcm11216421

68. Al-Batran SE, Pauligk C, Wirtz R, Werner D, Steinmetz K, Homann N, et al. The validation of matrix metalloproteinase-9 Mrna gene expression as a predictor of outcome in patients with metastatic gastric cancer. *Ann Oncol* (2012) 23(7):1699–705. doi: 10.1093/annonc/mdr552

69. Sachie Hiratsuka KN, Iwai S, Murakami M, Itoh T, Kijima H, Shipley JM, et al. Mmp9 induction by vascular endothelial growth factor receptor-1 is involved in lung-specific metastasis. *Cancer Cell* (2002) 2(4):289–300. doi: 10.1016/s1535-6108(02)00153-8

70. Murdocca M, De Masi C, Pucci S, Mango R, Novelli G, Di Natale C, et al. Lox-1 and cancer: an indissoluble liaison. *Cancer Gene Ther* (2021) 28(10-11):1088–98. doi: 10.1038/s41417-020-00279-0

71. Jiang L, Jiang S, Zhou W, Huang J, Lin Y, Long H, et al. Oxidized low density lipoprotein receptor 1 promotes lung metastases of osteosarcomas through regulating the epithelial-mesenchymal transition. *J Transl Med* (2019) 17(1):369. doi: 10.1186/s12967-019-2107-9

72. Hall BM, Gleiberman AS, Strom E, Krasnov PA, Frescas D, Vujcic S, et al. Immune checkpoint protein Vsig4 as a biomarker of aging in murine adipose tissue. *Aging Cell* (2020) 19(10):e13219. doi: 10.1111/acel.13219

73. Liao Y, Guo S, Chen Y, Cao D, Xu H, Yang C, et al. Vsig4 expression on macrophages facilitates lung cancer development. *Lab Invest* (2014) 94(7):706–15. doi: 10.1038/labinvest.2014.73

74. Su WP, Chen YT, Lai WW, Lin CC, Yan JJ, Su WC. Apolipoprotein E expression promotes lung adenocarcinoma proliferation and migration and as a potential survival marker in lung cancer. *Lung Cancer* (2011) 71(1):28–33. doi: 10.1016/j.lungcan.2010.04.009

75. Lee YS, Yeo IJ, Kim KC, Han SB, Hong JT. Inhibition of lung tumor development in Apoe knockout mice via enhancement of Trem-1 dependent Nk cell cytotoxicity. *Front Immunol* (2019) 10:1379. doi: 10.3389/fimmu.2019.01379

76. Oliveira G, Wu CJ. Dynamics and specificities of T cells in cancer immunotherapy. *Nat Rev Cancer* (2023) 23(5):295–316. doi: 10.1038/s41568-023-00560-y

77. Sanz-Pamplona R, Melas M, Maoz A, Schmit SL, Rennert H, Lejbkowicz F, et al. Lymphocytic infiltration in stage ii microsatellite stable colorectal tumors: A retrospective prognosis biomarker analysis. *PloS Med* (2020) 17(9):e1003292. doi: 10.1371/journal.pmed.1003292

78. Zitvogel L, Galluzzi L, Kepp O, Smyth MJ, Kroemer G. Type I interferons in anticancer immunity. *Nat Rev Immunol* (2015) 15(7):405–14. doi: 10.1038/nri3845

79. Wu Y, Biswas D, Usaite I, Angelova M, Boeing S, Karasaki T, et al. A local human Vδ1 T cell population is associated with survival in nonsmall-cell lung cancer. *Nat Cancer* (2022) 3(6):696–709. doi: 10.1038/s43018-022-00376-z

80. Myers JA, Miller JS. Exploring the Nk cell platform for cancer immunotherapy. *Nat Rev Clin Oncol* (2020) 18(2):85–100. doi: 10.1038/s41571-020-0426-7

81. Park MD, Reyes-Torres I, LeBerichel J, Hamon P, LaMarche NM, Hegde S, et al. Trem2 macrophages drive Nk cell paucity and dysfunction in lung cancer. *Nat Immunol* (2023) 24(5):792–801. doi: 10.1038/s41590-023-01475-4

82. Fridman WH, Meylan M, Petitprez F, Sun C-M, Italiano A, Sautès-Fridman C. B cells and tertiary lymphoid structures as determinants of tumour immune contexture and clinical outcome. *Nat Rev Clin Oncol* (2022) 19(7):441–57. doi: 10.1038/s41571-022-00619-z

83. Patil NS, Nabet BY, Müller S, Koeppen H, Zou W, Giltnane J, et al. Intratumoral plasma cells predict outcomes to Pd-L1 blockade in non-small cell lung cancer. *Cancer Cell* (2022) 40(3):289–300.e4. doi: 10.1016/j.ccell.2022.02.002

84. Speiser DE, Chijioke O, Schaeuble K, Münz C. Cd4+ T cells in cancer. *Nat Cancer* (2023) 4(3):317–29. doi: 10.1038/s43018-023-00521-2

85. Duan Z, Luo Y. Targeting macrophages in cancer immunotherapy. *Signal Transduct Target Ther* (2021) 6(1):127–47. doi: 10.1038/s41392-021-00506-6

86. Qin J, Zhang X, Tan B, Zhang S, Yin C, Xue Q, et al. Blocking P2x7-mediated macrophage polarization overcomes treatment resistance in lung cancer. *Cancer Immunol Res* (2020) 8(11):1426–39. doi: 10.1158/2326-6066.Cir-20-0123

87. Liu Y, Wang Y, Yang Y, Weng L, Wu Q, Zhang J, et al. Emerging phagocytosis checkpoints in cancer immunotherapy. *Signal Transduct Target Ther* (2023) 8(1):104–45. doi: 10.1038/s41392-023-01365-z

88. Liu B, Wang Z, Gu M, Zhao C, Ma T, Wang J. Geo data mining identifies Olr1 as a potential biomarker in Nsclc immunotherapy. *Front Oncol* (2021) 11:629333. doi: 10.3389/fonc.2021.629333

89. Ye Y, Kuang X, Xie Z, Liang L, Zhang Z, Zhang Y, et al. Small-molecule Mmp2/Mmp9 inhibitor Sb-3ct modulates tumor immune surveillance by regulating Pd-L1. *Genome Med* (2020) 12(1):83–101. doi: 10.1186/s13073-020-00780-z

90. Xu H, Zhang A, Han X, Li Y, Zhang Z, Song L, et al. Itgb2 as a prognostic indicator and a predictive marker for immunotherapy in gliomas. *Cancer Immunol Immunother* (2021) 71(3):645–60. doi: 10.1007/s00262-021-03022-2

91. Sun Y, Liu Y, Chu H. Nasopharyngeal carcinoma subtype discovery via immune cell scores from tumor microenvironment. *J Immunol Res* (2023) 2023:2242577. doi: 10.1155/2023/2242577

92. Zhang Y, Ma W, Fan W, Ren C, Xu J, Zeng F, et al. Comprehensive transcriptomic characterization reveals core genes and module associated with immunological changes via 1619 samples of brain glioma. *Cell Death Dis* (2021) 12 (12):1140–50. doi: 10.1038/s41419-021-04427-8

93. Fang G, Wang X. Prognosis-related genes participate in immunotherapy of renal clear cell carcinoma possibly by targeting dendritic cells. *Front Cell Dev Biol* (2022) 10:892616. doi: 10.3389/fcell.2022.892616

frontiers | Frontiers in Immunology

TYPE Original Research
PUBLISHED 05 December 2023
DOI 10.3389/fimmu.2023.1289753

OPEN ACCESS

EDITED BY
Zhangran Chen,
Xiamen University, China

REVIEWED BY
Tiezheng Hou,
University College London,
United Kingdom
Leonardo Stella,
Agostino Gemelli University Polyclinic
(IRCCS), Italy
Jianjun Liu,
Dalian Medical University, China

*CORRESPONDENCE
Fang Wu
wufang_wlx@126.com
Gang Chen
chen.gang@wmu.edu.cn
Yi Wang
wang.yi@wmu.edu.cn

†These authors have contributed equally to this work

RECEIVED 06 September 2023
ACCEPTED 16 November 2023
PUBLISHED 05 December 2023

CITATION
Zhao R, Li J, Chen B, Zhao J, Hu L, Huang K, Chen Q, Yao J, Lin G, Bao L, Lu M, Wang Y, Chen G and Wu F (2023) The enrichment of the gut microbiota Lachnoclostridium is associated with the presence of intratumoral tertiary lymphoid structures in hepatocellular carcinoma. *Front. Immunol.* 14:1289753. doi: 10.3389/fimmu.2023.1289753

The enrichment of the gut microbiota Lachnoclostridium is associated with the presence of intratumoral tertiary lymphoid structures in hepatocellular carcinoma

Rui Zhao[1†], Jiacheng Li[2†], Bo Chen[2†], Jungang Zhao[2], Leyin Hu[3], Kate Huang[3], Qiwen Chen[1], Jiangqiao Yao[2], Ganglian Lin[2], Lishimeng Bao[4], Mengmeng Lu[1], Yi Wang[5,6*], Gang Chen[2,6,7*] and Fang Wu[1*]

[1]Department of Gastroenterology, The First Affiliated Hospital of Wenzhou Medical University, Wenzhou, China, [2]Department of Hepatobiliary Surgery, The First Affiliated Hospital of Wenzhou Medical University, Wenzhou, China, [3]Department of Pathology, The First Affiliated Hospital of Wenzhou Medical University, Wenzhou, China, [4]The Second Clinical College, Wenzhou Medical University, Wenzhou, China, [5]Department of Epidemiology and Biostatistics, School of Public Health and Management, Wenzhou Medical University, Wenzhou, China, [6]Zhejiang-Germany Interdisciplinary Joint Laboratory of Hepatobiliary-Pancreatic Tumor and Bioengineering, Wenzhou, China, [7]Key Laboratory of Diagnosis and Treatment of Severe Hepato-Pancreatic Diseases of Zhejiang Province, The First Affiliated Hospital of Wenzhou Medical University, Wenzhou, Zhejiang, China

Backgrounds and aims: Immunotherapies have formed an entirely new treatment paradigm for hepatocellular carcinoma (HCC). Tertiary lymphoid structure (TLS) has been associated with good response to immunotherapy in most solid tumors. Nonetheless, the role of TLS in human HCC remains controversial, and recent studies suggest that their functional heterogeneity may relate to different locations within the tumor. Exploring factors that influence the formation of TLS in HCC may provide more useful insights. However, factors affecting the presence of TLSs are still unclear. The human gut microbiota can regulate the host immune system and is associated with the efficacy of immunotherapy but, in HCC, whether the gut microbiota is related to the presence of TLS still lacks sufficient evidence.

Methods: We performed pathological examinations of tumor and para-tumor tissue sections. Based on the location of TLS in tissues, all patients were divided into intratumoral TLS (It-TLS) group and desertic TLS (De-TLS) group. According to the grouping results, we statistically analyzed the clinical, biological, and pathological features; preoperative gut microbiota data; and postoperative pathological features of patients.

Results: In a retrospective study cohort of 60 cases from a single center, differential microbiota analysis showed that compared with the De-TLS group, the abundance of Lachnoclostridium, Hungatella, Blautia, Fusobacterium, and Clostridium was increased in the It-TLS group. Among them, the enrichment of

Lachnoclostridium was the most significant and was unrelated to the clinical, biological, and pathological features of the patients. It can be seen that the difference in abundance levels of microbiota is related to the presence of TLS.

Conclusion: Our findings prove the enrichment of Lachnoclostridium-dominated gut microbiota is associated with the presence of It-TLS in HCC patients.

KEYWORDS

hepatocellular carcinoma (HCC), tumor immune microenvironment (TIME), tertiary lymphoid structure (TLS), gut microbiota, Lachnoclostridium

Highlights

- **What is already known on this topic**

Previously, the presence of intratumoral tertiary lymphoid structures (TLS) has been demonstrated to correlate with favorable immunotherapy response and long-term prognosis in patients with hepatocellular carcinoma (HCC); however, factors influencing their presence remain elusive.

- **What this study adds**

Our study has, for the first time, demonstrated the association between gut microbiota and TLS presence. We found that the enrichment of Lachnoclostridium-dominated gut microbiota is associated with the presence of intratumoral TLS in HCC a patients.

- **How this study might affect research, practice, or policy**

This provides new insights into the research on how gut microbiota affects tumor immunotherapy, specifically by modulating the formation of intratumoral TLS.

Introduction

Primary liver cancer is the sixth most commonly diagnosed cancer type and the third leading cause of cancer death worldwide in 2020. Hepatocellular carcinoma (HCC) is the main pathological type of primary liver cancer, accounting for 75%–85% of all liver cancer cases (1). Over the past decade, the systemic therapies of tyrosine kinase inhibitors sorafenib and lenvatinib have been the first-line treatment for advanced HCC. Currently, immune checkpoint inhibitors (ICIs) and other immunotherapies are emerging as a major treatment approach in HCC due to significantly improved overall survival and lower recurrence rates in HCC patients (2–5). Despite these major advances, the full therapeutic potential of ICIs has not yet been fully realized because not all patients benefit from immunotherapy, and some HCC patients may even experience hyperprogressive disease after treatment (6, 7). Finding predictive biomarkers for good efficacy of immunotherapy can better guide the choice of clinical treatment plans, help improve patient prognosis, and solve problems pending in clinical treatment.

Tertiary lymphoid structures (TLS) are organized clusters of immune cells comprised by T and B cells and sometimes other immune cell type that develop in non-lymphoid tissues after birth. In TLS, germinal center-like aggregates of CD20+ B cells are surrounded by CD3+ T cells, resembling structures found in secondary lymphoid organs (8). TLS has emerged as a promising biomarker, as its presence in most solid tumors is closely linked with better outcomes and may predict response to ICIs (9, 10). However, the role of TLS in HCC is still debated. Recent research indicates significant functional differences depending on location within the tumor. Finkin et al. found TLS in para-tumor liver tissue increased the risk of HCC recurrence long after treatment (11). In contrast, Wolf Herman Fridman et al. found TLS within HCC tumors linked to lower odds of the cancer recurrence after surgery. They suggested that TLS inside tumors may help antitumor immunity by boosting local antigen presentation and immune cell maturation (12). Most importantly, the drivers of TLS formation in HCC and other cancers are still not fully understood.

The gut microbiota, as the largest symbiotic microbial community in humans, plays a critical role in directing the normal development of the immune system and regulating immune functions (13), including contributing to germinal center formation, regulating germinal center reactions (14), and promoting T- and B-cell activation (15, 16). Given the intertwined nature of the microbiota and the immune system, the microbiota is likely to influence the host's response to immunotherapy. Recent clinical studies have shown that changes in the gut microbiota profiles of patients responding to immunotherapy can predict the efficacy of immunotherapy, including in HCC (17). Specific gut microbes have been identified and shown to even affect the efficacy of ICI in tumor patients, including those with gastrointestinal tumors and distal intestinal tumors (18–20). Mechanistic explorations have shown that the gut

Abbreviations: ICIs, immune checkpoint inhibitors; HCC, hepatocellular carcinoma; TLS, tertiary lymphoid structure; It-TLS group, intratumoral TLS group; De-TLS group, desertic-TLS group; TILs, tumor infiltrating lymphocytes; HBV, hepatitis B virus infection; HCV, hepatitis C virus infection; NAFLD, nonalcoholic fatty liver disease; BCLC, Barcelona clinic liver cancer; AFP, alpha-fetoprotein; FFPE, formalin-fixed paraffin-embedded; TIME, tumor immune microenvironment.

microbiota increases the number of infiltrating lymphocytes in tumor tissues. In recent years, with a deepening understanding of the function of tumor infiltrating lymphocytes (TILs), recent studies have highlighted that TILs exert their effects by forming specific spatial structures such as TLS (21). However, little is known so far about whether the gut microbiota affects the formation of specific spatial structures by TILs. Previously, research clinical features by Timothy W. Hand et al. confirmed that specific gut microbiota can support the maturation of adjacent TLS in mouse colorectal cancer (22), but further investigation is needed to determine whether similar relationships exist in human patients with tumors outside the gut.

In this study, we found that the enrichment of Lachnoclostridium-dominated gut microbiota is associated with the presence of intratumoral TLS (It-TLS) in HCC patients in a single-center retrospective cohort (Figure 1).

Materials and methods

Study population and specimen collection

We conducted a retrospective analysis of 60 patients who underwent curative hepatectomy for HCC at the First Affiliated Hospital of Wenzhou Medical University between 1 January 2019 and 30 June 2022. All cases were pathologically and clinically diagnosed as HCC. Within 30 min of hepatectomy, HCC tumor tissues and adjacent non-tumor tissues (defined as >3 cm from the tumor margin) were collected. The tissues were evenly cut and immediately preserved in RNA later solution. All tissue samples were stored at −80°C within 24h. The tissue specimens were obtained from the surgically resected tissues and did not cause any additional interventions or risks to the patients. Patients had not been prescribed lactulose, proton pump inhibitors, non-steroidal anti-inflammatory drugs, antibiotics, probiotics, or prebiotics within 4 weeks prior to surgery. Fecal samples were obtained from all patients before surgery for 16S rRNA sequencing analysis. This study was approved by the Ethics Committee of the First Affiliated Hospital of Wenzhou Medical University, and the study protocol conforms to the ethical guidelines of the 1975 Declaration of Helsinki.

Clinical and biological features

We retrospectively obtained the following clinical and biological features of patients in the study cohort: age, sex, alcohol consumption (active or inactive at the time of surgery), hepatitis B virus (HBV) infection, hepatitis C virus (HCV) infection (eradicated or non-eradicated at the time of surgery), nonalcoholic fatty liver disease (NAFLD), other etiologies, Barcelona clinic liver cancer (BCLC) stage, and preoperative serum alpha-fetoprotein (AFP) levels. These clinical features were analyzed to determine their effects on the formation of TLS.

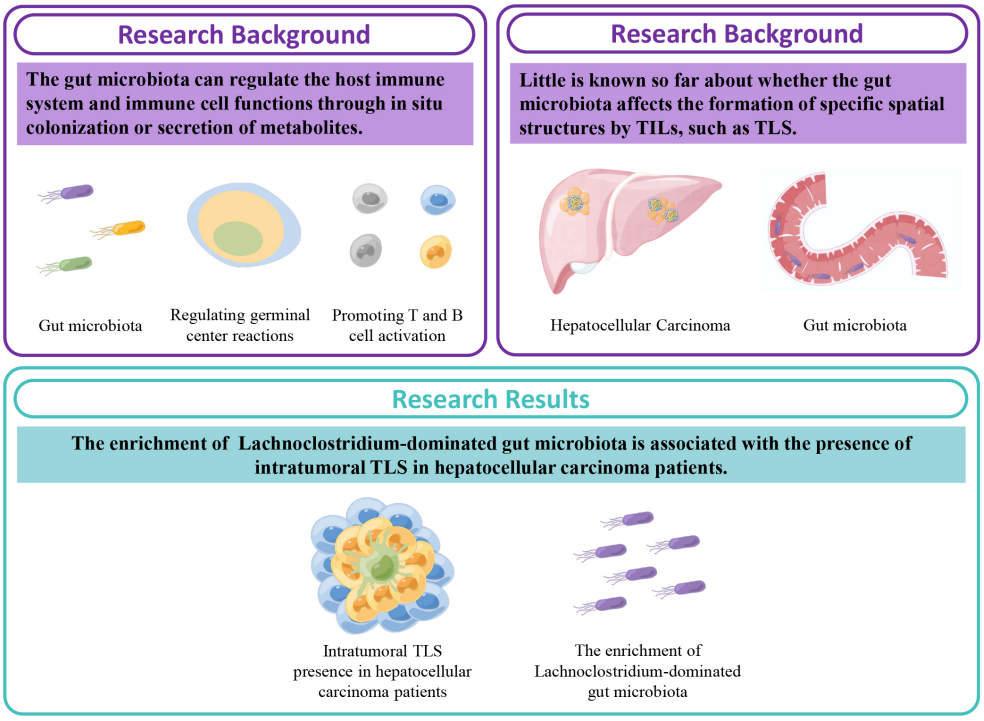

TILs, tumor infiltrating lymphocytes; **TLS**, tertiary lymphoid structures.

FIGURE 1
Graphical abstract, schematic diagram of this study. Our results for the first time demonstrate that the enrichment of the gut microbiota Lachnoclostridium taxa is associated with the presence of intratumoral tertiary lymphoid structures (TLS) in hepatocellular carcinoma.

H&E staining and multiplex immunohistochemistry

All tissues were prepared into 4-μm formalin-fixed paraffin-embedded (FFPE) sections. After dewaxing the xylene clear, the sections were deparaffinized via a series of decreasing concentrations of ethanol. The sections were then washed in deionized water and phosphate buffered saline (PBS).

For hematoxylin and eosin (H&E) staining, hematoxylin stained the nuclei and eosin stained the cytoplasm. For multiplex immunohistochemistry, antigenic epitopes were unmasked in a decloaking chamber using citrate buffer (10 mM sodium citrate and 0.05% Tween 20, pH 6). Rinsed in PBS, endogenous peroxidase activity was blocked by incubation in a 3% methanol solution of H2O2, blocked at 37°C with 5% bovine serum albumin for at least 30 min, then incubated with primary antibodies in a humidified chamber at 4°C overnight. The next day sections were incubated with anti-rabbit/mouse mixed IgG monoclonal antibodies at 37°C for 1h. Thereafter, chromogenic development was performed according to the kit manual. (Zsbio, Cat No. DS-0004).

Multiplex immunofluorescence

All FFPE blocks prepared from patient tumor tissue and corresponding para-tumor tissue were sectioned at a thickness of 4 μm on slides. Antigen retrieval was performed on all slides as described in "IHC staining." On the first day of the experiment, the sections were incubated with the first antibody (mouse antibody to human CD23) as described in "IHC," and stained with fluorescein isothiocyanate/cyanine-3 (FITC/CY3) the next day. Then, the antigen epitopes were revealed again under dark conditions using citrate buffer. The sections were then exposed to primary antibodies (including rabbit antibody to human CD3 and mouse antibody to human CD20) for 16h–20h at 4°C and to secondary antibodies conjugated to Alexa 594 and Alexa 488 for 1h at room temperature. Slides were counterstained with 4',6-diamidino-2-phenylindole to visualize cell nuclei and imaged on a Leica Stellaris 5 upright fluorescent microscope using a Leica Hyde S camera and the LAS X imaging suite.

Pathological examination

Tumor tissue sections were strictly distinguished from para-tumor tissue sections. All sections stained with H&E were observed under microscope. The following information was recorded: tumor size, satellite nodules, invasion of large blood vessels or microvessels, multinodularity, tumor differentiation according to the World Health Organization, and non-tumorous fibrotic septa based on the METAVIR staging system.

Meanwhile, pathologists identified and categorized TLS on slides. If at least one TLS was present in the field of view of the tumor tissue, the patient was considered to have TLS within the tumor tissue, which was finally confirmed by dual immunohistochemistry and immunofluorescence. All pathological sections were evaluated separately by two pathologists specializing in liver disease (Jiacheng, Li; Leyin, Hu). Different opinions were discussed and, in case of disagreement, the final decision was made by a third senior pathologist (Kate, Huang).

DNA extractions and PCR amplification

DNA from different samples was extracted using the cetyltrimethylammonium bromide according to manufacturer's instructions. The full-length 16S rRNA gene was amplified using primers 27F: 5′- AGRGTTTGATYNTGGCTCAG -3′ and 1492R: 5′- TASGGHTACCTTGTTASGACTT-3′, which were tagged with specific barcode per sample. PCR amplification was performed in a total volume of 20 μL reaction mixture containing 4 μL of 5 × FastPfu Buffer, 2 μL of 2.5 mM dNTPs, 0.8 μL of each primer (5 μM), 0.4 μL of FastPfu Polymerase, and 10 ng of template DNA, and PCR-grade water to adjust the volume. The PCR conditions to amplify the FL prokaryotic 16S rRNA gene consisted of an initial denaturation at 95°C for 2 min; 25 cycles of denaturation at 95°C for 30 s, annealing at 55°C for 30 s, and extension at 72°C for 1 min; and then final extension at 72°C for 5 min.

Library construction and sequencing

The PCR products were confirmed with 2% agarose gel electrophoresis, and purified using the AxyPrep DNA Gel Extraction Kit (Axygen Biosciences, Union City, CA, USA) according to the manufacturer's instructions. After quantified by QuantiFluorTM-ST (Promega, Madison, WI, USA), the amplicon pools were prepared for libraries construction. SMRTbell libraries were prepared using the Pacific Biosciences SMRTbellTM Template Prep kit 1.0 (PacBio, Menlo Park, CA, USA) and sequenced on PacBio RS II (LC-Bio Technology Co., Ltd., Hangzhou, China).

Data analysis

All clinical and biological features were translated into categorical variables, which were shown as number (percentage). Then chi-square test or Fisher exact test was performed to compare the composition differences.

Circular consensus sequence (CCS) reads were generated from raw subreads by SMRT Link (v6.0) with the following parameters: minPasses = 5; minPredictedAccuracy = 0.9. Then lima (v1.7.1) was used to distinguished CCS reads from different samples, and cutadapt (v1.9) was applied to identify primers. The CCS reads, which are between 1200 bp and 1650 bp, were remained after the length filtration. After dereplication and filtering chimeric sequences using DADA2, we obtained feature table and feature sequence. Alpha diversity and beta diversity were calculated by normalized to the same sequences randomly. Alpha diversity were applied in analyzing complexity of species diversity for a sample through five indices, including Chao1, observed species, goods coverage, Shannon, Simpson, and all these indices were calculated with QIIME2. Beta diversity was calculated by

QIIME2. The ASVs were annotated by aligned feature sequences with SILVA database (release 138). Other diagrams were implemented using the R packages.

Results

Cohort characteristics

In our cohort of 60 patients, males comprised 83.33% and patients over 60 years of age comprised 53.33%. The primary risk factor was HBV infection in 49 patients (81.67%), followed by alcohol consumption in 21 patients (35.00%). No patient had HCV infection. 20 patients (33.33%) had multiple risk factors. According to the BCLC staging system (2022 version), two patients (3.33%) had very early stage disease (Stage 0), 49 (81.67%) had early stage disease (Stage A), nine (15.00%) had intermediate stage disease (Stage B), and zero (0.00%) had advanced stage disease (Stage C). Elevated serum AFP levels were detected in 15 patients (25.00%) (Table 1).

Pathological findings and cohort grouping

In a retrospective cohort of 60 patients, we found TLS in 33 cases (55.00%). Given previous studies showing that TLS located in para-tumor parenchyma was associated with increased late recurrence risk in HCC and could serve as an ecological niche to maintain the survival of transformed hepatocytes (11), we further distinguished para-tumor TLS in cases with TLS. Among these, TLS was observed only within tumor tissues in eight cases (13.33%) but not in para-tumor tissues. These were identified as tumor tissue only (It-TLS group). In 27 cases (45.00%), no TLS was observed in either tumor or para-tumor tissues (desertic-TLS group, De-TLS). The grouping of this study is shown in Figure 2.

Identification of tertiary lymphoid structures

Two hepatopathologist examined tumor sections and para-tumor sections under microscopy. According to the recent expert consensus (23), dense lymphoid aggregates within the liver parenchyma containing ≥50 immunocyte nuclei were preliminarily identified as TLS, It-TLS was required to be surrounded by and/or embedded within the tumor matrix. We confirmed the presence of TLS using multiplex immunohistochemistry. CD3 was utilized to label peripheral T cells within the TLS, while CD20 was used to label B cells within the TLS. To further verify that the observed structures were TLS, we performed immunofluorescence staining on all sections containing presumed TLS and assessed the maturity of TLS by CD23 staining (Figure 3).

The presence of intratumoral TLS was unrelated to cohort characteristics

We performed statistical analyses between the It-TLS group and De-TLS. The results showed that all clinical, biological, or

TABLE 1 Clinical, biological, and pathological features of the HCC patients according to the presence of intratumoral TLS.

Variables	All patients (*n* =35)	It-TLS (*n* = 8)	De-TLS (*n* = 27)	*P*-value
Age, > 60 years	19 (54.29%)	5 (62.50%)	14 (51.85%)	0.700
Gender, male	28 (80.00%)	7 (87.50%)	21 (77.78%)	1.000
BCLC stage, B–C	4 (11.43%)	1 (12.50%)	3 (11.11%)	1.000
AFP, > 300 ng/ml	9 (25.71%)	1 (12.50%)	8 (29.63%)	0.684
Alcohol	11 (31.43%)	3 (37.50%)	8 (29.63%)	0.685
HCV	0 (0.00%)	0 (0.00%)	0 (0.00%)	/
HBV	28 (80.00%)	4 (50.00%)	24 (88.89%)	0.033
NAFLD	0 (0.00%)	0 (0.00%)	0 (0.00%)	/
Other etiology	6 (17.14%)	3 (37.50%)	3 (11.11%)	0.117
PS score, 1–2	22 (62.86%)	3 (37.50%)	19 (70.37%)	0.116
Tumor size, > 5cm	15 (42.86%)	2 (25.00%)	13 (48.15%)	0.419
Satellite nodules	8 (22.86%)	1 (12.50%)	7 (25.93%)	0.684
Microvascular invasion	16 (45.71%)	4 (50.00%)	12 (44.44%)	1.000
Poor differentiation	4 (11.43%)	0 (0.00%)	4 (14.81%)	0.553
Cirrhosis	22 (62.86%)	3 (37.50%)	19 (70.37%)	0.116

Statistical analysis was performed using chi-square tests. AFP, alpha-fetoprotein; BCLC, Barcelona Clinic Liver Cancer; HBV, hepatitis B virus; HCV, hepatitis C virus; NAFALD, Nonalcoholic fatty liver disease; TLS, tertiary lymphoid structure.

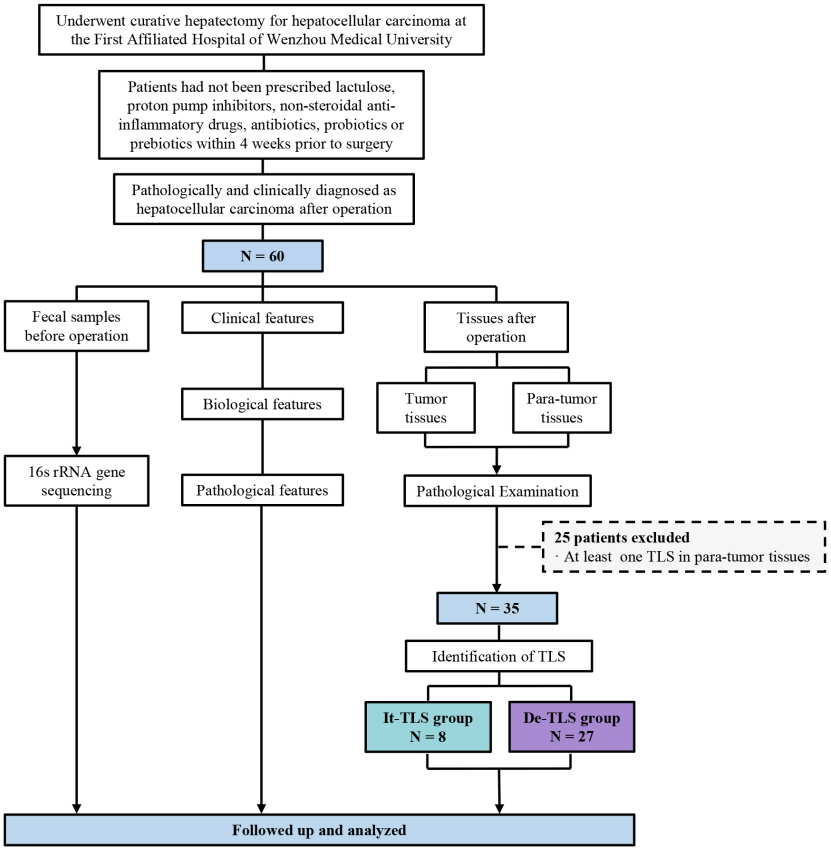

FIGURE 2
The flowchart of this study. TLS, tertiary lymphoid structure; It-TLS group, Intratumoral TLS group; De-TLS group, Desertic TLS group.

pathological features did not differ between HCC patients with or without It-TLS (It-TLS vs. De-TLS group, $p > 0.05$, chi-squared test) (Table 1). These findings indicate that underlying liver disease did not influence the presence of It-TLS.

Alterations in microbiota were associated with the presence of intratumoral TLS

Based on the above grouping, we performed 16s rRNA sequencing. Observed species and Chao1 were used to assess species richness. Shannon and Simpson reflected species abundance and evenness. Our results showed that there were no significant differences in α diversity between the It-TLS and De-TLS groups. The analysis of β diversity within groups showed no significant differences in the It-TLS and De-TLS groups. Analysis of the differentially abundant genera suggested that compared with the De-TLS group, the abundance of Lachnoclostridium, Hungatella, Blautia, Fusobacterium, Clostridium, Tyzzerella, and Clostridiales increased in the It-TLS group. Among them, the enrichment of Lachnoclostridium was the most significant. Collectively, these results indicate that differences in the abundance of microbiota were associated with the presence of TLS (Figure 4). We have consolidated the results pertaining to the comparison of microbiota data between the It-TLS group and the De-TLS group. The relevant data are accessible in Supplementary Figure S1.

Discussion

Immunotherapy has produced unprecedented durable therapeutic responses in HCC and other solid tumors, bringing revolutionary changes to cancer treatment (2). This clinical outcome has aroused people's interest in exploring immune components in the tumor microenvironment, namely, the tumor immune microenvironment (TIME) (24). TIME is closely related to tumor development, recurrence, and metastasis. As research deepens, some unexplained results have also emerged, for example, earlier studies focusing on cellular components in TIME showed that patients with similar immune cell infiltration had different prognoses (25), suggesting the necessity to explore the spatial structure of TIME in tumors to further deepen understanding of the impact of TIME on tumors. With the study of the spatial distribution of immune cells within tumors, some aggregation patterns of immune cells have attracted attention due to their functional consistency in multiple tumor types and different individuals and potential clinical value, such as TLS (26). Since the back-to-back studies published in Nature successfully demonstrated that TLS affected the objective response rate of ICB in melanoma

10.3389/fimmu.2023.1289753

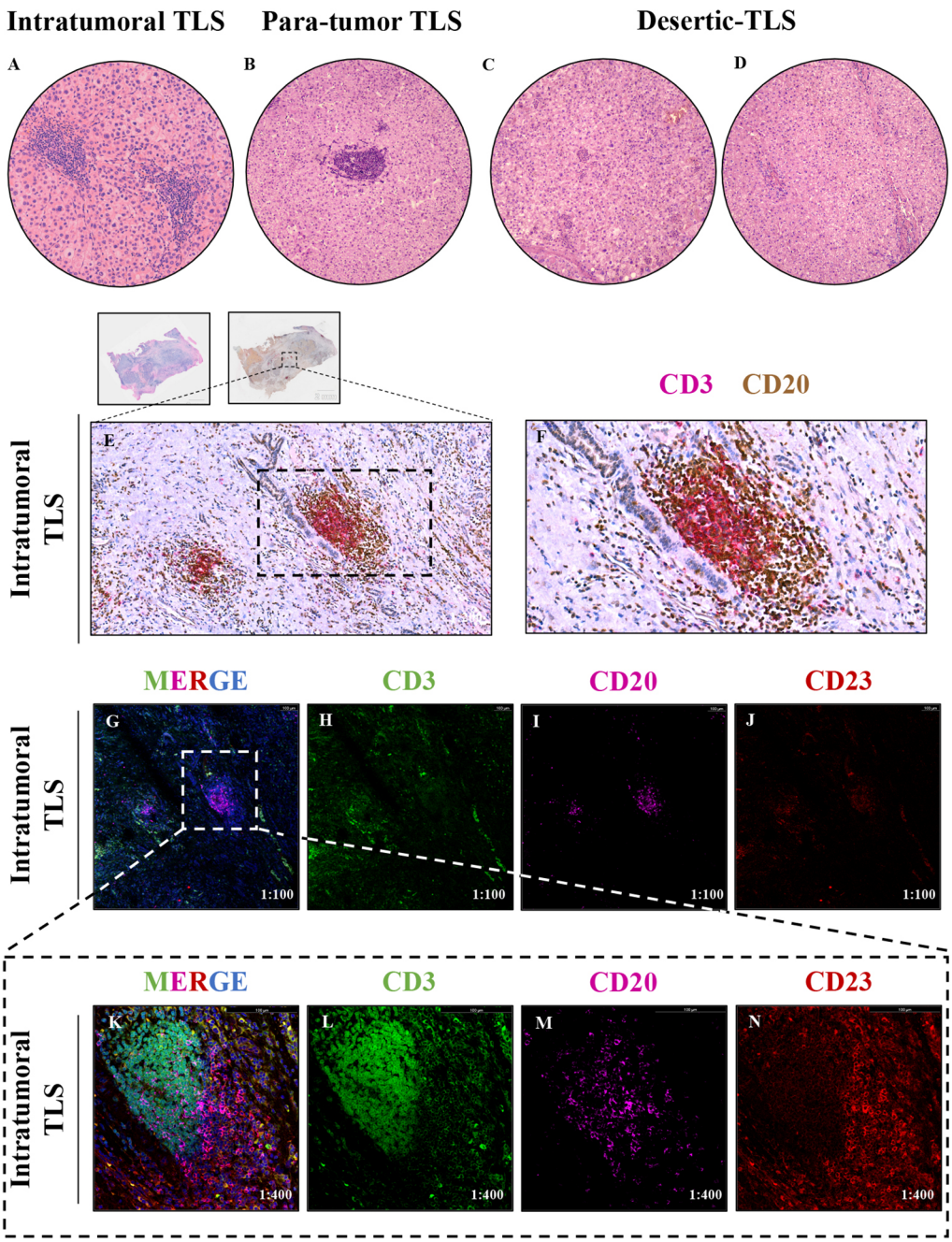

FIGURE 3
(A–D) The tertiary lymphoid structures (TLS) in tumor and para-tumor tissues of hepatocellular carcinoma were identified and grouped by H&E staining,1:200. **(A)** Tertiary lymphoid structure in tumor tissue, namely, intratumoral TLS group (It-TLS) group. **(B)** Tertiary lymphoid structure exists in para-tumor tissues. **(C, D)** TLS is not found in tumor tissue and para-tumor tissues, namely, desertic TLS group, De-TLS group. **(E, F)** Mature tertiary lymphoid structure in tumor tissue by multiplex immunohistochemistry, CD3+ T cells, CD20+ B cells, E 1:200, F 1:400. **(G–J)** CD3+ T cells, CD20+ B cells, and CD23+FDCs multiplex immunofluorescence, 1:100; **(K–N)** Representative regions CD3+ T cells, CD20+ B cells and CD23+FDCs multiplex immunofluorescence, 1:400.

and was associated with good patient prognosis (10, 27), similar conclusions have been obtained in most tumors (28–30). In particular, in a previous study by Mark Yarchoan, cabozantinib and nivolumab converted locally advanced HCC into a resectable disease, and significant enrichment of TLS was present in the tumor tissue of responders (31). Recently, Fridman et al's study showed that the presence of TLS in advanced soft tissue sarcoma could be used as a predictive biomarker to improve patients' drug selection for pembrolizumab treatment (32). These findings demonstrate the application prospect of TLS in helping patients choose clinical treatment regimens. To encapsulate, this seems to form a guideline for the "clinical benefit" of TLS in the tumor context.

Interestingly, this guideline is currently controversial in HCC: initially, Finkin et al's study challenged this tenet. Their study found

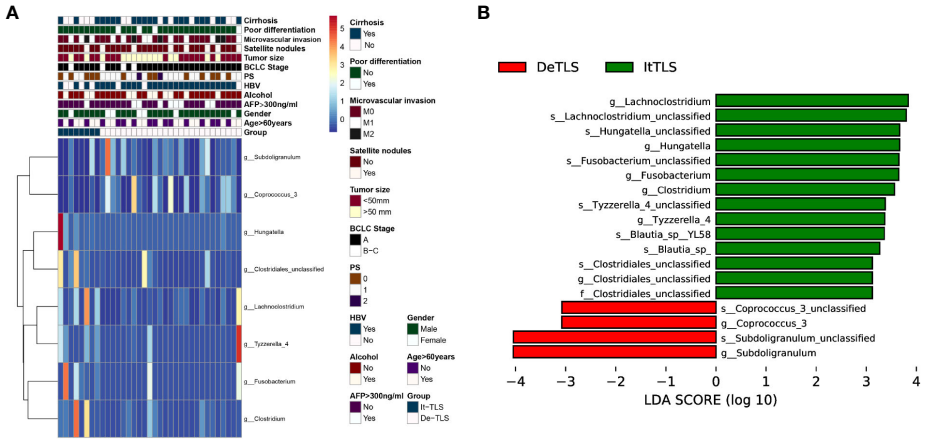

FIGURE 4
(A) Heatmaps of differential clinical, biological, and pathological features characteristics and flora features of HCC patients between It-TLS group and De-TLS group in our cohort, the heatmap was generated using the pheatmap R package. **(B)** Differential flora between It-TLS group and De-TLS group.

that ectopic TLS in HCC provided a growth environment for malignant hepatic progenitor cells (11), recently, Wenjie Song et al's study found that CD15+ neutrophil infiltration in HCC, and increased density of TLS around the tumor were associated with worse prognosis (33). Fridman et al's observed in early HCC that immature TLS formation was associated with overexpression of genes related to immunosuppression, immune failure, and tumor immune escape, promoting tumor immune evasion (34). However, Hong Wu et al's previous study showed that para-tumor TLS were associated with improved patient prognosis (35). Specifically, they found decreased infiltration of FOXP3+, CD68+, and PD1+ cells in para-tumor TLS. Valerie Chew et al's work showed that close interaction between tumor-infiltrating T cells and B cells was associated with enhanced local immune activation and contributed to better prognosis in HCC patients (36), supporting Fridman et al's finding that It-TLS in HCC had good clinical prognostic value (12). In summary, given the contradictory results of TLS on anti-tumor immunity in HCC, studying the specific cellular composition and origin of TLS in HCC may provide more effective information. Nonetheless, the factors influencing the formation of TLS in HCC are currently unclear, which greatly limits the exploration of TLS in HCC. Therefore, there is an urgent need to clarify the factors affecting the formation of It-TLS in HCC.

The microbiota in the host gut can regulate the host immune system. The role of the gut microbiota in the progression of gastrointestinal tumors is undoubtedly crucial. In particular, a recent series of studies have shown that the gut microbiota is involved in and affects anti-tumor immunity, including regulating patients' clinical responses to ICIs. The exact mechanisms by which the gut microbiota influences cancer immunotherapy are being gradually revealed, surprisingly not only in gastrointestinal tumors but also including pancreatic cancer and melanoma (19, 20). Previously, Giandomenica Iezzi et al's work demonstrated that microbiota abundance and high chemokine expression were associated with TILs recruitment (37). As a specific spatial form of TILs, Helicobacter hepaticus can promote TLS maturation in mouse CRC models (22). However, whether the gut microbiota is associated with TLS in HCC still lacks sufficient evidence.

To our knowledge, this is the first study to explore the relationship between gut microbiota and It-TLS in extraintestinal tumors. Our study shows that the presence of TLS in tumor tissues of HCC patients is associated with enrichment of specific gut microbial phyla, specifically, increased enrichment of Lachnoclostridium, Hungatella, Fusobacterium, and Clostridium in these patients, among which Lachnoclostridium enrichment in the tumor TLS group was most pronounced. Lachnoclostridium belongs to the family Lachnospiraceae (38). Although intestinal microbiota members belonging to the Lachnospiraceae family have been shown to play important roles in regulating the host's immune system, our understanding of the functional diversity of strains belonging to this family remains incomplete. Recently, Shuo Wang et al. found that Ruminococcus gnavus, a member of the Lachnospiraceae family, can act as an intratumoral bacterium to increase and degrade hemolytic glycerophospholipids that inhibit CD8+ T-cell activity. Maintaining CD8+ T-cell immune surveillance, thereby reducing colon tumor growth (18), and Lachnoclostridium is highly homologous to Ruminococcus gnavus (39). Previously, Peichang Lee et al. first demonstrated the important role of the gut microbiome-liver axis in the therapeutic response and survival of ICI treatment in HCC patients. In addition, in responders to immunotherapy with unresectable HCC, increased enrichment of Lachnoclostridium was found in fecal samples, which was associated with better overall survival (17), suggesting an important role of Lachnoclostridium in immunotherapy for HCC. In addition, analysis of the intratumoral microbiome in melanoma showed that Lachnoclostridium was positively correlated with the number of CD8+ T-cell infiltration in tumor tissues and affected patient survival (40). Lachnoclostridium has also been reported as a non-invasive marker to distinguish colorectal cancer from adenoma and is enriched in the intestine of patients with adenomas (41). Although our study has not yet revealed the specific mechanism

by which Lachnoclostridium influences the presence of TLS at the experimental animal level, published studies may allow us to speculate that Lachnoclostridium may affect lymphocyte recruitment or activation in HCC and promote TLS formation within tumor tissues, but this requires further validation (Figure 5).

For other differential flora between the It-TLS group and the De-TLS group, we focused on several sub-high abundance flora, including Hungatella, Fusobacterium, and Clostridium in addition to Lachnoclostridium. In a previous study of differential flora between colorectal adenomas and colorectal cancer, Hungatella hathewayi was enriched in the colorectal cancer group (42). In addition, previous studies have reported that Hungatella increased in cancer patients who did not respond to anti–PD-1 and chemotherapy combined treatment (43). Fusobacterium has recently been defined as a "notorious" expert in cancer immunotherapy by many studies. Jingyuan Fang et al. showed that succinic acid derived from F. nucleatum inhibited the cGAS–interferon-β pathway, thereby inhibiting anti-tumor responses by limiting the transport of CD8+ T cells (44), while Shuo Wang 's study found that Fusobacterium nucleatum can limit the function of Lachnospiraceae and promote tumor progression (18). In HCC tumor tissues, the enrichment of Fusobacterium was accompanied by a significant increase in processes such as fatty acid and lipid synthesis, which is thought to be a key factor in the effect of intratumoral microbes on tumor progression (45). Clostridium XIVa was enriched in the intestinal flora of patients with HBV-related HCC with high tumor burden and may affect disease progression through bile acid metabolism (46). To encapsulate, several other differential flora did not seem to show the function of promoting anti-tumor immunity in the body, but rather the ability to promote tumor progression, but their role in HCC still needs more experiments to prove. Finally, although we observed a significant enrichment of Subdoligranulum in the De-TLS group, we did not find studies on its mechanism of function in tumors. Instead, it has been more reported in inflammatory diseases and is related to regulating the function of Th17 cells (47).

In this single-center retrospective study, most of the patients had HBV-related HCC, without the other two common underlying chronic liver diseases of HCC–HCV infection and NAFLD. Therefore, our data may be more applicable to HBV-related HCC. In addition, our data also showed no statistical differences in either clinical or pathological features between It-TLS and De-TLS groups, which supports microbiota difference as an independent impact factor for TLS existence. However, some data may need further exploration. We found less than half of patients with It-TLS had liver cirrhosis, while over 70% patients in De-TLS group had cirrhosis (p = 0.1). Previous studies have shown decreased immune cell infiltration in HCC tissues of cirrhotic mice (48). However, there are few studies evaluating It-TLS formation in human HCC patients with liver cirrhosis, which could be a potential direction for future research.

In conclusion, our results for the first time demonstrate that the enrichment of the gut microbiota Lachnoclostridium taxa is associated with the presence of It-TLS in HCC. Our study provides a new line of reasoning for the mechanism by which gut microbes influence cancer immunotherapy, that is, by affecting the formation of specific spatial structures of tumor-infiltrating

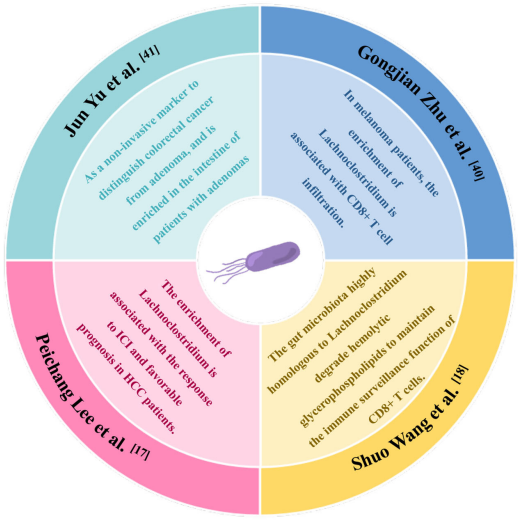

ICIs: immune checkpoint inhibitors; **HCC**: hepatocellular carcinoma.

FIGURE 5
Graphical abstract, summary of the evidence from previous studies supporting that enrichment of Lachnoclostridium-dominated gut microbiota promotes anti-tumor immunity.

lymphocytes–TLS, thereby promoting anti-tumor immunity. We show that the gut microbiota may be an interesting research focus. In the future, Related studies in experimental animals may have a positive impact on revealing the mechanism by which gut microbes regulate the formation of TLS in HCC tumors.

Limitation of the study

Regrettably, there are still some limitations in this study. First, due to the short follow-up time, we did not analyze the prognosis of patients, although previous studies have supported it, further study of the specific mechanisms is warranted. Second, due to the limitations of sequencing technology, we were unable to finely identify some differential flora. Finally, we did not study the causal relationship between changes in the intestinal microbiome and the existence of TLS in tumors. Further study of the mechanisms is essential to elucidate the exact interactions between gut microbiota and It-TLS, as well as identify potential therapeutic targets. In future studies, we plan to further confirm our view in a mouse model of primary hepatocellular carcinoma.

Data availability statement

The datasets presented in this article are not readily available because the privacy of the patients involved in the study needs to be protected, and the 16S rRNA sequencing data in the research is not readily available. Requests to access the datasets should be directed to Rui Zhao, wzykdx0412@126.com.

Ethics statement

The studies involving humans were approved by The ethics committee of the First Affiliated Hospital of Wenzhou Medical University. The studies were conducted in accordance with the local legislation and institutional requirements. The participants provided their written informed consent to participate in this study.

Author contributions

RZ: Writing – original draft, Writing – review & editing, Conceptualization, Data curation, Methodology, Project administration, Visualization. JL: Writing – original draft, Writing – review & editing, Conceptualization, Data curation, Methodology, Project administration. BC: Writing –original draft, Writing – review & editing, Conceptualization, Software, Project administration. JZ: Writing – original draft, Writing – review & editing, Conceptualization, Project administration. LH: Writing – original draft, Writing –review & editing, Visualization, Data curation. KH: Writing – review & editing, Visualization, Data curation. QC: Writing –review & editing, Data curation. JY: Writing – review & editing, Data curation. GL: Writing – review & editing, Data curation. LB: Writing – review & editing, Data curation. ML: Writing – review & editing, Data curation. YW: Writing – original draft, Writing – review & editing, Funding acquisition. GC: Writing – original draft, Writing – review & editing, Resources, Conceptualization, Supervision, Funding acquisition. FW: Writing –original draft, Writing – review & editing, Resources, Conceptualization, Supervision, Funding acquisition.

Funding

The author(s) declare financial support was received for the research, authorship, and/or publication of this article. This study was supported by National Natural Science Foundation of China (Grant numbers: 82072685), Huadong Medicine Joint Funds of the Zhejiang Provincial Natural Science Foundation of China under Grant No. LHDMY23H100001.

Conflict of interest

The authors declare that the research was conducted in the absence of any commercial or financial relationships that could be construed as a potential conflict of interest.

Publisher's note

Supplementary material

The Supplementary Material for this article can be found online at: https://www.frontiersin.org/articles/10.3389/fimmu.2023.1289753/full#supplementary-material

SUPPLEMENTARY FIGURE 1
The 16S rRNA data of the It-TLS group and De-TLS group were analyzed. Firstly, microbiota compositional analyses were undertaken. A stacked bar chart **(A)** delineated the top 30 species with the highest relative abundances at the genus level across different samples. A Venn diagram **(B)** depicted the species compositional similarities and overlaps between the two groups at the genus level. A Circos plot **(C)** visualized sample-species co-occurrence at the genus level, elucidating the correspondence between samples and species. Subsequently, analyses of microbiota diversity were conducted. Regarding α-diversity metrics, Observed species **(D)** and Chao1 **(E)** reflected species richness in samples irrespective of proportional abundances, whereas Shannon **(F)** and Simpson **(G)** indexes reflected both species richness and evenness. For β-diversity metrics, PCA **(H)** and PCoA **(I)** revealed variation in community compositions, and NMDS analysis **(J)** revealed differences among individuals. Finally, differential abundance analysis was performed to ascertain differentially abundant taxa. Fisher's exact test **(K)** identified differentially abundant microbiota. Taken together, the results demonstrate distinct gut microbiota between the It-TLS and De-TLS groups, with enrichment of Lachnoclostridium in the It-TLS group. All analyses were performed on the OmicStudio (https://www.omicstudio.cn/home).

References

1. Sung H, Ferlay J, Siegel RL, Laversanne M, Soerjomataram I, Jemal A, et al. Global Cancer Statistics 2020: GLOBOCAN estimates of incidence and mortality worldwide for 36 cancers in 185 countries. *CA Cancer J Clin* (2021) 71(3):209–49. doi: 10.3322/caac.21660

2. Llovet JM, Castet F, Heikenwalder M, Maini MK, Mazzaferro V, Pinato DJ, et al. Immunotherapies for hepatocellular carcinoma. *Nat Rev Clin Oncol* (2022) 19(3):151–72. doi: 10.1038/s41571-021-00573-2

3. Fulgenzi C, Scheiner B, Korolewicz J, Stikas C, Gennari A, Vincenzi B, et al. Efficacy and safety of frontline systemic therapy for advanced HCC: A network meta-analysis of landmark phase III trials. *JHEP Rep* (2023) 5(5):100702. doi: 10.1016/j.jhepr.2023.100702

4. Xia Y, Tang W, Qian X, Li X, Cheng F, Wang K, et al. Efficacy and safety of camrelizumab plus apatinib during the perioperative period in resectable hepatocellular carcinoma: a single-arm, open label, phase II clinical trial. *J Immunother Cancer* (2022) 10(4):e004656. doi: 10.1136/jitc-2022-004656

5. Peng S, Chen S, Hu W, Mei J, Zeng X, Su T, et al. Combination neoantigen-based dendritic cell vaccination and adoptive T-cell transfer induces antitumor responses against recurrence of hepatocellular carcinoma. *Cancer Immunol Res* (2022) 10(6):728–44. doi: 10.1158/2326-6066.CIR-21-0931

6. Zhang L, Wu L, Chen Q, Zhang B, Liu J, Liu S, et al. Predicting hyperprogressive disease in patients with advanced hepatocellular carcinoma treated with anti-programmed cell death 1 therapy. *EClinicalMed* (2021) 31:100673. doi: 10.1016/j.eclinm.2020.100673

7. Kim CG, Kim C, Yoon SE, Kim KH, Choi SJ, Kang B, et al. Hyperprogressive disease during PD-1 blockade in patients with advanced hepatocellular carcinoma. *J Hepatol* (2021) 74(2):350–9. doi: 10.1016/j.jhep.2020.08.010

8. Fridman WH, Meylan M, Petitprez F, Sun CM, Italiano A, Sautès-Fridman C. B cells and tertiary lymphoid structures as determinants of tumour immune contexture and clinical outcome. *Nat Rev Clin Oncol* (2022) 19(7):441–57. doi: 10.1038/s41571-022-00619-z

9. Ding GY, Ma JQ, Yun JP, Chen X, Ling Y, Zhang S, et al. Distribution and density of tertiary lymphoid structures predict clinical outcome in intrahepatic cholangiocarcinoma. *J Hepatol* (2022) 76(3):608–18. doi: 10.1016/j.jhep.2021.10.030

10. Helmink BA, Reddy SM, Gao J, Zhang S, Basar R, Thakur R, et al. B cells and tertiary lymphoid structures promote immunotherapy response. *Nature* (2020) 577(7791):549–55. doi: 10.1038/s41586-019-1922-8

11. Finkin S, Yuan D, Stein I, Taniguchi K, Weber A, Unger K, et al. Ectopic lymphoid structures function as microniches for tumor progenitor cells in hepatocellular carcinoma. *Nat Immunol* (2015) 16(12):1235–44. doi: 10.1038/ni.3290

12. Calderaro J, Petitprez F, Becht E, Laurent A, Hirsch TZ, Rousseau B, et al. Intra-tumoral tertiary lymphoid structures are associated with a low risk of early recurrence of hepatocellular carcinoma. *J Hepatol* (2019) 70(1):58–65. doi: 10.1016/j.jhep.2018.09.003

13. Matson V, Chervin CS, Gajewski TF. Cancer and the microbiome-influence of the commensal microbiota on cancer, immune responses, and immunotherapy. *Gastroenterol* (2021) 160(2):600–13. doi: 10.1053/j.gastro.2020.11.041

14. Waide ML, Polidoro R, Powell WL, Denny JE, Kos J, Tieri DA, et al. Gut microbiota composition modulates the magnitude and quality of germinal centers during plasmodium infections. *Cell Rep* (2020) 33(11):108503. doi: 10.1016/j.celrep.2020.108503

15. Barrow F, Khan S, Fredrickson G, Wang H, Dietsche K, Parthiban P, et al. Microbiota-driven activation of intrahepatic B cells aggravates NASH through innate and adaptive signaling. *Hepatol* (2021) 74(2):704–22. doi: 10.1002/hep.31755

16. Gao G, Shen S, Zhang T, Zhang J, Huang S, Sun Z, et al. Lacticaseibacillus rhamnosus Probio-M9 enhanced the antitumor response to anti-PD-1 therapy by modulating intestinal metabolites. *EBioMed* (2023) 91:104533. doi: 10.1016/j.ebiom.2023.104533

17. Lee PC, Wu CJ, Hung YW, Lee CJ, Chi CT, Lee IC, et al. Gut microbiota and metabolites associate with outcomes of immune checkpoint inhibitor-treated unresectable hepatocellular carcinoma. *J Immunother Cancer* (2022) 10(6):e004779. doi: 10.1136/jitc-2022-004779

18. Zhang X, Yu D, Wu D, Gao X, Shao F, Zhao M, et al. Tissue-resident Lachnospiraceae family bacteria protect against colorectal carcinogenesis by promoting tumor immune surveillance. *Cell Host Microbe* (2023) 31(3):418–432.e8. doi: 10.1016/j.chom.2023.01.013

19. Tintelnot J, Xu Y, Lesker TR, Schönlein M, Konczalla L, Giannou AD, et al. Microbiota-derived 3-IAA influences chemotherapy efficacy in pancreatic cancer. *Nature* (2023) 615(7950):168–74. doi: 10.1038/s41586-023-05728-y

20. Bender MJ, McPherson AC, Phelps CM, Pandey SP, Laughlin CR, Shapira JH, et al. Dietary tryptophan metabolite released by intratumoral Lactobacillus reuteri facilitates immune checkpoint inhibitor treatment. *Cell* (2023) 186(9):1846–1862.e26. doi: 10.1016/j.cell.2023.03.011

21. Zhang J, Huang D, Saw PE, Song E. Turning cold tumors hot: from molecular mechanisms to clinical applications. *Trends Immunol* (2022) 43(7):523–45. doi: 10.1016/j.it.2022.04.010

22. Overacre-Delgoffe AE, Bumgarner HJ, Cillo AR, Burr AHP, Tometich JT, Bhattacharjee A, et al. Microbiota-specific T follicular helper cells drive tertiary lymphoid structures and anti-tumor immunity against colorectal cancer. *Immunity* (2021) 54(12):2812–2824.e4. doi: 10.1016/j.immuni.2021.11.003

23. Vanhersecke L, Bougouin A, Crombé A, Brunet M, Sofeu C, Parrens M, et al. Standardized pathology screening of mature tertiary lymphoid structures in cancers. *Lab Invest.* (2023) 103(5):100063. doi: 10.1016/j.labinv.2023.100063

24. Fu T, Dai LJ, Wu SY, Xiao Y, Ma D, Jiang YZ, et al. Spatial architecture of the immune microenvironment orchestrates tumor immunity and therapeutic response. *J Hematol Oncol* (2021) 14(1):98. doi: 10.1186/s13045-021-01103-4

25. Su S. Effector Immune Cell Deployment: a revolutionized concept in cancer immunotherapy. *Sci China Life Sci* (2022) 66(8):1930–3. doi: 10.1007/s11427-022-2184-6

26. Schumacher TN, Thommen DS. Tertiary lymphoid structures in cancer. *Science* (2022) 375(6576):eabf9419. doi: 10.1126/science.abf9419

27. Cabrita R, Lauss M, Sanna A, Donia M, Skaarup Larsen M, Mitra S, et al. Tertiary lymphoid structures improve immunotherapy and survival in melanoma. *Nature* (2020) 577(7791):561–5. doi: 10.1038/s41586-019-1914-8

28. Lu Y, Zhao Q, Liao JY, Song E, Xia Q, Pan J, et al. Complement signals determine opposite effects of B cells in chemotherapy-induced immunity. *Cell* (2020) 180(6):1081–1097.e24. doi: 10.1016/j.cell.2020.02.015

29. He M, He Q, Cai X, Liu J, Deng H, Li F, et al. Intratumoral tertiary lymphoid structure (TLS) maturation is influenced by draining lymph nodes of lung cancer. *J Immunother Cancer* (2023) 11(4):e005539. doi: 10.1136/jitc-2022-005539

30. Zhang FP, Zhu K, Zhu TF, Liu CQ, Zhang HH, Xu LB, et al. Intra-tumoral secondary follicle-like tertiary lymphoid structures are associated with a superior prognosis of overall survival of perihilar cholangiocarcinoma. *Cancers (Basel)* (2022) 14(24):6107. doi: 10.3390/cancers14246107

31. Ho WJ, Zhu Q, Durham J, Popovic A, Xavier S, Leatherman J, et al. Neoadjuvant cabozantinib and nivolumab converts locally advanced HCC into resectable disease with enhanced antitumor immunity. *Nat Cancer.* (2021) 2(9):891–903. doi: 10.1038/s43018-021-00234-4

32. Italiano A, Bessede A, Pulido M, Bompas E, Piperno-Neumann S, Chevreau C, et al. Pembrolizumab in soft-tissue sarcomas with tertiary lymphoid structures: a phase 2 PEMBROSARC trial cohort. *Nat Med* (2022) 28(6):1199–206. doi: 10.1038/s41591-022-01821-3

33. Zhang T, Lei X, Jia W, Li J, Nie Y, Mao Z, et al. Peritumor tertiary lymphoid structures are associated with infiltrating neutrophils and inferior prognosis in hepatocellular carcinoma. *Cancer Med* (2023) 12(3):3068–78. doi: 10.1002/cam4.5227

34. Meylan M, Petitprez F, Lacroix L, Di Tommaso L, Roncalli M, Bougoüin A, et al. Early hepatic lesions display immature tertiary lymphoid structures and show elevated expression of immune inhibitory and immunosuppressive molecules. *Clin Cancer Res* (2020) 26(16):4381–9. doi: 10.1158/1078-0432.CCR-19-2929

35. Li H, Liu H, Fu H, Li J, Xu L, Wang G, et al. Peritumoral tertiary lymphoid structures correlate with protective immunity and improved prognosis in patients with hepatocellular carcinoma. *Front Immunol* (2021) 12:648812. doi: 10.3389/fimmu.2021.648812

36. Garnelo M, Tan A, Her Z, Yeong J, Lim CJ, Chen J, et al. Interaction between tumour-infiltrating B cells and T cells controls the progression of hepatocellular carcinoma. *Gut* (2017) 66(2):342–51. doi: 10.1136/gutjnl-2015-310814

37. Tosti N, Cremonesi E, Governa V, Basso C, Kancherla V, Coto-Llerena M, et al. Infiltration by IL22-producing T cells promotes neutrophil recruitment and predicts favorable clinical outcome in human colorectal cancer. *Cancer Immunol Res* (2020) 8(11):1452–62. doi: 10.1158/2326-6066.CIR-19-0934

38. Sorbara MT, Littmann ER, Fontana E, Moody TU, Kohout CE, Gjonbalaj M, et al. Functional and genomic variation between human-derived isolates of lachnospiraceae reveals inter- and intra-species diversity. *Cell Host Microbe* (2020) 28(1):134–146.e4. doi: 10.1016/j.chom.2020.05.005

39. Shen YC, Lee PC, Kuo YL, Wu WK, Chen CC, Lei CH, et al. An exploratory study for the association of gut microbiome with efficacy of immune checkpoint inhibitor in patients with hepatocellular carcinoma. *J Hepatocell Carcinoma.* (2021) 8:809–22. doi: 10.2147/JHC.S315696

40. Zhu G, Su H, Johnson CH, Khan SA, Kluger H, Lu L. Intratumour microbiome associated with the infiltration of cytotoxic CD8+ T cells and patient survival in cutaneous melanoma. *Eur J Cancer.* (2021) 151:25–34. doi: 10.1016/j.ejca.2021.03.053

41. Liang JQ, Li T, Nakatsu G, Chen YX, Yau TO, Chu E, et al. A novel faecal Lachnoclostridium marker for the non-invasive diagnosis of colorectal adenoma and cancer. *Gut* (2020) 69(7):1248–57. doi: 10.1136/gutjnl-2019-318532

42. Xia X, Wu W, Wong SH, Liu D, Kwong TNY, Nakatsu G, et al. Bacteria pathogens drive host colonic epithelial cell promoter hypermethylation of tumor suppressor genes in colorectal cancer. *Microbiome* (2020) 8(1):108. doi: 10.1186/s40168-020-00847-4

43. Wu Z, Zhang S, Li L, Huang Z, Huang D, Hu Y. The gut microbiota modulates responses to anti-PD-1 and chemotherapy combination therapy and related adverse

events in patients with advanced solid tumors. *Front Oncol* (2022) 12:887383. doi: 10.3389/fonc.2022.887383

44. Jiang SS, Xie YL, Xiao XY, Kang ZR, Lin XL, Zhang L, et al. Fusobacterium nucleatum-derived succinic acid induces tumor resistance to immunotherapy in colorectal cancer. *Cell Host Microbe* (2023) 31(5):781–797.e9. doi: 10.1016/j.chom.2023.04.010

45. He Y, Zhang Q, Yu X, Zhang S, Guo W. Overview of microbial profiles in human hepatocellular carcinoma and adjacent nontumor tissues. *J Transl Med* (2023) 21(1):68. doi: 10.1186/s12967-023-03938-6

46. Huang H, Ren Z, Gao X, Hu X, Zhou Y, Jiang J, et al. Integrated analysis of microbiome and host transcriptome reveals correlations between gut microbiota and clinical outcomes in HBV-related hepatocellular carcinoma. *Genome Med* (2020) 12 (1):102. doi: 10.1186/s13073-020-00796-5

47. Qin H, Fu Y, Zhou K, Song H, Fang G, Chen Q, et al. Toddalia asiatica extract attenuates adjuvant-induced arthritis by modulating colon Th17/Treg balance and colony homeostasis. *J Ethnopharmacol* (2023) 313:116542. doi: 10.1016/j.jep.2023.116542

48. Ke MY, Xu T, Fang Y, Ye YP, Li ZJ, Ren FG, et al. Liver fibrosis promotes immune escape in hepatocellular carcinoma *via* GOLM1-mediated PD-L1 upregulation. *Cancer Lett* (2021) 513:14–25. doi: 10.1016/j.canlet.2021.05.007

frontiers | Frontiers in Immunology

TYPE Original Research
PUBLISHED 12 December 2023
DOI 10.3389/fimmu.2023.1263633

OPEN ACCESS

EDITED BY
Takaji Matsutani,
Maruho, Japan

REVIEWED BY
Qiming Gong,
Affiliated Hospital of Youjiang Medical University for Nationalities, China
Ming Zheng,
Academy of Military Medical Sciences, China

*CORRESPONDENCE
Wenhua Xiao
w_hxiao@hotmail.com
Tao Wang
wangtao1117@gmail.com

†These authors have contributed equally to this work

RECEIVED 20 July 2023
ACCEPTED 22 November 2023
PUBLISHED 12 December 2023

CITATION
Dong W, Zhao H, Xiao S, Zheng L, Fan T, Wang L, Zhang H, Hu Y, Yang J, Wang T and Xiao W (2023) Single-cell RNA-seq analyses inform necroptosis-associated myeloid lineages influence the immune landscape of pancreas cancer.
Front. Immunol. 14:1263633.
doi: 10.3389/fimmu.2023.1263633

Single-cell RNA-seq analyses inform necroptosis-associated myeloid lineages influence the immune landscape of pancreas cancer

Weiwei Dong[1†], Huixia Zhao[2†], Shanshan Xiao[3], Liuqing Zheng[3], Tongqiang Fan[3], Li Wang[3], He Zhang[2], Yanyan Hu[1], Jingwen Yang[1], Tao Wang[3*] and Wenhua Xiao[1*]

[1]Senior Dept of Oncology, The Fifth Medical Center of People's Liberation Army (PLA) General Hospital, Beijing, China, [2]Dept of Oncology, The Forth Medical Center of People's Liberation Army (PLA) General Hospital, Beijing, China, [3]Department of Research and Development (R&D), Hangzhou Repugene Technology Co., Ltd., Hangzhou, China

Introduction: Tumor-infiltrating myeloid cells (TIMs) are key regulators in tumor progression, but the similarity and distinction of their fundamental properties in pancreatic ductal adenocarcinoma (PDAC) remain elusive.

Method: In this study, we conducted scRNA-seq data analysis of cells from 12 primary tumor (PT) tissues, 4 metastatic (Met) tumor tissues, 3 adjacent normal pancreas tissues (Para), and PBMC samples across 16 PDAC patients, and revealed a heterogeneous TIMs environment in PDAC.

Result: Systematic comparisons between tumor and non-tumor samples of myeloid lineages identified 10 necroptosis-associated genes upregulated in PDAC tumors compared to 5 upregulated in paratumor or healthy peripheral blood. A novel RTM (resident tissue macrophages), GLUL-SQSTM1- RTM, was found to act as a positive regulator of immunity. Additionally, HSP90AA1 +HSP90AB1+ mast cells exhibited pro-immune characteristics, and JAK3 +TLR4+ CD16 monocytes were found to be anti-immune. The findings were validated through clinical outcomes and cytokines analyses. Lastly, intercellular network reconstruction supported the associations between the identified novel clusters, cancer cells, and immune cell populations.

Conclusion: Our analysis comprehensively characterized major myeloid cell lineages and identified three subsets of myeloid-derived cells associated with necroptosis. These findings not only provide a valuable resource for understanding the multi-dimensional characterization of the tumor microenvironment in PDAC but also offer valuable mechanistic insights that can guide the design of effective immuno-oncology treatment strategies.

KEYWORDS

scRNA-seq, PDAC, TIMs, necroptosis, TME

Highlights

- ScRNA-seq revealed a heterogeneous tumor-infiltrating myeloid (TIMs) environment in PDAC.
- 10 necroptosis-associated genes were found to be upregulated in PDAC tumors, while 5 genes were upregulated in paratumor or healthy peripheral blood.
- A novel RTM subset, *GLUL*$^-$*SQSTM1*$^-$ RTM, was found to act as a positive regulator of immunity.
- *HSP90AA1*$^+$*HSP90AB1*$^+$ mast cells were identified to be pro-immune, while *HSP90AA1*$^-$*HSP90AB*$^-$ mast cells were anti-immune.
- *JAK3*$^+$*TLR4*$^+$ CD16 monocytes were found to have anti-immune characteristics, while *JAK3*$^-$*TLR4*$^-$ CD16 monocytes displayed pro-immune properties.

Introduction

Pancreatic cancer is a highly malignant tumor of the digestive system, with the most common subtype being pancreatic duct adenocarcinoma (PDAC), and its morbidity and mortality are increasing year by year worldwide (1). The insidious primary lesion determines that more than 80% of cases cannot undergo surgical resection due to regional or distant metastasis, and the postoperative recurrence rate is as high as 85% for resectable patients (2). For radiotherapy and chemotherapy, the mainstay therapeutic strategy, resistances are usually inevitable, leading to limited clinical benefits, especially for advanced patients. Recently, researchers reported the therapeutic potential of immunotherapy by recruiting and activating the host's T cells to recognize tumor-specific antigens, however, cancer cells developed mechanisms to escape the cytotoxicity effect of T cells. Moreover, the unique immunosuppressive microenvironment of pancreatic cancer hinders the promotion of anti-tumor immune responses through immune checkpoint manipulation (3–5). Therefore, it is urgent to explore novel therapeutic strategies that can significantly improve patient survival and prognosis (6).

Investigations of converting immune "cold" tumors into "hot" tumors are ongoing in immunotherapy. Regulated cell death (RCD), one of the hallmarks of cancer, has been identified as a potential therapeutic target due to its association with anti-tumor immunity. Necroptosis, a recently proposed form of cell death proposed (7), can be inhibited by Necrostain-1 and mediated by receptor-interacting serine/threonine protein kinase 1 (RIPK1) (8). Necroptosis often triggers a robust inflammatory response by releasing cellular contents into the extracellular environment, and this process has been implicated in the pathogenesis and progression of various diseases (9). It is reported that the impact of necroptosis on cancer development, whether inhibitory or promotive, often varies depending on the specific tumor type and stage (10).

The involvement of necroptosis in dysregulated tumor immune microenvironment (TIME) has been demonstrated, especially for myeloid lineages. For instance, damage-associated molecular patterns (DAMPs) were released by tumor cells through necroptosis to stimulate the antigen presentation by dendritic cells (DCs), further enhancing the cytotoxicity of CD8$^+$ T cells (11, 12). RIPK3, the effector of necroptosis, contributes to NF-κB activation, tissue repair of DC cells, and infiltration of CD8$^+$ T cell (13, 14). Previous studies have reported that the anti-tumor immune response can be activated by NF-κB signaling via necroptosis of fibroblasts (15, 16). However, the regulatory mechanisms of necroptosis in tumor progression in other studies seem to differ from the aforementioned processes. RIPK1 was found to be upregulated in tumor-associated macrophages (TAMs) during M2 Macrophages polarization in a PDAC mice model (17). Necroptosis mediated by RIPK3 promoted the accumulation of immunosuppressive myeloid-derived suppressor cells (MDSCs) in tumor microenvironment (TME) of pancreatic cancer through producing C-x-c motif chemokine ligand 1 (CXCL1) and CXCL5 (18, 19). In an intestinal tumor model, RIPK3 in intermediate MDSC subpopulation was found to increase tumor size (20). Taken together, these findings suggest that myeloid clusters and associated necroptosis may play critical roles in tumor progression and immune evasion.

The exploration of necroptosis-associated myeloid subpopulation can provide a better understanding of the mechanisms underlying immune evasion and therapy resistance in PDAC. Recently, single-cell transcriptomic has made remarkable breakthroughs in deciphering the heterogeneity at the individual cell level. Accumulating evidence has demonstrated the abundance of myeloid cells in tumor immune microenvironment (TIME) of PDAC, serving as key regulators in immune response and treatment resistance (21). By refining the clustering of tumor-associated macrophages (TAMs) in human and mouse samples, researchers have identified significant upregulation of proliferating tissue-resident macrophages and inflammatory macrophages in PDAC TIME received chemotherapy. Conversely, monocyte-derived antigen-presenting cells (APCs) and Marco+ macrophages highly expressed the scavenger receptor MARCO, showed decreased expression. Results from multiplex immunohistochemistry (mIHC) further supported the chemotherapy resistance of proliferating tissue-resident macrophages (22). The deficiency of DCs has been linked to dysfunctional T cell-mediated immunity in early-stage PDAC, indicating their vital role in immune escape and tumor progression (23). Although some progress have been made, further detailed characterization of myeloid cell lineage is needed, and the therapeutic application of myeloid cells in pancreatic cancer remains limited.

This study aims to further elucidate the unique microenvironment of PDAC, explore its intrinsic mechanisms in the tumor occurrence and progression, and provide a potential novel approach for the treatment of PDAC patients. Leveraging a publicly available scRNA-seq resource (24), we revealed a tumor-associated myeloid environment in PDAC. Specifically, we identified upregulated necroptosis genes and immune-related

novel clusters in PDAC. Furthermore, we discovered cell-specific signaling pathways and receptor-ligand pairs within these new clusters, which have the potentially to either promote or suppress tumor development. In general, utilizing this unique resource, we analyzed myeloid cell lineages, necroptosis-associated networks, and cell-cell crosstalk in PDAC. This sheds light on the myeloid ecosystems underlying PDAC initiation and progression, and may provide a myeloid-modulating therapeutic strategies from pre-clinical models to pancreatic cancer treatment.

Methods

Data source and preprocessing

The PDAC dataset GSE155698 (24) was downloaded from the GEO database, including 12 primary tumor (PT) patients, 4 metastatic (Met) patients, 3 adjacent normal pancreas tissue (Para) patients, and all samples were coupled with peripheral blood (Figure 1A). The original dataset contained a total of 25,236 genes and 142,353 cells. The raw UMI count matrices were processed using the R package Seurat (version 3.2.3) (25). The data underwent several filtering steps: 1) cells with a low number of unique detected genes (< 200) and a high number of 5000 were removed; 2) cells with more than 30,000 UMIs were discarded; 3) cells with mitochondrial content higher than 30% were removed; 4) cell cycle genes were regressed out. After excluding low-quality cells, 124,575 single cells remained for downstream analysis. Additionally, another publicly available scRNA-seq data from CRA001160 (26), including a total of 57,539 cells from 24 primary PDAC tumors and 11 control pancreases, was utilized to validate the findings.

Public clinical data and gene expression information were retrieved from the TCGA database (https://www.cbioportal.org/). A total of 178 samples from the TCGA-PAAD (Pancreatic adenocarcinoma) cohorts were included for further analysis.

Sing-cell RNA-seq data clustering and dimensional reduction

First, we performed data normalization on the merged data using the *NormalizeData* function and identified the first 2000 highly variable genes through the *FindVariableFeatures* function, which is based on the variance stabilization transformation ("*vst*"). Simultaneously, all genes were scaled using the *ScaleData* function, and the *RunPCA* function was applied to reduce the dimensionality of the data using PCA for previously identified highly variable genes. We selected a dimensionality reduction of 30 (dim = 30) and clustered the cells using the *FindNeighbors* and *FindClusters* functions with a resolution of 1.2, enabling the identification of distinct cell clusters. To further reduce dimensionality and visualize the data, we employed the UMAP and tSNE methods using the top 30 principal components. Specifically focusing on myeloid cell types, we repeated the clustering protocol to identify clusters within the aforementioned myeloid lineages. To address batch effects, we utilized the *runHarmony* function from the Harmony package (version 0.1.0) (27). Finally, we employed the

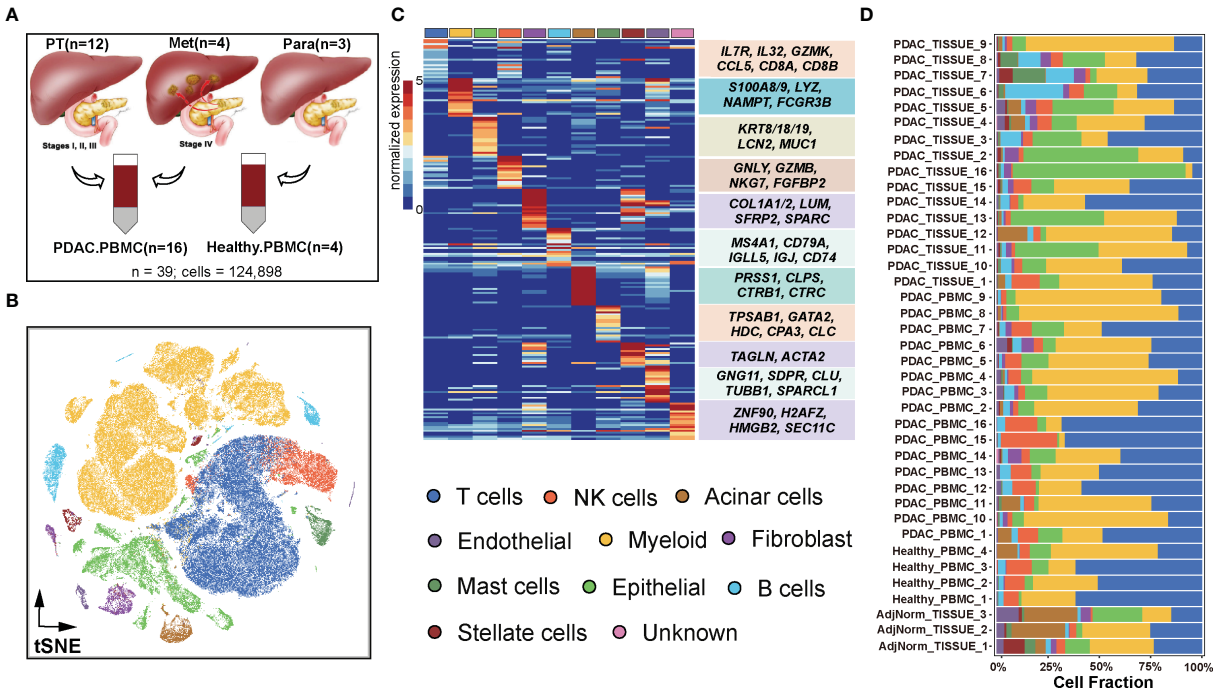

FIGURE 1
Dissection of the tumor microenvironment in PDAC. **(A)** Samples were collected from GSE155698. **(B)** Visualization of single-cell RNA-seq data of 124,575 cells by t-SNE. **(C)** Single-cell resolution heatmap of top expressed genes for each cell type. **(D)** Proportions of 11 cell types among 39 samples including 16 primary or metastatic tumor tissues coupled with 16 PDAC PBMC samples, 3 paratumor tissues and 4 healthy PBMC samples.

FindAllMarkers function to screen the marker genes of 40 subgroups, considering a log-fold change (logfc) threshold of 0.25 for differential expression and a minimum percentage (min.pct) of 0.25 for the expression ratio of the least differentially expressed genes. We applied a corrected p threshold of less than 0.05 to screen the significant marker genes.

Cell type identification

The annotation of each cell cluster was confirmed by the expression of canonical marker genes. Epithelial cells were identified using the higher expression of *EPCAM*, *ACTA2*, *KRT7*, *KRT8*, *KRT18*, *KRT19*, *CDH1*, *PRSS1*, *CTRB2*, *REG1A*, *CLU*, *MKI67*, *SPINK1*, *TFF1*, and *MUC1*, and other cell types were annotated using: T cells (*CD3D*, *CD3E*, *CD3G*, *CD4*, *CD8A*, *IL7R*, and *LEF1*), B cells (*MS4A1*, *CD79A*, *CD79B*, *CD52*, *CD19*, *SDC1*, *IGJ*, *IGLL5*, *CXCR4*, *KIT*, *CD27*, and *HLA-DRA*), NK (natural killer) cells (*NCR3*, *FCGR3A*, *NCAM1*, *KLRF1*, *KLRC1*, and *CD38*), acinar cells (*PRSS1*, *CTRB1*, *CTRB2*, *REG1B*, *SPINK1*, and *AMY2A*), mast cells (*TPSAB1*, and *CPA3*), fibroblast (*LUM*, *DCN*, *COL1A1*, *ACTA2*, *SPARC*, *CDH11*, *PDGFRA*, *PDGFRB*, *COL3A1*, *RGS5*, *IGFBP7*, *PDPN*, *MCAM*, *IL6*, *APOE*, *GLI1*, *GLI2*, *GLI3*, and *PDGFA*), myeloid cells (*CD14*, *ITGAM*, *MNDA*, *MPEG1*, *ITGAX*, *FCGR3A*, *FCGR3B*, *APOE*, *C1QA*, *MARCO*, *LYZ*, and *HLA-DRA*), stellate cells (*RGS5*, *ACTA2*, *PDGFRB*, and *ADIRF*), and endothelial cells (*CDH5*, *PLVAP*, *VMF*, *VLDN5*, *KDR*, and *PECAM1*).

Among myeloid cells, cell clusters were identified using genes previously reported. Mast cells were identified by the high expression of *KIT*, *CPA3*, and *TPSAB1*, and other myeloid lineages were annotated using: granulocytes (*CXCR2*, *FCGR3B*, *IFTIM2*, *SLC25A37*, *IL1R2*, *CXCR1*, *SIRPA*, and *S100A8*), macrophages (*C1QC*, *C1QA*, *APOE*, *CCL4*, *PLTP*, and *IL1B*), CD14 monocyte (*CD14*, *FCN1*, *S100A8*, and *S100A9*), CD16 monocyte (*FCGR3A*, *LST1*, and *LILRB2*), and DCs (dendritic cells) (*IL7R*, *CCR7*, *GZMB*, *LYZ*, *IL3RA*, and *IL32*).

Tissue distribution of clusters

We quantified the tissue preference of each cluster by calculating the ratio of observed to expected cell numbers (*Ro/e*) in different tissue (28, 29). The expected cell numbers for each combination of cell clusters and tissues were determined using the chi-square test. A cluster was considered enriched in a specific tissue if *Ro/e* value was greater than 1.

Differential expression and pathway analysis

To identify differentially expressed genes between two groups of clusters, we used the Wilcox method in the *FindMarkers* function in *Seurat* to evaluate the significance of each gene, with multiple hypothesis correction using the *Benjamini-Hochberg* procedure. Genes with adjusted *P*-values less than 0.05 were considered as differentially expressed genes. In addition, the log2 fold change (log2FC) for each gene was calculated by subtracting the log2 transformed mean count in each group.

KEGG (Kyoto Encyclopedia of Genes and Genomes) pathway enrichment was performed using the *clusterProfiler* package (version 3.14.3) (30), with a *Benjamini-Hochberg multiple testing adjustment*. Gene sets with FDR-corrected $P < 0.01$ were considered to be significantly enriched.

TCGA data analysis

Two endpoints (overall survival (OS) and disease-free interval (DFI) from the TCGA-PAAD) were used to analyze patients' clinical outcomes. We employed the Cox proportional hazards model implemented in the *survival* package to assess the correlation between selected genes and patients' survival. Kaplan-Meier survival curves were generated using the R function *ggsurvplot* from the *survminer* package.

Specifically, to examine the relationship between clusters and patients' survival, we utilized their signature genes. The signature genes including the following categories: macrophage (*C1QC*, *C1QA*, *APOE*, *MACRO*, *INHBA*, *IL1RN*, *CCL4*, *NLRP3*, *EREG*, *IL1B*, *LYVE1*, *PLTP*, *SEPP1*), granulocyte (*FCGR3B*, *IFITM2*, *CXCR2*, *S100A8*, *SLC25A37*, *CXCR1*, *IL1R2*), CD14 monocyte (*CD14*, *FCN1*, *S100A8*, *S100A9*, *S100A12*, *VCAN*, *CD36*), CD16 monocyte (*FCGR3A*, *LST1*, *LILRB2*, *IFITM2*, *SIGLEC10*, *CX3CR1*, *LILRB1*, *LIBRA1*, *TCF7L2*, *MTSS1*, *RHOC*), DCs (*GZMB*, *JCHAIN*, *MZB1*, *CLIC3*, *CXCL8*, *IL7R*, *CCR7*, *MMP7*, and *IL32*), and mast cells (*KIT*, *CPA3*, *TPSAB1*, *HDC*, *GATA2*, *HPGDS*, *TPSD1*, *SLC18A2*, *MS4A2*, *IL1RL1*, and *VWA5A*). The mean expression of the signature genes was used to classify samples into a high and low groups based on risk score (high: risk score > 0; low: risk score ≤ 0). The Cox model was employed to adjust for OS and status in the survival analysis.

Cell-cell interaction analysis

To investigate the potential interactions between different cell types in the TME of PDAC, we conducted cell-cell interaction analysis using *CellChat* (v1.1.3), which integrates a curated repository of ligand-receptor (L-R) pairs and employs a statistical framework (31). We combined $CD4^+$T cells, $CD8^+$T cells, B cells, NK cells, and epithelial cells with the newly identified clusters, including $GLUL^-SQSTM1^-$ RTM, $GLUL^+SQSTM1^+$ Macro., $HSP90AA1^+HSP90AB1^+$ Mast and $JAK3^+TLR4^+$ Mono. Interactions networks between cell clusters were investigated.

RNA fluorescence *in situ* hybridization

The samples used for RNA FISH were obtained from tumor paraffin sections of patients diagnosed with PDAC. Isolated cancer-associated cells were adhered onto laminin coated #1 coverslips (ThermoScientific) were fixed for 10 min at room temperature with

Fixation Buffer (3.7% formaldehyde in PBS), washed twice in 1x PBS and permeabilized with 70% EtOH at 4°C for at least an hour. RNA FISH was performed using 20-mer Stellaris Biosearch Probes for LINCMs and core gene conjugated to Quasar 670 or CAL Fluor Red 610. Briefly, cells were washed with Wash Buffer (10% formamide in 2x SSC) prior to overnight 37°C hybridization with target probes (125 nM) in Hybridization buffer (100 mg/ml Dextran Sulfate, 10% Formamide in 2x SSC). After hybridization, cells were washed in Wash Buffer for 30 min at 37°C, counterstained with DAPI (5 ng/ml in Wash Buffer) for 30 min at 37°C, and washed in 2x SSC at room temperature. Coverslips were transferred onto glass slides with mounting medium (Vectashield) and imaging was performed immediately on upright microscope (Nikon, Ni-E) with 100x Objective (Nikon) on a cooled CCD/CMOS camera (Qi-1, Qi-2, Nikon).

For the notable exception of S100A4, SQSTM1 and GLUL RNA FISH co-staining, RNA FISH was performed using 50-mer ZZ ACD RNAScope probes due to the short unique sequence of the antibodies available for probe design. Cells were fixed and permeabilized as described above in 70% EtOH, washed in 1x PBS and 1x Hybwash buffer for 10 and 30 min, respectively. They were then incubated with 1x Target Probe Mix at 40°C for 3 hours. Cells were washed thrice in 1x Hybwash at room temperature, incubated in 1x Pre Amp Mix for 40 min at 40°C, washed thrice in 1x Hybwash at r.t.p, incubated in 1x Amp Mix for 30 min at 40°C, washed twice in 1x Hybwash before incubation in 1x Label Probe Mix (Alexa Fluo 488, ATTO0550) at 40°C for 25 min. Cells were washed thrice in 1x Hybwash in dark at r.t.p, counterstained with DAPI (5ng/ml) prior to mount and imaging.

Statistical analysis

All statistical analyses were conducted using R software. Comparisons between two groups of samples were evaluated using Wilcoxon rank-sum test (Mann-Whitney U-test) for statistical analysis. Statistical significance was denoted as $^{*}P < 0.05$, $^{**}P < 0.01$, $^{***}P < 0.001$.

Results

Overall characteristics of the cell cluster composition in pancreatic cancer

To gain a comprehensive understanding of TME, and explore its heterogeneity between PDAC and normal tissues, we investigated 39 PDAC samples consisting of primary tumors, metastatic tumors, adjacent normal tissues and paired peripheral blood (Figure 1A) from GSE155698 (24). Based on canonical cell markers mentioned in Methods (Table S1), a total of 124,575 cells were classified into distinct cell populations, including T cells (39,372 cells, 31.61%), myeloid cells (48,054, 38.57%), epithelial cells (14,998, 12.04%), NK cells (7,758, 6.23%), fibroblast (2,617, 2.10%), B cells (4,548, 3.65%), acinar cells (2,488, 2.00%), mast cells (2,086, 1.67%), stellate cells (1,324, 1.06%), endothelial cells (1,238, 0.99%) and minor unknown cells (92, 0.74%) (Figures 1B, C, S1A).

Compared to primary tumors and paracancerous samples, metastatic tumors exhibited higher composition of T cells (34.52%, 27.55%, 23.59%, respectively) and epithelial cells (15.17%, 12.54%, 9.47%) (Figure S1B, Table S2). Conversely, compared to primary and metastatic tumor samples, adjacent normal tissues had higher proportions of stromal cells, including acinar cells (14.27%, 1.11%, 1.21, respectively), stellate cells (6.26%, 0.95%, 0.57%) and endothelial cells (3.90%, 0.92%, 0.89%) (Figure S1B, Table S2). As for PDAC samples across clinical stage I to IV, the proportions of epithelial cells continued to rise, from 5.58% to 15.17%, while myeloid cell compositions decreased from 71.63% to 35.13% (Figure S1C, Table S2). Among the PDAC samples, T cells (28.68%), myeloid cells (40.25%), and epithelial cells (12.86%) were the most abundant populations. In normal samples, T cells (51.88%), myeloid cells (27.00%), and NK cells (9.26%) accounted for 88.14% of the cell population (Table S2, Figure S1D). The peripheral blood from PDAC patients had a higher proportion of T cells (36.87% vs. 22.41%), myeloid cells (41.46% vs. 33.53%), and NK cells (7.53% vs. 3.95%) compared to solid tissue, whereas the proportion of epithelial cell was higher in solid tissue (20.19%) than peripheral blood (7.37%) (Figure S1E, Table S2).

Similar to previous studies (26, 32), there was significant variation in the portions of epithelial, stromal, and immune cells among the samples, which could be attributed to intrinsic differences in tumor stages or specific locations within tumor where biopsies were taken (Figure 1D). For example, PDAC patients 15 and 16 (stage II) exhibited a highly immune-rich microenvironment, with nearly 70% T cells in peripheral blood compared to only 10% in solid tissue. Furthermore, patients 15 and 16 (stage II) had higher T cell portions (70%) than patients 2 and 3 (stage IV, approximately 20%). These findings indicated that the formation and progression of metastases in PDAC may necessitate a more immunosuppressive TME compared to primary tumors.

B cell may play a tumor-suppressive role in PDAC

Subsequently, to assess the clinical significance of these cell types in PDAC, we identified the top 20 genes that predominantly determined the identity of each cell type through ROC analysis. The correlation between the expression levels of these genes and the patient prognosis was then computed using multivariate Cox regression on TCGA-PAAD data (Table S3). Our analysis revealed that genes exclusively expressed in C3 (epithelial cell) (ave.cox = 0.182), C13 (epithelial cell) (ave.cox = 0.182), C21 (epithelial cell) (ave.cor = 0.193) were associated with poor prognosis (Figure S2A), where ave.cox represents the average Pearson correlation coefficient. On the other hand, genes expressed in C0 (T cells) (ave.cox = -0.076) and C14 (B cells) (ave.cox = -0.062) were correlated with a favorable prognosis in PDAC, suggesting potential tumor-suppressive functions of these cells. It is worth noting that B cells are prominent features of PDAC tumors, although their roles in this disease remain controversial (33). Notably, higher expression levels of genes exclusively expressed in the C14 and C38 B cell types (such as *BCL11A* and

DNASE1L3) were positively associated with favorable prognoses (Figure S2B, Table S3), indicating the tumor-suppressive functions of C14 and C38 cells in the PDAC microenvironment. Correlation analysis revealed that *BCL11A* (R = 0.419, p = 3.52e-09) and *DNASE1L3* (R = 0.689, p < 2.2e-16) were positively correlated with CD8A (Figure S2C). Clinical outcomes demonstrated that higher expressions of *BCLAA1* and *DNASE1L3* were significantly associated with improved survival (Figures S2E, F). Additionally, these genes exhibited higher expression values in PDAC tumors compared to normal samples (Figure S2D), suggesting B cells may exert tumor-suppressive roles as tumor-infiltrating B cells. Consistent with our findings, previous studies have demonstrated that tumor-infiltrating B cells are a positive prognosis factor, both in PDAC and other cancers (34, 35).

Myeloid cells exert immune-suppressive potential

The presence and functional activities of myeloid cells in tumors have garnered increasing interest due to their relevance as modulators of anticancer therapies and potential targets for specific treatment. In this study, we focused on unraveling the potential roles of myeloid cells in PDAC (Figure 2). Correlation analysis showed that the genes exclusively expressed in C1 (ave.cox = 0.023), C4 (ave.cox = 0.019), C7 (ave.cox = 0.026), C10 (ave.cox = 0,023), C17 (ave.cox = 0.034), C22 (ave.cox = 0.042) (myeloid cell) were associated with poor prognosis (Figure 2A), suggesting the immune-suppressive functions of myeloid cells in the microenvironment of PDAC. Besides, Immune-suppressive markers as previously reported (37), *SPP1*, *MACRO*, *APOE*, *CD68*, and *SIPRA*, were exclusively expressed in myeloid cells (Figure 2B). Additionally, myeloid cells had a relatively higher stemness score compared to other stromal cells (Figure 2C).Previous studies have demonstrated that cancer progression involves a gradual loss of differentiated phenotype and the acquisition of progenitor-like, stem cell-like features (38). Furthermore, myeloid cells exhibited heterogeneous expression of immune checkpoint receptors (*CD86*, *HAVCR2*, *CD48*, and *VSIR*) (Figure 2D). Collectively, these findings suggest that myeloid cells may play an immune-suppressive role in the PDAC tumor environment, consistent with previous observations and supporting the notion that myeloid cells are a key immunosuppressive component in TME (39).

Characterization of major myeloid cell lineages

To investigate tumor-infiltrating myeloid cells (TIMs) in PDAC, we firstly excluded all cells from healthy samples,

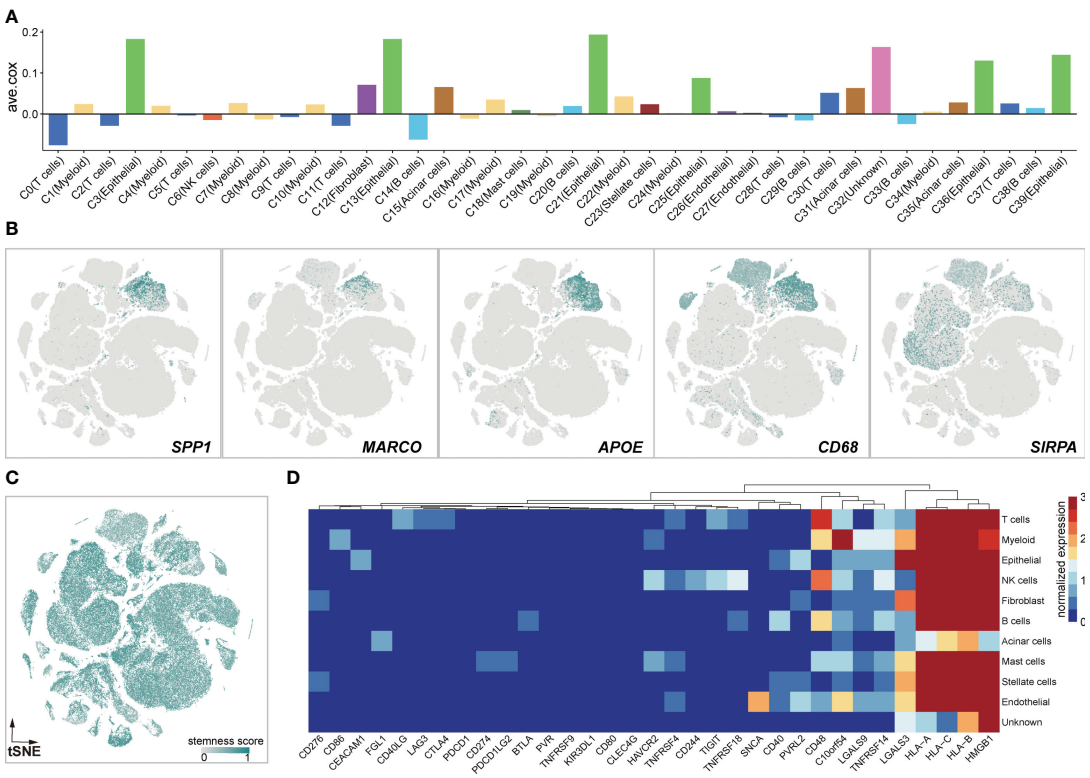

FIGURE 2
Myeloid cells exert immune-suppressive potentials. **(A)** Bar Graphs illustrating the average coefficients (ave.cor) for the prognostic effect of genes exclusively expressed in each clusters. Positive values of ave.cor indicate the associations with anti-tumor immunity and good clinical outcomes, opposite from negative ave.cor values. **(B)** Expression landscapes of immunosuppressive markers of *SPP1, MARCO, APOE, CD58*, and *SIRPA*. **(C)** The high stemness score profile of myeloid cells calculated by *scCancer* (36). **(D)** Heatmap of immune checkpoint inhibitors in 11 cell clusters.

resulting in 45,859 myeloid cells for further analysis. Subsequently, we performed unsupervised clustering and cell annotation of myeloid cells using canonical markers (Figures 3A, C), as described in the Methods section. It revealed the presence of 6 distinct subclusters within the myeloid lineage, including granulocytes (24,786, 54.0%), CD14 monocytes (8,713, 19.0%), macrophages (7,767, 16.9%), mast cells (1,999, 4.4%), CD16 monocytes (1,270, 2.8%), and dendritic cells (DCs) (1,324, 2.9%) (Figure 3B).

To visualize the distribution of cell populations of myeloid subclusters across different histologic types, we utilized unbiased hierarchical clustering algorithms and supervised annotation on PBMC samples(Figures S3A, B). Compared to adjacent normal tissues, tumor tissues exhibited overall increases in DCs, CD14 monocytes, and CD16 monocytes, indicating a redirected immune response (Figure S3C). Besides, PBMC samples predominantly consisted of granulocytes, while tumor and paratumor tissues exhibited abundant macrophages (Figure S3C). The distict cellular compositions suggested a heterogeneous TIMs environment in tumor.

We subsequently investigated the expression patterns of immune-suppressive markers mentioned above. The results revealed elevated expression of these markers in macrophages (Figure 3D), suggesting that macrophages may contribute to the immunosuppressive effects of TIMs in PDAC. To further assess the clinical impact of the signature (Figure 3C) for myeloid subclusters, including macrophages, mast cells, CD14 monocytes, CD16 monocytes and DCs, we utilized an independent PAAD cohort from TCGA. Patients with high expression of signature genes exhibited worse OS compared to those with low expression(two-sided log-rank test $p < 0.01$) (Figures 3E–I). These findings further underscored the immunosuppressive effects of myeloid lineages at the bulk level.

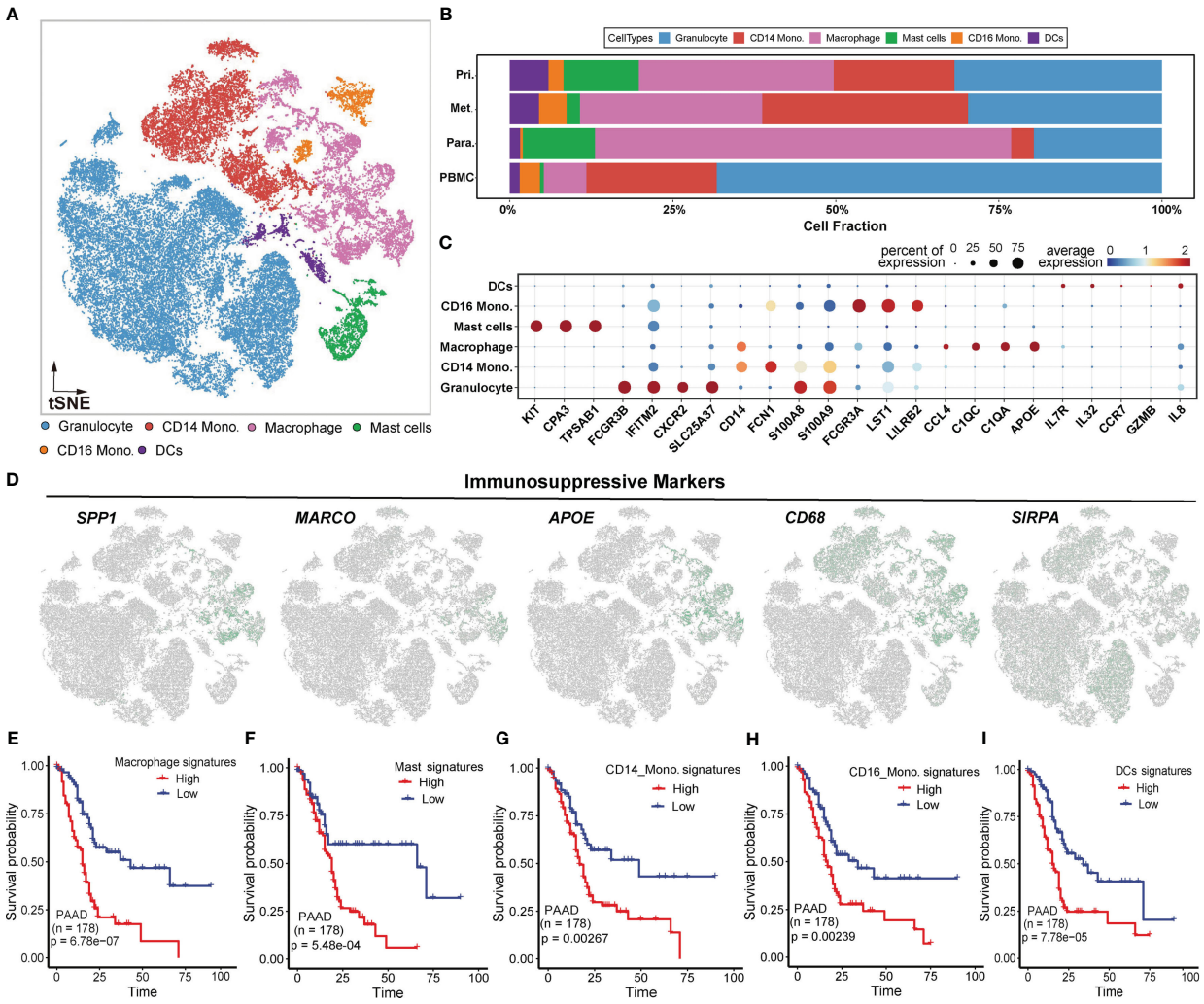

FIGURE 3
Myeloid-derived cell components in PDAC. **(A)** t-SNE plot showing 6 myeloid clusters of samples from PDAC patients. **(B)** Proportion of each myeloid cell lineage from the primary tumor, metastatic tumor, paracancerous tissue, and peripheral blood. **(C)** Bubble plot showing selected cell type-specific markers across all clusters. The size of dots represents the fraction of cells expressing a particular marker, and the intensity of the color indicates the levels of average mean expression. **(D)** t-SNE plots showing the expression of specific immunosuppressive markers, which were denoted in Figure B, in the myeloid subclusters. **(E–I)**. Kaplan-Meier survival analyses of some myeloid subclusters markers, including macrophage, mast cells, CD14 monocyte, CD16 monocyte, and DCs.

PDAC tumor progression is associated with necroptosis

In order to comprehensively investigate the diverse range of myeloid cell populations in PDAC, we first performed tissue prevalence analysis. Compared to paratumor samples, macrophages and mast cells were highly enriched in tumor tissues, suggesting the coexistence of host immune response and tumor escape in the PDAC milieu. Moreover, macrophages exhibited a higher enrichment in paratumor samples compared to primary and metastatic tumor samples, in contrast to CD14 monocytes and granulocytes (Figure S3C, left). Moreover, macrophages and mast cells exhibited a preferential enrichment in PDAC tissues rather than peripheral blood samples (Figure S3C, middle). Subsequently, we performed differential gene expression (DGE) analysis between tumor and paratumor samples (Figure 4A) and gene set enrichment analysis of each cluster's upregulated genes (Figures 4B-F). Strikingly, gene ontology (GO) characteristics related to necroptosis were detected across all myeloid lineages in tumor samples. Necroptosis can either elicit robust adaptive immune responses that may impede tumor progression, or it can recruit inflammatory responses that may potentially facilitate tumorigenesis, cancer metastasis and the generation of an immunosuppressive tumor microenvironment (40).

To investigate the potential enrichment of necroptosis in peripheral blood, we only kept myeloid cells from peripheral blood samples (Figure S3A). Compared with normal blood samples, blood samples from PDAC patients showed higher proportions of CD14 monocytes and lower proportions of DCs, and CD16 monocytes (Figure S3B), indicating a heterogeneous myeloid environment in peripheral blood. However, myeloid lineages showed comparable enrichment in peripheral blood except for DCs, CD16 monocytes, and macrophages (Figure S3C, right). We performed DGE and enrichment analyses of PBMC samples from PDAC or healthy individuals, and results demonstrated the presence of necroptosis in PBMC samples from PDAC (Figures S3D-I), indicating that the necroptosis event was not tissue-specific. To investigate the differences between tumor and paratumor tissues, we excluded myeloid cells from peripheral blood samples. DGE and enrichment analyses showed that necroptosis remained specifically enriched in all myeloid lineages within tumor tissues (Figures S4A-F). Moreover, we removed myeloid cells from adjacent normal samples to compare the differences between tumor

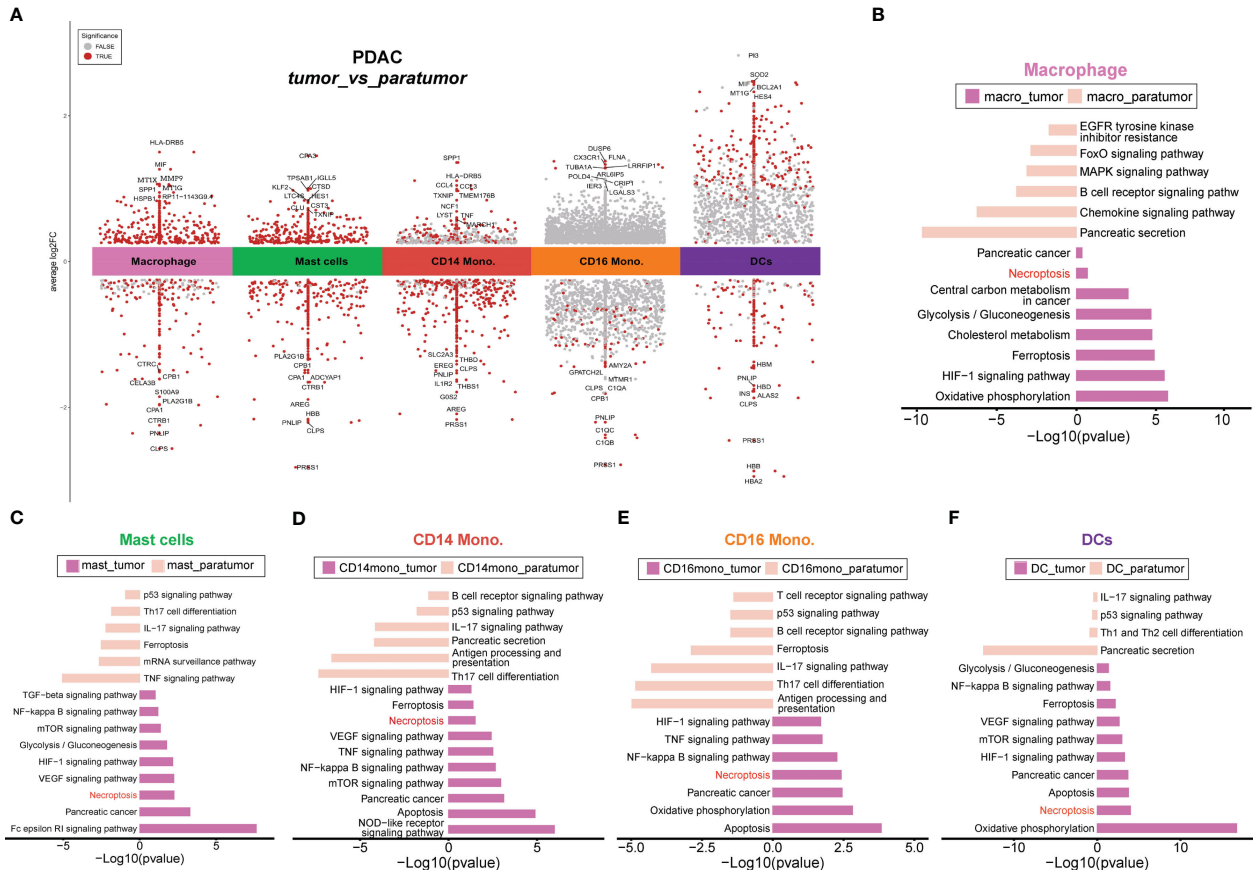

FIGURE 4
Differential gene analyses of PDAC tumors and paracancerous tissues. **(A)** Differential gene expression analysis showing up- and down-regulated genes across all cell types between tumor and paratumor samples from PDAC patients. The top 10 DE genes were shown, and the points dotted in red indicate significant genes. An adjusted p-value < 0.01 is indicated in red, while an adjusted p-value ≥ 0.01 is indicated in black. **(B–F)**. Differential pathways enriched in tumor and paratumor for each cell type.

tissue and peripheral blood from PDAC. The results showed that necroptosis was specifically enriched in all myeloid lineages from tumor tissues, rather than peripheral blood (Figures S5A-F), suggesting a propensity for necroptosis events to occur in solid tumor tissues. Detailed information on all DEGs and necroptosis-associated DEGs could be found in Tables S4, S5, respectively.

We next performed overlapping analyses to find key necroptosis-pathway-associated (NPA) DEGs that exhibited significant up- and down-regulation within each myeloid lineage (Figure 5; Figure S6). The results revealed specific patterns in the expression of NPA genes in different myeloid cell types within tumor tissues. In macrophages from tumor samples, two NPA genes, *GLUL* and *SQSTM1*, were found to be up-regulated (Figure 5A), while *SLC25A6* exhibited down-regulation (Figure 5B). Besides, in mast cells, two NPA genes *HSP90AA1* and *HSP90AB1* were up-regulated in tumor tissues (Figure 5A), whereas *BIRC3* was down-regulated (Figure 5B). Interestingly, *BIRC3* displayed an opposite expression pattern, being up-regulated in CD14 monocytes and CD16 monocytes but down-regulated in mast cells (Figure 5B), indicating potential distinct roles of this NPA gene in different cell types. Additionally, in CD16 monocytes, the remaining NPA genes, *JAK3*, *PPIA*, and *TLR4* were up-regulated in tumor tissues (Figure 5A), while *IFNGR1* was down-regulated in tumor samples (Figure 5B). In the case of DCs,

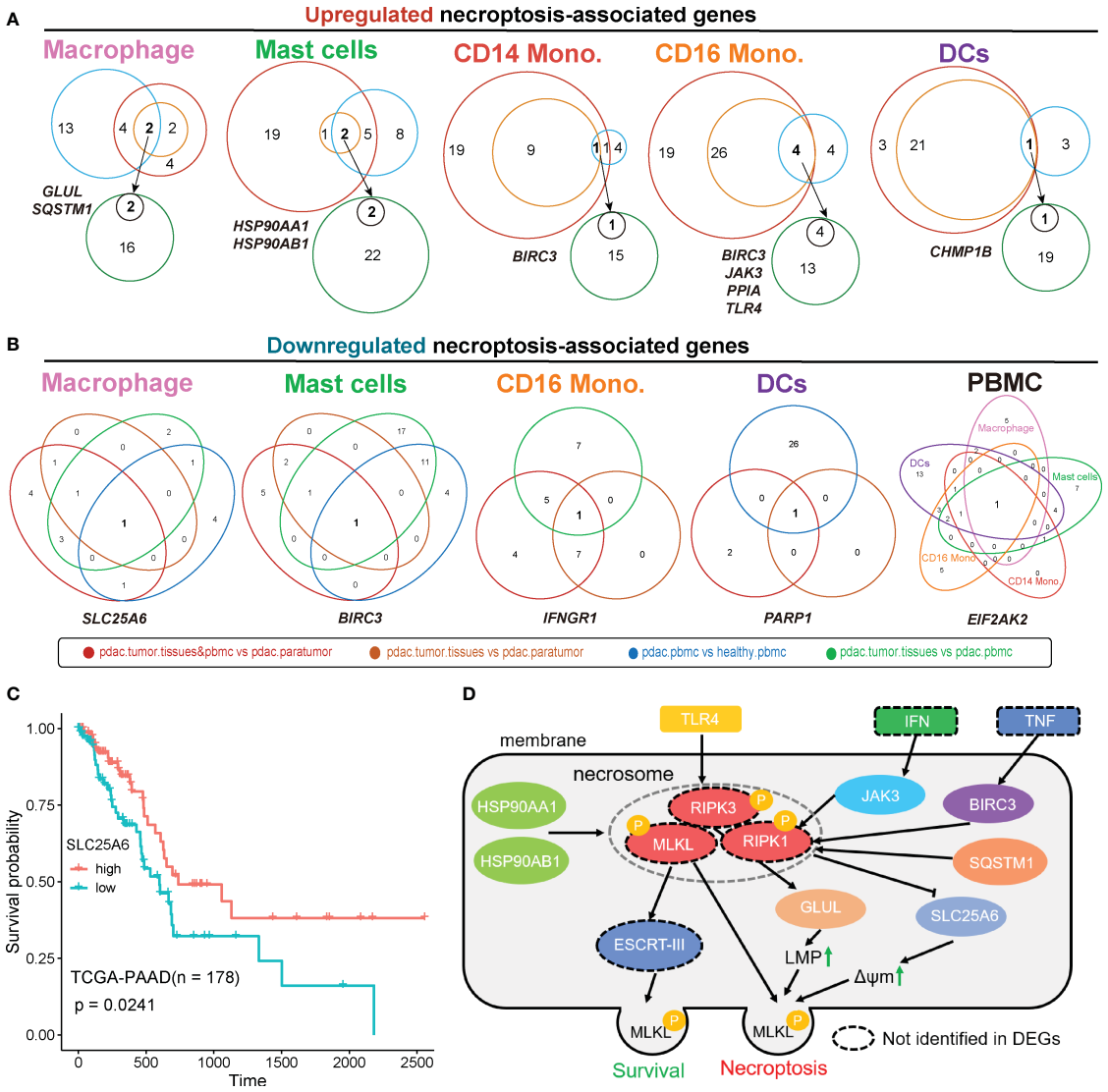

FIGURE 5
Overlapped differentially expressed genes were associated with necroptosis. Analysis of overlapped necroptosis-associated genes up-regulated **(A)** or down-regulated **(B)** in tumor for each cell type. **(C)** TCGA survival analysis of SLC25A6. **(D)** The predicted regulatory pathways of overlapped necroptosis-associated genes we identified based on public Necroptosis pathway network. Genes in dashed-circles were not identified in overlapped DEGs. 'pdac.tumor.tissues&pbmc vs pdac.paratumor', primary tumor tissues, metastatic tumor tissues and PBMCs samples from PDAC patients vs paratumor samples from PDAC patients.; 'pdac.tumor.tissues vs pdac.paratumor', primary tumors and metastatic tumors from PDAC patient vs paracarcinoma tissues from PDAC patient; 'pdac.pbmc vs healthy.pbmc', PBMCs of PDAC Patients vs PBMCs from healthy controls; 'pdac.tumor.tissues vs pdac.pbmc', primary tumor tissues and metastatic tumor tissues of PDAC patients vs PBMCs of PDAC patients; LMP, lysosome membrane permeabilization; ΔΨm, mitochondrial membrane potential.

the NPA gene, *CHMP1B* was up-regulated in tumor tissues (Figure 5A), while *PARP1* was down-regulated in tumor samples (Figure 5B).

Based on the Necroptosis pathway network (https://www.kegg.jp/pathway/map04217), several NPA DEGs that identified within PDAC myeloid cells were involved in this network, thereby the interactive relationship was mapped. This approach allowed us to gain insights into the underlying contribution of necroptosis in the context of myeloid cell-mediated immune responses within TME of PDAC. Of note, we designated this mapping as the representation of the necroptosis pathway associated with PDAC myeloid cells, while experimental studies are necessary to confirm their precise roles and interactions (Figure 5D). In this predicted simplified model, *TLR4* acts as an upstream regulator that promotes the phosphorylation of *RIPK3*, a key regulator of necroptosis (41). This phosphorylation event leads to the subsequent phosphorylation of *GLUL*, which contributes to increased lysosome membrane permeabilization (LMP), a common phenomenon in cancer cells (42). Besides, *JAK3*, a downstream signaling molecule of IFN, *BIRC3*, a downstream molecule of TNF, and *SQSTM1*, a dissociated molecule, work together to promote the phosphorylation of *RIPK1*, another core regulator of necroptosis (41). The phosphorylated *RIPK1*, in turn, represses the expression of *SLC25A6*, result in a transient increases in mitochondrial transmembrane potential ($\Delta\Psi m$), which is highly related to cancer malignancy (43). Moreover, *HSP90AA1* and *HSP90AB1* can simultaneously promote the phosphorylation of necrosome, including *RIPK1*, *RIPK3*, and *MLKL*. This leads to the activation of various necroptosis pathways, such as MLP, $\Delta\Psi m$ and mitochondrial fission (44). Mitochondrial fission facilitates the proliferation, metastasis, and drug resistance of cancer cells (45). Despite their necroptosis-promoting function, HSP90AA1 and HSP90AB1 can also act as upstream regulator of ESCRT-III, which helps maintain membrane integrity during the initiation of necroptosis, thereby promoting cell survival (46).

To explore the clinical relevance of necroptosis-associated genes that were down-regulated in tumor (Figure 5B), we conducted survival analysis. The results revealed that higher expression of *SLC25A6* was correlated with improved survival outcomes (Figure 5C). Interestingly, we observed a significantly higher expression of *SLC25A6* in *HSP90AA1*$^+$*HSP90AB1*$^+$ mast cells compared to *HSP90AA1*$^-$*HSP90AB1*$^-$ mast cells (Figure 6E). These findings indicated that *HSP90AA1* and *HSP90AB1* might have an unknown mechanism of targeting *SLC25A6* in necroptosis pathway (Figure 5D).

A novel immunological RTM population is specific to paratumor tissue

Based on the identified NPA genes mentioned above, we proceeded to investigate the relations within myeloid lineages. Firstly, myeloid cells from tumor and paratumor samples were selected for subsequent analysis (Figure 7A, left). Subsequently, an unsupervised clustering analysis was performed on macrophage subsets (Figure 7A, middle). Cluster 3, characterized by high expression of *ITGAX*, *CD86*, *HLA-DRA*, and *HLA-DRB1*, was identified as M1 macrophages (Figure 7B). Clusters 0, 2, 4, and 6 were classified as M2 macrophages as they highly expressed *SPP1*, *MACRO*, *APOE*, *FABP5*, and *LAMP1*. Clusters 1 and 5, which displayed elevated expression profiles of *S100A4*, *RGS1*, *CD74*, and *CSF1R*,were designated as RTM (resident tissue macrophage) subset.

Focusing on the expression profiles of NPA genes, including *GLUL* and *SQSTM1* in macrophages, strikingly, we found that *GLUL* and *SQSTM1* were elevated in all macrophage subsets except for a minor RTM cell population (Figure 7C). Therefore, we named this RMT subset as *GLUL*$^-$*SQSTM1*$^-$ RTM. Unexpectedly, this subset was deficient in tumor samples compared to paratumor samples (Figure 7D), indicating that *GLUL*$^-$*SQSTM1*$^-$ RTM may act as a positive regulator of immunity. To validate this hypothesis, we performed a correlation analysis of *GLUL*$^-$*SQSTM1*$^-$ RTM and CD8$^+$T cells using *GLUL*$^-$*SQSTM1*$^-$ RTM markers, including *PRSS1*, *CTRB1*, *CLPS*, *PLA2G1B*, *PNLIP* and *CPA1* (Figure 7E). The results showed positive correlations between these markers with CD8+T cells both in this cohort (Figure 7F) and TCGA-PAAD cohort (Figure 7G), which validated that *GLUL*$^-$*SQSTM1*$^-$ RTM represents an immunological cell population. Furthermore, to investigate whether this subpopulation directly interacts with epithelial cells, we performed correlation analyses. The results indicated that this subpopulation had no direct correlations with epithelial cells, neither in this cohort (Figure S7A) nor in the TCGA-PAAD cohort (Figure S7B). This suggests that this subpopulation may not directly exert immunological functions on epithelial cells.

Cytokines, which are small proteins crucial in controlling the growth and activity of the immune system, play a significant role in the immune and inflammatory responses of all cells in the body (47). Alternatively, cancers can respond to host-derived cytokines that promote growth, inhibit apoptosis and facilitate invasion and metastasis (48). In this study, we investigated the expression profiles of several cytokines in macrophages. The results showed that *ADM* (49), *CCL2* (50), *CCL4* (51), *CXCL3* (52), *MIF* (53), *SPP1* (54), *VEGFA* (55) and *VEGFB* (56), which have previously been reported to promote tumor progression and metastasis, were specifically deficient in *GLUL*$^-$*SQSTM1*$^-$ RTM (Figure 7H). This further emphasizes the immunological role of *GLUL*$^-$*SQSTM1*$^-$ RTM in TME.

HSP90AA1$^+$*HSP90AB1*$^+$ mast cells are pro-immune

After investigating macrophages, our focus shifted to mast cells (Figure 6). We extracted mast cells from the myeloid cell population to perform unsupervised clustering. A total of 6 clusters were identified, and cluster 3 lacked HSP90AA1 and HSP90AB1 expression. Consequently, we termed cluster 3 as *HSP90AA1*$^-$*HSP90AB1*$^-$ mast cells, while the remaining mast cells were classified as *HSP90AA1*$^+$*HSP90AB1*$^+$ mast cells (Figure 6A). To determine whether *HSP90AA1*$^+$*HSP90AB1*$^+$ mast cells exhibited pro-immune or anti-immune characteristics, we evaluated the correlations between *HSP90AA1*$^+$*HSP90AB1*$^+$ mast cell markers

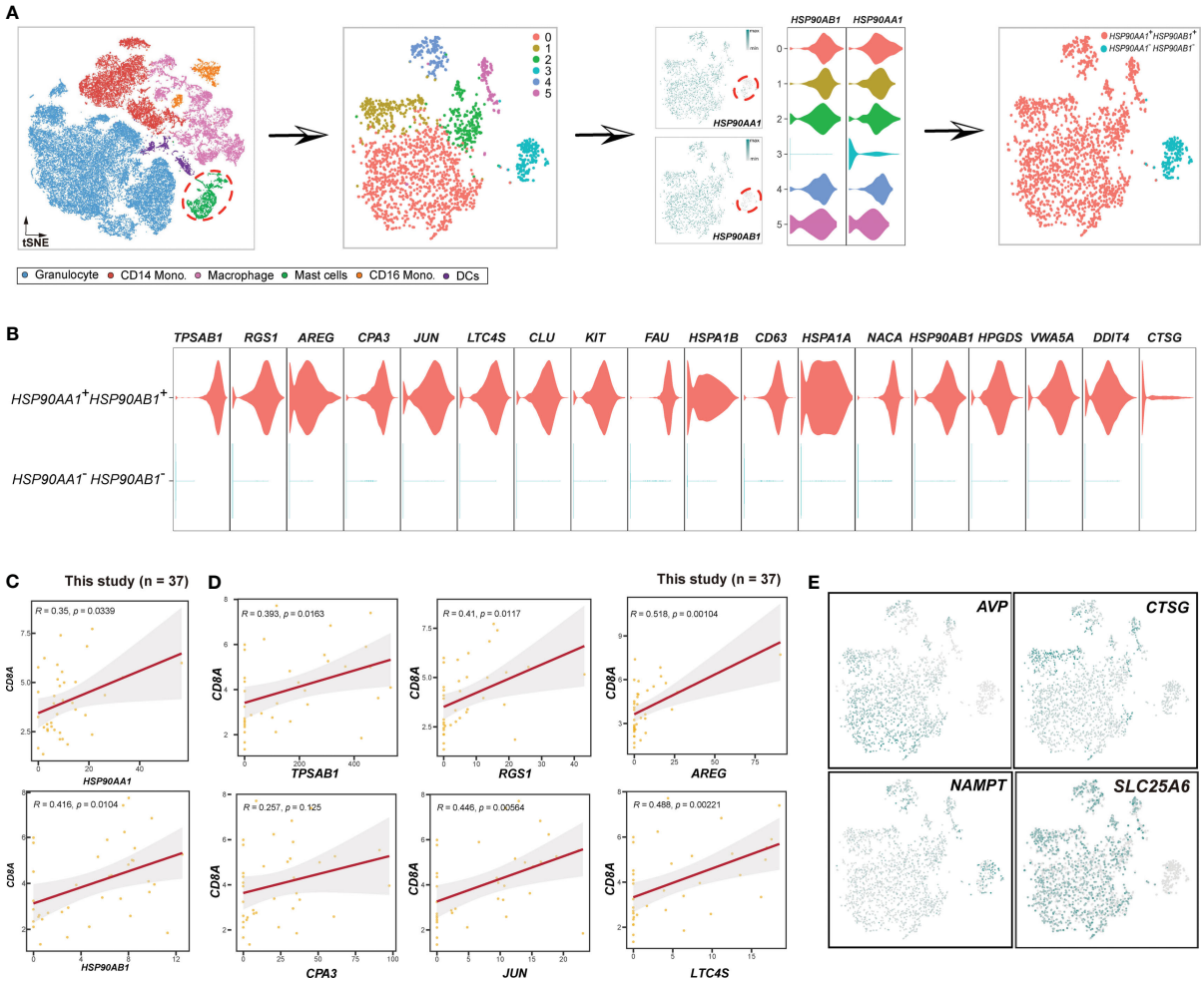

FIGURE 6
Schema to identify *HSP90AA1*$^+$*HSP90AB1*$^+$ mast cells. **(A)** Schema showing the procedures to distinguish mast cells based on *HSP90AA1* and *HSP90AB1*. **(B)** Violin plots displaying the expression of *HSP90AA1*$^+$*HSP90AB1*$^+$ mast cluster-specific genes. **(C)** Scatterplot showing the Spearman correlation between the *HSP90AA1*, *HSP90AB1*, and CD8A in this study. **(D)** Scatterplot illustrating the correlations between the top 6 *HSP90AA1*$^+$*HSP90AB1*$^+$ mast cluster-specific genes and *CD8A* in this study. **(E)** Expression patterns of cytokines (*AVP*, *CTSG*, *NAMPT*, *SLC25A6*) in mast cells.

(Figure 6B) and CD8$^+$T cells. The results showed that all of the *HSP90AA1*$^+$*HSP90AB1*$^+$ mast cell markers, including *HSP90AA1*, *HSP90AB1*, *TPSAB1*, *AREG*, *CPA3*, *JUN*, *LTC4S*, *CLU*, *KIT*, *FAU*, etc., exhibited positive correlations with *CD8A* (Figures 6C, D, S8A), demonstrating that *HSP90AA1*$^+$*HSP90AB1*$^+$ mast cell may act as positive regulator of immunity. In contrast, *HSP90AA1*$^-$*HSP90AB1*$^-$ mast cells were anti-immune, and their markers, including *CLC*, *RUNX1*, *FAM101B*, *SORL1*, *PIM1*, *CSF3R*, *ATP100*, *MAF*, *MYO1F*, etc. (Figure S8B), showed negative correlations with CD8$^+$ T cells (Figure S8C). To further investigate the novel mast clusters, we evaluated the expression patterns of certain cytokines (Figure 6E), including *AVP*, *CTSG*, and *NAMPT*. *AVP* (57) and *CTSG* (58), known to play important roles in inflammation and immune responses, were exclusively sufficient in *HSP90AA1*$^+$*HSP90AB1*$^+$ mast cells, while *NAMPT* (59), previously reported to be associated with maintaining cancer stemness, was highly expressed in *HSP90AA1*$^-$*HSP90AB1*$^-$ mast cells. Additionally, the expression of *CD8A* was significantly higher in *HSP90AA1*$^+$*HSP90AB1*$^+$ mast cells (Figure S8D), providing further supporting for the notion that *HSP90AA1*$^+$*HSP90AB1*$^+$ mast cells were immune-promoting.

JAK3$^+$*TLR4*$^+$ CD16 monocytes are anti-immune

Furthermore, we investigated CD16 monocytes (Figure 8). Firstly, we extracted CD16 monocytes from myeloid cells and performed unsupervised clustering. As a result, a total of 7 clusters were identified, in which clusters 1, 4, and 5 were all *JAK3*$^-$*TLR4*$^-$ (Figure 8A). Therefore, we classified CD16 monocytes into *JAK3*$^+$*TLR4*$^+$ CD16 monocytes and *JAK3*$^-$*TLR4*$^-$ CD16 monocytes (Figure 8A). We then proceeded to examine the distinctive features of these two clusters. In contrast to *HSP90AA1*$^+$*HSP90AB1*$^+$ mast cells, *JAK3*$^+$*TLR4*$^+$ CD16 monocytes were immunosuppressive, as indicated by the negative

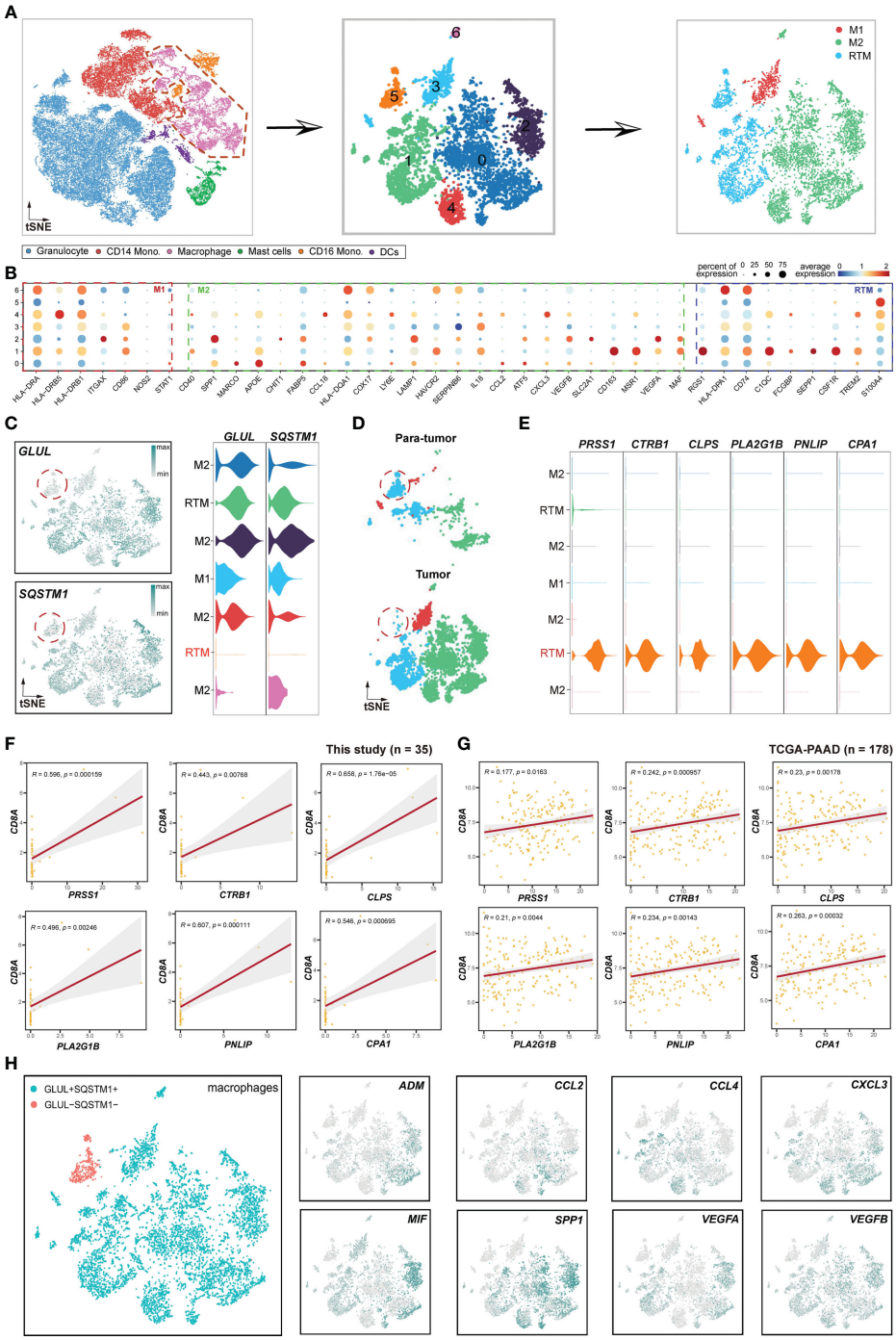

FIGURE 7
Pipeline to identify novel immunological RTM (resident tissue macrophage) population. **(A)** Schema illustrating the procedures for identifying the subclusters of macrophages. **(B)** Bubble plot displaying selected cell type-specific markers across all clusters. The size of dots represents the fraction of cells expressing a particular marker, and the color intensity indicates the level of average mean expression. **(C)** t-SNE plots showing the expression of *GLUL* and *SQSTM1*. **(D)** t-SNE plots showing the subclusters of macrophages between tumor and paratumor samples. **(E)** Violin plots presenting RTM (*GLUL*$^-$*SQSTM*$^-$) cluster-specific markers. **(F)** Correlations between the *GLUL*$^-$*SQSTM1*$^-$ RTM cluster-specific genes and CD8A. **(G)** TCGA validation of the genes illustrated in **(F)**. **(H)** Expression and distribution patterns of cytokines in macrophages. The left figure represents macrophage subsets, while the right figures are expression patterns of some cytokines.

correlation between their markers (*JAK3*, *TLR4*, *CRIP1*, *IFI6*, *ZBTB7A*, *ZYX*, etc.) (Figure 8B) and CD8$^+$T cells at a significant levels (Figures 8C, D). In contrast, *JAK3*$^-$*TLR4*$^-$ CD16 monocytes displayed upregulation of *EEF1D*, *MS4A4A*, *TMEM66*, and TNF (Figure S9A), all of which were positively correlated with CD8$^+$ T cells at significant levels (Figure S9B), suggesting a pro-immune role of *JAK3*$^-$*TLR4*$^-$ CD16 monocytes. Cytokine analysis further confirmed these results. *CAT* (60), *CECR1* (61), *GPI* (62), *HDGF* (63), and *MIF* (53), previously reported to promote tumor development and progression, were specifically abundant in

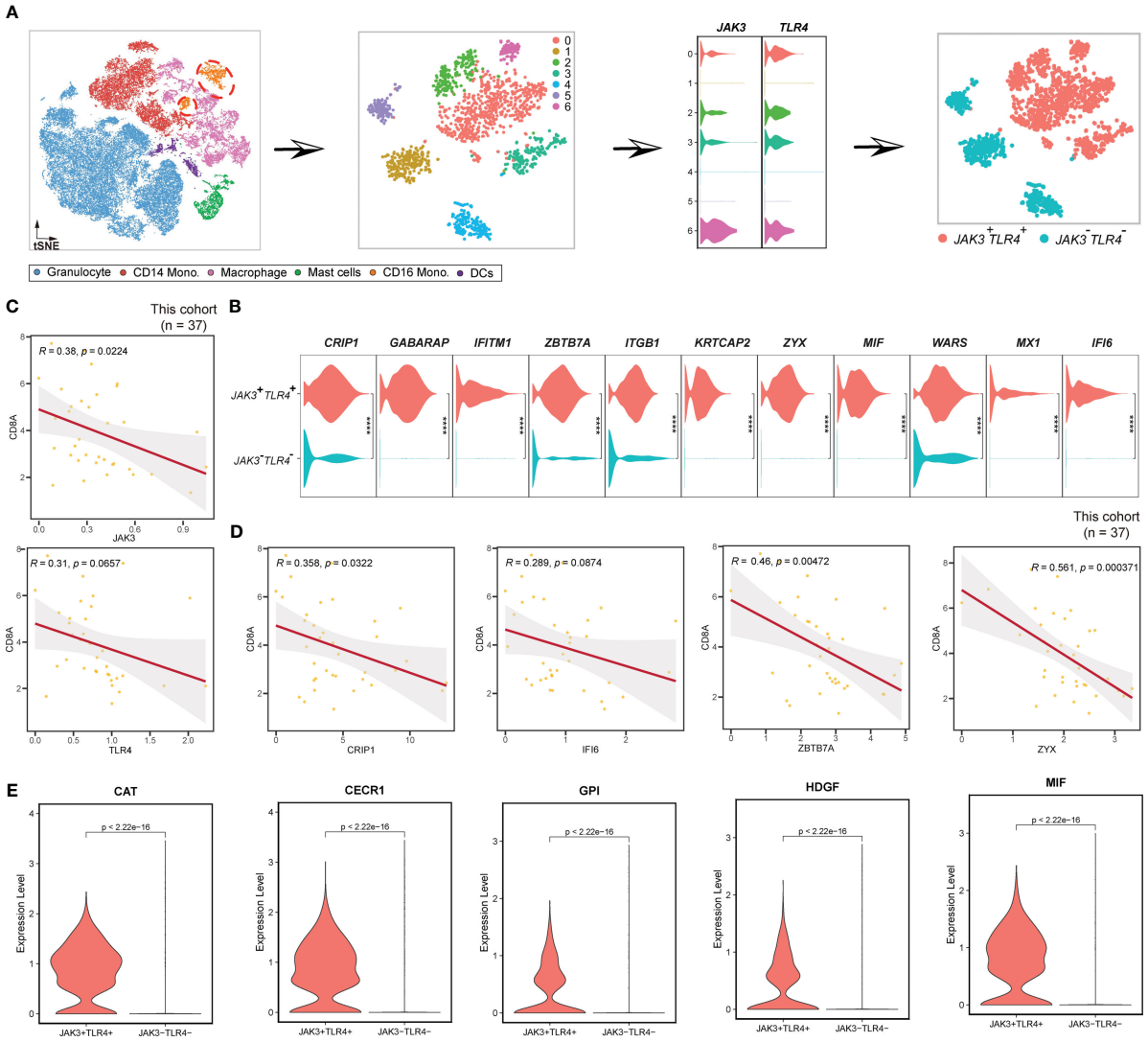

FIGURE 8
Pipeline to identify *JAK3*$^{+}$*TLR4*$^{+}$ CD16 monocytes. **(A)** Workflow showing the procedures to identify *JAK3*$^{+}$*TLR4*$^{+}$ mast cells. **(B)** Violin plots displaying the expression of *JAK3*$^{+}$*TLR4*$^{+}$ mast cluster-specific genes. **(C)** Scatterplot showing the correlations between *JAK3*, *TLR4*, and *CD8A* in this study. **(D)** Scatterplot illustrating the correlation between *JAK3*$^{+}$*TLR4*$^{+}$ mast cluster-specific genes and CD8A in this study. **(E)** Violin plot showing the expression profiles of some cytokines in CD16 monocytes. **** Represents a statistical significance level of P<0.0001.

JAK3^{+}*TLR4*$^{+}$ CD16 monocytes, rather than *JAK3*$^{-}$*TLR4*$^{-}$ CD16 monocytes (Figure 8E).

Furthermore, we explored the NPA genes in other myeloid cells, however, the correlations between these genes and *CD8A* were insignificant. For example, in *BIRC3*$^{+}$ CD14 monocytes, the marker *BIRC3*, did not show a significantly correlation with CD8^{+} T cells (Figure S10A). Moreover, in *BIRC3*$^{+}$ CD16 monocytes, although *BIRC3* exhibited a significant positive correlation with *CD8A*, other markers such as *APRT*, *C1QB*, *GABARAP*, and *IFITM1* were not correlated with CD8^{+} T cells (Figure S10B). Moreover, in *CHMP1B*$^{+}$ DCs, the marker *CHMP1B* was not correlated with CD8^{+} T cells (Figure S10C). These results indicated that these NPA genes may function as immune mediators in an unknown manner.

Cluster-specific cellular interaction networks that mediate immunity

To gain a comprehensive understanding of the interactions among the novel clusters and the T/B/NK/epithelial cell populations, as well as their collective contribution to the PDAC tumor microenvironment, we inferred a putative cellular interaction network based on the receptor-ligand database (31). Our findings unveiled specific interactions within various signaling pathways. Specifically, we observed that *EPO/EPOR* interaction of EPO signaling pathway was unique to the *GLUL*$^{-}$*SQSTM1*$^{-}$ RTM cluster. In this cluster, the ligand EPO was predominantly expressed in *GLUL*$^{-}$*SQSTM1*$^{-}$ RTM, while *EPOR* receptor was present in CD4^{+} T cells, CD8^{+} T cells, B cells, NK cells and epithelial cells

(Figure 9A). The *EPO/EPOR* interaction has been reported to initiate a signaling cascade that activated and recruited a variety of Src homology-2 (SH2) domain-containing proteins, subsequently triggering downstream signaling pathways such as ERK-1/2 and JAK-2 (64). Interestingly, a recent study has demonstrated that *EPO/EPOR* could reduce the variability of myeloma cell lines and malignant primary plasma cells (65). And *ANXA1/FPR1* interaction within the ANNEXIN signaling pathway was specific to *GLUL*$^{+}$*SQSTM1*$^{+}$ macrophage cells, and ligand *ANXA1* was specific to *GLUL*$^{+}$*SQSTM1*$^{+}$ macrophage, while receptor *FPR1* was in CD4^{+} T, CD8^{+} T, B, NK and epithelial cells (Figure 9B). *FPR1*, previously reported to promote chemotherapy-induced antitumor immune response (66), was demonstrated to act as a receptor for *ANXA1*, promoting cell death through the necroptosis pathway (67). Furthermore, we identified the *IL10/IL10RA* interaction within the IL10 signaling pathway, which was specific to *HSP90AA1*$^{+}$*HSP90AB1*$^{+}$ mast cell, in which ligand *IL10* was expressed in CD4^{+} T, CD8^{+} T, B, NK, and epithelial cells, while the receptor *IL10RA* was specific to *HSP90AA1*$^{+}$*HSP90AB1*$^{+}$ mast cell (Figure 9C). IL10- and IL10R-dependent signaling have been reported to play critical roles in controlling immune responses in both innate and adaptive immune systems (68). Finally, TNF-α (TNF)/TNFR1 (*TNFRSF1A*) interaction was found to be specific to *JAK3*$^{+}$*TLR4*$^{+}$ CD16 monocytes. In this interaction, the ligand TNF was specific to *JAK3*$^{+}$*TLR4*$^{+}$ CD16 monocytes, while receptor *TNFR1* was expressed in CD4^{+} T, CD8^{+} T, B, NK and epithelial cells (Figure 9D). TNF-α signaling meditated by *TNFR1* in the TME has been reported to promote gastric tumor development and maintain tumor cells in an undifferentiated state (69). Taken together, the intercellular interactions revealed a close relationship between immune cell and cancer cell dynamics, as well as the molecular features of novel clusters (Figure 10). These interactions may play a crucial role in determining the prognostic and therapeutic response in PDAC.

Validation of the existence of the novel clusters

We proceeded to validate the presence of *GLUL*$^{-}$*SQSTM1*$^{-}$ RTM, *HSP90AA1*$^{+}$*HSP90AB1*$^{+}$ mast cell, and *JAK3*$^{+}$*TLR4*$^{+}$ CD16 monocyte cellular clusters in other PDAC cohorts. To accomplish this, we analyzed publicly available scRNA-seq data from the CRA001160 dataset (26). In this dataset, 1,047, 3,098, and 1,464 cells were annotated as RTM, mast cells, and CD16 monocytes, respectively (Figure S1). To focus specifically on RTM, mast cells,

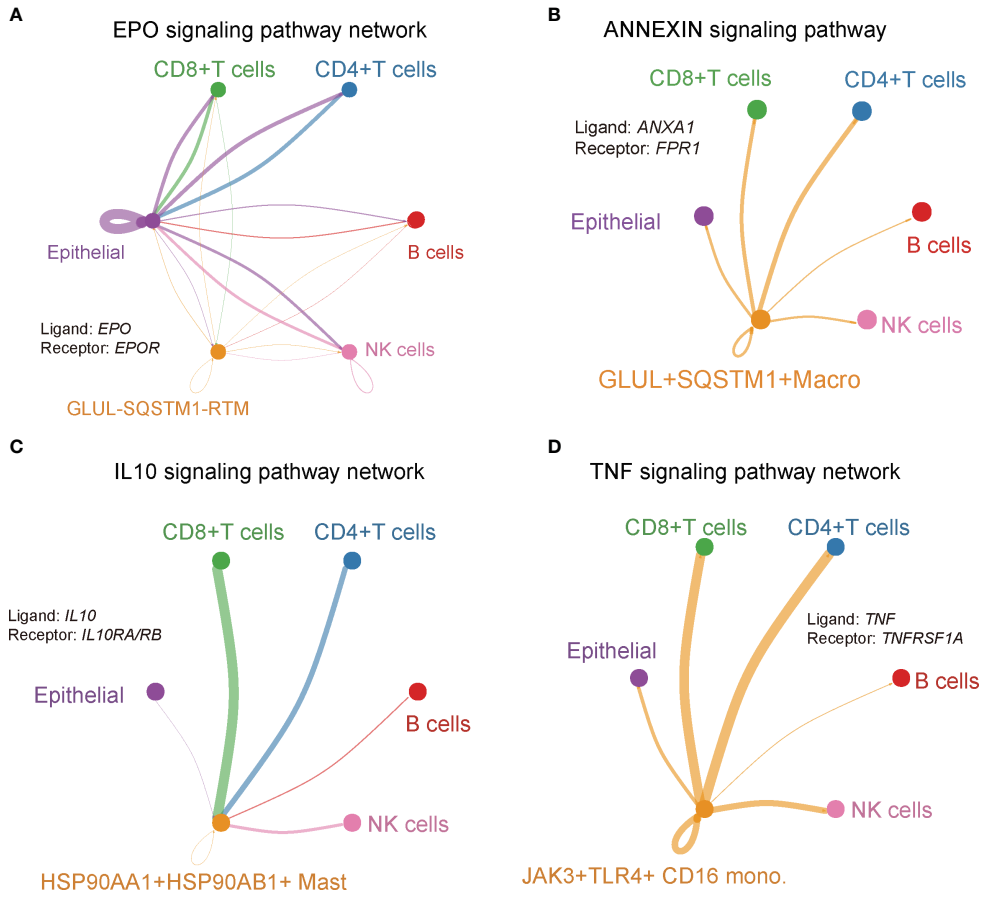

FIGURE 9
Cluster-specific interaction network. Signaling pathway network of ligand-receptor pairs that were specific in **(A)** *GLUL*$^{-}$*SQSTM1*$^{-}$ RTM, **(B)** *GLUL*$^{+}$*SQSTM1*$^{+}$ macro, **(C)** *HSP90AA1*$^{+}$*HSP90AB1*$^{+}$ mast, **(D)** *JAK3*$^{+}$*TLR4*$^{+}$ CD16 Mono.

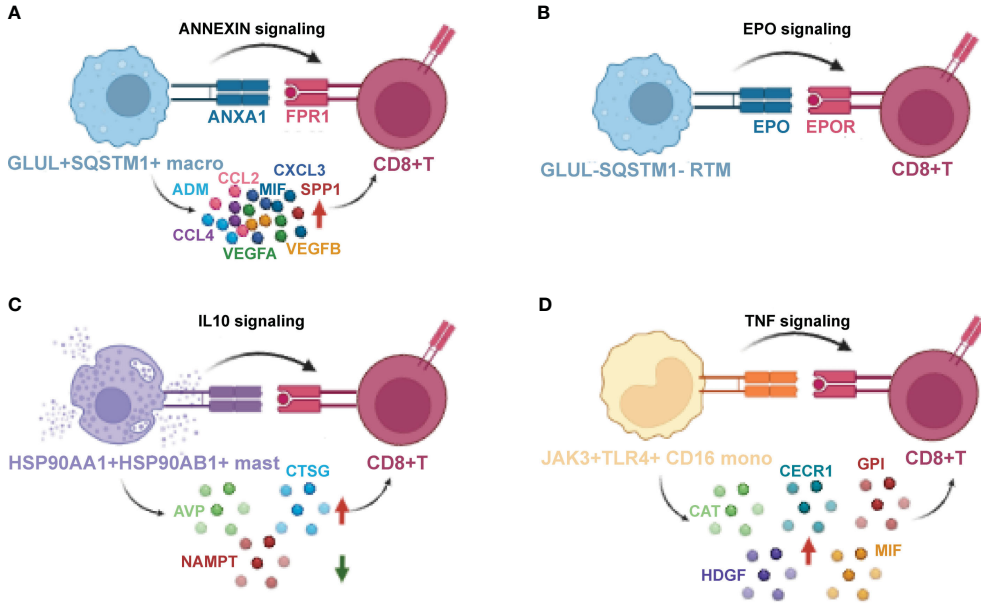

FIGURE 10
The crosstalk between novel myeloid-derived novel clusters, CD8$^+$T cells Macrophage **(A)**, GLUL-SQSTM1-Macrophage **(B)**, HSP90AA1$^+$ HSP90AB1$^+$ Mast **(C)** and JAK3$^+$ TLR4$^+$ CD16$^+$ Monocyte **(D)**, and CD8$^+$T cells that mediate immunity. Schematic for cellular crosstalk and corresponding signaling pathways in PDAC TIMs that contribute to immunity or immune suppression. The novel clusters secrete various cytokines and ligands that signal to their respective receptors, thus activating the corresponding signaling, respectively. Red arrows indicate up-regulated cytokines while green arrow indicates down-regulated cytokines.

and CD16 monocytes, we distinguished these cell types based on the expression of *GLUL*/*SQSTM1* (RTM), *HSP90AA1*/*HSP90AB1* (mast cell), and *JAK3*/*TLR4* (CD16 monocytes), respectively (Figure 11A). Consequently, we obtained 49 *GLUL*$^-$*SQSMT1*$^-$ RTM, 2,151 *HSP90AA1*$^+$*HSP90AB1*$^+$ mast cells, and 1,234 *JAK3*$^+$*TLR4*$^+$ CD16 monocytes (Figure 11A).

Although GLUL$^-$SQSMT1$^-$ RTM was specifically present in PDAC tumor tissues, it was noteworthy that the majority of RTM in the TME are characterized by the expression of GLUL and SQSTM1. Given the prevalence of GLUL$^+$SQSTM1$^+$RTM cells in PDAC tumor tissues, and their interaction with CD8$^+$T cells revealed by the cell chat analysis, it becomes apparent that a deeper exploration is warranted. To validate the expression of these genes at single-cell level, visualize their spatial distribution within complex tissue structures and validate co-expression patterns, functional gene interactions, we performed RNA fluorescence *in situ* hybridization (FISH) on paraffin sections of PDAC tumor tissue (Figure 11B).Our analysis revealed frequent overlap of the *GLUL*, *SQSTM1* and *S100A4*, providing evidence for the existence of the GLUL$^+$SQSTM1$^+$ RTM. Additionally, we conducted further investigations and confirmed the adjacent spatial relationship between the GLUL$^+$SQSTM1$^+$ RTM and CD8$^+$ T cells in PDAC solid tumors. This observation suggests potential functional interactions between these cell populations within the tumor microenvironment.

Discussion

It is well-established that necroptosis, a programmed form of necrosis or inflammatory cell death (70), has gained significant attention in cancer research due to its implications in pathogenesis and therapy (40, 71, 72). The involvement of necroptosis in recruiting immune cells, regulating pro- or anti-tumor components in TME, and modulating immune responses through the release of DAMPs, chemokines and other cytokines. However, the specific roles of necroptosis in PDAC have not been systematically described and remain to be deciphered. In this study, public scRNA-seq data from Gene Expression Omnibus (GEO) database was downloaded, which covered more than 124,000 cells of 16 PDAC patients across multiple immune-relevant tissue sites (24). Our analysis focused on charactering major myeloid cell lineages, and identifying three necroptosis-associated subsets of myeloid-derived cells. These findings provide a valuable resource for comprehensively understanding multi-dimensional characterization of the tumor microenvironment in PDAC.

In this study, we identified *HSP90AA1*$^+$*HSP90AB1*$^+$ mast cells that exerting anti-tumorigenic effects in PDAC, contributing to better clinical outcomes. the Heat shock protein 90 (HSP90) protein family, including *HSP90AA1* and *HSP90AB1*, plays prominent roles in various biological processes such as protein folding (73), apoptosis (74), cell-cycle regulation (75), as well as signal transduction (76). Of note, previous studies have suggested that HSP90 can influence the activation and stability of crucial regulators involved in the necroptosis process, such asRIPK1, RIPK3 and MLKL, thereby contributing to immune cell recruitment and immunogenic cell death of tumor cells (77–79). In addition, necroptosis is deemed to trigger an adaptive immune response by releasing cytokines (80). The novel mast cells were predicted to interact with CD8$^+$ T cells via IL10 signaling pathway, and highly expressed *AVP* and *CTSG*. Consistently, *AVP* (57) and

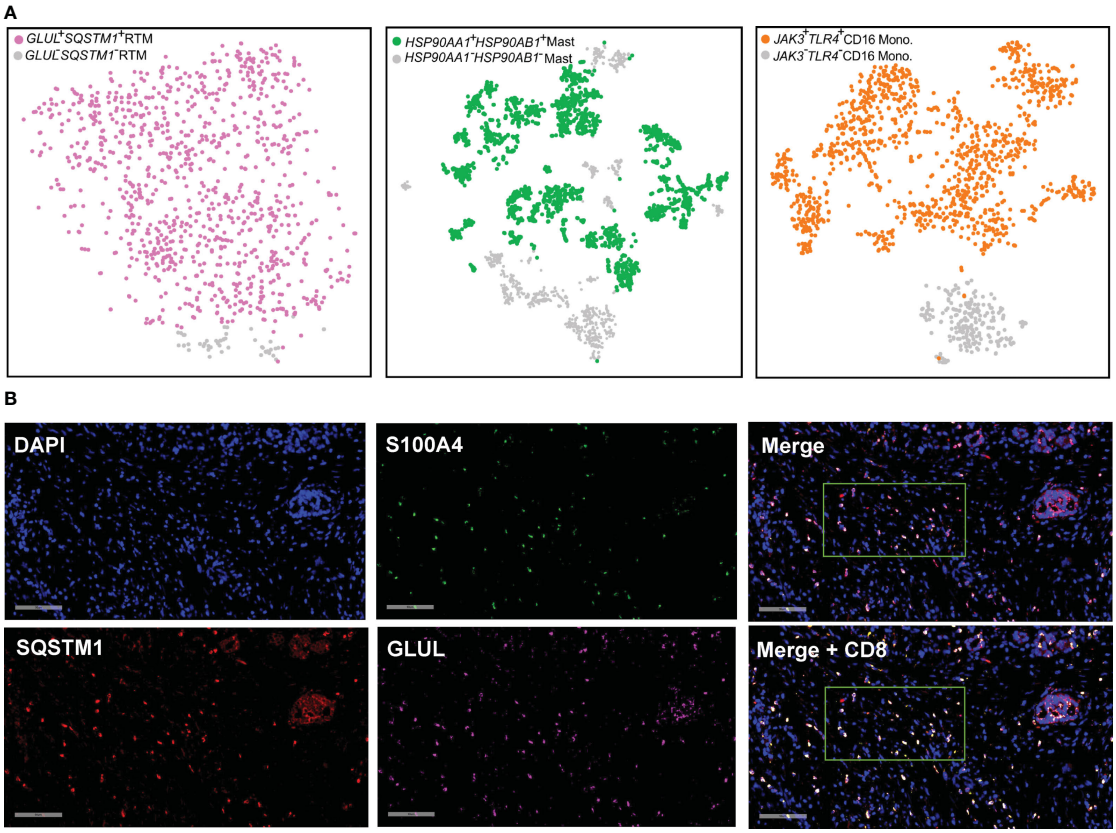

FIGURE 11
Detection and validation of the cellular clusters. **(A)** t-SNE plot combing *GLUL*$^{+}$*SQSTM1*$^{+}$ RTM (n = 998, in purple), *HSP90AA1*$^{+}$*HSP90AB1*$^{+}$ mast cells (n = 2,151, in blue), and *JAK3*$^{+}$*TLR4*$^{+}$ CD16 monocyte (n = 1,234, in orange) from PDAC (Peng et al., 2019). **(B)** RNA FISH staining in the PDAC tissues. One representative image for each gene is shown. Spectrum orange dots indicate GLUL, spectrum red dots indicate SQSTM1, spectrum green dots indicate S100A4, spectrum gold indicate CD8A. Scale bars, 90 μm.

CTSG (58) have been reported to play important roles in inflammation and immune response, and IL10 has been shown to potentiate IFN-γ and induct the cytotoxicity of CD8^{+} T cells (68, 81–83), thereby triggering anti-tumor immune responses. These findings collectively suggested that *HSP90AA1*$^{+}$*HSP90AB1*$^{+}$ mast cells are functionally important in necroptosis process and are involved in immune cell recruitment through the IL10 signaling pathway. Future research should focus on designing effective drugs that modulate HSP90 activity and developing diagnostic tools for accurate patient stratification for therapy with HSP90 agonists or HSP90 antagonist.

Another cluster of special interest is the *GLUL*$^{-}$*SQSTM1*$^{-}$ RTM subpopulation, which is enriched in PDAC tumor tissues and acts as a positive regulator of immunity. Glutamine synthetase (GLUL) has been associated with RIP3-mediated necroptosis (41), and the p62/SQSTM1 complex binding to necroptosis-related proteins RIP1 and RIP3 facilitates the transition from autophagy to necroptosis (84). Moreover, it has been reported that both GLUL and p62/SQSTM1 may influence the recruitment, activation and polarization of macrophage. *GLUL* is known to be associated with the differentiation and function of macrophage, more specifically, enhancing M2- polarization (85, 86). Exogenous p62/SQSTM1 has been shown to induce M1 polarization of macrophage through activation of the NF-κB pathway (87). Given the potential roles of GLUL and p62/SQSTM1 in macrophage polarization, we evaluating the expression levels of molecular markers in macrophages. For example, CCL2/CCR2 axis is a major player in macrophage polarizing towards to M2 phenotype (88, 89). Stimulation of CXCL13 may activate Akt pathway, suggesting an increase in M2 macrophage in renal cell carcinoma (90). The vascular endothelial growth factor (VEGF) family, including *VEGFA* and *VEGFB*, can contribute to M2 polarization in the decidua (91). *MIF* (92), *SPP1* (93) and *ADM* (94) have all been previously reported to be associated with a dominant M2 polarization and a loss of M1 function. In our study, the deficiency of these chemokines in *GLUL*$^{-}$*SQSMT1*$^{-}$ RTM cells may suggest the pro-inflammatory M1-polarized phenotype, thereby modulating the antitumor response. These results indicated that the GLUL^{-}SQSMT1^{-} RTM cells with a pro-immune profile may evade programmed necroptosis and abundantly infiltrate in the PDAC TME of patients with superior efficacy. The combination of *GLUL* and *SQSTM1* inhibitors in precisely characterized patients may have superior effects against cancer compared to immunotherapy alone.

The novel *JAK3*$^{+}$*TLR4*$^{+}$ CD16 monocyte subset exhibits anti-immune properties and is associated with unfavorable clinical outcomes. Janus Kinase 3 (*JAK3*) is a tyrosine kinase that belongs to the Janus family of kinases. Hyper-activation of the JAK3-STAT signaling pathway has been linked to tumor development and

progression by inducing factors associated with suppressive immune cell recruitment, angiogenesis and neo-vascularization (95–99). TLR4, a member of the toll-like receptor (TLR) family, can lead to the activation of NF-κB pathway, which is essential for necroptosis signaling, as well as the production of pro-inflammatory cytokines and angiogenetic factors (100, 101). In addition, we observed that this novel monocyte subset was predicted to interact with $CD8^+$ T cells via TNF-TNFR1 signaling pathway and expressed high levels of pro-tumor cytokines CAT, HDGF, CECER1, GPI and MIF. NFR1-dependent TNF signaling has been reported to impair the accumulation of tumor-infiltrating lymphocyte (TILs) and induce significant death of activated $CD8^+$ T cells (102, 103). HDGF is considered as an angiogenic and anti-apoptotic factor, contributing to tumorigenesis in several malignant diseases (104–106). MIF plays an essential role in inhibiting cytotoxic T lymphocytes (CTLs) and regulating lymphocyte transmigration (107, 108). CAT, CECR1 and GPI have all been previously associated with promoting tumor progression (60–62). Altogether, these results align with our observations. We hypothesized that this monocyte subset (*JAK3*$^+$*TLR4*$^+$ CD16 monocyte) contributes to shaping pro-tumor immunity in TME, ultimately accelerating malignant transformation and tumor progression. However, further investigation is needed to elucidate the underlying mechanisms. Compared to other JAKs, *JAK3* has a more restricted expression profile, primarily confined to immune system. Therefore, selective targeting of *JAK3* represents a potent immunosuppressant strategy that could minimize potential adverse effects. Inhibition of TLR4-related pathways has shown promising results in clinical trials for disease treatment with excessive immune response (109–111). Current study supports the notion that the discovery of *JAK3* and *TLR4* antagonists could be an ideal strategy for cancer treatment.

A major limitation of the current finding is the lack of sufficient experimental validation. For instance, the proposed NPA gene network was supposed only based on the expression profiles, and the underlying regulatory mechanism of necroptosis pathway in tumor progression remains obscure in real world. In addition, our study illustrated the indispensable roles of three novel myeloid subpopulations in tumor microenvironment and their associations with necroptosis, however, the underlying mechanisms need further investigation. And the expression profiles of GLUL and SQSTM1 of macrophages in normal samples were not explored. The implementation of advanced biological techniques and bioinformatics analysis in mammalian models of human pathological samples will be critical for gaining a better understanding of these subpopulations in the context of molecular mechanism and drug targeting.

Given the robust immunosuppressive and desmoplastic TME in PDAC, which contributes to adaptive or acquired resistance to therapy, investigating the relationship between necroptosis and tumor immunology holds promise for future treatment solutions. The identification of necroptosis-associated myeloid lineages can potentially serve as targets for therapeutic intervention, allowing for dynamically monitoring of the anti-tumor immune response and improvement of patient outcomes. Our findings provide a valuable resource for further investigation to gain deeper biological insights into the role of necroptosis in cancer. Considering the exceedingly complex and individually unique immune microenvironment of tumors, necroptosis signaling may generate a diverse array of inflammatory responses, ranging from facilitation of anti-tumor to pro-tumor signaling. The three novel necroptosis-associated myeloid subpopulations uncovered in our research may communicate with other cells to mediate ECM degradation and remodeling, signaling pathway regulation and immune cell polarization. These cells and their respective products hold potential as therapeutic targets in PDAC and other types of cancers, enabling the establishment of effective necroptosis-based cancer therapy regimens.

Data availability statement

The datasets presented in this study can be found in online repositories. The names of the repository/repositories and accession number(s) can be found in the article/Supplementary Material.

Ethics statement

The studies involving humans were approved by The Forth Medical Center of PLA General Hospital. The studies were conducted in accordance with the local legislation and institutional requirements. Written informed consent for participation in this study was provided by the participants' legal guardians/next of kin. Written informed consent was obtained from the individual(s) for the publication of any potentially identifiable images or data included in this article.

Author contributions

HXZ: Conceptualization, Methodology, Writing – original draft. WD: Conceptualization, Methodology, Writing – original draft. SX: Writing – original draft, Data curation, Software, Visualization. LZ: Data curation, Software, Visualization, Writing – original draft. TF: Data curation, Software, Visualization, Writing – original draft. LW: Writing – original draft, Investigation. HZ: Writing – review & editing. YH: Writing – review & editing. JY: Writing – review & editing. TW: Writing – review & editing, Conceptualization, Methodology, Resources, Supervision. WX: Conceptualization, Methodology, Resources, Supervision, Writing – review & editing.

Funding

The author(s) declare that no financial support was received for the research, authorship, and/or publication of this article.

Acknowledgments

We appreciate the assistance of the staff of the Senior Department of Oncology, The Fifth Medical Center of PLA

General Hospital, who collected and providing the samples used in RNA-Fish.

Conflict of interest

Authors TW, SX, LZ, TF and LW are employed by Hangzhou Repugene Technology Co Ltd.

The remaining authors declare that the research was conducted in the absence of any commercial or financial relationships that could be construed as a potential conflict of interest.

Publisher's note

Supplementary material

The Supplementary Material for this article can be found online at: https://www.frontiersin.org/articles/10.3389/fimmu.2023.1263633/full#supplementary-material

SUPPLEMENTARY FIGURE 1
Heterogeneity of TME in PDAC. **(A)** t-SNE plots of cells from 39 samples profiled in this study. Colored by cell types. **(B)** The proportion of 11 cell types among primary tumors, metastatic tumors and paratumor samples, respectively. **(C)** The histogram of 11 cell types among clinical-stage I-IV. **(D)** The percentage of cell types between PBMCs from PDAC Patients and PBMCs from healthy controls. **(E)** The proportion of 11 cell types compared between primary tissues and metastatic tumor tissues of PDAC patients with PBMC samples from PDAC patients.

SUPPLEMENTARY FIGURE 2
Functional analysis of B cells in PDAC. **(A)** Top 100 genes were used to calculate the cox coefficient for each cluster using TCGA (PAAD, n = 183) data. **(B)** t-SNE plots showing the expression of *BCL11A* and *DNASE1L3*. **(C)** Scatterplots showing the correlation between *BCL11A*, *DNASE1L3*, and *CD8A* using TCGA (PAAD, n = 183) data. **(D)** The body maps showing the expression of *BCL11A* and *DNASE1L3* between tumor and normal samples via GEPIA 2 (http://gepia2.cancer-pku.cn/#index). **(E)** Kaplan-Meier overall survival analysis of the high and low groups of *BCL11A* (top) and *DNASE1L3* (bottom). **(F)** DFS (Disease-Free Survival) analysis of the high and low groups of *BCL11A* (top) and *DNASE1L3* (bottom). The hazard ratio was calculated based on Cox PH Model, and 95% CI (Confidence Interval) was applied.

SUPPLEMENTARY FIGURE 3
Differential gene and pathway analysis for peripheral blood. **(A)** t-SNE plots of myeloid lineages of PBMC from healthy individuals and PDAC patients. **(B)** Proportion of each myeloid cell lineage in PBMC samples from PDAC patients and healthy controls. **(C)** Tissue prevalence estimated by Ro/e score of primary tumor/metastatic tumor/paratumor tissues from PDAC patients (left), tissue/PBMC (middle) from PDAC patient, and PBMCs from PDAC patient/healthy controls (right). **(D)** Top 10 differential up- or down-regulated genes across myeloid lineages of PBMCs from PDAC patient and normal samples. Red dots indicate statistically significant genes (adjusted p-value < 0.01). **(E–I)** Pathways enriched by DEGs of each cell type between PBMCs from PDAC patients and PBMCs from healthy controls.

SUPPLEMENTARY FIGURE 4
Differential genes and pathways between tumor and paratumor tissue of PDAC. **(A)** Differential gene expression analysis shows up- and down-regulated genes across all cell types between tumor and paratumor tissue from PDAC patients. The top 10 DE genes were shown, and the points dotted in red indicate significant genes. An adjusted p-value < 0.01 is indicated in red, while an adjusted p-value ≥ 0.01 is indicated in black. **(B–F)** Differential pathway enriched in tumor and paratumor from PDAC tissue for each cell type.

SUPPLEMENTARY FIGURE 5
Differential genes and pathways between PDAC tissue and peripheral blood. **(A)** Differential gene expression analysis showing up- and down-regulated genes across all cell types between tumor tissue samples and PBMC from PDAC patients. The top 10 DE genes were shown, and the points dotted in red indicate significant genes. An adjusted p-value < 0.01 is indicated in red, while an adjusted p-value ≥ 0.01 is indicated in black. **(B–E)** Differential pathway enriched in tissue and PBMC from PDAC patients for each cell type.

SUPPLEMENTARY FIGURE 6
Visualization of overlapped necroptosis-associated DE genes. Violin plots showing overlapped up-regulated **(A)** and down-regulated **(B)** necroptosis-associated genes (denoted in) in tumor. *P < 0.05, **P < 0.01, ***P < 0.001.

SUPPLEMENTARY FIGURE 7
The novel immunological RTM has no direct correlation with epithelial cells. **(A)** Scatterplots showing the correlation between the expression of GLUL$^-$ SQSTM1$^-$RTM cluster-specific genes (denoted in) and EPCAM. **(B)** TCGA validation of the correlations. Data are from TCGA-PAAD (n = 178).

SUPPLEMENTARY FIGURE 8
HSP90AA1$^-$*HSP90AB1*$^-$ mast cells are anti-immune. **(A)** Scatterplot showing the correlations between the rest of *HSP90AA1*$^+$*HSP90AB1*$^+$ mast cluster-specific genes (shown in) and CD8A in this study. **(B)** Violin plots showing the expression of *HSP90AA1*$^-$*HSP90AB*$^-$ mast cluster-specific genes. **(C)** Scatterplots showing the correlations between *HSP90AA1*$^-$*HSP90AB1*$^-$ mast cluster-specific genes and *CD8A* in this study. **(D)** Expression profiles of CD8A in *HSP90AA1*$^+$*HSP90AB1*$^+$ mast cells vs. *HSP90AA1*$^-$ *HSP90AB1*$^-$ mast cells.

SUPPLEMENTARY FIGURE 9
JAK3$^-$TLR4$^-$ CD16 monocytes are pro-immune. **(A)** Violin plots showing the expression of *JAK3*$^-$*TLR4*$^-$ mast cluster-specific high expression genes. **(B)** Scatterplots showing the correlations between the expression of *JAK3*, *TLR4*, and *CD8A* in this study.

SUPPLEMENTARY FIGURE 10
Several myeloid subsets may act as pro/anti-immune regulators in a non-necroptosis way. Workflow showing the procedures to distinguish CD14 monocyte **(A)**, CD16 monocyte **(B)**, and DCs **(C)** by *BIRC3*, *PPIA*, and *CHMP1B*, respectively.

References

1. Grossberg AJ, Chu LC, Deig CR, Fishman EK, Hwang WL, Maitra A, et al. Multidisciplinary standards of care and recent progress in pancreatic ductal adenocarcinoma. *CA Cancer J Clin* (2020) 70(5):375–403. doi: 10.3322/caac.21626

2. Schnelldorfer T, Adams DB, Warshaw AL, Lillemoe KD, Sarr MG. Forgotten pioneers of pancreatic surgery: beyond the favorite few. *Ann Surg* (2008) 247(1):191–202. doi: 10.1097/SLA.0b013e3181559a97

3. Foley K, Kim V, Jaffee E, Zheng L. Current progress in immunotherapy for pancreatic cancer. *Cancer Lett* (2016) 381(1):244–51. doi: 10.1016/j.canlet.2015.12.020

4. Royal RE, Levy C, Turner K, Mathur A, Hughes M, Kammula US, et al. Phase 2 trial of single agent Ipilimumab (anti-CTLA-4) for locally advanced or metastatic pancreatic adenocarcinoma. *J Immunother* (2010) 33(8):828–33. doi: 10.1097/CJI.0b013e3181eec14c

5. Brahmer JR, Tykodi SS, Chow LQ, Hwu WJ, Topalian SL, Hwu P, et al. Safety and activity of anti-PD-L1 antibody in patients with advanced cancer. *N Engl J Med* (2012) 366(26):2455–65. doi: 10.1056/NEJMoa1200694

6. Gamboa AC, Lee RM, Maithel SK. The role of radiation for pancreatic adenocarcinoma. *J Pancreatol* (2020) 3(2):72–80. doi: 10.1097/JP9.0000000000000045

7. Degterev A, Huang Z, Boyce M, Li Y, Jagtap P, Mizushima N, et al. Chemical inhibitor of nonapoptotic cell death with therapeutic potential for ischemic brain injury. *Nat Chem Biol* (2005) 1(2):112–9. doi: 10.1038/nchembio711

8. Holler N, Zaru R, Micheau O, Thome M, Attinger A, Valitutti S, et al. Fas triggers an alternative, caspase-8-independent cell death pathway using the kinase RIP as effector molecule. *Nat Immunol* (2000) 1(6):489–95. doi: 10.1038/82732

9. Green DR. The cell's dilemma, or the story of cell death: an entertainment in three acts. *FEBS J* (2016) 283(14):2568–76. doi: 10.1111/febs.13658

10. Wang Z, Guo LM, Zhou HK, Qu HK, Wang SC, Liu FX, et al. Using drugs to target necroptosis: dual roles in disease therapy. *Histol Histopathol* (2018) 33(8):773–89.

11. Kaczmarek A, Vandenabeele P, Krysko DV. Necroptosis: the release of damage-associated molecular patterns and its physiological relevance. *Immunity* (2013) 38 (2):209–23. doi: 10.1016/j.immuni.2013.02.003

12. Pasparakis M, Vandenabeele P. Necroptosis and its role in inflammation. *Nature* (2015) 517(7534):311–20. doi: 10.1038/nature14191

13. Yang H, Ma Y, Chen G, Zhou H, Yamazaki T, Klein C, et al. Contribution of RIP3 and MLKL to immunogenic cell death signaling in cancer chemotherapy. *Oncoimmunology* (2016) 5(6):e1149673. doi: 10.1080/2162402X.2016.1149673

14. Moriwaki K, Balaji S, McQuade T, Malhotra N, Kang J, Chan FK. The necroptosis adaptor RIPK3 promotes injury-induced cytokine expression and tissue repair. *Immunity* (2014) 41(4):567–78. doi: 10.1016/j.immuni.2014.09.016

15. Snyder AG, Hubbard NW, Messmer MN, Kofman SB, Hagan CE, Orozco SL, et al. Intratumoral activation of the necroptotic pathway components RIPK1 and RIPK3 potentiates antitumor immunity. *Sci Immunol* (2019) 4(36):eaaw2004. doi: 10.1126/sciimmunol.aaw2004

16. Yatim N, Jusforgues-Saklani H, Orozco S, Schulz O, Barreira da Silva R, Reis e Sousa C, et al. RIPK1 and NF-kappaB signaling in dying cells determines cross-priming of CD8(+) T cells. *Science* (2015) 350(6258):328–34. doi: 10.1126/science.aad0395

17. Wang W, Marinis JM, Beal AM, Savadkar S, Wu Y, Khan M, et al. RIP1 kinase drives macrophage-mediated adaptive immune tolerance in pancreatic cancer. *Cancer Cell* (2018) 34(5):757–74.e7. doi: 10.1016/j.ccell.2018.10.006

18. Seifert L, Werba G, Tiwari S, Ly NNG, Alothman S, Alqunaibit D, et al. Author Correction: The necrosome promotes pancreatic oncogenesis via CXCL1 and Mincle-induced immune suppression. *Nature* (2021) 591(7851):E28. doi: 10.1038/s41586-021-03322-8

19. Ando Y, Ohuchida K, Otsubo Y, Kibe S, Takesue S, Abe T, et al. Necroptosis in pancreatic cancer promotes cancer cell migration and invasion by release of CXCL5. *PLoS One* (2020) 15(1):e0228015. doi: 10.1371/journal.pone.0228015

20. Jayakumar A, Bothwell ALM. RIPK3-induced inflammation by I-MDSCs promotes intestinal tumors. *Cancer Res* (2019) 79(7):1587–99. doi: 10.1158/0008-5472.CAN-18-2153

21. Kadiyala P, Elhossiny AM, Carpenter ES. Using single cell transcriptomics to elucidate the myeloid compartment in pancreatic cancer. *Front Oncol* (2022) 12:881871. doi: 10.3389/fonc.2022.881871

22. Zhang J, Song J, Tang S, Zhao Y, Wang L, Luo Y, et al. Multi-omics analysis reveals the chemoresistance mechanism of proliferating tissue-resident macrophages in PDAC via metabolic adaptation. *Cell Rep* (2023) 42(6):112620. doi: 10.1016/j.celrep.2023.112620

23. Hegde S, Krisnawan VE, Herzog BH, Zuo C, Breden MA, Knolhoff BL, et al. Dendritic cell paucity leads to dysfunctional immune surveillance in pancreatic cancer. *Cancer Cell* (2020) 37(3):289–307.e9. doi: 10.1016/j.ccell.2020.02.008

24. Steele NG, Carpenter ES, Kemp SB, Sirihorachai VR, The S, Delrosario L, et al. Multimodal mapping of the tumor and peripheral blood immune landscape in human pancreatic cancer. *Nat Cancer* (2020) 1(11):1097–112. doi: 10.1038/s43018-020-00121-4

25. Butler A, Hoffman P, Smibert P, Papalexi E, Satija R. Integrating single-cell transcriptomic data across different conditions, technologies, and species. *Nat Biotechnol* (2018) 36(5):411–20. doi: 10.1038/nbt.4096

26. Peng J, Sun BF, Chen CY, Zhou JY, Chen YS, Chen H, et al. Single-cell RNA-seq highlights intra-tumoral heterogeneity and Malignant progression in pancreatic ductal adenocarcinoma. *Cell Res* (2019) 29(9):725–38. doi: 10.1038/s41422-019-0195-y

27. Korsunsky I, Millard N, Fan J, Slowikowski K, Zhang F, Wei K, et al. Fast, sensitive and accurate integration of single-cell data with Harmony. *Nat Methods* (2019) 16(12):1289–96. doi: 10.1038/s41592-019-0619-0

28. Zhang L, Yu X, Zheng L, Zhang Y, Li Y, Fang Q, et al. Lineage tracking reveals dynamic relationships of T cells in colorectal cancer. *Nature* (2018) 564(7735):268–72. doi: 10.1038/s41586-018-0694-x

29. Guo X, Zhang Y, Zheng L, Zheng C, Song J, Zhang Q, et al. Global characterization of T cells in non-small-cell lung cancer by single-cell sequencing. *Nat Med* (2018) 24(7):978–85. doi: 10.1038/s41591-018-0045-3

30. Yu G, Wang LG, Han Y, He QY. clusterProfiler: an R package for comparing biological themes among gene clusters. *OMICS* (2012) 16(5):284–7. doi: 10.1089/omi.2011.0118

31. Jin S, Guerrero-Juarez CF, Zhang L, Chang I, Ramos R, Kuan CH, et al. Inference and analysis of cell-cell communication using CellChat. *Nat Commun* (2021) 12 (1):1088. doi: 10.1038/s41467-021-21246-9

32. Chen K, Wang Q, Li M, Guo H, Liu W, Wang F, et al. Single-cell RNA-seq reveals dynamic change in tumor microenvironment during pancreatic ductal adenocarcinoma Malignant progression. *EBioMedicine* (2021) 66:103315. doi: 10.1016/j.ebiom.2021.103315

33. Spear S, Candido JB, McDermott JR, Ghirelli C, Maniati E, Beers SA, et al. Discrepancies in the tumor microenvironment of spontaneous and orthotopic murine models of pancreatic cancer uncover a new immunostimulatory phenotype for B cells. *Front Immunol* (2019) 10:542. doi: 10.3389/fimmu.2019.00542

34. Brunner M, Maier K, Rümmele P, Jacobsen A, Merkel S, Benard A, et al. Upregulation of CD20 positive B-cells and B-cell aggregates in the tumor infiltration zone is associated with better survival of patients with pancreatic ductal adenocarcinoma. *Int J Mol Sci* (2020) 21(5):1779. doi: 10.3390/ijms21051779

35. Wouters MCA, Nelson BH. Prognostic significance of tumor-infiltrating B cells and plasma cells in human cancer. *Clin Cancer Res* (2018) 24(24):6125–35. doi: 10.1158/1078-0432.CCR-18-1481

36. Shan Y, Liu C, Gu J. scCancer: a package for automated processing of single-cell RNA- Q25 seq data in cancer. *Brief Bioinform* (2021) 22(3):bbaa127. doi: 10.1093/bib/bbaa127

37. Elyada E, Bolisetty M, Laise P, Flynn WF, Courtois ET, Burkhart RA, et al. Cross-species single-cell analysis of pancreatic ductal adenocarcinoma reveals antigen-presenting cancer-associated fibroblasts. *Cancer Discovery* (2019) 9(8):1102–23. doi: 10.1158/2159-8290.CD-19-0094

38. Malta TM, Sokolov A, Gentles AJ, Burzykowski T, Poisson L, Weinstein JN, et al. Machine learning identifies stemness features associated with oncogenic dedifferentiation. *Cell* (2018) 173(2):338–54.e15. doi: 10.1016/j.cell.2018.03.034

39. Kemp SB, Pasca di Magliano M, Crawford HC. Myeloid cell mediated immune suppression in pancreatic cancer. *Cell Mol Gastroenterol Hepatol* (2021) 12(5):1531–42. doi: 10.1016/j.jcmgh.2021.07.006

40. Gong Y, Fan Z, Luo G, Yang C, Huang Q, Fan K, et al. The role of necroptosis in cancer biology and therapy. *Mol Cancer* (2019) 18(1):100. doi: 10.1186/s12943-019-1029-8

41. Vandenabeele P, Galluzzi L, Vanden Berghe T, Kroemer G. Molecular mechanisms of necroptosis: an ordered cellular explosion. *Nat Rev Mol Cell Biol* (2010) 11(10):700–14. doi: 10.1038/nrm2970

42. Serrano-Puebla A, Boya P. Lysosomal membrane permeabilization as a cell death mechanism in cancer cells. *Biochem Soc Trans* (2018) 46(2):207–15. doi: 10.1042/BST20170130

43. Zhang BB, Wang DG, Guo FF, Xuan C. Mitochondrial membrane potential and reactive oxygen species in cancer stem cells. *Fam Cancer* (2015) 14(1):19–23. doi: 10.1007/s10689-014-9757-9

44. Rayamajhi M, Miao EA. The RIP1-RIP3 complex initiates mitochondrial fission to fuel NLRP3. *Nat Immunol* (2014) 15(12):1100–2. doi: 10.1038/ni.3030

45. Ma Y, Wang L, Jia R. The role of mitochondrial dynamics in human cancer. *Am J Cancer Res* (2020) 10(5):1278–93.

46. Gong YN, Guy C, Olauson H, Becker JU, Yang M, Fitzgerald P, et al. ESCRT-III acts downstream of MLKL to regulate necroptotic cell death and its consequences. *Cell* (2017) 169(2):286–300.e16. doi: 10.1016/j.cell.2017.03.020

47. Arai KI, Lee F, Miyajima A, Miyatake S, Arai N, Yokota T. Cytokines: coordinators of immune and inflammatory responses. *Annu Rev Biochem* (1990) 59:783–836. doi: 10.1146/annurev.bi.59.070190.004031

48. Dranoff G. Cytokines in cancer pathogenesis and cancer therapy. *Nat Rev Cancer* (2004) 4(1):11–22. doi: 10.1038/nrc1252

49. Nakamura M, Han B, Nunobiki O, Kakudo K. Adrenomedullin: a tumor progression factor via angiogenic control. *Curr Cancer Drug Targets* (2006) 6 (7):635–43. doi: 10.2174/156800906778742442

50. Jin J, Lin J, Xu A, Lou J, Qian C, Li X, et al. CCL2: an important mediator between tumor cells and host cells in tumor microenvironment. *Front Oncol* (2021) 11:722916. doi: 10.3389/fonc.2021.722916

51. Mukaida N, Sasaki SI, Baba T. CCL4 signaling in the tumor microenvironment. *Adv Exp Med Biol* (2020) 1231:23–32. doi: 10.1007/978-3-030-36667-4_3

52. Xin H, Cao Y, Shao ML, Zhang W, Zhang CB, Wang JT, et al. Chemokine CXCL3 mediates prostate cancer cells proliferation, migration and gene expression changes in an autocrine/paracrine fashion. *Int Urol Nephrol* (2018) 50(5):861–8. doi: 10.1007/s11255-018-1818-9

53. Guda MR, Rashid MA, Asuthkar S, Jalasutram A, Caniglia JL, Tsung AJ, et al. Pleiotropic role of macrophage migration inhibitory factor in cancer. *Am J Cancer Res* (2019) 9(12):2760–73.

54. Zeng B, Zhou M, Wu H, Xiong Z, et al. SPP1 promotes ovarian cancer progression via Integrin beta1/FAK/AKT signaling pathway. *Onco Targets Ther* (2018) 11:1333–43. doi: 10.2147/OTT.S154215

55. Kim M, Jang K, Miller P, Picon-Ruiz M, Yeasky TM, El-Ashry D, et al. VEGFA links self-renewal and metastasis by inducing Sox2 to repress miR-452, driving Slug. *Oncogene* (2017) 36(36):5199–211. doi: 10.1038/onc.2017.4

56. Yang X, Zhang Y, Hosaka K, Andersson P, Wang J, Tholander F, et al. VEGF-B promotes cancer metastasis through a VEGF-A-independent mechanism and serves as a marker of poor prognosis for cancer patients. *Proc Natl Acad Sci U.S.A.* (2015) 112 (22):E2900–9. doi: 10.1073/pnas.1503500112

57. Chikanza IC, Grossman AS. Hypothalamic-pituitary-mediated immunomodulation: arginine vasopressin is a neuroendocrine immune mediator. *Br J Rheumatol* (1998) 37(2):131–6. doi: 10.1093/rheumatology/37.2.131

58. Gao S, Zhu H, Zuo X, Luo H. Cathepsin G and its role in inflammation and autoimmune diseases. *Arch Rheumatol* (2018) 33(4):498–504. doi: 10.5606/ArchRheumatol.2018.6595

59. Lucena-Cacace A, Umeda M, Navas LE, Carnero A. NAMPT as a dedifferentiation-inducer gene: NAD(+) as core axis for glioma cancer stem-like cells maintenance. *Front Oncol* (2019) 9:292. doi: 10.3389/fonc.2019.00292

60. Glorieux C, Calderon PB. Catalase, a remarkable enzyme: targeting the oldest antioxidant enzyme to find a new cancer treatment approach. *Biol Chem* (2017) 398 (10):1095–108. doi: 10.1515/hsz-2017-0131

61. Zhu C, Mustafa D, Zheng PP, van der Weiden M, Sacchetti A, Brandt M, et al. Activation of CECR1 in M2-like TAMs promotes paracrine stimulation-mediated glial tumor progression. *Neuro Oncol* (2017) 19(5):648–59. doi: 10.1093/neuonc/now251

62. Han J, Deng X, Sun R, Luo M, Liang M, Gu B, et al. GPI is a prognostic biomarker and correlates with immune infiltrates in lung adenocarcinoma. *Front Oncol* (2021) 11:752642. doi: 10.3389/fonc.2021.752642

63. Bao C, Wang J, Ma W, Wang X, Cheng Y. HDGF: a novel jack-of-all-trades in cancer. *Future Oncol* (2014) 10(16):2675–85. doi: 10.2217/fon.14.194

64. Chateauvieux S, Grigorakaki C, Morceau F, Dicato M, Diederich M. Erythropoietin, erythropoiesis and beyond. *Biochem Pharmacol* (2011) 82(10):1291–303. doi: 10.1016/j.bcp.2011.06.045

65. Vatsveen TK, Sponaas AM, Tian E, Zhang Q, Misund K, Sundan A, et al. Erythropoietin (EPO)-receptor signaling induces cell death of primary myeloma cells in vitro. *J Hematol Oncol* (2016) 9(1):75. doi: 10.1186/s13045-016-0306-x

66. Vacchelli E, Ma Y, Baracco EE, Sistigu A, Enot DP, Pietrocola F, et al. Chemotherapy-induced antitumor immunity requires formyl peptide receptor 1. *Science* (2015) 350(6263):972–8. doi: 10.1126/science.aad0779

67. Saito N, Qiao H, Yanagi T, Shinkuma S, Nishimura K, Suto A, et al. An annexin A1-FPR1 interaction contributes to necroptosis of keratinocytes in severe cutaneous adverse drug reactions. *Sci Transl Med* (2014) 6(245):245ra95. doi: 10.1126/scitranslmed.3008227

68. Shouval DS, Ouahed J, Biswas A, Goettel JA, Horwitz BH, Klein C, et al. Interleukin 10 receptor signaling: master regulator of intestinal mucosal homeostasis in mice and humans. *Adv Immunol* (2014) 122:177–210. doi: 10.1016/B978-0-12-800267-4.00005-5

69. Oshima H, Ishikawa T, Yoshida GJ, Naoi K, Maeda Y, Naka K, et al. TNF-alpha/TNFR1 signaling promotes gastric tumorigenesis through induction of Noxo1 and Gna14 in tumor cells. *Oncogene* (2014) 33(29):3820–9. doi: 10.1038/onc.2013.356

70. Nirmala JG, Lopus M. Cell death mechanisms in eukaryotes. *Cell Biol Toxicol* (2020) 36(2):145–64. doi: 10.1007/s10565-019-09496-2

71. Khoury MK, Gupta K, Franco SR, Liu B. Necroptosis in the pathophysiology of disease. *Am J Pathol* (2020) 190(2):272–85. doi: 10.1016/j.ajpath.2019.10.012

72. Su Z, Yang Z, Xie L, DeWitt JP, Chen Y. Cancer therapy in the necroptosis era. *Cell Death Differ* (2016) 23(5):748–56. doi: 10.1038/cdd.2016.8

73. Sidera K, Patsavoudi E. HSP90 inhibitors: current development and potential in cancer therapy. *Recent Pat Anticancer Drug Discovery* (2014) 9(1):1–20. doi: 10.2174/15748928113089990031

74. Takayama S, Reed JC, Homma S. Heat-shock proteins as regulators of apoptosis. *Oncogene* (2003) 22(56):9041–7. doi: 10.1038/sj.onc.1207114

75. Burrows F, Zhang H, Kamal A. Hsp90 activation and cell cycle regulation. *Cell Cycle* (2004) 3(12):1530–6. doi: 10.4161/cc.3.12.1277

76. Pratt WB. The role of the hsp90-based chaperone system in signal transduction by nuclear receptors and receptors signaling via MAP kinase. *Annu Rev Pharmacol Toxicol* (1997) 37:297–326. doi: 10.1146/annurev.pharmtox.37.1.297

77. Li D, Xu T, Cao Y, Wang H, Li L, Chen S, et al. A cytosolic heat shock protein 90 and cochaperone CDC37 complex is required for RIP3 activation during necroptosis. *Proc Natl Acad Sci U S A* (2015) 112(16):5017–22. doi: 10.1073/pnas.1505244112

78. Jacobsen AV, Lowes KN, Tanzer MC, Lucet IS, Hildebrand JM, Petrie EJ, et al. HSP90 activity is required for MLKL oligomerisation and membrane translocation and the induction of necroptotic cell death. *Cell Death Dis* (2016) 7(1):e2051. doi: 10.1038/cddis.2015.386

79. Zhao XM, Chen Z, Zhao JB, Zhang PP, Pu YF, Jiang SH, et al. Hsp90 modulates the stability of MLKL and is required for TNF-induced necroptosis. *Cell Death Dis* (2016) 7(2):e2089. doi: 10.1038/cddis.2015.390

80. Riegler AN, Brissac T, Gonzalez-Juarbe N, Orihuela CJ. Necroptotic cell death promotes adaptive immunity against colonizing pneumococci. *Front Immunol* (2019) 10:615. doi: 10.3389/fimmu.2019.00615

81. Chan IH, Wu V, Bilardello M, Mar E, Oft M, Van Vlasselaer P, et al. The potentiation of IFN-gamma and induction of cytotoxic proteins by pegylated IL-10 in human CD8 T cells. *J Interferon Cytokine Res* (2015) 35(12):948–55. doi: 10.1089/jir.2014.0221

82. Xi J, Xu M, Song Z, Li H, Xu S, Wang C, et al. Stimulatory role of interleukin 10 in CD8(+) T cells through STATs in gastric cancer. *Tumour Biol* (2017) 39 (5):1010428317706209. doi: 10.1177/1010428317706209

83. Mumm JB, Emmerich J, Zhang X, Chan I, Wu L, Mauze S, et al. IL-10 elicits IFNgamma-dependent tumor immune surveillance. *Cancer Cell* (2011) 20(6):781–96. doi: 10.1016/j.ccr.2011.11.003

84. Liu X, Liu L, Wang X, Jin Y, Wang S, Xie Q, et al. Necroptosis inhibits autophagy by regulating the formation of RIP3/p62/Keap1 complex in shikonin-induced ROS dependent cell death of human bladder cancer. *Phytomedicine* (2023) 118:154943. doi: 10.1016/j.phymed.2023.154943

85. Orecchioni M, Ghosheh Y, Pramod AB, Ley K. Macrophage Polarization: Different Gene Signatures in M1(LPS+) vs. Classically and M2(LPS-) vs. Alternatively Activated Macrophages. *Front Immunol* (2019) 10:1084. doi: 10.3389/fimmu.2019.01084

86. Liu PS, Wang H, Li X, Chao T, Teav T, Christen S, et al. alpha-ketoglutarate orchestrates macrophage activation through metabolic and epigenetic reprogramming. *Nat Immunol* (2017) 18(9):985–94. doi: 10.1038/ni.3796

87. Zhou B, Liu J, Zeng L, Zhu S, Wang H, Billiar TR, et al. Extracellular SQSTM1 mediates bacterial septic death in mice through insulin receptor signalling. *Nat Microbiol* (2020) 5(12):1576–87. doi: 10.1038/s41564-020-00795-7

88. Sierra-Filardi E, Nieto C, Domínguez-Soto A, Barroso R, Sánchez-Mateos P, Puig-Kroger A, et al. CCL2 shapes macrophage polarization by GM-CSF and M-CSF: identification of CCL2/CCR2-dependent gene expression profile. *J Immunol* (2014) 192 (8):3858–67. doi: 10.4049/jimmunol.1302821

89. Roca H, Varsos ZS, Sud S, Craig MJ, Ying C, Pienta KJ. CCL2 and interleukin-6 promote survival of human CD11b+ peripheral blood mononuclear cells and induce M2-type macrophage polarization. *J Biol Chem* (2009) 284(49):34342–54. doi: 10.1074/jbc.M109.042671

90. Xie Y, Chen Z, Zhong Q, Zheng Z, Chen Y, Shangguan W, et al. M2 macrophages secrete CXCL13 to promote renal cell carcinoma migration, invasion, and EMT. *Cancer Cell Int* (2021) 21(1):677. doi: 10.1186/s12935-021-02381-1

91. Wheeler KC, Jena MK, Pradhan BS, Nayak N, Das S, Hsu CD, et al. VEGF may contribute to macrophage recruitment and M2 polarization in the decidua. *PLoS One* (2018) 13(1):e0191040. doi: 10.1371/journal.pone.0191040

92. Wang X, Chen T, Leng L, Fan J, Cao K, Duan Z, et al. MIF produced by bone marrow-derived macrophages contributes to teratoma progression after embryonic stem cell transplantation. *Cancer Res* (2012) 72(11):2867–78. doi: 10.1158/0008-5472.CAN-11-3247

93. Zheng Y, Hao S, Xiang C, Han Y, Shang Y, Zhen Q, et al. The correlation between SPP1 and immune escape of EGFR mutant lung adenocarcinoma was explored by bioinformatics analysis. *Front Oncol* (2021) 11:592854. doi: 10.3389/fonc.2021.592854

94. Pang X, Shang H, Deng B, Wen F, Zhang Y. The interaction of adrenomedullin and macrophages induces ovarian cancer cell migration via activation of RhoA signaling pathway. *Int J Mol Sci* (2013) 14(2):2774–87. doi: 10.3390/ijms14022774

95. Walters DK, Mercher T, Gu TL, O'Hare T, Tyner JW, Loriaux M, et al. Activating alleles of JAK3 in acute megakaryoblastic leukemia. *Cancer Cell* (2006) 10 (1):65–75. doi: 10.1016/j.ccr.2006.06.002

96. Koo GC, Tan SY, Tang T, Poon SL, Allen GE, Tan L, et al. Janus kinase 3-activating mutations identified in natural killer/T-cell lymphoma. *Cancer Discovery* (2012) 2(7):591–7. doi: 10.1158/2159-8290.CD-12-0028

97. McKinney M, Moffitt AB, Gaulard P, Travert M, De Leval L, Nicolae A, et al. The genetic basis of hepatosplenic T-cell lymphoma. *Cancer Discovery* (2017) 7(4):369–79. doi: 10.1158/2159-8290.CD-16-0330

98. Nairismagi ML, Tan J, Lim JQ, Nagarajan S, Ng CC, Rajasegaran V, et al. JAK-STAT and G-protein-coupled receptor signaling pathways are frequently altered in

epitheliotropic intestinal T-cell lymphoma. *Leukemia* (2016) 30(6):1311–9. doi: 10.1038/leu.2016.13

99. Bains T, Heinrich MC, Loriaux MM, Beadling C, Nelson D, Warrick A, et al. Newly described activating JAK3 mutations in T-cell acute lymphoblastic leukemia. *Leukemia* (2012) 26(9):2144–6. doi: 10.1038/leu.2012.74

100. Lee CH, Wu CL, Shiau AL. Toll-like receptor 4 signaling promotes tumor growth. *J Immunother* (2010) 33(1):73–82. doi: 10.1097/CJI.0b013e3181b7a0a4

101. Karin M, Greten FR. NF-kappaB: linking inflammation and immunity to cancer development and progression. *Nat Rev Immunol* (2005) 5(10):749–59. doi: 10.1038/nri1703

102. Bernard V, Semaan A, Huang J, San Lucas FA, Mulu FC, Stephens BM, et al. Single-cell transcriptomics of pancreatic cancer precursors demonstrates epithelial and microenvironmental heterogeneity as an early event in neoplastic progression. *Clin Cancer Res* (2019) 25(7):2194–205. doi: 10.1158/1078-0432.CCR-18-1955

103. Ding X, Yang W, Shi X, Du P, Su L, Qin Z, et al. TNF receptor 1 mediates dendritic cell maturation and CD8 T cell response through two distinct mechanisms. *J Immunol* (2011) 187(3):1184–91. doi: 10.4049/jimmunol.1002902

104. Liu C, Wang L, Jiang Q, Zhang J, Zhu L, Lin L, et al. Hepatoma-derived growth factor and DDX5 promote carcinogenesis and progression of endometrial cancer by activating beta-catenin. *Front Oncol* (2019) 9:211. doi: 10.3389/fonc.2019.00211

105. Zhang C, Chang X, Chen D, Yang F, Li Z, Li D, et al. Downregulation of HDGF inhibits the tumorigenesis of bladder cancer cells by inactivating the PI3K-AKT signaling pathway. *Cancer Manag Res* (2019) 11:7909–23. doi: 10.2147/CMAR.S215341

106. Zhou Y, Zhou N, Fang W, Huo J. Overexpressed HDGF as an independent prognostic factor is involved in poor prognosis in Chinese patients with liver cancer. *Diagn Pathol* (2010) 5:58. doi: 10.1186/1746-1596-5-58

107. Abe R, Peng T, Sailors J, Bucala R, Metz CN. Regulation of the CTL response by macrophage migration inhibitory factor. *J Immunol* (2001) 166(2):747–53. doi: 10.4049/jimmunol.166.2.747

108. Tillmann S, Bernhagen J, Noels H. Arrest functions of the MIF ligand/receptor axes in atherogenesis. *Front Immunol* (2013) 4:115. doi: 10.3389/fimmu.2013.00115

109. Vargas-Caraveo A, Sayd A, Robledo-Montaña J, Caso JR, Madrigal JLM, García-Bueno B, et al. Toll-like receptor 4 agonist and antagonist lipopolysaccharides modify innate immune response in rat brain circumventricular organs. *Neuroinflamm* (2020) 17(1):6. doi: 10.1186s12974-019-1690-2

110. Ledeboer A, Liu T, Shumilla JA, Mahoney JH, Vijay S, Gross MI, et al. The glial modulatory drug AV411 attenuates mechanical allodynia in rat models of neuropathic pain. *Neuron Glia Biol* (2006) 2(4):279–91. doi: 10.1017/S1740925X0700035X

111. Rodgers KM, Hutchinson MR, Northcutt A, Maier SF, Watkins LR, Barth DS, et al. The cortical innate immune response increases local neuronal excitability leading to seizures. *Brain* (2009) 132(Pt 9):2478–86. doi: 10.1093/brain/awp177

frontiers | Frontiers in Immunology

TYPE Original Research
PUBLISHED 19 December 2023
DOI 10.3389/fimmu.2023.1298290

OPEN ACCESS

EDITED BY
Takaji Matsutani,
Maruho, Japan

REVIEWED BY
Zhirui Zeng,
Guizhou Medical University, China
Shunwang Cao,
The Second Affiliated Hospital of Guangzhou University of Chinese Medicine, China

*CORRESPONDENCE
Zhengdong Deng
dzd0915@tjh.tjmu.edu.cn
Jianming Wang
wjm18jgm@aliyun.com

RECEIVED 21 September 2023
ACCEPTED 24 November 2023
PUBLISHED 19 December 2023

CITATION
Shi Y, Feng Y, Qiu P, Zhao K, Li X, Deng Z and Wang J (2023) Identifying the programmed cell death index of hepatocellular carcinoma for prognosis and therapy response improvement by machine learning: a bioinformatics analysis and experimental validation.
Front. Immunol. 14:1298290.
doi: 10.3389/fimmu.2023.1298290

Identifying the programmed cell death index of hepatocellular carcinoma for prognosis and therapy response improvement by machine learning: a bioinformatics analysis and experimental validation

Yuanxin Shi[1], Yunxiang Feng[1], Peng Qiu[1], Kai Zhao[1], Xiangyu Li[1], Zhengdong Deng[2*] and Jianming Wang[1,3*]

[1]Department of Biliary and Pancreatic Surgery/Cancer Research Center Affiliated Tongji Hospital, Tongji Medical College, Huazhong University of Science and Technology, Wuhan, China, [2]Department of Pediatric Surgery, Tongji Hospital of Tongji Medical College, Huazhong University of Science and Technology, Wuhan, China, [3]Affiliated Tianyou Hospital, Wuhan University of Science and Technology, Wuhan, China

Background: Despite advancements in hepatocellular carcinoma (HCC) treatments, the prognosis for patients remains suboptimal. Cumulative evidence suggests that programmed cell death (PCD) exerts crucial functions in HCC. PCD-related genes are potential predictors for prognosis and therapeutic responses.

Methods: A systematic analysis of 14 PCD modes was conducted to determine the correlation between PCD and HCC. A novel machine learning-based integrative framework was utilized to construct the PCD Index (PCDI) for prognosis and therapeutic response prediction. A comprehensive analysis of PCDI genes was performed, leveraging data including single-cell sequencing and proteomics. GBA was selected, and its functions were investigated in HCC cell lines by *in vitro* experiments.

Results: Two PCD clusters with different clinical and biological characteristics were identified in HCC. With the computational framework, the PCDI was constructed, demonstrating superior prognostic predictive efficacy and surpassing previously published prognostic models. An efficient clinical nomogram based on PCDI and clinicopathological factors was then developed. PCDI was intimately associated with immunological attributes, and PCDI could efficaciously predict immunotherapy response. Additionally, the PCDI could predict the chemotherapy sensitivity of HCC patients. A multilevel panorama of PCDI genes confirmed its stability and credibility. Finally, the knockdown of GBA could suppress both the proliferative and invasive capacities of HCC cells.

Conclusion: This study systematically elucidated the association between PCD and HCC. A robust PCDI was constructed for prognosis and therapy response prediction, which would facilitate clinical management and personalized therapy for HCC.

KEYWORDS

hepatocellular carcinoma, immunotherapy, prognostic model, machine learning, programmed cell death

Introduction

Hepatocellular carcinoma (HCC) continues to be a leading cause of cancer-associated mortality, with its incidence increasing annually at a rapid rate. It is projected that by 2025, nearly one million new cases will be reported (1, 2). Standardized treatments such as surgical resection or liver transplantation for early-stage tumors, transarterial chemoembolization (TACE) for intermediate-stage tumors, and systemic therapies, including tyrosine kinase inhibitors (TKIs) and immune checkpoint inhibitors (ICIs) for advanced-stage tumors (3), have enhanced the prognosis of patients with HCC. However, the outcomes are still often short of expectations. Historically, clinical staging systems, such as the Barcelona Clinic Liver Cancer (BCLC) staging system, have played a central role in HCC management, serving as routine tools for clinicians to evaluate the conditions and therapeutic requirements of patients in practice (4). Nevertheless, the current clinical staging systems have limitations that may hinder their capacity to provide optimal therapeutic interventions to patients. They only focus on clinicopathological characteristics and do not take into account an individual's molecular biological characteristics (5). Therapeutic decisions relying solely on them were obviously unilateral and could lead to potential over- or undertreatment, contributing to suboptimal therapeutic outcomes. For HCC, which is characterized by high heterogeneity, the realization of personalized treatment is essential to improving patient prognosis (6, 7). Thus, it is imperative to identify novel biomarkers that can clarify the molecular biological profile of patients, aid in risk stratification, and ultimately optimize HCC treatments and prognosis.

Programmed cell death (PCD), also referred to as regulated cell death, is the gene-regulated autonomous process employed by cells to maintain homeostatic balance. The progression and treatment response of tumors are intricately associated with PCD. Broad crosstalk exists in the initiation and regulation of various PCD types, and this interaction has emerged as a prominent focus in tumor research. Alongside the recently identified disulfidptosis and cuproptosis, the mainly recognized types of PCD include apoptosis, necroptosis, ferroptosis, pyroptosis, autophagy, parthanatos, entosis, NETosis, lysosome-dependent cell death, alkaliptosis, and oxeiptosis (8). Disulfidptosis was discovered in UMRC6 cells characterized by high *SCL7A11* expression. It occurs under conditions of glucose deficiency, resulting in the accumulation of disulfide bonds, which cause abnormal cross-linking between actin and cytoskeletal proteins. Consequently, this leads to cytoskeletal contraction and the collapse of the actin network, ultimately resulting in cell death (9). Cuproptosis is induced by an overload of copper ions, and its regulation is closely tied to mitochondrial metabolism and the sulfuric acid pathway (10, 11). Apoptosis is the most classical form of PCD and is the primary target of current antitumor strategies (12). Anoikis is a specific case of intrinsic apoptosis, triggered by the loss of cellular contact with the extracellular matrix or other adjacent cells. It serves as an important inhibitor in the growth and metastasis of tumors (13–15). Necroptosis is considered an alternative mechanism to apoptosis, primarily mediated by *RIPK1*, *RIPK3*, and *MLKL*, and can be inhibited by Nec-1. Necroptosis plays a dual role in tumors, as it can inhibit tumor growth while promoting metastasis and immune suppression through inflammatory responses induced (16, 17). Ferroptosis is a cell death type resulting from iron-dependent lipid peroxidation. Targeting ferroptosis represents a promising antitumor strategy (18, 19). Pyroptosis is mediated by the *gasdermin* protein family and is also associated with tumor proliferation and metastasis (20). The potential anti-tumor effects of pyroptosis have gained increasing attention (21). The occurrence of autophagy relies on lysosomal degradation, and its role in tumors is complex (22). On the one hand, autophagy is an important mechanism for suppressing tumor formation, but once a tumor is established, the activation of autophagy could promote further progression (23). Parthanatos is a cell death reliant on PARP-1 and is widely implicated in pathological processes such as inflammatory damages and neoplasms leading to aberrant activation of PARP-1 (24). Entosis, initially discovered in certain tumors, is described as a phenomenon of cell cannibalism (25). NETosis is a specialized mechanism in neutrophils for resisting pathogens, characterized by the formation of neutrophil extracellular traps (NETs) through the release of chromatin covered with antibacterial proteins (26, 27). Lysosome-dependent cell death is often induced by an imbalance in the cellular internal environment, marked by lysosomal membrane permeabilization and the release of lysosomal contents into cytoplasm (28). Alkaliptosis was discovered during antitumor molecular screening of G protein-coupled receptors, and it is regulated by an elevation of intracellular pH levels (29, 30). Oxytosis is cell death mediated by reactive oxygen species, with *KEAP1-PGAM5-AIFM1* as the key axis regulating this process (31).

Owing to its close association with tumors, PCD has become a central focus in the field of oncology research. However,

comprehensive studies elucidating the relationship between PCD and HCC remain lacking. In the study, we performed a summative analysis of 14 PCD modes within HCC and developed the programmed cell death index (PCDI) using a machine learning algorithms-integrated framework. The PCDI could effectively characterize the heterogeneity of HCC patients, enabling risk stratifications among them and accurate prediction of their clinical prognosis and therapeutic response. This, in turn, could facilitate the personalized treatment and clinical management for HCC.

Materials and methods

Data collection and processing

The regulatory factors that govern 14 PCD modes were identified as PCD-related genes (Supplementary Table S1). These genes were sourced from the GSEA gene sets, KEGG, previous studies (32), and the Gene-Cards online platform (https://www.genecards.org/). A total of 1,937 nonredundant PCD-related genes were included for analysis.

Three independent HCC datasets containing clinical and transcriptomic data of patients, TCGA-LIHC, GSE76427, and ICGC-LIRI-JP, were acquired from TCGA database (https://portal.gdc.cancer.gov/), GEO database (https://www.ncbi.nlm.nih.gov/geo/), and ICGC database (https://icgc.org/), respectively. The transcriptomic data underwent conversion into TPM values using the "limma" package, followed by the removal of batch effects using the "SVA" package. Subsequently, the log2 transformation was conducted. A total of 711 HCC samples were included for analysis: 365 from TCGA-LIHC dataset, 231 from the ICGC-LIRI-JP dataset, and 115 from the GSE76427 dataset (Supplementary Table S2). TCGA-LIHC dataset served as the training dataset, while the GSE76427 and ICGC-LIRI-JP datasets were employed as validation datasets for the construction and evaluation of the PCDI.

Analysis of expression patterns and mutation characteristics of PCD-related genes

The "limma" package was employed to identify differentially expressed genes (DEGs) with these criteria of $p < 0.05$ and $|\log2FC| > 1$. A univariate Cox analysis was performed to identify prognostic genes, which were used in subsequent analyses. Mutation characteristics of prognostic PCD genes were described using the "mafTools" package. The copy number variation (CNV) characteristics of these genes were visualized through the GISTIC algorithm and the "RCircos" package.

Identification of PCD clusters

Unsupervised clustering analysis was performed to identify the distinct PCD clusters in HCC patients. PCA, t-SNE, and UMAP analyses were utilized to illustrate the differences in sample distribution between PCD clusters. The survival analysis was performed using the R packages "survival" and "survminer". The "Pheatment" package was utilized to visualize the expression patterns of PCD-related genes, immune checkpoint genes (ICGs), chemotherapy resistance-related genes (CRRGs), and clinicopathological characteristics between different PCD clusters. ICGs and CRRGs were obtained from previous studies (33, 34) and the Gene-Cards website. The "ESTIMATE" package was applied for calculating the TME score of patients, and their immune cell infiltration levels were evaluated through the ssGSEA algorithm.

Functional enrichment analysis

We employed various methods to elucidate the biological functional differences among HCC patients. For HCC patients in different PCD clusters, Gene Set Variation Analysis (GSVA), Gene Set Enrichment Analysis (GSEA), and GO/KEGG functional enrichment analyses were all used. The same methods were employed in the analysis of patients with different PCDI scores. GSEA was also applied to explore the potential functions of PCDI genes in patients with HCC. The criteria for GSVA and GO/KEGG analyses were both p-value < 0.05 and FDR < 0.05; for GSEA, the criteria were p-value < 0.05, FDR < 0.25, and NES > 1.

Construction and prognostic predictive value evaluation of the PCDI

To develop an accurate and robust PCDI, the following steps were adopted:

1. Using the univariate Cox analysis, 87 prognostic PCD genes were introduced for prognostic model construction.
2. We employed a machine learning algorithm integrated framework that incorporated 10 machine learning algorithms, such as random survival forest (RSF), partial least squares regression for Cox (plsRcox), supervised principal component (SuperPC), generalized boosted regression modeling (GBM), support vector machine (SVM), elastic net (Enet), LASSO, ridge, stepwise Cox, and CoxBoost. Via 10-fold cross-validation, we generated 88 algorithm combinations within TCGA-LIHC dataset for training prognostic models, and further validation was carried out in the GSE76427 and ICGC-LIRI-JP datasets. Upon comparison, the model that exhibited the highest average C-index among these three datasets was thus determined as the PCDI.
3. In this study, the PCDI was constructed through the combination of CoxBoost and RSF algorithms. The CoxBoost model was instantiated utilizing the "CoxBoost" software package, engineered to facilitate the estimation of Cox proportional hazards models through componentwise likelihood-based boosting techniques. For this model, the optimal regularization parameter, signifying the extent of shrinkage, was rigorously identified by employing the 10-

fold cross-validation strategy within the framework of the CoxBoost penalty function. The "RandomForestSRC" package was employed for the RSF model. This model comprised two parameters. Ntree was indicative of the number of trees constituting the forest, and mtry represented the quantity of arbitrarily selected variables designated for bifurcation at every individual node. A meticulous grid search was conducted on both ntree and mtry, assisted by the 10-fold cross-validation mechanism. All possible pairings of (ntree, mtry) were formulated, with the pairing boasting the superior C-index value recognized as the optimized parameters.

4. A comprehensive evaluation was subsequently carried out to assess the prognostic value of PCDI. Patients were categorized into dichotomous groups based on their PCDI score. Survival curves were generated to compare the prognosis between the two groups. ROC curves were applied to assess the predictive accuracy of PCDI, while chi-square analysis was performed to explore the correlation between PCDI and other clinicopathological features. The independent prognostic value of PCDI and other clinicopathological factors was compared through univariate and multivariate Cox analyses. The predictive efficacy of PCDI and other clinicopathological attributes was assessed through C-index curves and DCA curves. Additionally, the predictive efficacy of PCDI was compared with 102 other published prognostic models using C-index curves (Supplementary Table S12).

Construction and evaluation of the clinical nomogram

The "rms" and "regploy" packages were used to develop a clinical nomogram based on the PCDI and other clinicopathological factors, predicting the overall survival (OS) of patients with HCC. Calibration and ROC curves along with DCA were used to evaluate the predictive efficacy of the clinical nomogram.

Correlation analysis of PCDI with immunological, gene mutation, and stemness characteristics

Using various algorithms, including CIBERSORT-ABS, TIMER, and XCELL, we assessed the differences in immune cell infiltration levels between these two groups. The "ESTIMATE" package was utilized to calculate the tumor microenvironment (TME) score, while Gene Set Variation Analysis (GSVA) and single sample gene set enrichment analysis (ssGSEA) were performed to further explore the immunological functional status. Additionally, the correlation between PCDI and ICG expression patterns was investigated.

The "maftools" package was applied to describe different mutation statuses of patients between both groups. We also compared their different TMB and microsatellite instability (MSI) statuses. Moreover, we extracted the stemness index of HCC patients from "StemnessScores_RNAexp_20170127.2.tsv". Subsequent correlation analysis was performed between the PCDI and tumor stemness features.

Predictive value evaluation of the PCDI in immunotherapeutic responses

Employing the Tumor Immune Dysfunction and Exclusion (TIDE) algorithm (http://tide.dfci.harvard.edu/) and multiple immunotherapy cohorts, we discussed the value of the PCDI in immunotherapeutic response prediction. In TCGA-LIHC dataset, we calculated and compared the TIDE, dysfunction, and exclusion scores of HCC patients in the two groups. A correlation analysis between immunotherapeutic response and PCDI score was then performed. Subsequently, the predictive capability of PCDI for immunotherapeutic response was further validated in 10 cohorts: IMvigor210 (35), Checkmate (36), GSE175307, GSE179351, GSE165252, GSE103668, GSE78220, GSE91061, GSE35640, and GSE120644, which included the immunotherapeutic response data from tumor patients. Moreover, the GSE109221 cohort (sorafenib treatment for HCC) and GSE104580 cohort (TACE treatment for HCC) were included for an extensive assessment of the predictive value in HCC treatments.

Correlation analysis between PCDI and chemotherapeutic drug sensitivities

In TCGA-LIHC dataset, we detected the different expression patterns of CRRGs between patients in the high and low PCDI score groups. Furthermore, the "OncoPredict" package was applied in predicting various chemotherapeutic drug sensitivities between the two groups.

PCDI gene analysis based on single-cell transcriptomic data

GSE125449 was obtained from the GEO database, which encompassed single-cell transcriptomic profiles from 19 liver cancer patients. The "Seurat" package was employed for the initial data processing. For the GSE125449 dataset, quality control was conducted according to these criteria: (1) genes expressing in fewer than three cells were excluded; (2) cells expressing fewer than 500 genes were excluded; (3) cells expressing 500 to 10,000 genes were retained; (4) cells with mitochondrial gene expression exceeding 20% were excluded; and (5) cells with ribosomal gene expression exceeding 20% were excluded. The "NormalizeData" function was applied to normalize the data passed quality control measures. Highly variable genes were identified by the "FindVariableFeatures" function. The "ScaleData" function was utilized for scaling gene expression profiles.

Dimensionality reduction was executed using the "RunPCA" function, and the first 20 principal components (PCA) were selected for cluster analysis. The main cell types were annotated utilizing the "SingleR" package, with subsequent corrections based on markers in the original literature (37). The "CellChat" package was employed to assess cellular communication among different cell populations.

PCDI gene analysis based on proteomic and immunohistochemistry data

The HCC proteomic dataset PDC-000198 was obtained from the CPTAC database (https://pdc.cancer.gov/pdc/), with 151 samples with complete clinical information and proteomic data included. Using the "limma" package and the criteria of $p < 0.05$ and $|\log2FC| > 0.585$, we assessed the different expression patterns of PCDI genes between tumor and adjacent tissues at the protein level. Survival analysis was performed as described before. And immunohistochemistry data of PCDI genes was acquired from the Human Protein Atlas(HPA) database (https://www.proteinatlas.org/) for further analysis.

Cellular cultivation and transfection

The human HCC cell lines MHCC97H and HuH-7 were acquired from the Hepatic Surgery Center at the Affiliated Tongji Hospital of Huazhong University of Science and Technology. All cells underwent rigorous STR analysis to ensure they were free from mycoplasma contamination. HCC cells were cultured with Dulbecco's modified Eagle's medium (DMEM) (Cibco, Massachusetts, USA) added the 10% fetal bovine serum (FBS) (Gibco, USA) under the conditions of 37°C and 5% CO_2 atmospheric composition.

SiRNAs were transfected into MHCC97H and HuH-7 cells to downregulate *GBA* expression. The negative control siRNA (si-NC), si-*GBA*-1, si-*GBA*-2, and si-*GBA*-3 were designed and synthesized by Hippo Biotechnology (Huzhou, China), with detailed sequences provided in Supplementary Table S3. HCC cells under optimal conditions were seeded uniformly into six-well plates. Upon cell adhesion and achieving approximately 50% confluency, transfection was executed utilizing Lipofectamine 2000 (Invitrogen, Massachusetts, USA).

HCC tissue sample collection

Five paired HCC tumors and adjacent tissue samples were obtained from the Affiliated Tongji Hospital of Huazhong University of Science and Technology with the ethical authorization conferred by the Tongji Hospital Research Ethics Committee. The information on HCC patients is delineated in Supplementary Table S4.

Quantitative real-time PCR and Western blotting

The total RNA extraction was conducted with the TRIzol reagent (Vazyme, Nanjing, China). CDNA synthesis was carried out with ABScript III RT Master Mix (ABclonal, Wuhan, China). Quantitative real-time PCR (qRT-PCR) analysis was performed with Universal SYBR Green Fast qPCR Mix (ABclonal) in the CFX96 Touch™ Real-Time PCR Detection 203 System (Bio-Rad, California, USA). GAPDH served as the internal negative control, and the relative mRNA expression levels of target genes were quantified with the $2^{-\Delta\Delta CT}$ method.

Western blotting (WB) was carried out following the published protocols previously (38), and Image Lab software (Bio-Rad, California, USA) was used in data analysis. GAPDH served as the internal negative control for the comparison of protein expression levels across various groups. The primers and antibodies involved in this study are listed in Supplementary Table S5.

Functional experiments on proliferation, invasion, and migration *in vitro*

Cell Counting Kit-8 (CCK-8, ABclonal, Wuhan, China) assay and colony formation test were utilized for assessing the proliferative capacity of HCC cells. For the CCK-8 assay, MHCC97H and HuH-7 cells were seeded in 96-well plates at 3,000 cells/well density. Upon cell adhesion, the medium was substituted with DMEM supplemented with CCK-8 reagent (100 μL DMEM + 10 μL CCK-8 per well). Each group had five duplicate wells. The absorbance at 450 nm was measured after a 2-h incubation at 37°C. The CCK-8 assay spanned 3 days. For the colony formation test, HCC cells were seeded in six-well plates at 500 cells/well density. The culture medium was replaced every 3 days, following the same cell cultivation procedure as previously described. Cultivation was terminated after 2 weeks, and the cell colonies were fixed with paraformaldehyde (Solarbio Science and Technology Co., Beijing, China) for 25 min, followed by staining with the crystal violet dye (G1014, Servicebio, Wuhan, China) for 25 min. Cell colonies were counted under a microscope.

The Transwell assay and wound-healing test were both used for assessing the migratory and invasive capacity of HCC cells. For the transwell assay, MHCC97H and HuH-7 cells were cultured in a serum-free medium for 8 h. Subsequently, $5*10^4$ cells were resuspended in 200 μL of serum-free medium and uniformly seeded to the upper chamber of Transwell inserts (Corning, New York, USA), with Matrigel coating (BD Bioscience, New Jersey, USA) for invasion or with no Matrigel coating for migration. The lower chamber was filled with 700 μL of complete DMEM medium. After culturing for 36 h, the chambers were harvested. Cells that invaded or migrated to the lower surface of the chamber were fixed and stained as previously described. Cellular migration or invasion was quantified with ImageJ software, with the calculation of average cell counts from five randomly selected fields of view.

For the wound-healing test, HCC cells were uniformly seeded in six-well plates. Upon reaching a cellular confluence exceeding 95%, scratches were performed with a 200-μL pipette tip. At 0 h, 12 h, 24 h, and 48 h, nonadherent cells were removed carefully, and photographs were captured. The scratch closure rates were analyzed with ImageJ software.

All experiments were independently replicated three times.

Statistical analysis

In this study, statistical analysis was accomplished with R 4.3.0 and GraphPad Prism 8.0.1 software. The findings of *in vitro* experiments were typified by representative images from three independent replicates, conveyed as the mean ± standard deviation (SD). The Spearman's correlation coefficient was conducted for the correlation test between continuous variables. The Chi-square test was utilized to assess the correlation between categorical variables. The differences between groups were determined by the Wilcoxon rank-sum test, independent Student's *t*-test, or analysis of variance for continuous variables. The survival analysis was performed employing the Kaplan–Meier (KM) method, and the log-rank test was applied for the assessment of statistical significance. A p-value of < 0.05 indicated statistical significance.

Results

Landscape of expression and mutation in PCD-related genes

The comprehensive framework for this present study is depicted in Supplementary Figure S1.

By analyzing PCD-related gene expression profiles, we identified 756 DEGs. Among these, 721 genes exhibited upregulated expression in tumor tissues, while only 35 genes displayed downregulated expression (Supplementary Table S6). We further conducted univariate Cox regression analysis, revealing 87 prognostic PCD-related genes. Among these, 85 genes correlated with an unfavorable prognosis in HCC, while *ADRA1A* and *FABP4* were protective factors for patients (Supplementary Table S7). A subsequent analysis of the 87 prognostic PCD genes was conducted. As shown in Figure 1A, these PCD-related genes frequently exhibit CNVs. The top 5 genes with the highest amplification frequencies were *GBA*, *SQLE*, *USP21*, *GSDMC*, and *NDRG1*, while *SFN*, *E2F2*, *CDKN2A*, *BRCA2*, and *CDX2* displayed the highest frequencies of copy number loss. The chromosomal locations of CNVs are presented in Figure 1C. Additionally, we observed that PCD-related genes exhibited mutations in 125 samples, with *CDKN2A* exhibiting the highest mutation frequency (Figure 1B). Figure 1D depicts the expression network of the aforementioned PCD-related genes.

Identifying PCD clusters with distinct characteristics of clinicopathology, molecular patterns, and functions

In accordance with the expression profiles of the 87 prognostic PCD genes, we identified two PCD clusters (Supplementary Figures S2A–D). PCA, t-SNE, and UMAP analysis substantiated notable disparities in the distribution of patient samples between the two PCD clusters (Supplementary Figures S2E–G). As illustrated in Supplementary Figure S3A and Figure 2A, we found patients in cluster A exhibited higher expression levels of PCD-related genes and suffered advanced clinical stages and pathological grades. In Figure 2C, survival curves clearly demonstrate that patients in cluster A experienced worse survival outcomes. Concurrently, it was demonstrated that the expression levels of most ICGs and CRRGs increased in cluster A (Figure 2B; Supplementary Figure S3B). Furthermore, we observed notable variations in immune characteristics between patients in the two clusters. As depicted in Figures 2F, G, patients in cluster A displayed higher immune scores and immune cell infiltrations. For example, the infiltration levels of MDSCs, macrophages, monocytes, and Treg cells were elevated in cluster A, while only eosinophils exhibited reduced infiltration levels.

Distinct molecular biological functions were observed across the PCD clusters. GSVA (Supplementary Figures S4A, B) and GSEA results (Supplementary Figures S4C, D) revealed the activation of numerous tumor-associated biological processes and signaling pathways in cluster A. These processes encompassed epithelial-mesenchymal transition (EMT), cell proliferation (MYC targets, G2M checkpoints, E2F targets, cell cycle), and signaling pathways like WNT/β-Catenin, TGF-β, and PI3K/AKT. In contrast, cluster B exhibited the activation of several metabolism-associated biological processes, such as fatty acid metabolism and bile acid metabolism. These findings were corroborated by the results of the GO/KEGG analysis (Supplementary Figures S5A–D). In addition to disparities in tumor biological attributes, significant differences in various biological functions associated with PCD, such as apoptosis, necroptosis, and autophagy, were observed between the two clusters.

Construction and evaluation of the prognostic predictive value of PCDI

Based on 87 prognostic PCD genes, we employed a machine learning algorithms integrated framework that combined 10 different machine learning algorithms through 10-fold cross-validation. The PCDI was constructed by integrating CoxBoost and RSF algorithms, which demonstrated the highest average C-index across three datasets among 88 algorithm combinations (Figure 3A). With the CoxBoost algorithm, we identified *GBA*, *G6PD*, *ETV4*, *KIF20A*, *LAPTM4B*, *TRAF5*, and *SLC2A1* as the seven most valuable PCD-related genes (Figure 3B; Supplementary Table S8). Furthermore, the RSF algorithm enhanced the reliability of this model (Figure 3C). We observed elevated expression levels of seven PCDI genes in HCC tissues (Supplementary Table S6), all of which were associated with an unfavorable prognosis (Supplementary Table S7; Supplementary Figures S16A–G). Concurrently, through GSEA, we detected that PCDI genes could trigger the activation of crucial tumor-associated biological processes, such as proliferation, invasion, and metastasis. Moreover, *TRAF5* and *SLC2A1* may be linked to immunological regulation, such as inflammation responses, and chemokine and T-cell receptor signaling pathways (Supplementary Figures S6A–G).

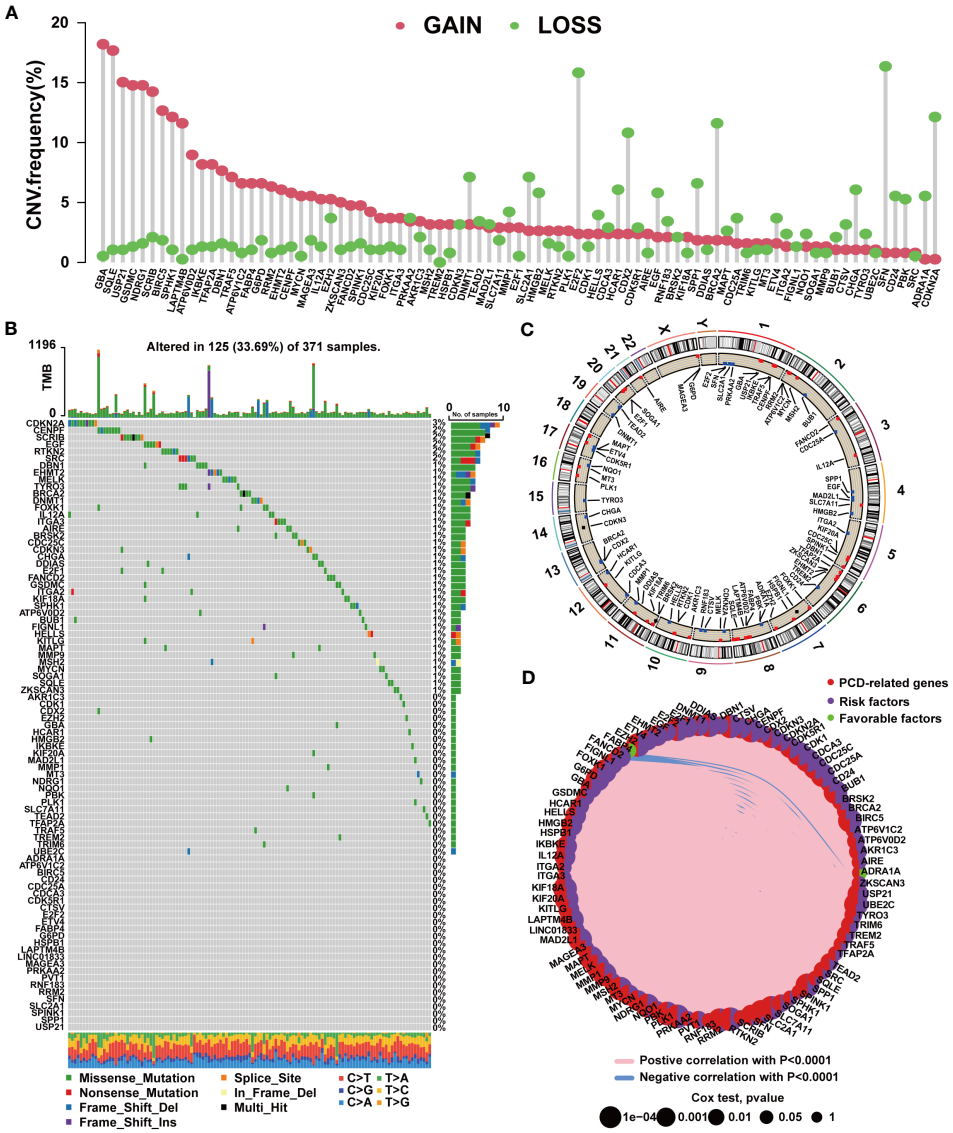

FIGURE 1
Mutation characteristics of PCD-related genes in HCC. **(A)** Characteristics of CNVs in PCD-related genes. **(B)** Characteristics of genetic variation in PCD-related genes. **(C)** Location of CNVs in PCD-related genes on chromosomes. **(D)** Expression correlation among PCD-related genes.

Subsequently, a comprehensive evaluation was performed for the prognostic predictive value of PCDI. In TCGA-LIHC dataset, survival curves demonstrated the PCDI could effectively predict the clinical outcomes of HCC patients, as indicated by survival metrics. Patients in the high PCDI score group suffered poor OS, PFS, DFS, and DSS compared to others (Figures 3D–G). ROC curves illustrated the accuracy of PCDI in prognostic prediction (Figure 4A). Notably, the highest accuracy was observed when utilizing the PCDI to predict OS, with the AUC values of 0.963 (95% CI: 0.945–0.981), 0.960 (95% CI: 0.926–0.983), and 0.946 (95% CI: 0.905–0.986) at 1 year, 3 years, and 5 years. Particularly, we found that PCDI scores for HCC patients in cluster A were significantly higher than those in cluster B, indicating congruence in terms of sample distribution (Figures 2D, E).

Afterward, we conducted a correlation analysis between PCDI and clinicopathological attributes. The PCDI exhibited a significant association with the advanced clinical stage, T stage, pathological grade, and vascular invasion status among HCC patients (Figures 4B, C). Independent prognostic analysis revealed PCDI as an independent risk factor for the OS, PFS, DFS, and DSS in HCC patients (Figures 4D, E). Through C-index and DCA curves, we observed that the PCDI exhibited superior predictive performance compared to other clinicopathological attributes in predicting OS, PFS, DFS, and DSS (Figures 4F, 5A–C; Supplementary Figure S7A–I). Additionally, when compared with 102 published prognostic predictive models, a C-index analysis affirmed the superiority of PCDI (Figures 6A–D).

Finally, the prognostic predictive value of PCDI was validated in the GSE76427 and ICGC-LIRI-JP datasets. Survival curves substantiated the capacity of PCDI to effectively predict the clinical outcomes of HCC patients in both datasets, indicating a worse OS in patients with higher PCDI scores (Figures 3H, I). In the

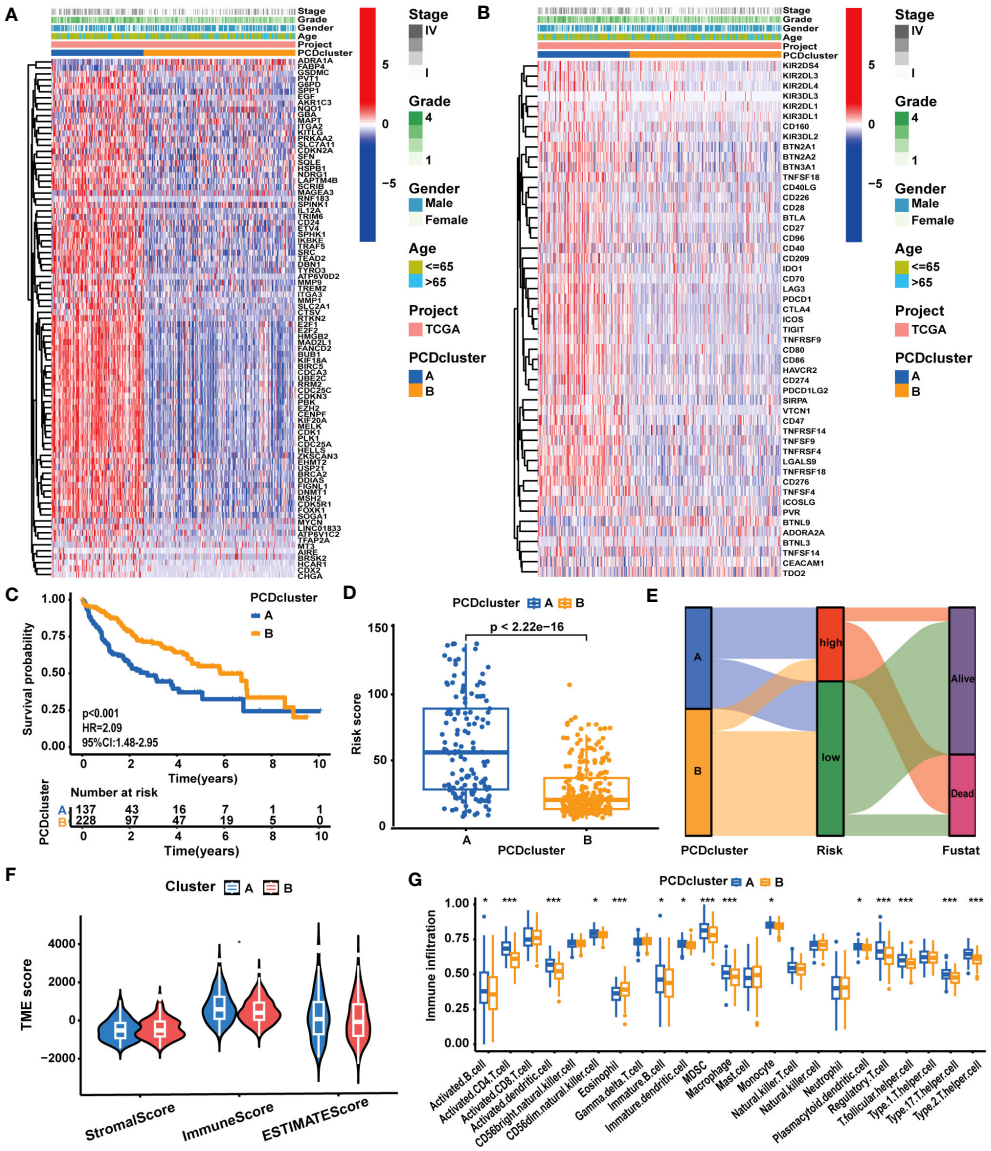

FIGURE 2
The correlation between PCD clusters, clinicopathological characteristics, and molecular patterns. **(A)** Different clinicopathological characteristics and PCD-related gene expression patterns between the two PCD clusters. **(B)** Different clinicopathological characteristics and ICG expression patterns between the two PCD clusters. **(C)** Different OS statuses of HCC patients between the two PCD clusters. **(D)** Correlation analysis between PCDI scores and PCD clusters. **(E)** Distribution of patients with different OS statuses across PCD clusters and PCDI score groups. **(F)** Different TME scores between the two PCD clusters. **(G)** Different immune cell infiltration patterns between the two PCD clusters. (*$p < 0.05$; **$p < 0.01$; ***$p < 0.001$.).

GSE76427 dataset, ROC curves presented the AUC values of PCDI as 0.629 (95% CI: 0.517–0.761), 0.631 (95% CI: 0.531–0.772), and 0.659 (95% CI: 0.556–0.790) at 1 year, 3 years, and 5 years in predicting OS (Supplementary Figure S8A), and in the ICGC-LIRI-JP dataset, the values were 0.757 (95% CI: 0.630–0.890), 0.726 (95% CI: 0.661–0.858), 0.692 (95% CI: 0.549–0.818) (Supplementary Figure S9A). In both datasets, Chi-square analysis revealed a significant correlation between PCDI and advanced clinical stages (Supplementary Figures S8B, C, S9B, C). Independent prognostic analysis demonstrated that the PCDI served as an independent risk factor for worse outcomes in HCC (Supplementary Figures S8D, E, S9D, E). C-index and DCA curves indicated excellent prognostic predictive performance of the PCDI in both datasets (Supplementary Figures S8F–I, S9F–I). When compared with published predictive models, the PCDI consistently demonstrated exemplary performance (Supplementary Figures S10A, B).

Construction and evaluation of the predictive efficacy of clinical nomograms

Owing to the remarkable prognostic predictive value of PCDI, we developed a clinical nomogram to facilitate the utilization of PCDI. In TCGA-LIHC dataset, the PCDI was integrated with other clinicopathological factors to establish a clinical nomogram for predicting the OS of patients. As shown in Figure 5D, the PCDI

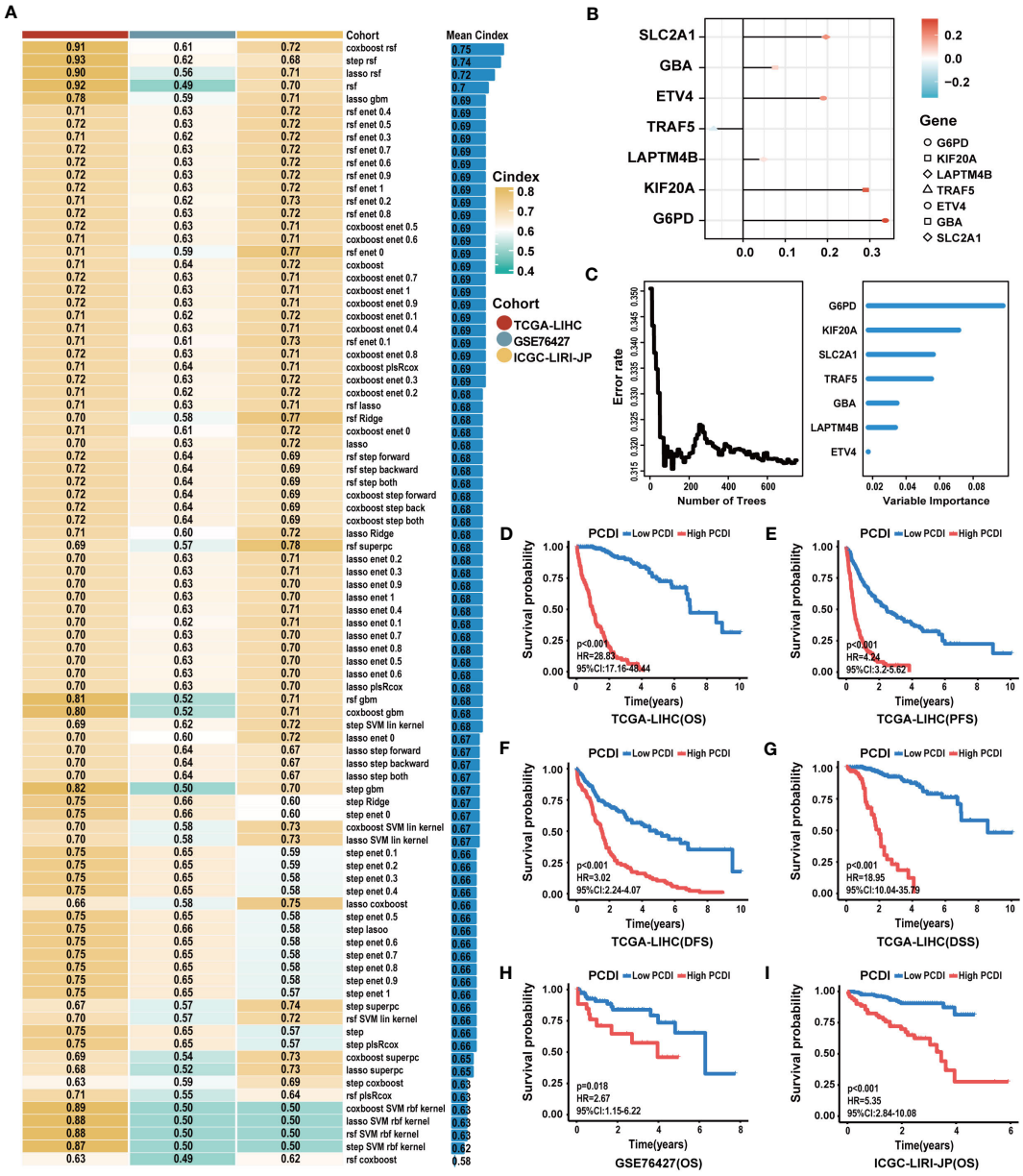

FIGURE 3
Construction of the PCDI based on an integrated framework for machine learning. **(A)** Combining 88 machine learning algorithms for prognostic models via 10-fold cross-validation and identifying the best one by C-index as the PCDI. **(B)** Determination of seven PCDI genes via the CoxBoost algorithm. **(C)** Determination of PCDI with minimal error and the importance of seven PCDI genes via the RSF algorithm. **(D–G)** Differences between patients in the high and low PCDI score groups for the OS, PFS, DFS, and DSS in TCGA-LIHC dataset. **(H, I)** Differences between patients in the high and low PCDI score groups for the OS in the GSE76427 and ICGC-LIRI-JP datasets.

score emerged as a significant variable in the clinical nomogram. Calibration and ROC curves indicated the exceptional predictive efficacy of this nomogram (Figures 5E, F). Furthermore, DCA curves validated the superior predictive efficacy of this clinical nomogram for OS compared to other clinicopathological factors (Figures 5G–I).

Subsequently, we applied a similar method to construct clinical nomograms in the GSE76427 and ICGC-LIRI-JP datasets. In the GSE76427 dataset, the PCDI score was the significant variable in the clinical nomogram (Supplementary Figure S11A), and a similar result was observed in the ICGC-LIRI-JP dataset (Supplementary Figure S12A). Calibration and ROC curves clearly demonstrated the favorable predictive performance of these clinical nomograms in predicting OS (Supplementary Figures S11B, C, S12B, C). Additionally, DCA curves affirmed the nice predictive performance of clinical nomograms for OS (Supplementary Figures S11D–F, S12D–F).

Clarifying the characteristics of immunology and biological function based on the PCDI score in HCC

To explore the correlation between PCDI and immunological features in HCC patients, we conducted a comprehensive

10.3389/fimmu.2023.1298290

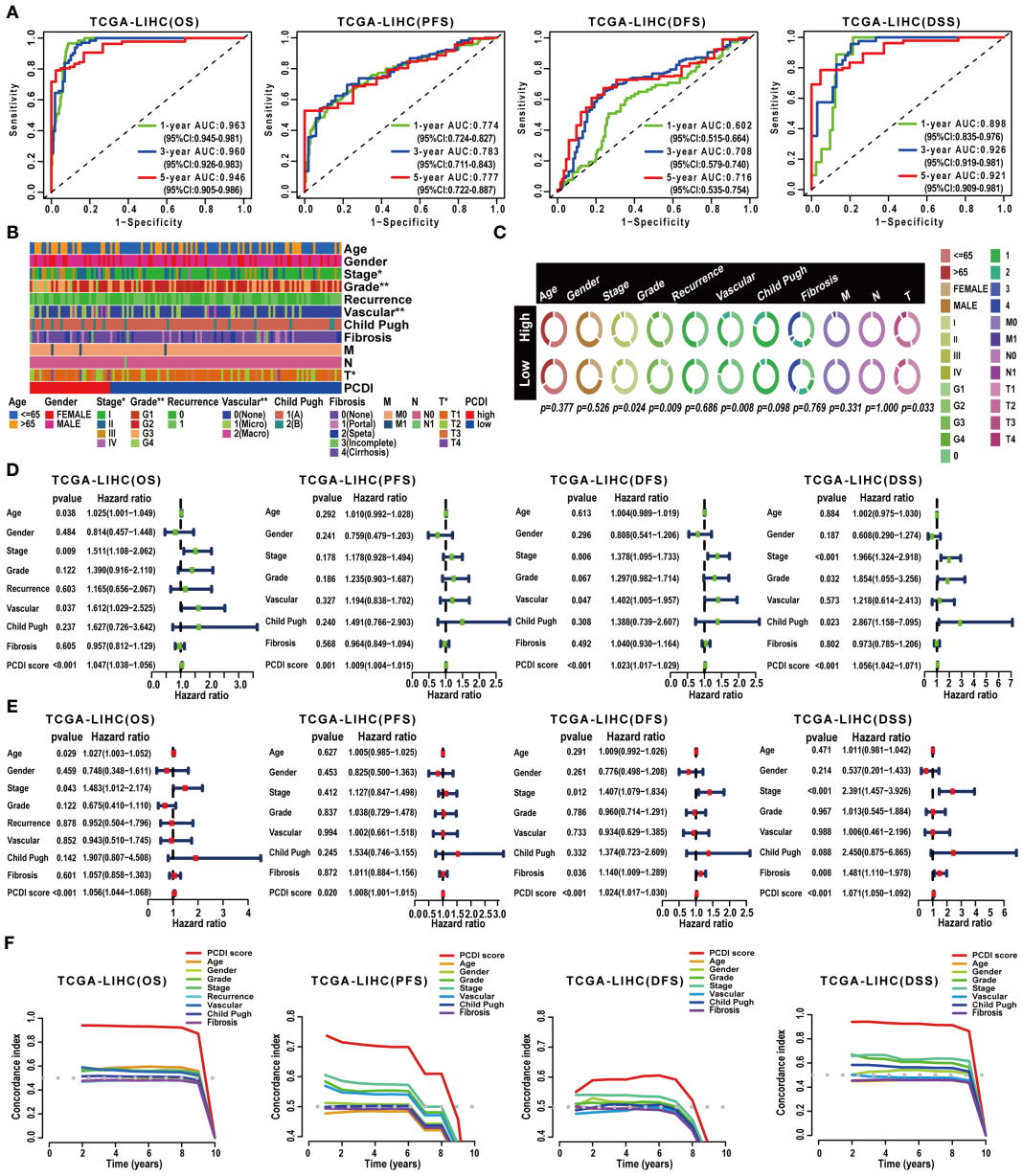

FIGURE 4
Validation of the prognostic predictive value of PCDI. **(A)** Evaluating the predictive accuracy of the PCDI for the OS, PFS, DFS, and DSS in TCGA-LIHC dataset with ROC curves. **(B, C)** Correlation analysis between clinicopathological characteristics and PCDI in TCGA-LIHC dataset. **(D)** Univariate Cox analysis revealing the impacts of PCDI and clinicopathological characteristics on OS, PFS, DFS, and DSS in TCGA-LIHC dataset. **(E)** Multivariate Cox analysis revealing the impacts of PCDI and clinicopathological characteristics on OS, PFS, DFS, and DSS in TCGA-LIHC dataset. **(F)** Comparing the prognostic predictive efficacy of PCDI and clinicopathological characteristics for the OS, PFS, DFS, and DSS in TCGA-LIHC dataset with C-index curves.

investigation. Using multiple immunological algorithms such as TIMER, CIBERSORT, and XCELL, we observed notable differences in immune cell infiltration levels between the high and low PCDI score groups (Figures 7A, B). Furthermore, we found that the infiltration levels of Treg cells, neutrophils, and M0 and M2 macrophages exhibited a significant positive correlation with PCDI scores, whereas $CD8^+$ T cells, $CD4^+$ T cells, and M1 macrophages displayed a significant negative correlation (Figures 7C–I). Employing the ESTIMATE algorithm, we found that the stromal and estimate scores of patients with higher PCDI scores were significantly decreased compared to those with lower PCDI scores. However, no statistically significant differences were observed in the immune scores between these two groups (Figure 7K). Additionally, we noticed that, compared to patients with lower PCDI scores, patients with higher PCDI scores exhibited significant suppression of type I/II IFN responses, T-cell co-stimulation, cytotoxic responses, and proinflammatory processes (Figure 7L). These findings indicated a potential suppressive immune microenvironment in the high PCDI score group and enhanced stromal cell infiltration in the TME of the low PCDI score group. Furthermore, a significant positive correlation was detected between stemness score and PCDI score, suggesting the potential

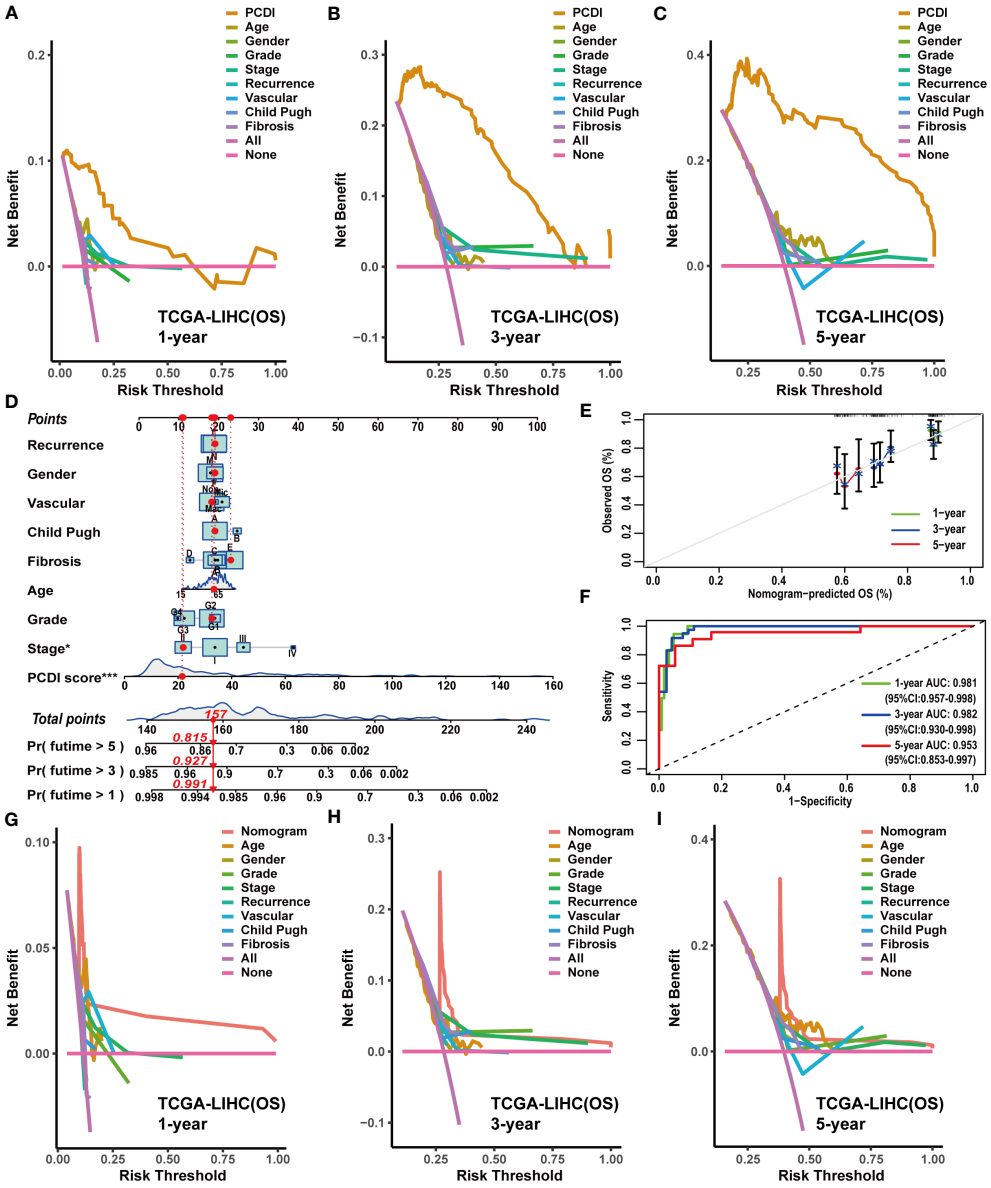

FIGURE 5
Construction and evaluation of the nomogram based on PCDI and clinicopathological characteristics. **(A–C)** Comparing the prognostic predictive efficacy of PCDI and clinicopathological characteristics for OS with DCA curves in TCGA-LIHC dataset. **(D)** Construction of a nomogram with PCDI and clinicopathological characteristics for predicting OS in TCGA-LIHC dataset. **(E)** Evaluating the predictive accuracy of a nomogram for the OS with calibration curves in TCGA-LIHC dataset. **(F)** Evaluating the predictive accuracy of a nomogram for the OS with ROC curves in TCGA-LIHC dataset. **(G–I)** Comparing the predictive efficacy of nomogram and clinicopathological characteristics for the OS in TCGA-LIHC dataset with DCA curves.

presence of active cancer stem cells in the TME of patients with higher PCDI scores (Figure 7J).

Subsequently, we compared the biological functional attributes between HCC patients in the high and low PCDI score groups. Through GSVA (Supplementary Figures S13A, B) and GSEA (Supplementary Figures S13C, D), we observed a significant activation of tumor-associated biological processes such as EMT, cell proliferation (MYC targets, E2F targets, G2M checkpoints, and cell cycle), and signaling pathways like WNT/β-catenin and PI3K/AKT/MTOR pathways in the high PCDI score group. Conversely, metabolic-associated processes, such as fatty acid metabolism and bile acid metabolism, were notably activated in the low PCDI score group. Furthermore, between these two groups, GO/KEGG analysis (Supplementary Figures S14A–D) revealed notable differences in various oncological biological functions and numerous cellular processes associated with cell replication, such as nuclear division and chromosomal disjunction regulation. Additionally, various metabolic-related processes exhibited distinct patterns.

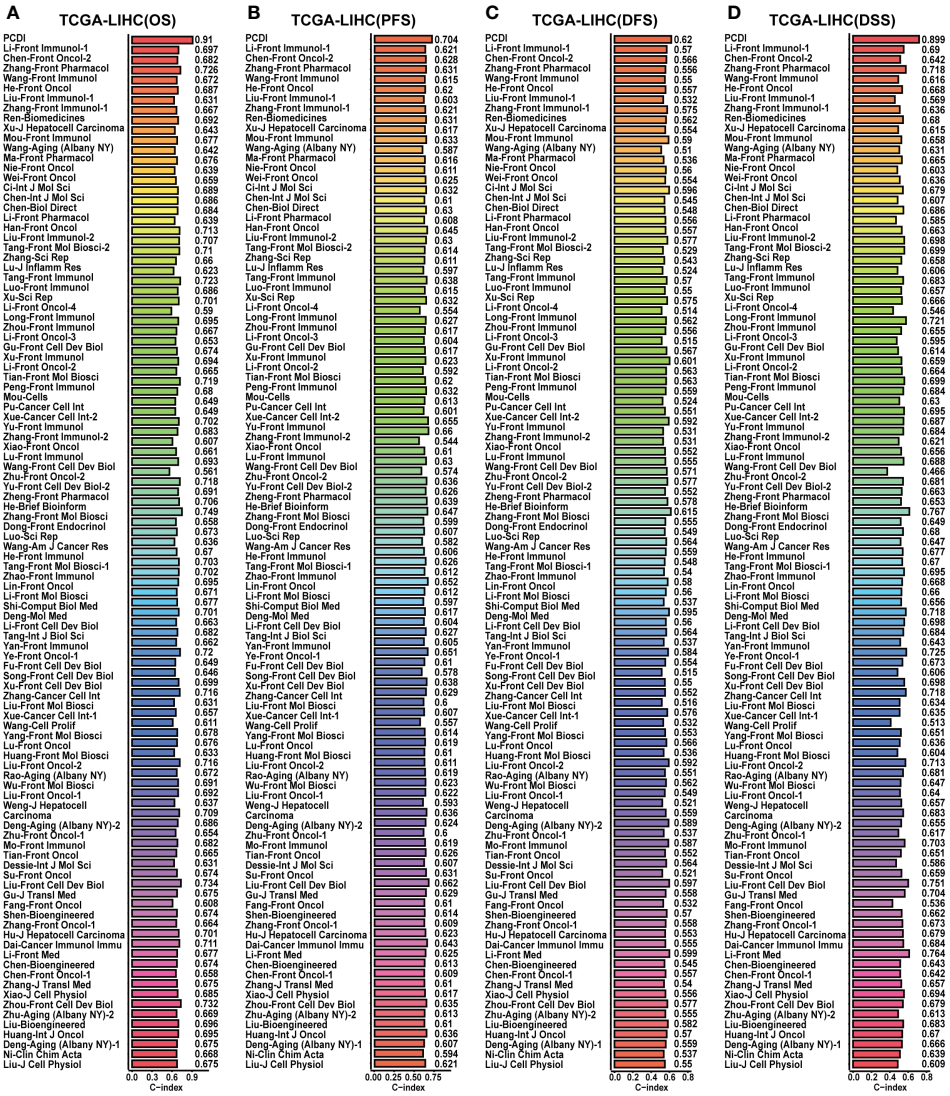

FIGURE 6
Comparison of the predictive value between PCDI and other models in TCGA-LIHC dataset. **(A)** Comparing the prognostic predictive efficacy of PCDI and other published models for OS by C-index analysis. **(B)** Comparing the prognostic predictive efficacy of PCDI and other published models for PFS by C-index analysis. **(C)** Comparing the prognostic predictive efficacy of PCDI and other published models for DFS by C-index analysis. **(D)** Comparing the prognostic predictive efficacy of PCDI and other published models for DSS by C-index analysis.

Clarifying ICG expression patterns and gene mutation statuses based on the PCDI score in HCC

We explored the correlation between PCDI and gene mutation statuses along with ICG expression patterns. We found a higher frequency of gene mutations in the high PCDI score group. Missense mutations were the predominant mutation type observed. *TP53* emerged as the most frequently mutated gene in the high PCDI score group, displaying the greatest disparity in mutation frequency between the two groups. Moreover, *CTNNB1* mutations were most prevalent in the low PCDI score group (Figures 8A, B). Further analysis indicated an obvious increase in TMB levels among patients in the high PCDI score group. Concurrently, patients with higher TMB levels were predominantly classified as cluster A (Figures 8C, D). Similarly, we observed a positive correlation between MSI levels and PCDI scores. Patients with high MSI levels were primarily clustered in the high PCDI score group (Figures 8E, F). Moreover, correlation analysis of PCDI and ICG expression patterns revealed that the expression of the majority of ICGs exhibited a significant positive correlation with PCDI scores (Figure 8G; Supplementary Table S9).

Evaluation and valuation of the predictive value of PCDI in immunotherapy responses

Considering the correlation between PCDI and TMB, MSI, and ICG expression patterns, we examined the predictive value of PCDI in patients' responses to immunotherapy.

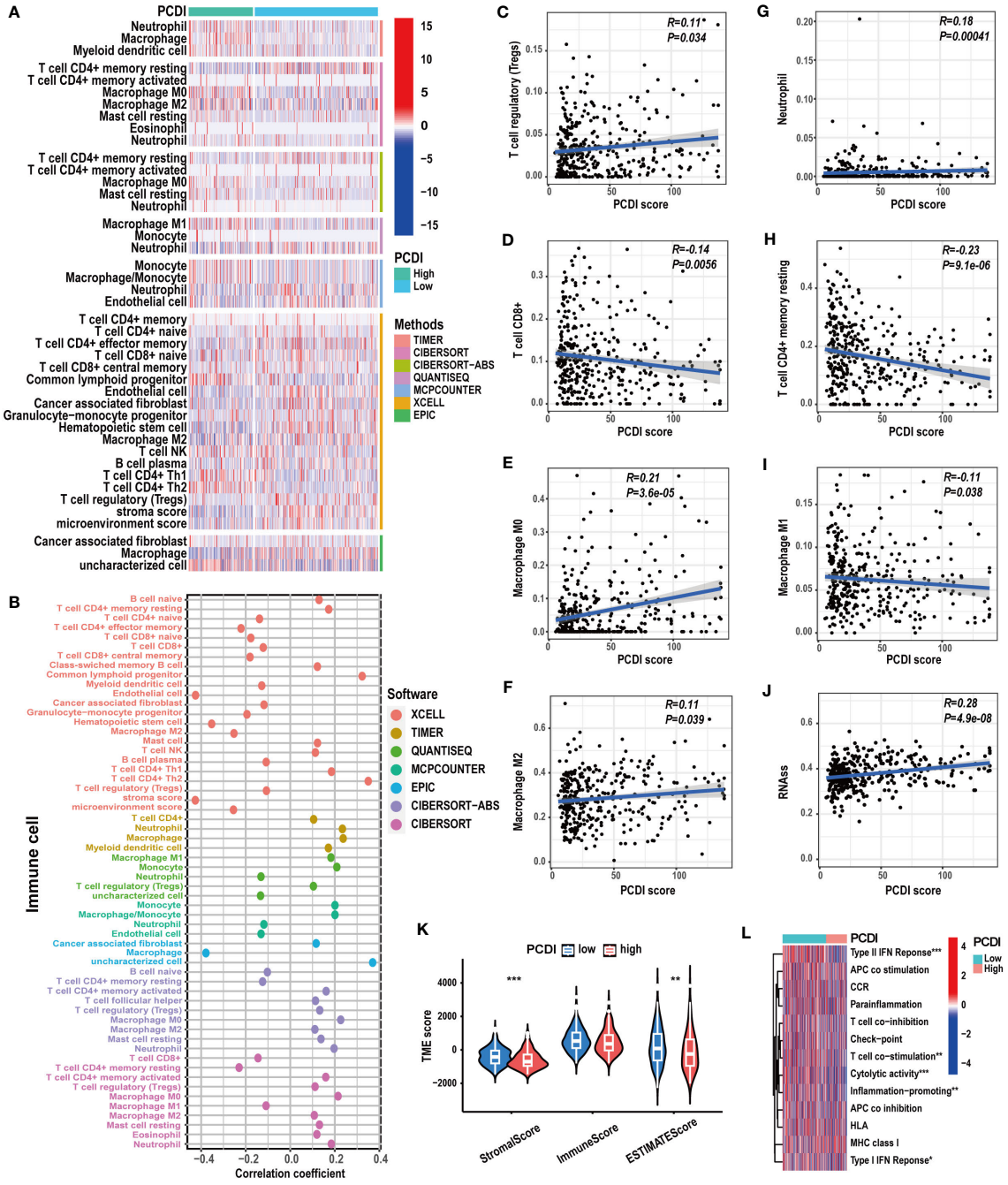

FIGURE 7
The correlation between immunological characteristics and PCDI. **(A, B)** Different immune cell infiltration patterns between the high and low PCDI score groups. **(C-I)** Correlation analysis of the immune cell infiltration levels and PCDI scores. **(J)** Correlation analysis of the stemness scores and PCDI scores. **(K)** Different TME scores between the high and low PCDI score groups. **(L)** Different immune function statuses between the high and low PCDI score groups. (*p < 0.05; **p < 0.01; ***p< 0.001).

In TCGA-LIHC dataset, we calculated the TIDE, dysfunction, and exclusion scores for HCC patients through the TIDE algorithm. We found the TIDE and dysfunction scores exhibited a notable reduction in the high PCDI score group, while the exclusion score demonstrated an increase (Figures 9A–C). These results suggested patients with higher PCDI scores could respond to immunotherapy easily. Further analysis indicated a significant relationship between higher PCDI scores and an increased response rate to immunotherapy. More patients responding to immunotherapy were found in the high PCDI score group (Figures 9D, E). These results reaffirmed our earlier findings, indicating that patients with higher PCDI scores were more responsive to immunotherapy. PCDI could be employed for immunotherapy response prediction in HCC patients.

Subsequently, we analyzed multiple immunotherapy cohorts to further validate the predictive efficacy of PCDI for immunotherapy

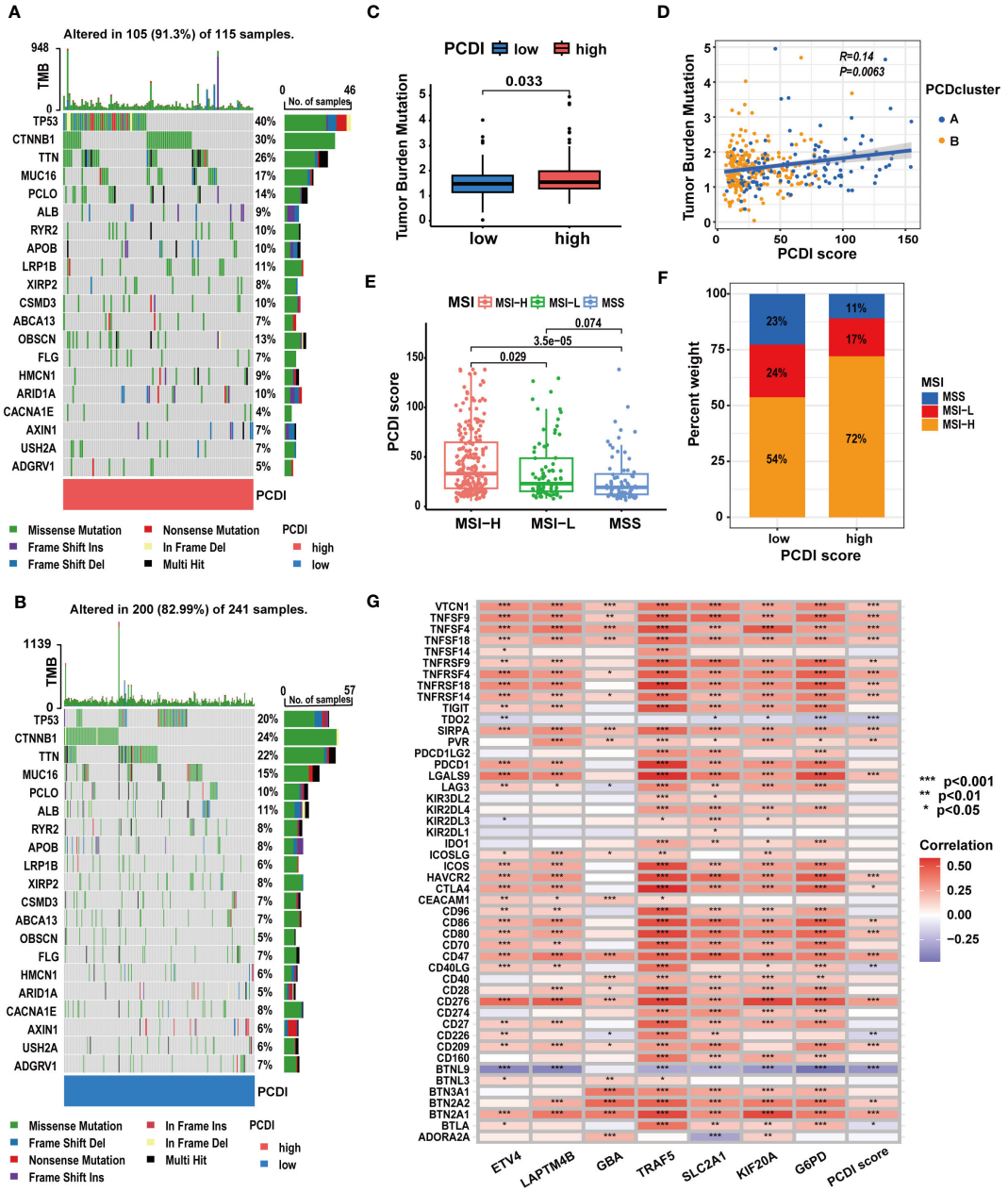

FIGURE 8
The correlation between mutation characteristics, ICG expression patterns, and PCDI. **(A, B)** Different genetic mutation characteristics between the high and low PCDI score groups. **(C)** Different TMB levels between the high and low PCDI score groups. **(D)** Correlation analysis of TMB, PCD clusters, and PCDI scores. **(E)** Correlation analysis of MSI statuses and PCDI scores. **(F)** Distribution of patients with different MSI statuses across PCDI score groups. **(G)** Correlation analysis of ICG expression levels and PCDI. (*p < 0.05; **p < 0.01; ***p< 0.001).

responses. In the IMvigor210 cohort, we found a higher PCDI score was significantly associated with a better response rate to immunotherapy, and more patients responding to immunotherapy were in the high PCDI score group (Figures 10A–E). Furthermore, we observed that the median levels of immune cell infiltration were elevated in patients with higher PCDI scores, but there was no significant difference. Additionally, there was no significant correlation between immune microenvironment statuses and PCDI scores, while tumor cell infiltration levels were positively associated with PCDI scores (Figures 10F–H). Moreover, in the GSE176307, Checkmate, GSE179351, GSE103668, and GSE78220 cohorts, patients in the higher PCDI score group demonstrated a greater likelihood of responding to immunotherapy (Supplementary Figures S15A–G); and in the GSE35640 and GSE120644 cohorts, patients in the low PCDI score group were more responsive to immunotherapy (Supplementary Figures S15I, J). In the GSE91061 cohort, PCDI appeared to have no association with the immunotherapy responses (Supplementary Figure S15H). Overall, the PCDI can effectively predict patients' responses to immunotherapy, and it can guide immunotherapy for patients based on PCDI scores. Particularly for HCC patients, those with higher PCDI scores could be better candidates for immunotherapy.

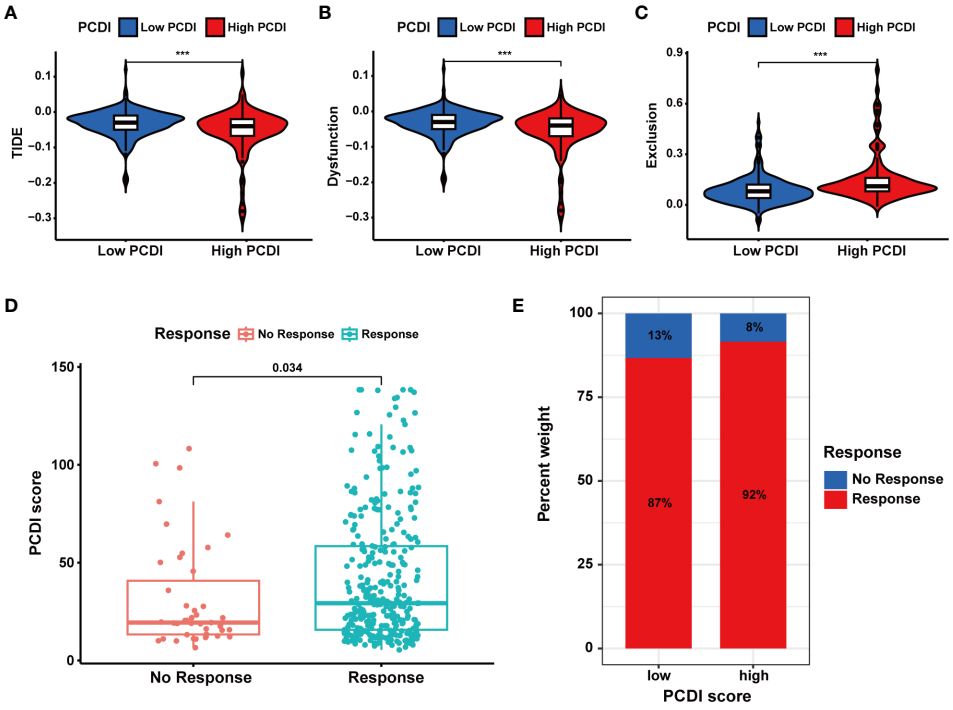

FIGURE 9
Evaluation of the predictive value of PCDI in immunotherapy responses based on TIDE algorithms. **(A)** Different TIDE scores between the high and low PCDI score groups. **(B)** Different dysfunction scores between the high and low PCDI score groups. **(C)** Different exclusion scores between the high and low PCDI score groups. **(D)** Correlation analysis of immunotherapy response statuses and PCDI scores. **(E)** The distribution of patients with different immunotherapy response statuses across the PCDI score groups.

Additionally, as shown in Supplementary Figures S15K, L, PCDI can also predict the responses of HCC patients to sorafenib and TACE treatments. Patients in the low PCDI score group were more likely to respond to sorafenib and TACE therapies, suggesting that patients with lower PCDI scores could be better candidates for these treatments.

Evaluation of the predictive value of PCDI in chemotherapy sensitivity for HCC

We further investigated the predictive value of the PCDI in chemotherapy. As depicted in Figure 11A, we found a significant positive correlation between the PCDI scores and the expression levels of most CRRGs. The results suggested the PCDI could be used for assessing the drug resistance of HCC patients, and PCDI genes may represent promising targets for overcoming chemotherapeutic resistance in HCC (Supplementary Table S10). Figure 11B visualizes the first nine CRRGs exhibited a positive correlation with the PCDI score. We employed the "OncoPredict" package to further validate the capability of PCDI in drug sensitivity prediction. As illustrated in Figure 11C, in the low PCDI score group, the imputed sensitivity score of oxaliplatin was significantly reduced, indicating a heightened sensitivity in patients with lower PCDI scores. Conversely, in the high PCDI score group, several drugs such as paclitaxel, docetaxel, vinblastine, cediranib, and bortezomib displayed lower imputed sensitive scores, implying a potential increase in sensitivity to these drugs in these patients.

Comprehensive analysis of the PCDI genes

To acquire a deeper understanding of the PCDI, we performed a comprehensive analysis of the PCDI genes in HCC.

At the single-cell level, we investigated the expression patterns and cellular communication characteristics of PCDI genes. Employing the t-SNE method for cluster analysis, we identified 21 cell clusters, which were annotated as eight primary cell populations (Figures 12A, B). Subsequently, we explored the expression patterns of seven PCDI genes across different cell populations (Figures 12C, D). We observed stable expression of PCD genes in malignant cells, with *LAPTM4B*, *G6PD*, *SLC2A1*, and *GBA* exhibiting the highest expression levels. Notably, besides malignant cells, PCDI genes are also expressed in immune and stromal cells. *G6PD* is mainly expressed in TAMs, *LAPTM4B* is predominantly expressed in tumor endothelial cells (TECs), *GBA* is expressed in both cell populations, and *TRAF5* is primarily expressed in cancer-associated fibroblasts (CAFs). Moreover, we conducted a cellular communication analysis. Given the limited research on *GBA* in HCC and its high expression level in malignant cells and suppressive immune cells, we selected it as the focal point of this analysis. We divided malignant cells into two groups: *GBA*+ and *GBA*−, based on their *GBA* expression levels (*GBA*+ indicating high expression, *GBA*− indicating low expression). We then compared the cellular communication characteristics between the two groups. The communication network among all cell populations is displayed in Figures 12E, F. Among all cell populations,

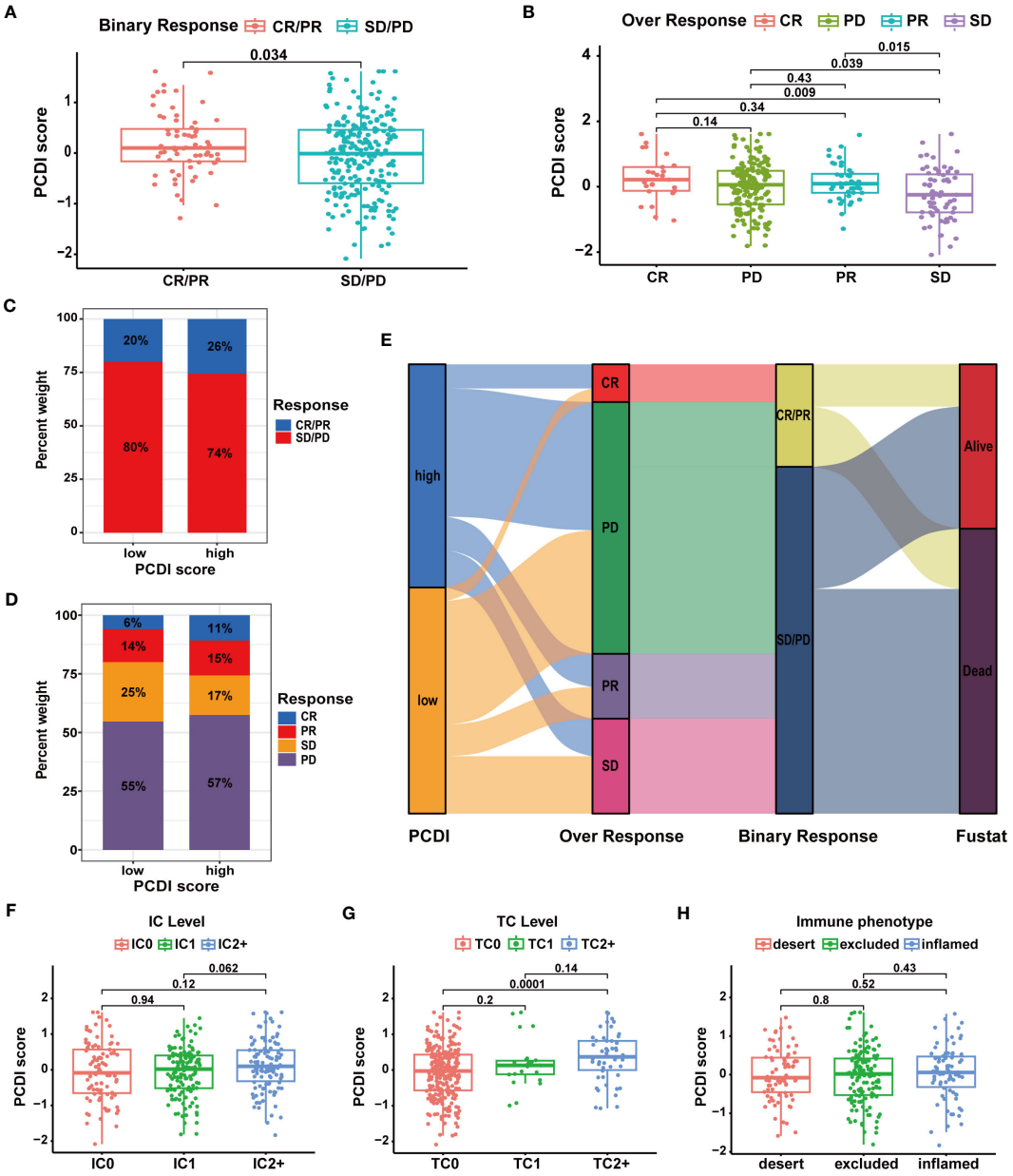

FIGURE 10
Validation of the predictive value of PCDI for immunotherapy response in the IMvigor210 cohort. **(A, B)** Correlation analysis of immunotherapy response statuses and PCDI scores. **(C, D)** The distribution of patients with different immunotherapy response statuses across the PCDI score groups. **(E)** The distribution of patients with different immunotherapy responses and OS statuses across the PCDI score groups. **(F)** Correlation between the levels of immune cells and PCDI scores. **(G)** Correlation between the levels of tumor cells and PCDI scores. **(H)** Correlation between TME characteristics and PCDI scores.

malignant cells exhibited the most extensive cell communication and showed the highest signal output intensity. TAMs, TECs, CAFs, and HPCs exhibited similar numbers of cellular interactions, with TAMs demonstrating the highest signal input strength. Notably, *GBA*+ malignant cells exhibited more extensive cell communication in terms of both quantity and strength. For specific cellular communication pathways, *GBA*+ malignant cells exhibited higher activation levels in pathways such as SPP1, GDF, ANGPTL, PARs, and PROS (Figure 12G). This suggested more active biological processes in *GBA*+ malignant cells, including cell proliferation, invasion, metastasis, angiogenesis, and inflammatory responses.

At the protein level, we explored the expression patterns and prognostic correlations of the PCDI genes. Utilizing the proteome dataset PDC-000198, we observed a significant upregulation in the expression of *GBA*, *G6PD*, and *KIF20A* in HCC tissue, which was associated with unfavorable clinical outcomes. Although *SLC2A1* and *TRAF5* exhibited no significant expression difference between HCC and adjacent tissues, they still displayed an association with a poor prognosis. Unfortunately, data for *LAPTM4B* and *ETV4* were not available in this dataset (Supplementary Table S11; Supplementary Figures S16H–L).

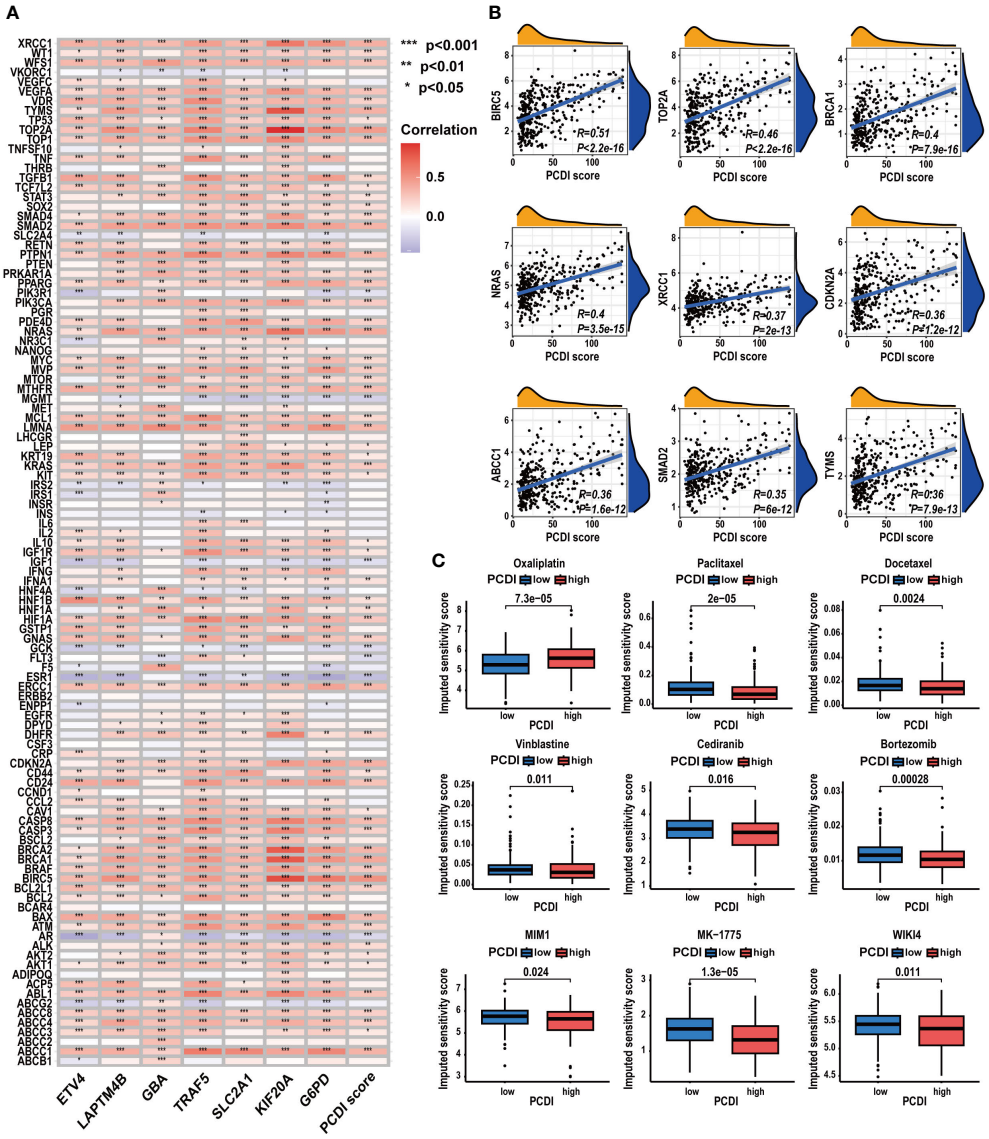

FIGURE 11
Correlation between CRRG expression patterns, chemotherapeutic drug sensitivities, and PCDI. **(A)** Correlation analysis of CRRG expression levels and PCDI. **(B)** Correlation analysis of multiple CRRG expression levels and PCDI scores. **(C)** Different drug sensitivities between the high and low PCDI score groups. (*p < 0.05; **p < 0.01; ***p< 0.001).

We subsequently acquired IHC data for PCDI genes from the HPA database. Among them, *GBA*, *G6PD*, and *KIF20A* demonstrated remarkably elevated expression levels in HCC tissue. Similarly, *SLC2A1* and *TRAF5* also displayed a modest difference between HCC tissue and normal tissue. Additionally, *LAPTM4B* exhibited notably heightened expression in HCC tissue, while *ETV4* exhibited slightly higher expression in HCC tissue (Figures 13A–G).

Functional evaluation of the PCDI genes

We then aimed to provide experimental evidence elucidating the involvement of PCDI genes in HCC. Building upon prior findings, a sequence of functional investigations focused on GBA was undertaken.

As shown in Figures 14A, B, both qRT-PCR and WB analyses consistently revealed a significant upregulation of GBA in tumor tissues. Afterward, we downregulated *GBA* expression levels in MHCC97H and HuH-7 through transfection of siRNAs. *GBA* knockdown was validated at both the mRNA and protein levels, and three distinct siRNAs, si-NC (control), si-*GBA*-1, and si-*GBA*-2, were selected for subsequent experiments (Figures 14C, D). The results of the CCK-8 assay and colony formation test revealed *GBA* knockdown significantly suppressed the proliferative capacity of MHCC97H and HuH-7 cells (Figures 14E, F). Simultaneously, WB analysis demonstrated *GBA* knockdown substantially reduced the expression levels of *CDK1*, *CDK2*, *CDK4*, and *c-MYC* in both two HCC cell lines (Figure 14G). These results indicated the integral role of *GBA* in the regulation of the cell cycle and tumor proliferation.

10.3389/fimmu.2023.1298290

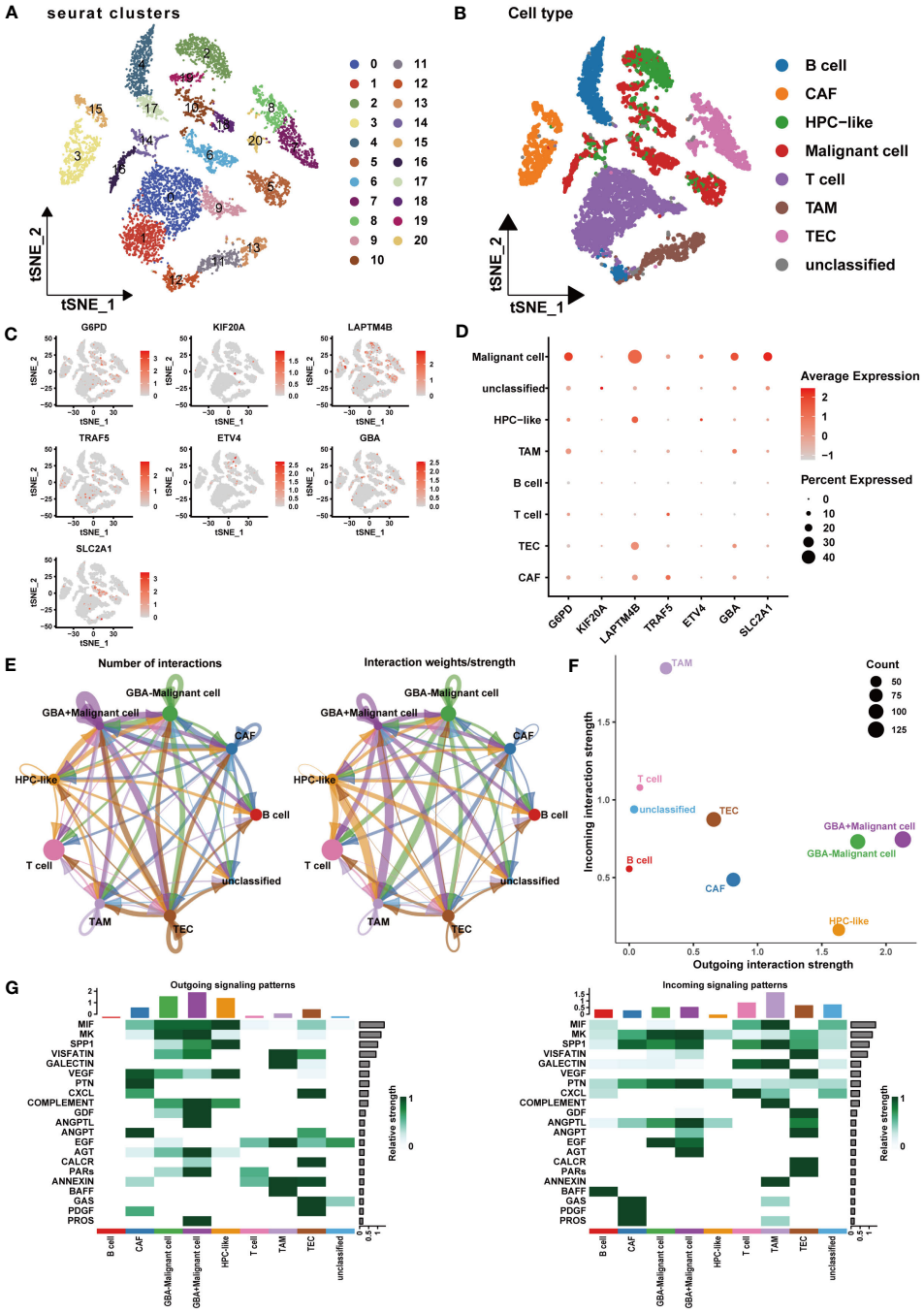

FIGURE 12
Expression patterns and cellular communication characteristics of the PCDI genes at single-cell level. **(A, B)** The results of cell clustering and annotation for the GSE125449 dataset. **(C, D)** The expression patterns of seven PCDI genes in different cell populations. **(E, F)** The cellular communication network among different cell populations. **(G)** The activated state of specific pathways in different cell populations.

Furthermore, our results suggest that *GBA* may also be involved in the invasive processes of the tumor. The wound-healing test revealed that the downregulation of *GBA* significantly attenuated the scratch closure rates of MHCC97H and HuH-7 cells (Figure 15A), suggesting a reduced migratory capacity of HCC cells. The Transwell assay further validated that *GBA* knockdown resulted in a diminished migratory and invasive capacity of HCC cells (Figure 15B). WB analysis illustrated that in both MHCC97H and HuH-7 cell lines, *GBA* knockdown notably decreased the expression levels of *N-cadherin*, *Vimentin*, *Snail*, and *MMP2*. Conversely, the expression levels of *E-cadherin* increased with the downregulation of *GBA* (Figure 15C). These findings suggested *GBA* was involved in the EMT in HCC cells, thereby enhancing their invasive and metastatic potential.

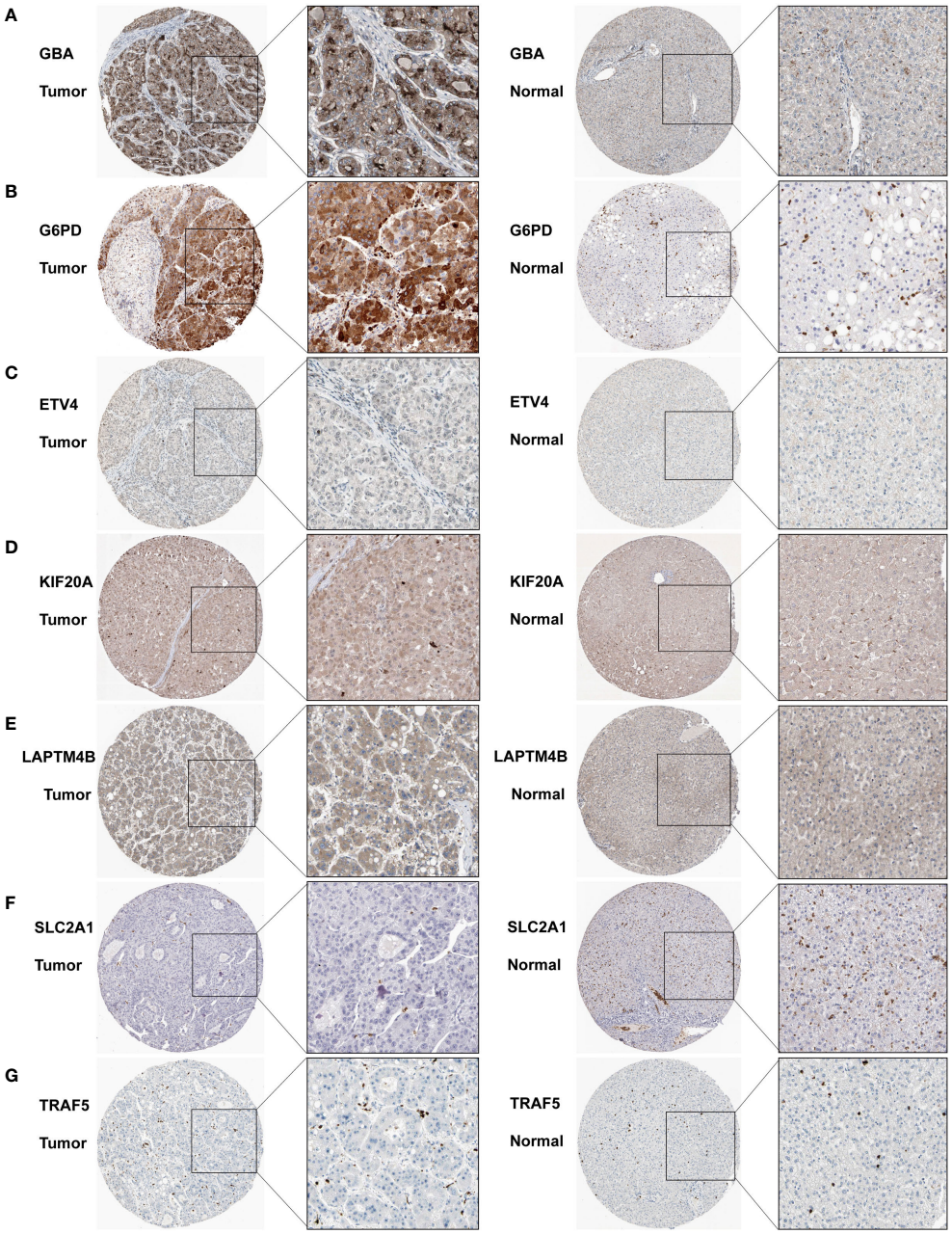

FIGURE 13
Immunohistochemistry results for the PCDI genes. **(A–G)** Different protein expression levels of PCDI genes between tumor and normal tissues in the HPA database.

Discussion

Despite notable advancements in HCC therapies, the clinical prognosis for patients remains unsatisfactory. Surgical interventions, such as resection and transplantation, are the optimal therapeutic strategies for early-stage HCC patients. However, over half of them experience a relapse within 5 years following a hepatectomy. While the recurrence rate is lower for liver transplant recipients, the widespread adoption of liver transplantation is constrained by the limited availability of donors (1, 39). For the majority of patients diagnosed with advanced-stage HCC, systemic treatments are the primary therapeutic approach. The application of TKIs and ICIs represents a significant transformation in the current systemic treatment for HCC. However, these treatments have only resulted in modest improvements in survival time, ranging from 1.2 to 5.8 months, which falls short of expectations (40–45). This may be attributed to the limited success of personalized treatment owing to tumor heterogeneity. Although clinical staging systems provide a foundation for HCC management, they are incapable of assessing the molecular biological characteristics of patients. This limitation is a significant hindrance to the implementation of personalized

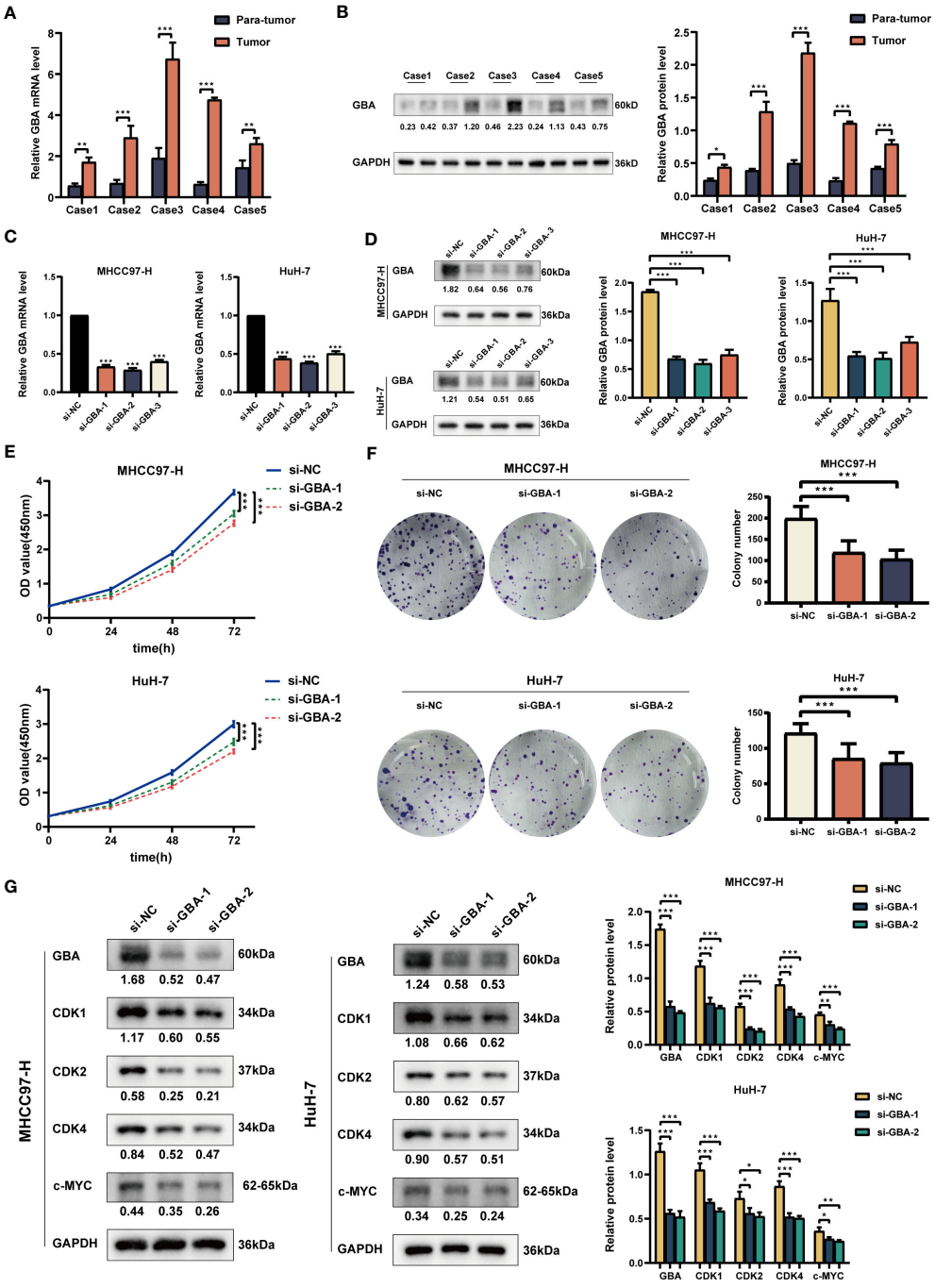

FIGURE 14
Experimental validation of GBA on proliferation. **(A)** Relative expression of GBA in HCC tumor tissues and para-tumor tissues at the mRNA level. **(B)** Expression of GBA in HCC tumor tissues and para-tumor tissues at the protein level. **(C, D)** Verification of GBA knockdown efficiency with siRNA at the mRNA and protein levels in MHCC97H and HuH-7 cells. **(E, F)** Effects of GBA knockdown on the proliferation capability of both cell lines detected with CCK-8 and colony formation assays. **(G)** Effects of GBA knockdown on cell cycle-associated markers in both cell lines detected by WB. (*$p < 0.05$; **$p < 0.01$; ***$p < 0.001$.).

treatments for HCC. Thus, there is an imperative requirement to identify potent biomarkers as complementary tools to existing staging systems for guiding therapeutic decisions, which could elevate the level of personalized treatment and enhance the clinical management of HCC, thus improving the prognosis.

Distinct from accidental cell death, PCD is a complex process characterized by intricate regulation and diverse operational patterns. Accumulated evidence has implicated various cell death modes as pivotal hallmarks of tumorigenesis, potentially serving as a theoretical foundation for innovative anticancer strategies (8). In this study, we presented a comprehensive examination of the correlation between 14 distinct PCD modes and the clinical characteristics along with the biological patterns of HCC for the first time. Initially, we investigated the expression patterns of PCD-

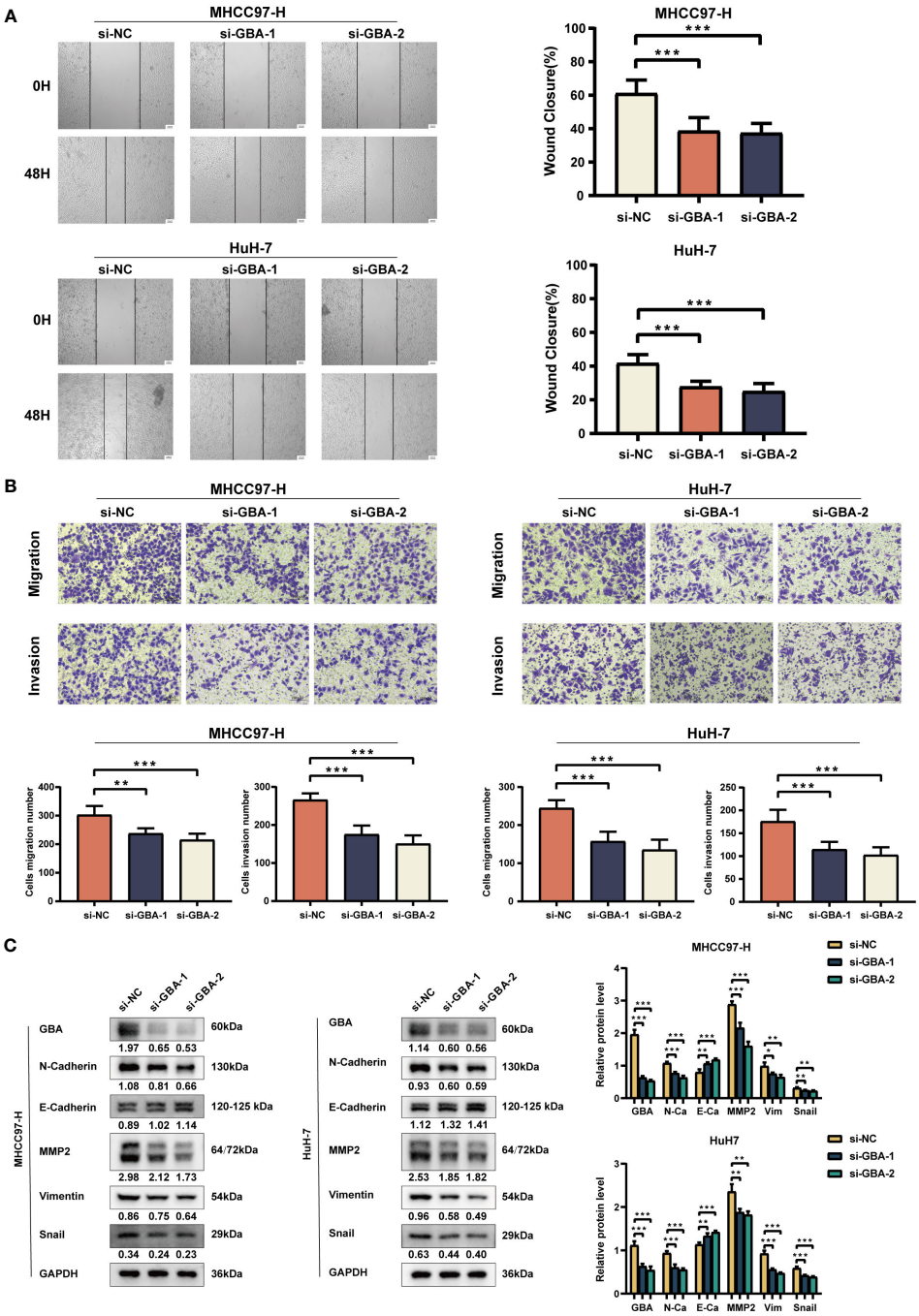

FIGURE 15
Experimental validation of GBA on invasion and migration. **(A)** Effects of GBA knockdown on the migration capability of both cell lines detected with a wound healing test. Scale bar: 100 μm (×40). **(B)** Effects of GBA knockdown on the migration and invasion capability of both cell lines detected with a Transwell assay. Scale bar: 100 μm (×200). **(C)** Effects of GBA knockdown on EMT-associated markers in both cell lines detected by WB. (*$p < 0.05$; **$p < 0.01$; ***$p < 0.001$.).

related genes in HCC. We identified 756 differentially expressed PCD-related genes, with 721 of them exhibiting increased expression in tumor tissues. Among these genes, we further identified 87 prognostic PCD genes, with 85 of them associated with an unfavorable prognosis. These findings indicated a potential role for PCD-related genes in HCC. Among the 87 prognostic-related PCD genes, CNVs were frequently observed, and approximately one-third of patients experienced mutations of these genes. Indeed, there is some evidence suggesting that mutations in specific genes could participate in PCD regulation and influenced tumorigenesis. For example, mutations in the *TP53* gene could disrupt various PCD pathways, playing a crucial role in HCC progression (46).

Subsequently, we identified two PCD clusters in HCC patients. These two PCD clusters exhibited notable differences in sample distribution, clinical attributes, and biological features. HCC patients

in cluster A displayed more severe clinical manifestations, such as advanced clinical stage, pathological grade, and poor prognosis. In addition to higher expression levels of PCD-related genes, HCC patients in cluster A also demonstrated elevated expression of ICGs and CRRGs compared to those in cluster B. Drug resistance mechanisms in HCC have been categorized into seven types, encompassing drug uptake and export, drug metabolism, alterations in drug targets, DNA repair, disruption in apoptosis/survival signals, adaptation to the TME, and phenotypic transition. These mechanisms can elucidate the roles of most CRRGs in regulating drug sensitivity in HCC (34). Similarly, ICGs could be categorized into three types: tumor cell dominant, immune cell dominant, and balanced type. HCC patients with higher expression of ICGs exhibited a favorable prognosis and were more likely to benefit from immunotherapy (33). These findings indicated a potential association between treatment responses for HCC patients and the expression patterns of ICGs and CRRGs, which could cause variable treatment responses. Despite patients in cluster A exhibiting higher immune scores and enhanced immune cell infiltration, the presence of cells including MDSCs, macrophages, monocytes, and Treg cells suggested the existence of an immunosuppressive microenvironment (47). In addition, we observed a significant activation of numerous tumor-associated biological functions and pathways in cluster A, such as EMT, cell proliferation (MYC targets, G2M checkpoints, E2F targets, and cell cycle), WNT/β-catenin, TGF-β, and PI3K/AKT signaling pathways. The characteristics of these HCC patients, including an unfavorable prognosis, increased proliferation, heightened invasiveness, and pathway activation, align with the proliferative subtype in the classical classification of HCC. Additionally, the activation of the WNT/β-catenin pathway has been defined as a hallmark of the nonproliferative subtype of HCC, which correlates with enhanced immune infiltration (48, 49). Notably, these features were also observed in HCC patients in cluster A. Our findings substantiate the close association between PCD clusters and the clinical and biological characteristics of HCC patients. We posited that focusing on PCD could offer a novel perspective for comprehending the pathogenesis, evolution, and treatment of HCC.

Afterward, we constructed the well-performing PCDI model, which could serve as a tool for prognostic prediction and therapeutic guidance in HCC. Indeed, with the advancements in gene sequencing and bioinformatics techniques, there has been an exponential increase in genomic and molecular data from both tissues and single cells. This abundance of data has led to the identification of numerous gene signatures (referred to as prognostic models) similar to the PCDI model. These gene signatures could be used to assess patients at a molecular level and group them based on shared phenotypes, such as clinical and molecular biological characteristics and responses to specific treatments. Thus, these signatures can assist clinicians in patient risk stratification and screening potential beneficiaries of certain treatments. For example, He et al. reported a coagulation pathway subtype in HCC with distinct immunological and prognostic features. They further developed a coagulation-related gene risk score to predict patient prognosis and treatment responses (50). Zeng et al. developed a hypoxia-driven gene signature for predicting and improving outcomes for HCC patients (51). Liu et al. established a prognostic model for HCC with cuproptosis-related genes and the RSF algorithm, which was used for patient risk stratification and treatment beneficiary selection (52). In diseases with complex etiologies and heterogeneity, such as HCC, these gene signatures, which were composed of multiple genes, demonstrated greater reliability compared to biomarkers such as *AFP*, *PD-L1*, and TMB (53). However, most gene signatures were constructed using a single algorithm, typically a regression algorithm (e.g., LASSO regression) or a machine learning algorithm (e.g., the RSF algorithm). This often resulted in decreased stability and generalizability, manifesting as a significant decrease in accuracy when tested on validation or external datasets. Furthermore, these studies frequently lack lateral comparisons among prognostic models, hindering the further validation of their predictive efficacy. These limitations may compromise the ability of most gene signatures to accurately predict and guide personalized treatment for HCC patients. In this study, we employed a novel framework that integrated 10 machine learning algorithms and generated 88 prognostic models via algorithmic combinations. The model composed of a CoxBoost and RSF algorithmic combination was identified as the best one, referred to as the PCDI. Compared to singular algorithms, the integration and combination of multiple algorithms could effectively reduce the dimensionality of variables, optimize stability and generalizability, and thereby enhance the performance of prognostic models. Furthermore, through extensive lateral comparisons, the superior performance of the PCDI model has been further substantiated. This also highlighted the potential utility of integrating and combining multiple algorithms in developing high-performance gene signatures.

In this study, the PCDI was comprised of seven genes: *GBA*, *G6PD*, *ETV4*, *KIF20A*, *LATPM4B*, *TRAF5*, and *SLC2A1*. *G6PD*, an essential rate-limiting enzyme of the pentose phosphate pathway, exhibits notable upregulation in HCC patients. *G6PD* was reported as a promoter in tumor growth, invasion, and metastasis, correlating with a poor prognosis. Concurrently, *G6PD* suppresses ferroptosis by downregulating *POR* expression. Targeting *G6PD* could potentially inhibit the progression of HCC (54, 55). *ETV4* expression was upregulated in HCC tissues, involved in the modulation of numerous oncogenes, proteins, and signaling pathways, thereby contributing to HCC progression (56). Increased *KIF20A* expression has been observed in mouse HCC models and could promote tumor proliferation. Knockdown of *KIF20A* in human HCC cell lines could also suppress cell growth and enhance their sensitivities to sorafenib and cisplatin (57, 58). *LATPM4B*, which was overexpressed in HCC, induced malignant behaviors, including proliferation, migration-invasion, and stem cell phenotypes (59, 60). *TRAF5* enhanced the ability of HCC in proliferation and invasion-metastasis. Reduction of *TRAF5* could induce necroptosis, thereby impeding HCC progression (61, 62). *SLC2A1* expression was upregulated in numerous solid tumors, including HCC. *SLC2A1* could promote HCC progression, and suppressing *SLC2A1* could induce immunogenic cell death in HCC (63, 64). Currently, few studies have addressed the role of *GBA* in HCC. One study suggested that *GBA* may be implicated in the antineoplastic activity of artemisinin against HCC (65). These results illuminated the complex involvement of the PCDI genes in

HCC. In our study, we also performed a multilevel investigation of PCDI genes based on single-cell transcriptomic data, transcriptomic data, proteomic data, and IHC data. At the single-cell level, we provided a possible explanation for the correlation between PCDI and biological characteristics in patients with HCC. PCDI genes are primarily expressed in malignant cells and are also observed in certain immune and stromal cells such as TAMs and CAFs. These findings suggested the presence of massive active tumor cells and a suppressive immune microenvironment in the tumor tissues of patients with high PCDI scores. This was consistent with the TME characteristics of patients in the high PCDI score group. At the mRNA and protein levels, our findings further validated the oncogenic potential of PCDI genes. Furthermore, we investigated the role of *GBA* in HCC. Single-cell analysis revealed that *GBA* is predominantly expressed in malignant cells, TAMs, and TECs. Concurrently, *GBA* promoted the formation of cellular communication between malignant cells and other cells, particularly between malignant cells and TAMs, TECs, and CAFs. Upon activation of specific signaling pathways, *GBA* could enhance malignant behaviors such as proliferation, invasion, metastasis, and angiogenesis. These observations provided preliminary evidence for the oncogenic role of *GBA* in HCC. In addition, we conducted more deep experimental studies subsequently. In HCC patient specimens, we validated the expression pattern of *GBA*, observing a significant upregulation of *GBA* expression in tumor tissues at both mRNA and protein levels. This result was consistent with relevant transcriptomic, proteomic, and IHC data. Next, we found *GBA* was intricately engaged in biological processes, including cell cycle regulation and EMT. Functional experiments and WB analysis further substantiated that *GBA* knockdown notably diminished the proliferative, migratory, and invasive capacity of HCC cells, which aligned with the results of single-cell analysis. Therefore, our findings exhibited novel evidence regarding the role of *GBA* in HCC. *GBA* promoted the malignant behaviors in HCC, including proliferation, invasion, and metastasis. In summary, our findings extended the understanding of PCDI genes in HCC and thereby enhanced the credibility of PCDI as a biomarker.

Subsequently, the PCDI was further validated. The PCDI exhibited robust predictive efficiency for clinical prognosis. In TCGA-LIHC dataset, we observed a significant correlation between the PCDI and clinical staging, pathological grade, T staging, and vascular invasion status among patients. The PCDI also emerged as an independent risk factor for the OS, PFS, DFS, and DSS. The accuracy and stability of the PCDI in predicting prognosis were assessed by ROC curves, C-index curves, and DCA curves, obviously outperforming other clinical indicators. These findings were independently validated in both the GSE76427 and ICGC-LIRI-JP datasets. Moreover, we compared the PCDI with 102 different prognostic models published in recent years. Most models exhibited good performance in the training dataset (TCGA-LIHC). However, the predictive performance obviously declined in the validation datasets (GSE76427 and ICGC-LIRI-JP). This decline should be attributed to overfitting in models developed through a single algorithm, resulting in reduced model generalizability. Notably, despite the decreased predictive performance in the validation datasets, the PCDI maintained superior performance over nearly all other models during the comparative analysis. This suggests that dimension reduction through the combination of machine learning algorithms is an effective approach for improving model generalizability. To assess the practical utility of PCDI in clinical settings, we developed clinical nomograms across the three datasets. Moreover, we observed a significant correlation between PCDI score groups and PCD clusters. Patients in the high PCDI score group and in PCD cluster A demonstrated a substantial overlap in sample distribution, indicating similar unfavorable prognoses and biological functional features. The alignment between PCDI score groups and PCD clusters undeniably bolstered the credibility of PCDI. In conclusion, these findings highlighted the superior predictive performance of the PCDI in clinical prognosis, affirming its suitability as a novel biomarker for prognostic evaluation in HCC patients.

The PCDI exhibited robust predictive efficiency for the immunotherapeutic responses of HCC patients. In the high PCDI score group, we observed a conspicuous immunosuppressive microenvironment characterized by enhanced immunosuppressive cell infiltration, including M2 macrophages, Treg cells, and neutrophils, along with impaired antitumor immune functions such as IFN response and T-cell co-stimulation, resembling the immunological features of cluster A. In addition, we discerned a significant positive correlation between stemness score and PCDI score, aligning with a previous study associating tumor stem cell status with immunological characteristics in solid tumors. This stem cell phenotype was found to inhibit anti-tumor immune functions (66). Given the close relationship between PCDI and immunological characteristics in HCC patients, we further investigated the potential of PCDI for predicting immunotherapeutic responses. Our results indicated that HCC patients in the high PCDI score group displayed elevated gene mutation frequencies. *TP53* was the most frequently mutated gene in the high PCDI score group, while *CTNNB1* was the most frequently mutated one in the low PCDI score group. Studies have shown that *TP53* and *CTNNB1* mutations are common in HCC, usually occurring in the early stages. *TP53* mutations lead to the loss of P53 function and could promote the recruitment of immunosuppressive cells, whereas *CTNNB1* mutations could enhance immune evasion and resistance to immunotherapy in tumor cells (67). Furthermore, we found a significant positive correlation between the PCDI score, TMB and MSI levels, and the expressions of most ICGs. TMB, MSI, and ICG expression patterns were considered crucial indicators for predicting immunotherapeutic responses in tumor patients. It is widely accepted that increased levels of TMB, MSI, and ICG expression correlated with a higher likelihood of positive responses to immunotherapy (33, 68–70). Therefore, we posit that HCC patients with higher PCDI scores could benefit more from immunotherapy. Subsequently, we validated this hypothesis through the TIDE algorithm. By calculating the TIDE scores, we observed that patients in the high PCDI score group exhibited significantly decreased TIDE scores. This suggested that patients with higher PCDI scores were more responsive to immunotherapy. Subsequent correlation analysis validated that the immunotherapeutic response rates of patients in the high PCDI score group were significantly higher than those in the low PCDI score group. These results provided more compelling evidence that the PCDI could predict immunotherapy responses in HCC

patients. Thereafter, a more comprehensive study was conducted to assess the predictive ability of PCDI in immunotherapeutic responses across multiple immunotherapy cohorts. Our findings revealed that in the IMvigor210, GSE176307, Checkmate, GSE179351, GSE103668, and GSE78220 cohorts, patients who responded to immunotherapy were predominantly found in the high PCDI score group. In the GSE35640 and GSE120644 cohorts, patients who responded to immunotherapy were primarily in the low PCDI score group. In the GSE91061 cohort, immunotherapeutic responses seemed unrelated to PCDI scores. In summary, the PCDI demonstrated excellent predictive capability regarding immunotherapy responses. Higher PCDI scores were associated with a greater likelihood of tumor patients benefiting from immunotherapy. These results highlighted the PCDI as a valuable tool for predicting the immunotherapy responses of tumor patients. In particular, HCC patients with higher PCDI scores were more suitable candidates for immunotherapy.

Additionally, we found that the PCDI could be employed to predict the chemotherapeutic sensitivity of patients with HCC. The expression levels of most CRRGs in patients with HCC showed a significant positive correlation with the PCDI score. This observation suggested that the PCDI could serve as an effective indicator for assessing chemotherapeutic resistance. Patients with higher PCDI scores may exhibit heightened resistance to chemotherapy. In the two HCC treatment cohorts, GSE109211 and GSE104580, we observed that patients with lower PCDI scores were more responsive to sorafenib and TACE treatments. When comparing the imputed sensitivity scores of drugs, HCC patients with lower PCDI scores demonstrated heightened sensitivity to oxaliplatin, whereas those with higher PCDI scores exhibited heightened sensitivity to inhibitors of cell mitosis and proliferation, such as paclitaxel, docetaxel, and vinblastine, as well as certain targeted drugs and small molecule inhibitors such as cediranib, bortezomib, MIM1, MK-1775, and WIKI4. In summary, the PCDI exhibited remarkable predictive efficacy in assessing the responses of HCC patients to various therapies, including immunotherapy. Overall, it holds promise as a novel biomarker for guiding personalized treatment in HCC.

Although we have demonstrated the robust performance and clinical value of the PCDI, it is necessary to recognize several constraints inherent in this study. Firstly, the data used here were all sourced from public databases, classifying it as a retrospective study. During the data processing phase, we excluded samples with incomplete clinical data, which reduced the usage of samples and might have influenced the analytical outcomes. Consequently, large-scale prospective studies are still necessary to comprehensively evaluate the precise value of the PCDI. Secondly, we provided a comprehensive landscape of the PCDI genes across multiple levels, including the transcriptome, proteome, and single-cell analyses. We also discussed the role of PCDI genes in HCC development based on existing research. Moreover, we contributed new experimental evidence supporting the role of GBA in the progression of HCC. All of these enhance the reliability of the PCDI as a biomarker for HCC. However, further research is necessary to elucidate the detailed mechanisms by which these genes regulate HCC progression and therapy responses. Lastly, additional therapeutic cohorts involving HCC patients are needed to further validate the predictive value of the PCDI in treatment responses among HCC patients.

In conclusion, we systematically analyzed the correlation between 14 programmed cell death modes and the clinical characteristics and biological patterns of HCC. We constructed a precise and robust PCDI model through a comprehensive array of machine-learning algorithms. The PCDI demonstrated remarkable accuracy in predicting the prognosis and treatment responses of HCC patients. It served as an effective biomarker for heterogeneity delineation and risk stratification. The application of PCDI has the potential to facilitate personalized treatment and clinical management for HCC patients, representing a significant contribution to clinical practice.

Data availability statement

The datasets presented in this study can be found in online repositories. The names of the repository/repositories and accession number(s) can be found in the article/Supplementary Material.

Ethics statement

The studies involving humans were approved by Tongji Hospital Research Ethics Committee. The studies were conducted in accordance with the local legislation and institutional requirements. The participants provided their written informed consent to participate in this study.

Author contributions

YS: Conceptualization, Data curation, Formal analysis, Investigation, Methodology, Visualization, Writing – original draft. YF: Investigation, Visualization, Writing – original draft. PO: Data curation, Writing – review & editing. KZ: Data curation, Writing – review & editing. XL: Data curation, Writing – review & editing. ZD: Project administration, Supervision, Writing – review & editing. JW: Funding acquisition, Project administration, Resources, Supervision, Writing – review & editing.

Funding

The author(s) declare financial support was received for the research, authorship, and/or publication of this article. The work was supported by the National Natural Science Foundation of China (No. 81874062, No. 82072730).

Acknowledgments

Thanks to all authors participating in this study and the support from the National Natural Science Foundation of China (No. 81874062, No. 82072730), as well as all public databases and websites mentioned previously.

Conflict of interest

The authors declare that the research was conducted in the absence of any commercial or financial relationships that could be construed as a potential conflict of interest.

Publisher's note

All claims expressed in this article are solely those of the authors and do not necessarily represent those of their affiliated organizations, or those of the publisher, the editors and the reviewers. Any product that may be evaluated in this article, or claim that may be made by its manufacturer, is not guaranteed or endorsed by the publisher.

Supplementary material

The Supplementary Material for this article can be found online at: https://www.frontiersin.org/articles/10.3389/fimmu.2023.1298290/full#supplementary-material

References

1. Vogel A, Meyer T, Sapisochin G, Salem R, Saborowski A. Hepatocellular carcinoma. *Lancet* (2022) 400(10360):1345–62. doi: 10.1016/S0140-6736(22)01200-4

2. Llovet JM, Kelley RK, Villanueva A, Singal AG, Pikarsky E, Roayaie S, et al. Hepatocellular carcinoma. *Nat Rev Dis Primers* (2021) 7(1):6. doi: 10.1038/s41572-020-00240-3

3. Llovet JM, De Baere T, Kulik L, Haber PK, Greten TF, Meyer T, et al. Locoregional therapies in the era of molecular and immune treatments for hepatocellular carcinoma. *Nat Rev Gastroenterol Hepatol* (2021) 18(5):293–313. doi: 10.1038/s41575-020-00395-0

4. Brown ZJ, Tsilimigras DI, Ruff SM, Mohseni A, Kamel IR, Cloyd JM, et al. Management of hepatocellular carcinoma: A review. *JAMA Surg* (2023) 158(4):410–20. doi: 10.1001/jamasurg.2022.7989

5. Park J-W, Chen M, Colombo M, Roberts LR, Schwartz M, Chen P-J, et al. Global patterns of hepatocellular carcinoma management from diagnosis to death: the bridge study. *Liver Int* (2015) 35(9):2155–66. doi: 10.1111/liv.12818

6. Khatib S, Pomyen Y, Dang H, Wang XW. Understanding the cause and consequence of tumor heterogeneity. *Trends Cancer* (2020) 6(4):267–71. doi: 10.1016/j.trecan.2020.01.010

7. Dagogo-Jack I, Shaw AT. Tumour heterogeneity and resistance to cancer therapies. *Nat Rev Clin Oncol* (2018) 15(2):81–94. doi: 10.1038/nrclinonc.2017.166

8. Peng F, Liao M, Qin R, Zhu S, Peng C, Fu L, et al. Regulated cell death (Rcd) in cancer: key pathways and targeted therapies. *Signal Transduct Target Ther* (2022) 7 (1):286. doi: 10.1038/s41392-022-01110-y

9. Liu X, Nie L, Zhang Y, Yan Y, Wang C, Colic M, et al. Actin cytoskeleton vulnerability to disulfide stress mediates disulfidptosis. *Nat Cell Biol* (2023) 25(3):404–14. doi: 10.1038/s41556-023-01091-2

10. Tsvetkov P, Coy S, Petrova B, Dreishpoon M, Verma A, Abdusamad M, et al. Copper induces cell death by targeting lipoylated tca cycle proteins. *Science* (2022) 375 (6586):1254–61. doi: 10.1126/science.abf0529

11. Xie J, Yang Y, Gao Y, He J. Cuproptosis: mechanisms and links with cancers. *Mol Cancer* (2023) 22(1):46. doi: 10.1186/s12943-023-01732-y

12. Carneiro BA, El-Deiry WS. Targeting apoptosis in cancer therapy. *Nat Rev Clin Oncol* (2020) 17(7):395–417. doi: 10.1038/s41571-020-0341-y

13. Galluzzi L, Vitale I, Aaronson SA, Abrams JM, Adam D, Agostinis P, et al. Molecular mechanisms of cell death: recommendations of the nomenclature committee on cell death 2018. *Cell Death Differ* (2018) 25(3):486–541. doi: 10.1038/s41418-017-0012-4

14. Gilmore AP. Anoikis. *Cell Death Differ* (2005) 12 Suppl 2:1473–7. doi: 10.1038/sj.cdd.4401723

15. Song J, Liu Y, Liu F, Zhang L, Li G, Yuan C, et al. The 14-3-3σ Protein promotes hcc anoikis resistance by inhibiting egfr degradation and thereby activating the egfr-dependent erk1/2 signaling pathway. *Theranostics* (2021) 11(3). doi: 10.7150/thno.51646

16. Christofferson DE, Yuan J. Necroptosis as an alternative form of programmed cell death. *Curr Opin Cell Biol* (2010) 22(2):263–8. doi: 10.1016/j.ceb.2009.12.003

17. Yan J, Wan P, Choksi S, Liu Z-G. Necroptosis and tumor progression. *Trends Cancer* (2022) 8(1):21–7. doi: 10.1016/j.trecan.2021.09.003

18. Dixon SJ, Lemberg KM, Lamprecht MR, Skouta R, Zaitsev EM, Gleason CE, et al. Ferroptosis: an iron-dependent form of nonapoptotic cell death. *Cell* (2012) 149 (5):1060–72. doi: 10.1016/j.cell.2012.03.042

19. Lei G, Zhuang L, Gan B. Targeting ferroptosis as a vulnerability in cancer. *Nat Rev Cancer* (2022) 22(7):381–96. doi: 10.1038/s41568-022-00459-0

20. Yu P, Zhang X, Liu N, Tang L, Peng C, Chen X. Pyroptosis: mechanisms and diseases. *Signal Transduct Target Ther* (2021) 6(1):128. doi: 10.1038/s41392-021-00507-5

21. Wei X, Xie F, Zhou X, Wu Y, Yan H, Liu T, et al. Role of pyroptosis in inflammation and cancer. *Cell Mol Immunol* (2022) 19(9):971–92. doi: 10.1038/s41423-022-00905-x

22. Mizushima N, Komatsu M. Autophagy: renovation of cells and tissues. *Cell* (2011) 147(4):728–41. doi: 10.1016/j.cell.2011.10.026

23. Levy JMM, Towers CG, Thorburn A. Targeting autophagy in cancer. *Nat Rev Cancer* (2017) 17(9):528–42. doi: 10.1038/nrc.2017.53

24. Fatokun AA, Dawson VL. Dawson TM. Parthanatos: mitochondrial-linked mechanisms and therapeutic opportunities. *Br J Pharmacol* (2014) 171(8):2000–16. doi: 10.1111/bph.12416

25. Overholtzer M, Mailleux AA, Mouneimne G, Normand G, Schnitt SJ, King RW, et al. A nonapoptotic cell death process, entosis, that occurs by cell-in-cell invasion. *Cell* (2007) 131(5):966–79. doi: 10.1016/j.cell.2007.10.040

26. Brinkmann V, Reichard U, Goosmann C, Fauler B, Uhlemann Y, Weiss DS, et al. Neutrophil extracellular traps kill bacteria. *Science* (2004) 303(5663):1532–5. doi: 10.1126/science.1092385

27. McDonald B, Urrutia R, Yipp BG, Jenne CN, Kubes P. Intravascular neutrophil extracellular traps capture bacteria from the bloodstream during sepsis. *Cell Host Microbe* (2012) 12(3):324–33. doi: 10.1016/j.chom.2012.06.011

28. Gómez-Sintes R, Ledesma MD, Boya P. Lysosomal cell death mechanisms in aging. *Ageing Res Rev* (2016) 32:150–68. doi: 10.1016/j.arr.2016.02.009

29. Song X, Zhu S, Xie Y, Liu J, Sun L, Zeng D, et al. Jtc801 induces ph-dependent death specifically in cancer cells and slows growth of tumors in mice. *Gastroenterology* (2018) 154(5):1480–93. doi: 10.1053/j.gastro.2017.12.004

30. Chen F, Zhu S, Kang R, Tang D, Liu J. Atp6v0d1 promotes alkaliptosis by blocking stat3-mediated lysosomal ph homeostasis. *Cell Rep* (2023) 42(1):111911. doi: 10.1016/j.celrep.2022.111911

31. Holze C, Michaudel C, Mackowiak C, Haas DA, Benda C, Hubel P, et al. Oxeiptosis, a ros-induced caspase-independent apoptosis-like cell-death pathway. *Nat Immunol* (2018) 19(2):130–40. doi: 10.1038/s41590-017-0013-y

32. Tang D, Kang R, Berghe TV, Vandenabeele P, Kroemer G. The molecular machinery of regulated cell death. *Cell Res* (2019) 29(5):347–64. doi: 10.1038/s41422-019-0164-5

33. Hu F-F, Liu C-J, Liu L-L, Zhang Q, Guo A-Y. Expression profile of immune checkpoint genes and their roles in predicting immunotherapy response. *Brief Bioinform* (2021) 22(3). doi: 10.1093/bib/bbaa176

34. Marin JJG, Macias RIR, Monte MJ, Romero MR, Asensio M, Sanchez-Martin A, et al. Molecular bases of drug resistance in hepatocellular carcinoma. *Cancers (Basel)* (2020) 12(6). doi: 10.3390/cancers12061663

35. Mariathasan S, Turley SJ, Nickles D, Castiglioni A, Yuen K, Wang Y, et al. Tgfβ Attenuates tumour response to pd-L1 blockade by contributing to exclusion of T cells. *Nature* (2018) 554(7693):544–8. doi: 10.1038/nature25501

36. Braun DA, Hou Y, Bakouny Z, Ficial M, Sant' Angelo M, Forman J, et al. Interplay of somatic alterations and immune infiltration modulates response to pd-1 blockade in advanced clear cell renal cell carcinoma. *Nat Med* (2020) 26(6):909–18. doi: 10.1038/s41591-020-0839-y

37. Ma L, Hernandez MO, Zhao Y, Mehta M, Tran B, Kelly M, et al. Tumor cell biodiversity drives microenvironmental reprogramming in liver cancer. *Cancer Cell* (2019) 36(4). doi: 10.1016/j.ccell.2019.08.007

38. Dobin A, Davis CA, Schlesinger F, Drenkow J, Zaleski C, Jha S, et al. Star: ultrafast universal rna-seq aligner. *Bioinformatics* (2013) 29(1):15–21. doi: 10.1093/bioinformatics/bts635

39. Krenzien F, Schmelzle M, Struecker B, Raschzok N, Benzing C, Jara M, et al. Liver transplantation and liver resection for cirrhotic patients with hepatocellular

carcinoma: comparison of long-term survivals. *J Gastrointestinal Surg Off J Soc For Surg Alimentary Tract* (2018) 22(5):840–8. doi: 10.1007/s11605-018-3690-4

40. Llovet JM, Ricci S, Mazzaferro V, Hilgard P, Gane E, Blanc J-F, et al. Sorafenib in advanced hepatocellular carcinoma. *N Engl J Med* (2008) 359(4):378–90. doi: 10.1056/NEJMoa0708857

41. Kudo M, Finn RS, Qin S, Han K-H, Ikeda K, Piscaglia F, et al. Lenvatinib versus sorafenib in first-line treatment of patients with unresectable hepatocellular carcinoma: A randomised phase 3 non-inferiority trial. *Lancet* (2018) 391(10126):1163–73. doi: 10.1016/S0140-6736(18)30207-1

42. Bruix J, Qin S, Merle P, Granito A, Huang Y-H, Bodoky G, et al. Regorafenib for patients with hepatocellular carcinoma who progressed on sorafenib treatment (Resorce): A randomised, double-blind, placebo-controlled, phase 3 trial. *Lancet* (2017) 389(10064):56–66. doi: 10.1016/S0140-6736(16)32453-9

43. Abou-Alfa GK, Meyer T, Cheng A-L, El-Khoueiry AB, Rimassa L, Ryoo B-Y, et al. Cabozantinib in patients with advanced and progressing hepatocellular carcinoma. *N Engl J Med* (2018) 379(1):54–63. doi: 10.1056/NEJMoa1717002

44. Zhu AX, Kang Y-K, Yen C-J, Finn RS, Galle PR, Llovet JM, et al. Ramucirumab after sorafenib in patients with advanced hepatocellular carcinoma and increased A-fetoprotein concentrations (Reach-2): A randomised, double-blind, placebo-controlled, phase 3 trial. *Lancet Oncol* (2019) 20(2):282–96. doi: 10.1016/S1470-2045(18)30937-9

45. Finn RS, Qin S, Ikeda M, Galle PR, Ducreux M, Kim T-Y, et al. Atezolizumab plus bevacizumab in unresectable hepatocellular carcinoma. *N Engl J Med* (2020) 382 (20):1894–905. doi: 10.1056/NEJMoa1915745

46. Su Y, Sai Y, Zhou L, Liu Z, Du P, Wu J, et al. Current insights into the regulation of programmed cell death by tp53 mutation in cancer. *Front Oncol* (2022) 12:1023427. doi: 10.3389/fonc.2022.1023427

47. Prieto J, Melero I, Sangro B. Immunological landscape and immunotherapy of hepatocellular carcinoma. *Nat Rev Gastroenterol Hepatol* (2015) 12(12):681–700. doi: 10.1038/nrgastro.2015.173

48. Hoshida Y, Nijman SMB, Kobayashi M, Chan JA, Brunet J-P, Chiang DY, et al. Integrative transcriptome analysis reveals common molecular subclasses of human hepatocellular carcinoma. *Cancer Res* (2009) 69(18):7385–92. doi: 10.1158/0008-5472.CAN-09-1089

49. Llovet JM, Pinyol R, Kelley RK, El-Khoueiry A, Reeves HL, Wang XW, et al. Molecular pathogenesis and systemic therapies for hepatocellular carcinoma. *Nat Cancer* (2022) 3(4):386–401. doi: 10.1038/s43018-022-00357-2

50. He Q, Yang J, Jin Y. Immune infiltration and clinical significance analyses of the coagulation-related genes in hepatocellular carcinoma. *Brief Bioinform* (2022) 23(4). doi: 10.1093/bib/bbac291

51. Zeng Z, Lei S, Wang J, Yang Y, Lan J, Tian Q, et al. A novel hypoxia-driven gene signature that can predict the prognosis of hepatocellular carcinoma. *Bioengineered* (2022) 13(5):12193–210. doi: 10.1080/21655979.2022.2073943

52. Liu R, Liu Y, Zhang F, Wei J, Wu L. A cuproptosis random forest cox score model-based evaluation of prognosis, mutation characterization, immune infiltration, and drug sensitivity in hepatocellular carcinoma. *Front Immunol* (2023) 14:1146411. doi: 10.3389/fimmu.2023.1146411

53. Pinto Marques H, Gomes da Silva S, De Martin E, Agopian VG, Martins PN. Emerging biomarkers in hcc patients: current status. *Int J Surg* (2020) 82S:70–6. doi: 10.1016/j.ijsu.2020.04.043

54. Du D, Liu C, Qin M, Zhang X, Xi T, Yuan S, et al. Metabolic dysregulation and emerging therapeutical targets for hepatocellular carcinoma. *Acta Pharm Sin B* (2022) 12(2):558–80. doi: 10.1016/j.apsb.2021.09.019

55. Cao F, Luo A, Yang C. G6pd inhibits ferroptosis in hepatocellular carcinoma by targeting cytochrome P450 oxidoreductase. *Cell Signal* (2021) 87:110098. doi: 10.1016/j.cellsig.2021.110098

56. Craig AJ, Silveira MAD. The role of etv4 in hcc: how transcription factors can inform immunotherapy combination treatments. *J Hepatol* (2023) 79(1):19–21. doi: 10.1016/j.jhep.2023.04.005

57. Blanc V, Riordan JD, Soleymanjahi S, Nadeau JH, Nalbantoglu I, Xie Y, et al. Apobec1 complementation factor overexpression promotes hepatic steatosis, fibrosis, and hepatocellular cancer. *J Clin Invest* (2021) 131(1). doi: 10.1172/JCI138699

58. Wu C, Qi X, Qiu Z, Deng G, Zhong L. Low expression of kif20a suppresses cell proliferation, promotes chemosensitivity and is associated with better prognosis in hcc. *Aging (Albany NY)* (2021) 13(18):22148–63. doi: 10.18632/aging.203494

59. Yang H, Xiong F, Wei X, Yang Y, McNutt MA, Zhou R. Overexpression of laptm4b-35 promotes growth and metastasis of hepatocellular carcinoma *in vitro* and *in vivo*. *Cancer Lett* (2010) 294(2):236–44. doi: 10.1016/j.canlet.2010.02.006

60. Liao J, Wang J, Xu Y, Wu Y, Wang M, Zhao Q, et al. Laptm4b-yap loop feedback amplification enhances the stemness of hepatocellular carcinoma. *iScience* (2023) 26 (6):106754. doi: 10.1016/j.isci.2023.106754

61. Ding G, Zeng Y, Yang D, Zhang C, Mao C, Xiao E, et al. Silenced lncrna ddx11-as1 or up-regulated microrna-34a-3p inhibits Malignant phenotypes of hepatocellular carcinoma cells via suppression of traf5. *Cancer Cell Int* (2021) 21(1):179. doi: 10.1186/s12935-021-01847-6

62. Wu G, Wu F, Zhou YQ, Lu W, Hu FL, Fan X. Silencing of traf5 enhances necroptosis in hepatocellular carcinoma by inhibiting ltbr-mediated nf-Kb signaling. *PeerJ* (2023) 11:e15551. doi: 10.7717/peerj.15551

63. Amann T, Hellerbrand C. Glut1 as a therapeutic target in hepatocellular carcinoma. *Expert Opin Ther Targets* (2009) 13(12):1411–27. doi: 10.1517/14728220903307509

64. Li Y, Song Z, Han Q, Zhao H, Pan Z, Lei Z, et al. Targeted inhibition of stat3 induces immunogenic cell death of hepatocellular carcinoma cells via glycolysis. *Mol Oncol* (2022) 16(15):2861–80. doi: 10.1002/1878-0261.13263

65. Chen W, Ma Z, Yu L, Mao X, Ma N, Guo X, et al. Preclinical investigation of artesunate as a therapeutic agent for hepatocellular carcinoma via impairment of glucosylceramidase-mediated autophagic degradation. *Exp Mol Med* (2022) 54 (9):1536–48. doi: 10.1038/s12276-022-00780-6

66. Miranda A, Hamilton PT, Zhang AW, Pattnaik S, Becht E, Mezheyeuski A, et al. Cancer stemness, intratumoral heterogeneity, and immune response across cancers. *Proc Natl Acad Sci USA* (2019) 116(18):9020–9. doi: 10.1073/pnas.1818210116

67. Montironi C, Castet F, Haber PK, Pinyol R, Torres-Martin M, Torrens L, et al. Inflamed and non-inflamed classes of hcc: A revised immunogenomic classification. *Gut* (2023) 72(1):129–40. doi: 10.1136/gutjnl-2021-325918

68. Marabelle A, Fakih M, Lopez J, Shah M, Shapira-Frommer R, Nakagawa K, et al. Association of tumour mutational burden with outcomes in patients with advanced solid tumours treated with pembrolizumab: prospective biomarker analysis of the multicohort, open-label, phase 2 keynote-158 study. *Lancet Oncol* (2020) 21(10):1353–65. doi: 10.1016/S1470-2045(20)30445-9

69. Ganesh K, Stadler ZK, Cercek A, Mendelsohn RB, Shia J, Segal NH, et al. Immunotherapy in colorectal cancer: rationale, challenges and potential. *Nat Rev Gastroenterol Hepatol* (2019) 16(6):361–75. doi: 10.1038/s41575-019-0126-x

70. Palmeri M, Mehnert J, Silk AW, Jabbour SK, Ganesan S, Popli P, et al. Real-world application of tumor mutational burden-high (Tmb-high) and microsatellite instability (Msi) confirms their utility as immunotherapy biomarkers. *ESMO Open* (2022) 7(1):100336. doi: 10.1016/j.esmoop.2021.100336

frontiers | Frontiers in Immunology

TYPE Original Research
PUBLISHED 04 January 2024
DOI 10.3389/fimmu.2023.1272108

OPEN ACCESS

EDITED BY
Takaji Matsutani,
Maruho, Japan

REVIEWED BY
Hanren Dai,
The First Affiliated Hospital of Anhui Medical University, China
Xiaojing Chang,
Second Hospital of Hebei Medical University, China
Chengliang Zhang,
Huazhong University of Science and Technology, China

*CORRESPONDENCE
Chuan Tong
tc6636@sina.com
Yao Wang
wangyao301@163.com

†These authors have contributed equally to this work

RECEIVED 03 August 2023
ACCEPTED 11 December 2023
PUBLISHED 04 January 2024

CITATION
Liu Y, Zhu J, Shen J, Lu Y, Pan K, Tong C and Wang Y (2024) A pan-cancer analysis of the prognostic implication and oncogenic role of tubulin epsilon and delta complex 2 (TEDC2) in human tumors. *Front. Immunol.* 14:1272108. doi: 10.3389/fimmu.2023.1272108

A pan-cancer analysis of the prognostic implication and oncogenic role of tubulin epsilon and delta complex 2 (TEDC2) in human tumors

Yang Liu[1†], Jie Zhu[2†], Jing Shen[3†], Yuting Lu[4], Ke Pan[1], Chuan Tong[4*] and Yao Wang[4*]

[1]Faculty of Hepato-Pancreato-Biliary Surgery, the First Medical Centre, Chinese PLA General Hospital, Beijing, China, [2]Senior Departments of Urology, the Third Medical Centre, Chinese PLA General Hospital, Beijing, China, [3]Department of Endocrinology, the Eighth Medical Center of PLA General Hospital, Beijing, China, [4]Department of Bio-therapeutic, the First Medical Center, Chinese PLA General Hospital, Beijing, China

Introduction: Tubulin epsilon and delta complex 2 (TEDC2) is widely expressed in various human tissues and primarily governs centriole stability. However, the biological significance of TEDC2 in pan-cancer is unclear.

Methods: In this study, we employed R software and various online bioinformatics analysis tools to investigate the functional attributes of TEDC2 in human tumours and its potential involvement in immune response. The status of TEDC2 expression was evaluated in samples from the TCGA and GEO datasets, as well as in tumour and corresponding normal samples from the TCGA database. Subsequently, Kaplan-Meier estimates, clinical correlations, and univariate Cox regressions were used to analyze the 33 types of tumors from TCGA and determine the prognostic significance of TEDC2. Moreover, nomogram models were formulated using three distinct tumours, namely kidney renal clear cell carcinoma (KIRC), lung adenocarcinoma (LUAD), and liver hepatocellular carcinoma (LIHC), to evaluate the prognostic significance of TEDC2 in tumours. Furthermore, TEDC2 was investigated for its correlation with the levels of immune cell infiltration, and a functional enrichment analysis was conducted to identify potential signalling pathways involving TEDC2.

Results: Differential analysis revealed that 16 tumour types expressed TEDC2 to a greater extent than normal tissues. The abnormal expression of TEDC2 can predict survival outcomes in patients with adrenocortical carcinoma (ACC), KIRC, kidney renal papillary cell carcinoma (KIRP), LUAD, LIHC, lower grade glioma (LGG), and thymoma (THYM). Subsequent results indicated that TEDC2 has the ability to influence ECM regulators, cell cycle, and Immune checkpoint-associated signalling pathways, which could potentially lead to a poor prognosis and tumour progression.

Discussion: TEDC2 has been identified as a potential therapeutic target that could predict the prognosis of multiple tumour types, making it a promising target for reversing tumour development.

KEYWORDS

immune infiltration, tumor microenvironment, pan-cancer, prognosis, TEDC2

Introduction

Globally, tumors pose a serious threat to public health, with incidence and mortality rates on the rise (1, 2). Despite significant advancements in tumor diagnosis and treatment, the 5-year overall survival rate for most tumors remains dismal (3). Therefore, there is an urgent need for novel approaches to diagnose and treat tumors. Currently, the utilization of tumor biomarkers has greatly enhanced the prognosis in certain types of tumors (4–6).

The rapid advancements in next-generation sequencing and bioinformatics have facilitated the accumulation of data, enabling a comprehensive understanding of the intricate biological characteristics of tumors from various perspectives. Concurrently, a growing number of databases, such as the Gene Expression Omnibus (GEO) and The Tumor Genome Atlas (TCGA), have been established to comprehensively analyze the pathogenesis of cancer. These databases have conducted molecular characterizations on more than 20,000 primary tumors and their corresponding normal samples, encompassing 33 different types of cancer. In a recent study, Pan et al. employed a pan cancer analysis approach to investigate the impact of abnormal expression of the RUNX gene on the prognosis of diverse tumors (7). This analysis involved the utilization of TCGA multi-omics data in conjunction with various online tools. Similarly, Xie et al. developed a "FOXOs score" system based on the TCGA database, which demonstrated a correlation with multiple immune features and the ability to accurately predict treatment efficacy across various GEO datasets (8). Consequently, the utilization of these extensive and multi-omics tumor datasets can serve as an effective means of identifying potential tumor biomarkers.

Tubulin epsilon and delta complex 2 (TEDC2), also named Chromosome 16 open reading frame 59 (C16orf59), is a protein coding gene. Some studies reported that TEDC2 is involved in the regulation of centriole stability, ciliary hedgehog signaling, and might contribute to the tumorigenesis of LUAD (9, 10) and central nervous system lymphoma (11), but no comprehensive study have been conducted on the immune characteristics and prognostic of TEDC2 in tumors. Furthermore, Meng et al. employed the monozygotic twin-pair database to identify alterations in DNA methylation subsequent to alcohol consumption (12). Their findings revealed a significant correlation between elevated methylation levels of cg07326074, situated within the TEDC2 gene, and alcohol intake. It is worth noting that prolonged alcohol consumption has been associated with immune dysfunction in the body (13), and it is widely recognized as a prominent risk factor in the development of diverse tumors (14–16). The observed methylation patterns linked to alcohol consumption are hypothesized to impact the functionality of the TEDC2 gene. Currently, there are no reports on the role of TEDC2 in pan-cancer. Therefore, we investigated the mechanisms of TEDC2 in tumors and its correlation with immune infiltration. In our study, we found that the expression of TEDC2 was unregulated in the majority of tumors, thereby affecting the prognosis of ACC, KIRC, KIRP, LUSC, LIHC, and MESO. According to immune infiltration analysis, TEDC2 expression was associated with multiple immune cells, and might affect tumor survival. Furthermore, enrichment analysis indicated that TEDC2 may be involved in the tumorigenesis by the cell cycle, ECM regulators, and Immune checkpoint-associated signaling pathways. Collectively, these findings indicate that TEDC2 plays multifaceted roles across tumors, can influence the prognosis and immune infiltration of some tumors, and could become a novel biomarker.

Materials and methods

Data acquisition

Expression profile data for 33 tumors and corresponding clinical data were obtained from The Cancer Genome Atlas (TCGA, https://portal.gdc.cancer.gov/). Additionally, the RNA-seq data of GSE10927 (10 normal tissues, 55 tumorous tissues), GSE15641 (23 normal tissues, 69 tumorous tissues), GSE36376 (193 normal tissues, 240 tumorous tissues), GSE51575 (26 normal tissues, 26 tumorous tissues), GSE63514 (24 normal tissues, 28 tumorous tissues), GSE116959 (11 normal tissues, 57 tumorous tissues), GSE13213 (117 tumorous tissues), GSE3141 (111 tumorous tissues), GSE214992 (32 cell line samples) and GSE91061 (37 tumorous tissues) were downloaded from Gene Expression Omnibus (GEO, https://www.ncbi.nlm.nih.gov/). The 100 genes most closely related to TEDC2 were obtained from The Gene Expression Profiling Interactive Analysis database (GEPIA2, http://gepia2.tumor-pku.cn/#index). The protein–protein interaction (PPI) network was analyzed in STRING (https://cn.string-db.org/).

Expression analysis of TEDC2

The mRNA expression levels of TEDC2 in normal tissues and tumors were analyzed and visualized using the ggplot2 package (version 3.4.2). The representative immunohistochemical results of TEDC2 in tumor tissues were obtained from the Human Protein Atlas (HPA, https://www.proteinatlas.org/).

Diagnostic and prognostic value of TEDC2

Kaplan–Meier survival analysis was employed to assess the association between TEDC2 expression and clinical outcomes, including overall survival (OS), disease specific survival (DSS), and progression free interval (PFI) in TCGA datasets. In addition, a receiver operating characteristic curve (ROC) was drawn for tumors in which TEDC2 affects prognosis. The ggplot2 package (version 3.4.2) was used to analyze and visualize the correlation between TEDC2 expression and multiple clinical parameters such as age, gender and pathologic stage.

Univariate Cox regression analysis of factors related to OS was performed for tumors in which TEDC2 affects prognosis. Tumors with $p < 0.05$ and three representative tumors (KIRC, LUAD, LIHC) were selected as the training set for constructing a nomogram model. Calibration curves were generated to assess the prediction accuracy of the nomograms at 1, 3, and 5 years.

Genetic alteration analysis

cBioPortal database (https://www.cbioportal.org/) (17, 18) was used to estimate TEDC2 genetic alterations in tumors using data from the TCGA Pan-Cancer Atlas Studies. According to the data set of TCGA Pan-Cancer Atras Studies, we calculated the mutation frequency and copy number change of TEDC2 gene in the "Cancer Type Summary" module. A mutation site plot of TEDC2 was created using the "Mutations" module.

To analyze the correlation between TEDC2 mutation status and SKCM, BRCA, and UCES prognosis, the molecular profile was selected as mutations based on "skin cutaneous melanoma (TCGA Pan-Cancer)", "breast invasive carcinoma (TCGA Pan-Cancer)", "uterine corpus endometrial carcinoma (TCGA Pan-Cancer)", and the survival plot was generated by dividing cases into altered and unaltered groups.

Immune infiltration analysis

The GSVA package (version 1.48.0) was used to perform Spearman correlation analysis of TEDC2 expression and immune cell infiltration, including activated DC (aDC), DC, immature DC (iDC), plasmacytoid DC (pDC), macrophages, mast cells, neutrophils, eosinophils, cytotoxic cells, B cells, NK cells, NK CD56bright cells, NK CD56dim cells, T cells, CD8 T cells, T central memory (Tcm), T effector memory (Tem), T helper cells, T gamma delta (Tgd), T follicular helper (Tfh), Th1 cells, Th2 cells, Th17 cells and Treg (19, 20).

Functional enrichment analysis and PPI network analysis

The GEPIA2 database was used to obtain the 100 genes most closely related to TEDC2. We performed Gene Ontology (GO) analysis, which includes biological pathway (BP), and molecular function (MF) and cellular component (CC) categories. We also performed Kyoto Encyclopedia of Genes and Genomes (KEGG) analysis based on the TEDC2 related genes to further explore the potential functions of TEDC2. Additionally, a PPI network of the 100 TEDC2 related genes was created from the STRING database (21), and the top 10 molecules were extracted by the cytoHubba plugin in the Cytoscape (version 3.7.1) software.

Differential expression analysis and gene set enrichment analysis

Samples were divided into high and low groups based on the median expression level of TEDC2. DESeq2 package (version 1.40.1) was used to analyze differential expression of TEDC2 in tumors in which can affect prognosis. Using $|\log2(FC)| > 2$ and $p.adj < 0.01$ as conditions for screening significantly different genes. Then, according to the results obtained from the differential expression analysis of TEDC2 in different tumors, GSEA was performed using the clusterProfiler package (version 4.8.0) (22, 23). Subsequently, these genes were enriched on the basis of the Hallmark gene sets database. Gene sets with normalized enrichment score (NES) > 1, and false discovery rate (FDR) < 0.05 were considered significant results.

Cell culture and transfection

Human normal liver cell line L02, human LUAD cell line A549 and human LIHC cell line HepG2 were obtained from the Cell Bank of the Chinese Academy of Sciences and cultured in Dulbecco's modified Eagle's medium (DMEM, Hyclone, USA) supplemented with 10% Fetal bovine serum (FBS, Gibco) and 100 units/mL penicillin at 37°C with 5% CO2. The small interfering RNAs (siRNAs) targeting human TEDC2 and a negative control were purchased from Shanghai Genechem Co., Ltd. The sequence of TEDC2 siRNA (siTEDC2) were 5'- GCGCACAGCGACA ATTGCAATTGGA-3', 5'- GCCAGAAACTAATGGAGAGGA-3' and the sequence negative control siRNA (siNC) was 5'-GCGGACAGCAACGTTAACTTCAGGA-3'. Transient transfections were conducted following the manufacturer's protocol (Entranster-R4000, Engreen Biosystem). A549 and HepG2 cells were seeded in 12 well plates one day prior to transfection and were transfected when the cell confluence reached 40%. The culture medium was replaced with fresh

medium after 6 hours of transfection. Finally, cells were harvested for further experiments after 24 hours of transfection.

Cell proliferation assays

To ascertain cellular proliferation, a quantity of 1×10^4 cells was introduced into a 24 well plate. The cells were cultivated in DMEM supplemented with 10% Fetal bovine serum, with the medium being refreshed on a daily basis. Subsequently, at 24, 48, 72 and 96 hour intervals, the cells were harvested, diluted with a trypan blue working solution, and enumerated using an automatic cell counter Arthur (NanoEntek, Germany) to establish a growth curve. Each measurement was performed in triplicate, and a minimum of three independent experiments were conducted.

Real-time PCR

The SYBR Premix Ex Taq was employed for the purpose of gene mRNA expression detection in various cell types through the utilization of real-time PCR on the ABI7500 instrument. In order to ensure consistency, three tests were conducted on each sample, with β-Actin serving as the standardization control. The relative mRNA concentration was determined by averaging the results of the three replicates, and the $2^{-\triangle\triangle CT}$ method was employed to calculate the expression levels. The specific primer sequence can be found in Supplementary Table 1.

Cell cycle assay

4×10^5 harvested cells were incubated in phosphate buffered saline (PBS, Hyclone, USA) containing 0.1% Triton X-100 (Sigma, USA) and 0.2 mg/mL RNaseA (Sigma, USA), followed by fixation in 75% alcohol at 4°C for 60 minutes. After three washes with cold PBS, 7-amino dactinomycin (7-AAD, BD, USA) was added and incubated at 37°C for 30 minutes. Subsequently, cell cycle analysis was performed using flow cytometry (BECKMAN COULTER, USA). Each measurement was repeated three times, and a minimum of three experiments were conducted.

Wound healing assay

A density of 4×10^5 cells was inoculated into each well of a 6 well plate. Following overnight incubation, the cell monolayer was scraped using sterile pipette tips. The floating cells were then washed with PBS and cultured with DMEM. Migration images along the scratch line were captured at intervals of 0, 6, and 12 hours using an optical microscope. The measurement of wound area was conducted using Image J software from the National Institutes of Health in Bethesda, USA. The migration rate (%) was calculated as $((A - B)/A) \times 100\%$, where A represents the wound area at 0 hours and B represents the wound area at 6 and 12 hours. The experiments were conducted in triplicates independently.

Transwell assay

Cell migration and invasion experiments were conducted using a 24 well plate with an 8 μm pore chamber (Corning, USA). For the invasion experiment, the upper chamber of the Transwell pore chamber was coated with a 1:8 dilution of Matrigel matrix gel (BD, USA). Prior to experimentation, cells were cultured in DMEM medium without FBS for 12 hours to induce starvation treatment. Subsequently, the cells were suspended in DMEM medium without FBS and added to the upper chamber at a concentration of 1×10^5 cells per well. Simultaneously, DMEM medium containing 10% FBS was added to the lower chamber, and the plate was incubated in an incubator for a duration of different time points. Following incubation, the residual cells adhered to the filter membrane surface should be delicately removed using a cotton swab. Subsequently, the cells that migrated to the lower surface of the filter membrane ought to be fixed with methanol for a duration of 20 minutes, followed by staining with a 0.1% Crystal violet solution for the same duration. To ensure accuracy, the microscope should be inverted to observe the lower surface and the counting process should be repeated three times. It is important to note that the steps involved in the cell migration experiment closely resemble those of the invasion experiment, with the exception that no gel coating is applied.

Statistical analysis

Spearman rank test and Wilcoxon rank-sum test were respectively performed to examine correlation between two groups and the expression difference. Log-rank test was used to compare survival differences between groups. Univariate and multivariate Cox proportional hazard regression analyses were performed to screen the factors influencing the prognosis. Statistical analyses were performed using GraphPad Prism 9 and R (version 4.3) software. P values < 0.05 were considered statistically significant. (*p < 0.05, **p < 0.01, ***p < 0.001, and ****p < 0.0001)

Results

The expression of TEDC2 across tumors

The workflow in the current study is demonstrated in Figure 1. The aberrant expression of genes in tumor samples was related to probably participate in tumorigenesis. To clarify the expression of TEDC2 across tumors, normalized TCGA data were analyzed. The results showed that TEDC2 was significantly upregulated in many tumors compared to corresponding normal tissues, including KIRP, KIRC, LIHC, STAD, LUAD and so on (Figure 2A). TEDC2 expression was also analyzed in 23 types of tumors and paired normal tissues, and the result was roughly in consistent with the unpaired samples (Figure 2B). Furthermore, the differential expression of TEDC2 between tumors and normal tissues was verified by the data sets GSE10927, GSE15641, GSE36376, GSE51575, GSE63514 and GSE116959. The results showed that

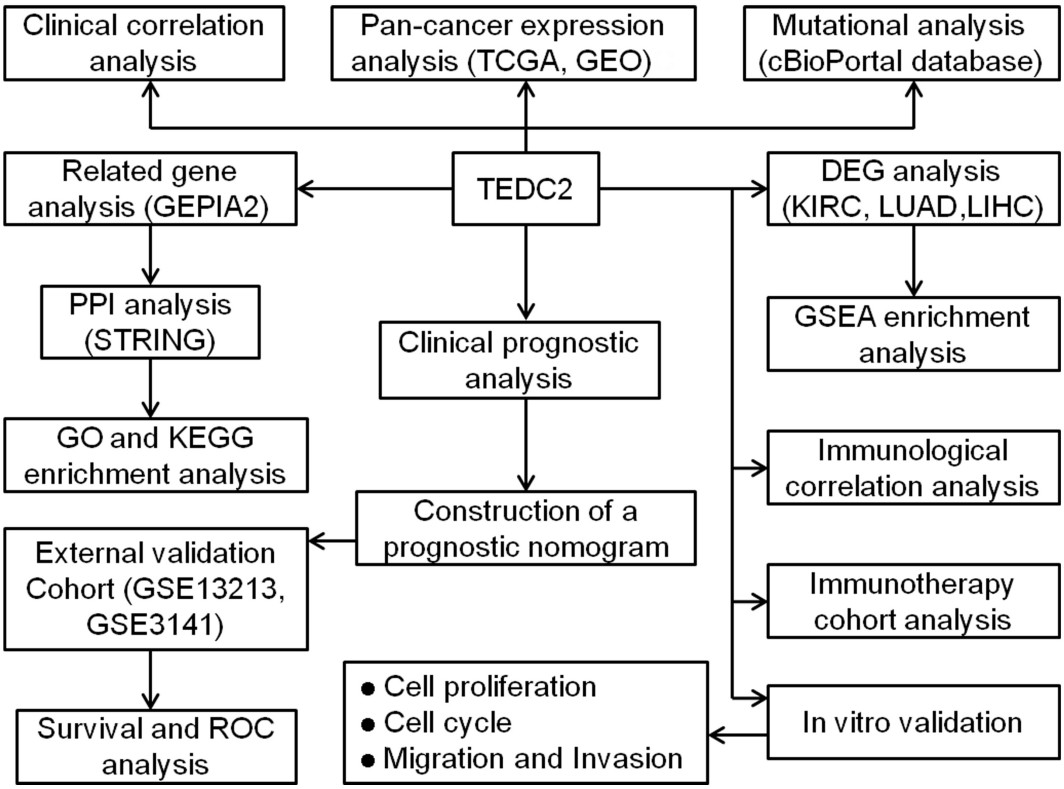

FIGURE 1
Workflow diagram of this study.

the expression of TEDC2 in many tumors was higher than normal tissues (Figure 2C). In order to substantiate these findings, we conducted an analysis of the immunohistochemistry of TEDC2 across various tumors within the HPA database, results demonstrated that a noteworthy increase in the expression of the TEDC2 protein within certain tumor samples (Figure 2D).

Genetic alteration analysis of TEDC2 across tumors

We observed the genetic alteration status of TEDC2 in different tumor samples of the TCGA cohorts. We found that all cholangiocarcinoma cases with genetic alteration (~3% frequency) had miss mutation of TEDC2, and adrenocortical carcinoma tumor samples had the highest TEDC2 genetic alteration frequency (>4%). It is worth noting that amplification, deep deletion, and miss mutation were the main types of frequent genetic alterations in TEDC2. (Supplementary Figure 1A). A total of 76 TEDC2 mutations, including 13 truncating mutations, 57 missense mutations, 4 splice mutation and 2 fusion mutations were detected in TCGA tumor samples (Supplementary Figure 1B). In addition, we assessed whether genetic variation of TEDC2 is associated with clinical survival prognoses with different types of tumor. The results showed that the altered TEDC2 did not cause a significant difference in overall survival (Supplementary Figure 1C). It is noteworthy that the occurrence of TEDC2 mutation is relatively infrequent in the majority of tumors, thus necessitating additional validation through the inclusion of a larger dataset comprising clinical patient information.

The association between TEDC2 expression and prognosis across tumors

To explore the prognostic value of TEDC2 across tumours, Kaplan–Meier survival analysis was performed to assess the association between TEDC2 expression and clinical outcome. We investigated the association between TEDC2 expression and OS in tumours (Figure 3A), and the results showed that high expression of TEDC2 was associated with significantly shorter OS in ACC (HR = 7.129, 95% CI 2.838–17.907, $p < 0.001$) , KIRC (HR = 1.843, 95% CI 1.358–2.5, $p < 0.001$), LUAD (HR = 1.681, 95% CI 1.256–2.251, $p < 0.001$) and LIHC (HR = 2.026, 95% CI 1.421–2.888, $p < 0.001$) (Figure 3B). Subsequently, we investigated the association between TEDC2 expression and DSS and PFI in tumours, which was roughly in agreement with the result of OS (Supplementary Figure 2).

Construction and validation of a nomogram on TEDC2

We further explored the relationship between TEDC2 expression and clinic pathological features in these tumors. The

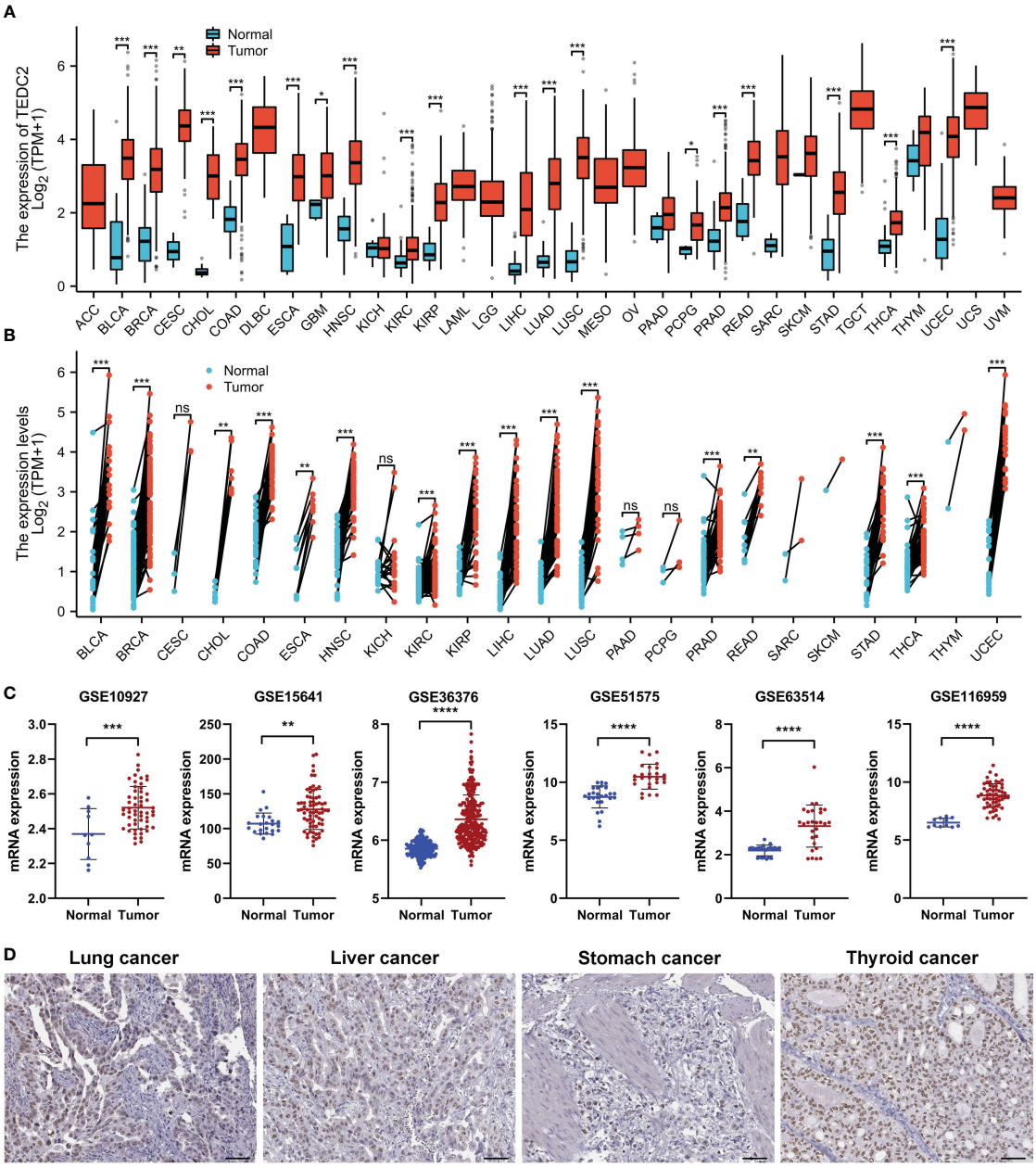

FIGURE 2
The mRNA expression of TEDC2 in pan-cancer. **(A)** TEDC2 expression in 33 tumors in TCGA database. **(B)** TEDC2 expression in paired samples of 22 tumors in TCGA database. **(C)** TEDC2 expression in the six GEO database. **(D)** The IHC images of TEDC2 in tumor tissues extracted from the HPA. (ns, *p < 0.05, **p < 0.01, ***p < 0.001, and ****p < 0.0001).

results showed that the expression of TEDC2 in KIRP, KIRC, ACC, LUAD and LIHC was correlated with pathological stage (Figure 4A). Moreover, the expression of TEDC2 in LUAD was correlated with age and gender (Supplementary Figure 3). The ROC curves were also presented for six tumors whose prognosis was associated with TEDC2 expression (Figure 4B), suggesting the diagnostic ability of TEDC2 in these tumors.

To establish a quantitative prognostic approach for diverse tumor patients, we initially identified, via unvaried Cox analysis, a significant association between the prognosis of multiple tumor patients and the expression of TEDC2, age, and T stage (Supplementary Tables 2-7). Subsequently, we integrated these factors into a multivariate Cox model and developed a nomogram model encompassing age, T stage, and TEDC2 expression in three representative tumors (KIRC, LUAD, and LIHC) to validate their prognostic significance. The findings demonstrate that the nomogram model exhibits a high level of accuracy in predicting OS (Figures 5A, C, E). We further used calibration curves to evaluate the prediction accuracy of the nomogram model at 1, 3, and 5-years. These results showed that the nomogram models had high accuracy in predicting OS (Figures 5B, D, F). Furthermore, in the external validation set, individual risk scores were computed for each patient, and

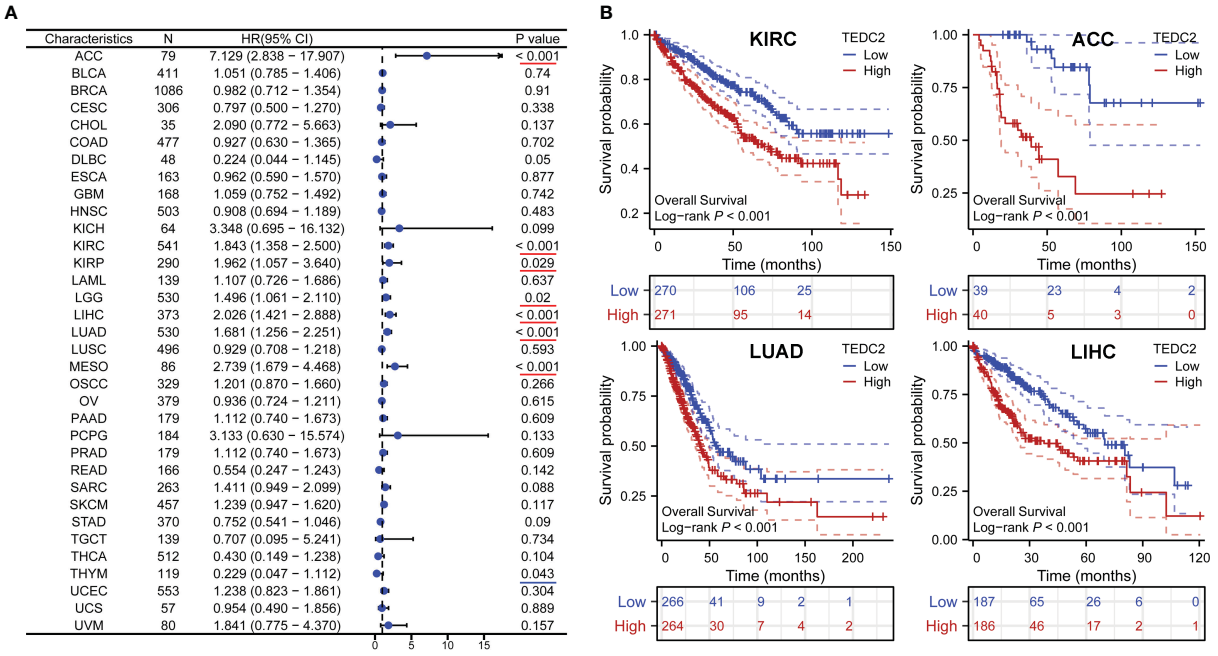

FIGURE 3
The correlation between TEDC2 expression and OS in pan-cancer. **(A)** Forest plots showed the effect of TEDC2 expression on OS in pan-cancer. The presence of a red underline signifies an unfavorable prognosis for TEDC2, whereas a blue underline denotes a favorable prognosis for TEDC2. **(B)** The effects of TEDC2 expression on OS in KIRC, LUAD, ACC and LIHC, respectively.

subsequently, they were categorized into high-risk and low-risk groups based on the median. Comparative analysis of survival curves revealed a significantly superior survival rate among patients in the low-risk group as opposed to those in the high-risk group. Additional ROC curves demonstrate that risk signatures possess commendable diagnostic capabilities (Supplementary Figure 4A, B).

Functional enrichment analysis

To elucidate the biological function of TEDC2 in tumors, we used GEPIA2 to obtain the top 100 genes with similar expression patterns for TEDC2 in all tumor types. GO enrichment analysis showed that TEDC2 related genes were closely related to nuclear chromosome segregation, nuclear division, condensed chromosome and ligand-gated ion channel activity. KEGG pathway analysis indicated that TEDC2 related genes may participate in to the cell cycle, neuroactive ligand-receptor and oocyte meiosis (Figure 6A).

Additionally, a PPI network of the 100 TEDC2 related genes was created from the STRING database (Figure 6B), and the top 10 genes were extracted by the cytoHubba plugin in the Cytoscape (version 3.7.1) software (Figure 6C). The top 10 genes deeply involved in the regulation of cell proliferation and cell cycle (24–27). Furthermore, we analyzed the correlation between the top 10 genes and TEDC2 expression in KIRC and LIHC. The top 10 genes were plotted in heatmaps. On the right side of heatmaps, significant pairs were identified by Spearman correlation analysis for each of these genes with TEDC2 (Figure 6D). The results showed TEDC2 expression correlated positively with these genes, suggesting that TEDC2 may be involved in tumor growth.

In order to elucidate the function of TEDC2, differential gene expression analysis on TEDC2 low (0-30%) and high (70-100%) expression samples was conducted in KIRC, LUAD, and LIHC. KIRC identified 280 genes with significant differential expression, with 222 upregulated and 58 downregulated genes in the high TEDC2 expression group. LUAD identified 755 genes with significant differential expression, with 395 upregulated and 360 downregulated genes in the high TEDC2 expression group. LIHC identified 400 genes with significant differential expression, with 351 upregulated and 59 downregulated genes in the high TEDC2 expression group (Supplementary Figure 5A). Subsequently, we used all genes with log2(FC) values for GSEA analysis. Interestingly, a high degree of similarity was found between the enriched gene sets in the three tumors, which included cell cycle checkpoints, cell cycle, cell cycle mitotic and mitotic prometaphase (Supplementary Figure 5B).

Expression of TEDC2 combined with immune infiltration affects overall survival

As we have known that tumor-infiltrated lymphocyte cells play a key role in tumorigenesis and affect the prognosis of tumor patients (28–30). Therefore, we next examine whether TEDC2 is related with the immune infiltration level in specific tumors. We found that TEDC2 expression was negatively correlated with most infiltrated immune cells including CD8 T cells, macrophages, eosinophils, DC cells, cytotoxic cells, and NK cells (Figure 7A, Supplementary Figure 6). Noteworthy, TEDC2 expression in LIHC was significantly negatively correlated with the enrichment of NK

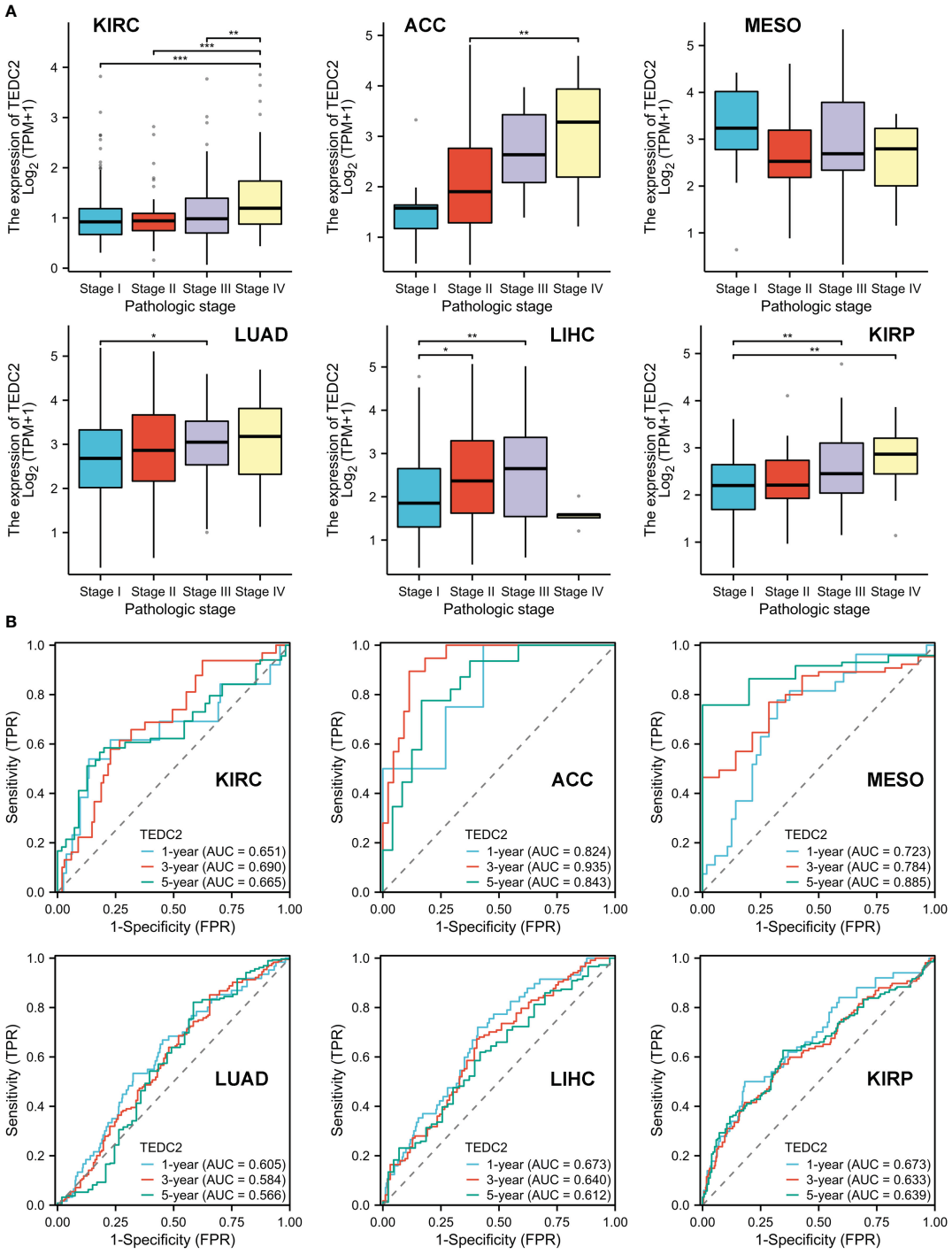

FIGURE 4
The correlation between TEDC2 expression and clinic pathological parameters. **(A)** The expression of TEDC2 was correlated with pathologic in ACC, KIRC, MESO, LUAD, LIHC and KIRP. **(B)** The time-dependent ROC curve of the diagnostic value of TEDC2 in patients with ACC, KIRC, MESO, LUAD, LIHC and KIRP. (*p < 0.05, **p < 0.01, ***p < 0.001).

cells (R = −0.208, p < 0.001), CD8 T cells (R = −0.272, p < 0.001) and eosinophils (R = −0.374, P < 0.001). On the contrary, TEDC2 expression was significantly positively correlated with the enrichment of Th2 cells (R = 0.671, p < 0.001) (Figure 7B). Considering that TEDC2 may be a potential oncogene in LIHC, the relationship between TEDC2 and various cytokines (IFNG, TNF, GZMB, PRF1, IL2, IL4, IL4, IL10, TGFA, TGFB1, and TGFB2) and immune checkpoints (PDCD1, CD274, TIGIT, LAG3, HAVCR2, CTLA4, and PDCD1LG2) was assessed (Figures 7C, D). As a result, we found that the expression of TEDC2 is positively correlated with IFNG, but there is no significant associated with the anti-tumor cytokines GZMB and PRF1. Additionally, TEDC2 expression is positively associated with the immunosuppressive factors IL4, IL10, TGFA and TGFB1.

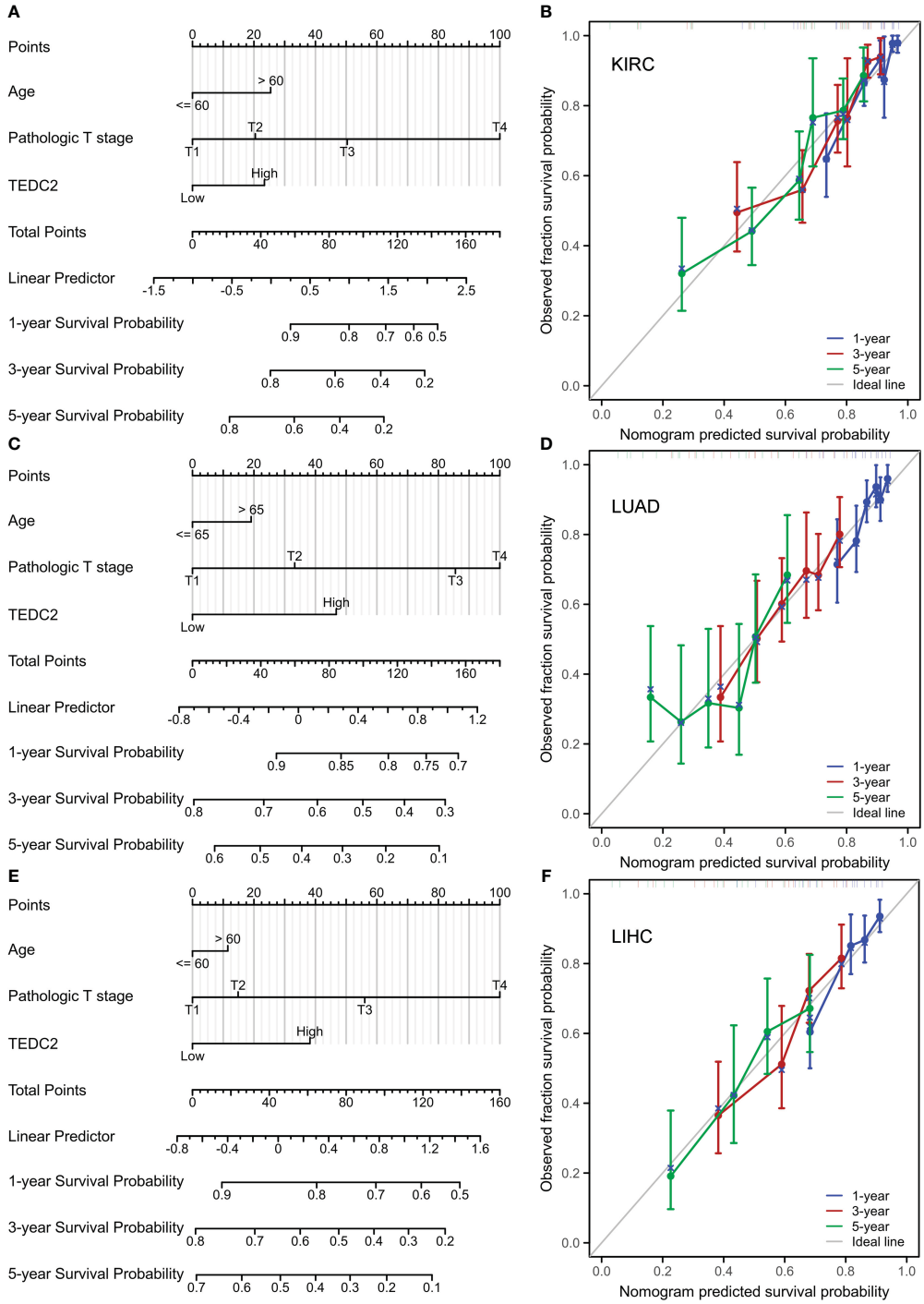

FIGURE 5
Nomogram models were constructed and evaluated in KIRC, LUAD and LIHC. **(A)** The establishment of a nomogram model combined with the expression of TEDC2 in KIRC. **(B)** Calibration curves were generated to assess the prediction accuracy of the nomograms at 1, 3, and 5 years. **(C)** The establishment of a nomogram model combined with the expression of TEDC2 in LUAD. **(D)** Calibration curves were generated to assess the prediction accuracy of the nomograms at 1, 3, and 5 years in LUAD. **(E)** The establishment of a nomogram model combined with the expression of TEDC2 in LIHC. **(F)** Calibration curves were generated to assess the prediction accuracy of the nomograms at 1, 3, and 5 years in LIHC.

Importantly, the expression levels of TEDC2 had a significant positive correlation with PDCD1, CD274, HAVCR2, LAG3, TIGIT, CTLA4 in LIHC. It is worth noting that we conducted a concise examination of the TEDC2 expression and its prognostic association within four cohorts pertaining to immunotherapy, specifically encompassing two adoptive T cell therapies (Supplementary Figure 7A, B) and two immune checkpoint blockade therapies (Supplementary Figure 7C, D). We found that the expression of TEDC2 is comparatively diminished in the subset of individuals responding to immunotherapy, and in contrast to

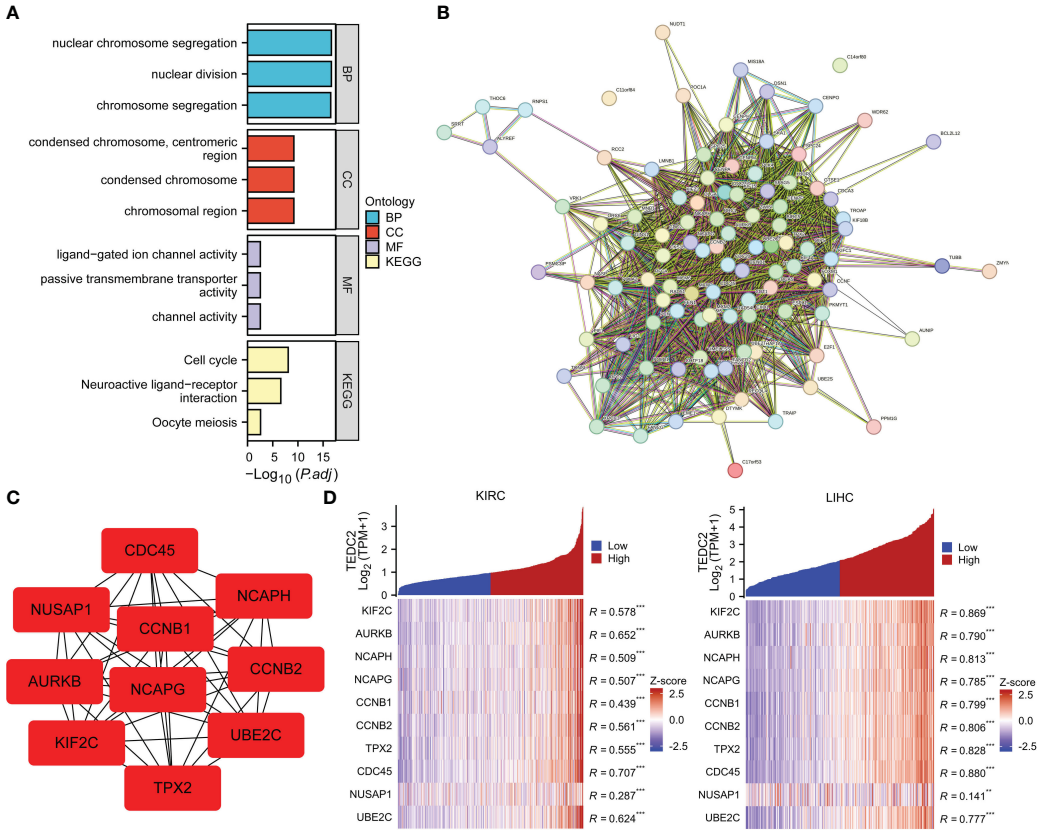

FIGURE 6
Functional enrichment analysis of TEDC2 related genes. **(A)** GO enrichment (BP, MF and CC) and KEGG pathways analysis based on top 100 TEDC2 related genes. **(B)** PPI network diagram of the top 100 TEDC2 related genes. **(C)** PPI network diagram of the top 10 TEDC2 related genes. **(D)** Correlation analysis of TEDC2 expression and top 10 TEDC2 related genes in KIRC and LIHC in the TCGA database. (**p < 0.01 and ***p < 0.001).

those with low TEDC2 expression, patients exhibiting high TEDC2 expression exhibit a markedly reduced survival rate. These results suggested that TEDC2 might mediate the carcinogenic process of tumor by influencing the immunosuppressive microenvironment.

Based on the above results, TEDC2 was associated with immune infiltration of LIHC. We analyzed the effect on tumor survival by combining the expression of TEDC2 and immune cell infiltration. Then, we performed KM plotter analysis of TEDC2 expression in LIHC following CD8 T cells, NK cells and Th2 cells. We found that higher TEDC2 levels in LIHC in enriched CD8 T cells and NK cells had a worse prognosis (Figure 7E). These results suggested that immune infiltration might influence the prognosis of tumor with high TEDC2 expression to some extent.

In vitro experimental verification

Based on the above bioinformatics analysis, TEDC2 may be one of the important factors driving the occurrence and development of various tumors. It can activate cell proliferation, induce immune dysfunction, and ultimately lead to poor prognosis. Then, we validated whether knocking down TEDC2 can inhibit the malignant biological behavior of tumor cells in two cell lines, A549 and HepG2.

Based on the HPA database, our findings revealed that the A549 and HepG2 cell exhibited comparatively elevated levels of TEDC2 expression. Furthermore, when compared to the L02 cell line, which represents the normal human liver, the expression of TEDC2 in both A549 and HepG2 cell demonstrated a significant increase (Supplementary Figure 8A, B). The knockdown efficiency of siteDC2 was initially assessed using real-time PCR, which revealed that siRNA effectively reduced the mRNA levels of TEDC2 in both A549 and HepG2 cells (Figure 8A, Supplementary Figure 9A). Additionally, the growth curve analysis demonstrated that the reduction of TEDC2 significantly impeded the proliferation of A549 and HepG2 cells (Figure 8B, Supplementary Figure 9B). Following this, flow cytometry was employed to examine the impact of TEDC2 knockdown on the cell cycle. The findings of this study indicate that the TEDC2 knockdown group exhibited a significant increase in the proportion of A549 and HepG2 cells in the G1 phase of the cell cycle, accompanied by a significant decrease in the S and G2 phases, when compared to the SINC group (Figure 8C, Supplementary Figure 9C). These results suggest that the inhibition of TEDC2 can impede the progression of tumor cells through the G1 phase, thereby inhibiting cell proliferation. Additionally, the migration and invasion capabilities of A549 and HepG2 cells were assessed using wound healing and transwell experiments after

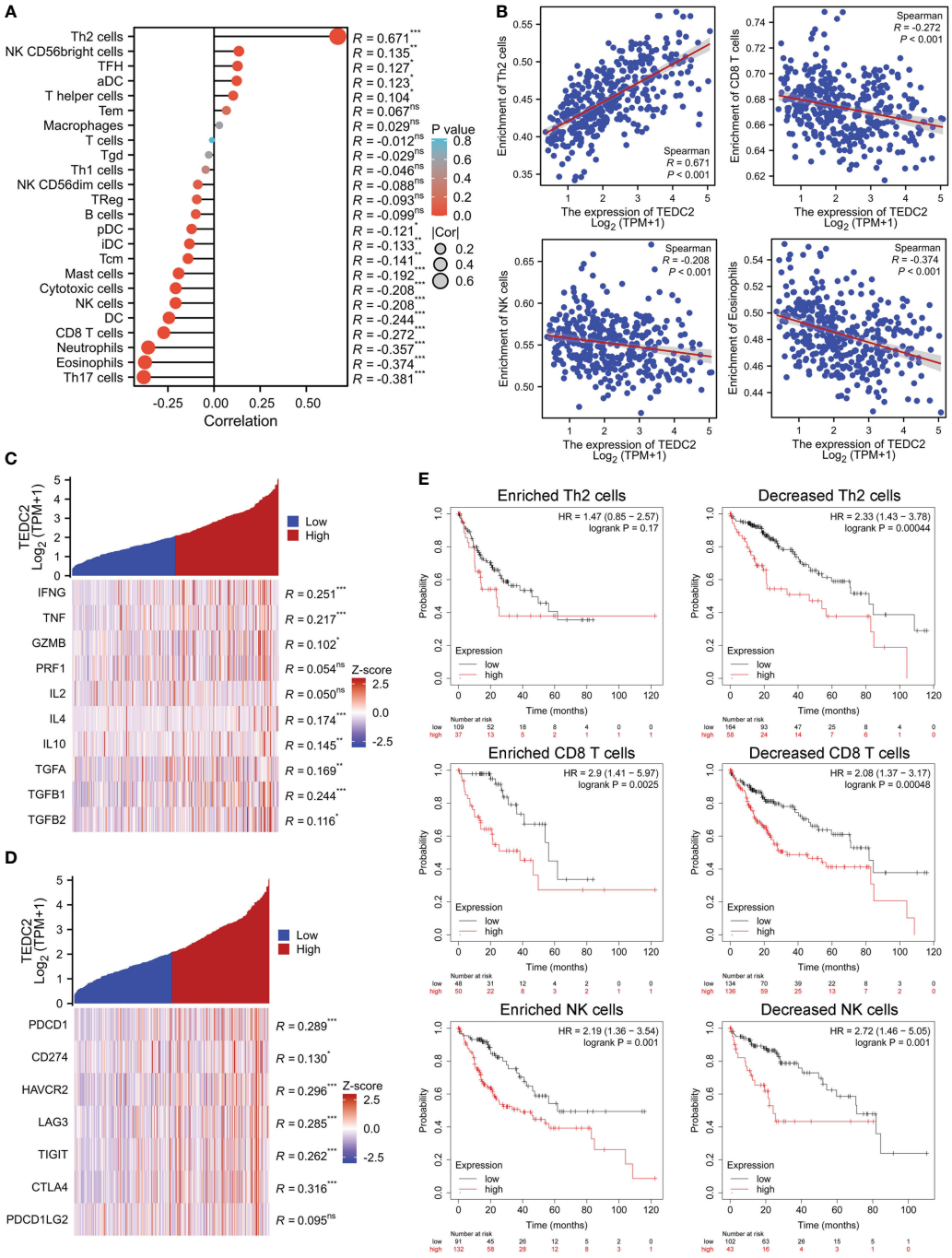

FIGURE 7
The correlation between immune cell infiltration and TEDC2 expression in LIHC. **(A)** The correlation of TEDC2 expression with the infiltration of different immune cells by ssGSEA algorithm. **(B)** The correlation of TEDC2 expression with eosinophils, NK cells, CD8 T cells and Th2 cells, respectively. **(C)** Correlation analysis of TEDC2 expression and immune related cytokines in LIHC. **(D)** Correlation analysis of TEDC2 expression and immune checkpoint molecules in LIHC. **(E)** Correlations between TEDC2 expression and OS in different immune cell subgroups in LIHC patients were determined by Kaplan–Meier survival plotter. (ns, *p < 0.05, **p < 0.01 and ***p < 0.001).

TEDC2 knockdown. The outcomes revealed a significant reduction in both migration and invasion abilities of the tumor cells following TEDC2 knockdown (Figures 8D, E and Supplementary Figure 9D).

In conclusion, these findings strongly indicate that TEDC2 assumes a critical role in the etiology and progression of various tumors.

Discussion

Tumors pose a grave threat to human lives. Despite significant efforts being made to improve tumor diagnosis and treatment, the 5-year overall survival rate for most tumors remains very low (31, 32).. Thus, new methods for diagnosing and treating tumors are

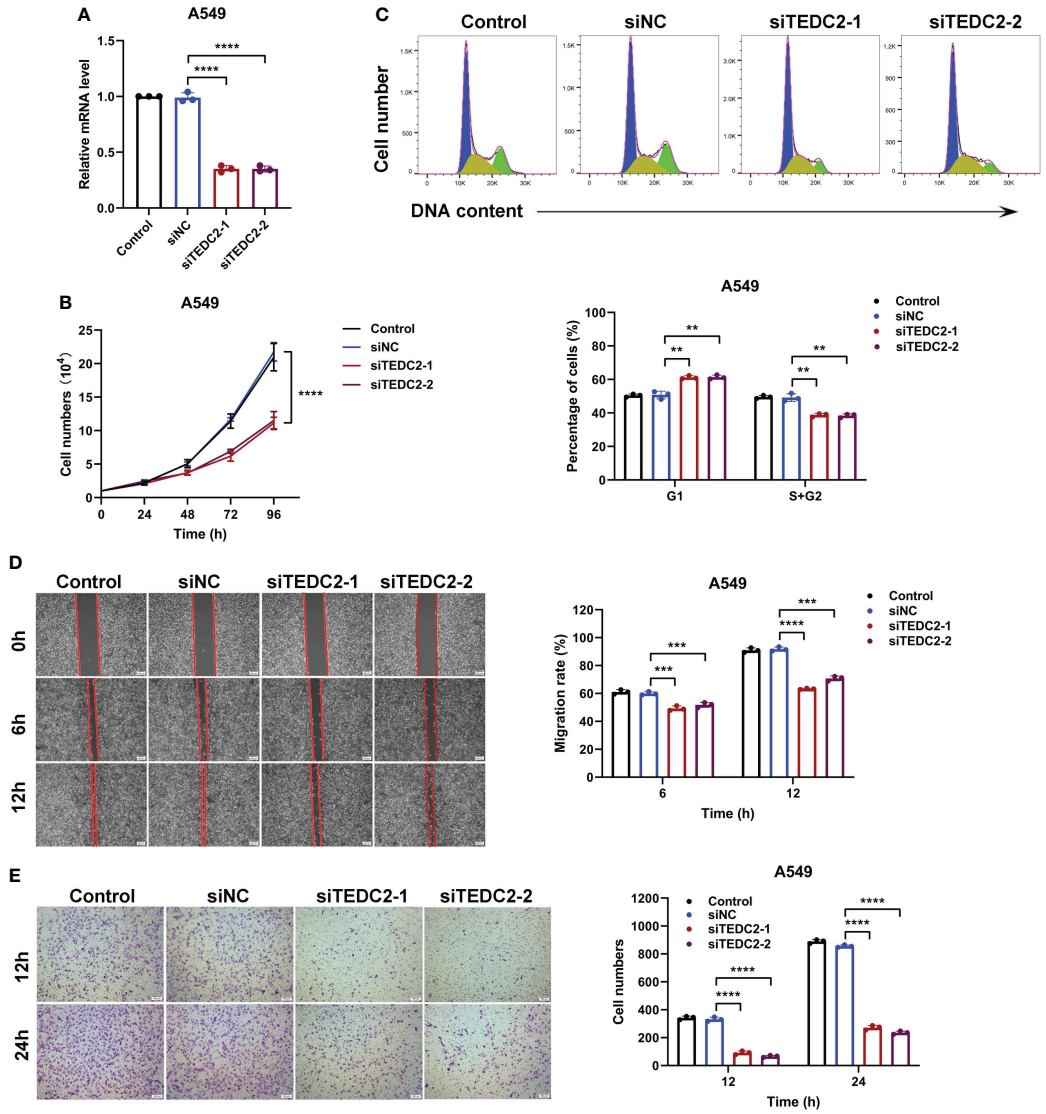

FIGURE 8
The *in vitro* proliferation and metastasis of A549 cells can be inhibited by the knockout of TEDC2. **(A)** The efficiency of siRNA knockout was evaluated through PCR. **(B)** The survival curves of cells treated with various methods were analyzed. **(C)** Flow cytometry was employed to detect the cell cycle of the Control, siNC, siTEDC2-1, and siTEDC2-2 groups. **(D)** The wound healing experiment was conducted to assess the impact of TEDC2 knockdown on cell migration, and the wound healing ratio was measured following 6 and 12 hours of incubation. **(E)** The Transwell experiment was employed to investigate the influence of TEDC2 knockdown on cell invasion, and the quantitative findings were presented in the Bar chart located on the right. The experiments were conducted in triplicates independently. (**p < 0.01, ***p < 0.001 and ****p < 0.0001).

urgently needed. The TCGA database utilized multi-omics data to analyze 33 common tumor types, providing an unprecedented opportunity to detect gene functions in different tumor types (33, 34). In recent years, numerous studies have been conducted to identify and characterize pan-cancer molecular biomarkers and their functions, thanks to the advancement of bioinformatics algorithms and databases. In this study, we conducted a thorough analysis by utilizing an open-access database to investigate the prognostic significance and carcinogenic mechanism of TEDC2 across diverse tumor types.

After analyzing data from GEO and TCGA databases, we found that TEDC2 expression was significantly upregulated in various types of tumors, such as ACC, KIRC, LUAD, LIHC, MESO, STAD, and more. To investigate whether TEDC2 could serve as a prognostic marker for tumors, we examined the correlation between TEDC2 expression and the prognosis of different tumor patients. The Kaplan–Meier survival analysis revealed that high TEDC2 expression was associated with adverse survival outcomes in patients with ACC, KIRP, KIRC, LUAD, LIHC, and MESO. These outcomes included OS, PFS, and DSS. Using pan-cancer data, Cox regression analysis identified TEDC2 high expression as an independent risk factor for poor prognosis in tumors. Based on these results, it can be concluded that TEDC2 not only is an overexpressed gene but also serves as a significant prognostic factor for tumor patients.

Based on the above findings, we investigated its downstream mechanisms for carcinogenesis and risk. Firstly, we performed

TEDC2 coexpression and functional enrichment analysis. This result indicated that most genes coexpressed with TEDC2 were mainly enriched in cell cycle progression such as nuclear division, chromosome segregation and chromosome condensation, suggesting that these genes could promote tumor growth via accelerating the cell cycle phase. Then, we conducted GSEA databases to analyze the biological functions of TEDC2 in KIRC, LUAD and LIHC. Interestingly, the three tumors showed a high degree of similarity between the enriched gene sets including ECM regulators, cell cycle mitotic and cell cycle checkpoints. To ascertain the precise contribution of TEDC2 in the advancement of tumors, we conducted a comprehensive examination of the biological attributes associated with TEDC2 knockdown in A549 and HepG2 cell lines. Suppression of TEDC2 effectively impedes the cell cycle progression of tumor cells during the G1 phase, consequently impeding cell proliferation. Concurrently, TEDC2 knockdown significantly curtails the migratory and invasive capabilities of tumor cells. These findings further substantiate the potential involvement of TEDC2 in the proliferation of tumor cells.

More and more evidence showed that tumor immune microenvironment plays an important role in tumors. TEDC2 has been identified as a potential oncogenic gene linked to immune infiltration in the tumor microenvironment in two recent studies focusing on hepatocellular carcinoma and laryngeal squamous cell carcinoma (35, 36). In our study, we found that TEDC2 expression was negatively correlated with most infiltrated immune cells, including DC cells, macrophages, CD8 T cells, cytotoxic cells, NK cells and eosinophils, suggesting that TEDC2 might induce tumor immunosuppression. Subsequently, we conducted a detailed analysis in LIHC on the correlation between tumor immune related cytokines and immune checkpoints with TEDC2. The results showed that TEDC2 expression was positively correlated with the immunosuppressive factors IL4, IL10, TGFA, and TGFB1, and with the immune checkpoint molecules such as PDCD1, CTLA4, LAG3, CD274 and HAVCR2. PDCD1 is a negative regulator of T cell function that promotes disease progression in patients with many types of tumors (37, 38). HAVCR2 and LAG3 can work synergistically to promote the exhaustion of effector T cells and inhibit anti-tumor function (39–41). However, the molecular mechanisms underlying TEDC2 and these immune checkpoint molecules are unknown, and require further research. These results suggested that TEDC2 may be involved in modulating the tumor immune microenvironment, suggesting that TEDC2 could be used to develop a new targeted immunotherapy for certain tumors and benefit a large number of tumor patients.

Conclusions

In conclusion, we found that TEDC2 is associated with prognosis and functions by modulating the immune microenvironment and cell proliferation of various tumors. Admittedly, there are limitations to our study. On the one hand, since all data in this study were obtained from online databases, data heterogeneity is inevitable. On the other hand, some uncommon tumor types have relatively small sample sizes, which can lead to inaccurate results. Finally, this study solely employed bioinformatics methods to analyze the association between TEDC2 and different tumors, and simple experimental verification was conducted. To determine the precise molecular function of TEDC2 in tumor development, additional experiments are required.

Data availability statement

The raw data supporting the conclusions of this article will be made available by the authors, without undue reservation.

Author contributions

YL: Data curation, Writing – original draft. JZ: Data curation, Writing – original draft. JS: Data curation, Writing – original draft, Software. YTL: Writing – original draft, Methodology. KP: Writing – original draft, Investigation. CT: Conceptualization, Writing – review & editing. YW: Conceptualization, Project administration, Writing – review & editing.

Funding

The author(s) declare that no financial support was received for the research, authorship, and/or publication of this article.

Conflict of interest

The authors declare that the research was conducted in the absence of any commercial or financial relationships that could be construed as a potential conflict of interest.

Publisher's note

Supplementary material

The Supplementary Material for this article can be found online at: https://www.frontiersin.org/articles/10.3389/fimmu.2023.1272108/full#supplementary-material

References

1. Sung H, Ferlay J, Siegel RL, Laversanne M, Soerjomataram I, Jemal A, et al. Global cancer statistics 2020: GLOBOCAN estimates of incidence and mortality worldwide for 36 cancers in 185 countries. *CA Cancer J Clin* (2021) 71:209–49. doi: 10.3322/caac.21660

2. Siegel RL, Miller KD, Fuchs HE, Jemal A. Cancer statistics, 2021. *CA Cancer J Clin* (2021) 71:7–33. doi: 10.3322/caac.21654

3. Cao W, Chen HD, Yu YW, Li N, Chen WQ. Changing profiles of cancer burden worldwide and in China: a secondary analysis of the global cancer statistics 2020. *Chin Med J (Engl)* (2021) 134:783–91. doi: 10.1097/CM9.0000000000001474

4. Liu J, Lichtenberg T, Hoadley KA, Poisson LM, Lazar AJ, Cherniack AD, et al. An integrated TCGA pan-cancer clinical data resource to drive high-quality survival outcome analytics. *Cell* (2018) 173:400–416.e11. doi: 10.1016/j.cell.2018.02.052

5. Zhang Z, Wu L, Li J, Chen J, Yu Q, Yao H, et al. Identification of ZBTB9 as a potential therapeutic target against dysregulation of tumor cells proliferation and a novel biomarker in Liver Hepatocellular Carcinoma. *J Transl Med* (2022) 20:602. doi: 10.1186/s12967-022-03790-0

6. Wang Y, Wan X, Du S. Integrated analysis revealing a novel stemness-metabolism-related gene signature for predicting prognosis and immunotherapy response in hepatocellular carcinoma. *Front Immunol* (2023) 14:1100100. doi: 10.3389/fimmu.2023.1100100

7. Pan S, Sun S, Liu B, Hou Y. Pan-cancer Landscape of the RUNX Protein Family Reveals their Potential as Carcinogenic Biomarkers and the Mechanisms Underlying their Action. *J Transl Int Med* (2022) 10:156–74. doi: 10.2478/jtim-2022-0013

8. Xie J, Zhang J, Tian W, Zou Y, Tang Y, Zheng S, et al. The pan-cancer multi-omics landscape of FOXO family relevant to clinical outcome and drug resistance. *Int J Mol Sci 23* (2022) 23(24):15647. doi: 10.3390/ijms232415647

9. Fang L, Yu W, Zhu P, Yu G, Ye B. TEDC2 correlated with prognosis and immune microenvironment in lung adenocarcinoma. *Sci Rep* (2023) 13:5006. doi: 10.1038/s41598-023-32238-8

10. Hsu MK, Wu IC, Cheng CC, Su JL, Hsieh CH, Lin YS, et al. Triple-layer dissection of the lung adenocarcinoma transcriptome: regulation at the gene, transcript, and exon levels. *Oncotarget* (2015) 6:28755–73. doi: 10.18632/oncotarget.4810

11. Lim DH, Kim WS, Kim SJ, Yoo HY, Ko YH. Microarray gene-expression profiling analysis comparing PCNSL and non-CNS diffuse large B-cell lymphoma. *Anticancer Res* (2015) 35:3333–40.

12. Lu M, Xueying Q, Hexiang P, Wenjing G, Hagg S, Weihua C, et al. Genome-wide associations between alcohol consumption and blood DNA methylation: evidence from twin study. *Epigenomics* (2021) 13:939–51. doi: 10.2217/epi-2021-0039

13. Malherbe DC, Messaoudi I. Transcriptional and epigenetic regulation of monocyte and macrophage dysfunction by chronic alcohol consumption. *Front Immunol* (2022) 13:911951. doi: 10.3389/fimmu.2022.911951

14. Bagnardi V, Rota M, Botteri E, Tramacere I, Islami F, Fedirko V, et al. Alcohol consumption and site-specific cancer risk: a comprehensive dose-response meta-analysis. *Br J Cancer* (2015) 112:580–93. doi: 10.1038/bjc.2014.579

15. Rock CL, Thomson C, Gansler T, Gapstur SM, McCullough ML, Patel AV, et al. American Cancer Society guideline for diet and physical activity for cancer prevention. *CA Cancer J Clin* (2020) 70:245–71. doi: 10.3322/caac.21591

16. Jung KJ, Baek JW, Shin SY, Jee SH. Genetically determined alcohol consumption and cancer risk in Korea. *Epidemiol Health* (2023) 45:e2023077. doi: 10.4178/epih.e2023077

17. Cerami E, Gao J, Dogrusoz U, Gross BE, Sumer SO, Aksoy BA, et al. The cBio cancer genomics portal: an open platform for exploring multidimensional cancer genomics data. *Cancer Discovery* (2012) 2:401–4. doi: 10.1158/2159-8290.CD-12-0095

18. Gao J, Aksoy BA, Dogrusoz U, Dresdner G, Gross B, Sumer SO, et al. Integrative analysis of complex cancer genomics and clinical profiles using the cBioPortal. *Sci Signal 6* (2013) 6, pl1. doi: 10.1126/scisignal.2004088

19. Hanzelmann S, Castelo R, Guinney J. GSVA: gene set variation analysis for microarray and RNA-seq data. *BMC Bioinf* (2013) 14:7. doi: 10.1186/1471-2105-14-7

20. Bindea G, Mlecnik B, Tosolini M, Kirilovsky A, Waldner M, Obenauf AC, et al. Spatiotemporal dynamics of intratumoral immune cells reveal the immune landscape in human cancer. *Immunity* (2013) 39:782–95. doi: 10.1016/j.immuni.2013.10.003

21. Szklarczyk D, Gable AL, Lyon D, Junge A, Wyder S, Huerta-Cepas J, et al. STRING v11: protein-protein association networks with increased coverage, supporting functional discovery in genome-wide experimental datasets. *Nucleic Acids Res* (2019) 47:D607–13. doi: 10.1093/nar/gky1131

22. Subramanian A, Tamayo P, Mootha VK, Mukherjee S, Ebert BL, Gillette MA, et al. Gene set enrichment analysis: a knowledge-based approach for interpreting genome-wide expression profiles. *Proc Natl Acad Sci U.S.A.* (2005) 102:15545–50. doi: 10.1073/pnas.0506580102

23. Yu G, Wang LG, Han Y, He QY. clusterProfiler: an R package for comparing biological themes among gene clusters. *OMICS* (2012) 16:284–7. doi: 10.1089/omi.2011.0118

24. Broderick R, Nasheuer HP. Regulation of Cdc45 in the cell cycle and after DNA damage. *Biochem Soc Trans* (2009) 37:926–30. doi: 10.1042/BST0370926

25. Wei P, Zhang N, Xu Y, Li X, Shi D, Wang Y, et al. TPX2 is a novel prognostic marker for the growth and metastasis of colon cancer. *J Transl Med* (2013) 11:313. doi: 10.1186/1479-5876-11-313

26. Xie B, Wang S, Jiang N, Li JJ. Cyclin B1/CDK1-regulated mitochondrial bioenergetics in cell cycle progression and tumor resistance. *Cancer Lett* (2019) 443:56–66. doi: 10.1016/j.canlet.2018.11.019

27. Zhang R, Ai J, Wang J, Sun C, Lu H, He A, et al. NCAPG promotes the proliferation of hepatocellular carcinoma through the CKII-dependent regulation of PTEN. *J Transl Med* (2022) 20:325. doi: 10.1186/s12967-022-03519-z

28. Grisaru-Tal S, Itan M, Klion AD, Munitz A. A new dawn for eosinophils in the tumor microenvironment. *Nat Rev Cancer* (2020) 20:594–607. doi: 10.1038/s41568-020-0283-9

29. Tosolini M, Kirilovsky A, Mlecnik B, Fredriksen T, Mauger S, Bindea G, et al. Clinical impact of different classes of infiltrating T cytotoxic and helper cells (Th1, th2, treg, th17) in patients with colorectal cancer. *Cancer Res* (2011) 71:1263–71. doi: 10.1158/0008-5472.CAN-10-2907

30. Grisaru-Tal S, Rothenberg ME, Munitz A. Eosinophil-lymphocyte interactions in the tumor microenvironment and cancer immunotherapy. *Nat Immunol* (2022) 23:1309–16. doi: 10.1038/s41590-022-01291-2

31. Chen GM, Chen C, Das RK, Gao P, Chen CH, Bandyopadhyay S, et al. Integrative bulk and single-cell profiling of premanufacture T-cell populations reveals factors mediating long-term persistence of CAR T-cell therapy. *Cancer Discovery* (2021) 11:2186–99. doi: 10.1158/2159-8290.CD-20-1677

32. DiSiena M, Perelman A, Birk J, Rezaizadeh H. Esophageal cancer: an updated review. *South Med J* (2021) 114:161–8. doi: 10.14423/SMJ.0000000000001226

33. Schaub FX, Dhankani V, Berger AC, Trivedi M, Richardson AB, Shaw R, et al. Pan-cancer alterations of the MYC oncogene and its proximal network across the cancer genome atlas. *Cell Syst* (2018) 6:282–300.e2. doi: 10.1016/j.cels.2018.03.003

34. Way GP, Sanchez-Vega F, La K, Armenia J, Chatila WK, Luna A, et al. Machine learning detects pan-cancer ras pathway activation in the cancer genome atlas. *Cell Rep* (2018) 23:172–180.e3. doi: 10.1016/j.celrep.2018.03.046

35. Huang C, He J, Dong Y, Huang L, Chen Y, Peng A, et al. Identification of novel prognostic markers associated with laryngeal squamous cell carcinoma using comprehensive analysis. *Front Oncol* (2021) 11:779153. doi: 10.3389/fonc.2021.779153

36. Deng Z, Huang K, Liu D, Luo N, Liu T, Han L, et al. Key candidate prognostic biomarkers correlated with immune infiltration in hepatocellular carcinoma. *J Hepatocell Carcinoma* (2021) 8:1607–22. doi: 10.2147/JHC.S337067

37. Altorki NK, Markowitz GJ, Gao D, Port JL, Saxena A, Stiles B, et al. The lung microenvironment: an important regulator of tumor growth and metastasis. *Nat Rev Cancer* (2019) 19:9–31. doi: 10.1038/s41568-018-0081-9

38. Sharpe AH, Pauken KE. The diverse functions of the PD1 inhibitory pathway. *Nat Rev Immunol* (2018) 18:153–67. doi: 10.1038/nri.2017.108

39. Ruffo E, Wu RC, Bruno TC, Workman CJ, Vignali DAA. Lymphocyte-activation gene 3 (LAG3): The next immune checkpoint receptor. *Semin Immunol* (2019) 42:101305. doi: 10.1016/j.smim.2019.101305

40. Topalian SL, Taube JM, Anders RA, Pardoll DM. Mechanism-driven biomarkers to guide immune checkpoint blockade in cancer therapy. *Nat Rev Cancer* (2016) 16:275–87. doi: 10.1038/nrc.2016.36

41. Wolf Y, Anderson AC, Kuchroo VK. TIM3 comes of age as an inhibitory receptor. *Nat Rev Immunol* (2020) 20:173–85. doi: 10.1038/s41577-019-0224-6

frontiers | Frontiers in Immunology

TYPE Original Research
PUBLISHED 11 January 2024
DOI 10.3389/fimmu.2023.1289548

OPEN ACCESS

EDITED BY
Takaji Matsutani,
Maruho, Japan

REVIEWED BY
Irene Bertolini,
Wistar Institute, United States
Andre Patrick Arrigo,
UniversitéClaude Bernard Lyon 1,
France

*CORRESPONDENCE
Shengni Hua
huashengni0401@163.com

†These authors have contributed equally to this work

RECEIVED 06 September 2023
ACCEPTED 26 December 2023
PUBLISHED 11 January 2024

CITATION
Zhang Z, Ju M, Tang Z, He Z and Hua S (2024) DNAJC8: a prognostic marker and potential therapeutic target for hepatocellular carcinoma.
Front. Immunol. 14:1289548.
doi: 10.3389/fimmu.2023.1289548

DNAJC8: a prognostic marker and potential therapeutic target for hepatocellular carcinoma

Zhibo Zhang†, Mingxiu Ju†, Zhongming Tang, Zhen He and Shengni Hua*

Department of Radiation Oncology, Zhuhai People's Hospital, Zhuhai Hospital Affiliated with Jinan University, Zhuhai, China

Background: Hepatocellular carcinoma (HCC) is the most common type of liver cancer, accounting for ~90% of the total cases. DnaJ heat shock protein family member C8 (DNAJC8), belonging to the heat shock protein 40 (HSP40) family, is known to regulate cancer biology function. However, the role of DNAJC8 on HCC development remains unknown.

Methods: The Cancer Genome Atlas, GTEx, cBioPortal, and Human Protein Atlas were used to analyze the expression and clinical significance of DNAJC8 in HCC. Two HCC cell lines, MHCC-97H and Huh-7, were utilized to determine the biological function of DNAJC8.

Results: DNAJC8 expression was upregulated in HCC tissues and correlated with poor clinical prognosis. It was closely related to spliceosome, nucleocytoplasmic transport, and cell cycle and might be involved in the formation of tumor immunosuppressive microenvironment. Knockdown of DNAJC8 severely inhibited HCC cell proliferation and induced apoptosis.

Conclusion: Our study demonstrate that *DNAJC8* functions as an oncogene in HCC and hence may be used as a potential therapeutic target and prognostic marker for HCC.

KEYWORDS

DNAJC8, hepatocellular carcinoma, bioinformatics analysis, apoptosis, tumor immune microenvironment

Abbreviations: HCC, Hepatocellular carcinoma; DNAJC8, DnaJ heat shock protein family member C8; HSP40, heat shock protein 40; EMT, epithelial mesenchymal transition; ROC, receiver operating characteristic; GO, Gene Ontology; MF, molecular function; CC, cellular component; BP, biological process; KEGG, Kyoto Encyclopedia of Genes and Genomes; GSVA, Gene set variation analysis; CCK-8, Cell Counting Kit-8; EdU, 5-Ethynyl-20-deoxyuridine; ANOVA, one-way analysis of variance.

Introduction

Hepatocellular carcinoma (HCC) is the most common primary liver malignancy, and surgical resection is still the main treatment for it (1). However, due to the concealment of liver cancer, it is often diagnosed at the advanced stage. Systemic treatment is the only effective method for these patients (2). Unfortunately, drugs targeting HCC are mostly multi-target kinase inhibitors, such as sorafenib and lenvatinib (3). Furthermore, individual sensitivity and drug resistance greatly limit their clinical application (4, 5). Therefore, more and more attention are paid to non-kinase target proteins, such as ASCT2, SPR (6, 7). Thus, exploring novel non-kinase treatment targets of HCC is urgently needed.

Heat shock proteins (HSPs) are a type of evolutionarily highly conserved proteins. They are induced by a range of environmental stimuli, especially high temperature, and act as intracellular homeostasis protectors (8). After binding to other proteins, HSP help amino acid chains to fold correctly, eliminating damaged amino acid chains, and avoid cell death (9, 10). The HSP40/DNAJ family is the largest HSP family, containing at least 49 members, which can be divided into three subclasses: DNAJA, DNAJB, and DNAJC (11). Most of the members contain a "J" domain that can bind to HSP70 and activate its ATPase activity to regulate protein folding, unfolding, translation, translocation, and degradation (12). It has increasingly been shown that HSP40/DNAJ family is involved in the regulation of cancer biological functions (13, 14); DNAJA3 can induce apoptosis of breast cancer by regulating p53 (15), and reduce angiogenesis of sarcoma and cervical cancer by destabilizing HIF-1 (16); DNAJB4 arrests lung cancer cell cycle through the STAT1/p21 signaling pathway (17); DNAJB6 inhibits the epithelial mesenchymal transition (EMT) process of breast cancer cells by up-regulating DKK1 and inhibiting Wnt/β-catenin signaling pathway (18); DNAJB1 suppresses p53-dependent apoptosis by destabilizing PDCD5 (19); DNAJC6 can promote the metastasis of HCC via enhancing EMT progression (20). Some studies have shown that DNAJC8 is related to heat tolerance of bee and human spinocerebellar ataxia 3 polyglutamine formation (21). DNAJC8 is also involved in the glycolysis of cervical cancer cells under the regulation of TIG1 (22). However, there is still a lack of research on DNAJC8, especially on its role in cancer.

In this study, through bioinformatics analyses (sample expression, clinical correlation, gene enrichment, and immune infiltration) of data from multiple public databases and *in vitro* cell experiments (siRNA interference), we detected the expression features and function of DNAJC8 and proved that it can serve as an oncogene in HCC. Thus, DNAJC8 may be a potential prognostic and therapeutic target for HCC.

Materials and methods

DNAJC8 expression analysis

Paired HCC samples from The Cancer Genome Atlas (TCGA) database (https://portal.gdc.cancer.gov/) were used. The protein expression of DNAJC8 was obtained from UALCAN database (https://ualcan.path.uab.edu/index.html). The immunohistochemical results were obtained from The Human Protein Atlas (www.proteinatlas.org/). Copy number and methylation levels were evaluated using the Liver Hepatocellular Carcinoma (TCGA, PanCancer Atlas) dataset of cBioPotal (www.cbioportal.org/). The genetic variation information was obtained from TCGA Liver Cancer dataset of UCSC XENA and analyzed using the maftools package in R software (3.6.3).

Clinical prognostic analysis

Survival time and clinical pathological characteristics from TCGA-LIHC datasets were analyzed using the survival (3.2.10) and survminer (0.4.9) packages in R software, respectively. According to the median expression level of DNAJC8, the patients were divided into two groups: high expression group and low expression group. A receiver operating characteristic (ROC) curve was obtained using the pROC package (1.17.0.1). Survival analysis results were obtained from GEPIA (http://gepia.cancer-pku.cn/).

Enrichment analyses of co-expressed genes

Gene Ontology (GO) (molecular function [MF], cellular component [CC], biological process [BP]) and Kyoto Encyclopedia of Genes and Genomes (KEGG) pathway analyses were performed using the clusterProfiler package (3.14.3) in R software (3.6.3). Gene set variation analysis (GSVA) was done using the GSVA package (1.40.1). Protein–protein interaction network analysis was performed online by STRING database (http://string-db.org).

Immune infiltration analysis

HCC sample expression data GSE98638 was analyzed online through ImmuCellAI using ssGSEA. TCGA-LIHC expression data (https://portal.gdc.cancer.gov/) was analyzed using estimate (1.0.13) package in R software (3.6.3) via ssGSEA method. Immune checkpoint analysis was performed online using the "correlation analysis" function of GEPIA.

Immunohistochemistry

11 pairs of HCC tissues fixed with 4% paraformaldehyde were dehydrated and paraffin-embedded and then sectioned. The sections were put into an oven to dry at 63 degrees for 1 hour. Dewaxing was performed with LEICAST5020 (Dako). After antigen repair was completed, the sections were incubated with DNAJC8 antibody at 4 degrees overnight. Blocking, secondary antibody binding, and DAB chromogenic staining was performed with Autostainer Link 48 (Dako). After 1 minute of hematoxylin staining, the sections were immersed in 0.25% hydrochloric acid

alcohol for 10 seconds and washed with water for 5 minutes. After sealing with neutral resin, the sections were photographed. The score standard for the intensity of staining was as follows: 0, negative; 1, weak; 2, medium; 3, strong. The extent of staining was scored as: 0, 0%; 1, 1–25%; 2, 26–50%; 3, 51–75%; 4, 76–100%.

Cell culture

All cell lines in the experiments were obtained from Procell Life Science & Technology Co., Ltd. MHCC-97H and Huh-7 cells were cultured using Dulbecco's modified Eagle medium (Gibco, Waltham, MA, USA) with 10% fetal bovine serum (Gibco) in a 37°C incubator with 5% CO_2 (Thermo Fisher Scientific, Waltham, MA, USA).

siRNA transient transfection

Cells in rapid growth phase were collected and plated in 6-well plates at a density of 200,000 cells per well. After 12 h of incubation, the mixture containing 5 μL siRNA for DNAJC8 (RiboBio, Guangzhou, China) and 5 μL RNAiMAX (Invitrogen, Carlsbad, CA, USA) was added to every well. The cells were cultured in a 37°C incubator with 5% CO_2 for 48–72 h for further analysis. the siDNAJC8-1 sequence was 'GATTGAAGCTCAAGAAAAA'; the siDNAJC8-2 sequence was 'GCAGTTATCCATCTTGGTG'.

qRT-PCR

Total RNA was isolated from the cell lines using the RNA-Quick Purification Kit (Yishan, Shanghai, China). Approximately 1 μg RNA was reverse-transcribed into cDNA, using the HiScript III RT SuperMix (Vazyme, Nanjing, China), and qRT-PCR was performed using the AceQ Universal SYBR qPCR Master Mix (Vazyme). GAPDH was used as internal control. The primer sequence of *DNAJC8* was that the forward sequence was 'CCAAACGGGAAAGAGAGTGGCA'; the reverse sequence was 'ACTTTCGGTGGTCTCAGGAAGG'.

Western blotting

Western blotting was performed according to our previous reports. The DNAJC8 antibody (ab138506) was obtained from Abcam (1:1000; Abcam, Cambridge, UK). The Bax (50599-2-lg), P53 (10442-1-AP), DNAJB1 (13174-1-AP), Hsp70 (10995-1-AP) and Hsp90 (13171-1-AP) antibody was obtained from Proteintec (Chicago, USA).

Cell Counting Kit-8 assay

Cells were plated in 96-well plates at a density of 3000 cells per well, and CCK8 solution (Dojindo, Kumamoto, Japan; 10 μL/well) was added at 12, 24, 48, and 96 h. The mixture was incubated at 37° C for 2 h, and the absorbance at 450 nm wavelength was recorded (Thermo Fisher Scientific, Waltham, MA, USA).

Colony formation

Cells were plated in a 6-well plate at a density of 2000 cells per well. When the clone was formed, the wells were fixed with 4% paraformaldehyde for 2 h, washed with phosphate-buffered saline, and stained with crystal violet for 24 h.

5-Ethynyl-20-deoxyuridine assay

The cells were plated in a 96-well plate at a density of 3000 cells per well. Proliferating cells were examined using the Cell-Light EdU Apollo488 *In Vitro* Kit (RiboBio), according to the manufacturer's protocol.

Apoptosis analysis

The cells were plated in a 6-well plate at a density of 200,000 cells per well. Annexin V-FITC/PI Apoptosis Detection Kit (Vazyme) were used to analyze the programmed cell death. All operations were carried out according to the manufacturer's protocol.

Statistical analysis

Data are presented as the mean ± standard error of the mean of at least three independent experiments. All statistical analyses were performed using SPSS software (Abbott Laboratories, Chicago, IL, USA). The Student's *t*-test was used to determine the significance between groups. Comparisons among multiple groups were analyzed using one-way analysis of variance (ANOVA) and Dunnett's multiple comparisons. For CCK-8 results, a multi-way ANOVA was adopted. Two-sided *p*-values were calculated, and different numbers of asterisks indicate different levels of statistical significance (*$p< 0.05$, **$p< 0.01$, and ***$p< 0.001$).

Results

DNAJC8 expression is upregulated in HCC

TCGA cohort data showed that the DNAJC8 mRNA level in HCC tissues was considerably increased than that in adjacent or normal tissues (Figure 1A). DNAJC8 protein expression was upregulated in HCC tissues compared to that in normal liver tissues, according to UALCAN (Figure 1B) and Human Protein Atlas database (Figure 1C). DNAJC8 expression was negatively correlated with promoter methylation level (r=-0.3, $p<0.0001$) but positively related to gene copy number (r=0.46, $p<0.0001$) (Figure 1D). Notably, 37% of patients with high DNAJC8 expression had TP53 mutations, while CTNNB1

10.3389/fimmu.2023.1289548

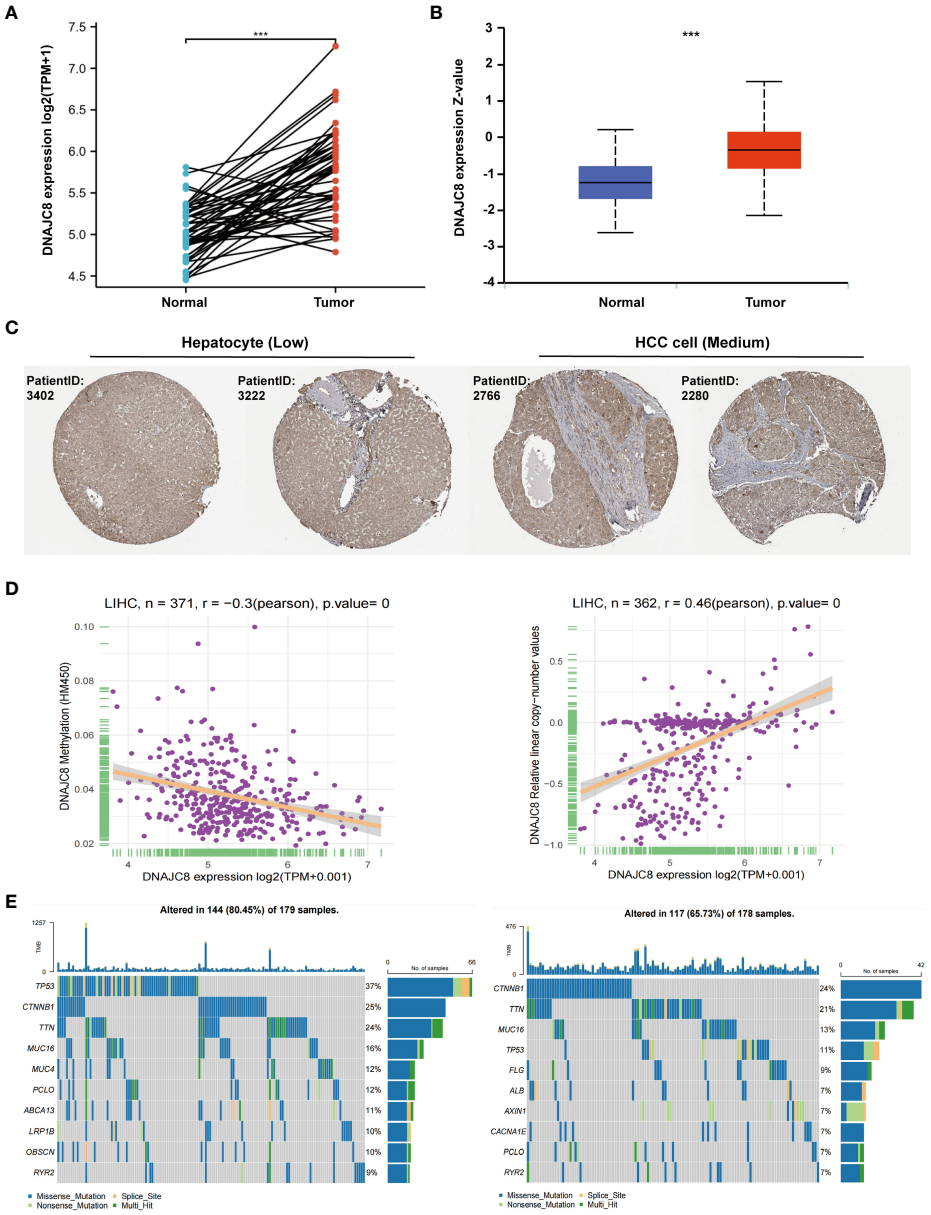

FIGURE 1
DNAJC8 expression is upregulated in HCC. **(A)** mRNA expression of DNAJC8 in paired samples from TCGA. **(B)** Protein expression of DNAJC8 between normal and tumor tissue from UALCAN. **(C)** Expression difference of DNAJC8 in Human Protein Atlas database. **(D)** The respective relationship between DNAJC8 expression and methylation (left), copy number (right). **(E)** Relationship between gene mutation and DNAJC8 expression (left: high; right: low). ***: $p<0.001$.

mutations were the most common in patients with low DNAJC8 expression (Figure 1E; Supplementary Figure 1A). These results suggested that DNAJC8 expression was higher in HCC and it may serve as an oncogene.

DNAJC8 expression is closely associated with HCC prognosis

Survival analysis showed that HCC patients with higher DNAJC8 levels showed significantly poor prognosis in overall survival (HR=1.74, $p<0.005$), progression-free survival (HR=1.52, $p<0.05$), and disease-specific survival (HR=1.59, $p<0.05$) in TCGA cohort (Figure 2A). The ROC curve also indicated that DNAJC8 expression could distinguish tumors from non-tumors (AUC=0.906) (Figure 2B). Survival analysis results from GEPIA database verified the above results (Figure 2C). Furthermore, there was an upward trend of DNAJC8 expression in patients with advanced stage tumor ($p<0.05$) and vascular invasion ($p<0.05$) (Figure 2D). Logistics regression analysis confirmed that the expression level of DNAJC8 was correlated with T stage ($p<0.05$), pathological stage ($p<0.05$), and vascular invasion ($p<0.005$)

10.3389/fimmu.2023.1289548

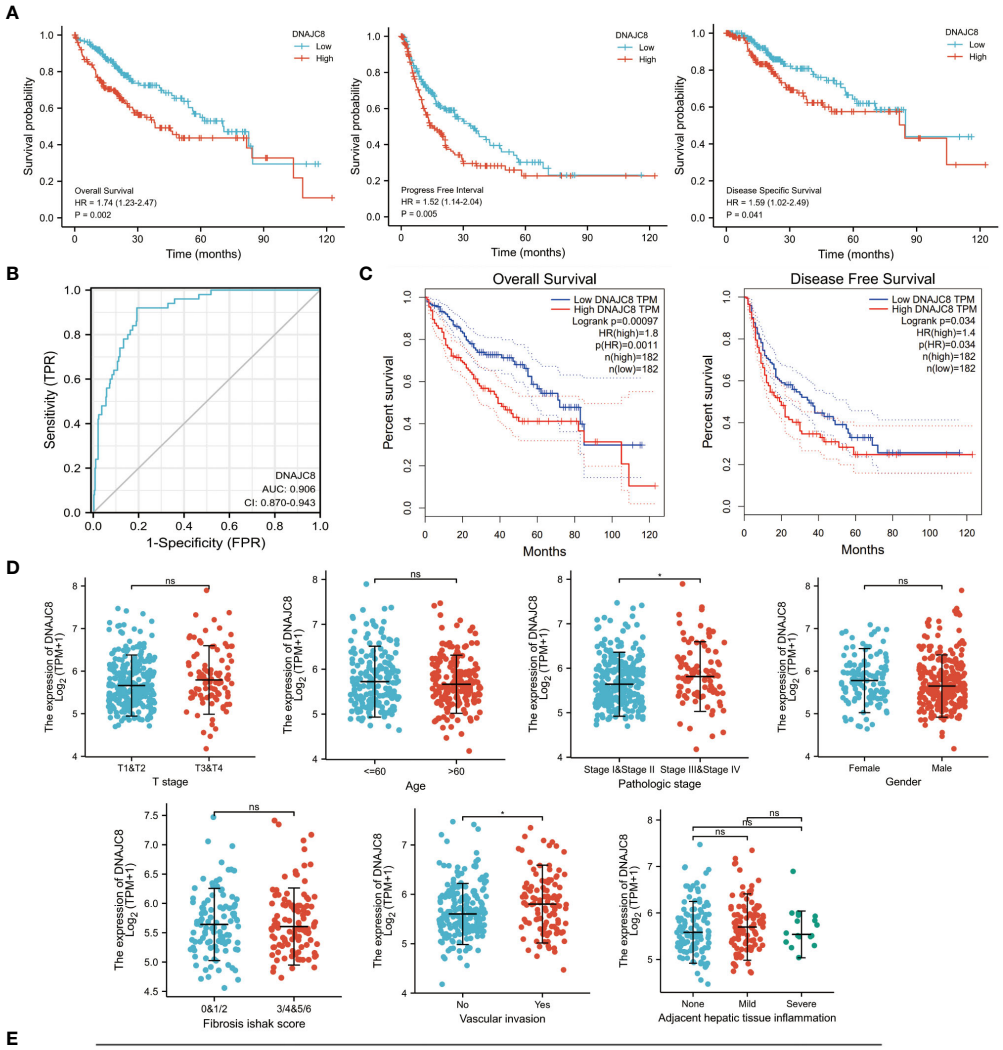

E

Characteristics	Total(N)	Odds Ratio(OR)	P value	
T stage (T3&T4 vs. T1&T2)	371	1.648 (1.027-2.666)	0.040	*
Age (>60 vs. <=60)	373	0.781 (0.519-1.173)	0.234	
Pathologic stage (Stage III&Stage IV vs. Stage I&Stage II)	350	1.833 (1.129-3.008)	0.015	*
Gender (Male vs. Female)	374	0.659 (0.424-1.018)	0.061	
Fibrosis ishak score (3/4&5/6 vs. 0&1/2)	215	0.882 (0.514-1.510)	0.647	
Vascular invasion (Yes vs. No)	318	2.013 (1.263-3.231)	0.003	**
Adjacent hepatic tissue inflammation (Severe vs. None&Mild)	237	0.935 (0.345-2.458)	0.891	

FIGURE 2
DNAJC8 expression is closely associated with HCC prognosis. **(A)** Survival analysis of DNAJC8 expression (left: overall survival; middle: progression-free survival; right: disease-specific survival) in TCGA. **(B)** The ROC curve of DNAJC8. **(C)** Survival analysis of DNAJC8 expression in GEPIA. **(D)** Relationship between DNAJC8 expression and clinical characteristics. **(E)** Logistics regression analysis between DNAJC8 and clinical characteristics. *: $p<0.05$; **: $p<0.01$.

(Figure 2E). Therefore, DNAJC8 can be used as an independent prognostic indicator for HCC patients.

Enrichment analysis of DNAJC8-related genes

In order to identify the genetic alterations and enriched biological functions mediated by DNAJC8, we first picked out the genes significantly correlated with DNAJC8 and found differentially expressed genes, including *zcchc17* (r=0.85, $p<0.01$), *rpa2* (r=0.82, $p<0.01$), *ppp1r8* (r=0.83, $p<0.01$), *capzb* (r=0.80, $p<0.01$), *kdm1a* (r=0.77, $p<0.01$), *cdc42* (r=0.82, $p<0.01$), *hnrnpr* (r=0.80, $p<0.01$), *srsf4* (r=0.79, $p<0.01$), *ythdf2* (r=0.76, $p<0.01$), *szrd1* (r=0.75, $p<0.01$), *apoc2* (r=-0.41, $p<0.01$), *c8g* (r=-0.34, $p<0.01$), *hp* (r=-0.38, $p<0.01$), *c3* (r=-0.37, $p<0.01$), *itih4* (r=-0.36, $p<0.01$), *APOA1* (r=-0.33, $p<0.01$), *CFB* (r=-0.28, $p<0.01$), *A1BG* (r=-0.32, $p<0.01$), *SERPINA3* (r=-0.21, $p<0.01$), *APOC1* (r=-

10.3389/fimmu.2023.1289548

0.42, $p<0.01$) (Figure 3A). We then conducted enrichment analyses in terms of MFs, CCs, and BPs and KEGG pathways analyses (Figure 3B). GSVA correlation analysis was performed (Figure 3C). They all showed that the signaling pathways associated with DNAJC8 were spliceosome (KEGG, $p<0.01$), nucleocytoplasmic transport (KEGG, $p<0.01$), DNA replication (KEGG $p<0.01$), mRNA surveillance pathway (KEGG, $p<0.01$), cell cycle (KEGG, $p<0.01$), mitotic spindle (GSVA, r=0.54, $p<0.01$), G2M_checkpoint (GSVA, r=0.53, $p<0.01$), PI3K_Akt_mTOR_signaling (GSVA, r=0.53, $p<0.01$), MYC_targets_V1 (GSVA, r=0.52, $p<0.01$), E2F_targets (GSVA, r=0.50, $p<0.01$), spermatogenesis (GSVA, r=0.45, $p<0.01$), fatty_acid_metabolism (GSVA, r=-0.30, $p<0.01$), coagulation (GSVA, r=-0.30, $p<0.01$), bile_acid_metabolism (GSVA, r=-0.31, $p<0.01$), and xenobiotic_metabolism (GSVA, r=-0.36, $p<0.01$). Finally, through the string database analysis, we found that DNAJB6 (score=0.746), CCT5 (score=0.782), HSPA14 (score=0.732), DNAJC18 (score=0.860), U2SURP (score=0.839),

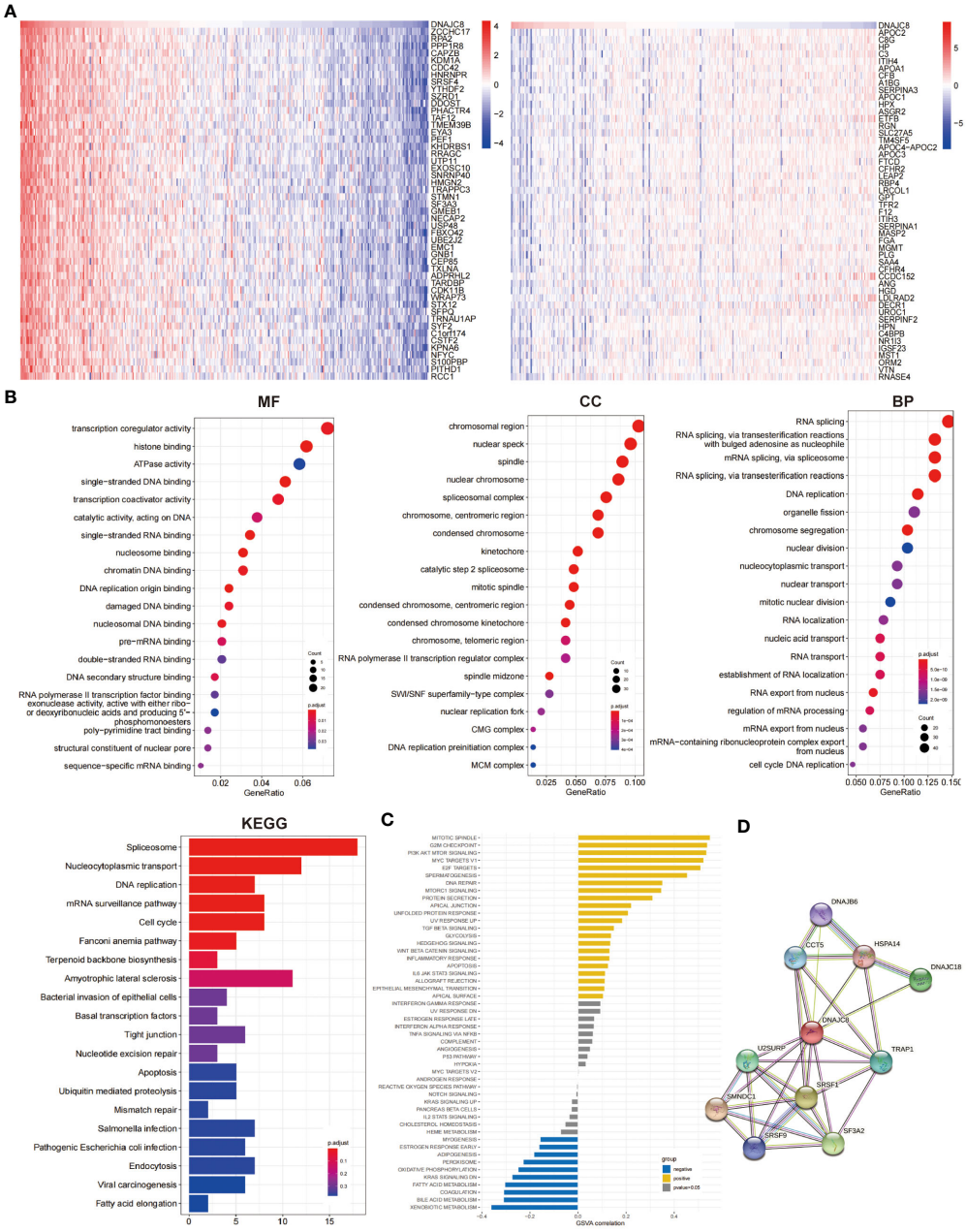

FIGURE 3
Enrichment analysis of DNAJC8-related genes. **(A)** The heat map of DNAJC8-related genes (left: positive correlation; right: negative correlation). **(B)** GO and KEGG analysis about DNAJC8-related genes. **(C)** GSVA analysis of DNAJC8-related genes. **(D)** PPI analysis of DNAJC8.

TRAP1 (score=0.811), SMNDC1 (score=0.940), SRSF1 (score=0.929), SRSF9 (score=0.751), and SF3A2 (score=0.885) may have protein-protein interactions with DNAJC8 (Figure 3D; Supplementary Figure 1B).

Abnormal expression of DNAJC8 affects tumor immune microenvironment

The composition or function of stromal cells, especially immune cells in tumor microenvironment can affect cancer progression. GSE datasets analysis showed that the expression of DNAJC8 was positively correlated with the enrichment of NK CD56 bright (r=0.185, p<0.001), T helper (r=0.269, p<0.001), and Th2 cells (r=0.382, p<0.001), while negatively correlated with the enrichment of Th17 cells (r=-0.171, p<0.001), killer toxic cells (r=-0.181, p<0.001), DC cells (r=-0.190, p<0.001), and pDC cells (r=-0.231, p<0.001) (Figure 4A). TCGA data analysis revealed that DNAJC8 expression was positively correlated with the infiltration of B cells (r=0.24, p<0.0001), CD8_naive (r=0.16, p<0.005), DC (r=0.16, p<0.005), Tr1 (r=0.18, p<0.001), nTreg (r=0.25, p<0.0001), and iTreg cells (r=0.22, p<0.0001), while negatively correlated with

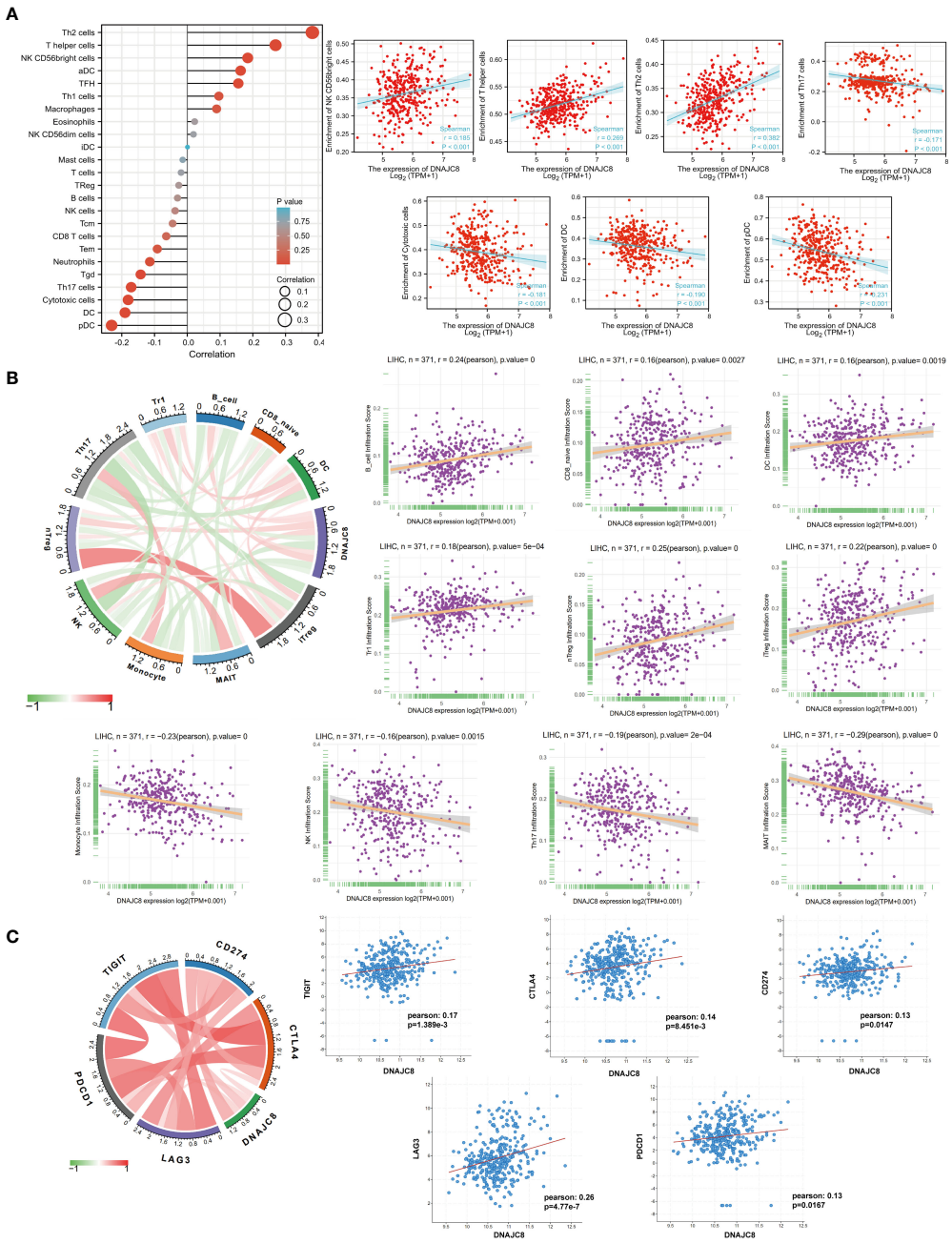

FIGURE 4
Abnormal expression of DNAJC8 affects tumor immune microenvironment. **(A)** Immune infiltration analysis using GSE datasets. **(B)** Immune infiltration analysis using TCGA datasets. **(C)** Relationship between DNAJC8 and immune checkpoints.

10.3389/fimmu.2023.1289548

the infiltration of monocytes (r=-0.23, p<0.0001), NK (r=-0.16, p<0.005), Th17 (r=-0.19, p<0.001), and MAIT cells (r=-0.29, p<0.0001) (Figure 4B). In addition, DNAJC8 levels was positively correlated with the expression of immune molecular checkpoint TIGIT (r=0.17, p<0.01), CTLA4 (r=0.14, p<0.01), CD274 (r=0.13, p<0.05), LAG3 (r=0.26, p<0.0001), and PDCD1 (r=0.13, p<0.05) (Figure 4C). These data indicated that DNAJC8 may be involved in the formation of tumor immunosuppressive microenvironment.

DNAJC8 knockdown inhibits HCC cell proliferation and induces apoptosis

Consistent with the above results of TCGA, DNAJC8 expression in tumor tissues was much higher than that in adjacent tissues in seven pairs of HCC patients' samples (Figure 5A). Meanwhile, immunohistochemical result further confirmed the upregulated DNAJC8 expression in the tumor tissues (Figure 5C). In order to explore the biological roles of DNAJC8, among the nine HCC cell lines, MHCC-97H and Huh-7 with relatively high DNAJC8 expression were selected for subsequent functional experiments (Figure 5B). DNAJC8 was successfully knockdown as shown in Supplementary Figures 1C, D. The proliferation ability of HCC cells with inhibited DNAJC8 expression was considerably impaired according to CCK-8 assays (Figure 6A), clone formation assays (Figure 6B), and EdU assays (Figure 6C). Furthermore, interference with DNAJC8 expression can induce apoptosis in HCC cells (Figure 6D). The expression of pro-apoptotic protein Bax was upregulated after DNAJC8 knockdown (Figure 6E). These indicated that DNAJC8 could promote the proliferation and inhibit apoptosis of HCC cells.

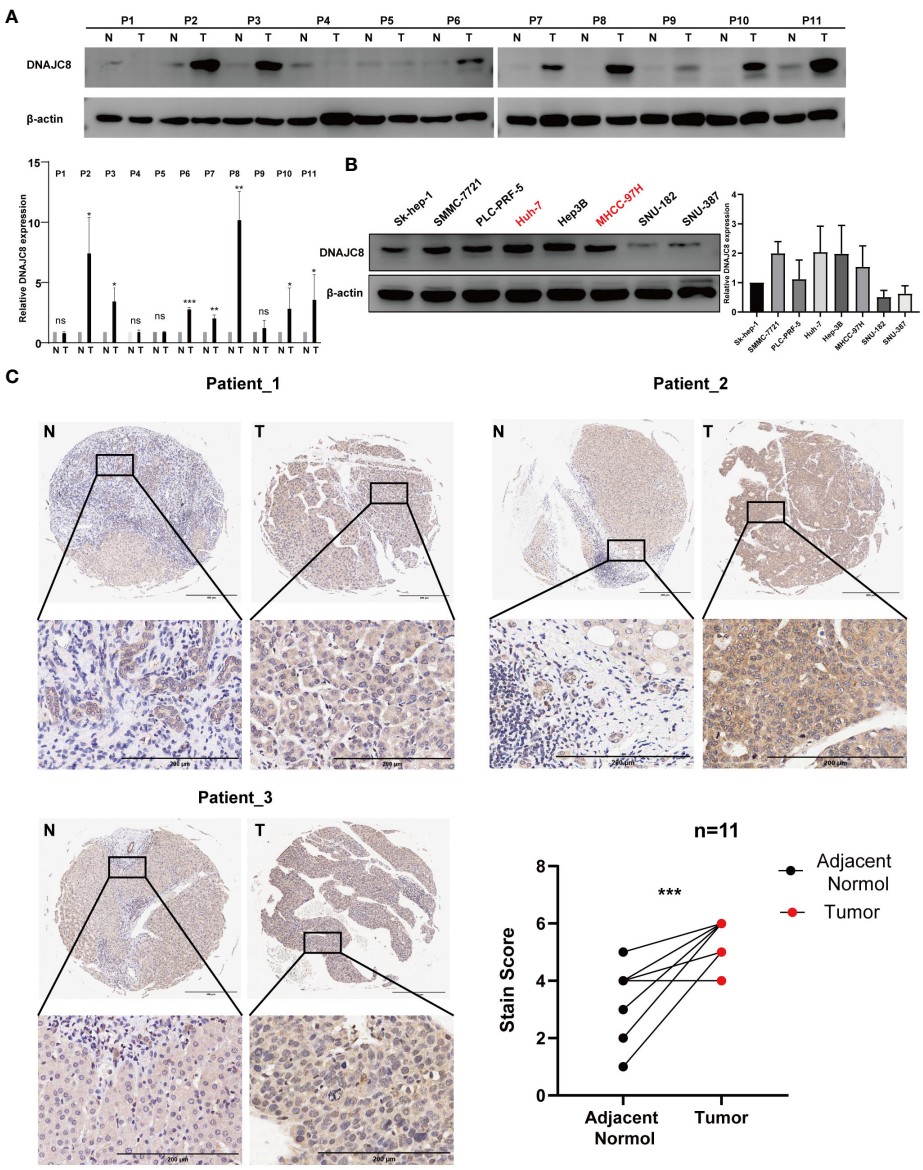

FIGURE 5
DNAJC8 expression in patients and cell lines. **(A)** Expression of DNAJC8 in paired samples from HCC patients. **(B)** Expression of DNAJC8 in HCC cell lines. **(C)** Immunohistochemical staining of HCC patient tissues (n=11). *: p<0.05; **: p<0.01; ***: p<0.001.

Discussion

DNAJC8, a member of HSP40 family, reports about its functional effects especially in tumor are scarce. Our study found that DNAJC8 expression was upregulated in HCC and has prognosis implications, indicating it may mediate the regulation of biological functions in HCC. HSP40 binds to HSP70 and activates its ATPase activity, which is mainly performed by His-Pro-Asp (HPD) motif in the conserved J region (23). Except for the conserved J region, there is no sequence similarity between DNAJCs and DNAJAs/DNAJBs (24). Hence, it is difficult to predict the function of DNAJCs according to DNAJAs and DNAJBs. Based on the context, it is necessary to analyze the function of DNAJC8 using bioinformatics analyses.

Analysis of TCGA data showed that HCC patients with higher expression of DNAJC8 have higher TP53 mutation frequencies. The

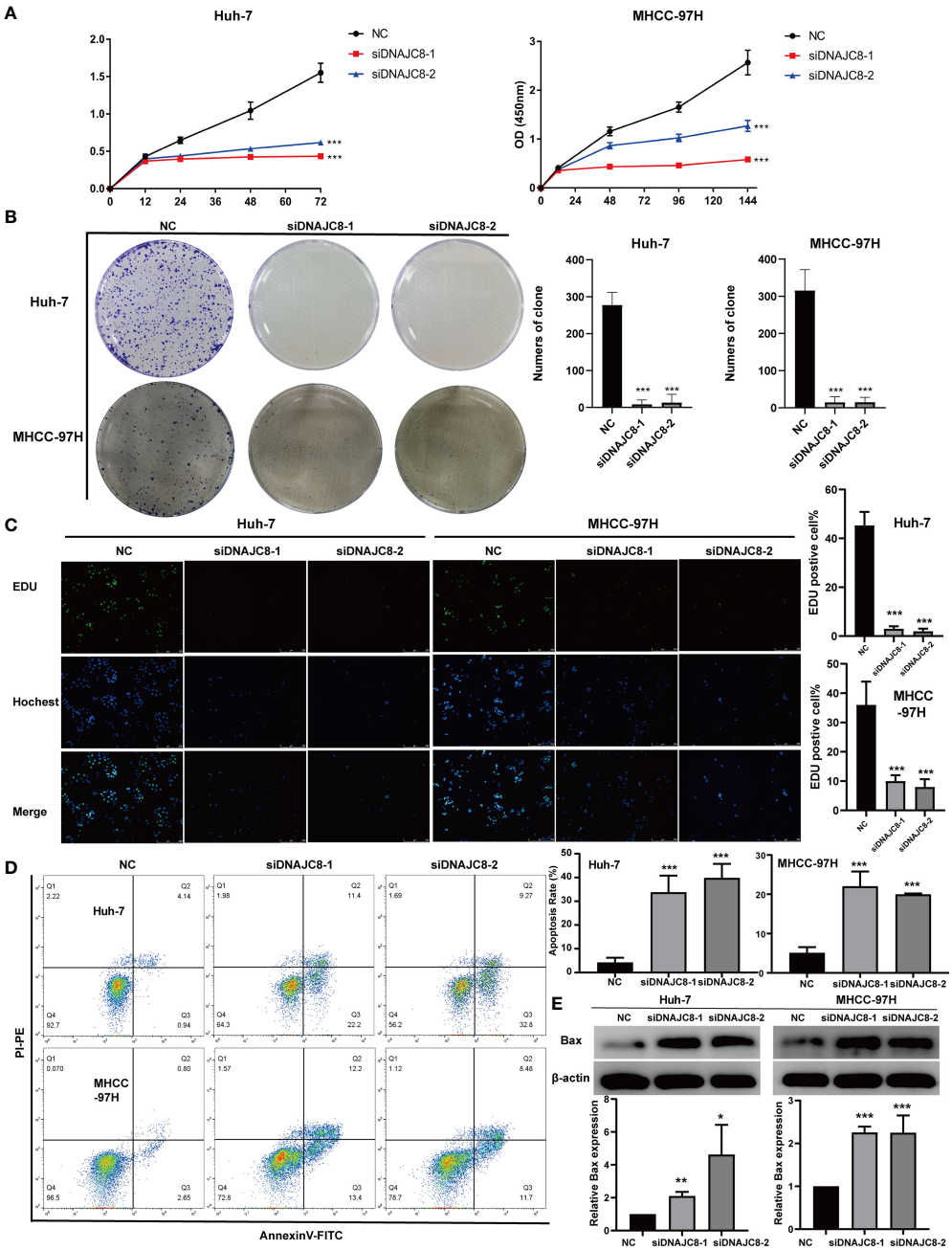

FIGURE 6
DNAJC8 knockdown inhibits HCC cell proliferation and induces apoptosis. **(A)** Growth curve of Huh-7 and MHCC-97H. **(B)** Colony formation assay of Huh-7 and MHCC-97H. **(C)** EDU assay of Huh-7 and MHCC-97H. **(D)** Apoptosis analysis of Huh-7 and MHCC-97H. **(E)** The up-regulation of Bax caused by the knock down of DNAJC8. *: $p<0.05$; **: $p<0.01$; ***: $p<0.001$.

relationship between HSP40 family and TP53 has been extensively verified. DNAJA1/HDJ2 directly binds to mutant TP53 (R175H, C176F) to prevent its ubiquitin-proteasome degradation (25). DNAJA3/Tid1 can bind to wild-type or mutant TP53, promoting its mitochondrial translocation, and thus inducing apoptosis (26). DNAJC7 can bind to the DNA binding region of TP53, stabilizing TP53 and further activating it to promote apoptosis (27). However, DNAJC2/ZRF1 promotes tumor development by inhibiting the function of wild-type TP53 (28). Thus, TP53 pathway most likely participate in the mechanistic regulation of DNAJC8. Moreover, DNAJC8 co-expressed gene sets analysis showed these significantly correlated genes were mainly involved in the regulation of chromatin and spindle regions, and their functions were mostly related to DNA binding. GO and KEGG analyses showed that DNAJC8 was associated with DNA replication, spindle function, and chromosome segregation. GSVA analysis showed a strong positive correlation between DNAJC8, mitotic spindle and G2/M checkpoint. These analyses suggest that the abnormal expression of DNAJC8 is associated with cell cycle. Combined with the fact that TP53 is an important regulatory protein in G2/M phase (29, 30), we hypothesized that DNAJC8 regulates HCC cell proliferation mediated by the TP53 pathway. However, we detected the expression of P53 protein after DNAJC8 knockdown, but no significant difference was found (Supplementary Figure 2B). According to the Cellosaurus database (https://www.cellosaurus.org/), both Huh-7 (c.659A>G) and MHCC-97H (c.151G>T) have P53 mutation, so it may not be appropriate to explore the regulatory relationship between DNAJC8 and P53 using these two cell lines. We will use HCC cells with different states of P53 in the future to explore the detailed regulatory mechanism.

The relationship between HSP40 family and tumor immune microenvironment remains unclear. Thus, exploring the interaction between DNAJC8 and immune cell infiltration will help us further understand the underlying mechanism of DNAJC8. Our analysis verified that the infiltration of killer cells (mononuclear-macrophages, NK, CD8+T, and MAIT cells) decreased, while the infiltration of helper cells (Th2, Tr1, nTreg, iTreg, NK CD56 bright), playing an immunomodulatory role and inhibiting the function of killer cells, increased in HCC tissues with higher DNAJC8 expression. These indicate that DNAJC8 is associated with tumor immunosuppressive microenvironment. However, the infiltration trend of DC cells was not consistent between the two databases analyses. Therefore, further verification in the follow-up study is needed. In addition, immune checkpoint molecular expression analysis also confirmed that five immune checkpoint molecular were significantly positively correlated with DNAJC8 expression, suggesting that DNAJC8 may promote tumor immune escape through checkpoint pathway. Therefore, the high expression of DNAJC8 is significantly related to immunosuppression microenvironment of cancer and detailed experimental investigation is needed in the future.

In order to investigate the function of DNAJC8, we used siRNA technology to knockdown DNAJC8 in MHCC-97H (TP53:c.151G>T) and Huh-7 (TP53:c.659A>G) cell lines. The results demonstrate that cell proliferation was inhibited and apoptosis was induced. In fact, clinical correlation analysis indicated that DNAJC8 expression was closely related to vascular invasion, and the HSP40 family had been proved to play an important role in tumor metastasis. Zhang et al. found that DNAJB6 promote rectal cancer cell invasion through IQGAP1/erk signaling pathway (31). It has been reported that DNAJA1 can stabilized the expression of EF1A1 by binding *miR-205-5p* to enhance the metastasis progress (32). Therefore, DNAJC8 is also likely to be involved in modulation of cancer metastasis. As DNAJC8 knockdown significantly injured cells *in vitro*, migration-related experiments were not explored.

Conclusions

DNAJC8 expression is upregulated in HCC and can serve as a prognostic indicator for HCC. DNAJC8 promotes the proliferation and inhibits apoptosis of HCC cells and interferes with the tumor immune response. Undoubtedly, DNAJC8 is worthy of further exploration as a therapeutic target for HCC.

Data availability statement

The datasets presented in this study can be found in online repositories. The names of the repository/repositories and accession number(s) can be found in the article/Supplementary Material.

Ethics statement

The studies involving humans were approved by the institutional review board of Zhuhai Hospital Affiliated with Jinan University. The studies were conducted in accordance with the local legislation and institutional requirements. The participants provided their written informed consent to participate in this study.

Author contributions

ZZ: Writing – original draft, Data curation, Methodology, Software. MJ: Writing – original draft, Validation. ZT: Writing – original draft, Software. ZH: Writing – original draft, Investigation. SH: Writing – original draft, Writing – review & editing, Funding acquisition, Project administration, Supervision.

Funding

The author(s) declare financial support was received for the research, authorship, and/or publication of this article. This work was supported by the National Nature Science Foundation of China (Grant No. 81902460), Scientific Research Startup Foundation of Zhuhai

People's Hospital (Grant No. 2020KYQD-01), and Xiangshan Talent Foundation of Zhuhai People's Hospital (Grant No. 2021XSYC-09).

Acknowledgments

We would like to thank Editage (www.editage.cn) for English language editing.

Conflict of interest

The authors declare that the research was conducted in the absence of any commercial or financial relationships that could be construed as a potential conflict of interest.

Publisher's note

Supplementary material

The Supplementary Material for this article can be found online at: https://www.frontiersin.org/articles/10.3389/fimmu.2023.1289548/full#supplementary-material

References

1. Llovet J, Zucman-Rossi J, Pikarsky E, Sangro B, Schwartz M, Sherman M, et al. Hepatocellular carcinoma. *Nat Rev Dis Primers* (2016) 2:16018. doi: 10.1038/nrdp.2016.18

2. Rimassa L, Personeni N, Czauderna C, Foerster F, Galle P. Systemic treatment of HCC in special populations. *J Hepatol* (2021) 74:931–43. doi: 10.1016/j.jhep.2020.11.026

3. Faivre S, Rimassa L, Finn R. Molecular therapies for HCC: Looking outside the box. *J Hepatol* (2020) 72:342–52. doi: 10.1016/j.jhep.2019.09.010

4. Huang A, Yang X, Chung W, Dennison A, Zhou J. Targeted therapy for hepatocellular carcinoma. *Signal Transduct Target Ther* (2020) 5:146. doi: 10.1038/s41392-020-00264-x

5. Jiang L, Li L, Liu Y, Lu L, Zhan M, Yuan S, et al. Drug resistance mechanism of kinase inhibitors in the treatment of hepatocellular carcinoma. *Front Pharmacol* (2023) 14:1097277. doi: 10.3389/fphar.2023.1097277

6. Jin H, Wang S, Zaal EA, Wang C, Wu H, Bosma A, et al. A powerful drug combination strategy targeting glutamine addiction for the treatment of human liver cancer. *Elife* (2020) 9:e56749. doi: 10.7554/eLife.56749

7. Wu Y, Du H, Zhan M, Wang H, Chen P, Du D, et al. Sepiapterin reductase promotes hepatocellular carcinoma progression via FoxO3a/Bim signaling in a nonenzymatic manner. *Cell Death Dis* (2020) 11:248. doi: 10.1038/s41419-020-2471-7

8. Piano A, Valbonesi P, Fabbri E. Expression of cytoprotective proteins, heat shock protein 70 and metallothioneins, in tissues of Ostrea edulis exposed to heat and heavy metals. *Cell Stress chaperones* (2004) 9:134–42. doi: 10.1379/483.1

9. Hartl FU, Martin J. Molecular chaperones in cellular protein folding. *Curr Opin Struct Biol* (1995) 5:92–102. doi: 10.1016/0959-440x(95)80014-r

10. Davenport EL, Moore HE, Dunlop AS, Sharp SY, Workman P, Morgan GJ, et al. Heat shock protein inhibition is associated with activation of the unfolded protein response pathway in myeloma plasma cells. *Blood* (2007) 110:2641–9. doi: 10.1182/blood-2006-11-053728

11. Kampinga H, Hageman J, Vos M, Kubota H, Tanguay R, Bruford E, et al. Guidelines for the nomenclature of the human heat shock proteins. *Cell Stress chaperones* (2009) 14:105–11. doi: 10.1007/s12192-008-0068-7

12. Cyr D, Langer T, Douglas M. DnaJ-like proteins: molecular chaperones and specific regulators of Hsp70. *Trends Biochem Sci* (1994) 19:176–81. doi: 10.1016/0968-0004(94)90281-x

13. Kim H, Hong S. Multi-faceted roles of DNAJB protein in cancer metastasis and clinical implications. *Int J Mol Sci* (2022) 23(23):14970. doi: 10.3390/ijms232314970

14. Babi A, Menlibayeva K, Bex T, Doskaliev A, Akshulakov S, Shevtsov M. Targeting heat shock proteins in Malignant brain tumors: from basic research to clinical trials. *Cancers* (2022) 14(21):5435. doi: 10.3390/cancers14215435

15. Trinh D, Elwi A, Kim S. Direct interaction between p53 and Tid1 proteins affects p53 mitochondrial localization and apoptosis. *Oncotarget* (2010) 1:396–404. doi: 10.18632/oncotarget.100902

16. Bae M, Jeong J, Kim S, Kim S, Kang H, Kim D, et al. Tid-1 interacts with the von Hippel-Lindau protein and modulates angiogenesis by destabilization of HIF-1alpha. *Cancer Res* (2005) 65:2520–5. doi: 10.1158/0008-5472.Can-03-2735

17. Tsai M, Wang C, Chang G, Chen C, Chen H, Cheng C, et al. A new tumor suppressor DnaJ-like heat shock protein, HLJ1, and survival of patients with non-small-cell lung carcinoma. *J Natl Cancer Institute* (2006) 98:825–38. doi: 10.1093/jnci/djj229

18. Menezes M, Mitra A, Shevde L, Samant R. DNAJB6 governs a novel regulatory loop determining Wnt/β-catenin signalling activity. *Biochem J* (2012) 444:573–80. doi: 10.1042/bj20120205

19. Cui X, Choi H, Choi Y, Park S, Sung G, Lee Y, et al. DNAJB1 destabilizes PDCD5 to suppress p53-mediated apoptosis. *Cancer Lett* (2015) 357:307–15. doi: 10.1016/j.canlet.2014.11.041

20. Yang T, Li X, Li X, Li M, Gao P. DNAJC6 promotes hepatocellular carcinoma progression through induction of epithelial-mesenchymal transition. *Biochem Biophys Res Commun* (2014) 455:298–304. doi: 10.1016/j.bbrc.2014.11.011

21. Li G, Zhao H, Guo H, Wang Y, Cui X, Li H, et al. Analyses of the function of DnaJ family proteins reveal an underlying regulatory mechanism of heat tolerance in honeybee. *Sci total Environ* (2020) 716:137036. doi: 10.1016/j.scitotenv.2020.137036

22. Wang C, Shyu R, Wu C, Chen M, Lee M, Lin Y, et al. Tazarotene-induced gene 1 interacts with DNAJC8 and regulates glycolysis in cervical cancer cells. *Mol Cell* (2018) 41:562–74. doi: 10.14348/molcells.2018.2347

23. Kityk R, Kopp J, Mayer M. Molecular mechanism of J-domain-triggered ATP hydrolysis by Hsp70 chaperones. *Mol Cell* (2018) 69:227–237.e224. doi: 10.1016/j.molcel.2017.12.003

24. Kampinga H, Craig E. The HSP70 chaperone machinery: J proteins as drivers of functional specificity. *Nat Rev Mol Cell Biol* (2010) 11:579–92. doi: 10.1038/nrm2941

25. Xu D, Tong X, Sun L, Li H, Jones R, Liao J, et al. Inhibition of mutant Kras and p53-driven pancreatic carcinogenesis by atorvastatin: Mainly via targeting of the farnesylated DNAJA1 in chaperoning mutant p53. *Mol carcinogenesis* (2019) 58:2052–64. doi: 10.1002/mc.23097

26. Ahn B, Trinh D, Zajchowski L, Lee B, Elwi A, Kim S. Tid1 is a new regulator of p53 mitochondrial translocation and apoptosis in cancer. *Oncogene* (2010) 29:1155–66. doi: 10.1038/onc.2009.413

27. Kubo N, Wu D, Yoshihara Y, Sang M, Nakagawara A, Ozaki T. Co-chaperon DnaJC7/TPR2 enhances p53 stability and activity through blocking the complex formation between p53 and MDM2. *Biochem Biophys Res Commun* (2013) 430:1034–9. doi: 10.1016/j.bbrc.2012.11.121

28. Imamura T, Komatsu S, Ichikawa D, Miyamae M, Okajima W, Ohashi T, et al. Overexpression of ZRF1 is related to tumor Malignant potential and a poor outcome of gastric carcinoma. *Carcinogenesis* (2018) 39:263–71. doi: 10.1093/carcin/bgx139

29. Hafner A, Bulyk ML, Jambhekar A, Lahav G. The multiple mechanisms that regulate p53 activity and cell fate. *Nat Rev Mol Cell Biol* (2019) 20:199–210. doi: 10.1038/s41580-019-0110-x

30. Müller I, Strozyk E, Schindler S, Beissert S, Oo HZ, Sauter T, et al. Cancer Cells Employ Nuclear Caspase-8 to Overcome the p53-Dependent G2/M Checkpoint through Cleavage of USP28. *Mol Cell* (2020) 77:970–984.e977. doi: 10.1016/j.molcel.2019.12.023

31. Zhang T, Jiang Y, Shang L, Shi Z, Liang J, Wang Z, et al. Overexpression of DNAJB6 promotes colorectal cancer cell invasion through an IQGAP1/ERK-dependent signaling pathway. *Mol carcinogenesis* (2015) 54:1205–13. doi: 10.1002/mc.22194

32. Yi L, He S, Cheng Z, Chen X, Ren X, Bai Y. DNAJA1 stabilizes EF1A1 to promote cell proliferation and metastasis of liver cancer mediated by miR-205-5p. *J Oncol* (2022) 2022:2292481. doi: 10.1155/2022/2292481

frontiers | Frontiers in Immunology

TYPE Original Research
PUBLISHED 15 January 2024
DOI 10.3389/fimmu.2023.1292019

OPEN ACCESS

EDITED BY
Takaji Matsutani,
Maruho, Japan

REVIEWED BY
Antonella Antignani,
National Institutes of Health, United States
Ghanbar Mahmoodi Chalbatani,
Mayo Clinic Arizona, United States

*CORRESPONDENCE
Yi-Yuan Yang
yangyuan@tmu.edu.tw
Liang-Tzung Lin
ltlin@tmu.edu.tw

†These authors have contributed equally to this work

RECEIVED 10 September 2023
ACCEPTED 11 December 2023
PUBLISHED 15 January 2024

CITATION
Liu C-H, Leu S-J, Lee C-H, Lin C-Y, Wang W-C, Tsai B-Y, Lee Y-C, Chen C-L, Yang Y-Y and Lin L-T (2024) Production and characterization of single-chain variable fragment antibodies targeting the breast cancer tumor marker nectin-4. *Front. Immunol.* 14:1292019. doi: 10.3389/fimmu.2023.1292019

Production and characterization of single-chain variable fragment antibodies targeting the breast cancer tumor marker nectin-4

Ching-Hsuan Liu[1,2†], Sy-Jye Leu[1,3†], Chi-Hsin Lee[4,5], Cheng-Yuan Lin[4], Wei-Chu Wang[5], Bor-Yu Tsai[6], Yu-Ching Lee[7], Chi-Long Chen[8], Yi-Yuan Yang[4,5,9*] and Liang-Tzung Lin[1,3*]

[1]Department of Microbiology and Immunology, School of Medicine, College of Medicine, Taipei Medical University, Taipei, Taiwan, [2]Department of Microbiology & Immunology, Dalhousie University, Halifax, Nova Scotia, Canada, [3]Graduate Institute of Medical Sciences, College of Medicine, Taipei Medical University, Taipei, Taiwan, [4]School of Medical Laboratory Science and Biotechnology, College of Medical Science and Technology, Taipei Medical University, Taipei, Taiwan, [5]Ph.D. Program in Medical Biotechnology, College of Medical Science and Technology, Taipei Medical University, Taipei, Taiwan, [6]Navi Bio-Therapeutics Inc., Taipei, Taiwan, [7]The Center of Translational Medicine, Taipei Medical University, Taipei, Taiwan, [8]Department of Pathology, School of Medicine, College of Medicine, Taipei Medical University and Taipei Medical University Hospital, Taipei, Taiwan, [9]Core Laboratory of Antibody Generation and Research, Taipei Medical University, Taipei, Taiwan

Background: Nectin-4 is a novel biomarker overexpressed in various types of cancer, including breast cancer, in which it has been associated with poor prognosis. Current literature suggests that nectin-4 has a role in cancer progression and may have prognostic and therapeutic implications. The present study aims to produce nectin-4-specific single-chain variable fragment (scFv) antibodies and evaluate their applications in breast cancer cell lines and clinical specimens.

Methods: We generated recombinant nectin-4 ectodomain fragments as immunogens to immunize chickens and the chickens' immunoglobulin genes were amplified for construction of anti-nectin-4 scFv libraries using phage display. The binding capacities of the selected clones were evaluated with the recombinant nectin-4 fragments, breast cancer cell lines, and paraffin-embedded tissue sections using various laboratory approaches. The binding affinity and *in silico* docking profile were also characterized.

Results: We have selected two clones (S21 and L4) from the libraries with superior binding capacity. S21 yielded higher signals when used as the primry antibody for western blot analysis and flow cytometry, whereas clone L4 generated cleaner and stronger signals in immunofluorescence and

immunohistochemistry staining. In addition, both scFvs could diminish attachment-free cell aggregation of nectin-4-positive breast cancer cells. As results from ELISA indicated that L4 bound more efficiently to fixed nectin-4 ectodomain, molecular docking analysis was further performed and demonstrated that L4 possesses multiple polar contacts with nectin-4 and diversity in interacting residues.

Conclusion: Overall, the nectin-4-specific scFvs could recognize nectin-4 expressed by breast cancer cells and have the merit of being further explored for potential diagnostic and therapeutic applications.

KEYWORDS

phage display, single-chain variable fragment antibody, nectin-4, tumor marker, breast cancer

1 Introduction

The recombinant antibody molecule single-chain variable fragment (scFv) has emerged as a compelling variant of intact monoclonal antibodies (mAb) due to its reduced molecular size and lower production cost. scFv is an engineered antibody fragment comprising the heavy and light chains' variable domains (V_H and V_L) joined by a short flexible peptide linker. It retains complete monovalent targeting affinity and specificity (1), rendering it theoretically viable for all bench and bedside applications currently relying on intact mAb. Moreover, as a minimized antibody lacking the fragment crystallizable (Fc) domain, scFv exhibits superior pharmacokinetic properties, notably enhanced tumor penetration and low retention rates in non-target organs (2, 3). Furthermore, with regard to production, there is relative ease in and preference for constructing scFv due to the advancement in genetic engineering and phage display technology (3), an *in vitro* method that can produce highly diverse libraries for high-affinity antibody selection (4). scFv can also be efficiently and economically produced in bacteria expression systems since they do not require glycosylation (5). Finally, scFv has excellent potential to be modified and developed into diverse immunoconjugates with varied and enhanced functionality for clinical and laboratory uses (3). As a promising alternative to intact mAb, scFv variants have entered clinical development, representing about 40% of clinically evaluated antibody fragments (6), with cancer being the top target of patented scFvs (3).

Nectin-4, also known as poliovirus receptor-related 4 (PVRL4), is an immunoglobulin (Ig) superfamily member of the nectin family which regulates the formation of cell-cell junctions (7). This adhesion junction protein has three Ig-like domains in its extracellular portion, including one variable (V) type domain and two constant (C) type domains. In contrast to the other members of the nectin family, nectin-4 is highly expressed in the placenta (hence also an embryonic protein) but modestly expressed in the trachea and skin and is absent in most normal human tissues (8). Recently, nectin-4 has been identified as a tumor marker in several types of carcinoma, including lung (9), breast (10), ovarian (11), esophageal (12), gastric (13), pancreatic (14), liver (15), colon (16), and bladder (17) cancers, and has been suggested to promote carcinogenesis (18–22). The upregulation of nectin-4 was first reported in breast cancer, especially in ductal carcinomas, and positively correlated with basal-like markers, which often implies poor prognosis (10). This observation was further supported by a bigger dataset where nectin-4-high triple-negative breast cancer patients had shorter metastasis-free survival (23). Nectin-4 expression is also related to shorter disease-free survival and relapse-free survival in luminal A (24) and luminal B human epidermal growth factor receptor 2 (HER2)-negative (25) breast cancers, suggesting that nectin-4 could be a potential prognostic marker and a therapeutic target of breast cancer.

Given the high level of expression and importance of nectin-4 in cancers, including breast cancer, and the benefits of scFv as an emerging diagnostic and therapeutic tool, we produced anti-nectin-4 scFvs using phage display and characterized their use for detecting nectin-4 in breast cancer cell lines and tissue sections. Their impact on breast cancer cells were also evaluated.

2 Materials and methods

2.1 Construction and purification of nectin-4 protein fragments

Two recombinant protein fragments, r342p and r864p, were constructed based on the extracellular region of human nectin-4 (accession number: NM_030916). Fragment r342p contained only the membrane-distal V-type domain, while r864p contained all

three Ig-like domains. The nucleotide sequence of r342p and r864p were amplified from vectors containing nectin-4 (26) and cloned into the pET-21a vector. The plasmids were amplified in *Escherichia coli* (*E. coli*) with broth containing 50 μl/ml ampicillin and induced by 1 mM isopropyl β-D-1-thiogalactopyranoside (IPTG) at 37°C overnight for protein expression. Pellets were then collected and resuspended in histidine (His) binding buffer containing 6 M urea. The cell membrane was disrupted by sonication and precipitated to release the proteins. Recombinant nectin-4 fragments were purified from the supernatants using Ni Sepharose High Performance (GE Healthcare Life Science, Pittsburgh, PA, USA) according to the manufacturer's instructions. The purified nectin-4 fragments were further analyzed with sodium dodecyl sulfate-polyacrylamide gel electrophoresis (SDS-PAGE) and western blot.

2.2 Immunization and purification of chicken polyclonal IgY

The experimental protocol for chicken immunization was approved by the Institutional Animal Care and Use Committee of Taipei Medical University (TMU). Purified nectin-4 fragments r342p or r864p were dissolved in phosphate buffered saline (PBS) and mixed with complete (for the first immunization) or incomplete Freund's adjuvant (Sigma-Aldrich, St. Louis, MO, USA). The solutions were then intramuscularly injected into female Leghorn (*Gallus domesticus*) hens for four (r864p) or five (r342p) dosages at the interval of 7 days as previously described (27). Eggs were collected before and after each immunization. Polyclonal IgY were then purified from the egg yolks using the previously reported dextran sulfate method (28) and analyzed for their binding capacity to the recombinant nectin-4 fragments using western blot and enzyme-linked immunosorbent assay (ELISA).

2.3 Construction of scFv libraries

Monoclonal scFv antibodies were generated using the previously described phage display method (29, 30) with a few modifications. To establish the cDNA libraries, the immunized hens were sacrificed after the final immunization, and total RNA was extracted from the spleens using Trizol Reagent (Invitrogen, Carlsbad, CA, USA) following the manufacturer's instructions. After reverse transcription-PCR (RT-PCR), the synthesized cDNA was used to amplify the variable regions of light chains (V_L) and heavy chains (V_H) of chicken immunoglobulin genes with the primers (Supplementary Table S1): CSCVHo-F and CSCG-B were used to amplify V_H with a short linker (GQSSRSS), CSCVHo-FL and CSCG-B were used to amplify V_H with a long linker (GQSSRSSGGGGSSGGGGS), and CSCVK and CKJo-B were used to amplify V_L. This would generate a short linker library and a long linker library for each immunogen. The purified V_H and V_L DNA fragments were then pooled and further amplified with CSC-F and CSC-B primers to generate full-length scFv genes. These full-length scFv genes were cloned into a pComb3X vector with SfiI (New England Biolabs, Ipswich, MA, USA) to generate constructs that encoded a 6x His tag and a HA tag in their C terminus. The purified plasmids were electroporated into *E. coli*, and the transformed bacteria were then infected with M13 helper phages. Recombinant phages in the supernatant were collected by precipitation with 4% polyethylene glycol 8000 (PEG-8000; Sigma-Aldrich) and 3% NaCl (Merck, Darmstadt, Germany) and resuspended in PBS.

To isolate and amplify the phage-displayed scFv libraries with high specificity, the biopanning steps were carried out using a similar method as previously described (27). Four rounds of biopanning were performed to selectively amplify the phages that displayed nectin-4-specific scFv antibodies. After the fourth round of biopanning, total DNA from the amplified phages was purified and used to transform the heat-shock competent TOP10F' *E. coli*. Colonies were picked and amplified, after which 0.5 mM IPTG was added to induce scFv expression. Bacterial cultures were then collected, resuspended in His-binding buffer (20 mM sodium phosphate, 0.5 M NaCl, 20 mM imidazole, pH 7.4), and lysed by sonication to release the His-tagged scFvs, which were purified using Ni^{2+} Sepharose columns as previously described (27). The V_L and V_H genes of the scFv clones were sequenced by Genomics (Taipei, Taiwan) using the OmpA primers. Amino acid sequences of the clones were then determined and aligned to those of the chicken immunoglobulin germline using the BioEdit alignment program.

2.4 Cell culture

MCF-7, MDA-MB-231, BT-474, MDA-MB-453, and Vero cells were acquired from the American Type Culture Collection (ATCC; Manassas, VA, USA). All cells were maintained in Dulbecco's Modified Eagle Medium (Gibco, Thermo Fisher Scientific, Waltham, CA, USA) containing 10% fetal bovine serum (FBS; Gibco), 10 μg/ml of gentamicin (Gibco) and 0.5 μg/ml of Amphotericin B (Gibco). Vero cell overexpressing human nectin-4 (Vero-hNectin-4) was generated using a retroviral transduction method and cultured in the above medium containing additional 1 mg/ml of G418 (InvivoGen, San Diego, CA, USA).

2.5 Western blot analysis

Purified proteins or whole cell lysates were analyzed using standard western blot analysis. Briefly, samples were separated by SDS-PAGE, and the gel was then stained with Coomassie blue for protein visualization or transferred to a polyvinylidene fluoride (PVDF) membrane for blocking and antibody incubations. For the detection of recombinant nectin-4, the membrane was incubated with mouse anti-His IgG (1:3000; Bioman Scientific, New Taipei City, Taiwan) and secondary horseradish peroxidase (HRP)-conjugated rabbit anti-mouse IgG (1:5000; Jackson ImmunoResearch, West Grove, PA, USA). The membrane was then visualization by 3, 3'-diaminobenzidine tetrahydrochloride (DAB) staining. For the detection of endogenous nectin-4 from whole cell lysates using scFv, the membrane was incubated with scFv (10 μg/ml), mouse anti-HA secondary antibody (1:5000; Cat#

66006-1, Proteintech, Rosemont, IL, USA), and HRP-conjugated anti-mouse tertiary antibody (1:5000; Cat# 7076, Cell Signaling Technology, Danvers, Massachusetts, USA). Finally, the membrane was stained with Clarity Western ECL Substrate (Bio-Rad) and visualized by ImageQuant™ LAS 4000 (GE Healthcare Life Science).

2.6 Indirect ELISA

For the indirect ELISA, 96-well half-area plates were coated with either recombinant nectin-4 fragment or BSA (0.25 μg per well) and blocked with 5% skim milk. To determine the binding capacity of IgY, the coated wells were incubated with serially diluted chicken IgY and incubated with HRP-conjugated donkey anti-chicken IgY (1:5000; Jackson ImmunoResearch). To determine the expression of nectin-4-specific scFvs on the phages after biopanning, 2x diluted phages were added to the wells and further incubated with HRP-conjugated mouse anti-M13 phage antibody (1:3000; GE Healthcare Life Science). To determine the binding capacity of scFvs, the coated wells were incubated with serially diluted scFv primary antibody, goat anti-chicken light chain secondary antibody (1:3000; Bethyl, Montgomery, TX, USA), and the tertiary HRP-conjugated donkey anti-goat IgG (1:5000). All incubations were carried out at 37°C for 1 h, and washing steps with PBST were included between all incubations. After the final incubation, the wells were washed and stained with 3,3',5,5'-tetramethylbenzidine (TMB; Sigma), and the reaction was stopped by 1 N HCl before the absorbance was read at 450 nm using a Synergy HT plate reader (BioTek, Winooski, VT, USA).

2.7 Competitive ELISA

Free nectin-4 fragment r864p was serially diluted and mixed with S21 (20 μg/ml, approximately 666.67 nM) or L4 (1 μg/ml, approximately 33.33 nM) and incubated at 25°C for 1 h, before the mixture was added to plates coated with r864p and incubated at 37°C for 1 h. The blocking, washing, staining, and detection steps were performed using the abovementioned methods. The dissociation constant KD is approximately equal to the concentration of free antigen when the half-maximal ELISA signal is acquired (31). KD values were calculated with variable slope nonlinear regression analysis using GraphPad 9.

2.8 Cell-based ELISA

Cells seeded in 24-well plates (2 x 10^5 cells/well) were washed and fixed with 4% paraformaldehyde (PFA; Affymetrix, Santa Clara, CA, USA) before incubation in 3% BSA in PBS blocking buffer for 1 h at 37°C. The cells were then incubated with various concentrations of scFvs and goat anti-chicken light chain secondary antibody (1:5000). Subsequently, the cells were washed and further incubated with the tertiary HRP-conjugated donkey anti-goat IgG (1:10000). All incubations were carried out at 37°C for 1 h. After the final incubation, the cells were washed and stained with TMB as described above.

2.9 Flow cytometry

Cells (5 x 10^4 cells/sample) were fixed with 10% ethanol and blocked in 3% FBS in PBS blocking buffer. For detection of cell surface nectin-4 using scFv, cells were incubated with scFv primary antibody (37.5 μg/ml), goat anti-chicken light chain secondary antibody (1:400), and rabbit anti-goat IgG Fluor 488-labeled tertiary antibody (1:400; AnaSpec, Fremont, CA, USA). Staining with the commercial PE-conjugated anti-Nectin-4 antibody (FAB2659P, R&D Systems) and its isotype control (IC0041P, R&D Systems) were performed following the manufacturer's instructions and included for comparison. Data were acquired with the BD FACSCalibur Cell Analyzer (BD Biosciences, San Jose, CA, USA).

2.10 Immunofluorescence staining

Cells seeded in 96-well plates (2 x 10^4 cells/well) were washed and fixed with 4% PFA for 10 min at room temperature, then incubated in 3% BSA in PBS blocking buffer for 1 h at room temperature. After which, cells were incubated with scFv primary antibody (0.1 μg/ml), mouse anti-HA secondary antibody (1:500), and goat anti-mouse Alexa Fluor 488 (1:300; Thermo Fisher Scientific) tertiary antibody. All antibody dilutions were prepared in 3% BSA blocking buffer. Finally, the cells were stained with Hoechst nuclear stain (1:500; Sigma-Aldrich) and examined using Invitrogen EVOS™ FL Cell Imaging System (Thermo Fisher Scientific).

2.11 Immunohistochemistry staining

Paraffin sections of breast ductal carcinomas and adjacent non-tumor tissues were obtained from Taipei Medical University Joint Biobank as approved by the TMU-Joint Institutional Review Board. Informed consent was waived. Before staining, sections were deparaffinized with xylene and ethanol, and antigen retrieval was performed using the heat-induced method at 121°C for 10 min. Endogenous HRP was inactivated by treating the sections with 3% hydrogen peroxide for 5 min. The sections were then blocked with Background Sniper (Biocare Medical, Pacheco, CA, USA) for 15 min at room temperature. For scFv staining, the slides were incubated with scFv primary antibody (10 μg/ml), mouse anti-HA secondary antibody (1 μg/ml), and the Starr Trek Universal HRP Detection System (Biocare Medical, Pacheco, CA, USA), and counter-stained with hematoxylin. For the commercial anti-nectin-4 antibody staining, the slides were incubated with a polyclonal rabbit anti-nectin-4 antibody (1:600; Cat# HPA010775, Sigma-Aldrich) and visualized with the Starr Trek Universal HRP Detection System and hematoxylin as described above.

2.12 Clustering assay

Self-clustering of breast cancer cells was analyzed as previously reported (18). Cells were first detached with enzyme-free cell dissociation buffer (Thermo Fisher Scientific) and resuspended in complete medium. Then 1 x 10^5 cells were transferred to an Eppendorf tube and incubated in 1 ml complete medium with or without scFv (10 μg/ml) at room temperature. After 1 h, cells were poured into 6-well plates and visualized using Invitrogen EVOS™ FL Cell Imaging System for counting. A total of 5 random fields were analyzed for each well, and clusters with over 5 cells were counted.

2.13 Protein-protein docking analysis

The homology model of the scFv L4 was created using SWISS-MODEL (Swiss Institute of Bioinformatics; Basel, Switzerland) based on a scFv template (PDBID: 5VF6) (32). Protein-protein docking was performed using ClusPro 2.0's antibody docking mode (33). The nectin-4 crystal structure was obtained from the PDB database (PDBID: 4FRW) and used as the ligand molecule, whereas the scFv homology model was used as the receptor molecule. All models were analyzed using the PyMOL Molecular Graphics System (Version 1.7.4, Schrödinger, LLC; Portland, OR, USA) (34).

3 Results

3.1 Generation of nectin-4-specific polyclonal IgY from immunized chickens

Like the other members in the nectin family, nectin-4 has three Ig-like domains in its extracellular portion, including one V-type and two C-type domains (8). To generate polyclonal antibodies against nectin-4, we immunized chickens with recombinant nectin-4 fragments r342p (V domain) and r864p (V-C-C domains). The nectin-4 fragments, after SDS-PAGE and Coomassie blue staining, appeared at the positions of approximately 15 kDa (r342p; Figure 1A) and 35 kDa (r864p; Figure 1B), respectively. Polyclonal IgY antibodies purified from the immunized chickens were used as primary antibodies to detect these protein fragments

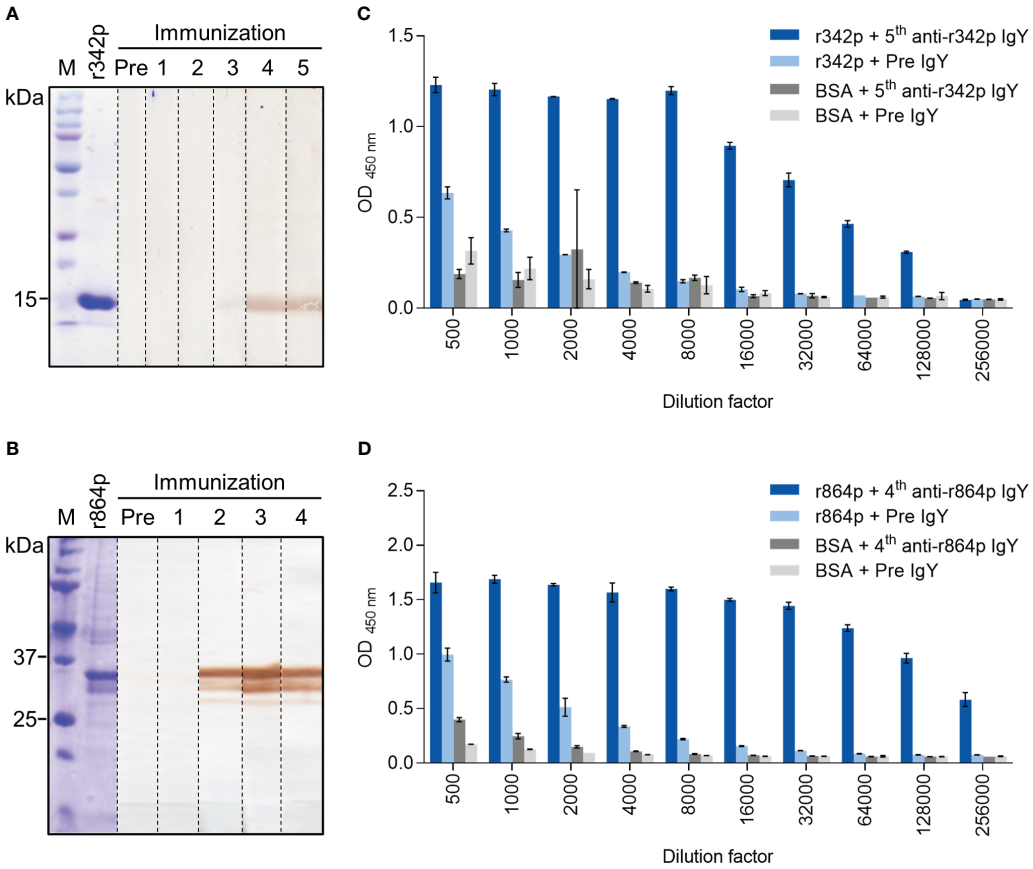

FIGURE 1
Binding analyses of polyclonal IgY against recombinant nectin-4 fragments r342p and r864p. Hens were immunized with nectin-4 fragments r342p or r864p for 5 or 4 cycles, respectively, and polyclonal IgY was purified from the egg yolks after each immunization cycle. **(A, B)** The r342p and r864p fragments were visualized on SDS-PAGE gel with Coomassie blue staining or transferred to PVDF membrane and immunoblotted with the IgY collected before ("Pre") or after each immunization cycle. The molecular weight marker (M) is shown on the left. Representative data are shown. **(C, D)** Pre-immunization IgY ("Pre IgY") or IgY collected after the last immunization cycle ("5^{th} anti-r342p IgY" or "4^{th} anti-r864p IgY") were serially diluted and evaluated by immunogen- or BSA-coated plate-based indirect ELISA. BSA served as a negative control antigen (mean ± SD, N=2).

on western blots. As shown in Figure 1A, the presence of anti-r342p antibodies became prominent after 4 cycles of immunization. On the other hand, anti-r864p antibodies were generated after 2 cycles of immunization (Figure 1B). The binding specificity of these antibodies was further evaluated with ELISA. As shown in Figures 1C, D, the anti-r342p and anti-r864p antibodies were specific and bound robustly to their immunogens (O.D. > 1.0 for anti-r342p IgY, and O.D. > 1.5 for anti-r864p IgY) with minimal reactivity to BSA. In contrast, the pre-immunization IgY did not show specific binding to the nectin-4 fragments or BSA. These results indicate that we successfully generated nectin-4-specific polyclonal IgY, which were used for the following construction of scFv phage libraries.

3.2 ScFv clones in the anti-r342p long linker and anti-r864p short linker phage libraries demonstrate the best nectin-4-binding ability

We next attempted to produce anti-nectin-4 scFv antibodies using the phage display method. Four scFv phage libraries were generated based on the amplified chicken antibody sequences, namely the anti-r342p short linker library, anti-r342p long linker library, anti-r864p short linker library, and anti-r864p long linker library. These four libraries were subjected to four rounds of biopanning to amplify the phages that expressed nectin-4-specific scFv antibodies. Phages collected before and after each round of biopanning were then analyzed with ELISA for their binding capacity to r864p, the recombinant nectin-4 fragment containing all three extracellular Ig-like domains. As shown in Figure 2A, after 3 rounds of biopanning, the binding capacity of the anti-r342p long linker and anti-r864p short linker libraries substantially increased. In contrast, the anti-r342p short linker and anti-r864p long linker libraries had low binding activity to the nectin-4 fragment. None of the libraries reacted to BSA.

To express the scFv antibodies from the anti-r342p long linker and anti-r864p short linker libraries, total DNA from the phages were extracted after the fourth-round biopanning and used to transform TOP10F' *E. coli* cells. Thirteen and 26 colonies were randomly picked from the anti-r342p long linker and anti-r864p short linker libraries, respectively, for protein purification. Seven colonies from the anti-r342p long (L) linker library and 12 colonies from the anti-r864p short (S) linker library were then selected for sequence analysis based on their specific binding to nectin-4. The V_L and V_H amino acid sequences of

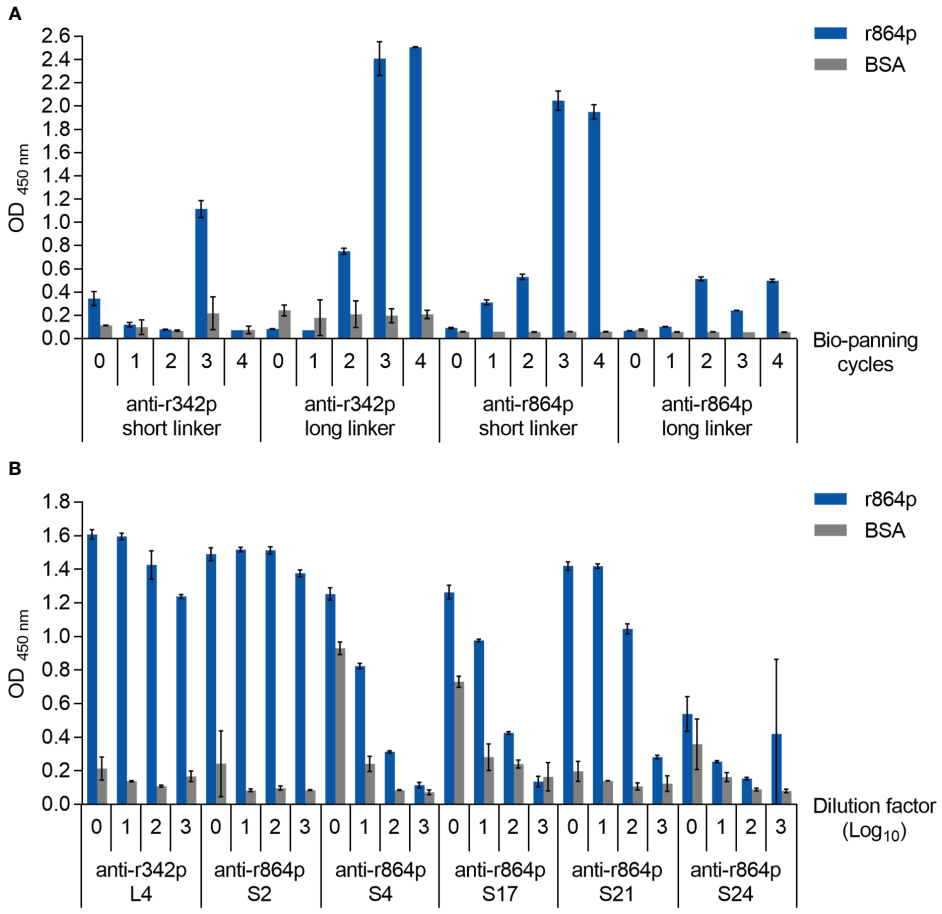

FIGURE 2
Construction of anti-nectin-4 scFv libraries. **(A)** Anti-r342p and anti-r864p phages from each biopanning cycle were diluted 10x and evaluated for their binding capacity to r864p using plate-based indirect ELISA. BSA served as a negative control antigen (mean ± SD, N=2). **(B)** Purified scFvs from the representative clones were serially diluted (starting concentration: 10 μg/ml) and evaluated for their binding capacity by r864p-coated plate-based indirect ELISA. BSA served as a negative control antigen (mean ± SD, N=2).

each clone were aligned to those of the chicken immunoglobulin germline. Based on the alignment results, the mutations were mainly found in the complementarity-determining regions (CDR), which generate the paratope for antigen binding. The 7 colonies from the anti-r342p long linker library shared identical amino acid sequences (representative clone: L4), and the 12 colonies from the anti-r864p short linker library resulted in 5 different sequences (representative clones: S2, S4, S17, S21, and S24). After assessing the binding capacity of the representative clones as primary antibodies using ELISA (Figure 2B), clones L4 and S21 were selected for subsequent characterization due to their superior activity of recognizing nectin-4 fragment r864p. Clone S2 was not further pursued due to its lower production yield.

3.3 Clones L4 and S21 successfully recognize nectin-4 expressed on breast cancer cells

To evaluate the application of L4 and S21, we next examined whether these scFvs could detect endogenous nectin-4 expressed in human breast cancer cell lines, including MCF-7 (luminal type A), BT-474 (luminal type B HER2-positive), and MDA-MB-453 (triple negative) (10, 26, 35). The nectin-4-negative MDA-MB-231 breast cancer cells served as a negative control. When used in western blotting as primary antibodies, S21, but not L4, successfully detected nectin-4 in the whole cell lysates at approximately 60 kDa (Figure 3A). Both clones could recognize the endogenous nectin-4 in MCF-7 cells using cell-based ELISA, with S21 generating higher signals than L4 after serial dilutions (Figure 3B). In flow cytometry analysis, S21 also produced a comparable staining pattern to the commercial PE-conjugated anti-nectin-4 antibody FAB2659P (Figure 3C). When used for immunofluorescence surface staining, both L4 and S21 could stain nectin-4 on MCF-7 cells (Figure 4A). Notably, L4 produced little background in the nectin-4-negative MDA-MB-231 breast cancer cell (Figure 4B), whereas S21 generated higher background (data not shown). L4 could also stain the other nectin-4-positive breast cancer cell lines (including BT-474 and MDA-MB-453) and Vero-hNectin-4 cells. These results suggest that the two clones, S21 and L4, could have different research applications, with L4 having the additional advantage for cell staining.

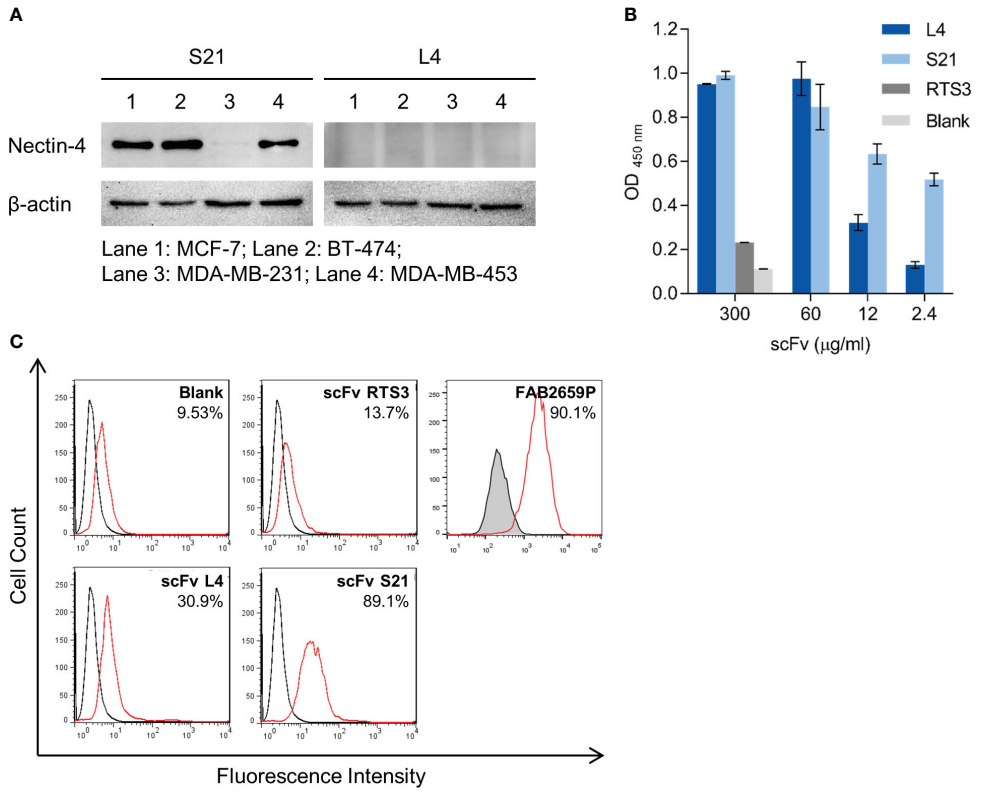

FIGURE 3
In vitro binding analyses of the anti-nectin-4 scFvs S21 and L4. **(A)** The scFvs (10 μg/ml) were used as primary antibodies to detect endogenous nectin-4 in MCF-7, BT-474, and MDA-MB-453 cells in western blot. MDA-MB-231 served as a negative control. Representative data are shown. **(B)** The scFvs were used as primary antibodies to stain MCF-7 cells in cell-based ELISA (mean ± SD, N=2). RTS3 (an anti-snake venom scFv) served as an unrelated control. A control with only the secondary and tertiary antibodies ('Blank') was included. **(C)** The scFvs were used as primary antibodies to stain MCF-7 cells in flow cytometry (37.5 μg/ml). Black and red solid lines indicate unstained and stained samples. The blank and RTS3 controls were also included. The commercial PE-conjugated anti-nectin-4 antibody (FAB2659P, R&D Systems; red solid line) and its isotype control (IC0041P, R&D Systems; tinted with black line) were included for comparison. Representative data are shown.

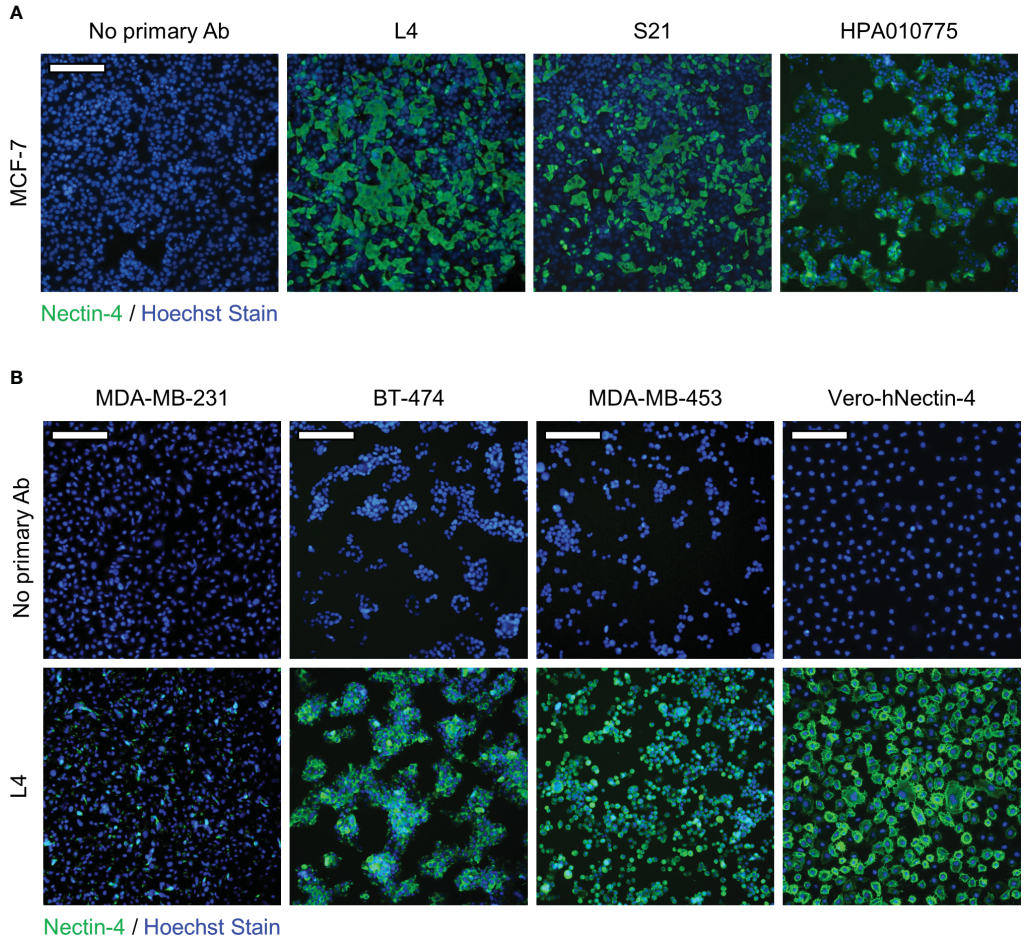

FIGURE 4
Immunofluorescence staining of breast cancer cell lines with anti-nectin-4 scFv clones. Clone L4 or S21 was used as the primary antibody (0.1 μg/ml) to detect endogenous nectin-4 in **(A)** MCF-7, **(B)** BT474, and MDA-MB-453 cells. Scale bar = 200 μm. Representative data are shown. MDA-MB-231 served as a negative control, and Vero-hNectin-4 served as a positive control. A control with only the secondary and tertiary antibodies ('No primary antibody') was included. Staining with the commercial anti-nectin-4 antibody (HPA010775; Sigma-Aldrich) was included for comparison.

3.4 Immunohistochemistry staining of paraffin-embedded breast cancer tissue sections using scFv L4

To validate the feasibility of using the nectin-4-specific scFv L4 on clinical samples as a diagnostic tool, we further performed immunohistochemistry (IHC) staining of breast ductal carcinoma paraffin-embedded tissue sections with the scFv. As shown in Figure 5, L4 yielded comparable staining results to the commercial anti-nectin-4 antibody HPA010775 (Sigma-Aldrich), with minimal background on the non-tumor tissues (NT) and strong signals on the tumor tissues (T1-T5) of different molecular subtypes. This suggests the high sensitivity of scFv L4 binding to native nectin-4 molecule, which supports its potential to be further developed as a tumor-marker-specific diagnostic and/or therapeutic agent.

3.5 Assessment of the scFvs' anti-breast cancer effect *in vitro*

Given that nectin-4 plays a vital role in the carcinogenesis of breast cancer, we further explored whether the scFvs could inhibit cell growth *in vitro*. Our initial results indicated that the scFvs are not significantly cytotoxic to nectin-4-positive and nectin-4-negative breast cancer cell monolayers (Supplementary Figure S1). Nonetheless, considering nectin-4's contribution to cell-to-cell attachment and tumor cells' anchorage-independent growth (18), we then performed a clustering assay to evaluate whether the scFvs could inhibit breast cancer cell aggregation, which is important for tumor formation (18). As shown in Figure 6, nectin-4-positive breast cancer cells easily formed cell clusters in suspension. More importantly, such self-clustering phenomenon was decreased by the treatment of both scFvs (Figure 6), indicating their ability to inhibit nectin-4-positive tumor cell aggregation.

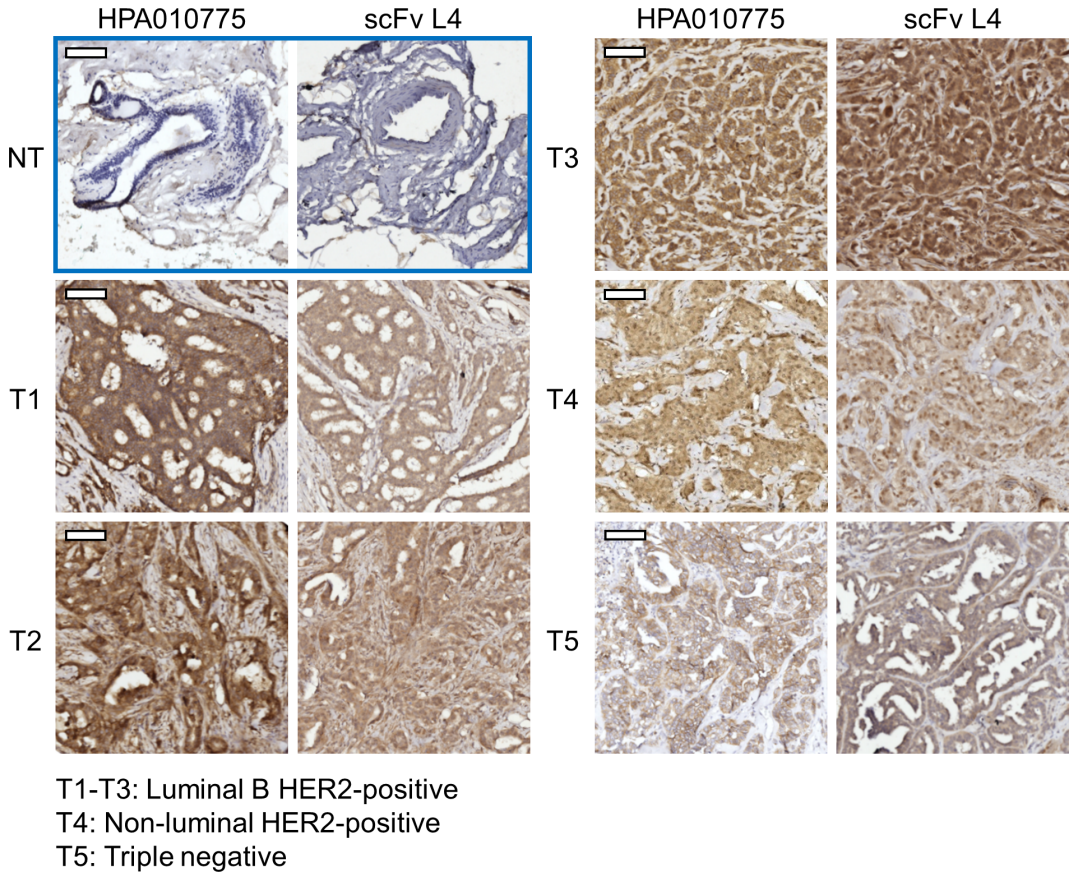

FIGURE 5
Anti-nectin-4 scFv L4 staining of breast cancer clinical specimens. ScFv L4 was used as the primary antibody (10 µg/ml) for immunohistochemistry staining of breast ductal carcinoma paraffin-embedded tissue sections (T1-T5 from five different patients) and compared with the commercial anti-nectin-4 antibody HPA010775. Non-tumor (NT) tissues were included as a negative control. Scale bar = 100 µm.

3.6 Characterizing the interaction between scFvs and the ectodomain of nectin-4

We next attempted to characterize the interaction between the scFvs and nectin-4. A binding curve analysis using non-competitive ELISA indicated that L4 binds to the recombinant nectin-4 fragment r864p efficiently, reaching 50% and 100% binding at 1.14 nM and 41.67 nM, respectively (Figure 7A). Subsequently, a competitive ELISA was conducted to determine the dissociation constant KD, which was approximately 4.17 µM. In contrast, a

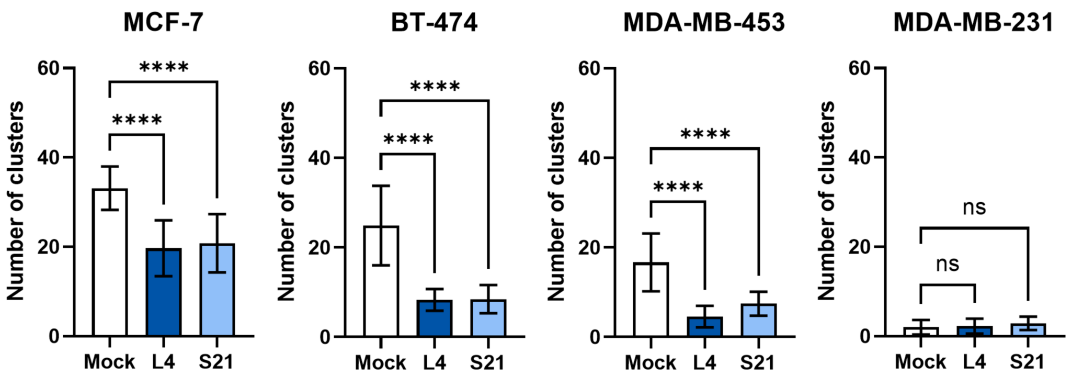

FIGURE 6
Self-clustering of breast cancer cells with or without anti-nectin-4 scFvs. Nectin-4-positive cells MCF-7, BT474, and MDA-MB-453 were dissociated and allowed to aggregate in medium with or without scFv (10 µg/ml). Cells were then poured into 6-well plates and visualized for counting. Five random fields in the wells were counted for clusters (more than 5 cells) using bright-field microscopy (4X objective lens magnification). Nectin-4-negative MDA-MB-231 cells served as a negative control. Data presented are mean ± SD (N=3). One-way ANOVA with Dunnett's multiple comparisons test was performed to determine the difference between Mock and scFv treatment groups of each cell line. (****$p \leq 0.0001$; ns, not significant).

higher concentration of S21 was required to reach 50% binding (130.5 nM) and saturation in the non-competitive ELISA (Figure 7B), although the estimated KD (4.09 μM) is similar to that of L4.

To further predict possible binding sites between scFv and nectin-4, we selected L4 as an example to perform a protein-protein docking with the ectodomain of nectin-4. The sequence of scFv L4 is shown in Supplementary Figure S2. The homology model of L4 was generated and docked onto the nectin-4 homodimer structure (PDBID: 4FRW; Figure 8A). Our docking analysis indicated that L4 returned a probable binding frame on the tip of nectin-4 dimer and targeted the amino acids 57Asp, 58Ser, 85Lys, 88Leu, 100Gln, 101Pro, 105Arg, and 106Asn on nectin-4 (Figure 8B). This diversity in binding residues between L4 and nectin-4 potentially contributes to the efficient recognition of the soluble nectin-4 ectodomain by L4 as observed in the ELISA analyses (Figure 7).

4 Discussion

Multiple studies have suggested that nectin-4 may contribute to carcinogenesis. The extracellular portion of nectin-4 interacts with nectin-1 on the adjacent cell to promote cell-to-cell attachment, and it also interacts with integrin β4 on the same cell to activate the Src family kinases (SFKs) that sustain anchorage-independent growth of human mammary epithelial cells (18). Given the pleiotropic role of SFKs in cellular events, including cell cycle progression, cell survival, adhesion, and migration, and in pathophysiological disorders, including cancers (36), activation of SFKs by nectin-4 could contribute to cancer transformation from multiple pathways. The soluble nectin-4 ectodomain, which could be detected in the sera of breast cancer (37), lung cancer (9), and ovarian cancer (11, 38) patients, has been shown to interact with endothelial integrin β4 to promote angiogenesis in breast cancer through the Src-regulated PI3K/Akt pathway (19). This suggests that targeting or neutralizing the soluble nectin-4 in patient sera may be a potential therapeutic approach. In addition, nectin-4 is also considered a breast cancer stem cell marker, as its presence enhances cell invasion and epithelial-mesenchymal transition and activates the Wnt/β-catenin pathway through the PI3K/Akt axis (20). More recently, a study further identified nectin-4 as a cancer-specific ligand of the inhibitory receptor T-cell immunoreceptor with Ig and ITIM domains (TIGIT), and their interaction was found to inhibit the antitumor activity of nature killer (NK) cells (21). Consistent with these findings, clinical nectin-4 expression positively correlates with tumor size, histopathological grading, angiogenic markers, metastasis, and recurrence (22).

Given the importance of nectin-4 in tumor initiation and progression, antibodies against nectin-4 could be a helpful diagnostic/therapeutic tool. In the current study, we successfully

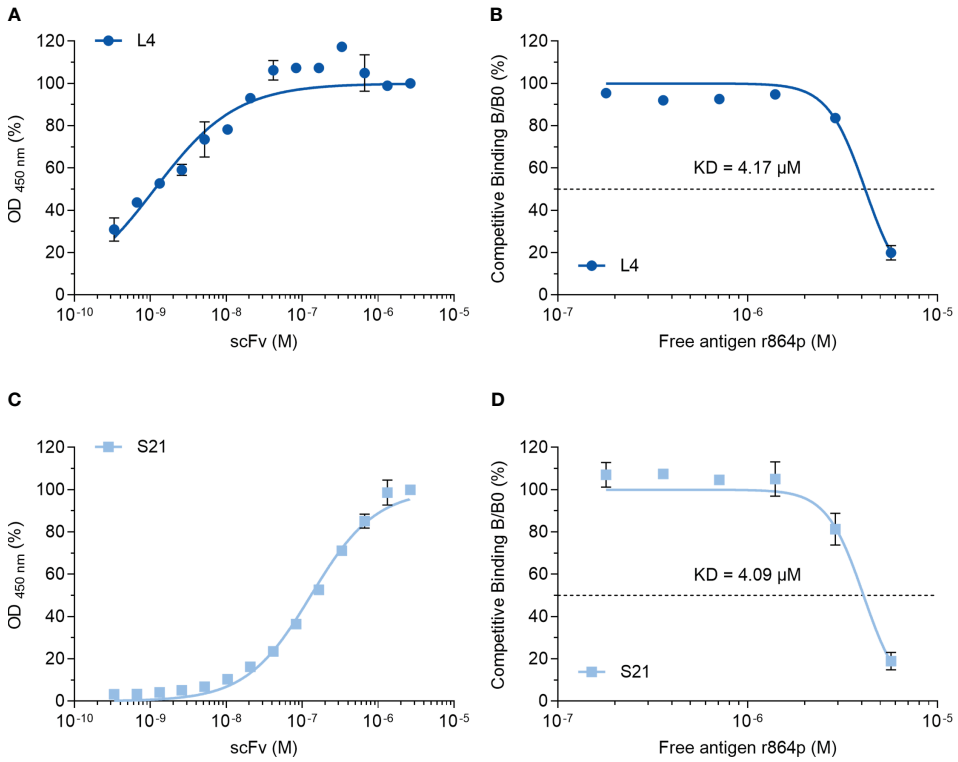

FIGURE 7
Binding curve and affinity determination of anti-nectin-4 scFvs. **(A)** Indirect ELISA showing the binding curve of L4 to nectin-4 ectodomain r864p fixed on plates. **(B)** Competitive ELISA of L4 to determine the dissociation constant (KD). Free r864p was serially diluted and incubated with L4 before the mixture was added to plates coated with r864p. **(C)** Indirect ELISA showing the binding curve of S21 to nectin-4 ectodomain r864p fixed on plates. **(D)** Competitive ELISA of S21 to determine the dissociation constant (KD). Free r864p was serially diluted and incubated with S21 before the mixture was added to plates coated with r864p. Mean ± SD are shown (N=2).

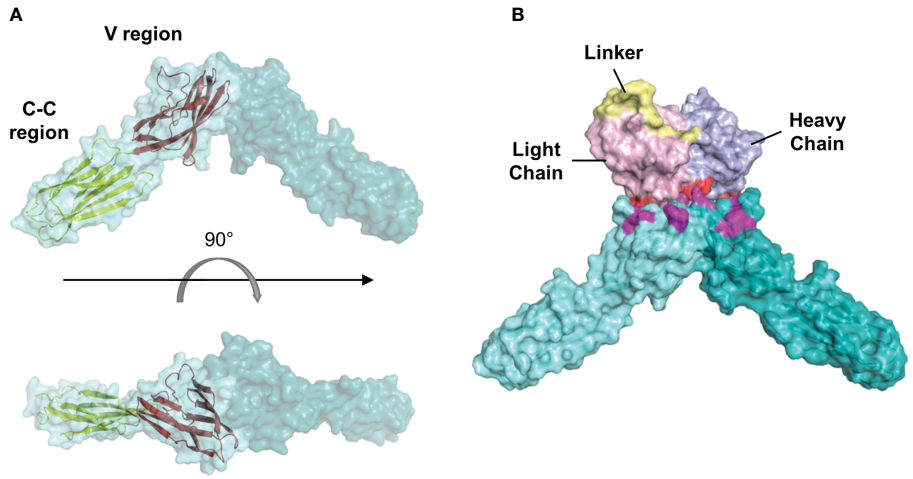

FIGURE 8
Molecular docking analysis of the interaction between scFv L4 and nectin-4. **(A)** Structure of human nectin-4 homodimer (4FRW) showing its one variable (V) and two constant (C-C) regions. **(B)** A representative docking frame showing the interaction between scFv L4 and nectin-4 homodimer structure. Polar contacts on the scFv (red) and nectin-4 (magenta) are shown.

generated nectin-4-targeted scFv libraries using the phage display technique (Figures 1, 2). Selected clones L4 and S21 recognized the recombinant ectodomain of nectin-4 (Figure 2B) and successfully detected the endogenous nectin-4 in several breast cancer cell lines. Specifically, S21 demonstrated better performance in western blot and flow cytometry analyses (Figure 3), whereas L4 displayed high sensitivity and produced little background signal in immunofluorescence staining of 4% PFA-fixed cells (Figure 4) and IHC staining of paraffin-embedded breast cancer tissue sections (Figure 5). This could possibly be explained by molecular docking results indicating that L4 has a predicted binding site on the V loop junction of the nectin-4 dimer (Figure 8), which would only appear in its native conformation. S21, on the other hand, might recognize an epitope on the nectin-4 monomer that would be exposed upon cell dissociation. L4 is also more efficiently bound to fixed nectin-4 ectodomain in the non-competitive ELISA (Figure 7). These results suggest that S21 may be useful for laboratory applications such as flow cytometry and western blot detection, whereas L4 may be suitable for immunostaining, IHC, and potential development into a clinical diagnostic tool. Since the immunogens were based on the ectodomain, these scFvs could be utilized for both staining of the dissected tissues (Figure 5) and measuring the shed or soluble nectin-4 in patient sera and ascites, which can be indicative of disease status, therapeutic effect, and prognosis (9–11). In addition, since nectin-4 has been proposed as a new therapeutic target for antibody-based cancer treatment (39) and oncolytic measles virotherapy, which utilizes nectin-4 as a receptor (40–42), the scFvs could also be useful for screening suitable candidates to receive such nectin-4-targeted treatments.

Antibody-based therapeutics have been extensively studied in the past few decades, especially in the field of cancer treatment (43). Well-known examples include the HER2-directed mAbs, their derivatives conjugated with chemotherapeutic or immunotherapeutic drugs (44), and mAbs that target the vascular endothelial growth factor (VEGF) (45) for breast cancer treatment. Supporting the role of nectin-4 in cancer progression, it has been shown that blocking nectin-4 with antibodies could inhibit the growth of cell line-derived (18) and patient-derived (23) breast cancer mouse xenografts and augment the antitumor activity of NK cells (21). Importantly, our results also demonstrate that the scFvs can reduce the formation of attachment-free breast cancer cell aggregation (Figure 6), which can disrupt cell-cell contact and slow down tumor growth (18). Further analyses of the scFvs' impact on tumor sphere formation and *in vivo* tumor suppression are underway. In addition, although the scFvs alone are not directly cytotoxic (Supplementary Figure S1), they can be explored through other strategies. For example, their anti-clustering effect could be useful in combination with cytotoxic anticancer agents to boost the anticancer effect. Moreover, conjugation with drugs or reporters is another popular strategy to increase the applicability of non-cytotoxic antibodies. For instance, in the therapeutic antibody-drug conjugate (ADC) enfortumab vedotin, the microtubule-disrupting agent monomethyl auristatin E (MMAE) was conjugated to the non-cytotoxic nectin-4-directed mAb AGS-22M6E to increase its tumor-killing effect. It was shown that enfortumab vedotin could inhibit breast, bladder, pancreatic, and lung cancer xenografts in mouse models (17) and has been further evaluated in multicenter phase 2 (EV-201; NCT03219333) and global phase 3 (EV-301; NCT03474107) trials, with preliminary results showing 44%-52% objective response rate (ORR) (46, 47) and prolonged survival compared to chemotherapy (48) in metastatic urothelial cancer patients who previously received platinum chemotherapy and anti-PD-1/PD-L1 immunotherapy. Based on the above observations, enfortumab vedotin has been granted accelerated approval by the U.S. Food and Drug Administration (FDA) for the treatment of metastatic urothelial cancer (39). It has also been shown that anti-nectin-4 antibody conjugated with the zirconium isotope ^{89}Zr ([^{89}Zr]AGS-22M6) could serve as a reagent for positron emission tomography (PET) evaluation of nectin-4-positive tumors and metastases *in vivo* (49). Nectin-4-targeting mAb conjugates ^{99m}Tc-HYNIC-mAb$_{Nectin-4}$ and mAb$_{Nectin-4}$-ICG (Indocyanine green) were also developed for

immuno-single photon emission computed tomography (SPECT) diagnostic imaging and photothermal therapy in TNBC-bearing mice (50). With a smaller size and faster clearance compared to intact mAbs, scFvs are highly suitable for the development of therapeutic or diagnostic purposes (2). Taking advantage of the better penetration of scFvs in target tumors (3), more scFv conjugates are being evaluated in clinical trials for cancer indications (51). Given that scFv L4 displayed high sensitivity and specificity in recognizing the native form of nectin-4 on breast cancer cell monolayer and tissue sections (Figures 4, 5) and its ability to prevent nectin-4-positive tumor cell cluster formation (Figure 6), the scFv and its derivatives may be further developed and investigated for their diagnostic and therapeutic values. As scFv L4 was derived from chicken provenance, potential issues of immunogenicity and the scFv's binding affinity to human nectin-4 could be further improved by humanization procedures (52).

Based on the protein-protein docking, we predicted multiple interacting residues on scFv L4 with the physiologically relevant nectin-4 homodimer (Figure 8). The amino acids' diversity and the number of polar contacts that scFv L4 possesses in its interaction with nectin-4 homodimer (Figure 8) could, in theory, provide stability of the complex. In addition, the physical structure of L4 also has a non-occluded cleft between the light and heavy chains, which is broad and could potentially contribute to its binding affinity to nectin-4; whether this is because of the increased flexibility of the longer linker or because of the intra-sequence interactions warrants further analysis. Likewise, further in-depth examination of the quantitative binding energy and molecular dynamics simulation combined with biophysical analyses could also help better characterize L4's complete protein binding profile.

In conclusion, we produced nectin-4-specific scFvs based on chicken IgY using the phage display method in this study. Two selected scFv clones could capture the ectodomain of nectin-4 and recognize endogenous nectin-4 on several breast cancer cell lines, with scFv L4 demonstrating better sensitivity and specificity to identify nectin-4 in its native form. Importantly, while the scFvs are non-cytotoxic, they could inhibit the self-clustering of nectin-4-positive breast cancer cells. Molecular docking analysis further revealed that the scFv L4 possibly binds to the tip of the nectin-4 homodimer junction. These results highlight the potential of developing the scFv clones for laboratory or clinical uses, either as a diagnostic tool or a therapeutic candidate for combination or drug conjugation to target nectin-4-positive cancers, including breast cancer.

Data availability statement

The original contributions presented in the study are included in the article/Supplementary Material. Further inquiries can be directed to the corresponding authors.

Ethics statement

The studies involving humans were approved by TMU-Joint Institutional Review Board. The studies were conducted in accordance with the local legislation and institutional requirements. The human samples used in this study were acquired from Taipei Medical University Joint Biobank. Written informed consent for participation was not required from the participants or the participants' legal guardians/next of kin in accordance with the national legislation and institutional requirements. The experimental protocol for chicken immunization was approved by the Institutional Animal Care and Use Committee of Taipei Medical University.

Author contributions

C-HLiu: Formal analysis, Investigation, Methodology, Writing – original draft, Writing – review & editing. S-JL: Conceptualization, Formal analysis, Funding acquisition, Methodology, Resources, Supervision, Writing – review & editing. C-HLee: Formal analysis, Investigation, Methodology, Writing – review & editing. C-YL: Formal analysis, Investigation, Writing – review & editing. W-CW: Formal analysis, Investigation, Writing – review & editing. B-YT: Resources, Writing – review & editing. Y-CL: Formal analysis, Writing – review & editing. C-LC: Methodology, Resources, Writing – review & editing. Y-YY: Conceptualization, Formal analysis, Funding acquisition, Methodology, Resources, Supervision, Writing – review & editing. L-TL: Conceptualization, Formal analysis, Funding acquisition, Methodology, Resources, Supervision, Writing – original draft, Writing – review & editing.

Funding

The author(s) declare financial support was received for the research, authorship, and/or publication of this article. The study was supported by funding from the Ministry of Science and Technology of Taiwan (MOST109-2622-B-038-005 to S-JL; MOST109-2320-B-038-053 to Y-YY; MOST107-2320-B-038-034-MY3 and MOST110-2320-B-038-041-MY3 to L-TL), the Ministry of Health and Welfare of Taiwan (MOHW110-TDU-B-212-144014 to Y-YY), the Aim for the Top University Project – Cancer Translational Center of Taipei Medical University (TMUTOP103005-4 to L-TL), and the 2023 Neuro TMULille Program (111-3800-014-400 to L-TL). The funders have no role in the design of the study and collection, analysis, and interpretation of data and in writing the manuscript.

Acknowledgments

The authors would like to acknowledge Dr. Chih-Yeu Fang, Shu Hui Wong, and Jonathan Y. Wang for providing technical support.

Conflict of interest

B-YT is the chairman of Navi Bio-Therapeutics Inc. Taipei, Taiwan. The company has no role in the study's experimental design, data collection, or interpretation.

The remaining authors declare that the research was conducted in the absence of any commercial or financial relationships that could be construed as a potential conflict of interest.

Publisher's note

All claims expressed in this article are solely those of the authors and do not necessarily represent those of their affiliated organizations, or those of the publisher, the editors and the reviewers. Any product that may be evaluated in this article, or claim that may be made by its manufacturer, is not guaranteed or endorsed by the publisher.

Supplementary material

The Supplementary Material for this article can be found online at: https://www.frontiersin.org/articles/10.3389/fimmu.2023.1292019/full#supplementary-material

References

1. Holliger P, Hudson PJ. Engineered antibody fragments and the rise of single domains. *Nat Biotechnol* (2005) 23(9):1126–36. doi: 10.1038/nbt1142

2. Monnier PP, Vigouroux RJ, Tassew NG. *In vivo* applications of single chain Fv (Variable domain) (scFv) fragments. *Antibodies* (2013) 2(2):193–208. doi: 10.3390/antib2020193

3. Pucca MB, Bertolini TB, Barbosa JE, Galina VSR, Porto GS. Therapeutic monoclonal antibodies: scFv patents as a marker of a new class of potential biopharmaceuticals. *Braz J Pharm Sci* (2011) 47(1):31–8. doi: 10.1590/S1984-82502011000100005

4. Alfaleh MA, Alsaab HO, Mahmoud AB, Alkayyal AA, Jones ML, Mahler SM, et al. Phage display derived monoclonal antibodies: from bench to bedside. *Front Immunol* (2020) 11:1986. doi: 10.3389/fimmu.2020.01986

5. Nelson AL, Reichert JM. Development trends for therapeutic antibody fragments. *Nat Biotechnol* (2009) 27(4):331–7. doi: 10.1038/nbt0409-331

6. Nelson AL. Antibody fragments: hope and hype. *MAbs* (2010) 2(1):77–83. doi: 10.4161/mabs.2.1.10786

7. Takai Y, Miyoshi J, Ikeda W, Ogita H. Nectins and nectin-like molecules: roles in contact inhibition of cell movement and proliferation. *Nat Rev Mol Cell Biol* (2008) 9 (8):603–15. doi: 10.1038/nrm2457

8. Reymond N, Lecocq E, Adelaide J, Dubreuil P, Lopez M. Nectin4/PRR4, a new afadin-associated member of the nectin family that trans-interacts with nectin1/PRR1 through V domain interaction. *J Biol Chem* (2001) 276(46):43205–15. doi: 10.1074/jbc.M103810200

9. Takano A, Ishikawa N, Nishino R, Masuda K, Yasui W, Inai K, et al. Identification of nectin-4 oncoprotein as a diagnostic and therapeutic target for lung cancer. *Cancer Res* (2009) 69(16):6694–703. doi: 10.1158/0008-5472.CAN-09-0016

10. Fabre-Lafay S, Monville F, Garrido-Urbani S, Berruyer-Pouyet C, Ginestier C, Reymond N, et al. Nectin-4 is a new histological and serological tumor associated marker for breast cancer. *BMC Cancer* (2007) 7:73. doi: 10.1186/1471-2407-7-73

11. Derycke MS, Pambuccian SE, Gilks CB, Kalloger SE, Ghidouche A, Lopez M, et al. Nectin 4 overexpression in ovarian cancer tissues and serum: potential role as a serum biomarker. *Am J Clin Pathol* (2010) 134(5):835–45. doi: 10.1309/AJCPGXK0FR4MHIHB

12. Deng H, Shi H, Chen L, Zhou Y, Jiang J. Over-expression of Nectin-4 promotes progression of esophageal cancer and correlates with poor prognosis of the patients. *Cancer Cell Int* (2019) 19:106. doi: 10.1186/s12935-019-0824-z

13. Zhang Y, Chen P, Yin W, Ji Y, Shen Q, Ni Q. Nectin-4 promotes gastric cancer progression via the PI3K/AKT signaling pathway. *Hum Pathol* (2018) 72:107–16. doi: 10.1016/j.humpath.2017.10.034

14. Nishiwada S, Sho M, Yasuda S, Shimada K, Yamato I, Akahori T, et al. Nectin-4 expression contributes to tumor proliferation, angiogenesis and patient prognosis in human pancreatic cancer. *J Exp Clin Cancer Res* (2015) 34:30. doi: 10.1186/s13046-015-0144-7

15. Ma J, Sheng Z, Lv Y, Liu W, Yao Q, Pan T, et al. Expression and clinical significance of Nectin-4 in hepatocellular carcinoma. *Onco Targets Ther* (2016) 9:183–90. doi: 10.2147/OTT.S96999

16. Zhang J, Liu K, Peng P, Li S, Ye Z, Su Y, et al. Upregulation of nectin-4 is associated with ITGB1 and vasculogenic mimicry and may serve as a predictor of poor prognosis in colorectal cancer. *Oncol Lett* (2019) 18(2):1163–70. doi: 10.3892/ol.2019.10417

17. Challita-Eid PM, Satpayev D, Yang P, An Z, Morrison K, Shostak Y, et al. Enfortumab vedotin antibody-drug conjugate targeting nectin-4 is a highly potent therapeutic agent in multiple preclinical cancer models. *Cancer Res* (2016) 76 (10):3003–13. doi: 10.1158/0008-5472.CAN-15-1313

18. Pavlova NN, Pallasch C, Elia AE, Braun CJ, Westbrook TF, Hemann M, et al. A role for PVRL4-driven cell-cell interactions in tumorigenesis. *Elife* (2013) 2:e00358. doi: 10.7554/eLife.00358

19. Siddharth S, Nayak A, Das S, Nayak D, Panda J, Wyatt MD, et al. The soluble nectin-4 ecto-domain promotes breast cancer induced angiogenesis via endothelial Integrin-beta4. *Int J Biochem Cell Biol* (2018) 102:151–60. doi: 10.1016/j.biocel.2018.07.011

20. Siddharth S, Goutam K, Das S, Nayak A, Nayak D, Sethy C, et al. Nectin-4 is a breast cancer stem cell marker that induces WNT/beta-catenin signaling via Pi3k/Akt axis. *Int J Biochem Cell Biol* (2017) 89:85–94. doi: 10.1016/j.biocel.2017.06.007

21. Reches A, Ophir Y, Stein N, Kol I, Isaacson B, Charpak Amikam Y, et al. Nectin4 is a novel TIGIT ligand which combines checkpoint inhibition and tumor specificity. *J Immunother Cancer* (2020) 8(1):e000266. doi: 10.1136/jitc-2019-000266

22. Sethy C, Goutam K, Nayak D, Pradhan R, Molla S, Chatterjee S, et al. Clinical significance of a pvrl 4 encoded gene Nectin-4 in metastasis and angiogenesis for tumor relapse. *J Cancer Res Clin Oncol* (2020) 146(1):245–59. doi: 10.1007/s00432-019-03055-2

23. MR M, Cabaud O, Josselin E, Finetti P, Castellano R, Farina A, et al. Nectin-4: a new prognostic biomarker for efficient therapeutic targeting of primary and metastatic triple-negative breast cancer. *Ann Oncol* (2017) 28(4):769–76. doi: 10.1093/annonc/mdw678

24. Lattanzio R, Ghasemi R, Brancati F, Sorda RL, Tinari N, Perracchio L, et al. Membranous Nectin-4 expression is a risk factor for distant relapse of T1-T2, N0 luminal-A early breast cancer. *Oncogenesis* (2014) 3:e118. doi: 10.1038/oncsis.2014.32

25. Rajc J, Gugic D, Frohlich I, Marjanovic K, Dumencic B. Prognostic role of Nectin-4 expression in luminal B (HER2 negative) breast cancer. *Pathol Res Pract* (2017) 213(9):1102–8. doi: 10.1016/j.prp.2017.07.019

26. Noyce RS, Bondre DG, Ha MN, Lin LT, Sisson G, Tsao MS, et al. Tumor cell marker PVRL4 (nectin 4) is an epithelial cell receptor for measles virus. *PLoS Pathog* (2011) 7(8):e1002240. doi: 10.1371/journal.ppat.1002240

27. Lee CH, Leu SJ, Lee YC, Liu CI, Lin LT, Mwale PF, et al. Characterization of chicken-derived single chain antibody fragments against venom of Naja Naja Atra. *Toxins (Basel)* (2018) 10(10):383. doi: 10.3390/toxins10100383

28. Akita EM, Nakai S. Comparison of four purification methods for the production of immunoglobulins from eggs laid by hens immunized with an enterotoxigenic *E. coli* strain. *J Immunol Methods* (1993) 160(2):207–14. doi: 10.1016/0022-1759(93)90179-b

29. Andris-Widhopf J, Rader C, Steinberger P, Fuller R, Barbas CF 3rd. Methods for the generation of chicken monoclonal antibody fragments by phage display. *J Immunol Methods* (2000) 242(1-2):159–81. doi: 10.1016/s0022-1759(00)00221-0

30. Barbas CF,I, Burton DR, Scott JK, Silverman GJ. Phage Display: A Laboratory Manual. New York: Cold Spring Harbor Laboratory Press (2001).

31. Bumke MA, Neri D. Affinity measurements by band shift and competition ELISA. In: Kontermann RDS, editor. *Antibody Engineering*. Berlin, Heidelberg: Springer (2001).

32. Waterhouse A, Bertoni M, Bienert S, Studer G, Tauriello G, Gumienny R, et al. SWISS-MODEL: homology modelling of protein structures and complexes. *Nucleic Acids Res* (2018) 46(W1):W296–303. doi: 10.1093/nar/gky427

33. Brenke R, Hall DR, Chuang GY, Comeau SR, Bohnuud T, Beglov D, et al. Application of asymmetric statistical potentials to antibody-protein docking. *Bioinformatics* (2012) 28(20):2608–14. doi: 10.1093/bioinformatics/bts493

34. *The PyMOL Molecular Graphics System, Version 1.7*. Schrodinger, LLC.

35. Neve RM, Chin K, Fridlyand J, Yeh J, Baehner FL, Fevr T, et al. A collection of breast cancer cell lines for the study of functionally distinct cancer subtypes. *Cancer Cell* (2006) 10(6):515–27. doi: 10.1016/j.ccr.2006.10.008

36. Kumar A, Jaggi AS, Singh N. Pharmacology of Src family kinases and therapeutic implications of their modulators. *Fundam Clin Pharmacol* (2015) 29(2):115–30. doi: 10.1111/fcp.12097

37. Fabre-Lafay S, Garrido-Urbani S, Reymond N, Goncalves A, Dubreuil P, Lopez M. Nectin-4, a new serological breast cancer marker, is a substrate for tumor necrosis factor-alpha-converting enzyme (TACE)/ADAM-17. *J Biol Chem* (2005) 280 (20):19543–50. doi: 10.1074/jbc.M410943200

38. Buchanan PC, Boylan KLM, Walcheck B, Heinze R, Geller MA, Argenta PA, et al. Ectodomain shedding of the cell adhesion molecule Nectin-4 in ovarian cancer is mediated by ADAM10 and ADAM17. *J Biol Chem* (2017) 292(15):6339–51. doi: 10.1074/jbc.M116.746859

39. U.S. Food and Drug Administration. *FDA grants accelerated approval to enfortumab vedotin-ejfv for metastatic urothelial cancer*. Available at: https://www.fda.gov/drugs/resources-information-approved-drugs/fda-grants-accelerated-approval-enfortumab-vedotin-ejfv-metastatic-urothelial-cancer (Accessed 17 April 2020).

40. Liu CH, Wong SH, Tai CJ, Tai CJ, Pan YC, Hsu HY, et al. Ursolic acid and its nanoparticles are potentiators of Oncolytic measles virotherapy against breast cancer cells. *Cancers (Basel)* (2021) 13(1). doi: 10.3390/cancers13010136

41. Tai CJ, Liu CH, Pan YC, Wong SH, Tai CJ, Richardson CD, et al. Chemovirotherapeutic treatment using camptothecin enhances oncolytic measles virus-mediated killing of breast cancer cells. *Sci Rep* (2019) 9(1):6767. doi: 10.1038/s41598-019-43047-3

42. Kuo YT, Liu CH, Wong SH, Pan YC, Lin LT. Small molecules baicalein and cinnamaldehyde are potentiators of measles virus-induced breast cancer oncolysis. *Phytomedicine* (2021) 89:153611. doi: 10.1016/j.phymed.2021.153611

43. Corraliza-Gorjon I, Somovilla-Crespo B, Santamaria S, Garcia-Sanz JA, Kremer L. New strategies using antibody combinations to increase cancer treatment effectiveness. *Front Immunol* (2017) 8:1804. doi: 10.3389/fimmu.2017.01804

44. Costa RLB, Czerniecki BJ. Clinical development of immunotherapies for HER2 (+) breast cancer: a review of HER2-directed monoclonal antibodies and beyond. *NPJ Breast Cancer* (2020) 6:10. doi: 10.1038/s41523-020-0153-3

45. Masoud V, Pages G. Targeted therapies in breast cancer: New challenges to fight against resistance. *World J Clin Oncol* (2017) 8(2):120–34. doi: 10.5306/wjco.v8.i2.120

46. Rosenberg JE, O'donnell PH, Balar AV, Mcgregor BA, Heath EI, Yu EY, et al. Pivotal trial of Enfortumab vedotin in urothelial carcinoma after platinum and anti-programmed death 1/programmed death ligand 1 therapy. *J Clin Oncol* (2019) 37 (29):2592–600. doi: 10.1200/JCO.19.01140

47. Yu EY, Petrylak DP, O'donnell PH, Lee JL, van der Heijden MS, Loriot Y, et al. Enfortumab vedotin after PD-1 or PD-L1 inhibitors in cisplatin-ineligible patients with advanced urothelial carcinoma (EV−201): a multicentre, single-arm, phase 2 trial. *Lancet Oncol* (2021) 22(6):872–82. doi: 10.1016/S1470-2045(21)00094-2

48. Powles T, Rosenberg JE, Sonpavde GP, Loriot Y, Duran I, Lee JL, et al. Enfortumab vedotin in previously treated advanced urothelial carcinoma. *N Engl J Med* (2021) 384(12):1125–35. doi: 10.1056/NEJMoa2035807

49. Campbell DO, Noda A, Verlinsky A, Snyder J, Fujita Y, Murakami Y, et al. Preclinical evaluation of an anti-nectin-4 immunoPET reagent in tumor-bearing mice and biodistribution studies in cynomolgus monkeys. *Mol Imaging Biol* (2016) 18(5):768–75. doi: 10.1007/s11307-016-0953-x

50. Shao F, Pan Z, Long Y, Zhu Z, Wang K, Ji H, et al. Nectin-4-targeted immunoSPECT/CT imaging and photothermal therapy of triple-negative breast cancer. *J Nanobiotechnol* (2022) 20(1):243. doi: 10.1186/s12951-022-01444-3

51. Kaplon H, Muralidharan M, Schneider Z, Reichert JM. Antibodies to watch in 2020. *MAbs* (2020) 12(1):1703531. doi: 10.1080/19420862.2019.1703531

52. Tsai K-C, Chang C-D, Cheng M-H, Lin T-Y, Lo Y-N, Yang T-W, et al. Chicken-derived humanized antibody targeting a novel epitope F2pep of fibroblast growth factor receptor 2: potential cancer therapeutic agent. *ACS Omega* (2019) 4(1):2387–97. doi: 10.1021/acsomega.8b03072

frontiers | Frontiers in Oncology

TYPE Original Research
PUBLISHED 15 January 2024
DOI 10.3389/fonc.2023.1206882

OPEN ACCESS

EDITED BY
Takaji Matsutani,
Maruho, Japan

REVIEWED BY
Luo Yuhao,
Southwest Medical University, China
Ray Manneh,
Society of Oncology and Hematology of Cesar, Colombia
Abdallah Flaifel,
National Institutes of Health (NIH), United States

*CORRESPONDENCE
Xishi Jin
jinxishi@tom.com
Dapang Rao
raodapang@tom.com

RECEIVED 16 April 2023
ACCEPTED 27 November 2023
PUBLISHED 15 January 2024

CITATION
Zhang J, Jiang H, Rao D and Jin X (2024) Clear cell renal cell carcinoma: immunological significance of alternative splicing signatures. *Front. Oncol.* 13:1206882. doi: 10.3389/fonc.2023.1206882

Clear cell renal cell carcinoma: immunological significance of alternative splicing signatures

Jiayu Zhang, Hongyi Jiang, Dapang Rao* and Xishi Jin*

Department of Urology, The Second Affiliated Hospital of Wenzhou Medical University, Wenzhou, China

Background: Renal cell carcinoma (RCC) accounts for 90% of renal cancers, of which clear cell carcinoma (ccRCC) is the most usual histological type. The process of alternative splicing (AS) contributes to protein diversity, and the dysregulation of protein diversity may have a great influence on tumorigenesis. We developed a prognostic signature and comprehensively analyzed the role of tumor immune microenvironment (TIME) and immune checkpoint blocking (ICB) treatment in ccRCC.

Methods: To identify prognosis-related AS events, univariate Cox regression was used and functional annotation was performed using gene set enrichment analysis (GSEA). In this study, prognostic signatures were developed based on multivariate Cox, univariate Cox, and LASSO regression models. Moreover, to assess the prognostic value, the proportional hazards model, Kruskal–Wallis analysis, and ROC curves were used. To obtain a better understanding of TIME in ccRCC, the ESTIMATE R package, single sample gene set enrichment analysis (ssGSEA) algorithm, CIBERSORT method, and the tumor immune estimation resource (TIMER) were applied. The database was searched to verify the expression of *C4OF19* in tumor and normal samples. Regulatory networks for AS-splicing factors (SFs) were visualized using Cytoscape 3.9.1.

Results: There were 9,347 AS cases associated with the survival of ccRCC patients screened. A total of eight AS prognostic signatures were developed with stable prognostic predictive accuracy based on splicing subtypes. In addition, a qualitative prognostic nomogram was developed, and the prognostic prediction showed high effectiveness. In addition, we found that the combined signature was significantly associated with the diversity of TIME and ICB treatment-related genes. *C4ORF19* might become an important prognostic factor for ccRCC. Finally, the AS-SF regulatory network was established to clearly reveal the potential function of SFs.

Conclusion: We found novel and robust indicators (i.e., risk signature, prognostic nomogram, etc.) for the prognostic prediction of ccRCC. A new and reliable prognostic nomogram was established to quantitatively predict

the clinical outcome. The AS-SF networks could provide a new way for the study of potential regulatory mechanisms, and the important roles of AS events in the context of TIME and immunotherapy efficiency were exhibited. *C4ORF19* was found to be a vital gene in TIME and ICB treatment.

KEYWORDS

clear cell renal carcinoma (ccRCC), alternative splicing (AS), tumor immune microenvironment (TIME), prognosis, immunotherapy

1 Introduction

Over the past decades, the global incidence of renal cell carcinoma (RCC) is increasing (1, 2). Among urinary cancers, the mortality rate of renal cell carcinoma ranks first in the world (2). As the main subtype of renal cell carcinoma, clear cell renal carcinomas (ccRCCs) are among the most malignant tumors in urology, responsible for approximately 90,000 deaths annually (3). Approximately 30% of patients with ccRCC have metastases at the first diagnosis, and 20%–40% have recurrence after tumor resection (4, 5). In traditional clinical work, there are some good prognostic biomarkers developed in RCC. However, these approaches may be unreliable due to heterogeneity within the patients (6). Consequently, there is an urgent need for a new approach to predict clinical results more accurately, so as to provide help in choosing treatment strategies.

In recent years, more and more evidence has emphasized the role of immune response as an essential feature of the occurrence and development of ccRCC and therapeutic outcomes (3). Immunotherapy has attracted great attention because of its encouraging results in a variety of malignant tumors (7). Therefore, the most effective strategies were identifying ccRCC patients with molecular signatures, improving prognostic accuracy, and optimizing immunotherapy based on molecular risk distributions.

Alternative splicing (AS) is defined as the process of producing different mRNA splicing isomers from pre-mRNA by different splicing methods (8). AS events were well known for involving AT, AP, AD, AA, ME, ES, and RI. In post-transcriptional regulation, alternative splicing plays a critical role, and more and more studies indicate that alternative splicing is closely linked to cancer cell invasion and metastasis (3, 9, 10). In addition, we learned that splicing factors had a great influence on the regulation of AS events (11). There was a need to mention that abnormal splicing factors could contribute to oncogenic splicing isoforms (12, 13). Unfortunately, there was a lack of adequate understanding of the relationship between the prognostic signature, immunotherapy, and TIME.

In this study, as a result of an integrated analysis of AS events, we characterized TIME and discovered potential molecular mechanisms involved in tumorigenesis. The AS pattern of the KIRC cohort in TCGA was described, and the correlation between AS events and survival was verified using comprehensive bioinformatic analysis. Afterward, the predictive prognostic signatures based on AS events were built and then proven. Next, to meet the clinical application and promote development, we made an AS-clinicopathologic nomogram which could effectively predict the prognosis and guide clinical work. After that, we comprehensively analyzed the association of the prognostic signature newly established with TIME complexity and immune checkpoint blocking (ICB) treatment outcomes. Furthermore, we found a new key gene—*C4ORF19*, and the underlying role of *C4ORF19* in ccRCC was investigated. In the end, we established the AS-SF regulatory network to clarify the underlying mechanisms of ccRCC occurrence and development. The AS-SF networks could provide a new way for the study of potential regulatory mechanisms.

Abbreviations: AS, alternative splicing; seven subtypes of AS events; AA, alternate acceptor site; AD, alternate donor site; AP, alternate promoter; AT, alternate terminator; ES, exon skip; ME, mutually exclusive exons; RI, retained intron; AUC, area under the curve; CTLA-4, cytotoxic T-lymphocyte antigen 4; CD274, also known as PD-L1;ccRCC, clear cell renal carcinoma; HAVCR2, also known as TIM3; ICB, immune checkpoint blockade; IDO1, indoleamine 2,3-dioxygenase 1; LASSO, least absolute shrinkage and selection operator; OS, overall survival; PD-1, programmed cell death 1; PD-L1, programmed cell death-ligand 1; PD-L2, programmed cell death-ligand 2; PDCD1, also known as PD-1; PDCD1LG2, also known as PD-L2; PSI, percent spliced index—a visual ratio to quantify splicing events from 0 to 1; RNA, ribonucleic acid; ROC, receiver operating characteristic; SFs, splicing factors; ssGSEA, single sample gene set enrichment analysis; TCGA, The Cancer Genome Atlas; TICs, tumor-infiltrating immune cells; TIME, tumor immune microenvironment; TIMER, tumor immune estimation resource; TIM-3, T-cell immunoglobulin domain and mucin domain-containing molecule-3; TNM, tumor, node, metastasis; Tregs, regulatory T cells SpliceSeq: http://bioinformatics.mdanderson.org/TCGASpliceSeq); The Cancer Genome Atlas (TCGA): http://cancergenome.nih.gov; TIMER: http://timer.cistrome.org/; CIBERSORT: https://cibersort.stanford.edu/.

2 Materials and methods

2.1 Multiomics data acquisition

The transcriptome and survival data of the ccRCC patients in this study came from The Cancer Genome Atlas portal website

(TCGA). Also, the AS data of TCGA came from SpliceSeq, and the SF expression data were obtained from the SpliceAid 2 database (www.intron i.it/spliceaid.html). All analyses strictly followed TCGA's published guidelines, and the detailed analysis flowchart can be found in Figure 1.

2.2 AS profile recognition process

When setting the PSI value above 0.75 as the point for filtration, samples were partitioned. Using the UpSetR software package, the UpSet plot was drawn and seven subtypes of AS events were found. We named AS by splicing types, ID numbers in splicing sequences, and corresponding parental gene names. There was a case that *C4orf19* was the corresponding parent gene name, 69001 was the ID number in SpliceSeq, and AT was the splicing type in "*C4orf19*|69001|AT".

2.3 Screening AS events associated with survival

When we detected the PSI standard deviation less than 0.01, the data of AS events were deleted. The connection between the overall survival (OS) and AS events was found in the univariate Cox regression analysis (Additional file 1: Table 1), which was exhibited in the UpSet map and volcano map. In addition, each bubble chart of the seven subtypes summarized the 20 most important AS events.

2.4 Prognostic signature and nomogram

Firstly, candidate models for each splicing pattern were determined by least absolute shrinkage and selection operator (LASSO) regression analysis, in which way we could also avoid model overfitting. Next, multivariate Cox regression analysis was applied to screen prognostic predictors from the identified AS events. Because the pattern of AS events in post-transcriptional modification was independent of each subtype, the AS events identified in each of the splicing subtypes described above were integrated and then another prognostic feature was generated. Afterward, risk scores were calculated according to the formula: risk score = βAS event1 × PSIAS event1 + ⋯ + βAS eventn × PSIAS eventn. The specific formulas for each prognostic signature can be found in Additional file 1: Table 2. Consequently, the low-risk group and the high-risk group were born by the calculated median risk scores. The "survival" R package was employed to analyze K–M survival curves. The predictive value of this prognostic signature was validated by using time-dependent receiver operating characteristic (ROC) curves. Then, univariate and multivariate Cox regression analyses were exploited to ascertain whether this signature could be used as an independent prognostic factor. In addition, stratified survival analysis further verified whether prognostic performance in patients was independent of clinical data including age; sex; pathological grade; T, N, and M categories; and tumor stage. Then, we calculate the AUC from the ROC curve to systematically measure the value of the accuracy of the model for 1-, 2-, and 3-year OS. Finally, to accurately calculate the OS of ccRCC patients, we established prognostic nomograms to obtain the survival probabilities of 1, 2, and 3 years. Then, there was a calibration curve showing the prognostic value of the AS-constructed nomogram. It should be noted that the model was highly predictive when the calibration curve was close to 45°.

2.5 Risk score and characteristics of tumor-infiltrating immune cells

Information on immune infiltrates such as B cells from each specimen was downloaded from TIMER. The ssGSEA algorithm of the R package "GSEAbase" was performed to elucidate the enrichment of two different risk subgroups in 29 gene sets related to immune function. Subsequently, we calculated the purity of the tumor and the degree of cell invasion (stromal and immune cells) using the R package "ESTIMATE" to validate the significantly different characteristics of the TIME between the low-risk and high-risk groups. The proportion of 22 immune cell types in the

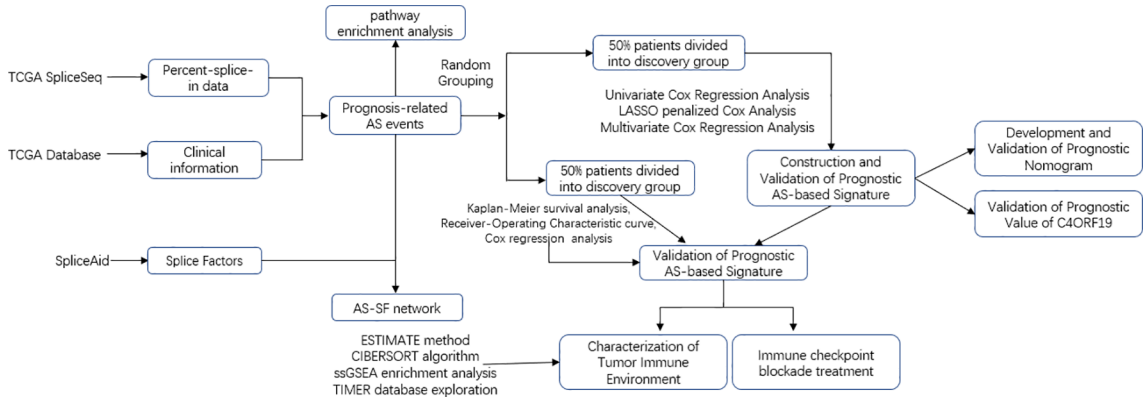

FIGURE 1
Overall research design. Flow process diagram presenting the process of comprehensive analysis.

tumor sample was recognized by assessing the relative subsections of RNA transcripts from CIBERSORT.

2.6 ICB treatment

According to existing research, the expression level of key genes associated with immune checkpoint blockade might have a close relationship with the clinical results of ICB treatment (14, 15). Six key genes (PD-L1, IDO1, PD-L2, PD-1, CTLA-4, and TIM-3) of immune checkpoint blockade therapy in ccRCC (16, 17) were obtained. Afterward, to investigate the potential role of risk score in immune checkpoint blockade therapy of ccRCC, AS-based prognostic characteristics were significantly related to the expression levels of four key genes for immune checkpoint blockade. At last, the expression levels of 47 immune checkpoint genes (i.e., CTLA4, BTLA, etc.) were compared in low-risk and high-risk patients.

2.7 Splicing regulatory network

A total of 404 SFs derived from a previous study (18) are exhibited in Additional file 1: Table 3, and the RNA-seq profiles of SFs can be found in the TCGA database. In addition, we conducted a Spearman correlation analysis to assess the connection between SFs and survival-related AS events. p <0.001 and correlation coefficient >0.6 were the cutoff values. In the end, Cytoscape (version 3.9.1) was applied to build an underlying SF-AS regulatory network.

2.8 Experimental proof

2.8.1 Immunohistochemistry

From Outdo Biotech (Shanghai, China), we purchased one ccRCC tissue microarray (TMA, Cat. HKid-CRCC060PG-01). TMA HKID-CRCC060PG-01 contained 30 paired adjacent tissues and 30 ccRCC tissues. Moreover, Outdo Biotech (Shanghai, China) also provided detailed clinicopathological features of this TMA, and TMA was approved ethically by the Clinical Research Ethics Committee, Outdo Biotech (Shanghai, China).

On TMA samples of ccRCC tissues, immunohistochemistry (IHC) was performed according to the standard procedure. For antigen retrieval, EDTA was used, and the primary antibodies were incubated overnight at 4°C. The primary antibody used in the study was anti-*C4ORF19* (1:500 dilution; Cat. PA5-60368, RRIDP: AB_2639064, Thermo Fisher Scientific). Lastly, using Aperio Digital Pathology Slide Scanners, stained TMA was scanned to visualize antibody staining and hematoxylin counterstaining.

2.8.2 Real-time polymerase chain reaction

Human renal cancer tissue and adjacent/normal tissue came from the biological sample library of the Second Affiliated Hospital of Wenzhou Medical University (Yuying Children's Hospital of Wenzhou Medical University). The sample numbers were KI220001, KI220002, KI220003, LI220005, and KI220006. Quantitative real-time polymerase chain reaction (qRT-PCR) was performed (approval nos. 2022-K-151-01, 2022-K-151-02, and 2022-K-151-03 by the ethics committee).

According to the extraction standards provided by the reagent manufacturer, TRIzol kit (Invitrogen, Carlsbad, CA, USA) was used to extract total RNA (tRNA). We used a NanoDrop 2000 spectrophotometer to determine RNA concentration and purity. In the following steps, total RNA was reverse-transcribed into cDNA using the RevertAid First Strand cDNA Synthesis Kit (TaKaRa:Tokyo, Japan). SYBR Green detection reagent (TaKaRa) and LightCycler® 96 Real-Time PCR System (Roche, IN, USA) were used for quantitative polymerase chain reaction (qPCR). Finally, the $2^{-\Delta\Delta Cq}$ method was used to examine gene expression data. All primers were synthesized by Sangon Biotech (Shanghai, China). The sequences of all primers used in qPCR are shown in Table 1.

2.9 Statistical analysis

In this study, for comparisons between two different groups, we used the Wilcoxon test, and for comparisons between more than two groups, we used the Kruskal–Wallis test. OS was the time between diagnosis and death. The K–M log-rank test was employed to plot the survival curse. Moreover, the Pearson correlation test was applied to explore the correlation between risk score, clinical variables, and degree of immune cell infiltration and immune checkpoint. When the result of the CIBERSORT algorithm $p \geq 0.05$, further study was abandoned. Then, in order to verify the independent prognostic prediction abilities of risk signatures, univariate and multivariate analyses were carried out by the Cox regression model. For 1-, 2-, and 3-year OS, we used ROC curves to evaluate their prognostic value. p <0.05 was regarded as statistically significant. All statistical analyses were performed using R software in version 4.1.2.

3 Results

3.1 Basic information on patients and AS events in ccRCC

Five hundred thirty-seven patients with ccRCC were obtained from the TCGA database, and 11 patients without complete

TABLE 1 Sequences of all primers used in qPCR.

Genes	Forward primer sequence (5′–3′)	Reverse primer sequence (5′–3′)
C4orf19	CAGCCTGGGTGACAGTGCAA	AACCAGCTCGGTCCCTTCCT
GADPH	GCGGGGCTCTCCAGAACATC	TCCACCACTGACACGTTGGC

information were rejected. Therefore, 526 patients in total were included. Table 2 presents the basic clinical data of all ccRCC patients. In addition, by using the UpSet plot (Figure 2A), we analyzed the AS event profiles comprehensively and displayed gene intersections among the seven subtypes of AS events. It could be seen that ES was the most frequent splicing pattern, while ME was the least frequent.

3.2 Finding survival-related AS events

Univariate Cox regression analysis showed that 9,347 AS events were significantly associated with survival ($p < 0.05$). Furthermore, a detailed record of the data can be found in Additional file 1: Table 1. In Figure 2B, the gene interactions among the seven types of survival-related AS events are shown. Moreover, ES was still the main splicing pattern. On the other hand, the volcano map was designed to present the distribution of AS events (Figure 3A), and the top 20 AS events with significant survival correlation from seven subtypes were summarized by using the bubble graphs (Figures 3B–H).

3.3 Establishment of the verified prognostic signature

In this study, the prognostic abilities of the survival-related AS events found in the previous step were evaluated by using the stepwise LASSO algorithm and multivariate Cox regression analysis. Moreover, the LASSO regression analysis results of ALL AS events and seven AS event subtypes are exhibited in Figures 4A, B, 5A–G, 6A–G. Next, the best survival-related AS events, which were determined by multivariate Cox analysis, were performed to build eight AS prognostic signatures, namely, AA, AD, AP, AT, ES, ME, RI, and ALL. The formulas for each prognostic signature are detailed in Additional file 1: Table 2. Using the median risk score as a standard for further study, ccRCC patients were ranked into low- and high-risk groups. The distribution of eight different AS events (AA, AP, AT, AD, ME, RI, ES, and ALL) and their PSI values in the two subgroups and patients was exhibited in the heatmap (Figures 4C, 7A, D, 8A, D, 9A, D, 10A). In the same way, the distribution of risk score (Figures 4D, 7B, E, 8B, E, 9B, E, 10B) and the dot plot of survival status (Figures 4E, 7C, F, 8C, F, 9C, F, 10C) indicated a lower overall survival in the higher-risk patients. Furthermore, the Kaplan–Meier curve also confirmed that in the low-risk subgroup, patients had a significantly better prognosis than those in the high-risk subgroup (Figures 4A, 11A, C, E, G, 12A, C, E, G; all $P < 0.05$). The results showed that the areas under the risk score curves of 1-, 2- and 3-year survival were all greater than 0.70, indicating that the established prognostic signature had highly sensitive and specific survival prediction ability (Figures 4G, 11B, D, F, G, 12B, D, F, G). Moreover, the risk score might become an independent prognostic signature of the ccRCC (univariate Cox model in Figures 4H and 13A, C, E, G, I, K, M and multivariate Cox regression analysis in Figures 4I and 13B, D, F, H, J, L, N).

TABLE 2 Baseline data of all ccRCC patients.

Characteristics	Type	*N*	Proportion
Age	≤65	352	65.55%
	>65	185	34.45%
Gender	Female	191	35.57%
	Male	346	64.43%
Grade	G1–2	244	45.44%
	G3–4	285	53.07%
	Unknown	8	1.49%
Stage	I–II	326	60.71%
	III–IV	208	38.73%
	Unknown	3	0.56%
T stage	T1–2	344	64.06%
	T3–4	193	35.94%
M stage	M0	426	79.33%
	M1	79	14.71%
	Unknown	32	5.96%
N stage	N0	240	44.69%
	N1	17	3.17%
	Unknown	280	52.14%

3.4 Construction of the verified nomogram

According to the difference in the risk score in different subtypes of clinical variables, clinical significance was explored. With the progression of tumor grade (most $p < 0.05$, Figure 14A); clinicopathological stage (most $p < 0.05$, Figure 14B); and T, M, and N stages (most $p < 0.05$, Figures 14C–E), the risk score significantly rose, suggesting that prognostic risk score had a positive correlation with tumor progression. Next, the prognostic nomogram established for forecasting the prognosis of ccRCC patients is exhibited in Figure 14F. It was well known that there was a great prognostic capability of 1-, 2-, and 3-year OS in the nomogram plot when the calibration curve was close to the diagonal (Figures 14G–I).

3.5 Risk score and TIME characterization

In order to further investigate the possibility of using risk score as an immune indicator, we performed correlation analyses between risk score and immune score (from the ESTIMATE algorithm), ssGSEA characteristics, and TIC subtypes and levels (from the CIBERSORT method). The high-risk patients achieved a higher immune score and ESTIMATE score and lower tumor purity (Figures 15A–C), which suggested higher immune infiltration. However, there was no significant difference in stromal score (Figure 16). Then, in Figures 15D, E, immune-related signatures

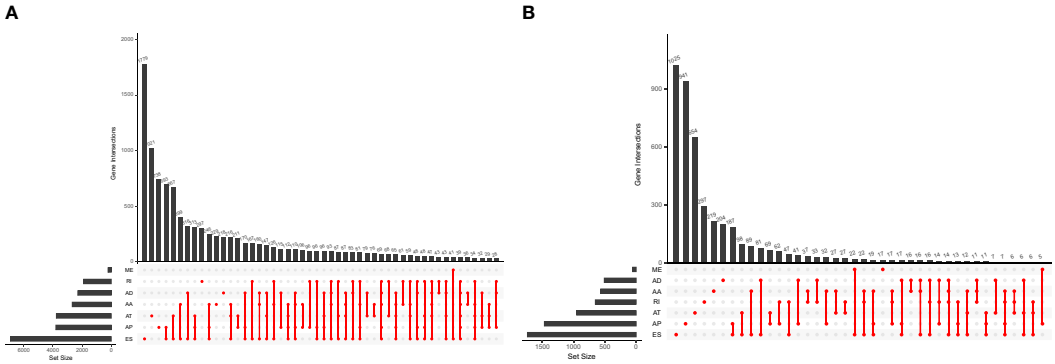

FIGURE 2
(A) The UpSet plot of gene interactions among the seven types of AS events in the TCGA KIRC cohort. **(B)** The UpSet plot of gene interactions among the seven types of prognostic relevant AS events.

were shown to differ between the two subgroups, where immunological scores corresponding to immune-related signatures were exhibited for each patient in the low-/high-risk group. The results revealed that the infiltration of immune cells such as CD8+ T cells, macrophages, T helper cells, Tfh, Th1 cells, Th2 cells, and TIL and the immune signatures such as parainflammation, T-cell co-inhibition, T-cell co-stimulation, checkpoint, inflammation-promoting, and cytolytic activity were significantly increased with increased risk score (Figure 15F). On the contrary, iDCs, mast cells, and type IIIFN response were significantly decreased with increased risk score (Figure 15F). The CIBERSORT algorithm results showed that the proportion of CD8+ T cells, activated CD4 memory T cells, follicular helper T cells, Tregs, and M0 macrophages was positively associated with risk score, and the proportion of naive B cells, memory B cells, M1 macrophages, M2 macrophages, resting dendritic cells, and resting mast cells was negatively associated with risk score (Figure 15G). In conclusion, the ALL prognostic signature could be a kind of new method to clarify the ccRCC immunoregulatory network.

3.6 Correlation between the ALL prognostic signature and ICB key therapy

With the increasing attention paid to ICB therapy in clinical work, immune checkpoint inhibitors have greatly changed the

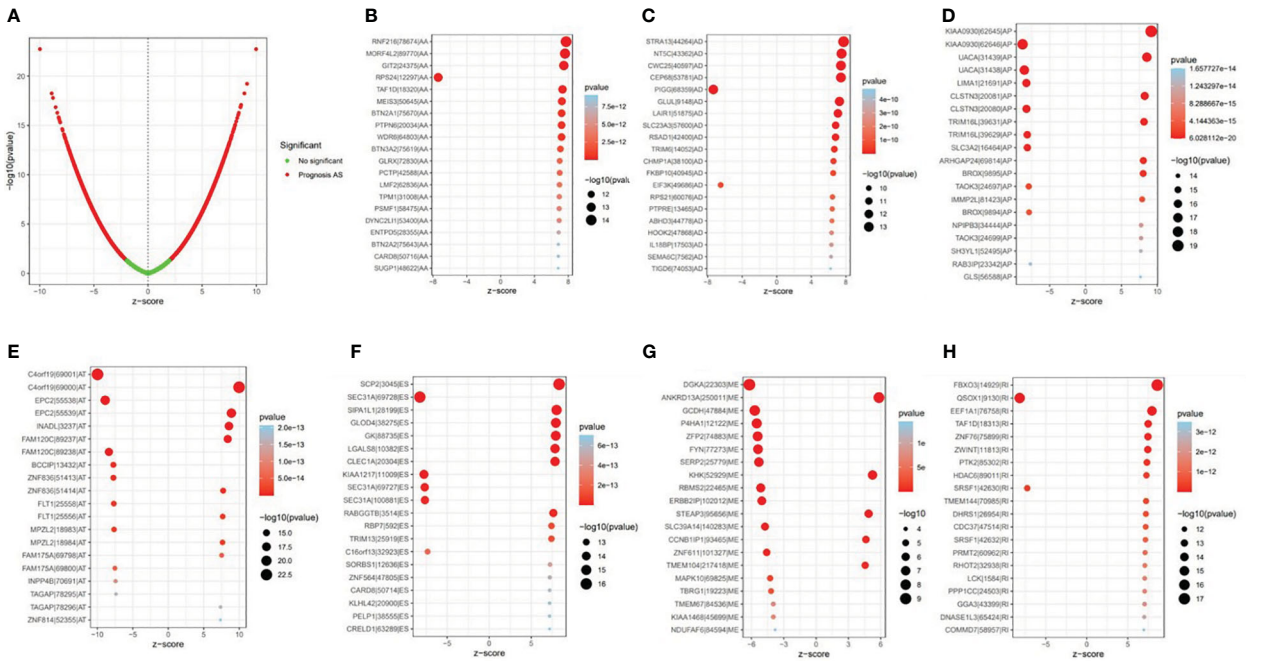

FIGURE 3
The survival-relevant alternative splicing (AS) events. **(A)** The volcano plots of survival-relevant AS events. The most significant survival-relevant AAs, ADs, APs, ATs, ESs, MEs, and RIs in the TCGA KIRC cohort **(B–H)**.

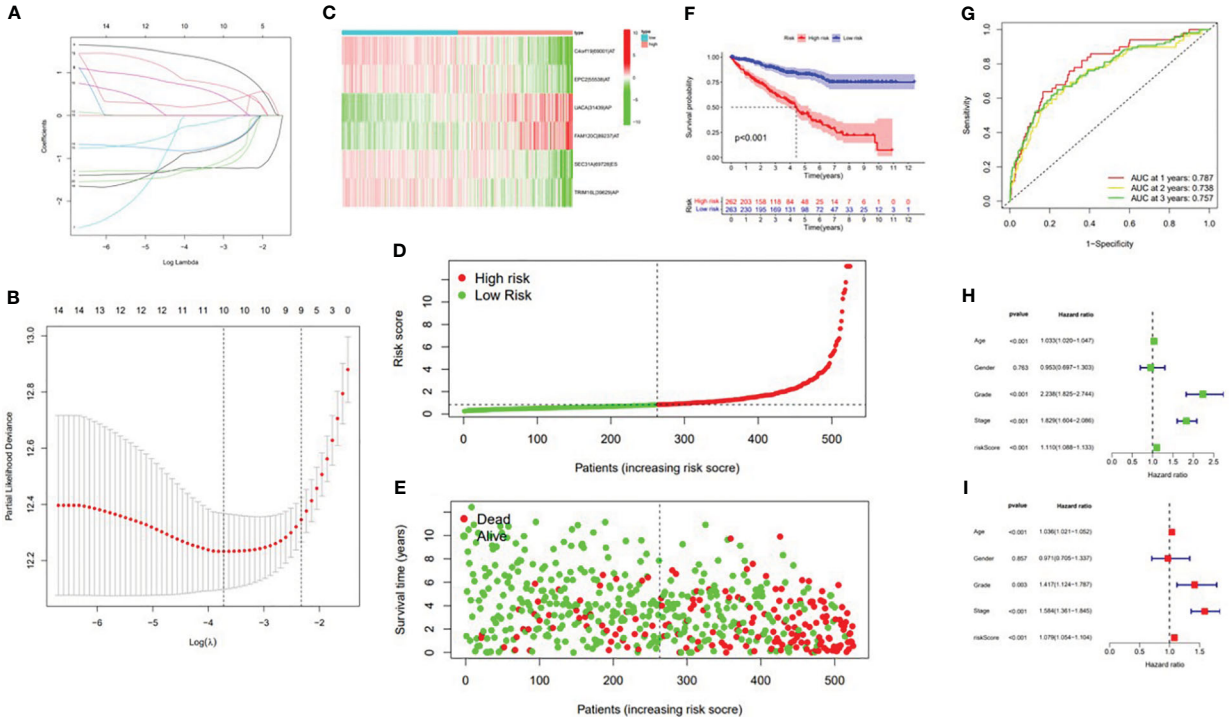

FIGURE 4
Confirmation of the ALL AS-based prognostic signature. **(A)** Least absolute shrinkage and selection operator (LASSO) coefficient profiles of the whole AS events. **(B)** Ten times cross-validation for tuning parameter selection in the LASSO regression. **(C)** Heatmap of the percent spliced index (PSI) value of ALL signature AS events in clear cell renal carcinoma (ccRCC). The colors from red to green show a trend from high expression to low expression. **(D)** Distribution of the ALL signature risk score. **(E)** The survival status and duration of ccRCC patients. **(F)** The K–M curve presenting survival in the high-risk and low-risk sets. **(G)** ROC analysis of the risk scores for overall survival prediction. The AUC was calculated for ROC curves, and sensitivity and specificity were calculated to assess score performance. Proportional hazards model results. **(H)** Univariate Cox regression results. **(I)** Multivariate Cox regression results.

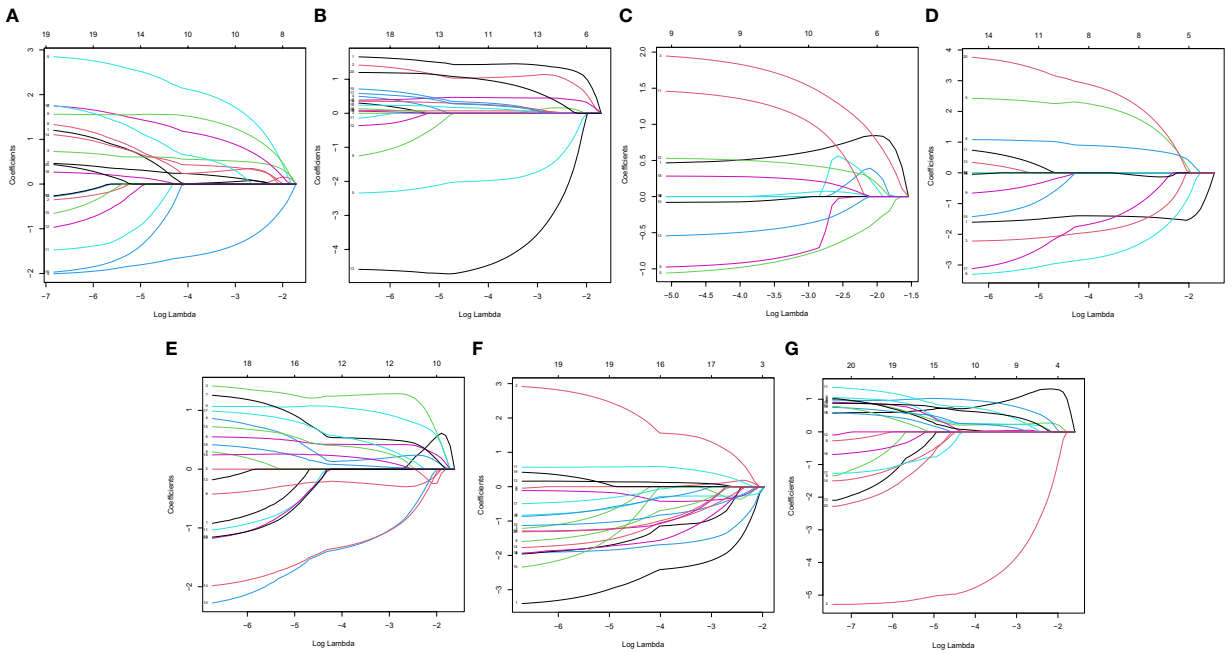

FIGURE 5
LASSO coefficient of prognostic relevant AS events. **(A)** AA. **(B)** AD. **(C)** AP. **(D)** AT. **(E)** ES. **(F)** ME. **(G)** RI.

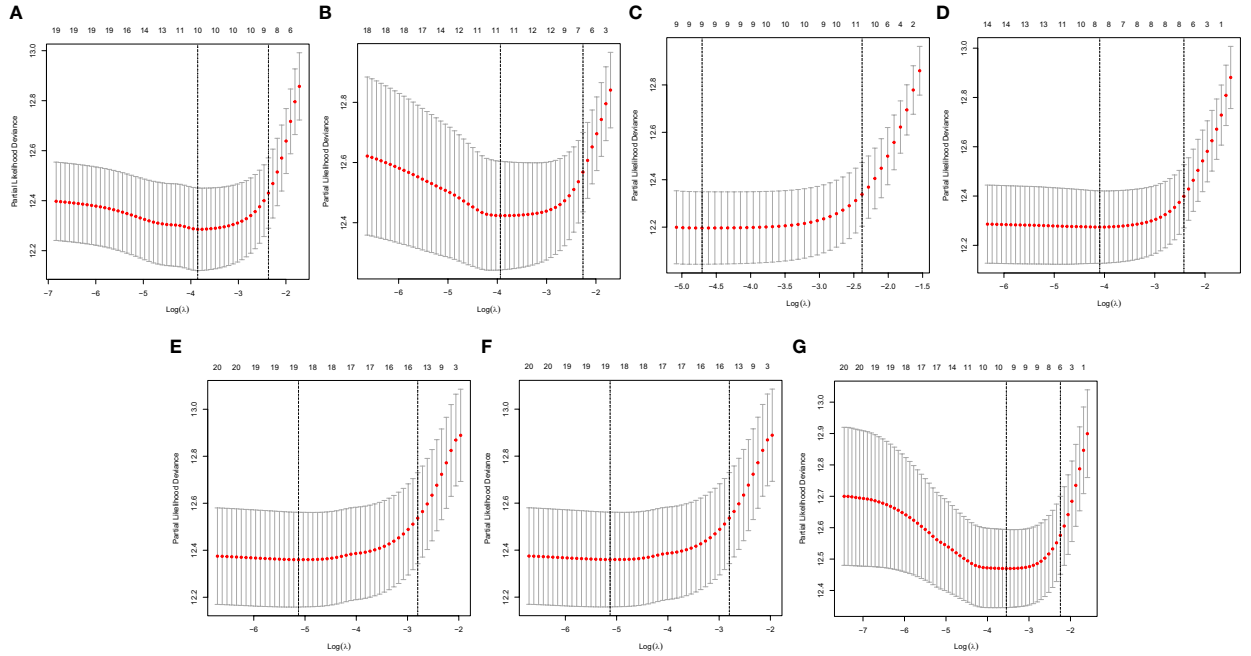

FIGURE 6
A graph of the error rate of cross-validation. **(A)** AA. **(B)** AD. **(C)** AP. **(D)** AT. **(E)** ES. **(F)** ME. **(G)** RI.

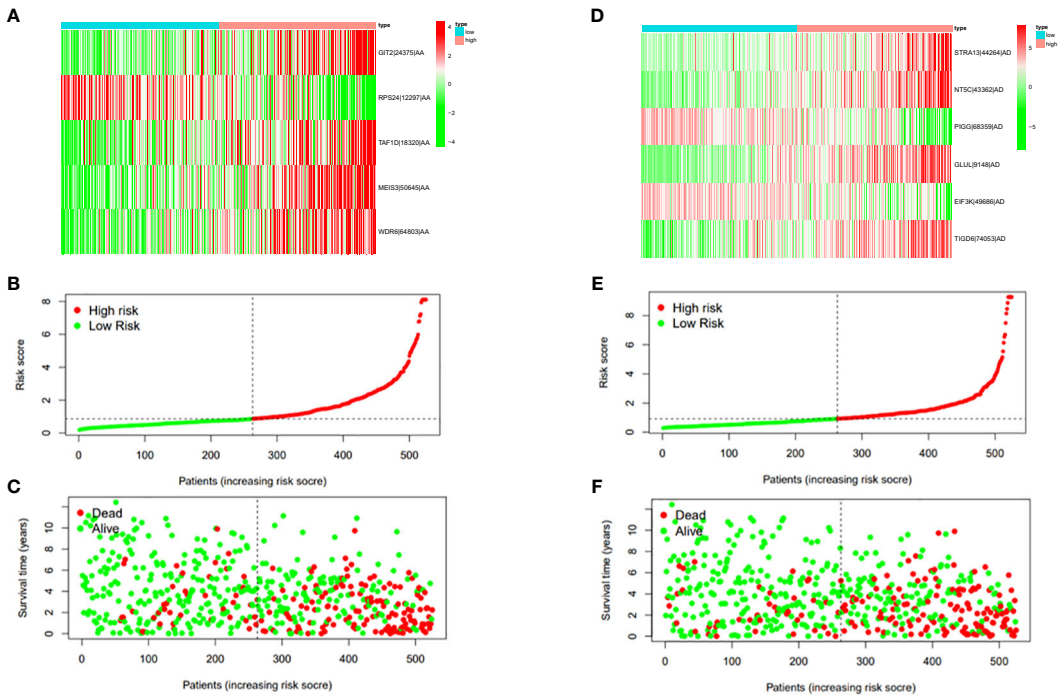

FIGURE 7
(A) Heatmap of the PSI value of AA events in ccRCC. The colors from red to green show a trend from high expression to low expression. **(B)** Distribution of the AA prognostic signature risk score. **(C)** The survival status and duration of ccRCC patients in the AA prognostic signature. **(D)** Heatmap of the PSI value of AD events in ccRCC. The colors from red to green show a trend from high expression to low expression. **(E)** Distribution of the AD prognostic signature risk score. **(F)** The survival status and duration of ccRCC patients in the AD prognostic signature.

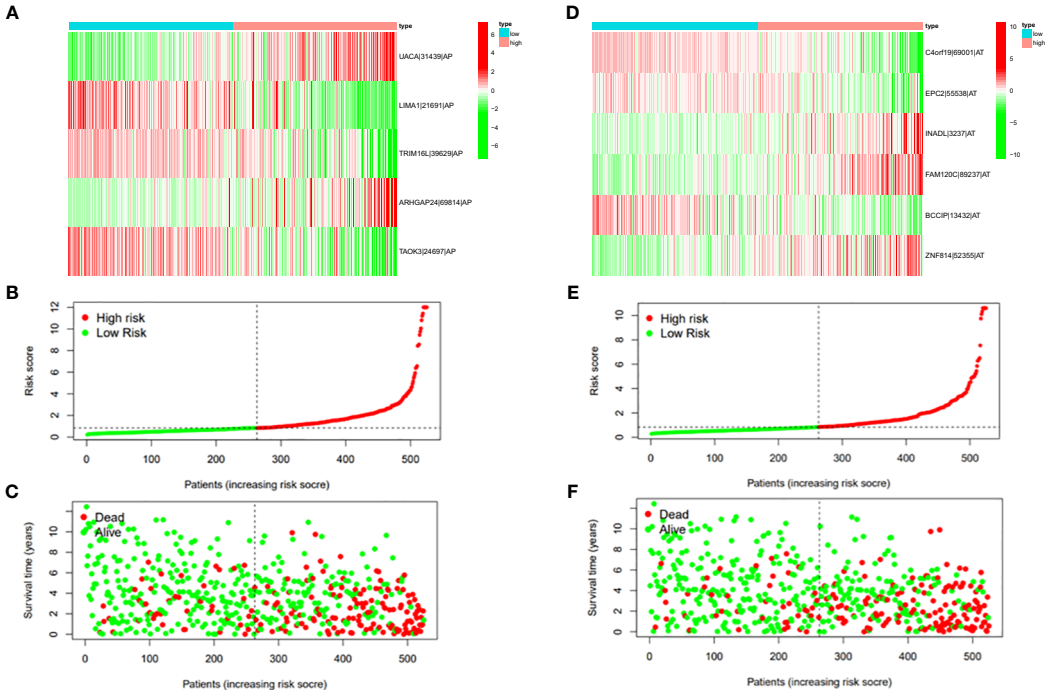

FIGURE 8
(A) Heatmap of the PSI value of AP events in ccRCC. The colors from red to green show a trend from high expression to low expression. **(B)** Distribution of the AP prognostic signature risk score. **(C)** The survival status and duration of ccRCC patients in the AP prognostic signature. **(D)** Heatmap of the PSI value of AT events in ccRCC. The colors from red to green show a trend from high expression to low expression. **(E)** Distribution of the AT prognostic signature risk score. **(F)** The survival status and duration of ccRCC patients in the AT prognostic signature.

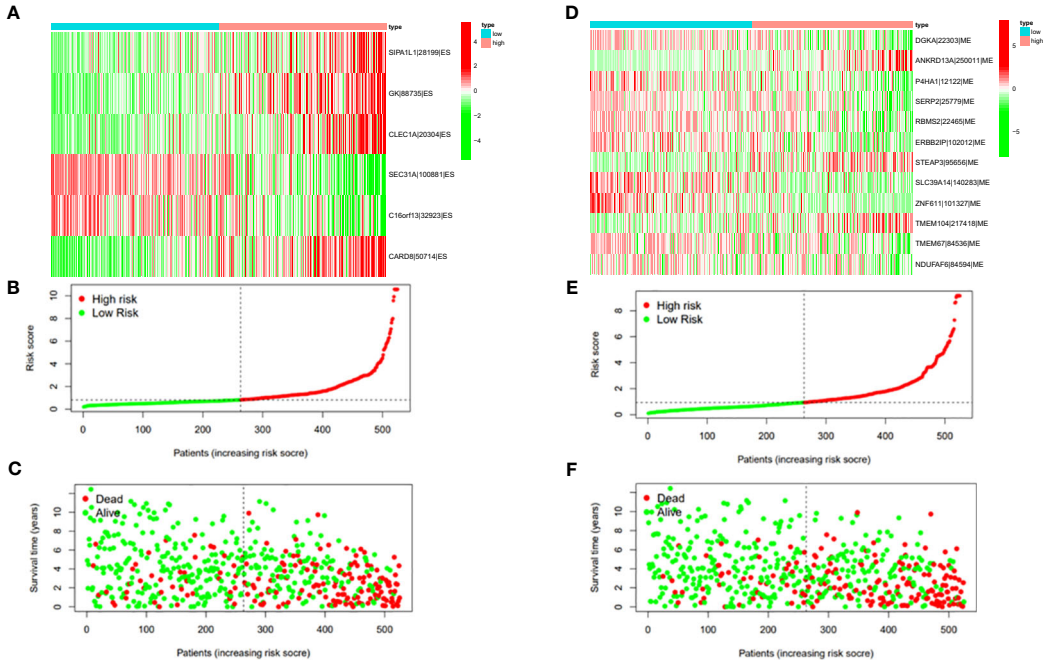

FIGURE 9
(A) Heatmap of the PSI value of ES events in ccRCC. The colors from red to green show a trend from high expression to low expression. **(B)** Distribution of the ES prognostic signature risk score. **(C)** The survival status and duration of ccRCC patients in the ES prognostic signature. **(D)** Heatmap of the PSI value of ME events in ccRCC. The colors from red to green show a trend from high expression to low expression. **(E)** Distribution of the ME prognostic signature risk score. **(F)** The survival status and duration of ccRCC patients in the ME prognostic signature.

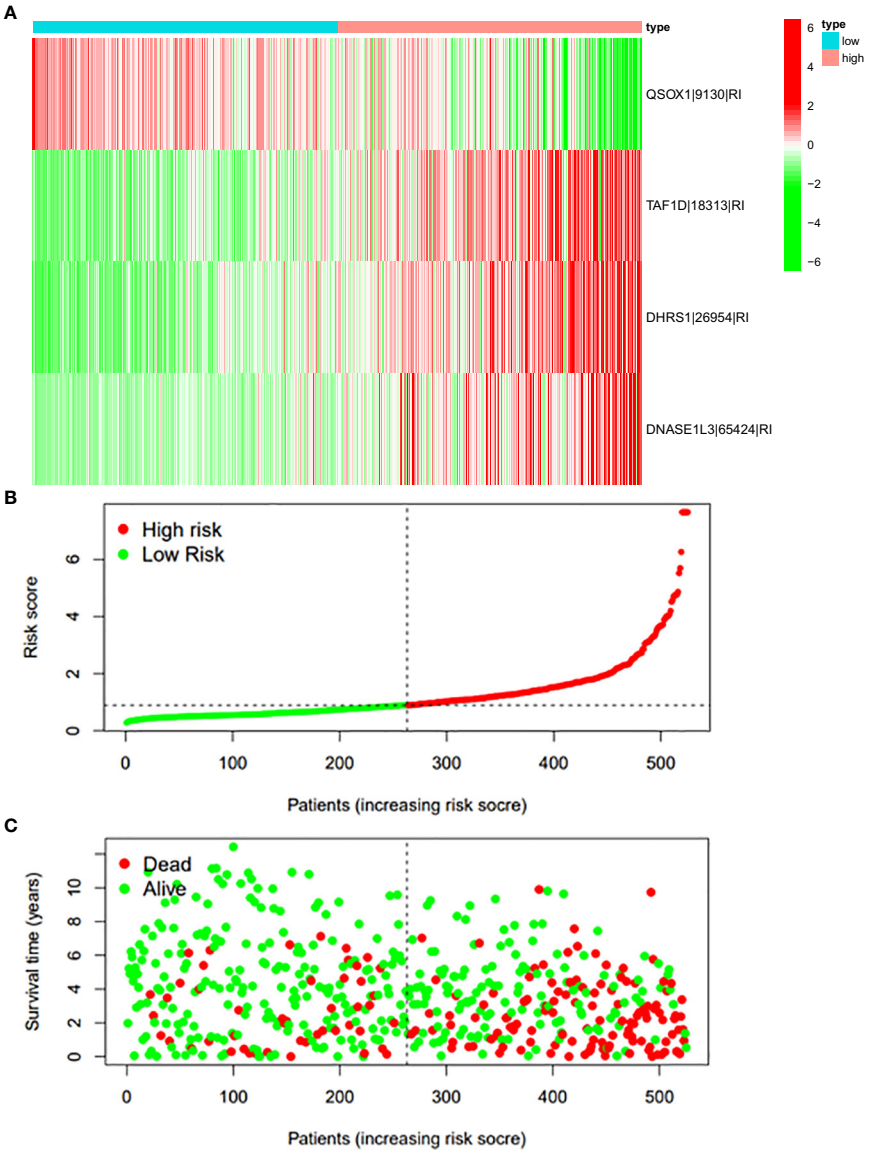

FIGURE 10
(A) Heatmap of the PSI value of RI events in ccRCC. The colors from red to green show a trend from high expression to low expression. **(B)** Distribution of the RI prognostic signature risk score. **(C)** The survival status and duration of ccRCC patients in the RI prognostic signature.

clinical decision-making of cancer oncology (19, 20). We screened out six key immune checkpoint inhibitor genes (PDCD1, CD274, PDCD1LG2, CTLA-4, HAVCR2, and IDO1) (21, 22) for further analysis. Then, to uncover the potential role of risk signature in ICB therapy for ccRCC, we comprehensively analyzed the association between the ALL prognostic signature and ICB key targets (Figure 17A). The results showed that the ALL prognostic signature had a significant positive association with PDCD1 (r = 0.3; p = 6.1e−12; Figure 17B) and CTLA4 (r = 0.33; p = 8.8e−15; Figure 17D) and a significant negative association with HAVCR2 (r = −0.13; p = 0.0035; Figure 17C) and CD274 (r = −0.13; p = 0.0025; Figure 17E). Furthermore, 36 of the 47 (i.e., HHLA2, CD44, etc.) ICB key gene expression levels between the low- and high-risk groups were significantly dysregulated in the further correlation analysis (Figure 17F). These results suggested that the level of the ALL prognostic signature does affect the expression changes of ICB key genes, which could be a valuable factor.

3.7 Role of *C4ORF19* in the prognosis and ICB treatment of vital genes

In this study, we found only one prognostic AS-related gene, *C4ORF19*, whose expression level was significantly downregulated. According to the TCGA database, the expression level of *C4ORF19* in normal adjacent tissues was higher than that in tumor tissues (Figure 18A). The IHC experiment showed that the expression level of *C4ORF19* in ccRCC tissue was significantly lower than that in normal tissue, and the experimental results of qPCR also confirmed this point (p = 0.0115) (Figure 19). It could be clearly seen that the

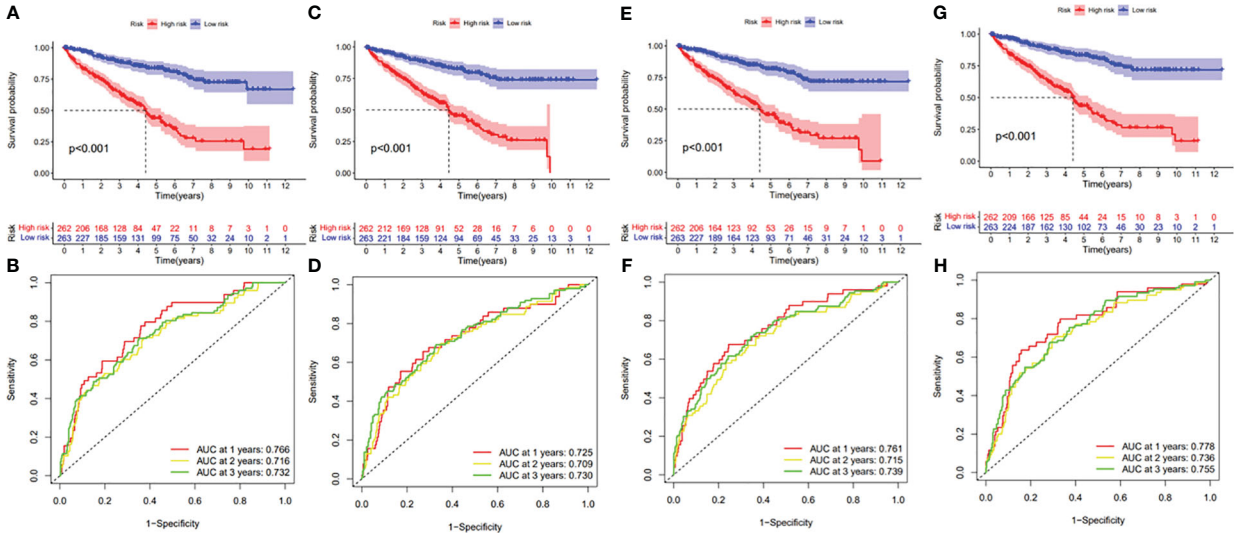

FIGURE 11
(A) Kaplan–Meier curve presenting survival in the AA prognostic signature. **(B)** ROC analysis of the risk scores in the AA prognostic signature. **(C)** Kaplan–Meier curve presenting survival in the AD prognostic signature. **(D)** ROC analysis of the risk scores in the AD prognostic signature. **(E)** Kaplan–Meier curve presenting survival in the AP prognostic signature. **(F)** ROC analysis of the risk scores in the AP prognostic signature. **(G)** Kaplan–Meier curve presenting survival in the AT prognostic signature. **(H)** ROC analysis of the risk scores in the AT prognostic signature.

expression levels of *C4ORF19* in different tumor grades (Figure 18C, almost $p < 0.05$), different pathological stages (Figure 18D, almost $p < 0.05$), T state, M state, and gender (Figures 18E–G, almost $p < 0.05$) had significant statistical significance. In order to further assess the prognostic value of *C4ORF19* in ccRCC, K–M analyses were performed between patients with low and high expression of *C4ORF19*. A higher *C4ORF19* expression level significantly correlated with a longer overall survival time, as illustrated in

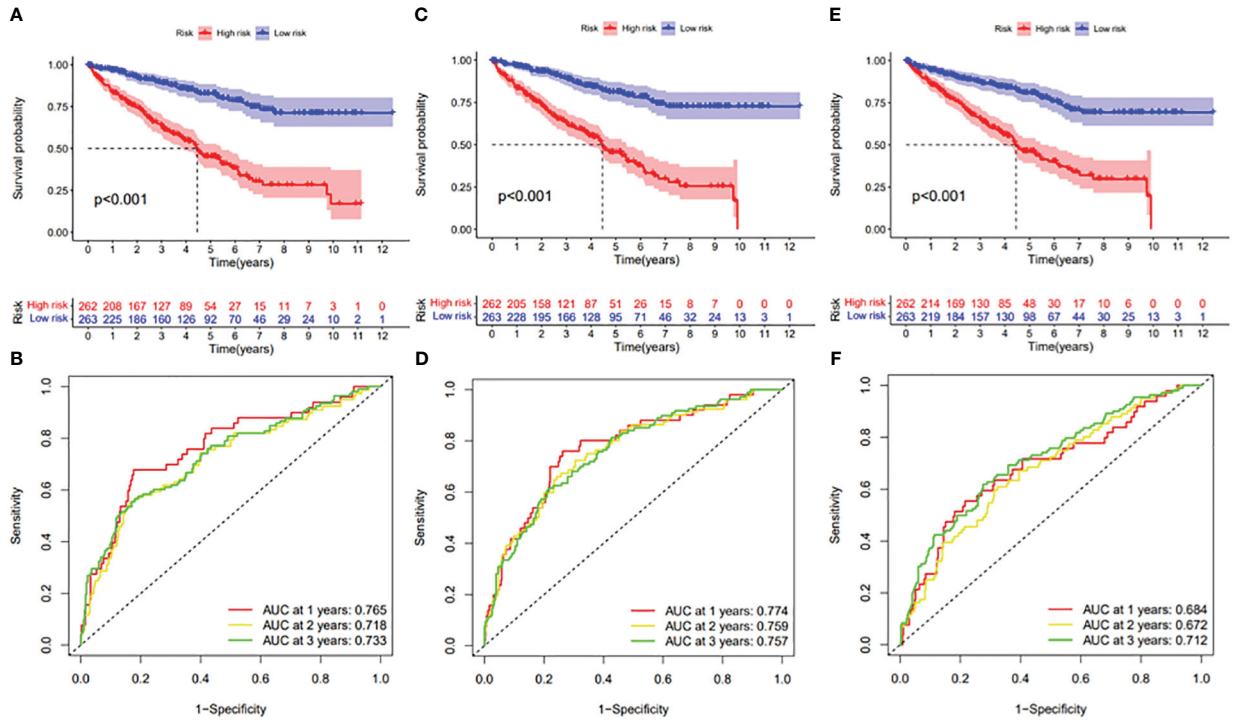

FIGURE 12
(A) Kaplan–Meier curve presenting survival in the ES prognostic signature. **(B)** ROC analysis of the risk scores in the ES prognostic signature. **(C)** Kaplan–Meier curve presenting survival in the ME prognostic signature. **(D)** ROC analysis of the risk scores in the ME prognostic signature. **(E)** Kaplan–Meier curve presenting survival in the RI prognostic signature. **(F)** ROC analysis of the risk scores in the RI prognostic signature.

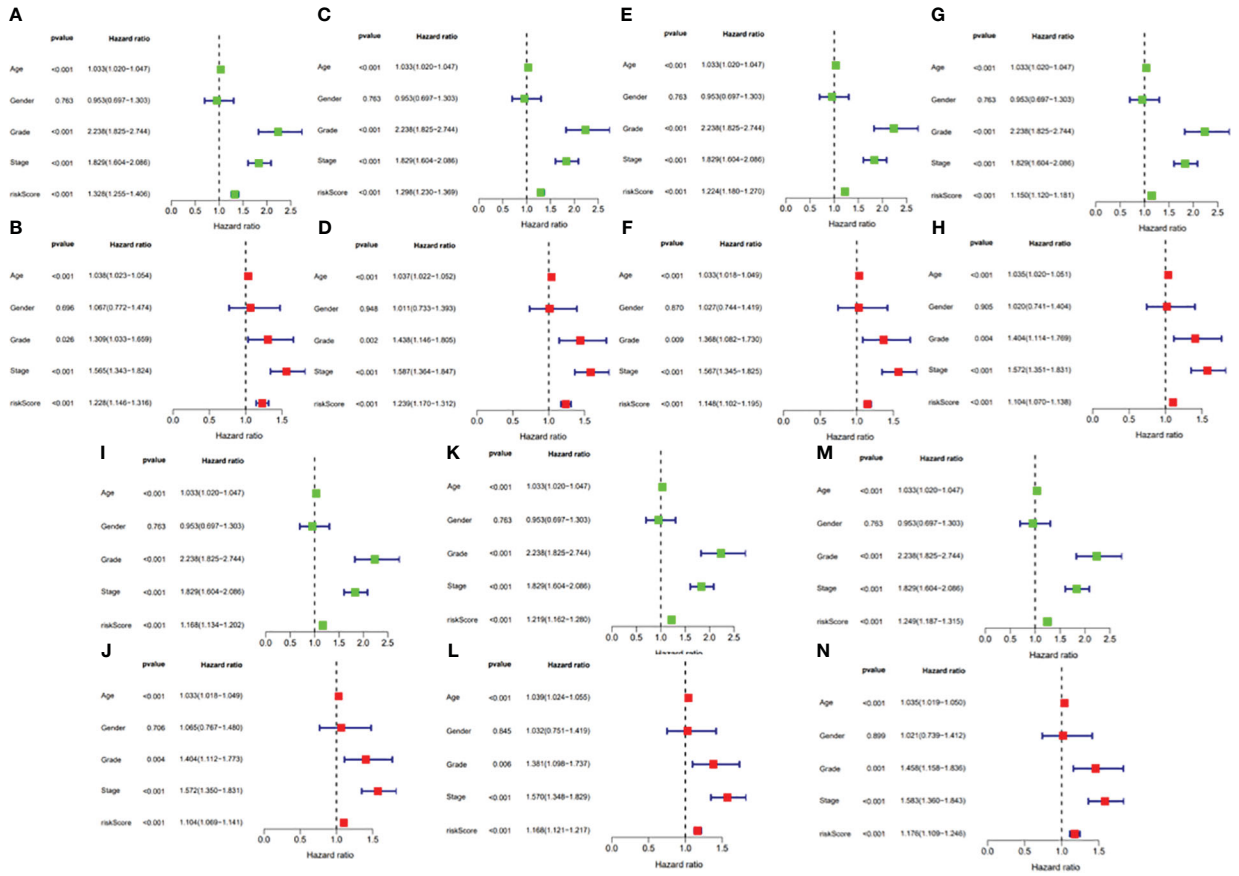

FIGURE 13
(A) Univariate Cox regression analyses in the AA prognostic signature. **(B)** Multivariate Cox regression analyses in the AA prognostic signature. **(C)** Univariate Cox regression analyses in the AD prognostic signature. **(D)** Multivariate Cox regression analyses in the AD prognostic signature. **(E)** Univariate Cox regression analyses in the AP prognostic signature. **(F)** Multivariate Cox regression analyses in the AP prognostic signature. **(G)** Univariate Cox regression analyses in the AT prognostic signature. **(H)** Multivariate Cox regression analyses in the AT prognostic signature. **(I)** Univariate Cox regression analyses in the ES prognostic signature. **(J)** Multivariate Cox regression analyses in the ES prognostic signature. **(K)** Univariate Cox regression analyses in the ME prognostic signature. **(L)** Multivariate Cox regression analyses in the ME prognostic signature. **(M)** Univariate Cox regression analyses in the RI prognostic signature. **(N)** Multivariate Cox regression analyses in the RI prognostic signature.

Figure 18B ($p < 0.001$). Moreover, in 28 of 47 immune check blockade-associated genes (i.e., PDCD1, CTLA4, etc.), there were significant dysregulations in the expression levels between the low *C4ORF19* group and high *C4ORF19* group in different subgroups (Figure 18H). Then, a possible role for *C4ORF19* in ICB treatment of ccRCC was explored by analyzing the association between *C4ORF19* and ICB key targets adjusted for tumor purity using TIMER. The TIMER results exhibited that *C4ORF19* had a significant positive correlation with CD274 ($r = 0.361$; $p = 1.21e{-}15$) and HAVCR2 ($r = 0.137$; $p = 3.15e{-}03$) and a significant negative correlation with PDCD1 ($r = -0.129$; $p = 5.46e{-}03$) and CTLA4 ($r = -0.095$; $p = 4.11e{-}02$; Figure 18I), suggesting that *C4ORF19* may play a vital role in the ICB treatment of ccRCC.

3.8 *C4ORF19* in TIME

Firstly, we classified ccRCC patients into high/low *C4ORF19* groups for further study according to the median *C4ORF19* expression level. The ESTIMATE results showed significantly higher stromal and immune scores in the low *C4ORF19* group than in the high *C4ORF19* group, suggesting more infiltration of stromal and immune cells and lower tumor purity in the low *C4ORF19* group (Figures 20A–D). Moreover, the relationship between the gene copy number of the different mutation types and main immune cells is exhibited in Figure 20E. Afterward, a positive correlation was found between *C4ORF19* expression level and B-cell infiltration, while a negative correlation was found between *C4ORF19* expression level and CD8+ T-cell infiltration. There was no significant difference in the expression level of *C4ORF19* when CD4+ T cells, macrophages, and neutrophils were infiltrated (Figure 20F). The consequences of ssGSEA presented that the infiltration fraction of aDCs, CD8+ T cells, DCs, macrophages, pDCs, Th1 cells, Th2 cells, NK cells, parainflammation, T helper cells, Tfh, TIL, APC co-stimulation, checkpoint, T-cell co-stimulation, CCR, cytolytic activity, inflammation-promoting, and IFN-response type-I were significantly increased when the *C4ORF19* expression level was

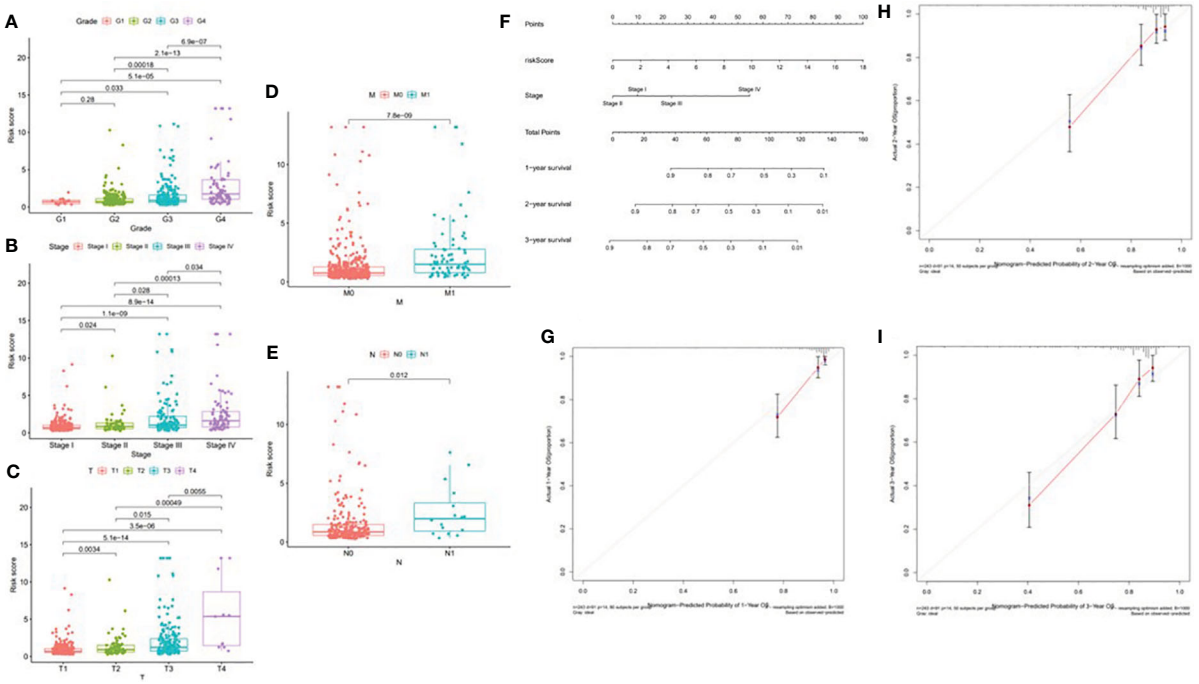

FIGURE 14
Correlation of risk score with clinical features and construction of nomogram. **(A)** Correlation of risk score with tumor grade. **(B)** Correlation of risk score with clinicopathological stage. **(C)** Correlation of risk score with T status. **(D)** Correlation of risk score with M status. **(E)** Correlation of risk score with N status. **(F)** A nomogram was constructed by stage and risk signature for predicting the survival of ccRCC patients. **(G)** One-year nomogram calibration curves. **(H)** Two-year nomogram calibration curves. **(I)** Three-year nomogram calibration curves.

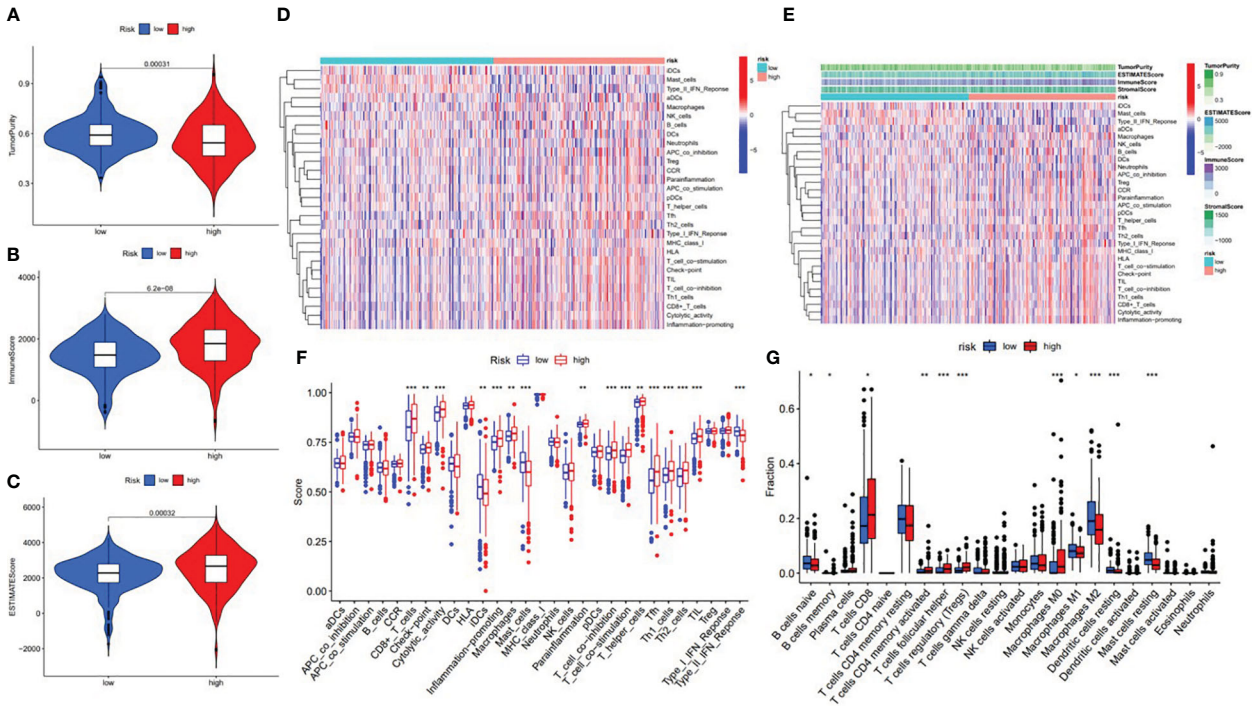

FIGURE 15
Correlation between infiltrating immune cells and the ALL AS-based prognostic signature. **(A)** Comparison of tumor purity between the low- and high-risk groups. **(B)** Comparison of immune score between the low- and high-risk groups. **(C)** Comparison of ESTIMATE score between the low- and high-risk groups. **(D)** Heatmap exhibited enrichment of 29 immune signatures of the low-/high-risk groups. Blue represents low activity and red represents high activity. **(E)** Heatmap of 29 immune signatures and immune scores of two different risk score groups. Blue represents low activity and red represents high activity. **(F)** Difference of enrichment of immune-related signatures between the low-risk and high-risk groups. **(G)** Distinction of infiltrating immune cell subpopulations and levels between the low-/high-risk groups. * means p<0.05, * * means p<0.01, * * * means p<0.001.

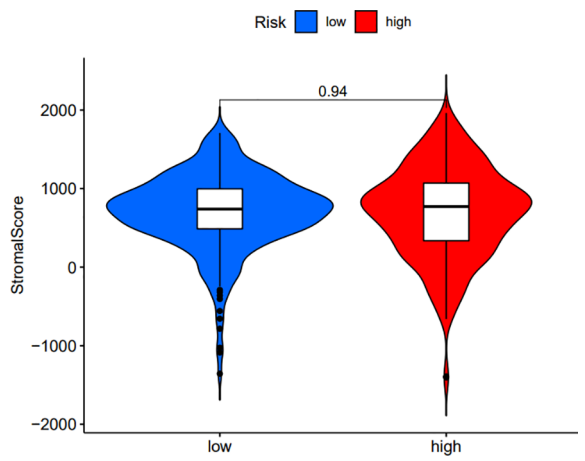

FIGURE 16
Comparison of the stromal score between the low-/high-risk groups.

declining (Figure 20G). The consequences of the CIBERSORT analysis of the TCGA cohort presented that the proportions of plasma cells, Tregs, activated memory CD4 T cells, and M0 macrophages were significantly higher and the proportions of monocytes and resting dendritic cells were significantly lower in patients with low *C4ORF19* expression (Figure 20H).

3.9 Establishment of the SF-AS regulatory network

The upregulated and downregulated genes were the results of the correlation analysis with the corresponding gene expression levels in tumor samples (Additional file 1: Table 4). Finally, to better explain the underlying mechanisms of AS regulation, we used 351 upregulated AS events (yellow diamond), 88 downregulated AS events (green triangle), and 31 SFs (blue hexagon; Figure 21) to establish the correlation network between SF expression level and PSI value of prognostic AS events. In the regulation network, the most important four nodes (Additional file 1: Table 4) consisting of two upregulated AS events (METTL3|26596|RI and FADS3|16305|RI) and two SFs (DDX39B and LUC7L) were identified. As a result, these SFs had great potential to further mediate the occurrence and development of tumors in ccRCC as key regulatory factors involved in abnormal AS regulation.

4 Discussion

Among urinary cancers, the mortality rate of renal cell carcinoma ranks first in the world (2). In addition to being one of the most malignant urologic tumors, ccRCC is also one of the most common subtypes of renal cell carcinoma (3). Genetic, molecular, and clinicopathological characteristics of ccRCC could not

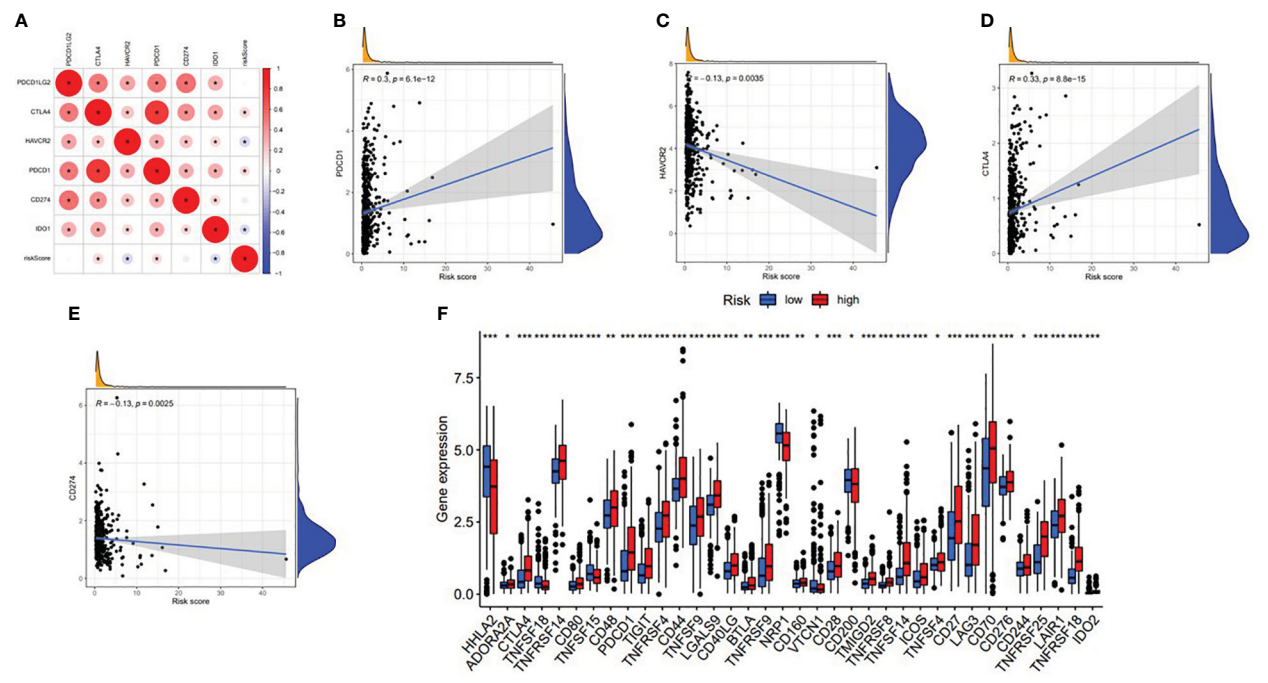

FIGURE 17
Association between the ALL AS-based prognostic signature and key immune checkpoint genes. **(A)** Correlation analyses between immune checkpoint inhibitors CD274, PDCD1, PDCD1LG2, CTLA4, HAVCR2, and IDO1 and risk score. **(B)** Correlation between risk score and PDCD1. **(C)** Correlation between risk score and HAVCR2. **(D)** Correlation between risk score and CTLA4. **(E)** Correlation between risk score and CD274. **(F)** Comparison of immune checkpoint blockade-related gene expression levels between the low-risk group and high-risk groups. *means p<0.05, * * means p<0.01, * * * means p<0.001.

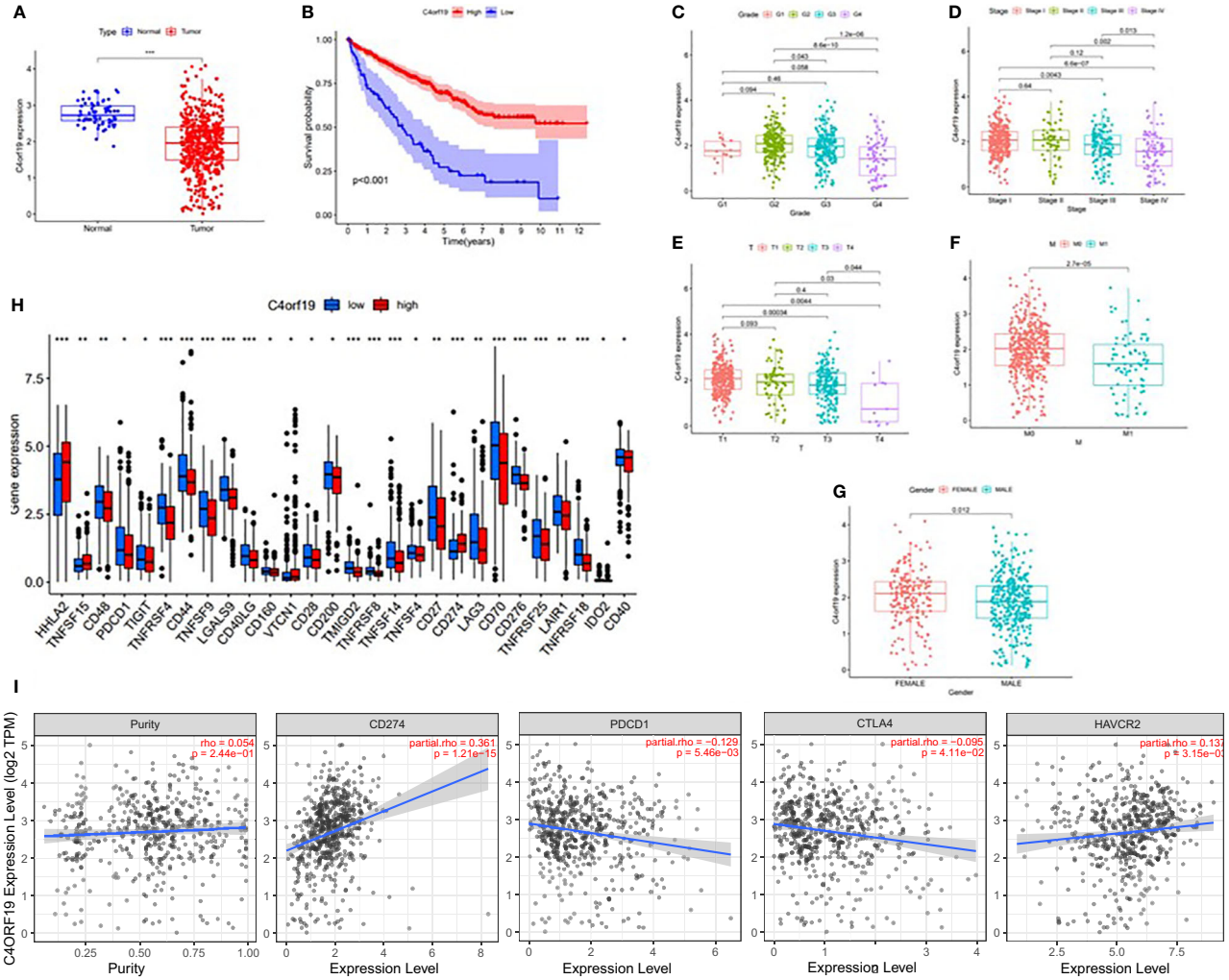

FIGURE 18
The clinical significance of *C4ORF19* in ccRCC. **(A)** *C4ORF19* was of lower expression in ccRCC tumor tissue than in normal tissue. **(B)** Higher ZDHHC16 expression levels revealed longer overall survival. **(C)** Correlation of *C4ORF19* expression with tumor grade. **(D)** Correlation of *C4ORF19* expression with major pathological stages. **(E)** Correlation of *C4ORF19* expression with T status. **(F)** Correlation of *C4ORF19* expression with M status. **(G)** Correlation of *C4ORF19* expression with gender. **(H)** Comparison of immune checkpoint blockade-related gene expression levels between the low *C4ORF19* group and high *C4ORF19* group. **(I)** Correlation of *C4ORF19* with CD274, PDCD1, CTLA4, and HAVCR2. *means p<0.05, * * means p<0.01, * * * means p<0.001.

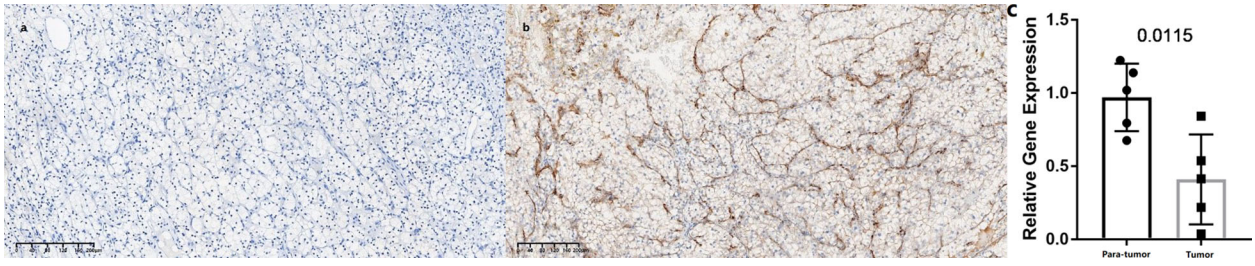

FIGURE 19
Expression levels of *C4ORF19* in ccRCC tissues. **(A)** Representative microphotographs revealed *C4ORF19* expression in tumor tissues using IHC staining. Brown, *C4ORF19*. Blue, hematoxylin. Bar = 200 μm. **(B)** Representative microphotographs revealed *C4ORF19* expression in paratumor tissues using IHC staining. Brown, *C4ORF19*. Blue, hematoxylin. Bar = 200 μm. **(C)** qPCR showed low expression of *C4ORF19* in ccRCC tissue.

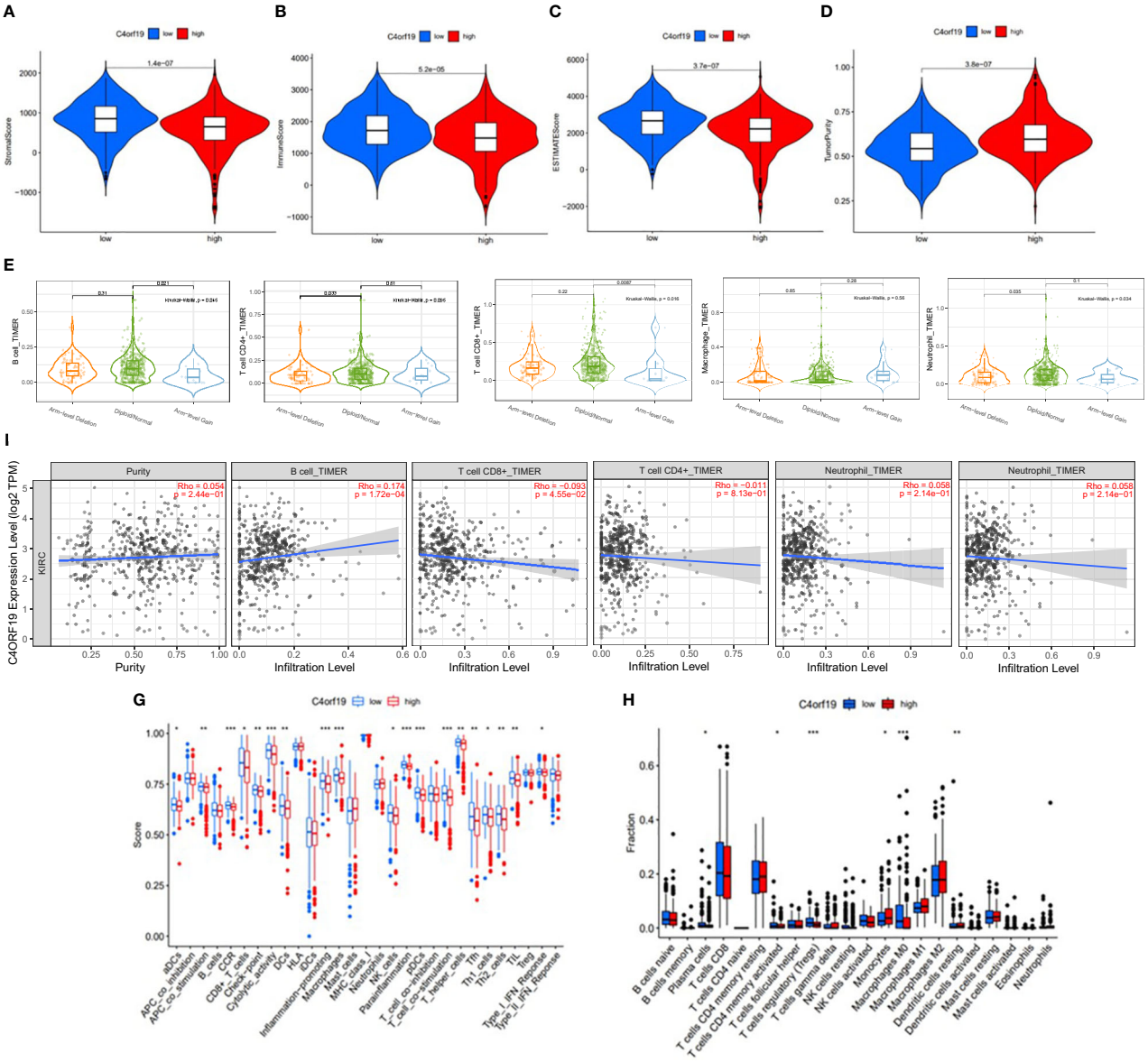

FIGURE 20
The role of *C4ORF19* in TIME features. **(A)** Comparison of stromal score between the low/high *C4ORF19* groups. **(B)** Comparison of immune score between the low/high *C4ORF19* groups. **(C)** Comparison of ESTIMATE score between the low/high *C4ORF19* groups. ESTIMATE score. **(D)** Comparison of tumor purity between the low/high *C4ORF19* groups. **(E)** Copy number of immune cells in ccRCC. **(F)** Relationship between *C4ORF19* expression level with B cells, CD8+ T cells, CD4+ T cells, macrophages, and neutrophils. **(G)** Comparison of ssGSEA enrichment between the low/high *C4ORF19* groups. **(H)** Comparison of CIBERSORT results between the low/high *C4ORF19* groups. *means p<0.05, * * means p<0.01, * * * means p<0.001.

accurately forecast clinical therapy outcomes and the prognosis of patients (23). RCC has dissimilar immunological features in pathogenesis and treatment. Thus, there is a great need to further investigate powerful prognostic tools to predict immunotherapeutic outcomes and to recognize patients for whom immunotherapy might be effective.

Growing studies have proven that AS, which refers to a post-transcriptional modification procedure, functions in physiological and pathological processes (8). The irregular regulation of AS generally indicated that tumors occurred and developed, including ccRCC (10). Therefore, dysregulated expressed genes have the potential to be utilized as new prognostic indicators and effective therapeutic targets. Unfortunately, we still lacked enough understanding of the relationship of the AS prognostic signature with TIME and immunotherapy results in ccRCC.

In this study, we made full use of univariate Cox regression analysis. As a result, we found 9,347 AS events to be significantly associated with survival, in order to further explore the prognostic value of AS events. Afterward, based on a comprehensive bioinformatics analysis, we summarized and validated eight (AP, AD, AA, AT, ME, RI, ES, ALL) prognostic predictive signatures, all of which showed strong predictive abilities in ccRCC. In addition, when ccRCC patients were grouped according to clinicopathological stage and tumor grade, these signatures still

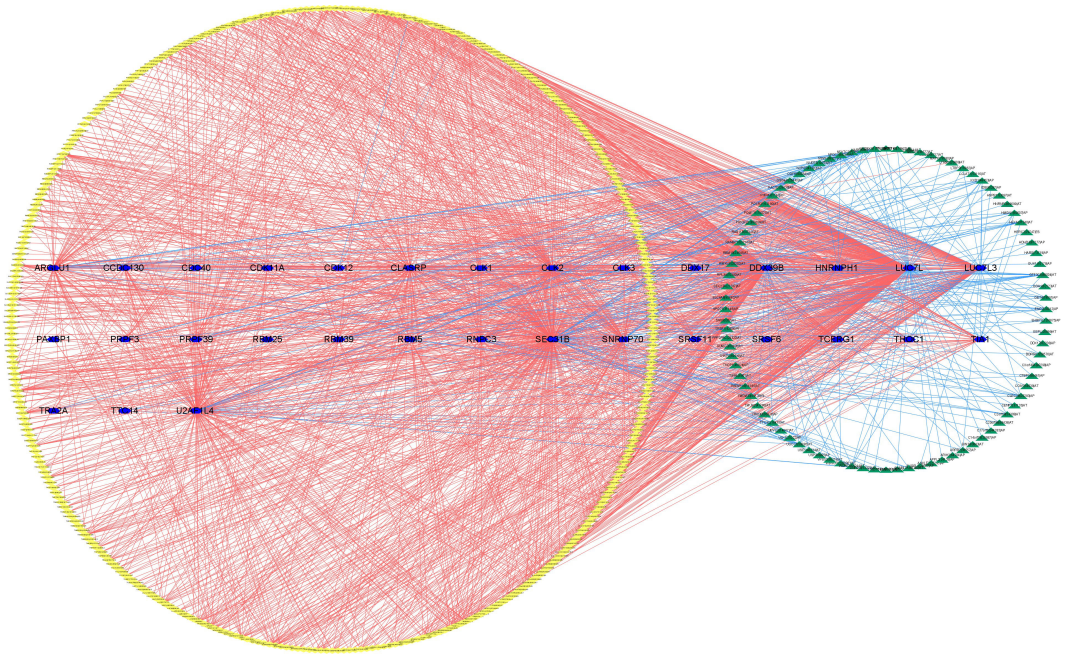

FIGURE 21
The regulatory network between SFs and survival-related AS events. The yellow or green nodes indicated that the AS events were positively or negatively correlated with survival. Blue hexagons symbolized SFs. The positive/negative correlations ($r > 0.6$ or $r \leq 0.6$) between SFs and AS events were shown with red/blue lines.

had excellent predictive ability. We drew a nomogram to better serve the clinic. As expected, the predicted results of the nomogram were in good agreement with the actual results. As mentioned above, we developed and presented the SF-AS regulatory network to interpret the underlying mechanisms of AS regulation.

Although our new nomogram shows good predictive ability, we believe that the nomogram we created using risk score and stage cannot replace the IMDC score model and the nomograms based on clinical data at present (24, 25). This is because we did not classify renal clear cell carcinoma into metastatic and non-metastatic types, making it difficult to make accurate comparisons. Therefore, external validation of big data may be a more acceptable method to assess the effectiveness of our nomogram. However, this does not mean that our new nomogram is an invalid effort. Our proposed risk score has the potential to be an independent factor in predicting the prognosis of renal clear cell carcinoma.

By exploring the role of AS events in TIME with the method described above, we found that there was generally a high level of infiltration and a more active immune state in the high-risk group, which indicates that immune recognition and antitumor effects are present. Moreover, these results suggested that risk scores could facilitate the prediction of immunotherapy outcomes. Unfortunately, we had no way to explore the association between risk score and ICB treatment outcomes because there was no ICB treatment dataset in the ccRCC cohort. Then, risk score had a significantly positive relationship with PDCD1 and CTLA4 and a significantly negative relationship with HAVCR2 and IDO1. Furthermore, it was worth mentioning that risk score was significantly connected with 36 (i.e., HHLA2, etc.) ICB gene expression levels. These results above confirmed that risk scores did have the potential to help develop more scientific and personalized immunotherapy strategies.

C4ORF19 (Chromosome 4 Open Reading Frame 19) is a protein-coding gene. Wang W. et al. reported that regulated *C4ORF19* could promote colon adenocarcinoma cell proliferation, invasion, and migration (26). However, our understanding of the role of *C4ORF19* in clear cell renal carcinoma is not clear so far. This study indicated that *C4ORF19* was significantly downregulated in cell lines, largely suggesting a poor prognosis for ccRCC. In ICB immunotherapy for ccRCC, the *C4ORF19* expression level correlated significantly with clinicopathological stage, tumor grade, and key genes (i.e., IDO1). However, the potential biological role of *C4ORF19* was unclear and required further study.

In general, ccRCC patients with higher risk scores or lower levels of *C4ORF19* expression had higher levels of immune cell infiltration in the tumor environment, suggesting immunophenotypic activation, but shorter overall survival. Therefore, we hypothesized that the ICB pathways might influence the antitumor effect of immune cells, and the risk score was related to the expression of immune checkpoint blockade targets.

This study had the following advantages in exploring new prognostic factors for ccRCC. First of all, as a result of this study, we were able to uncover the role of AS events in the formation of TIME diversity and complexity as well as their role in the prediction of ICB therapy outcomes, which had not been clarified. In addition, to uncover the comprehensive landscape of TIME in ccRCC, the ESTIMATE R package, ssGSEA algorithm, CIBERSORT method, and TIMER database exploration were employed. Finally, the study

emphasized the biological function of *C4ORF19* in clear cell renal carcinoma for the first time.

The current research also had several shortcomings. First of all, the AS events in ccRCC were investigated using the public TCGA cohort, which was not validated using the in-house cohort. In addition, the effectiveness of prognostic indicators including the ALL prognostic signature and prognostic nomogram still needed to be verified through clinical trials. Furthermore, the conclusion that the key gene *C4ORF19* was downregulated in ccRCC tumor tissue still required a larger number of experiments.

5 Conclusion

All in all, we systematically analyzed the prognostic value of RNA splicing patterns in order to strengthen the prognostic prediction of ccRCC. The nomogram we developed using risk score and stage is not as effective in predicting prognosis compared with the nomogram based on clinical data. Despite this, our proposed risk score has the potential to be an independent factor in predicting the prognosis of ccRCC. In addition, the promising targets for ccRCC antitumor therapy were identified from the AS-SF regulatory network. After comprehensive bioinformatics analysis of AS events, the AS atlas was closely correlated with the TIME characteristics and immunotherapy of ccRCC. However, these findings still required more experimental and clinical exploration to verify. At the same time, the mechanism of tumor occurrence and development of ccRCC and the impact of these AS events still need to be further explored.

Data availability statement

The datasets presented in this study can be found in online repositories. The names of the repository/repositories and accession number(s) can be found in the article/Supplementary Material.

Ethics statement

The studies involving humans were approved by the Hospital Ethics Committees of the second Affiliated Hospital of Wenzhou Medical University. The studies were conducted in accordance with the local legislation and institutional requirements. The participants provided their written informed consent to participate in this study.

Author contributions

JZ mainly completes bioinformatics analysis and article writing; HJ mainly completes experimental verification; As the first corresponding author, XJ guides the whole process; As the second corresponding author, DR provides experimental help. All authors contributed to the article and approved the submitted version.

Funding

The author(s) declare that no financial support was received for the research, authorship, and/or publication of this article.

Conflict of interest

The authors declare that the research was conducted in the absence of any commercial or financial relationships that could be construed as a potential conflict of interest.

Publisher's note

Supplementary material

The Supplementary Material for this article can be found online at: https://www.frontiersin.org/articles/10.3389/fonc.2023.1206882/full#supplementary-material

References

1. Makhov P, Joshi S, Ghatalia P, Kutikov A, Uzzo RG, Kolenko VM. Resistance to systemic therapies in clear cell renal cell carcinoma: mechanisms and management strategies. *Mol Cancer Ther* (2018) 17(7):1355–64. doi: 10.1158/1535-7163.MCT-17-1299

2. Mou Y, Wu J, Zhang Y, Abdihamid O, Duan C, Li B. Low expression of ferritinophagy-related NCOA4 gene in relation to unfavorable outcome and defective immune cells infiltration in clear cell renal carcinoma. *BMC Cancer* (2021) 21(1):18. doi: 10.1186/s12885-020-07726-z

3. Xu WH, Xu Y, Wang J, Wan FN, Wang HK, Cao DL, et al. Prognostic value and immune infiltration of novel signatures in clear cell renal cell carcinoma microenvironment. *Aging (Albany NY)* (2019) 11(17):6999–7020. doi: 10.18632/aging.102233

4. Crispen PL, Breau RH, Allmer C, Lohse CM, Cheville JC, Leibovich BC, et al. Lymph node dissection at the time of radical nephrectomy for high-risk clear cell renal cell carcinoma: indications and recommendations for surgical templates. *Eur Urol* (2011) 59(1):18–23. doi: 10.1016/j.eururo.2010.08.042

5. Hsieh JJ, Purdue MP, Signoretti S, Swanton C, Albiges L, Schmidinger M, et al. Renal cell carcinoma. *Nat Rev Dis Primers* (2017) 3:17009. doi: 10.1038/nrdp.2017.9

6. Xiao L, Zou G, Cheng R, Wang P, Ma K, Cao H, et al. Alternative splicing associated with cancer stemness in kidney renal clear cell carcinoma. *BMC Cancer* (2021) 21(1):703. doi: 10.1186/s12885-021-08470-8

7. Grosser R, Cherkassky L, Chintala N, Adusumilli PS. Combination immunotherapy with CAR T cells and checkpoint blockade for the treatment of solid tumors. *Cancer Cell* (2019) 36(5):471–82. doi: 10.1016/j.ccell.2019.09.006

8. Nilsen TW, Graveley BR. Expansion of the eukaryotic proteome by alternative splicing. *Nature* (2010) 463(7280):457–63. doi: 10.1038/nature08909

9. Zhao Z, Li GZ, Liu YQ, Huang RY, Wang KY, Jiang HY, et al. Characterization and prognostic significance of alternative splicing events in lower-grade diffuse gliomas. *J Cell Mol Med* (2020) 24(22):13171–80. doi: 10.1111/jcmm.15924

10. Climente-González H, Porta-Pardo E, Godzik A, Eyras E. The functional impact of alternative splicing in cancer. *Cell Rep* (2017) 20(9):2215–26. doi: 10.1016/j.celrep.2017.08.012

11. Tripathi V, Ellis JD, Shen Z, Song DY, Pan Q, Watt AT, et al. The nuclear-retained noncoding RNA MALAT1 regulates alternative splicing by modulating SR splicing factor phosphorylation. *Mol Cell* (2010) 39(6):925–38. doi: 10.1016/j.molcel.2010.08.011

12. El Marabti E, Younis I. The cancer spliceome: reprograming of alternative splicing in cancer. *Front Mol Biosci* (2018) 5:80. doi: 10.3389/fmolb.2018.00080

13. Yang Q, Zhao J, Zhang W, Chen D, Wang Y. Aberrant alternative splicing in breast cancer. *J Mol Cell Biol* (2019) 11(10):920–9. doi: 10.1093/jmcb/mjz033

14. Atkins MB, Tannir NM. Current and emerging therapies for first-line treatment of metastatic clear cell renal cell carcinoma. *Cancer Treat Rev* (2018) 70:127–37. doi: 10.1016/j.ctrv.2018.07.009

15. Goodman A, Patel SP, Kurzrock R. PD-1-PD-L1 immune-checkpoint blockade in B-cell lymphomas. *Nat Rev Clin Oncol* (2017) 14(4):203–20. doi: 10.1038/nrclinonc.2016.168

16. Xu W, Atkins MB, McDermott DF. Checkpoint inhibitor immunotherapy in kidney cancer. *Nat Rev Urol* (2020) 17(3):137–50. doi: 10.1038/s41585-020-0282-3

17. Cimadamore A, Massari F, Santoni M, Lopez-Beltran A, Cheng L, Scarpelli M, et al. PD1 and PD-L1 inhibitors for the treatment of kidney cancer: the role of PD-L1 assay. *Curr Drug Targets* (2020) 21(16):1664–71. doi: 10.2174/1389450121666200324151056

18. Seiler M, Peng S, Agrawal AA, Palacino J, Teng T, Zhu P, et al. Cancer genome atlas research network, Buonamici S, Yu L. Somatic mutational landscape of splicing factor genes and their functional consequences across 33 cancer types. *Cell Rep* (2018) 23(1):282–96. doi: 10.1016/j.celrep.2018.01.088

19. Wang Y, Wu L, Tian C, Zhang Y. PD-1-PD-L1 immune-checkpoint blockade in Malignant lymphomas. *Ann Hematol* (2018) 97(2):229–37. doi: 10.1007/s00277-017-3176-6

20. Mahoney KM, Freeman GJ, McDermott DF. The next immune-checkpoint inhibitors: PD-1/PD-L1 blockade in melanoma. *Clin Ther* (2015) 37(4):764–82. doi: 10.1016/j.clinthera.2015.02.018

21. Kim JE, Patel MA, Mangraviti A, Kim ES, Theodros D, Velarde E, et al. Combination therapy with anti-PD-1, anti-TIM-3, and focal radiation results in regression of murine gliomas. *Clin Cancer Res* (2017) 23(1):124–36. doi: 10.1158/1078-0432.CCR-15-1535

22. Nishino M, Ramaiya NH, Hatabu H, Hodi FS. Monitoring immune-checkpoint blockade: response evaluation and biomarker development. *Nat Rev Clin Oncol* (2017) 14(11):655–68. doi: 10.1038/nrclinonc.2017.88

23. Kim MC, Jin Z, Kolb R, Borcherding N, Chatzkel JA, Falzarano SM, et al. Updates on immunotherapy and immune landscape in renal clear cell carcinoma. *Cancers (Basel)* (2021) 13(22):5856. doi: 10.3390/cancers13225856

24. Heng DY, Xie W, Regan MM, Harshman LC, Bjarnason GA, Vaishampayan UN, et al. External validation and comparison with other models of the International Metastatic Renal-Cell Carcinoma Database Consortium prognostic model: a population-based study. *Lancet Oncol* (2013) 14(2):141–8. doi: 10.1016/S1470-2045(12)70559-4

25. Zhang G, Wu Y, Zhang J, Fang Z, Liu Z, Xu Z, et al. Nomograms for predicting long-term overall survival and disease-specific survival of patients with clear cell renal cell carcinoma. *Onco Targets Ther* (2018) 11:5535–44. doi: 10.2147/OTT.S171881

26. Wang W, Lin X, Yu R, Zhou S, Liu Y, Jia H, et al. Down-regulated *C4orf19* confers poor prognosis in colon adenocarcinoma identified by gene co-expression network. *J Cancer* (2022) 13(4):1145–59. doi: 10.7150/jca.63635

frontiers | Frontiers in Immunology

TYPE Original Research
PUBLISHED 17 January 2024
DOI 10.3389/fimmu.2023.1301945

OPEN ACCESS

EDITED BY
Takaji Matsutani,
Maruho, Japan

REVIEWED BY
Liang-min Fu,
The First Affiliated Hospital of Sun Yat-sen University, China
Shahid Banday,
University of Massachusetts Medical School, United States

*CORRESPONDENCE
Bin Fu
urofbin@163.com
Jianqiang Nie
jianqiang1614@163.com
Xiaoqiang Liu
shaw177@163.com

†These authors have contributed equally to this work and share first authorship

RECEIVED 25 September 2023
ACCEPTED 07 December 2023
PUBLISHED 17 January 2024

CITATION
Yang H, Ma L, Deng W, Fu B, Nie J and Liu X (2024) Prognostic biomarker DARS2 correlated with immune infiltrates in bladder tumor. *Front. Immunol.* 14:1301945. doi: 10.3389/fimmu.2023.1301945

Prognostic biomarker DARS2 correlated with immune infiltrates in bladder tumor

Hailang Yang[1†], Li Ma[2†], Wen Deng[1,3], Bin Fu[1,3*], Jianqiang Nie[1*] and Xiaoqiang Liu[1,3*]

[1]Department of Urology, The First Affiliated Hospital, Jiangxi Medical College, Nanchang University, Nanchang, China, [2]Department of Pathology, The First Affiliated Hospital, Jiangxi Medical College, Nanchang University, Nanchang, China, [3]Jiangxi Institute of Urology, Nanchang, China

Background: DARS2 is a pivotal member of the Aminoacyl-tRNA synthetases family that is critical for regulating protein translation. However, the biological role of DARS2 in bladder cancer remains elusive.

Methods: We analyzed the correlation between DARS2 expression and prognosis, tumor stage, and immune infiltration in bladder cancer using The Cancer Genome Atlas (TCGA) database. We validated findings in clinical samples from The First Affiliated Hospital of Nanchang University and explored the biological functions of DARS2 using cell and animal models.

Results: We found DARS2 to be upregulated in bladder cancer, associated with tumor progression and poor prognosis. Immune infiltration analysis suggested that DARS2 may facilitate immune evasion by modulating PD-L1. Cell and animal experiments validated that DARS2 knockdown and overexpress can inhibit or increase cancer cell proliferation, metastasis, tumorigenesis, immune escape, and PD-L1 levels.

Conclusions: Our study reveals DARS2 as a potential prognostic biomarker and immunotherapy target in BLCA.

KEYWORDS

DARS2, bladder cancer, prognosis, immune infiltration, PD-L1

1 Introduction

Bladder cancer (BLCA) is the most common malignancy of the urinary tract and one of the most prevalent cancers worldwide (1). Globally, it is the ninth most prevalent cancer, and among males, it ranks sixth most common (2). Approximately 70-80% of patients are diagnosed with non-muscle-invasive BLCA at the initial diagnosis. However, up to 20% of patients progress to advanced, high-grade muscle-invasive BLCA, with a 5-year survival rate of less than 50% (3). Despite significant advancements in the treatment of BLCA, including targeted therapies and immunotherapy, the survival rates for BLCA have not shown significant improvement over the past three

decades (4, 5). Therefore, investigating the underlying mechanisms of BLCA development and identifying novel therapeutic targets is of paramount importance for improving patient prognosis.

aminoacyl-tRNA synthetases (ARS) are critical enzymes that catalyze the synthesis of proteins by transferring amino acids onto their corresponding homologous transfer RNAs (tRNAs) (6–8). ARS constitutes an evolutionarily conserved and essential enzyme family responsible for catalyzing the linkage of tRNA with its cognate amino acid, facilitating translation (9).ARS was once considered a family of 'housekeeping' enzymes; however, it is now known that they play diverse roles, including involvement in transcription, translation, splicing, inflammation, angiogenesis, and apoptosis. ARS also serves as regulators and signaling molecules in various immune diseases, infectious diseases, and tumor immunity (9–11).

The gene encoding mitochondrial Aspartyl-tRNA synthetase 2 (DARS2), DARS2 encodes mitochondrial ARS, which specifically catalyzes the aminoacylation of aspartyl-tRNA. Mutations in this gene are associated with leukoencephalopathy with brainstem and spinal cord involvement and lactate elevation, a white matter brain disorder characterized by brainstem and spinal cord involvement and elevated lactate levels (12, 13). DARS2 is a significant member of the ARS family and is implicated in tumorigenesis (14, 15). Sukru's group discovered that the deficiency of DARS2 leads to the activation of various stress responses in a tissue-specific manner. Depletion of DARS2 in the heart and skeletal muscles results in a severe disruption of mitochondrial protein synthesis (14, 15). It has been discovered that HBV inhibits NFAT5 via the miR-30e-5p/mitogen-activated protein kinase signaling pathway upstream of NFAT5. Furthermore, HBV enhances hepatocellular carcinoma tumor development by suppressing NFAT5 through downstream target genes, including DARS2 (16). It reported an upregulation of DARS2 expression in lung adenocarcinoma and highlighted its role in regulating the proliferation, invasion, and apoptosis of lung adenocarcinoma cells. Moreover, DARS2 overexpression was associated with poor prognosis in lung adenocarcinoma (17). However, the biological role of DARS2 in BLCA has not yet been completely researched.

In this study, we investigated the expression levels of DARS2 in BLCA and corresponding adjacent tissues, analyzing the infiltration of immune cells. We further explored the association between DARS2 expression and overall survival. Additionally, we delved into the impact of DARS2 interference on tumor cell proliferation, invasion, migration, and PD-L1 expression. To gain a more comprehensive understanding of its role in tumor immune regulation, we conducted co-culture experiments with DARS2 and Jurkat cells, with further validation through animal experiments. Collectively, all these research findings affirm the potential of DARS2 as a novel prognostic marker guiding BLCA treatment.

2 Methods

2.1 Data source

mRNA expression data and clinical information for BLCA were downloaded from The Cancer Genome Atlas (TCGA) (https://portal.gdc.cancer.gov), while pan-cancer data for DARS2 were obtained from TIMER2 (http://timer.cistrome.org/) (18).To further validate the protein expression of DARS2 in BLCA, we collected surgical specimens of BLCA and normal bladder tissues from six patients during surgery. Additionally, we selected pathological specimens from 37 BLCA samples and 10 normal bladder tissue samples at the First Affiliated Hospital of Nanchang University for immunohistochemistry (IHC) and collected clinical information from these patients. All patient specimens underwent histological diagnosis by two pathologists. This study was approved by the Ethics Committee of the First Affiliated Hospital of Nanchang University, Ethics license number (2022):CDYFYYLK (11–031); CDYFY-IACUC-202308QR018.

2.2 Survival analysis

Patients were stratified into high-expression and low-expression groups based on DARS2 expression levels in the TCGA dataset and IHC expression in specimens collected from the First Affiliated Hospital of Nanchang University. OS (Overall Survival) analysis was performed using the 'survival' and 'survminer' R packages to analyze and visualize survival information for both the TCGA dataset and patients collected from the First Affiliated Hospital of Nanchang University.

2.3 Immunoinfiltration and gene expression correlation analysis

TIMER2 is a comprehensive resource for studying molecular features of tumor-immune interactions across various cancer types (https://cistrome.shinyapps.io/timer/) (18). We utilized TIMER2 to analyze the correlation between DARS2 expression and the infiltration of seven immune cell types, including $CD4^+$T cells, $CD8^+$T cells, B cells, NK (Natural Killer) cells, macrophages, MDSCs (Myeloid-Derived Suppressor Cells), CAFs (Cancer-Associated Fibroblasts), macrophages, and Treg (Regulatory T) cells.

We also analyzed the genes of three immune checkpoints, including PD1 (Programmed Cell Death 1, also known as PDCD1), PD-L1 (Programmed Cell Death 1 Ligand 1, also known as CD274), and CTLA4 (Cytotoxic T-Lymphocyte-Associated Protein 4), using the Genetic correlation module on TIMER2 (adjusted for tumor purity) with statistical methods based on Spearman's rank correlation coefficient. Furthermore, we conducted preliminary validation of DARS2 and PD-L1 expression using five pairs of BLCA tissues.

2.4 Gene set enrichment analysis

Performing Gene Set Enrichment Analysis (GSEA) using gene sets from the MSigDB collection between the high and low DARS2 expression groups (19). Identifying potential signaling pathways regulated by DARS2 using the 'clusterProfiler' package.

2.5 Cell culture and transfection

The human urothelial carcinoma cell lines T24, J82, EJ, and the normal urothelial cell line SV-HUC were obtained from the Cell Bank of the Shanghai Institute of Cell Biology, Chinese Academy of Sciences, China. T24, J82, EJ, and SV-HUC cells were cultured in DMEM, RPMI-1640, and F12K media, respectively, supplemented with 10% fetal bovine serum (FBS, Hyclone) and 100 U/mL penicillin/streptomycin, and were grown at 37°C with 5% CO_2. T24 and EJ cells were seeded in six-well plates at a density of $2x10^5$ cells per well.

2.6 Primers and SiRNA knockdown fragments

DARS2:
Forward Primer: CGAGATGAAGGTTCAAGACCAGA
Reverse Primer: GCCAGGAATACTGGAGCAAACC
β-Actin:
Forward Primer: TCTTCCAGCCTTCCTTCCT
Reverse Primer: AGCACTGTGTTGGCGTACAG
DARS2 SiRNA Interference Fragments:
si-1: GCGTAGTTTCCAAATGCAGTA
si-2: GCCACCTATGGAACTGATAAA
si-3: GCCAACACTATGACTTGGTTT
Lentiviral Interference Fragment (shRNA):
shRNA: GCGTAGTTTCCAAATGCAGTA
Lentiviral Vector: pLV3-U6-MCS-shRNA-EF1a-CopGFP-Puro
Overexpression DARS2:
Forward Primer: TGCTCGCCTTCCTCTTTCAG
Reverse Primer: AGGGAGGCTAAGCGAGGTTT

2.7 Jurkat cell co-culture system

Tumor cells were seeded onto a 12-well plate and allowed to adhere. Following attachment, Jurkat cells, pre-cultured for 24 hours with 1ug/mL PHA and 50ng/mL PMA, were introduced into the upper chamber of a migration apparatus. The semi-permeable membrane of the migration chamber, featuring a pore size of 0.4um, adeptly prevented reciprocal cell transmigration between the upper and lower compartments. Maintaining a proportion of 1:8 for tumor cells to Jurkat cells, a 24-hour co-cultivation ensued, with subsequent collection of culture medium for IL-2(Human IL-2 ELISA Kit EK102, MULTISCIENCES) level assessment through ELISA. Concurrently, CCK-8 reagent was employed to evaluate the cell viability of tumor cells in both the control group (without Jurkat cells group) and the co-culture group. Finally, the co-cultured tumor cells were subjected to crystal violet staining to portray any remaining cells visually.

2.8 Other reagents

DARS2 antibody: Sourced from Wuhan Boster Biotechnology Co., Ltd., Catalog Number A06034-1.GAPDH antibody: Obtained from Wuhan Sanying Biotechnology Co., Ltd., Catalog Number 60004-1-Ig.Ki67 antibody:Obtain from Wuhan Servicebio, GB151142-100. Anti-mouse HRP-conjugated secondary antibody: Supplied by Wuhan Sanying Biotechnology Co., Ltd., Catalog Number KFA025.Anti-rabbit HRP-conjugated secondary antibody: Provided by Wuhan Sanying Biotechnology Co., Ltd., Catalog Number KFA005.PD-L1 antibody: Procured from Wuhan Sanying Biotechnology Co., Ltd., Catalog Number 28076-1-AP.Lipo 2000 transfection reagent: Purchased from Sigma-Aldrich, Massachusetts, USA.PEI transfection reagent: Obtained from Wuhan Sanying Biotechnology Co., Ltd. DAB staining solution: Sourced from Background Soledad Technology Co., Ltd.

2.9 Ethical approval

This study was approved by the Ethics Committee of the First Affiliated Hospital of Nanchang University, Ethics license number (2022):CDYFYYLK (11–031); CDYFY- IACUC-202308QR018.

3 Results

3.1 Upregulation of DARS2 expression in BLCA

We analyzed TCGA data to investigate the expression of DARS2 in tumor and normal tissues. Our findings revealed that DARS2 expression was significantly higher than that in normal tissues across 25 types of tumors, such as BLCA, BRCA, CESC,etc (Figure 1A). Furthermore, our analysis of TCGA data demonstrated a significant upregulation of DARS2 expression in BLCA ($P<0.001$, Figure 1B). Additionally, analysis of paired mRNA expression data from TCGA showed a significant increase in DARS2 expression in tumor tissues ($P<0.001$, Figure 1C).

Subsequently, qPCR was performed to validate the mRNA expression levels of DARS2 in BLCA using paired samples from five patients. The results showed an increase in DARS2 mRNA expression in four pairs of cancer tissues compared to adjacent normal tissues (Figure 1D). Protein immunoblotting results further demonstrated elevated expression of DARS2 in both cancer cell lines and tumor tissues (Figures 1E, F). We employed Ki67 to assess the malignancy level of ten pairs of bladder cancer tissues, because a higher proportion of Ki67-positive cells correlates with increased malignancy. Immunohistochemical (IHC) analysis of the ten pairs of bladder cancer tissues indicated a heightened expression of DARS2 in bladder cancer compared to normal bladder mucosal epithelial tissues ($P<0.05$, Figures 1G, H). Additionally, we observed that high-grade bladder cancer exhibited elevated levels of DARS2 expression compared to low-grade bladder cancer. This trend was consistent with the Ki67 staining results, where high-grade bladder cancer showed a higher proportion of Ki67-positive cells compared to the low-grade counterpart.

Subsequently, patients were grouped based on clinical characteristics to determine the correlation between DARS2

10.3389/fimmu.2023.1301945

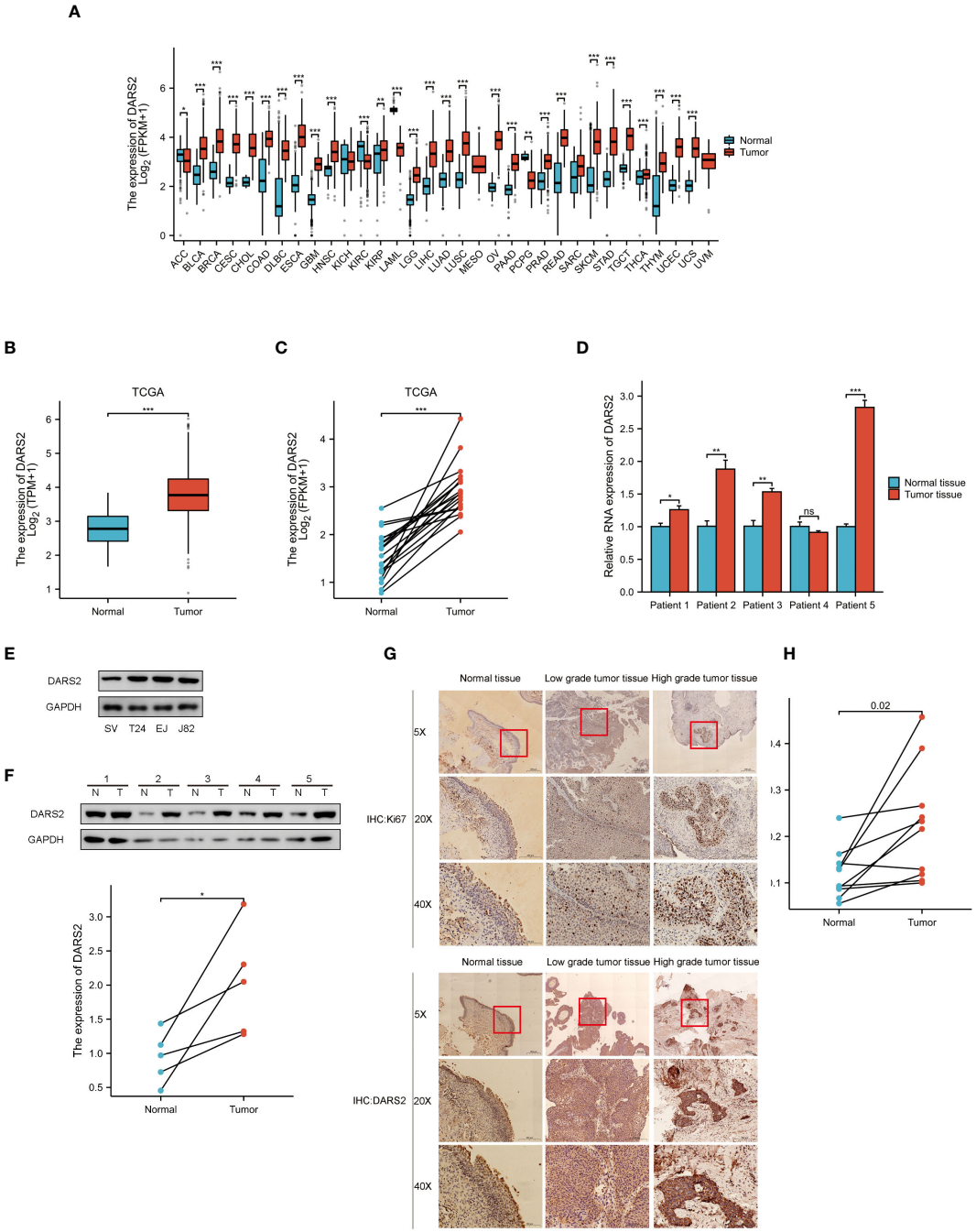

FIGURE 1
DARS2 Expression in BLCA. **(A)** DARS2 Pan-Cancer Analysis. **(B)** TCGA Analysis of DARS2 Expression in BLCA. **(C)** The expression of DARS2 in paired bladder cancer in TCGA. **(D)** qPCR analysis of DARS2 expression in 5 pairs of bladder cancer tissues. **(E)** Expression of DARS2 in bladder cancer cells and normal urothelial cells by western blot. **(F)** Western blot analysis of DARS2 expression in 5 pairs of bladder cancer tissues. **(G)** Immunohistochemistry of DARS2 and Ki67 in bladder cancer tissues. **(H)** Immunohistochemical analysis of DARS2 in 10 pairs of bladder cancer tissues. *P<0.05, **P<0.01, ***P<0.001. ns, no statistical difference.

expression levels and clinical features. TCGA analysis results revealed significant differences in higher DARS2 expression across histological grade ($P < 0.001$), pathological stage ($P < 0.05$), T stage ($P < 0.05$), and M stage ($P < 0.01$) (Supplementary Table 1). Furthermore, to further confirm the relationship between clinical features of tumors and DARS2 protein expression, we conducted clinical baseline data analysis based on the results of IHC analysis in 37 patient samples. The patients were divided into high and low DARS2 expression groups based on the median DARS2 expression. The analysis showed significant differences in higher DARS2 expression concerning N stage ($P < 0.05$), M stage ($P < 0.05$), and histological grade ($P < 0.05$) (Supplementary Table 2). Notably, the results for M stage and histological grade from IHC analysis were consistent with the TCGA results.

In summary, these findings suggest that DARS2 expression is upregulated in BLCA at both the transcriptional and translational levels.

3.2 DARS2 as an independent prognostic factor in BLCA

To determine the prognostic value of DARS2 in BLCA, we divided patients in the TCGA dataset into DARS2 low-expression and DARS2 high-expression groups based on the median DARS2 expression for survival analysis. High DARS2 expression was associated with poorer overall survival (OS) in BLCA (HR = 1.48, P < 0.01) (Figure 2A).

To further validate the prognostic role of DARS2, we analyzed follow-up data from collected patients. Based on IHC analysis results, patients were categorized into high-expression and low-expression groups. The analysis revealed that patients in the high-expression group had worse OS (HR = 3.02, P < 0.01) (Figure 2B).

Next, we performed univariate and multivariate Cox regression analyses on clinical data from TCGA to determine the correlation between overall survival in BLCA and multiple factors. Univariate analysis showed that six clinical features, including T3 stage (HR = 1.970, P < 0.001), T4 stage (HR = 2.987, P < 0.001), N stage (HR = 2.250, P < 0.001), M stage (HR = 3.112, P < 0.005), age >70 (HR = 1.424, P < 0.05), and DARS2 expression (HR = 1.480, P < 0.005), were significantly associated with patient overall survival (Supplementary Table 3; Figure 2C). Multivariate analysis data revealed that DARS2 expression (HR = 1.953, P = 0.022) is an independent prognostic factor (Supplementary Table 3).

3.3 Identification and enrichment analysis of differentially expressed genes

Through gene differential analysis, a total of 466 genes were identified as differentially expressed genes (DEGs) between the high DARS2 group and the low DARS2 group (Figure 3A). To identify signaling pathways regulated by abnormal DARS2 expression, we compared the DARS2 high-expression and low-expression groups using a signature gene set based on the TCGA dataset.

The analysis results indicated the top five upregulated pathways as follows: Formation of the cornified envelope; WP retinoblastoma gene in cancer; G2 mDNA damage checkpoint; Processing of DNA double-strand break ends; Meiosis (Figure 3B)

Conversely, the top five downregulated pathways were identified as Initial triggering of complement; Complement cascade; Scavenging of heme from plasma; Creation of C4 and C2 activators; and CD22 mediated by regulation (Figure 3C)

These findings provide insights into the potential pathways and processes influenced by DARS2 dysregulation in BLCA, offering valuable information for further mechanistic investigations and therapeutic targeting.

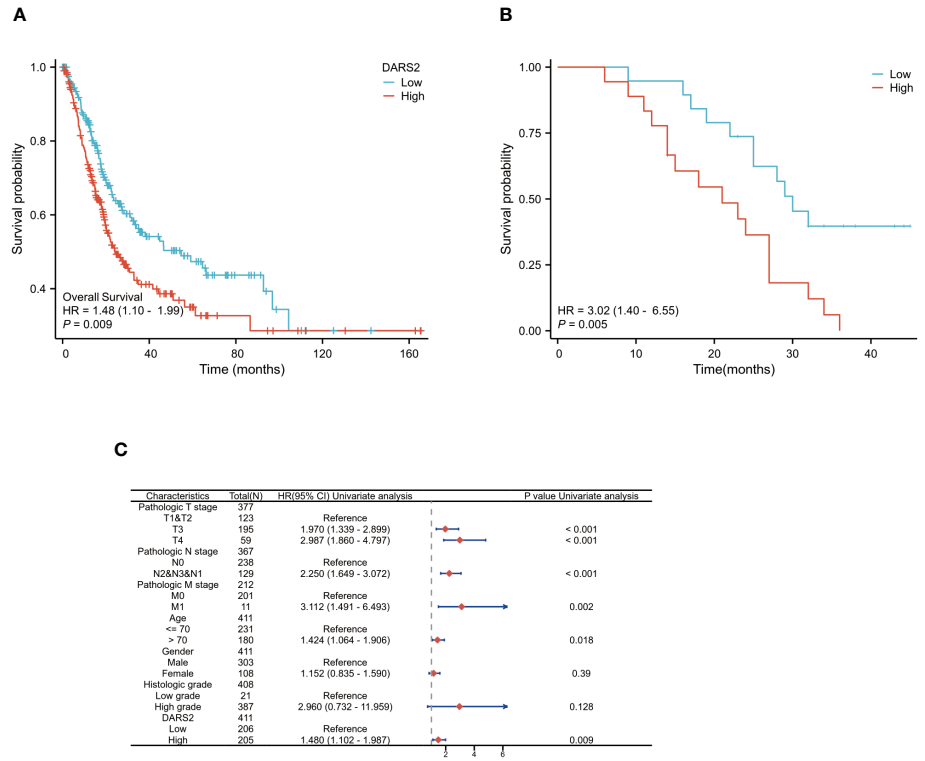

FIGURE 2
DARS2 as an Independent Prognostic Factor in BLCA. **(A)** Kaplan-Meier analysis of OS in the TCGA BLCA. **(B)** Kaplan-Meier analysis of OS in the 37 cases of BLCA immunohistochemistry. **(C)** DARS2 expression distribution and survival status.

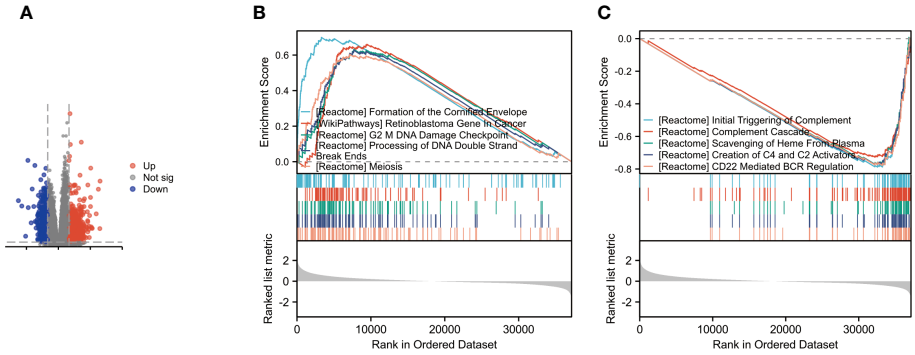

FIGURE 3
Identification and Enrichment Analysis of Differentially Expressed Genes. **(A)** Volcano plot for differentially expressed genes between high and low expression of DARS2 in BLCA patients. **(B)** GSEA revealed the top five are positively correlated. **(C)** GSEA revealed the top five are poorly correlated.

3.4 DARS2 regulates bladder cancer cell proliferation, migration, and invasion

The above results indicate that DARS2 is upregulated in BLCA, suggesting its crucial role in BLCA tumorigenesis. Therefore, we used siRNA to knock down DARS2 expression (Figure 4A) to observe its biological effects on T24 and EJ cells. We chose Si-1 and Si-2 for cell experiments. We assessed the impact of DARS2 on cell proliferation using CCK8 and EDU assays. Our results showed that knocking down DARS2 inhibited cell proliferation (Figures 4B, C). Furthermore, we found that migration and invasion abilities were reduced in T24 and EJ cells with reduced DARS2 expression (Figure 4D).

In addition, we conducted an overexpression experiment of DARS2 in bladder cancer cells and assessed relevant indicators. Our research revealed that the overexpression of DARS2 significantly promotes cell proliferation, invasion, and migration, in stark contrast to the experimental results of DARS2 knockdown (Supplementary Figures 1A-D).

In summary, these results indicate that DARS2 can affect cell proliferation, migration, and invasion.

3.5 DARS2 expression correlates with immune infiltration and PD-L1 expression

Our analysis using TIMER2 showed that DARS2 expression was negatively correlated with immune-active cells, including $CD4^+$ T cells (R= -0.251, P < 0.001) and NK cells (R= -0.067, P < 0.001). Conversely, DARS2 expression was positively correlated with immunosuppressive cells, such as MDSCs (R= 0.372, P < 0.001) and macrophages (R= 0.196, P < 0.01). Interestingly, DARS2 expression was positively correlated with $CD8^+$T cells (R= 0.203, P < 0.001) (Supplementary Figure 2A).

It is known that blocking immune checkpoint receptors such as PD-1/PD-L1 and CTLA-4 can alleviate $CD8^+$T cell exhaustion and reactivate immune cell cytotoxicity to eliminate antigen-expressing tumor cells (20). Therefore, we analyzed the correlation between DARS2 expression and the expression of PD-1, PD-L1 (CD274), and CTLA-4 using TIMER2. We found that DARS2 expression was positively correlated with PD-L1 expression (R= 0.202, P < 0.001), but showed no significant correlation with PD-1 and CTLA-4 (Supplementary Figure 2B).

To validate the expression patterns of DARS2 and PD-L1, we conducted protein immunoblotting on five pairs of clinical samples derived from patients. The results revealed elevated expression of both DARS2 and PD-L1 in cancer tissues compared to adjacent non-cancerous tissues across all five sample sets. Furthermore, correlation analysis of the results from 10 samples demonstrated a positive association between the expression levels of DARS2 and PD-L1 (Figure 5K).

Subsequently, we performed knockdown and overexpression experiments targeting DARS2. Following interference or overexpression of DARS2, we observed a corresponding downregulation or upregulation of PD-L1 expression, respectively (Figures 5A, B). In response to these findings, we designed co-culture experiments to investigate the impact of cellular immunity of DARS2 on PD-L1 expression.

We established a co-culture model. We induced Jurkat cell activation with 50ng/mL PMA and 10ug/mL PHA for 24 hours, resulting in increased IL-2 levels post-activation (Figure 5C). Subsequently, using a 12-well plate, we co-cultured cells, either solely Jurkat cells or Jurkat cells in a 1:5 ratio with tumor cells, for 24 hours. Previous research has indicated that high PD-L1 expression can inhibit the function of Jurkat cells, leading to a reduction in IL-2 expression (21).Consistent with the mentioned study, we observed a decrease in IL-2 levels in the co-culture medium containing tumor cells (Figure 5D).

We then conducted co-cultures after knockdown and overexpression of DARS2, maintaining conditions consistent with the explored co-culture settings. Notably, the knockdown of DARS2 resulted in an increase in IL-2 levels in the co-culture medium, while overexpression led to a decrease in IL-2 levels (Figures 5E, G).

Finally, we investigated the activity of residual tumor cells after co-culture. In the co-culture setting, we observed lower activity in tumor cells of the DARS2 knockdown group compared to the control group. Conversely, overexpression of DARS2 resulted in heightened activity of tumor cells in the co-culture (Figures 5F, H).

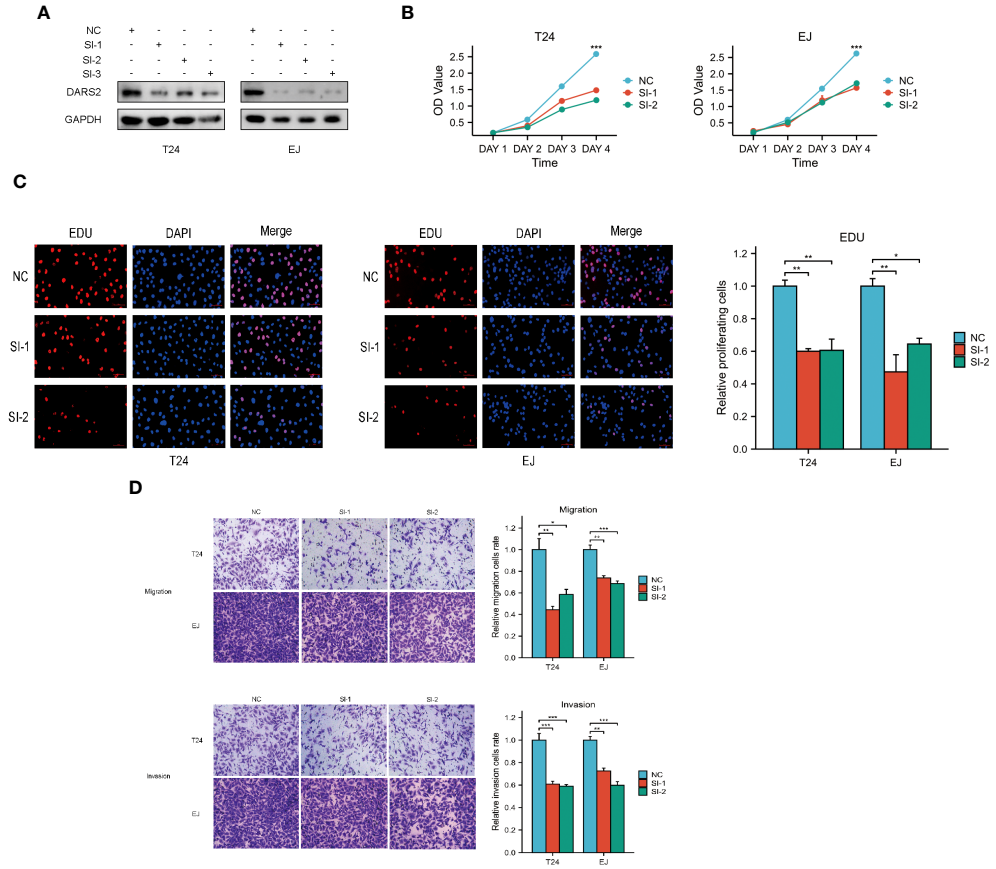

FIGURE 4
DARS2 Regulates Bladder Cancer Cell Proliferation, Migration, and Invasion. **(A)** DARS2 knockdown in T24 and EJ cells. **(B, C)** The impact of DARS2 on proliferation in T24 and EJ cells via CCK8, EDU. **(D)** The impact of DARS2 on migration and invasion in T24 and EJ cells. *P<0.05, **P<0.01, ***P<0.001.

Crystal violet staining of residual live cells post-co-culture aligned with the observed cell viability patterns (Figures 5I, J).

This indicates that in the immune microenvironment, elevated expression of DARS2 can lead to a reduction in the cytotoxicity of Jurkat cells against tumor cells. Conversely, lower expression of DARS2 results in increased susceptibility of tumor cells to Jurkat cell-mediated cytotoxicity. PD-L1 plays a crucial role in the cytotoxic process of Jurkat cells against tumor cells. Moreover, DARS2 has the ability to influence the expression of PD-L1.

Therefore, DARS2 expression plays a significant role in immune infiltration and may serve as a potential biomarker for immune therapy response in BLCA patients.

3.6 Knockdown of DARS2 inhibits tumor formation in nude mice

In order to further study the impact of DARS2 on bladder cancer, we used T24 cells to conduct tumorigenesis experiments in nude mice.we found that T24 cells with DARS2 knockdown formed smaller subcutaneous tumors in nude mice compared to the NC group in animal experiments (Figures 6A, B). IHC images of tumor tissues showed a decrease in both DARS2, cell proliferation markers Ki67 and the immune marker PD -L1 after DARS2 knockdown (Figure 6C). The above experiments show that DARS2 can affect the proliferation and tumor formation of bladder cancer.

4 Discussion

BLCA remains one of the most common malignancies of the urinary tract and one of the most prevalent cancers globally (1, 2). Approximately 70-80% of patients are diagnosed with non-muscle-invasive BLCA initially, but up to 20% progress to high-grade, high-stage muscle-invasive BLCA, with a 5-year survival rate of less than 50% (3, 22). Despite the significant advances in BLCA treatment, such as targeted therapies and immunotherapies, the survival rates for BLCA have not significantly improved (1, 23). Therefore, it is crucial to explore novel biomarkers for BLCA.

DARS2 is responsible for producing the enzyme that ensures the correct translation of the genetic code by attaching amino acids to their corresponding tRNA molecules in the mitochondria (9, 11, 24). Liu and colleagues discovered that DARS2 can serve as a prognostic marker for non-adenocarcinomas and promote the proliferation, invasion, and migration of lung adenocarcinoma cells while inhibiting cell apoptosis (17, 25, 26). It suggests that

10.3389/fimmu.2023.1301945

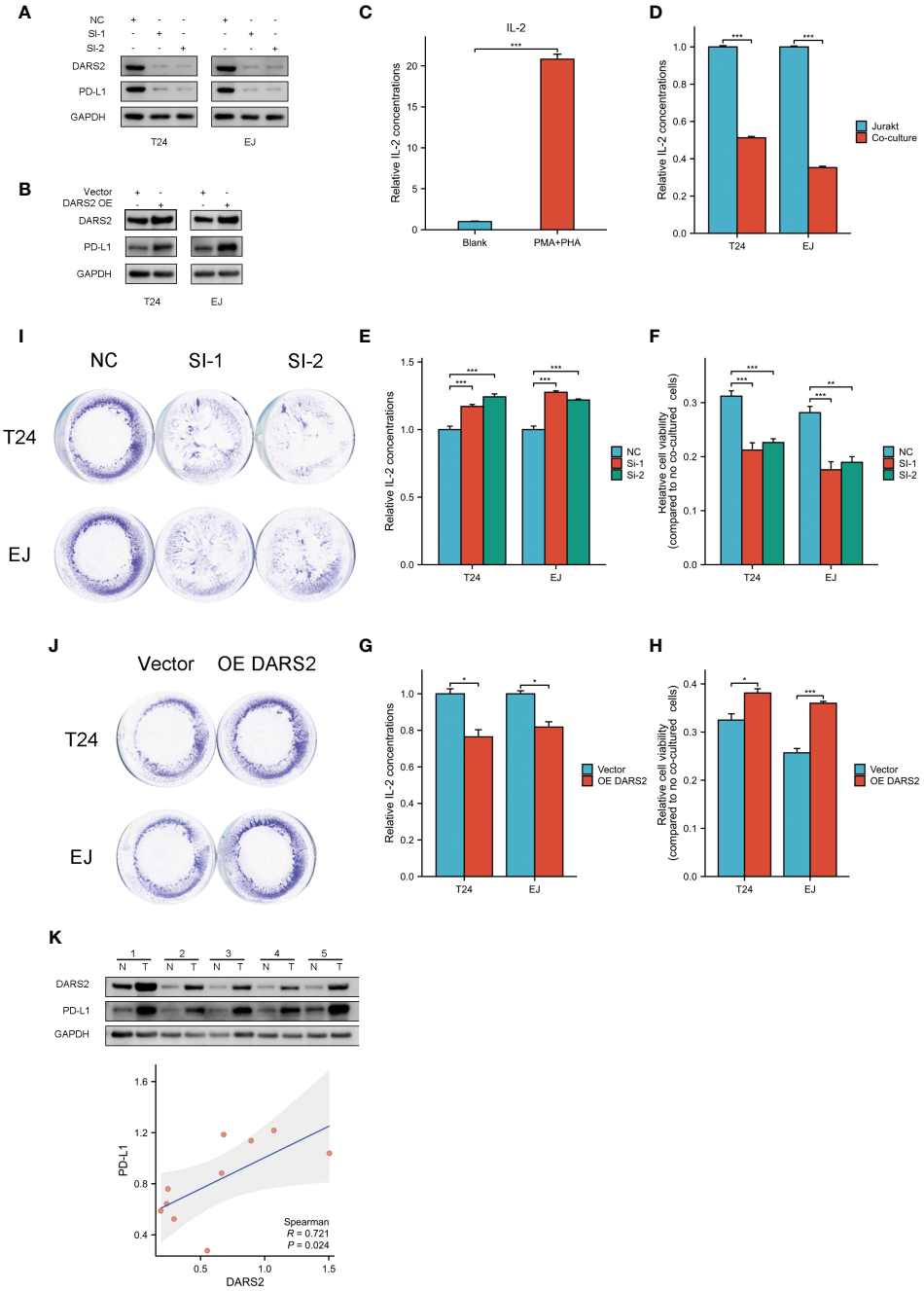

FIGURE 5
Bladder cancer cells and Jurkat cells co-cultured. **(A, B)** PD-L1 changes after interference and overexpression of DARS2. **(C)** Relative concentration of IL-2 in culture medium after activation of jurkat cells by PMA and PHA. **(D)** Relative concentration of IL-2 in the culture medium after co-culture of activated Jurkat cells and untreated bladder cancer cells. **(E, G)** Relative concentration of IL-2 in the co-culture system after knocking down and overexpressing DRAS2. **(F, H)** Viability of residual surviving tumor cells in co-culture system after knockdown and overexpression of DRAS2 **(I, J)** Crystal violet staining of remaining surviving tumor cells in the co-culture system after knocking down and overexpressing DRAS2. **(K)** Expression of DARS2 and PD-L1 in bladder cancer cells and normal urothelial cells by western blot and analysis of the correlation between shigeDARS2 and PD-L1. *P<0.05, **P<0.01, ***P<0.001.

DARS2 may be proposed as a new biomarker to distinguish between multiple myeloma and lung adenocarcinoma (27). It has been found that DARS2 is an oncogene in hepatocellular carcinoma and can promote the progression of the hepatocellular carcinoma cell cycle while inhibiting apoptosis in HCC cells (16, 17). Although Wu's team discovered that DARS2 can predict overall survival in BLCA and serve as a predictive model for assessing clinical outcomes (28). However, there have been no reported studies on the biological role of DARS2 in BLCA.

Our research findings indicate that patients with high DARS2 expression have a poorer prognosis. In terms of biological function, interfering with DARS2 expression can inhibit the proliferation, invasion, and migration of BLCA, while overexpression of DARS2 has been demonstrated to promote the malignant progression of tumors.

10.3389/fimmu.2023.1301945

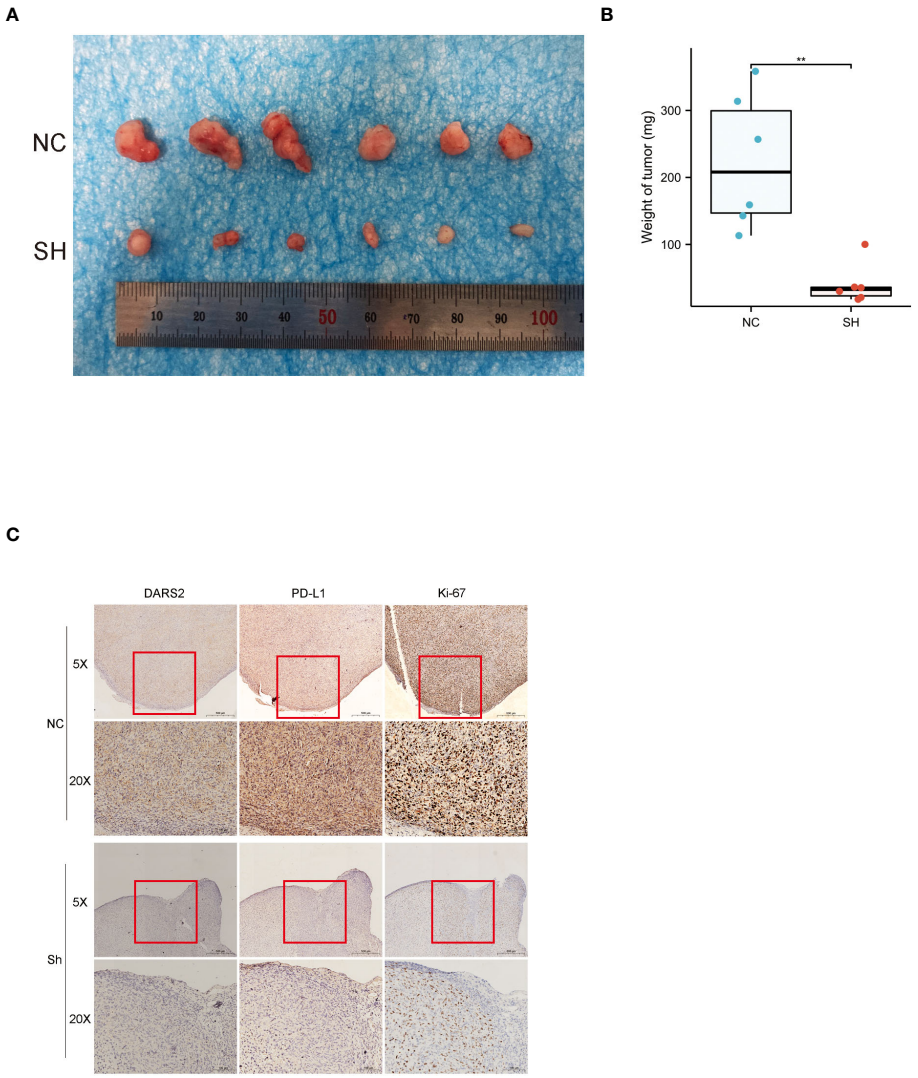

FIGURE 6
(A, B) subcutaneous tumor formation in nude mice. **(C)** Immunohistochemical staining of DARS2, PD-L1 and Ki67 in subcutaneous tumor samples from nude mice. *P<0.05, **P<0.01, ***P<0.001.

Our investigation into PD-L1 reveals that both the downregulation and upregulation of DARS2 may result in a corresponding decrease or increase in PD-L1 expression. Recent research has unveiled that knocking down DARS2 leads to a diminished expression of p-ERK1/2, while DARS2 overexpression prompts an elevation in p-ERK1/2 levels (29). Previous studies have substantiated the role of the ERK-MAPK pathway in modulating PD-L1 expression across diverse cell types, where the regulation of p-ERK1/2 expression can intricately impact PD-L1 levels (30–34). Drawing from these insights, we posit that DARS2 likely modulates PD-L1 expression through the regulation of p-ERK1/2.

In addition, our immune infiltration analysis indicates a positive correlation between the expression of DARS2 and CD8+ T cells. In the context of immunotherapy, CD8+ T cells play a pivotal role, secreting cytokines such as IFN-γ, TNF-α, and IL-2 to exert cytotoxic effects on tumor cells (35). In studies of bladder cancer prognostic markers, Wang found that CLIC1, as a prognostic marker, showed a negative correlation with CD8+ T cells. Patients with low CLIC1 expression exhibited increased infiltration of CD8+ T cells, correlating with a better prognosis (36). However, our study revealed that in patients with high DARS2 expression, there is an increased infiltration of CD8+ T cells, but paradoxically, a worse prognosis. Further classification of CD8+ T cells identified precursor-exhausted and terminally exhausted subtypes (37, 38). Precursor-exhausted CD8+ T cells typically lack effector molecules for tumor cell cytotoxicity, while terminally exhausted cells release cytokines for tumor killing but express high levels of immune checkpoints such as PD-1 (39). In contrast to Wang's findings (36), we speculate that the upregulation of PD-L1 induced by high DARS2 expression may weaken the cytotoxicity of CD8+ T cells against tumor cells. Our experiments, involving DARS2 knockdown and overexpression, confirm concurrent upregulation or downregulation of PD-L1 with DARS2. Additionally, DARS2 knockdown led to a smaller decrease in IL-2 secretion by Jurkat cells in the co-culture system compared to the control group. IL-2 is a critical factor for T cell

proliferation, survival, and immune function, while the binding of PD-L1/PD-1 induces CD8+ T cell apoptosis and loss of anti-tumor function (40–42). Therefore, highly infiltrated CD8+ T cells may not fully exert their cytotoxic effects in tumors due to the high expression of PD-L1 on the surface of tumor cells. Moreover, we observed that tumor cells with high DARS2 expression exhibit enhanced relative activity, while the knockdown group showed the opposite, further confirming the stronger immunosuppressive effect of tumor cells with high DARS2 expression.

On the other hand, we found a positive correlation between DARS2 expression and macrophage infiltration. Tumor-associated macrophages (TAMs) are immune cells in the tumor microenvironment expressing various immune checkpoints influencing immune function. TAMs can be classified into M1 and M2 types, with M1 playing a crucial role in innate immunity, while M2 is considered to have a protective effect on tumors (43). Multiple studies suggest that PD-L1 induces the conversion of M1 macrophages to the M2 phenotype, promoting tumor occurrence and development (44–47). The correlation between high DARS2 expression and PD-L1 may induce the conversion of macrophages to the M2 type, thereby weakening the immune cell's cytotoxicity against tumors. In summary, high DARS2 expression may promote tumor development by altering the immune microenvironment of BLCA. Given DARS2's impact on PD-L1 expression, it could potentially serve as a novel predictive indicator for immune therapy responses.

This study yielded several key findings. Firstly, we confirmed and validated the association of upregulated DARS2 expression with poor prognosis in BLCA. Secondly, we delved into the impact of DARS2 on the biological functions of bladder cancer cells, establishing a connection between DARS2 expression and an immunosuppressive tumor microenvironment, including its correlation with PD-L1 expression. This was further corroborated by our co-culture system, demonstrating the influence of DARS2 on the cytotoxicity of immune cells. Lastly, we conducted *in vivo* experiments to validate the impact of DARS2 knockdown on tumor formation. However, our study has some limitations. In one part, the sample size is relatively small, and the correlation between DARS2 and PD-L1 expression needs further validation in larger clinical cohorts. Another part, how DARS2 regulates the relationship between tumors and the immune microenvironment is not yet clear. In-depth investigations into these mechanisms may pave the way for novel immune therapy strategies, such as combining DARS2 inhibitors with immune checkpoint inhibitors to improve the prognosis of BLCA patients.

Data availability statement

The original contributions presented in the study are included in the article/Supplementary Material. Further inquiries can be directed to the corresponding authors.

Ethics statement

The studies involving humans were approved by the First Affiliated Hospital of Nanchang University. The studies were conducted in accordance with the local legislation and institutional requirements. The participants provided their written informed consent to participate in this study. The animal study was approved by the First Affiliated Hospital of Nanchang University. The study was conducted in accordance with the local legislation and institutional requirements.

Author contributions

YH: Writing – original draft, Writing – review & editing. LM: Writing – review & editing. NJ: Writing – review & editing. WD: Writing – review & editing. XL: Writing – review & editing. BF: Writing – review & editing.

Funding

The author(s) declare financial support was received for the research, authorship, and/or publication of this article. This study was supported by the National Natural Science Foundation of P.R. China (Grant Nos 8 1560419, 81960512, 82260511).

Acknowledgments

The authors sincerely thank all participants involved in this study.

Conflict of interest

The authors declare that the research was conducted in the absence of any commercial or financial relationships that could be construed as a potential conflict of interest.

Publisher's note

Supplementary material

The Supplementary Material for this article can be found online at: https://www.frontiersin.org/articles/10.3389/fimmu.2023.1301945/full#supplementary-material

References

1. Dobruch J, Oszczudłowski M. Bladder cancer: current challenges and future directions. *Medicina (Kaunas Lithuania)* (2021) 57(8). doi: 10.3390/medicina57080749

2. Sung H, Ferlay J, Siegel RL, Laversanne M, Soerjomataram I, Jemal A, et al. Global cancer statistics 2020: globocan estimates of incidence and mortality worldwide for 36 cancers in 185 countries. *CA: Cancer J Clin* (2021) 71(3):209–49. doi: 10.3322/caac.21660

3. Kohada Y, Hayashi T, Hsi RS, Yukihiro K, Sentani K, Goto K, et al. Recurrence- and progression-free survival in intermediate-risk non-muscle-invasive bladder cancer: the impact of conditional evaluation and subclassification. *BJU Int* (2021) 127(4):473–85. doi: 10.1111/bju.15209

4. Berdik C. Unlocking bladder cancer. *Nature* (2017) 551(7679):S34–S5. doi: 10.1038/551S34a

5. Hu J, Chen J, Ou Z, Chen H, Liu Z, Chen M, et al. Neoadjuvant immunotherapy, chemotherapy, and combination therapy in muscle-invasive bladder cancer: A multi-center real-world retrospective study. *Cell Rep Med* (2022) 3(11):100785. doi: 10.1016/j.xcrm.2022.100785

6. Lee SW, Cho BH, Park SG, Kim S. Aminoacyl-trna synthetase complexes: beyond translation. *J Cell Sci* (2004) 117:3725–34. doi: 10.1242/jcs.01342

7. Onuora S. Aminoacyl-trna synthetases function as alarmins in ra. *Nat Rev Rheumatol* (2023) 19(9):538. doi: 10.1038/s41584-023-01020-5

8. Yu YC, Han JM, Kim S. Aminoacyl-trna synthetases and amino acid signaling. *Biochim Biophys Acta (BBA) - Mol Cell Res* (2021) 1868(1):118889. doi: 10.1016/j.bbamcr.2020.118889

9. Nie A, Sun B, Fu Z, Yu D. Roles of aminoacyl-trna synthetases in immune regulation and immune diseases. *Cell Death Dis* (2019) 10(12):901. doi: 10.1038/s41419-019-2145-5

10. Park SG, Ewalt KL, Kim S. Functional expansion of aminoacyl-trna synthetases and their interacting factors: new perspectives on housekeepers. *Trends Biochem Sci* (2005) 30(10):569–74. doi: 10.1016/j.tibs.2005.08.004

11. Jafarnejad SM, Kim SH, Sonenberg N. Aminoacylation of proteins: new targets for the old arsenal. *Cell Metab* (2018) 27(1):1–3. doi: 10.1016/j.cmet.2017.12.012

12. Köhler C, Heyer C, Hoffjan S, Stemmler S, Lücke T, Thiels C, et al. Early-onset leukoencephalopathy due to a homozygous missense mutation in the dars2 gene. *Mol Cell Probes* (2015) 29(5):319–22. doi: 10.1016/j.mcp.2015.06.005

13. Martikainen MH, Ellfolk U, Majamaa K. Impaired information-processing speed and working memory in leukoencephalopathy with brainstem and spinal cord involvement and elevated lactate (Lbsl) and dars2 mutations: A report of three adult patients. *J Neurol* (2013) 260(8):2078–83. doi: 10.1007/s00415-013-6940-0

14. Lee EY, Kim S, Kim MH. Aminoacyl-trna synthetases, therapeutic targets for infectious diseases. *Biochem Pharmacol* (2018) 154:424–34. doi: 10.1016/j.bcp.2018.06.009

15. Zhou Z, Sun B, Nie A, Yu D, Bian M. Roles of aminoacyl-trna synthetases in cancer. *Front Cell Dev Biol* (2020) 8:599765. doi: 10.3389/fcell.2020.599765

16. Qin X, Li C, Guo T, Chen J, Wang HT, Wang YT, et al. Upregulation of dars2 by hbv promotes hepatocarcinogenesis through the mir-30e-5p/mapk/nfat5 pathway. *J Exp Clin Cancer Res CR* (2017) 36(1):148. doi: 10.1186/s13046-017-0618-x

17. Jiang Y, You J, Wu C, Kang Y, Chen F, Chen L, et al. High expression of dars2 indicates poor prognosis in lung adenocarcinoma. *J Clin Lab Anal* (2022) 36(10):e24691. doi: 10.1002/jcla.24691

18. Li T, Fu J, Zeng Z, Cohen D, Li J, Chen Q, et al. Timer2.0 for analysis of tumor-infiltrating immune cells. *Nucleic Acids Res* (2020) 48(W1):W509–w14. doi: 10.1093/nar/gkaa407

19. Subramanian A, Tamayo P, Mootha VK, Mukherjee S, Ebert BL, Gillette MA, et al. Gene set enrichment analysis: A knowledge-based approach for interpreting genome-wide expression profiles. *Proc Natl Acad Sci United States America* (2005) 102(43):15545–50. doi: 10.1073/pnas.0506580102

20. Farhood B, Najafi M, Mortezaee K. Cd8(+) cytotoxic T lymphocytes in cancer immunotherapy: A review. *J Cell Physiol* (2019) 234(6):8509–21. doi: 10.1002/jcp.27782

21. Rong W, Wan N, Zheng X, Shi G, Jiang C, Pan K, et al. Chrysin inhibits hepatocellular carcinoma progression through suppressing programmed death ligand 1 expression. *Phytomedicine* (2022) 95:153867. doi: 10.1016/j.phymed.2021.153867

22. Wallerand H, Bernhard JC, Culine S, Ballanger P, Robert G, Reiter RE, et al. Targeted therapies in non-muscle-invasive bladder cancer according to the signaling pathways. *Urologic Oncol* (2011) 29(1):4–11. doi: 10.1016/j.urolonc.2009.07.025

23. Pond GR, Agarwal A, Ornstein M, Garcia J, Gupta R, Grivas P, et al. Clinical outcomes of platinum-ineligible patients with advanced urothelial carcinoma treated with first-line pd1/L1 inhibitors. *Clin genitourinary Cancer* (2021) 19(5):425–33. doi: 10.1016/j.clgc.2021.04.008

24. Sacks D, Baxter B, Campbell BCV, Carpenter JS, Cognard C, Dippel D, et al. Multisociety consensus quality improvement revised consensus statement for endovascular therapy of acute ischemic stroke. *Int J* (2018) 13(6):612–32. doi: 10.1177/1747493018778713

25. Zhang X, Dong W, Zhang J, Liu W, Yin J, Shi D, et al. A novel mitochondrial-related nuclear gene signature predicts overall survival of lung adenocarcinoma patients. *Front Cell Dev Biol* (2021) 9:740487. doi: 10.3389/fcell.2021.740487

26. Liu XS, Zeng J, Zhang YH, Zhang Y, Gao Y, Liu C, et al. Dars2 is a prognostic biomarker and correlated with immune infiltrates and cuproptosis in lung adenocarcinoma. *Am J Cancer Res* (2023) 13(3):818–34.

27. Ucer O, Kocaman N. New candidates in the differential diagnosis of Malignant mesothelioma from benign mesothelial hyperplasia and adenocarcinoma; dars2 and suprabasin. *Tissue Cell* (2022) 79:101920. doi: 10.1016/j.tice.2022.101920

28. Wu Y, Liu Z, Wei X, Feng H, Hu B, Liu B, et al. Identification of the functions and prognostic values of rna binding proteins in bladder cancer. *Front Genet* (2021) 12:574196. doi: 10.3389/fgene.2021.574196

29. Fang T, Jiang J, Yu W, Li R, Tian H. Dars2 promotes the occurrence of lung adenocarcinoma *via* the erk/C-myc signaling pathway. *Thorac Cancer* (2023). doi: 10.1111/1759-7714.15152

30. Jiang X, Zhou J, Giobbie-Hurder A, Wargo J, Hodi FS. The activation of mapk in melanoma cells resistant to braf inhibition promotes pd-L1 expression that is reversible by mek and pi3k inhibition. *Clin Cancer Res* (2013) 19(3):598–609. doi: 10.1158/1078-0432.Ccr-12-2731

31. Qian Y, Deng J, Geng L, Xie H, Jiang G, Zhou L, et al. Tlr4 signaling induces B7-H1 expression through mapk pathways in bladder cancer cells. *Cancer Invest* (2008) 26(8):816–21. doi: 10.1080/07357900801941852

32. Jalali S, Price-Troska T, Bothun C, Villasboas J, Kim HJ, Yang ZZ, et al. Reverse signaling *via* pd-L1 supports Malignant cell growth and survival in classical hodgkin lymphoma. *Blood Cancer J* (2019) 9(3):22. doi: 10.1038/s41408-019-0185-9

33. Zerdes I, Matikas A, Bergh J, Rassidakis GZ, Foukakis T. Genetic, transcriptional and post-translational regulation of the programmed death protein ligand 1 in cancer: biology and clinical correlations. *Oncogene* (2018) 37(34):4639–61. doi: 10.1038/s41388-018-0303-3

34. Han Y, Liu D, Li L. Pd-1/pd-L1 pathway: current researches in cancer. *Am J Cancer Res* (2020) 10(3):727–42.

35. McLane LM, Abdel-Hakeem MS, Wherry EJ. Cd8 T cell exhaustion during chronic viral infection and cancer. *Annu Rev Immunol* (2019) 37:457–95. doi: 10.1146/annurev-immunol-041015-055318

36. Wang W, Huang G, Lin H, Ren L, Fu L, Mao X. Label-free lc-ms/ms proteomics analyses reveal clic1 as a predictive biomarker for bladder cancer staging and prognosis. *Front Oncol* (2022) 12:1102392. doi: 10.3389/fonc.2022.1102392

37. Yu A, Hu J, Fu L, Huang G, Deng D, Zhang M, et al. Bladder cancer intrinsic lrfn2 drives anticancer immunotherapy resistance by attenuating cd8(+) T cell infiltration and functional transition. *J immunotherapy Cancer* (2023) 11(10). doi: 10.1136/jitc-2023-007230

38. Siddiqui I, Schaeuble K, Chennupati V, Fuertes Marraco SA, Calderon-Copete S, Pais Ferreira D, et al. Intratumoral tcf1(+)Pd-1(+)Cd8(+) T cells with stem-like properties promote tumor control in response to vaccination and checkpoint blockade immunotherapy. *Immunity* (2019) 50(1):195–211.e10. doi: 10.1016/j.immuni.2018.12.021

39. Kallies A, Zehn D, Utzschneider DT. Precursor exhausted T cells: key to successful immunotherapy? *Nat Rev Immunol* (2020) 20(2):128–36. doi: 10.1038/s41577-019-0223-7

40. Niederlova V, Tsyklauri O, Kovar M, Stepanek O. Il-2-driven cd8(+) T cell phenotypes: implications for immunotherapy. *Trends Immunol* (2023) 44(11):890–901. doi: 10.1016/j.it.2023.09.003

41. Zhang P, Wang Y, Miao Q, Chen Y. The therapeutic potential of pd-1/pd-L1 pathway on immune-related diseases: based on the innate and adaptive immune components. *Biomedicine pharmacotherapy = Biomedecine pharmacotherapie* (2023) 167:115569. doi: 10.1016/j.biopha.2023.115569

42. Chen M, Bie L, Ying J. Cancer cell-intrinsic pd-1: its role in Malignant progression and immunotherapy. *Biomedicine pharmacotherapy = Biomedecine pharmacotherapie* (2023) 167:115514. doi: 10.1016/j.biopha.2023.115514

43. Yunna C, Mengru H, Lei W, Weidong C. Macrophage M1/M2 polarization. *Eur J Pharmacol* (2020) 877:173090. doi: 10.1016/j.ejphar.2020.173090

44. Mantovani A, Sozzani S, Locati M, Allavena P, Sica A. Macrophage polarization: tumor-associated macrophages as a paradigm for polarized M2 mononuclear phagocytes. *Trends Immunol* (2002) 23(11):549–55. doi: 10.1016/s1471-4906(02)02302-5

45. Wei Y, Liang M, Xiong L, Su N, Gao X, Jiang Z. Pd-L1 induces macrophage polarization toward the M2 phenotype *via* erk/akt/mtor. *Exp Cell Res* (2021) 402(2):112575. doi: 10.1016/j.yexcr.2021.112575

46. Pang X, Wang SS, Zhang M, Jiang J, Fan HY, Wu JS, et al. Oscc cell-secreted exosomal cmtm6 induced M2-like macrophages polarization *via* erk1/2 signaling pathway. *Cancer immunology immunotherapy CII* (2021) 70(4):1015–29. doi: 10.1007/s00262-020-02741-2

47. Hartley GP, Chow L, Ammons DT, Wheat WH, Dow SW. Programmed cell death ligand 1 (Pd-L1) signaling regulates macrophage proliferation and activation. *Cancer Immunol Res* (2018) 6(10):1260–73. doi: 10.1158/2326-6066.Cir-17-0537

frontiers | Frontiers in Immunology

TYPE Original Research
PUBLISHED 19 January 2024
DOI 10.3389/fimmu.2024.1291938

OPEN ACCESS

EDITED BY
Takaji Matsutani,
Maruho, Japan

REVIEWED BY
Chi-Ming Li,
Amgen, United States
Pingping Chen,
University of Miami, United States

*CORRESPONDENCE
Kefeng Ding
dingkefeng@zju.edu.cn
Yang Tang
tyx90@zju.edu.cn

†These authors have contributed equally to this work

RECEIVED 10 September 2023
ACCEPTED 04 January 2024
PUBLISHED 19 January 2024

CITATION
Wei J, Ge X, Qian Y, Jiang K, Chen X, Lu W, Yang H, Fu D, Fang Y, Zhou X, Xiao Q, Tang Y and Ding K (2024) Development and verification of a combined immune- and cancer-associated fibroblast related prognostic signature for colon adenocarcinoma.
Front. Immunol. 15:1291938.
doi: 10.3389/fimmu.2024.1291938

Development and verification of a combined immune- and cancer-associated fibroblast related prognostic signature for colon adenocarcinoma

Jingsun Wei[1,2,3†], Xiaoxu Ge[1,2,3†], Yucheng Qian[1,2,3], Kai Jiang[1,2,3], Xin Chen[1,2,3], Wei Lu[1,2,3], Hang Yang[1,2,3], Dongliang Fu[1,2,3], Yimin Fang[1,2,3], Xinyi Zhou[1,2,3], Qian Xiao[1,2,3], Yang Tang[1,2,3*] and Kefeng Ding[1,2,3*]

[1]Department of Colorectal Surgery and Oncology (Key Laboratory of Cancer Prevention and Intervention, China National Ministry of Education, Key Laboratory of Molecular Biology in Medical Sciences), The Second Affiliated Hospital, Zhejiang University School of Medicine, Hangzhou, Zhejiang, China, [2]Department of Colorectal Surgery and Oncology, Zhejiang Provincial Clinical Research Center for Cancer, Hangzhou, Zhejiang, China, [3]Department of Colorectal Surgery and Oncology, Cancer Center of Zhejiang University, Hangzhou, Zhejiang, China

Introduction: To better understand the role of immune escape and cancer-associated fibroblasts (CAFs) in colon adenocarcinoma (COAD), an integrative analysis of the tumor microenvironment was performed using a set of 12 immune- and CAF-related genes (ICRGs).

Methods: Univariate and least absolute shrinkage and selection operator (LASSO) Cox regression analyses were used to establish a prognostic signature based on the expression of these 12 genes (*S1PR5*, *AEN*, *IL20RB*, *FGF9*, *OSBPL1A*, *HSF4*, *PCAT6*, *FABP4*, *KIF15*, *ZNF792*, *CD1B* and *GLP2R*). This signature was validated in both internal and external cohorts and was found to have a higher C-index than previous COAD signatures, confirming its robustness and reliability. To make use of this signature in clinical settings, a nomogram incorporating ICRG signatures and key clinical parameters, such as age and T stage, was developed. Finally, the role of S1PR5 in the immune response of COAD was validated through in vitro cytotoxicity experiments.

Results: The developed nomogram exhibited slightly improved predictive accuracy compared to the ICRG signature alone, as indicated by the areas under the receiver operating characteristic curves (AUC, nomogram:0.838; ICRGs:0.807). The study also evaluated the relationships between risk scores (RS) based on the expression of the ICRGs and other key immunotherapy variables, including immune checkpoint expression, immunophenoscore (IPS), and microsatellite instability (MSI). Integration of these variables led to more precise prediction of treatment efficacy, enabling personalized immunotherapy for COAD patients. Knocking down S1PR5 can enhance the efficacy of PD-1 monoclonal antibody, promoting the cytotoxicity of T cells against HCT116 cells ((p<0.05).

Discussion: These findings indicate that the ICRG signature may be a valuable tool for predicting prognostic risk, evaluating the efficacy of immunotherapy, and tailoring personalized treatment options for patients with COAD.

KEYWORDS

immune, CAF, prognosis, colon adenocarcinoma, TME

Introduction

Colorectal cancer (CRC) is one of the most common malignant tumors worldwide, with China and the United States ranking second and fourth, respectively, in incidence and fifth and second, respectively, in mortality (1). In 2020, it was estimated that over 1.9 million patients would be newly diagnosed with CRC, including anal cancer, resulting in approximately 935,000 deaths, accounting for roughly 10% of both newly diagnosed cancers and cancer deaths worldwide (2). CRC is mainly treated with surgery, radiation and chemotherapy, although immune checkpoint inhibitors have played an increasingly important role in its recent treatment. The KEYNOTE-177 clinical study indicated that pembrolizumab should be the standard first-line treatment for patients with microsatellite instability-high or mismatch repair-deficient (MSI-H/dMMR) metastatic CRC (mCRC) (3). Only 13% of CRC patients, however, are MSI-H, with the remaining CRC patients being insensitive to immunotherapy (4). These differences in treatment outcomes may be attributed primarily to the heterogeneity and complexity within the tumor microenvironment (TME) (5). A prognostic signature specific to the TME of CRC patients may therefore aid in the effective delivery of immunotherapy.

The TME consists mainly of blood vessels, cancer-associated fibroblasts (CAFs), the extracellular matrix (ECM), and tumor-infiltrating immune cells (6). CAFs in the TME have several critical functions, including remodeling of the extracellular matrix (ECM), engaging in reciprocal signaling interactions with cancer cells and communicating with infiltrating leukocytes (7). Both the CAFs and tumor-infiltrating immune cells in the TME are indispensable in regulating the occurrence and development of tumors. CAFs can secrete a variety of cytokines and regulate immune cells through a variety of pathways. Signals from other cells within the TME can also influence CAF function. For example, activation of T cells can induce their production of interferon-gamma (IFNγ), a cytokine that can stimulate CAFs to increase the expression of programmed death-ligand 1 (PD-L1), with PD-L1 subsequently inhibiting the activity of T cells (8).

Prognostic predictive signatures based solely on immune-related genes have been developed. For example, a prognostic signature based on immune-related genes was found to predict survival in CRC patients and may reflect the state of the TME (9). In addition, a prognostic signature was designed based on subsets of CAFs in CRC and their interactions with nonspecific immune cells (10). These findings indicate the importance of investigating the prognostic implications of interactions between the immune system and CAFs.

The present study utilized RNA sequencing to assess differential gene expression of CAFs stimulated with activated peripheral blood mononuclear cells (aPBMCs) in patients with colorectal adenocarcinoma (COAD). Immune- and CAF-related gene signatures in COAD were subjected to systematic and comprehensive integrative analyses, with the prognostic value of these signatures were analyzed. A prognostic nomogram was developed to provide a quantitative analytic tool for predicting prognostic risk in patients with COAD.

Materials and methods

Data acquisition

Gene expression levels and clinical information of 476 patients with COAD patients and 41 normal individuals were obtained from the Cancer Genome Atlas (TCGA) database (https://portal.gdc.cancer.gov/). In addition, gene expression levels and clinical information of 566 patients with COAD were obtained from the GSE39582 dataset in the Gene Expression Omnibus (GEO) database (https://www.ncbi.nlm.nih.gov/geo/). The latter patients were randomly allocated into two groups, a training group (70%) and a testing group (30%). The testing group in the TCGA-COAD cohort and the GEO cohort were used as internal validation sets. Immune-related genes were obtained from the ImmPort database (https://www.immport.org) (11). CAFs were stimulated by aPBMCs, and changes in expression of CAF genes were determined by RNA sequencing.

Preparation of primary cancer-associated fibroblasts

CRC tumor tissue samples were collected from three patients of the Second Affiliated Hospital of Zhejiang University, School of Medicine. CRC tissue samples were obtained from fresh, surgically

resected samples and transferred to the laboratory in phosphate-buffered saline (PBS; Gibco, Carlsbad, CA) containing 10% povidone iodine within 30 min. The tissue samples were rinsed three times in PBS containing 500 U/mL streptomycin and penicillin, minced with surgical scissors into 2–4 mm^3 pieces and plated in 60 mm-culture plates in RPMI 1640 containing 10% fetal bovine serum (FBS; Gibco, Brazil), 100 U/mL streptomycin and penicillin and 2.5 μg/mL amphotericin B. To ensure adherence to the culture plate, the tissue specimens were not submerged in culture medium. The tissue samples were cultured at 37°C in an atmosphere containing 5% CO2, with the culture medium changed every 3–4 days. One to three weeks after plating, the proliferating fibroblasts could be observed near the minced tissue. The primary CAFs were subsequently passaged and the remaining tissues were discarded. The study protocol was approved by the ethical review board of our institution (Approval number 2022-1130), and all patients provided written informed consent for tumor resection.

Preparation of peripheral blood mononuclear cells

Withdraw 6 ml of peripheral blood from one healthy individual, placed it in an anticoagulant tube with Ethylene Diamine Tetraacetic Acid (EDTA), and gently mixed by rocking it back and forth to prevent blood coagulation. The blood samples were collected from the Second Affiliated Hospital of Zhejiang University, School of Medicine. Fresh anticoagulant-treated blood samples were diluted 1:1 with PBS, with each sample layered onto 3 mL of Ficoll-Paque plus solution (Sigma). After centrifugation at 400 g for 15 min, the lymphocyte layer was collected and washed in PBS. Erythrocytes were eliminated with red blood cell lysis buffer, and the cells were again washed in PBS. The samples were centrifuged, and the pellets, consisting of peripheral blood mononuclear cells (PBMCs), were resuspended in RPMI1640 supplemented with 10% FBS and 1% penicillin/streptomycin and incubated overnight in a Petri dish to allow monocyte adherence. The following day, the cells in suspension were transferred to a second culture bottle. PBMCs were activated by incubation with anti-CD3/anti-CD28 dynabeads (Thermofisher, US) for 24 hours, yielding preparations of aPBMCs.

Co-culture of CAFs and aPBMCs

PBMCs in DMEM were prepared as described above. Following centrifugation and resuspension, a 20 μl aliquot was transferred to cell counting plate (Counter Star Company) and counted with a cell counter (Counter Star Company). The PBMCs were diluted to a concentration of 150,000 cells/100 μl, with a 100 μl aliquot of diluted PBMCs transferred to each well of a 96-well plate. A suitable volume of anti-CD3/anti-CD28 Dynabeads (Gibco, Human) was washed with a magnet stand, followed by removal of the supernatant, resuspension in DMEM culture medium, and addition of a 3 μl aliquot of suspended Dynabeads to each well of the 96-well plate containing PBMCs. The experimental group co-cultured CAFs and aPBMCs in a 6-well plate for 24 hours. 2 x 10^5 aPBMCs were placed in the upper transwell chamber (6-well plate chamber, 0.4μm pore size), with 2 x 10^5 CAFs in the lower chamber. The control group co-cultured unactivated PBMCs with CAFs for 24 hours. The experiment was conducted with 3 biological replicates.Subsequently, samples from both groups of CAFs were collected for RNA sequencing to detect the expression level of differential genes. And the P-value<0.05 and |log2 (fold change) > 1| were considered as CAF-related differentially expressed genes (CRGs).

Clustering of non-negative matrix factorization

Non-negative matrix factorization (NMF) is a matrix factorization technique used to divide a matrix into two non-negative matrices. DEGs in tumor and normal samples were screened out based on a |log2 (fold change) > 1| and a false discovery rate (FDR) < 0.05. DEGs correlating with prognosis were screened out by univariate COX regression analysis, and the COAD samples were classified based on the expression of prognostic relevant genes using the "NMF" package. The number of clusters K was set in the range of 2 to 10.

Development of the combined immune- and CAF related prognostic signature

Prognostic genes in the TCGA training cohort were identified by univariate Cox regression analysis, followed by least absolute shrinkage and selection operator (LASSO) Cox regression analysis using the "glmnet" package. Based on the median risk score (RS), the training cohort was divided into two groups, a low-risk and a high-risk group. The results obtained from the TCGA training cohort were subsequently validated in the TCGA test cohort and the GEO cohort. After the construction of the ICRG prognostic signature, the resulting RS was combined with the clinicopathological information obtained from patient records, and a prognostic nomogram predicting outcomes in patients with COAD was constructed. The predictive ability of the nomogram was assessed by determining survival risks. The calibration curves were drawn using the "rms" package.

Evaluation of the responses to immunotherapy

Comprehensive immunogenomic data were obtained from the Cancer Immunome Database (TCIA) (https://tcia.at/home). The relationships between ICRG signatures and predicted responses to treatment were analyzed based on four immune checkpoints: PD1, PD-L1,PD-L2 and CTLA4.In addition, the association between ICRG signatures and MSI was assessed to determine the efficacy of immunotherapy.

T cell cytotoxicity assay

The plates were incubated for 48 hours to obtain aPBMCs, the anti-CD3/anti-CD28 Dynabeads were removed magnetically, and the cells were resuspended in DMEM containing IL-2 (10 ng/ml) for another 5 days. This process can cool aPBMC to prevent non-specific killing. HCT116 cells were transfected with negative control short interfering RNA (si-NC) or si-S1PR5 for 48 hours and plated at 10,000 cells per well in 96-well plates. The siRNA sequences are as follows (5'→3'): si-NC: UUCUCCGAACGUGUCACGUTT;si-S1PR5-1:CCGCUAUCUGUGCACUCUA(dT)(dT); si-S1PR5-2: CAUCGUGCUAGAGAAUCUA(dT)(dT).The next day, 40,000 aPBMCs and anti-PD1 monoclonal antibody (4 μg/ml) were added as appropriate to each well. Killed HCT116 cells were measured after 48-72 hours, with the results verified by microscopy and crystal violet staining.

ELISA assay for IFNγ expression

After co-culturing PBMCs with HCT116, the supernatant was collected and centrifuged to remove the cells. The Human IFNγ ELISA kit (Code: EK0373, Boster, China) was used to detect the expression of IFNγ in the supernatant. The supernatant was added to each well of the enzyme-labeled plate in 100ul aliquots. The plate was then covered with a sealing membrane and incubated at 37°C for 90 minutes. After the liquid was removed from the enzyme-labeled plate, the working solution of biotinylated anti-human IFNG antibody (excluding the TMB blank colorimetric wells) was added, and the plate was sealed for another 90 minutes at 37°C. Following a wash, 100ul of ABC working solution was added to each well (excluding the TMB blank colorimetric wells), and the plate was sealed for 30 minutes at 37°C. After the wash, 90ul of TMB color development solution was added to each well and incubated at 37°C in the dark for 25 minutes. Subsequently, 100ul of stop solution was added to each well. The OD value at 450nm was measured using an enzyme immunoassay analyzer, with the TMB blank colorimetric well set as the control.

Statistical analysis

Univariate and multivariate Cox hazard regression analyses were performed using the "survival" package of R software. Pearson correlation analysis was performed using the "corrplot" package of R software. Differences between two groups were evaluated using the Wilcoxon test, and receiver operator characteristic (ROC) curves and areas under the curve (AUC) analyzed using the "timeROC" package in R sofware. Survival outcomes were determined by the Kaplan-Meier method and compared by log-rank tests. All statistical analyses were performed using R software (version 4.2.1), with P-values <0.05 considered statistically significant.

Results

Classification of COAD subtypes according to the NMF algorithm

CAFs and aPBMCs were co-cultured for 24 hours, and gene expression levels in CAFs were measured by RNA-sequence analysis. A total of 2013 CRGs were identified, and 2483 immune-related genes (IRGs) were obtained from https://www.immport.org/ (Supplementary Table 1). These CRGs and IRGs were combined, with 3415 ICRGs screened during follow-up. Analysis of the levels of expression of these ICRGs in normal and colon cancer samples from the TCGA database, resulted in the selection of 1095 significantly DEGs with FDR<0.05 and |log2 (fold change) > 1|. The NFM algorithm was applied to these 1095 DEGs to identify three molecular subtypes (Figure 1A). The appropriate rank values were determined by analyzing the cophenetic, silhouette, and dispersion metrics (Supplementary Figures 1, 2), with a heatmap showing the expression of genes in the different clusters (Figure 1B). Kaplan–Meier analysis showed that overall survival (OS) (P=0.05) and progression free survival (PFS) (P=0.002) were significantly lower in Cluster 2 than in Clusters 1 and 3 (Figures 1C, D). Evaluation of the status of the TME showed that immune cell infiltration and stromal infiltration were significantly higher in Cluster 1 than in Clusters 2 and 3 (P<0.001) (Figure 1E). Furthermore, analysis of the infiltration of 10 types of immune cells showed that immune cell infiltration was highest in Cluster 1 and lowest in Cluster 2 (Figure 1F). The higher level of immune cell infiltration in Cluster 1 may indicate that this cluster was associated with a stronger immune response than the other clusters. A heatmap showed that the infiltration of endothelial cells, fibroblasts, myeloid dendritic cells and cells of the monocytic lineage was higher in Cluster 1 than in the other two clusters (Figure 1G).

Construction of an ICRG prognostic signature by LASSO Cox regression analysis

The TCGA-COAD cohort was randomly split into two subgroups, a training cohort (70%) and a testing cohort (30%), which showed no significant differences in clinical characteristics (Supplementary Table 2). Based on the above results, we performed univariate analysis on 1905 significantly different ICRGs and selected 47 prognostic-related ICRGs, followed by application of the LASSO-Cox regression algorithm to the selected ICRGs in the TCGA training cohort. Based on coefficients of independent variables and optimal log values of lambda in LASSO regression analysis, 23 genes were identified (Figures 2A, B). Risk scores (RS) were subsequently calculated by multivariate Cox regression analysis, resulting in an ICRG signature based on 12 genes (*SIPR5, AEN, IL20RB, FGF9, OSBPL1A, HSF4, PCAT6, FABP4, KIF15, ZNF792, CD1B* and *GLP2R*) (Figure 2C), along with their corresponding coefficients (Supplementary Table 3).

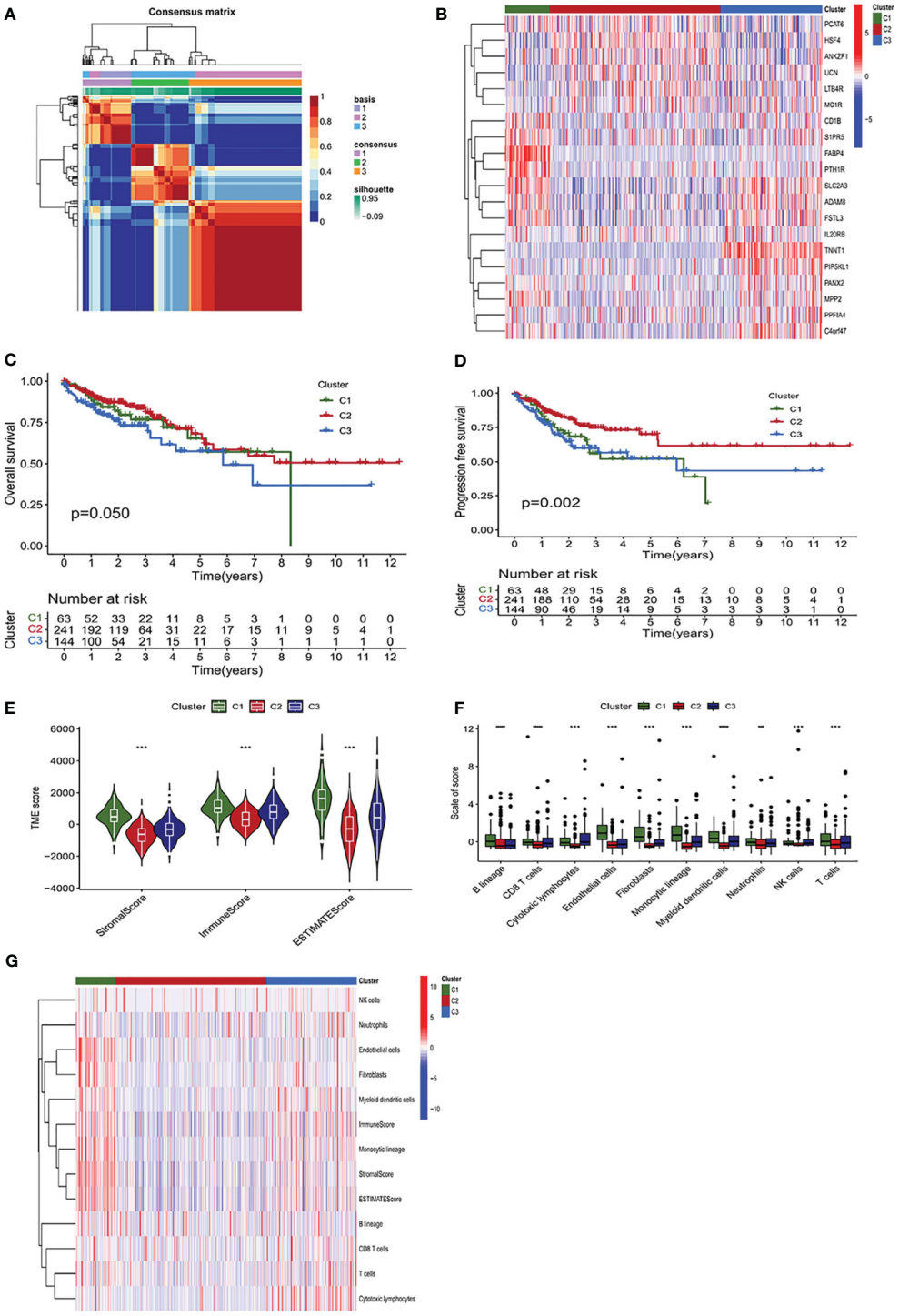

FIGURE 1
Identification of molecular subtypes of colon adenocarcinoma (COAD) using a non-negative matrix factorization (NMF) algorithm. **(A)** Heatmap of an NMF consensus matrix of K = 3. **(B)** Unsupervised clustering of the immune- and CAF-related genes (ICRGs) expression profiles of the three clusters. The heatmap displayed the expression levels of ICRG within the three clusters based on NMF classification. **(C, D)** Analysis of the differences in survival among the three clusters based on the NMF algorithm. Kaplan–Meier analysis of the **(C)** overall survival (OS) and **(D)** progression-free survival (PFS) of patients with the three subtypes of COAD. **(E)** Comparison of the TME scores of the three subtypes using the estimate algorithm. The TME scores were divided into stromalscore, immunescore, and estimatescore, with cluster 2 having the lowest scores, showing significant discrepancies (P<0.001). **(F)** Comparison of MCP counter algorithm-derived immune scores of the three subtypes. The bar chart showed the infiltration levels of immune cells in the tumor immune microenvironment of three subgroups. **(G)** Immune scores of immune cells for ESTIMATE and MCP counter algorithms displayed on the heatmap. P < 0.05, **P < 0.01, ***P <0.001, ****P<0.0001.

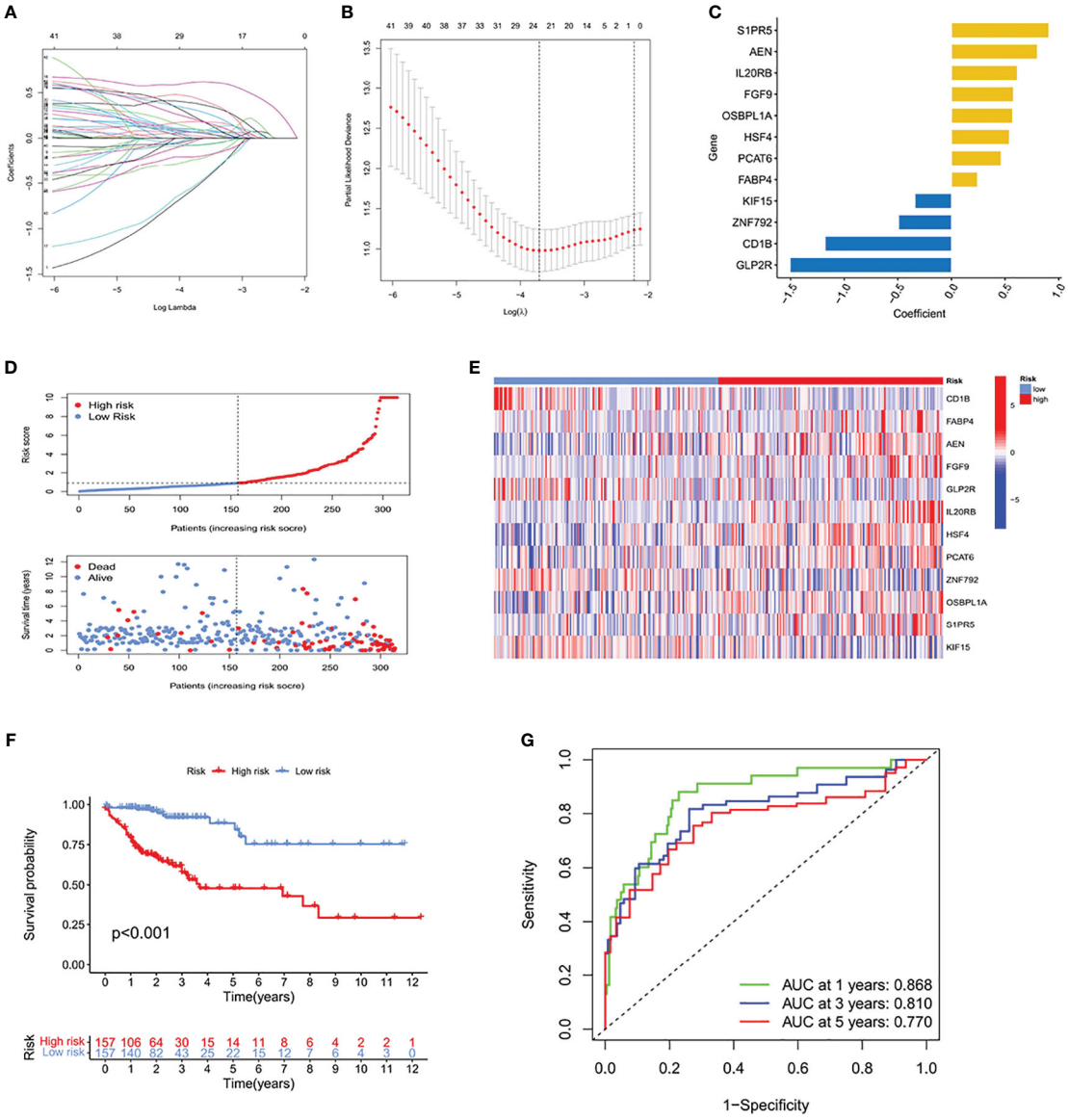

FIGURE 2
Determination of a prognostic signature for ICRGs by LASSO Cox regression analysis of the TCGA training cohort. **(A)** Determination of the coefficients of independent variables by LASSO Cox regression analysis. **(B)** Calculation of the optimal lambda value, as indicated by the first black dotted line from the left on the logarithmic scale. **(C)** Bar chart showing the correlation coefficients of each gene that constituted the ICRG prediction signature. **(D)** Distribution of risk score (RS) and survival status according to the ICRG prediction signature. **(E)** Heat map depicting the gene expression profiles of the ICRGs included in high-risk and low-risk groups based on the prognostic signature. **(F)** Kaplan-Meier analysis comparing survival rates in the high-risk and low-risk groups, which were classified based on the median RS. The prognosis of patients in the high-risk group was significantly lower than that of the low-risk group, with statistical significance (P<0.001). **(G)** ROC curves showing the predictive accuracy of the ICRG prognostic signature at 1, 3, and 5 years.

Based on the median RS, the TCGA training cohort was divided into two groups, those with high RS and low RS, to predict the prognosis of patients with COAD. A risk plot was generated to show played the distribution of RSs and their relationship to survival outcomes and a heatmap showed the levels of expression levels of risk genes in the high and low RS groups (Figures 2D, E, Supplementary Table 4). Kaplan–Meier analysis showed that patient prognosis was significantly lower in the high than in the low RS group (P<0.001) (Figure 2F). Analysis of the areas under the curve (AUCs) of the ICRG risk model showed that the 1-, 3, and 5-year AUCs were 0.868, 0.810 and 0.770, respectively (Figure 2G). These results showed that this prognostic model based on ICRGs had good predictive performance in patients with COAD.

Validation of the ICRG prognostic signature

To further evaluate the predictive value of this ICRG risk model, it was used to analyze the TCGA testing cohort and TCGA-COAD

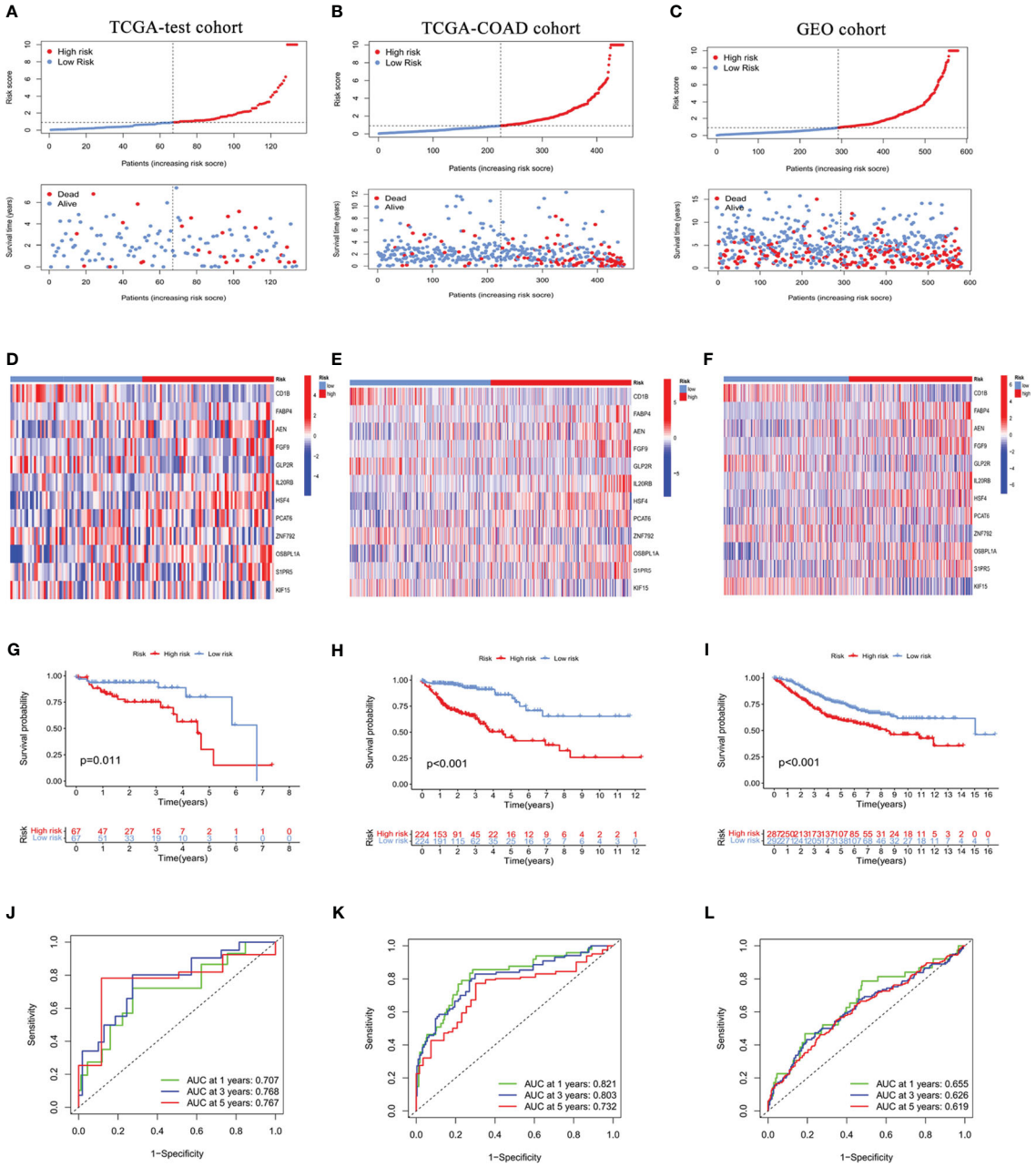

FIGURE 3
Internal and external validation of the prognostic value of the ICRG signature in the TCGA testing cohort **(A, D, G, J)**, the entire TCGA-COAD cohort **(B, E, H, K)**, and the GEO cohort **(C, F, I, L)**. **(A-C)** Distribution of risk scores (RS) and survival status in the internal and external cohorts. **(D-F)** Heat maps showing the gene expression profiles of the ICRGs in high-risk and low-risk groups. **(G-I)** Kaplan-Meier analysis comparing the survival rates in the high-risk and low-risk groups based on ICRG signature. **(J-L)** ROC curves showing the predictive accuracy of the IMRG prognostic signature at 1, 3, and 5 years.

cohort for internal validation and the GEO cohort for external validation. Each of these cohorts was divided into two groups, those with high and low RS. The relationships between the distribution of risk groups and patient survival status are shown in Figures 3A–C, with a heatmap showing the expression of ICRGs in this risk model (Figures 3D–F). Kaplan-Meier analysis of survival in the testing cohorts was also performed to validate the prognostic value of this ICGR risk model. Patient prognoses were significantly higher in the low than in the high RS groups in the TCGA testing cohort (P=0.011), the TCGA-COAD cohort (P<0.001) and the GEO cohort (P<0.001) (Figures 3G–I). Moreover, the 1-year AUCs of the risk model in the TCGA testing cohort, the TCGA-COAD

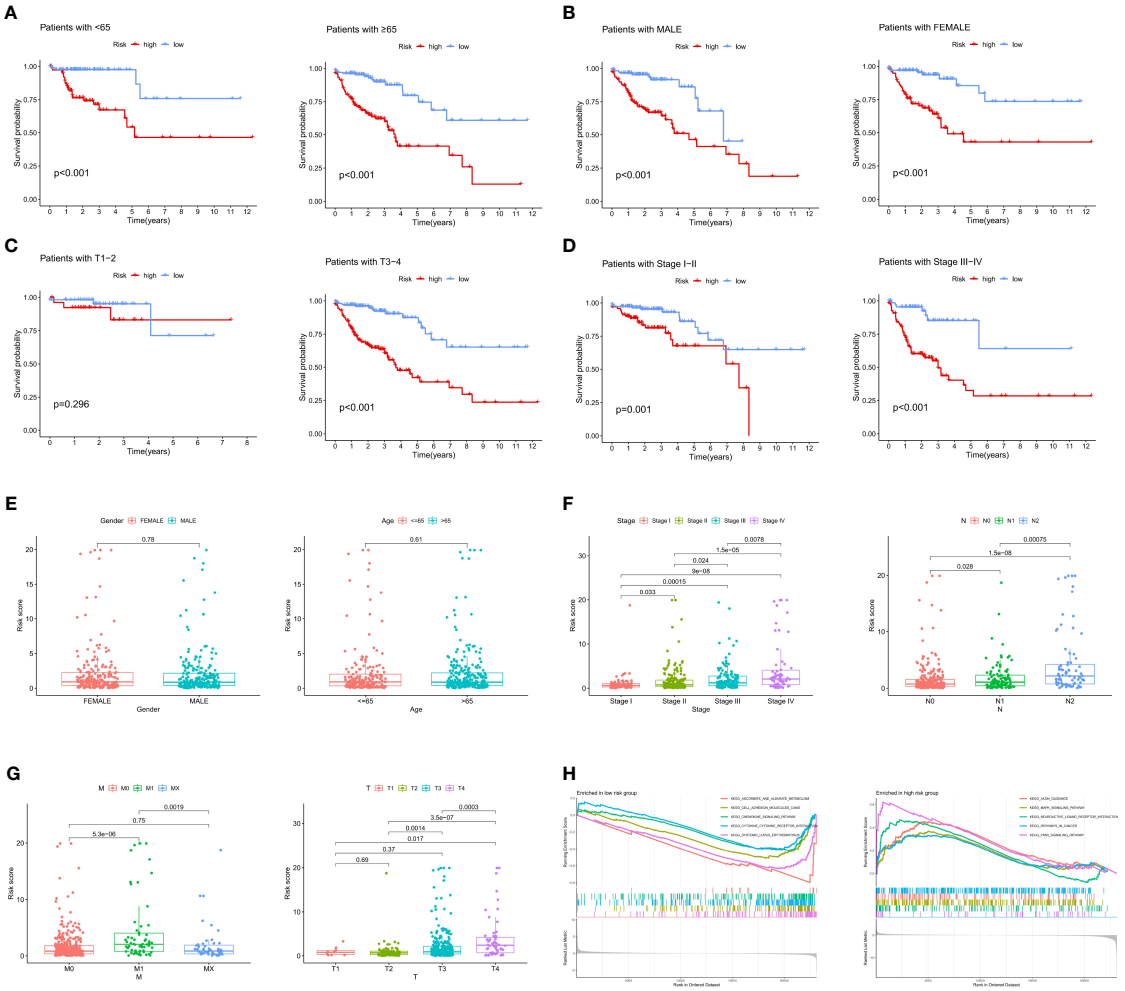

FIGURE 4
Correlations between the ICRG prognostic signature and clinical features in patients with COAD. **(A–D)** Kaplan-Meier analysis of overall survival (OS) in COAD patients assorted by **(A)** age (<65 vs. ≥ 65 years), **(B)** sex (males vs. females), **(C)** TNM stage (TI-II vs. TIII-IV) and **(D)** tumor stage (I-II vs. III-IV). **(E–G)** Relationships between risk scores (RS) and clinical characteristics, including age, sex, TNM stage and tumor stage. **(H)** Results of GSEA enrichment analysis in both the high-risk and low-risk groups.

cohort and the GEO cohort were 0.707, 0.821 and 0.655, respectively, validating the good predictive performance of this model in patients with COAD (Figures 3J–L).

Relationships between the ICRG prognostic signature and clinical characteristics

To further explore the associations between the ICRG prognostic signature and patients' clinical characteristics, RSs were compared in the TCGA-COAD cohort using independent t tests. Based on their clinical characteristics, patients were grouped into high and low risk groups and differences in prognosis were determined. Prognosis was significantly worse in patients in the high-risk than in the low-risk group based on clinical characteristics, such as age (P<0.001), gender (P<0.001), T3-4 status (P<0.001) and stage (P<0.001) (Figures 4A–D). Analyses of differences in RSs between groups classified by clinical features showed that RS was not affected by age or gender (Figure 4E). In contrast, RSs increased gradually and significantly as tumor stage and TNM increased (Figures 4F, G). These results demonstrated that this prognostic signature based on ICRGs showed a high degree of overall predictive power across various clinical characteristics.

In addition, the entire TCGA-COAD cohort was subjected to gene set enrichment analysis (GSEA) to identify gene sets significantly associated with both the low-risk and high-risk groups. Genes enriched in the low-risk group were associated with chemokine and cytokine pathways, whereas genes enriched in the high-risk group were associated with tumor-related signaling pathways (Figure 4H). Pathway enrichment analysis therefore showed that changes in signaling pathways and

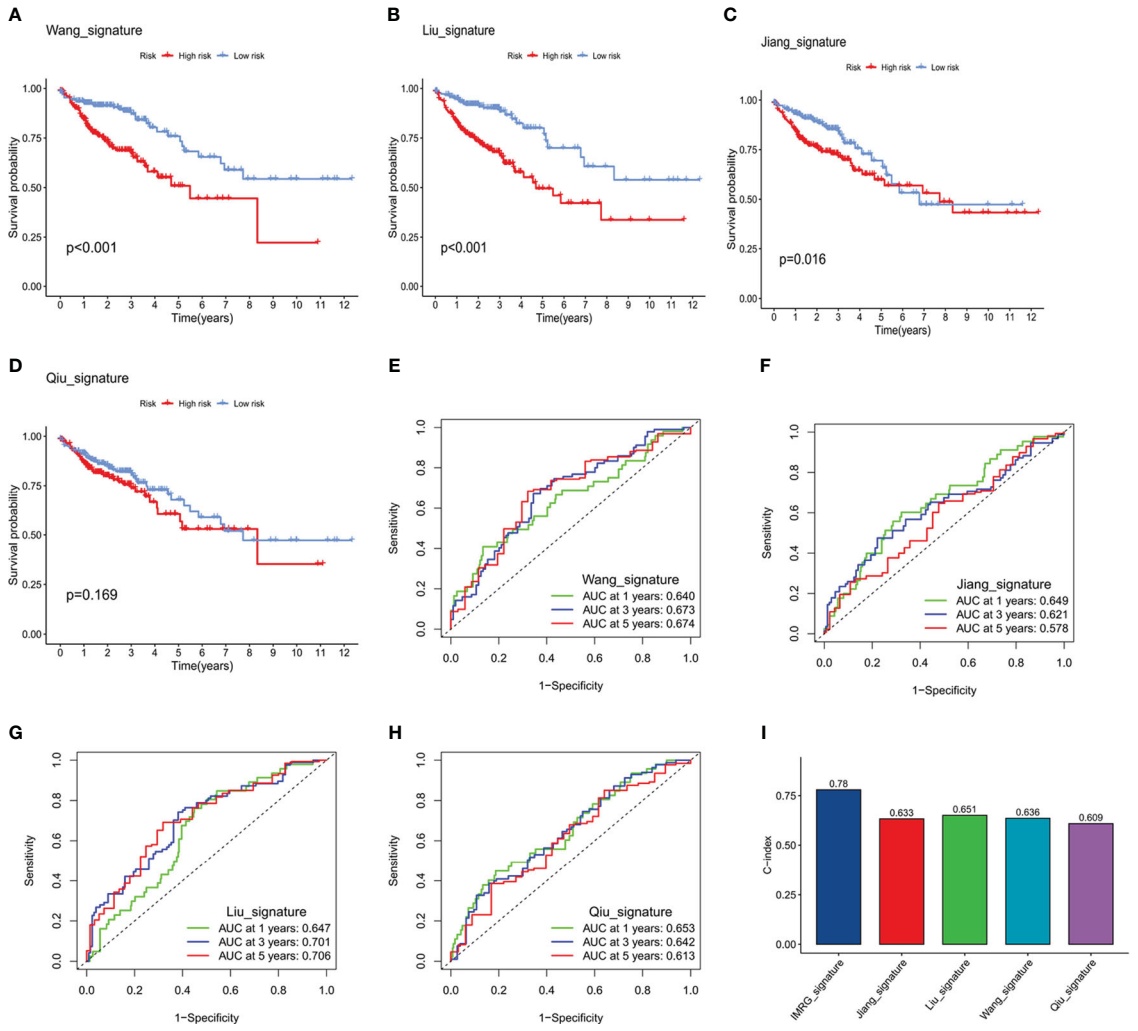

FIGURE 5
Comparison of the predictive accuracy of the ICRG prognostic signature with that of four previously published signatures. **(A-D)** Kaplan–Meier survival curve analysis of the four published signatures. **(E-H)** ROC curves showing the predictive accuracy of the four published signatures. **(I)** Comparison of the C-indices of the ICRG prognostic model with that of the other four prognostic models.

chemokines could lead to differences in immune states in low- and high-risk groups.

Comparison of the ICRG prognostic forecasting model with other published models

The relative predictive ability of the immune- and CAF-associated model described in this study was compared with the predictive ability of four previously-described prognostic models (12–15). To ensure the comparability of these signatures, the same method for calculating and converting the RS was applied to the entire TCGA-COAD cohort. Three of the previously published signatures were effective in categorizing the COAD samples into high- and low-risk groups, with the differences being statistically significant (Figures 5A–D). However, ROC curve analysis showed that the AUCs in the present model were higher than those of the four previously published signatures. Specifically, the present model had AUCs of 0.821, 0.803, and 0.732 for 1-, 3-, and 5-year survival, respectively (Figures 5E–H). In addition, the C-index of the present model was highest at 0.78, whereas the four other signatures had C-indices of 0.651 (16), 0.633 (17), 0.636 (18), and 0.609 (19). These results suggest that the prognostic performance of the ICRG prognostic signature consistently outperformed other evaluated signatures (Figure 5I).

Development of a nomogram using the ICRG prognostic signature and assessment of its clinical relevance

The clinical suitability of the ICRG prognostic signature was determined by Cox regression analyses of the TCGA-COAD

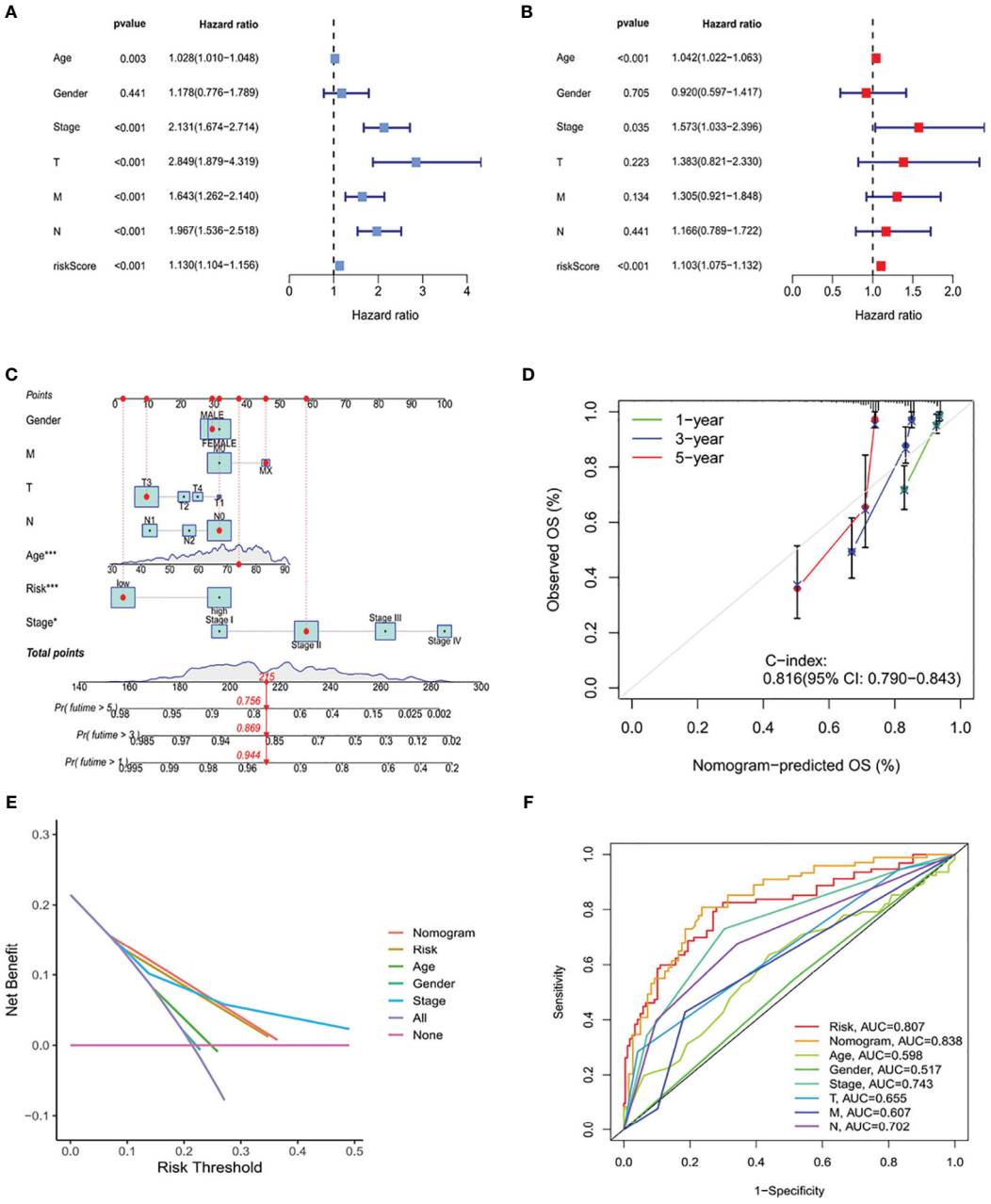

FIGURE 6
Construction of a nomogram based on the ICRG prognostic signature and evaluation of its clinical significance in the TCGA-COAD cohort. **(A, B)** Univariate and multivariate Cox regression analyses assessing the relationships between risk scores (RS) and clinical characteristics of patients in the TCGA-COAD cohort. **(C)** Development of a nomogram model predicting 1-, 3-, and 5-year overall survival (OS) in the TCGA-COAD cohort. The nomogram assigned points to each variable, with the points added to calculate a total score for each patient. Based on this score, the bottom scale was used to predict the probability of OS at the specified time points. **(D)** Calibration curve evaluating the agreement between the predicted probabilities of survival at 1-, 3-, and 5-years generated by the nomogram and the actual survival outcomes. The graph visually displays the degree of consistency between the predicted and observed survival rates. **(E)** DCA curve analysis of the clinical value of the nomogram model. **(F)** Comparison the ROC curves of clinical factors and the risk model. The nomogram model demonstrates better accuracy and performance in predicting the survival of patients with COAD.

cohort. RS correlated significantly with prognosis on both univariate ($P < 0.001$) (Figure 6A) and multivariate ($P < 0.001$) (Figure 6B) regression analyses. A reliable nomogram predicting survival risk for individuals was constructed based on multiple regression analysis, which found that three variables, age, stage, and RS, had P values <0.05 (Figure 6C). Moreover, calibration curves suggested a strong correlation between the survival rates predicted by the nomogram and the actual survival rates (Figure 6D).

Decision curve analysis (DCA) can be used to evaluate the practical clinical benefit of the nomogram. These curves are based

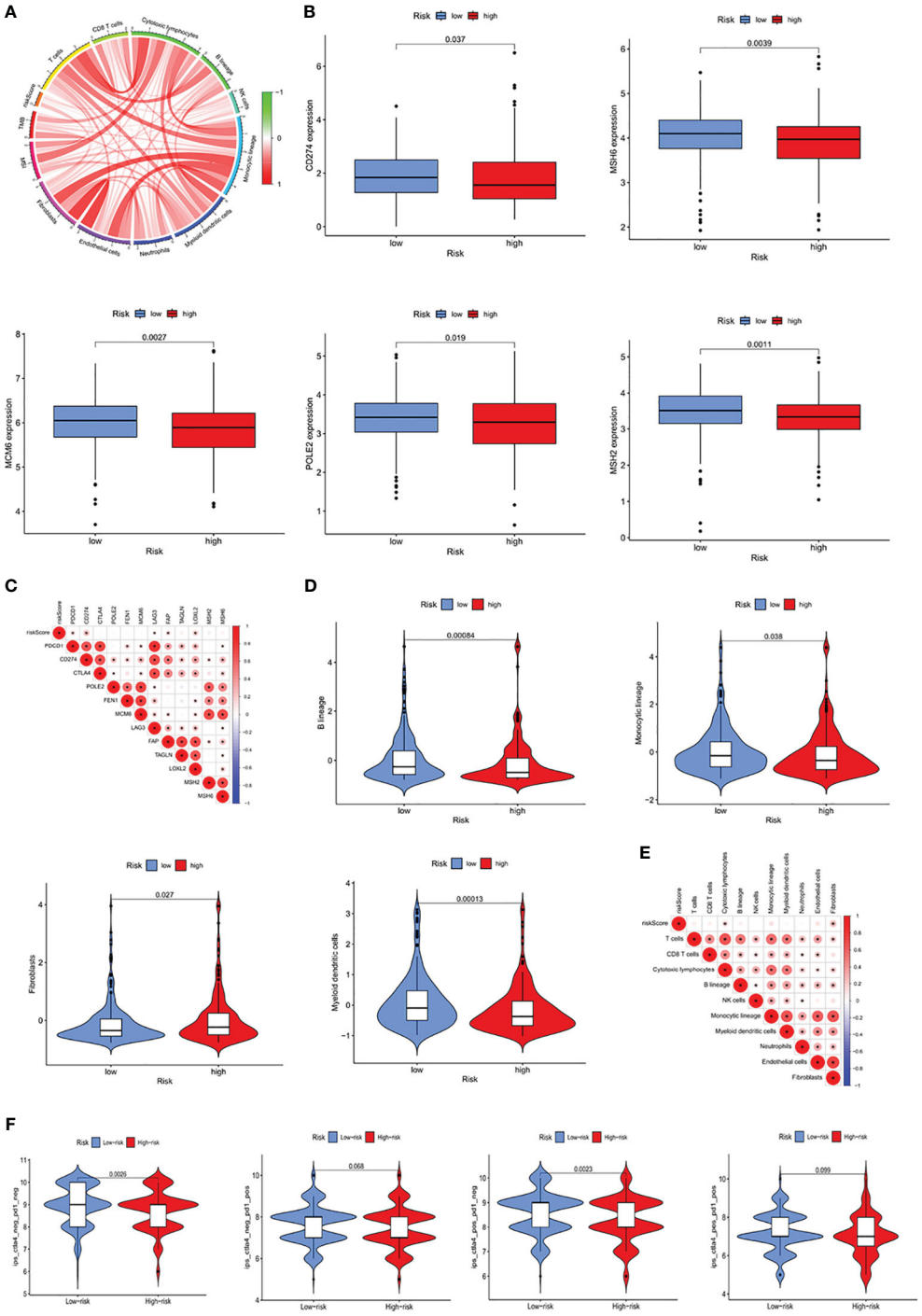

FIGURE 7
Prognostic ability of the ICRG signature to predict patient response to immunotherapy. **(A)** Correlation analyses of RS, MSI, and immune-related cells. **(B)** Comparative expression of immune checkpoint molecules (e.g. *CD274, MSH6, MCM6, POLE2* and *MSH2*) in the high- and low-risk groups. **(C)** Heatmap showing the correlations between RS and immune checkpoint expression. **(D)** Comparative immune cell infiltration in the high- and low-risk groups. **(E)** Heatmap showing the correlations between RS and immune cell infiltration. **(F)** Correlation between RS and four IPS scores associated with a single ICI (anti-CTLA4 or anti-PD1) or their combination.

on a series of possible thresholds and can compare the net benefit of the model with other decision strategies. If the net benefit of the nomogram was higher than that of other decision strategies, then this model was considered to have clinical value. DCA showed that the nomogram had better predictive ability than any other predictors (Figure 6E). In additionally, the nomogram had an AUC of 0.838, outperforming other variables (Figure 6F). Thus, these findings showed that the ICRG-based nomogram correlated significantly with patient prognosis, suggesting that this nomogram could effective aid in predicting cancer progression.

Ability of the ICRGs prognostic signature to predict response to immunotherapy

To better understand the impact of the IMRG prognostic signature on immunotherapy outcomes, the correlations between RSs and the level of immune infiltration within the TME were analyzed. RS showed a positive correlation with the infiltration of cytotoxic lymphocytes and fibroblasts (Figure 7A). Moreover, the levels of expression of immune checkpoint proteins, including *CD274, CTLA4, MSH6, MCM6, POLE2*, and *MSH2*, were found to differ significantly in the high- and low-risk groups (Figure 7B), indicating a close relationship between RS and immune checkpoint proteins (Figure 7C). The proportions of B cells, monocytes, and myeloid dendritic cells were lower, whereas the proportions of fibroblasts were higher, in the high- than in the low-risk group (Figure 7D). Furthermore, correlation analysis showed that RS correlated significantly with cytotoxic lymphocytes and fibroblasts (Figure 7E). Analysis of the correlation between RS and IPS, which are valuable predictors of the effectiveness of immunotherapy, showed significant differences in IPS and IPS-CTLA4 between the high- and low-risk groups (Figure 7F). These results suggested that the prognostic signature based on ICRGs could indicate immune infiltration status and predict patient response to immunotherapy.

Downregulation of S1PR5 improved the efficacy of anti-PD1 treatment in CRC

T cell killing experiments were performed to verify the role of S1PR5 in CRC immunity. PBMCs from healthy donors were activated for 48 hours with CD3/CD28 beads to obtain aPBMCs. To reduce non-specific killing, aPBMCs were incubated in the cold for 5 days and co-cultured with HCT116 cells in which S1PR5 had been knocked down, followed by the addition of anti-PD1 to test the effect of S1PR5 on T cell killing ability (Figure 8A). Western blotting showed that transfection of S1PR5 siRNA downregulated S1PR5 protein expression in HCT116 cells (Figure 8B). Crystal violet staining results showed that knock down of S1PR5 did not significantly increase the cytotoxic capacity of T cells, whereas the addition of anti-PD1 monoclonal antibody significantly enhanced the cytotoxic capacity of T cells (P<0.01) (Figures 8C, D). IFNγ was

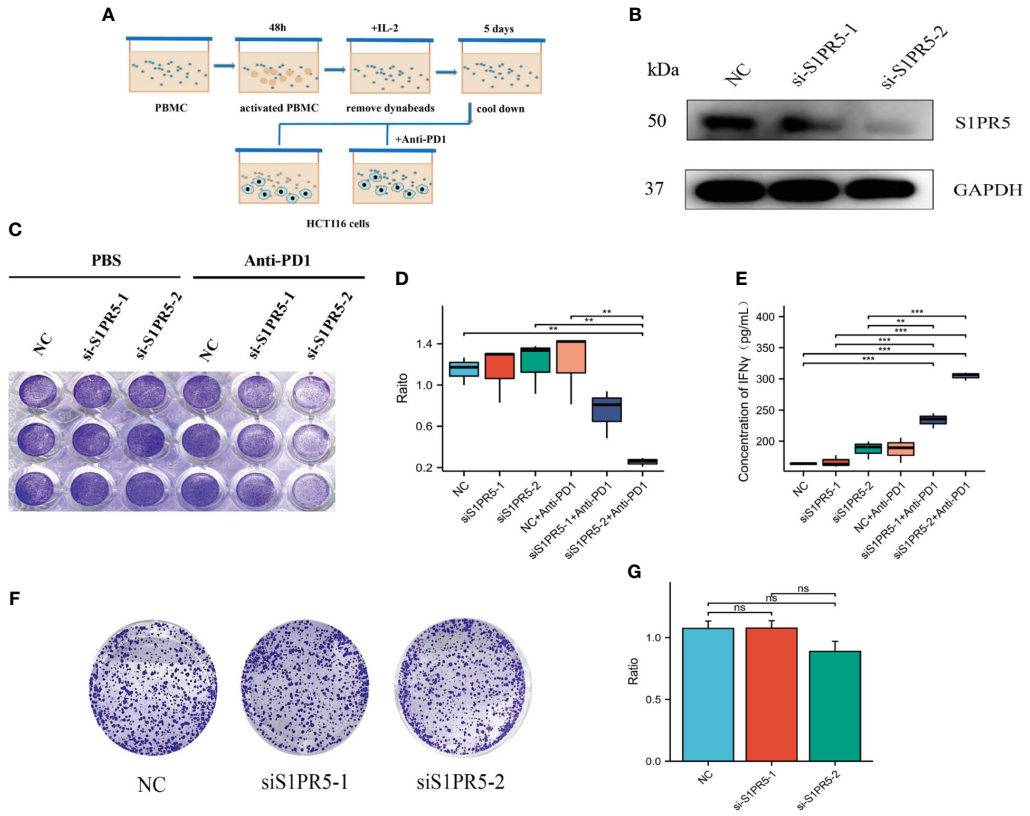

FIGURE 8
Effect of S1PR5 knockdown on the therapeutic efficacy of anti-PD1 monoclonal antibody. **(A)** Diagram of the T-cell killing assay. **(B)** Effect of si-S1PR5 on the expression of S1PR5 protein, as shown by western blotting. **(C-E)** Effect of S1PR5 knockdown and anti-PD1 antibody on T-cell cytotoxicity, as shown by crystal violet staining, with fewer tumor cells and a smaller staining area indicating stronger T-cell killing ability. Knockdown of S1PR5 alone did not significantly enhance T-cell killing ability (p>0.05), whereas the combination of S1PR5 knockdown and treatment with anti-PD1 antibody significantly enhancing T-cell killing ability (p<0.05). The expression level of IFNγ in cell culture supernatants is detected using ELISA method. Knocking down S1PR5 alone or using PD1 monoclonal antibody treatment did not significantly upregulate the expression levels of IFNγ, while the combination of s1PR5 knockdown with PD1 monoclonal antibody treatment significantly upregulated the expression levels of IFNγ (P<0.001). **(F, G)** Clonogenic assay, showing that S1PR5 knockdown did not affect the proliferation of HCT116 cells (p>0.05).

one of the markers of T cell activation and can effectively reflect the cytotoxicity of T cells. We concurrently performed an ELISA-based detection of the protein expression level of IFNγ in the cell supernatant. The experimental results indicated a significant upregulation in the expression of IFNγ in the group with knockdown of S1PR5 combined with PD1 monoclonal antibody ($P<0.001$), suggesting that the knockdown of S1PR5 significantly enhanced the efficacy of PD1 monoclonal antibody, thereby promoting the cytotoxicity of T cells (Figure 8E). To exclude cytotoxicity resulting from cell proliferation, the effects of S1PR5 on colorectal cancer cell proliferation were evaluated by testing clone formation. S1PR5 knockdown did not affect clone formation by HCT116 cells, suggesting that S1PR5 does not affect tumor proliferation ($P>0.05$) (Figures 8F, G). Taken together, these results indicate that knocking down S1PR5 can effectively enhance the therapeutic efficacy of anti-PD1 and promote the killing ability of T cells, suggesting that inhibition of S1PR5 could promote the therapeutic effects of anti-PD1.

Discussion

The emergence of cancer immunotherapies and immune checkpoint inhibitors (ICIs) has enhanced the ability to treat cancer patients. To date, the programmed cell death-1 (PD-1)/programmed cell death ligand-1 (PD-L1) signaling pathway has been the most extensively studied pathway in tumor immunotherapy (20). Activation of this pathway can inhibit T cell proliferation, differentiation and secretion of cytokines, thus inhibiting T cell activity, impairing tumor immunosurveillance and triggering tumor immune tolerance and escape (21). Although ICIs have changed the treatment pattern of many tumors, the therapeutic effects of ICIs in some tumors are not obvious. One of the main factors affecting the therapeutic effects of ICIs is the complex TMEs, which are composed of CAFs and immune cells. CAFs play an important role in tumor immunity. Activation of the immune system and T cells can trigger the expression of multiple inflammatory cytokines by CAFs (22). This can result in a polarized imbalance of immune cells in the TME, making it difficult even for existing immune cells to effectively attack tumor cells (22). Simultaneously, CAFs can inhibit the function of immune cells, reducing the effectiveness of immune responses (23). The significant roles played by immune cells and CAFs in the TME suggest that the model described in the present study, based on the expression of immune and CAF-related genes, will accurately predict prognosis in patients with COAD. A thorough evaluation of immune and CAF-related genes in COAD can aid in the identification of new methods and pathways that can improve the efficacy of immunotherapy and enhance patient prognosis.

Co-cultivation of aPBMCs with CAFs enabled detection of changes in gene expression levels in CAFs and identification of CAF-related genes. Combining CAF-related genes with immune genes enabled identification of ICRGs, including those differentially expressed in the TCGA database. The TCGA-COAD cohort was divided into three subtypes using the NMF algorithm, and 1095 DEGs were classified. Findings from the ESTIMATE (24) and MCP counter showed that the degree of immune cell infiltration was higher in Cluster 2 than in Clusters 1 and 3, a difference that may have contributed to poorer prognosis in Cluster 2. These findings also suggest that the TME in Cluster 2 may be immunosuppressive. A prognostic signature based on 12 ICRGs was assessed in the TCGA training cohort using univariate and LASSO Cox regression analyses. The resulting predictive model categorized patients into high and low-risk groups based on their median RS, with further analysis showing that pathological and TNM stages were more advanced in the high-risk group. Regardless of clinical factors, however, this prognostic model showed exceptional predictive performance and was successfully validated in both internal and external cohorts. The C-index of this ICRG prognostic signature was notably better than the C-indices of four previously described signatures. Overall, these findings indicate that the prognostic signature based on ICRGs has superior prognostic ability than other prognostic signatures.

The ICRG model described in this study was based on 12 genes, all of which are involved in both tumors and the immune system. For example, CD1B plays significant roles in antigen presentation in the immune system (25) and in the progression of various solid malignancies (18). The present study showed that the gene with the highest coefficient was S1PR5 (0.90782435), suggesting that higher levels of expression of S1PR5 in CRC patients were associated with greater risk of progression and poorer prognosis. Sphingosine-1-phosphate (S1P), a metabolite of cell membrane sphingolipids, is a ubiquitous lysophospholipid signaling molecule that regulates various biological functions through binding to five subtypes of S1P receptors (S1PR1–S1PR5), all of which belong to the family of G-protein coupled receptors (GPCRs). Inhibitors have been developed against all S1PRs or specific S1PRs, with some of them being utilized clinically as immunomodulators. For example, fingolimod is an inhibitor that binds to S1PR1, 3, 4, and 5 (16).

Although S1PR5 was originally believed to be primarily located in the nervous system, recent research has indicated that it is also involved in the proliferation and migration of gastric and esophageal cancer cell lines (17). For example, the level of expression of S1PR5 was found to be significantly higher in malignant than in benign colon tissues (19). However, the role of S1PR5 in CRC immunity has not yet been determined. The results of the present study suggested that knocking down S1PR5 can significantly promote T cell killing ability and enhance the therapeutic effect of anti-PD1 antibody. These results indicated that S1PR5 played an important role in the development of CRC, and may become a new target in the treatment of CRC.

The present study had several strengths. First, the prognostic ICRG signature was validated in several datasets, including internal and external cohorts, making it highly reliable and robust. Second, a highly useful nomogram was developed to assist in quantitative calculations, suggesting that this nomogram may be useful in clinical applications. Third, this study found that S1PR5 could affect T-cell cytotoxicity, making it a potential target for intervention.

This study also had several limitations. Most importantly, the development of both the ICRG prognostic signature and the nomogram was based on a retrospective analysis of data. This prognostic signature and nomogram will therefore require validation in large multicenter prospective patient cohorts.

Conclusion

The present study described the development of an ICRG prognostic signature, which incorporated immune- and CAF-related genes. This signature was found to be more accurate in predicting both prognostic risk and the efficacy of immunotherapy in patients with COAD. This prognostic signature was subsequently used to develop a personalized quantitative nomogram, which can be valuable in designing personalized treatments of patients with COAD.

Data availability statement

The datasets presented in this study can be found in online repositories. The names of the repository/repositories and accession number(s) can be found in the article/Supplementary Material.

Ethics statement

The studies involving humans were approved by Human Body Research Ethics Committee of the Second Hospital Affiliated to Zhejiang University School of Medicine. The studies were conducted in accordance with the local legislation and institutional requirements. The participants provided their written informed consent to participate in this study.

Author contributions

JW: Writing – original draft. XG: Writing – original draft. YQ: Writing – original draft. KJ: Writing – review & editing. XC: Writing – review & editing. WL: Writing – review & editing. HY: Writing – review & editing. DF: Writing – review & editing. YF: Writing – review & editing. YZ: Writing – review & editing. QX: Writing – review & editing. YT: Writing – review & editing. KD: Writing – review & editing.

Funding

The author(s) declare financial support was received for the research, authorship, and/or publication of this article. This study was funded by the National Natural Science Foundation of China (grant no. 81902959), the Fundamental Research Funds for the Central Universities (No. 226-2022-00009), the Natural Science Foundation of China (grant no. 82072360) and Project of the regional diagnosis and treatment center of the Health Planning Committee (No. JBZX-201903 to KD).

Acknowledgments

We are deeply grateful to all the participants who contributed to the TCGA-COAD and GEO cohorts.

Conflict of interest

The authors declare that the research was conducted in the absence of any commercial or financial relationships that could be construed as a potential conflict of interest.

Publisher's note

Supplementary material

The Supplementary Material for this article can be found online at: https://www.frontiersin.org/articles/10.3389/fimmu.2024.1291938/full#supplementary-material

References

1. Xia C, Dong X, Li H, Cao M, Sun D, He S, et al. Cancer statistics in China and United States, 2022: profiles, trends, and determinants. *Chin Med J (Engl)* (2022) 135 (5):584–90. doi: 10.1097/CM9.0000000000002108

2. Sung H, Ferlay J, Siegel RL, Laversanne M, Soerjomataram I, Jemal A, et al. Global cancer statistics 2020: GLOBOCAN estimates of incidence and mortality worldwide for 36 cancers in 185 countries. *CA Cancer J Clin* (2021) 71(3):209–49. doi: 10.3322/caac.21660

3. Diaz LA Jr., Shiu KK, Kim TW, Jensen BV, Jensen LH, et al. Pembrolizumab versus chemotherapy for microsatellite instability-high or mismatch repair-deficient metastatic colorectal cancer (KEYNOTE-177): final analysis of a randomised, open-label, phase 3 study. *Lancet Oncol* (2022) 23(5):659–70. doi: 10.1016/S1470-2045(22)00197-8

4. Zhang C, Ding H, Sun S, Luan Z, Liu G, Li Z. Incidence and detection of high microsatellite instability in colorectal cancer in a Chinese population: a meta-analysis. *J Gastrointest Oncol* (2020) 11(6):1155–63. doi: 10.21037/jgo-20-487

5. Ganesh K, Stadler ZK, Cercek A, Mendelsohn RB, Shia J, Segal NH, et al. Immunotherapy in colorectal cancer: rationale, challenges and potential. *Nat Rev Gastroenterol Hepatol* (2019) 16(6):361–75. doi: 10.1038/s41575-019-0126-x

6. Thomas PD, Kahn M. Kat3 coactivators in somatic stem cells and cancer stem cells: biological roles, evolution, and pharmacologic manipulation. *Cell Biol Toxicol* (2016) 32(1):61–81. doi: 10.1007/s10565-016-9318-0

7. Rimal R, Desai P, Daware R, Hosseinnejad A, Prakash J, Lammers T, et al. Cancer-associated fibroblasts: Origin, function, imaging, and therapeutic targeting. *Adv Drug Delivery Rev* (2022) 189:114504. doi: 10.1016/j.addr.2022.114504

8. Gocher AM, Workman CJ, Vignali DAA. Interferon-gamma: teammate or opponent in the tumour microenvironment? *Nat Rev Immunol* (2022) 22(3):158–72. doi: 10.1038/s41577-021-00566-3

9. Qian Y, Wei J, Lu W, Sun F, Hwang M, Jiang K, et al. Prognostic risk model of immune-related genes in colorectal cancer. *Front Genet* (2021) 12:619611. doi: 10.3389/fgene.2021.619611

10. Zhao Z, Li W, Zhu L, et al. Construction and verification of a fibroblast-related prognostic signature model for colon cancer. *Front Genet* (2022) 13:908957. doi: 10.3389/fgene.2022.908957

11. Bhattacharya S, Andorf S, Gomes L, Dunn P, Schaefer H, Pontius J, et al. ImmPort: disseminating data to the public for the future of immunology. *Immunol Res* (2014) 58(2-3):234–9. doi: 10.1007/s12026-014-8516-1

12. Wang J, Yu S, Chen G, Kang M, Jin X, Huang Y, et al. A novel prognostic signature of immune-related genes for patients with colorectal cancer. *J Cell Mol Med* (2020) 24(15):8491–504. doi: 10.1111/jcmm.15443

13. Liu X, Fang X, Lu L, Liu G. Prognostic significance and immune landscape of a fatty acid metabolism-related gene signature in colon adenocarcinoma. *Front Genet* (2022) 13:996625. doi: 10.3389/fgene.2022.996625

14. Jiang HZ, Yang B, Jiang YL, Liu X, Chen DL, Long FX, et al. Development and validation of prognostic models for colon adenocarcinoma based on combined immune-and metabolism-related genes. *Front Oncol* (2022) 12:1025397. doi: 10.3389/fonc.2022.1025397

15. Qiu C, Shi W, Wu H, Zou S, Li J, Wang D, et al. Identification of molecular subtypes and a prognostic signature based on inflammation-related genes in colon adenocarcinoma. *Front Immunol* (2021) 12:769685. doi: 10.3389/fimmu.2021.769685

16. Sukocheva OA. Expansion of sphingosine kinase and sphingosine-1-phosphate receptor function in normal and cancer cells: from membrane restructuring to mediation of estrogen signaling and stem cell programming. *Int J Mol Sci* (2018) 19 (2):420. doi: 10.3390/ijms19020420

17. Huang YL, Chang CL, Tang CH, Lin YC, Ju TK, Huang WP, et al. Extrinsic sphingosine 1-phosphate activates S1P5 and induces autophagy through generating endoplasmic reticulum stress in human prostate cancer PC-3 cells. *Cell Signal* (2014) 26 (3):611–8. doi: 10.1016/j.cellsig.2013.11.024

18. Luis G, Godfroid A, Nishiumi S, Cimino J, Blacher S, Maquoi E, et al. Tumor resistance to ferroptosis driven by Stearoyl-CoA Desaturase-1 (SCD1) in cancer cells and Fatty Acid Biding Protein-4 (FABP4) in tumor microenvironment promote tumor recurrence. *Redox Biol* (2021) 43:102006. doi: 10.1016/j.redox.2021.102006

19. Wang C, Mao J, Redfield S, Mo Y, Lage JM, Zhou X. Systemic distribution, subcellular localization and differential expression of sphingosine-1-phosphate receptors in benign and Malignant human tissues. *Exp Mol Pathol* (2014) 97(2):259–65. doi: 10.1016/j.yexmp.2014.07.013

20. Doroshow DB, Bhalla S, Beasley MB, Sholl LM, Kerr KM, Gnjatic S, et al. PD-L1 as a biomarker of response to immune-checkpoint inhibitors. *Nat Rev Clin Oncol* (2021) 18(6):345–62. doi: 10.1038/s41571-021-00473-5

21. Sun C, Mezzadra R, Schumacher TN. Regulation and function of the PD-L1 checkpoint. *Immunity* (2018) 48(3):434–52. doi: 10.1016/j.immuni.2018.03.014

22. Mao X, Xu J, Wang W, Liang C, Hua J, Liu J, et al. Crosstalk between cancer-associated fibroblasts and immune cells in the tumor microenvironment: new findings and future perspectives. *Mol Cancer* (2021) 20(1):131. doi: 10.1186/s12943-021-01428-1

23. Maia A, Schollhorn A, Schuhmacher J, Gouttefangeas C. CAF-immune cell crosstalk and its impact in immunotherapy. *Semin Immunopathol* (2023) 45(2):203–14. doi: 10.1007/s00281-022-00977-x

24. Yoshihara K, Shahmoradgoli M, Martinez E, Vegesna R, Kim H, Torres-Garcia W, et al. Inferring tumour purity and stromal and immune cell admixture from expression data. *Nat Commun* (2013) 4:2612. doi: 10.1038/ncomms3612

25. James CA, Xu Y, Aguilar MS, Jing L, Layton ED, Gilleron M, et al. CD4 and CD8 co-receptors modulate functional avidity of CD1b-restricted T cells. *Nat Commun* (2022) 13(1):78. doi: 10.1038/s41467-021-27764-w

frontiers | Frontiers in Immunology

TYPE Original Research
PUBLISHED 19 January 2024
DOI 10.3389/fimmu.2024.1295693

OPEN ACCESS

EDITED BY
Takaji Matsutani,
Maruho, Japan

REVIEWED BY
Peng Huang,
Nanjing Medical University, China
Alok Kumar,
Kyoto University, Japan

*CORRESPONDENCE
Yadong Guo
1731191@tongji.edu.cn
Xin Ge
xin.ge@tongji.edu.cn

†These authors have contributed equally to this work

RECEIVED 17 September 2023
ACCEPTED 03 January 2024
PUBLISHED 19 January 2024

CITATION
Dong C, Guo Y, Yang Y and Ge X (2024) Comprehensive analysis of PSME3: from pan-cancer analysis to experimental validation. *Front. Immunol.* 15:1295693. doi: 10.3389/fimmu.2024.1295693

Comprehensive analysis of PSME3: from pan-cancer analysis to experimental validation

Chengyuan Dong[1,2†], Yadong Guo[3*†], Yanrong Yang[4†] and Xin Ge[1*]

[1]Department of Clinical Medicine, Shanghai Tenth People's Hospital, School of Medicine, Tongji University, Shanghai, China, [2]School of Medicine, Anhui University of Science and Technology, Huainan, China, [3]Department of Urology, Shanghai Tenth People's Hospital, School of Medicine, Tongji University, Shanghai, China, [4]Tongji University Cancer Center, School of Medicine, Tongji University, Shanghai, China

PSME3 plays a significant role in tumor progression. However, the prognostic value of PSME3 in pan-cancer and its involvement in tumor immunity remain unclear. We conducted a comprehensive study utilizing extensive RNA sequencing data from the TCGA (The Cancer Genome Atlas) and GTEx (Genotype-Tissue Expression) databases. Our research revealed abnormal expression levels of PSME3 in various cancer types and unveiled a correlation between high PSME3 expression and adverse clinical outcomes, especially in cancers like liver cancer (LIHC) and lung adenocarcinoma (LUAD). Functional enrichment analysis highlighted multiple biological functions of PSME3, including its involvement in protein degradation, immune responses, and stem cell regulation. Moreover, PSME3 showed associations with immune infiltration and immune cells in the tumor microenvironment, indicating its potential role in shaping the cancer immune landscape. The study also unveiled connections between PSME3 and immune checkpoint expression, with experimental validation demonstrating that PSME3 positively regulates CD276. This suggests that PSME3 could be a potential therapeutic target in immunotherapy. Additionally, we predicted sensitive drugs targeting PSME3. Finally, we confirmed in both single-factor Cox and multiple-factor Cox regression analyses that PSME3 is an independent prognostic factor. We also conducted preliminary validations of the impact of PSME3 on cell proliferation and wound healing in liver cancer. In summary, our study reveals the multifaceted role of PSME3 in cancer biology, immune regulation, and clinical outcomes, providing crucial insights for personalized cancer treatment strategies and the development of immunotherapy.

KEYWORDS

immunotherapy, PSME3, tumor markers, CD276, LIHC

1 Introduction

Cancer, a leading cause of mortality in the world, is a persistent public health issue (1, 2). Immunotherapy has emerged as a promising approach for treating various cancer types, such as melanoma, lung cancer, and lymphoma (3–5). However, not all patients respond equally to immunotherapy (6), and there is a need for further identification of biomarkers and the development of personalized approaches to maximize its effectiveness. Therefore, pan-cancer studies of target genes are useful for analyzing molecular abnormalities and potential associations in different types of cancer (7). This facilitates advances in combination therapy and individualized therapy.

PSME3, also known as Proteasome Activator Complex Subunit 3, plays a crucial role in regulating essential cellular processes. For instance, PSME3 facilitates the breakdown of the cell cycle inhibitor p21 to stimulate cell proliferation (8). It also serves as a regulator by targeting the mouse double minute 2 homolog/P53 complex (9). PSME3 mediates the secretion of tumor interleukin-1 and necrosis factor-alpha as a transcriptional regulator (10). Furthermore, in pancreatic cancer, PSME3 targets the cellular myelocytomatosis oncogene (c-Myc) to stimulate lactate secretion (11). It also regulates tumor biological functions such as tumor angiogenesis, cell senescence or apoptosis, and lipid and energy metabolism (12–16). For instance, PSME3 participates in angiogenesis by influencing protein kinase (PKA) conversion in the cyclic adenosine monophosphate/PKA signaling pathway (15). Furthermore, it can control the growth of cells with cancer and the onset of BRCA and lung cancer by degrading the steroid receptor co-activators 3, P21, and P53 (8, 9, 17). It regulates energy metabolism in mice by influencing Sirt1-mediated autophagy (12).

The tumor microenvironment (TME) is an active facilitator of cancer progression during tumor growth rather than a silent bystander (18). An in-depth investigation of the dynamic regulatory mechanism of stromal and immune components in the TME and elucidation of the immune phenotype of tumor-immune interactions may provide new cancer treatment targets (19). PSME3 can create a positive feedback cycle with nuclear factor kappa-B (NF-κB), promote the development of colitis and related colon cancer, and mediate the cross-linking between NF-κB and Yes-associated protein pathways (10). Hence, These findings suggest that PSME3 may have a potential role in the immune microenvironment.

However, despite the previous reports on PSME3 in the mentioned cancer types, there hasn't been a comprehensive pan-cancer study conducted to date. In this study, we conducted a comprehensive investigation aimed at exploring the differential expression of PSME3 in various cancers, its prognostic value, clinical pathological staging, metastasis, and biological functions. We also focused on the role of PSME3 in the tumor immune microenvironment, which was further validated through flow cytometry analysis to gain a deeper understanding of its involvement in immune processes. Additionally, we predicted potential drugs targeting PSME3. Finally, we established the independent prognostic value of PSME3 in LIHC. These research findings provide valuable clues for the development of new targeted therapies.

2 Materials and methods

2.1 Data preparation and analysis of differential expression

GTEx databases (https://commonfund.nih.gov/GTEx) was used to gather the gene expression information for different tissues. The TCGA transcriptome data were found using UCSC Xena (https://xena.ucsc.edu/) On the expression data and matching tumor types, a log2 transformation and t-test were run. Boxplots were created using the "ggplot" R tool.

2.2 PSME3 immunohistochemical staining

The HPA database (https://www.proteinatlas.org/) provides the expression and distribution patterns of approximately 26,000 types of proteins in human tissues and organs. We downloaded immunohistochemistry images of various types of tumor tissues and their corresponding normal tissues from the HPA database.

2.3 Survival analysis

Overall Survival (OS) and Recurrence-Free Survival (RFS) were visualized and analyzed using the KMPlot website (https://kmplot.com/analysis/).

2.4 Gene set enrichment analysis

The top 100 co-expressed genes in the TCGA dataset were obtained from GEPIA2.0 (http://gepia2.cancer-pku.cn). The PSME3 protein-protein interaction (PPI) network was constructed using the online network tool Search Tool for the Retrieval of Interacting Genes and Proteins (STRING) (https://www.string-db.org/). Enrichment analysis was performed using the R package clusterProfiler (version 3.14.3).

2.5 Examination of the immune function of PSME3 in the pan-cancer microenvironment

We calculated immuneScore, stromalScore, and ESTIMATEScore using the Sanegrbox website (http://sangerbox.com/) to evaluate the immune and stromal components. To analyze the association between PSME3 and immune cells, we employed six different immune algorithms, including TIMER, xCell, MCP-counter, CIBERSORT, EPIC, and QuanTIseq. The analysis of immune checkpoints was also conducted using the Sanegrbox website. Additionally, we

utilized the SpatialDB online tool to analyze spatial transcriptome data of PSME3 in the mouse brain. We used the TISMO tumor immune network tool (http://tismo.cistrome.org/) to compare gene expression levels before and after cytokine treatment, as well as before and after PDL1 and CTLA-4 treatments in cell lines.

2.6 Single-cell sequencing analysis

Using the Tumor Immune Single Cell Center (TISCH) (http://tisch.comp-genomics.org/home/), a single-cell RNA (scRNA)-seq database focused on the TME, we compared the LIHC PSME3 expression in various cell types.

2.7 Drug sensitivity of PSME3 in the pan-cancer analysis

We downloaded the NCI-60 compound activity data and RNA-seq from the Genomic of Drug Sensitivity in Cancer (GDSC) (https://www.cancerrxgene.org/) databases. Expression profiling and the examination of PSME3 drug sensitivity in the pan-cancer analysis were performed. The 'limma', 'ggplot2', and 'ggpubr' R packages were used.

2.8 Univariate and multivariate cox regression

We conducted univariate Cox regression analysis on liver cancer patients, examining gene expression in relation to overall survival. Multivariate Cox regression was employed to assess independent risk factors within the same cohort. Genes and factors with a false discovery rate (FDR) < 0.05 were deemed significantly associated with patient survival. The outcomes of both univariate and multivariate Cox regression were obtained and visualized using the R package forestplot.

2.9 Development of a nomogram

This study employed the Cox regression model and the R package rms to devise an OS prediction nomogram. The nomogram was designed with endpoints set at 1, 2, 3, and 5-year overall survival rates for liver cancer.

2.10 Cell culture

The human liver cancer cells (Hut7), human lung cancer cells (A549), human bladder cancer cells (T24), and HEK 293T cells were purchased from the ATCC cell repository. At 37°C and 5% CO2 in a humid incubator, cells were grown in DMEM medium supplemented with 10% heat-inactivated fetal bovine serum, penicillin (100 units/mL) from Gibco, and streptomycin (100 ug/mL) from Gibco.

2.11 Plasmid construction and lentivirus transfection

The primer sequences of shRNA were synthesized by Shanghai Biotech. sh1-PSME3 target sequence is 5'-CGTGACAGAGA TTGATGAGAA -3'. sh2-PSME3 target sequence is 5'-GCATCTTATCTGGACCAGATT-3'. sh2-PSME3 target sequence is 5'-GCATCTTATCTGGACCAGATT-3'. The PCR instrument was annealed using the combined primers, and the annealing procedures were 37°C (30 min); 95°C (5 min); 95°C (1°C lower per cycle, 1s lower 0.2°C, 20 cycles); 75°C (1°C lower per cycle, 1s lower 0.1°C, 20 cycles); and 12°C (permanent). Finally, the annealed product and vector backbone pLKO.1 were ligated using a high-performance ligase.

Virus packaging was performed in HEK 293T cells according to the ratio pMD2G: psPAX2: plasmid: PEI = 1:2:4:12 (ug:ug:ug:ul). T24 cells were infected at a density of approximately 40%, and virus and medium were added in equal proportions along with 1x of infection reagent PB. Fluid was changed on day 2, and plasmid-resistant drugs were started on day 3 of screening. The pCDNA3.1-Flag-PSME3 overexpression plasmid originates from our laboratory.

2.12 Western blotting

Cell lysates were used to obtain total proteins. Proteins were electrotransferred onto polyvinylidene difluoride (PVDF) membranes following SDS-PAGE, and the membranes were sealed with 5% skim milk before being incubated. The membrane was then incubated with Anti-PSME3 antibody (ab180829), Anti-Flag antibody(ab95045), Alpha Tubulin antibody (11224-1-AP), Proteintech, and anti-Actin antibody (ab197345). Incubate for 14–16 hours after dilution at the corresponding ratio. Rabbit secondary antibody (Abcam ab97051) diluted 1:4000 was incubated for 1 h at room temperature, and burst scanning was performed using a high-sensitivity ECL chemiluminescence test kit (Chengdu Gechi Bio 2212ECL013).

2.13 Flow cytometry

We prepared cell flow antibodies (dilution ratio 1:100) using Purified anti-human CD276 (B7-H3) antibodies (BioLegend Cat. No. 331602). Resuspended cells were stained on ice for half an hour, washed twice, and fixed using 1% paraformaldehyde. The samples were obtained on the machine using BD Diva software (BD Biosciences). And the data were analyzed using Flowjo 10.

2.14 Cell proliferation analysis

To assess the effect of PSME3 silencing on Hut7 cell proliferation, we conducted CCK-8 cell proliferation assays. Cells were seeded in 96-well plates, and CCK-8 reagent was added at different time points (24 hours and 48 hours). Cell proliferation capacity was evaluated by measuring absorbance.

2.15 Scratch wound healing assay

Cells were seeded in 6-well culture plates and allowed to grow to a uniform monolayer. Subsequently, a uniform scratch was created in the cell monolayer using a 200μL pipette tip. The ability of cells to heal in the scratched area was photographed, recorded, and compared at different time points.

2.16 Data analysis

All experimental data were subjected to statistical analysis using appropriate biostatistical methods, including t-tests and analysis of variance. Experimental results were considered statistically significant when the p-value was less than 0.05.

3 Results

3.1 Differential expression based on PSME3

We conducted an in-depth analysis of RNA sequencing data from the TCGA and GTEx databases. The analysis of the TCGA database reveals a significant upregulation of PSME3 gene mRNA expression in 15 distinct cancer types compared to normal tissues. These cancer types encompass bladder cancer (BLCA), breast cancer (BRCA), cervical squamous cell carcinoma (CESC), cholangiocarcinoma (CHOL), colon adenocarcinoma (COAD), esophageal cancer (ESCA), glioblastoma multiforme (GBM), head and neck squamous cell carcinoma (HNSC), kidney renal clear cell carcinoma (KIRC), LIHC, LUAD, lung squamous cell carcinoma (LUSC), rectum adenocarcinoma (READ), stomach adenocarcinoma (STAD), and uterine corpus endometrial carcinoma (UCEC). Only two cancer types, kidney chromophobe (KICH) and thyroid carcinoma (THCA), exhibit lower PSME3 gene expression when compared to normal tissues (Figure 1A).

Considering the limited availability of normal tissue data within the TCGA dataset, we conducted a comprehensive analysis by seamlessly integrating gene expression data sourced from the GTEx database, which offers a larger dataset of paired normal tissues. The combined analysis demonstrates a prominent elevation in PSME3 mRNA expression across several cancer types, including BLCA, BRCA, CESC, CHOL, COAD, Diffuse Large B-Cell Lymphoma (DLBC), ESCA, GBM, HNSC, KICH, Kidney Renal Papillary Cell Carcinoma (KIRP), Acute Myeloid Leukemia (LAML), Low-Grade Glioma (LGG), LIHC, LUAD, LUSC, Ovarian Cancer (OV), Pancreatic Ductal Adenocarcinoma (PAAD), PRAD, READ, Skin Cutaneous Melanoma (SKCM), STAD, Testicular Germ Cell Tumor (TGCT), Thymoma (THYM), and UCEC. Only in adrenocortical carcinoma (ACC), kidney renal clear cell carcinoma (KIRC), and kidney chromophobe (KICH) do we observe a contrasting trend (Figure 1B).

We conducted a further analysis of the expression patterns of PSME3 in different cancers concerning pathological staging and metastasis. The data indicates a correlation between the expression of PSME3 and the pathological staging as well as tumor metastasis in cases of LUAD, LIHC, and KIRC (Figures 1C, D).

In the previously mentioned tumors exhibiting mRNA level differences, we proceeded with an analysis of PSME3 protein expression using the UALCAN database. The results revealed a significant increase in PSME3 protein expression in LIHC, UCEC, BRCA, OV, HNSC, PAAD, GBM, COAD, and LUAD. These findings are consistent with our previous research outcomes (Figure 2A). Furthermore, immunohistochemical data from the HPA database provided additional support for our discoveries (Figure 2B). These findings may contribute to a deeper understanding of the biological functions of PSME3 in various cancers and shed light on its potential clinical diagnostic value.

3.2 The prognostic significance of PSME3 expression in pan-cancer

We conducted a pan-cancer analysis using the Kaplan-plot tool to assess the prognostic significance of PSME3. The results revealed that in LIHC, HNSC, LUAD, OV, THCA, and CESC, high PSME3 expression was associated with poorer OS, with a hazard ratio (HR) greater than 1 (Figure 3A; $P < 0.05$). However, in gastric cancer STAD (Supplementary Figure 1A), high PSME3 expression was correlated with better OS. Furthermore, in HNSC, LIHC, BLCA, LUAD, LUSC, and PCPG, high PSME3 expression was linked to worse RFS (Figure 3B; $HR > 1$, $P < 0.05$), while in STAD, ESCA, KIRC, and OV, high PSME3 expression was associated with better RFS (Supplementary Figure 1B).

In summary, the PSME3 particularly in LIHC and LUAD, exhibits significantly elevated expression levels. This elevated expression is associated with poor clinical prognosis and cancer progression, indicating its potential clinical utility. Further research into the biological functions of PSME3 will contribute to the development of more effective cancer treatment strategies.

3.3 The biological functions of PSME3

Our study commenced by analyzing proteins that interact with PSME3 and exploring co-expressed genes. Subsequently, we conducted functional enrichment analysis. In the STRING database, we identified ten proteins known to interact with PSME3: PSME1, PSME2, PSMA5, PSMD8, PSMD14, PSMEIP1, NCOA3, RXRA, TNF, and IFNG. These proteins collectively constitute a PPI network (Figure 4A). Furthermore, we validated

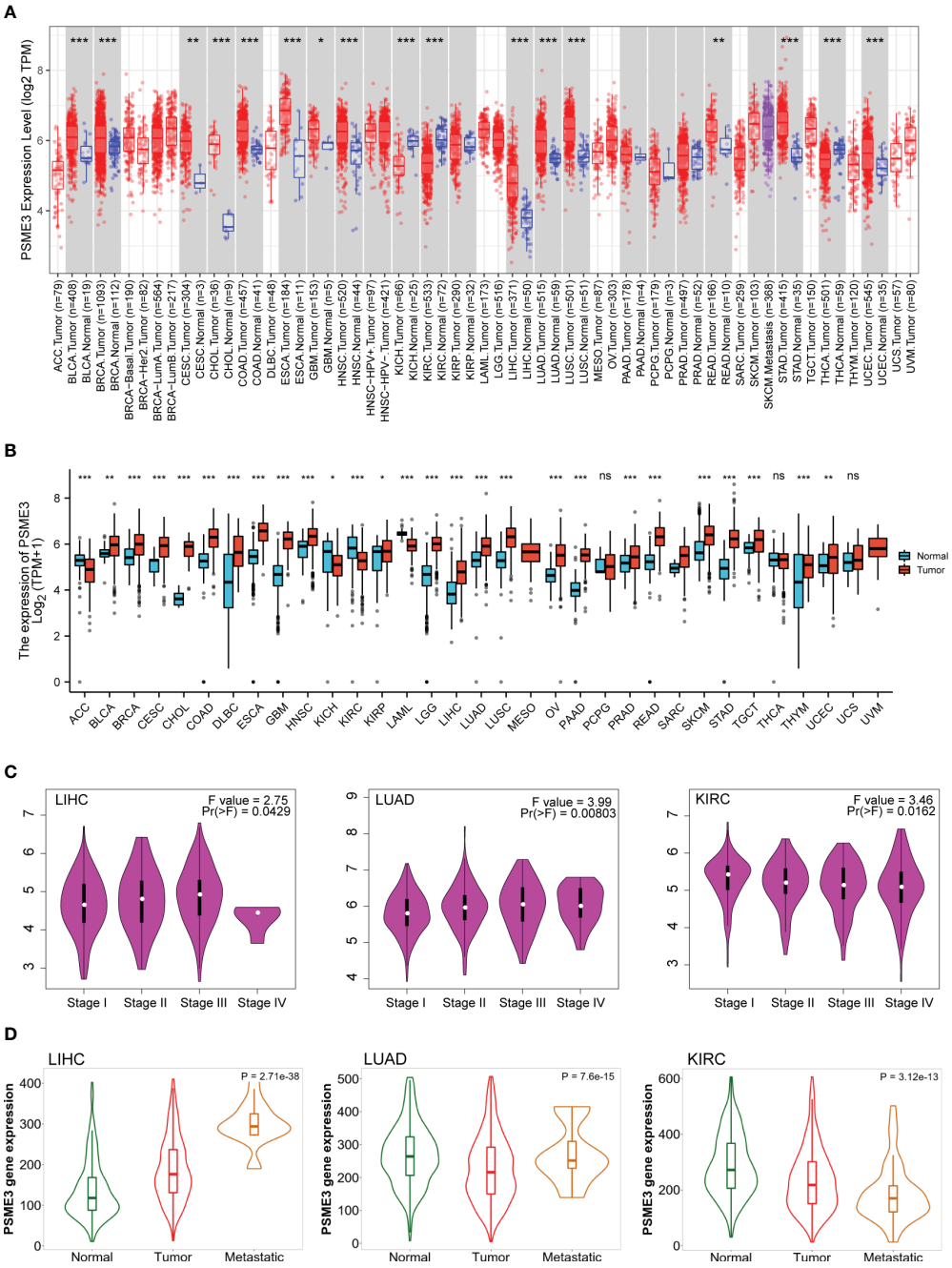

FIGURE 1
Differential expression of PSME3 **(A)** PSME3 mRNA expression levels in 33 different tumor types derived from TCGA database. Red columns represent cancer samples, and blue columns represent normal samples. *P<0.05, **P<0.01. **(B)** Comparison of PSME3 expression between tumor and normal tissues, combining data from TCGA and GTEx. *P<0.05, **P<0.01, ****P<0.001, NS (no significant differences). **(C)** Violin plots illustrating PSME3 mRNA levels at pathological stages (stages I, II, III, and IV) in various cancers. **(D)** Relationship between PSME3 expression and metastasis in different tumors [log2 transcript per million (TPM) + 1]; only cancers with statistically significant differences between pathological stages are presented.

the co-expression patterns of PSME3 using GEPIA 2. This analysis unveiled the top 100 genes closely associated with PSME3 (Supplementary Table 1), with the top 10 genes listed as follows: LSM12P1 (R = 0.74), PIGW (R = 0.71), LSM12 (R = 0.67), CCDC43 (R = 0.67), RAB5C (R = 0.67), KPNA1 (R = 0.66), RABM12 (R = 0.66), CPSF2 (R = 0.66), URB2 (R = 0.67), and KPNB1 (R = 0.69) (Figure 4B).

Through Go and KEGG functional enrichment analysis, our research has unveiled the pivotal roles played by PSME3 and its interacting proteins in a multitude of biological processes. These processes encompass protein degradation, antigen processing and presentation, immune rejection reactions, autoimmune diseases and inflammation, regulation of hematopoietic stem cell differentiation, and amino acid metabolism (Figures 4C, D). Additionally, the functional

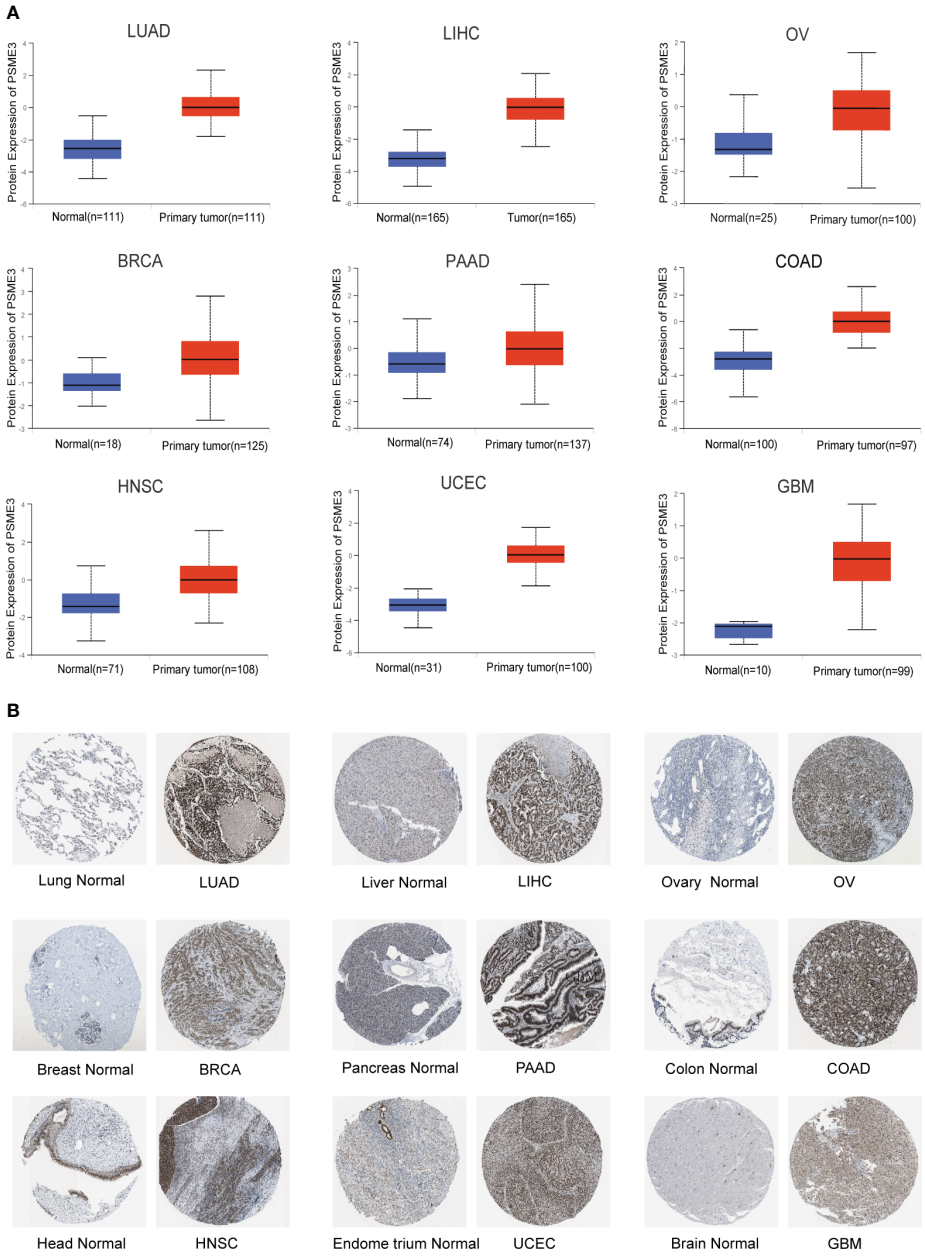

FIGURE 2
(A) Differential expression of PSME3 protein in various tumor and normal tissues from the UALCAN database. **(B)** Immunohistochemical images comparing PSME3 protein expression in normal (left) and tumor (right) tissues.

enrichment analysis of the top 100 genes co-expressed with PSME3 has revealed a wide spectrum of cellular processes, including RNA processing, protein synthesis, organelle functions, and signal transduction pathways (Figures 4E, F). These findings underscore the multifunctionality of PSME3 in cell biology, immunology.

3.4 Immune infiltration and immune cell analysis based on PSME3

Research on PSME3 within the domain of tumor immunity has been relatively limited in scope. However, given its potential significance in this field, there is a critical need for further exploration and expansion of PSME3 research. As immune infiltrating cells play a pivotal role in cancer development, we conducted an analysis to determine the estimated score, immune score, and stromal score of PSME3 in various cancers (Figures 4E, F). It's worth noting that in specific cancer types such as COAD, KIRC, READ, DLBC, PAAD, UVM, KICH, and LAML, PSME3 exhibited a positive correlation with the Stromal Score. Additionally, a positive correlation was observed between PSME3 and Immune Score in COAD, DLBC, PAAD, UVM, KICH, and LAML. Furthermore, the Immune Scores in COAD, READ, PAAD, UVM, KICH, and LAML displayed a positive correlation with the estimates (Figures 5A–C).

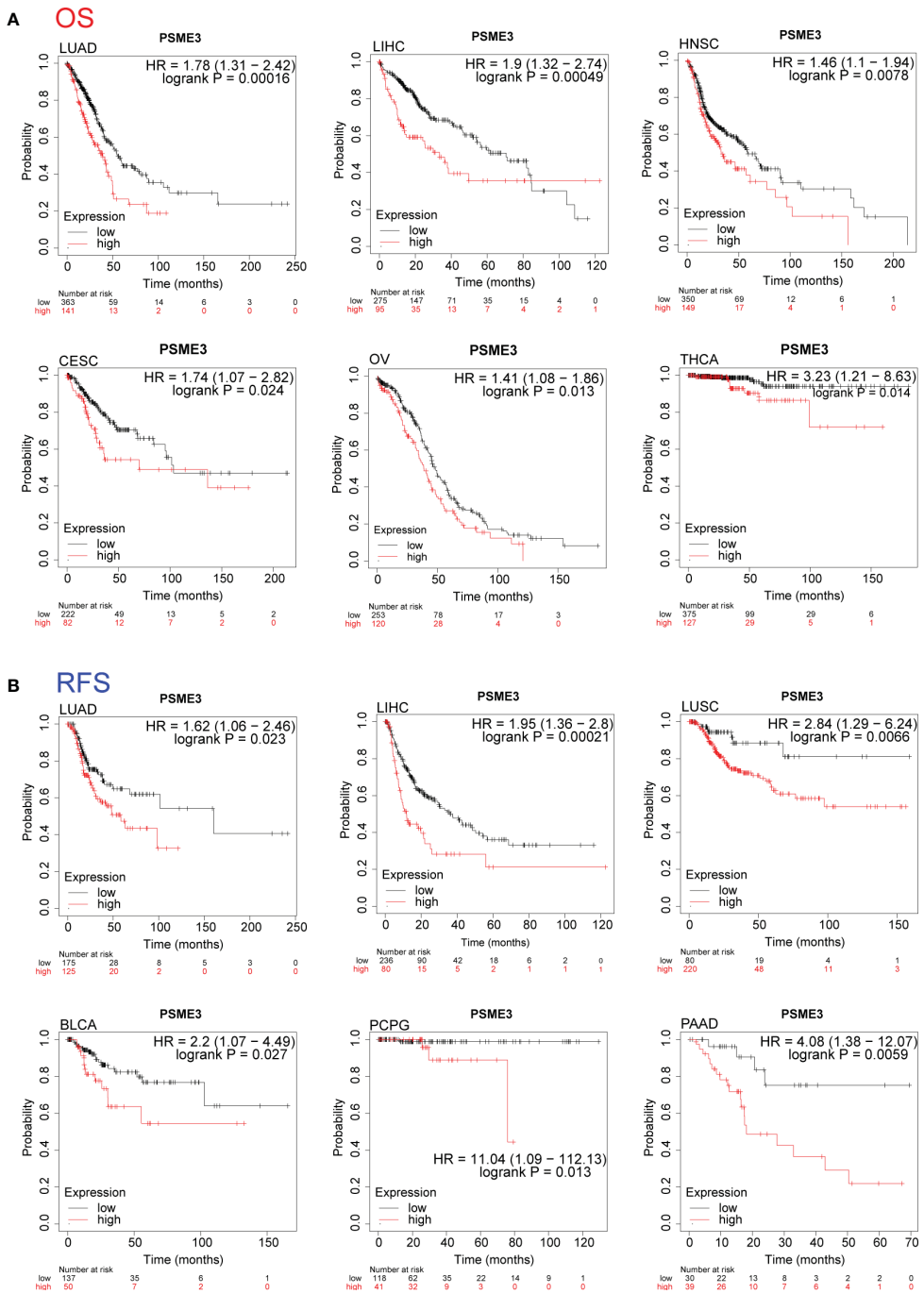

FIGURE 3
(A) Kaplan-Meier analysis of the relationship between high and low expression of PSME3 and OS(HR>1, P<0.05). **(B)** Kaplan-Meier analysis of the relationship between high and low expression of PSME3 and RFS (HR>1, P<0.05).

Furthermore, we employed six different techniques to assess immune cell involvement, aiming to elucidate the relationship between PSME3 and immune cells. These methods included EPIC (Figure 5D), QuanTIseq (Figure 5E), CIBERSORT (Supplementary Figure 2A), TIMER (Supplementary Figure 2B), XCell (Supplementary Figure 2C), and MCP-counter (Supplementary Figure 2D). Notably, higher levels of PSME3 exhibited a robust positive correlation with neutrophils, B cells, CD4 T cells, CD8 T cells, and M2 macrophages in cancers such as HNSC, KIRC, KICH, PRAD, and UVM. To further validate these findings, we conducted a spatial transcriptional analysis in the mouse brain, confirming the spatial co-expression of PSME3 with the M2 macrophage biomarkers CD68 and CD163. The geographical distribution patterns of PSME3, CD68, and CD163 markers showed significant overlap (Figure 5F).

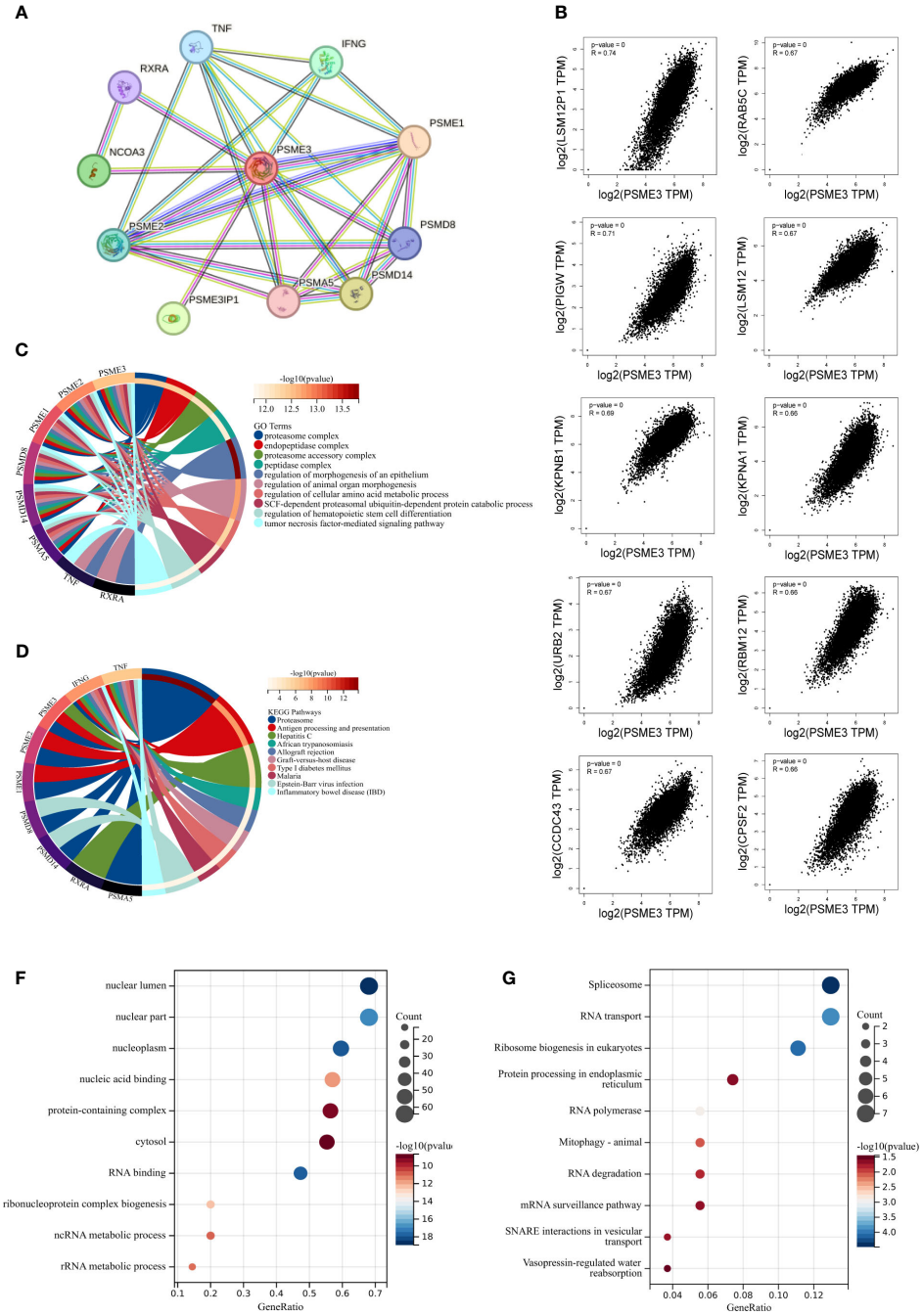

FIGURE 4
The enrichment analysis of PSME3 in pan-cancer: **(A)** Interaction network of PSME3's interacting proteins as retrieved using the protein-protein interaction search tool (STRING). **(B)** Correlation between PSME3 and the top 10 co-expressed genes. **(C)** Functional enrichment analysis of GO pathways associated with PSME3 and its interacting proteins. **(D)** Functional enrichment analysis of KEGG pathways associated with PSME3 and its interacting proteins. **(E)** Functional enrichment analysis of GO pathways associated with PSME3 and its co-expressed genes. **(F)** Functional enrichment analysis of KEGG pathways associated with PSME3 and its co-expressed genes.

Furthermore, results from immune subtype analysis indicated that elevated expression of PSME3 was associated predominantly with the C2 subtype in BLCA, UCEC, STAD, and LUAD, suggesting a primary association with IFN-gamma. Meanwhile, the increased presence of PSME3 in the C4 subtype of LUSC and KIRC implied an association with lymphocyte exhaustion (Figure 5G).

3.5 Association between PSME3 and immune checkpoint

Antitumor immunity is a powerful predictor of immunotherapy response associated with MSI (Microsatellite Instability), TMB (Tumor Mutational Burden) (20). Immune checkpoint inhibitor

10.3389/fimmu.2024.1295693

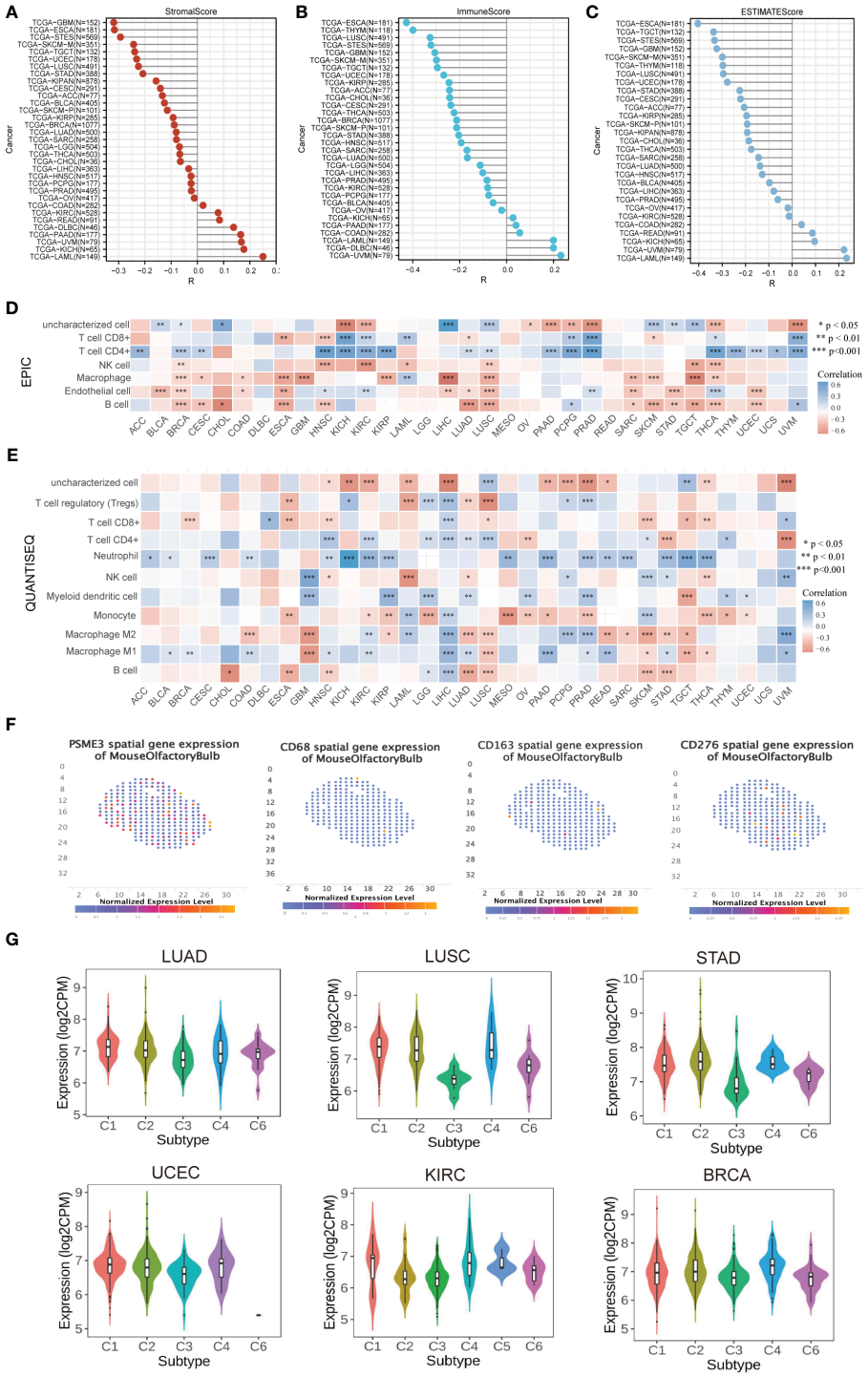

FIGURE 5
Correlation and Immune Cell Infiltration Analysis **(A)** Stick map illustrating the correlation between PSME3 and StromalScore. **(B)** Stick map illustrating the correlation between PSME3 and ImmuneScore. **(C)** Stick map illustrating the correlation between PSME3 and ESTIMATEScore. **(D)** Immune cell infiltration analysis conducted using EPIC. **(E)** Immune cell infiltration analysis conducted using QuanTiseq. *P<0.05, **P<0.01, NS (no significant differences). **(F)** Spatial transcription sections displaying the spatial expression patterns of PSME3, CD68, CD276, and CD163 markers. Dot colors represent the expression levels of the markers. **(G)** Correlations between PSME3 and immune subtypes were analyzed with the TSIDB online tool.

therapy's effects can be detected by MSI-H/dMMR and a high TMB (TMB-H) (21). In our study, we utilized the Pearson correlation coefficient to assess the association between the PSME3 gene expression levels and TMB as well as MSI. We looked into the correlation between PSME3 expression levels and those of MSI, TMB. The expression levels of PSME3 were positively correlated with TMB in LUAD, UCEC, BLCA, UCEC, STAD, SKCM, OV, LGG, and HNSC; this was negatively correlated with TMB in

THCA (Figure 6A). Furthermore, the expression of PSME3 was negatively correlated with MSI in UCEC and UVM while being positively correlated with MSI in COAD, DLBC, LGG, PRAD, and THCA (Figure 6B). Based on the association between PSME3 expression and the mutation markers TMB and MSI, we further investigated the link between PSME3 expression and mature MMR genes. From the results, in 33 cancer types (excluding LGG), PSME3 was positively correlated with MMR gene expression (Figure 6C).

Immunological checkpoints (ICPs) represent the most promising targets for tumor immunotherapy since they regulate the entry of immune cells into TME (21). When investigating the relationship between immune checkpoint expression and PSME3, we observed that among the 33 cancers, CD276 and CD274 exhibited the highest positive correlation with PSME3, followed by VEGFA, HMGB1, THR4, BTNA2, and ENTDD1 (Figure 6D). Spatial transcriptome results also indicated an overlap between

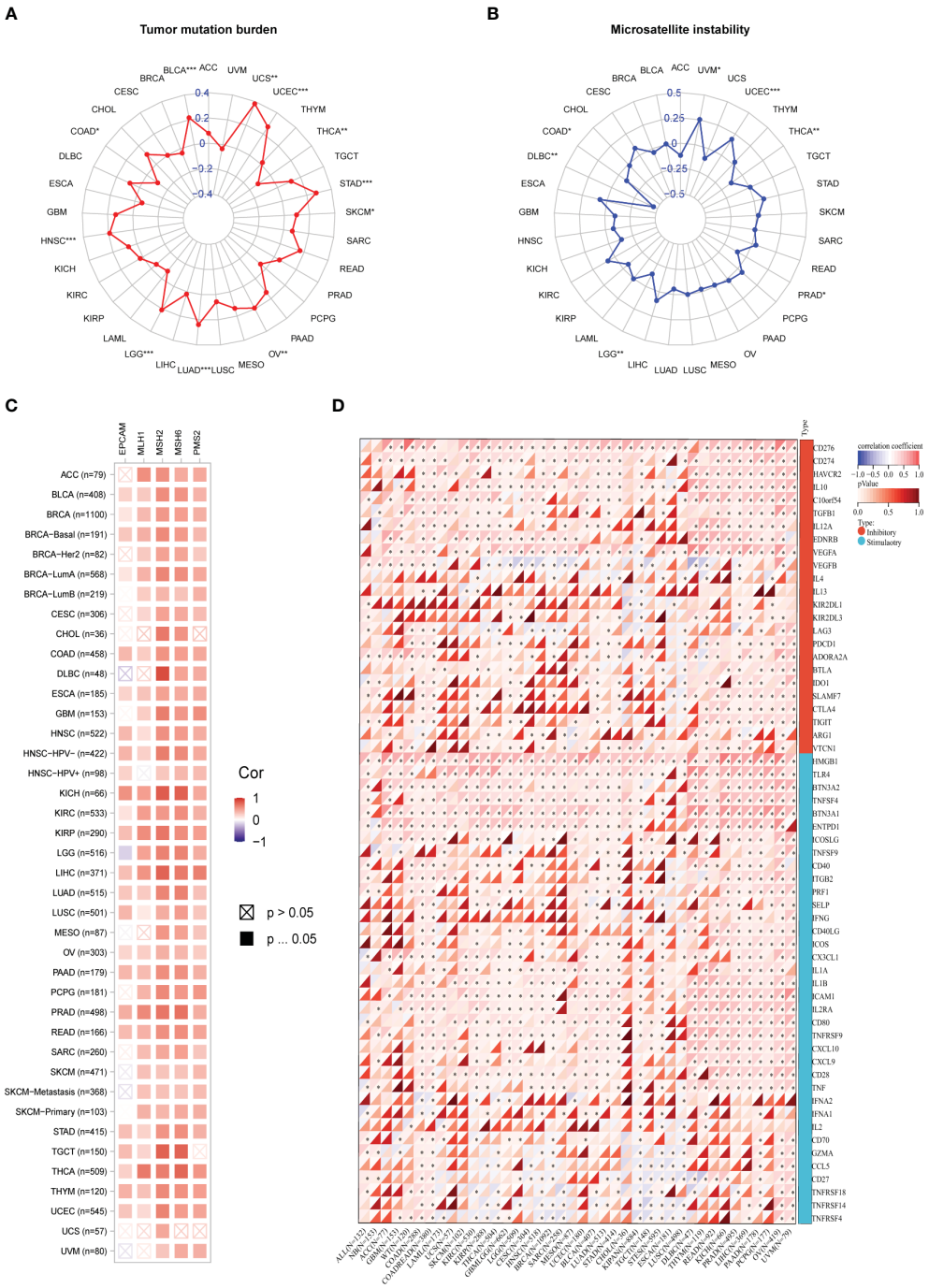

FIGURE 6
(A) Correlation Between PSME3 mRNA Expression and TMB. **(B)** Correlation Between PSME3 mRNA Expression and MSI. **(C)** Heatmap illustrating the expression of PSME3 and MMR pathway genes. **(D)** Heatmap depicting the relationship between immune checkpoint genes and PSME3 expression in pan-cancer analysis. *P < 0.05, **P < 0.01, ***P < 0.001.

CD276 and PSME3 (Figure 5F). In summary, the correlation between PSME3 and immune checkpoint expression offers crucial insights into the intricate dynamics within the tumor microenvironment. Continued research in this field could lead to significant progress in personalized cancer treatment strategies.

3.6 To validate the involvement of PSME3 in the regulation of CD276

To further confirm the association between PSME3 and immune checkpoints, we conducted flow cytometry analysis after modulating PSME3 expression in 293T cells (Figure 7A) and silencing PSME3 in liver cancer Hut7, lung adenocarcinoma A549, and bladder cancer T24 cells (Figures 7B-D). The experimental findings unequivocally demonstrated that PSME3 plays a positive regulatory role in CD276 expression. Intervening to reduce the expression of CD276 by targeting PSME3 is a promising treatment strategy that may contribute to enhancing the efficacy of immunotherapy.

3.7 Immunotherapy response and sensitive medication prediction

We initiated our study by employing the TISMO network tool, which revealed that cytokine therapy, particularly interferons (IFNβ and IFNγ), exhibited promising therapeutic effects in mouse models with high PSME3 expression, especially in various cancer types such as lung cancer, breast cancer, melanoma, and colorectal cancer (Figure 8A). Additionally, our observations indicated that the expression levels of PSME3 can predict the response to immunotherapy with PDL1 and CTLA4 in gastric adenocarcinoma and breast cancer in mouse models (Figure 8B). These findings provide crucial insights into the potential role of PSME3 in immunotherapy and its association with treatment responses, offering valuable information for future research and the development of immunotherapeutic strategies.

Acetalax, sapitinib, and dasatinib were the top three medications that were positively linked with PSME3 expression, according to analyses of correlations between PSME3 expression and drug sensitivity based on the GDSC dataset (Figure 8C). Contrarily, the top three medications that were adversely linked with PSME3 expression were TW 37, daporinad, and telomerase inhibitor IX (Figure 8D).

3.8 PSME3 as an independent predictor in LIHC

Our previous findings indicate a close correlation between high PSME3 expression and the progression and prognosis of LIHC, with a significant role in liver cancer immunity. For this reason, we proceeded to explore the biological functions and independent prognostic value of of PSME3 in LIHC. We identified PSME3 as an independent prognostic indicator in LIHC through both univariate and multivariate COX regression analyses. (Figures 9A, B). Additionally, we constructed a PSME3-based nomogram to better assist in evaluating patient prognosis in clinical practice (Figure 9C). The area under the curve (AUC) for the 1-year, 2-year, 3-year, and 5-year OS in the line chart were 0.775, 0.709, 0.725, and 0.699, respectively (Figure 9D). Moreover, calibration curves were generated to evaluate the performance of the line chart (Figure 9E). These curves demonstrated a close proximity between the predictive curve of the model and the ideal curve.These results indicate a robust predictive performance.

Meanwhile, we conducted independent survival prognosis analyses in TCGA and ICGC databases to further confirm the predictive capacity of high PSME3 expression for a poorer prognosis in liver cancer patients (Figures 9F, G). Furthermore, clinical relevance indicated an association between high PSME3 expression and specific tumor staging (T1-T4/I/II/III/IV stages), irrespective of age (Supplementary Figure 3A).

To better elucidate the potential mechanisms through which PSME3 influences patient prognosis, we analyzed single-cell sequencing data and observed a noteworthy correlation between PSME3 and CD4Tconv, CD8T, CD8Tex and Tprolif (Supplementary Figure 3B). Additionally, KEGG pathway enrichment analysis revealed significant associations between PSME3 expression and pathways related to neuroactive ligand receptor interactions and primary bile acid biosynthesis (Figure 9H).

Finally, we conducted initial validation of the general functions of PSME3 in liver cancer. Both CCK-8 assays and wound healing assays provided confirmation of PSME3's impact on Hut7 cell proliferation. The results were unequivocal, demonstrating that the knockdown of PSME3 significantly decreased the proliferation capacity of Hut7 cells compared to the control group. Additionally, the healing capacity of the PSME3 knockdown group remained notably inferior to that of the control group (Figures 9I-K).

4 Discussion

Immune checkpoint inhibitors (ICIs) play a pivotal role in cancer immunotherapy by modulating immune responses to help restore the body's immune response against tumors. Despite the significant achievements of immune checkpoint inhibitors like PD-1/PD-L1 inhibitors in some cancer treatments, resistance to therapy in some patients and inconsistent efficacy remain challenges. Therefore, the search for new immune checkpoints or biomarkers to predict the effectiveness of immunotherapy becomes particularly important. In our research, we have demonstrated that PSME3 could serve as a promising prognostic biomarker, especially in the context of future cancer immunotherapy, holding potential significance.

Finding biomarkers useful for broad-spectrum cancer diagnosis is aided by the analysis of differential gene expression. Protein analysis offers compelling evidence for the identification of prognostic biomarkers for early diagnosis (22, 23). Our research results indicate that abnormal PSME3 mRNA expression is observed in nearly all types of cancer within the TCGA dataset.

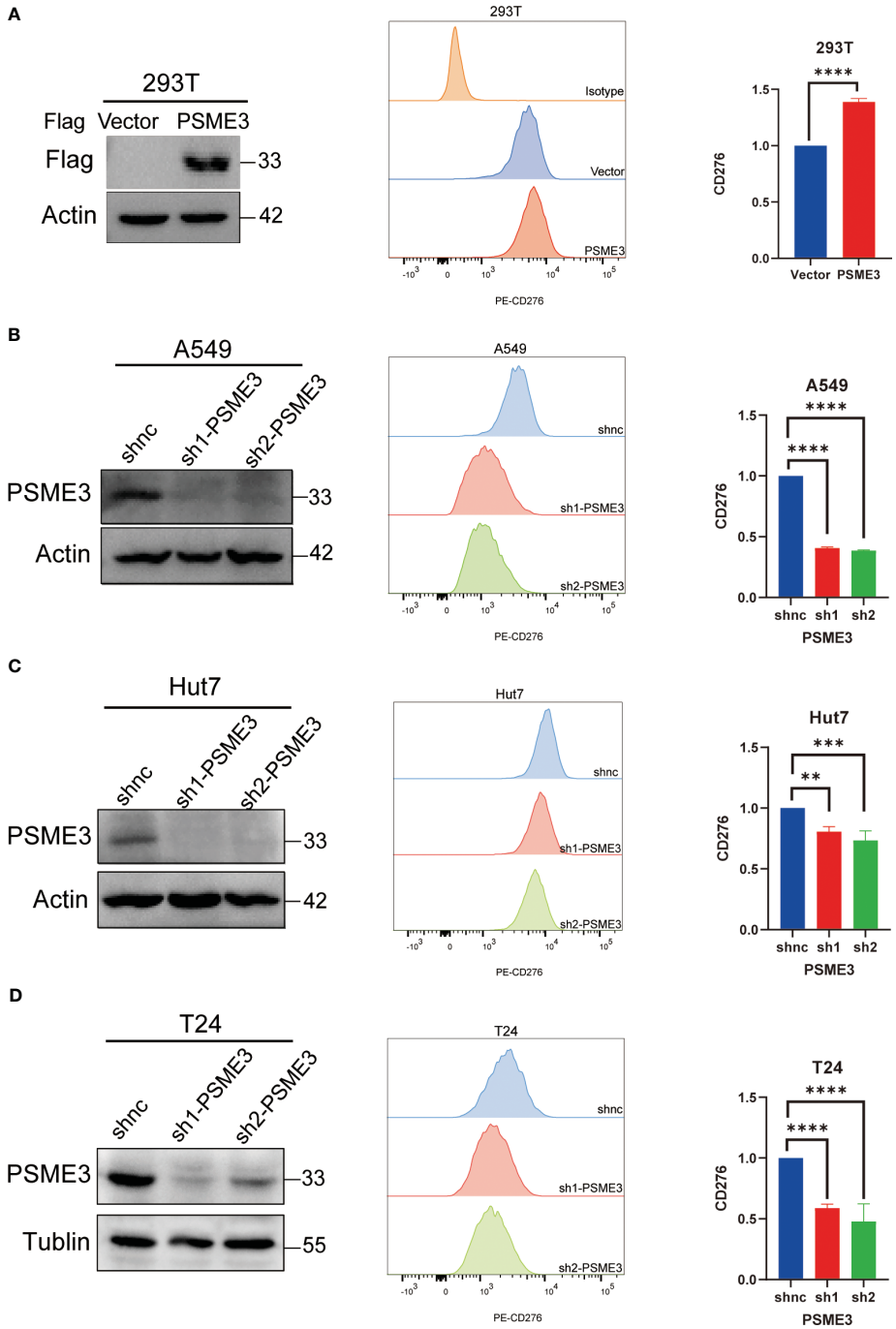

FIGURE 7
(A) CD276 Expression with PSME3 Overexpression in 293T Cells. **(B)** CD276 Expression with PSME3 Knockdown in A549 Cells. **(C)** CD276 Expression with PSME3 Knockdown in Hut7 Cells. **(D)** CD276 Expression with PSME3 Knockdown in T24 Cells. Left: Western blot results; Center: Flow cytometry histograms; Right: Quantified data in a bar graph. **P<0.05, **P<0.01, ****P<0.001.*

Importantly, our immunohistochemical analysis provides further confirmation, strongly supporting the high consistency between PSME3 protein levels and mRNA expression across various cancer types. Furthermore, we find associations between PSME3 expression and tumor staging as well as metastasis in kidney, liver, and lung cancers. Most significantly, high PSME3 expression is significantly correlated with OS and RFS.

Previous reports have also mentioned the abnormal expression of PSME3 in various types of cancer, including thyroid cancer, head and neck cancer, and osteosarcoma, which is consistent with our research findings (24–29). The investigators found that the prognosis of patients with PSME3-negative tumor tissue was significantly better than that of the PSME3-positive group (30); Roessler M. et al. identified PSME3 as a new serum tumor marker

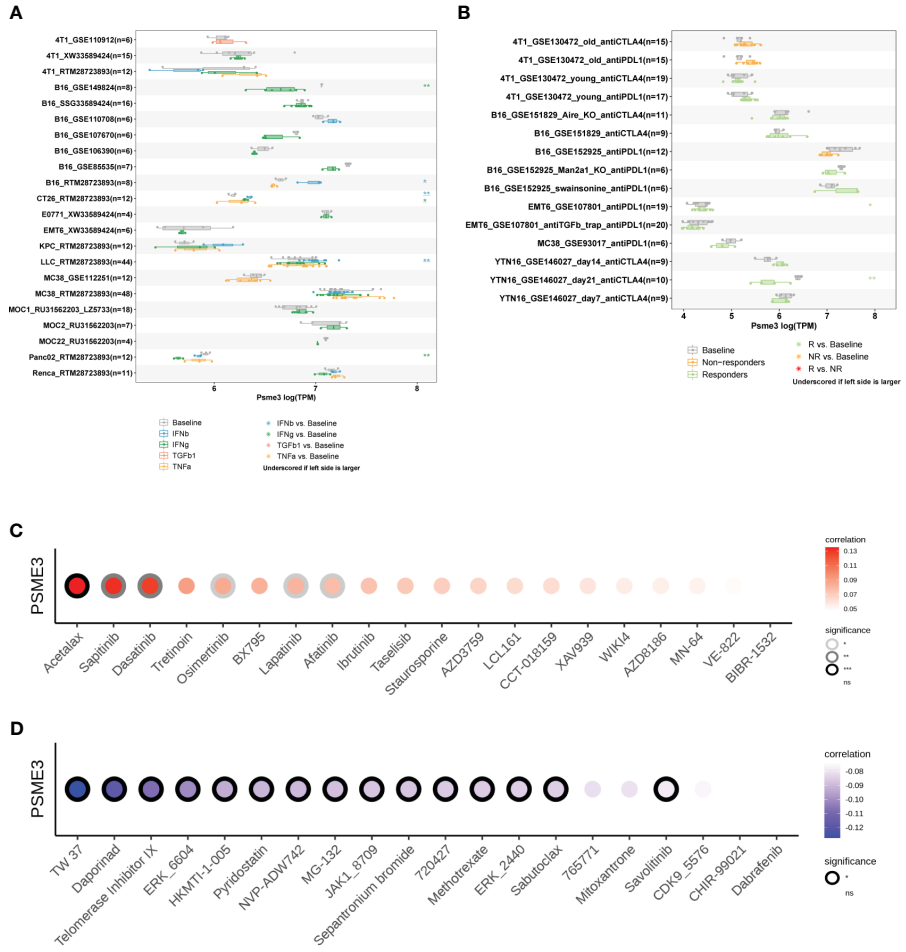

FIGURE 8
(A) Multiple boxplots illustrate the expression of PSME3 in cancer cell lines before and after cytokine treatment, as obtained from the TISMO web tool. Significance levels are indicated as follows: *, **, and *** represent P values of < 0.05, < 0.01, and < 0.001, respectively. **(B)** Multiple boxplots depict the expression of PSME3 in cancer cell lines before and after PDL1 or CTLA4 treatment, as obtained from the TISMO web tool. Significance levels are denoted as follows: *, **, and *** denote P values of < 0.05, < 0.01, and < 0.001, respectively. Based on drug sensitivity analysis in GDSC (Genomics of Drug Sensitivity in Cancer), the following are the top 15 drugs that are positively correlated **(C)** and negatively correlated **(D)** with PSME3 expression, as shown in the figure. *P<0.05, **P<0.01, NS (no significant differences).

for colorectal cancer based on mass spectrometry analysis as early as 2006 (31). It further indicated that PSME3 is a potential prognostic biomarker for various cancers.

PSME3 is a proteasomal activator that functions by activating the 20S proteasome to degrade proteins (32–34). Our functional enrichment analysis has revealed that PSME3 is involved in multiple biological functions, such as protein degradation, lipid metabolism, immune responses, and stem cell regulation, among others. These findings align with previous research, for example, PSME3 targets several key proteins involved in cell cycle regulation, including the cell cycle arrest protein P21, and two cell cycle-dependent kinase inhibitors, P16 and P14 (8, 35). Additionally, the deficiency of PSME3 disrupts the function of MDM2, leading to the stabilization of p53 and the upregulation of p21, consequently resulting in cell cycle arrest (9). PSME3 regulates autophagy and hepatocyte lipid metabolism by affecting Sirt1 (12).

The immune microenvironment plays a significant role in the TME (36). Immune cell invasions can either inhibit or promote the development and progression of tumors, including tumor escape, invasion, metastasis, and treatment (37, 38). Our results indicated an association between elevated PSME3 expression and the presence of CD8T, and M2 macrophages. Our research also unveiled the association of PSME3 with immune checkpoints, with experimental validation demonstrating that PSME3 positively regulates CD276 expression. This suggests that PSME3 might be a potential therapeutic target in immunotherapy.

Additionally, we predicted sensitive drugs targeting PSME3, providing crucial clues for future treatment strategies. In further analyses, we discovered a close correlation between high PSME3 expression and adverse clinical outcomes and cancer progression in LIHC. The independent prognostic value of PSME3 in LIHC was validated, underscoring its significance in assessing the prognosis of liver cancer patients. We also constructed a prognostic model based on PSME3, which exhibited high predictive performance. Finally, through experimental validation, we confirmed the impact of

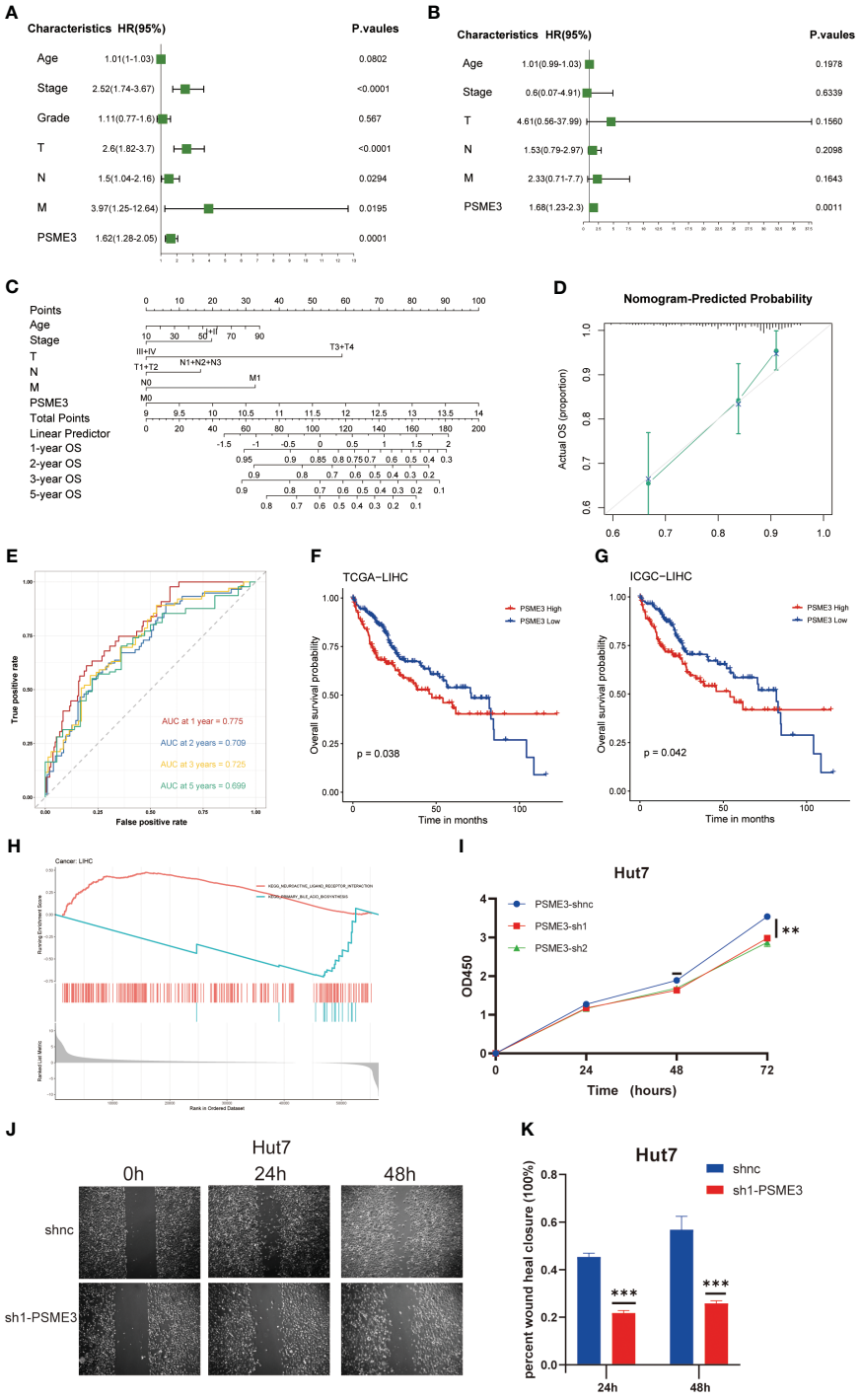

FIGURE 9
PSME3 as an independent predictor in LIHC. **(A, B)** Prognostic implications of PSME3 in liver carcinoma through univariate and multifactorial COX analysis. **(C)** Construction of a nomogram utilizing PSME3 expression. **(D)** Nomogram correction analysis diagram. **(E)** In the TCGA liver cancer cohort, calibration plots illustrating the 1-year, 2-year, 3-year, and 5-year OS probabilities were displayed (*p<0.05; **p<0.01; ***p<0.001; ****p<0.0001; ns p>0.05). Independent survival prognosis analysis of PSME3 in TCGA **(F)** and ICGC **(G)** datasets. **(H)** GSEA was performed with the KEGG signature of PSME3 in LIHC. Different color curves represent different functions or pathways. The peaks of the rising and falling curves indicate positive and negative regulation of PSME3, respectively. **(I)** Evaluation of PSME3 expression in the Hut7 liver cancer cell line using the CCK-8 assay. **(J, K)** Bar chart representing the quantified data of PSME3 expression in the Hut7 liver cancer cell line following scratch assay. *P < 0.05, **P < 0.01, ***P < 0.001 compared to the control group.

PSME3 on liver cancer cell proliferation and wound healing, further supporting its biological function in liver cancer.

In summary, our research revealed the multifaceted role of PSME3 in cancer biology, immune regulation, and clinical prognosis, providing crucial insights for the development of personalized cancer treatment strategies and immunotherapy research. PSME3 holds the potential to become a significant target in future cancer therapies, but further research is needed to elucidate its detailed mechanisms and application prospects.

5 Conclusion

PSME3 emerges as a key factor positively regulating the immune checkpoint CD276 in various cancers, including LIHC, LUAD, and BLCA. Therefore, it holds the potential to become a promising target for immunotherapy. Additionally, PSME3 has been confirmed as an independent prognostic factor in LIHC, impacting not only immune regulation but also aspects like liver cancer cell proliferation and wound healing. These discoveries provide crucial insights for the development of future cancer treatment strategies, with the potential to enhance the survival rates and overall quality of life for cancer patients.

Data availability statement

The original contributions presented in the study are included in the article/Supplementary Material. Further inquiries can be directed to the corresponding author.

Author contributions

CD: Conceptualization, Data curation, Methodology, Validation, Visualization, Writing – original draft, Writing – review & editing. YG: Supervision, Validation, Writing – review & editing. YY: Formal Analysis, Methodology, Writing – review & editing. XG: Conceptualization, Funding acquisition, Resources, Supervision, Writing – review & editing.

Funding

The author(s) declare financial support was received for the research, authorship, and/or publication of this article. The National Natural Science Foundation of China awarded grants for this project (81874198 and 82073086).

Acknowledgments

We thank Dr. Ping Wang's lab at Tongji University School of Medicine for their help.

Conflict of interest

The authors declare that the research was conducted in the absence of any commercial or financial relationships that could be construed as a potential conflict of interest.

Publisher's note

Supplementary material

The Supplementary Material for this article can be found online at: https://www.frontiersin.org/articles/10.3389/fimmu.2024.1295693/full#supplementary-material

SUPPLEMENTARY FIGURE 1
(A) Kaplan-Meier analysis of the relationship between high and low expression of PSME3 and OS(HR<1, P<0.05). **(B)** Kaplan-Meier analysis of the relationship between high and low expression of PSME3 and RFS (HR<1, P<0.05).

SUPPLEMENTARY FIGURE 2
Immune cell infiltration was assessed using various methods, including cell-type identification by estimating the relative subset of RNA transcripts (CIBERSORT) **(A)**, TIMER **(B)**, xCell **(C)**, and MCP-counter **(D)**. The results are presented in the form of a heatmap.

SUPPLEMENTARY FIGURE 3
The clinical correlation analysis of PSME3 with different ages and pathological stages. Single-cell analysis based on the LIHC-GSE98638 dataset: (left:) Provides an overview of the distribution of CD4Tconv, CD8T, CD8Tex, Tprolif, and Treg cells at the single-cell level. (center) Illustrates the expression distribution of PSME3 in LIHC. (right) Presents a violin plot depicting the single-cell expression profile based on PSME3.

References

1. Siegel RL, Miller KD, Fuchs HE, Jemal A. Cancer statistics, 2021. *CA: Cancer J Clin* (2021) 71(1):7–33. doi: 10.3322/caac.21654

2. Sung H, Ferlay J, Siegel RL, Laversanne M, Soerjomataram I, Jemal A, et al. Global cancer statistics 2020: GLOBOCAN estimates of incidence and mortality worldwide for 36 cancers in 185 countries. *CA: Cancer J Clin* (2021) 71(3):209–49. doi: 10.3322/caac.21660

3. Ansell SM, Lesokhin AM, Borrello I, Halwani A, Scott EC, Gutierrez M, et al. PD-1 blockade with nivolumab in relapsed or refractory Hodgkin's lymphoma. *N Engl J Med* (2015) 372(4):311–9. doi: 10.1056/NEJMoa1411087

4. Larkin J, Chiarion-Sileni V, Gonzalez R, Grob JJ, Cowey CL, Lao CD, et al. Combined nivolumab and ipilimumab or monotherapy in untreated melanoma. *N Engl J Med* (2015) 373(1):23–34. doi: 10.1056/NEJMoa1504030

5. Robert C, Ribas A, Wolchok JD, Hodi FS, Hamid O, Kefford R, et al. Anti-programmed-death-receptor-1 treatment with pembrolizumab in ipilimumab-refractory advanced melanoma: a randomised dose-comparison cohort of a phase 1 trial. *Lancet* (2014) 384(9948):1109–17:2014. doi: 10.1016/S0140-6736(14)60958-2

6. Brahmer JR, Tykodi SS, Chow LQ, Hwu WJ, Topalian SL, Hwu P, et al. Safety and activity of anti-PD-L1 antibody in patients with advanced cancer. *N Engl J Med* (2012) 366(26):2455–65. doi: 10.1056/NEJMoa1200694

7. Weinstein JN, Collisson EA, Mills GB, Shaw KR, Ozenberger BA, Ellrott K, et al. The Cancer Genome Atlas Pan-Cancer analysis project. *Nat Genet* (2013) 45(10):1113–20. doi: 10.1038/ng.2764

8. Li X, Amazit L, Long W, Lonard DM, Monaco JJ, O'Malley BW. Ubiquitin- and ATP-independent proteolytic turnover of p21 by the REGgamma-proteasome pathway. *Mol Cell* (2007) 26(6):831–42. doi: 10.1016/j.molcel.2007.05.028

9. Zhang Z, Zhang R. Proteasome activator PA28 gamma regulates p53 by enhancing its MDM2-mediated degradation. *EMBO J* (2008) 27(6):852–64. doi: 10.1038/emboj.2008.25

10. Sun J, Luan Y, Xiang D, Tan X, Chen H, Deng Q, et al. The 11S proteasome subunit PSME3 is a positive feedforward regulator of NF-κB and important for host defense against bacterial pathogens. *Cell Rep* (2016) 14(4):737–49. doi: 10.1016/j.celrep.2015.12.069

11. Guo J, Hao J, Jiang H, Jin J, Wu H, Jin Z, et al. Proteasome activator subunit 3 promotes pancreatic cancer growth *via* c-Myc-glycolysis signaling axis. *Cancer Lett* (2017) 386:161–7. doi: 10.1016/j.canlet.2016.08.018

12. Dong S, Jia C, Zhang S, Fan G, Li Y, Shan P, et al. The REGγ proteasome regulates hepatic lipid metabolism through inhibition of autophagy. *Cell Metab* (2013) 18(3):380–91. doi: 10.1016/j.cmet.2013.08.012

13. Li L, Zhao D, Wei H, Yao L, Dang Y, Amjad A, et al. REGγ deficiency promotes premature aging *via* the casein kinase 1 pathway. *Proc Natl Acad Sci U States A* (2013) 110(27):11005–10. doi: 10.1073/pnas.1308497110

14. Sun L, Fan G, Shan P, Qiu X, Dong S, Liao L, et al. Regulation of energy homeostasis by the ubiquitin-independent REGγ proteasome. *Nat Commun* (2016) 7:12497. doi: 10.1038/ncomms12497

15. Liu S, Lai L, Zuo Q, Dai F, Wu L, Wang Y, et al. PKA turnover by the REGγ-proteasome modulates FoxO1 cellular activity and VEGF-induced angiogenesis. *J Mol Cell Cardiol* (2014) 72:28–38. doi: 10.1016/j.yjmcc.2014.02.007

16. Li X, Lonard DM, Jung SY, Malovannaya A, Feng Q, Qin J, et al. The SRC-3/AIB1 coactivator is degraded in a ubiquitin- and ATP-independent manner by the REGgamma proteasome. *Cell* (2006) 124(2):381–92. doi: 10.1016/j.cell.2005.11.037

17. Liu J, Yu G, Zhao Y, Zhao D, Wang Y, Wang L, et al. REGgamma modulates p53 activity by regulating its cellular localization. *J Cell Sci* (2010) 123(Pt 23):4076–84. doi: 10.1242/jcs.067405

18. Anderson NM, Simon MC. The tumor microenvironment. *Curr Biol CB* (2020) 30(16):R921–r5. doi: 10.1016/j.cub.2020.06.081

19. Binnewies M, Roberts EW, Kersten K, Chan V, Fearon DF, Merad M, et al. Understanding the tumor immune microenvironment (TIME) for effective therapy. *Nat Med* (2018) 24(5):541–50. doi: 10.1038/s41591-018-0014-x

20. Picard E, Verschoor CP, Ma GW, Pawelec G. Relationships between immune landscapes, genetic subtypes and responses to immunotherapy in colorectal cancer. *Front Immunol* (2020) 11:369. doi: 10.3389/fimmu.2020.00369

21. Schizas D, Charalampakis N, Kole C, Economopoulou P, Koustas E, Gkotsis E, et al. Immunotherapy for pancreatic cancer: A 2020 update. *Cancer Treat Rev* (2020) 86:102016. doi: 10.1016/j.ctrv.2020.102016

22. Borrebaeck CA. Precision diagnostics: moving towards protein biomarker signatures of clinical utility in cancer. *Nat Rev Cancer* (2017) 17(3):199–204. doi: 10.1038/nrc.2016.153

23. Sawyers CL. The cancer biomarker problem. *Nature* (2008) 452(7187):548–52. doi: 10.1038/nature06913

24. Chen H, Gao X, Sun Z, Wang Q, Zuo D, Pan L, et al. REGγ accelerates melanoma formation by regulating Wnt/β-catenin signalling pathway. *Exp Dermatol* (2017) 26 (11):1118–24. doi: 10.1111/exd.13394

25. Kontos CK. Surrogate prognostic biomarkers in OSCC: the paradigm of PA28γ Overexpression. *EBioMedicine* (2015) 2(8):784–5. doi: 10.1016/j.ebiom.2015.07.032

26. Liu S, Zheng LL, Zhu YM, Shen HJ, Zhong Q, Huang J, et al. Knockdown of REGγ inhibits the proliferation and migration and promotes the apoptosis of multiple myeloma cells by downregulating NF-κB signal pathway. *Hematol (Amsterdam Netherlands)* (2018) 23(5):277–83. doi: 10.1080/10245332.2017.1385194

27. Okamura T, Taniguchi S, Ohkura T, Yoshida A, Shimizu H, Sakai M, et al. Abnormally high expression of proteasome activator-gamma in thyroid neoplasm. *J Clin Endocrinol Metab* (2003) 88(3):1374–83. doi: 10.1210/jc.2002-021413

28. Qi L, He W. REGγ Is associated with lymph node metastasis and T-stage in papillary thyroid carcinoma. *Med Sci Monit* (2018) 24:1373–8. doi: 10.12659/MSM.905664

29. He J, Cui L, Zeng Y, Wang G, Zhou P, Yang Y, et al. REGγ is associated with multiple oncogenic pathways in human cancers. *BMC Cancer* (2012) 12:75. doi: 10.1186/1471-2407-12-75

30. Yi Z, Yang D, Liao X, Guo F, Wang Y, Wang X. PSME3 induces epithelial-mesenchymal transition with inducing the expression of CSC markers and immunosuppression in breast cancer. *Exp Cell Res* (2017) 358(2):87–93. doi: 10.1016/j.yexcr.2017.05.017

31. Roessler M, Rollinger W, Mantovani-Endl L, Hagmann ML, Palme S, Berndt P, et al. Identification of PSME3 as a novel serum tumor marker for colorectal cancer by combining two-dimensional polyacrylamide gel electrophoresis with a strictly mass spectrometry-based approach for data analysis. *Mol Cell Proteomics MCP* (2006) 5 (11):2092–101. doi: 10.1074/mcp.M600118-MCP200

32. Ciechanover A. The ubiquitin-proteasome pathway: on protein death and cell life. *EMBO J* (1998) 17(24):7151–60. doi: 10.1093/emboj/17.24.7151

33. Mao I, Liu J, Li X, Luo H. REGgamma, a proteasome activator and beyond? *Cell Mol Life Sci CMLS* (2008) 65(24):3971–80. doi: 10.1007/s00018-008-8291-z

34. Ben-Nissan G, Sharon M. Regulating the 20S proteasome ubiquitin-independent degradation pathway. *Biomolecules* (2014) 4(3):862–84. doi: 10.3390/biom4030862

35. Chen X, Barton LF, Chi Y, Clurman BE, Roberts JM. Ubiquitin-independent degradation of cell-cycle inhibitors by the REGgamma proteasome. *Mol Cell* (2007) 26 (6):843–52. doi: 10.1016/j.molcel.2007.05.022

36. Wu T, Dai Y. Tumor microenvironment and therapeutic response. *Cancer Lett* (2017) 387:61–8. doi: 10.1016/j.canlet.2016.01.043

37. Galli F, Aguilera JV, Palermo B, Markovic SN, Nisticò P, Signore A. Relevance of immune cell and tumor microenvironment imaging in the new era of immunotherapy. *J Exp Clin Cancer Res CR* (2020) 39(1):89. doi: 10.1186/s13046-020-01586-y

38. Man YG, Stojadinovic A, Mason J, Avital I, Bilchik A, Bruecher B, et al. Tumor-infiltrating immune cells promoting tumor invasion and metastasis: existing theories. *J Cancer* (2013) 4(1):84–95. doi: 10.7150/jca.5482

frontiers | Frontiers in Immunology

TYPE Original Research
PUBLISHED 26 January 2024
DOI 10.3389/fimmu.2024.1258475

OPEN ACCESS

EDITED BY
Takaji Matsutani,
Maruho, Japan

REVIEWED BY
Silvia D'Amico,
National Research Council (CNR), Italy
Xiufei Chen,
University of Oxford, United Kingdom

*CORRESPONDENCE
Haigang Jin
jhgwzxshp@163.com
Zhenyu Wang
wzyxshp@163.com

†These authors have contributed equally to this work

RECEIVED 14 July 2023
ACCEPTED 04 January 2024
PUBLISHED 26 January 2024

CITATION
Li P, Wang S, Wan H, Huang Y, Yin K, Sun K, Jin H and Wang Z (2024) Construction of disulfidptosis-based immune response prediction model with artificial intelligence and validation of the pivotal grouping oncogene c-MET in regulating T cell exhaustion.
Front. Immunol. 15:1258475.
doi: 10.3389/fimmu.2024.1258475

Construction of disulfidptosis-based immune response prediction model with artificial intelligence and validation of the pivotal grouping oncogene c-MET in regulating T cell exhaustion

Pengping Li[1†], Shaowen Wang[2†], Hong Wan[3†], Yuqing Huang[1], Kexin Yin[1], Ke Sun[1], Haigang Jin[1*] and Zhenyu Wang[1*]

[1]Department of Thyroid and Breast Surgery, The First People's Hospital of Xiaoshan District, Xiaoshan Affiliated Hospital of Wenzhou Medical University, Hangzhou, Zhejiang, China, [2]Neuromedicine Center, The University of Hong Kong-Shenzhen Hospital, Shenzhen, Guangdong, China, [3]Department of General Surgery, Breast Surgery, The First Affiliated Hospital of Anhui Medical University, Hefei, China

Background: Given the lack of research on disulfidptosis, our study aimed to dissect its role in pan-cancer and explore the crosstalk between disulfidptosis and cancer immunity.

Methods: Based on TCGA, ICGC, CGGA, GSE30219, GSE31210, GSE37745, GSE50081, GSE22138, GSE41613, univariate Cox regression, LASSO regression, and multivariate Cox regression were used to construct the rough gene signature based on disulfidptosis for each type of cancer. SsGSEA and Cibersort, followed by correlation analysis, were harnessed to explore the linkage between disulfidptosis and cancer immunity. Weighted correlation network analysis (WGCNA) and Machine learning were utilized to make a refined prognosis model for pan-cancer. In particular, a customized, enhanced prognosis model was made for glioma. The siRNA transfection, FACS, ELISA, etc., were employed to validate the function of c-MET.

Results: The expression comparison of the disulfidptosis-related genes (DRGs) between tumor and nontumor tissues implied a significant difference in most cancers. The correlation between disulfidptosis and immune cell infiltration, including T cell exhaustion (Tex), was evident, especially in glioma. The 7-gene signature was constructed as the rough model for the glioma prognosis. A pan-cancer suitable DSP clustering was made and validated to predict the prognosis. Furthermore, two DSP groups were defined by machine learning to predict the survival and immune therapy response in glioma, which was validated in CGGA. PD-L1 and other immune pathways were highly enriched in the core blue gene module from WGCNA. Among them, c-MET was validated as a tumor driver gene and JAK3-STAT3-PD-L1/PD1 regulator in glioma and T cells. Specifically, the down-regulation of c-MET decreased the proportion of PD1+ CD8+ T cells.

Conclusion: To summarize, we dissected the roles of DRGs in the prognosis and their relationship with immunity in pan-cancer. A general prognosis model based on machine learning was constructed for pan-cancer and validated by external datasets with a consistent result. In particular, a survival-predicting model was made specifically for patients with glioma to predict its survival and immune response to ICIs. C-MET was screened and validated for its tumor driver gene and immune regulation function (inducing t-cell exhaustion) in glioma.

KEYWORDS

disulfidptosis, tumor immunity, prognosis prediction, artificial intelligence (AI), glioma

1 Background

Regulated cell death (RCD) refers to a controlled and orderly type of cellular death (1, 2). The subtypes of these death modalities have been enriched with more and more RCDs uncovered, for instance, apoptosis (3–5), autophagy (6–8), necroptosis (9), ferroptosis (10), pyroptosis (11), cuproptosis (12), disulfidptosis (13), etc. Disulfidptosis is the latest type of RCD proposed in 2023 by Gan et al. (13). What distinguishes it from other forms of cell death is the feature that the aberrant accumulation of disulfides without enough nicotinamide adenine dinucleotide phosphate (NADPH) supply from glucose can induce this specific cell death (13–17). Disulfidptosis holds potential as an alternative therapeutic tactic for patients resistant to existing therapies.

Cancer is a notoriously formidable disease that is characterized by abnormal growth and division. Many types of cancer can metastasize to surrounding tissues or even distant organs. Until now, 14 hallmarks of cancer have been discovered, which have been summarized well by Douglas Hanahan (18). Resisting cell death, as one of the classical hallmarks, is always the fundamental and final objective for all other hallmarks. With each discovery of an innovative modality of cell death from apoptosis to cuproptosis, our understanding of cancer will be expanded further in that perspective. Numerous RCD-related prognostic signatures have been made and validated by different researchers. In the recent decade, ferroptosis (19, 20), pyroptosis (21–23), cuproptosis (24–27) have been well-explored in many types of cancer based on the cancer genome atlas (TCGA), gene expression omnibus (GEO), international cancer genome consortium (ICGC), etc. These studies give us a deeper understanding of RCD in the context of cancer.

Machine learning (ML), a subdomain of artificial intelligence (AI), can be divided into supervised, unsupervised, and reinforcement learning. In the era of big data, it can be applied everywhere (28, 29). And in oncology, ML techniques have also been employed to gain insights into the complex interactions between tumors and the immune system. For instance, in lymphoma, artificial neural networks were taken advantage of to construct an immune-oncology panel to differentiate molecular subtypes and predict prognosis (30). In solid tumors, ML-assisted analysis based on genomics or radiomics also gives us better models to identify treatment success rates (31–34).

However, to our knowledge, there are only limited studies on disulfidptosis. Given the lack of research on this phenomenon, our study aimed to delve into the role of disulfidptosis in pan-cancer relying on well-recognized databases by constructing a prognostic signature related to disulfidptosis. We mainly focused on investigating the crosstalk between disulfidptosis and tumor immune responses.

2 Methods

2.1 Data collection

Clinical features and gene expression of TCGA, ICGC, and PCAWG patients were obtained in UCSC Xena (http://xena.ucsc.edu). The validated transcriptomic data and clinical characteristics from glioma were fetched from CGGA (http://www.cgga.org.cn). The external gene expression and prognosis datasets of LUAD, UVM, and HNSC (GSE30219, GSE31210, GSE37745, GSE50081, GSE22138, GSE41613) were downloaded from GEO (https://www.ncbi.nlm.nih.gov/geo/). DRGs (ACTB, TLN1, CAPZB, STN, FLNB, IQGAP1, ACTN4, MYL6, FLNA, MYH9, MYH10, PDLIM1, CD2AP, and INF2) were extracted from Gan et al.' disulfidptosis paper (13). Different immune cell infiltration markers were obtained from the cancer immunome atlas (TCIA) (35), Genecard (https://www.genecards.org/), GEPIA (http://gepia2.cancer-pku.cn/#index), Cibersot (https://cibersortx.stanford.edu/). The prognosis of different c-MET level glioblastoma patients treated with anti-PD1 therapy was obtained from Kaplan Meier-plotteR (http://kmplot.com/analysis/index.php?p=background).

2.2 Bioinformatic analysis

2.2.1 Pathway score calculation and immune cell infiltration

ssGSEA was used to assess immune activity, function, and programmed cell death pathways in each sample. Immune cell marker genes were used for analysis. ESTIMATE calculated immune, stromal, estimate scores, and tumor purity based on immune and stromal cell proportions. TIMER and CIBERSORT predicted infiltrating immune cell composition. Immune checkpoint inhibitors were compared across clusters and risk groups. By analyzing ssGSEA, ESTIMATE, immune cell infiltration, and immune checkpoints, we gained a comprehensive understanding of the tumor immune landscape. Infiltration immune cell fractions were calculated in CIBERSORT in R4.2.0, and the estimate package in R4.2.0 predicted the immune score.

2.2.2 Prognosis model construction

Univariate Cox regression, LASSO regression, and multivariate Cox regression were used to construct the gene signature. The previous survival and ROC analyses were made using survival and survivalROC packages in R4.2.0.

2.2.3 DRGs-based subgroups identification

ConsensusClusterPlus package in R4.2.0 was used to perform consensus clustering analysis based on the DRGs (parameter: maxK=10, reps=50). AI modeling for DRGs-based prognosis model was developed by six AI functions, including extreme gradient boosting (XGboost, xgboost package in R4.2.0), support vector machine (SVM, e1071 packages in R4.2.0), multi-logistic (nnet packages in R4.2.0), random forest (RF, randomForest package in R4.2.0), deep learning (DL, h2o package in R4.2.0) and K-Nearest Neighbor (KNN, kknn package in R4.2.0). During the model construction, randomly select 75% as the training cohort and randomly select 25% as the testing cohort. Gene expression value was standardized to range "0~1" with preProcess function (caret and tidyverse packages).

2.2.4 Tumor mutation analysis

We analyzed somatic mutations in TCGA data using "maftools" and calculated TMB for each group. Furthermore, we visualized somatic mutations of selected genes in the signature using cBioPortal. This analysis helped understand mutations and their potential role in disulfidptosis.

2.2.5 Drug sensitivity prediction

Drug sensitivity prediction was performed by the oncoPredict package in R4.2.0. This package leverages machine learning algorithms trained on large datasets of cancer cell lines to estimate the response of individual patient tumors to a wide range of therapeutic agents. By analyzing the gene expression profiles of the tumor samples, oncoPredict can identify potential therapeutic targets and guide personalized treatment strategies.

2.3 Biological experiments

2.3.1 Cell culture and reagents

Ln299 and Jurkat cell lines were purchased from the Chinese Academy of Science cell bank with STR matching analysis. Cells were cultured in recommended conditions. Co-culture was done by placing the transwell containing Jurkat cells (2.5×10^5) or alive PBMC (2.5×10^5) in the 6-well plate seeded with ln299 cells (20 x 10^4). Cabozantinib (BMS-907351) was purchased from Selleck.

2.3.2 SiRNA transfection

Ln299 cells were transfected with c-MET small interfering RNA (siRNA) (5′-AAG GAC CGG UUC AUC AAC UUC-3′) or non-targeting negative control siRNA (RiboBio, China) using LipofectamineTM 3000 (Invitrogen, USA) according to the manufacturer's protocol.

2.3.3 5-ethynyl-2′-deoxyuridine and live/dead staining

The live/dead staining kit was purchased from YEASEN Biotech, the Edu staining kit was purchased from APExBIO (K1077), and OPTI-MEM was purchased from (ThermoFisher, Gibco). 1×10^5 ln299 cells were seeded into 24-well plates. The treated cells were stained according to the kits' instructions and then observed under an inverted microscope.

2.3.4 Western blotting

Total cellular proteins were extracted using lysis buffer (5 mM EDTA, 300 mM NaCl, 0.1% NP-40, 0.5 mM NaF, 0.5 mM Na3VO4, 0.5 mM PMSF, and 10 μg/mL each of aprotinin, pepstatin, and leupeptin; Sigma-Aldrich). 30–50 μg protein was separated using 10% SDS-PAGE and transferred to polyvinylidene difluoride membranes (Millipore, Bedford, MA, USA). Then immunoblotting was performed using antibodies against c-MET (25869-1-AP, Proteintech), PD-L1 (28076-1-AP, Proteintech), p-JAK3 (29101-1-AP, Proteintech), JAK3 (80331-1-RR, Proteintech), p-STAT3 (#9145, Cell Signaling Technology), STAT3 (#9139, Cell Signaling Technology), GAPDH (AF7021, Affinity Biosciences), IL-2 (16806-1-AP, Proteintech), INF-γ (15365-1-AP, Proteintech), PD1 (18106-1-AP, Proteintech), beta-tubulin (10068-1-AP, Proteintech). The immunoblots were visualized using an enhanced chemiluminescence detection system (Amersham Pharmacia Biotech, Uppsala, Sweden).

2.3.5 PBMCs extraction

Simply, PBMCs were isolated via Ficoll-Paque density gradient centrifugation: 5 mL of peripheral blood was collected from healthy female volunteers, diluted with PBS at a 1:1 ratio, followed by gentle mixing. Add 10 mL of the diluted blood to 2 mL of Ficoll liquid (density 1.077). The clear stratification of blood and Ficoll liquid confirmed success. Carefully transferred the sample to the centrifuge and spin at 500 g for 15 minutes. Removed the centrifuge tube with care, aspirate the white thin film layer in the

middle, representing individual nucleated cells. Wash the isolated nucleated cells with 10 mL of PBS, centrifuge at 250 g for 10 minutes, and discarded the supernatant. Repeat the washing step once and the suspended cells were frozen in vials at 100 million cells/mL in HI FBS with 5% DMSO after washing. Stored in liquid nitrogen, they were revived gradually and washed in pre-warmed RPMI with FBS and pen/strep. Following a 4-5 hour incubation at 37°C, viability was assessed using Trypan blue (0.1%).

2.3.6 Flow cytometry

The co-cultured PBMC were stained with Fixable Viability Stain (Thermo, L34965) and Fc receptor blocking reagent [Ultra-LEAF™ Purified anti-mouse CD16/32 (101320, BioLegend)]. Next, they were stained with CD-3 (BD 557943), PD-1 (BD 561273), and CD8 antibody (thermo, A15448). The prepared single-cell suspensions were filtered through 40-μm nylon meshes (352340, Corning). Results were then acquired using BD Calibur, BD Fortessa, or Miltenyi MACSQuant systems. Data were analyzed with FlowJo_V10 software (TreeStar).

2.3.7 ELISA

Supernatants from PBMC co-cultured with glioma cell line were collected and analyzed using ELISA kits for IL2(Proteintech, KE00017), IFN-γ (Proteintech, KE00146), CXCR9 (Proteintech, KE00165). The levels of each cytokine were compared between the c-MET knockdown group and control groups.

2.4 Statistical analysis

Statistical analyses were performed with R (4.2.0) and GraphPad Prism (version 8.0.1). Discontinuous data were expressed as numbers/percentages, and continuous data were expressed as mean ± standard deviation (SD). $P < 0.05$ was considered a statistically significant difference.

3 Results

3.1 The expression landscape and prognosis significance of DRGs in pan-cancer

In TCGA, the 14 validated disulfidptosis-related genes (DRGs) - ACTB, TLN1, CAPZB, STN, FLNB, IQGAP1, ACTN4, MYL6, FLNA, MYH9, MYH10, PDLIM1, CD2AP, and INF2 - were generally expressed in all 33 types of cancer (Figure 1A). The correlation analysis between the DRGs indicated that MYH9 and ACTN4 were the most positively related gene pair, while MYH10 and PDL1M1 were the most negatively related (Figure 1B). And the DRGs' expression comparison between tumor and nontumor tissues implied a significant difference in most types of them (Figure 1C). MYH10 showed the highest 2.34-fold change between glioma and normal brain tissues among all the DRGs (Figure 1D). Moreover, the univariate Cox regression of the DRGs showed that almost all 14 DRGs could predict prognosis well in patients with glioma, kidney carcinoma (KCA), kidney renal clear cell carcinoma (KIRC), etc. (Figure 1E). Interestingly, DRGs were the completely hazardous factors in glioma (Figure 1F).

3.2 The correlation between immunity and disulfidptosis in pan-cancer

Following the ssGSEA analysis of different immune cell infiltration and programmed cell death, the correlation analysis indicated a strong association between disulfidptosis and most immune cells. For the most significant glioma, the R-value between disulfidptosis and exhausted T cells (TEX_Genecard), central memory CD8 T cell, effector memory CD8 T cell, gamma delta T cell, regulatory T cell, macrophage was over 0.5 (Figure 2A). Interestingly, the correlation between disulfidptosis and other modalities of cell death like ferroptosis (R-value = 0.651), necroptosis (R-value = 0.612), pyroptosis (R-value = 0.609), immunogenic cell death (ICD) (R-value = 0.559) are also very high in glioma compared with other types of cancer (Figure 2A). The univariate Cox regression indicated that T cell exhaustion (Tex), immature B cell infiltration, etc., were the dangerous factors in glioma patients. In contrast, the activated NK cells' infiltration was a beneficial factor for survival (Figure 2B). More importantly, a higher T cell exhaustion (TEX_GEPIA or TEX_Genecard) could predict a lousy prognosis in the glioma cohort from TCGA (Figure 2C).

3.3 Gene signature construction based on disulfidptosis for prognosis of patients with cancer

The univariate Cox regression, least absolute shrinkage and selection operator (LASSO) regression, and multivariate Cox regression were used to construct a gene signature for each type of cancer. Except for thyroid cancer (THCA) and uveal melanoma (UVM), the gene signatures that could predict the prognosis for patients with all other types of cancer, respectively, were successfully made (Figure 3). For the top 6 gene signatures ranked by c-index, i.e., the gene signature in adrenocortical carcinoma (ACC), pheochromocytoma and paraganglioma (PCPG), lymphoid neoplasm diffuse large B-cell lymphoma (DLBC), prostate adenocarcinoma (PRAD), kidney chromophobe (KICH), and thymoma (THYM), the receiver operating characteristic (ROC) curves showed a very high area under the curve (AUC) for 1-year, 2-year, 3-year, 4-year, and 5-year survival (Figure 3). And in glioma that showed the most outstanding relation between disulfidptosis and immune cell infiltration (Figures 2A, B), its 7-gene signature (risk score = 1.56709174 * APOBEC3C + (-3.2556028) * GLUD1 + (-2.0800874) * KIAA1671 + 1.08729963 * KIF4A + (-7.9141641) * RPL3 + 1.83720741 * TAGLN2 + 1.89252831 * TSPAN31) (Figures 4A–C) was further validated by dividing the TCGA cohort into a training group and a testing group. And both the

10.3389/fimmu.2024.1258475

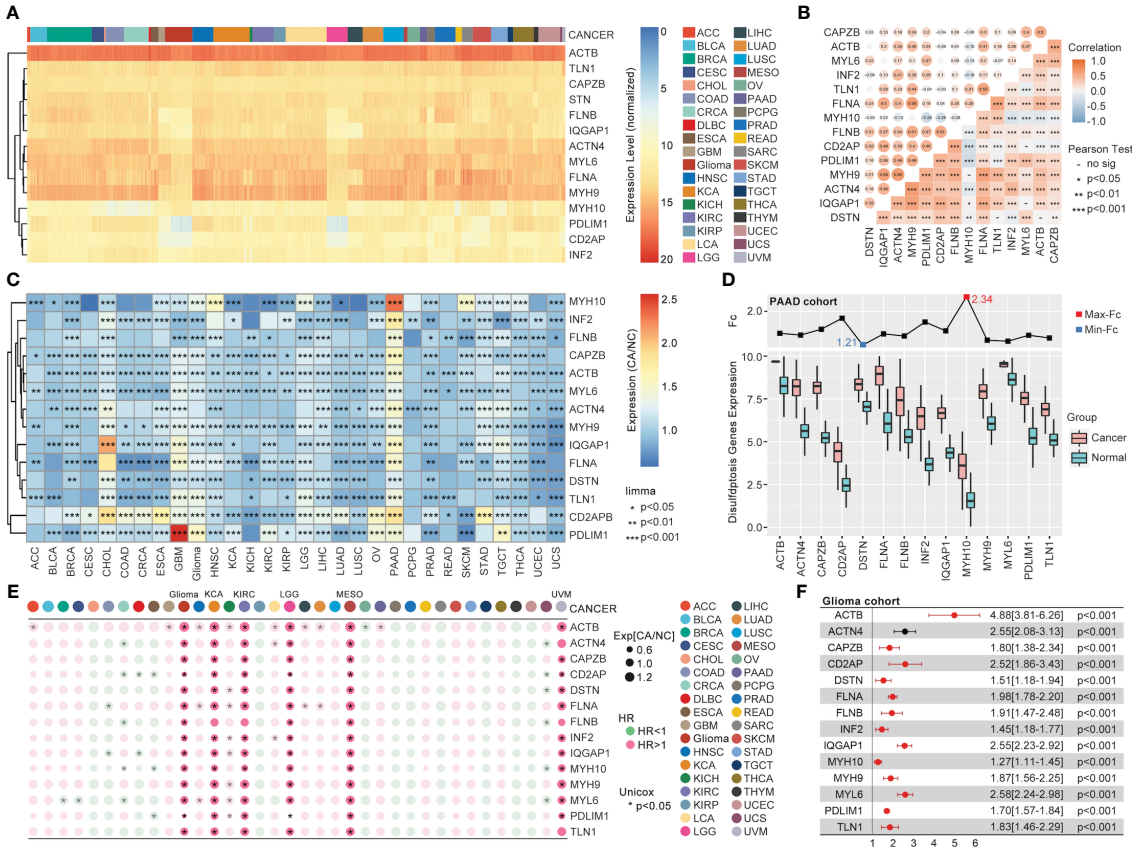

FIGURE 1
The pan-cancer landscape of DRGs. **(A)** The expression of 14 validated DRGs in all types (36) of cancer from TCGA. **(B)** The expression correlation analysis of DRGs, in which no significance of correlation was observed between MYH9 and MYH10, DSTN and TLN1, CD2AP and MYL6, IQGAP1 and MYL6, DSTN and ACTB. **(C)** The expression difference of DRGs between tumor samples (TCGA) and non-tumor samples (para tumor from TCGA + normal tissues from GTEx) in each type of cancer, expression difference existed in all DRGs in GBM, PAAD, PRAD, and TGCT. **(D)** The expression comparison between glioma tissues from TCGA and normal brain tissues from GTEx. **(E)** Univariate Cox regression analysis of DRGs in each type of cancer. **(F)** Univariate Cox regression analysis of DRGs in glioma, in which all DRGs were risk factors in glioma (HR>1, P<0.001).

Kaplan–Meier (KM) analysis and ROC curve (0.5-year, 1-year, 3-year, 5-year, and 10-year) indicated significant results in the training group, testing group, and the whole group (Figures 4D, E). Then, the multivariant Cox analysis of the gene signature and the clinical characteristics implied that the gene signature was an independent hazard factor for the prognosis of patients with glioma (Figure 4F). The nomogram indicated the relation of age, gender, DRGs gene signature, and the survival probability (0.5-year, 1-year, 3-year, 5-year, 7-year, and 10-year) for glioma patients (Figure 4G). Furthermore, the model based on age, gender, and DRGs gene signature was validated in the Chinese Glioma Genome Atlas (CGGA) with AUC over 0.72 (Figure 4I). In both glioma patients from TCGA and CGGA, there was a consistency between the predictive model and survival rate in the real world (Figures 4J, K).

3.4 Unsupervised pan-cancer clustering analysis based on DRGs and tumor mutation burden comparison

The unsupervised clustering analysis based on the 14 DRGs' expression was used to categorize the TCGA cohort into disulfidptosis (DSP)1, DSP2, and DSP3 groups (Figures 5A–E). The KM analysis suggested the DSP groups had significantly different survival in the disease-free interval (DFI), disease-specific survival (DSS), overall survival (OS), and progression-free interval (PFI) (Figure 5F). In line with the KM analysis of pan-cancer, the KM analysis or univariate Cox regression in individual cancer type indicated that the 3 DSP clusters could serve as a significant survival-related factor in colon adenocarcinoma (COAD), CRCA [COAD + rectum adenocarcinoma (READ)], glioblastoma multiforme (GBM), glioma, head and neck squamous cell carcinoma (HNSC), kidney chromophobe (KICH), kidney renal clear cell carcinoma (KIRC), lung adenocarcinoma (LUAD), lung carcinoma (LCA), stomach adenocarcinoma (STAD), uterine corpus endometrial carcinoma (UCEC), and uveal melanoma (UVM) (Figures 5G–I). Next, the top 10 mutated genes (TP53, TTN, MUC16, etc.) were listed and compared among DSP1, DSP2, and DSP3 groups (Figures 6A, C). Besides, the disulfidptosis, stromal score, immune score, tumor purity, Tex, and tumor mutation burden (TMB) were significantly different among the 3 DSP groups (Figure 6B). Since the previous 7-gene model included APOEBC3C, the TMB between APOBEC-enriched and APOBEC-unenriched groups was also compared in

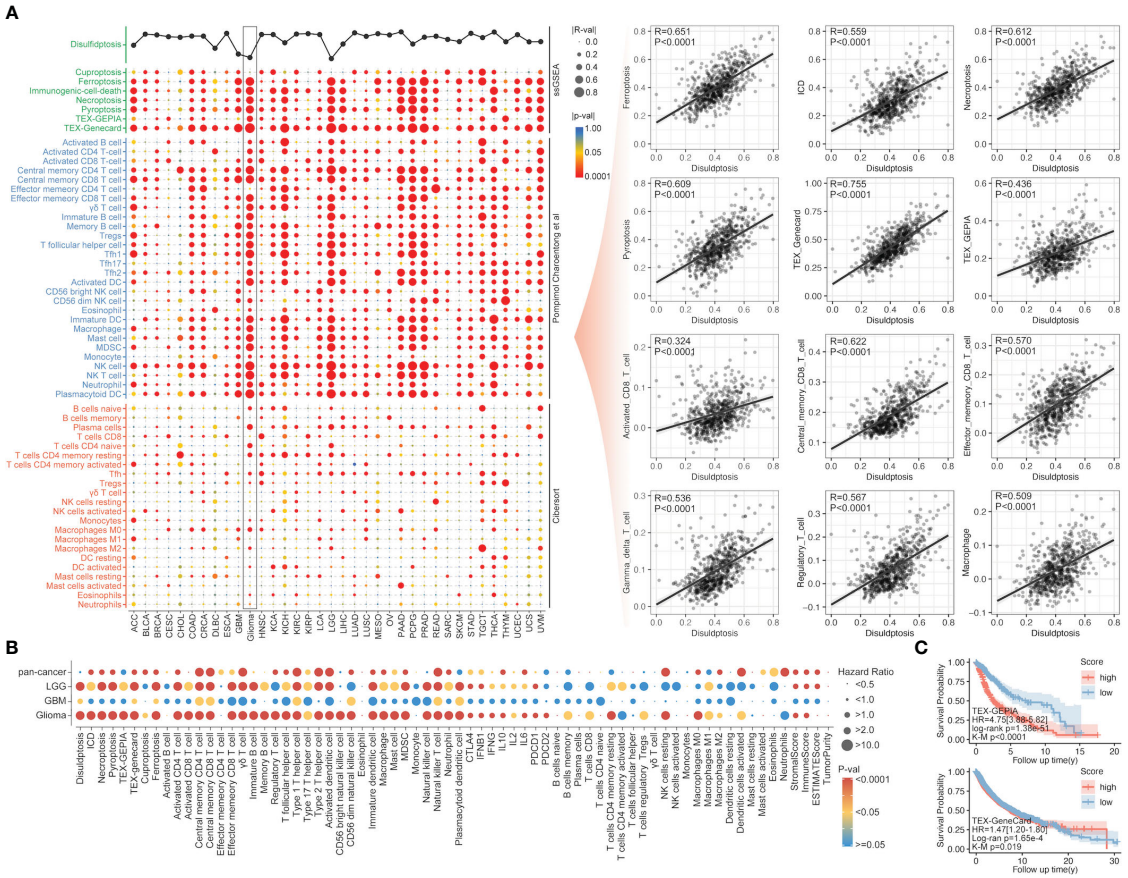

FIGURE 2
The correlation of immunity and other PCDs with disulfidptosis. **(A)** The correlation analysis between disulfidptosis and immune cell infiltration/other PCDs, in which disulfidptosis score was positively correlated with PCDs, including ferroptosis, ICD, necroptosis, and pyroptosis, and disulfidptosis was positive correlated with TEX, CD8+ T cells. **(B)** The univariate Cox regression of disulfidptosis, immune cell infiltration, and other PCDs in glioma, LGG, GBM, and pan-cancer. **(C)** The Kaplan–Meier survival analysis of Tex_GEPIA and Tex_GeneCard in pan-cancer, a higher score of both parameters was accompanied by worse prognosis in glioma (p<0.0001) evaluated by K-M analysis or unicox regression analysis.

each DSP group (Figure 6D). Immune cell infiltration and immune molecules differed greatly among the 3 DSP groups (Figures 6E, F). Each cancer type's total T-cell infiltration ratio was also listed to give a whole landscape (Figure 6G). In particular, the glioma, in which DRGs models showed the most significant relationship with survival and immunity, implicated a significant difference in disulfidptosis, Tex_GEPIA, Tex_genecard, CD8 (+) T cell subtypes, immune score, and tumor purity between the two DSP subgroups (Figures 6H–J).

3.5 Refined DSP models construction and validation by WGCNA and machine learning in pan-cancer

The weighted correlation network analysis (WGCNA) was used to extract the gene module most associated with disulfidptosis, immune cell infiltration, etc. (Figures 7A–C). Next, the ten hub genes (PRSS8, CRB3, ILDR1, ELF3, TMEM184A, AP1M2, TMC4, TJP3, CLDN7, HOXB7) within this cyan module were further abstracted by the STRING database and cytoHubba (Figures 7D, E). The refined DSP models based on the ten hub genes were then constructed by employing the best method of machine learning-randomForest, in which the training and testing cohorts have the highest AUC (Figure 7F). Moreover, compared with the original DSP groups, it could better predict the prognosis in pan-cancer patients (Figure 7G). The refined DSP models could differentiate the prognosis more evidently in patients with glioma (Figure 7H). After that, the new DSP model was also validated in pan-cancer cohorts from PCAWG and ICGC, glioma from CGGA, LUAD from GEO (GSE30219, GSE31210, GSE37745, GSE50081), and UVM from GEO (GSE22138) with significant p-value (Figures 8A–F).

3.6 Enhanced refined DSP models construction in glioma

Since the refined DSP model performed exceptionally well in glioma among all the types of cancer, the unsupervised consensus clustering and non-negative matrix factorization (NMF) clustering were further utilized to categorize the DRGs into different groups (Figures 9A, C). Finally, the more practical and evident two-DSP-group classification by the NMF method was chosen for further construction of gene signature. Compared with a lack of

10.3389/fimmu.2024.1258475

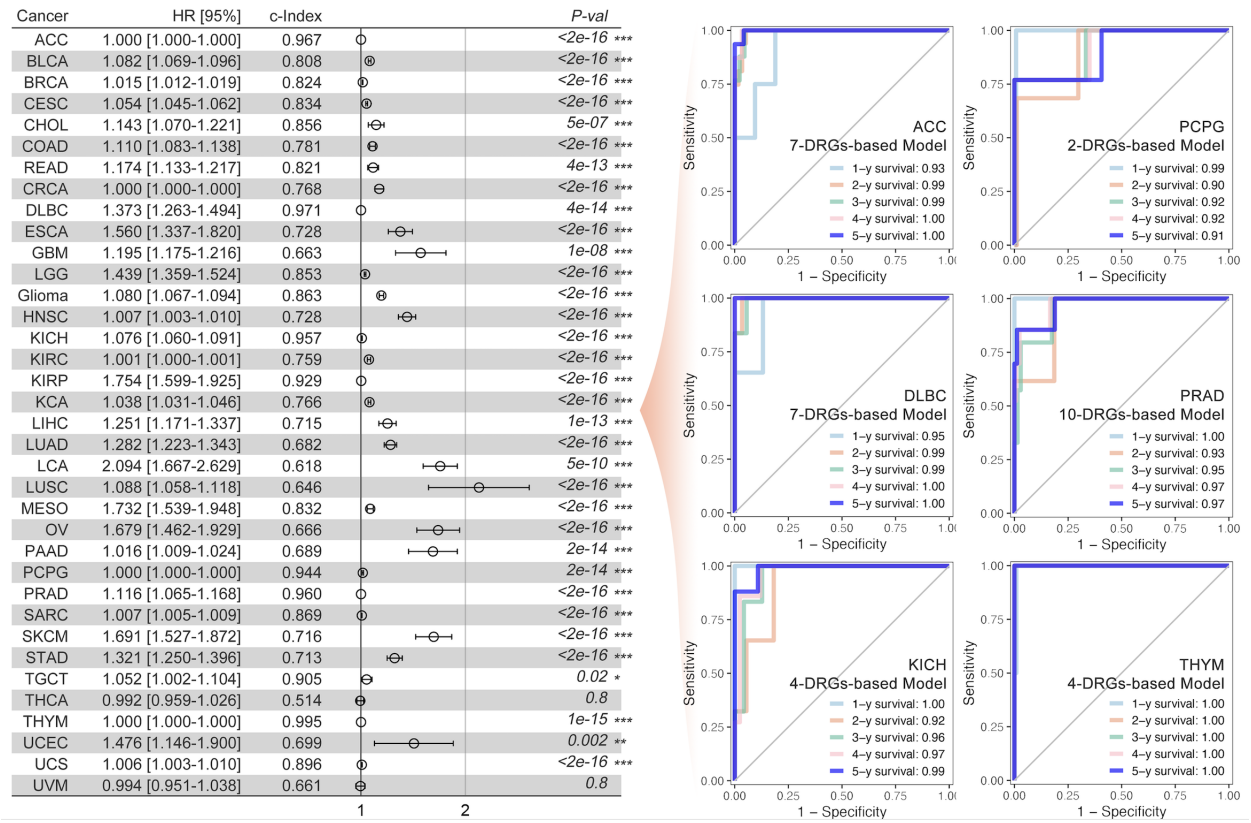

FIGURE 3
DRGs-based prognosis model and ROC curve. The DRGs-based gene signature for prognosis was constructed for each type of cancer (the left part), and the multi-gene-based model index was greater than 0.9 in ACC, DLBC, KICH, KIRP, PCPG, THYM, and TGCT. Multi-gene-based models for all cancer types were significantly constructed. The 1-year, 2-year, 3-year, 4-year, and 5-year ROC curve of the abovementioned gene signature was made for patients with ACC, PCPG, DLBC, PRAD, KICH, and THYM, respectively (the right part). * p<0.05, **p<0.01, ***p<0.001.

significance between the survival of some subtypes by the consensus clustering (Figure 9B), the KM analysis indicated a significant difference ($p < 0.0001$) between DSP1 and DSP2 with Hazard Ratio (HR) equal to 5.47 (Figure 9D). Furthermore, the blue module, most correlated with DSP subtypes classification and immune cell infiltration, was extracted by WGCNA (Figures 9E–G). Ten hub genes (IL2RB, CD96, CD3D, HOXC9, HOXC5, SLAMF6, GZMH, CD3E, GZMK, and GZMA) from this module were screened by cytoHubba to construct an enhanced refined DSP clustering model by ML in glioma (Figure 9H). Surprisingly, the glioma-customized DSP model trained from TCGA could predict survival well in the glioma cohort from CGGA (Figures 9I, J). Moreover, The DSP1 has a 3-fold immune therapy response rate than the DSP2 group by oncoPredict package prediction (R.4.2.0).

3.7 The c-MET mechanism exploration by experiments

The pathway enrichment of the blue gene module implied that these genes might be involved in PD1 regulation (Figures 10A–C). The c-MET inspired us to explore its function further since it was one of the top 2 genes in both the blue module and tumor driver genes (TDG) (36) (Figure 10D). High expression of c-MET was associated with poor survival among glioma patients from TCGA and CGGA (Figures 10D, E). More importantly, the survival tendency in glioblastoma patients receiving anti-PD1 therapy agreed with the previous two cohorts (Figure 10F). Interestingly, its expression differed significantly between tumor and nontumor samples in over 90% of cancer types (Figure 10G). Interestingly, most immune markers in glioma had an expression difference between the high-c-MET and low-c-MET groups (Figures 10H, I). The expression of c-MET was positively linked with PD-L1, PD2, IL-10, IRF1, JAK3, and STAT3 (Figure 10J). Furthermore, the *in-vitro* experiment results indicated that the knockdown of c-MET could decrease the survival (Figure 11A) and proliferation (Figure 11B) of glioblastoma cell line ln299, which could be further enhanced by the combination treatment with cabozantinib (2μM, a c-MET inhibitor) (Figures 11A, B). In line with our previous data, the decrease of c-MET could down-regulated the p-JAK3, p-STAT3, and PD-L1 (Figure 11C). Furthermore, the Jurkat T cell co-cultured with the ln299 of c-MET knockdown obtained a higher level of IL-2, IFN-γ, and PD-1 (Figure 11D).

To further verify the regulation of c-MET on PD1/PDL1, peripheral blood mononuclear cells (PBMC) were extracted from healthy females. Through the co-culture of PBMC and glioma cells, our data showed that down-regulation of c-MET in Ln299 significantly

10.3389/fimmu.2024.1258475

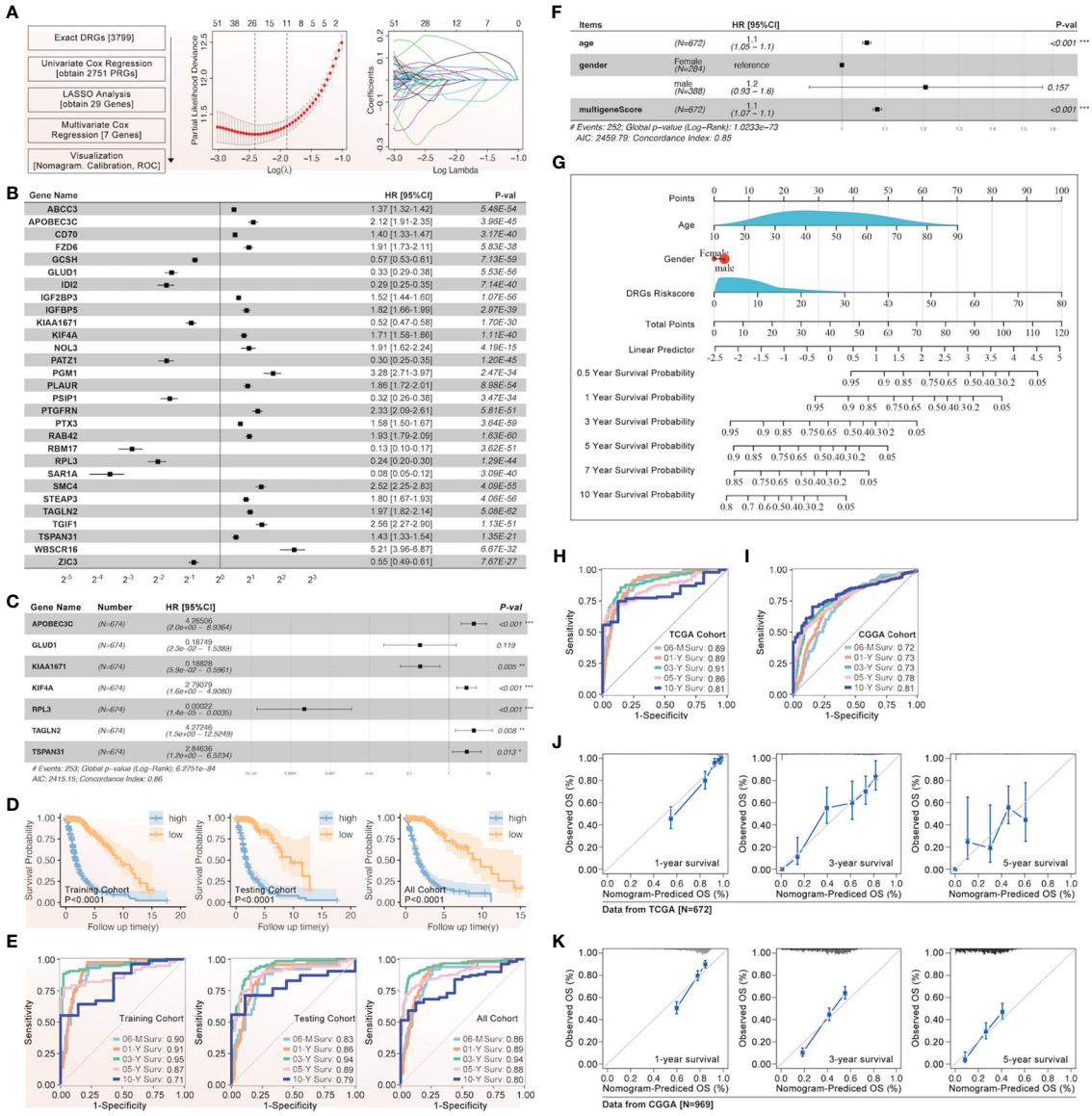

FIGURE 4
The gene signature of prognosis based on DRGs in glioma. **(A)** The flow chart and the LASSO regression results were listed, after which 29 genes were screened out, and **(B)** their effect on the prognosis of glioma was evaluated by univariate Cox, attached with HR and p-value. **(C)** The gene signature of glioma prognosis was made by multivariate Cox regression, in which APOBEC3C, GLUD1, KIAA1671, KIF4A, RPL3, TAGLN2, and TSPAN31 were input into the model. **(D)** The Kaplan–Meier curves were made in the training, testing, and all glioma cohorts from TCGA, and all displayed a similar result that a higher risk score was accompanied by a worse prognosis in glioma. **(E)** The ROC curves of 0.5-year, 1-year, 3-year, 5-year, and 10-year were presented in the training, testing, and all glioma cohorts from TCGA. **(F)** The gene signature based on DRGs and clinical characteristics for glioma were shown with HR value, in which age, gender, and multi-gene-based risk score were input into the model. **(G)** The glioma nomogram of gene signature based on DRGs and clinical characteristics. The glioma ROC curve of gene signature based on DRGs and clinical characteristics in TCGA **(H)** and CGGA **(I)**. The glioma nomogram prediction of gene signature based on DRGs and clinical characteristics in TCGA **(J)** and CGGA **(K)**. *p<0.05, **p<0.01, ***p<0.001.

decreased the activation of STAT3 and the expression level of PDL1 in this cell (Figure 12A). In contrast, the expression level of IL2, IFN-γ, CD8 and CXCR9 were elevated in PBMC (Figure 12A). Furthermore, extracellular level of IL2, IFN-γ, and CXCL9 were also significantly increased in the culture media (Figure 12B). Next, FACS was applied to detect the c-MET-mediated CD8+ T cell immunity inhibition. In Figure 12C, we found that the proportion of CD8+ T cells was increased a little after co-culture with glioma cells while it could return to normal level (Figure 12C). However, this phenomenon was very marginal compared with the PD1 change in CD8+ T cells. The CD3+ CD8+ T cells with high PD-1 expression elevated from 8.8% to 16% after co-cultured with ln299 cells. In contrast, the knockdown of c-MET almost reversed the T-cell exhaustion completely (Figure 12D).

Discussion

Disulfidptosis was a new modality of programmed cell death coined by Gan et al. in 2023 (13), with very little further research on cancer immunity. Our study explored the DRGs' role in 33 types of

10.3389/fimmu.2024.1258475

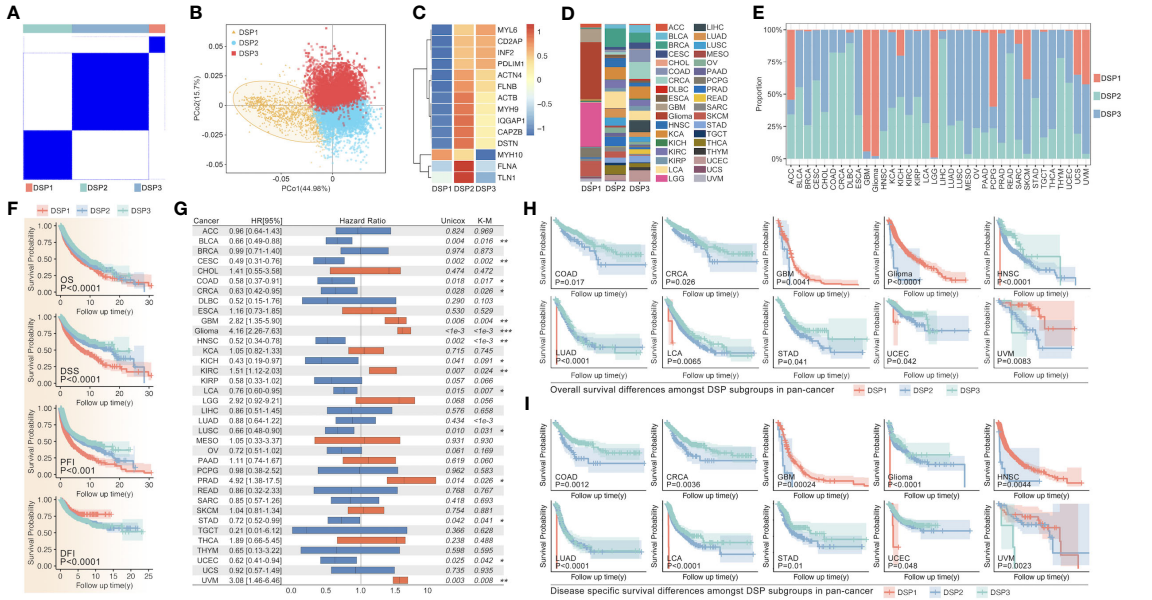

FIGURE 5
DRGs-based clustering and prognosis analysis in pan-cancer. **(A)** The unsupervised clustering of DRGs in pan-cancer based on the 14 DRGs (MYL6, CD2AP, INF2, PDLIM1, ACTN4, FLNB, ACTB, MYH9, IQGAP1, CAPZB, DSTN, MYH10, FLNA, TLN1). **(B)** PCA analysis shows the sample distribution amongst subgroups (DSP1, DSP2, DSP3). **(C)** DRGs expression profile feature in subgroups. **(D)** Tumor sample distribution amongst subgroups. **(E)** Subgroup distribution proportion in 36 kinds of cancer. **(F)** OS, DSS, PFI, and DFI analysis among different DSP groups in pan-cancer were all significant (p<0.001). **(G)** The univariate Cox regression (OS) of DSP clusters in every type of cancer from TCGA, in which significance was observed in BLCA, CESC, COAD, CRCA, Glioma, HNSC, KICH, KIRC, LCA, LUAD, LUSC, PRAD, STAD, UCEC and UVM. OS analysis **(H)** and DSS analysis **(I)** in COAD, CRCA, GBM, glioma, HNSC, LUAD, LCA, STAD, and UCEC. * p<0.05, **p<0.01, ***p<0.001.

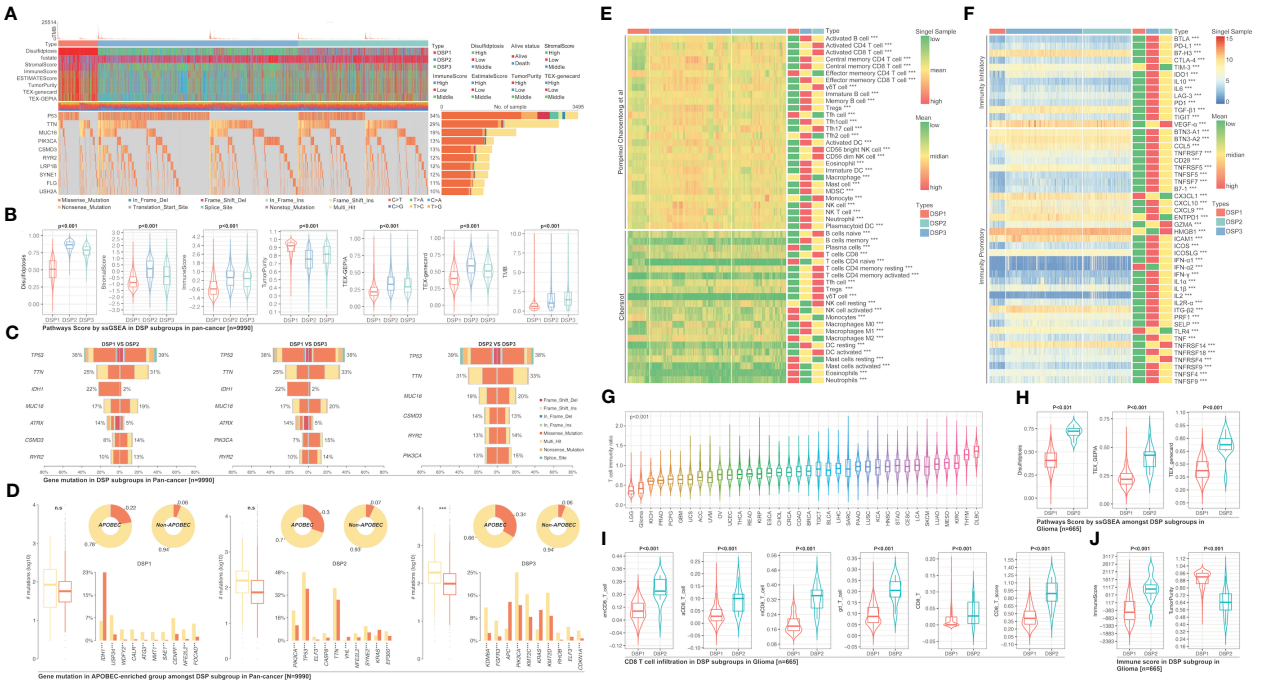

FIGURE 6
Gene mutation comparison among DSP groups in pan-cancer. **(A)** Gene mutation landscape among DSP groups in pan-cancer. **(B)** Pathways score in DSP groups in pan-cancer. **(C)** Mutation comparison between every two DSP groups. **(D)** Mutation comparison between APOBEC-enriched and non-APOBEC-enriched patients in each DSP group. Immune cell infiltration **(E)** Immune cell infiltration in DSP group, **(F)** Immunocheck points expression in DSP groups. **(G)** Immune score status in 36 types of cancer. **(H)** Disulfidptosis score, TEX_GEPIA, and TEX_gencard were higher in DSP2 in glioma (p<0.001). **(I)** Various types of CD8+ T cells infiltration differences in DSP groups in glioma (p<0.001). **(J)** Immune score and tumor purity differences in DSP groups in glioma (p<0.001). **p<0.01, ***p<0.001; ns, significant.

10.3389/fimmu.2024.1258475

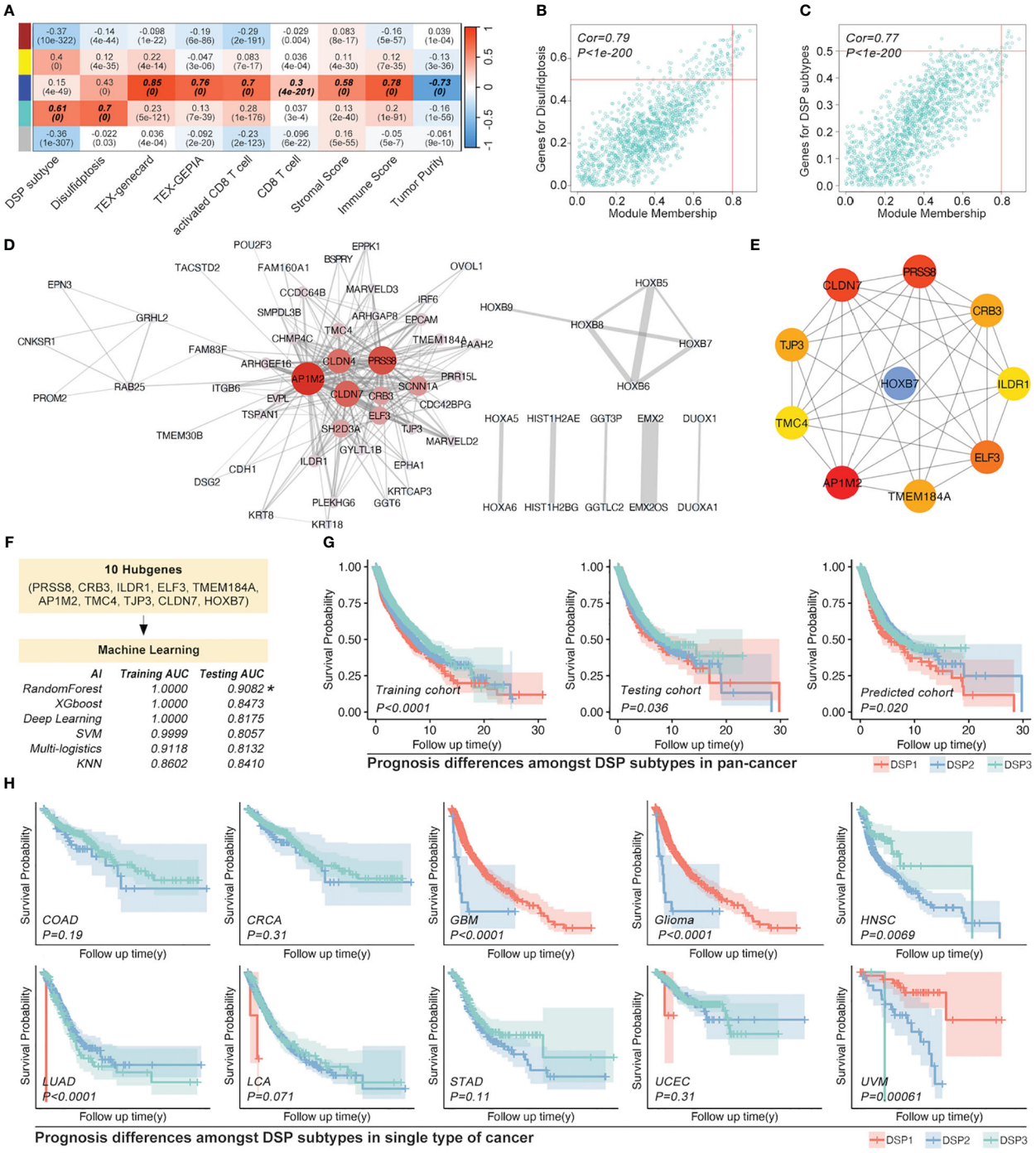

FIGURE 7
Refined prognostic model construction in pan-cancer by WGCNA and Machine learning. **(A)** Gene modules correlated with DSP pathways and immune cell infiltration by WGCNA, in which **(B, C)** module gene cohorts were most linked with DSP grouping and disulfidptosis (Cor=0.79, p<1e-200), while deep blue module gene cohorts were most correlated with immune cell infiltration (Cor=0.77, p<1e-200). **(D)** Gene interaction network about top 50 DSP grouping related genes in cyan module gene cohorts **(E)** Hub genes of the cyan gene module. **(F)** Refined prognostic model construction based on pan-cancer by supervised machine learning, in which random forest algorithm displayed as the most efficient (Training AUC=0.9082). **(G)** K-M analysis indicated the prognosis differences amongst DSP groups in the training cohort, testing cohort (original groups), and predicted group (AI-identified group using test cohort data). **(H)** Refined prognostic model performance in the OS analysis of COAD, CRCA, GBM, glioma, HNSC, LUAD, LCA, STAD, and UCEC.

cancer in detail. The limma package and univariate Cox regression indicated that the 14 validated DRGs did not only manifest significantly different expressions between tumors and normal + para tumor tissues, but they could also predict differential survival in glioma, KCA, KIRC, MESO, and UVM (Figures 1C, E). In particular, each gene of the 14 DRGs could play a significant role in the prognosis of patients with glioma (Figure 1F). Although some genes in the DRGs had been reported to be involved in glioma, our

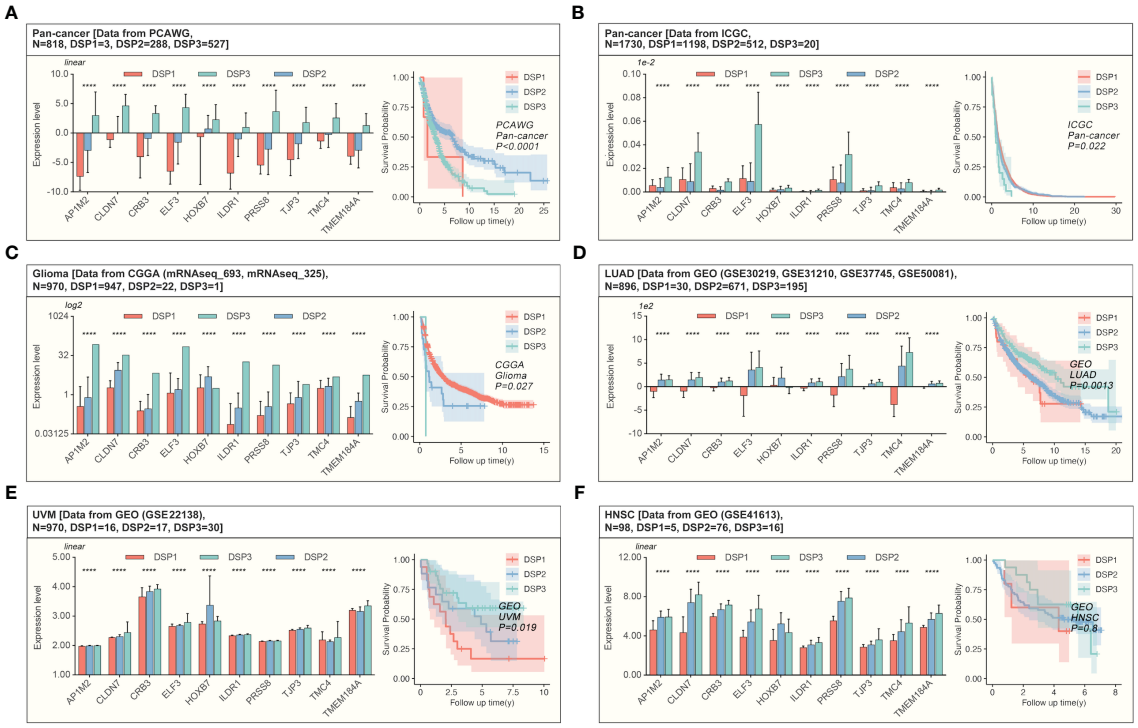

FIGURE 8
Validation of the refined prognostic model in external datasets. Expression of DRGs and validation of the refined prognostic model in pan-cancer from **(A, B)** PCAWG (p<0.0001) or ICGC (p=0.022), both of them showed significant prognosis differences in AI-identified DSP subgroups. **(C)** The Glioma cohort from CGGA manifested significant prognosis differences amongst AI-identified DSP groups (p=0.027). **(D)**, LUAD from GEO datasets (GSE30219, GSE31210, GSE37745, GSE50081) presented significant prognosis differences amongst AI-identified DSP groups (p=0.0013), **(E)** UVM from GSE22138 showed significant prognosis difference amongst AI-identified DSP groups (p=0.019) **(F)** HNSC from GSE41613 (exhibited insignificant prognosis difference amongst AI-identified DSP groups (p=0.8). ****p<0.0001.

results implicated how the disulfidptosis pathway is regulated by these genes in glioma deserves more research (37–42).

Besides other types of PCDs, the correlation analysis showed that the disulfidptosis was also closely related to immune cell infiltration, including Tex_Genecard, Tex_GEPIA, CD8 (+) T cells, regulatory T cells, and macrophages (Figure 2A). Our data even suggested that disulfidptosis-postively-related Tex by both gene cards and GEPIA was a harmful factor in the prognosis of glioma (Figure 2B). PCD of different cells in the tumor microenvironment (TME) has been found to complicate cancer therapy. On the one hand, evidence suggested that cancer cells undergoing PCD in TME might render them more difficult to survive (43–46). On the other hand, other immune components undergoing RCD in the TME could alter immune attacks on tumor cells. For instance, the necroptosis induced in the TME was reported to enhance the immune surveillance from the BATF3 (+) conventional dendritic cells 1 (cDC1) and CD8 (+) T cells, leading to the release of many immunostimulatory cytokines (47–51). However, necroptosis induction in pancreatic cancer was found to protect the tumor cell from attacks by immune cells (52). While pyroptosis could induce antitumor effects by increasing the infiltration of dendritic cells (DC), CD4 (+) T cells, and CD8 (+) T cells (53, 54). For ferroptosis, it was reported to promote immunogenicity, induce DCs' phenotypic development, and elicit a vaccination-like response (55). The expression of cuproptosis-related genes was positively correlated with PD-L1 expression and negatively associated with regulatory T-cell infiltration in melanoma (56). To our knowledge, our study was the first to explore disulfidptosis and tumor immune infiltration in pan-cancer patients and gave a complete picture of disulfidptosis' role in immune regulation.

Our study even constructed a rough gene signature based on disulfidptosis genes to predict the survival of all patients of every cancer from TCGA (Figure 3). In ACC, PCPG, DLBC, PRAD, KICH, and THYM, the DRGs-based model could predict 1-year, 2-year, 3-year, 4-year, and 5-year survival with over 0.9 AUC (Figure 3). The gene signature based on PCD-related genes has always been a popular research direction. However, there is still a lack of the DRGs-related prognostic gene signature (57–62). Our research is the first to make a gene signature for each type of cancer patient from TCGA. Moreover, we further analyzed the DRGs-based model in glioma in which Tex and immune cell infiltration was strongly associated with disulfidptosis (Figure 2B). In both the TCGA and CGGA glioma cohorts, the gene signature's predictive effect was significant and consistent (Figures 4D, E, H–K). To further dissect the role of disulfidptosis in pan-cancer, we clustered the 14 validated DRGs by their expression pattern in pan-cancer. The three DSP groups had significantly different OS, DSS, PFI, and DFI in pan-cancer (Figure 5F). More importantly, DSP groups also had disparate DFI and OS in COAD, CRCA, GBM, glioma, HNSC, LUAD, LCA, STAD, UCEC, and UVM (Figures 5F–I). The consistent survival significance of DSP clustering indicated that this new form of PCD was important in these types of cancer. Further tumor mutation burden (TMB) analysis suggested that the TP53, TTN, and IDH1 mutations may be

10.3389/fimmu.2024.1258475

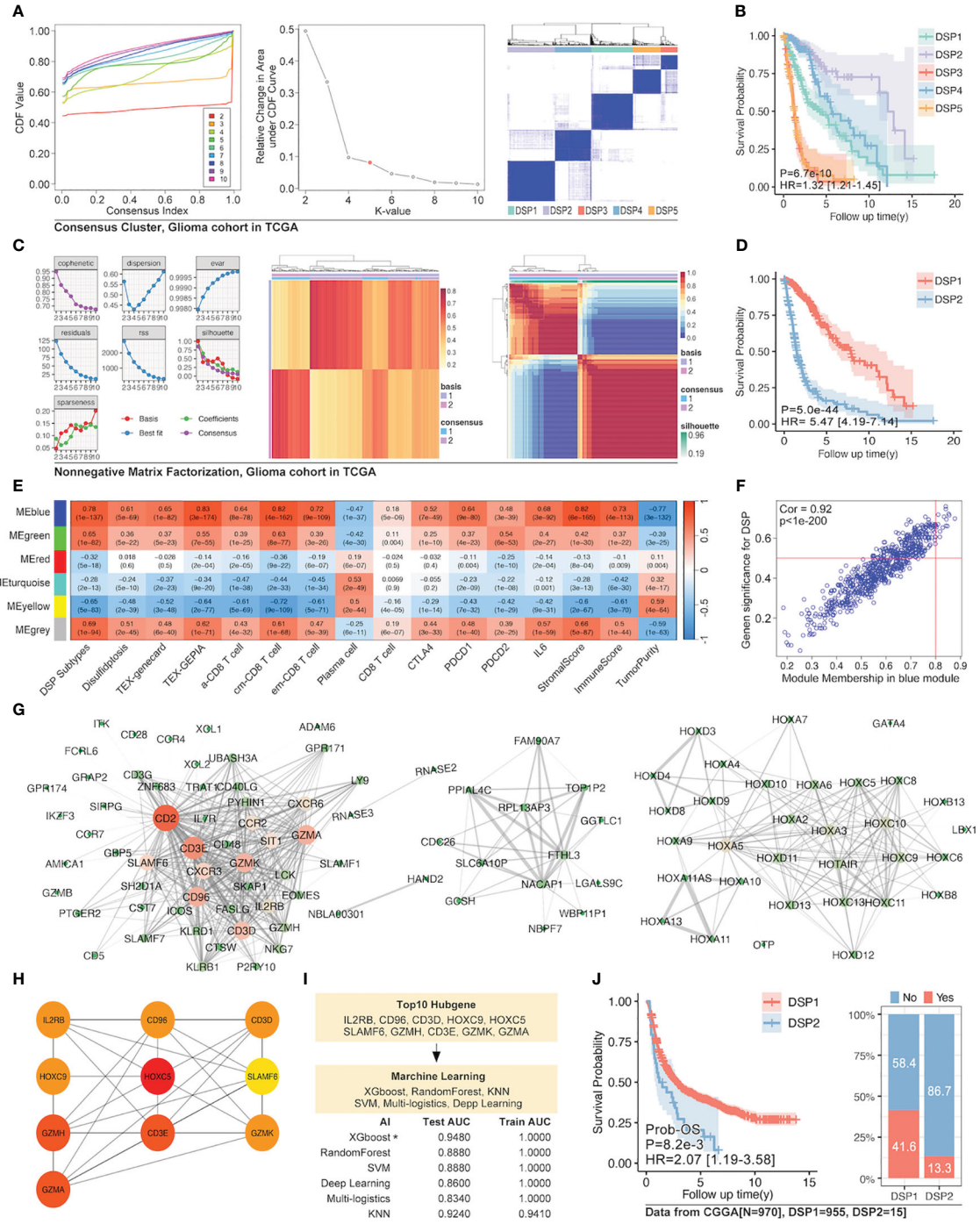

FIGURE 9
Enhanced prognostic model in glioma by WGCNA and machine learning. **(A)** Unsupervised consensus clustering of 14 validated DRGs **(B)** and its survival analysis in the glioma cohort, which displayed a significant difference in prognosis (p=6.7e-10). **(C)** The clustering of 14 validated DRGs by Non-negative Matrix Factorization (NMF) divided the glioma cohort into two groups with **(D)** significantly different prognoses (p=5e-44). **(E)** WGCNA for NMF clustering DSP groups, in which blue module gene cohort was the most correlated to DSP grouping, immune cell infiltration, and immunecheckpoint expression (p<0.0001). **(F)** The correlation analysis of the blue gene module from WGCNA and DSP subtypes. The blue gene module **(G)** and its hub genes **(H)** network. **(I)** Enhanced prognostic model based on hub genes for patients with glioma by machine learning, among which the xgboost algorithm showed the best accuracy (testing AUC=0.9480). **(J)** The validation of the enhanced prognostic model in glioma patients from CGGA by KM analysis and immune checkpoint inhibitors response prediction (p<0.001).

involved in the disulfidptosis. Despite the regulation on nearly all previously reported PCD by TP53, no studies have explored its role in disulfidptosis until now (63). Our data provided many possible candidates to uncover more mechanisms of disulfidptosis. Consistent with the previous immune cell infiltration analysis, our result showed that there was a higher Tex within the DSP2 than DSP1 in glioma patients (Figure 6G), which gave more evidence that disulfidptosis was closely linked with Tex (Figure 6I).

10.3389/fimmu.2024.1258475

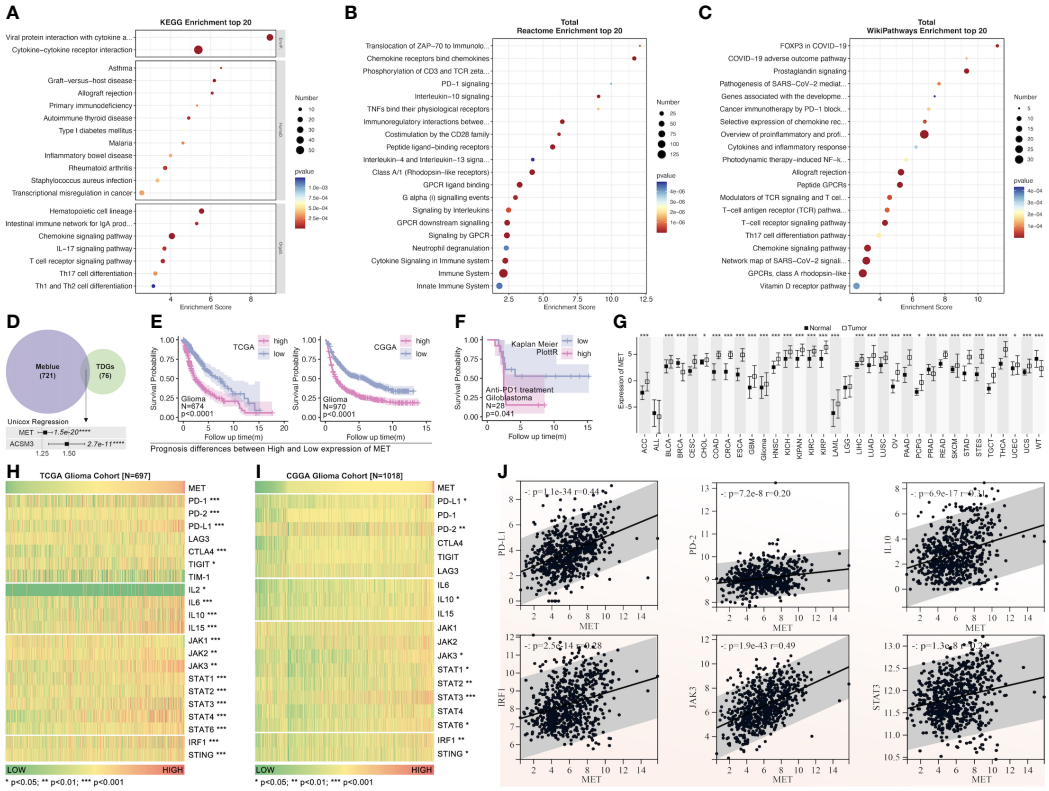

FIGURE 10
The pathway enrichment and tumor driver genes analysis from the blue gene module. Pathway enrichment of blue gene module by KEGG **(A)**, Reactome **(B)**, and WikiPathways **(C)**. **(D)** The tumor driver genes' extraction from the blue module. **(E)** The c-MET survival analysis of patients with glioma from TCGA and CGGA (HR>1.25, p=1.5e-20). **(F)** The c-MET prognosis analysis was validated in the glioblastoma cohort receiving anti-PD1 treatment from "Kaplan-Meier Plotter" (http://kmplot.com/analysis/index). **(G)** The expression of c-MET in pan-cancer and non-tumor tissues(data from TCGA and GTEx). The immune markers expression was based on the c-MET expression in the glioma cohort from TCGA **(H)** and CGGA **(I)**. **(J)** The expression correlation analysis between different immune markers (PDL1, PD2, IL10, IRF1, JAK3, STAT3) and c-MET in the glioma cohort from TCGA. *p<0.05, **p<0.01, ***p<0.001, ****p<0.0001

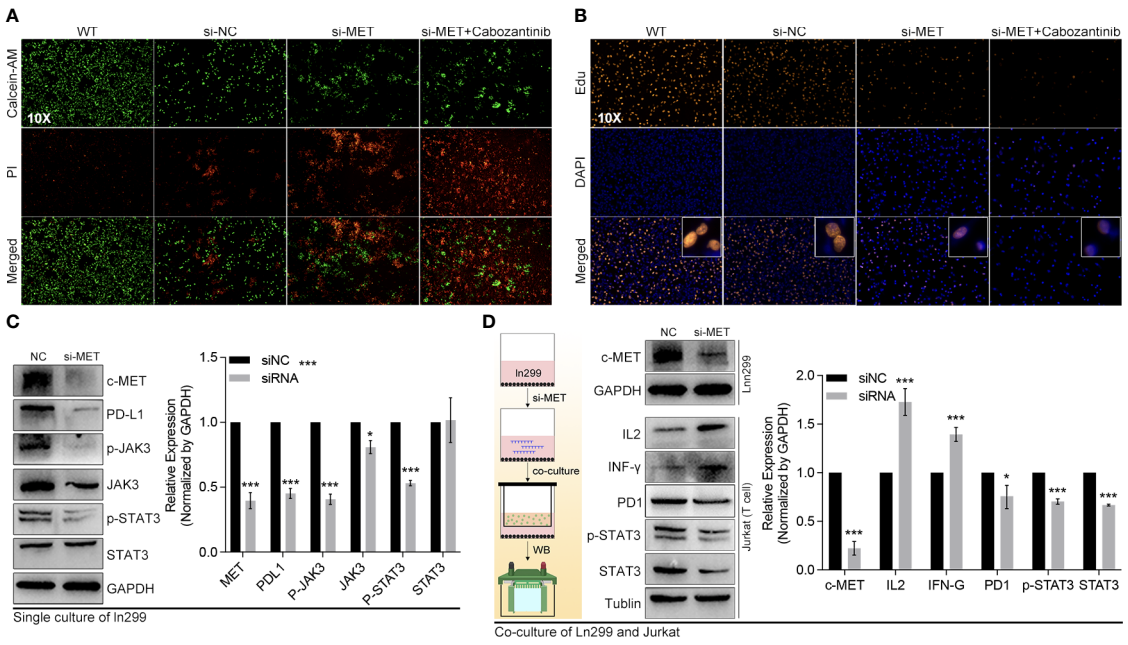

FIGURE 11
C-MET was a tumor driver gene and could inhibit the JAK3-STAT3 pathway. **(A)** The live and dead cell staining by Calcein and PI, in which siRNA-c-MET treatment increases the dead cell proportion induced by cabozantinib treatment. **(B)** The Edu and DAPI staining of the ln299 cell line. **(C)** The protein expression alteration after c-MET knockdown in the ln299 cell line, in which PDL1, p-JAK3, JAK3, and pSTAT3 were down-regulated, while **(D)** the expression of IL2 and IFN-γ were up-regulated in the Jurkat cell line in co-culture system. *p<0.05, ***p<0.001.

10.3389/fimmu.2024.1258475

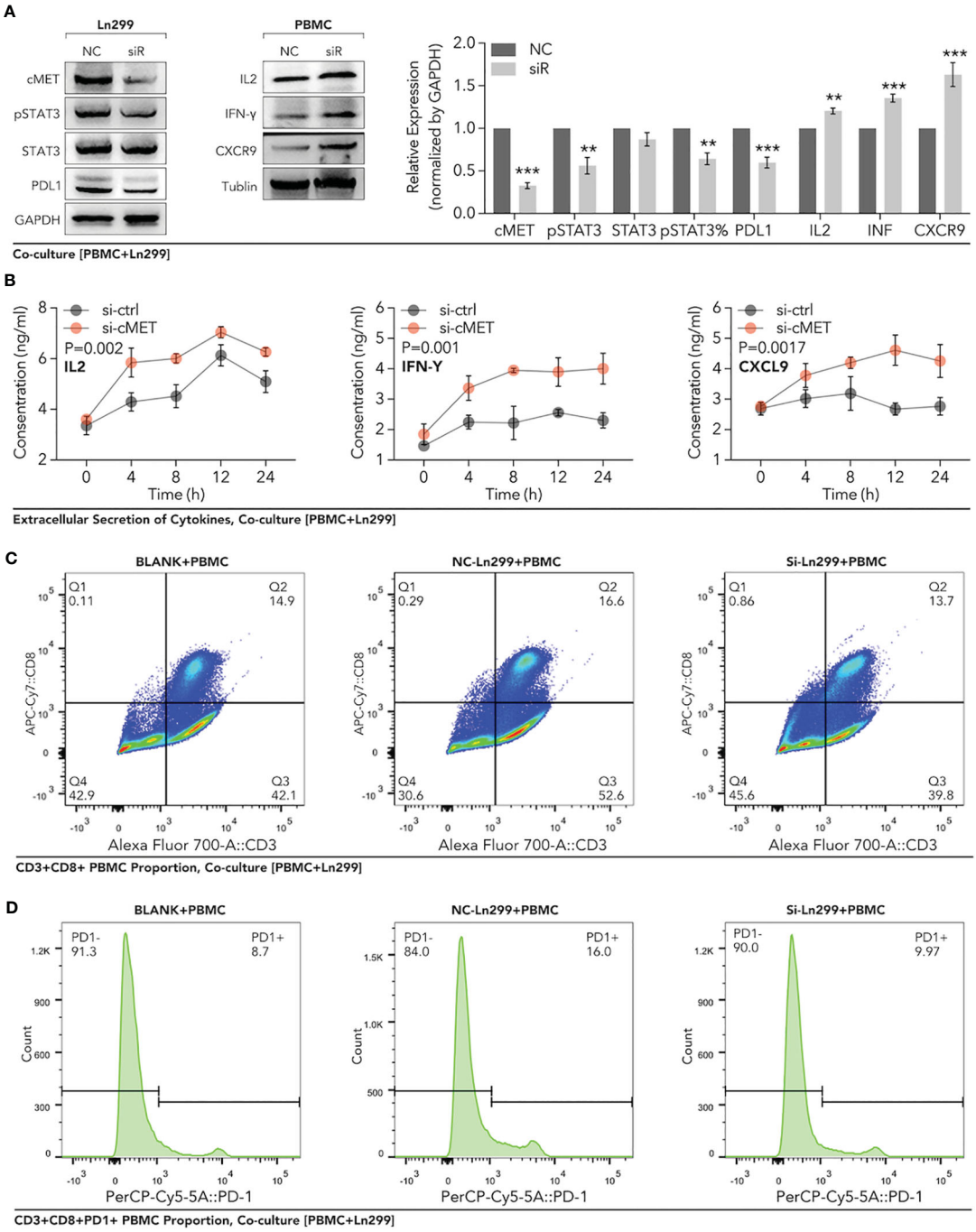

FIGURE 12
Down-regulation of c-MET within glioma enhanced the PBMC-derived CD8+ T cell function and proportion in the co-culture system. Glioma cell line Ln299 cells were treated with c-MET siRNA for 24h and co-cultured with PBMC for another 24h. **(A)** WB was used to detect the relevant protein expression in Ln299 and PBMC, in which PDL1, STAT3, pSTAT3, and pSTAT3 were down-regulated in Ln299. At the same time, IL2, IFN-γ, and CXCR9 were up-regulated in PBMC. **(B)** ELISA was applied to detect extracellular protein levels in the co-culture system, in which IL2, IFN-γ, and CXCL9 were higher in the si-c-MET group than those in the NC group. **(C)** The proportion of PD1+ PBMC was decreased by the down-regulation of c-MET in ln299 a little. **(D)** PD1+ CD3+CD8+ T cells were reduced evidently in the si-c-MET group than those in the NC group. **p<0.01, ***p<0.001.

To further obtain a refined DSP model, WGCNA, followed by machine learning, was employed to explore the most relevant gene modules with disulfidptosis. Ten hub genes, including PRSS8, CRB3, ILDR1, ELF3, TMEM184A, AP1M2, TMC4, TJP3, CLDN7, and HOXB7, were extracted from the most related gene module (Figure 7E). Next, randomForest machine learning, dependent on the ten hub genes, produced the best prognosis model by virtue of categorizing different DSP groups in pan-cancer, which was even validated in external databases (Figures 7G, 8A–F). Our study proposed a generally effective prognosis model for pan-cancer. Interestingly, it worked exceptionally well in glioma, LUAD, and UVM. Combined with the abovementioned results, it inspired us to

continue analyzing disulfidptosis in glioma. A specific prognosis model for patients with glioma was constructed based on ten hub genes (IL2RB, CD96, CD3D, HOXC9, HOXC5, SLAMF6, GZMH, CD3E, GZMK, and GZMA) (Figures 9H, I). Glioma was divided into DSP1 and DSP2 groups, where the DSP1 group was predicted to have a much higher response rate to immune checkpoint inhibitors (ICIs) than the DSP2 group (Figure 9J).

Finally, our further mechanism exploration revealed that c-MET might play a vital role in the interaction between disulfidptosis and glioma immunity. The high expression of c-MET could even predict a poor prognosis in glioblastoma patients receiving anti-PD1 treatment (Figure 10F). This tumor driver gene also manifested a positive relation with the JAK3-STAT3-PD-L1 pathway (Figure 10J). JAK/STAT signaling is reported to play pivotal roles in tumor immunity, including the maintenance of activated T cells (64–68). This phenomenon was further validated in *in-vitro* experiments where we co-cultured the c-MET-knockdown glioblastoma cell line with the Jurkat T cell line (Figures 11A–D, 12A–D). The promotion of cell death and inhibition of cell proliferation by c-MET knockdown indicated that it could serve as a tumor driver gene. Its regulation on JAK3-STAT3-PD1/PD-L1 in T cells indicated the crosstalk between disulfidptosis and T-cell exhaustion. Targeting c-MET by siRNA or cabozantinib might be a promising way to enhance the T cell function implicated by the decreased high-PD1 T cells proportion and the increased CXCR9, CXCL9, IL2, and INF-γ (Figures 11D, 12A–D). Although we uncovered many potential and exciting candidates for further research on disulfidptosis and cancer immunity, more efforts are needed to validate their functions.

Conclusions

To summarize, we dissected the expression of DRGs between cancerous and noncancerous tissues, their roles in the prognosis, and their relationship with immunity in pan-cancer. A general prognosis model based on machine learning was constructed for pan-cancer and validated by external datasets with a consistent result. In particular, a DSP prognosis model was made specifically for patients with glioma to predict its survival and immune response to ICIs. Many potential candidates were screened, among which c-MET was validated for its TDG and immune regulation roles (inducing t-cell exhaustion) in glioma.

Data availability statement

The original contributions presented in the study are included in the article/Supplementary Material. Further inquiries can be directed to the corresponding authors.

Ethics statement

The studies involving humans were approved by Medical Ethics Committee of The First People's Hospital of Xiaoshan District. The studies were conducted in accordance with the local legislation and institutional requirements. The participants provided their written informed consent to participate in this study.

Author contributions

PL: Funding acquisition, Software, Validation, Writing – original draft. SW: Data curation, Investigation, Methodology, Software, Writing – original draft. HW: Formal analysis, Investigation, Supervision, Validation, Writing – original draft. YH: Data curation, Formal analysis, Writing – original draft. KY: Methodology, Software, Writing – original draft. KS: Formal analysis, Investigation, Supervision, Writing – original draft. ZW: Funding acquisition, Project administration, Writing – review & editing. HJ: Formal analysis, Writing – review & editing, Funding acquisition, Project administration.

Funding

The author(s) declare financial support was received for the research, authorship, and/or publication of this article. This work was supported by grants from the Medical and Health Science and Technology Project of Hangzhou (No. B20220666), the Hangzhou Agricultural and Social Development Scientific Research Project (20211231Y117), and the Medical and Health Science and Technology Project of Zhejiang (No. 2023KY224).

Acknowledgments

Thanks for the support from The First People's Hospital of Xiaoshan District and the researchers who share their data in TCGA, GEO, CGGA, and ICGC databases.

Conflict of interest

The authors declare that the research was conducted in the absence of any commercial or financial relationships that could be construed as a potential conflict of interest.

Publisher's note

Supplementary material

The Supplementary Material for this article can be found online at: https://www.frontiersin.org/articles/10.3389/fimmu.2024.1258475/full#supplementary-material

SUPPLEMENTARY FIGURE 1
Gating strategy for PBMC co-cultured with Ln299 cells. **(A)** The gating detail for PBMC only. **(B)** The gating detail for PBMC co-cultured with ln299 cell for 48h. **(C)** The gating detail for PBMC co-cultured with c-MET-knockdown ln299 cell for 48h.

References

1. Tang D, Kang R, Berghe TV, Vandenabeele P, Kroemer G. The molecular machinery of regulated cell death. *Cell Res* (2019) 29:347–64. doi: 10.1038/s41422-019-0164-5

2. Peng F, Liao M, Qin R, Zhu S, Peng C, Fu L, et al. Regulated cell death (RCD) in cancer: key pathways and targeted therapies. *Signal Transduct Target Ther* (2022) 7:286. doi: 10.1038/s41392-022-01110-y

3. Kerr JF, Wyllie AH, Currie AR. Apoptosis: a basic biological phenomenon with wide-ranging implications in tissue kinetics. *Br J Cancer* (1972) 26:239–57. doi: 10.1038/bjc.1972.33

4. Paweletz N. Walther Flemming: pioneer of mitosis research. *Nat Rev Mol Cell Biol* (2001) 2:72–5. doi: 10.1038/35048077

5. Kerr JF. History of the events leading to the formulation of the apoptosis concept. *Toxicology* (2002) 181-182:471–4. doi: 10.1016/S0300-483X(02)00457-2

6. Klionsky DJ. Autophagy: from phenomenology to molecular understanding in less than a decade. *Nat Rev Mol Cell Biol* (2007) 8:931–7. doi: 10.1038/nrm2245

7. Nakatogawa H, Suzuki K, Kamada Y, Ohsumi Y. Dynamics and diversity in autophagy mechanisms: lessons from yeast. *Nat Rev Mol Cell Biol* (2009) 10:458–67. doi: 10.1038/nrm2708

8. Deter RL, De Duve C. Influence of glucagon, an inducer of cellular autophagy, on some physical properties of rat liver lysosomes. *J Cell Biol* (1967) 33:437–49. doi: 10.1083/jcb.33.2.437

9. Degterev A, Huang Z, Boyce M, Li Y, Jagtap P, Mizushima N, et al. Chemical inhibitor of nonapoptotic cell death with therapeutic potential for ischemic brain injury. *Nat Chem Biol* (2005) 1:112–9. doi: 10.1038/nchembio711

10. Dixon SJ, Lemberg KM, Lamprecht MR, Skouta R, Zaitsev EM, Gleason CE, et al. et al: Ferroptosis: an iron-dependent form of nonapoptotic cell death. *Cell* (2012) 149:1060–72. doi: 10.1016/j.cell.2012.03.042

11. Cookson BT, Brennan MA. Pro-inflammatory programmed cell death. *Trends Microbiol* (2001) 9:113–4. doi: 10.1016/S0966-842X(00)01936-3

12. Tsvetkov P, Coy S, Petrova B, Dreishpoon M, Verma A, Abdusamad M, et al. et al: Copper induces cell death by targeting lipoylated TCA cycle proteins. *Science* (2022) 375:1254–61. doi: 10.1126/science.abf0529

13. Liu X, Nie L, Zhang Y, Yan Y, Wang C, Colic M, et al. et al: Actin cytoskeleton vulnerability to disulfide stress mediates disulfidptosis. *Nat Cell Biol* (2023) 25:404–14. doi: 10.1038/s41556-023-01091-2

14. Zhao S, Wang L, Ding W, Ye B, Cheng C, Shao J, et al. Crosstalk of disulfidptosis-related subtypes, establishment of a prognostic signature and immune infiltration characteristics in bladder cancer based on a machine learning survival framework. *Front Endocrinol (Lausanne)* (2023) 14:1180404. doi: 10.3389/fendo.2023.1180404

15. Zheng P, Zhou C, Ding Y, Duan S. Disulfidptosis: a new target for metabolic cancer therapy. *J Exp Clin Cancer Res* (2023) 42:103. doi: 10.1186/s13046-023-02675-4

16. Machesky LM. Deadly actin collapse by disulfidptosis. *Nat Cell Biol* (2023) 25:375–6. doi: 10.1038/s41556-023-01100-4

17. Zhong Z, Zhang C, Ni S, Ma M, Zhang X, Sang W, et al. NFATc1-mediated expression of SLC7A11 drives sensitivity to TXNRD1 inhibitors in osteoclast precursors. *Redox Biol* (2023) 63:102711. doi: 10.1016/j.redox.2023.102711

18. Hanahan D. Hallmarks of cancer: new dimensions. *Cancer Discovery* (2022) 12:31–46. doi: 10.1158/2159-8290.CD-21-1059

19. Tang B, Zhu J, Li J, Fan K, Gao Y, Cheng S, et al. et al: The ferroptosis and iron-metabolism signature robustly predicts clinical diagnosis, prognosis and immune microenvironment for hepatocellular carcinoma. *Cell Commun Signal* (2020) 18:174. doi: 10.1186/s12964-020-00663-1

20. Zhuo S, Chen Z, Yang Y, Zhang J, Tang J, Yang K. Clinical and biological significances of a ferroptosis-related gene signature in glioma. *Front Oncol* (2020) 10:590861. doi: 10.3389/fonc.2020.590861

21. Ye Y, Dai Q, Qi H. A novel defined pyroptosis-related gene signature for predicting the prognosis of ovarian cancer. *Cell Death Discovery* (2021) 7:71. doi: 10.1038/s41420-021-00451-x

22. Shao W, Yang Z, Fu Y, Zheng L, Liu F, Chai L, et al. The pyroptosis-related signature predicts prognosis and indicates immune microenvironment infiltration in gastric cancer. *Front Cell Dev Biol* (2021) 9:676485. doi: 10.3389/fcell.2021.676485

23. Ju A, Tang J, Chen S, Fu Y, Luo Y. Pyroptosis-related gene signatures can robustly diagnose skin cutaneous melanoma and predict the prognosis. *Front Oncol* (2021) 11:709077. doi: 10.3389/fonc.2021.709077

24. Zhang Z, Zeng X, Wu Y, Liu Y, Zhang X, Song Z. Cuproptosis-related risk score predicts prognosis and characterizes the tumor microenvironment in hepatocellular carcinoma. *Front Immunol* (2022) 13:925618. doi: 10.3389/fimmu.2022.925618

25. Bian Z, Fan R, Xie L. A novel cuproptosis-related prognostic gene signature and validation of differential expression in clear cell renal cell carcinoma. *Genes (Basel)* (2022) 13. doi: 10.3390/genes13050851

26. Han J, Hu Y, Liu S, Jiang J, Wang H. A newly established cuproptosis-associated long non-coding RNA signature for predicting prognosis and indicating immune microenvironment features in soft tissue sarcoma. *J Oncol* (2022) 2022:8489387. doi: 10.1155/2022/8489387

27. Zhang G, Sun J, Zhang X. A novel Cuproptosis-related LncRNA signature to predict prognosis in hepatocellular carcinoma. *Sci Rep* (2022) 12:11325. doi: 10.1038/s41598-022-15251-1

28. Cedars MI. Artificial Intelligence in assisted reproductive technology: how best to optimize this tool of the future. *Fertil Steril* (2023). doi: 10.1016/j.fertnstert.2023.05.150

29. Chen M, Copley SJ, Viola P, Lu H, Aboagye EO. Radiomics and artificial intelligence for precision medicine in lung cancer treatment. *Semin Cancer Biol* (2023). doi: 10.1016/j.semcancer.2023.05.004

30. Carreras J, Hiraiwa S, Kikuti YY, Miyaoka M, Tomita S, Ikoma H, et al. et al: artificial neural networks predicted the overall survival and molecular subtypes of diffuse large B-cell lymphoma using a pancancer immune-oncology panel. *Cancers (Basel)* (2021) 13.

31. Sheehy J, Rutledge H, Acharya UR, Loh HW, Gururajan R, Tao X, et al. Gynecological cancer prognosis using machine learning techniques: A systematic review of the last three decades (1990-2022). *Artif Intell Med* (2023) 139:102536. doi: 10.1016/j.artmed.2023.102536

32. Vrdoljak J, Krešo A, Kumrić M, Martinović D, Cvitković I, Grahovac M, et al. : the role of AI in breast cancer lymph node classification: A comprehensive review. *Cancers (Basel)* (2023) 15. doi: 10.3390/cancers15082400

33. Brunese MC, Fantozzi MR, Fusco R, De Muzio F, Gabelloni M, Danti G, et al. et al: update on the applications of radiomics in diagnosis, staging, and recurrence of intrahepatic cholangiocarcinoma. *Diagnostics (Basel)* (2023) 13.

34. Yang X, Wu J, Chen X. Application of artificial intelligence to the diagnosis and therapy of nasopharyngeal carcinoma. *J Clin Med* (2023) 12. doi: 10.3390/jcm12093077

35. Charoentong P, Finotello F, Angelova M, Mayer C, Efremova M, Rieder D, et al. Pan-cancer immunogenomic analyses reveal genotype-immunophenotype relationships and predictors of response to checkpoint blockade. *Cell Rep* (2017) 18:248–62. doi: 10.1016/j.celrep.2016.12.019

36. Martínez-Jiménez F, Muiños F, Sentís I, Deu-Pons J, Reyes-Salazar I, Arnedo-Pac C, et al. A compendium of mutational cancer driver genes. *Nat Rev Cancer* (2020) 20:555–72. doi: 10.1038/s41568-020-0290-x

37. Liu W, Cai T, Li L, Chen H, Chen R, Zhang M, et al. et al: miR-200a regulates nasopharyngeal carcinoma cell migration and invasion by targeting MYH10. *J Cancer* (2020) 11:3052–60. doi: 10.7150/jca.40438

38. Wang Y, Yang Q, Cheng Y, Gao M, Kuang L, Wang C. Myosin heavy chain 10 (MYH10) gene silencing reduces cell migration and invasion in the glioma cell lines U251, T98G, and SHG44 by inhibiting the Wnt/β-catenin pathway. *Med Sci Monit* (2018) 24:9110–9. doi: 10.12659/MSM.911523

39. Li H, Lei B, Xiang W, Wang H, Feng W, Liu Y, et al. Differences in protein expression between the U251 and U87 cell lines. *Turk Neurosurg* (2017) 27:894–903.

40. Heuser VD, Kiviniemi A, Lehtinen L, Munthe S, Kristensen BW, Posti JP, et al. Multiple formin proteins participate in glioblastoma migration. *BMC Cancer* (2020) 20:710. doi: 10.1186/s12885-020-07211-7

41. Buehler M, Yi X, Ge W, Blattmann P, Rushing E, Reifenberger G, et al. et al: Quantitative proteomic landscapes of primary and recurrent glioblastoma reveal a protumorigeneic role for FBXO2-dependent glioma-microenvironment interactions. *Neuro Oncol* (2023) 25:290–302. doi: 10.1093/neuonc/noac169

42. Liu Z, Wei Y, Zhang L, Yee PP, Johnson M, Zhang X, et al. Induction of store-operated calcium entry (SOCE) suppresses glioblastoma growth by inhibiting the Hippo pathway transcriptional coactivators YAP/TAZ. *Oncogene* (2019) 38:120–39. doi: 10.1038/s41388-018-0425-7

43. Suhail Y, Cain MP, Vanaja K, Kurywchak PA, Levchenko A, Kalluri R. Systems biology of cancer metastasis. *Cell Syst* (2019) 9:109–27. doi: 10.1016/j.cels.2019.07.003

44. Spill F, Reynolds DS, Kamm RD, Zaman MH. Impact of the physical microenvironment on tumor progression and metastasis. *Curr Opin Biotechnol* (2016) 40:41–8. doi: 10.1016/j.copbio.2016.02.007

45. Liu W, Chakraborty B, Safi R, Kazmin D, C-y C. McDonnell DP: Dysregulated cholesterol homeostasis results in resistance to ferroptosis increasing tumorigenicity and metastasis in cancer. *Nat Commun* (2021) 12:5103. doi: 10.1038/s41467-021-25354-4

46. Chen X, Zeh HJ, Kang R, Kroemer G, Tang D. Cell death in pancreatic cancer: from pathogenesis to therapy. *Nat Rev Gastroenterol Hepatol* (2021) 18:804–23. doi: 10.1038/s41575-021-00486-6

47. Lin S-Y, Hsieh S-Y, Fan Y-T, Wei W-C, Hsiao P-W, Tsai D-H, et al. Necroptosis promotes autophagy-dependent upregulation of DAMP and results in immunosurveillance. *Autophagy* (2018) 14:778–95. doi: 10.1080/15548627.2017.1386359

48. Aaes TL, Kaczmarek A, Delvaeye T, De Craene B, De Koker S, Heyndrickx L, et al. Vaccination with necroptotic cancer cells induces efficient anti-tumor immunity. *Cell Rep* (2016) 15:274–87. doi: 10.1016/j.celrep.2016.03.037

49. Workenhe ST, Nguyen A, Bakhshinyan D, Wei J, Hare DN, MacNeill KL, et al. *De novo* necroptosis creates an inflammatory environment mediating tumor susceptibility to immune checkpoint inhibitors. *Commun Biol* (2020) 3:645. doi: 10.1038/s42003-020-01362-w

50. Park H-H, Kim H-R, Park S-Y, Hwang S-M, Hong SM, Park S, et al. RIPK3 activation induces TRIM28 derepression in cancer cells and enhances the anti-tumor microenvironment. *Mol Cancer* (2021) 20:1–20. doi: 10.1186/s12943-021-01399-3

51. Snyder AG, Hubbard NW, Messmer MN, Kofman SB, Hagan CE, Orozco SL, et al. Intratumoral activation of the necroptotic pathway components RIPK1 and RIPK3 potentiates antitumor immunity. *Sci Immunol* (2019) 4:eaaw2004. doi: 10.1126/sciimmunol.aaw2004

52. Seifert L, Werba G, Tiwari S, Giao Ly NN, Alothman S, Alqunaibit D, et al. The necrosome promotes pancreatic oncogenesis via CXCL1 and Mincle-induced immune suppression. *Nature* (2016) 532:245–9. doi: 10.1038/nature17403

53. Wang X, Lin W, Liu T, Xu Z, Wang Z, Cao Z, et al. Cross-talk of pyroptosis and tumor immune landscape in lung adenocarcinoma. *Transl Lung Cancer Res* (2021) 10:4423–44. doi: 10.21037/tlcr-21-715

54. Erkes DA, Cai W, Sanchez IM, Purwin TJ, Rogers C, Field CO, et al. Mutant BRAF and MEK inhibitors regulate the tumor immune microenvironment via pyroptosis. *Cancer Discovery* (2020) 10:254–69. doi: 10.1158/2159-8290.CD-19-0672

55. Xu H, Ye D, Ren M, Zhang H, Bi F. Ferroptosis in the tumor microenvironment: perspectives for immunotherapy. *Trends Mol Med* (2021) 27:856–67. doi: 10.1016/j.molmed.2021.06.014

56. Lv H, Liu X, Zeng X, Liu Y, Zhang C, Zhang Q, et al. Comprehensive analysis of cuproptosis-related genes in immune infiltration and prognosis in melanoma. *Front Pharmacol* (2022) 13:930041. doi: 10.3389/fphar.2022.930041

57. Chen H, Yang W, Li Y, Ma L, Ji Z. Leveraging a disulfidptosis-based signature to improve the survival and drug sensitivity of bladder cancer patients. *Front Immunol* (2023) 14:1198878. doi: 10.3389/fimmu.2023.1198878

58. Feng Z, Zhao Q, Ding Y, Xu Y, Sun X, Chen Q, et al. Identification a unique disulfidptosis classification regarding prognosis and immune landscapes in thyroid carcinoma and providing therapeutic strategies. *J Cancer Res Clin Oncol* (2023). doi: 10.21203/rs.3.rs-2910118/v1

59. Liu F, Yuan D, Liu X, Zhuo S, Liu X, Sheng H, et al. A demonstration based on multi-omics transcriptome sequencing data revealed disulfidptosis heterogeneity within the tumor microenvironment of esophageal squamous cell carcinoma. *Discovery Oncol* (2023) 14:96. doi: 10.1007/s12672-023-00711-5

60. Qi C, Ma J, Sun J, Wu X, Ding J. The role of molecular subtypes and immune infiltration characteristics based on disulfidptosis-associated genes in lung adenocarcinoma. *Aging (Albany NY)* (2023) 15:5075–95. doi: 10.18632/aging.204782

61. Wang T, Guo K, Zhang D, Wang H, Yin J, Cui H, et al. Disulfidptosis classification of hepatocellular carcinoma reveals correlation with clinical prognosis and immune profile. *Int Immunopharmacol* (2023) 120:110368. doi: 10.1016/j.intimp.2023.110368

62. Yang L, Liu J, Li S, Liu X, Zheng F, Xu S, et al. Based on disulfidptosis, revealing the prognostic and immunological characteristics of renal cell carcinoma with tumor thrombus of vena cava and identifying potential therapeutic target AJAP1. *J Cancer Res Clin Oncol* (2023). doi: 10.1007/s00432-023-04877-x

63. Xiong C, Ling H, Hao Q, Zhou X. Cuproptosis: p53-regulated metabolic cell death? *Cell Death Differ* (2023) 30:876–84. doi: 10.1038/s41418-023-01125-0

64. Han Y, Amin HM, Frantz C, Franko B, Lee J, Lin Q, et al. Restoration of shp1 expression by 5-AZA-2'-deoxycytidine is associated with downregulation of JAK3/STAT3 signaling in ALK-positive anaplastic large cell lymphoma. *Leukemia* (2006) 20:1602–9. doi: 10.1038/sj.leu.2404323

65. Johnston JA, Kawamura M, Kirken RA, Chen YQ, Blake TB, Shibuya K, et al. Phosphorylation and activation of the Jak-3 Janus kinase in response to interleukin-2. *Nature* (1994) 370:151–3. doi: 10.1038/370151a0

66. Macchi P, Villa A, Giliani S, Sacco MG, Frattini A, Porta F, et al. Mutations of Jak-3 gene in patients with autosomal severe combined immune deficiency (SCID). *Nature* (1995) 377:65–8. doi: 10.1038/377065a0

67. Witthuhn BA, Silvennoinen O, Miura O, Lai KS, Cwik C, Liu ET, et al. Involvement of the Jak-3 Janus kinase in signalling by interleukins 2 and 4 in lymphoid and myeloid cells. *Nature* (1994) 370:153–7. doi: 10.1038/370153a0

68. Yin Y, Zhang TT, Zhang DY. [Research progress of JAK-3 kinase and its inhibitors]. *Yao Xue Xue Bao* (2016) 51:1520–9.

10.3389/fimmu.2024.1258475

Glossary

ACC	Adrenocortical carcinoma
AUC	Area under the curve
AI	Artificial intelligence
CGGA	Chinese Glioma Genome Atlas
COAD	Colon adenocarcinoma
cDC1	Conventional dendritic cells 1
CRCA	COAD + rectum adenocarcinoma
DC	Dendritic cells
DFI	Disease-free interval
DSS	Disease-specific survival
DSP	Disulfidptosis
DRGs	Disulfidptosis-related genes
Edu	5-ethynyl-2′-deoxyuridine
GEO	Gene expression omnibus
GBM	Glioblastoma multiforme
HR	Hazard Ratio
HNSC	Head and neck squamous cell carcinoma
ICIs	Immune checkpoint inhibitors
ICD	Immunogenic cell death
ICGC	International Cancer Genome Consortium
KCA	Kidney carcinoma
KICH	Kidney chromophobe
KIRC	Kidney renal clear cell carcinoma
LASSO	Least absolute shrinkage and selection operator
LUAD	Lung adenocarcinoma
LCA	Lung carcinoma
DLBC	Lymphoid neoplasm diffuse large B-cell lymphoma
ML	Machine learning
NADPH	Nicotinamide adenine dinucleotide phosphate
NMF	Non-negative matrix factorization
OS	Overall survival
PBMC	peripheral blood mononuclear cells
PCPG	Pheochromocytoma and paraganglioma
PFI	Progression-free interval
PRAD	Prostate adenocarcinoma
ROC	Receiver operating characteristic
RCD	Regulated cell death
ssGSEA	Single-sample Gene Set Enrichment Analysis
siRNA	Small interfering RNA
STAD	Stomach adenocarcinoma
Tex	T cell exhaustion
TCGA	The Cancer Genome Atlas
TCIA	The Cancer Immunome Atlas
THCA	Thyroid cancer
THYM	Thymoma
TDG	Tumor driver genes
TME	Tumor microenvironment
TMB	Tumor mutation burden
UCEC	Uterine corpus endometrial carcinoma
UVM	Uveal melanoma
WGCNA	Weighted correlation network analysis

(Continued)

Continued

frontiers | Frontiers in Immunology

TYPE Original Research
PUBLISHED 26 February 2024
DOI 10.3389/fimmu.2024.1280525

OPEN ACCESS

EDITED BY
Antonella Sistigu,
Agostino Gemelli University Polyclinic (IRCCS), Italy

REVIEWED BY
Chengdong Liu,
Southern Medical University, China
Yasir Hameed,
Islamia University of Bahawalpur, Pakistan

*CORRESPONDENCE
Haixia Zhu
00zlingling@163.com
Yuan Liu
1409554480@qq.com

RECEIVED 20 August 2023
ACCEPTED 12 February 2024
PUBLISHED 26 February 2024

CITATION
Lin W, Zhang S, Gu C, Zhu H and Liu Y (2024) GLIPR2: a potential biomarker and therapeutic target unveiled – Insights from extensive pan-cancer analyses, with a spotlight on lung adenocarcinoma. *Front. Immunol.* 15:1280525. doi: 10.3389/fimmu.2024.1280525

GLIPR2: a potential biomarker and therapeutic target unveiled – Insights from extensive pan-cancer analyses, with a spotlight on lung adenocarcinoma

Wei Lin[1,2], Siming Zhang[1], Chunyan Gu[3], Haixia Zhu[1*] and Yuan Liu[1*]

[1]Cancer Research Center Nantong, Affiliated Tumor Hospital of Nantong University, Nantong, China, [2]Jiangsu Key Laboratory of Neuropsychiatric Diseases and Institute of Neuroscience, Soochow University, Suzhou, China, [3]Department of Pathology, Affiliated Nantong Hospital 3 of Nantong University (Nantong Third People's Hospital), Nantong, China

Background: Glioma pathogenesis related-2 (GLIPR2), an emerging Golgi membrane protein implicated in autophagy, has received limited attention in current scholarly discourse.

Methods: Leveraging extensive datasets, including The Cancer Genome Atlas (TCGA), Genotype Tissue Expression (GTEx), Human Protein Atlas (HPA), and Clinical Proteomic Tumor Analysis Consortium (CPTAC), we conducted a comprehensive investigation into GLIPR2 expression across diverse human malignancies. Utilizing UALCAN, OncoDB, MEXPRESS and cBioPortal databases, we scrutinized GLIPR2 mutation patterns and methylation landscapes. The integration of bulk and single-cell RNA sequencing facilitated elucidation of relationships among cellular heterogeneity, immune infiltration, and GLIPR2 levels in pan-cancer. Employing ROC and KM analyses, we unveiled the diagnostic and prognostic potential of GLIPR2 across diverse cancers. Immunohistochemistry provided insights into GLIPR2 expression patterns in a multicenter cohort spanning various cancer types. *In vitro* functional experiments, including transwell assays, wound healing analyses, and drug sensitivity testing, were employed to delineate the tumor suppressive role of GLIPR2.

Results: GLIPR2 expression was significantly reduced in neoplastic tissues compared to its prevalence in healthy tissues. Copy number variations (CNV) and alterations in methylation patterns exhibited discernible correlations with GLIPR2 expression within tumor tissues. Moreover, GLIPR2 demonstrated diagnostic and prognostic implications, showing pronounced associations with the expression profiles of numerous immune checkpoint genes and the relative abundance of immune cells in the neoplastic microenvironment. This multifaceted influence was evident across various cancer types, with lung adenocarcinoma (LUAD) being particularly prominent. Notably, patients with LUAD exhibited a significant decrease in GLIPR2 expression within practical

clinical settings. Elevated GLIPR2 expression correlated with improved prognostic outcomes specifically in LUAD. Following radiotherapy, LUAD cases displayed an increased presence of GLIPR2$^+$ infiltrating cellular constituents, indicating a notable correlation with heightened sensitivity to radiation-induced therapeutic modalities. A battery of experiments validated the functional role of GLIPR2 in suppressing the malignant phenotype and enhancing treatment sensitivity.

Conclusion: In pan-cancer, particularly in LUAD, GLIPR2 emerges as a promising novel biomarker and tumor suppressor. Its involvement in immune cell infiltration suggests potential as an immunotherapeutic target.

KEYWORDS

pan-cancer analysis, GLIPR2, LUAD, tumor suppressor, immune infiltration

1 Introduction

Cancer constitutes a significant contributor to global mortality and the profound compromise of well-being, exerting its impact on a universal scale (1). Presently, the absence of a comprehensive remedy for cancer is notably conspicuous. The year 2020 bore witness to the encroachment of Coronavirus Disease 2019 (COVID-19), resulting in considerable impediments to both the diagnosis and management of cancer (2). As a concrete illustration, the restriction of healthcare access consequent to the closure of medical facilities precipitated setbacks in the identification and treatment of malignant conditions. These setbacks, in turn, led to a transient decline in cancer incidence, succeeded by a subsequent upsurge in disease progression, culminating in escalated mortality rates. Despite substantial advancements in the sphere of oncological intervention, including immunotherapy, precision-targeted therapy, and radiation therapy (3–5), the 5-year overall survival (OS) rate for afflicted patients persistently eludes attainment of satisfactory levels.

Recent years have witnessed a revolutionary transformation in cancer research with the emergence of high-throughput sequencing technologies and comprehensive molecular analyses (6, 7). These innovations have brought to light novel biomarkers and therapeutic targets with the potential to profoundly impact the realms of cancer diagnosis, prognosis, and treatment strategies. Amid these emerging contenders, glioma pathogenesis related-2 (GLIPR2) has ascended in significance as a hub gene, owing to its multifaceted involvement across diverse domains of disease biology (8, 9).

GLIPR2, also recognized as Golgi-associated plant pathogenesis-related protein 1 (GAPR1), stands as a multifunctional protein that has garnered escalating attention due to its dual engagement in both normal cellular processes and the intricacies of cancer biology. GLIPR2 has been associated with a spectrum of cellular functions encompassing the regulation of autophagy and its entwinement in various neoplastic conditions (10, 11).

To comprehensively elucidate the functional and clinical implications of GLIPR2 across diverse cancer subtypes, this investigation integrates a multitude of analytical methodologies. Differential expression analysis, diagnostic curve evaluation, mutation scrutiny, methylation analysis, and examination of immune infiltration collectively depict the pivotal role of GLIPR2 in cancer pathogenesis. Moreover, validation of the discerned findings through scrutiny of a cohort of non-small cell lung cancer (NSCLC) patients from Nantong Tumor Hospital augments the clinical pertinence of the study. Finally, several lines of experiments indicated the tumor-suppressor function of GLIPR2 in suppressing malignant phenotype and facilitating the sensitivity of treatments. By amalgamating disparate datasets and deploying an array of bioinformatics techniques, this inquiry aspires to unravel the intricate interplay between the dysregulation of GLIPR2 and the evolution of malignancies. Furthermore, by illuminating the molecular mechanisms underpinning its participation and its potential as a diagnostic, prognostic, and therapeutic target, this exploration contributes to a heightened comprehension of the intricacies of cancer biology. It also charts a course for the formulation of precision medicine approaches.

2 Methods and materials

2.1 Data collection and preprocessing for pan-cancer patients

RNA sequencing data, along with survival information and clinical phenotypic characteristics, were gathered from The Cancer Genome Atlas (TCGA) repository (https://www.cancer.gov/ccg/research/genome-sequencing/tcga), housed within the University of California Santa Cruz (UCSC) Xena platform (http://www.genome.ucsc.edu/). We utilized the STAR (Spliced Transcripts Alignment to a Reference) pipeline to process the

RNAseq data, extracting transcripts per million (TPM) values for downstream analysis. Our data filtering strategy involved removing samples lacking clinical information and the exclusion of duplicate entries to ensure the integrity and reliability of the dataset. Following these filtering criteria, we performed data normalization using the $\log_2$ transformation of the TPM values, with the addition of one to accommodate zero values ($\log_2$(value +1)). After thorough data refinement and normalization procedures, a comprehensive cohort comprising 10,924 samples of malignant tumor tissues and 727 samples of adjacent paracancerous tissues was assembled for analysis. Simultaneously, non-neoplastic control tissues sourced from the Genotype Tissue Expression (GTEx) project (https://www.gtexportal.org) were procured to complement the dataset. Furthermore, a subset encompassing 301 patients with NSCLC, all of whom possessed pertinent clinical records related to their survival durations, was curated from the clinical archives of the Affiliated Tumor Hospital of Nantong University. Lastly, 18 paired samples (cervical squamous cell carcinoma and endocervical adenocarcinoma: CESC, lung adenocarcinoma: LUAD; lung squamous cell carcinoma: LUSC) from Nantong third hospital were included to describe the expression of GLIPR2. Written informed consent was obtained from each participating patient in this study. The ethics committee of the Affiliated Tumor Hospital of Nantong University and Nantong Third People's Hospital approved this study.

2.2 Expression analysis of GLIPR2

The architectural conformation and subcellular localization (A-431, U-251MG and U20S cell lines) of GLIPR2 were inferred from data accessible in the Human Protein Altas (HPA) repository (https://www.proteinatlas.org/). To elucidate GLIPR2 RNA expression profiles, we harnessed the integrated resources of TCGA (https://www.cancer.gov/ccg/research/genome-sequencing/tcga), coupled with the GTEx consortium, and employed TIMER2.0 (http://timer.cistrome.org/) as a complementary resource. Transforming the expression data through a logarithmic base 2 conversion, we subjected the resultant values to t-tests. Statistical significance was established at a threshold of $P < 0.05$, delineating distinctions in expression patterns between malignant and healthy tissue contexts. Computational analysis was executed employing the R programming language (Version R4.2.1), while the visualization of data distributions was facilitated by means of the "ggpubr" package integrated within the R environment. Furthermore, the HPA repository in conjunction with the Clinical Proteomic Tumor Analysis Consortium (CPTAC) database (https://ualcan.path.uab.edu/) were harnessed to scrutinize the abundance and localization of GLIPR2 at the protein level.

2.3 Diagnostic analysis of GLIPR2

In the diagnostic analysis of GLIPR2, we leveraged data from XENA database to assess the potential applicability of GLIPR2 in cancer diagnostics. The evaluation involved the construction of receiver operating characteristic (ROC) curves, aiming to discern the area under the curve (AUC) values. Notably, an AUC exceeding 0.5 indicates substantial diagnostic efficacy. The ROC curve analysis was performed using the Xiantao Academic Online Tool (https://www.xiantaozi.com/), which integrates data from the XENA database processed through the Toil pipeline. This approach unifies samples from the GTEx project with cancer tissue samples from TCGA.

2.4 Copy number variation and methylation analysis of GLIPR2

The investigation of distinct neoplastic contexts has involved a thorough examination of the mutational spectra inherent to GLIPR2. To achieve this objective, the computational framework provided by the cBioPortal tool (http://www.cbioportal.org/) was utilized. The initiation of the analytical process entailed the input of "GLIPR2" within the "Query" module, facilitating interaction with the extensive dataset known as the "TCGA Pan Cancer Atlas Studies" cohort. The interplay between the pertinent genetic locus and the various malignancies within this dataset reveals nuanced insights. Through the "cancer type summary" and "mutation" modules, a comprehensive depiction of GLIPR2 genomic perturbations emerges, elucidating intricate details regarding their spatial distribution, typological attributes, and numerical prevalence.

The assessment of methylation status in GLIPR2 across diverse cancer types and their corresponding adjacent tissues was conducted using the UALCAN repository (http://ualcan.path.uab.edu/analysis.html). Changes in DNA methylation profiles could impact gene expression, with regulation primarily influenced by methylation of CpG sites proximal to the promoters (12). To ascertain differentially methylated promoter regions, MEXPRESS was employed to calculate the association between GLIPR2 expression and DNA methylation (https://mexpress.ugent.be/).

2.5 Immune infiltration analysis of GLIPR2

The ESTIMATE algorithm was employed to analyze the disparity in stromal score and immune score utilizing the package "estimate" (Version R4.2.1) (13). The examination of the associations between GLIPR2 expression and the tumor mutation burden (TMB), as well as homologous recombination deficiency (HRD), across distinct tumors sourced from TCGA cohorts, was conducted through the Sanger Box platform. Pearson's rank correlation test was executed, yielding both the partial correlation (cor) and corresponding *p*-value. Explorations into the connections between GLIPR2 expression and immunomodulatory genes, alongside tumor-infiltrating immune cells (TIICs) across multiple tumors. These immune cells encompass B cells, $CD4^+$ T memory cells, $CD8^+$ T cells, NK cells, monocytes, macrophages, neutrophils, among others. Subsequently, a series of algorithms were formulated to quantify the extent of TIICs infiltration within the tumor

microenvironment (TME), leveraging bulk RNA-seq data. However, diverse algorithms and marker gene sets related to TIICs may engender calculation discrepancies. In order to circumvent these inconsistencies, we carried out a comprehensive determination of TIICs infiltration levels using six distinct independent algorithms: CIBERSORT (14), MCP-counter (15), EPIC (16), quanTIseq (17), XCELL (18), and TIMER (19).

2.6 Immunotherapy alone and combined with single-cell sequencing cohorts

The cohorts designated for immunotherapy, both in isolation and in conjunction with single-cell sequencing, were retrieved from authoritative databases. Immunotherapy cohorts were sourced from the BEST database (https://rookieutopia.com/appdirect/BEST/) (20). Single-cell expression profiles subsequent to immunotherapeutic interventions were procured from the TISCH database (http://tisch.comp-genomics.org/).

2.7 Tissue microarray construction and immunohistochemistry

The real-world cohort study utilized a tumor and paracancer tissue microarray (TMA) obtained from the Affiliated Tumor Hospital of Nantong University (Supplementary Table S1). The construction process of the TMA has been previously described (21). For the immunohistochemical (IHC) staining, the primary anti-GLIPR2 antibody (1:20, SantaCruz Biotechnology, sc-398529, USA) was employed. Following three washes with phosphate-buffered saline (PBS), the tissue sections were incubated with a secondary antibody (Poly-HRP-goat-anti-mouse antibody) for 20 minutes at 37°C, followed by staining with a diaminobenzidine solution. Subsequently, the TMA slides were scanned using the Nikon microscopy system (Japan). The labeling intensity was estimated as negative (0), weak (1), moderate (2) or strong (3). The extent of staining, defined as the percentage of positively stained cells, was scored as 1 (≤10%), 2 (11–50%), 3 (51–80%) and 4 (>80%). The total immunoreactive score (IRS) was obtained by multiplying the staining intensity score and the staining extent score and ranked from 0 to 12 (22, 23). The evaluation of staining intensity was carried out by two pathologists independently, who were kept blinded to the associated clinical data.

2.8 Cell culture and plasmid transfection

Beas-2b, H1299, and PC9 cells were cultured in RPMI 1640 medium supplemented with 10% fetal bovine serum (Gibco, Grand Island, NY, USA), and 1% Penicillin-Streptomycin (NCM Biotech, China). Similarly, A549 cells were nurtured in F-12K medium with 10% FBS. The maintenance of all cell lines in their respective culture media ensured optimal growth and experimental conditions. Additionally, regular screening for Mycoplasma species was conducted prior to any experimental procedures.

The plasmids for GLIPR2 overexpression and control were constructed by Shanghai Jikai Gene Technology Co. Ltd. Initially, high-fidelity PCR amplification was employed to obtain the GLIPR2 cDNA, which was subsequently inserted into the Age I site of the GV208 plasmid. Following this, the purified plasmid was transformed into competent cells for amplification, followed by plasmid extraction for subsequent use. H1299 cells in the logarithmic growth phase were seeded in six-well plates at a density of 5×10^5 cells per well, with three replicates per group. Upon achieving 60%-70% confluence, H1299 cells were transfected with the plasmid using Lipofectamine 3000 (Life Technologies).

2.9 Quantitative real-time PCR

The protocol for RNA extraction and quantitative real-time PCR (qRT-PCR) followed established procedures as outlined in the literature (21). Upon cell thawing, a minimum of three passages was conducted before commencing experimental procedures. Subsequently, cells underwent centrifugation at 12,000 × g and were suspended in TRIzol reagent (Invitrogen, USA) for RNA extraction. RNA purification involved chloroform extraction followed by isopropanol precipitation. Post RNA extraction, concentrations were determined and normalized through dilution processes. A total of 500 ng of RNA was reverse transcribed into cDNA utilizing the M-MLV kit per the manufacturer's instructions (Accurate Biology, China). QPCR were performed using iQ SYBR green (AG11701, Accurate Biology, China) on a BioRad CFX97 instrument. A standard curve was generated by 1:10 dilutions of a reference cDNA sample to amplify all target PCR products. Transcript abundance was determined by normalization to human GAPDH (Sangon Biotech, China). Experimental samples were compared against this standard curve to ascertain relative transcript abundance. The primer sequences used for GLIPR2 amplification are provided as follows: forward primer, 5′-GAAGATGGGCGTGGGGAAGG-3'; reverse primer, 5′-TTACTT CTTCG GCGGCAGGAC-3'.".

2.10 Immunofluorescence

The immunofluorescence protocol for cellular analysis was conducted in accordance with previously outlined procedures (24). Briefly, the cells underwent a series of procedures including three washes with PBS, fixation with 4% paraformaldehyde for 20 minutes, and treatment with 1% Triton X-100 for 10 minutes. Subsequent to a 1-hour blocking step, the cells were incubated with anti-GLIPR2 antibody sourced from Santa Cruz, diluted to 1:20, and maintained at 4°C for 18 hours. Following this, the cells were exposed to donkey anti-mouse 555 secondary antibody, diluted to 1:500 (Millipore, USA). DAPI staining of the nucleus was conducted for 5 minutes. Finally, high-resolution images of the

stained sections were captured using a scanning microscope (Nikon, Japan).

2.11 Cell invasion and wound healing assay

H1299 cell invasiveness was assessed utilizing 24-well transwell chambers (8μm, Corning, Lowell, MA, USA). In a succinct sequence, following a 24-hour incubation period, the chambers underwent cleansing with cotton swabs, fixation with 4% paraformaldehyde for 20 minutes, and subsequent staining with crystal violet. The enumeration of cells was conducted in three randomly selected fields within each chamber, and the resultant values were averaged.

For the evaluation of migratory potential, a single-cell suspension was introduced into a 6-well plate and cultivated until cells reached 90%-100% confluency. Subsequently, a controlled and vertical scratch was generated using a 200 μl pipette tip, creating a wound. Detached cells were systematically purged with PBS, and the medium was subsequently replaced with 1 ml of serum-free medium. The 24-well plate was positioned in the Live Cell Imaging System (Leica, Brunswick, Saxony, Germany), capturing images of the wound at both 0 h and 24 h. Measurements of wound distances were taken, and the rate of wound healing was evaluated.

2.12 Drug sensitivity analysis

H1299 cells were seeded into 96-well plates at a density of 5*10^3 cells per well. Following plasmid transfection, the cells were exposed to varying concentrations of cisplatin (MedChemExpress, USA) at 12.5, 25, and 50 μM, or subjected to irradiation with X-rays at doses of 2, 4, 6, and 8 Gy, administered at a dose rate of 1 Gy. After 48 hours, cell proliferation was assessed using a colorimetric assay employing the cell counting Kit-8 (CCK-8; Bimake, Houston, TX, USA), following the manufacturer's instructions.

2.13 Statistical analysis

Data processing, statistical analysis, and visualization were comprehensively performed using the R 4.2.1 software package. For datasets exhibiting normal distribution, the unpaired Student t-test was applied, whereas for datasets deviating from normal distribution, the Wilcoxon test was employed. Pearson's correlation coefficients were utilized to evaluate the association between two continuous variables. Considering the potential impact of skewed data, Spearman's correlation analysis was also performed to ensure a comprehensive examination of the relationship. The prognostic value was evaluated by Kaplan-Meier analysis. A significance level of $P < 0.05$ was considered indicative of statistical significance. All reported *p*-values resulting from TCGA data, were subjected to adjustment for multiple testing using the Benjamini-Hochberg procedure to control the false discovery rate (FDR).

3 Results

3.1 Procedural overview and expression analysis of GLIPR2 in cancer

The study's procedural overview is depicted in Figure 1. Primarily, the current understanding underscored that the protein structure of GLIPR2 comprised multiple α-folds, as delineated in Figure 2A. It is predominantly distributed in the cytoplasm, and intriguingly, its observation in the U-251MG cell line reveals co-localization with microtubule proteins, suggesting its potential involvement in the constitution of the cellular cytoskeleton (Figure 2B). Analysis of GLIPR2 gene expression patterns was executed using the TIMER 2.0 database. The derived outcomes revealed a prevailing downregulation of GLIPR2 across a spectrum of cancers (Figure 2C), inclusive of but not limited to bladder urothelial carcinoma (BLCA), breast invasive carcinoma (BRCA), colon adenocarcinoma (COAD), kidney chromophobe (KICH), LUAD, LUSC, pancreatic adenocarcinoma (PAAD), prostate adenocarcinoma (PRAD), CESC, and rectum adenocarcinoma (READ). Employing the HPA database, the investigation into the protein expression profile of GLIPR2 across various malignancies transpired. As portrayed in Figure 2D, heightened expression of GLIPR2 was conspicuous within tissues like the nasopharynx, bronchus, lung, esophagus, rectum, prostate, cervix, appendix, spleen, and bone marrow. Notably, a discernable trend emerged, where most malignancies exhibited moderate cytoplasmic positivity, whereas colorectal, breast, gastric, and pancreatic cancers displayed a general lack of such positivity. To gain deeper insights into GLIPR2 expression patterns, an exploration encompassing TCGA, GTEx and CPTAC datasets was conducted. These endeavors elucidated an augmented GLIPR2 expression in BLCA, BRCA, cholangiocarcinoma (CHOL), amongst others, in contrast to a diminution in breast, colon, ovarian cancers, among others (Figures 2E, F). Cumulatively, these findings intimated that GLIPR2 evinced dysregulation across diverse cancer types, thus postulating its pivotal involvement in the sphere of cancer diagnosis.

3.2 Genetic alterations and methylation patterns of GLIPR2 in various cancers

The cBioPortal tool revealed noteworthy variations in the genetic makeup of GLIPR2, exhibiting distinct patterns of alteration frequencies across different malignancies. In the context of acute myeloid leukemia (LAML), a deep deletion event was detected at a prevalence rate of 0.5%. Furthermore, diffuse large B-cell lymphoma (DLBC) demonstrated an amplification frequency of 2.08%, followed by uterine carcinosarcoma (UCS) at 1.75%, ovarian serous cystadenocarcinoma (OV) at 1.03%, skin cutaneous melanoma (SKCM) at 0.9%, testicular germ cell tumors (TGCT) at 0.67%, PRAD at 0.61%, liver hepatocellular carcinoma (LIHC) at 0.27%, and brain lower grade glioma (LGG) at 0.19%. In addition, the identified alterations encompassed diverse combinations of two

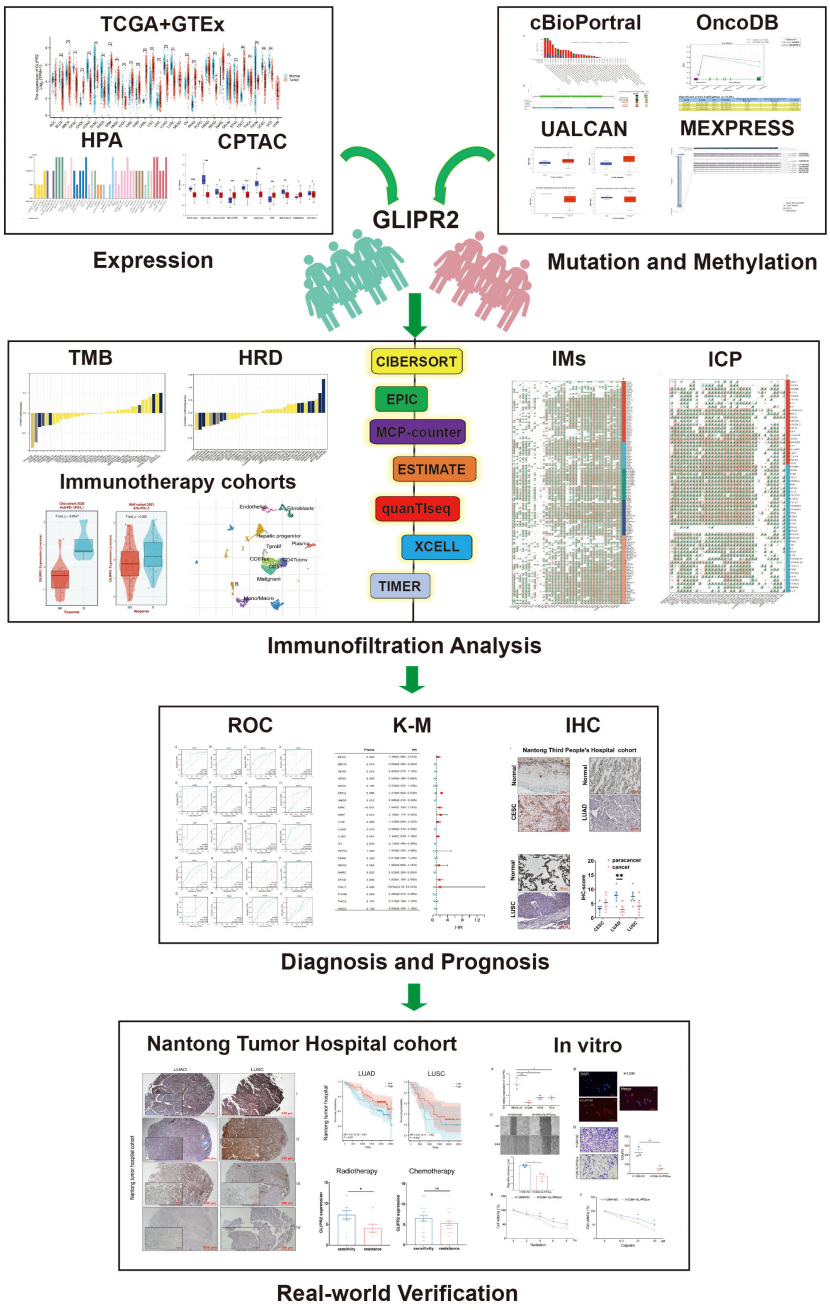

FIGURE 1
The flow chart of the study.

or more mutational types within other implicated tumor types (Supplementary Figure S1A). Notably, within GLIPR2, a total of 34 variants of uncertain significance (VUS) were identified across various tumor contexts (Supplementary Figure S1B; Supplementary Table S2).

Aberrant DNA methylation patterns are implicated in gene dysregulation in cancer (25). To investigate the causal relationship between aberrant expression patterns of GLIPR2 and methylation, we utilized the UALCAN database (26) along with OncoDB (27) to explore abnormal GLIPR2 methylation patterns in both normal and tumor tissues. Furthermore, we utilized MEXPRESS (28) to examine the correlation between GLIPR2 expression and CpG islands in tumor tissues. By integrating gene methylation differences between cancer and normal groups from the UALCAN database (Supplementary Figure S2), we observed that the reduced expression in LUAD, THCA, and PRAD may be associated with increased methylation (Figures 2C, 3A–C). Conversely, in cancers where methylation abnormalities are decreased, such as HNSC, elevated expression appears to synchronize with decreased methylation (Figure 2C; Supplementary Figure S2).

To further refine the macroscopic dysregulation of methylation expression into microscopic differences at methylation sites, we

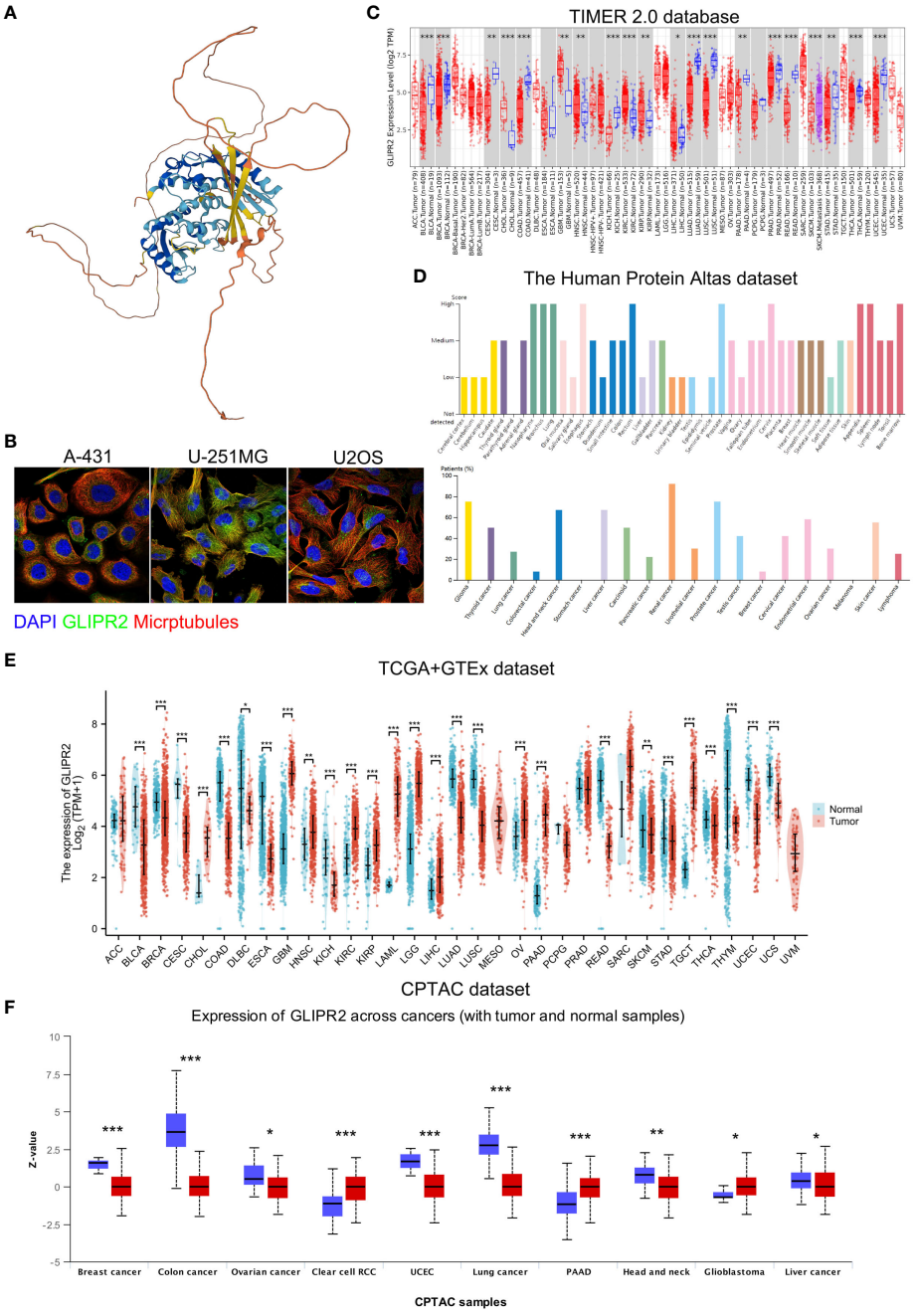

FIGURE 2
Comprehensive overview of GLIPR2 in cancer. **(A)** Representation of the molecular structure of GLIPR2. **(B)** Visualization of GLIPR2's subcellular distribution within cells. **(C)** Analysis of GLIPR2 gene expression at the RNA level across diverse cancer types, providing insights into the transcriptomic landscape. **(D)** Examination of GLIPR2 expression at the protein level, showcasing tissue-specific spatial distribution and prevalence among cancer patients. **(E)** Comparative analysis of GLIPR2 expression at the RNA level, highlighting differences between normal and cancerous tissues. **(F)** Comprehensive proteomic analysis depicting GLIPR2 expression across different cancers, complementing the preceding panels with a protein-level perspective. *$P < 0.05$, **$P < 0.01$, ***$P < 0.001$.

conducted further validation through OncoDB database. We identified that in comparison to adjacent normal tissues, LUAD exhibited high methylation at the cg06484397 and cg13644528 sites, THCA showed elevated methylation at cg14062007, and PRAD displayed increased methylation at cg13644528 (Figures 3D–F). In MEXPRESS database, changes in methylation sites cg06484397 (R = -0.115) and cg13644528 (R= -0.272) in LUAD were negatively correlated with GLIPR2 expression, while in PRAD, methylation at cg13644528 (R= -0.166) showed a negative correlation with GLIPR2 expression (Figures 3G–I). These commonalities suggest that targeting cg06484397 and cg13644528 in LUAD, as well as cg13644528 in PRAD, may restore normal GLIPR2 expression levels. Thus, these sites could serve as potential therapeutic targets for gene therapy in LUAD and PRAD.

10.3389/fimmu.2024.1280525

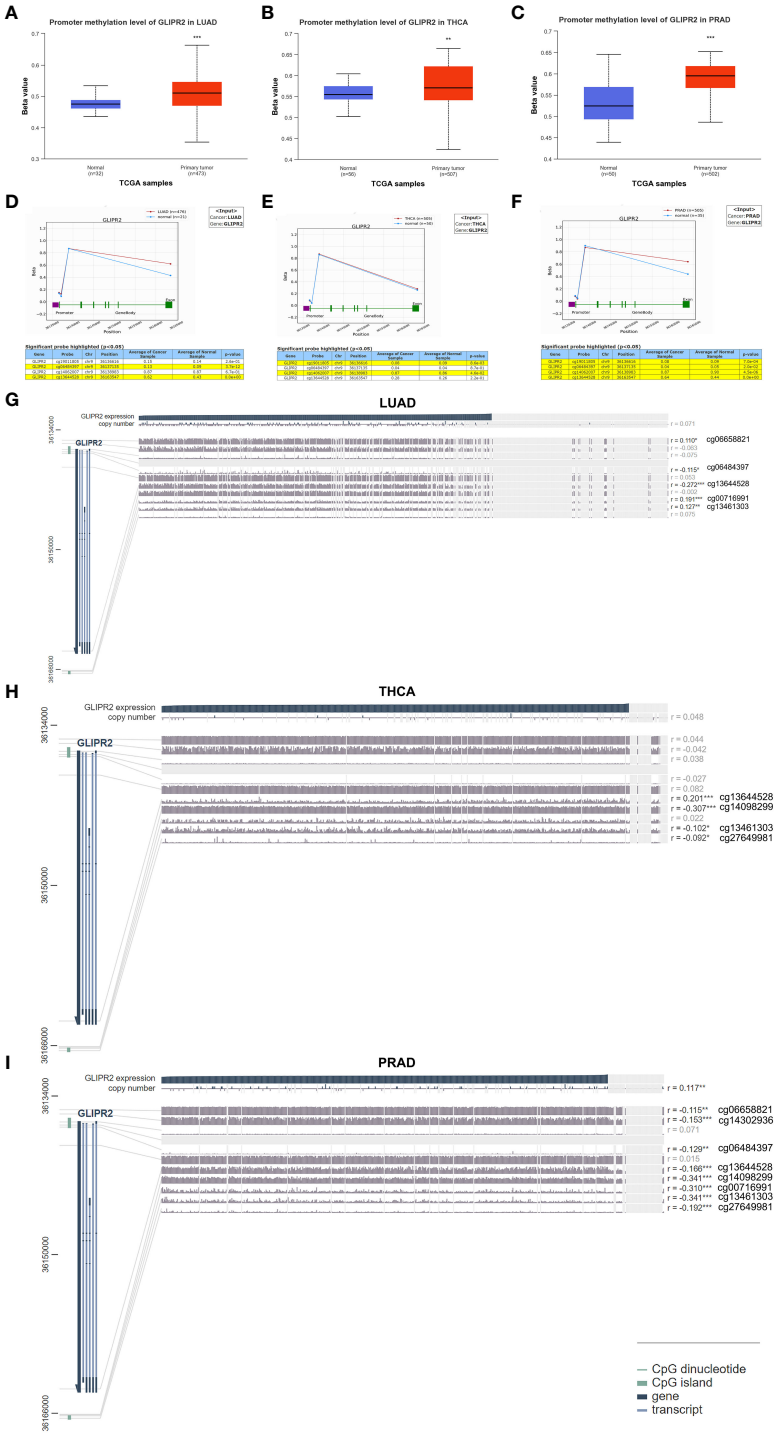

FIGURE 3
Methylation analysis of GLIPR2. Methylation analysis of GLIPR2 in lung adenocarcinoma (LUAD, **A**), thyroid carcinoma (THCA, **B**), and prostate adenocarcinoma (PRAD, **C**) and normal tissues was conducted using the UALCAN database. Exploration of GLIPR2 methylation status in LUAD **(D)**, THCA **(E)**, and PRAD **(F)** was performed via the OncoDB database. Visualization of the methylation sites within the GLIPR2 DNA sequence associated with gene expression was accomplished using MEXPRESS in LUAD **(G)**, THCA **(H)**, and PRAD **(I)**. The GLIPR2 expression is represented by the blue line. *Pearson*'s correlation coefficients and p-values for methylation sites and query gene expression are provided on the right side. $^{**}P < 0.01$, $^{***}P < 0.001$.

3.3 Advancing immune landscape characterization and immunotherapeutic potential of GLIPR2 in diverse cancers

The substantial influence exerted by the TME on the progression of cancer is universally acknowledged. Comprising a complex interplay of tumor cells, stromal elements, and immune components, the TME orchestrates intricate and dynamic interactions (29). The Estimation of Stromal and Immune cells in Malignant Tumor tissues using ESTIMATE algorithm have emerged as a robust computational tool for quantifying the infiltration of stromal and immune cells, thereby revealing immune scores and stromal scores. Our investigation into the expression of GLIPR2 has uncovered a positive correlation with immune scores in several cancer types, including low-grade glioma (LGG), CESC, LUAD, as well as other neoplastic tissues. However, it is important to note the observed negative correlation in GBM, although the *p*-value of 0.07 and correlation coefficient (r) of -0.15 suggest that this association may not reach conventional levels of statistical significance (Figure 4A).

Employing the metrics of TMB and HRD, the potential of GLIPR2 as an indicator of immunotherapeutic responses across diverse cancer types was ascertained. The examination revealed a positive nexus between GLIPR2 expression and TMB in COAD ($P < 0.001$), READ ($P < 0.001$), and BRCA ($P = 0.014$). Conversely, an inverse relationship transpired in LUAD ($P = 0.007$), PRAD ($P = 0.002$), LIHC ($P = 0.016$), UCS ($P = 0.029$), and CHOL ($P = 0.043$) (Figure 4B; Supplementary Table S3). Moreover, a positive correlation between GLIPR2 expression and HRD materialized in LGG ($P = 0.049$), BRCA ($P < 0.001$), SARC ($P = 0.006$), LIHC ($P = 0.003$), OV ($P = 0.002$), BLCA ($P < 0.001$), and KICH ($P = 0.005$). In contrast, a negative correlation was discerned in LUAD ($P = 0.003$), stomach and esophageal carcinoma (STES, $P < 0.001$), stomach adenocarcinoma (STAD, $P < 0.001$), HNSC ($P = 0.008$), LUSC ($P < 0.001$), THYM ($P = 0.048$), TGCT ($P = 0.029$), and SKCM ($P = 0.037$) (Figure 4C; Supplementary Table S4).

The TCGA dataset underwent deconvolution through a composite application of computational algorithms, including CIBERSORT, EPIC, MCP-counter, quanTIseq, XCELL, and TIMER (Figures 5A–F). The findings underscored substantial disparities in the inferred proportions of distinct cell populations across these algorithmic methodologies. Nonetheless, a consistent pattern emerged in the prevalence of M0 (naïve) macrophages and uncharacterized cellular entities between adjacent and tumor cohorts, aligning coherently across the entire spectrum of accessible techniques. Notably, the neoplastic specimens were conspicuously infiltrated by M1 macrophages and regulatory T (Treg) cells. Of distinct significance, the estimates pertaining to M1 macrophages and Treg cells were uniquely achievable through CIBERSORT, quanTIseq, and XCELL. The resulting revelations collectively unveiled a marked augmentation in the incidence of Treg cells and M1 macrophages within the tumor milieu, except for the CIBERSORT algorithm which indicated a reduction in Treg cell abundance. Concurrently, the abundance of $CD8^+$ T cells, estimable through CIBERSORT, MCP-counter, quanTIseq, XCELL, and TIMER algorithms, exhibited a conspicuous elevation within tumor specimens, except for the EPIC estimate which indicated a notable decline. Notably, QuanTIseq emerged as the solitary technique enabling the quantification of cellular fractions, thus facilitating comprehensive comparisons within and between samples. Further elucidation of the statistical significance of inter-algorithmic divergences is provided in Supplementary Table S5.

In the context of our comprehensive pan-cancer analysis aimed at deciphering the immunological implications of GLIPR2, the identification of specific malignancies conducive to anti-GLIPR2 immunotherapy holds paramount significance. Our findings elucidated a discernible positive correlation of GLIPR2 with most immunomodulatory elements across various cancers, including kidney papillary cell carcinoma (KIRC), OV, pan-kidney cohort (KIPAN), LIHC, BRCA, LUAD, THCA, PAAD and BLCA (Supplementary Figure S3; Supplementary Tables S6, S7). Notably, the emergence of immune checkpoint (ICP) blockade proteins as promising candidates for cancer immunotherapy prompted us to conduct a meticulous evaluation of the intricate interplay between GLIPR2 expression levels and the expressions of ICP genes across various malignancies. Remarkably, GLIPR2 exhibited a consistently positive correlation with the expression of ICP genes across various cancers, including LUAD, KIPAN, LIHC, BRCA, THCA, PAAD, KIRC, OV, BLCA (Figure 5G; Supplementary Tables S8, S9).

Analysis of immunotherapy cohort data suggests that GLIPR2 expression level is closely related to the patient's response to immunotherapy (Figure 6A). To further reveal the underlying mechanisms, we analyzed the immune cell types in the gene profiles of pan-cancer receiving immunotherapy by single cell sequencing. GLIPR2 expression was found to be enriched in monocyte/macrophage, NK, and T proliferation cells, suggesting potential roles in immune cell recruitment and alterations in the immune microenvironment. Intriguingly, this expression pattern of GLIPR2 was robust to pan-cancer (Figures 6B–H).

In concise summation, the prominent role of GLIPR2 in shaping the landscape of immune infiltration across diverse cancers is manifest, firmly positioning it as a compelling candidate for pioneering immunotherapeutic interventions within the realm of oncology.

3.4 Deciphering prognostic and diagnostic significance of GLIPR2

Cancer diagnosis and prognosis monitoring are critical elements in mitigating cancer-related mortality (30). Markers demonstrating both prognostic and predictive value across diverse cancers warrant meticulous investigation to substantiate their clinical utility. In this study, we employed ROC curves to assess the discriminative potential of GLIPR2 expression levels between malignant and non-neoplastic tissues. In the context of evaluating diagnostic performance, the AUC was selected as the principal metric to measure the discriminative efficacy of our model. In adherence to established conventions, an initial threshold of AUC > 0.5 was employed to delineate performance surpassing random chance. The graphical representation of these ROC curves is

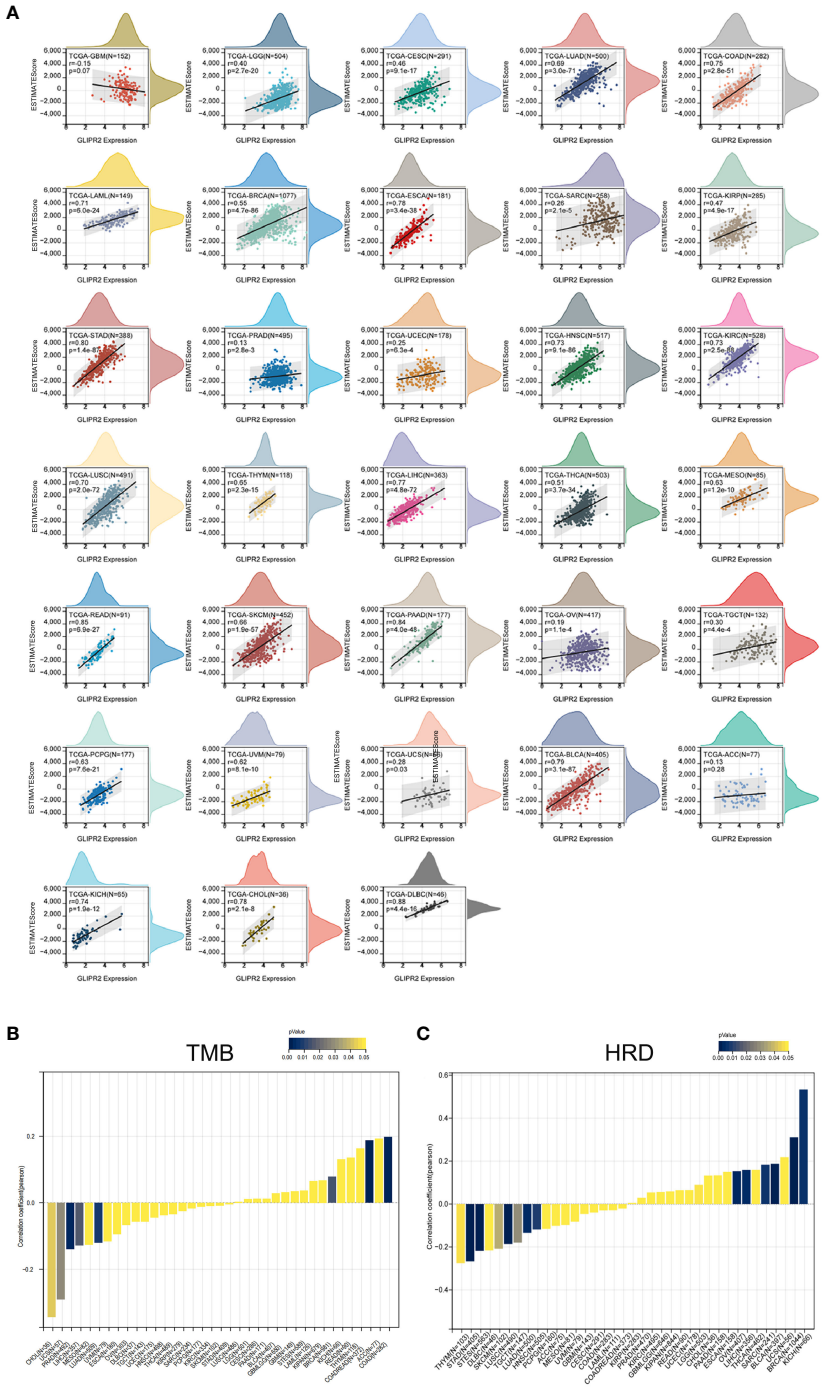

FIGURE 4
Immune assessment of GLIPR2: estimation, correlation, and association. **(A)** Estimate score. **(B)** Correlation with tumor mutation burden. **(C)** Correlation with homologous recombination repair defects.

illustrated in Supplementary Figure S4 (Supplementary Table S10). The derived AUC values provided compelling evidence that GLIPR2 exhibited a robust capacity to effectively discriminate between malignancy and normalcy across diverse cancer types. However, our primary emphasis is on highlighting exceptional diagnostic accuracy. Consequently, we specifically emphasize instances where the AUC exceeds the threshold of 0.9. Noteworthy observations include CESC (AUC=0.977), CHOL (AUC=0.975), COAD (AUC=0.943), colorectal adenocarcinoma (CEAD, AUC=0.988), KICH (AUC=0.924), LUAD (AUC=0.987), LUSC (AUC=0.994), and PAAD (AUC=0.925), thereby reinforcing the diagnostic potential attributed to GLIPR2 (Figure 7A). Subsequently, KM analysis was employed to assess the prognostic value of pan-cancer GLIPR2 levels in patients. In the majority of cancers, such as BRCA, CESC, HNSC, LUAD, OV, SARC and THYM, GLIPR2, acting as a protective factor, demonstrated a

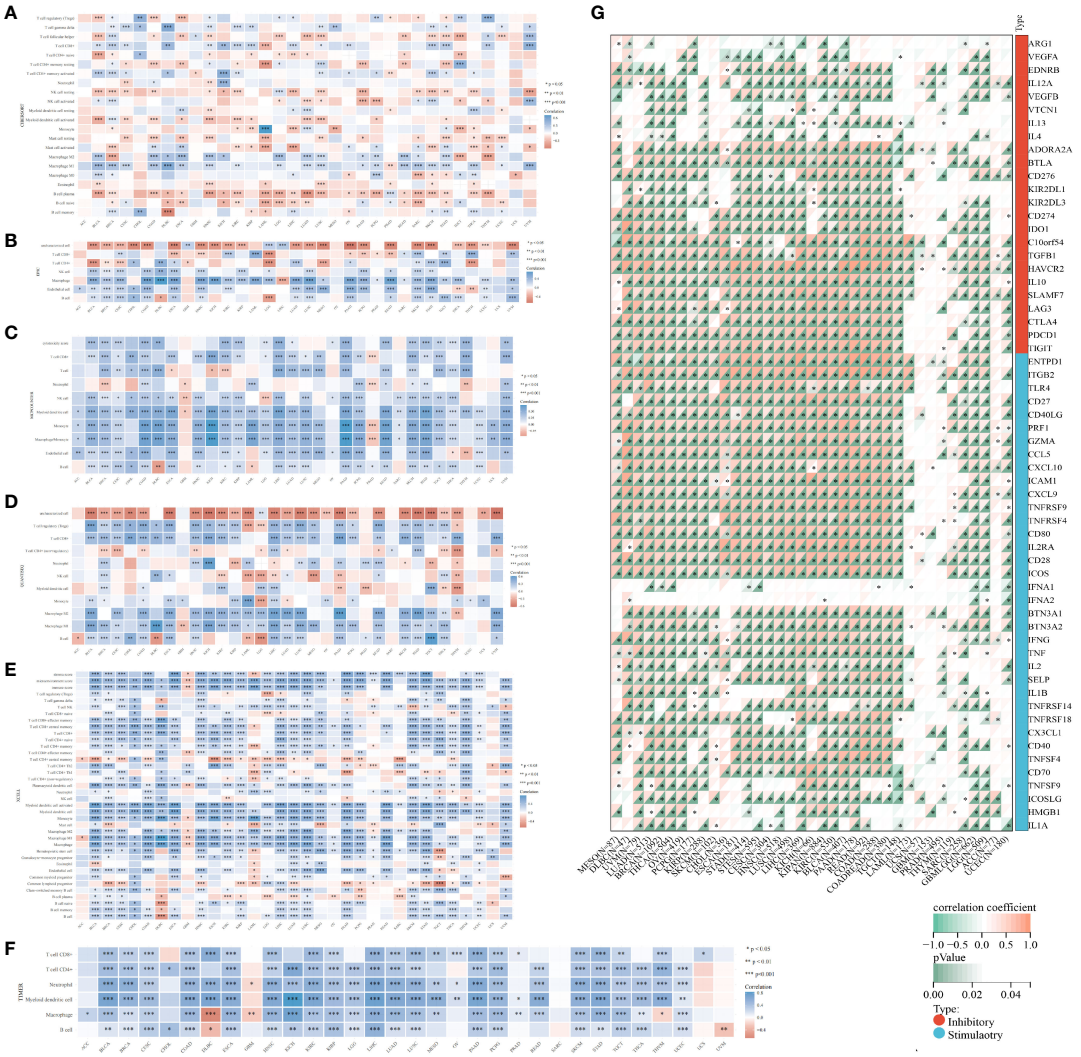

FIGURE 5
Algorithmic exploration of immune cell infiltration and immunomodulation. Immune cell infiltration was rigorously assessed through a series of mRNA-based immune infiltration prediction algorithms, including CIBERSORT **(A)**, EPIC **(B)**, MCP-counter **(C)**, quanTIseq **(D)**, XCELL **(E)**, and TIMER **(F)**. **(G)** Correlation of GLIPR2 expression levels with immune checkpoint-related genes, darker colors correspond to smaller *p*-values, indicating a higher level of statistical significance in the correlation. *$P < 0.05$, **$P < 0.01$, ***$P < 0.001$.

reduced risk of death. Conversely, in cancers such as BLCA, KIRC, KIRP, LUSC and STAD, an elevated expression of GLIPR2 was associated with an increased risk of mortality (Figure 7B) Integrated prognostic and diagnostic analysis identified LUAD, LUSC, and CESC as cancers most likely to benefit from the GLIPR2 biomarker (Figure 7C). Pathological validation revealed a pronounced decrease in GLIPR2 expression in LUAD (Figure 7D; Supplementary Figure S6).

3.5 Predictive merit of GLIPR2 infiltration for NSCLC in a real-world cohort

NSCLC, known for its status as the most prevalent and lethal cancer globally (31), became the primary focus of our investigation following a comprehensive pan-cancer assessment of GLIPR2. Then we embarked on a focused inquiry within a NSCLC cohort sourced from Nantong Tumor Hospital. Notably, within the context of LUAD, IHC scores for GLIPR2 in stage III and IV cases exhibited statistically significant decrease in comparison to stages I and II, a trend that was not evident in LUSC specimens (Figures 8A–C).

In consideration of these compelling findings, we undertook meticulous survival analyses predicated upon the levels of GLIPR2$^+$ infiltration within the cohorts of LUAD and LUSC patients derived from Nantong Tumor Hospital. Within the realm of LUAD, heightened expression of GLIPR2 was associated with a favorable prognosis, whereas discerning significant survival disparities of GLIPR2 expression was not observed in the context of LUSC (Figure 8D). Expanding our investigative scope to encompass the extensively accessible TCGA dataset, we observed congruence between outcomes derived from the Nantong Tumor Hospital cohort and the TCGA dataset (Supplementary Figure S5). This concordance substantially bolsters the veracity of our findings on a broader scale.

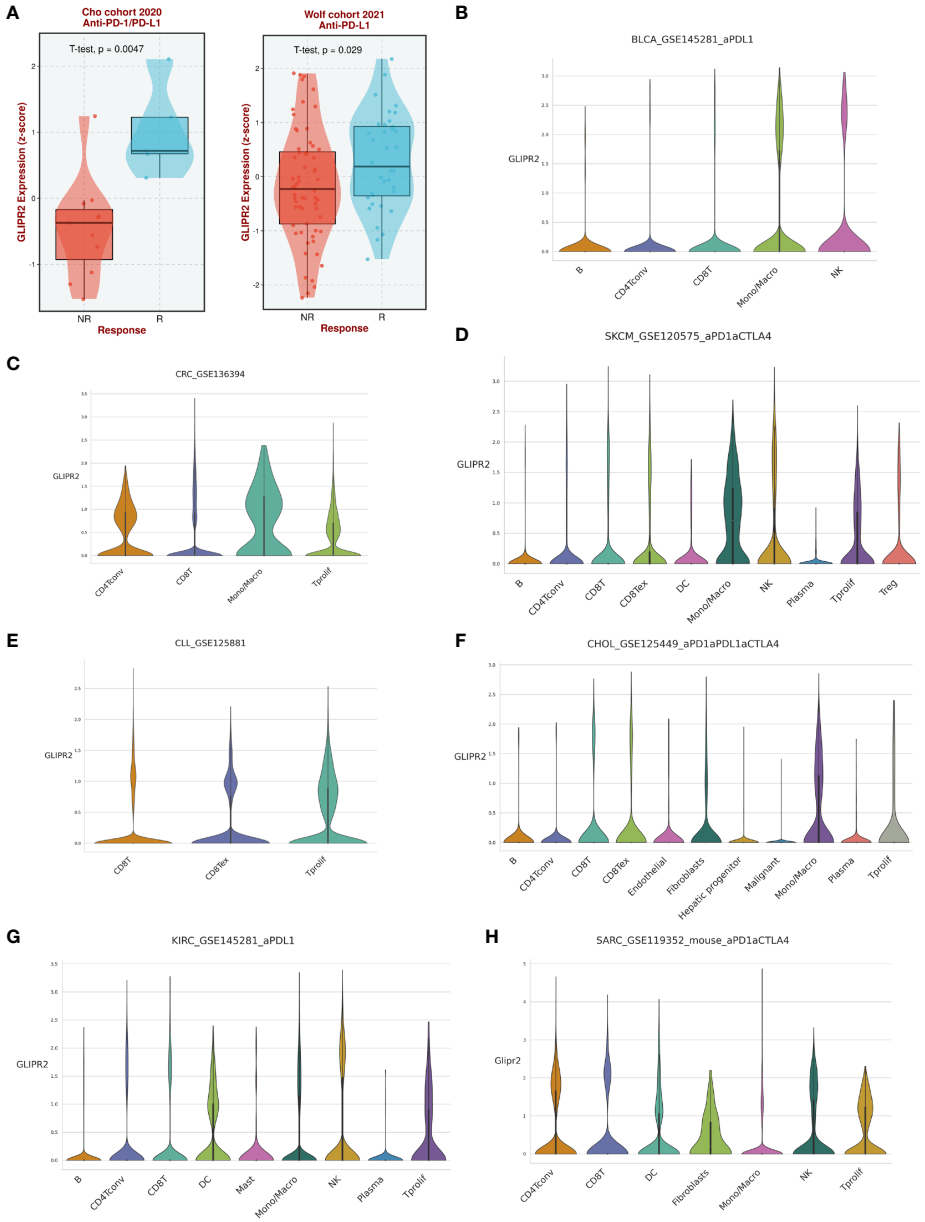

FIGURE 6
The expression of GLIPR2 predicts a more favorable immunotherapy outcome in patients. **(A)** Patients with high GLIPR2 expression have a better clinical response to immune therapy. **(B–H)** Distribution of GLIPR2 expression in different clusters of cancer-resident immune cells at single cell level.

In an effort to comprehensively gauge the predictive potential of GLIPR2 infiltration density to therapeutic responses, we delved into various treatment modalities. Specifically, we dissected post-radiotherapy LUAD patients, post-chemotherapy LUAD patients, post-radiotherapy LUSC patients, and post-chemotherapy LUSC patients. Notably, amidst post-radiotherapy LUAD patients, those evincing augmented GLIPR2^{+} infiltration levels exhibited correspondingly elevated levels of expression in radiation-sensitive cases in comparison to their radiation-resistant counterparts. This discernment underscores the latent utility of GLIPR2 expression as a predictive biomarker within the context of radiotherapy response within the LUAD patient stratum (Figure 8E).

3.6 GLIPR2 acts as a tumor suppressor in LUAD, suppress various malignant phenotypes of H1299 cells *in vitro*

In order to substantiate the functional implications of GLIPR2, a series of *in vitro* experiments were conducted. The mRNA expression of GLIPR2 exhibited a noteworthy elevation in normal

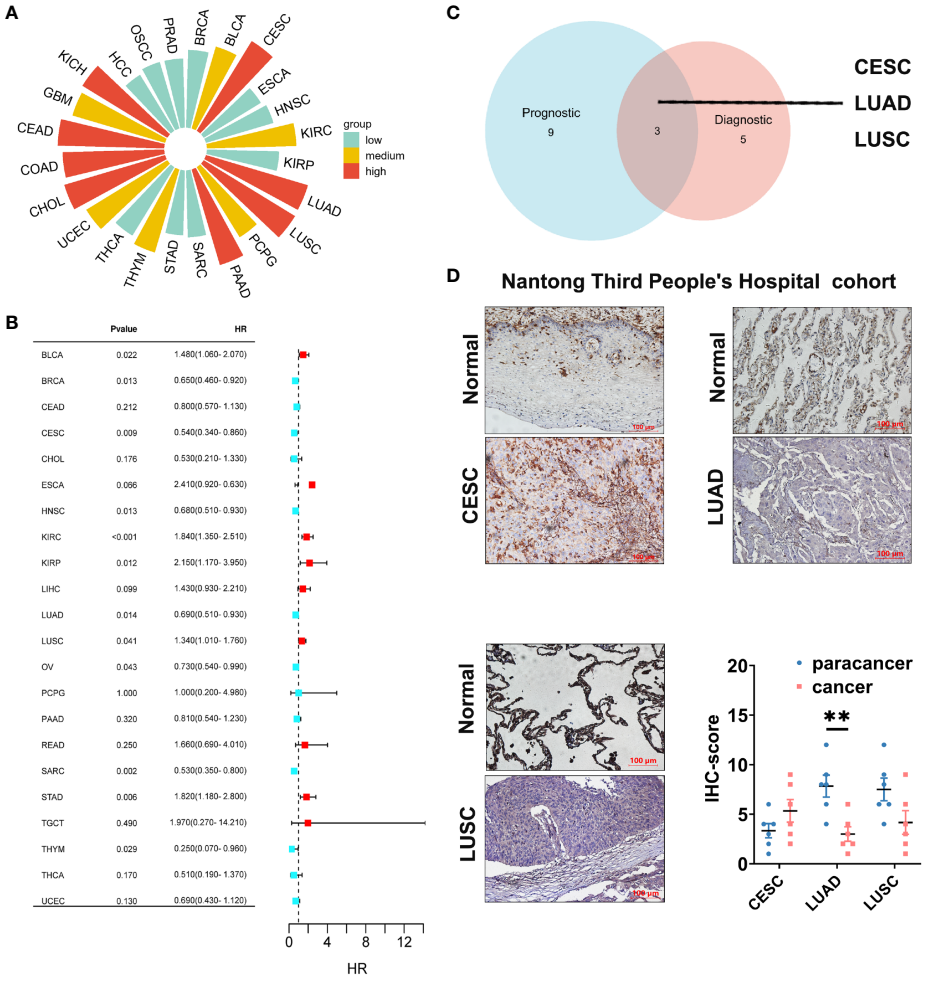

FIGURE 7
Diagnostic and prognostic value analysis of GLIPR2. **(A)** Prognostic value of GLIPR2 in pan-cancer. **(B)** Prognostic value of GLIPR2 in pan-cancer. **(C)** The intersection of different cancer between the diagnostic and the prognostic value. **(D)** The protein expression of GLIPR2 among CESC, LUAD and LUSC in Nantong Third People' Hospital cohort, scale bar = 100 μm (n = 6, $^{**}P < 0.01$).

lung epithelial cells in comparison to LUAD cell lines (Figure 9A). The H1299 cell line, characterized by the lowest GLIPR2 expression, was subsequently selected for further investigations. Immunofluorescence staining demonstrated a diffuse cytosolic distribution of GLIPR2 in H1299 cells (Figure 9B). Functional gain experiments involving GLIPR2 overexpression in the H1299 cell line revealed a pronounced inhibition of migration (Figure 9C) and invasion (Figure 9D). Moreover, augmentation of GLIPR2 attenuated radiotherapy resistance (Figure 9E) and concurrently induced susceptibility to chemotherapy (Figure 9F) in H1299 cells.

Collectively, the culmination of these findings collectively underscores the significant implications of GLIPR2 in the domain of LUAD. These observations accentuate its potential as both a prognostic and predictive marker, particularly in the context of radiotherapy to predict treatment responses. The multifaceted facets of GLIPR2 impact on therapeutic outcomes highlight its promise for translational applications within the clinical management of post-radiotherapy LUAD patients.

4 Discussion

In this present investigation, we employed a comprehensive array of bioinformatics analytical methodologies to investigate the potential implications of the GLIPR2 gene in cancer progression. Our findings reveal a marked reduction in GLIPR2 expression, strongly associated with the clinical stage across a diverse spectrum of malignancies Additionally, ROC curve analysis highlights the latent potential of GLIPR2 as a promising diagnostic biomarker across various cancer subtypes, including but not limited to CESC, CHOL, COAD, CEAD, KICH, LUAD, and LUSC.

Genetic mutations, particularly when coupled with DNA methylation alterations, exert profound influences on tumorigenesis (32, 33). Our study observed a significant downregulation of GLIPR2 expression in most types of cancer, accompanied by a simultaneous increase in the mutation rates associated with methylation events. This dual phenomenon suggests a potential role of GLIPR2 in cancer pathogenesis and

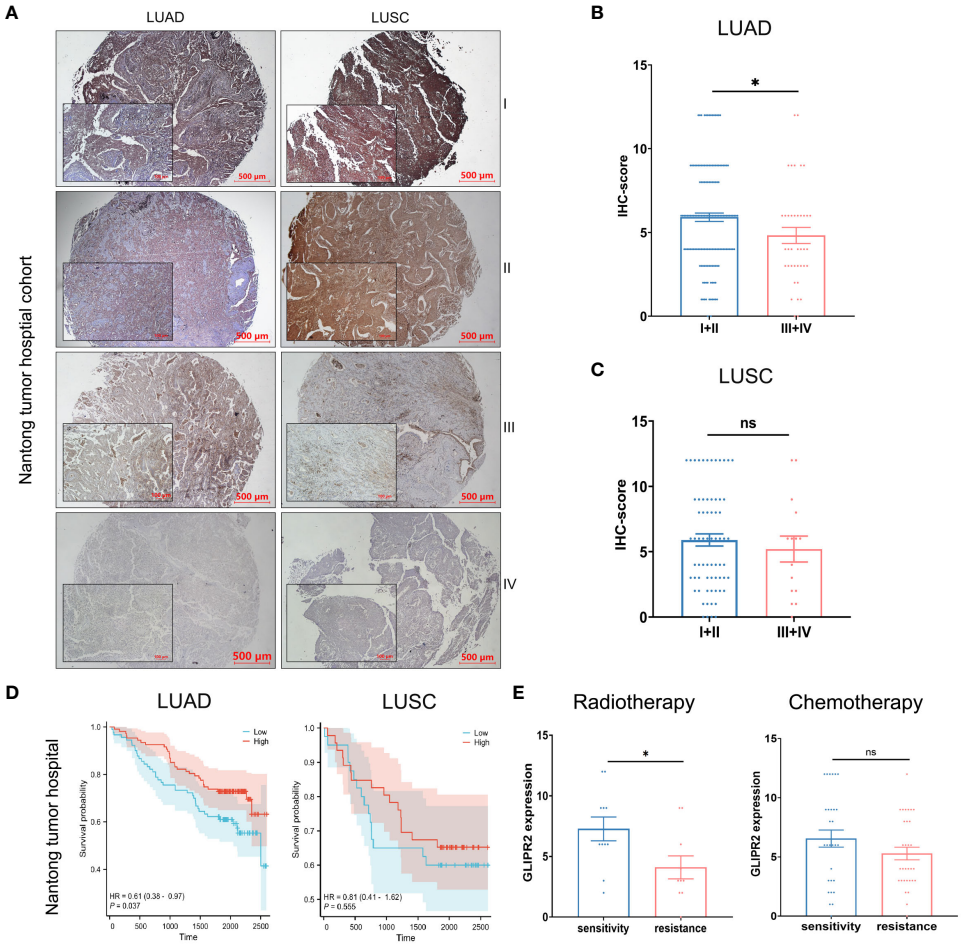

FIGURE 8
Protein expression and prognostic analysis of GLIPR2 in a real-world cohort. **(A)** Representative expression patterns of GLIPR2 in tumor and peritumor regions, scale bar = 500 μm. **(B, C)** GLIPR2 expression in different stages of LUAD and LUSC, scale bar = 500 μm [**(B)**, n = 194; **(C)**, n = 83]. **(D)** Overall survival (OS) curves according to GLIPR2^{+} infiltration level of patients in Nantong Tumor Hospital cohort. **(E)** The predictive value of GLIPR2 expression was explored in the context of therapeutic interventions, encompassing post-radiotherapy and post-chemotherapy LUAD patients in Nantong Tumor Hospital cohort (Radiotherapy, n = 10-11; Chemotherapy, n = 29-31). *$P < 0.05$, "ns" means "not significant".

highlights the intricate relationship between gene expression regulation and epigenetic modifications. The concurrent rise in methylation mutation rates further underscores the intricate epigenetic landscape in cancer progression. Methylation alterations, particularly in the promoter regions of tumor suppressor genes, can lead to transcriptional silencing and contribute to tumorigenesis. The observed correlation between GLIPR2 downregulation and increased methylation mutation rates suggests a potential mechanism through which cancer cells may evade the tumor-suppressive effects of GLIPR2. The identification of this association opens avenues for exploring GLIPR2 as a potential therapeutic target. Strategies aimed at reversing or mitigating the methylation alterations linked to GLIPR2 downregulation could represent novel therapeutic interventions in cancer treatment. Genetic mutations involve enduring alterations in the DNA sequence, modifying gene functionalities, dysregulation, and anomalous activations or inactivation, thereby contributing to tumor inception and progression (34–36). Such mutations include point mutations, insertions, deletions, and inversions, leading to modifications in the protein structure and function encoded by the genes (37). Conversely, DNA methylation is an epigenetic modification involving the addition of methyl groups to DNA molecules (38). While DNA methylation regulates normative cells, aberrant patterns are frequently encountered in cancerous cells. In malignancies, methylation is frequently associated with gene silencing, precipitating the subdued expression of normative genes (39). These methylation alterations impinge upon tumor suppressor genes and oncogenes, influencing cellular proliferation, survival, and invasive propensities. Within the intricate milieu of diverse TME, a total of thirty-four mutations, characterized by an indeterminate degree of significance, were delineated via a comprehensive analysis of GLIPR2. Particularly salient is the observation that amidst this collection of mutations, a conspicuous elevation in the levels of GLIPR2 methylation was discerned in LUAD, whereas a converse pattern was manifest in

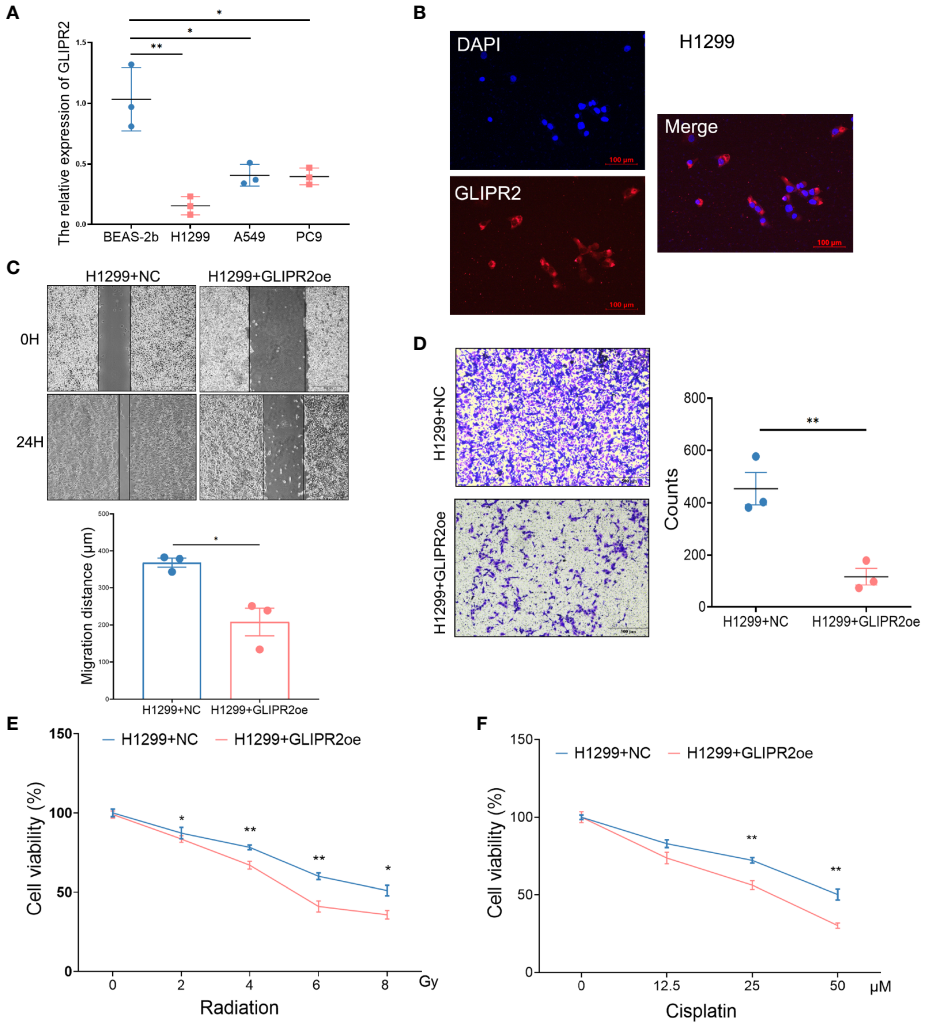

FIGURE 9
Functional experiments of GLIPR2 *in vitro*. **(A)** Distinct LUAD cell lines and normal lung epithelial cell lines exhibit varying patterns of GLIPR2 expression (n = 3). **(B)** Immunofluorescence analysis reveals predominant cytoplasmic distribution of GLIPR2 in H1299 cell, scale bar = 100 μm. **(C, D)** GLIPR2 block cell migration (C, n = 3) and invasion (D, n = 3) in H1299 cell line. **(E, F)** Elevated expression of GLIPR2 in H1299 cells enhances both radiosensitivity (n = 4) and chemosensitivity (n = 4). *$P < 0.05$, **$P < 0.01$.

LUSC. Galvanized by these discernments, the designation of NSCLC as the focal point for subsequent validation endeavors was judiciously warranted.

LUAD and LUSC represent prominent subtypes of lung cancer, exhibiting both shared characteristics and distinguishing features. Emerging within pulmonary tissues, these subtypes diverge in terms of their cellular origins, molecular profiles, and clinical presentations (40, 41). LUAD originates from lung glandular cells, which contribute to mucus and other secretions, whereas LUSC arises from lung squamous epithelial cells characterized by their flattened morphology. Mutations in genes such as epidermal growth factor receptor (EGFR) and anaplastic lymphoma kinase (ALK) are frequently implicated in LUAD (42), while the p53 gene mutations are prevalent in LUSC (43). In our study, upon subjecting NSCLC tissues to rigorous *in vitro* experimentation, a pronounced down-regulation in the expression of GLIPR2 became evident. Strikingly, IHC scores associated with GLIPR2 in stage III and IV LUAD instances displayed a statistically significant augmentation compared to stage I and II. In contrast, such a trend was not replicated within the context of LUSC specimens. Furthermore, a focused scrutiny of LUAD revealed an intensified manifestation of GLIPR2, correlating with a conspicuously improved prognosis. Conversely, no overt discordance in consequential survival outcomes emerged with respect to GLIPR2 expression within the purview of LUSC. Particularly pivotal is the observation that among LUAD patients subjected to post-radiotherapy, heightened levels of $GLIPR2^{+}$ infiltration correlated with an augmented frequency of expression in radiation-sensitive cases, in contradistinction to their radiation-resistant counterparts. Collectively, these findings collectively posit the plausible implication of GLIPR2 in the mechanistic underpinnings governing the genesis and pathological progression of LUAD.

GLIPR2 was first discovered within the human genome, displaying a broad expression profile. Notably, investigations into GLIPR2's interactions have uncovered a Tat-beclin 1 peptide derived from beclin 1, demonstrating autophagy-inducing

properties with potential therapeutic applications, particularly in the context of HIV-1 Nef interaction (44). In the realm of colorectal cancer (CRC), GLIPR2's correlation with glycolysis-related genes and its involvement in epithelial-to-mesenchymal transition (EMT) suggested its pivotal role in tumor progression (45). Furthermore, in hepatocellular carcinoma (HCC), GLIPR2's upregulation in hypoxia contributes to migration and invasion through the hypoxia/GLIPR-2/EMT axis (46). In our study, we confirmed GLIPR' broad expression profile, notably elevated in lung, prostate, colon, and rectum, while comparatively diminished in cerebral cortex, parathyroid gland, epididymis, and soft tissues (10). Additionally, our investigation extends GLIPR2's relevance to cancer immunity, emphasizing its role in the TME. Our results aligned with previous studies, revealing positive correlations between GLIPR2 expression and immune cell content in the TME across various cancers (47). In particular, our analysis, consistent with ESTIMATE analysis, establishes a positive association between GLIPR2 and the infiltration levels of various immune cells in the TME of LUAD, including $CD4^+$ T cells, $CD8^+$ T cells, MDSCs, NKT cells, Tregs, B cells, myeloid dendritic cells, monocytes, and macrophage M2. These findings position GLIPR2 as a potential biomarker for LUAD immunotherapy, intricately linked to the extent of immune cell infiltration. Collectively, these studies, including our own, underscore GLIPR2's versatile roles in autophagy, cancer, and immune response, emphasizing its significance as a diagnostic marker and therapeutic target across diverse pathological conditions.

Our study explores the multifaceted role of GLIPR2 in NSCLC, leveraging insights from a real-world cohort at Nantong Tumor Hospital. The progressive reduction in GLIPR2 expression with LUAD tumor progression suggests its potential involvement in underlying mechanisms driving LUAD development. Notably, GLIPR2's prognostic relevance is histotype-specific, exhibiting significance in LUAD but not in LUSC, indicative of distinct molecular pathways governing these NSCLC subtypes. In-depth analyses of treatment cohorts, particularly post-radiotherapy cases, establish GLIPR2 as a prognostic indicator in LUAD. Furthermore, our *in vitro* experiments, while acknowledging their limitations in capturing the tumor immune microenvironment complexity, demonstrate GLIPR2 augmentation sensitizing tumor cells to radiotherapy. This aligns with clinical findings, emphasizing GLIPR2's potential as a predictive biomarker for radiotherapy response. Discrepancies between clinical and *in vitro* results are discussed within the clinical complexity of chemotherapy, underscoring the challenges of interpreting *in vitro* findings in the context of combination therapy and varied pharmacological mechanisms. These insights necessitate cautious interpretation of *in vitro* results and stress the importance of clinical validation. Looking ahead, these findings lay the foundation for future investigations into the underlying molecular mechanisms driving observed correlations. Mechanistic studies and analyses of larger patient cohorts will provide deeper insights into GLIPR2's functional relevance in NSCLC pathobiology, potentially guiding personalized therapeutic strategies.

In conclusion, this study utilized diverse bioinformatics approaches to comprehensively investigate the roles of GLIPR2 in NSCLC, highlighting its potential implications in cancer development, diagnosis, mutation, methylation, and immune infiltration. These findings not only provide novel perspectives on our understanding of cancer biology but also offer crucial leads for early LUAD diagnosis and therapeutic target development.

Data availability statement

The original contributions presented in the study are included in the article/Supplementary Material. Further inquiries can be directed to the corresponding authors.

Ethics statement

The studies involving humans were approved by the clinical archives of the Affiliated Tumor Hospital of Nantong University and Nantong Third People's Hospital. The studies were conducted in accordance with the local legislation and institutional requirements. The participants provided their written informed consent to participate in this study.

Author contributions

WL: Conceptualization, Supervision, Visualization, Writing – original draft, Writing – review & editing. SZ: Formal analysis, Investigation, Validation, Writing – review & editing. CG: Funding acquisition, Supervision, Writing – review & editing. HZ: Funding acquisition, Supervision, Writing – review & editing. LY: Conceptualization, Formal analysis, Supervision, Visualization, Writing – review & editing.

Funding

The author(s) declare financial support was received for the research, authorship, and/or publication of this article. This study was supported by Nantong Municipal Health Commission Project Fund (M2022041, MS2022069), Nantong Science and Technology Project Fund (JC22022025).

Conflict of interest

The authors declare that the research was conducted in the absence of any commercial or financial relationships that could be construed as a potential conflict of interest.

Publisher's note

Supplementary material

The Supplementary Material for this article can be found online at: https://www.frontiersin.org/articles/10.3389/fimmu.2024.1280525/full#supplementary-material

SUPPLEMENTARY FIGURE 1
Mutation patterns of GLIPR2 across pan-cancer spectrum. **(A)** Representation of GLIPR2 genetic alterations in various cancer types. **(B)** Illustration of GLIPR2 variants of uncertain significance (VUS) across diverse tumor contexts.

SUPPLEMENTARY FIGURE 2
Promoter methylation patterns of GLIPR2 across pan-cancer types.

SUPPLEMENTARY FIGURE 3
Correlation of GLIPR2 expression levels with related immunomodulatory genes.

SUPPLEMENTARY FIGURE 4
Diagnostic potential of GLIPR2 across pan-cancer types. **(A–X)** Receiver operating characteristic (ROC) curves depicting the performance of GLIPR2 in terms of its diagnostic value for PCPG, BLCA, BRCA, CESC, CHOL, COAD, CEAD, ESCA, GBM, HNSC, KICH, KIRC, KIRP, HCC, LUAD, LUSC, SARC, PAAD, PRAD, STAD, THCA, THYM, UCEC, and OSCC.

SUPPLEMENTARY FIGURE 5
Overall survival (OS) curves according to GLIPR2^{+} infiltration level of patients in TCGA database.

SUPPLEMENTARY FIGURE 6
The intensity and positive cells of GLIPR2 among CESC, LUAD and LUSC in Nantong Third People' Hospital cohort (n = 6, *$P < 0.05$).

References

1. Gintant G, Burridge P, Gepstein L, Harding S, Herron T, Hong C, et al. Use of human induced pluripotent stem cell-derived cardiomyocytes in preclinical cancer drug cardiotoxicity testing: A scientific statement from the American heart association. *Circ Res*. (2019) 125:e75–92. doi: 10.1161/RES.0000000000000291.

2. Alagoz O, Sethi AK, Patterson BW, Churpek M, Safdar N. Effect of timing of and adherence to social distancing measures on COVID-19 burden in the United States : A simulation modeling approach. *Ann Intern Med*. (2021) 174:50–7. doi: 10.7326/M20-4096.

3. Mun EJ, Babiker HM, Weinberg U, Kirson ED, Von Hoff DD. Tumor-treating fields: A fourth modality in cancer treatment. *Clin Cancer Res*. (2018) 24:266–75. doi: 10.1158/1078-0432.CCR-17-1117.

4. Finck AV, Blanchard T, Roselle CP, Golinelli G, June CH. Engineered cellular immunotherapies in cancer and beyond. *Nat Med*. (2022) 28:678–89. doi: 10.1038/s41591-022-01765-8.

5. Zhou B, Lin W, Long Y, Yang Y, Zhang H, Wu K, et al. Notch signaling pathway: architecture, disease, and therapeutics. *Signal Transduct Target Ther*. (2022) 7:95. doi: 10.1038/s41392-022-00934-y.

6. Hong M, Tao S, Zhang L, Diao LT, Huang X, Huang S, et al. RNA sequencing: new technologies and applications in cancer research. *J Hematol Oncol*. (2020) 13:166. doi: 10.1186/s13045-020-01005-x.

7. Pai JA, Satpathy AT. High-throughput and single-cell T cell receptor sequencing technologies. *Nat Methods*. (2021) 18:881–92. doi: 10.1038/s41592-021-01201-8.

8. Aalberts M, Van Dissel-Emiliani FM, Van Adrichem NP, Van Wijnen M, Wauben MH, Stout TA, et al. Identification of distinct populations of prostasomes that differentially express prostate stem cell antigen, annexin A1, and GLIPR2 in humans. *Biol Reprod*. (2012) 86:82. doi: 10.1095/biolreprod.111.095760.

9. Zhao Y, Zou Z, Sun D, Li Y, Sinha SC, Yu L, et al. GLIPR2 is a negative regulator of autophagy and the BECN1-ATG14-containing phosphatidylinositol 3-kinase complex. *Autophagy*. (2021) 17:2891–904. doi: 10.1080/15548627.2020.1847798.

10. Eisenberg I, Barash M, Kahan T, Mitrani-Rosenbaum S. Cloning and characterization of a human novel gene C9orf19 encoding a conserved putative protein with an SCP-like extracellular protein domain. *Gene*. (2002) 293:141–8. doi: 10.1016/S0378-1119(02)00703-5.

11. Gibbs GM, Roelants K, O'bryan MK. The CAP superfamily: cysteine-rich secretory proteins, antigen 5, and pathogenesis-related 1 proteins–roles in reproduction, cancer, and immune defense. *Endocr Rev*. (2008) 29:865–97. doi: 10.1210/er.2008-0032.

12. Yan Y, Gao R, Trinh TLP, Grant MB. Immunodeficiency in pancreatic adenocarcinoma with diabetes revealed by comparative genomics. *Clin Cancer Res*. (2017) 23:6363–73. doi: 10.1158/1078-0432.CCR-17-0250.

13. Yoshihara K, Shahmoradgoli M, Martínez E, Vegesna R, Kim H, Torres-Garcia W, et al. Inferring tumour purity and stromal and immune cell admixture from expression data. *Nat Commun*. (2013) 4:2612. doi: 10.1038/ncomms3612.

14. Scholkopf B, Smola AJ, Williamson RC, Bartlett PL. New support vector algorithms. *Neural Comput*. (2000) 12:1207–45. doi: 10.1162/089976600300015565.

15. Breiman L. Random forests. *Mach Learn*. (2001) 45:5–32. doi: 10.1023/A:1010933404324.

16. Holtsträter C, Schrörs B, Bukur T, Löwer M. Bioinformatics for cancer immunotherapy. *Methods Mol Biol*. (2020) 2120:1–9. doi: 10.1007/978-1-0716-0327-7_1

17. Degenhardt F, Seifert S, Szymczak S. Evaluation of variable selection methods for random forests and omics data sets. *Brief Bioinform*. (2019) 20:492–503. doi: 10.1093/bib/bbx124.

18. Lin X, Deng J, Deng H, Yang Y, Sun N, Zhou M, et al. Comprehensive analysis of the immune microenvironment in checkpoint inhibitor pneumonitis. *Front Immunol*. (2021) 12:818492. doi: 10.3389/fimmu.2021.818492.

19. Racle J, De Jonge K, Baumgaertner P, Speiser DE, Gfeller D. Simultaneous enumeration of cancer and immune cell types from bulk tumor gene expression data. *Elife*. (2017) 6:e26476. doi: 10.7554/eLife.26476.

20. Liu Z, Liu L, Weng S, Xu H, Xing Z, Ren Y, et al. BEST: a web application for comprehensive biomarker exploration on large-scale data in solid tumors. *J Big Data*. (2023) 10:165. doi: 10.1186/s40537-023-00844-y.

21. Liu Y, Lin W, Yang Y, Shao J, Zhao H, Wang G, et al. Role of cuproptosis-related gene in lung adenocarcinoma. *Front Oncol*. (2022) 12:1080985. doi: 10.3389/fonc.2022.1080985.

22. Guo Z, Zhang X, Zhu H, Zhong N, Luo X, Zhang Y, et al. TELO2 induced progression of colorectal cancer by binding with RICTOR through mTORC2. *Oncol Rep*. (2021) 45:523–34. doi: 10.3892/or.

23. Lorenzi L, Lonardi S, Vairo D, Bernardelli A, Tomaselli M, Bugatti M, et al. E-cadherin expression and blunted interferon response in blastic plasmacytoid dendritic cell neoplasm. *Am J Surg Pathol*. (2021) 45:1428–38. doi: 10.1097/PAS.0000000000001747.

24. Lin W, Liu Y, Zhou Y, Lin M, Liu C, Tang Y, et al. Methyltransferase-like 3 modulates visceral hypersensitivity through regulating the nuclear export of circKcnk9 in YTHDC1-dependent manner. *Mol Pain*. (2022) 18:17448069221144540. doi: 10.1177/17448069221144540.

25. Torres CM, Biran A, Burney MJ, Patel H, Henser-Brownhill T, Cohen AS, et al. The linker histone H1.0 generates epigenetic and functional intratumor heterogeneity. *Science*. (2016) 353(6307):aaf1644. doi: 10.1126/science.aaf1644.

26. Chandrashekar DS, Bashel B, Balasubramanya S, Creighton CJ, Ponce-Rodriguez I, Chakravarthi B, et al. UALCAN: A portal for facilitating tumor subgroup gene expression and survival analyses. *Neoplasia*. (2017) 19:649–58. doi: 10.1016/j.neo.2017.05.002.

27. Tang G, Cho M, Wang X. OncoDB: an interactive online database for analysis of gene expression and viral infection in cancer. *Nucleic Acids Res*. (2022) 50:D1334–d1339. doi: 10.1093/nar/gkab970.

28. Koch A, Jeschke J, Van Criekinge W, Van Engeland M, De Meyer T. MEXPRESS update 2019. *Nucleic Acids Res*. (2019) 47:W561–w565. doi: 10.1093/nar/gkz445.

29. Xiao Y, Yu D. Tumor microenvironment as a therapeutic target in cancer. *Pharmacol Ther*. (2021) 221:107753. doi: 10.1016/j.pharmthera.2020.107753.

30. Zhang J, Shi J, Zhang H, Zhu Y, Liu W, Zhang K, et al. Localized fluorescent imaging of multiple proteins on individual extracellular vesicles using rolling circle amplification for cancer diagnosis. *J Extracell Vesicles*. (2020) 10:e12025. doi: 10.1002/jev2.12025.

31. Ganti AK, Klein AB, Cotarla I, Seal B, Chou E. Update of incidence, prevalence, survival, and initial treatment in patients with non-small cell lung cancer in the US. *JAMA Oncol*. (2021) 7:1824–32. doi: 10.1001/jamaoncol.2021.4932.

32. Klutstein M, Nejman D, Greenfield R, Cedar H. DNA methylation in cancer and aging. *Cancer Res*. (2016) 76:3446–50. doi: 10.1158/0008-5472.CAN-15-3278.

33. Khan AA, Liu X, Yan X, Tahir M, Ali S, Huang H. An overview of genetic mutations and epigenetic signatures in the course of pancreatic cancer progression. *Cancer Metastasis Rev*. (2021) 40:245–72. doi: 10.1007/s10555-020-09952-0.

34. Lima ZS, Ghadamzadeh M, Arashloo FT, Amjad G, Ebadi MR, Younesi L. Recent advances of therapeutic targets based on the molecular signature in breast cancer: genetic mutations and implications for current treatment paradigms. *J Hematol Oncol*. (2019) 12:38. doi: 10.1186/s13045-019-0725-6.

35. Chen S, Zhao Y, Liu S, Zhang J, Assaraf YG, Cui W, et al. Epigenetic enzyme mutations as mediators of anti-cancer drug resistance. *Drug Resist Update*. (2022) 61:100821. doi: 10.1016/j.drup.2022.100821.

36. Mertz TM, Collins CD, Dennis M, Coxon M, Roberts SA. APOBEC-induced mutagenesis in cancer. *Annu Rev Genet*. (2022) 56:229–52. doi: 10.1146/annurev-genet-072920-035840.

37. Stitziel NO, Khera AV, Wang X, Bierhals AJ, Vourakis AC, Sperry AE, et al. ANGPTL3 deficiency and protection against coronary artery disease. *J Am Coll Cardiol*. (2017) 69:2054–63. doi: 10.1016/j.jacc.2017.02.030.

38. Dmitrijeva M, Ossowski S, Serrano L, Schaefer MH. Tissue-specific DNA methylation loss during ageing and carcinogenesis is linked to chromosome structure, replication timing and cell division rates. *Nucleic Acids Res*. (2018) 46:7022–39. doi: 10.1093/nar/gky498.

39. Chen H, Orozco LD, Wang J, Rau CD, Rubbi L, Ren S, et al. DNA methylation indicates susceptibility to isoproterenol-induced cardiac pathology and is associated with chromatin states. *Circ Res*. (2016) 118:786–97. doi: 10.1161/CIRCRESAHA.115.305298.

40. Wang C, Yu Q, Song T, Wang Z, Song L, Yang Y, et al. The heterogeneous immune landscape between lung adenocarcinoma and squamous carcinoma revealed by single-cell RNA sequencing. *Signal Transduct Target Ther*. (2022) 7:289. doi: 10.1038/s41392-022-01130-8.

41. Zhang L, Zhang Y, Wang C, Yang Y, Ni Y, Wang Z, et al. Integrated single-cell RNA sequencing analysis reveals distinct cellular and transcriptional modules associated with survival in lung cancer. *Signal Transduct Target Ther*. (2022) 7:9. doi: 10.1038/s41392-021-00824-9.

42. He D, Wang D, Lu P, Yang N, Xue Z, Zhu X, et al. Single-cell RNA sequencing reveals heterogeneous tumor and immune cell populations in early-stage lung adenocarcinomas harboring EGFR mutations. *Oncogene*. (2021) 40:355–68. doi: 10.1038/s41388-020-01528-0.

43. Xu F, Lin H, He P, He L, Chen J, Lin L, et al. A TP53-associated gene signature for prediction of prognosis and therapeutic responses in lung squamous cell carcinoma. *Oncoimmunology*. (2020) 9:1731943. doi: 10.1080/2162402X.2020.1731943.

44. Shoji-Kawata S, Sumpter R, Leveno M, Campbell GR, Zou Z, Kinch L, et al. Identification of a candidate therapeutic autophagy-inducing peptide. *Nature*. (2013) 494:201–6. doi: 10.1038/nature11866.

45. Pudova EA, Kudryavtseva AV, Fedorova MS, Zaretsky AR, Shcherbo DS, Lukyanova EN, et al. HK3 overexpression associated with epithelial-mesenchymal transition in colorectal cancer. *BMC Genomics*. (2018) 19:113. doi: 10.1186/s12864-018-4477-4.

46. Huang SG, Zhang LL, Niu Q, Xiang GM, Liu LL, Jiang DN, et al. Hypoxia promotes epithelial–mesenchymal transition of hepatocellular carcinoma cells *via* inducing GLIPR-2 expression. *PloS One*. (2013) 8:e77497. doi: 10.1371/journal.pone.0077497.

47. Wu HW, Sheard MA, Malvar J, Fernandez GE, Declerck YA, Blavier L, et al. Anti-CD105 antibody eliminates tumor microenvironment cells and enhances anti-GD2 antibody immunotherapy of neuroblastoma with activated natural killer cells. *Clin Cancer Res*. (2019) 25:4761–74. doi: 10.1158/1078-0432.CCR-18-3358.

Frontiers in Immunology

Explores novel approaches and diagnoses to treat immune disorders.

The official journal of the International Union of Immunological Societies (IUIS) and the most cited in its field, leading the way for research across basic, translational and clinical immunology.

Discover the latest Research Topics

See more →

Frontiers

Avenue du Tribunal-Fédéral 34
1005 Lausanne, Switzerland
frontiersin.org

Contact us

+41 (0)21 510 17 00
frontiersin.org/about/contact